



pennsylvania

DEPARTMENT OF TRANSPORTATION

Monitoring of Integral Abutment Bridges and Design Criteria Development

FINAL REPORT

June 15, 2009

By Jeffrey A. Laman and Woo Seok Kim

The Thomas D. Larson
Pennsylvania Transportation Institute

COMMONWEALTH OF PENNSYLVANIA
DEPARTMENT OF TRANSPORTATION

CONTRACT No. 510602
PROJECT No. PSU-002

PENNSTATE



1. Report No. FHWA-PA-2009-005-PSU 002	2. Government Accession No.	3. Recipient's Catalog No.	
4. Title and Subtitle Monitoring of Integral Abutment Bridges and Design Criteria Development		5. Report Date June 15, 2009	
		6. Performing Organization Code PSU-2006-08	
7. Author(s) Jeffrey A. Laman and Woo Seok Kim		8. Performing Organization Report No. LTI 2009-05	
9. Performing Organization Name and Address The Thomas D. Larson Pennsylvania Transportation Institute The Pennsylvania State University 201 Transportation Research Building University Park, PA 16802-4710		10. Work Unit No. (TRAIS)	
		11. Contract or Grant No. 510602, PSU 002	
12. Sponsoring Agency Name and Address The Pennsylvania Department of Transportation Bureau of Planning and Research Commonwealth Keystone Building 400 North Street, 6 th Floor Harrisburg, PA 17120-0064		13. Type of Report and Period Covered Final Report. 4/16/07 – 6/15/09	
		14. Sponsoring Agency Code	
15. Supplementary Notes COTR: Bev Miller, bevemiller@state.pa.us , 717-783-4338			
16. Abstract It has been observed that Pennsylvania integral abutment bridge behavior is much different from that predicted by current design methodologies. Thermally induced displacement magnitudes are typically on the order of 10 percent to 25 percent of predicted values. Thermally induced rotations and displacements are, in certain locations, opposite predicted rotations and displacements. Thermally induced stresses are not currently incorporated into design aids and guidelines and are not insignificant. Design methodologies must consider actual field observations such that the design accurately predicts the structural behavior. Proper application of integral abutments can then be made considering the findings of this study with new integral abutment bridge designs. In addition, PennDOT integral abutment design requirements will represent the state-of-the-art. The objective of this project was to revise and make more accurate integral abutment bridge design criteria based on observed structural behavior and results of numerical parametric studies. Observed behaviors were on the basis of field monitoring conducted at 4 integral abutment bridge sites and a weather station utilizing previously installed instrumentation and data acquisition systems. Integral abutment bridge engineering data were continuously collected over the entire contract period at bridges 109, 203, 211, and 222 and compiled, processed and evaluated. Numerical parametric studies were conducted on the basis of 2D and 3D finite element models, developed and calibrated to the observed integral abutment behavior, in order to evaluate the field performance of integral abutments and establish the range of potential applications for integral abutment bridge construction in Pennsylvania.			
17. Key Words Bridge, integral abutment, rotation, displacement		18. Distribution Statement No restrictions. This document is available from the National Technical Information Service, Springfield, VA 22161	
19. Security Classif. (of this report) Unclassified	20. Security Classif. (of this page) Unclassified	21. No. of Pages 650	22. Price

This work was sponsored by the Pennsylvania Department of Transportation and the U.S. Department of Transportation, Federal Highway Administration. The contents of this report reflect the views of the authors, who are responsible for the facts and the accuracy of the data presented herein. The contents do not necessarily reflect the official views or policies of the Federal Highway Administration, the U.S. Department of Transportation, or the Commonwealth of Pennsylvania at the time of publication. This report does not constitute a standard, specification, or regulation.

TABLE OF CONTENTS

Executive Summary	xxxi
Chapter 1. Introduction	1
1.1 Problem Statement	1
1.2 Objectives	1
1.3 Project Tasks	2
Chapter 2. Bridge and Weather Station Descriptions	4
2.1 Bridge 109 Description	5
2.2 Bridge 203	13
2.3 Bridge 211	21
2.4 Bridge 222	28
2.5 Weather Station	36
Chapter 3. Historical Overview of the Research	40
Chapter 4. Measured Bridge Response	63
4.1 Introduction	63
4.2 Bridge 109	63
4.3 Bridge 203	96
4.4 Bridge 211	119
4.5 Bridge 222	149
4.6 Weather Station	173
4.7 Concluding Remarks	179
Chapter 5. Numerical Modeling and Response Prediction	183
5.1 Introduction	183
5.2 Model Components	184
5.2.1 Material Properties	185

5.2.2 Abutment-backfill Interaction.....	188
5.2.3 Soil-pile Interaction	190
5.2.4 Abutment-Backwall Construction Joint.....	197
5.3 Loading	200
5.3.1 Backfill Pressure	200
5.3.2 Time-dependent Effects	201
5.3.2.1 Concrete Creep.....	202
5.3.2.2 Concrete Shrinkage.....	204
5.3.2.3 Relaxation of Prestressing Steel.....	204
5.3.2.4 Age-Adjusted Effective Modulus (AAEM) Method	205
5.3.2.5 Time-Dependent Effects in Indeterminate Structures.....	208
5.3.3 Temperature Load.....	208
5.3.4 Temperature Gradient	210
5.4 IAB Model Description.....	213
5.4.1 Bridge 109 Numerical Model	213
5.4.2 Bridge 203 Numerical Model	217
5.4.3 Bridge 211 Numerical Model	219
5.4.4 Bridge 222 Numerical Model	220
5.5 Comparison of Predicted to Measured Response	221
5.5.1 Bridge 109.....	221
5.5.2 Bridge 203.....	231
5.5.3 Bridge 211.....	237
5.5.4 Bridge 222.....	247
5.6 Concluding Remarks.....	257
 Chapter 6. Integral Abutment Bridge Parametric Study	 258
6.1 Introduction.....	258
6.2 Primary Parameters.....	259
6.2.1 Girder Material.....	259
6.2.2 Bridge Length	260
6.2.3 Backfill Height.....	263

6.2.4 Construction Joint Stiffness	264
6.3 General Parameters	266
6.3.1 Bridge Construction Timeline.....	266
6.3.2 Thermal Expansion Coefficient	268
6.4 Description of Numerical Models.....	272
6.5 Parametric Study Results	273
6.5.1 Girder Axial Force	273
6.5.2 Girder Moment.....	283
6.5.3 Pile Moment.....	292
6.5.4 Pile Lateral Force.....	297
6.5.5 Pile Head Displacement.....	302
6.6 Concluding Remarks.....	307
 Chapter 7. Integral Abutment Bridge Thermal Loading Analysis.....	 312
7.1. Scope.....	313
7.2. Approximate Method of Analysis.....	315
7.2.1 Introduction.....	315
7.2.2 Superstructure Moments	317
7.2.3 Superstructure Axial Forces.....	319
7.2.4 Pile Head Moments.....	320
7.2.5 Pile Axial Forces.....	322
7.2.6 Pile Lateral Forces	322
7.2.7 Abutment/Pile-head Displacements.....	323
7.2.8 Graphs for Approximate Analysis	324
7.2.8.1 Bridge Axial Force.....	324
7.2.8.2 Bridge Total Bending Moment	331
7.2.8.3 Minimum Number of Laterally Supporting Piles	344
7.2.8.4 Pile Head/Abutment Displacement.....	347
7.3. Structure Numerical Modeling	351
7.3.1 Introduction.....	351
7.3.2 Simplified 2D Analysis.....	352

7.3.2.1 Symmetry Considerations	352
7.3.2.2 Boundary Conditions	353
7.3.2.2 Pile-Soil Interface	354
7.3.2.3 Backwall- and Abutment-Soil Interface	357
7.3.2.4 Abutment and Backwall Elements.....	358
7.3.2.5 Pier Elements	358
7.3.2.6 Superstructure Elements	358
7.3.2.7 Elastomeric Bearing Element	359
7.3.2.8 Backwall-to-Abutment Construction Joint	359
7.3.3 Refined 3D Analysis	360
7.3.3.1 Boundary Conditions	360
7.3.3.2 Pile-Soil Interface	361
7.3.3.3 Backwall- and Abutment-Soil Interface	362
7.3.3.4 Abutment and Backwall Elements.....	363
7.3.3.5 Pier Elements	363
7.3.3.6 Superstructure Elements	364
7.3.3.7 Elastomeric Bearing Element	365
7.3.3.8 Backwall-Abutment Joint	366
7.4. Bridge Structure Material Properties	367
7.4.1 Introduction.....	367
7.4.2 Concrete Elastic Modulus	367
7.4.3 Thermal Expansion Coefficient	368
7.4.4 Time-dependent effects.....	371
7.5. Loading Environment	374
7.5.1 Introduction.....	374
7.5.2 Thermal Gradient.....	374
7.5.3 Temperature Load.....	376
7.5.4 Backfill Pressure	377
 Chapter 8. Integral Abutment Bridge Analysis Examples.....	 379
8.1 Example 1: Single-span Concrete Girder Bridge.....	383

8.1.1 Example 1: Approximate Analysis Method.....	388
8.1.1.1 Girder Axial Force	388
8.1.1.2 Girder Bending Moment	389
8.1.1.3 Pile Head Moment	393
8.1.1.4 Pile Lateral Force.....	394
8.1.1.5 Pile Head/abutment Displacement.....	395
8.1.2 Example 1: Two-Dimensional Model Analysis.....	396
8.1.2.1 Bridge Components	397
8.1.2.1.1 Girder and Deck.....	398
8.1.2.1.2 Abutment/Back-wall	399
8.1.2.1.3 Construction Joints.....	399
8.1.2.1.4 Steel H-Piles.....	401
8.1.2.1.5 Soil Springs.....	401
8.1.2.1.6 Miscellaneous Components (diaphragms, interior supports, bearings)	404
8.1.2.2 Loads.....	404
8.1.2.2.1 Sinusoidal Temperature Fluctuation Simulation	405
8.1.2.2.2 Temperature Gradient	406
8.1.2.2.3 Backfill Pressure	408
8.1.2.2.4 Time-dependent Loads.....	410
8.1.2.3 Example 1: 2D Analysis Results.....	412
8.1.2.3.1 Girder Axial Force	413
8.1.2.3.2 Girder Bending Moment	413
8.1.2.3.3 Pile Lateral Force.....	414
8.1.2.3.4 Pile Moment.....	415
8.1.2.3.5 Pile Head Displacement.....	416
8.1.3 Example 1: Three-dimensional Analysis Model.....	418
8.1.3.1 Bridge Components	420
8.1.3.1.1 Girder and Deck.....	421
8.1.3.1.2 Abutment/Backwall	422
8.1.3.1.3 Construction Joints.....	424
8.1.3.1.4 Pile Foundations.....	428

8.1.3.1.5 Miscellaneous Components	431
8.1.3.2 Loads.....	431
8.1.3.2.1 Temperature Load.....	431
8.1.3.2.2 Temperature Gradient	432
8.1.3.2.4 Time-dependent Loads.....	439
8.1.3.3 Example 1: 3D Analysis Results.....	440
8.1.3.3.1 Girder Axial Force	441
8.1.3.3.2 Girder Bending Moment	442
8.1.3.3.3 Pile Lateral Force	443
8.1.3.3.4 Pile Moment.....	444
8.1.3.3.5 Pile Head Displacement.....	446
8.1.4 Example 1 Analysis Results.....	446
8.1.4.1 Girder Axial Force	447
8.1.4.2 Girder Bending Moment	448
8.1.4.3 Pile Lateral Force	448
8.1.4.4 Pile Moment.....	449
8.1.4.5 Pile Head Displacement.....	450
8.2 Example 2: 2-span Steel Girder Bridge	452
8.2.1 Example 2: Approximate Analysis Method.....	457
8.2.1.1 Girder Axial Force	457
8.2.1.2 Girder Bending Moment	458
8.2.1.3 Pile Head Moment	459
8.2.1.4 Pile Lateral Force	461
8.2.1.5 Pile Head/Abutment Displacement.....	461
8.2.2 Example 2: Two-Dimensional Model Analysis.....	462
8.2.2.1 Bridge Components	464
8.2.2.1.1 Girder and Deck.....	464
8.2.2.1.2 Abutment/Back-wall.....	466
8.2.2.1.3 Construction Joints.....	466
8.2.2.1.4 Steel H-Piles.....	468
8.2.2.1.5 Soil Springs.....	468

8.2.2.1.6 Miscellaneous Components (diaphragms, interior supports, bearings)	471
8.2.2.2 Loads	471
8.2.2.2.1 Sinusoidal Temperature Fluctuation Simulation	472
8.2.2.2.2 Temperature Gradient	475
8.2.2.2.3 Backfill Pressure	476
8.2.2.2.4 Time-dependent Loads	479
8.2.2.3 Example 2: 2D Analysis Results	479
8.2.2.3.1 Girder Axial Force	480
8.2.2.3.2 Girder Bending Moment	480
8.2.2.3.3 Pile Lateral Force	481
8.2.2.3.4 Pile Moment	482
8.2.2.3.5 Pile Head Displacement	483
8.2.3 Example 2: Three-dimensional Analysis Model	484
8.2.3.1 Bridge Components	486
8.2.3.1.1 Girder and Deck	487
8.2.3.1.2 Abutment/Backwall	488
8.2.3.1.3 Construction Joints	490
8.2.3.1.4 Pile Foundations	494
8.2.3.1.5 Miscellaneous Components	497
8.2.3.2 Loads	497
8.2.3.2.1 Temperature Load	497
8.2.3.2.2 Temperature Gradient	498
8.2.3.2.3 Backfill Pressure	502
8.2.3.2.4 Time-dependent Loads	505
8.2.3.3 Example 2: 3D Analysis Results	505
8.2.3.3.1 Girder Axial Force	506
8.2.3.3.2 Girder Bending Moment	507
8.2.3.3.3 Pile Lateral Force	508
8.2.3.3.4 Pile Moment	510
8.2.3.3.5 Pile Head Displacement	512
8.2.4 Example 2 Analysis Results	512

8.2.4.1 Girder Axial Force	513
8.2.4.2 Girder Bending Moment	514
8.2.4.3 Pile Lateral Force	514
8.2.4.4 Pile Moment	515
8.2.4.5 Pile Head Displacement	516
8.3 Example 3: 3-span Concrete Girder Bridge	518
8.3.1 Example 3: Approximate Analysis Method	523
8.3.1.1 Girder Axial Force	523
8.3.1.2 Girder Bending Moment	525
8.3.1.3 Pile Head Moment	526
8.3.1.4 Pile Lateral Force	528
8.3.1.5 Pile Head/abutment Displacement	528
8.3.2 Example 3: Two-Dimensional Model Analysis	529
8.3.2.1 Bridge Components	531
8.3.2.1.1 Girder and Deck	531
8.3.2.1.2 Abutment/Back-wall	532
8.3.2.1.3 Construction Joints	533
8.3.2.1.4 Steel H-Piles	534
8.3.2.1.5 Soil Springs	534
8.3.2.1.6 Miscellaneous Components (diaphragms, interior supports, bearings)	537
8.3.2.2 Loads	538
8.3.2.2.1 Sinusoidal Temperature Fluctuation Simulation	538
8.3.2.2.2 Temperature Gradient	539
8.3.2.2.3 Backfill Pressure	541
8.3.2.2.4 Time-dependent Loads	544
8.3.2.3 Example 3: 2D Analysis Results	546
8.3.2.3.1 Girder Axial Force	547
8.3.2.3.2 Girder Bending Moment	547
8.3.2.3.3 Pile Lateral Force	548
8.3.2.3.4 Pile Moment	549
8.3.2.3.5 Pile Head Displacement	550

8.3.3 Example 3: Three-dimensional Analysis Model.....	551
8.3.3.1 Bridge Components	555
8.3.3.1.1 Girder and Deck.....	555
8.3.3.1.2 Abutment/Backwall	557
8.3.3.1.3 Construction Joints.....	559
8.3.3.1.4 Pile Foundations.....	563
8.3.3.1.5 Miscellaneous Components	566
8.3.3.2 Loads.....	566
8.3.3.2.1 Temperature Load.....	566
8.3.3.2.2 Temperature Gradient	567
8.3.3.2.3 Backfill Pressure	571
8.3.3.2.4 Time-dependent Loads.....	574
8.3.3.3 Example 3: 3D Analysis Results.....	575
8.3.3.3.1 Girder Axial Force	576
8.3.3.3.2 Girder Bending Moment.....	577
8.3.3.3.3 Pile Lateral Force.....	578
8.3.3.3.4 Pile Moment.....	580
8.3.3.3.5 Pile Head Displacement.....	582
8.3.4 Example 3 Analysis Results.....	582
8.3.4.1 Girder Axial Force	583
8.3.4.2 Girder Bending Moment	583
8.3.4.3 Pile Lateral Force.....	584
8.3.4.5 Pile Head Displacement.....	586
 Chapter 9. Discussion of PennDOT IAB Analysis and Design Provisions.....	 588
9.1 PennDOT IAB Design Procedure.....	588
9.2 PennDOT IAB Design Spreadsheet Discussion	590
9.3 Implementation Plan	600
9.4 Concluding Remarks.....	602

Chapter 10. Summary and Conclusions.....	603
10.1 Summary	603
10.2 Conclusions.....	606
 Bibliography	 612

LIST OF FIGURES

Figure 2.1. Location of Four Selected I-99 IABs	4
Figure 2.2. Site Plan of Bridge 109.....	7
Figure 2.3. Elevation of Bridge 109.....	8
Figure 2.4. Transverse Section of Bridge 109	9
Figure 2.5. Cross-Section of Bridge 109 Abutment 1	10
Figure 2.6. Elevation of Bridge 109 Abutment 1.....	11
Figure 2.7. Foundation Plan of Bridge 109 Abutment 1.....	12
Figure 2.8. Site Plan of Bridge 203.....	15
Figure 2.9. Elevation of Bridge 203.....	16
Figure 2.10. Transverse Section of Bridge 203	17
Figure 2.11. Cross-Section of Bridge 203 Abutment 2	18
Figure 2.12. Elevation of Bridge 203 Abutment 2.....	19
Figure 2.13. Foundation Plan of Bridge 203 Abutment 2.....	20
Figure 2.14. Site Plan of Bridge 211.....	22
Figure 2.15. Elevation of Bridge 211.....	23
Figure 2.16. Transverse Section of Bridge 211	24
Figure 2.17. Cross-Section of Bridge 211 Abutment 1	25
Figure 2.18. Elevation of Bridge 211 Abutment 1.....	26
Figure 2.19. Foundation Plan of Bridge 211 Abutment 1.....	27
Figure 2.20. Site Plan of Bridge 222.....	29
Figure 2.21. Elevation of Bridge 222.....	31
Figure 2.22. Transverse Section of Bridge 222	32
Figure 2.23. Cross-Section of Bridge 222 Abutment 1	33
Figure 2.24. Elevation of Bridge 222 Abutment 1.....	34
Figure 2.25. Foundation Plan of Bridge 222 Abutment 1.....	35
Figure 2.26. Photograph of Weather Station	36
Figure 2.27. Schematic of Wireless Network	37
Figure 2.28. AirLink Redwing CDMA 3110 VZW	38
Figure 2.29. SC32B.....	39

Figure 2.30. Null modem cable.....	39
Figure 3.1. Bridge 109 Instrumentation Plan.....	43
Figure 3.2. Bridge 109 Cross-Section through North Abutment (Section A-A)	45
Figure 3.3. Bridge 109 Abutment 2 Elevation (Section B-B).....	46
Figure 3.4. Structure 109 Cross-Section Through South Abutment (Section C-C).....	47
Figure 3.5. Structure 109 Abutment 1 Elevation (Section D-D)	48
Figure 3.6. Structure 203 Instrumentation Plan.....	49
Figure 3.7. Structure 203 Cross-Section Through Abutment 2 (Section A-A)	50
Figure 3.8. Structure 203 Abutment 2 Elevation (Section B-B).....	51
Figure 3.9. Structure 211 Instrumentation Plan.....	52
Figure 3.10. Structure 211 Cross-Section Through Abutment 2 (Section A-A)	53
Figure 3.11. Structure 211 Abutment 2 Elevation (Section B-B).....	54
Figure 3.12. Structure 211 Abutment 1 Elevation (Section C-C).....	55
Figure 3.13. Structure 211 Cross-Section Through Abutment 1 (Section D-D)	56
Figure 3.14. Structure 222 Instrumentation Plan.....	57
Figure 3.15. Structure 222 Cross-Section Through Abutment 2 (Section A-A)	58
Figure 3.16. Structure 222 Abutment 2 Elevation (Section B-B).....	59
Figure 3.17. Structure 222 Abutment 1 Elevation (Section C-C).....	60
Figure 3.18. Structure 222 Cross-Section Through Abutment 1 (Section D-D)	61
Figure 3.19. Weather Station	62
Figure 4.1. Bridge 109: Extensometers on Abutment 1.....	70
Figure 4.2. Bridge 109: Extensometers on Abutment 2.....	71
Figure 4.3. Bridge 109: Pressure Cells on Abutment 1	72
Figure 4.4. Bridge 109: Pressure Cells on Abutment 2	73
Figure 4.5. Bridge 109: Tiltmeters on Abutment 1.....	74
Figure 4.6. Bridge 109: Tiltmeters on Abutment 2.....	75
Figure 4.7. Bridge 109: Tiltmeters on Girders near Abutment 1	76
Figure 4.8. Bridge 109: Tiltmeters on Girders near Abutment 2.....	77
Figure 4.9. Bridge 109: Moments on North Pile under Abutment 1	78
Figure 4.10. Bridge 109: Moments on South Pile under Abutment 1	79
Figure 4.11. Bridge 109: Moments on North Pile under Abutment 2	80

Figure 4.12. Bridge 109: Moments on South Pile under Abutment 2	81
Figure 4.13. Bridge 109: Axial Forces on North Pile under Abutment 1	82
Figure 4.14. Bridge 109: Axial Forces on South Pile under Abutment 1	83
Figure 4.15. Bridge 109: Axial Forces on North Pile under Abutment 2	84
Figure 4.16. Bridge 109: Axial Forces on South Pile under Abutment 2	85
Figure 4.17. Bridge 109: Interior Girder Moments near Abutment 1	86
Figure 4.18. Bridge 109: Exterior Girder Moments near Abutment 1	87
Figure 4.19. Bridge 109: Interior Girder Moments near Abutment 2	88
Figure 4.20. Bridge 109: Exterior Girder Moments near Abutment 2	89
Figure 4.21. Bridge 109: Interior Girder Axial Forces near Abutment 1	90
Figure 4.22. Bridge 109: Exterior Girder Axial Forces near Abutment 1	91
Figure 4.23. Bridge 109: Interior Girder Axial Forces near Abutment 2	92
Figure 4.24. Bridge 109: Exterior Girder Axial Forces near Abutment 2	93
Figure 4.25. Bridge 109: Sister-Bar Gages near Abutment 1	94
Figure 4.26. Bridge 109: Sister-Bar Gages near Abutment 2	95
Figure 4.27. Bridge 203: Extensometers on Abutment 2	102
Figure 4.28. Bridge 203: Pressure Cells on Abutment 2	103
Figure 4.29. Bridge 203: Tiltmeter on Abutment 2	104
Figure 4.30. Bridge 203: Tiltmeter on Girders near Abutment 2	105
Figure 4.31. Bridge 203: Pile Moments under Abutment 2	106
Figure 4.32. Bridge 203: Pile Axial Forces in Shallow Soil Strata under Abutment 2 ...	107
Figure 4.33. Bridge 203: East Pile Axial Forces in Deep Soil Strata under Abutment 2	108
Figure 4.34. Bridge 203: West Pile Axial Forces in Deep Soil Strata under Abutment 2	109
Figure 4.35. Bridge 203: Interior Girder Moments at Midspan	110
Figure 4.36. Bridge 203: Exterior Girder Moments at Midspan	111
Figure 4.37. Bridge 203: Interior Girder Moments at Endspan	112
Figure 4.38. Bridge 203: Exterior Girder Moments at Endspan	113
Figure 4.39. Bridge 203: Interior Girder Axial Forces at Midspan	114
Figure 4.40. Bridge 203: Exterior Girder Axial Forces at Midspan	115

Figure 4.41. Bridge 203: Interior Girder Axial Forces at Endspan	116
Figure 4.42. Bridge 203: Exterior Girder Axial Forces at Endspan	117
Figure 4.43. Bridge 203: Sister-Bar Gages.....	118
Figure 4.44. Bridge 211: Extensometers on Abutment 1.....	125
Figure 4.45. Bridge 211: Extensometers on Abutment 2.....	126
Figure 4.46. Bridge 211: Pressure Cells on Abutment 1	127
Figure 4.47. Bridge 211: Pressure Cells on Abutment 2	128
Figure 4.48. Bridge 211: Tiltmeters on Abutment 1.....	129
Figure 4.49. Bridge 211: Tiltmeters on Abutment 2.....	130
Figure 4.50. Bridge 211: Tiltmeters on Girders near Abutment 1.....	131
Figure 4.51. Bridge 211: Tiltmeters on Girders near Abutment 2.....	132
Figure 4.52. Bridge 211: North Pile Moments under Abutment 1	133
Figure 4.53. Bridge 211: South Pile Moments under Abutment 1	134
Figure 4.54. Bridge 211: North Pile Moments under Abutment 2	135
Figure 4.55. Bridge 211: South Pile Moments under Abutment 2	136
Figure 4.56. Bridge 211: Pile Axial Forces under Abutment 1	137
Figure 4.57. Bridge 211: Pile Axial Forces under Abutment 2	138
Figure 4.58. Bridge 211: Interior Girder Moments near Abutment 1.....	139
Figure 4.59. Bridge 211: Exterior Girder Moments near Abutment 1.....	140
Figure 4.60. Bridge 211: Interior Girder Moments near Abutment 2.....	141
Figure 4.61. Bridge 211: Exterior Girder Moments near Abutment 2.....	142
Figure 4.62. Bridge 211: Interior Girder Axial Forces near Abutment 1	143
Figure 4.63. Bridge 211: Exterior Girder Axial Forces near Abutment 1	144
Figure 4.64. Bridge 211: Interior Girder Axial Forces near Abutment 2	145
Figure 4.65. Bridge 211: Exterior Girder Axial Forces near Abutment 2	146
Figure 4.66. Bridge 211: Sister-bar Gages in Approach Slab near Abutment 1.....	147
Figure 4.67. Bridge 211: Sister-bar Gages in Approach Slab near Abutment 2.....	148
Figure 4.68. Bridge 222: Extensometers on Abutment 1.....	154
Figure 4.69. Bridge 222: Extensometers on Abutment 2.....	155
Figure 4.70. Bridge 222: Pressure Cells on Abutment 1	156
Figure 4.71. Bridge 222: Pressure Cells on Abutment 2	157

Figure 4.72. Bridge 222: Tiltmeter on Abutment 1	158
Figure 4.73. Bridge 222: Tiltmeter on Girders near Abutment 1	159
Figure 4.74. Bridge 222: North Pile Moments under Abutment 1	160
Figure 4.75. Bridge 222: South Pile Moments under Abutment 1	161
Figure 4.76. Bridge 222: North Pile Moments under Abutment 2	162
Figure 4.77. Bridge 222: South Pile Moments under Abutment 2	163
Figure 4.78. Bridge 222: North Pile Axial Forces under Abutment 1	164
Figure 4.79. Bridge 222: South Pile Axial Forces under Abutment 1	165
Figure 4.80. Bridge 222: North Pile Axial Forces under Abutment 2	166
Figure 4.81. Bridge 222: South Pile Axial Forces under Abutment 2	167
Figure 4.82. Bridge 222: Girder Moments near Abutment 1	168
Figure 4.83. Bridge 222: Girder Moments near Abutment 2	169
Figure 4.84. Bridge 222: Girder Axial Forces near Abutment 1	170
Figure 4.85. Bridge 222: Girder Axial Forces near Abutment 2	171
Figure 4.86. Bridge 222: Sister-Bar Gages	172
Figure 4.87. Ambient Air Temperature	175
Figure 4.88. Relative Humidity	176
Figure 4.89. Air Pressure	177
Figure 4.90. Solar Radiation	178
Figure 5.1. Bridge 109 Soil Properties under Abutment 1	186
Figure 5.2. Bridge 109 Soil Properties under Abutment 2	186
Figure 5.3. Bridge 203 Soil Properties under Abutment 2	187
Figure 5.4. Bridge 211 Soil Properties under Abutment 1	187
Figure 5.5. Bridge 211 Soil Properties under Abutment 2	187
Figure 5.6. Bridge 222 Soil Properties under Abutment 1	188
Figure 5.7. Bridge 222 Soil Properties under Abutment 2	188
Figure 5.8. Qualitative Lateral Earth Pressure at the Abutment and Backwall	189
Figure 5.9. Straight Bar Under Axial and Transverse Loading	191
Figure 5.10. p - y Curve at Pile Head - Clay above Water Table	193
Figure 5.11. p - y Curve at 11.5 Ft below Pile Head – Sand	193
Figure 5.12. Lateral Displacement Due to 5-kip Load at Pile Head	194

Figure 5.13. Pile Bending Moment Due to 5 kip Load at Pile Head	194
Figure 5.14. Pile Shear Force Due to 5 kip Load at Pile Head	195
Figure 5.15. Qualitative Diagram of Elasto-Plastic p - y Curve	196
Figure 5.16. Moment-Curvatures of Construction Joints and Abutment Members	198
Figure 5.17. Construction Joint Reinforcement and Behavior	199
Figure 5.18. Creep Coefficient.....	203
Figure 5.19. ACI 209 Aging Coefficient for Bridge 222.....	203
Figure 5.20. ACI 209 Shrinkage Strains for Bridge 222	204
Figure 5.21. Strain at Top Fiber of Bridge 222 Girder	207
Figure 5.22. Strain at Bottom Fiber of Bridge 222 Girder.....	207
Figure 5.23. Ambient Temperature Versus Girder Temperature (Bridge 222)	209
Figure 5.24. Ambient Temperature Versus Deck Slab Concrete Temperature (Bridge 109)	209
Figure 5.25. Temperature Model Based on 7-Day Average Ambient.....	211
Figure 5.26. Temperature Gradient of Cross-Section.....	213
Figure 5.27. Temperature Variation with Temperature Gradient	213
Figure 5.28. Completed Structure 109 Numerical Model.....	214
Figure 5.29. At-Rest Pressure Application	216
Figure 5.30. Bridge 109 Pier Exploded View.....	217
Figure 5.31. Complete Bridge 203 Numerical Model	218
Figure 5.32. Complete Bridge 211 Numerical Model	219
Figure 5.33. Bridge 222 Numerical Model.....	220
Figure 5.34: Measured and Predicted Bridge 109 Top Extensometer at Abutment 1	223
Figure 5.35: Measured and Predicted Bridge 109 Bottom Extensometer at Abutment 1.....	224
Figure 5.36: Measured and Predicted Bridge 109 Top Extensometer at Abutment 2	225
Figure 5.37: Measured and Predicted Bridge 109 Bottom Extensometer at Abutment 2.....	226
Figure 5.38: Measured and Predicted Bridge 109 Top Pressure Cell at Abutment 1	227
Figure 5.39: Measured and Predicted Bridge 109 Bottom Pressure Cell at Abutment 1.....	228

Figure 5.40: Measured and Predicted Bridge 109 Top Pressure Cell at Abutment 2	229
Figure 5.41: Measured and Predicted Bridge 109 Bottom Pressure Cell at Abutment 2.....	230
Figure 5.42: Bridge 203 Top Extensometer Comparison	231
Figure 5.43: Bridge 203 Bottom Extensometer Comparison.....	234
Figure 5.44: Bridge 203 Top Pressure Cell Comparison.....	235
Figure 5.45: Bridge 203 Bottom Pressure Cell Comparison	236
Figure 5.46: Measured and Predicted Bridge 211 Top Extensometer at Abutment 1	239
Figure 5.47: Measured and Predicted Bridge 211 Bottom Extensometer at Abutment 1.....	240
Figure 5.48: Measured and Predicted Bridge 211 Top Extensometer at Abutment 2	241
Figure 5.49: Measured and Predicted Bridge 211 Bottom Extensometer at Abutment 2.....	242
Figure 5.50: Measured and Predicted Bridge 211 Top Pressure Cell at Abutment 1	243
Figure 5.51: Measured and Predicted Bridge 211 Bottom Pressure Cell at Abutment 1.....	244
Figure 5.52: Measured and Predicted Bridge 211 Top Pressure Cell at Abutment 2	245
Figure 5.53: Measured and Predicted Bridge 211 Bottom Pressure Cell at Abutment 2.....	246
Figure 5.54: Measured and Predicted Bridge 222 Top Extensometer at Abutment 1	249
Figure 5.55: Measured and Predicted Bridge 222 Bottom Extensometer at Abutment 1.....	250
Figure 5.56: Measured and Predicted Bridge 222 Top Extensometer at Abutment 2	251
Figure 5.57: Measured and Predicted Bridge 222 Bottom Extensometer at Abutment 2.....	252
Figure 5.58: Measured and Predicted Bridge 222 Top Pressure Cell at Abutment 1	253
Figure 5.59: Measured and Predicted Bridge 222 Bottom Pressure Cell at Abutment 1.....	254
Figure 5.60: Measured and Predicted Bridge 222 Top Pressure Cell at Abutment 2	255
Figure 5.61: Measured and Predicted Bridge 222 Bottom Pressure Cell at Abutment 2.....	256

Figure 6.1. Typical Cross-Section for Parametric Study	259
Figure 6.2. Backfill Height Parameter	263
Figure 6.3. Rotational Stiffness of Construction Joints.....	265
Figure 6.4. Typical Bridge Construction Timeline.....	268
Figure 6.5. Backfill Pressure Versus Abutment Displacement.....	270
Figure 6.6. Subgrade Modulus of Monitored Bridges	271
Figure 6.7. Soil Properties under Bridge 211 Abutment 1	271
Figure 6.8: Girder Material Influence on Girder Tensile Axial Force.....	275
Figure 6.9: Girder Material Influence on Girder Compressive Axial Force.....	276
Figure 6.10: Construction Joint Stiffness Influence on Girder Tensile Axial Force	277
Figure 6.11: Construction Joint Stiffness Influence on Girder Compressive Axial Force	278
Figure 6.12: Backfill Height Influence on Girder Tensile Axial Force.....	279
Figure 6.13: Backfill Height Influence on Girder Compressive Axial Force.....	280
Figure 6.14: Bridge Length Influence on Girder Tensile Axial Force	281
Figure 6.15: Bridge Length Influence on Girder Compressive Axial Force	282
Figure 6.16: Girder Material Influence on Positive Girder Moment.....	284
Figure 6.17: Girder Material Influence on Negative Girder Moment	285
Figure 6.18: Construction Joint Stiffness Influence on Positive Girder Moment.....	286
Figure 6.19: Construction Joint Stiffness Influence on Negative Girder Moment.....	287
Figure 6.20: Backfill Height Influence on Positive Girder Moment	288
Figure 6.21: Backfill Height Influence on Negative Girder Moment.....	289
Figure 6.22: Bridge Length Influence on Positive Girder Moment.....	290
Figure 6.23: Bridge Length Influence on Negative Girder Moment	291
Figure 6.24: Girder Material Influence on Pile Moment	293
Figure 6.25: Construction Joint Stiffness Influence on Pile Moment.....	294
Figure 6.26: Backfill Height Influence on Pile Moment	295
Figure 6.27: Bridge Length Influence on Pile Moment.....	296
Figure 6.28: Girder Material Influence on Pile Lateral Force	298
Figure 6.29: Construction Joint Stiffness Influence on Pile Lateral Force.....	299
Figure 6.30: Backfill Height Influence on Pile Lateral Force	300

Figure 6.31: Bridge Length Influence on Pile Lateral Force	301
Figure 6.32: Girder Material Influence on Pile Displacement.....	303
Figure 6.33: Construction Joint Stiffness Influence on Pile Displacement	304
Figure 6.34: Backfill Height Influence on Pile Displacement.....	305
Figure 6.35: Bridge Length Influence on Pile Displacement	306
Figure 6.36: Correlation between Approximate Analysis and 2D Model Prediction.....	310
Figure 7.1. Backfill Height Parameter	316
Figure 7.2. Pile Response Displacement, Moment, and Shear Profile	320
Figure 7.3. Bridge Total Compressive Axial Force.....	325
Figure 7.4. Bridge Total Tensile Axial Force.....	328
Figure 7.5. Bridge Total Positive Bending Moment at mid-span of the exterior span....	332
Figure 7.6. Bridge Total Negative Bending Moment at Mid-Span of the Exterior Span.....	335
Figure 7.7. Bridge Total Positive Bending Moment at Abutment.....	338
Figure 7.8. Bridge Total Negative Bending Moment at Abutment	341
Figure 7.9. Minimum Number of Laterally Supporting Piles.....	345
Figure 7.10. Maximum Pile Head Displacement.....	348
Figure 7.11. Simplified 2D Numerical Model	354
Figure 7.12. Full and Condensed Soil-Pile Interaction Model	355
Figure 7.13. Abutment-Backfill Numerical Implementation Modification.....	358
Figure 7.14. Cross-Section of 3D Model Superstructure.....	365
Figure 7.15. Abutment to Backwall Construction Joint	367
Figure 7.16. Concrete Strain under Variable Stress.....	372
Figure 7.17. Temperature Gradient for Transformed Section	375
Figure 8.1: Bridge Elevation, Top – Example 1, Middle – Example 2, Bottom – Example 3	381
Figure 8.2. Typical Example Bridge Cross-Section and Abutment Dimensions	382
Figure 8.3: Example 1 Bridge Elevation.....	384
Figure 8.4: Example 1 Bridge Dimensions.....	385
Figure 8.5: Example 1 Bridge Section A-A.....	386
Figure 8.6: Moment Diagram of 2D Model.....	390

Figure 8.7: Single Span Bridge Thermal Behavior.....	391
Figure 8.8: Typical IAB Pile Displacement, Moment, and Shear Response.....	394
Figure 8.9: 2D Example 1 ANSYS Bridge Model	396
Figure 8.10: 2D Example 1 ANSYS Model Perspective View	397
Figure 8.11: Beam Element (BEAM189) Cross Section for Superstructure	398
Figure 8.12: Construction Joint Rotational Stiffness.....	400
Figure 8.13: Comparison of p - y Curve by the API Equation and Lpile	403
Figure 8.14: Temperature Model	406
Figure 8.15: Temperature Variation with Temperature Gradient.....	407
Figure 8.16: Backfill Pressure.....	408
Figure 8.17: Backfill Pressure Modeling.....	409
Figure 8.18: Backfill Pressure in 2D Numerical Model	410
Figure 8.19: Time-dependent Load Application.....	411
Figure 8.20: Temperature Load Application in Offset Element Section.....	412
Figure 8.21: Example 1: 2D Analysis—Girder Axial Force (Static and Time-History)	413
Figure 8.22: Example 1: 2D Analysis—Girder Bending Moment (Static and Time-history)	414
Figure 8.23: Example 1: 2D Analysis - Pile Lateral Force (Static and Time-history) ...	415
Figure 8.24: Example 1: 2D Analysis - Pile Moment (Static and Time-history)	416
Figure 8.25: Example 1: 2D Analysis - Pile Head Displacement (Static and Time-History)	417
Figure 8.26: Example 1, 3D Schematic ANSYS Bridge Model– Isometric View	419
Figure 8.27: Example 1, Solid 3D Bridge Model – Isometric View	420
Figure 8.28: Cross Section of BT72 Girder (units are inches)	421
Figure 8.29: Girder and Deck Slab Connection.....	422
Figure 8.30: Example 1 3D Abutment and Back-wall – Viewed from Backfill.....	423
Figure 8.31: Strains in Doubly Reinforced Beam.....	425
Figure 8.32: Moment-Rotation Curve.....	427
Figure 8.33: Example 1 Abutment to Back-wall Construction Joint Modeling	428
Figure 8.34: HP12×74 Foundation Pile Section	429

Figure 8.35: Foundation Pile Section Soil Spring Definition	430
Figure 8.36: Temperature Gradient for BT72 Girder in Pennsylvania	432
Figure 8.37: Temperature Gradient for BT72 Girder and Deck Slab	436
Figure 8.38: Backfill Pressure Contour in Example 1 3D Model	436
Figure 8.39: Example 1 3D Analysis Abutment Backfill Pressure	437
Figure 8.40: Example 1 3D Analysis Backfill Pressure Tributary Area for Spring	437
Figure 8.41: Backfill-Abutment Interaction Spring Property	439
Figure 8.42: Example Bridge 1 3D Analysis Girder Axial Force Comparison	441
Figure 8.43: Example Bridge 1 3D Analysis Girder Bending Moment	442
Figure 8.44: Example 1 3D Analysis Model Pile Lateral Force	444
Figure 8.45: Example Bridge 1 Pile Moment by 3D Analysis	445
Figure 8.46: Example Bridge 1 Pile Head Displacement by 3D Analysis	446
Figure 8.47: Example Bridge 1 Girder Axial Force Comparison	447
Figure 8.48: Example Bridge 1 Girder Bending Moment Comparison	448
Figure 8.49: Example Bridge 1 Pile Lateral Force Comparison	448
Figure 8.50: Example Bridge 1 Pile Moment Comparison	450
Figure 8.51: Example Bridge 1 Pile Head Displacement Comparison	451
Figure 8.52: Example Bridge 2 Girder Section	452
Figure 8.53: Example Bridge 2 Elevation	453
Figure 8.54: Example Bridge 2 Dimensions	454
Figure 8.55: Example Bridge 2 Section A-A	455
Figure 8.56: Typical IAB Pile Displacement, Moment, and Shear Response	460
Figure 8.57: 2D Example 2 ANSYS Bridge Model	463
Figure 8.58: 2D Example 2 ANSYS Model Perspective View	464
Figure 8.59: Beam Element (BEAM189) Cross Section for Superstructure	465
Figure 8.60: Construction Joint Rotational Stiffness	467
Figure 8.61: Comparison of p - y Curve by the API Equation and L_{pile}	470
Figure 8.62: Temperature Model	473
Figure 8.63: Temperature Load Application in Offset Element Section	474
Figure 8.64: Temperature Variation with Temperature Gradient	476
Figure 8.65: Backfill Pressure	477

Figure 8.66: Backfill Pressure Modeling	478
Figure 8.67: Backfill Pressure in 2D Numerical Model	479
Figure 8.68: Example 2: 2D Analysis—Girder Axial Force (Static and Time-History)	480
Figure 8.69: Example 2: 2D Analysis—Girder Bending Moment (Static and Time-history)	481
Figure 8.70: Example 2: 2D Analysis - Pile Lateral Force (Static and Time-history) ...	482
Figure 8.71: Example 2: 2D Analysis - Pile Moment (Static and Time-history)	483
Figure 8.72: Example 2: 2D Analysis— Pile Head Displacement (Static and Time-history)	484
Figure 8.73: Example 2 3D Schematic ANSYS Bridge Model– Isometric View	485
Figure 8.74: Example 2 Solid 3D Bridge Model – Isometric View	486
Figure 8.75: Cross Section of Steel Plate Girder	487
Figure 8.76: Girder and Deck Slab Connection.....	488
Figure 8.77: Example 2 3D Abutment and Back-wall – Viewed from Backfill.....	489
Figure 8.78: Strains in Doubly Reinforced Beam.....	491
Figure 8.79: Moment-Rotation Curve.....	493
Figure 8.80: Example 2 Abutment to Back-wall Construction Joint Modeling	494
Figure 8.81: HP12×74 Foundation Pile Section	495
Figure 8.82: Foundation Pile Section Soil Spring Definition	496
Figure 8.83: Temperature Gradient for BT72 Girder in Pennsylvania.....	498
Figure 8.84: Temperature Gradient for Steel Girder and Deck Slab	501
Figure 8.85: Backfill Pressure Contour in Example 2 3D Model.....	502
Figure 8.86: Example 2 3D Analysis Abutment Backfill Pressure	503
Figure 8.87: Example 2 3D Analysis Backfill Pressure Tributary Area for Spring	503
Figure 8.88: Backfill-Abutment Interaction Spring Property	505
Figure 8.89: Example Bridge 2 3D Analysis Girder Axial ForceComparison	507
Figure 8.90: Example Bridge 2 3D Analysis Girder Bending Moment	508
Figure 8.91: Example 2 3D Analysis Model Pile Lateral Force.....	509
Figure 8.92: Example Bridge 2 Pile Moment by 3D Analysis	511
Figure 8.93: Example Bridge 2 Pile Head Displacement by 3D Analysis	512

Figure 8.94: Example Bridge 2 Girder Axial Force Comparison.....	513
Figure 8.95: Example Bridge 2 Girder Bending Moment Comparison.....	514
Figure 8.96: Example Bridge 2 Pile Lateral Force Comparison.....	515
Figure 8.97: Example Bridge 2 Pile Moment Comparison.....	516
Figure 8.98: Example Bridge 2 Pile Head Displacement Comparison.....	517
Figure 8.99: Example 3 Bridge Elevation.....	519
Figure 8.100: Example 3 Bridge Cross-Section and Abutment Elevation	520
Figure 8.101: Example 3 Bridge Section A-A.....	521
Figure 8.102: Typical IAB Pile Displacement, Moment, and Shear Response.....	527
Figure 8.103: 2D Example 3 ANSYS Bridge Model	530
Figure 8.104: 2D Example 3 ANSYS Model Perspective View	531
Figure 8.105: Beam Element (BEAM189) Cross Section for Superstructure	532
Figure 8.106: Construction Joint Rotational Stiffness.....	533
Figure 8.107: Comparison of p - y Curve by the API Equation and L_{pile}	537
Figure 8.108: Temperature Model	539
Figure 8.109: Temperature Variation with Temperature Gradient.....	541
Figure 8.110: Backfill Pressure.....	542
Figure 8.111: Backfill Pressure Modeling.....	543
Figure 8.112: Backfill Pressure in 2D Numerical Model	544
Figure 8.113: Time-dependent Load Application.....	545
Figure 8.114: Temperature Load Application in Offset Element Section	546
Figure 8.115: Example 3: 2D Analysis—Girder Axial Force (Static and Time-History)	547
Figure 8.116: Example 3: 2D Analysis—Girder Bending Moment (Static and Time-history)	548
Figure 8.117: Example 3: 2D Analysis - Pile Lateral Force (Static and Time-history) ..	549
Figure 8.118: Example 3: 2D Analysis - Pile Moment (Static and Time-history)	550
Figure 8.119: Example 3: 2D Analysis— Pile Head Displacement (Static and Time-History)	551
Figure 8.120: Example 3 3D Schematic ANSYS Bridge Model– Isometric View	553
Figure 8.121: Example 3 Solid 3D Bridge Model – Isometric View	554

Figure 8.122: Cross Section of BT81 Girder	556
Figure 8.123: Girder and Deck Slab Connection.....	557
Figure 8.124: Example 3 3D Abutment and Back-wall – Viewed from Backfill.....	558
Figure 8.125: Strains in Doubly Reinforced Beam.....	560
Figure 8.126: Moment-Rotation Curve.....	562
Figure 8.127: Example 3 Abutment to Back-wall Construction Joint Modeling	563
Figure 8.128: HP12×74 Foundation Pile Section	564
Figure 8.129: Foundation Pile Section Soil Spring Definition	565
Figure 8.130: Temperature Gradient for BT81 Girder in Pennsylvania.....	567
Figure 8.131: Temperature Gradient for BT81 Girder and Deck Slab	571
Figure 8.132: Backfill Pressure Contour in Example 3 3D Model.....	571
Figure 8.133: Example 3 3D Analysis Abutment Backfill Pressure	572
Figure 8.134: Example 3 3D Analysis Backfill Pressure Tributary Area for Spring	572
Figure 8.135: Backfill-Abutment Interaction Spring Property	574
Figure 8.136: Example 3 Bridge 3D Analysis Girder Axial Force Comparison.....	576
Figure 8.137: Example 3 Bridge 3D Analysis Girder Bending Moment	577
Figure 8.138: Example 3 3D Analysis Model Pile Lateral Force.....	579
Figure 8.139: Example 3 Bridge Pile Moment by 3D Analysis	581
Figure 8.140: Example 3 Bridge Pile Head Displacement by 3D Analysis	582
Figure 8.141: Example 3 Bridge Girder Axial Force Comparison.....	583
Figure 8.142: Example 3 Bridge Girder Bending Moment Comparison.....	584
Figure 8.143: Example 3 Bridge Pile Lateral Force Comparison.....	585
Figure 8.144: Example 3 Bridge Pile Moment Comparison.....	586
Figure 8.145: Example 3 Bridge Pile Head Displacement Comparison.....	587

LIST OF TABLES

Table 2.1. Structural Parameters of the Selected IABs.....	5
Table 2.2. Details of Cell Modems and Cell Numbers	37
Table 4.1. Bridge 109 Maximum Abutment Displacement.....	64
Table 4.2. Bridge 109 Pile Strain Gage Depths Below Bottom of Abutment and Maximum Measured Moment.....	66
Table 4.3. Bridge 203 Maximum Abutment Displacement.....	97
Table 4.4. Bridge 203 Pile Strain Gage Depths Below Bottom of Abutment and Maximum Measured Moment.....	98
Table 4.5. Bridge 203 Pile Strain Gage Depths Below Bottom of Abutment and Maximum Measured Axial Force	99
Table 4.6. Bridge 211 Maximum Abutment Displacement.....	120
Table 4.7. Bridge 211 Pile Strain Gage Depths Below Bottom of Abutment and Maximum Measured Moment.....	122
Table 4.8. Bridge 222 Maximum Abutment Displacement.....	149
Table 4.9. Bridge 222 Pile Strain Gage Depths Below Bottom of Abutment and Maximum Measured Moment.....	151
Table 4.10. Summary of Maximum Abutment Displacements and Backfill Pressures...	179
Table 4.11. Summary of Maximum Girder and Abutment Rotations	180
Table 4.12. Summary of Maximum Pile Moments and Axial Forces	181
Table 4.13. Summary of Maximum Girder Moments and Axial Forces	181
Table 4.14. Summary of Maximum Compressive Sister-Bar Strain	182
Table 5.1. Bridges 109, 203, 211, 222 Material Properties	185
Table 5.2. Construction Joint Reinforcing Details.....	197
Table 5.3. Coefficients of the Mathematical Temperature Model.....	212
Table 5.4. Bridge 109 Elastomeric Bearing Properties.....	216
Table 6.1. Primary Parameters and Ranges	259
Table 6.2. Girder Sections and Dimensions for Parametric Study	261
Table 6.3. Construction Joint Reinforcing Details.....	265
Table 6.4. Deck Placement Date of Field Tested IABs	267

Table 6.5. Integral Backwall Placement Date of Field Tested IABs	267
Table 6.6. Variation of Concrete Thermal Expansion Coefficient	269
Table 6.7. Backfill Properties	269
Table 7.1. Backfill Properties and Range Determination	316
Table 7.2. Soil Layer Properties and Range Determination	316
Table 7.3. Thermal Expansion Coefficient by Aggregate Type	370
Table 8.1. Example Bridges.....	380
Table 8.2. Example 1 Component Concrete and Steel Strength.....	387
Table 8.3. Soil Layer Properties for Soil Pile Stiffness (<i>P</i>)	387
Table 8.4. Backfill Properties for Backfill Stiffness (<i>B</i>).....	387
Table 8.5: Superstructure Composite Section Property of Single Span Prestressed Girder IAB	398
Table 8.6: <i>p-y</i> curve ordinates for a depth of 10'-0"	403
Table 8.7. Example 2 Component Concrete and Steel Strength.....	456
Table 8.8. Soil Layer Properties for Soil Pile Stiffness (<i>P</i>)	456
Table 8.9. Backfill Properties for Backfill Stiffness (<i>B</i>).....	456
Table 8.10: Superstructure Composite Section Property of Steel Girder IAB	466
Table 8.11: <i>p-y</i> curve ordinates for a depth of 10'-0"	470
Table 8.12. Example 3 Component Concrete and Steel Strength.....	522
Table 8.13. Soil Layer Properties for Soil Pile Stiffness (<i>P</i>)	522
Table 8.14. Backfill Properties for Backfill Stiffness (<i>B</i>).....	522
Table 8.15: Superstructure Composite Section Property of 3-Span Prestressed Girder IAB	532
Table 8.16: <i>p-y</i> curve ordinates for a depth of 10'-0"	536
Table 9.1: PennDOT IAB Design Spreadsheet Evaluation	591
Table 9.2: PennDOT DM-4 IAB Design Discussion.....	595

Executive Summary

The primary objectives of this research project included: (1) connection of wireless data transfer at the four previously instrumented IABs and weather station; (2) continuous monitoring and collection of engineering bridge response data; (3) conduct of a parametric study to determine IAB behavior trends relative to several variables over practical ranges; (4) development of a preliminary, approximate analysis procedure to be used for initial design; (5) development of an accurate 2D and 3D analysis methodologies calibrated to measured response; and (6) presentation of three IAB analysis examples that include steel and concrete superstructures of three different lengths and illustrate the approximate, 2D, and 3D analysis methodologies.

To effectively present bridge field monitoring results and details of the numerical studies of this research project, this report consists of nine chapters: Chapter 1 presents project objectives and tasks; Chapter 2 presents detailed dimensions and locations of the four instrumented IABs and weather station; Chapter 3 summarizes the previous PennDOT/PSU research projects conducted on the four IABs; Chapter 4 presents processed data and measurements from all instruments installed at each of the four IABs and the weather station; Chapter 5 presents the developed IAB numerical modeling methodologies; Chapter 6 presents the parametric study conducted in order to observe overall trends for several key variables including results; Chapter 7 discusses the three IAB analyses methods; Chapter 8 presents the three detailed IAB analyses examples; and Chapter 9 presents an overall Summary and Conclusions.

The present study utilized a wireless connection between the base computer and bridge monitoring sites to download data approximately once per month. The data loggers and instrumentation were installed under two previous research contracts (Laman et al. 2003, 2006): research conducted from October 2000 to March 2003 installed instruments on bridges 203, 211, and 222, and research conducted from June 2005 to July 2006 installed instruments on bridge 109. The four instrumented IABs and weather station are located on the I-99 extension near Port Matilda in central Pennsylvania and, therefore, all thermal loading data are based on data collected there. Data loggers installed at bridges 203, 222, 211, and 109 were activated in November 2002, November 2003, September 2004, and July 2006, respectively. Measured bridge response data at each site are composed of longitudinal abutment displacements, abutment earth pressures, abutment and girder rotations, H-pile bending moments about the weak axis and axial forces, girder axial forces and moments, and approach slab strains.

Four 3D numerical models were developed and calibrated to predict IAB responses for bridges 109, 203, 211, and 222. Key features of the models include soil-pile interaction, backfill-abutment interaction, construction joint behavior, seasonal temperature fluctuation, superstructure temperature gradient, time-dependent effects, and backfill pressure. Comparisons between measured bridge responses and predicted bridge responses are presented and discussed. Based on the numerical modeling methodologies developed in this study, an extensive parametric study utilizing these 3D numerical modeling methodologies was performed to determine trends of IAB responses. The parameters considered include girder material, bridge length, backfill height and construction joint stiffness. Girder materials considered are prestressed concrete girders

and steel plate girders with cast-in-place deck slab concrete. The four bridge lengths of the study are single-span 100 ft, two-span 200 ft, three-span 400 ft and four-span 600 ft. Based on the monitored bridge dimensions, backfill heights range from 10 to 20 ft. The construction joint between the backwall and abutment was included in three levels: (1) a hinged joint; (2) the PennDOT standard reinforcement detail (#5 rebars at 9 inches); and (3) a rigid joint. Thus, the 3D parametric study results in 72 study cases. Each was analyzed based on an AASHTO extreme temperature static analysis for both temperature rise and fall. Variations of girder axial force, girder moment, pile lateral force, pile moment and pile head displacement with respect to the four parameters were investigated and discussed. In addition, a parametric study utilizing 486 2D numerical models was performed considering six parameters: (1) girder material, (2) thermal expansion coefficient, (3) bridge length, (4) backfill height, (5) backfill stiffness, and (6) pile soil stiffness. The parametric study results provided a basis to establish goodness-of-fit curves for the approximate analysis. Response equations for maximum and minimum girder axial force, maximum and minimum girder moment at the girder end adjacent to the abutments, maximum and minimum girder moment at the girder mid-span in the end span, maximum pile lateral force, maximum pile moment, and maximum pile head displacement have been developed.

The three bridge analysis methods developed as part of this study, (1) approximate analysis method, (2) 2D analysis methodology, and (3) 3D analysis methodology are described in detail and each of the analysis methods was demonstrated with three integral abutment bridge examples. The bridge analysis example are: (1) single-span 100-ft

prestressed concrete girder bridge; (2) two-span steel plate girder bridge; and (3) three-span 400-ft prestressed concrete girder bridge.

Chapter 1

Introduction

1.1 Problem Statement

It has been observed that Pennsylvania integral abutment bridge behavior is much different from that predicted by current design methodologies. Thermally induced displacement magnitudes are typically on the order of 10 percent to 25 percent of predicted values. Thermally induced rotations and displacements are, in certain locations, opposite from predicted rotations and displacements. Thermally induced stresses are not currently incorporated into design aids and guidelines and are not insignificant. Design methodologies must consider actual field observations such that the design accurately predicts the structural behavior. Proper application of integral abutments can then be made considering the findings of this study with new integral abutment bridge designs. In addition, PennDOT integral abutment design requirements will represent the state-of-the-art.

1.2 Objectives

The objective of this project is to revise and make more accurate integral abutment bridge design criteria based on observed structural behavior and results of numerical parametric studies. Observed behaviors will be on the basis of field monitoring conducted at four integral abutment bridge sites and a weather station using previously installed instrumentation and data acquisition systems. Integral abutment bridge engineering data will be continuously collected over the entire contract period at bridges 109, 203, 211, and 222 and will be compiled, processed, and evaluated. Numerical parametric studies will be conducted on the basis of 2D and 3D finite element models developed and calibrated to the observed integral abutment behavior in order to

evaluate the field performance of integral abutments and establish the range of potential applications for integral abutment bridge construction in Pennsylvania.

1.3 Project Tasks

Task 1: Install Wireless Data Transfer

Each of the five data acquisition systems (bridges 109, 203, 211, and 222 and the weather station) are capable of transferring acquired data via cell phone to a central computing location for reduction, processing, and storage. The communication devices will be installed with all required coordination with the communications vendor to enable this capability to streamline operations.

Task 2: Continuously Collect Data, Perform Monthly Downloads, Perform Data Reduction

Integral abutment bridge engineering data will be continuously collected and downloaded every two weeks to four weeks. As data are downloaded, they will be reduced and compiled, and backup will be performed.

Task 3: Continuously Maintain PennDOT Instrumentation and Data Acquisition

Equipment

Because of the sensitive nature of the installed instrumentation and data acquisition equipment, continuous maintenance oversight and repair oversight of PennDOT instrumentation and data acquisition equipment will be provided to ensure the lowest possible level of interruption to data acquisition. Because of the unforeseeable nature of equipment and instrumentation repair costs other than incidentals, all repair costs are considered outside the scope of this work order.

Task 4: Perform Parametric Study of Integral Abutment Bridges

A parametric study will be performed considering the major, anticipated integral abutment

details of 1) length, 2) material--steel or concrete, 3) abutment height, and 4) abutment joint stiffness to form the basis of new integral abutment bridge design guidelines. Base-line parametric study models will be calibrated with field data and previously developed 3D finite element models for accuracy.

Task 5: Develop Preliminary Integral Abutment Design Procedures and Interim Report

On the basis of observed integral abutment bridge behavior and initial results from the Task 4 parametric study, preliminary short-span integral abutment design protocols, criteria, and methodologies will be presented in a final report.

Task 6: Develop Integral Abutment Design Procedures

On the basis of observed integral abutment bridge behavior and the Task 4 parametric study, integral abutment design protocols, criteria, and methodologies will be revised or developed. Three integral abutment design examples will be provided to illustrate the application of the design procedures and demonstrate effectiveness of the proposed revisions to integral abutment design protocols, criteria, and methodologies.

Task 7: Draft Final Report

Upon completion of the study, a draft final report summarizing all findings will be provided to PennDOT for review. An Implementation Plan that provides details on the broader use of the results of this project will be included in the draft final report.

Task 8: Final Report

Three bound and two unbound copies of the final report will be provided to PennDOT, taking into consideration comments received from PennDOT on the draft final report.

Chapter 2

Bridge and Weather Station Descriptions

The four IABs and weather station were selected based on a range of bridge lengths and number of spans. The selected integral abutment bridges include bridges 109, 203, 211, and 222, all located on I-99 in central Pennsylvania as shown in Figure 2.1. Table 2.1 presents the major structural parameters of the selected IABs.

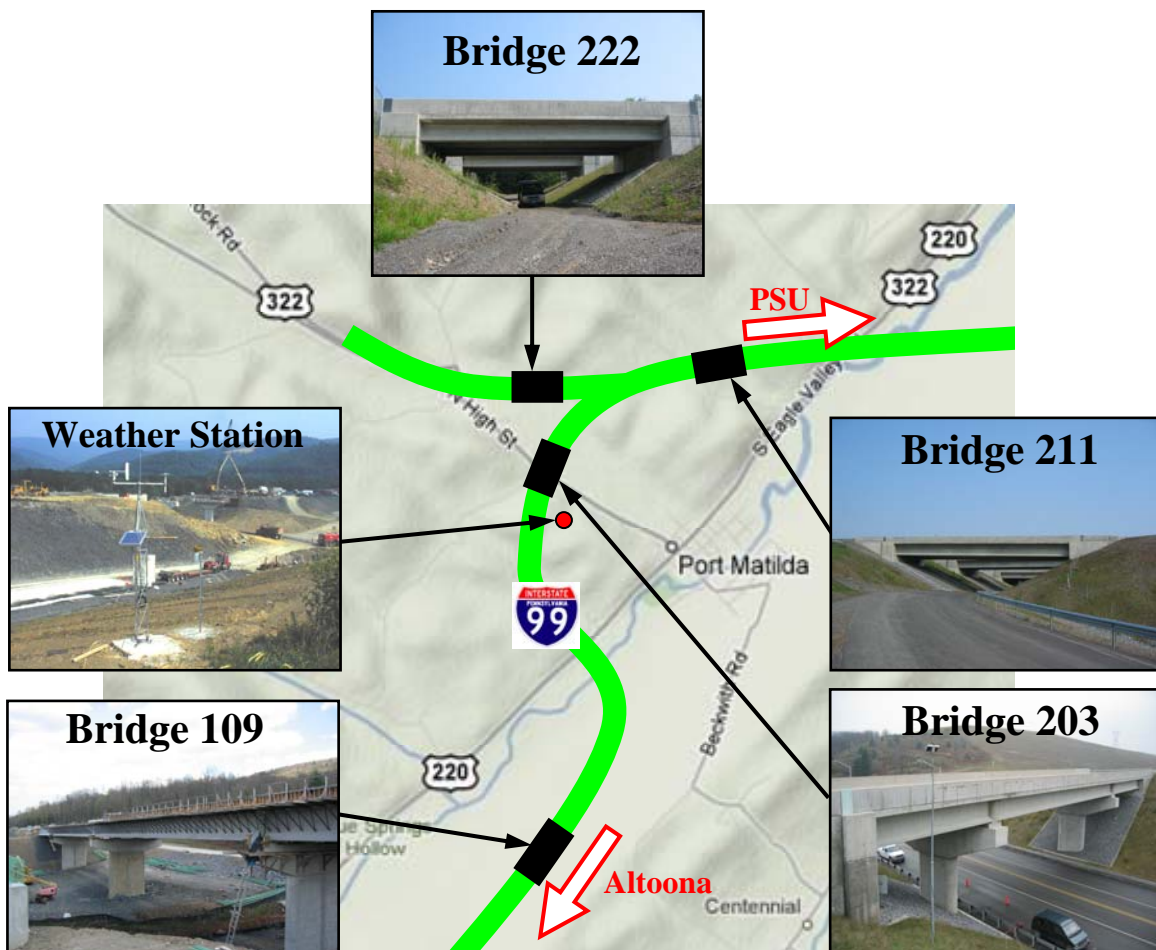


Figure 2.1. Location of Four Selected I-99 IABs.

Table 2.1. Structural Parameters of the Selected IABs.

Bridge No.	Girder Type	No. of Spans	Integral Abutment (Skew Angle)	Spans m (ft)	Design Section
109	P/S I (AASHTO Type I-Beam 28/78)	4	Both (90°)	88-122-122-88 = 420	A10
203	P/S I (AASHTO I-Beam V)	3	North Only (90°)	47-88-37 = 172	C11
211	P/S I (AASHTO Type I-Beam 28/78)	1	Both (90°)	114	A11
222	P/S I (PA. I-Beam 24/48)	1	Both (90°)	62	A11

2.1 Bridge 109 Description

Bridge 109 is located two miles west of Port Matilda, PA (see Figure 2.1 and Table 2.1). The composite slab on the girder structure consists of simply supported girders bearing on reinforced concrete piers and abutments (see Figure 2.2 and 2.3). The AASHTO Type I-Beam 28/78 prestressed concrete girders are spaced at 11 ft 6 inches and cast integrally with both abutments (see Figure 2.4 and 2.5). Construction details develop live load continuity in the four-span structure. The total abutment height is approximately 11 ft 5 inches, which is not in conformance with the current BD-667 Standard of 4 ft 6 inches. The piers are designed as semi-rigid, self-supporting substructures with $3 \frac{3}{32}$ -inch elastomeric bearing pads that allow movement between the pier and the superstructure. Both abutments are integral with a single row of (12) HP12x74 piles bending about the weak axis in response to longitudinal movements (see Figure 2.6). A 25-ft-long by 18-inch-thick reinforced concrete approach slab is to be constructed at both ends of the bridge. The deck is 9 inches thick, including a 1-inch integral wearing surface, and reinforced with epoxy-coated deformed steel bars. The roadway pavement and the approach slab at both ends of the bridge have neoprene strip seal expansion joints

separating them that allow a 4-inch movement capacity. A 1-inch-thick foam board has been placed between the abutment and the backfill to reduce backfill passive pressure. Tapered wing walls have been used for bridge 109 (see Figure 2.7).

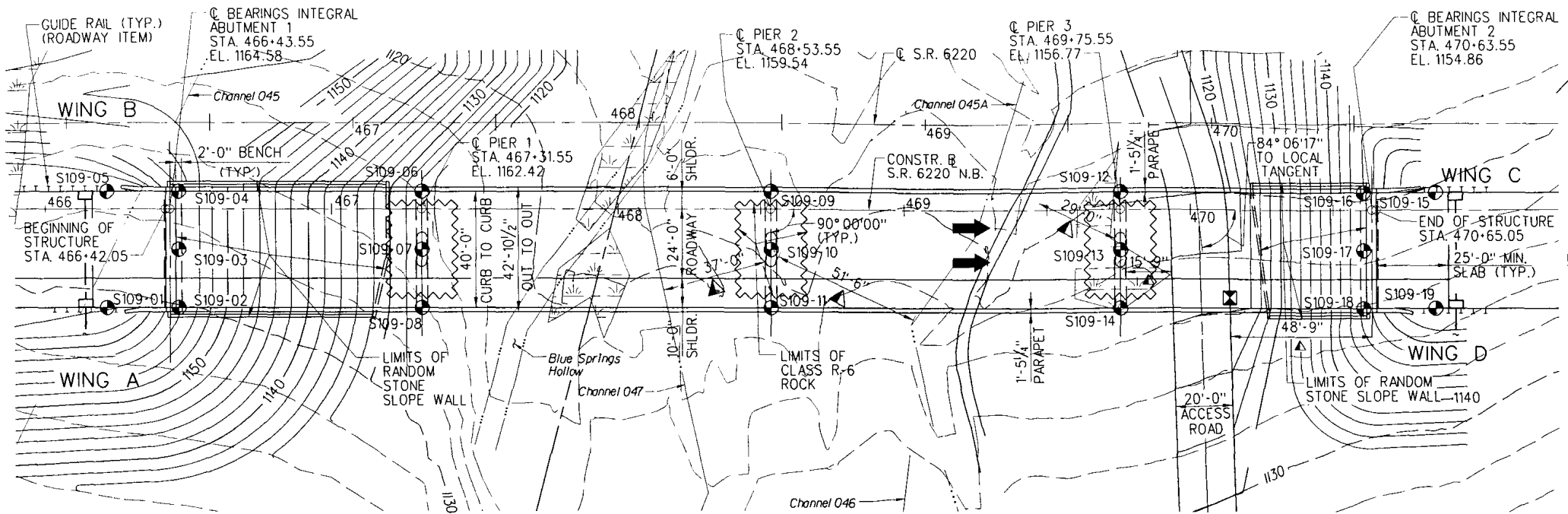


Figure 2.2. Site Plan of Bridge 109.

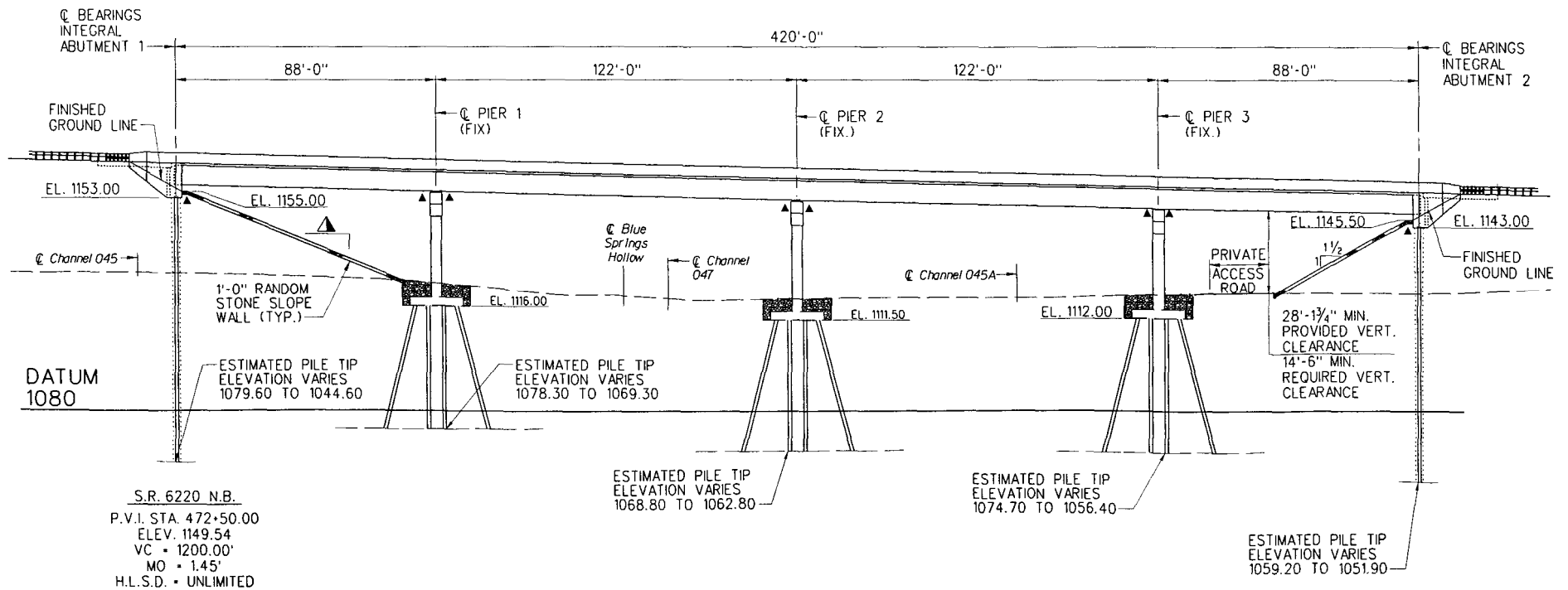
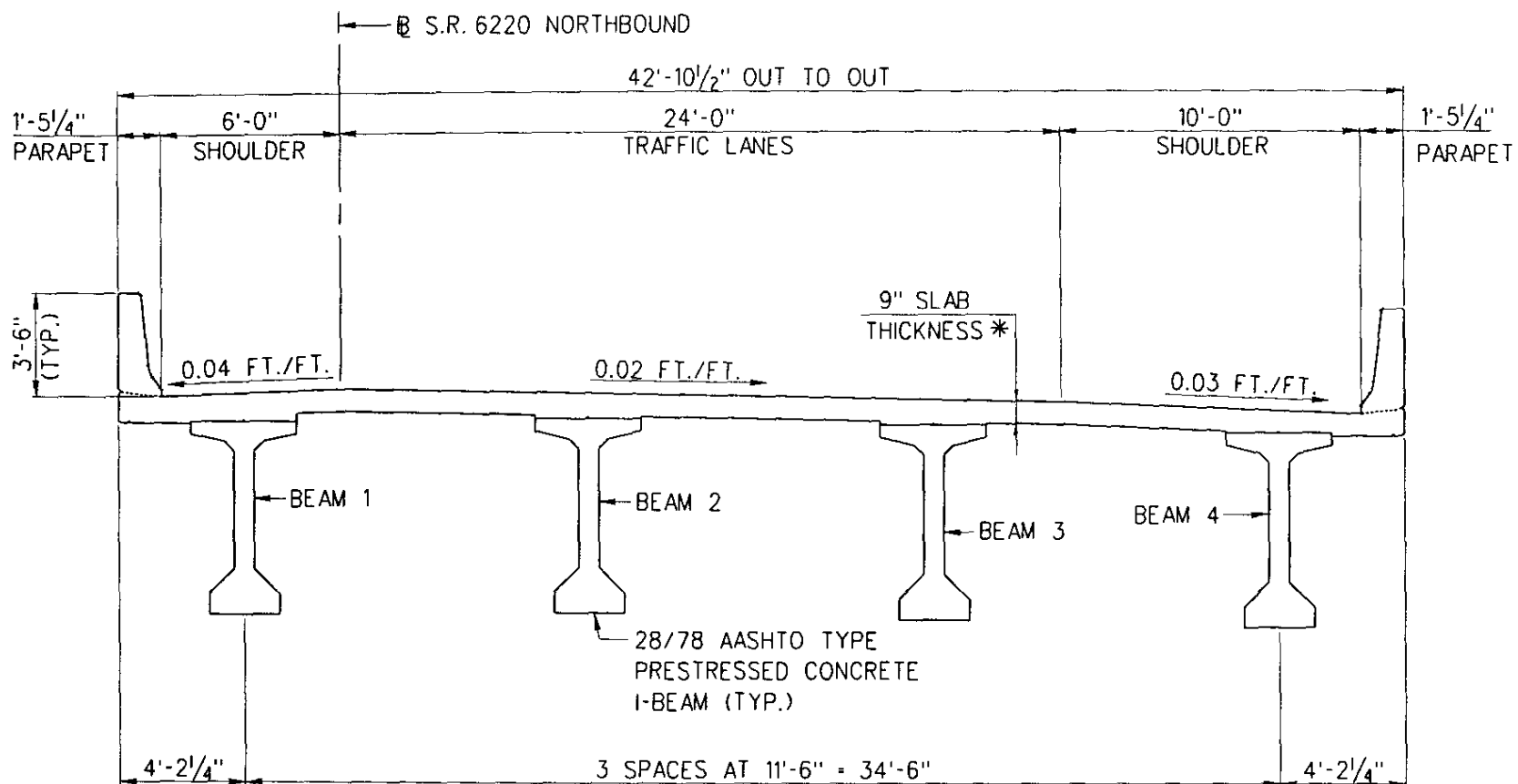


Figure 2.3. Elevation of Bridge 109.



* INCLUDES 1/2" INTEGRAL WEARING SURFACE AND AN ADDITIONAL 1/2" DECK THICKNESS TO ALLOW FOR REFLECTIVE PAVEMENT MARKERS AND MILLED SHOULDER RUMBLE STRIPS (ROADWAY ITEM).

Figure 2.4. Transverse Section of Bridge 109.

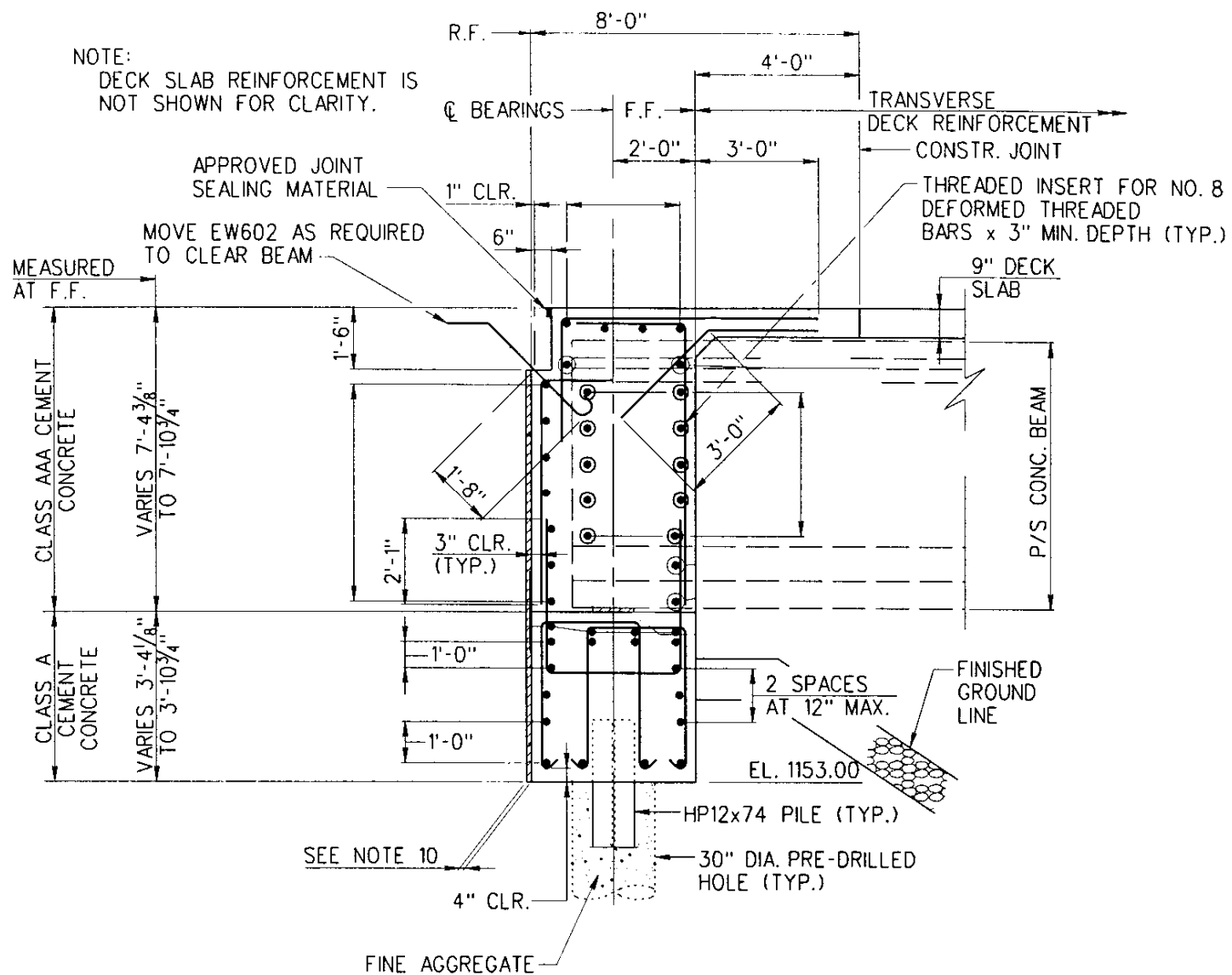


Figure 2.5. Cross-Section of Bridge 109 Abutment 1.

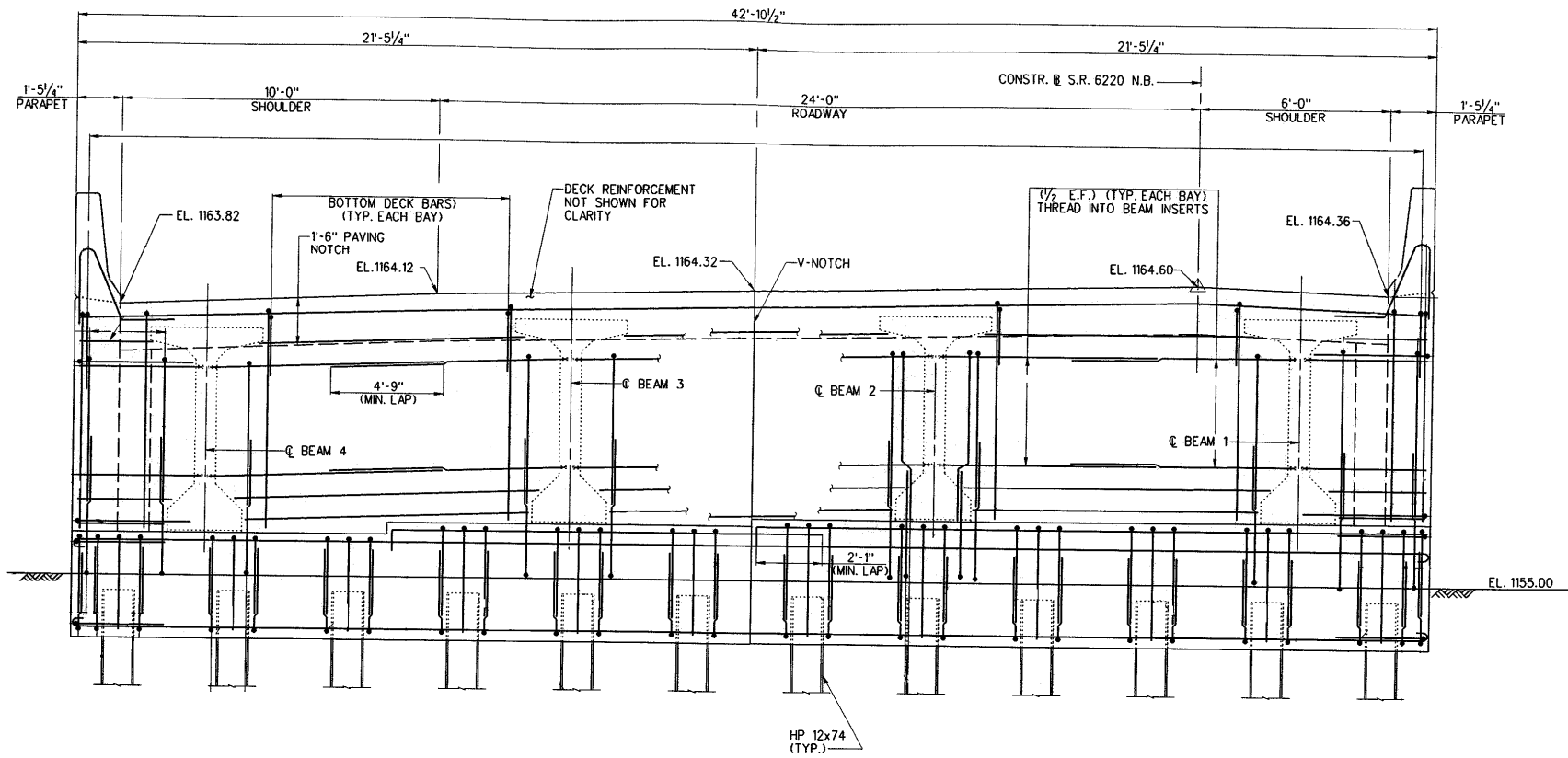


Figure 2.6. Elevation of Bridge 109 Abutment 1.

2.2 BRIDGE 203

Bridge 203 is located in Port Matilda, PA (see Figure 2.1 and Table 2.1). The composite slab on girder structure consists of simply supported girders bearing on reinforced concrete piers and abutments (see Figure 2.8 and Figure 2.9). The AASHTO Type I-Beam V prestressed concrete girders are spaced at 11 ft 9½ inches and are cast integrally with both abutments (see Figure 2.10 and Figure 2.11). Live load continuity is developed for this three-span structure. The total abutment height of the integral abutment (abutment 2) is approximately 19 ft 2 inches, which is not in conformance with the current BD-667 Standard of 4 ft 6 inches. Piers are designed as semi-rigid, self-supporting substructures with 2¾-inch elastomeric bearing pads that allow movement between the pier and the superstructure. The south abutment is designed as fixed without longitudinal movement accommodation. At the south abutment, rock is removed 2 ft below the bottom of the abutment, and Class C concrete is placed up to the underside of the foundation. The abutment is cast using the Class C concrete surface as a construction form. The north abutment is integral with a single row of eight steel HP12x74 piles bending about the weak axis from longitudinal movements (see Figure 2.12). Therefore, all movement in the structure is intended to occur at the north end of the bridge at the integral abutment. A 25-ft-long by 18-inch-thick reinforced concrete approach slab is constructed at both ends of the bridge. The deck is 9 inches thick, including a 1-inch integral wearing surface, and is reinforced with epoxy-coated deformed steel bars. A neoprene strip seal expansion joint separates the roadway pavement and approach slab at both ends of the bridge, allowing a 4-inch movement capacity. A 1-inch-thick foam board sheet separates the abutment from the backfill to reduce backfill passive pressure. A

2-inch-thick foam board sheet separates the abutment from the wing wall to isolate the components (see Figure 2.13).

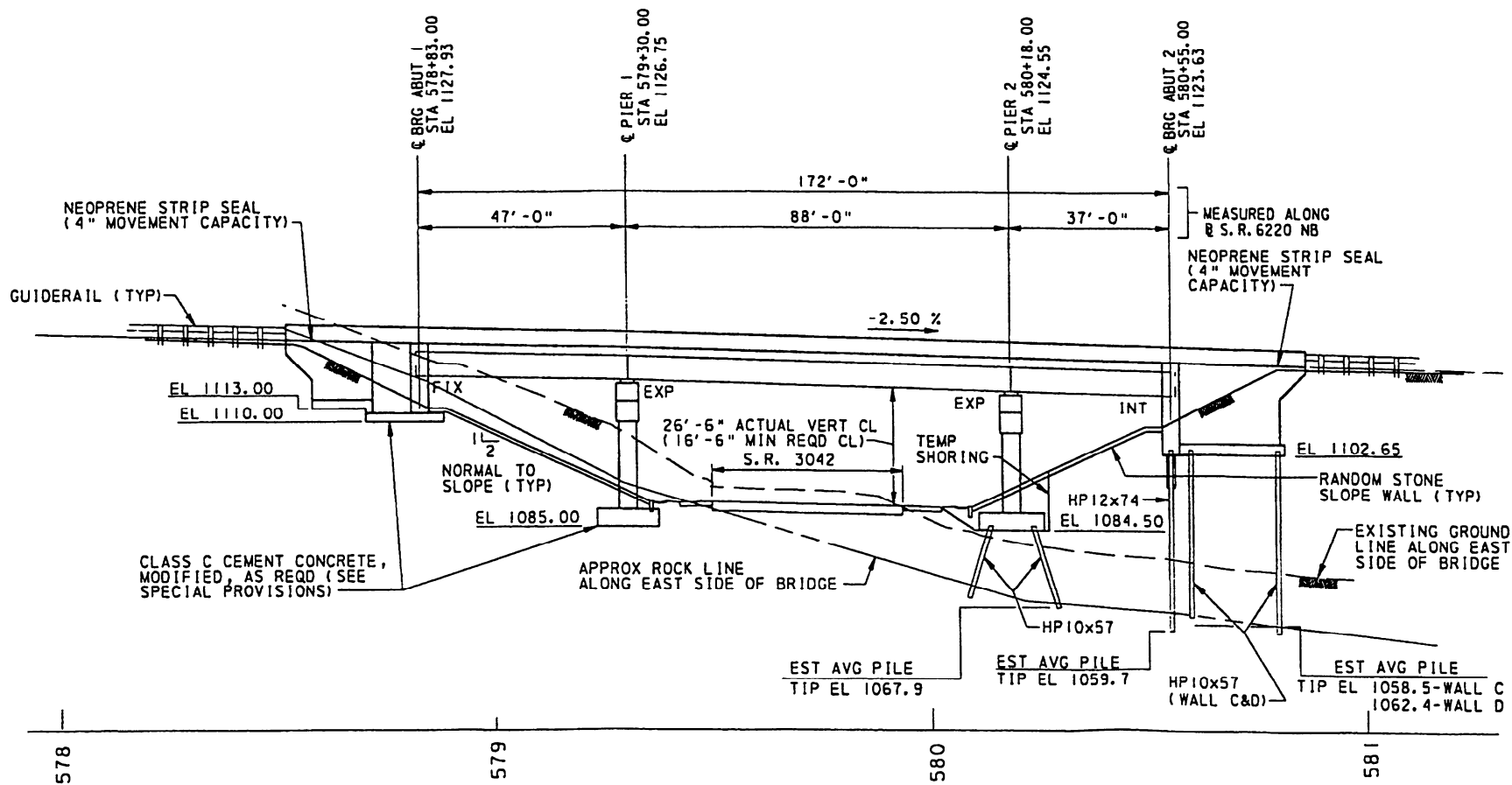


Figure 2.9. Elevation of Bridge 203.

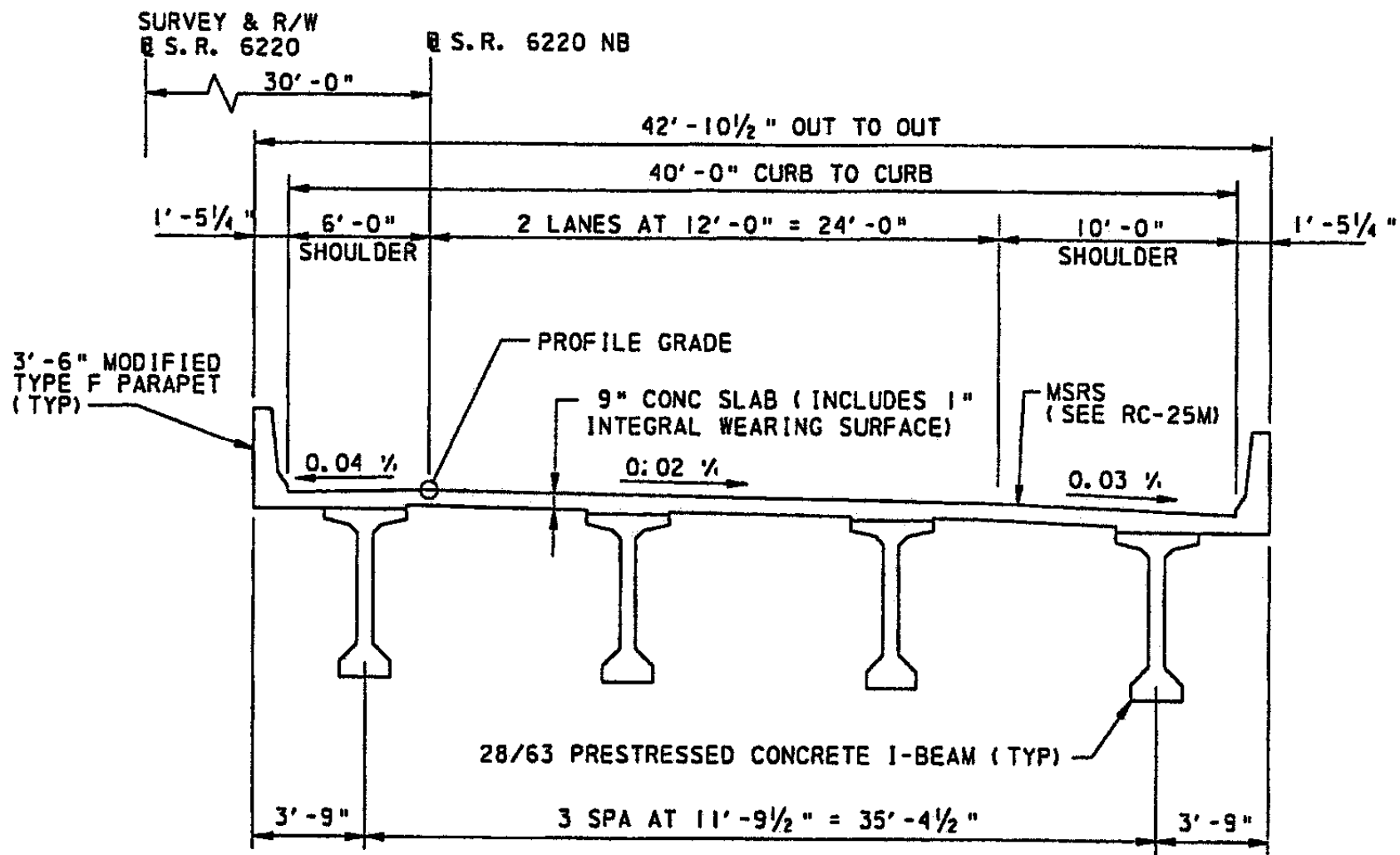


Figure 2.10. Transverse Section of Bridge 203.

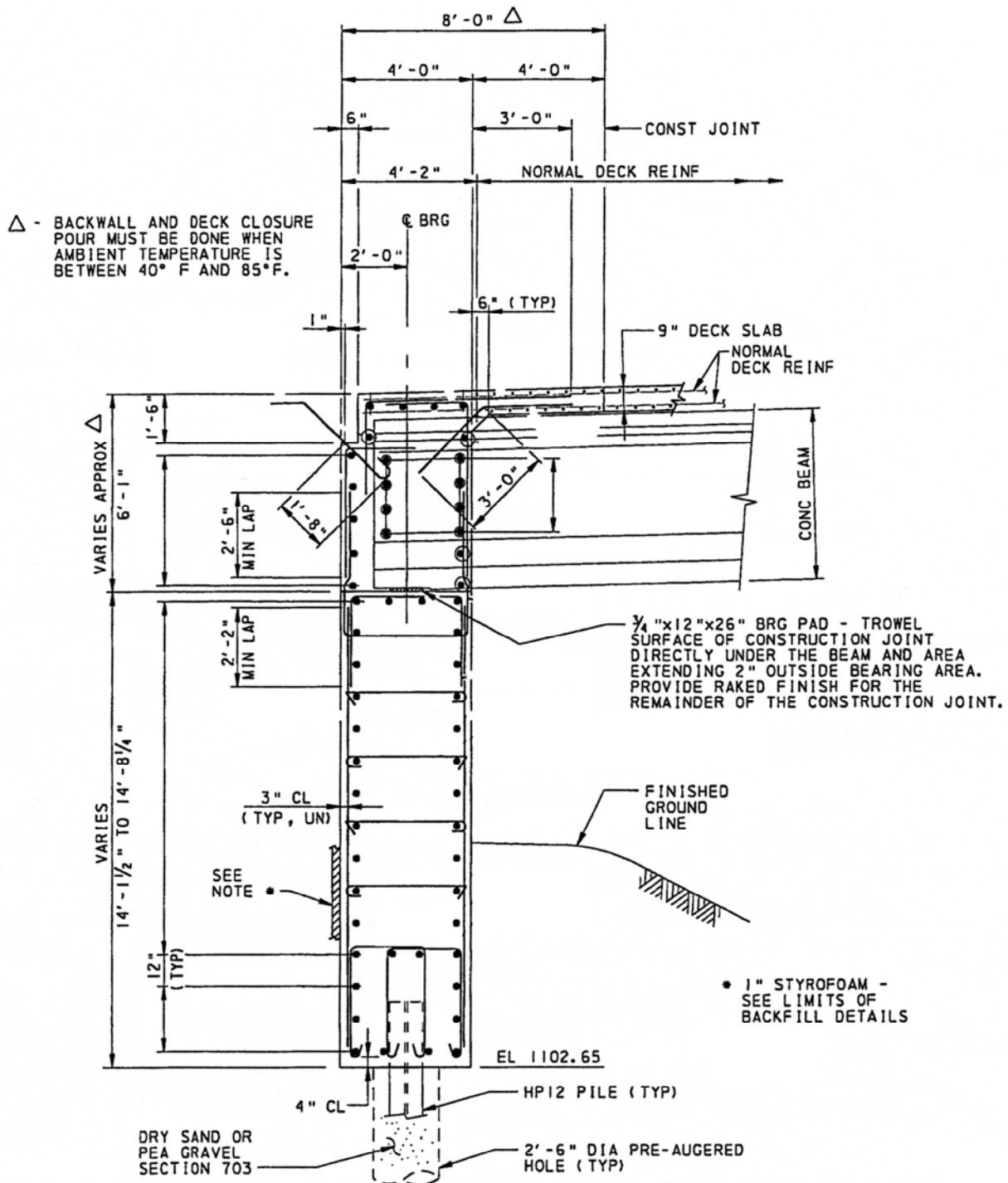


Figure 2.11. Cross-Section of Bridge 203 Abutment 2.

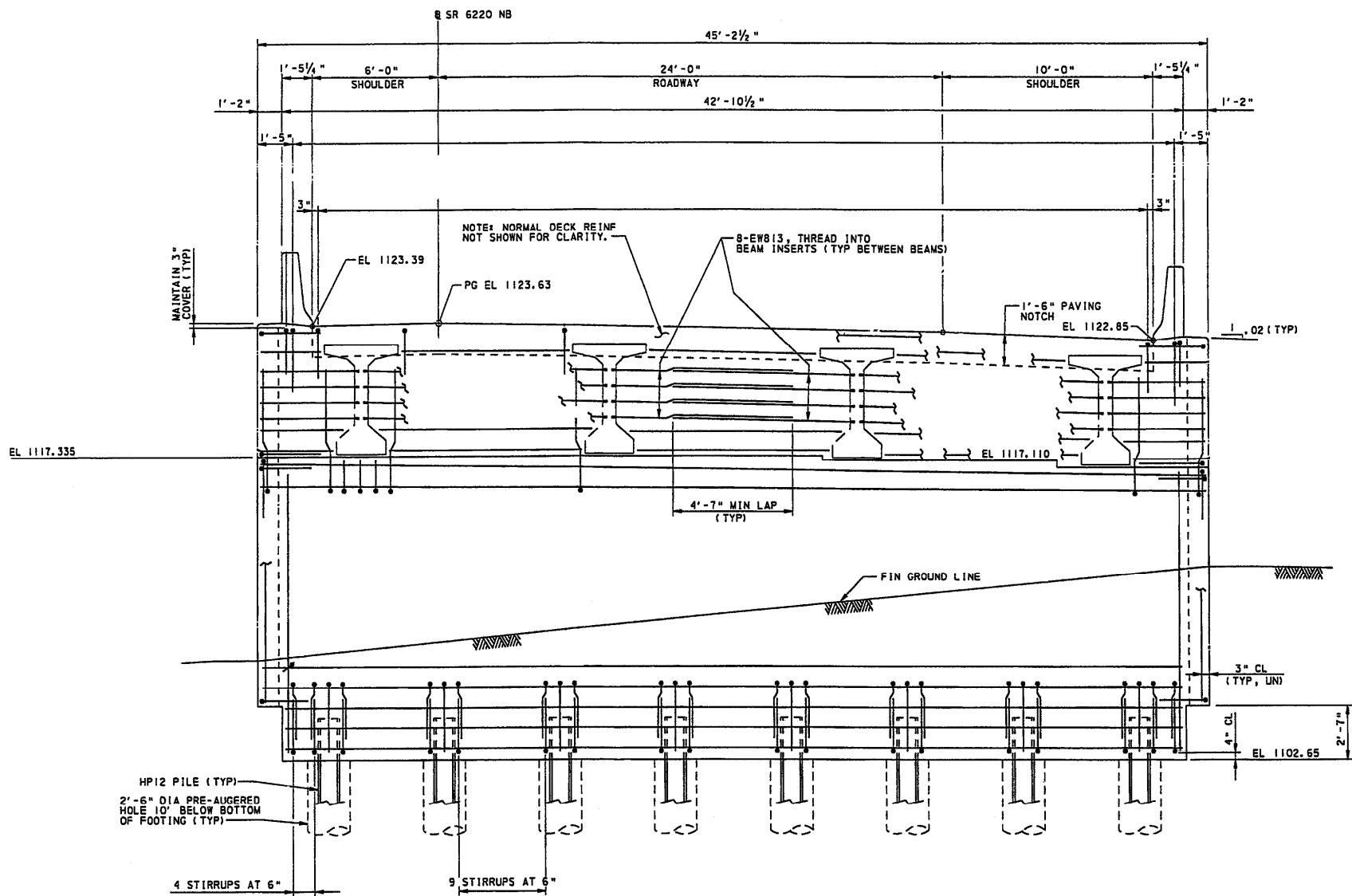


Figure 2.12. Elevation of Bridge 203 Abutment 2.

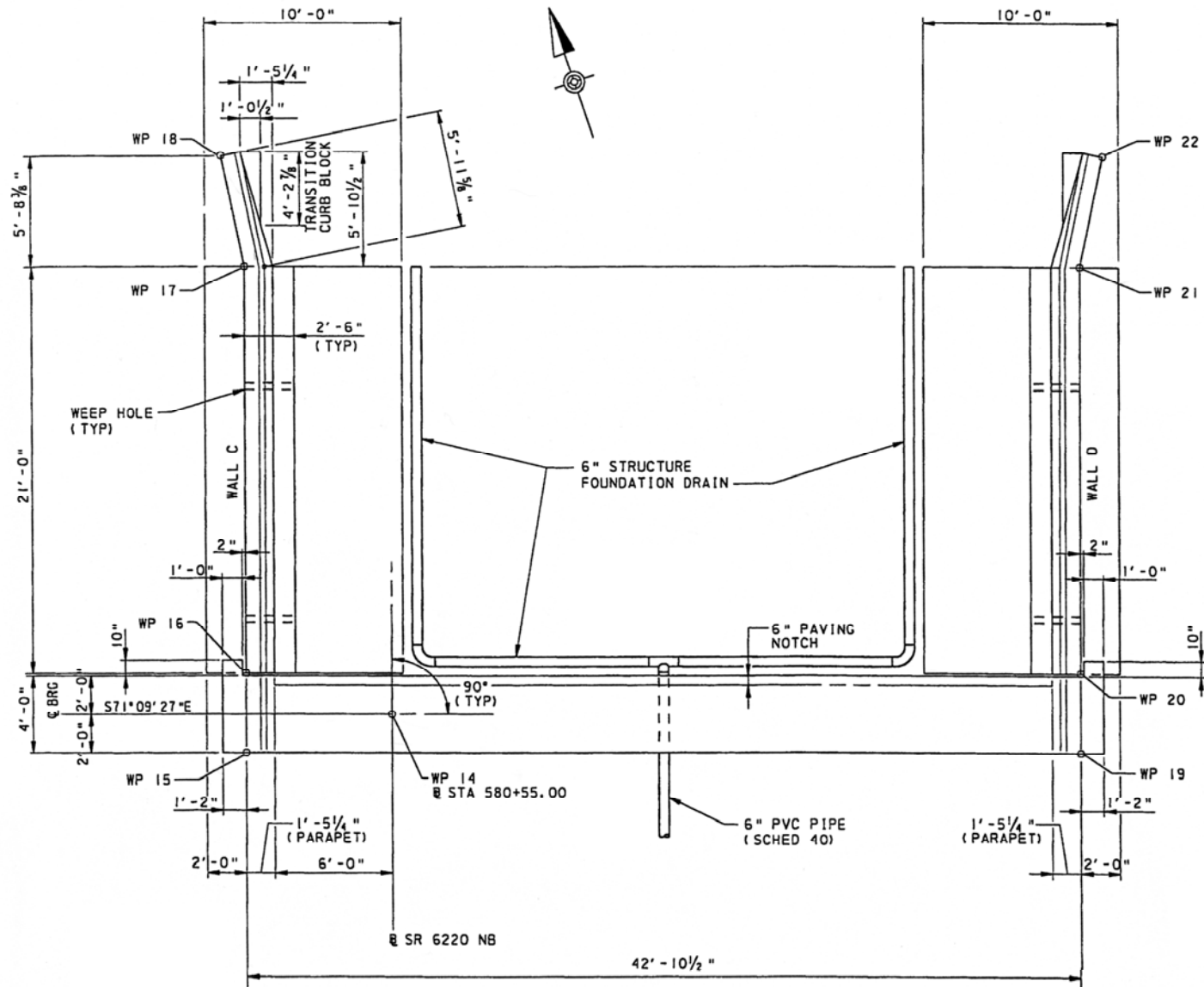


Figure 2.13. Foundation Plan of Bridge 203 Abutment 2.

2.3 BRIDGE 211

Bridge 211 is located in Port Matilda, PA (see Figure 2.1 and Table 2.1). The single-span composite structure consists of simply supported girders bearing on reinforced concrete integral abutments with a span of 114 ft (see Figure 2.14 and Figure 2.15). The four AASHTO Type I-Beam 28/78 prestressed concrete girders are spaced at 11 ft 1½ inches and are cast integrally with both abutments (see Figure 2.16 and Figure 2.17). The total abutment height is approximately 14 ft 3 inches, which is not in conformance with the current BD-667 Standard of 4 ft 6 inches. Each abutment has a single row of (11) HP12x74 piles bending about the weak axis in response to longitudinal movements (see Figure 2.18). A 25-ft-long by 18-inch-thick reinforced concrete approach slab will be constructed at both ends of the bridge. The deck is 9 inches thick, including a 1-inch integral wearing surface, and reinforced with epoxy-coated deformed steel bars. The roadway pavement and the approach slab at both ends of the bridge have neoprene strip seal expansion joints separating them that allow a 4-inch movement capacity. A 1-inch foam board sheet separates the abutment from the backfill to limit passive soil pressure. A 2-inch-thick foam board sheet separates the abutment wing wall to isolate component movements (see Figure 2.19).

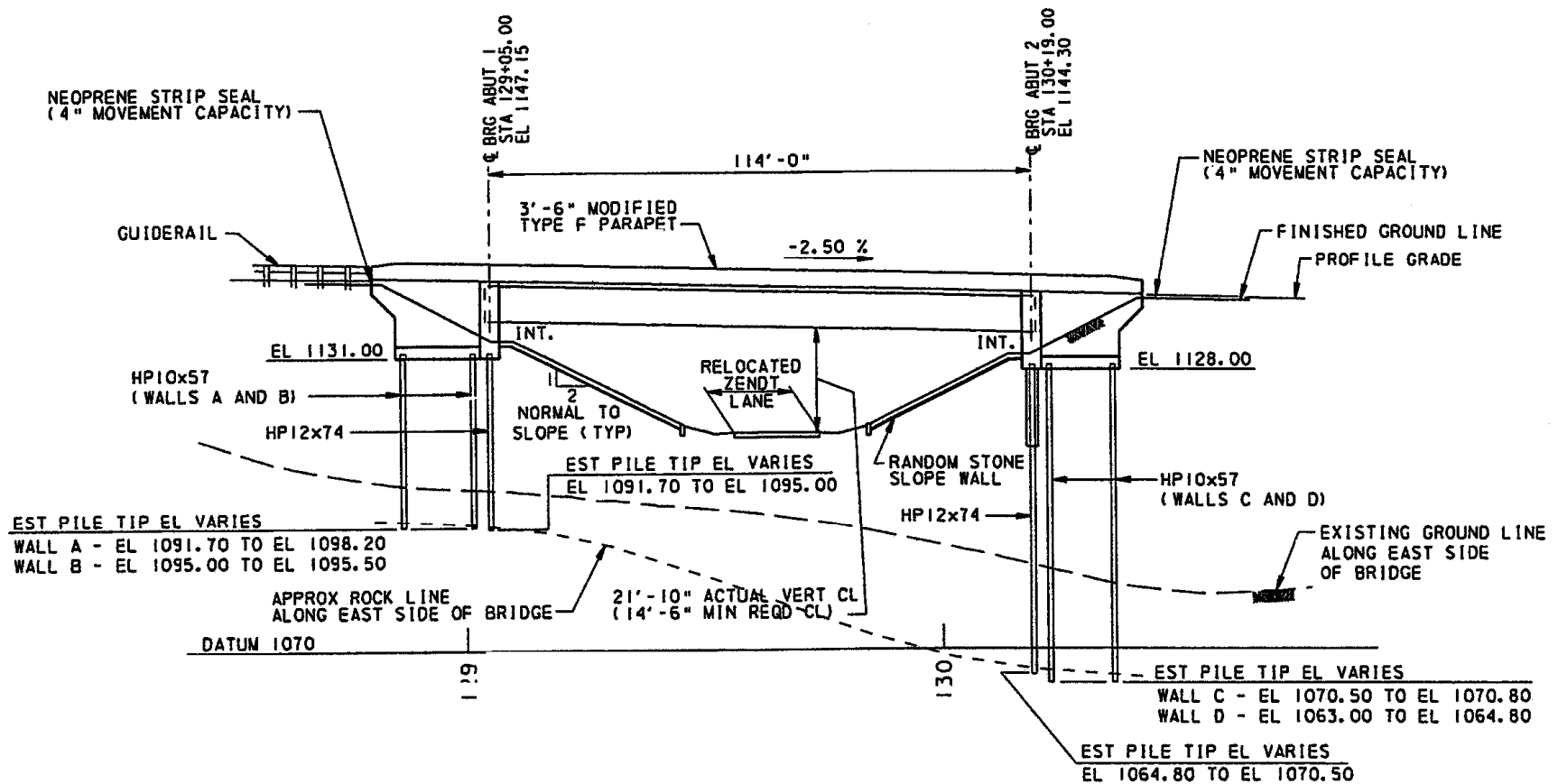


Figure 2.15. Elevation of Bridge 211.

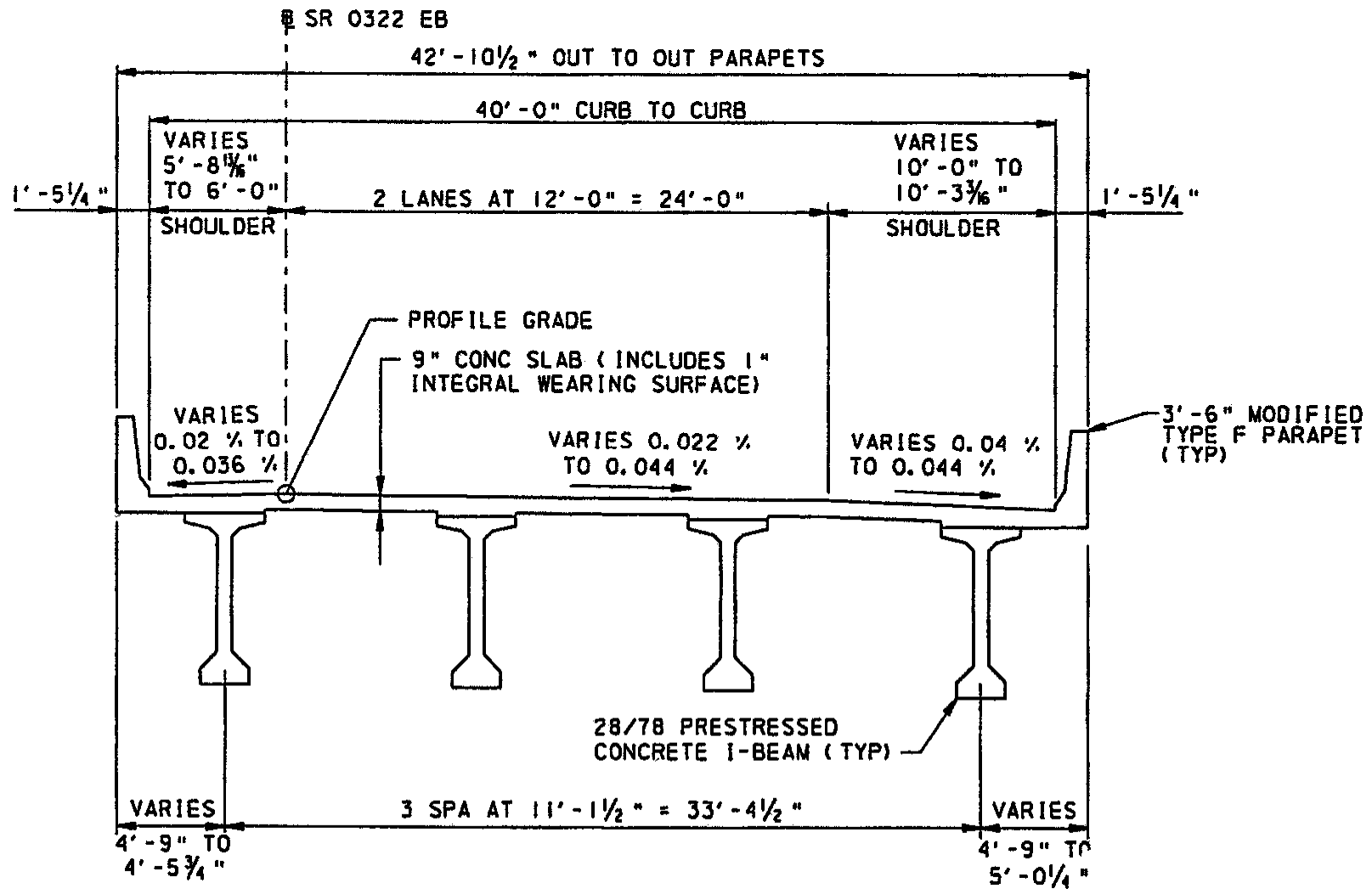


Figure 2.16. Transverse Section of Bridge 211.

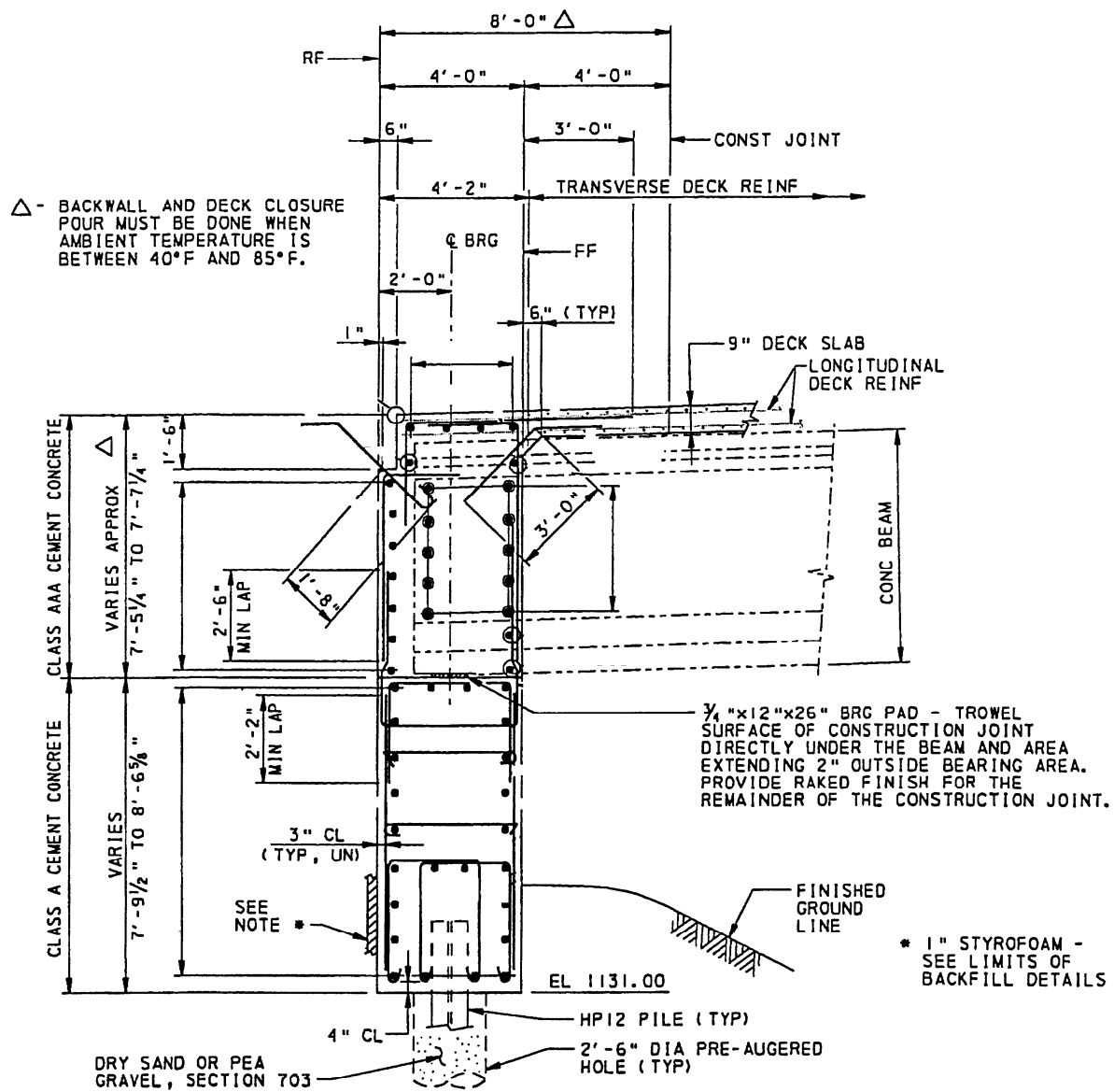


Figure 2.17. Cross-Section of Bridge 211 Abutment 1.

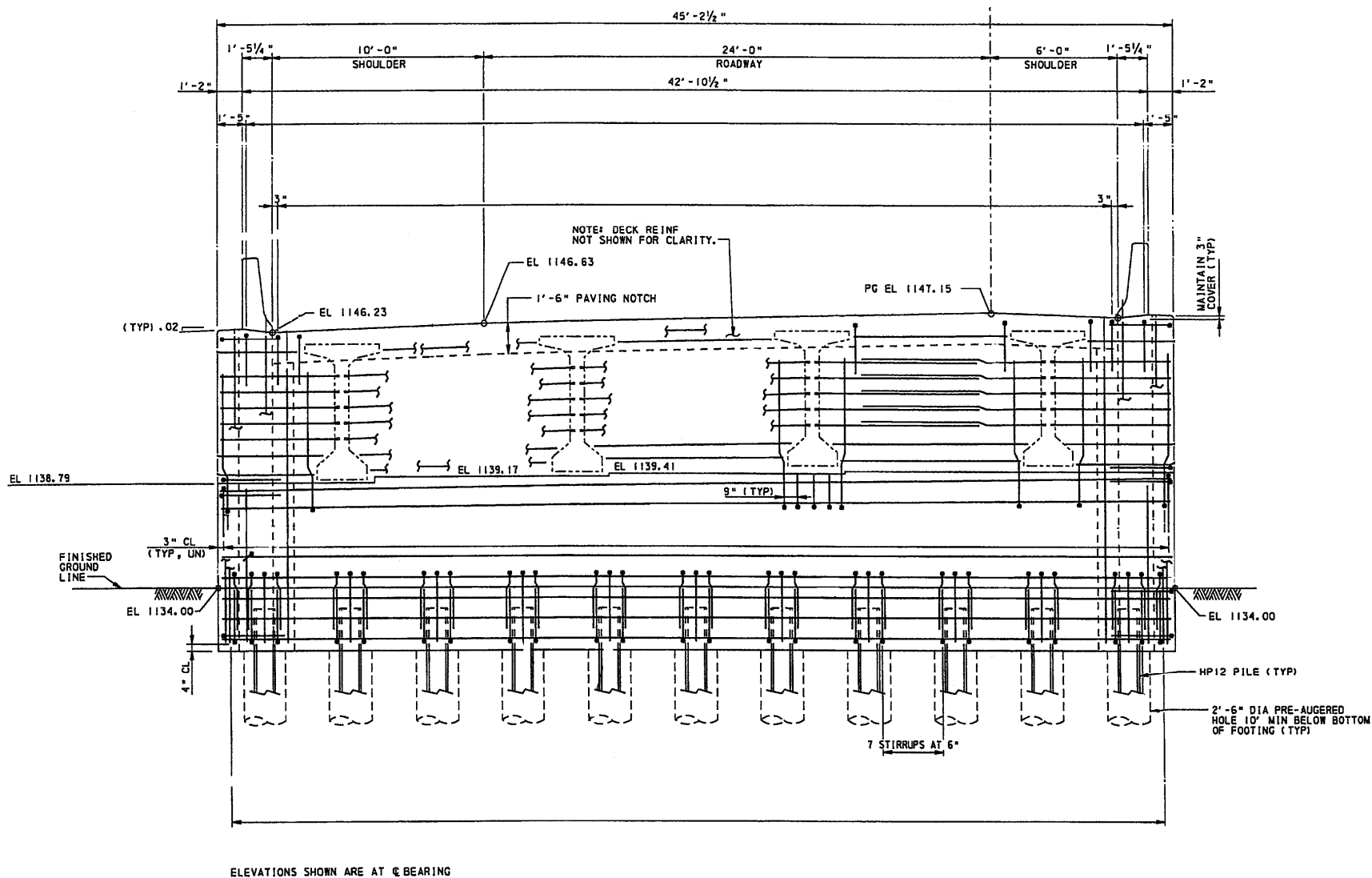


Figure 2.18. Elevation of Bridge 211 Abutment 1.

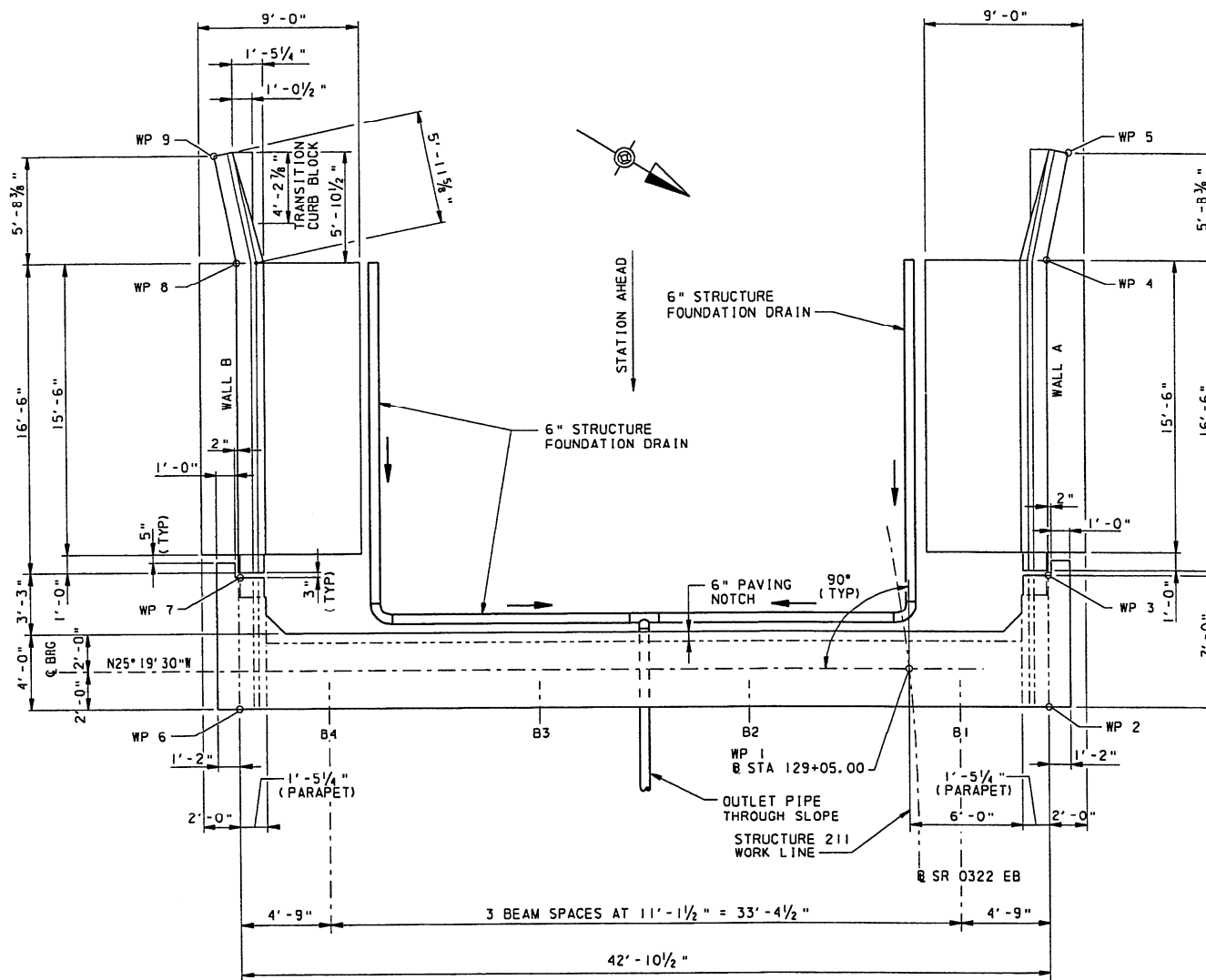


Figure 2.19. Foundation Plan of Bridge 211 Abutment 1.

2.4 BRIDGE 222

Bridge 222 is located in Port Matilda, PA (see Figure 2.1 and Table 2.1). The single-span composite slab on girder structure consists of four simply supported girders bearing on reinforced concrete integral abutments with a span of 62 ft (see Figures 2.20 and 2.21). The four PA I-Beam 24/48 prestressed concrete girders are spaced at 11 ft 9½ inches and are cast integrally with both abutments (see Figure 2.22 and 2.23). The total abutment height is approximately 12 ft 9 inches, which is not in conformance with the current BD-667 Standard of 4 ft 6 inches.

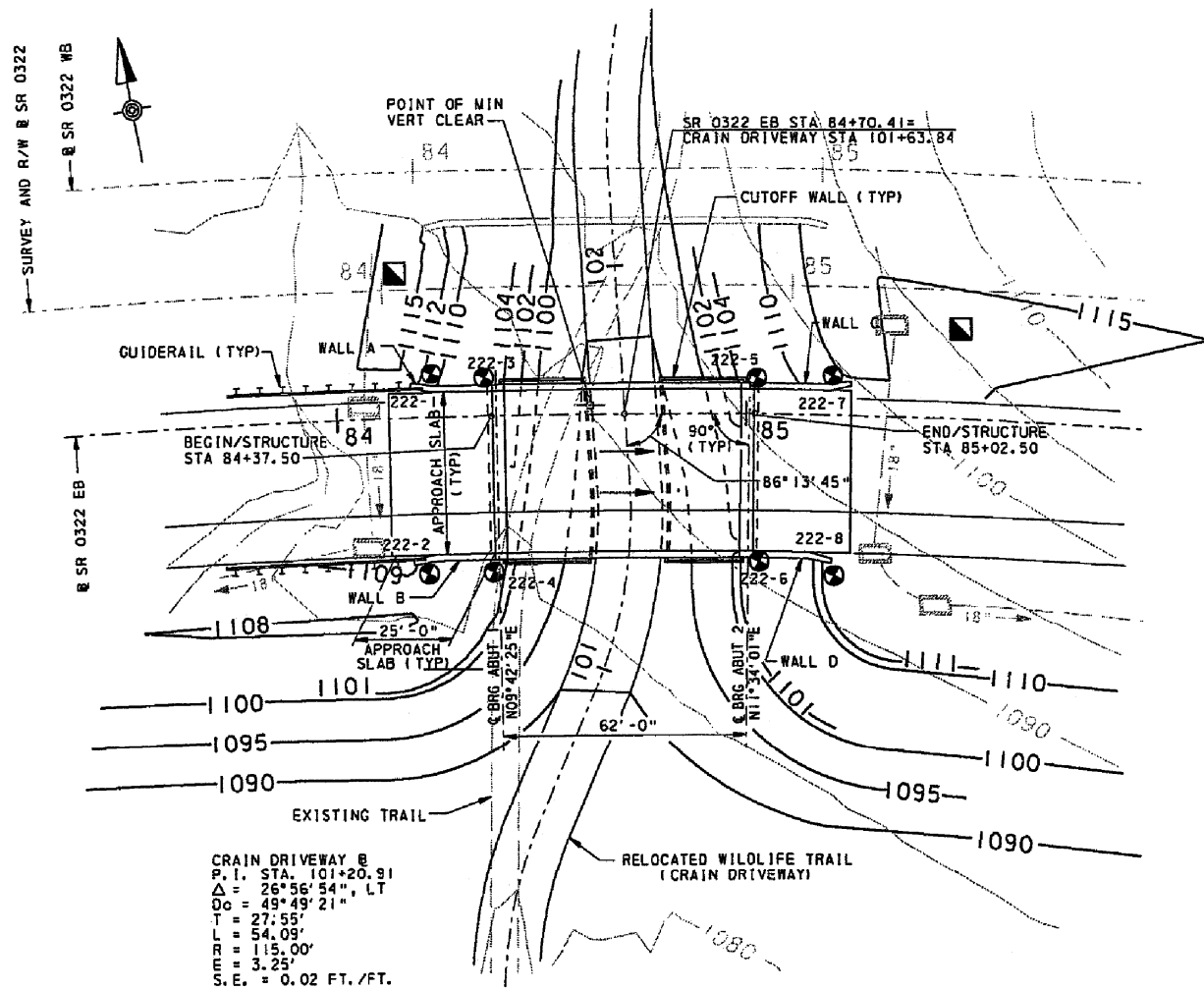


Figure 2.20. Site Plan of Bridge 222.

The abutment at the west end of the bridge has a single row of (11) HP12x74 piles, and the abutment at the east end of the bridge has a single row of (9) HP12x74 piles bending about the weak axis in response to longitudinal movements (see Figure 2.24). There is a 25-ft- by 18-inch-thick reinforced concrete approach slab at both ends of the bridge. The deck is 9½ inches thick, including a 1-inch integral wearing surface, and is reinforced with epoxy-coated deformed steel bars. The roadway pavement and approach slab is separated by a neoprene strip seal expansion joint that allows 4 inches of movement capacity. Behind the abutment is a 1-inch-thick foam board sheet intended to reduce backfill passive soil pressure. A 2-inch-thick foam board sheet between the abutment and wing wall isolates component movements (see Figure 2.25).

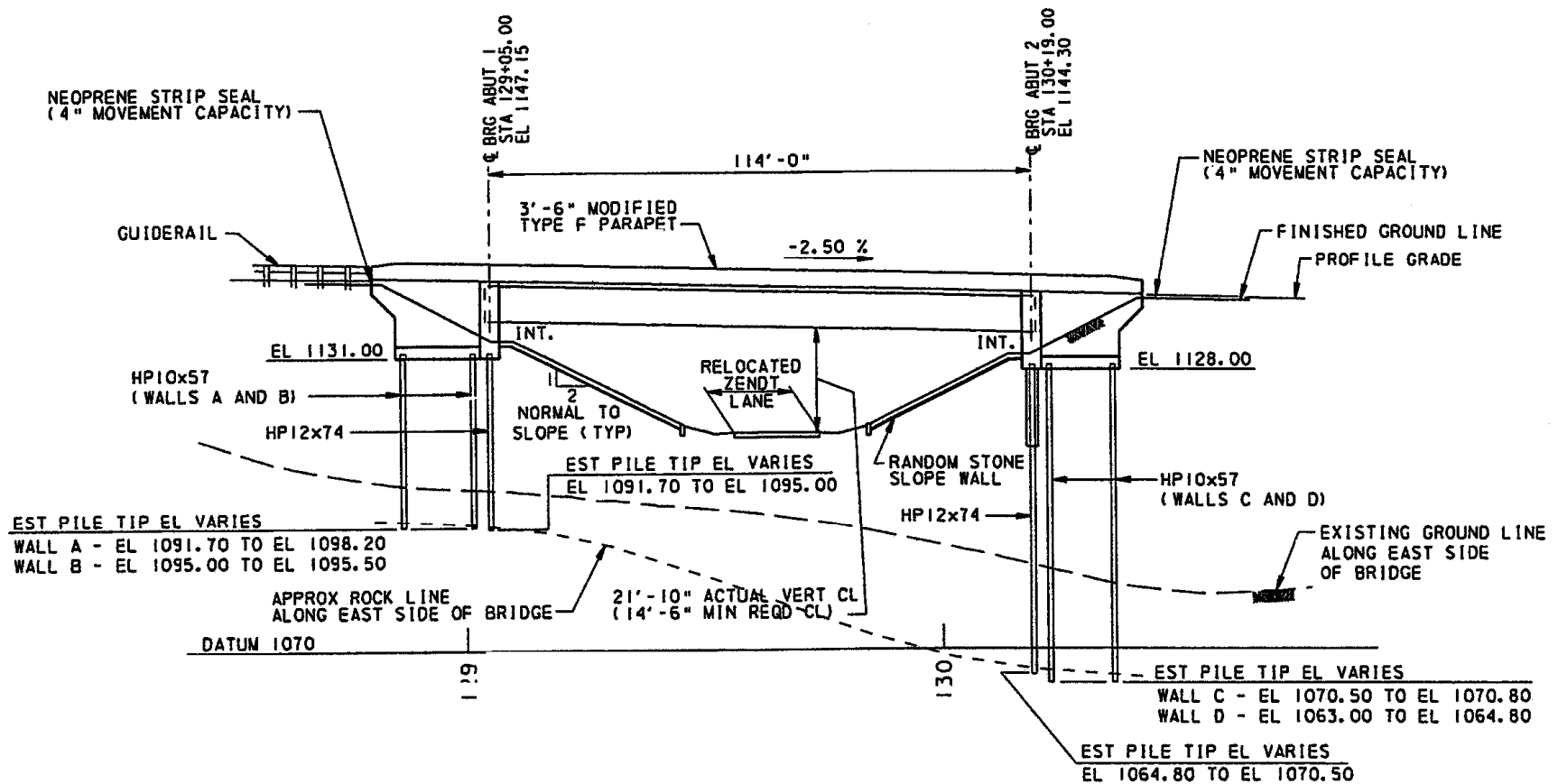


Figure 2.21. Elevation of Bridge 222.

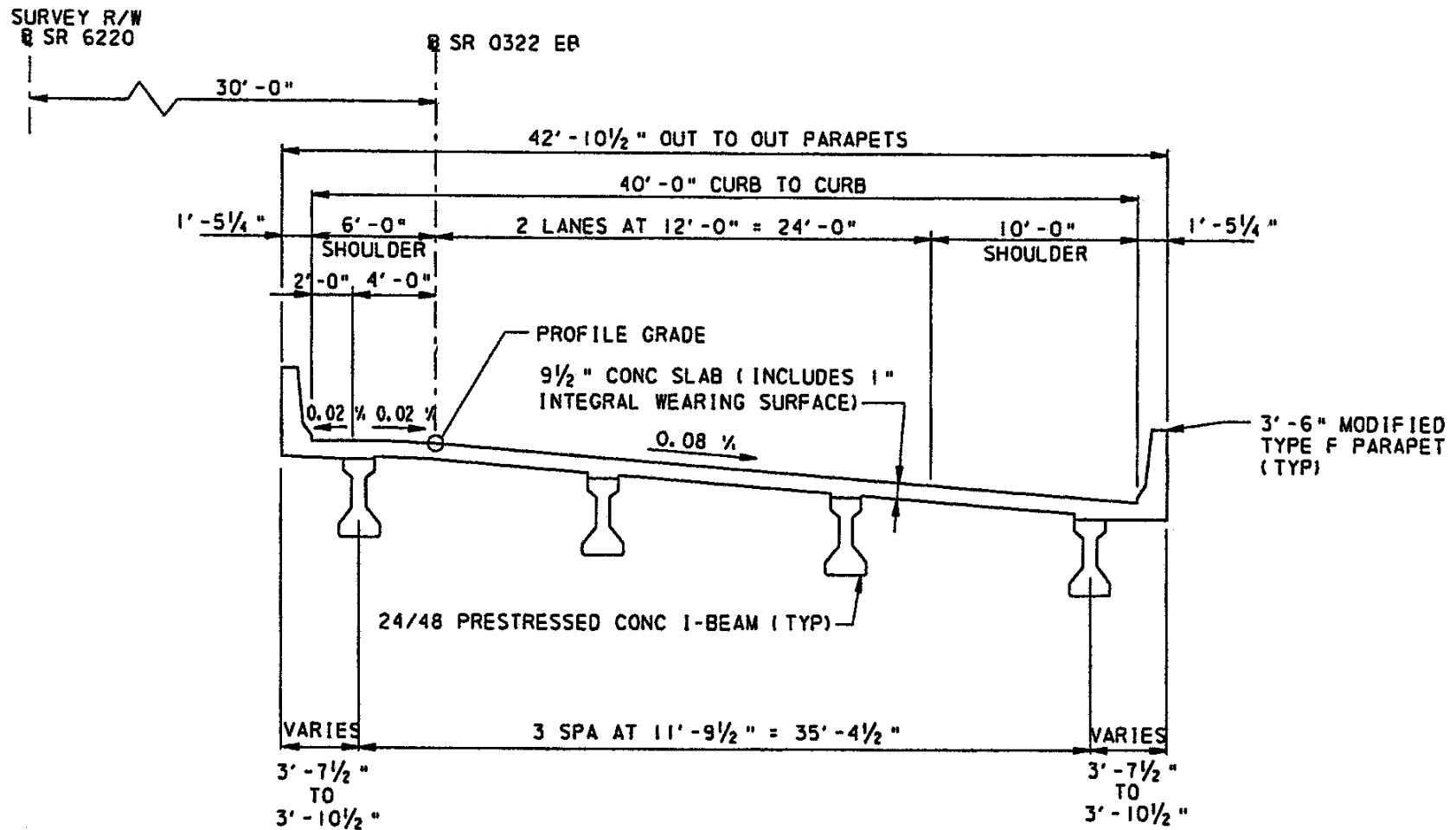


Figure 2.22. Transverse Section of Bridge 222.

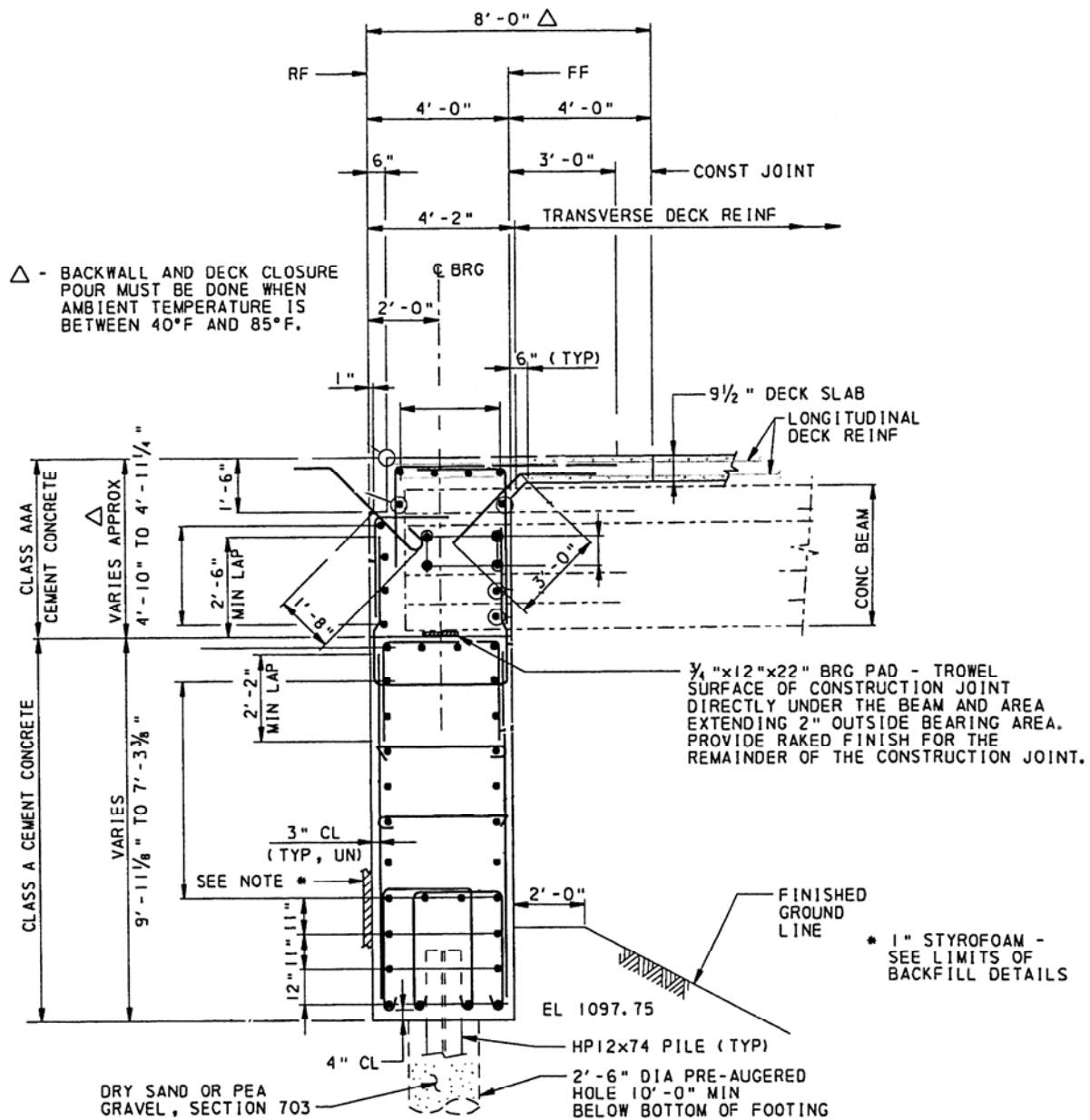


Figure 2.23. Cross-Section of Bridge 222 Abutment 1.

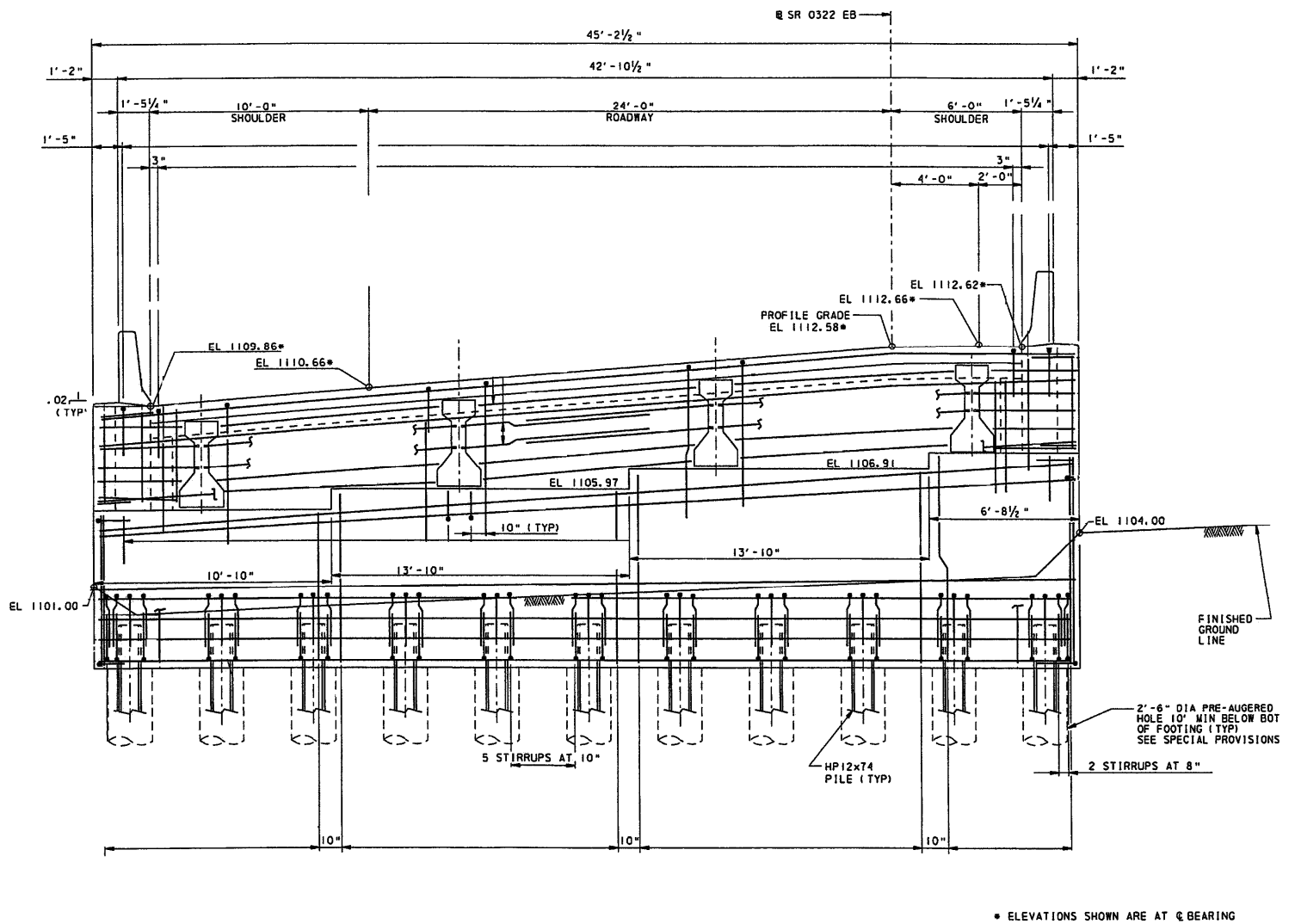


Figure 2.24. Elevation of Bridge 222 Abutment 1.

2.5 Weather Station

The weather station was installed near bridge 203 in Port Matilda, PA, on June 11, 2002. Collection of data from the weather station began in August 2002. Data monitored includes ambient air temperature, relative humidity, precipitation, wind speed, wind direction, and solar radiation as indicated in Figure 2.26.



Figure 2.26. Photograph of Weather Station.

2.6 Wireless Data Transfer Network

Each of the five data acquisition systems operating at bridges 109, 203, 211, and 222 and the weather station are capable of transferring acquired data via modem and cell phone to a central computing location for reduction, processing, and storage. Integral abutment bridge engineering data have been continuously collected and downloaded every two weeks to four weeks. AirLink Redwing CDMA 3110 VZW communication modems are installed at each site and connected to an antenna and the data acquisition systems. Each modem is assigned a unique electronic serial

number (ESN) by the manufacturer that identifies it to the cell service provider (see Table 2.2).

A schematic wireless network is illustrated in Figure 2.27.

Table 2.2. Details of Cell Modems and Cell Numbers.

Location	Modem ESN	Cell Phone No.
Bridge 109	09900-644-688	814-404-1253
Bridge 203	09900-477-259	814-404-0014
Bridge 211	09900-644-710	814-404-9613
Bridge 222	09900-648-389	814-933-6585
Weather	09900-643-977	814-404-0699

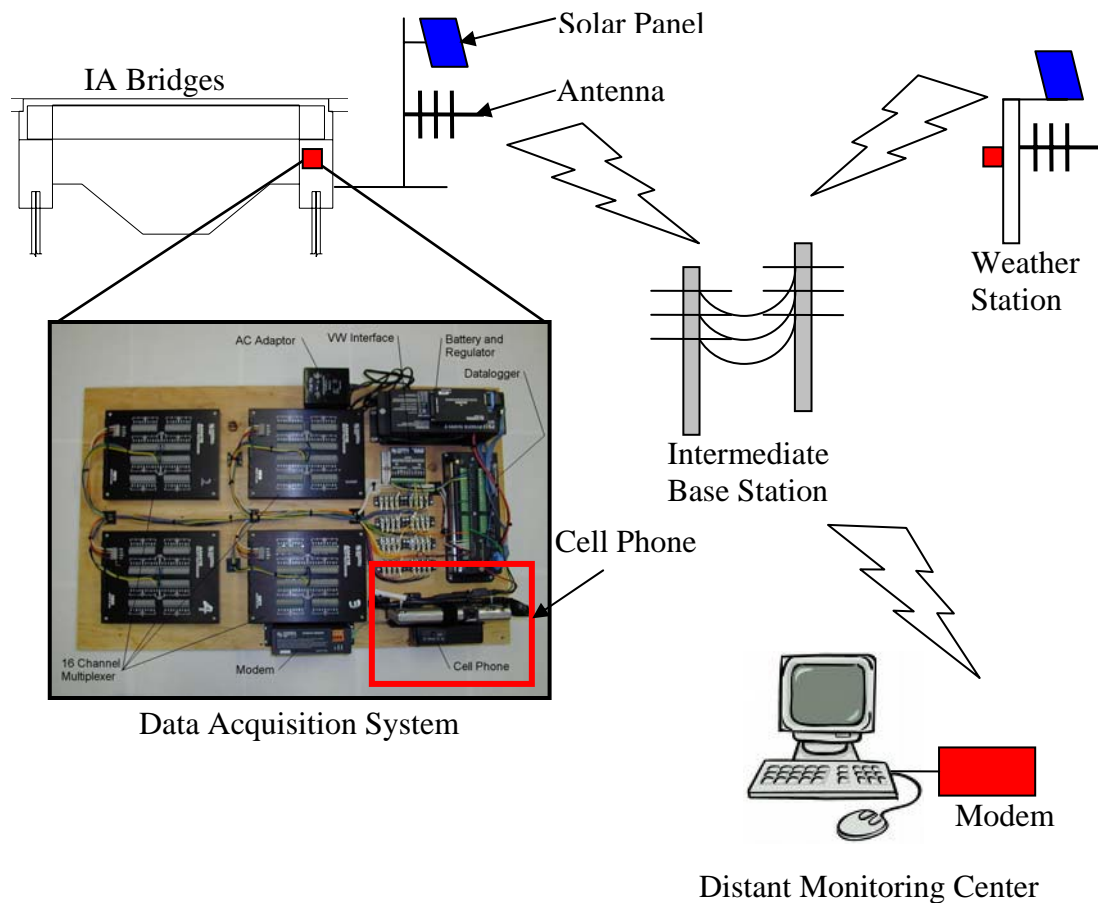


Figure 2.27. Schematic of Wireless Network.

AirLink Redwing CDMA 3110 VZW Communication Modems

The Airlink Redwing communication modem (see Figure 2.28) is ideal for bridge monitoring applications that require real-time communications. The Redwing cell phone modem is based on CDMA (Code Division Multiple Access), which is the highly secured digital radio network technology used by many cellular providers. The modem can communicate at speeds between 60 and 144 kbps. For compatibility with the data acquisition system CR10X (Campbell Scientific, Inc.), the band rate is set to 9600 bps with 8 data bits. System power is provided by a solar panel mounted on a mast and powered by a regulated, 7.5 amp-hour, deep-cycle battery.



Figure 2.28. AirLink Redwing CDMA 3110 VZW.

SC32B Interface

The SC32B (see Figure 2.29) optically isolated interface connects the RS232 port to the Campbell Scientific CR10X datalogger serial I/O. The interface isolates the connected electrical system (data terminal equipment) from the datalogger, protecting against a ground loop, normal static discharge, and noise. The SC32B also converts datalogger logic levels to RS232 logic levels that are required to communicate with the external modem.

Null Modem Cable

A null modem cable (see Figure 2.30) is required only when the RS232 device is connected to an SC32B and is configured as external data communication equipment. The null modem directly connects between two data terminal equipments using an RS232 serial cable.



Figure 2.29. SC32B.



Figure 2.30. Null modem cable.

Chapter 3

Historical Overview of the Research

The present research being conducted to monitor and evaluate the behavior of I-99 integral abutment bridges was initiated in October 2000. Four integral abutment bridges (IABs) on the I-99 extension and one weather station, all in the Port Matilda, PA, vicinity, were selected prior to construction during the initial stages of the research for detailed field monitoring. Monitoring of bridges 203, 222, 211, and 109 commenced in November 2002, September 2004, November 2003, and September 2005, respectively, and has continued uninterrupted to the present. In addition to the field monitoring program, an extensive numerical modeling effort has been conducted, including two-dimensional, three-dimensional, and parametric studies. Results of the earlier stages of research are presented in reports by Laman *et al.* (2003, 2006), which include an extensive literature review of IAB field monitoring, detailed description of the field monitoring system, current IAB design specifications, evaluation of current IAB PennDOT design tools, and development of IAB analysis methodologies. This interim report is an extension of the research documentation as more data are collected, design methodologies are developed, and examples are presented.

IAB instrumentation and subsequent monitoring has been a significant effort, understood to be the largest, most extensive study of its kind ever conducted nationally. A total of 240 instruments have been installed on the monitored bridges during construction. Sixty-four vibrating wire-based instruments are installed on bridge 109 (Figures 3.1 through 3.5), bridge 203 (Figures 3.6 through 3.8), and bridge 211 (Figures 3.9 through 3.13). Forty-eight vibrating wire-based instruments are installed on bridge 222 (Figures 3.14 through 3.18). Bridge response data include longitudinal abutment displacements, abutment earth pressures, abutment and girder rotations, H-pile bending strain about the weak axis and axial strain, girder strains, and approach slab strains. Weather station (Figure 3.19) collected data consist of ambient temperature, relative humidity, air pressure, solar radiation, wind speed, wind direction, and precipitation. The

collection of field data, beginning from the construction completion of each respective bridge, continued with the absence of vehicle traffic until December 2007. The monitoring program continues to the present, with I-99 open to vehicle traffic.

Based on the collected field data, numerical analysis methodologies have been developed and calibrated to predict integral abutment bridge behavior. Two-dimensional, simplified three-dimensional, and complex three-dimensional numerical models have been developed. In addition, the PennDOT IAB design spreadsheet has been evaluated by comparing the spreadsheet results to the field data, whereas the PennDOT IAB design spreadsheet was intended for use within the geometrical confines of PennDOT Standard BD-667.

Research Conducted from October 2000 to March 2003

The primary research objective during this time period was to investigate, design, procure, develop, and assemble remote, long-term, data acquisition systems for each of the four selected IABs. In addition, a comprehensive literature review of previous and related studies was conducted. During the time period between October 2000 and March 2003, the bridge 203 data acquisition system was installed, and a complete weather-monitoring station was constructed. In conjunction with the bridge monitoring, numerical models of each of the four bridges were developed that formed the initial basis of IAB analysis methodologies. The full report of this time period is available (Laman, et al, 2003).

Research Conducted from June 2005 to July 2006

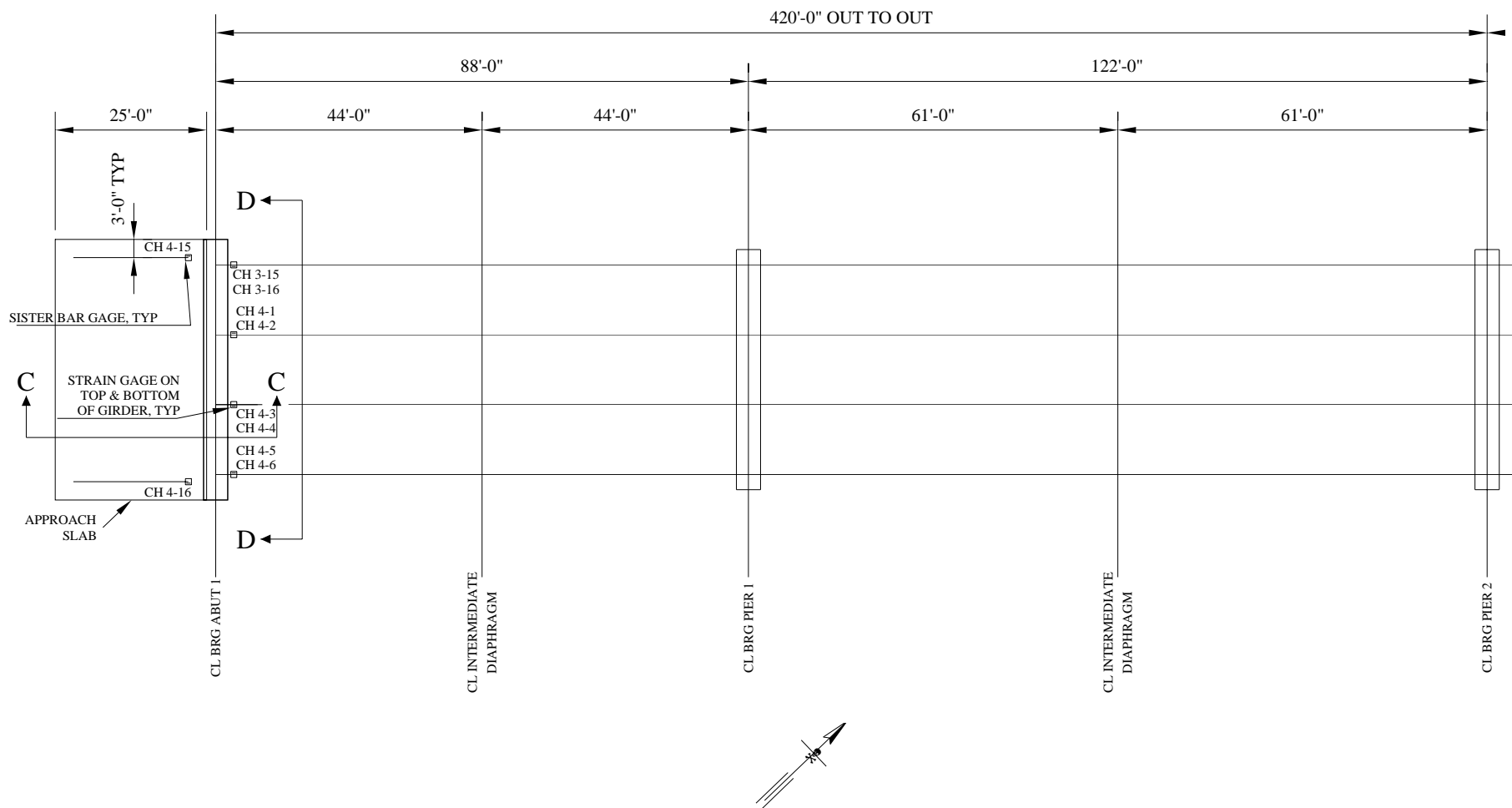
The project involved the instrumentation of bridge 109 and continued monitoring and collection of engineering bridge response data at the three previously instrumented bridges and the weather station. The development of three-dimensional numerical models for bridges 203, 211, and 222 and evaluation of the PennDOT IA Design Spreadsheet was completed. Observed bridge response was compared to predicted bridge response to calibrate the numerical models.

Evaluation of the PennDOT IA Design Spreadsheet was performed, evaluating all four instrumented bridges, to provide suggested program improvements. Predicted bridge response based on the PennDOT IAB program was also compared to the original design to evaluate the Spreadsheet. The full report for this time period is available in Laman, et al, 2006.

Research Conducted from March 2007 to Present

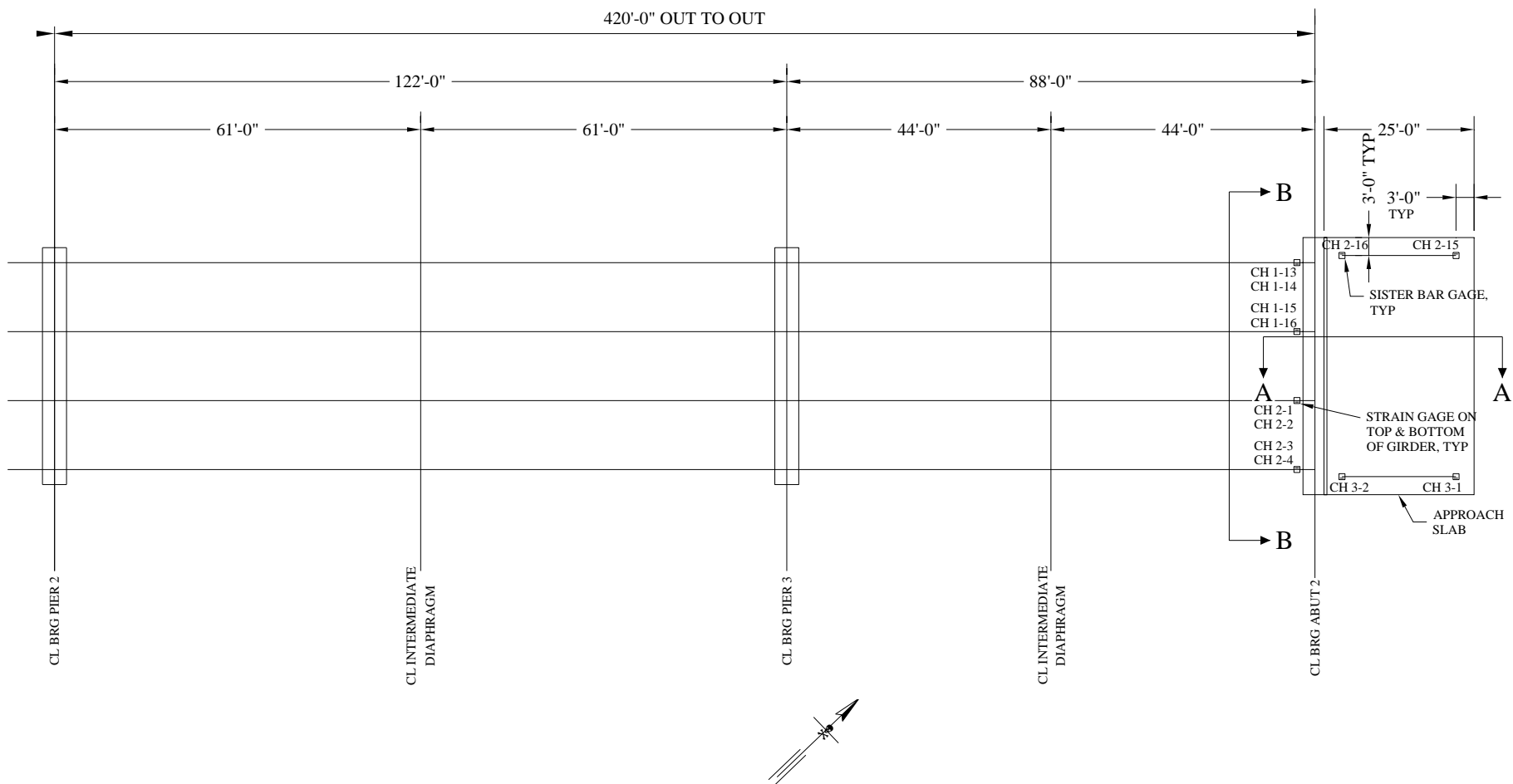
The objective of the present project is to revise and make more accurate IAB design criteria based on observed structural behavior and results of numerical parametric studies. IAB engineering data have been, and continue to be, collected at bridges 109, 203, 211, and 222 and be compiled, processed, and evaluated. Numerical 2D and 3D parametric studies are continuing based on calibrated models developed from observed IAB behavior in order to establish the range of potential applications for integral abutment bridge analysis and design. It has been observed that IAB behavior is significantly different from that predicted by past analysis schemes. Thermally induced displacement magnitudes are typically much smaller than predicted values. Thermally induced rotations and displacements are, in certain locations, opposite predicted rotations and displacements. Thermally induced stresses are not currently incorporated into design aids and guidelines; however, this project has determined that the stresses are not insignificant.

The present research consists of a number of tasks, including installation of wireless data transfer equipment at each of the five data acquisition locations, continuous data collection and reduction activities, acquisition system maintenance, parametric study of multiple variables, and the development of integral abutment analysis and design procedures with examples. This report is an interim presentation of the progress on this work.



(a) Span 1 and 2

Figure 3.1. Bridge 109 Instrumentation Plan.



(a) Span 3 and 4

Figure 3.1. Bridge 109 Instrumentation Plan.

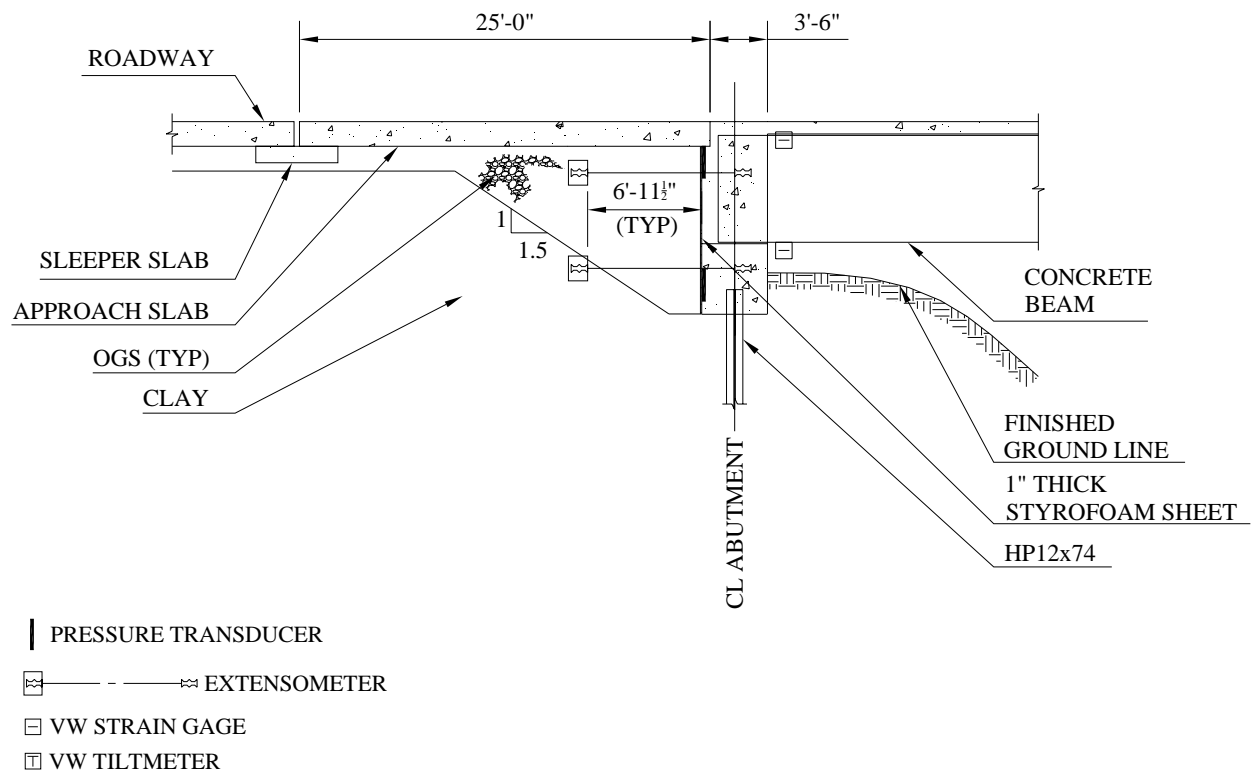


Figure 3.2. Bridge 109 Cross-Section through North Abutment (Section A-A).

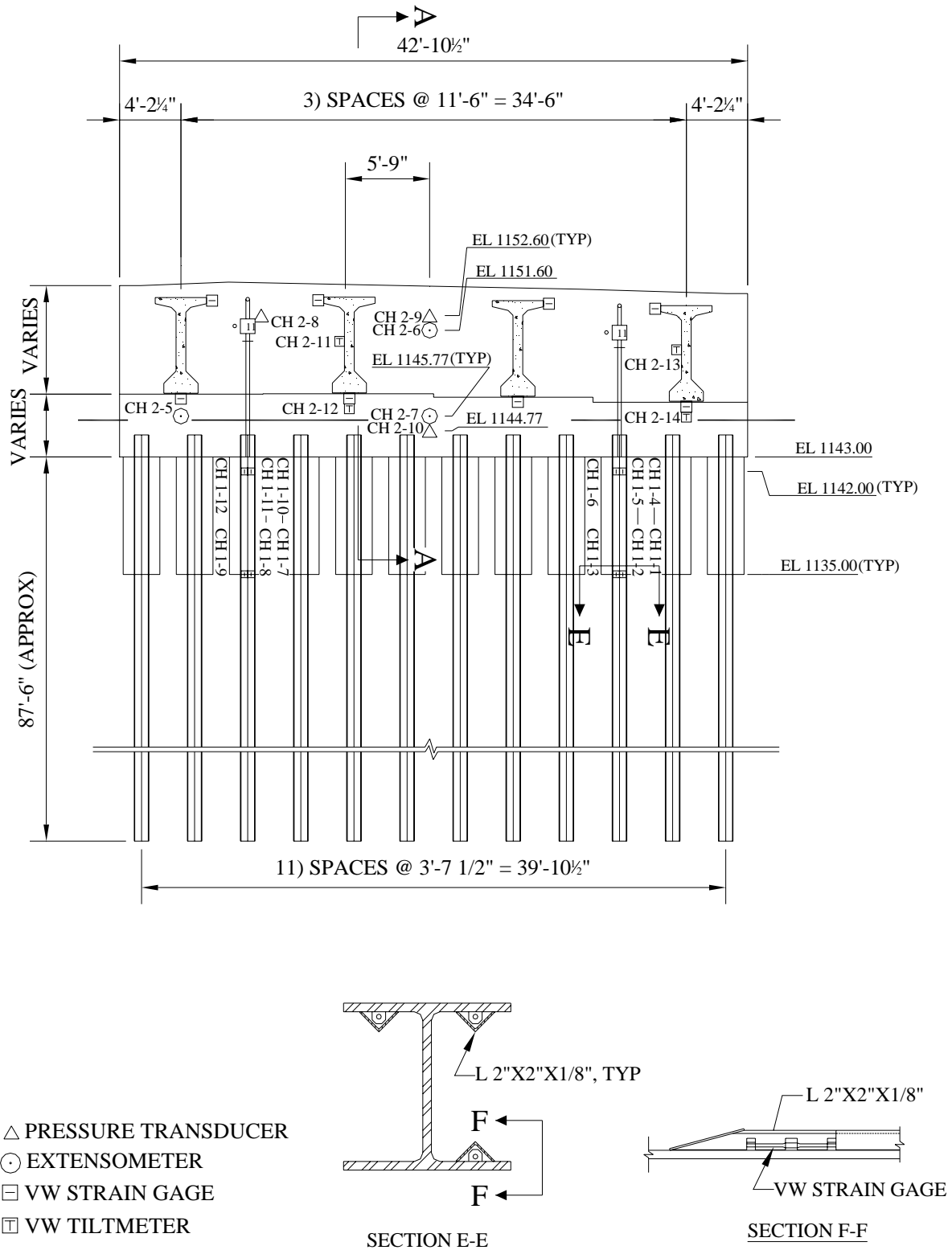


Figure 3.3. Bridge 109 Abutment 2 Elevation (Section B-B).

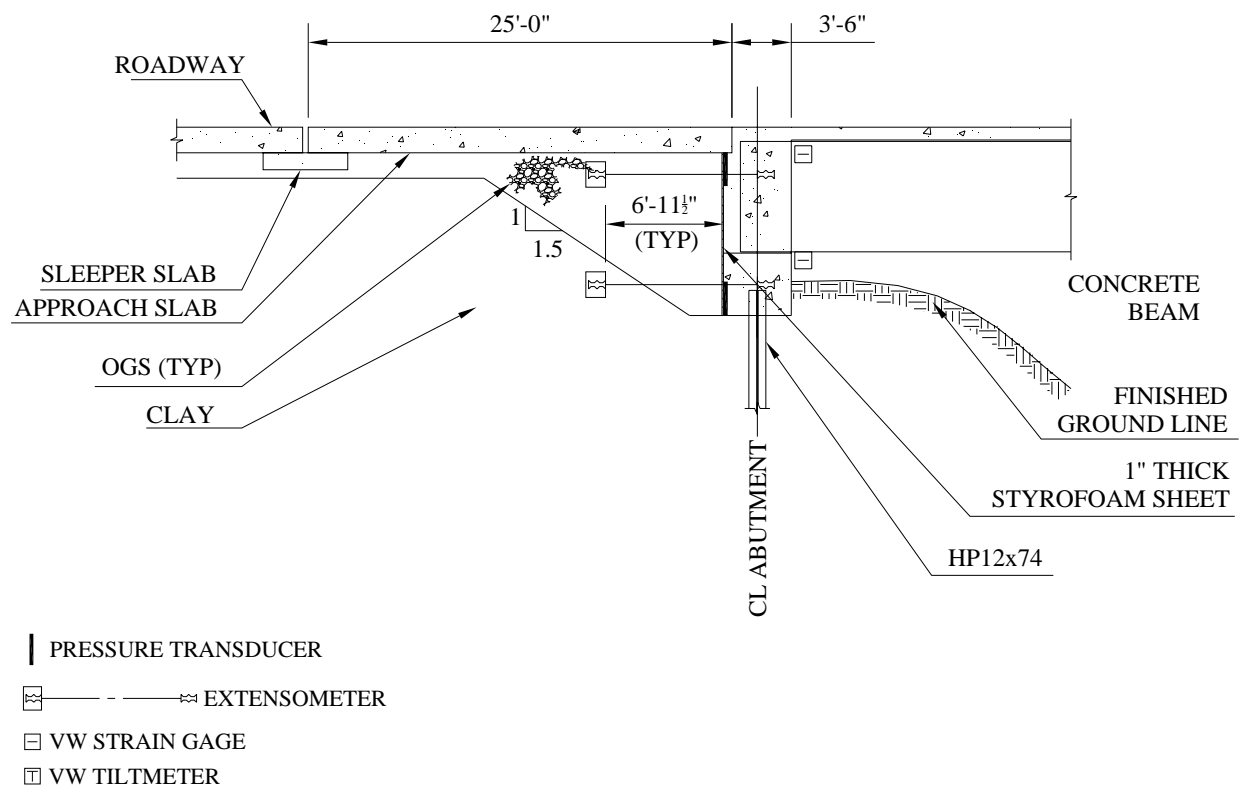


Figure 3.4. Structure 109 Cross-Section Through South Abutment (Section C-C).

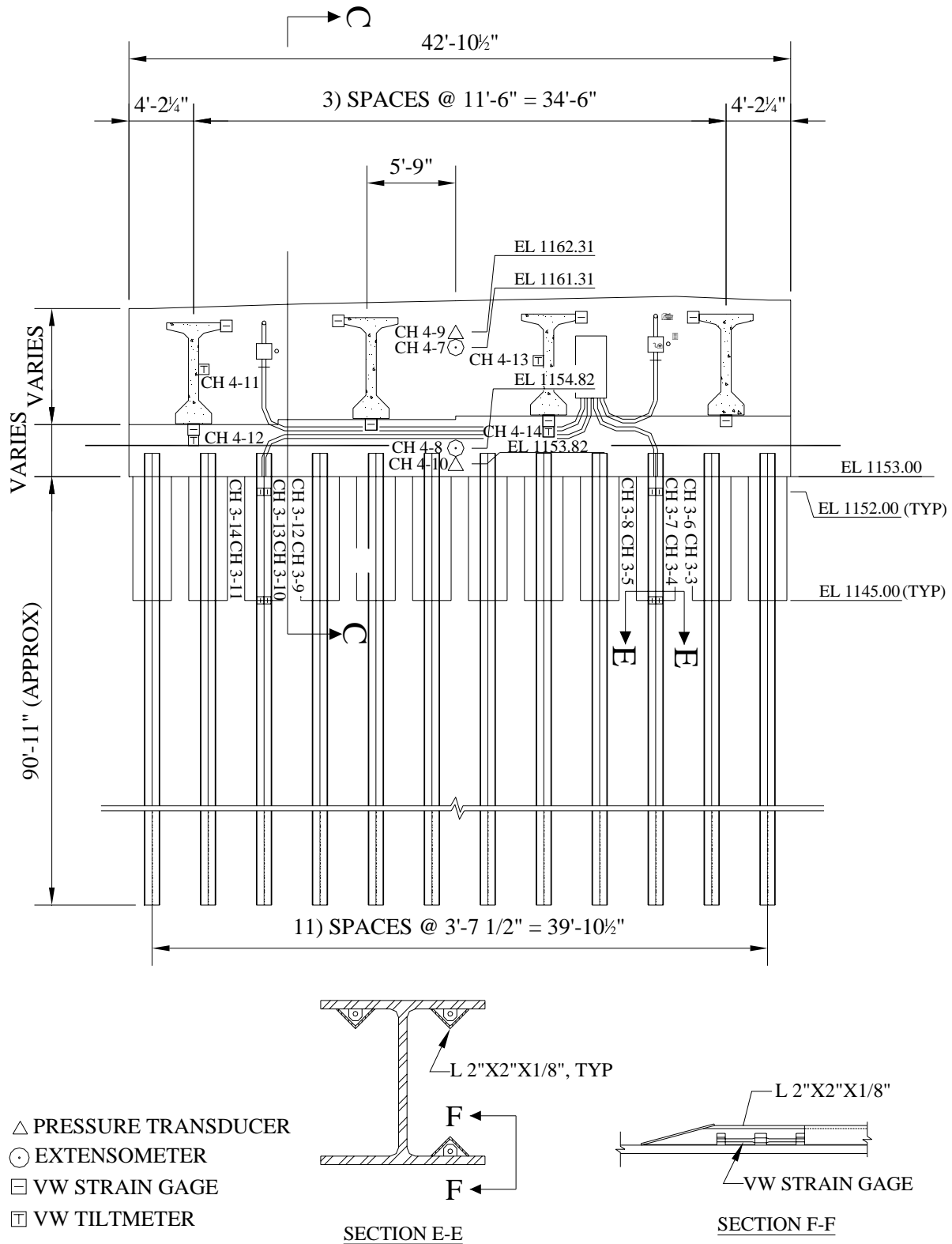


Figure 3.5. Structure 109 Abutment 1 Elevation (Section D-D).

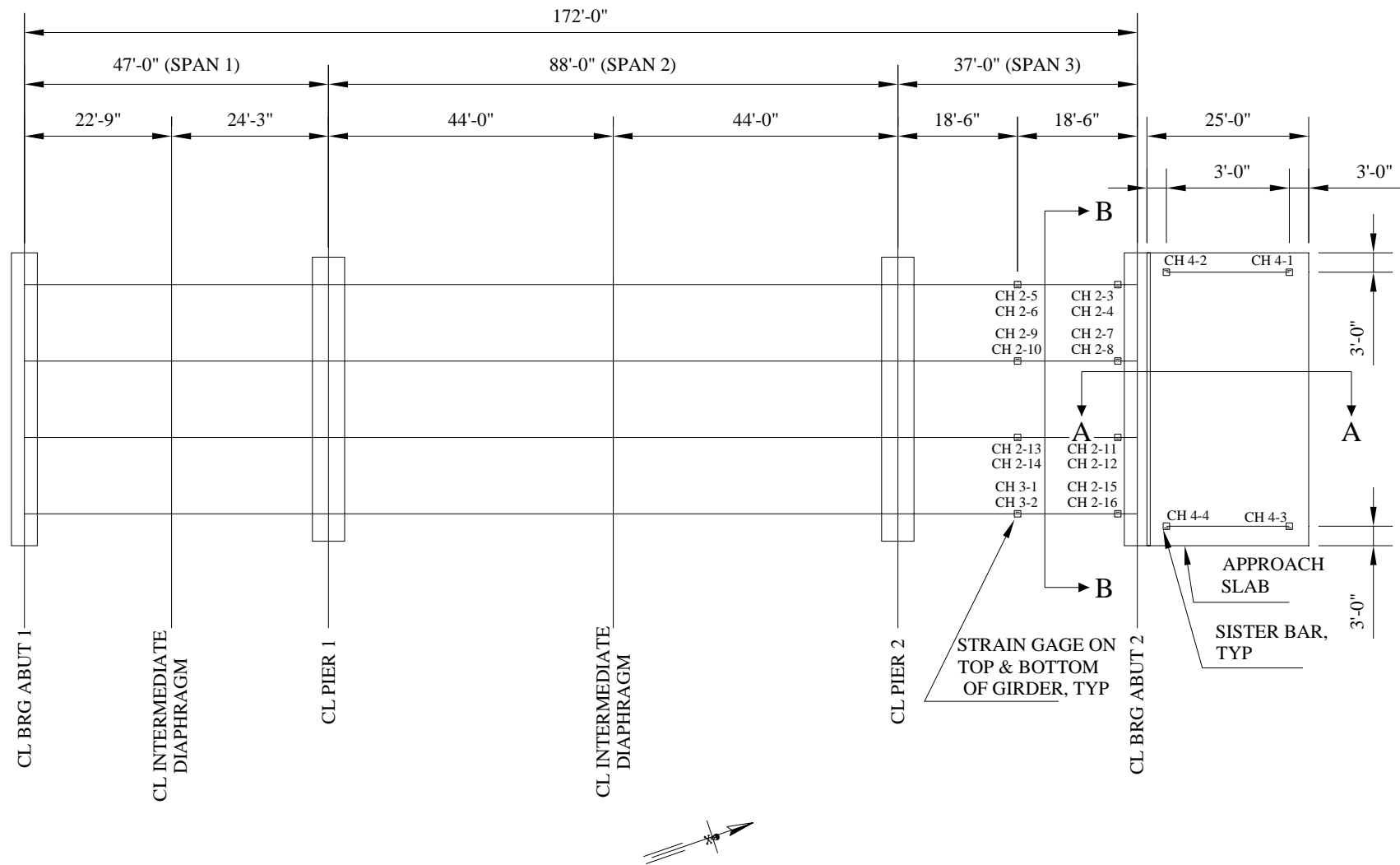


Figure 3.6. Structure 203 Instrumentation Plan.

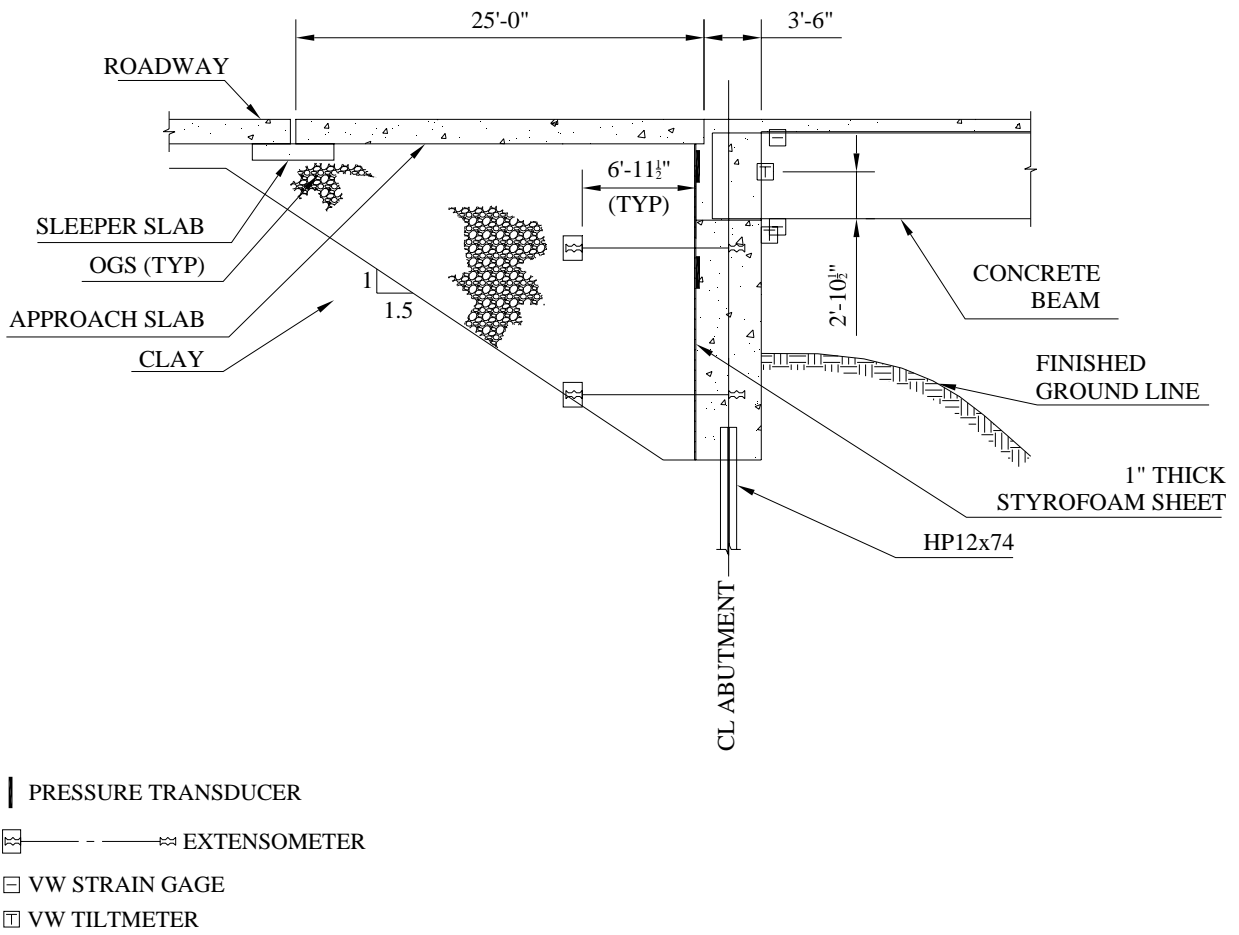


Figure 3.7. Structure 203 Cross-Section Through Abutment 2 (Section A-A).

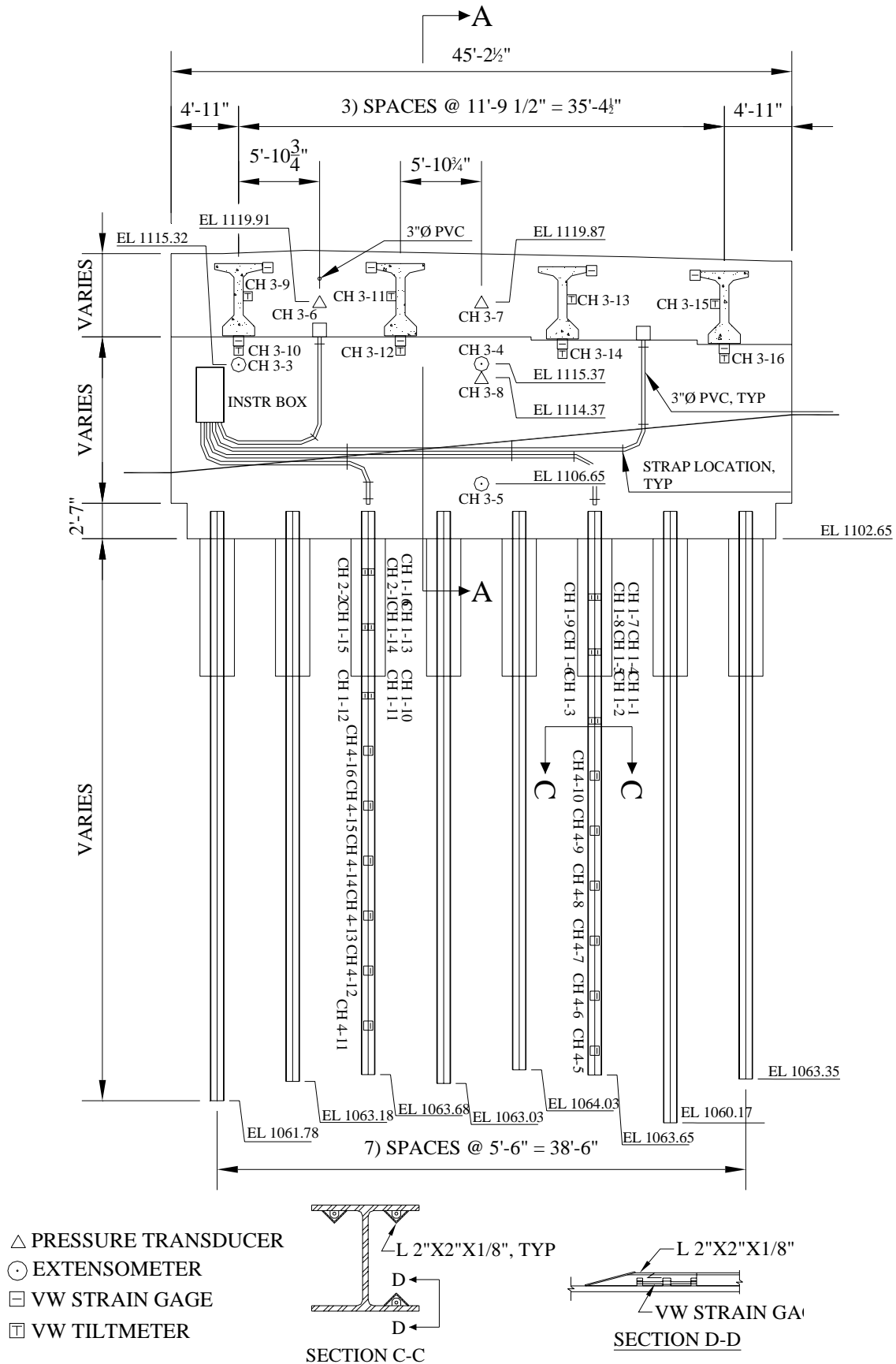


Figure 3.8. Structure 203 Abutment 2 Elevation (Section B-B).

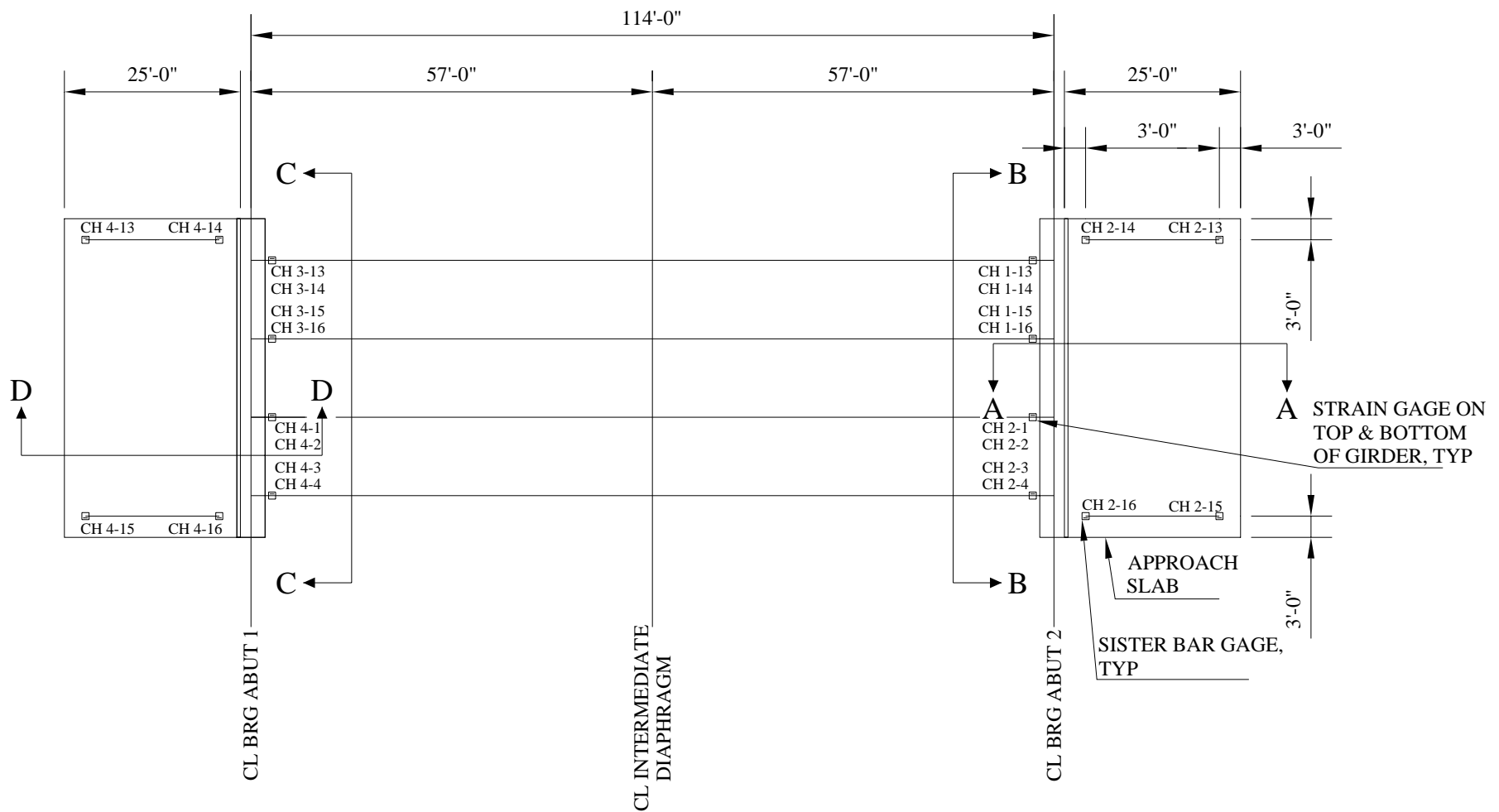


Figure 3.9. Structure 211 Instrumentation Plan.

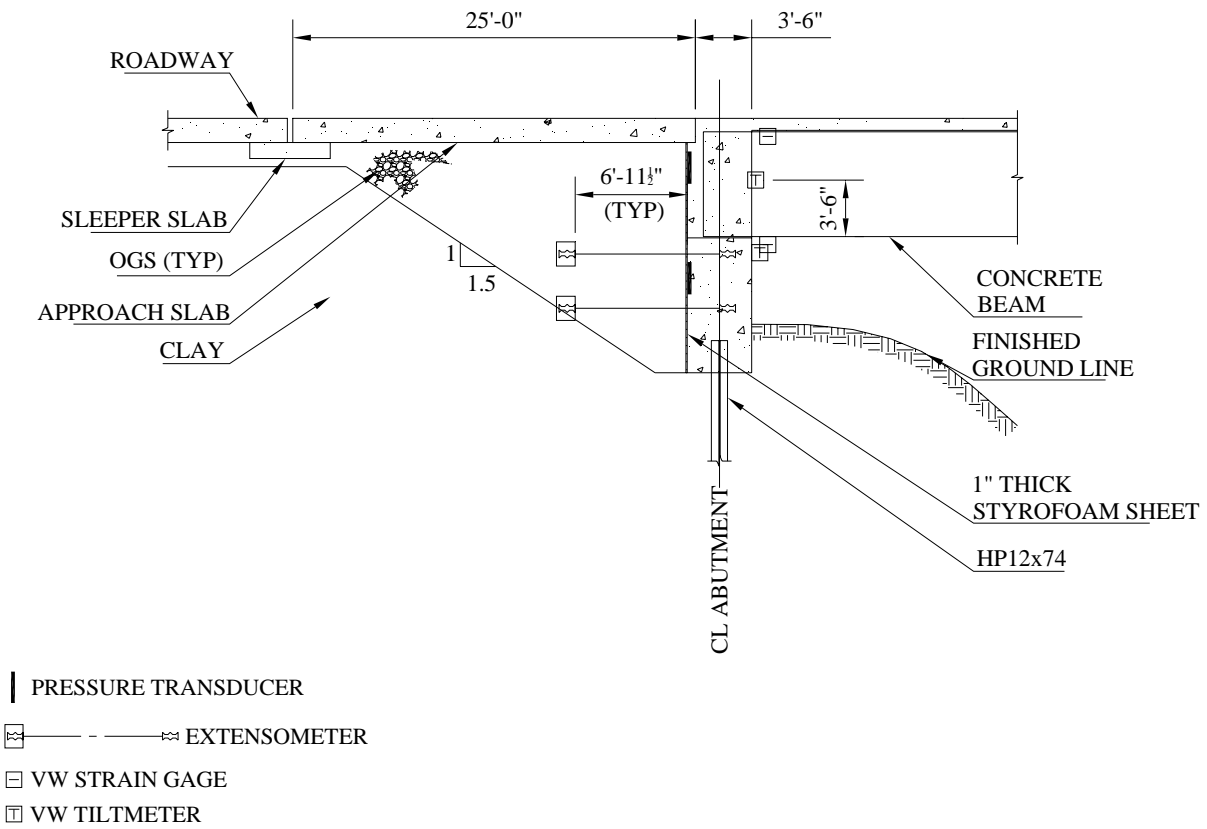


Figure 3.10. Structure 211 Cross-Section Through Abutment 2 (Section A-A).

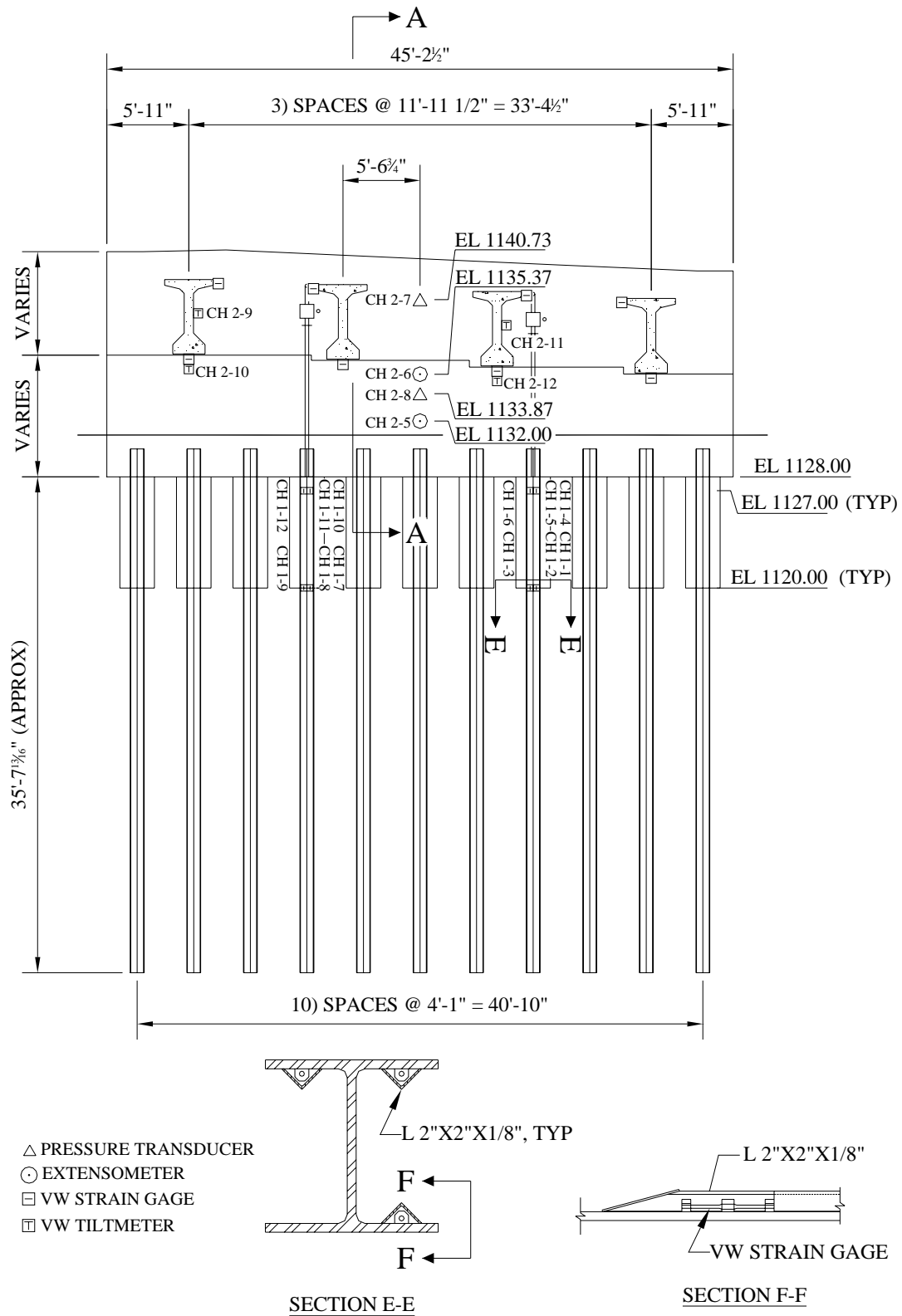


Figure 3.11. Structure 211 Abutment 2 Elevation (Section B-B).

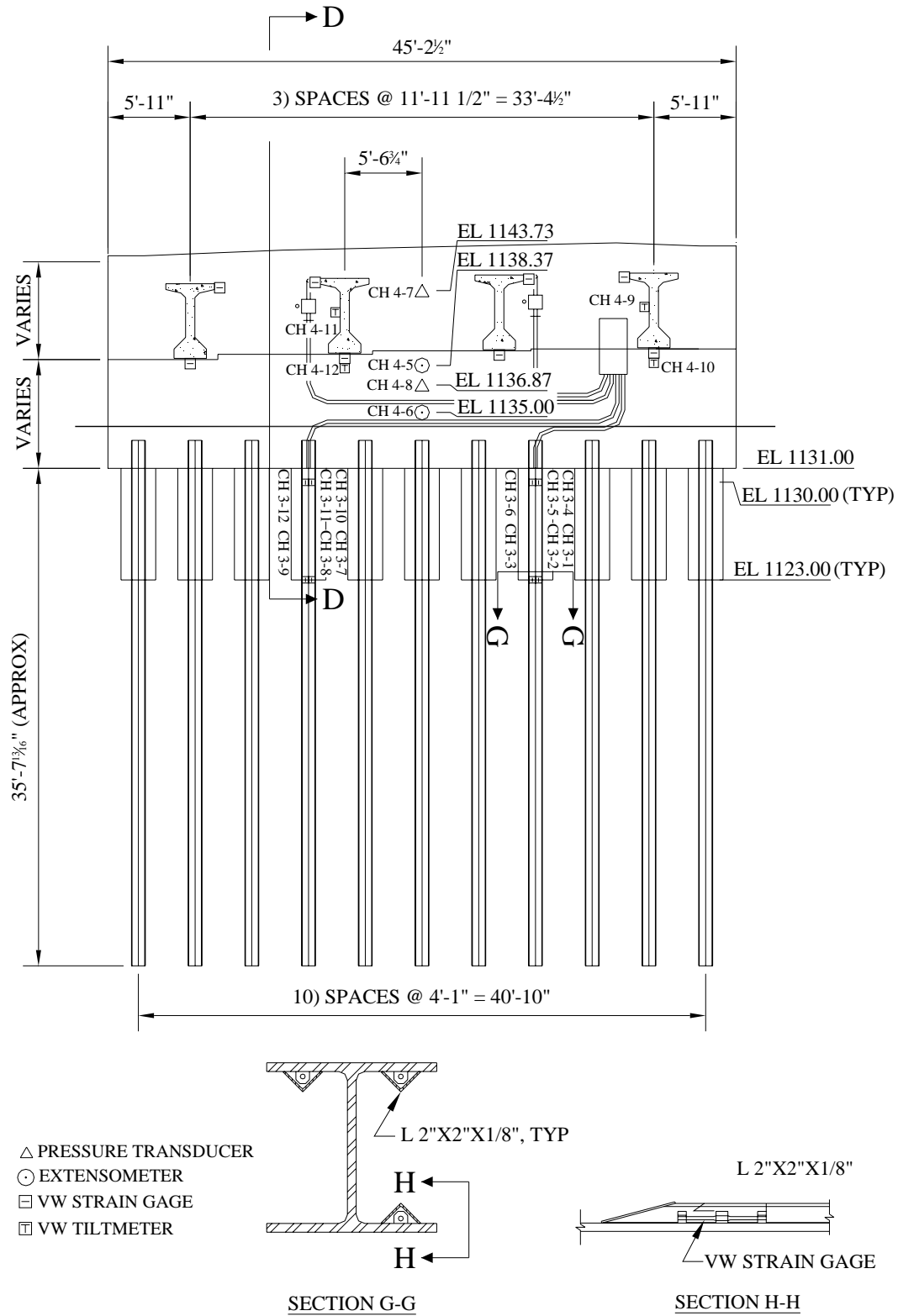
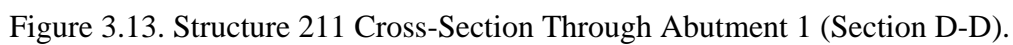


Figure 3.12. Structure 211 Abutment 1 Elevation (Section C-C).



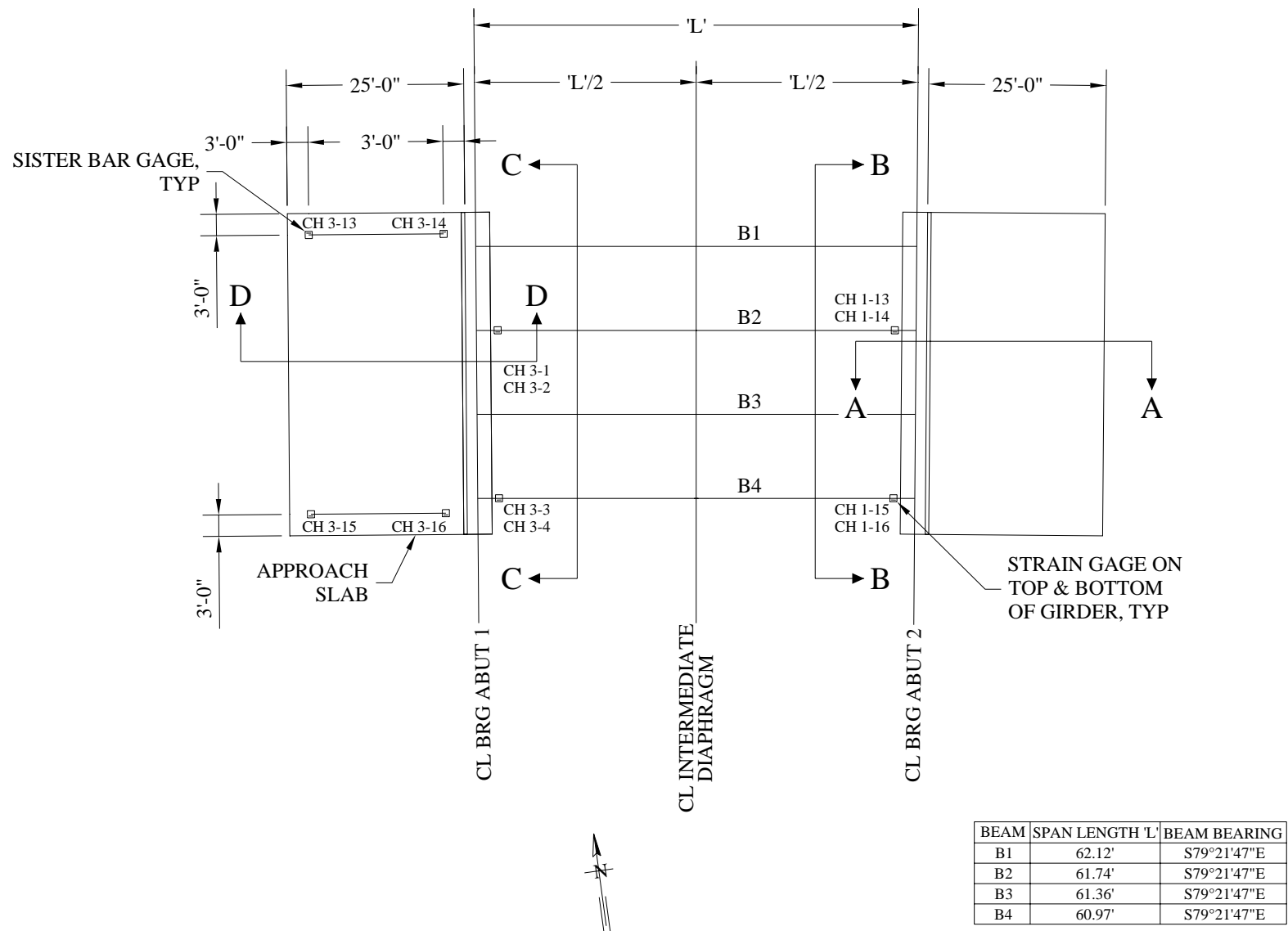


Figure 3.14. Structure 222 Instrumentation Plan.

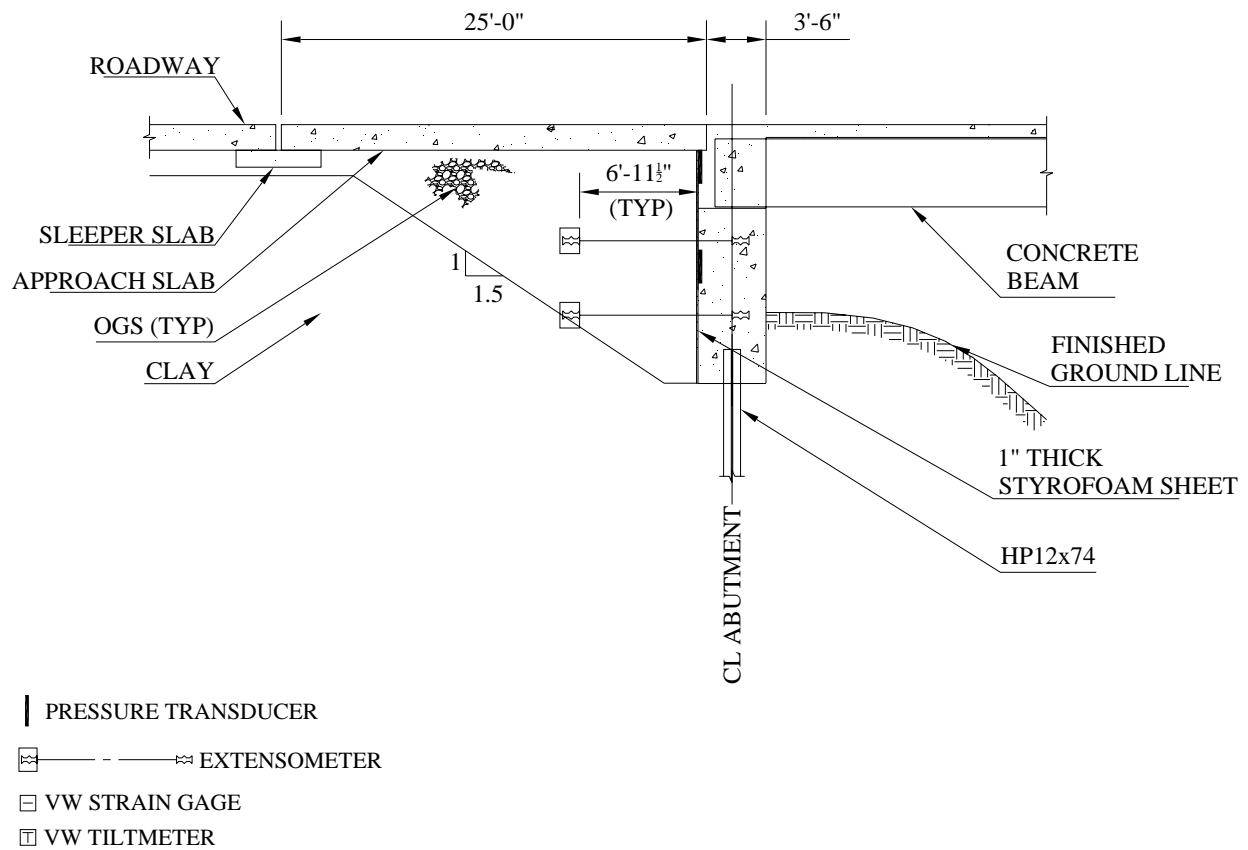


Figure 3.15. Structure 222 Cross-Section Through Abutment 2 (Section A-A).

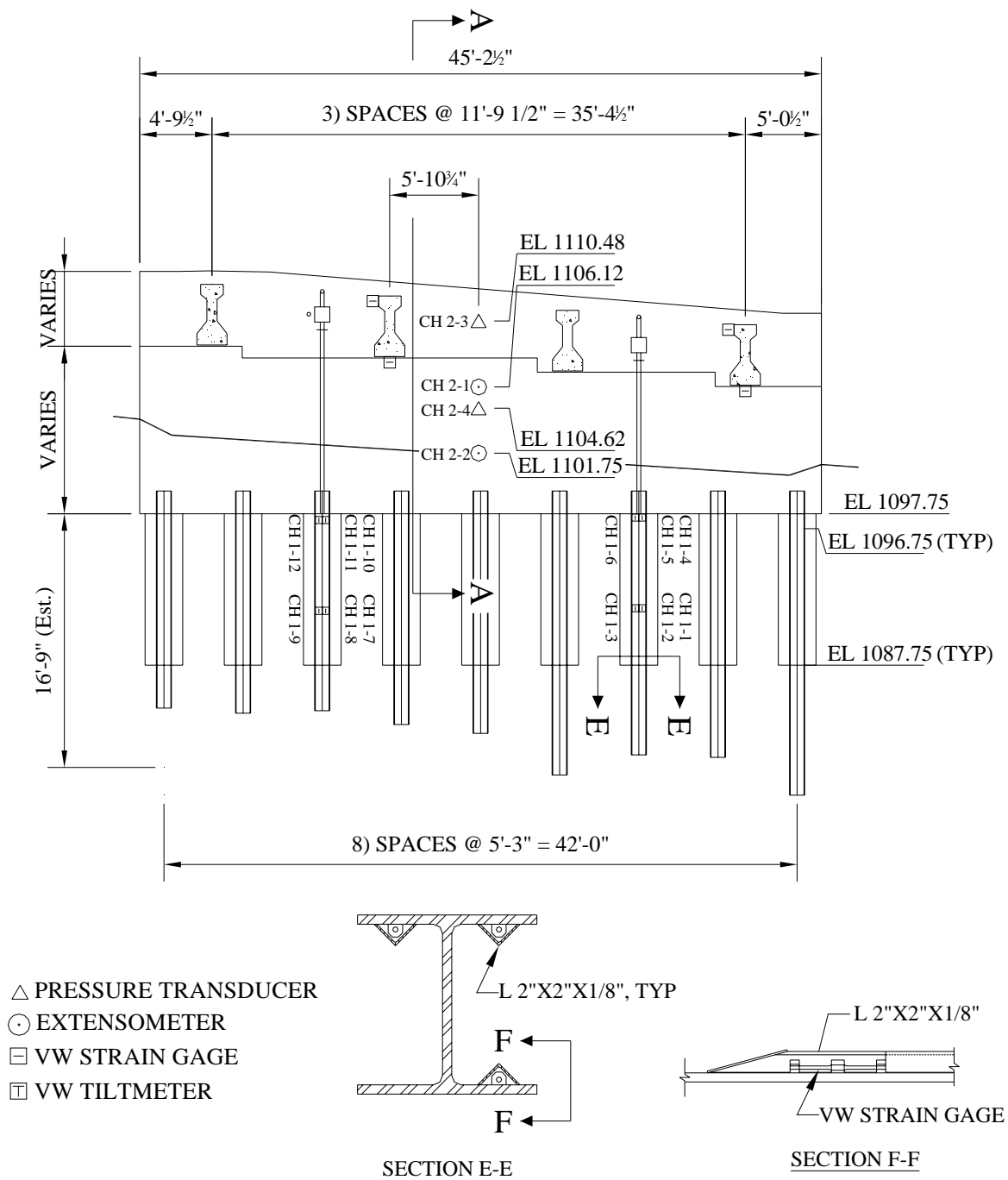


Figure 3.16. Structure 222 Abutment 2 Elevation (Section B-B).

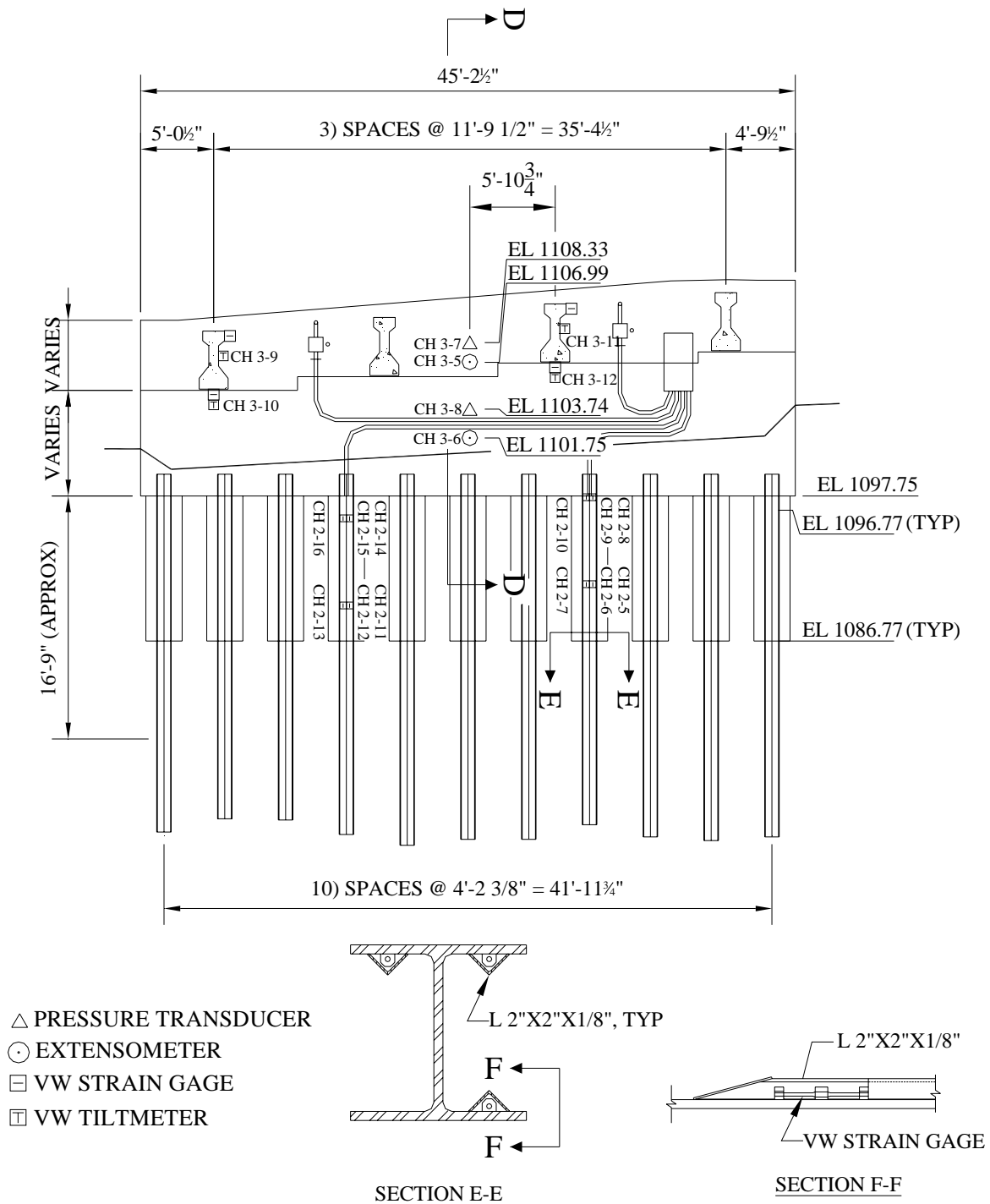


Figure 3.17. Structure 222 Abutment 1 Elevation (Section C-C).

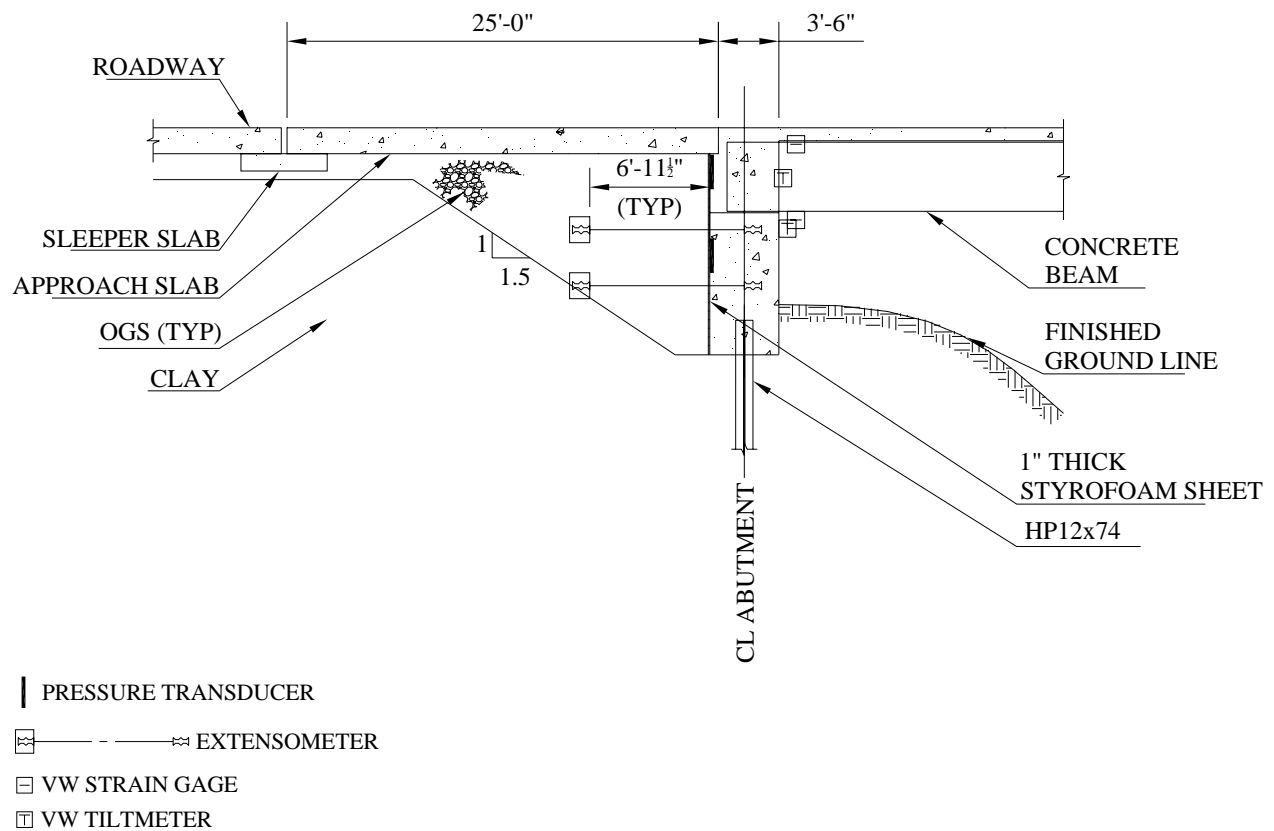


Figure 3.18. Structure 222 Cross-Section Through Abutment 1 (Section D-D).

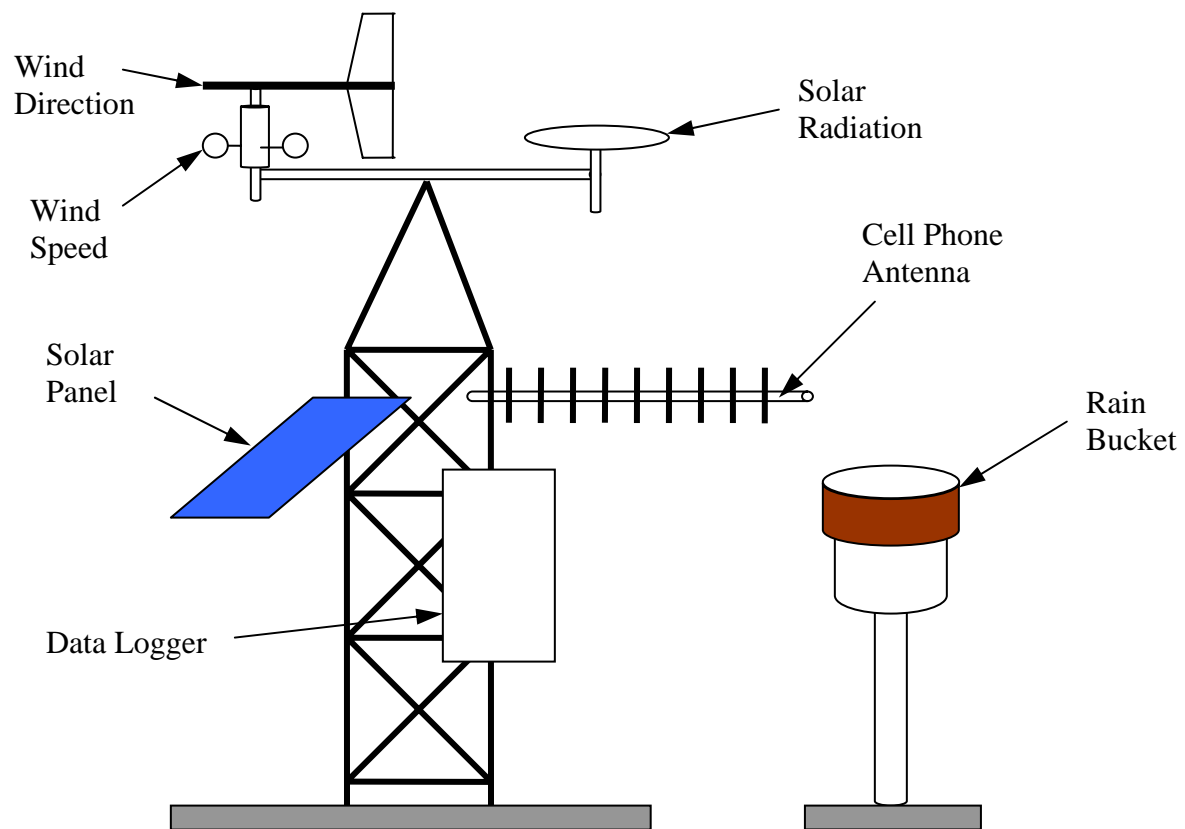


Figure 3.19. Weather Station.

Chapter 4

Measured Bridge Response

4.1 Introduction

Collection of strain, displacement, and rotation data at bridges 203, 211, 222, and 109 began in November 2002, September 2004, November 2003, and July 2006, respectively. Weather station data collection began in August 2002. All collected IAB data are periodically (monthly) downloaded from each bridge site as unprocessed electronic readings, converted to engineering units of strain, length, or rotation, and then further reduced in certain cases to units of moment and force. Weather station data are also downloaded periodically (monthly) downloaded and processed to obtain the environmental information needed from the electronic readings. As the data accumulated over time, they have been appended to data files and the graphs presented herein for evaluation and analysis. The sampling rate for all instruments is set to a period of 15 minutes. To permit data management, four representative data per day are plotted for evaluation (12:00 a.m., 6:00 a.m., 12:00 p.m., and 6:00 p.m.). Graphs of response versus calendar day in this chapter includes reduced field collected data, seven-day averages, and maximum and minimum envelopes in order to present the overall tendency and daily variations of the actual bridge response.

4.2 Bridge 109

Data obtained from bridge 109 instruments consist of 5 extensometers, 5 pressure cells, 8 tiltmeters, 24 strain gages on four piles, 16 strain gages on 4 prestressed concrete girders, and 6 sister bar gages. Abutment 2 H-piles were driven in September 2005, and

initial strain gage measurements were recorded as zero values. Abutment 1 H-piles were driven in December 2005. The strain gage channel 1-2 located at the bottom of the south pile under abutment 2 had no signal after pile driving, with the cause presumed to be damage due to the severe conditions. Therefore, no moment data are available for the east pile of abutment 2, while pile axial forces are computed from the remaining two strain gages (channel 1-1 and 1-3). The extensometer (channel 2-7) at the bottom center of abutment 2 was also determined to be damaged after installation after several failed attempts at repair.

Collected data from extensometers at abutments 1 and 2 are presented in Figure 4.1 and Figure 4.2, respectively. The extensometers measure bridge abutment longitudinal movement as a result of superstructure expansion and contraction. Maximum abutment displacement contraction and expansion are presented in Table 4.1. The bottom extensometer data at abutment 1 and the top and bottom extensometer at abutment 2 indicate continuous movement of the lower abutment toward the bridge. Contraction displacements of approximately 0.4 inches at both abutments occur every year.

Table 4.1. Bridge 109 Maximum Abutment Displacement.

Abutment		Abutment 1		Abutment 2	
Location		Top (in)	Bottom (in)	Top (in)	Bottom (in)
Maximum (Contraction)	Displacement	1.207	1.289	1.935	2.029
	Period	Winter 08/09	Winter 08/09	Winter 08/09	Winter 08/09
Minimum (Expansion)	Displacement	-0.276	-0.448	-0.169	0.071
	Period	Summer 07	Summer 06	Summer 06	Summer 06

Pressure cell data is presented in Figure 4.3 and Figure 4.4. Two pressure cells measure abutment 1 backfill pressure, and the other three pressure cells measure abutment 2 backfill pressure. Backfill pressures at the bottom of both abutments vary over a wide range with large amplitudes relative to the daily thermal displacements. The backfill pressure at the top of both abutments varies within a narrow range. Backfill pressures obtained from the abutment 1 bottom pressure cell are greater by as much as 15 psi, which was expected due to the approximately 8-ft deeper placement. The pressure difference between the bottom and top pressure cells increased during summer (approximately 6.4 psi), while the difference decreased during winter (approximately 2.3 psi). Backfill pressures at the abutment 2 top pressure cell are very similar to abutment 1, while the abutment 2 bottom pressure cell measured a 1 to 8 psi lower pressure than abutment 1. At abutment 1, the top and bottom pressure cell indicated maximum backfill pressures of 8.5 psi (summer 2006) and 37.0 psi (summer 2008). At abutment 2, the top north, top center, and bottom center pressure cells indicated maximum backfill pressures of 10.6 psi (summer 2007), 7.3 psi (summer 2008), and 28.3 psi (summer 2008), respectively.

Abutment tiltmeter data are presented in Figures 4.5 and 4.6. Two tiltmeters are mounted on each abutment under the centerline of girders 1 and 3. The two abutment 1 tiltmeters indicate an abutment rotation variation corresponding to temperature variation, while the two abutment 2 tiltmeters indicate observably less fluctuation. During the winter, abutment inclination increased toward the bridge, corresponding to the measured longitudinal displacements. The lower-bound abutment 2 rotation at the centerline of girder 3 decreased (starting from initial zero) from 0.034 to 0.012 to -0.07 degrees over a

3-year period. Maximum changes in rotation of abutment 1 at the centerline of girders 1 and 3 were 0.184 degrees (summer 2008) and 0.087 degrees (summer 2008). Maximum rotation of abutment 2 was 0.139 degrees (summer 2008) and 0.139 degrees (summer 2008).

Girder tiltmeter data are presented in Figures 4.7 and 4.8. One tiltmeter was placed directly on the web of girders 1 and 3 near both abutments. Both girders rotated with a trend that corresponds to seasonal temperature variation. Tiltmeters near abutment 1 measured a maximum rotation of 0.135 degrees (winter 2008/2009) at girder 1 and 0.096 degrees (winter 2007/2008) at girder 3. Tiltmeters near abutment 2 measured a maximum rotation of 0.152 degrees (winter 2008/2009) at girder 1 and 0.157 degrees (winter 2008/2009) at girder 3.

Pile bending moments about the weak axis at four piles, two each (north and south) at abutments 1 and 2, are presented in Figure 4.9 through Figure 4.12. The position of the gages and maximum measured moments are shown in Table 4.2. The H-pile bending strengths are $\phi M_{yielding} = 127$ ft-kip and $\phi M_{plastic} = 194$ ft-kip (based on $F_y = 50$ ksi).

Table 4.2. Bridge 109 Pile Strain Gage Depths Below Bottom of Abutment and Maximum Measured Moment.

	Abutment 1		Abutment 2	
	Placement	Max. Moment	Placement	Max. Moment
North Pile	0' - 9"	107.4 ft-kips	2' - 3"	57.4 ft-kips
	7' - 9"	65.0 ft-kips	9' - 3"	N/A*
South Pile	1' - 2"	108.3 ft-kips	1' - 3"	56.2 ft-kips
	8' - 2"	63.2 ft-kips	8' - 3"	38.9 ft-kips

* channel 1-2 was damaged after pile driving.

Pile axial forces are presented in Figure 4.13 through Figure 4.16. The average pile axial force measured, including dead loads and down drag forces accumulated over the

monitoring period, are abutment 1 north pile top = 22.3 kips, abutment 1 north pile bottom = 221 kips, abutment 1 south pile top = 157 kips, abutment 1 south pile bottom = 411 kips, abutment 2 north pile top = 110 kips and abutment 2 north pile bottom = 150 kips. The abutment 1 north pile axial force at the top does not fluctuate and remains constant at 22 kips. The abutment 1 south pile axial force at the top varies slightly with time, corresponding to temperature fluctuations. The magnitude of the abutment 1 axial force at the top is approximately 40 kips. Abutment 2 north pile axial force at the top varies, corresponding to temperature, with an amplitude of approximately 3 kips. Due to damage of channel 1-1 and 1-4, axial forces on the bottom and top location of the south pile indicated a malfunction after pile driving.

Girder moments derived from measured strain are presented in Figure 4.17 to Figure 4.20. Two strain gages are located 1 ft from each girder end, one at the top and one at the bottom flange. All girder moments tend to decrease compared to the preceding year, i.e., negative moments become more negative. The increasingly negative moments are more pronounced in exterior girders. Both interior girder responses are similar, varying within the upper and lower bound of positive 1,400 ft-kip and negative 1,500 ft-kip. Both exterior girder moments vary within the upper and lower bound of positive 1,800 and negative 3,900 ft-kip. The same trend is observed for girders adjacent to abutment 2.

Girder axial forces are presented in Figure 4.21 to Figure 4.24. The difference between interior and exterior girder axial force can be clearly observed. Interior girder axial response varies within a range of 1,000 kips. However, the tension force in exterior girders increase. Girder axial force near abutments 1 and 2 increased approximately 300 kips and 60 kips compared to the preceding year.

Sister-bar strain data at the approach slab on abutments 1 and 2 are presented in Figure 4.25 and Figure 4.26, respectively. The north sister bar near abutment 1 and all four sister bar gages near abutment 2 indicate a similar compression strain, ranging from 100 to 200 $\mu\epsilon$. The south sister bar gage near abutment 1 indicates less compression strain, ranging from 30 to 130 $\mu\epsilon$. Sister-bar gages indicated initial changes in compressive strain from 0 to 100 $\mu\epsilon$ due to concrete creep and shrinkage. Daily temperature variation correlation with all sister-bar strain were high during summer (approximately 30 $\mu\epsilon$), while daily strain changes during winter were less than 10 $\mu\epsilon$.

Bridge 109 Processed Response Data Figure List:

Figure 4.1. Bridge 109: Extensometers on Abutment 1.

Figure 4.2. Bridge 109: Extensometers on Abutment 2.

Figure 4.3. Bridge 109: Pressure Cells on Abutment 1.

Figure 4.4. Bridge 109: Pressure Cells on Abutment 2.

Figure 4.5. Bridge 109: Tiltmeters on Abutment 1.

Figure 4.6. Bridge 109: Tiltmeters on Abutment 2.

Figure 4.7. Bridge 109: Tiltmeters on Girders near Abutment 1.

Figure 4.8. Bridge 109: Tiltmeters on Girders near Abutment 2.

Figure 4.9. Bridge 109: Moments on North Pile under Abutment 1.

Figure 4.10. Bridge 109: Moments on South Pile under Abutment 1.

Figure 4.11. Bridge 109: Moments on North Pile under Abutment 2.

Figure 4.12. Bridge 109: Moments on South Pile under Abutment 2.

Figure 4.13. Bridge 109: Axial Forces on North Pile under Abutment 1.

Figure 4.14. Bridge 109: Axial Forces on South Pile under Abutment 1.

Figure 4.15. Bridge 109: Axial Forces on North Pile under Abutment 2.

Figure 4.16. Bridge 109: Axial Forces on South Pile under Abutment 2.

Figure 4.17. Bridge 109: Interior Girder Moments near Abutment 1.

Figure 4.18. Bridge 109: Exterior Girder Moments near Abutment 1.

Figure 4.19. Bridge 109: Interior Girder Moments near Abutment 2.

Figure 4.20. Bridge 109: Exterior Girder Moments near Abutment 2.

Figure 4.21. Bridge 109: Interior Girder Axial Forces near Abutment 1.

Figure 4.22. Bridge 109: Exterior Girder Axial Forces near Abutment 1.

Figure 4.23. Bridge 109: Interior Girder Axial Forces near Abutment 2.

Figure 4.24. Bridge 109: Exterior Girder Axial Forces near Abutment 2.

Figure 4.25. Bridge 109: Sister-Bar Gages near Abutment 1.

Figure 4.26. Bridge 109: Sister-Bar Gages near Abutment 2.

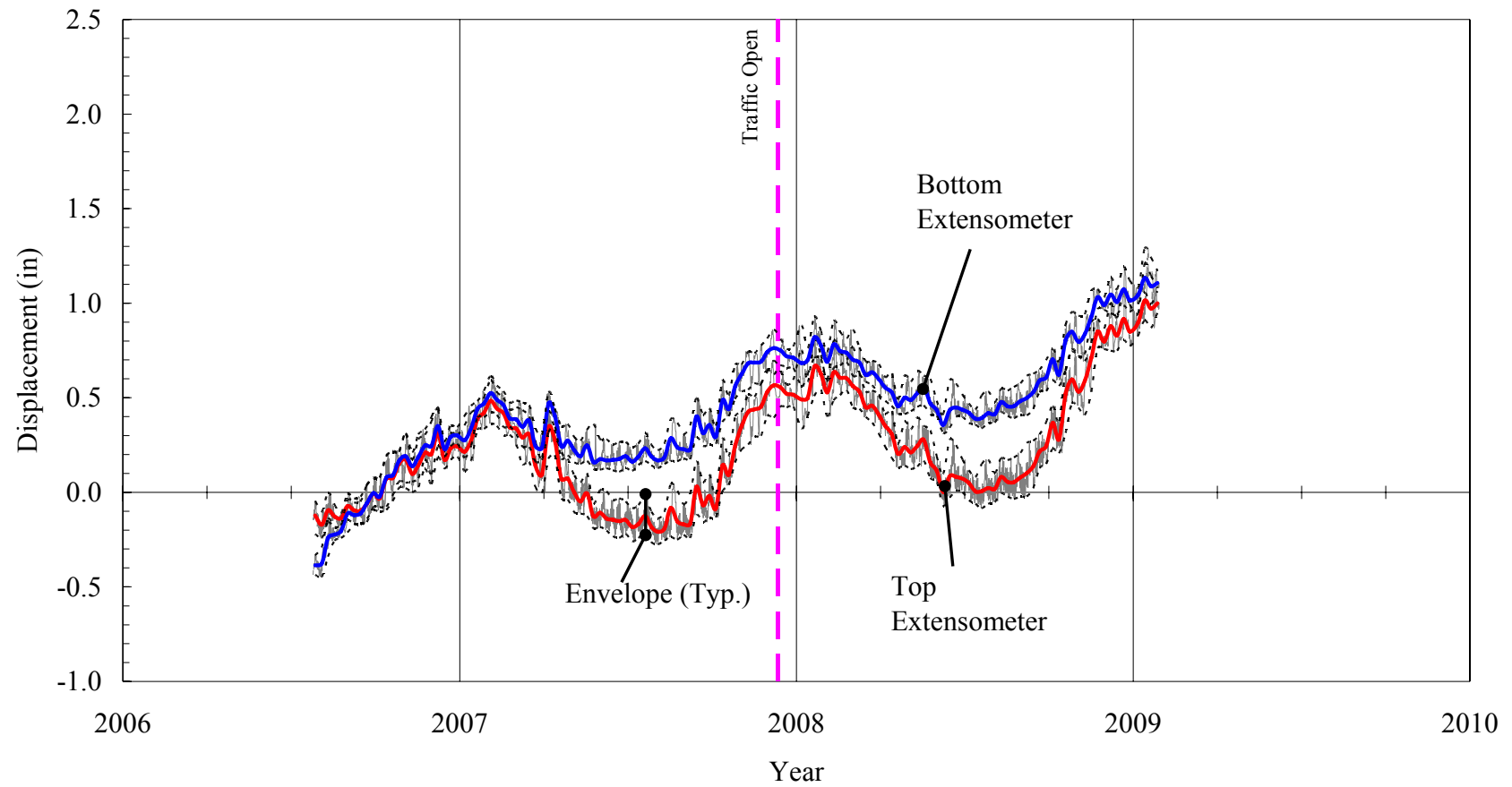


Figure 4.1. Bridge 109: Extensometers on Abutment 1.

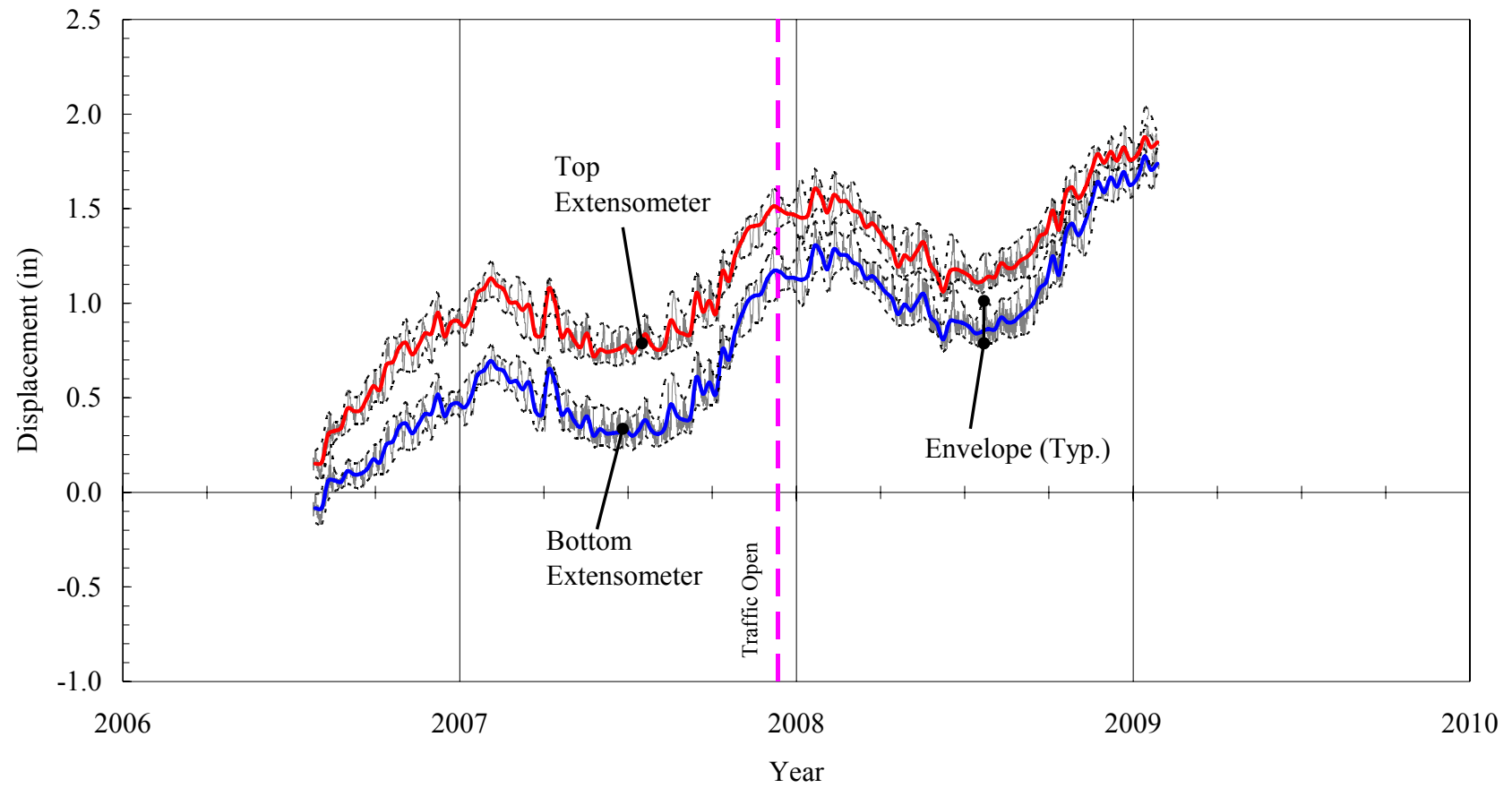


Figure 4.2. Bridge 109: Extensometers on Abutment 2.

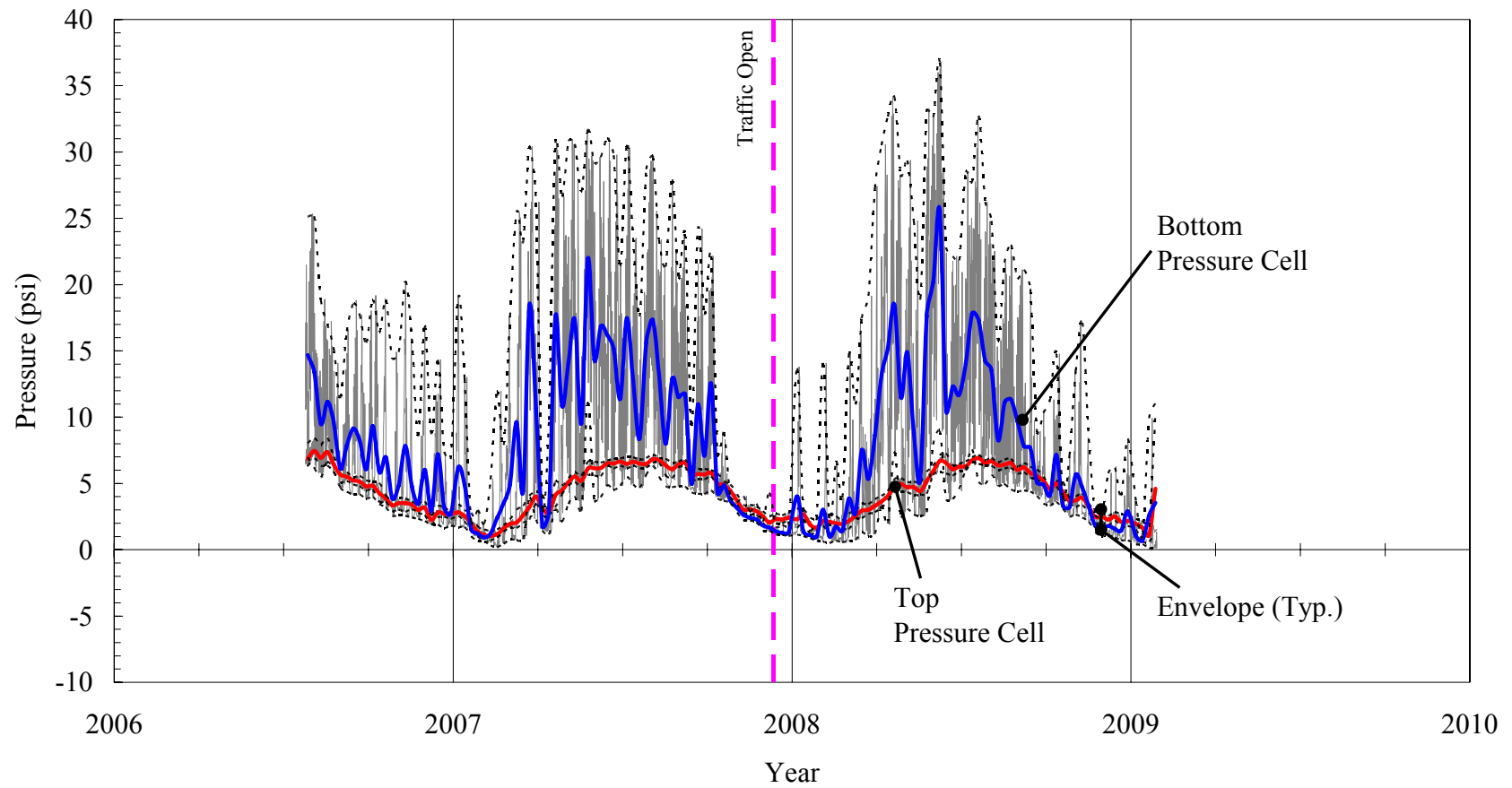


Figure 4.3. Bridge 109: Pressure Cells on Abutment 1.

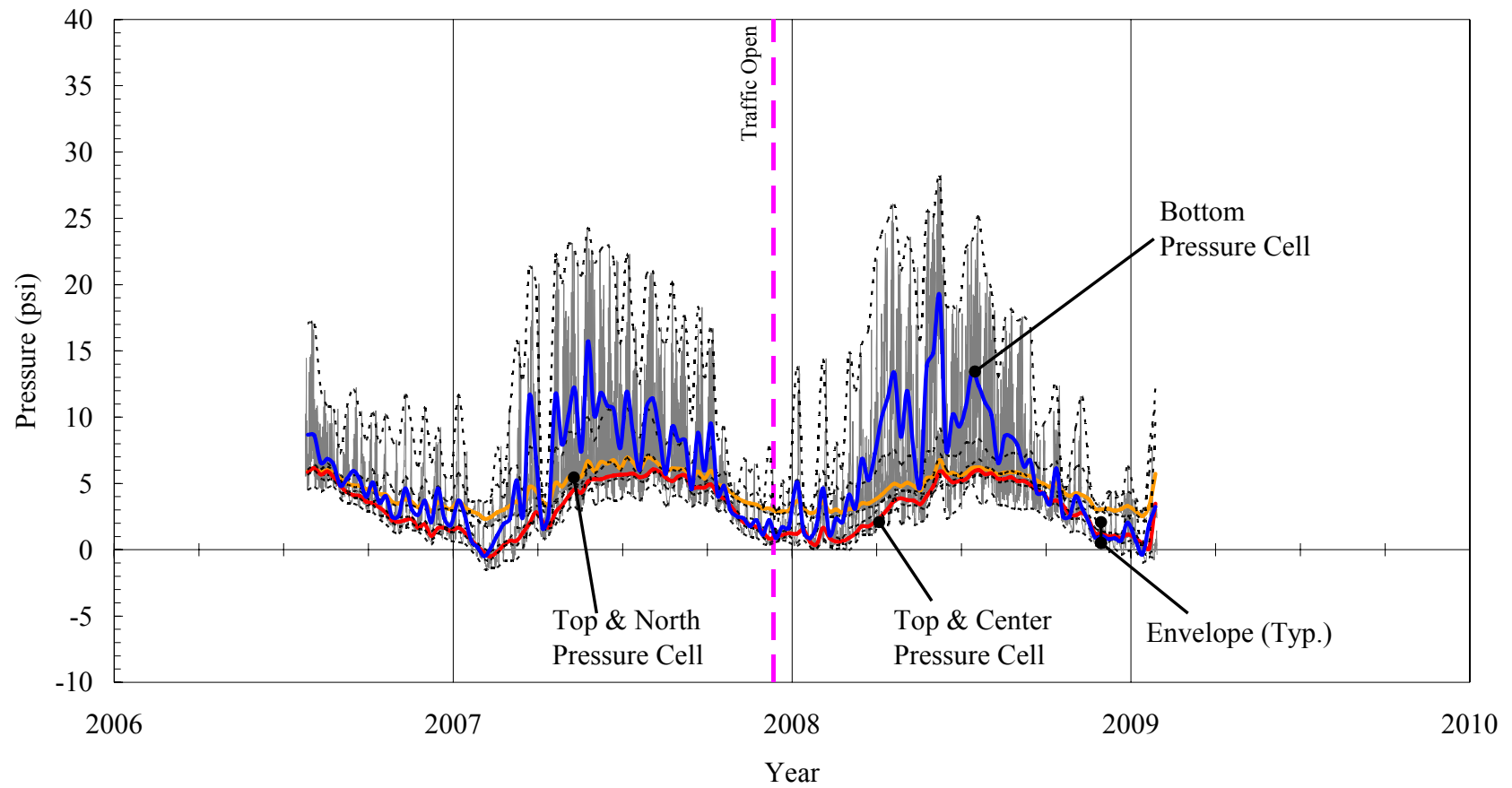


Figure 4.4. Bridge 109: Pressure Cells on Abutment 2.

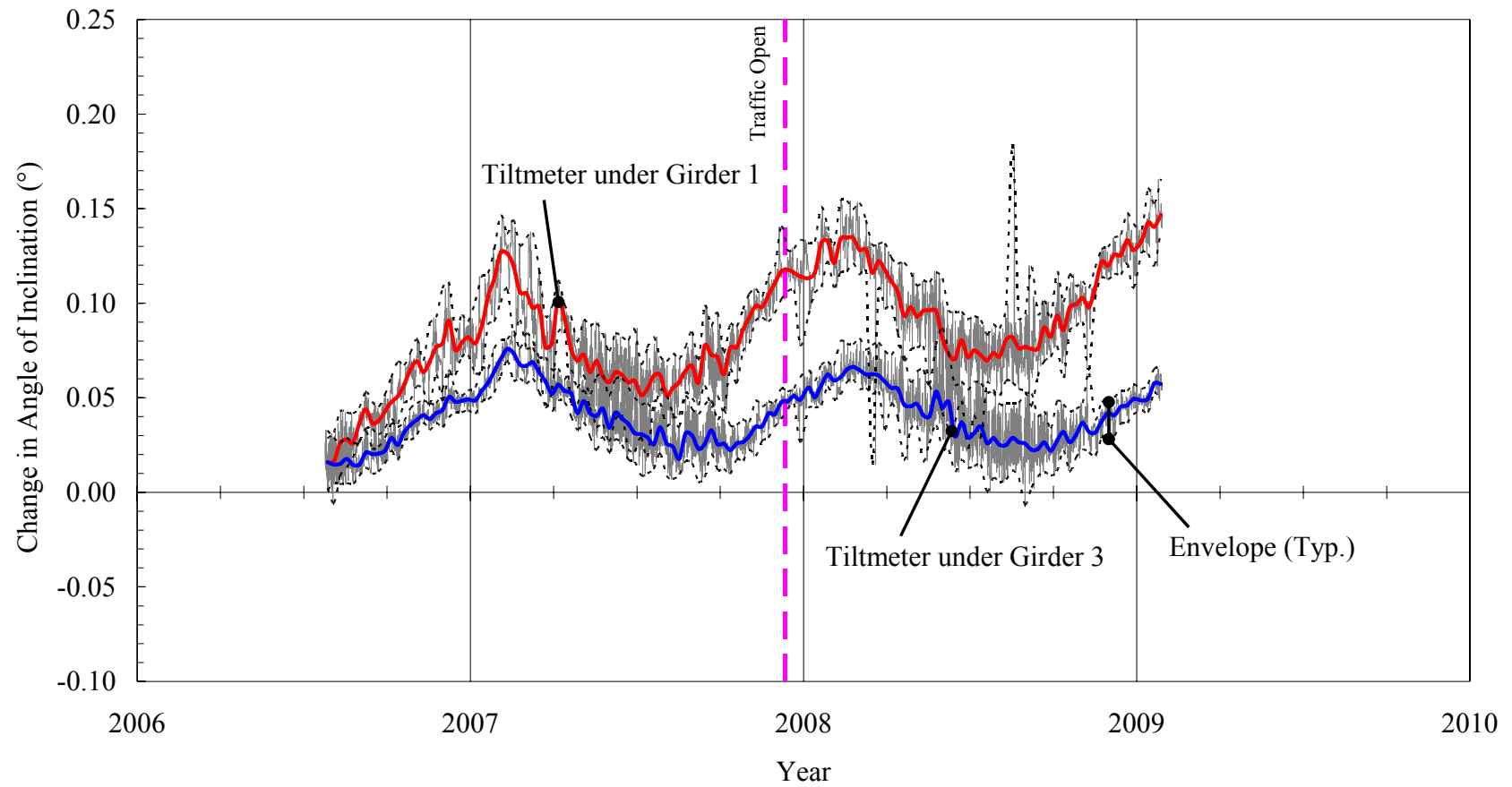


Figure 4.5. Bridge 109: Tiltmeters on Abutment 1.

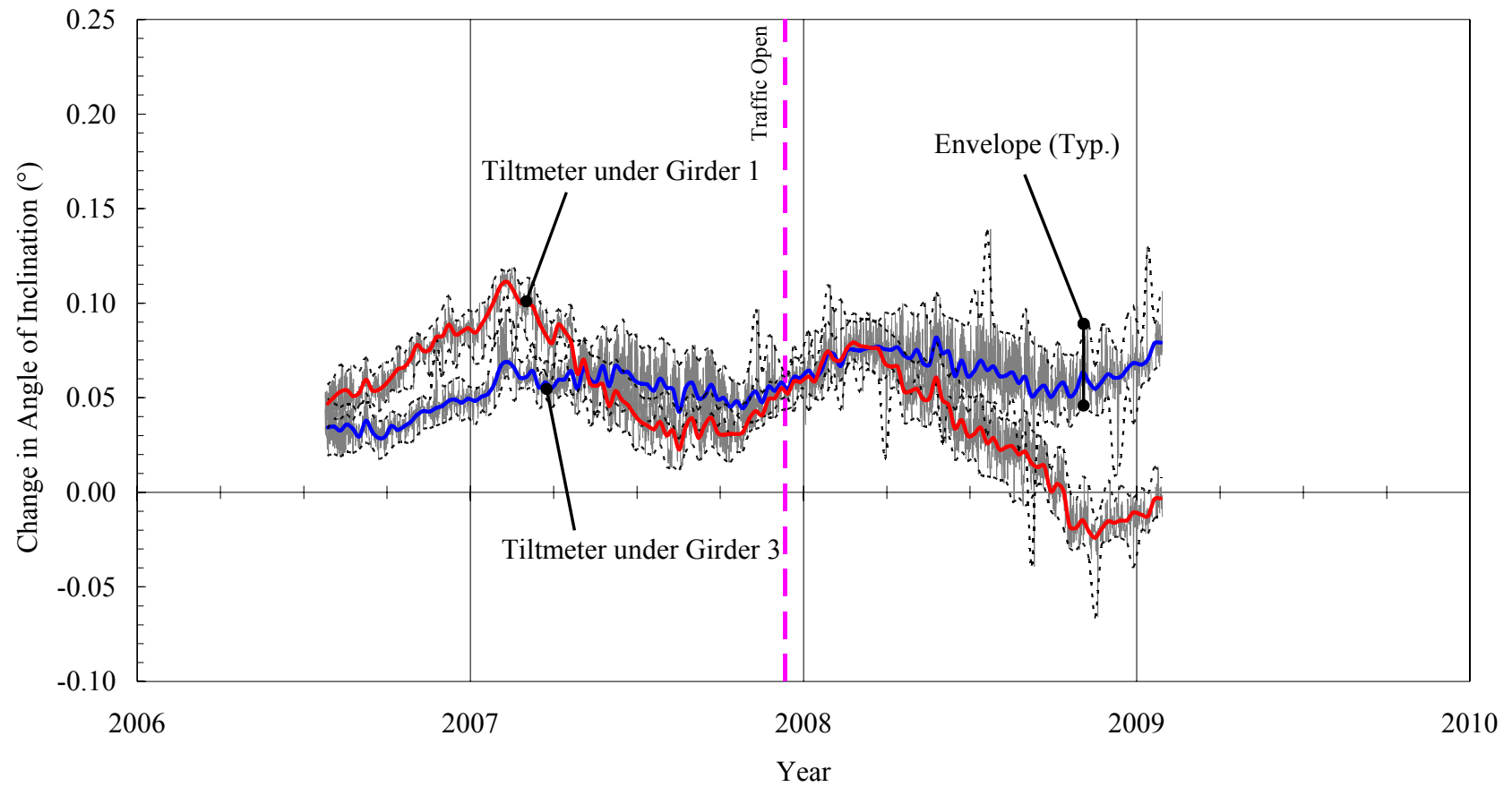


Figure 4.6. Bridge 109: Tiltmeters on Abutment 2.

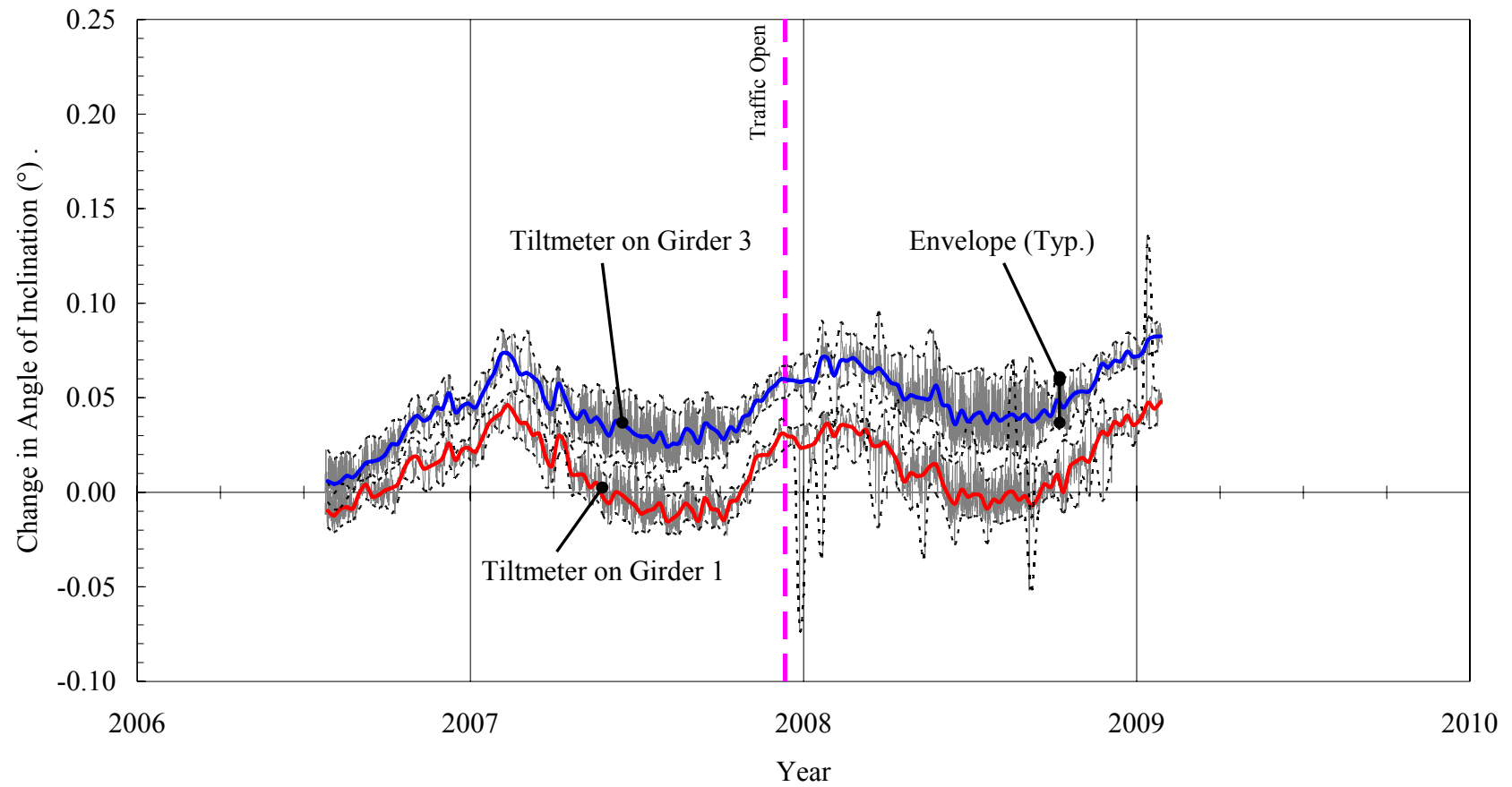


Figure 4.7. Bridge 109: Tiltmeters on Girders near Abutment 1.

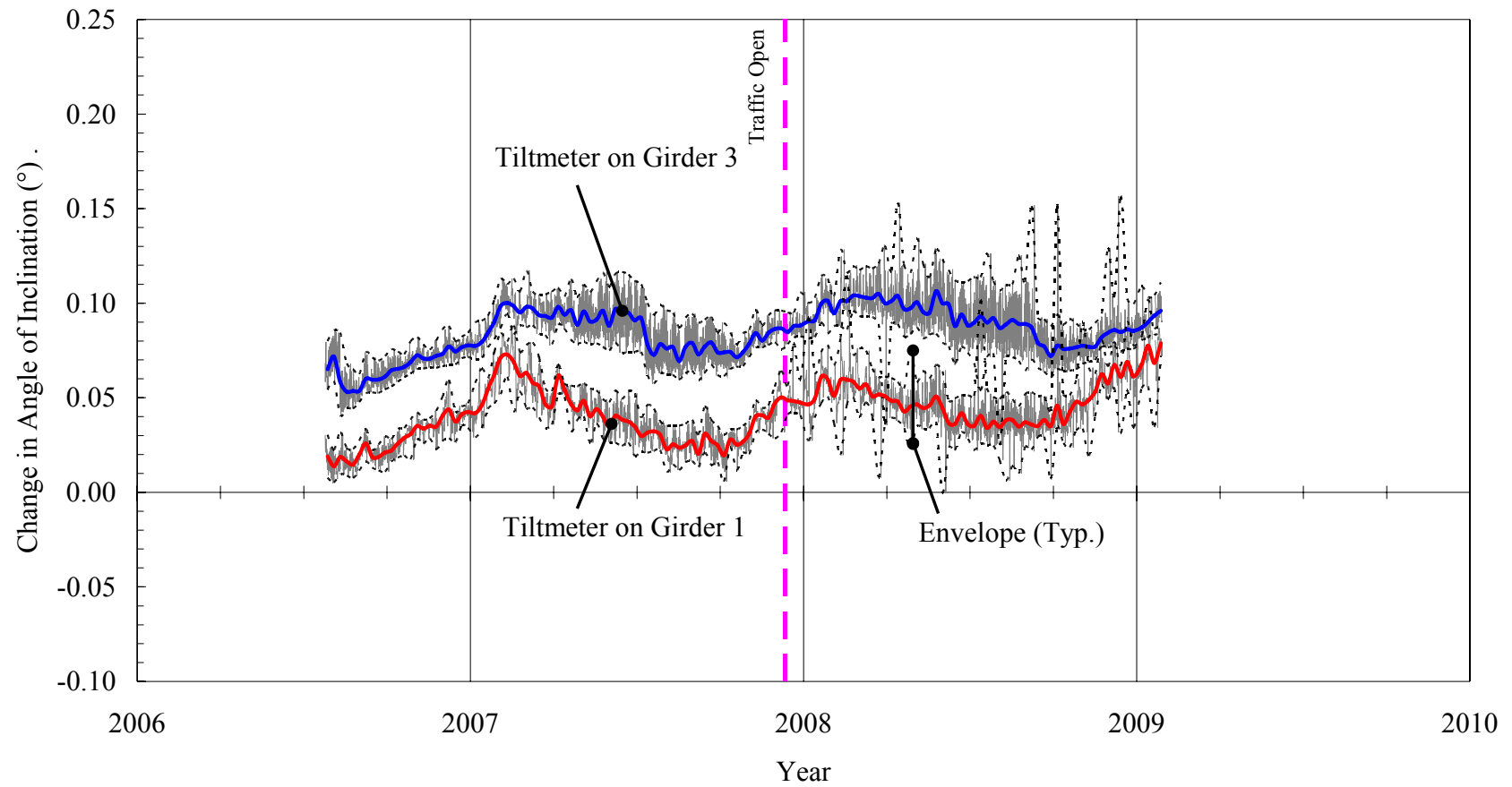


Figure 4.8. Bridge 109: Tiltmeters on Girders near Abutment 2.

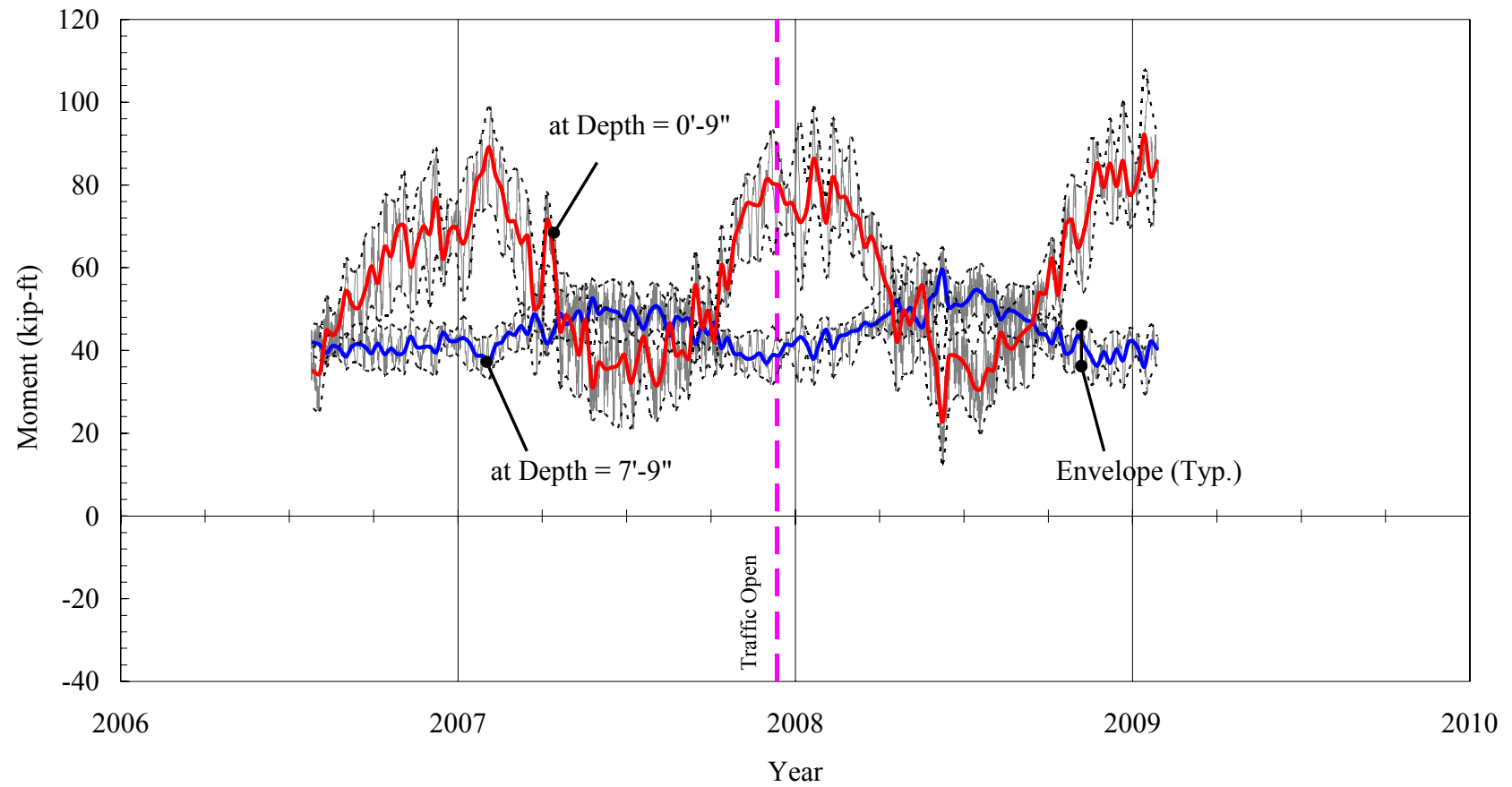


Figure 4.9. Bridge 109: North Pile Moments under Abutment 1.

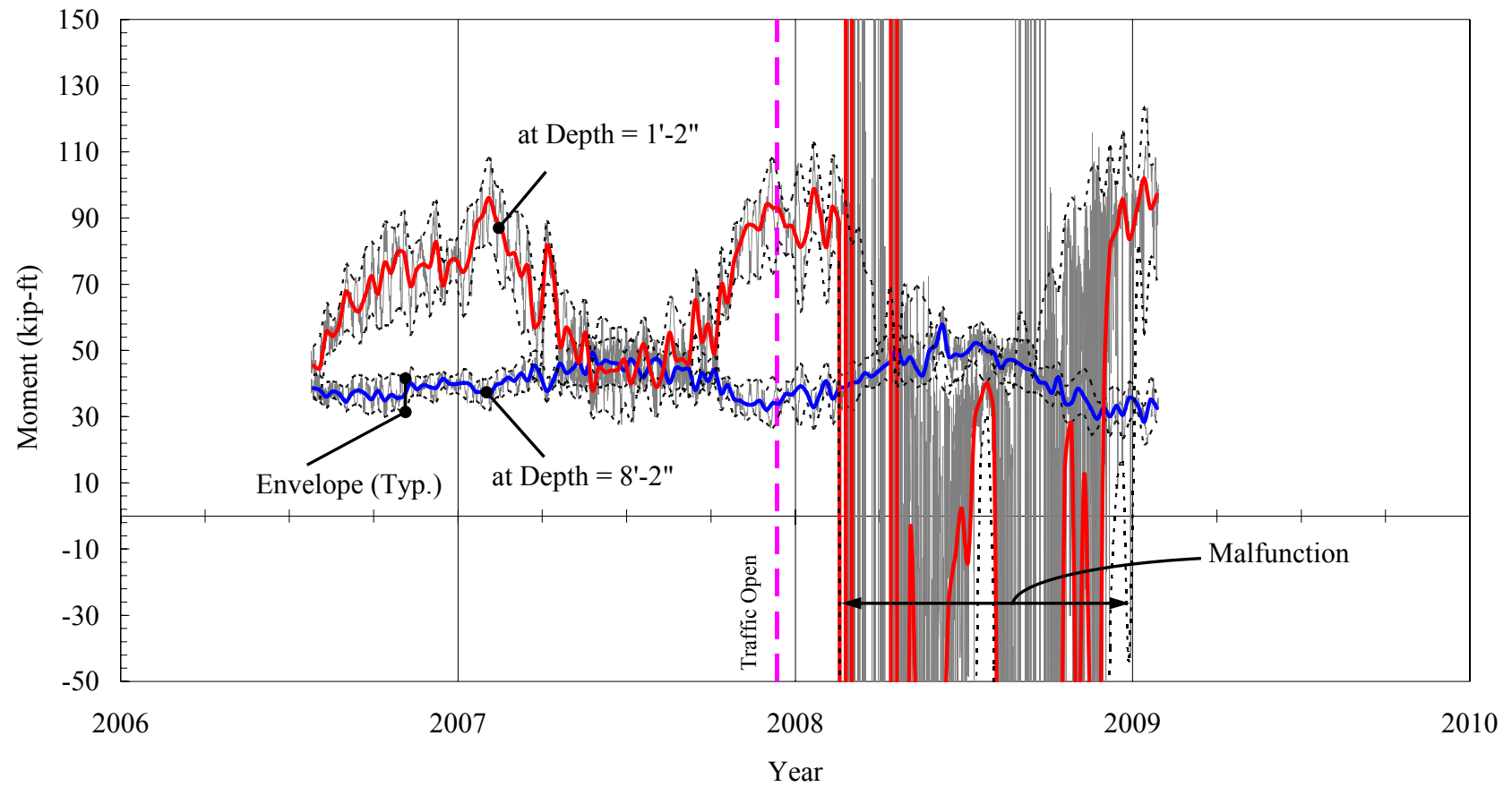


Figure 4.10. Bridge 109: South Pile Moments under Abutment 1.

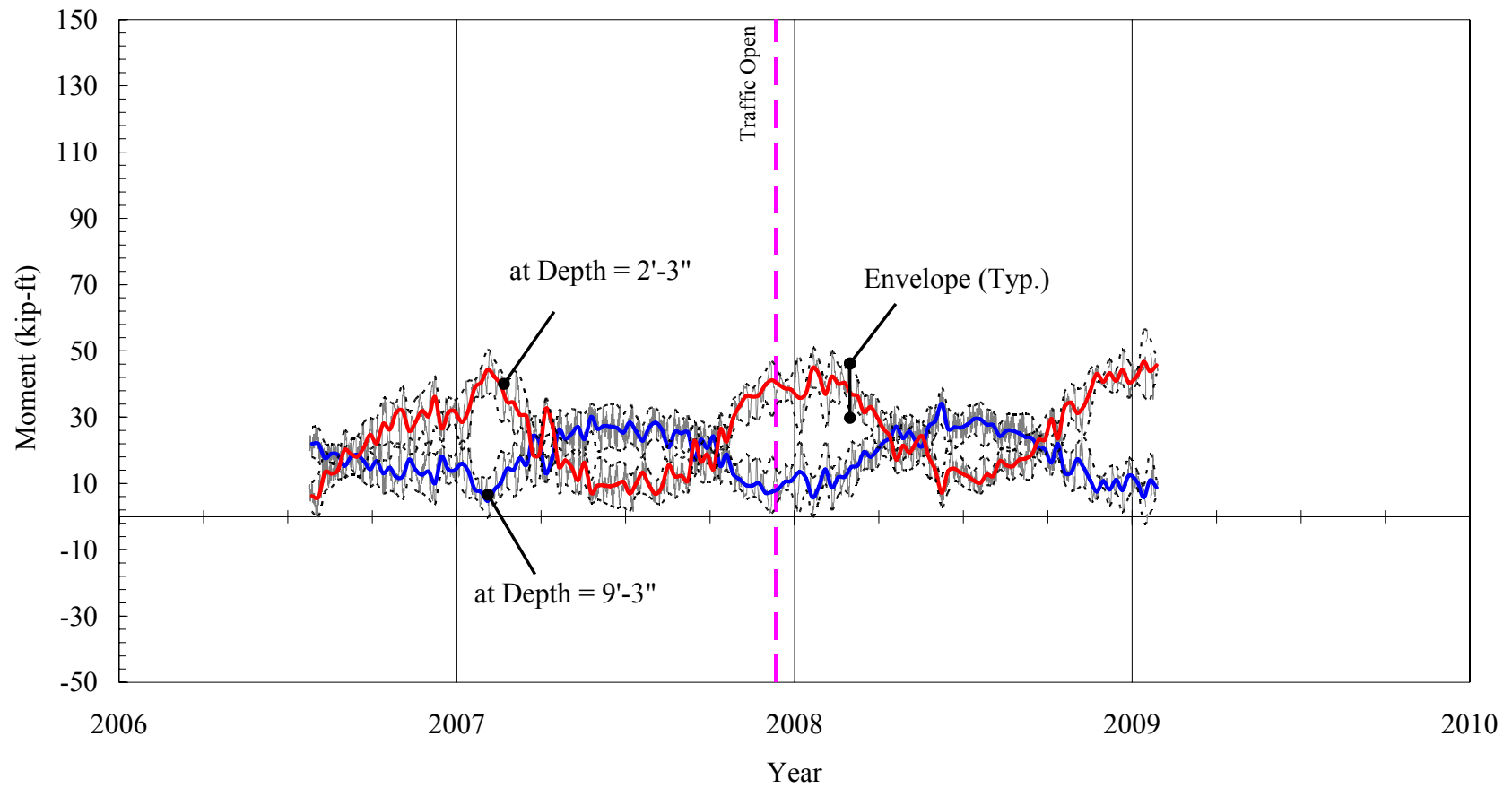


Figure 4.11. Bridge 109: North Pile Moments under Abutment 2.

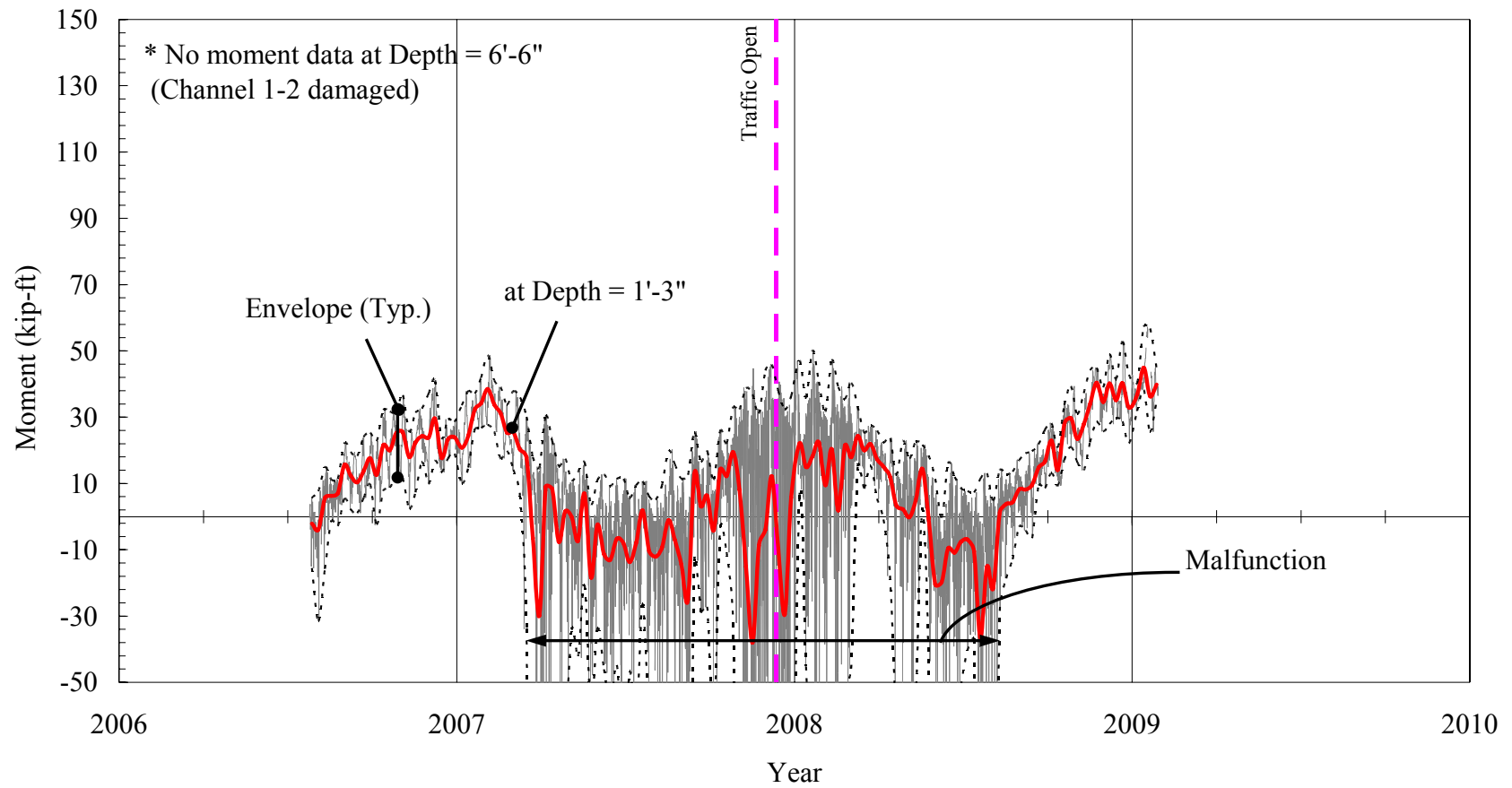


Figure 4.12. Bridge 109: South Pile Moments under Abutment 2.

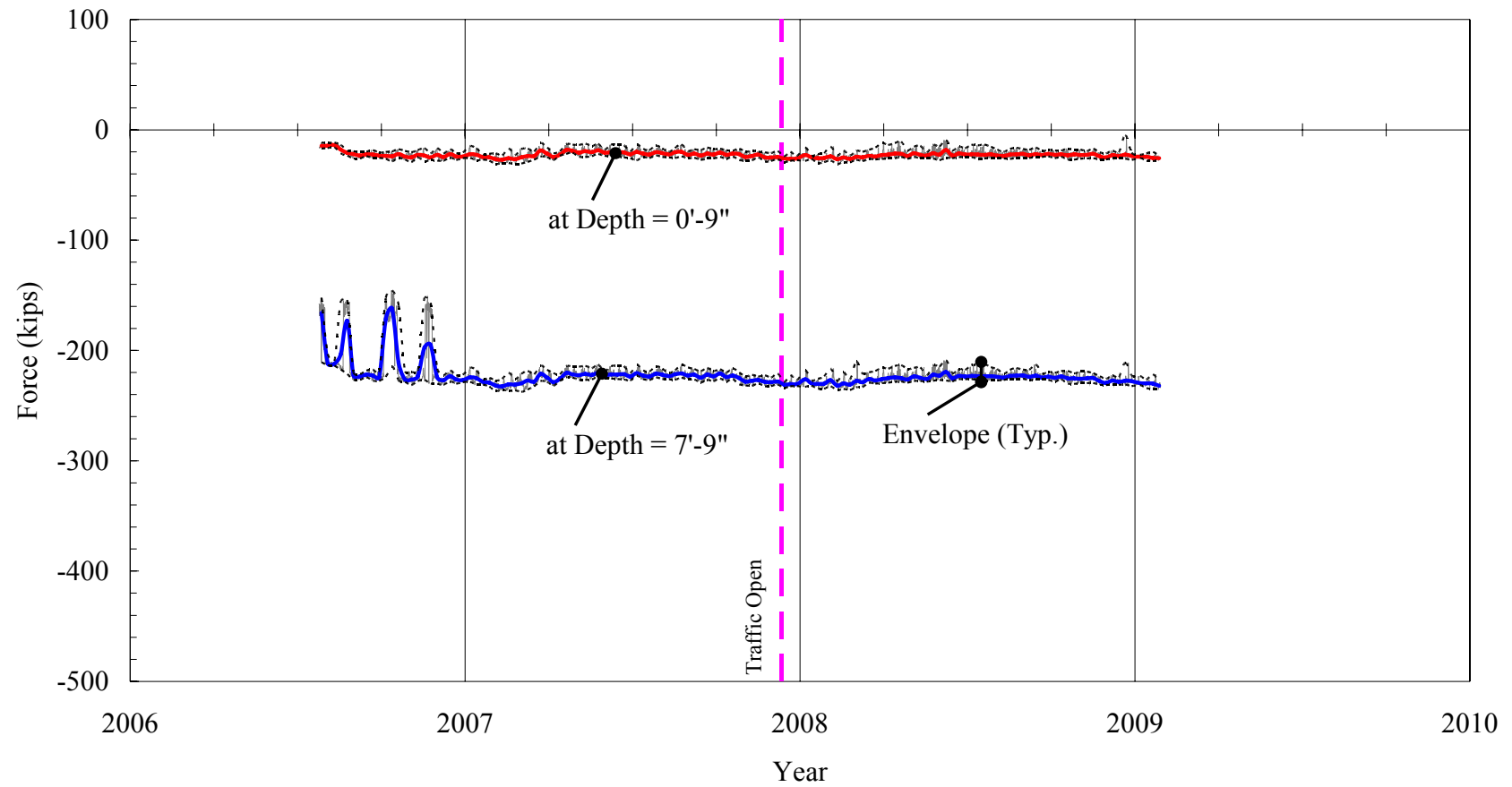


Figure 4.13. Bridge 109: Axial Force on North Pile under Abutment 1.

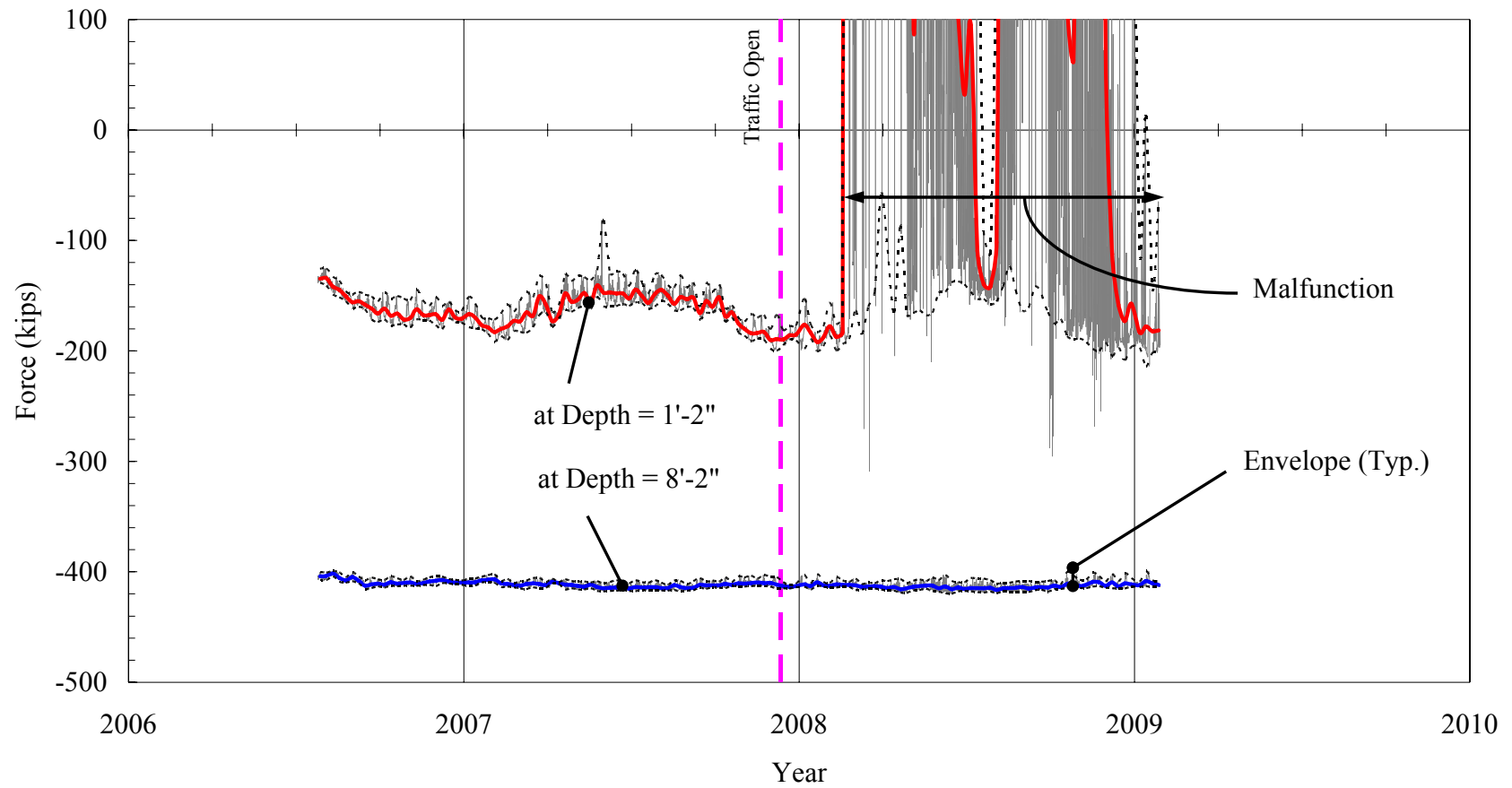


Figure 4.14. Bridge 109: Axial Force on South Pile under Abutment 1.

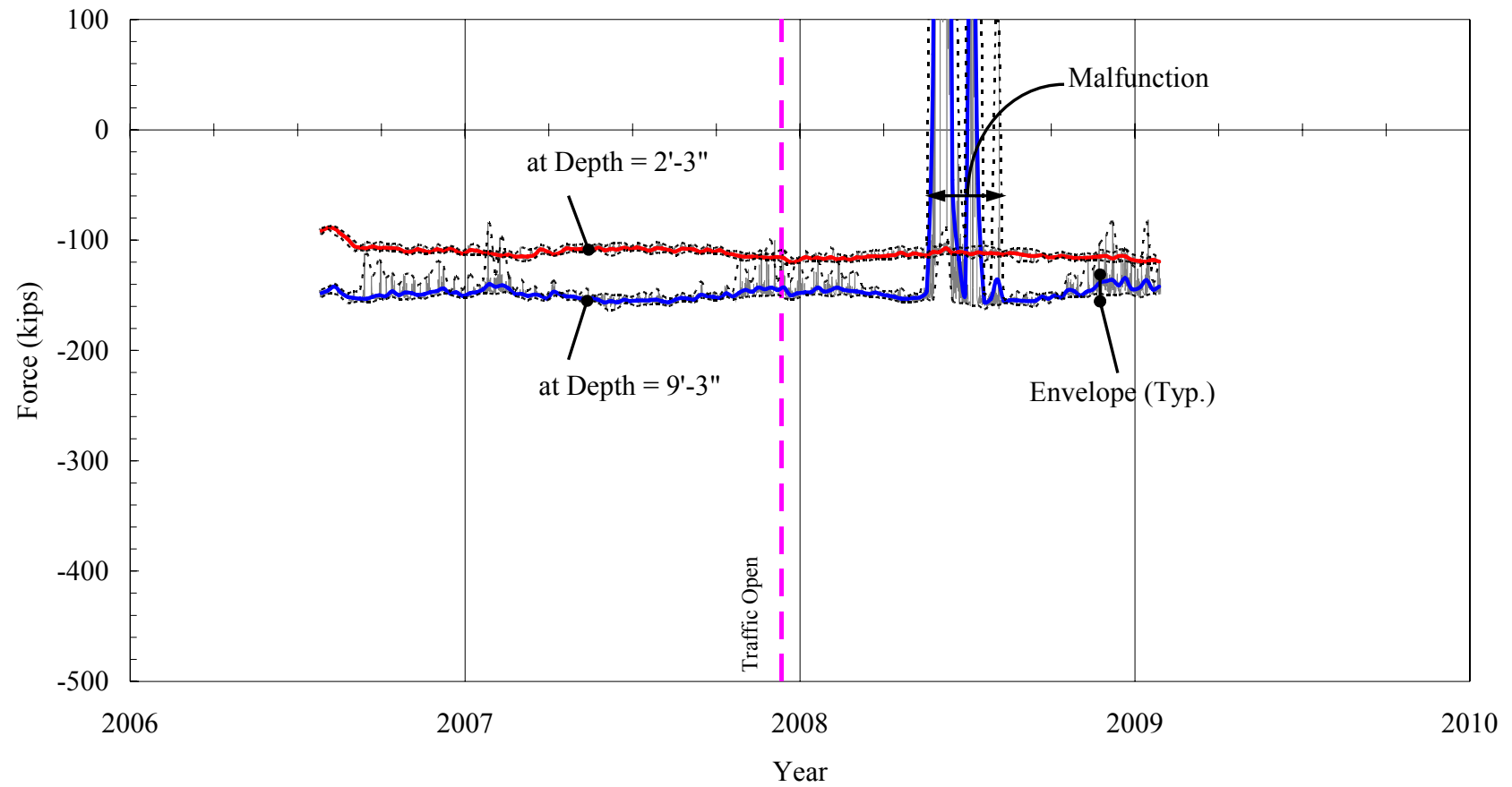


Figure 4.15. Bridge 109: Axial Force on North Pile under Abutment 2.

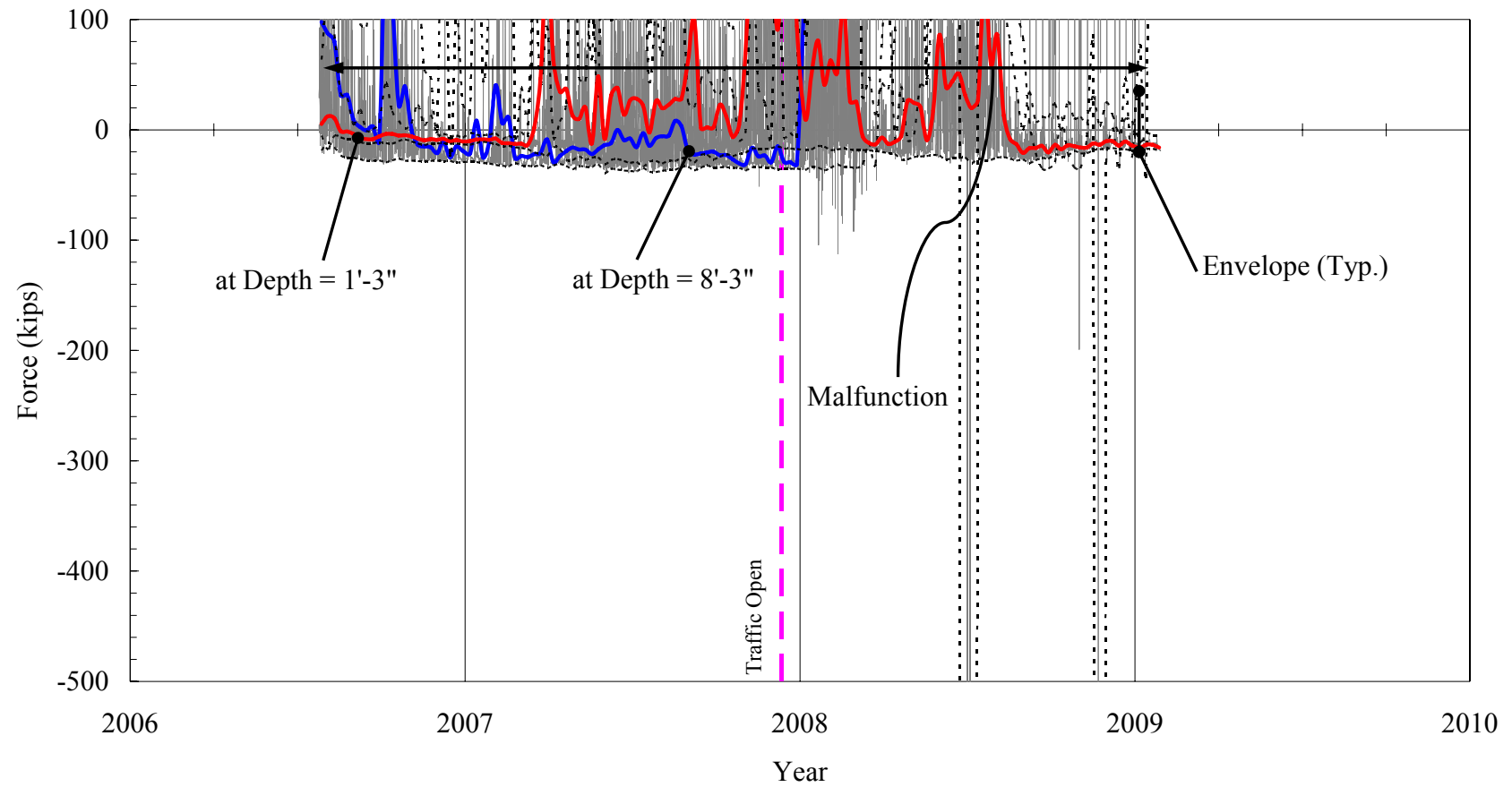


Figure 4.16. Bridge 109: Axial Force on South Pile under Abutment 2.

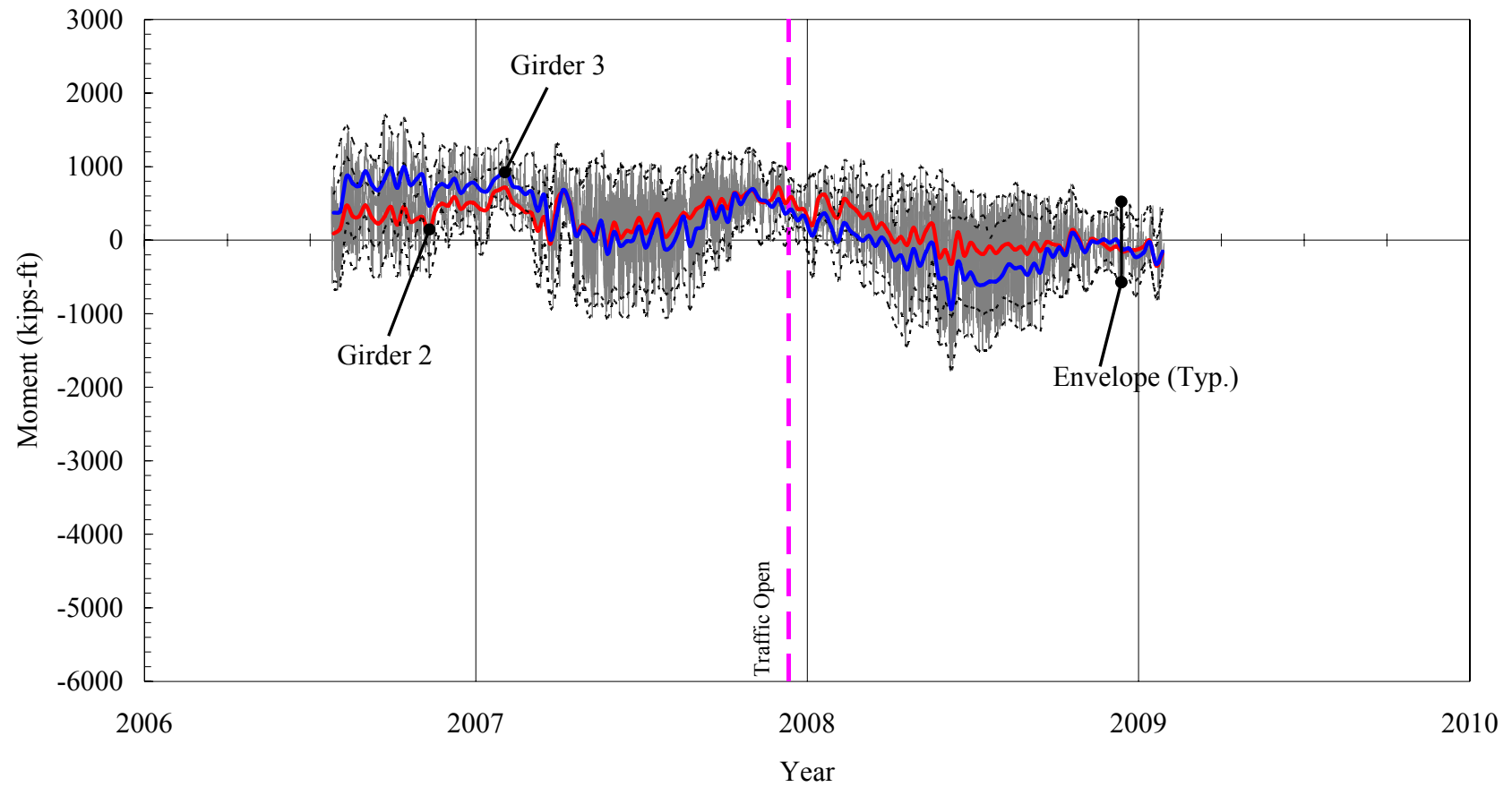


Figure 4.17. Bridge 109: Interior Girder Moments near Abutment 1.

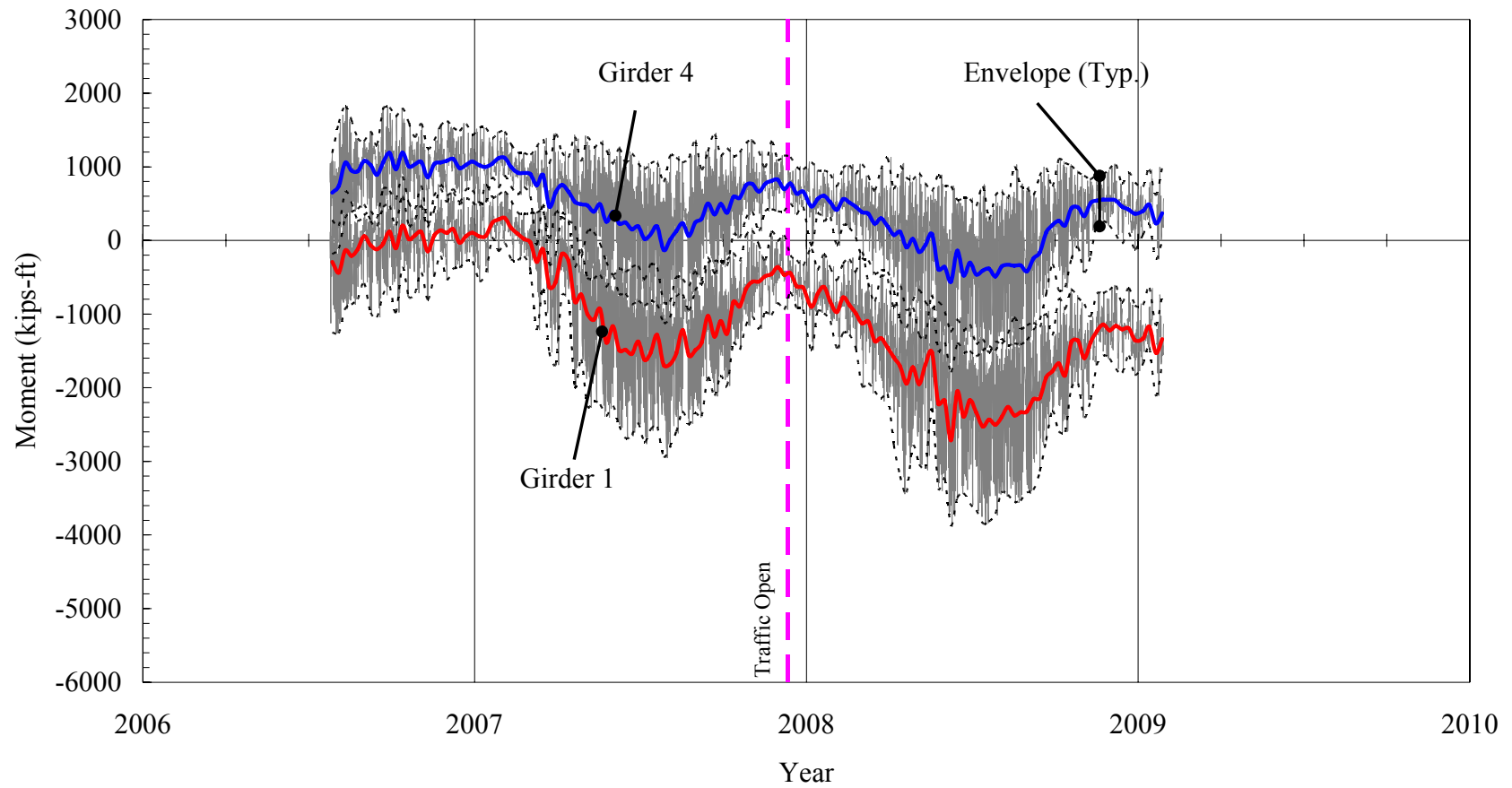


Figure 4.18. Bridge 109: Exterior Girder Moments near Abutment 1.

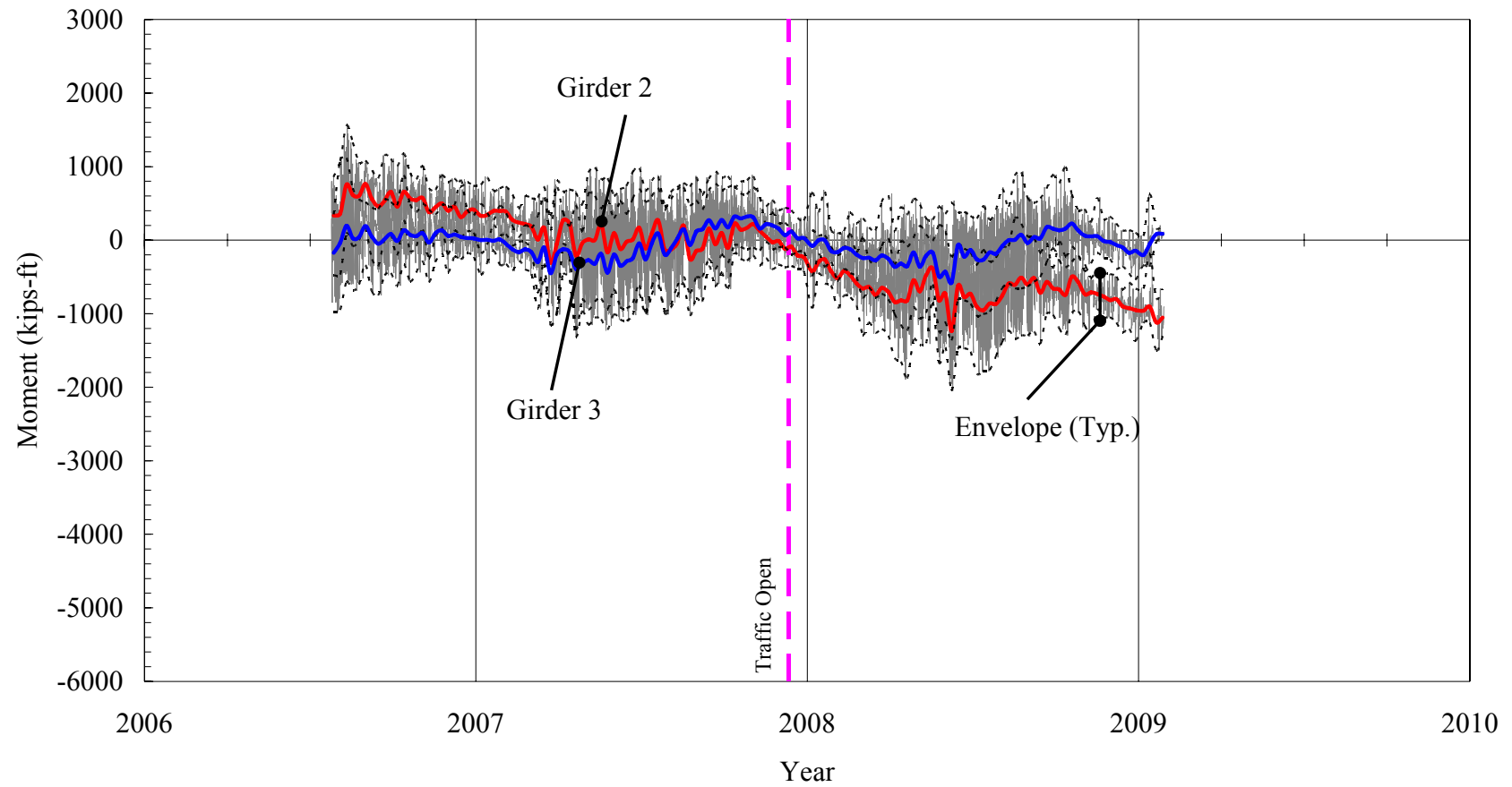


Figure 4.19. Bridge 109: Interior Girder Moments near Abutment 2.

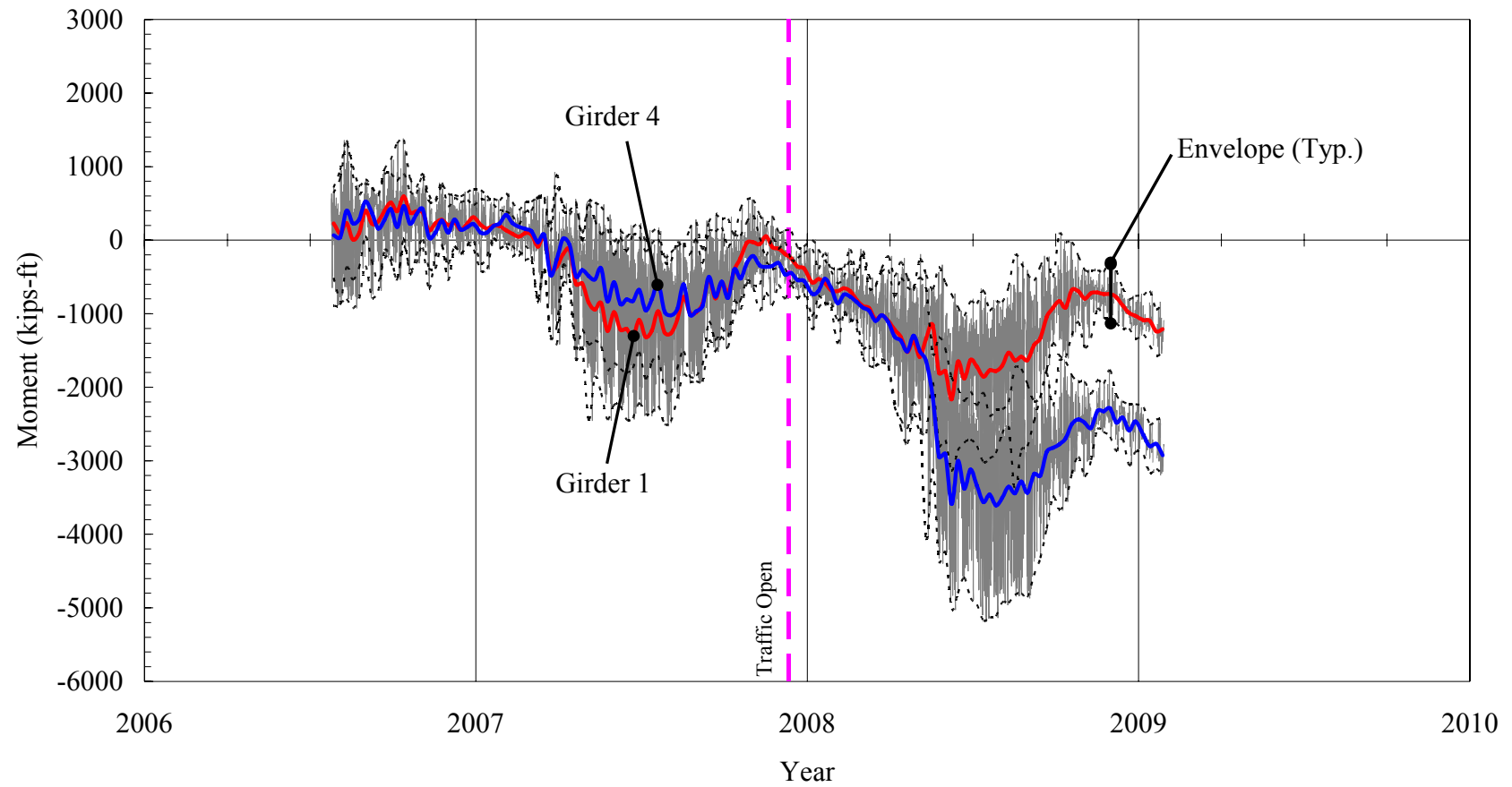


Figure 4.20. Bridge 109: Exterior Girder Moments near Abutment 2.

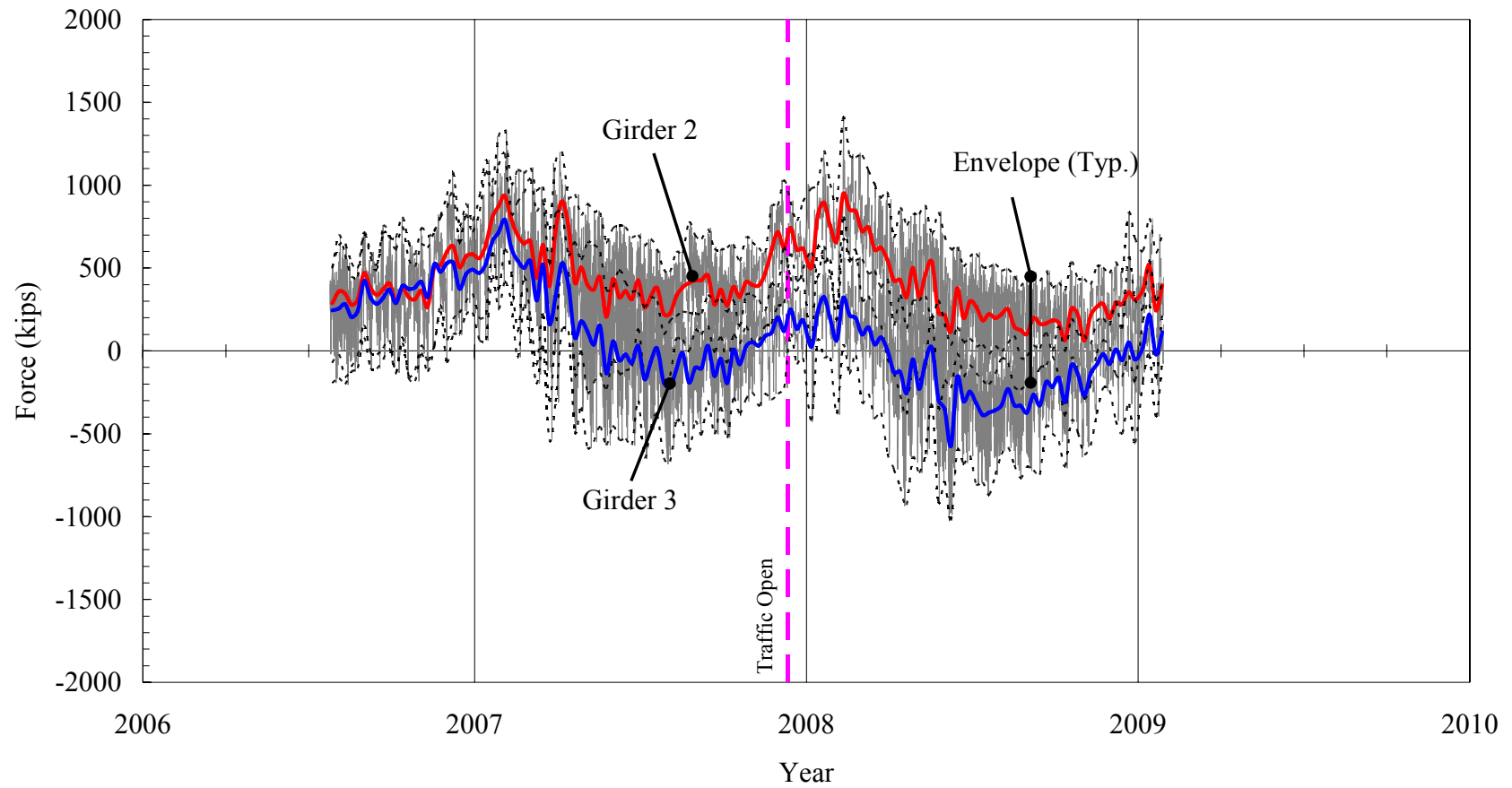


Figure 4.21. Bridge 109: Interior Girder Axial Forces near Abutment 1.

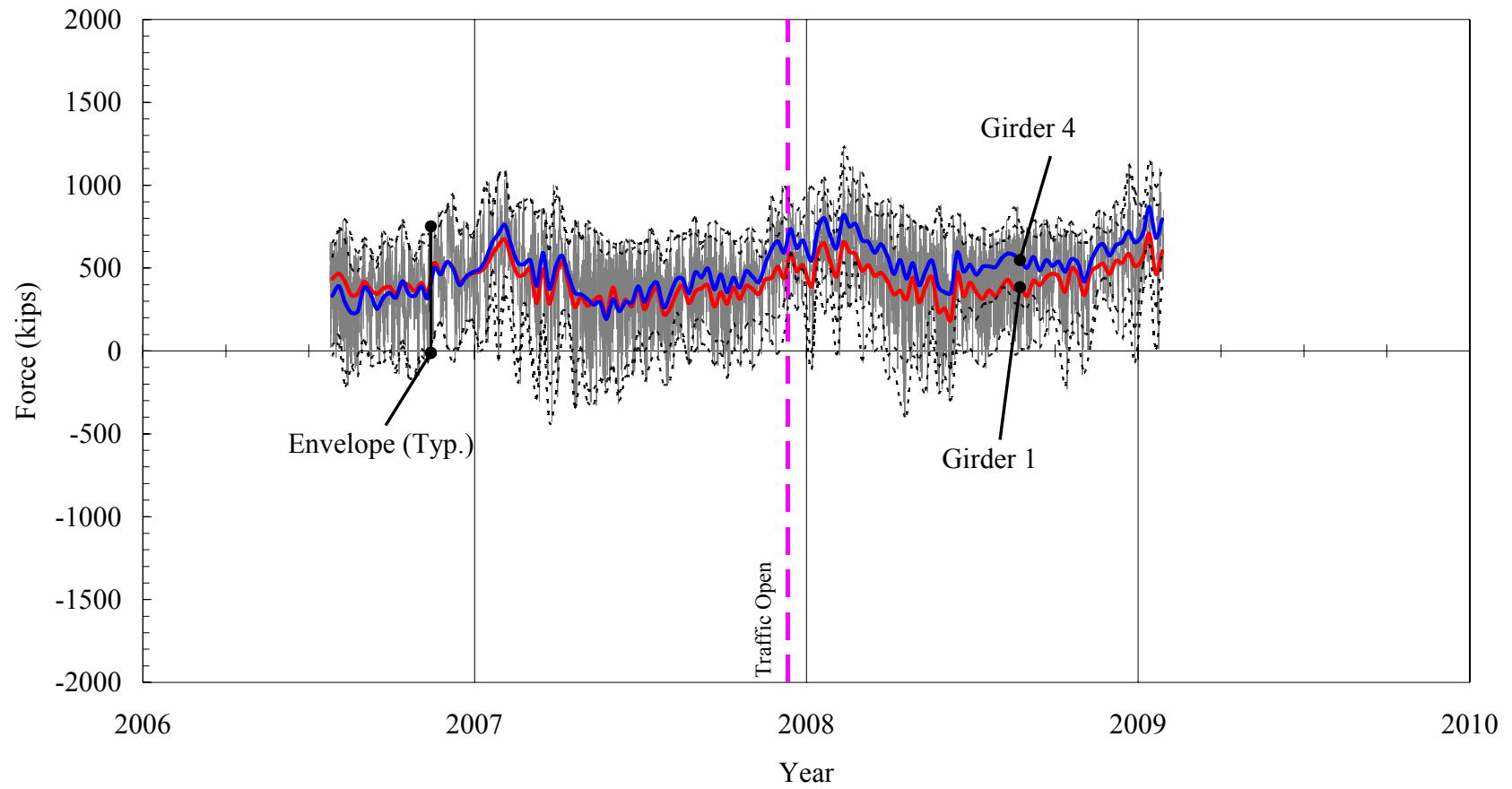


Figure 4.22. Bridge 109: Exterior Girder Axial Forces near Abutment 1.

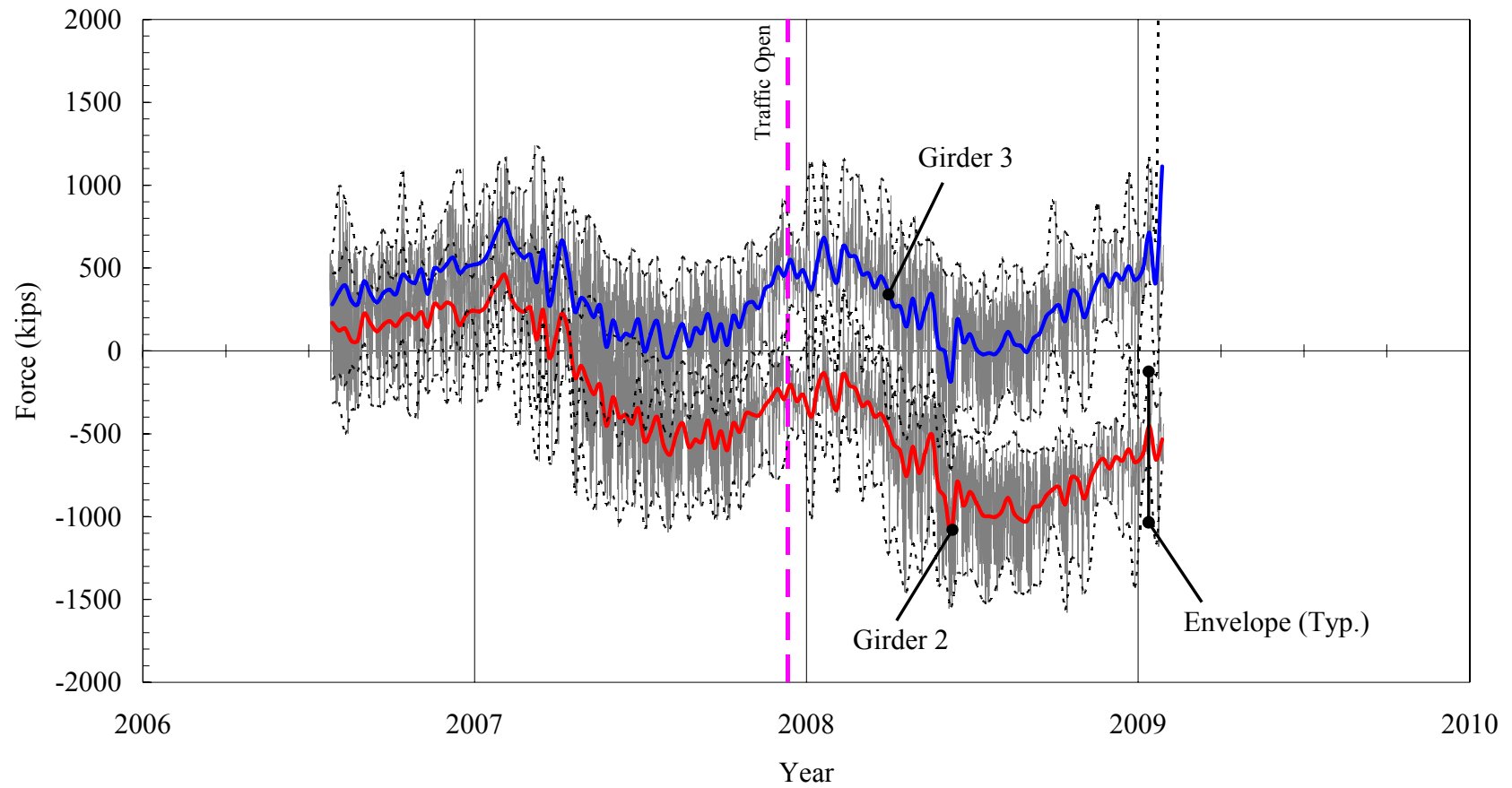


Figure 4.23. Bridge 109: Interior Girder Axial Forces near Abutment 2.

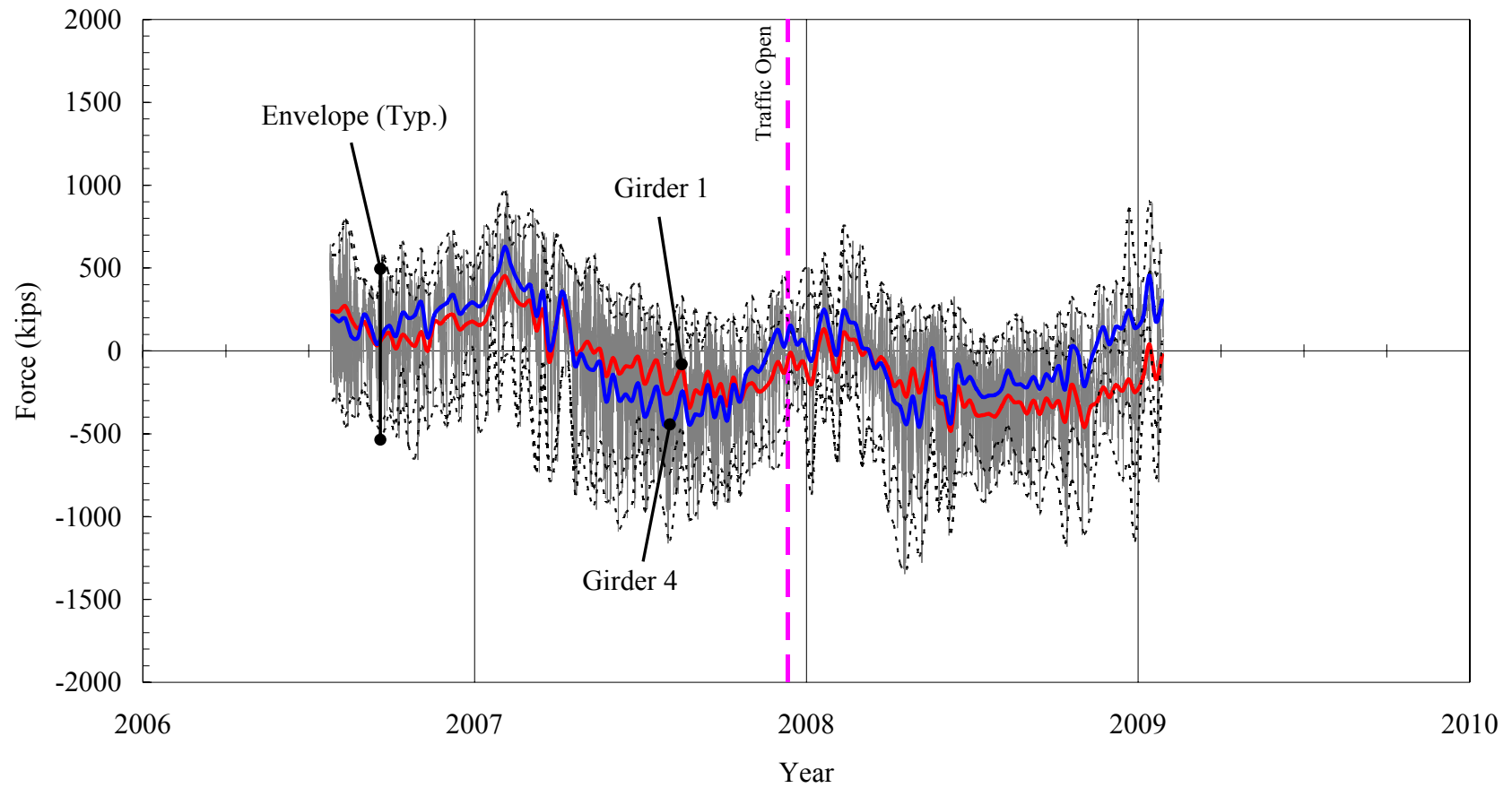


Figure 4.24. Bridge 109: Exterior Girder Axial Forces near Abutment 2.

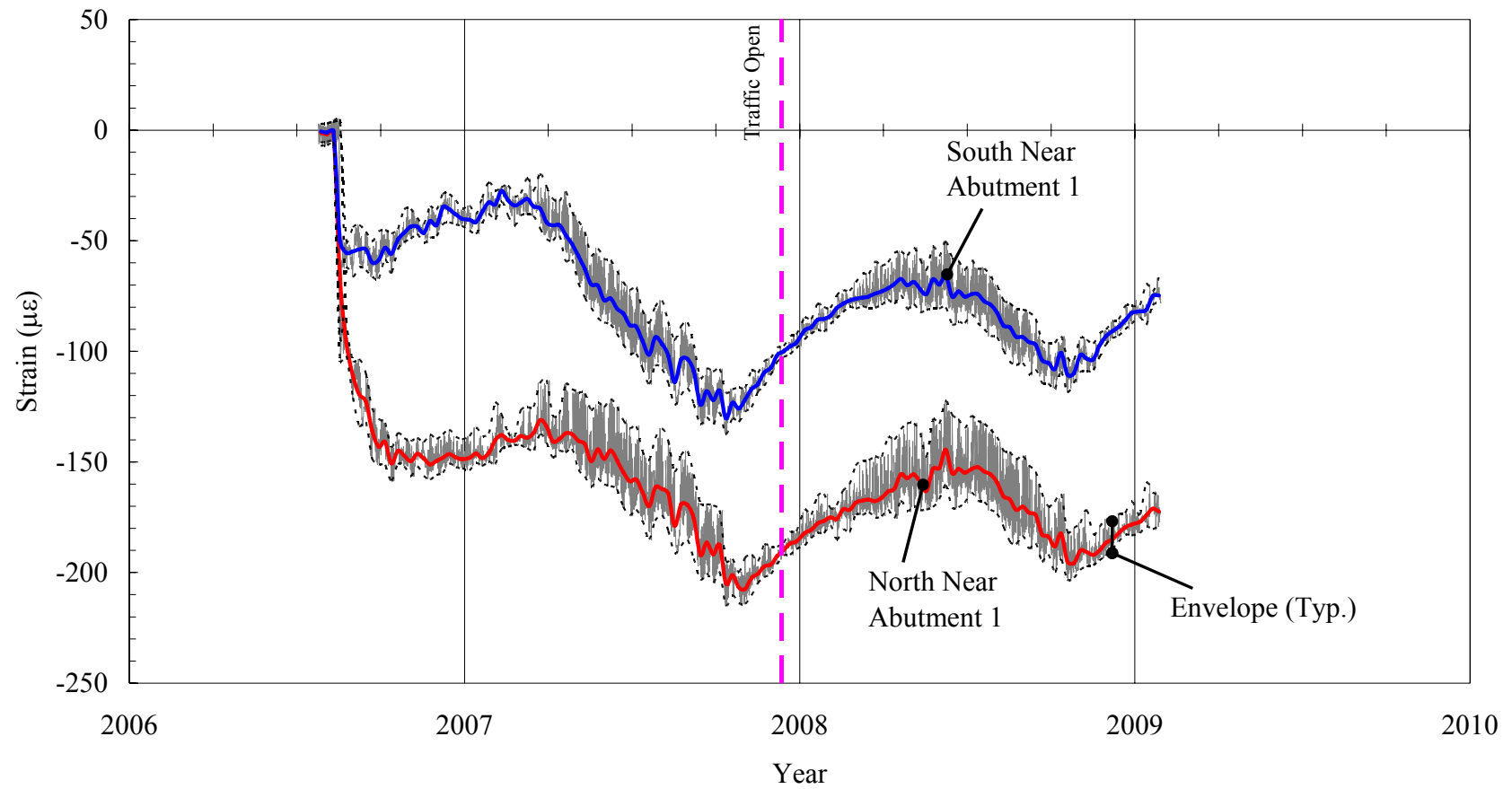


Figure 4.25. Bridge 109: Sister-Bar Gages in Approach Slab near Abutment 1.

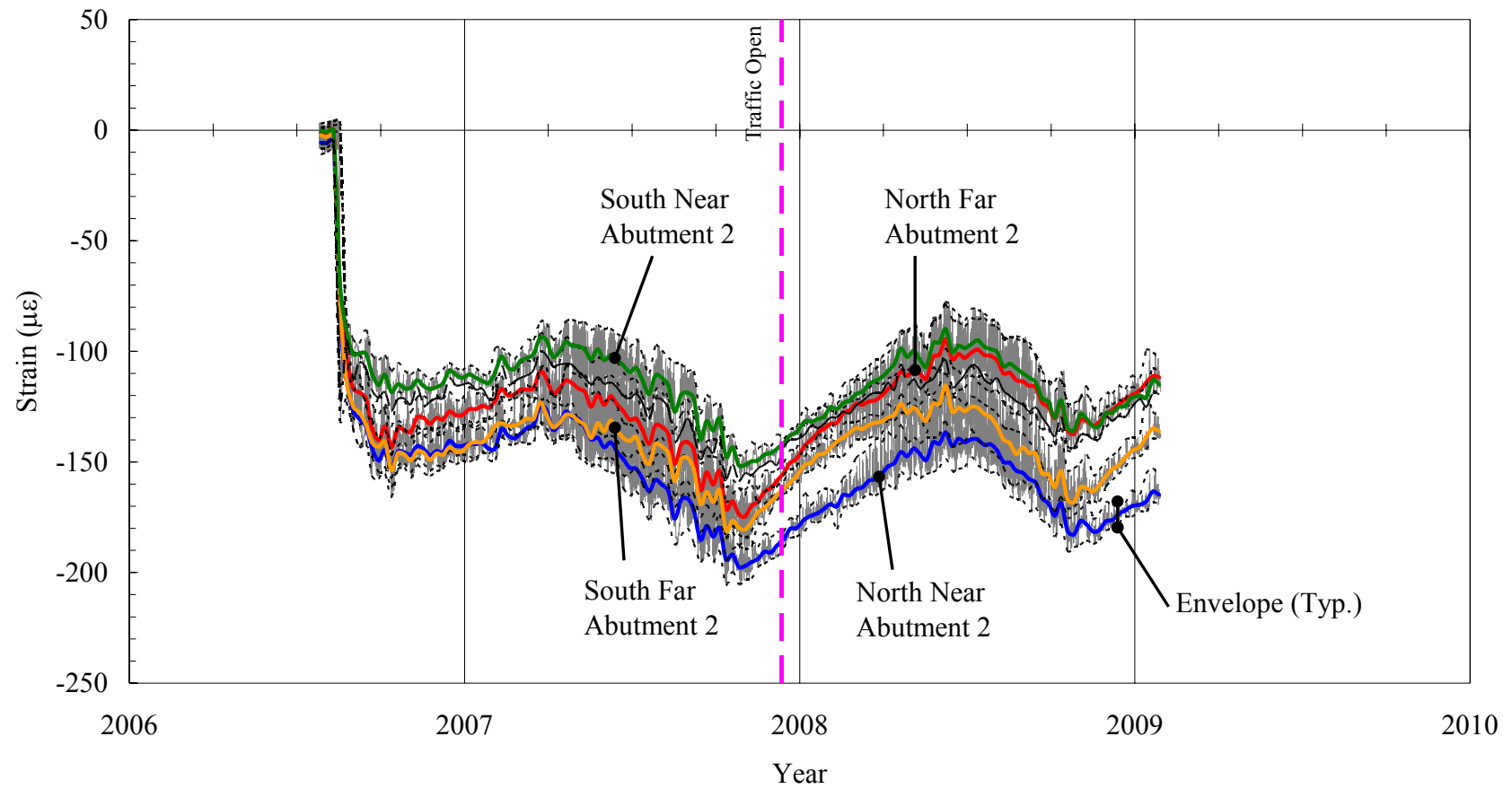


Figure 4.26. Bridge 109: Sister-Bar Gages in Approach Slab near Abutment 2.

4.3 Bridge 203

Data obtained from bridge 203 instruments consist of 3 extensometers, 3 pressure cells, 8 tiltmeters, 30 strain gages on two piles, 16 strain gages on 4 prestressed concrete girders, and 4 sister bar gages. All initial pile strain gage measurements were recorded as zero values after pile driving. The strain gage channels 1-4, 1-7, and 1-9 on the east pile and 4-16 on the west pile had no signal after pile driving, with the cause presumed to be damage due to the severe conditions. On the east pile, channels 1-2, 4-8, and 4-12 were additionally damaged since September 2004, October 2004, and December 2006, respectively.

Collected data from extensometers at abutments 2 are presented in Figure 4.27. The extensometers measure bridge abutment longitudinal movement as a result of superstructure expansion and contraction. Maximum abutment displacement contraction and expansion are presented in Table 4.3. The middle west and bottom center extensometer at abutment 2 indicate continuous movement of the lower abutment toward the bridge. Contraction displacements of approximately 0.06, -0.01, and 0.04 inches occur at the middle west, middle center, and bottom center location of abutment 2 every years.

Pressure cell data are presented in Figure 4.28. Three pressure cells measure abutment 2 backfill pressure. Backfill pressures at the bottom of abutment 2 vary over a wide range with large amplitudes relative to the daily thermal displacements. The backfill pressure at the top west and top center of abutment 2 vary within a narrow range. Backfill pressures obtained from the abutment 1 bottom pressure cell are 3.3 and 2.3 psi greater than the top west and top center pressure cell. The top west, top center, and bottom center

pressure cells indicated maximum backfill pressures of 13.7 psi (summer 2006), 16.1 psi (summer 2008), and 20.3 psi (summer 2006), respectively.

Table 4.3. Bridge 203 Maximum Abutment Displacement.

Abutment		Abutment 2		
Location		Middle West (in)	Middle Center (in)	Bottom Center (in)
Maximum (Contraction)	Displacement	0.626	0.123	0.299
	Period	Winter 08/09	Winter 06/07	Winter 08/09
Minimum (Expansion)	Displacement	-0.124	-0.195	-0.003
	Period	Winter 02/03	Summer 06	Winter 02/03

Note: Abutment 1 is not an integral abutment.

Abutment tiltmeter data are presented in Figure 4.29. Four tiltmeters are mounted on each abutment under the centerline of four girders. The two tiltmeters under girders 2 and 3 indicate an abutment rotation variation corresponding to temperature variation, while the two tiltmeters under girders 1 and 4 indicate observably less fluctuation. During the winter, abutment inclination increased toward the bridge, corresponding to the measured longitudinal displacements. The lower-bound abutment 2 rotation at the centerline of girder 2 increased (starting from initial zero) from 0.048 to 0.143 to 0.169 to 0.189 to 0.208 to 0.207 degrees over a 6-year period. The lower-bound abutment 2 rotation at the centerline of girder 3 increased (starting from initial zero) from 0.026 to 0.092 to 0.103 to 0.112 to 0.122 to 0.133 degrees over a 6-year period. Maximum changes in rotation of abutment 2 at the centerline of girders 1, 2, 3, and 4 were 0.142 degrees (summer 2008), 0.322 degrees (summer 2008), 0.248 degrees (summer 2008), and 0.187 degrees (summer 2008).

Girder tiltmeter data are presented in Figure 4.30. Four tiltmeters were placed directly on the web of each girder near abutment 2. Girders rotated with a trend that corresponds with seasonal temperature variation. Tiltmeters near abutment 2 measured a maximum rotation of 0.036 degrees at girder 1, 0.181 degrees at girder 2, 0.127 degrees at girder 3, and 0.255 degrees at girder 4.

Pile bending moments about the weak axis at two piles, east and west at abutment 2, are presented in Figure 4.31. The position of the gages and maximum measured moments are shown in Table 4.4. The H-pile bending strengths are $\phi M_{yielding} = 127$ ft-kip and $\phi M_{plastic} = 194$ ft-kip (based on $F_y = 50$ ksi).

Table 4.4. Bridge 203 Pile Strain Gage Depths Below Bottom of Abutment and Maximum Measured Moment.

	Abutment 2	
	Placement	Max. Moment
East Pile	4' - 3"	N/A*
	8' - 3"	N/A*
	13' - 3"	-16.2 ft-kips
West Pile	2' - 5"	80.4 ft-kips
	6' - 5"	28.3 ft-kips
	11' - 5"	-11.3 ft-kips

* channels 1-4 and 1-7 were damaged after pile driving.

Pile axial forces are presented in Figures 4.32 through 4.34. The average pile axial force measured, including dead loads and down drag forces accumulated over the monitoring period, are: east pile at the bottom location = 71 kips, west pile at the top location = 127 kips, and west pile at the bottom location = 84 kips. Maximum measure axial forces on each pile are presented in Table 4.5.

Table 4.5. Bridge 203 Pile Strain Gage Depths Below Bottom of Abutment and Maximum Measured Axial Force.

Abutment 2			
East Pile		West Pile	
Placement	Max. Axial Force	Placement	Max. Axial Force
4' - 3"	N/A	2' - 5"	149.9
8' - 3"	N/A	6' - 5"	99.7
13' - 3"	86.3	11' - 5"	93.5
17' - 3"	102.3	19' - 5"	98.0
25' - 3"	103.5	23' - 5"	87.6
29' - 3"	92.4	27' - 5"	108.0
33' - 3"	74.7	31' - 5"	88.9
37' - 3"	51.4	35' - 5"	81.7

* channels 1-4 and 1-7 were damaged after pile driving.

Girder moments derived from measured strain are presented in Figure 4.35 to Figure 4.38. Girder moments were measured at the girder center and the girder end on the exterior span near abutment 2. Two strain gages are located at the girder center, one at the top and one at the bottom flange. Two strain gages are located 1 ft from each girder end, one at the top and one at the bottom flange. At the girder center, only girder 1 indicates a positive moment increasing trend, while other girders had a negative moment increasing trend. At the girder center, moment measurements at girders 2 and 3 indicate opposite fluctuations to each other. Maximum positive moments of girder 1, 2, 3 and 4 are 1749, 172, 442 and 760 ft-kip. Maximum negative moments of girders 1, 2, 3 and 4 are 283, 2885, 3160, and 1567 ft-kip. At the girder end, maximum positive moments for girders 1, 2, and 3 are 440, 2330, and 1745 ft-kip, and no positive moments were measured at girder 4. Maximum negative moments for girders 1, 2, 3, and 4 are 1309, 2419, 412, and 1,562 ft-kip.

Girder axial forces are presented in Figure 4.39 to Figure 4.42. The girder axial forces varied irregularly. At the girder center, maximum tensile axial forces 1, 2, 3, and 4 at the girder center measured 2219, 1312, 2627, and 1248 kips, and maximum compressive axial force measured 1.0, 658, 655, and 1361 kips. At the girder end, maximum tensile axial forces at girders 1, 2, 3, and 4 measured 982, 1885, 2006, and 2179 kips, and maximum compressive axial force reached 1132, 723, 66, and 0.0 kips.

Sister-bar strain data at the approach slab on abutments 1 and 2 are presented in Figure 4.43. The sister-bar gages near abutment 2 indicate a similar compression strain, ranging from -270 to -150 $\mu\epsilon$. The east sister-bar gage far from abutment 1 indicates less compression strain, ranging from -170 to +10 $\mu\epsilon$. Sister-bar gages indicated initial changes in compressive strain from 0 to 250 $\mu\epsilon$ due to concrete creep and shrinkage. Daily temperature variation correlation with all sister-bar strain were high during summer (approximately 30 $\mu\epsilon$), while daily strain changes during winter were less than 10 $\mu\epsilon$.

Bridge 203 Processed Response Data Figure List:

Figure 4.27. Bridge 203: Extensometers on Abutment 2.

Figure 4.28. Bridge 203: Pressure Cells on Abutment 2.

Figure 4.29. Bridge 203: Tiltmeter on Abutment 2.

Figure 4.30. Bridge 203: Tiltmeter on Girders near Abutment 2.

Figure 4.31. Bridge 203: Pile Moments under Abutment 2.

Figure 4.32. Bridge 203: Pile Axial Forces in Shallow Soil Strata under Abutment 2.

Figure 4.33. Bridge 203: East Pile Axial Forces in Deep Soil Strata under Abutment 2.

Figure 4.34. Bridge 203: West Pile Axial Forces in Deep Soil Strata under Abutment 2.

Figure 4.35. Bridge 203: Interior Girder Moments at Midspan.

Figure 4.36. Bridge 203: Exterior Girder Moments at Midspan.

Figure 4.37. Bridge 203: Interior Girder Moments at Endspan.

Figure 4.38. Bridge 203: Exterior Girder Moments at Endspan.

Figure 4.39. Bridge 203: Interior Girder Axial Forces at Midspan.

Figure 4.40. Bridge 203: Exterior Girder Axial Forces at Midspan.

Figure 4.41. Bridge 203: Interior Girder Axial Forces at Endspan.

Figure 4.42. Bridge 203: Exterior Girder Axial Forces at Endspan.

Figure 4.43. Bridge 203: Sister-Bar Gages.

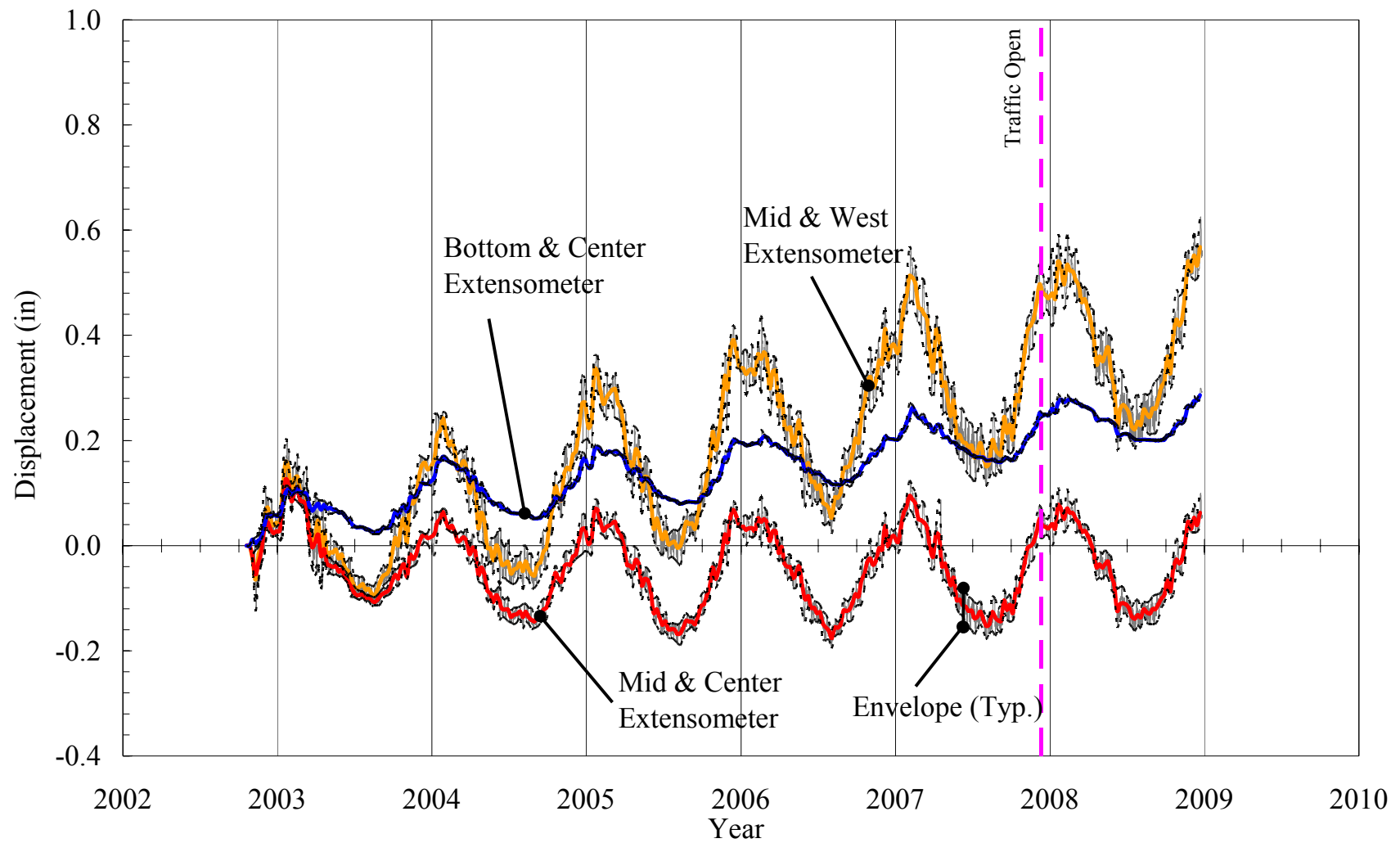


Figure 4.27. Bridge 203: Extensometers on Abutment 2.

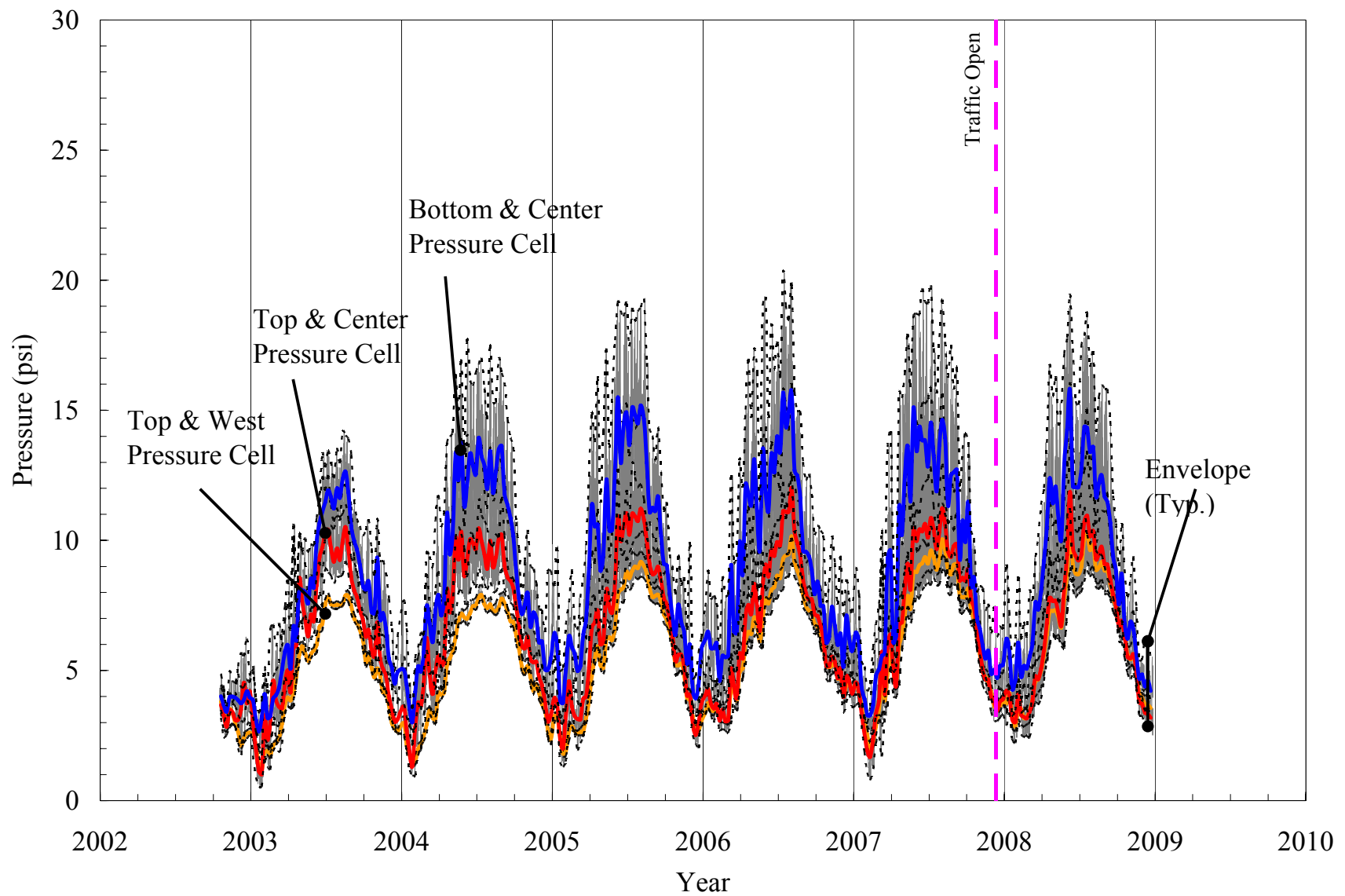


Figure 4.28. Bridge 203: Pressure Cells on Abutment 2.

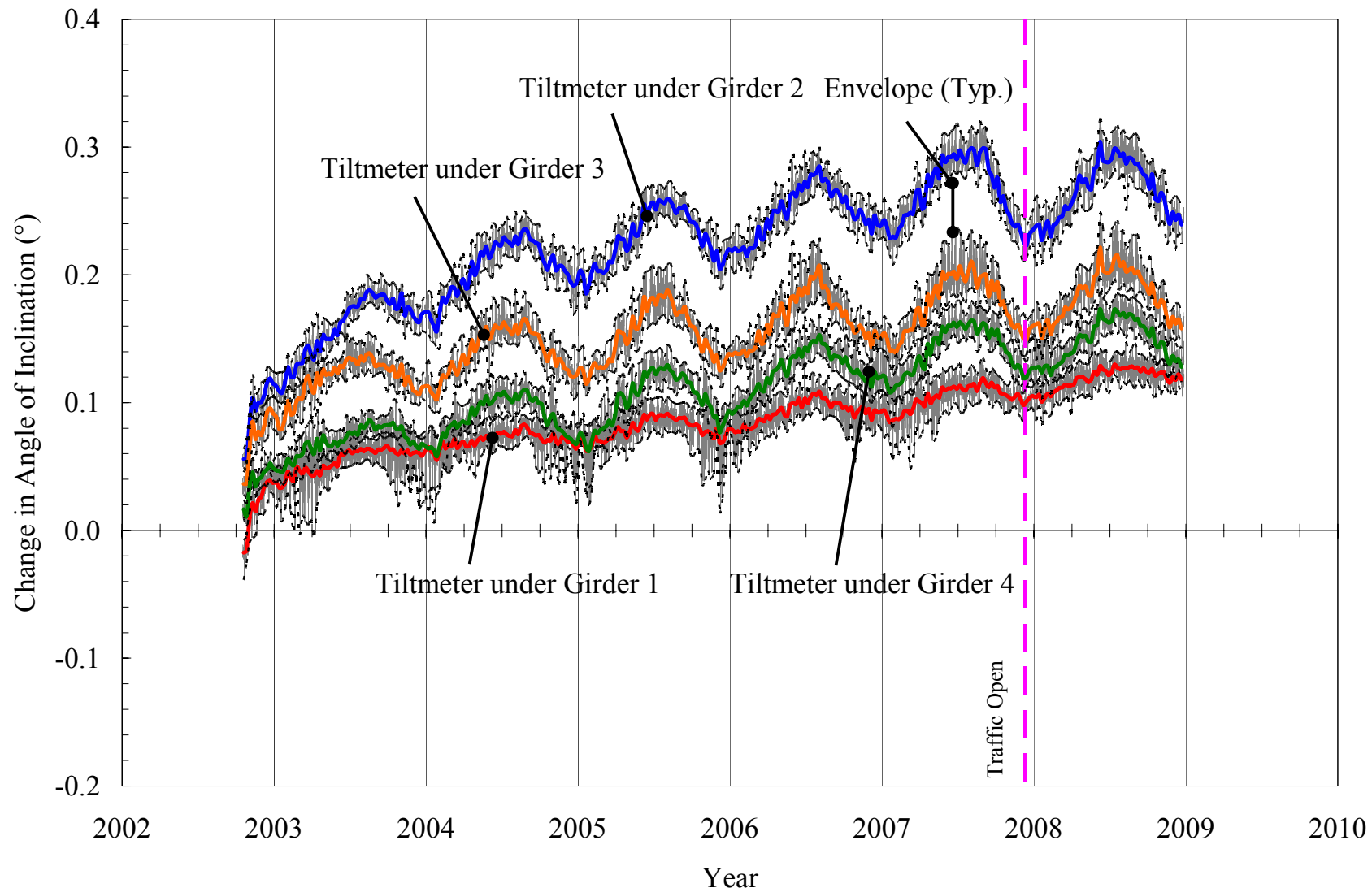


Figure 4.29. Bridge 203: Tiltmeters on Abutment 2.

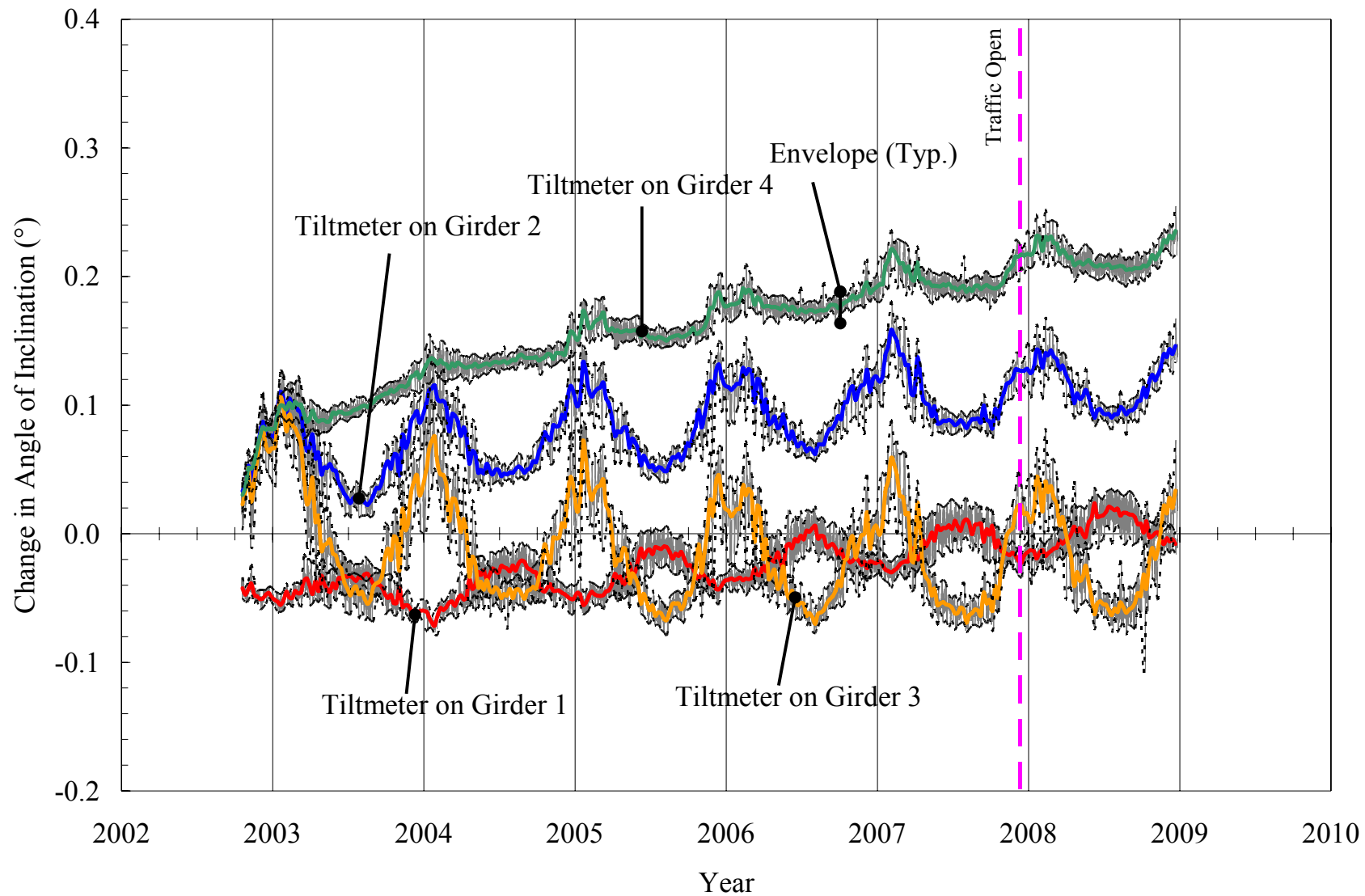


Figure 4.30. Bridge 203: Tiltmeters on Girders near Abutment 2.

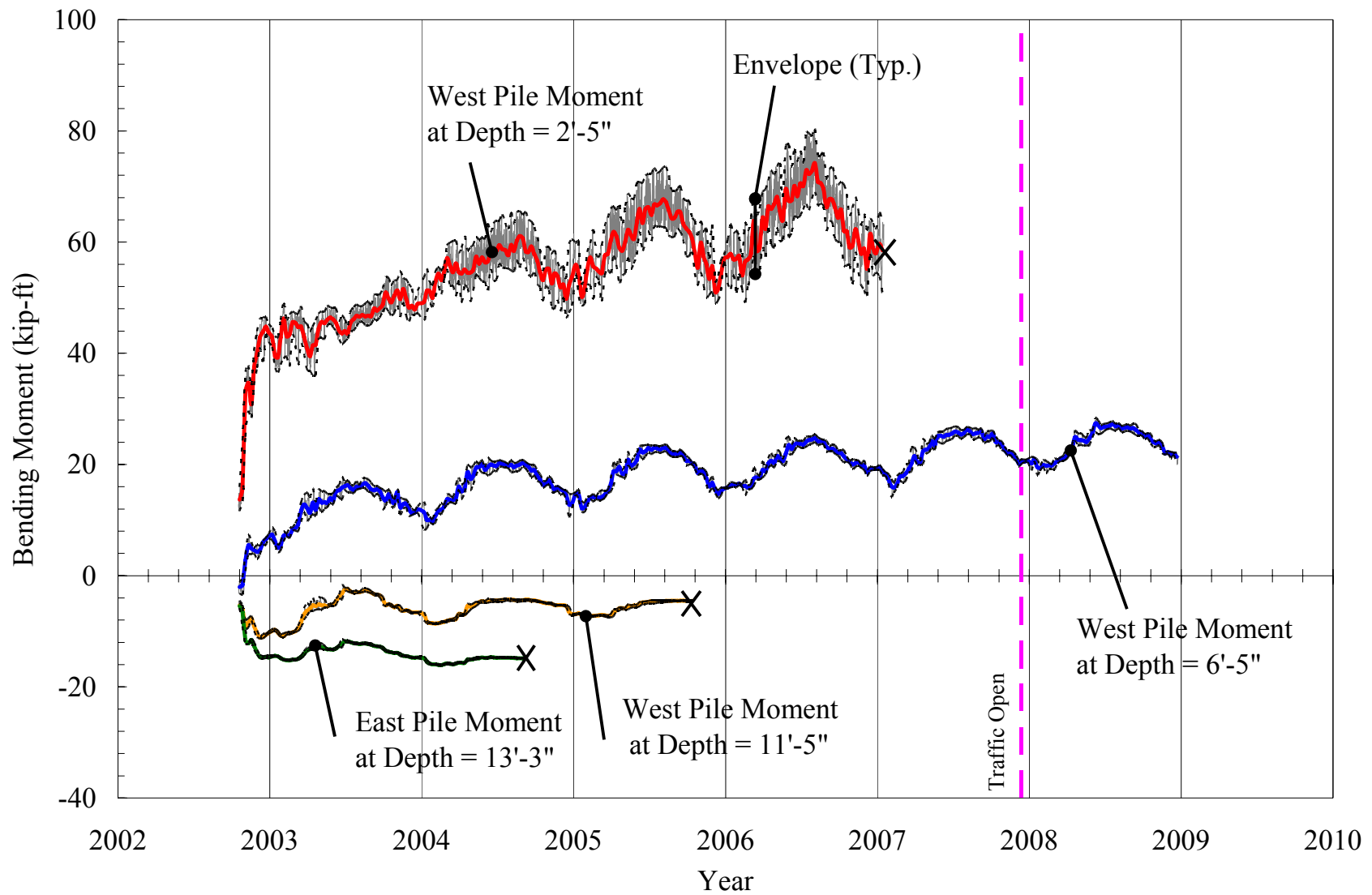


Figure 4.31. Bridge 203: Pile Moments under Abutment 2.

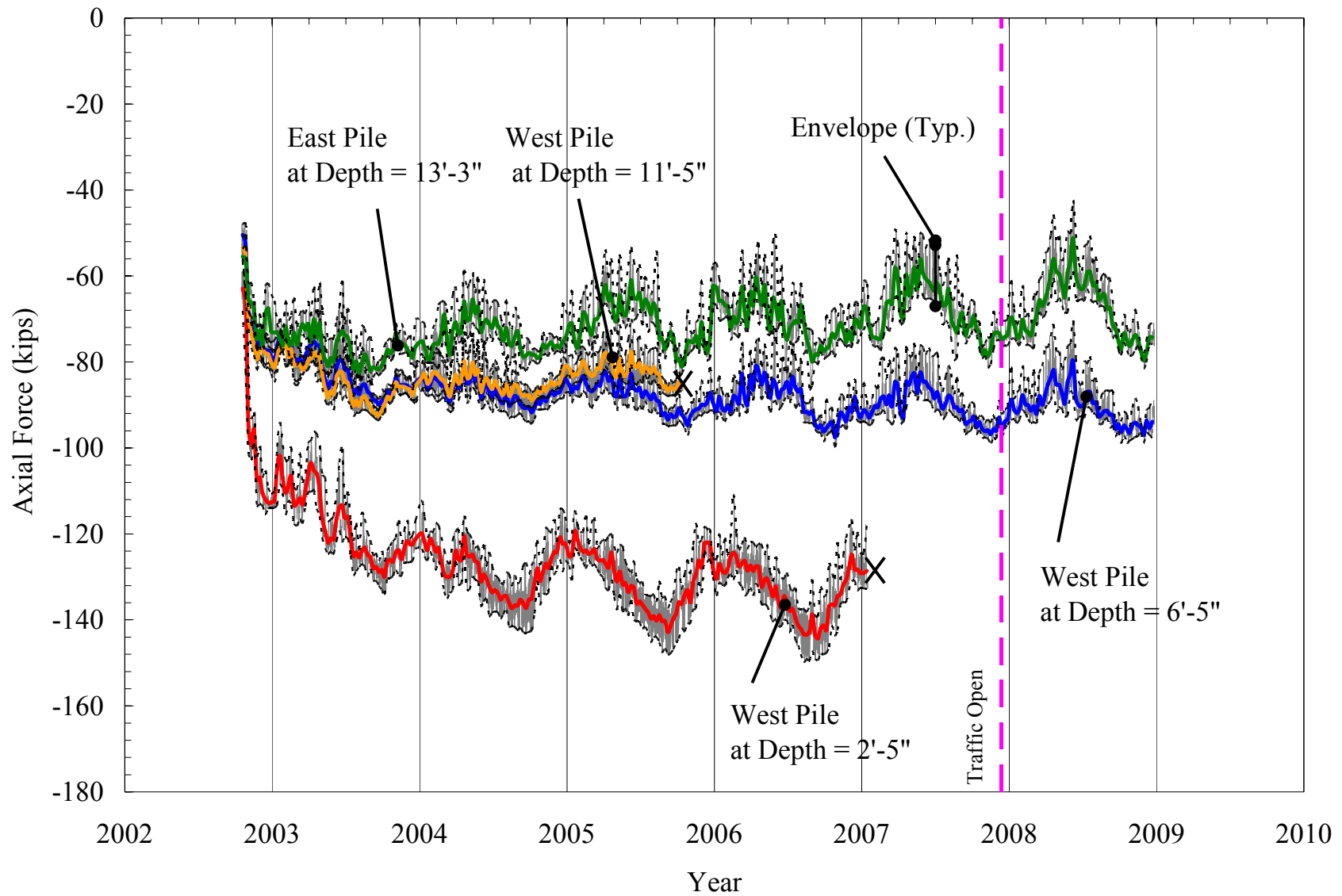


Figure 4.32. Bridge 203: Pile Axial Forces in the Shallow Soil Strata under Abutment 2.

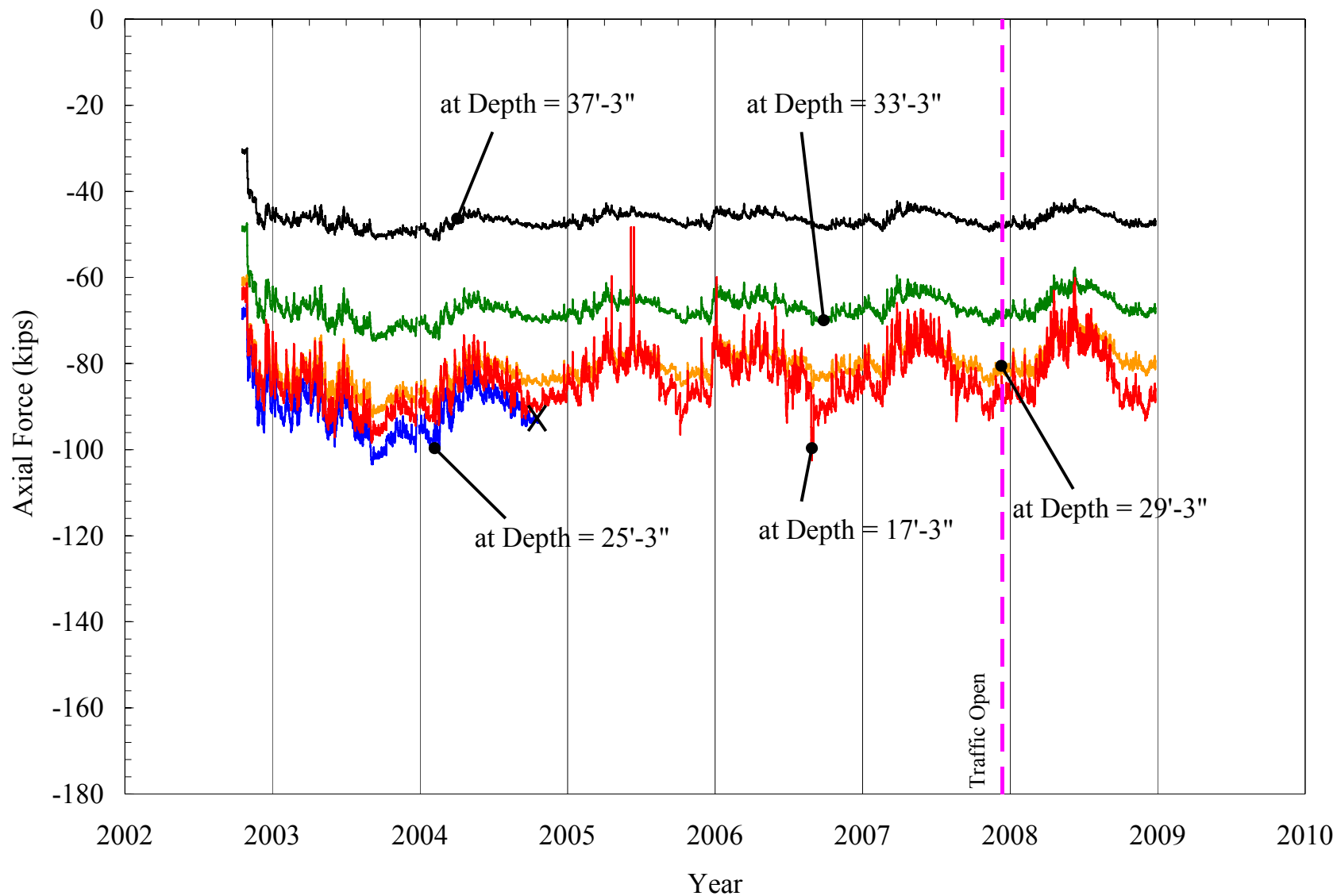


Figure 4.33. Bridge 203: East Pile Axial Forces in the Deep Soil Strata under Abutment 2.

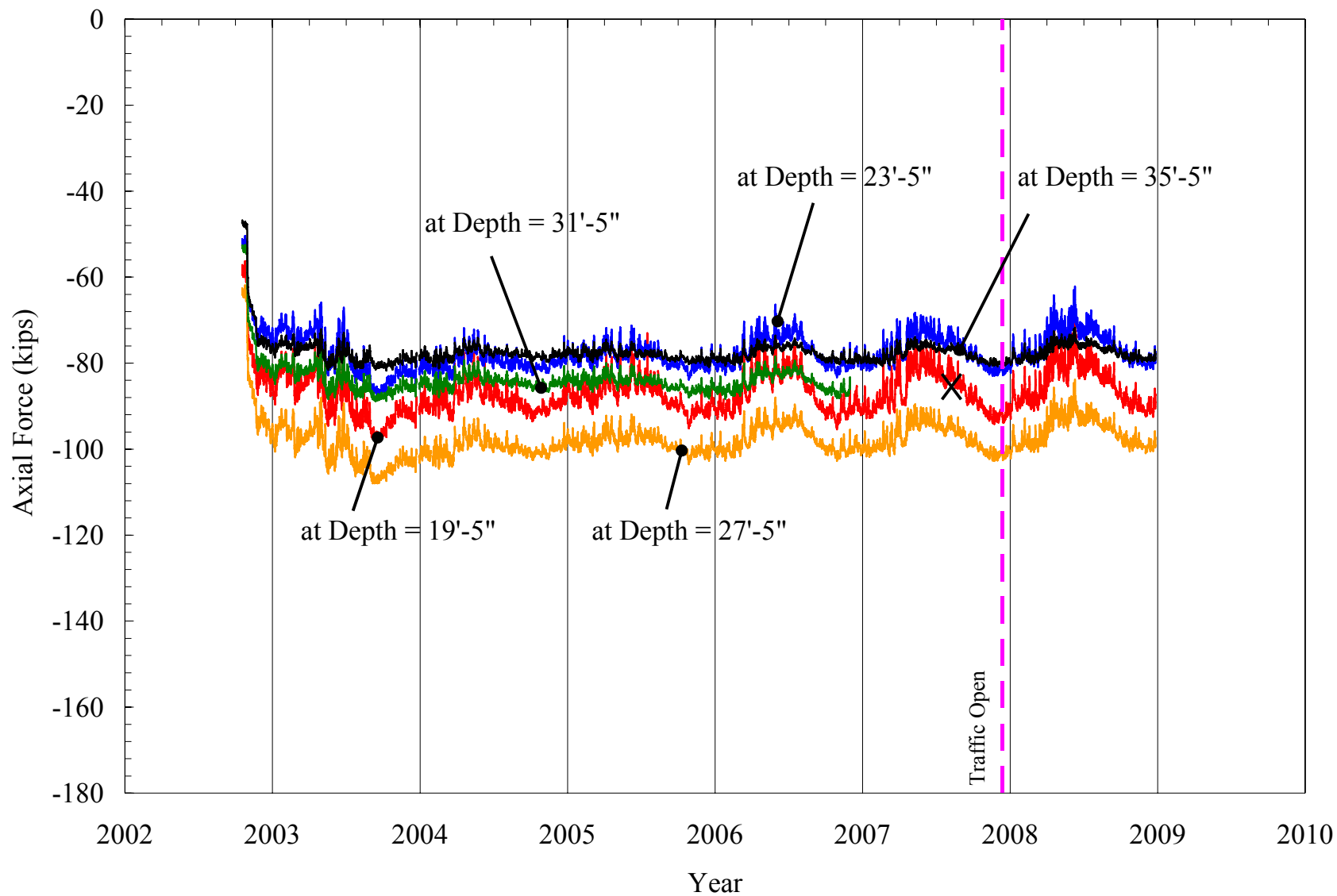


Figure 4.34. Bridge 203: West Pile Axial Forces in the Deep Soil Strata under Abutment 2.

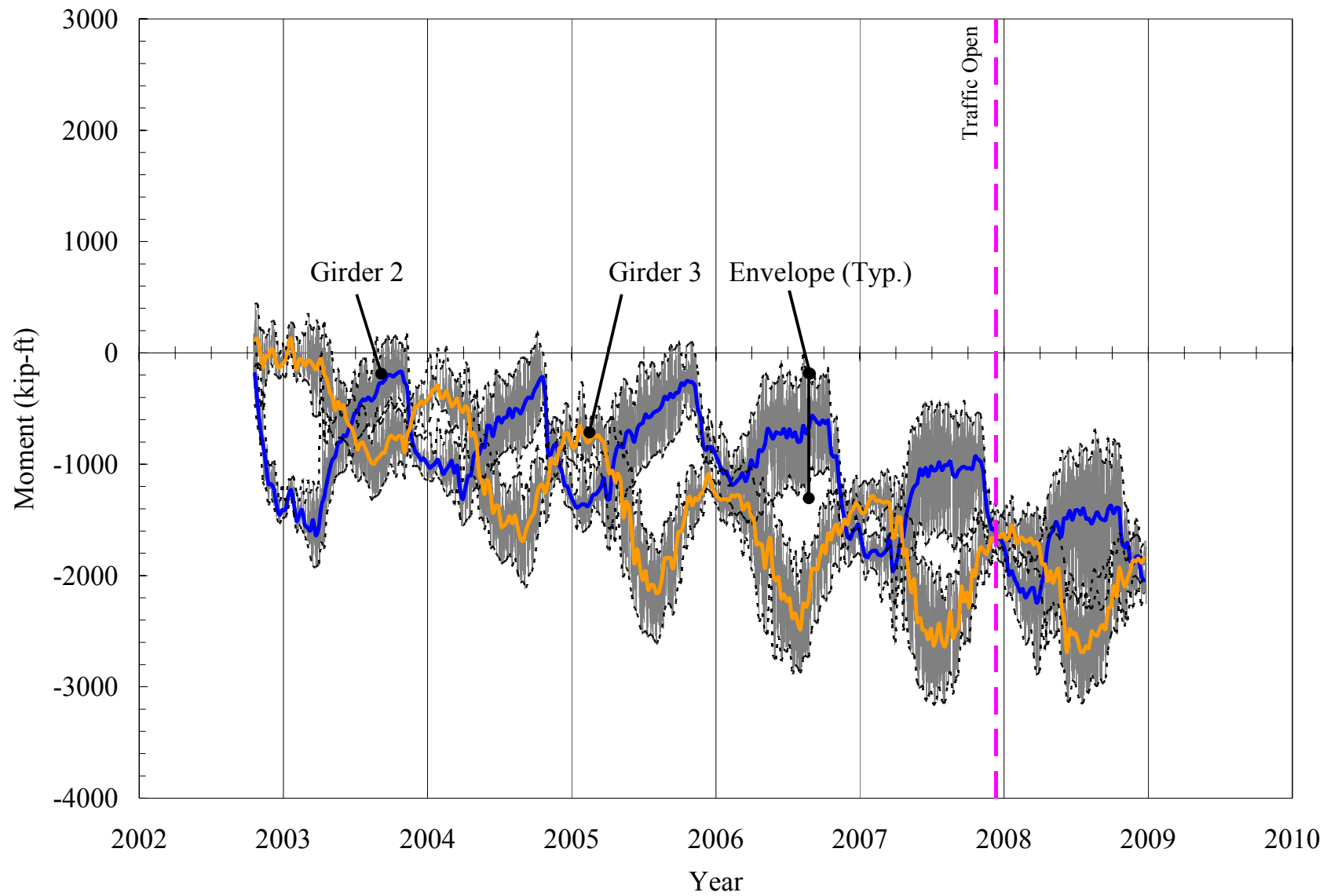


Figure 4.35. Bridge 203: Interior Girder Moments at Midspan.

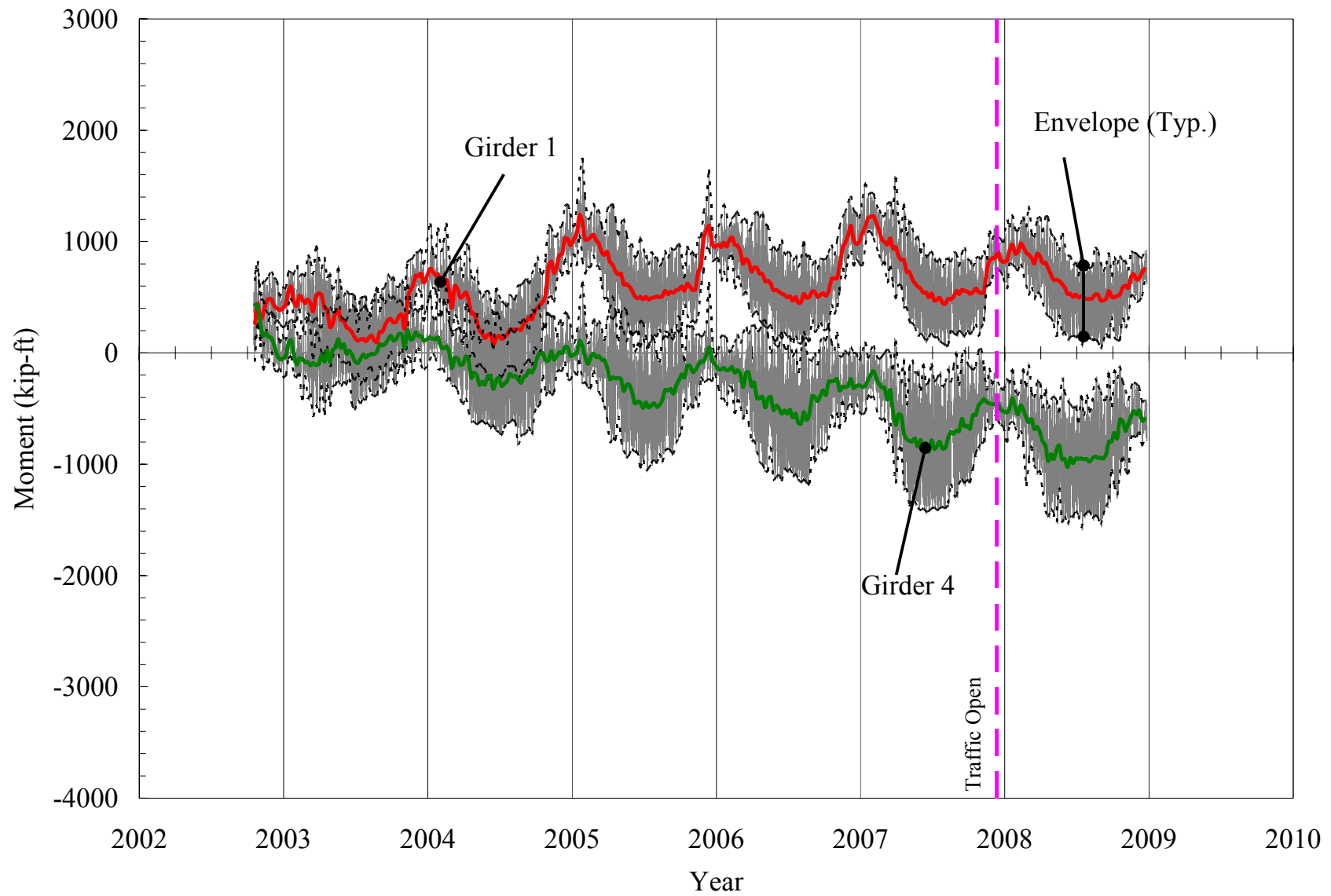


Figure 4.36. Bridge 203: Exterior Girder Moments at Midspan.

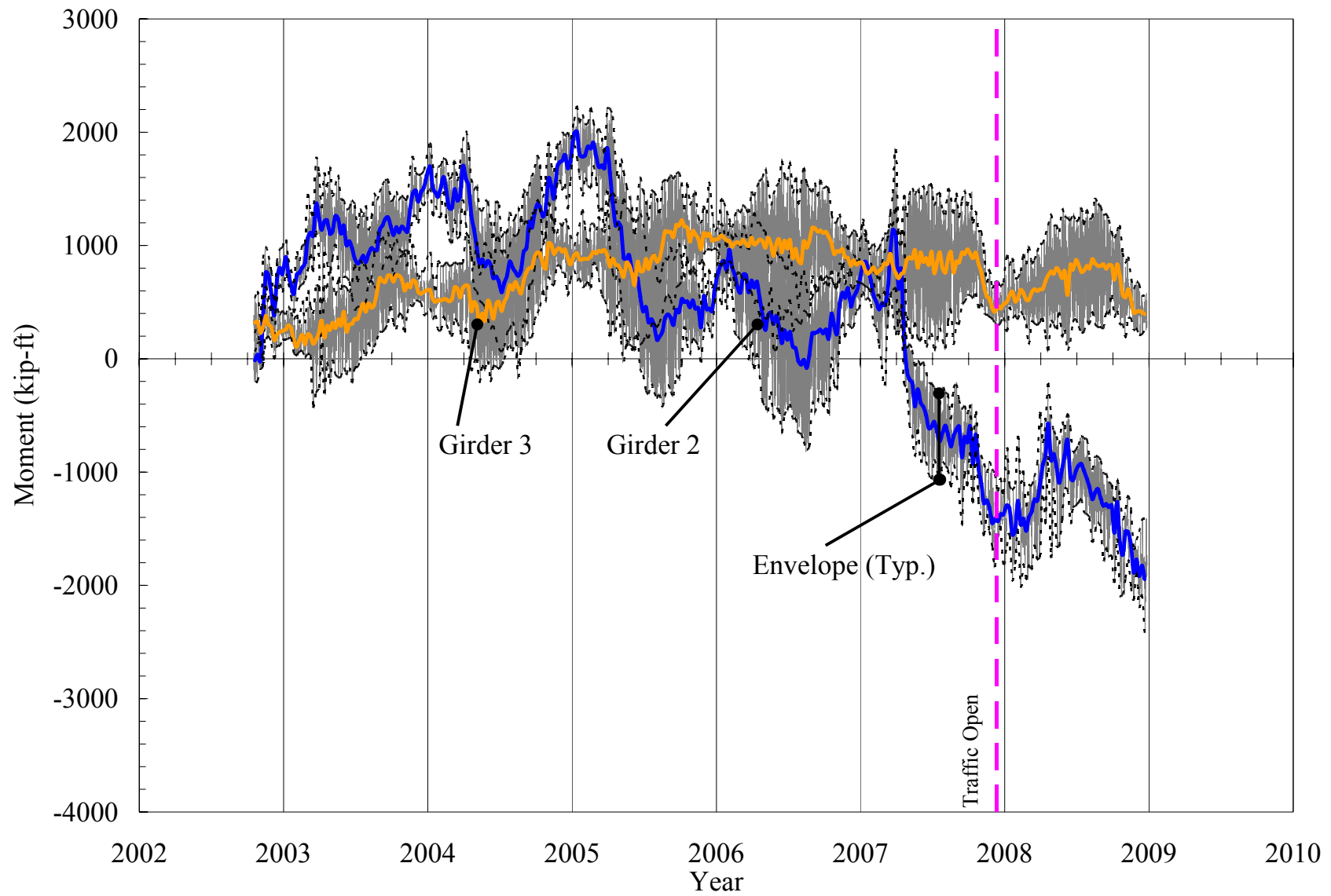


Figure 4.37. Bridge 203: Interior Girder Moments at Endspan.

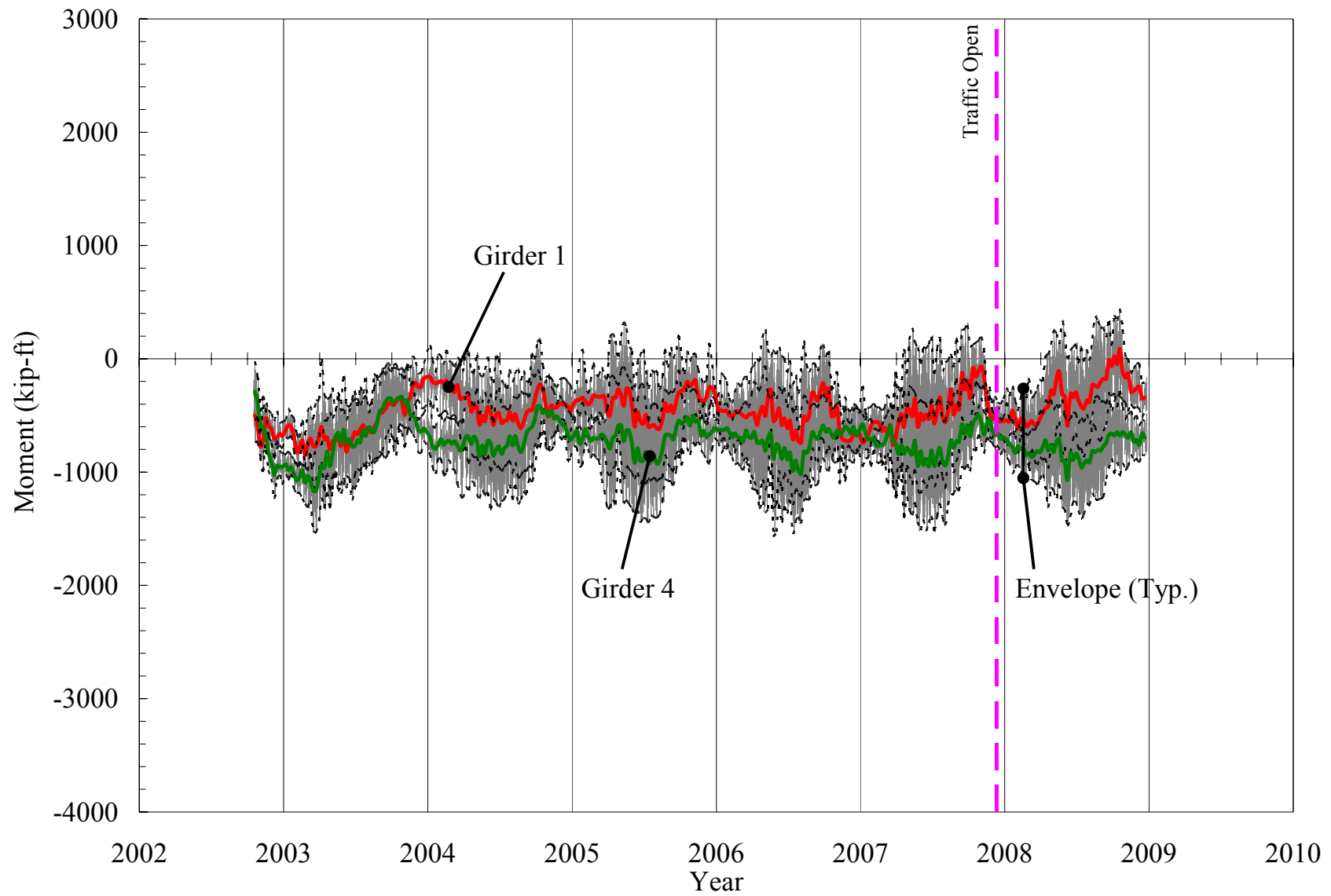


Figure 4.38. Bridge 203: Exterior Girder Moments at Endspan.

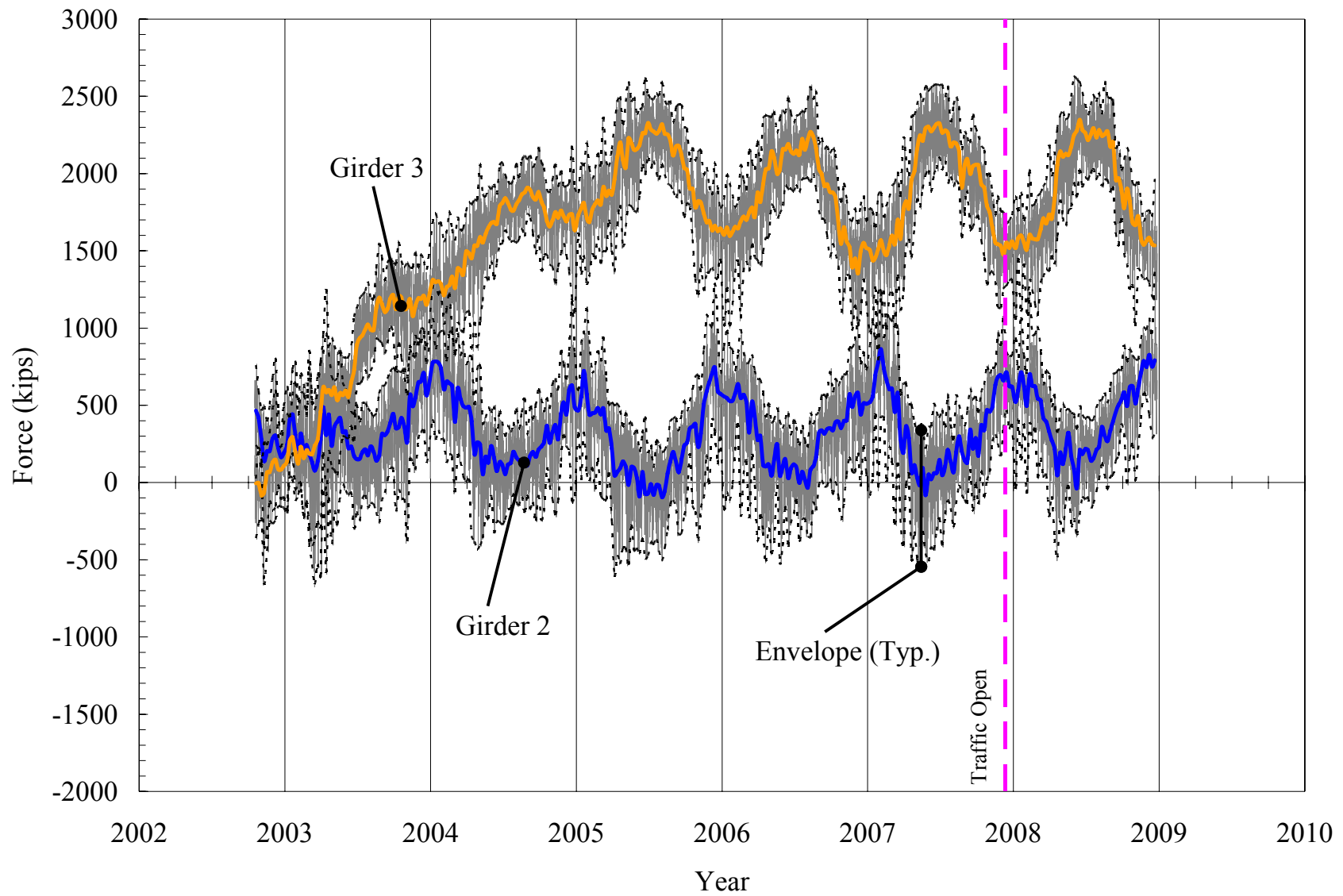


Figure 4.39. Bridge 203: Interior Girder Axial Forces at Midspan.

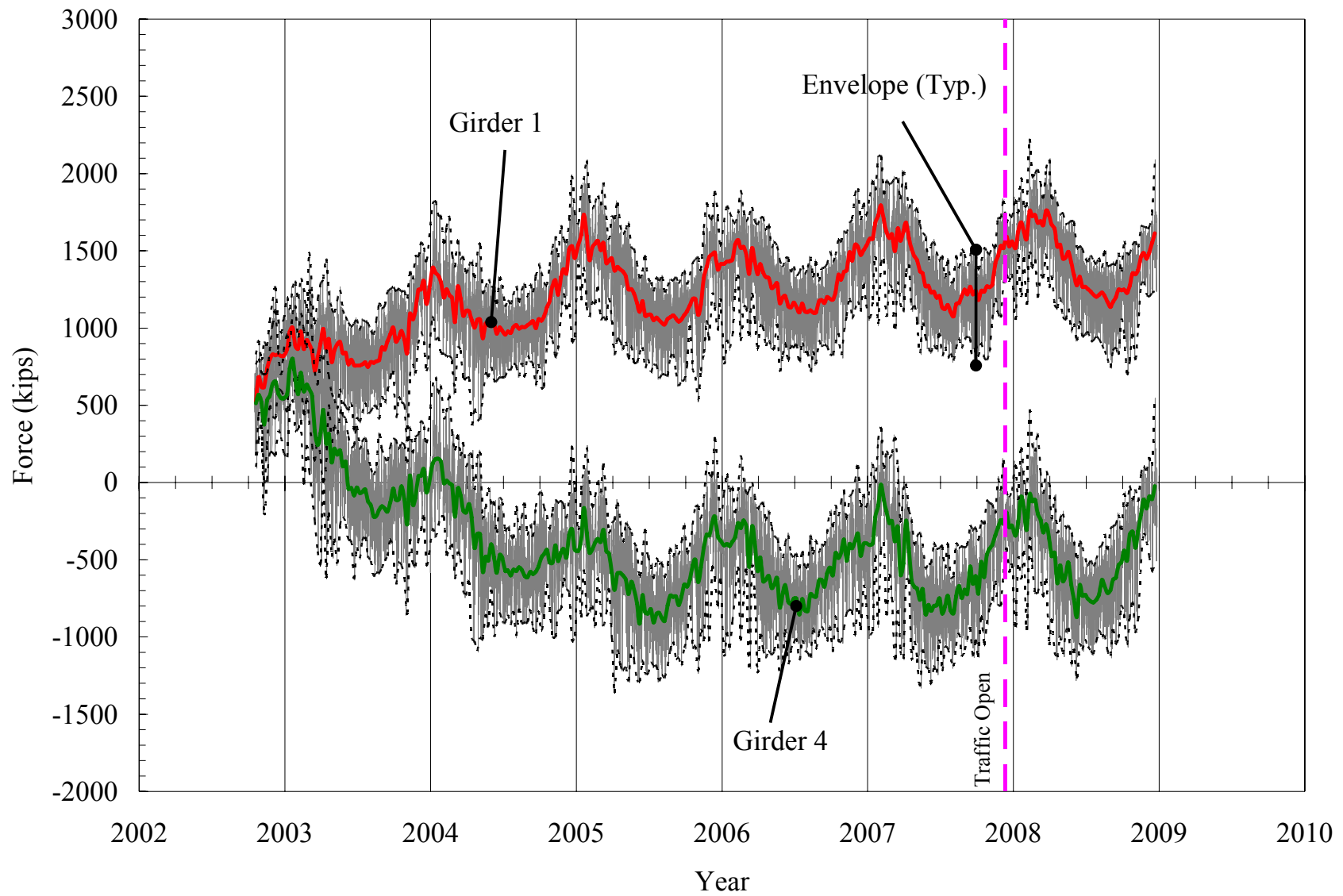


Figure 4.40. Bridge 203: Exterior Girder Axial Forces at Midspan.

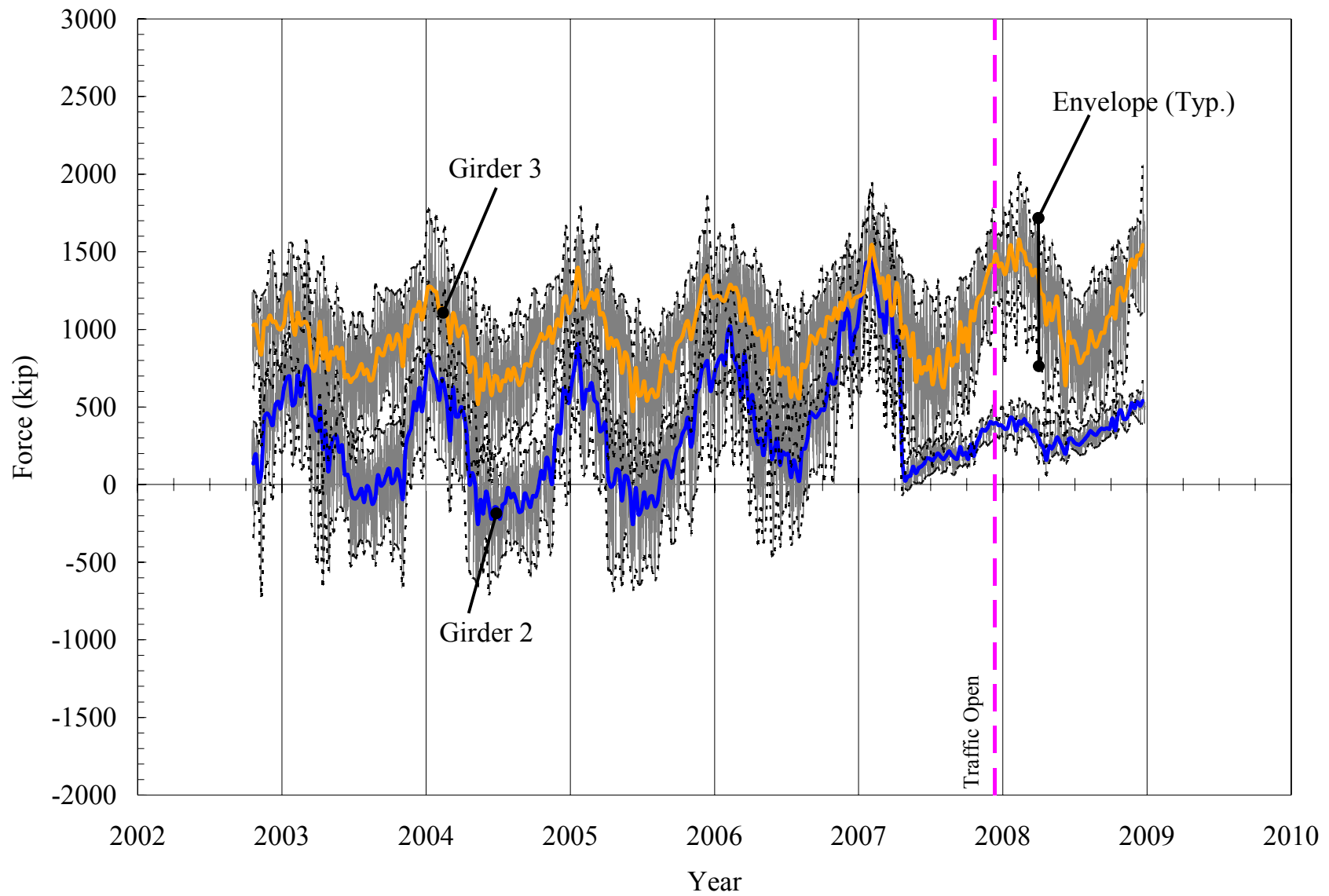


Figure 4.41. Bridge 203: Interior Girder Axial Forces at Endspan.

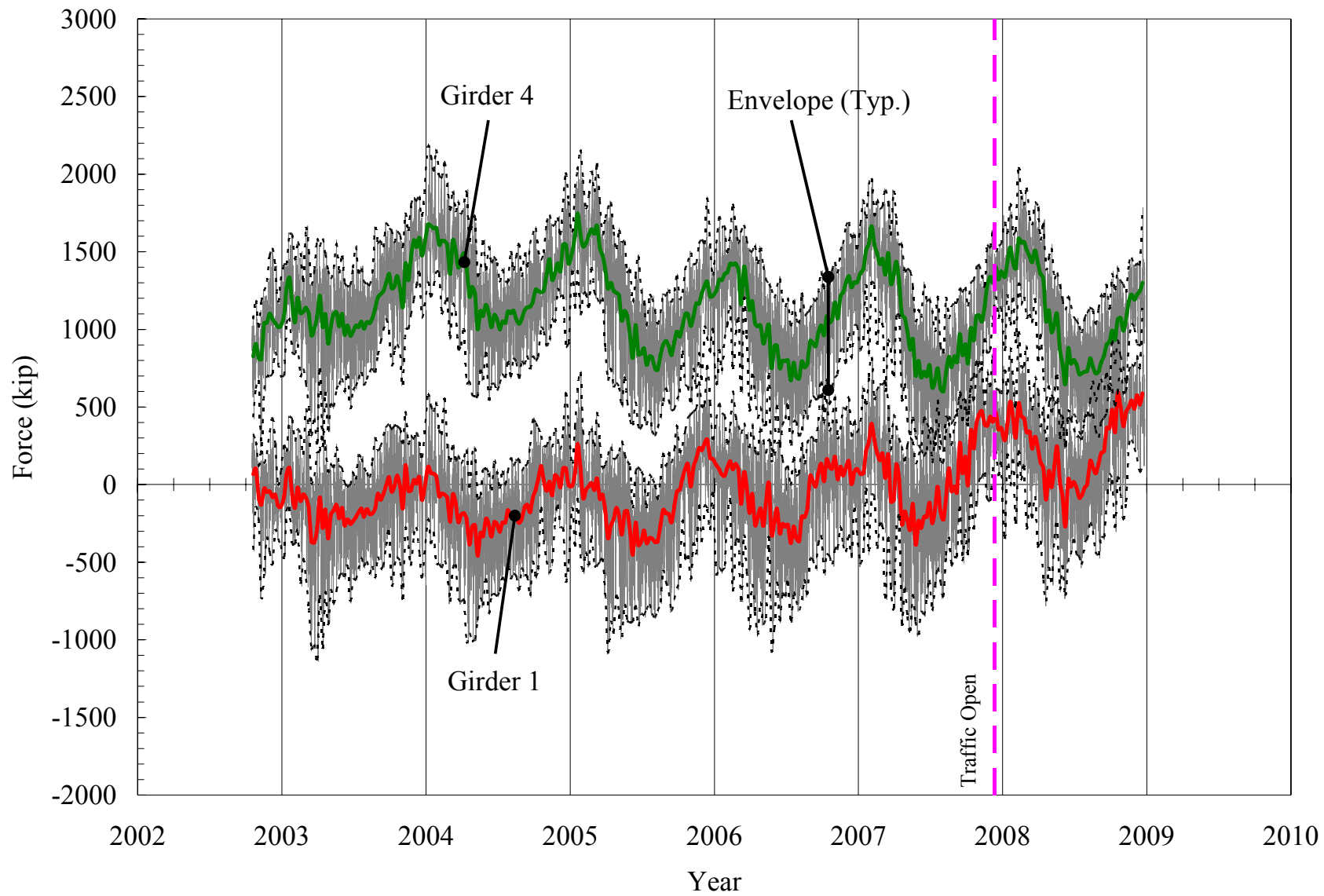


Figure 4.42. Bridge 203: Exterior Girder Axial Forces at Endspan.

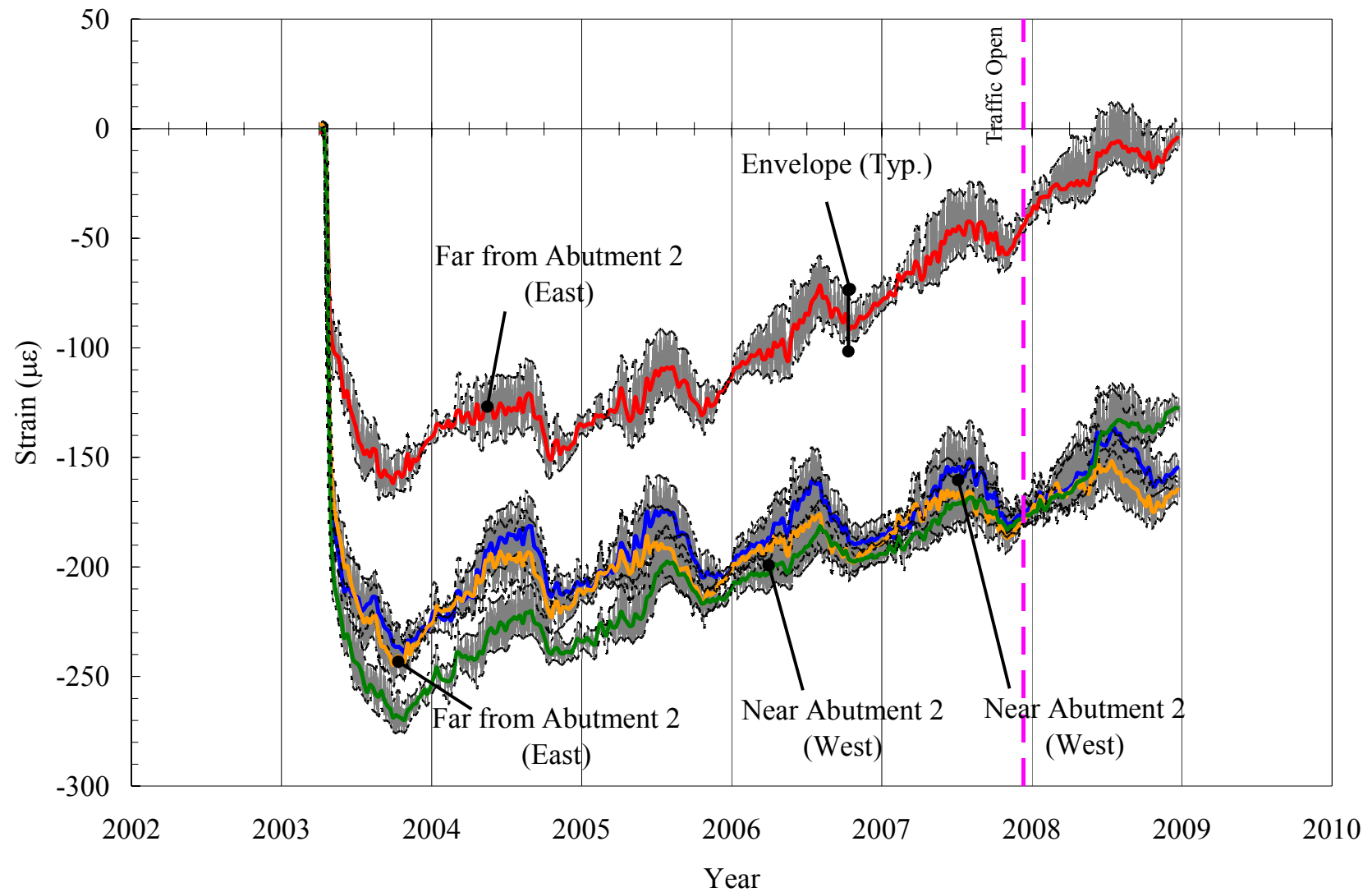


Figure 4.43. Bridge 203: Sister-Bar Gages in Approach Slab near Abutment 2.

4.4 Bridge 211

Data obtained from bridge 211 instruments consist of 4 extensometers, 4 pressure cells, 8 tilt meters, 24 strain gages on four piles, 16 strain gages on 4 prestressed concrete girders, and 8 sister-bar gages. All initial pile strain gage measurements were recorded as zero values after pile driving. The strain gage channel 1-1 located at the bottom of the south pile had no signal since November 2007. The strain gage channels 1-10 and 1-12 at the top of the north pile under abutment 2 had no signals since June 2006. Therefore, no moment and axial force data are available for the top location of the north pile and the bottom location of the south pile under abutment 2 since June 2006 and November 2007, respectively.

Collected data from extensometers at abutments 1 and 2 are presented in Figure 4.44 and Figure 4.45, respectively. The extensometers measure bridge abutment longitudinal movement as a result of superstructure expansion and contraction. Maximum abutment displacement contraction and expansion are presented in Table 4.6. The top and bottom extensometer data at abutment 1 indicate continuous movement of the lower abutment toward the bridge. The top and bottom extensometer data at abutment 2 indicate relatively less abutment movement toward the bridge. At abutment 1, contraction displacements of the top and bottom location occur approximately 0.022 and 0.049 inches every year. At abutment 2, contraction displacements of the top and bottom location occur approximately 0.017 and 0.005 inches every year.

Pressure cell data is presented in Figure 4.46 and Figure 4.47. Two pressure cells measure abutment 1 backfill pressure, and the other two pressure cells measure abutment

2 backfill pressure. Backfill pressures at the bottom of abutment 2 vary over a wide range, with large amplitudes relative to the daily thermal displacements.

Table 4.6. Bridge 211 Maximum Abutment Displacement.

Abutment		Abutment 1		Abutment 2	
Location		Top (in)	Bottom (in)	Top (in)	Bottom (in)
Maximum (Contraction)	Displacement	0.239	0.282	0.178	0.110
	Period	Winter 07/08	Winter 08/09	Winter 07/08	Winter 04/05
Minimum (Expansion)	Displacement	-0.002	-0.012	-0.007	-0.013
	Period	Summer 04	Summer 04	Summer 04	Summer 04

At abutment 1, despite a 7-ft depth difference between the top and bottom pressure cell, the top pressure cell indicated approximately 1.0 psi higher earth pressure with larger amplitudes than the bottom pressure cell during summers. During winters, the top pressure cell indicated approximately 0.55 psi lower earth pressure than the bottom pressure cell. The backfill pressure in abutment 1 varied from -0.67 to 16.6 psi, and the backfill pressure at abutment 2 varied from -0.47 to 12.3 psi. At abutment 2, the bottom pressure cell indicated higher earth pressure (difference = approximately 1.1 psi) during the first 3 years, but both top and bottom pressure cells measured similar earth pressure to each other thereafter. At abutment 1, the top and bottom pressure cells indicated maximum backfill pressures of 16.6 psi (summer 2008) and 11.4 psi (summer 2007). At abutment 2, the top and bottom pressure cells indicated maximum backfill pressures of 11.0 psi (summer 2006) and 12.3 psi (summer 2006).

Abutment tiltmeter data are presented in Figure 4.48 and Figure 4.49. Two tiltmeters are mounted on each abutment under the centerline of girders 1 and 3. The tiltmeters at both abutments indicate an abutment rotation variation corresponding to temperature variation. The tiltmeter under the centerline of girder 3 indicated opposite abutment rotations compared to the other three tiltmeters. During the winter, abutment inclination increased toward the bridge, corresponding to the measured longitudinal displacements. The lower-bound abutment 1 rotation at the centerline of girder 1 increased (starting from initial zero) from -0.011 to 0.011 to 0.019 to 0.029 to 0.037 degrees over a 4-year period. The lower-bound abutment 2 rotation at the centerline of girder 1 increased (starting from initial zero) from 0.013 to 0.041 to 0.060 to 0.064 to 0.071 degrees over a 4-year period. Maximum changes in rotation of abutment 1 at the centerline of girders 1 and 3 were 0.144 degrees (winter 2007/2008) and 0.232 degrees (summer 2008). Rotation of abutment 2 was 0.162 degrees (winter 2007/2008) and 0.162 degrees (winter 2007/2008).

Girder tiltmeter data are presented in Figure 4.50 and Figure 4.51. One tiltmeter was placed directly on the web of girders 1 and 3 near both abutments. Girder 3 rotated with a trend that corresponds to seasonal temperature variation, while girder 1 did not have a seasonal variation. Tiltmeters near abutment 1 measured a maximum rotation of 0.109 degrees at girder 1 and 0.225 degrees at girder 3. Tiltmeters near abutment 2 measured a maximum rotation of 0.151 degrees at girder 1 and 0.062 degrees at girder 3.

Pile bending moments about the weak axis at four piles, 2 each (north and south) at abutments 1 and 2, are presented in Figures 4.52 through 4.55. The position of the gages and maximum measured moments are shown in Table 4.7. The H-pile bending strengths are $\phi M_{yielding} = 127$ ft-kip and $\phi M_{plastic} = 194$ ft-kip (based on $F_y = 50$ ksi).

Table 4.7. Bridge 211 Pile Strain Gage Depths Below Bottom of Abutment and Maximum Measured Moment.

	Abutment 1		Abutment 2	
	Placement	Max. Moment	Placement	Max. Moment
North Pile	2' - 7"	43.7 ft-kips	0' - 6"	34.5 ft-kips
	9' - 7"	-5.4 ft-kips	7' - 6"	- 10.0 ft-kips*
South Pile	1' - 1"	25.4 ft-kips	(-)0' - 6"	15.1 ft-kips
	8' - 1"	8.4 ft-kips	6' - 6"	5.3 ft-kips

* maximum negative moment for the pile with a negative moment increasing trend.

Pile axial forces are presented in Figure 4.56 through Figure 4.57. The average pile axial force measured, including dead loads and down drag forces accumulated over the monitoring period, are abutment 1 north pile = 105 kips, abutment 1 south pile = 103 kips, abutment 2 north pile = 90 kips, and abutment 2 south pile = 93 kips.

Girder moments derived from measured strain are presented in Figures 4.58 to 4.61. Two strain gages are located 1 ft from each girder end, one at the top and one at the bottom flange. All girder moments tend to decrease compared to the preceding year, i.e., negative moments become more negative. The increasingly negative moments are more pronounced in exterior girders. Except girder 4 moments near abutment 2, all girders responses near both abutments are similar, varying within the upper and lower bound of 1050ft-kip and -3450 ft-kip.

Girder axial forces are presented in Figures 4.62 to 4.65. Girder axial forces near abutment 1 varied within a range of -1500 to 1100 kips. Girder axial forces near abutment 2 varied within a range of -880 to 1560 kips. During the first winter (winter 2004/2005), all girders reached their maximum tensile axial force: near abutment 1, girder 1 = 976 kips, girder 2 = 1088 kips, girder 3 = 944 kips and girder 4 = 1092 kips; near abutment 2, girder 1 = 1210 kips, girder 2 = 1221 kips, girder 3 = 1561 kips and

girder 4 = 1336 kips. Compressive girder axial force near abutments 1 and 2 increased approximately 189 kips and 69 kips compared to the preceding year.

Sister-bar strain data at the approach slab on abutments 1 and 2 are presented in Figures 4.66 and 4.67, respectively. Four sister-bar gages near abutment 1 and the other four sister-bar gages near abutment 2 indicate a similar compression strain, ranging from 40 to 120 $\mu\epsilon$. Sister-bar gages indicated initial changes in compressive strain from 0 to 80 $\mu\epsilon$ due to concrete creep and shrinkage. Daily temperature variation correlation with all sister-bar strain were high during summer (approximately 30 $\mu\epsilon$), while daily strain changes during winter were less than 10 $\mu\epsilon$.

Bridge 211 Processed Response Data Figure List:

Figure 4.44. Bridge 211: Extensometers on Abutment 1.

Figure 4.45. Bridge 211: Extensometers on Abutment 2.

Figure 4.46. Bridge 211: Pressure Cells on Abutment 1.

Figure 4.47. Bridge 211: Pressure Cells on Abutment 2.

Figure 4.48. Bridge 211: Tiltmeters on Abutment 1.

Figure 4.49. Bridge 211: Tiltmeters on Abutment 2.

Figure 4.50. Bridge 211: Tiltmeters on Girders near Abutment 1.

Figure 4.51. Bridge 211: Tiltmeters on Girders near Abutment 2.

Figure 4.52. Bridge 211: North Pile Moments under Abutment 1.

Figure 4.53. Bridge 211: South Pile Moments under Abutment 1.

Figure 4.54. Bridge 211: North Pile Moments under Abutment 2.

Figure 4.55. Bridge 211: South Pile Moments under Abutment 2.

Figure 4.56. Bridge 211: Pile Axial Forces under Abutment 1.

Figure 4.57. Bridge 211: Pile Axial Forces under Abutment 2.

Figure 4.58. Bridge 211: Interior Girder Moments near Abutment 1.

Figure 4.59. Bridge 211: Exterior Girder Moments near Abutment 1.

Figure 4.60. Bridge 211: Interior Girder Moments near Abutment 2.

Figure 4.61. Bridge 211: Exterior Girder Moments near Abutment 2.

Figure 4.62. Bridge 211: Interior Girder Axial Forces near Abutment 1.

Figure 4.63. Bridge 211: Exterior Girder Axial Forces near Abutment 1.

Figure 4.64. Bridge 211: Interior Girder Axial Forces near Abutment 2.

Figure 4.65. Bridge 211: Exterior Girder Axial Forces near Abutment 2.

Figure 4.66. Bridge 211: Sister-bar Gages in Approach Slab near Abutment 1.

Figure 4.67. Bridge 211: Sister-bar Gages in Approach Slab near Abutment 2.

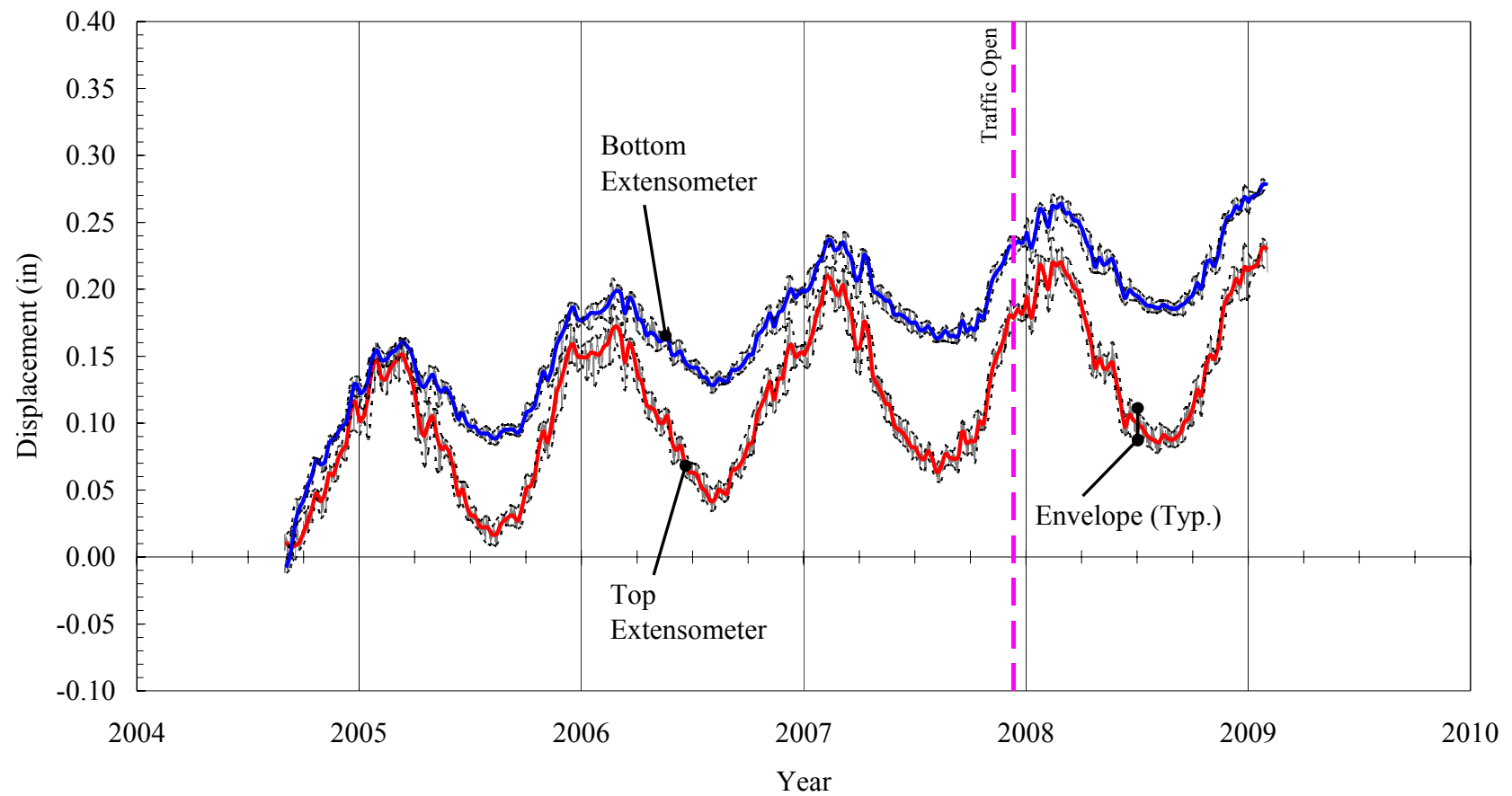


Figure 4.44. Bridge 211: Extensometers on Abutment 1.

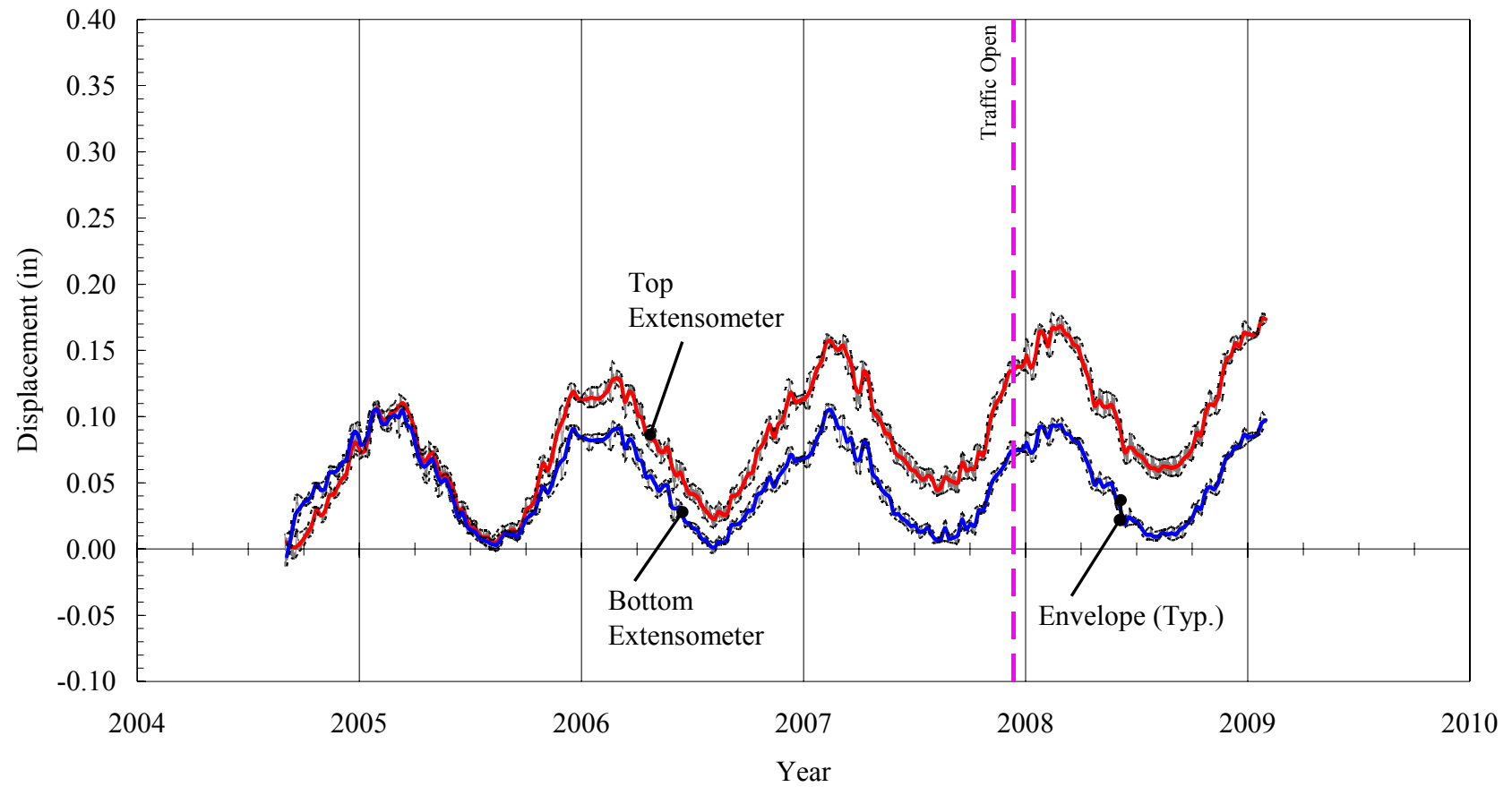


Figure 4.45. Bridge 211: Extensometers on Abutment 2.

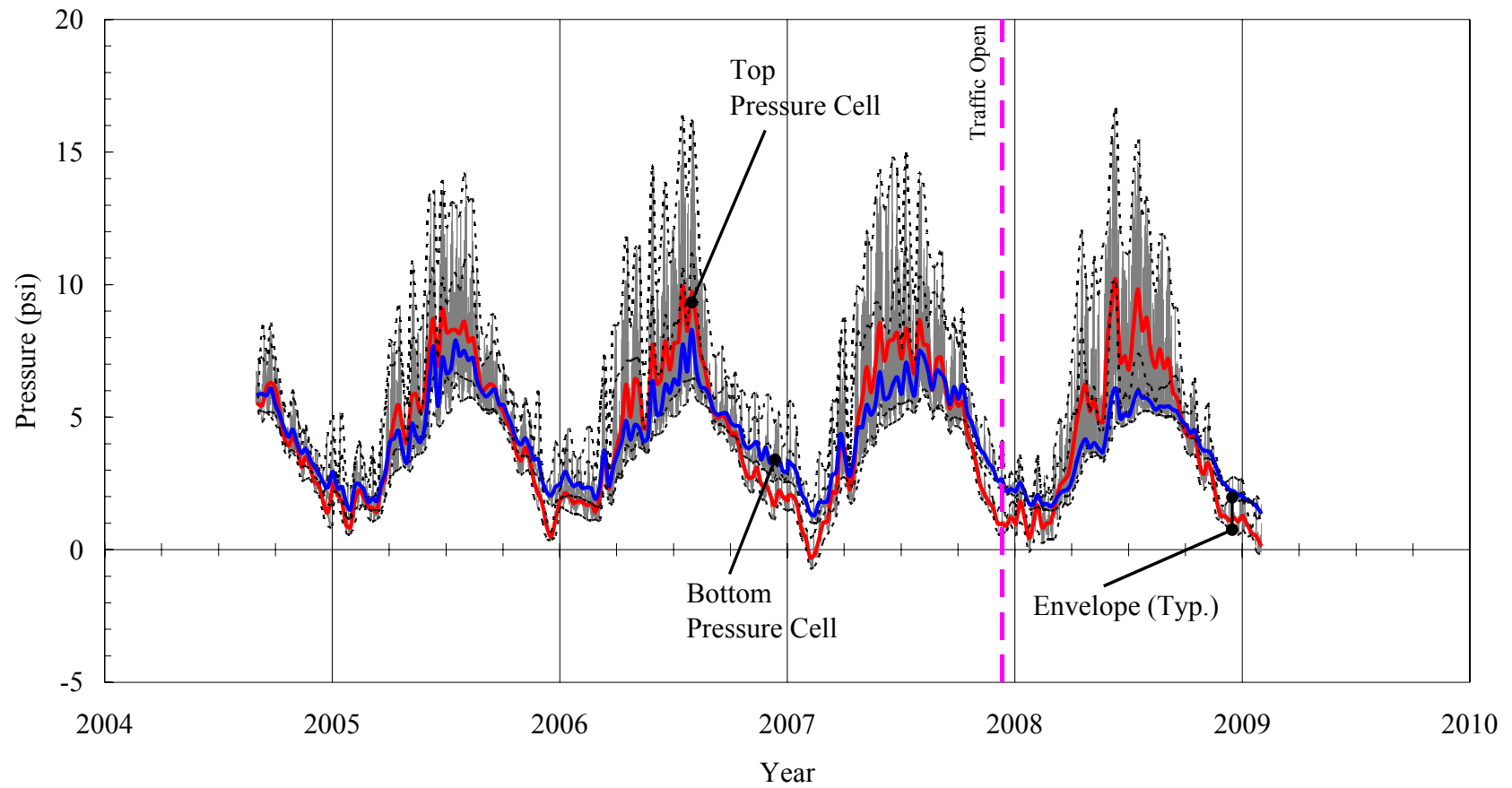


Figure 4.46. Bridge 211: Pressure Cells on Abutment 1.

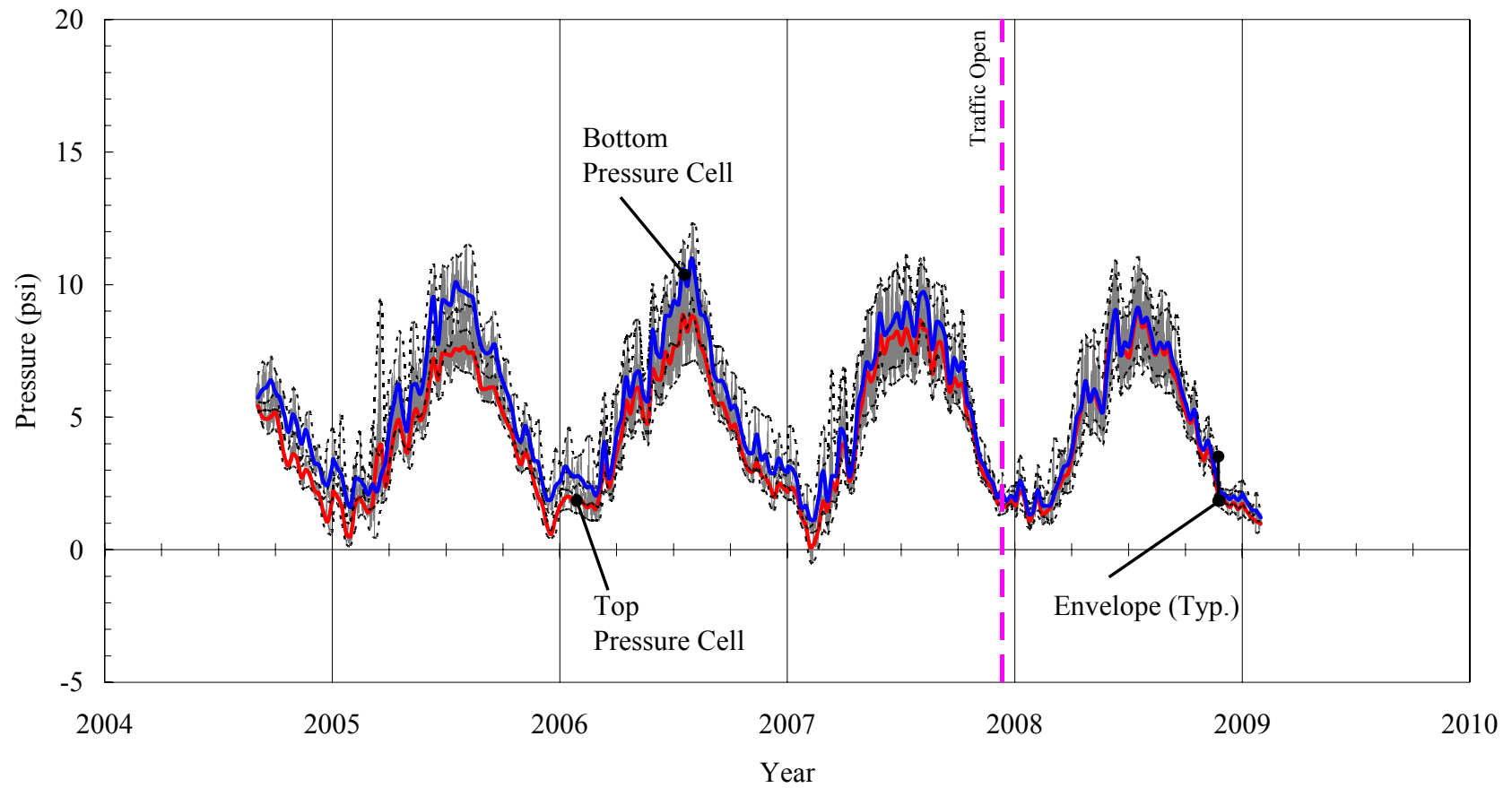


Figure 4.47. Bridge 211: Pressure Cells on Abutment 2.

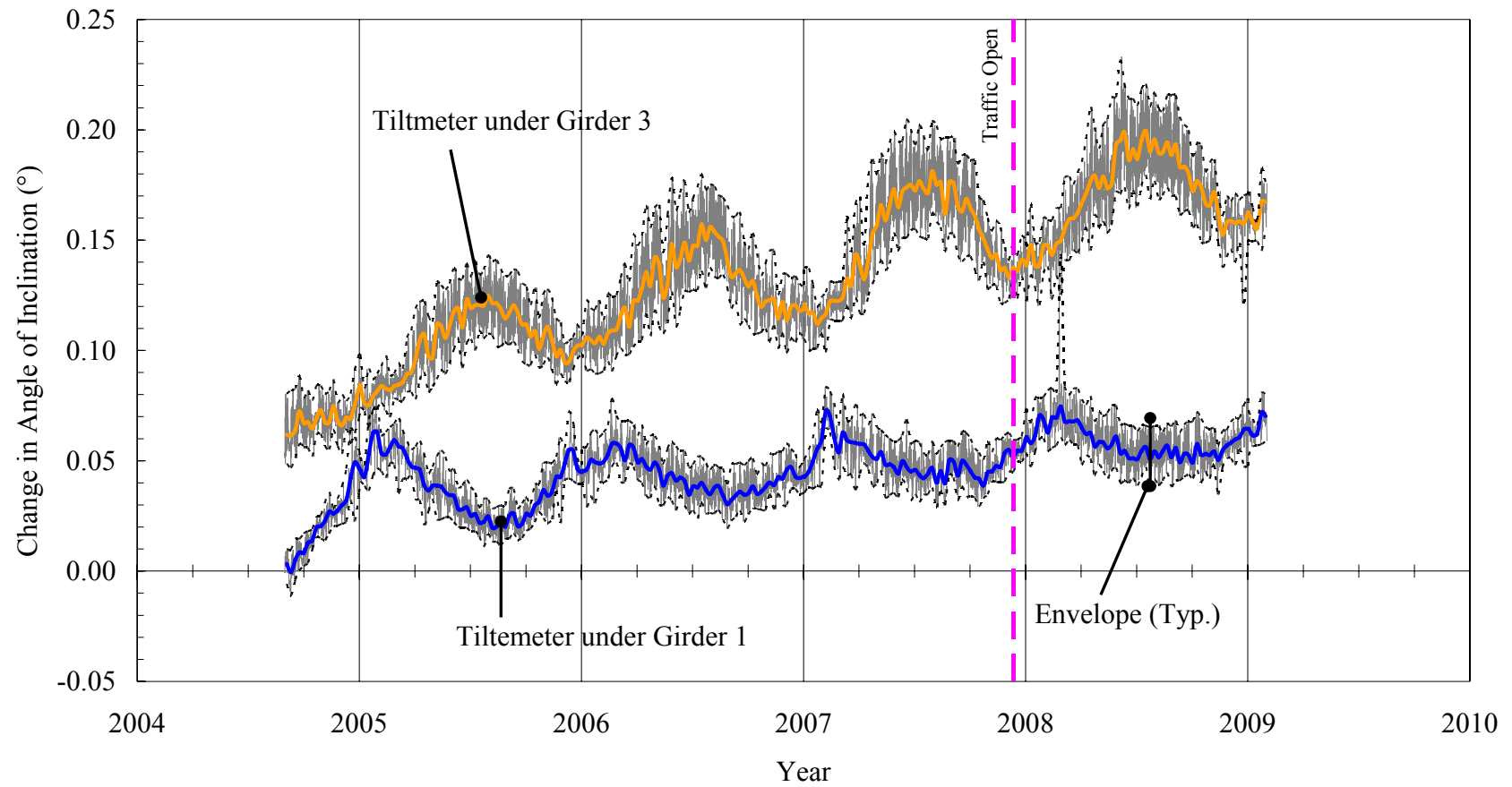


Figure 4.48. Bridge 211: Tiltmeters on Abutment 1.

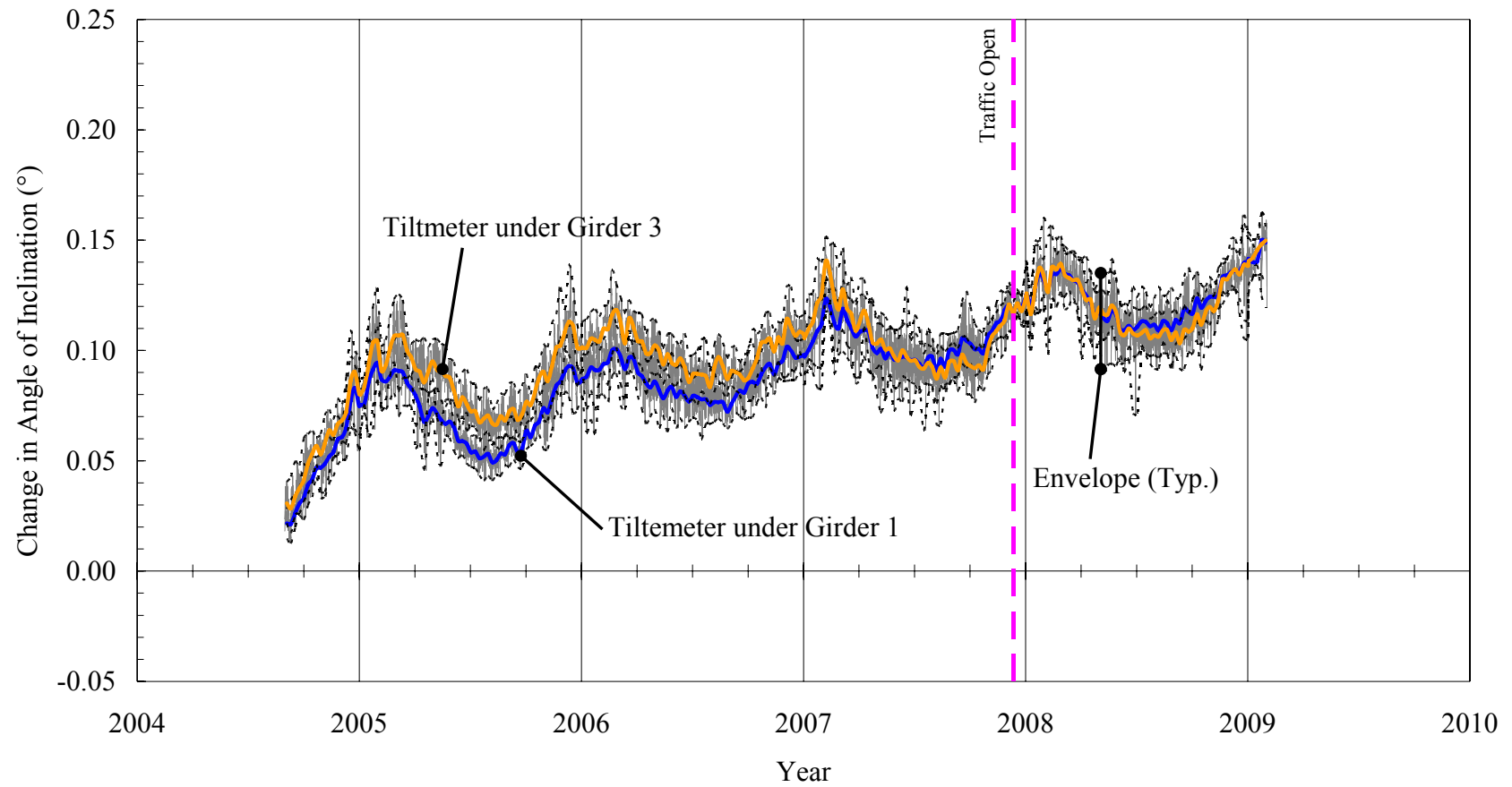


Figure 4.49. Bridge 211: Tiltmeters on Abutment 2.

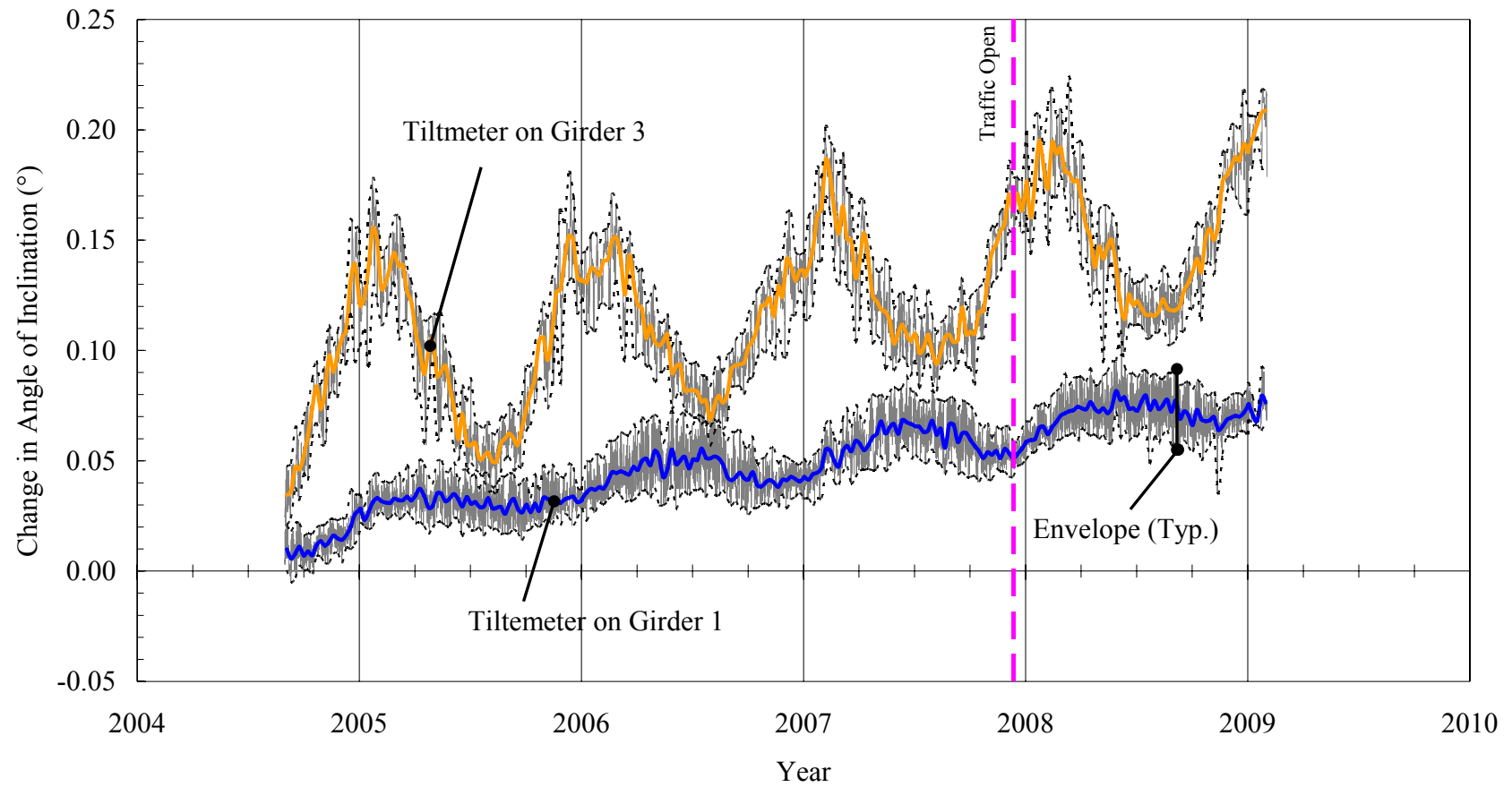


Figure 4.50. Bridge 211: Tiltmeters on Girders near Abutment 1.

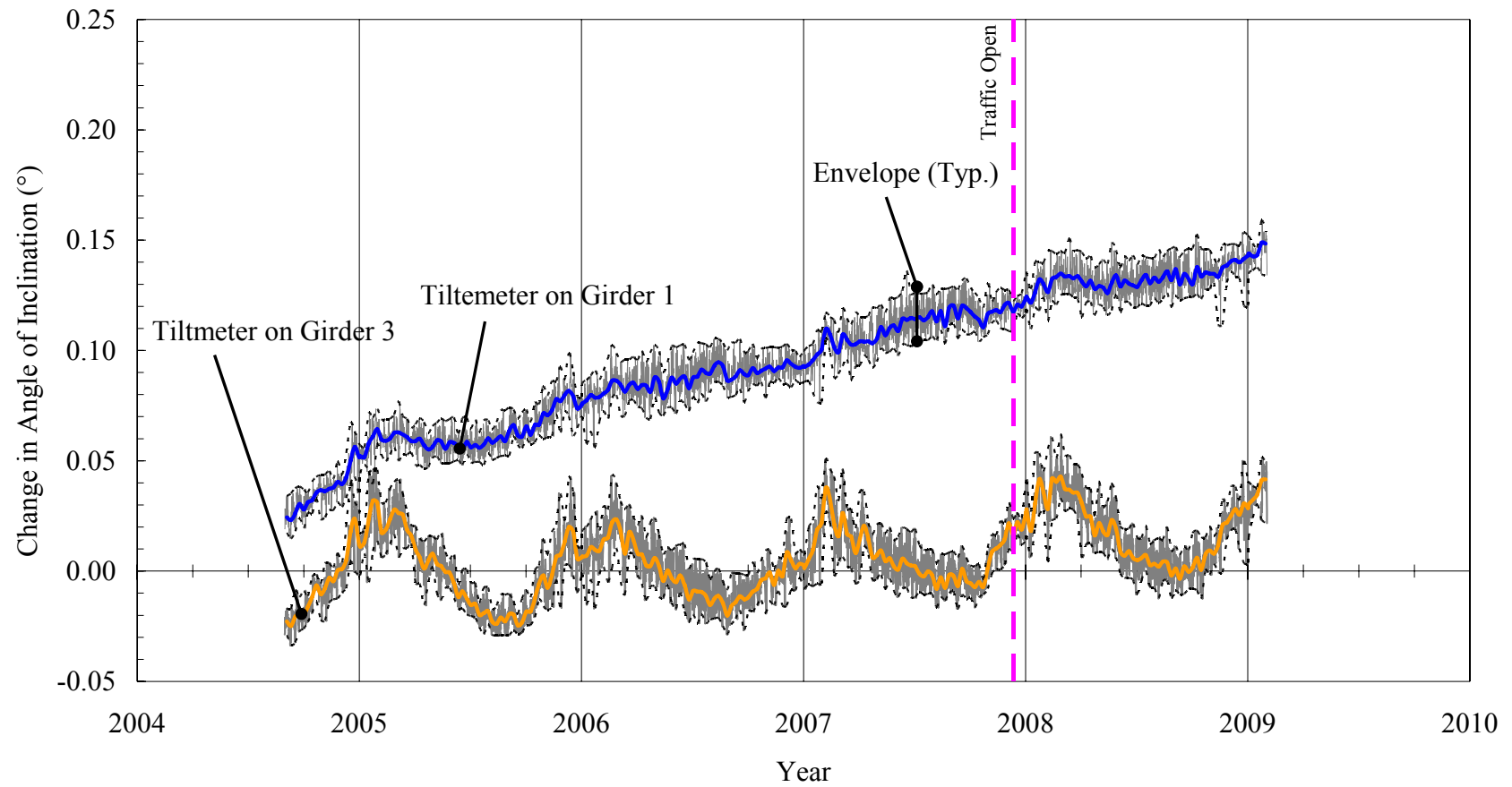


Figure 4.51. Bridge 211: Tiltmeters on Girders near Abutment 2.

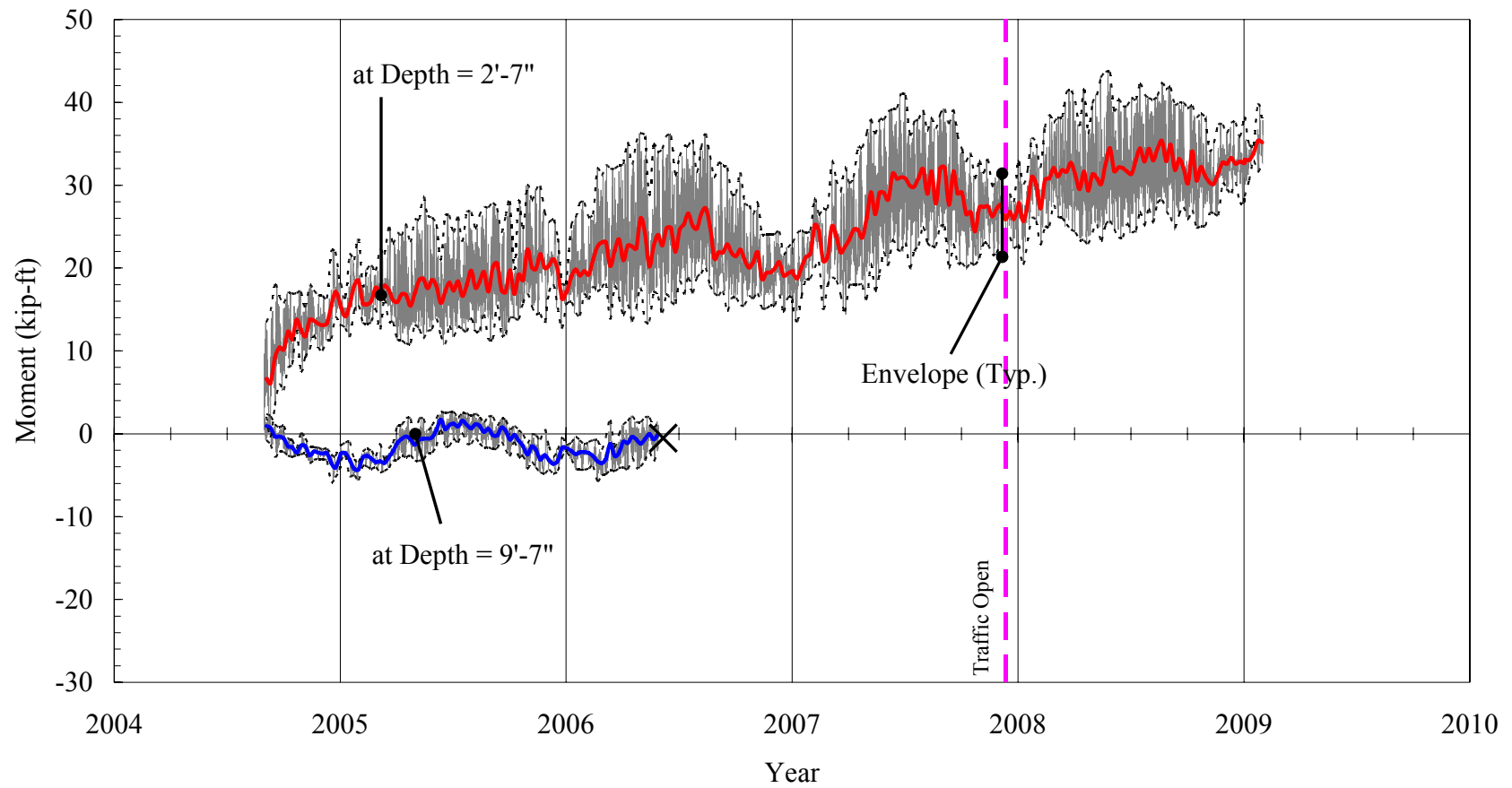


Figure 4.52. Bridge 211: North Pile Moments under Abutment 1.

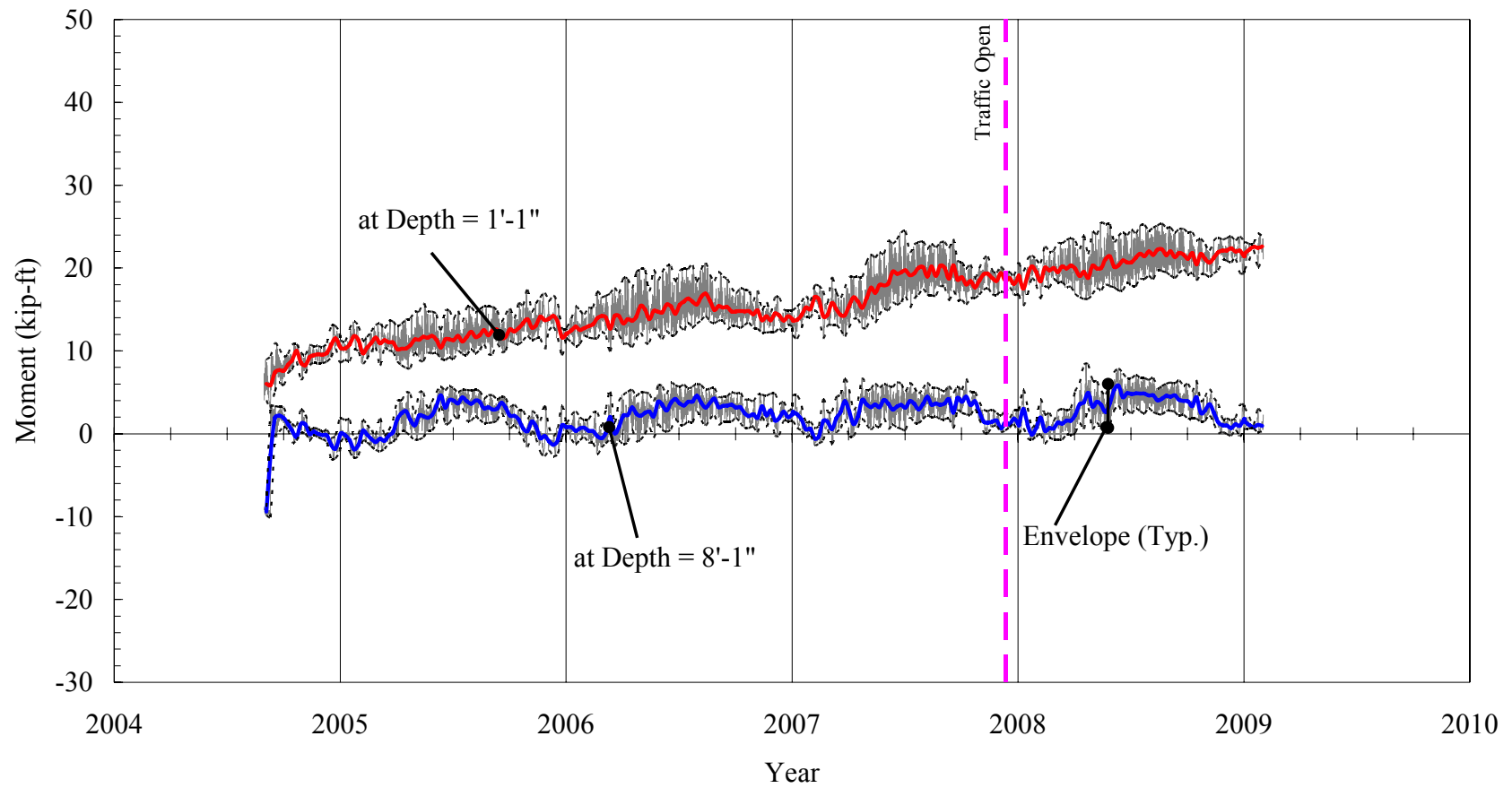


Figure 4.53. Bridge 211: South Pile Moments under Abutment 1.

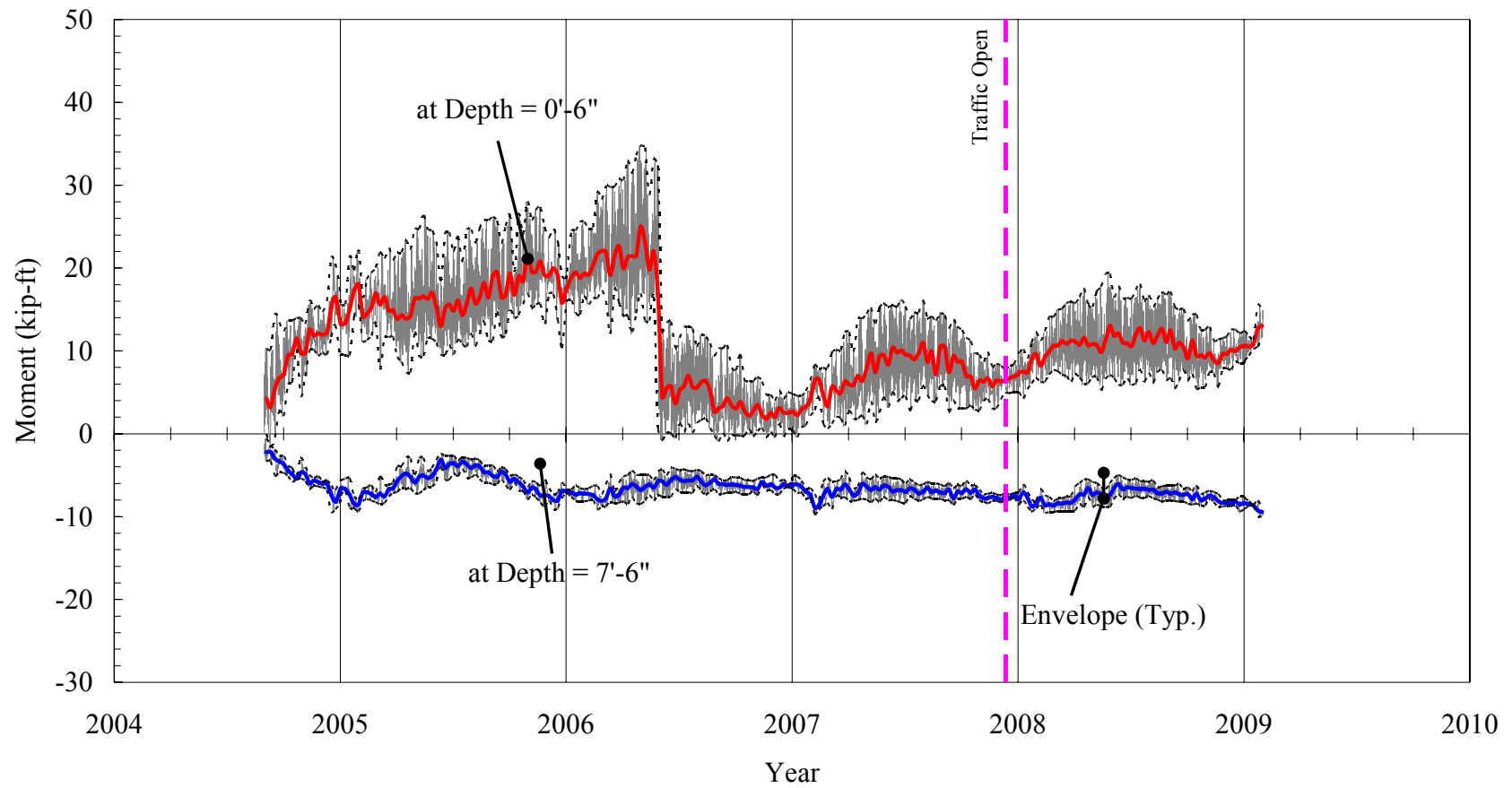


Figure 4.54. Bridge 211: North Pile Moments under Abutment 2.

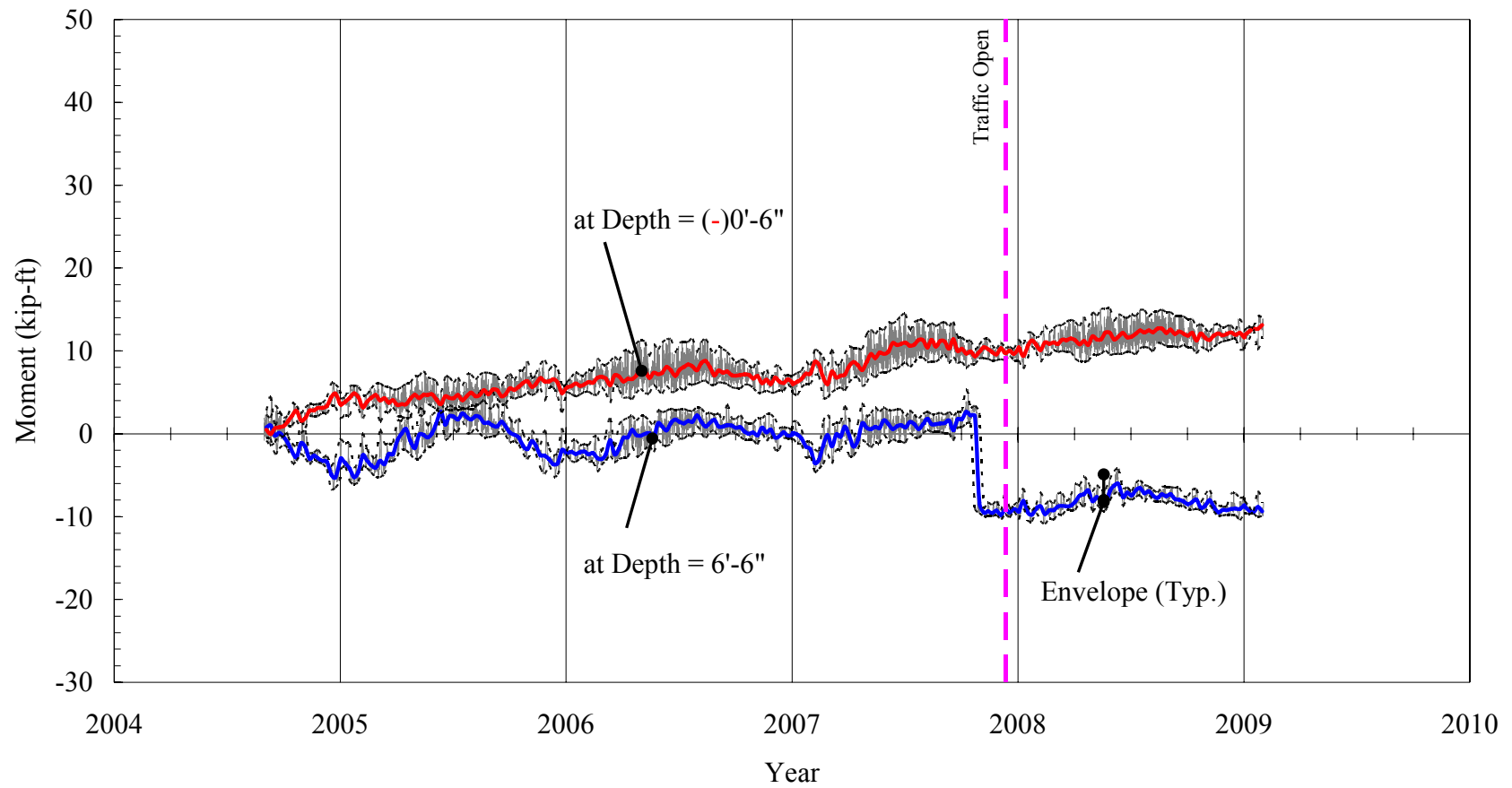


Figure 4.55. Bridge 211: South Pile Moments under Abutment 2.

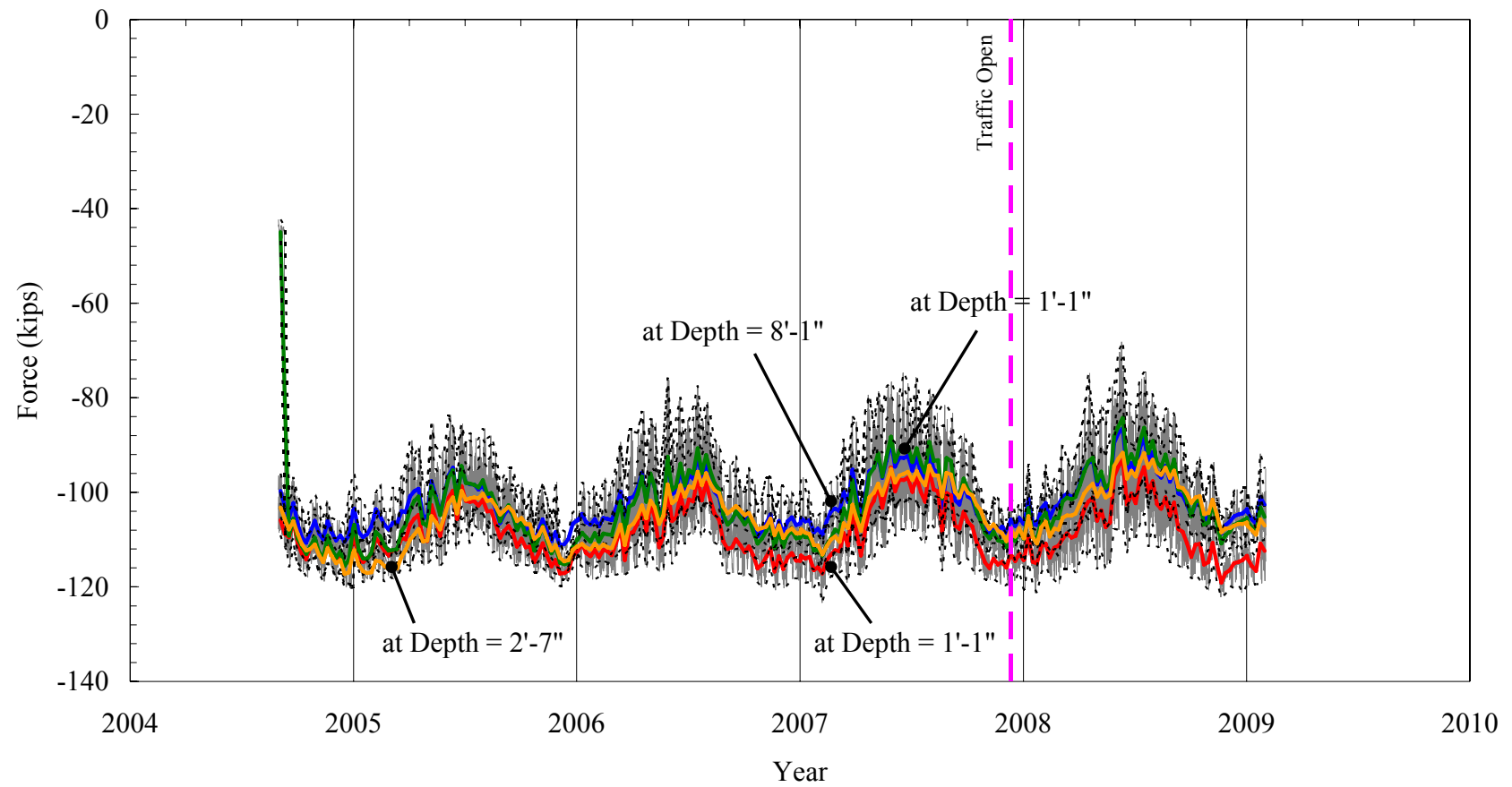


Figure 4.56. Bridge 211: Pile Axial Forces under Abutment 1.

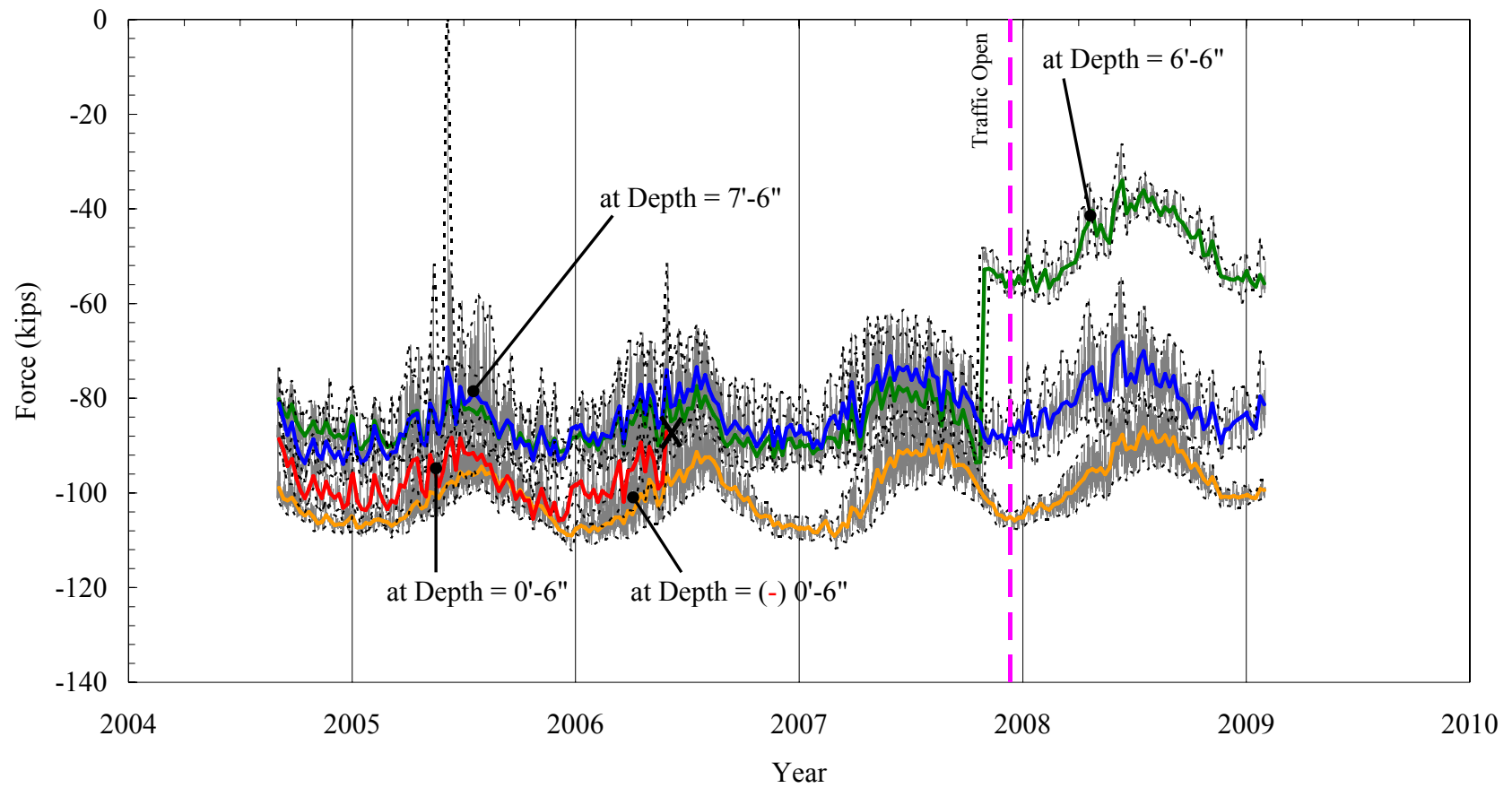


Figure 4.57. Bridge 211: Pile Axial Forces under Abutment 2.

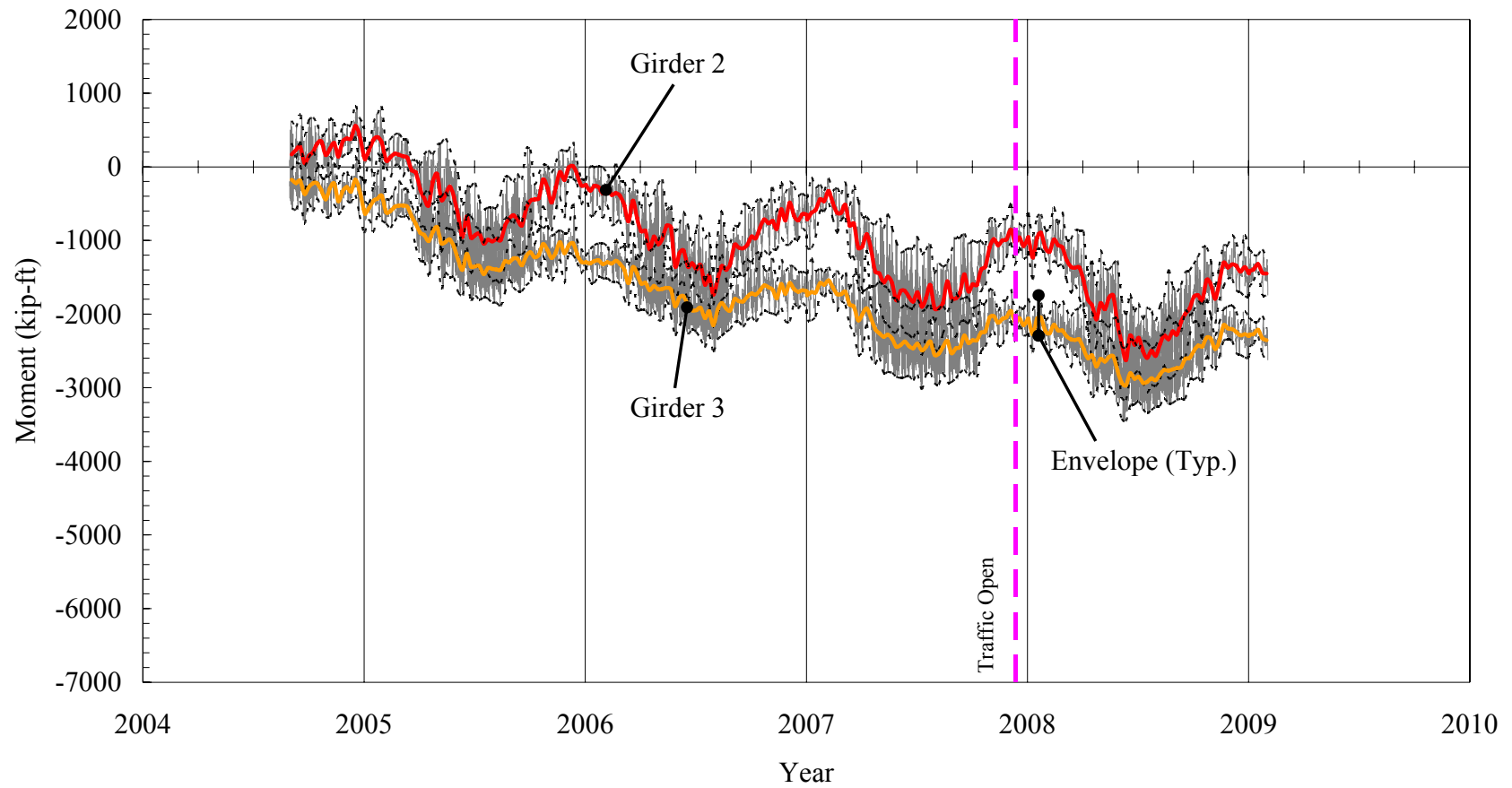


Figure 4.58. Bridge 211: Interior Girder Moments near Abutment 1.

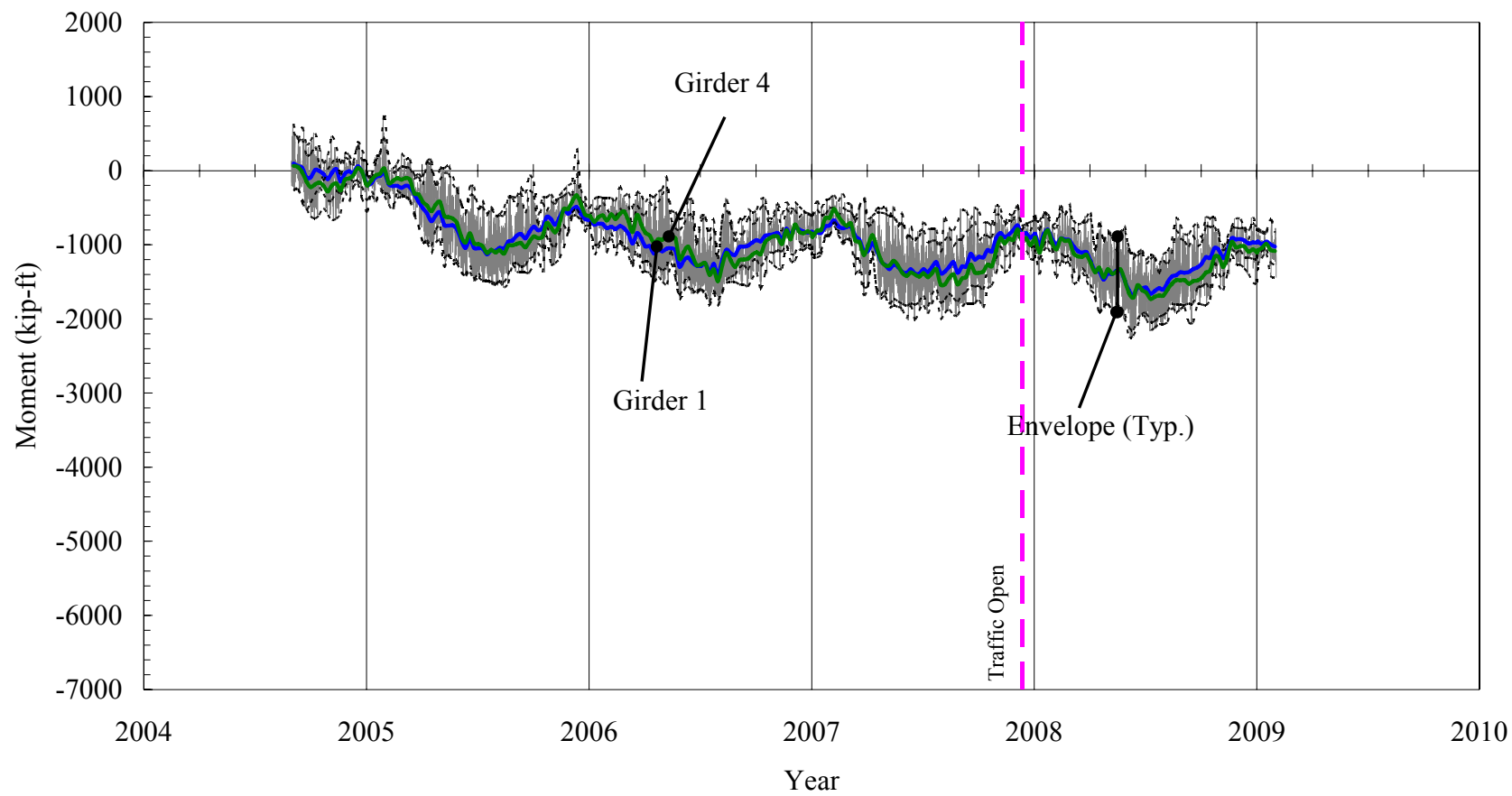


Figure 4.59. Bridge 211: Exterior Girder Moments near Abutment 1.

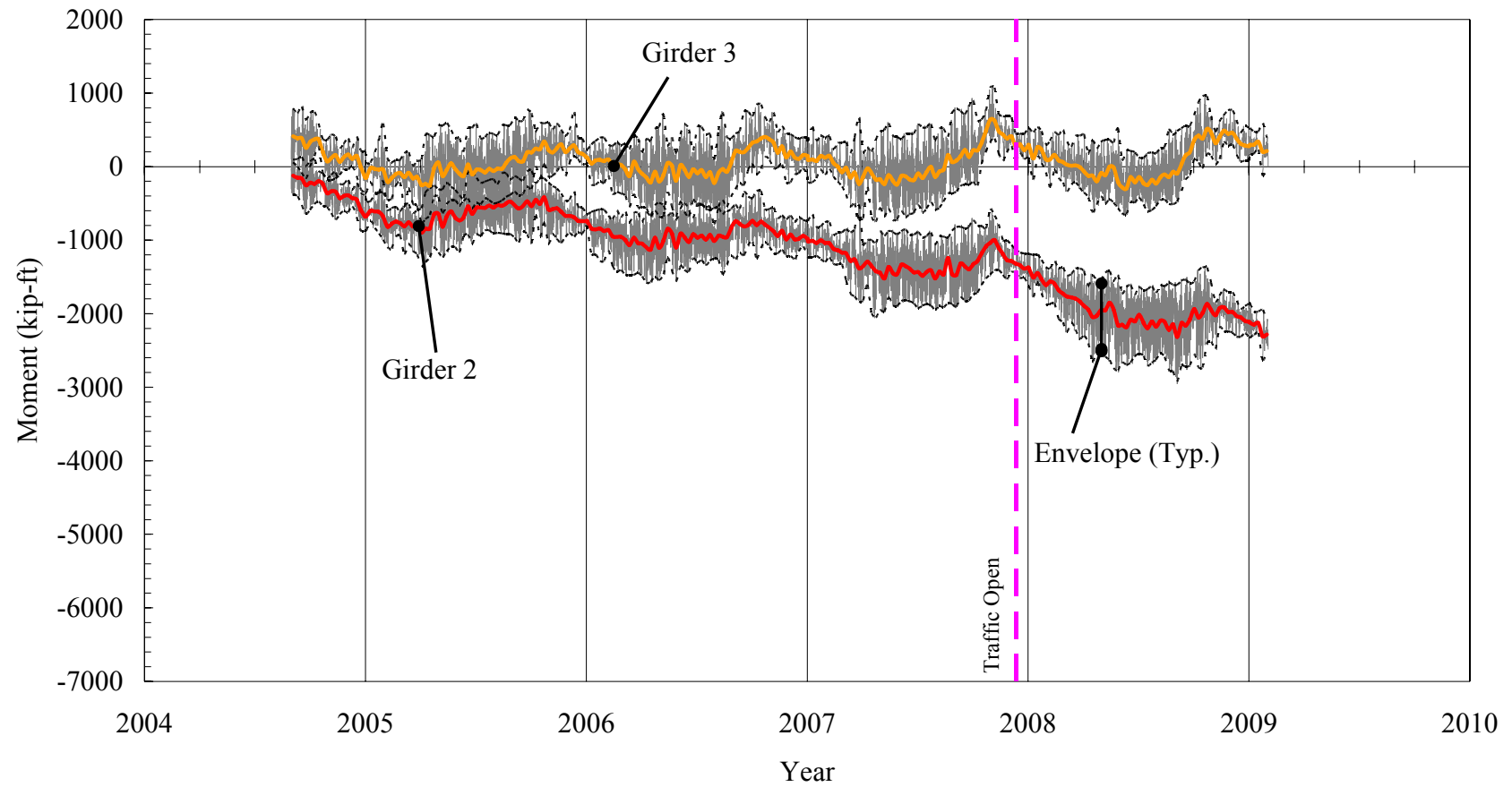


Figure 4.60. Bridge 211: Interior Girder Moments near Abutment 2.

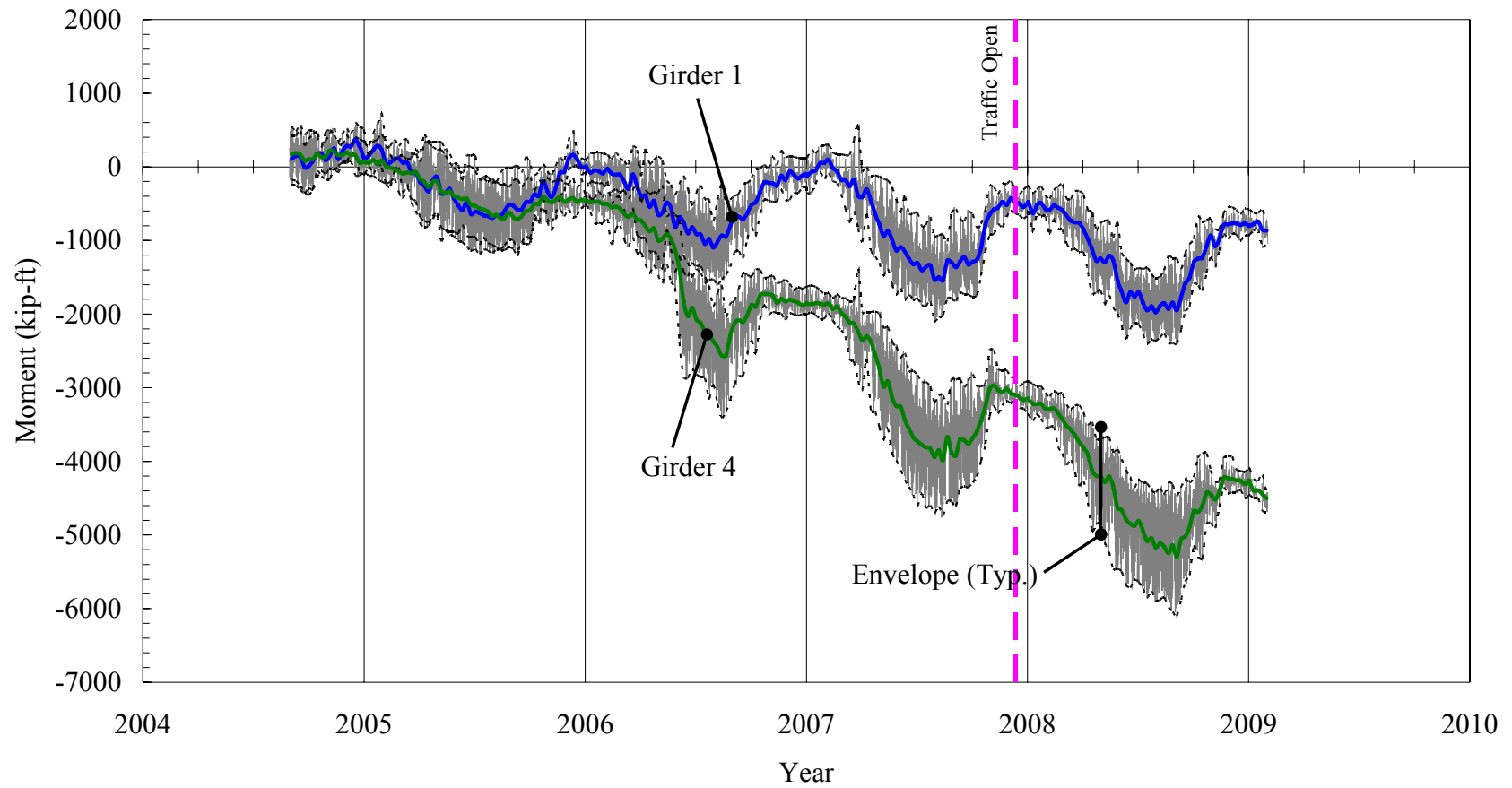


Figure 4.61. Bridge 211: Exterior Girder Moments near Abutment 2.

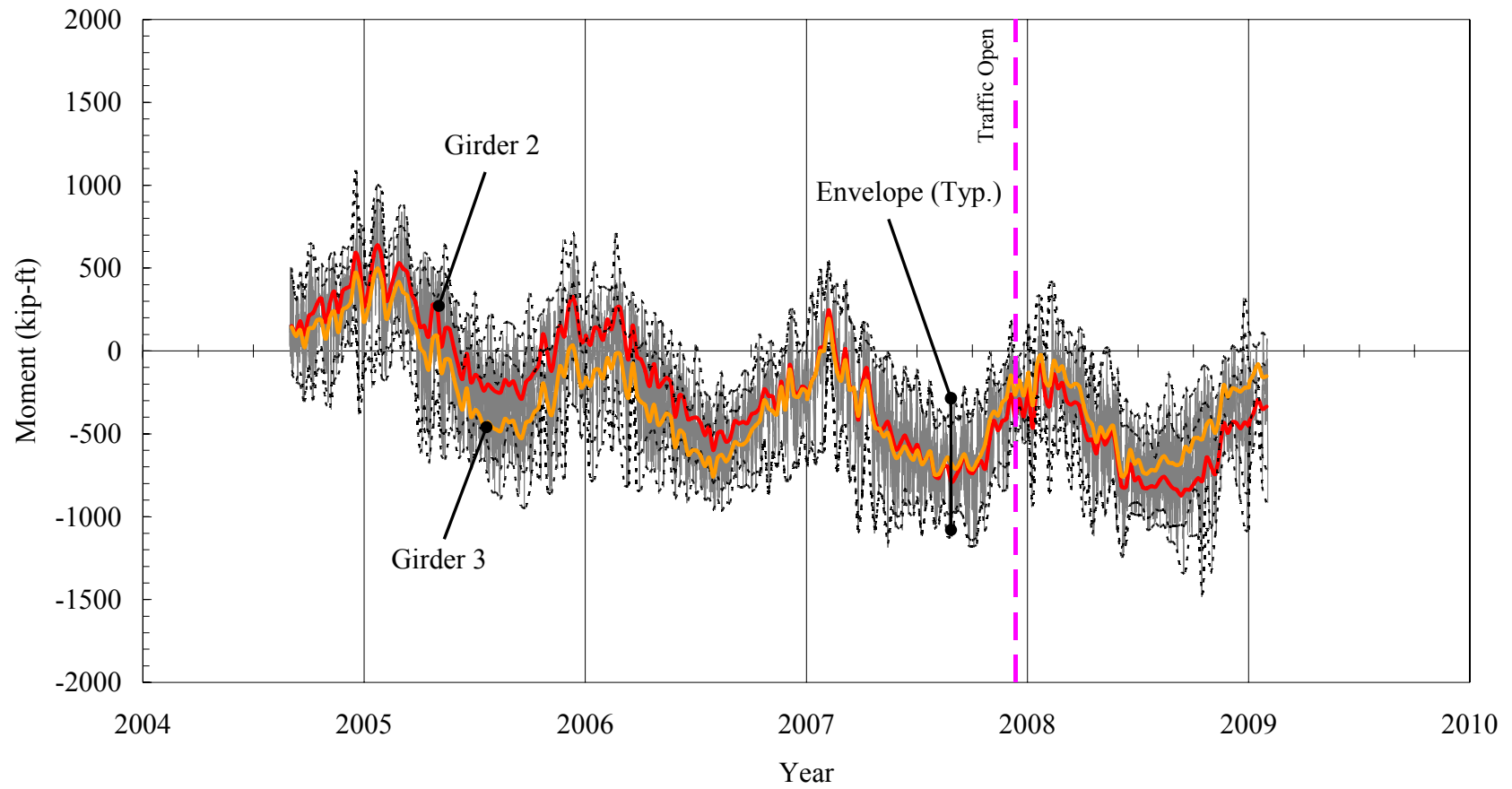


Figure 4.62. Bridge 211: Interior Girder Axial Forces near Abutment 1.

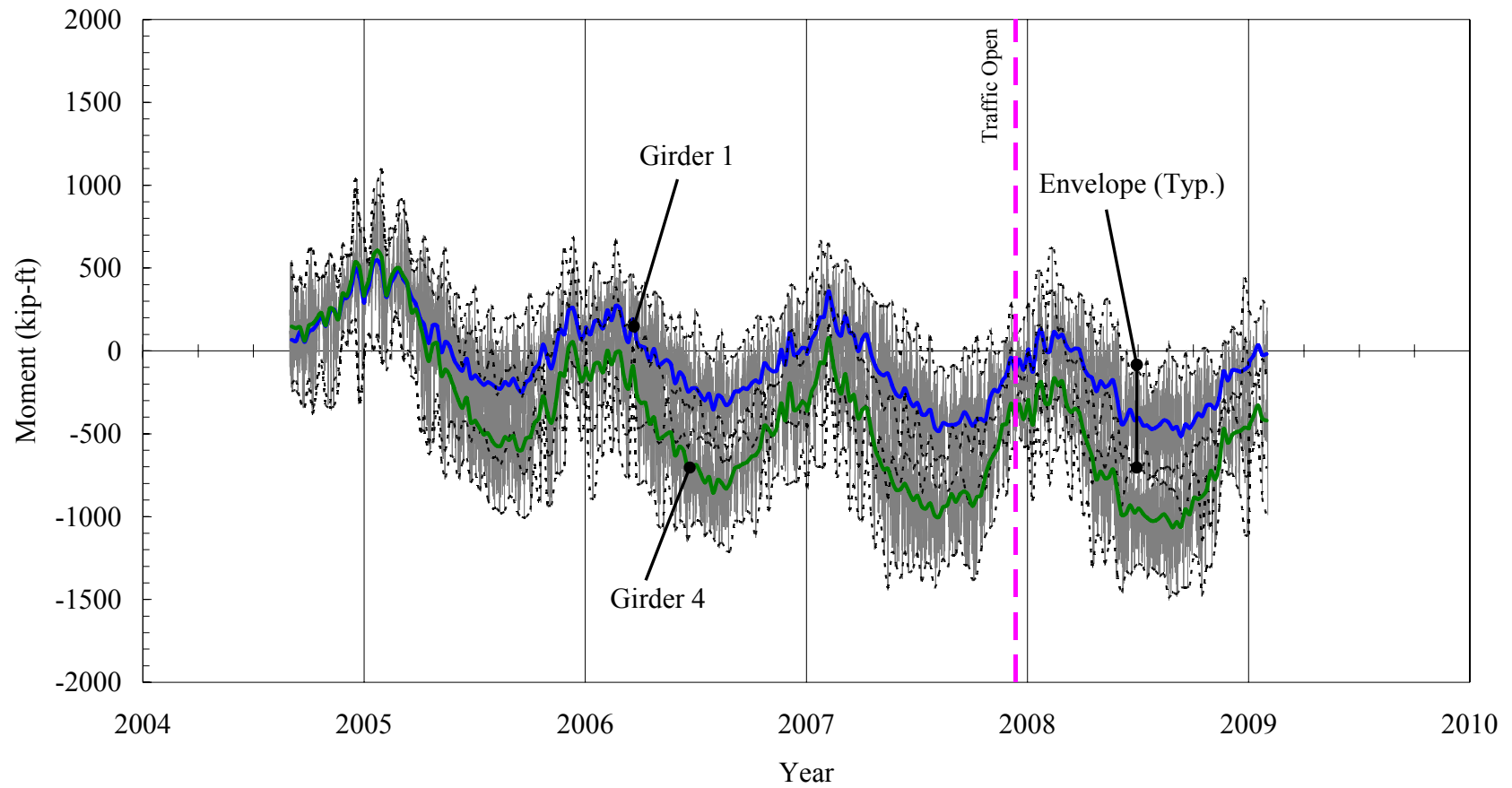


Figure 4.63. Bridge 211: Exterior Girder Axial Forces near Abutment 1.

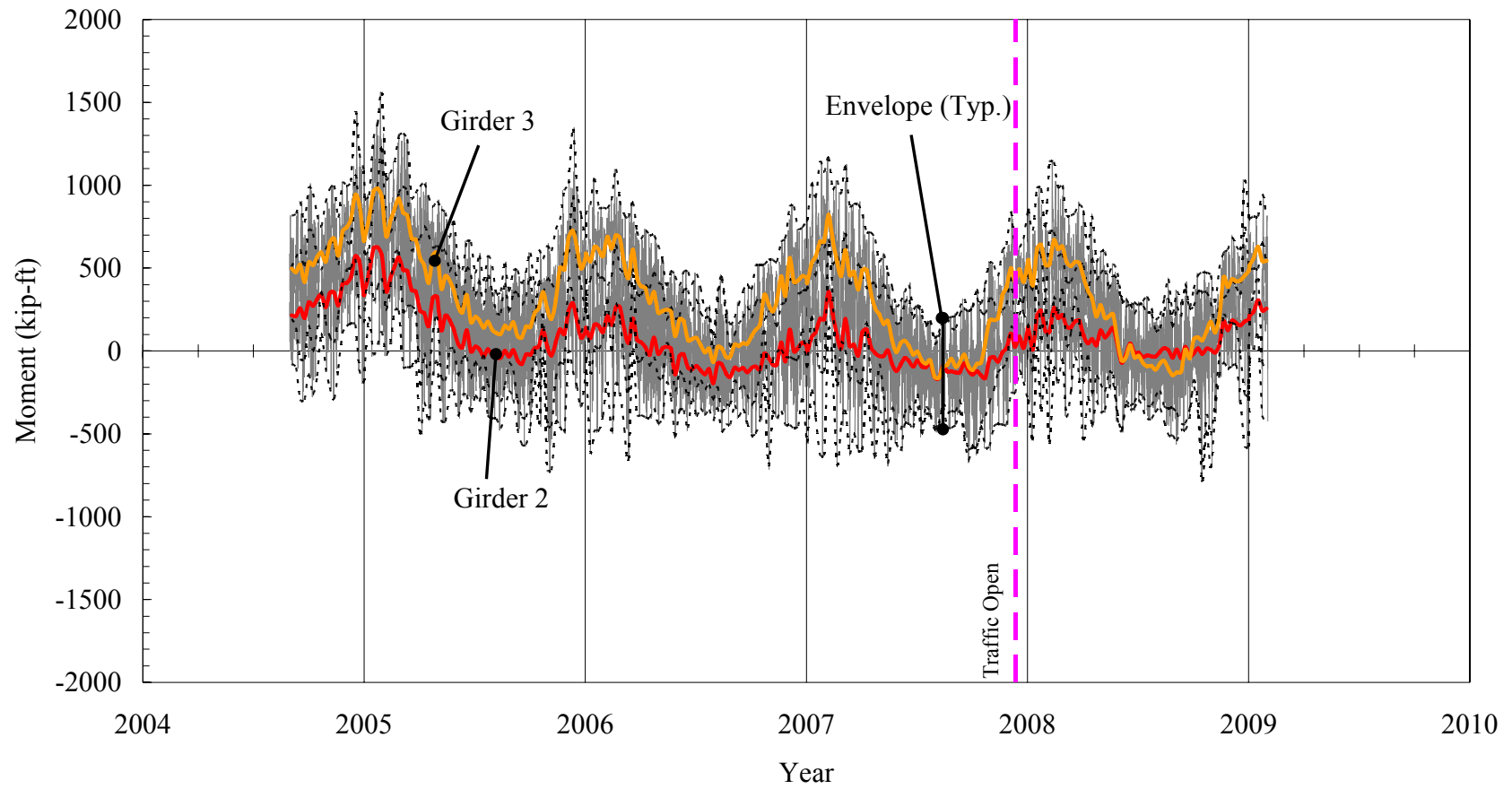


Figure 4.64. Bridge 211: Interior Girder Axial Forces near Abutment 2.

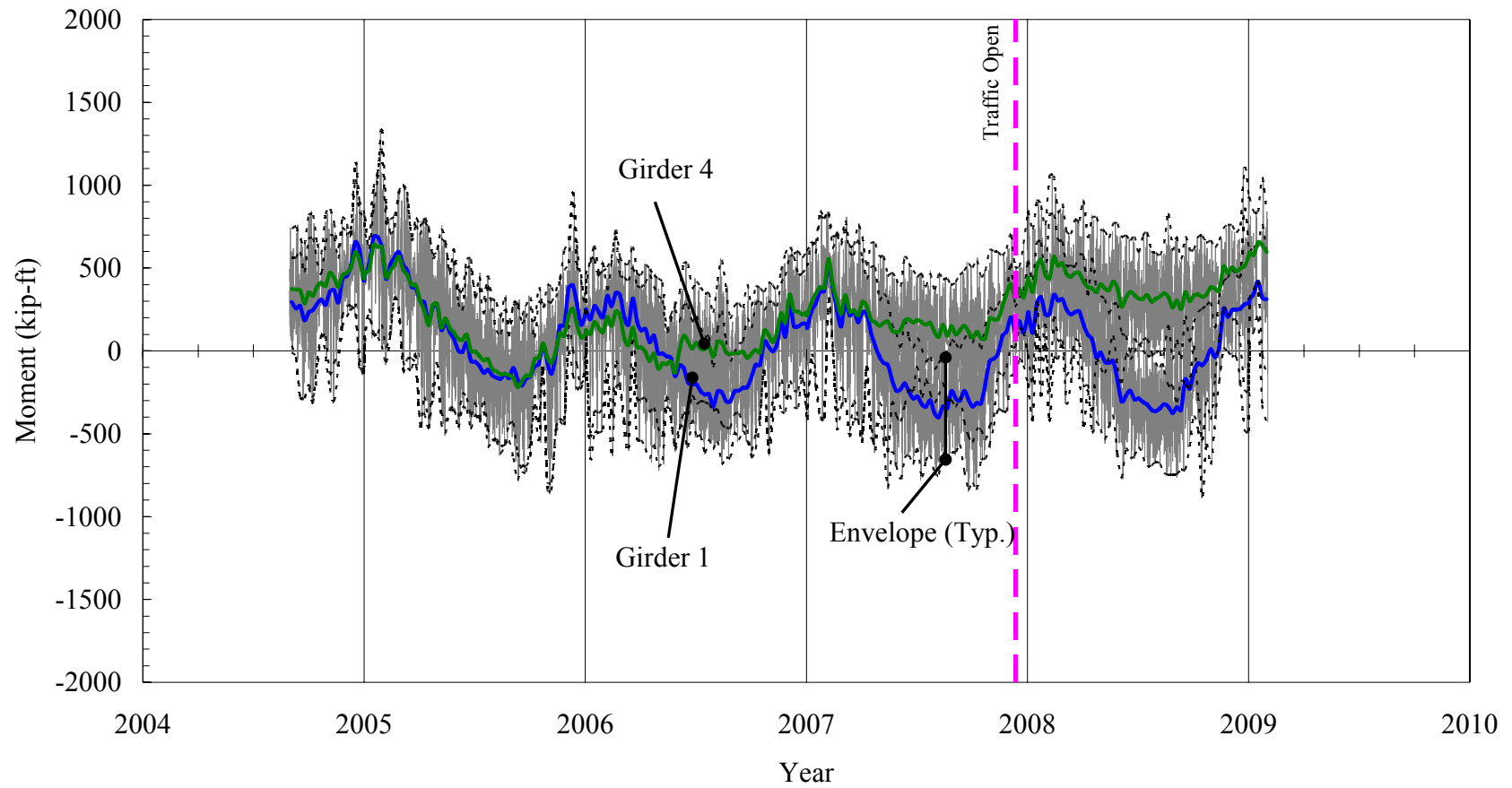


Figure 4.65. Bridge 211: Exterior Girder Axial Forces near Abutment 2.

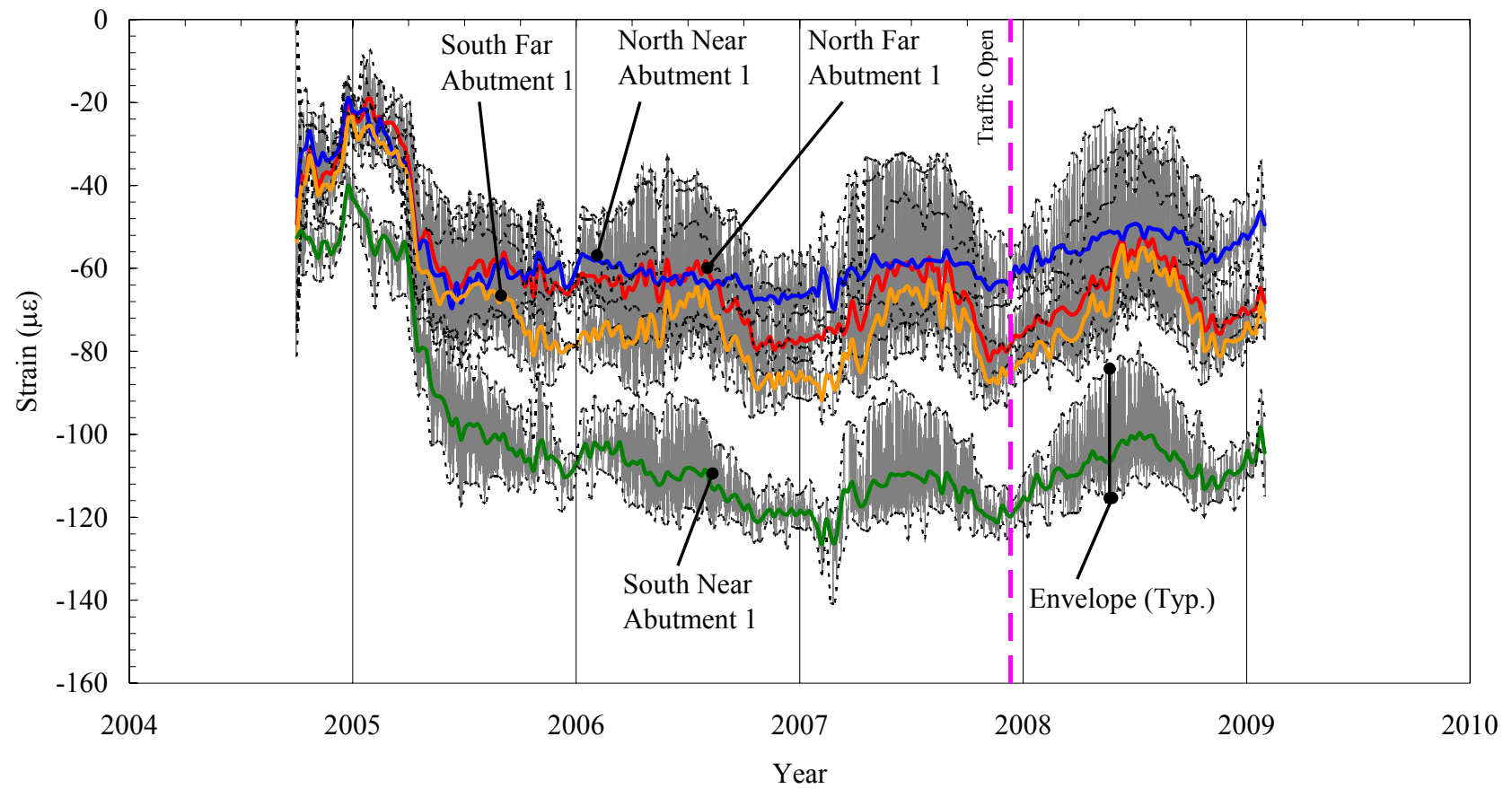


Figure 4.66. Bridge 211: Sister-Bar Gages in Approach Slab near Abutment 1.

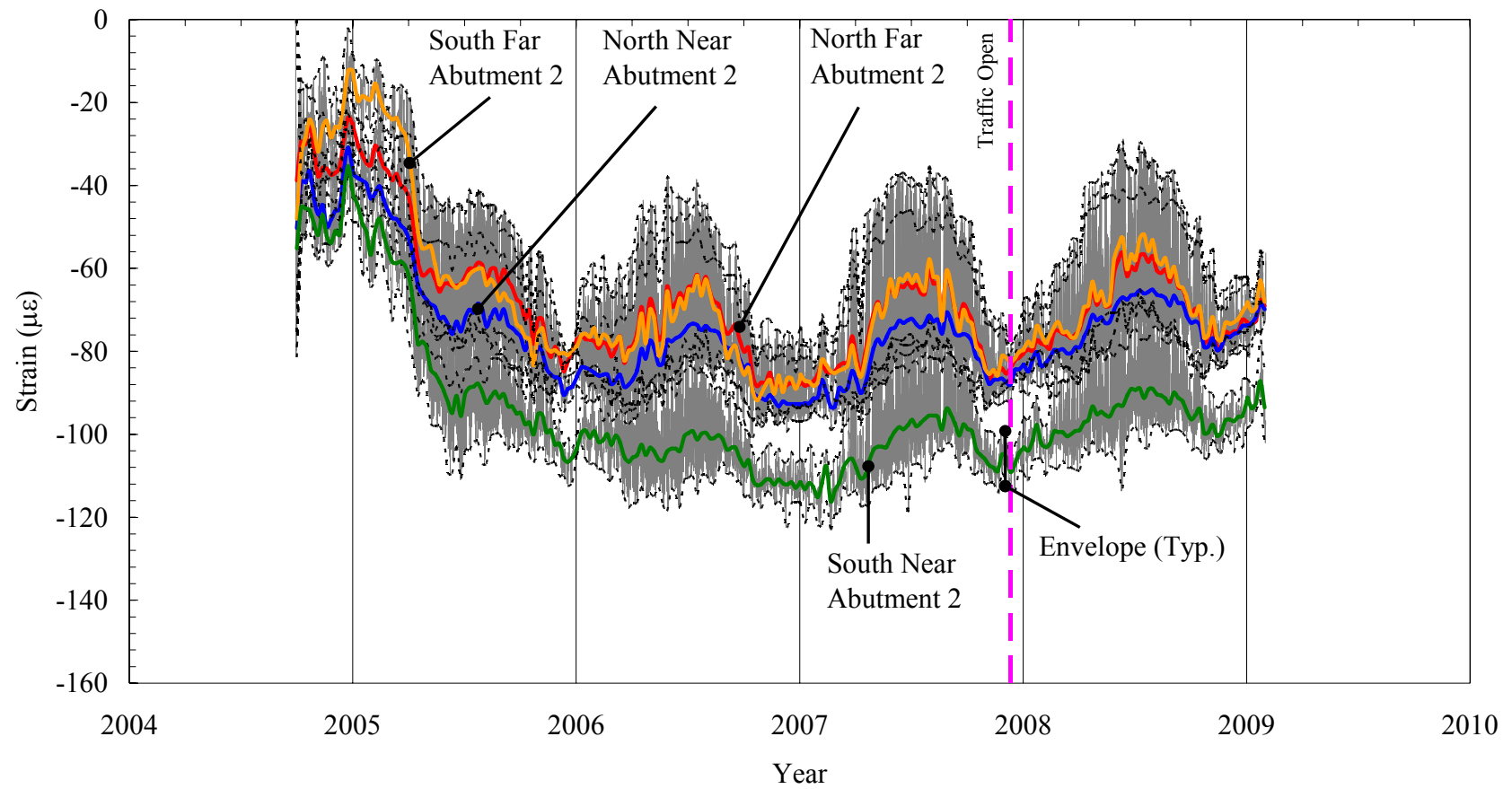


Figure 4.67. Bridge 211: Sister-Bar Gages in Approach Slab near Abutment 2.

4.5 Bridge 222

Data obtained from bridge 222 instruments consist of 4 extensometers, 4 pressure cells, 4 tilt meters, 24 strain gages on four piles, 8 strain gages on two prestressed concrete girders, and 4 sister-bar gages. The strain gage channel 1-2 located at the bottom of the south pile under abutment 2 malfunctioned from summer 2005 to fall 2006. Channel 1-12, located at the top of the north pile under abutment 2, malfunctioned during November 2008. The sister-bar gage channel 3-16, located near abutment 1, malfunctioned during August 2007.

Collected data from extensometers at abutments 1 and 2 are presented in Figure 4.68 and Figure 4.69, respectively. The extensometers measure bridge abutment longitudinal movement as a result of superstructure expansion and contraction. Maximum abutment displacement contraction and expansion are presented in Table 4.8. The top and bottom extensometer data at abutment 1 and the bottom extensometer at abutment 2 indicate continuous movement of the lower abutment toward the bridge. Contraction displacements occur 0.003 inches at the top of abutment 1, 0.030 inches at the bottom of abutment 2, and 0.005 inches at the bottom of abutment 2. Expansion displacement of 0.012 inches at the top of abutment 1 occurs every year.

Table 4.8. Bridge 222 Maximum Abutment Displacement.

Abutment		Abutment 1		Abutment 2	
Location		Top (in)	Bottom (in)	Top (in)	Bottom (in)
Maximum (Contraction)	Displacement	0.056	0.186	0.038	0.052
	Period	Winter 07/08	Winter 08/09	Winter 03/04	Winter 03/04
Minimum (Expansion)	Displacement	-0.028	-0.001	-0.061	-0.001
	Period	Summer 04	Summer 04	Summer 08	Summer 04

Pressure cell data are presented in Figures 4.70 and 4.71. Two pressure cells measure abutment 1 backfill pressure, and the other two pressure cells measure abutment 2 backfill pressure. Backfill pressures at the top of both abutments vary over a wide range, with large amplitudes relative to the daily thermal displacements. The backfill pressure at the bottom of both abutments varies within a narrow range. Backfill pressures obtained from both top pressure cells are greater by as much as 2.5 psi during winter, which was expected, despite of the approximately 4 ft 7 inches and 5 ft 10 inches shallower placement. The top and bottom pressure measurements were very similar to each other during summer. At abutment 1, the top and bottom pressure cells indicated maximum backfill pressures of 15.9 psi (summer 2005) and 15.8 psi (summer 2006). At abutment 2, the top and bottom center pressure cells indicated maximum backfill pressures of 24.0 psi (summer 2006) and 16.0 psi (summer 2006), respectively.

Abutment tiltmeter data are presented in Figure 4.72. Two tiltmeters are mounted on abutment 1 under the centerline of girders 2 and 4. The two abutment 1 tiltmeters indicate an abutment rotation variation corresponding to temperature variation. During the winter, abutment inclination increased toward the bridge, corresponding to the measured longitudinal displacements. The lower-bound abutment 1 rotation at the centerline of girder 2 increased (starting from initial zero) from -0.003 to 0.060 to 0.098 to 0.108 to 0.129 to 0.137 degrees over a 5-year period. The lower-bound abutment 1 rotation at the centerline of girder 4 increased (starting from initial zero) from -0.042 to 0.005 to 0.014 to 0.027 to 0.041 to 0.047 degrees over a 5-year period. Maximum changes in rotation of abutment 1 at the centerline of girders 2 and 4 were 0.184 degrees (winter 2007/2008) and 0.096 degrees (winter 2007/2008).

Girder tiltmeter data are presented in Figure 4.73. One tiltmeter was placed directly on the web of girders 2 and 4 near abutment 1. Both girders rotated with a trend that corresponds to seasonal temperature variation. Tiltmeters near abutment 1 measured a maximum rotation of 0.160 degrees at girder 2 and 0.135 degrees at girder 4.

Pile bending moments about the weak axis at four piles, two each (north and south) at abutments 1 and 2, are presented in Figures 4.74 through 4.77. The position of the gages and maximum measured moments are shown in Table 4.9. The H-pile bending strengths are $\phi M_{yielding} = 127$ ft-kip and $\phi M_{plastic} = 194$ ft-kip (based on $F_y = 50$ ksi).

Table 4.9. Bridge 222 Pile Strain Gage Depths Below Bottom of Abutment and Maximum Measured Moment.

	Abutment 1		Abutment 2	
	Placement	Max. Moment	Placement	Max. Moment
North Pile	1' - 3"	43.1 ft-kips	0' - 5"	46.4 ft-kips
	7' - 3"	47.4 ft-kips	6' - 5"	4.8 ft-kips
South Pile	1' - 7"	40.1 ft-kips	0' - 3"	36.7 ft-kips
	7' - 7"	16.6 ft-kips	6' - 3"	29.5 ft-kips*

* Maximum moment excludes the period between summer 2005 and fall 2006

Pile axial forces are presented in Figure 4.78 through 4.81. The average pile axial force measured, including dead loads and down drag forces accumulated over the monitoring period, are: at the top of abutment 1 north pile = 10 kips, at the bottom of abutment 1 north pile = 73 kips, at the top of abutment 1 south pile = 57 kips, at the bottom of abutment 1 south pile = 80 kips, at the top of abutment 2 north pile = 21 kips, at the bottom of abutment 2 north pile = 66 kips, at the top of abutment 2 south pile = 42 kips, and at the bottom of abutment 2 south pile = 103 kips.

Girder moments derived from measured strain are presented in Figures 4.82 and 4.83. Two strain gages are located 1 ft from each girder end, one at the top and one at the

bottom flange. All girder moments, except girder 4 near abutment 1, tend to decrease compared to the preceding year, i.e., negative moments become more negative. Girder 4 near abutment 1 moment varied within the upper and lower bound of 750 ft-kip and -790 ft-kip. Girders 2 and 4 moments adjacent to abutment 2 measured very similar variation.

Girder axial forces are presented in Figures 4.84 to 4.85. Girder axial forces at girder 4 near abutment 1 did not exhibit a clear trend with respect to seasonal temperature variation, varying within -600 to 1350 kips. Girder axial forces near abutment 2 indicated a clear trend with respect to seasonal temperature variation, varying within -4 to 645 kips.

Sister-bar strain data at the approach slab on abutment 1 are presented in Figure 4.86. All four sister-bar gages near abutment 1 indicate a similar compression strain, ranging from 30 to 150 $\mu\epsilon$. Sister-bar gages indicated initial changes in compressive strain from 0 to 100 $\mu\epsilon$ due to concrete creep and shrinkage. Daily temperature variation correlation with all sister-bar strain were high during summer (approximately 30 $\mu\epsilon$), while daily strain changes during winter were less than 10 $\mu\epsilon$.

Bridge 222 Processed Response Data Figure List:

Figure 4.68. Bridge 222: Extensometers on Abutment 1.

Figure 4.69. Bridge 222: Extensometers on Abutment 2.

Figure 4.70. Bridge 222: Pressure Cells on Abutment 1.

Figure 4.71. Bridge 222: Pressure Cells on Abutment 2.

Figure 4.72. Bridge 222: Tiltmeter on Abutment 1.

Figure 4.73. Bridge 222: Tiltmeter on Girders near Abutment 1.

Figure 4.74. Bridge 222: North Pile Moments under Abutment 1.

Figure 4.75. Bridge 222: South Pile Moments under Abutment 1.

Figure 4.76. Bridge 222: North Pile Moments under Abutment 2.

Figure 4.77. Bridge 222: South Pile Moments under Abutment 2.

Figure 4.78. Bridge 222: North Pile Axial Forces under Abutment 1.

Figure 4.79. Bridge 222: South Pile Axial Forces under Abutment 1.

Figure 4.80. Bridge 222: North Pile Axial Forces under Abutment 2.

Figure 4.81. Bridge 222: South Pile Axial Forces under Abutment 2.

Figure 4.82. Bridge 222: Girder Moments near Abutment 1.

Figure 4.83. Bridge 222: Girder Moments near Abutment 2.

Figure 4.84. Bridge 222: Girder Axial Forces near Abutment 1.

Figure 4.85. Bridge 222: Girder Axial Forces near Abutment 2.

Figure 4.86. Bridge 222: Sister-Bar Gages.

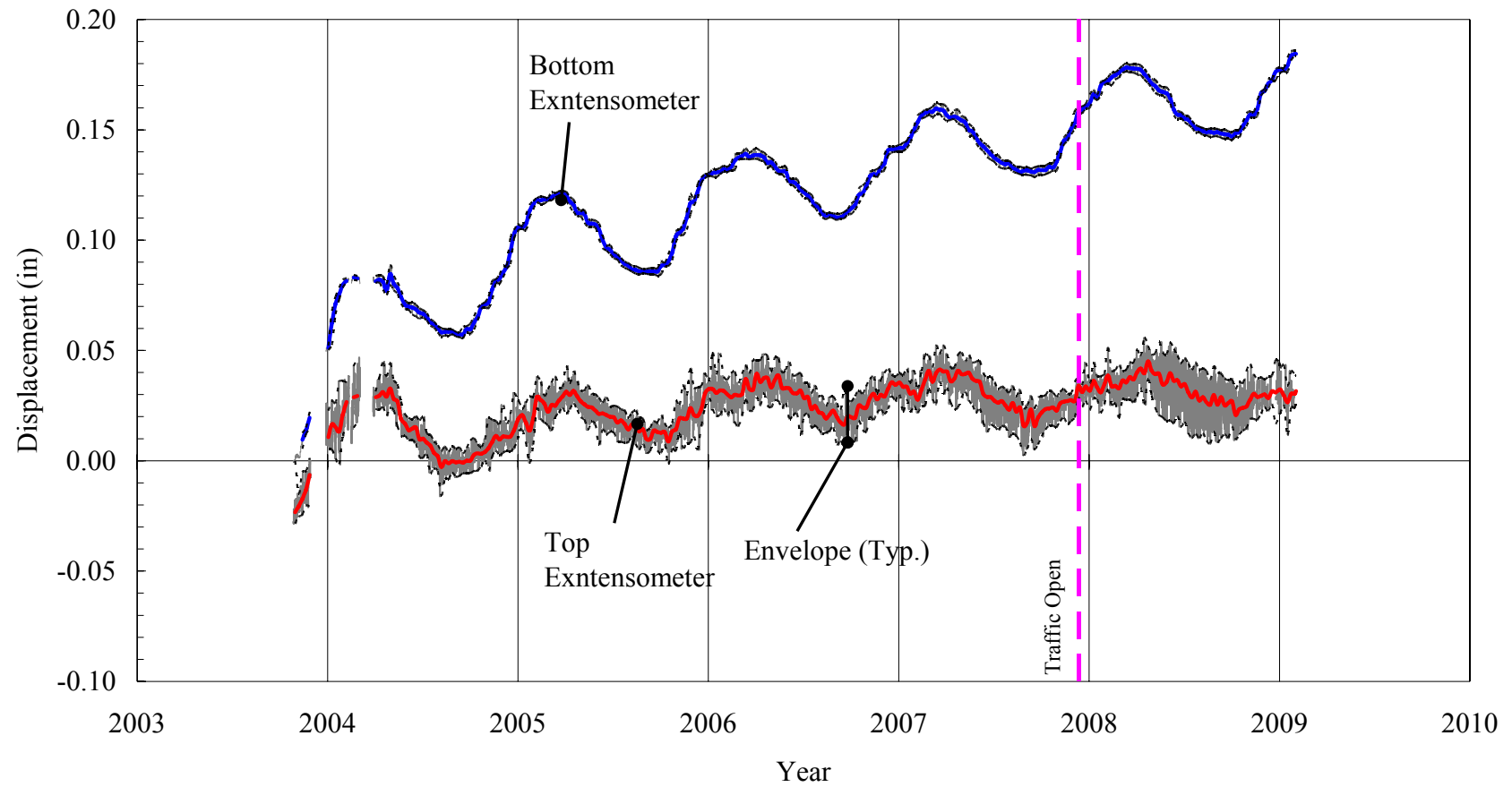


Figure 4.68. Bridge 222: Extensometer on Abutment 1.

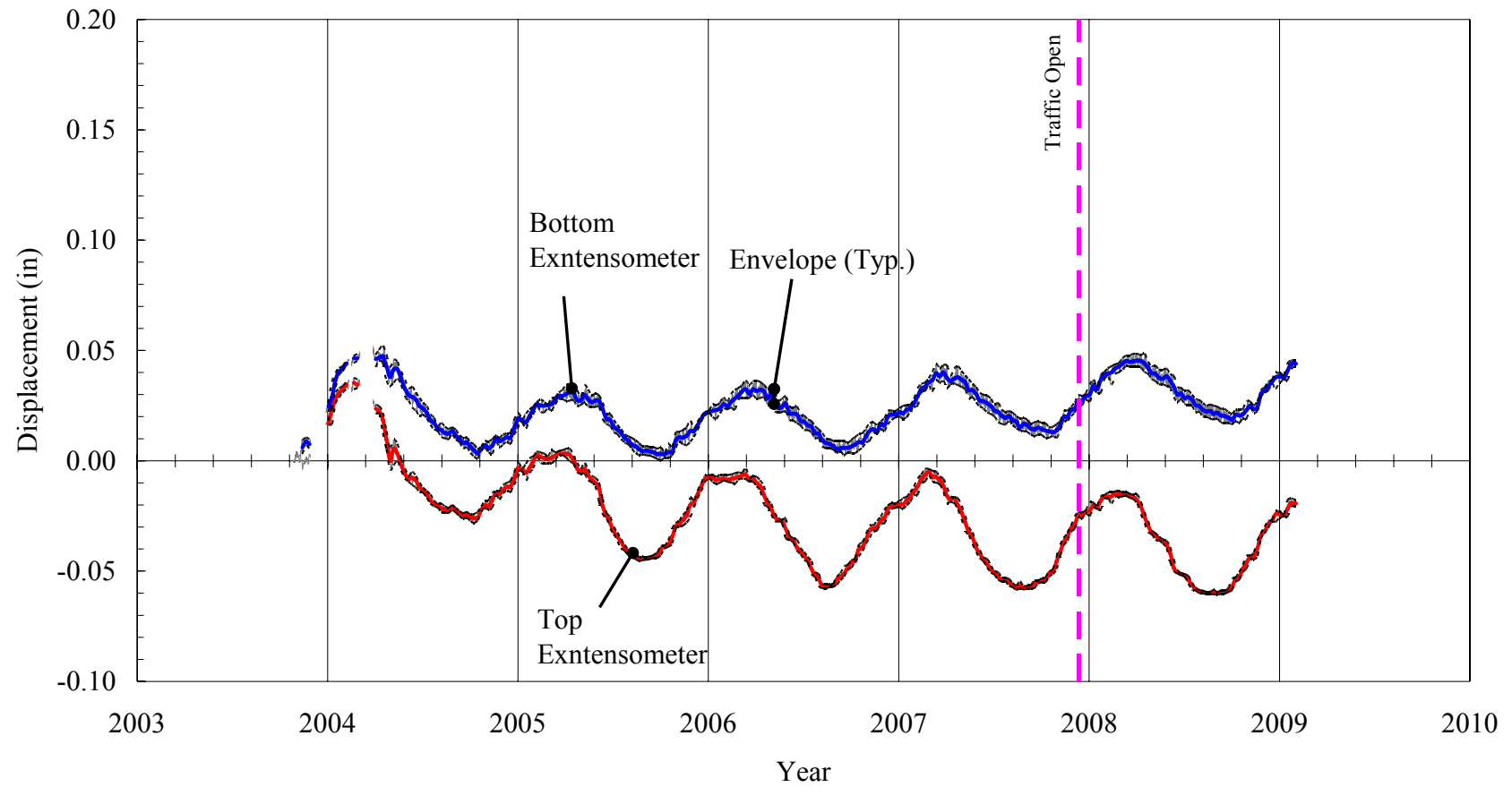


Figure 4.69. Bridge 222: Extensometers on Abutment 2.

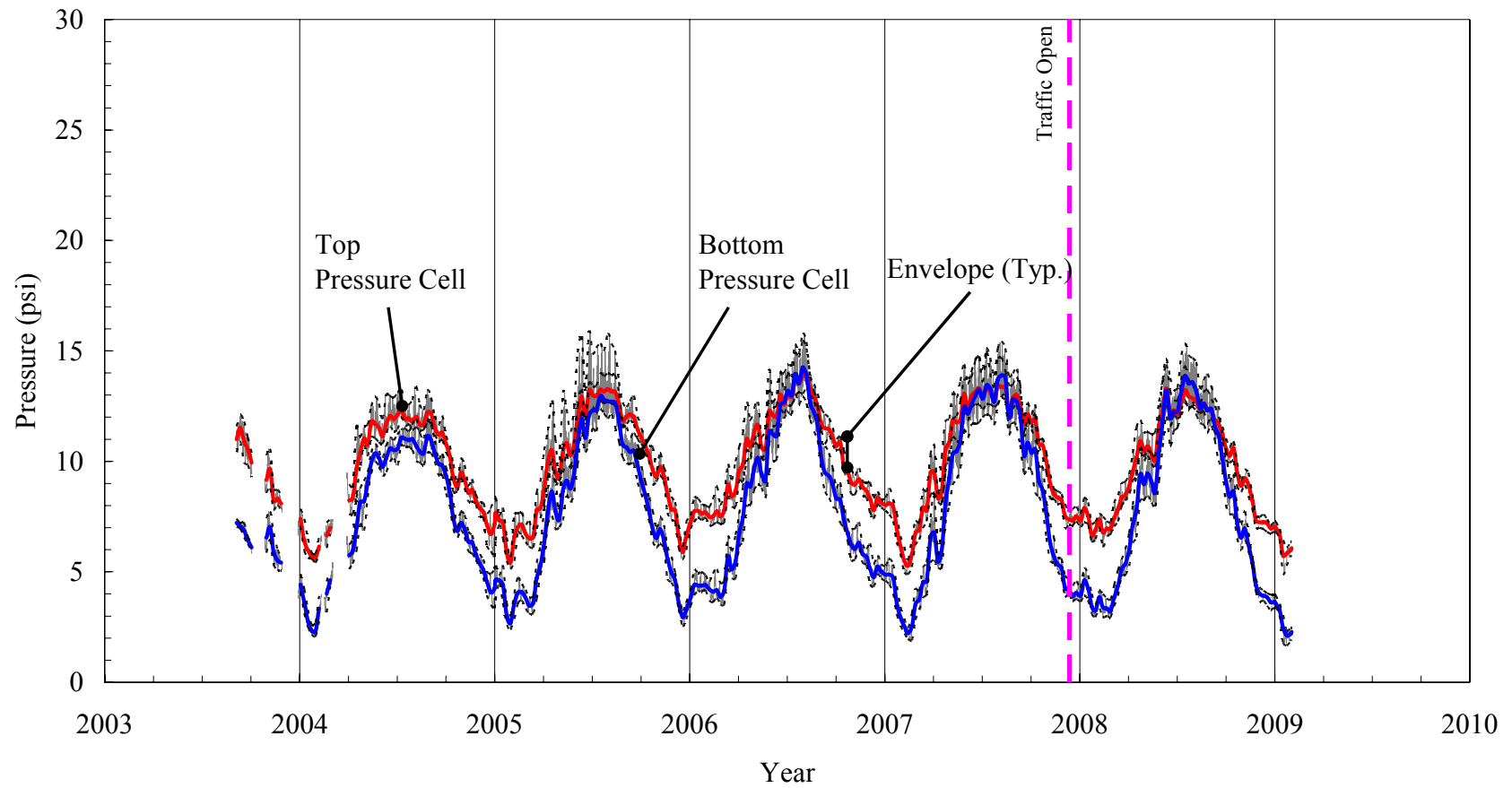


Figure 4.70. Bridge 222: Pressure Cells on Abutment 1.

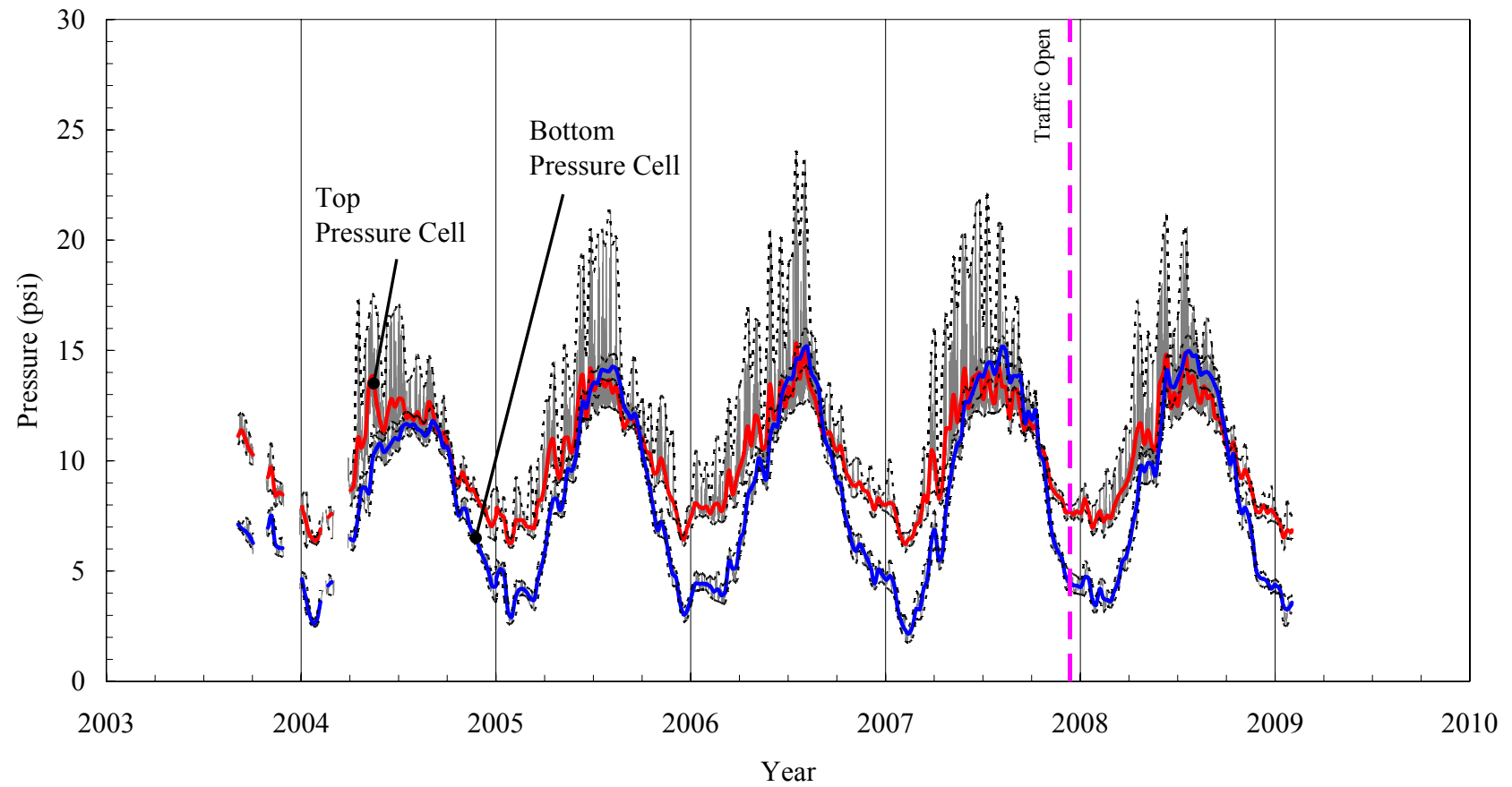


Figure 4.71. Bridge 222: Pressure Cells on Abutment 2.

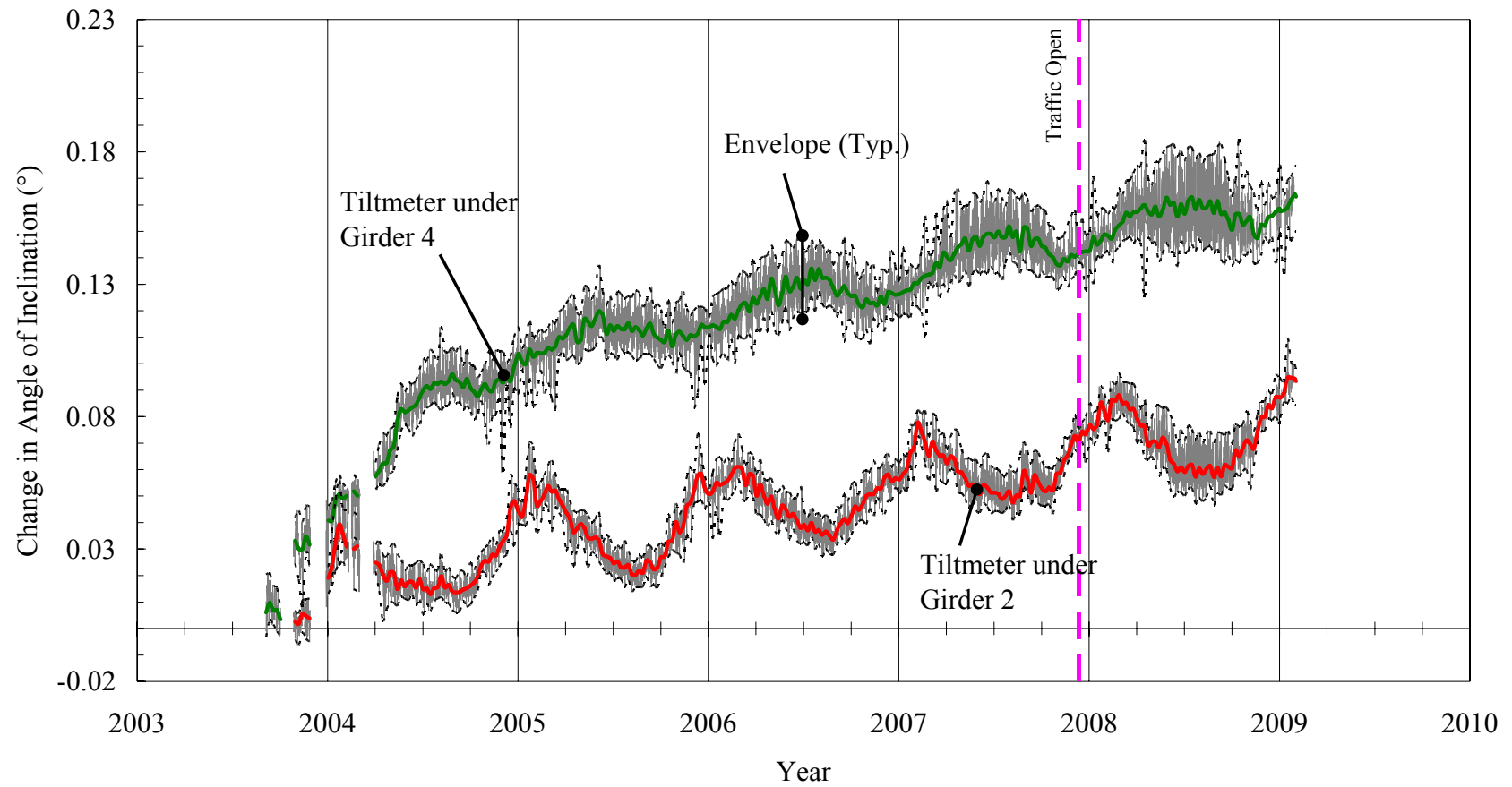


Figure 4.72. Bridge 222: Tiltmeters on Abutment 1.

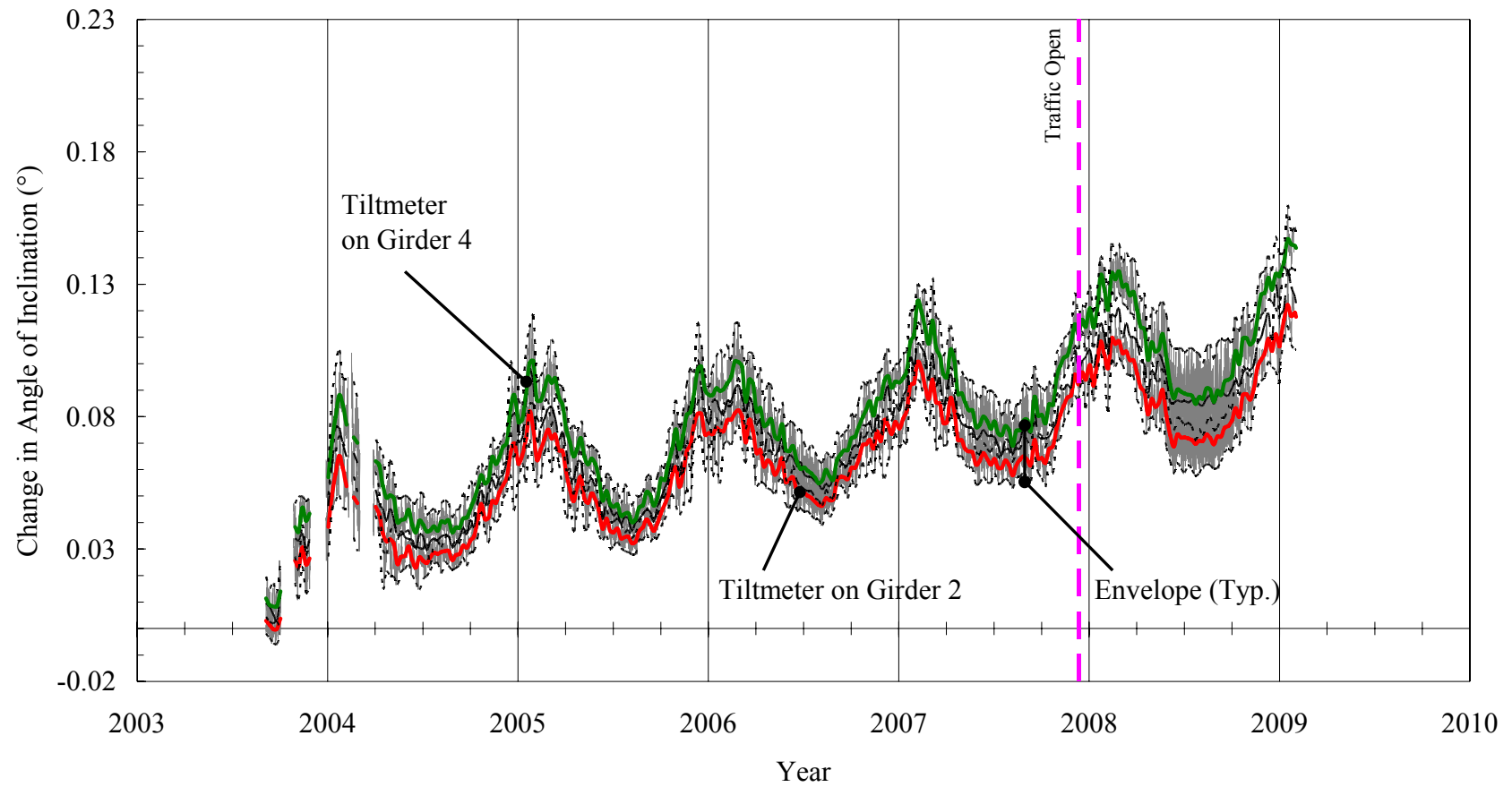


Figure 4.73. Bridge 222: Tiltmeters on Girders near Abutment 1.

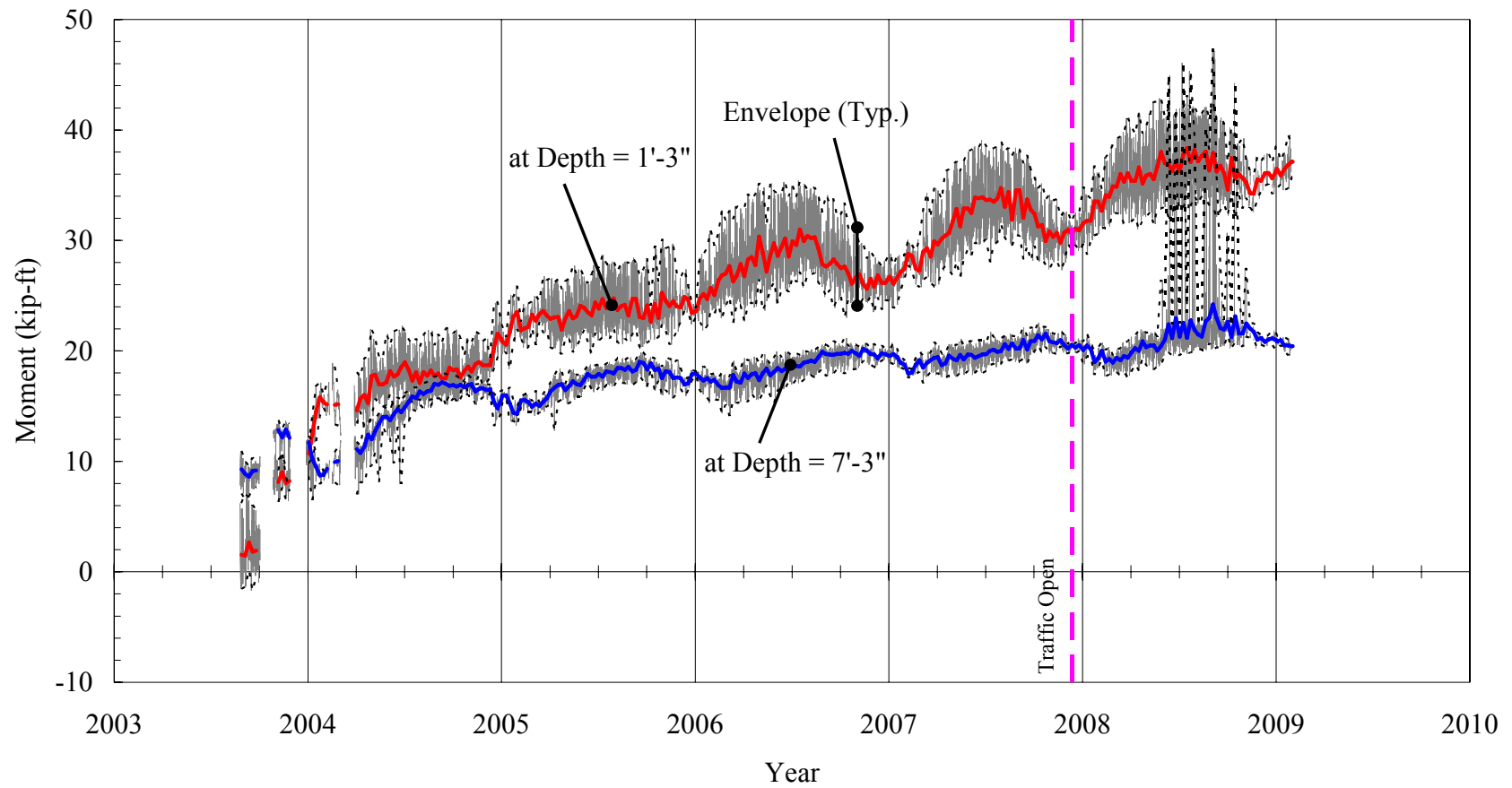


Figure 4.74. Bridge 222: North Pile Moments under Abutment 1.

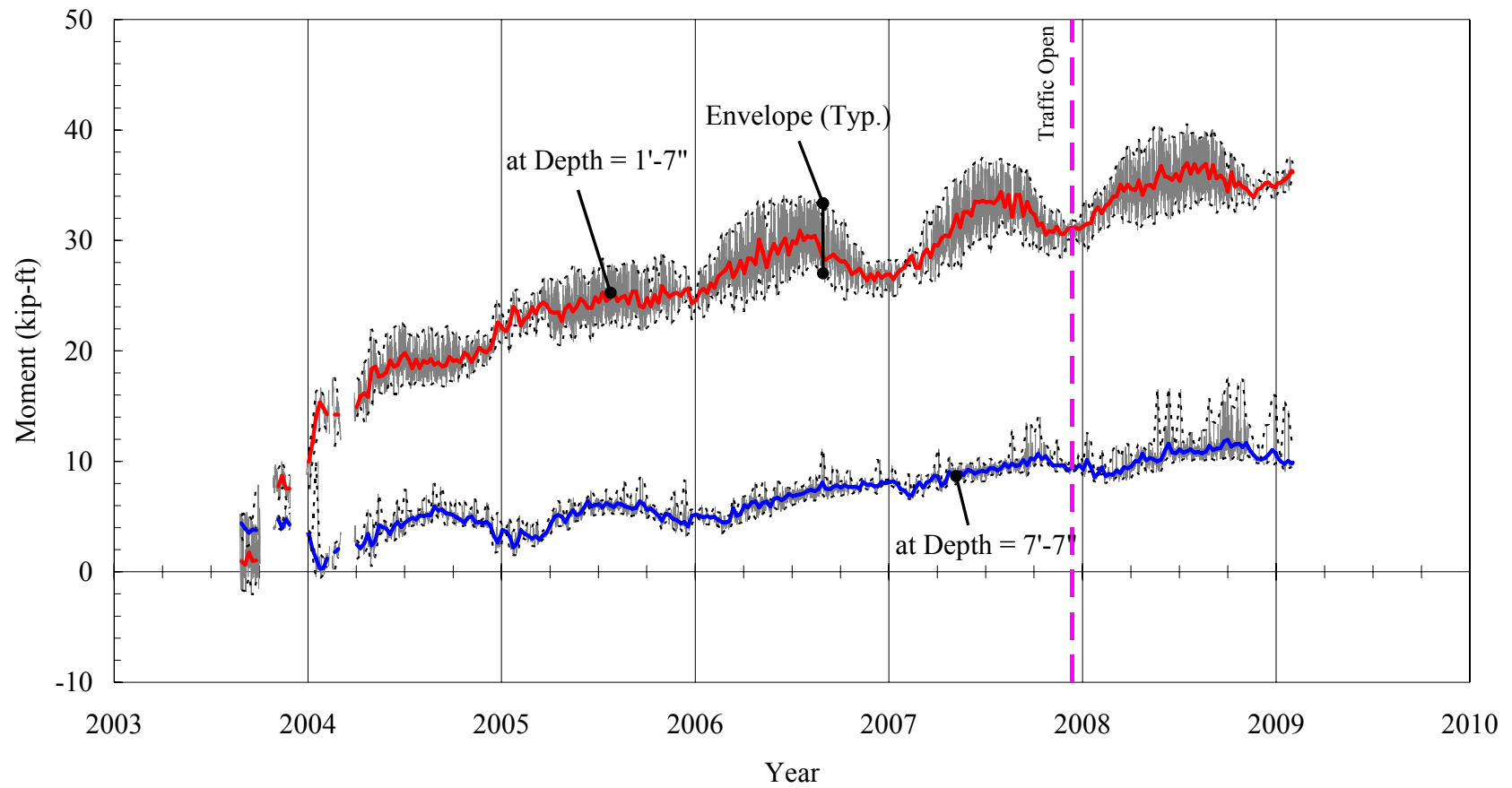


Figure 4.75. Bridge 222: South Pile Moments under Abutment 1.

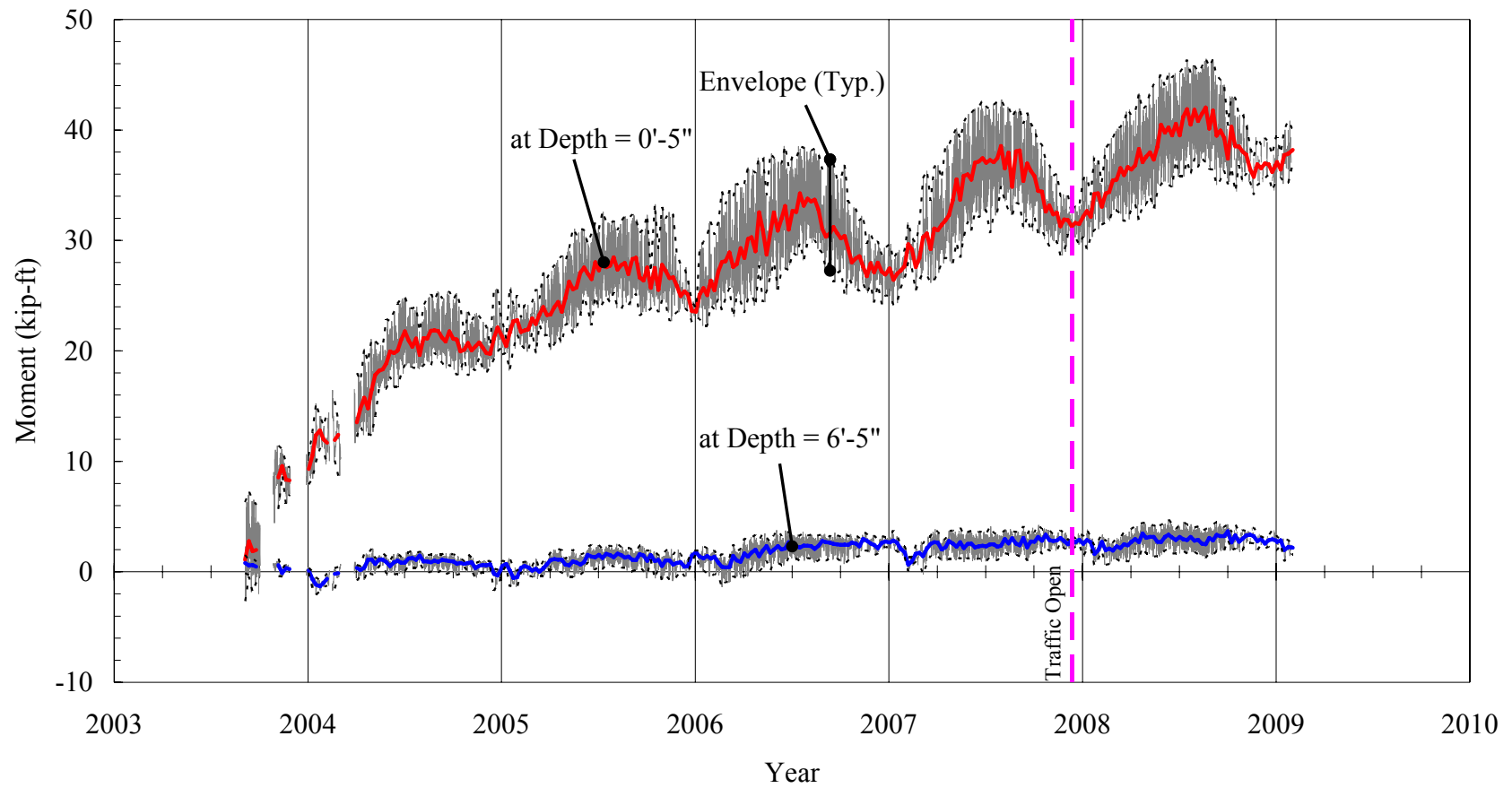


Figure 4.76. Bridge 222: North Pile Moments under Abutment 2.

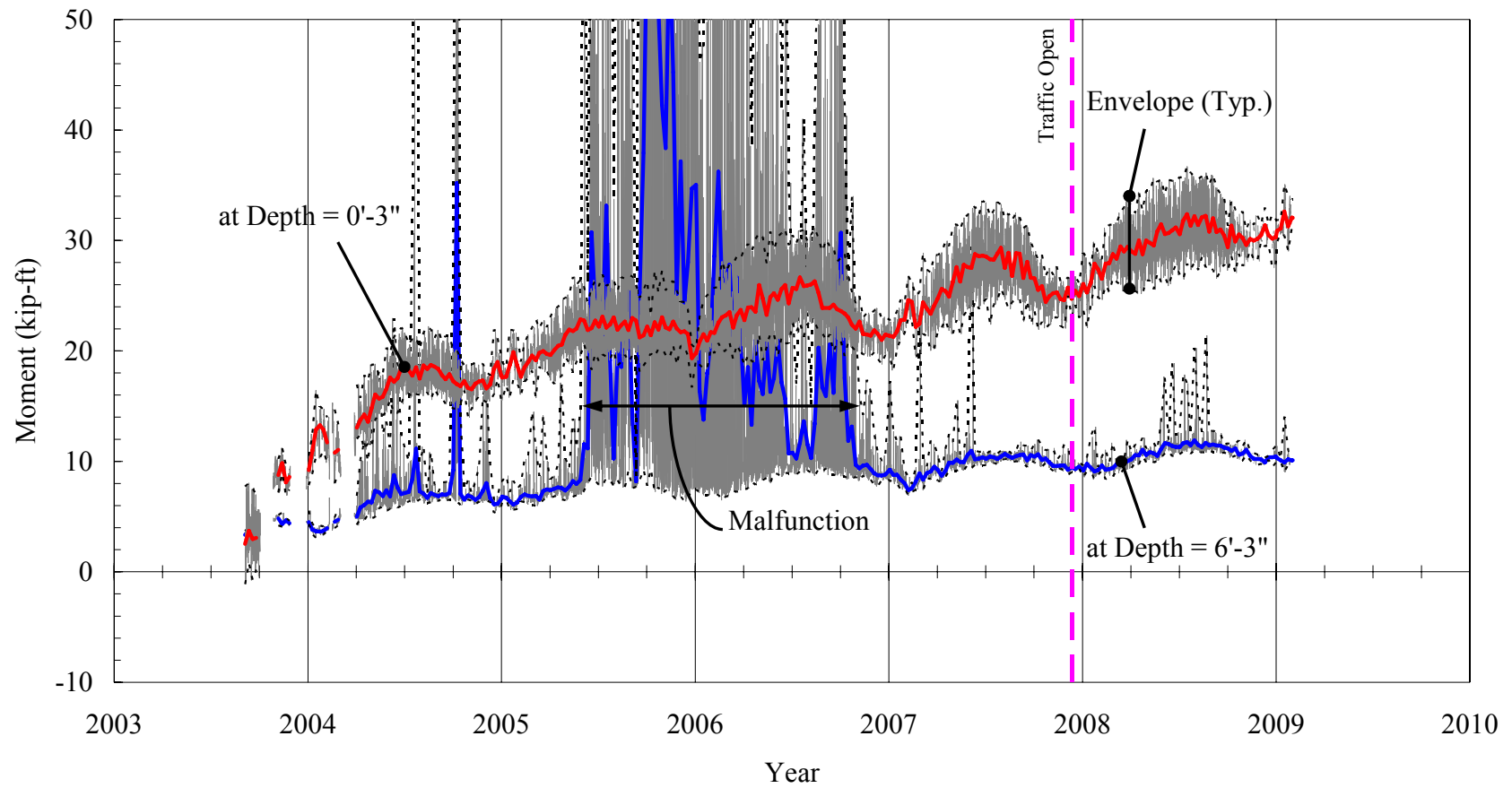


Figure 4.77. Bridge 222: South Pile Moments under Abutment 2.

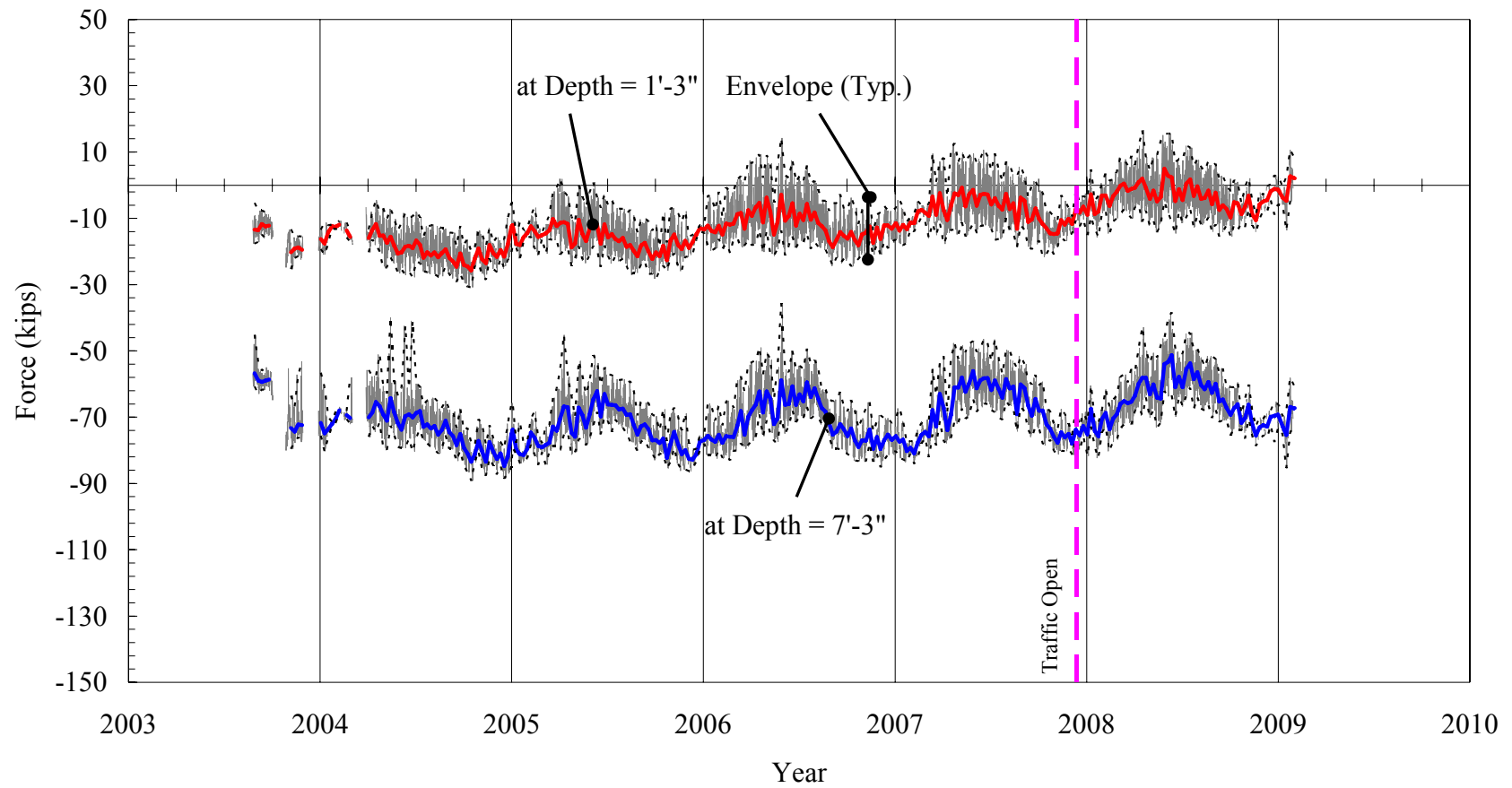


Figure 4.78. Bridge 222: North Pile Axial Forces under Abutment 1.

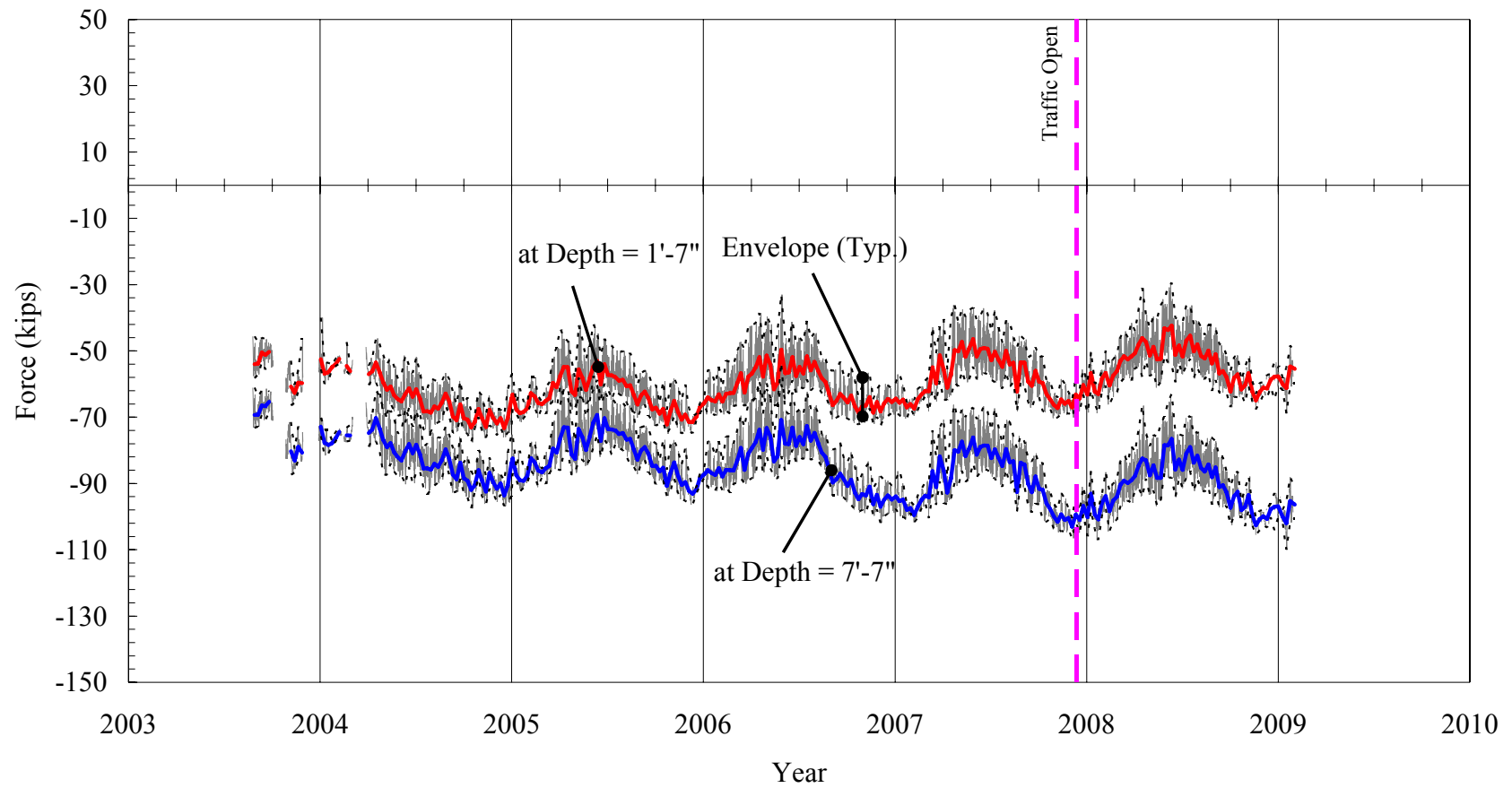


Figure 4.79. Bridge 222: South Pile Axial Forces under Abutment 1.

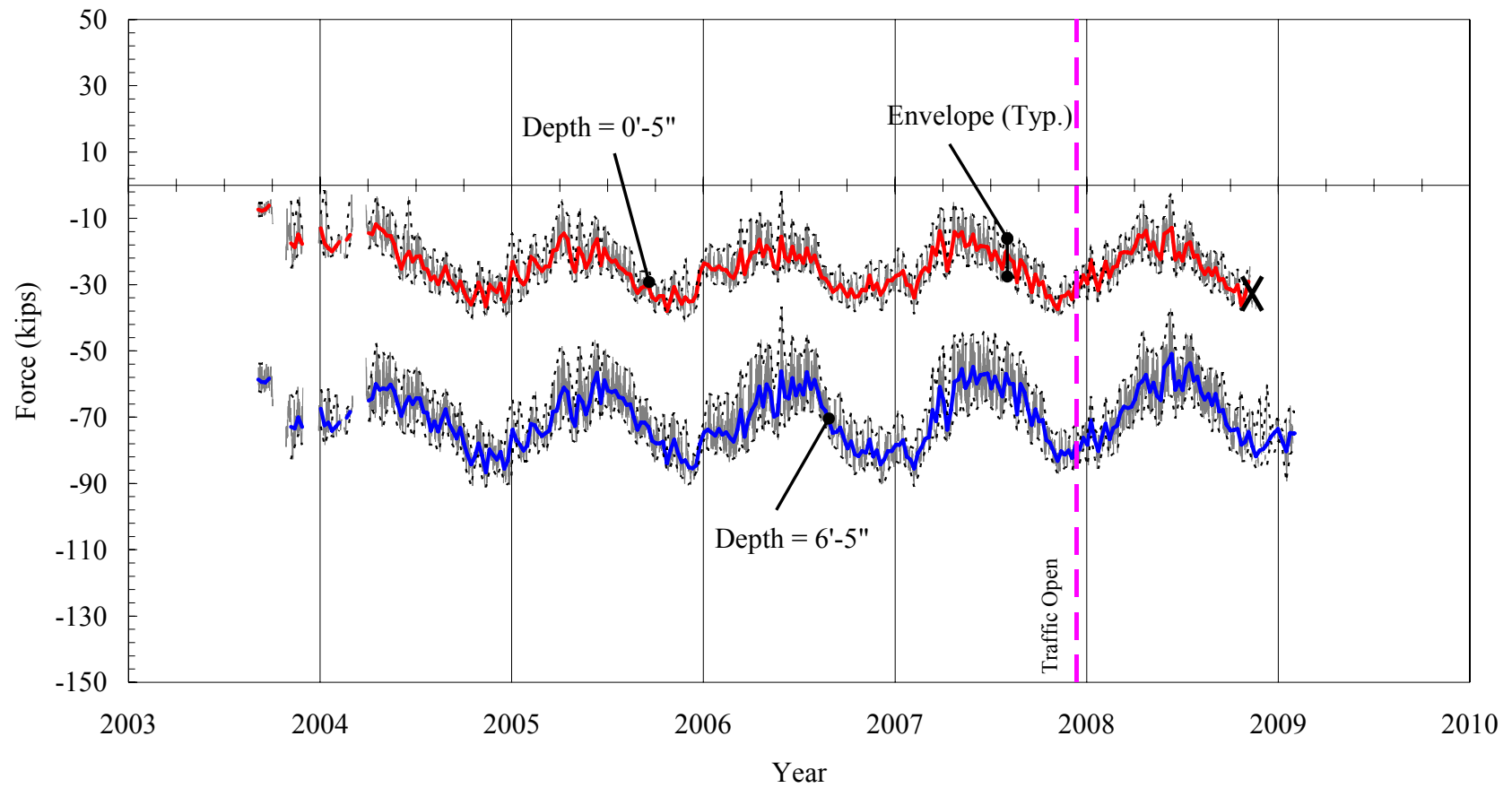


Figure 4.80. Bridge 222: North Pile Axial Forces under Abutment 2.

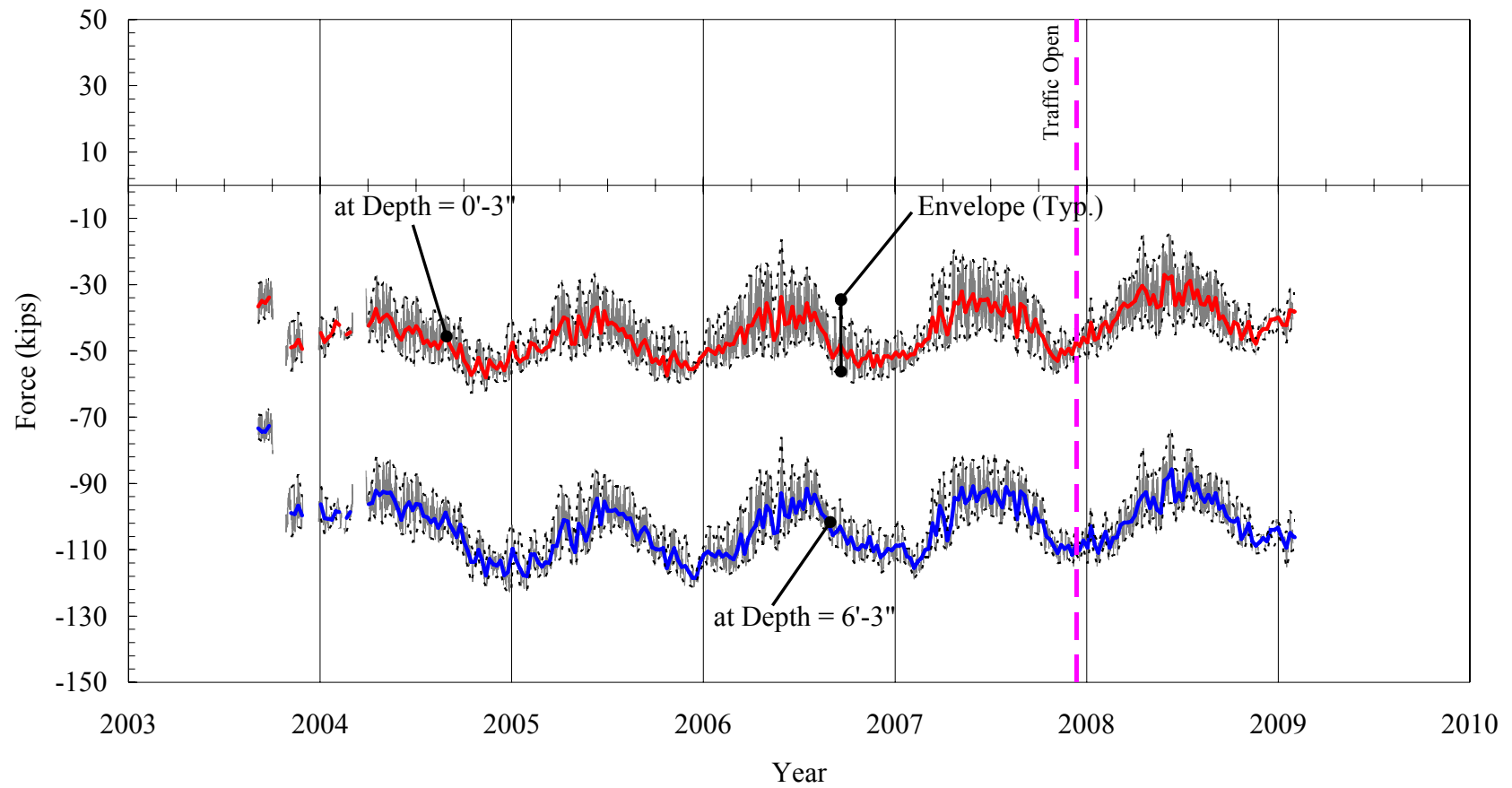


Figure 4.81. Bridge 222: South Pile Axial Forces under Abutment 2.

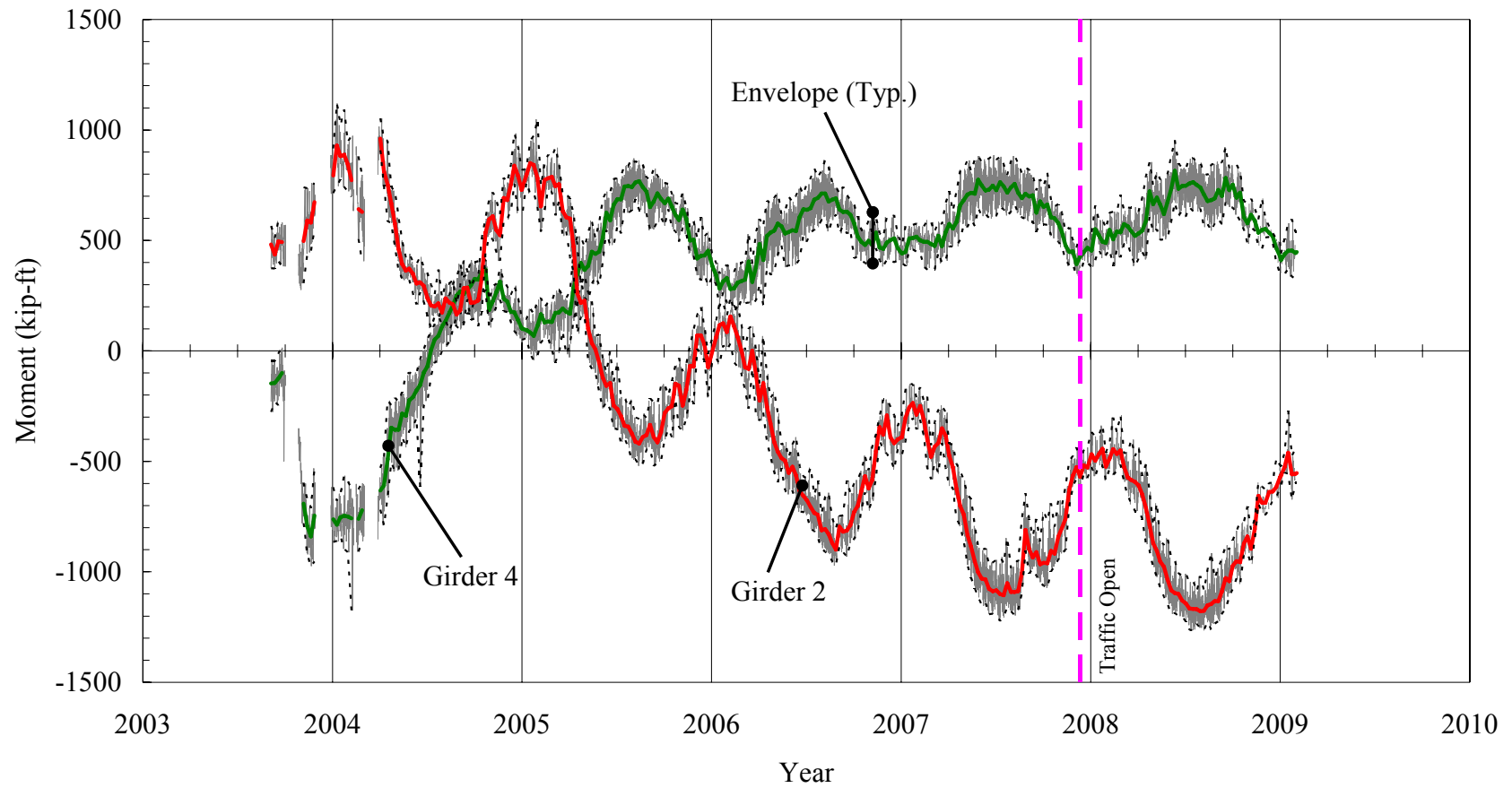


Figure 4.82. Bridge 222: Girder Moments near Abutment 1.

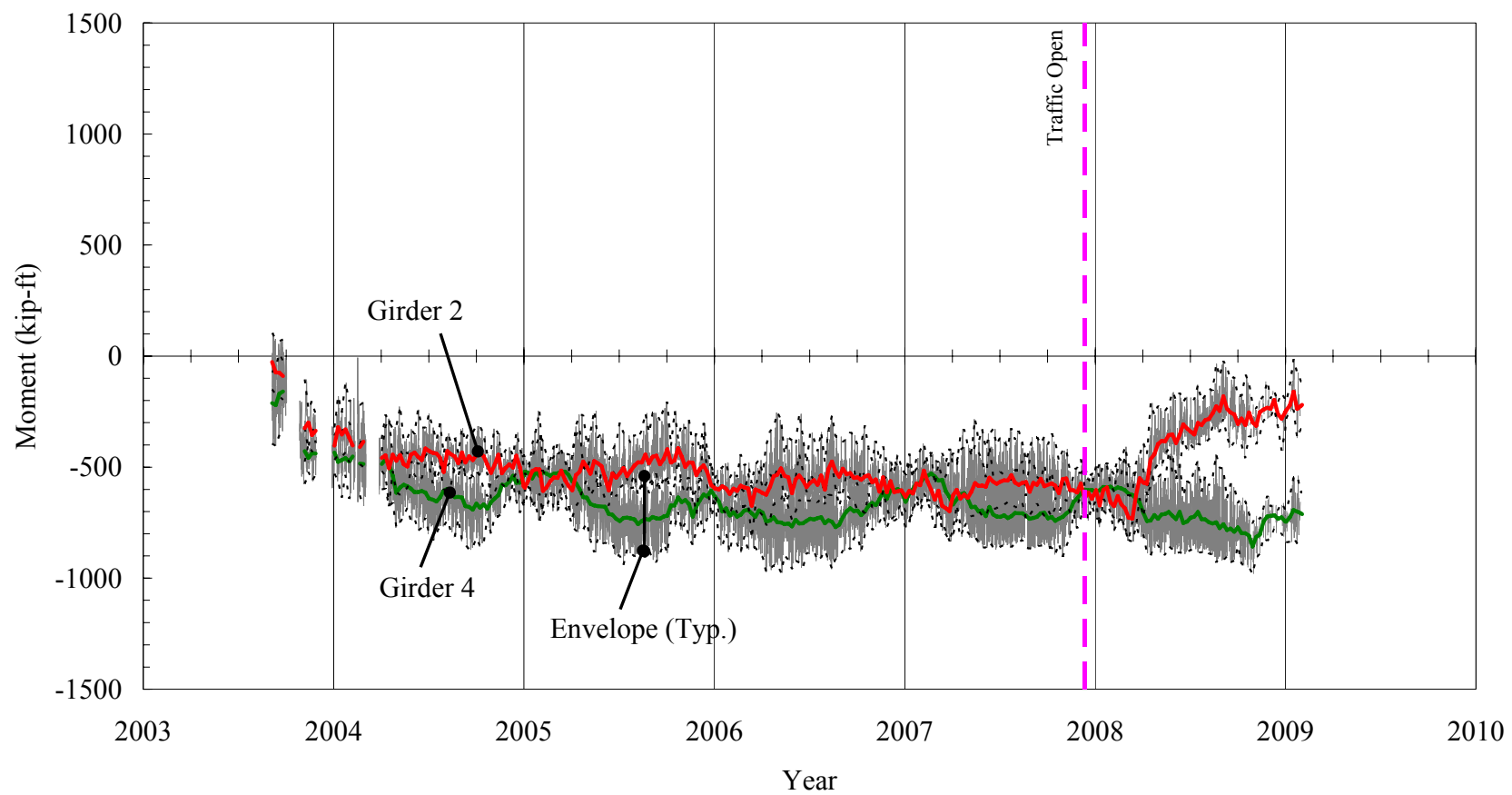


Figure 4.83. Bridge 222: Girder Moments near Abutment 2.

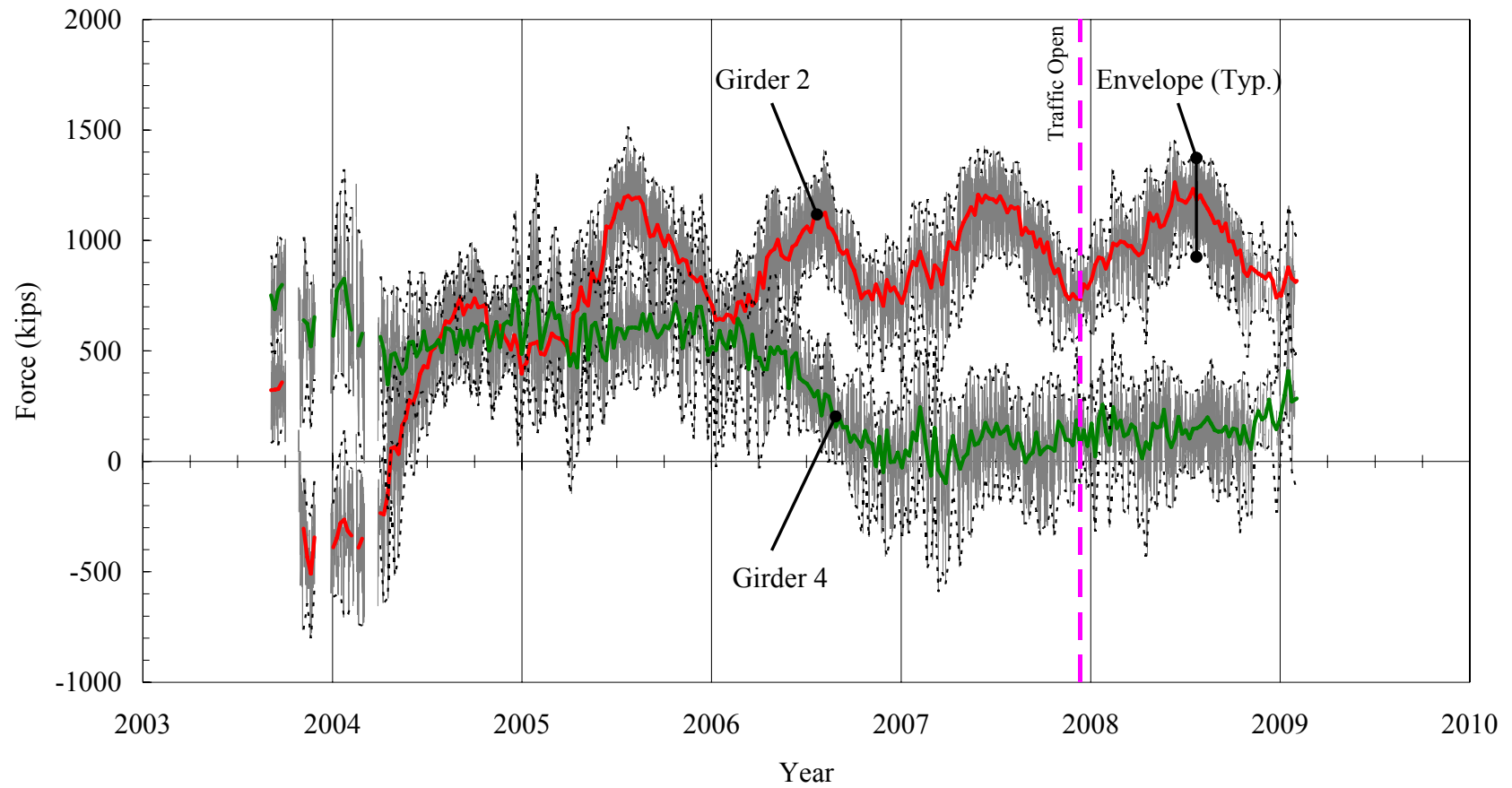


Figure 4.84. Bridge 222: Girder Axial Forces near Abutment 1.

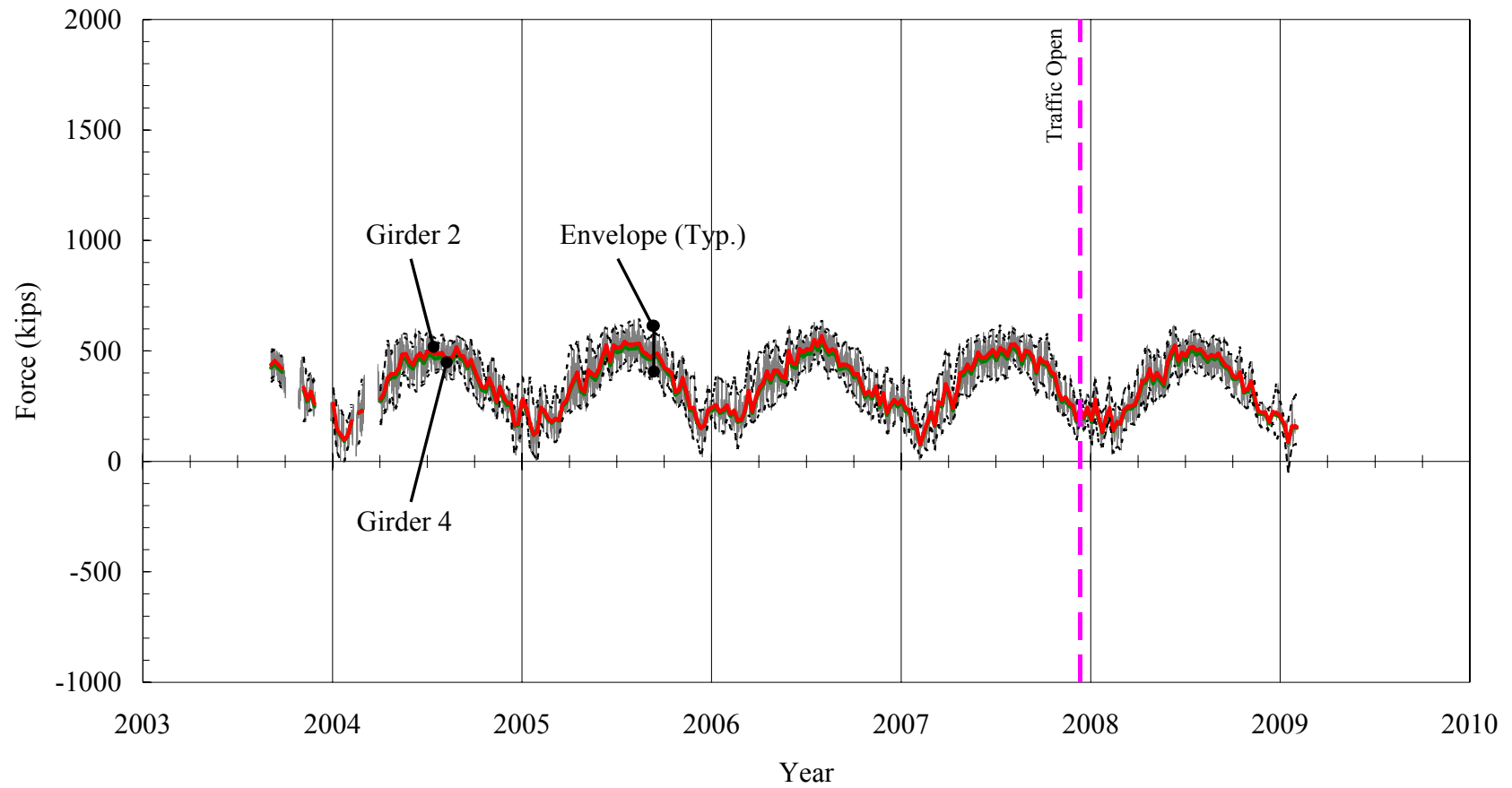


Figure 4.85. Bridge 222: Girder Axial Forces near Abutment 2.

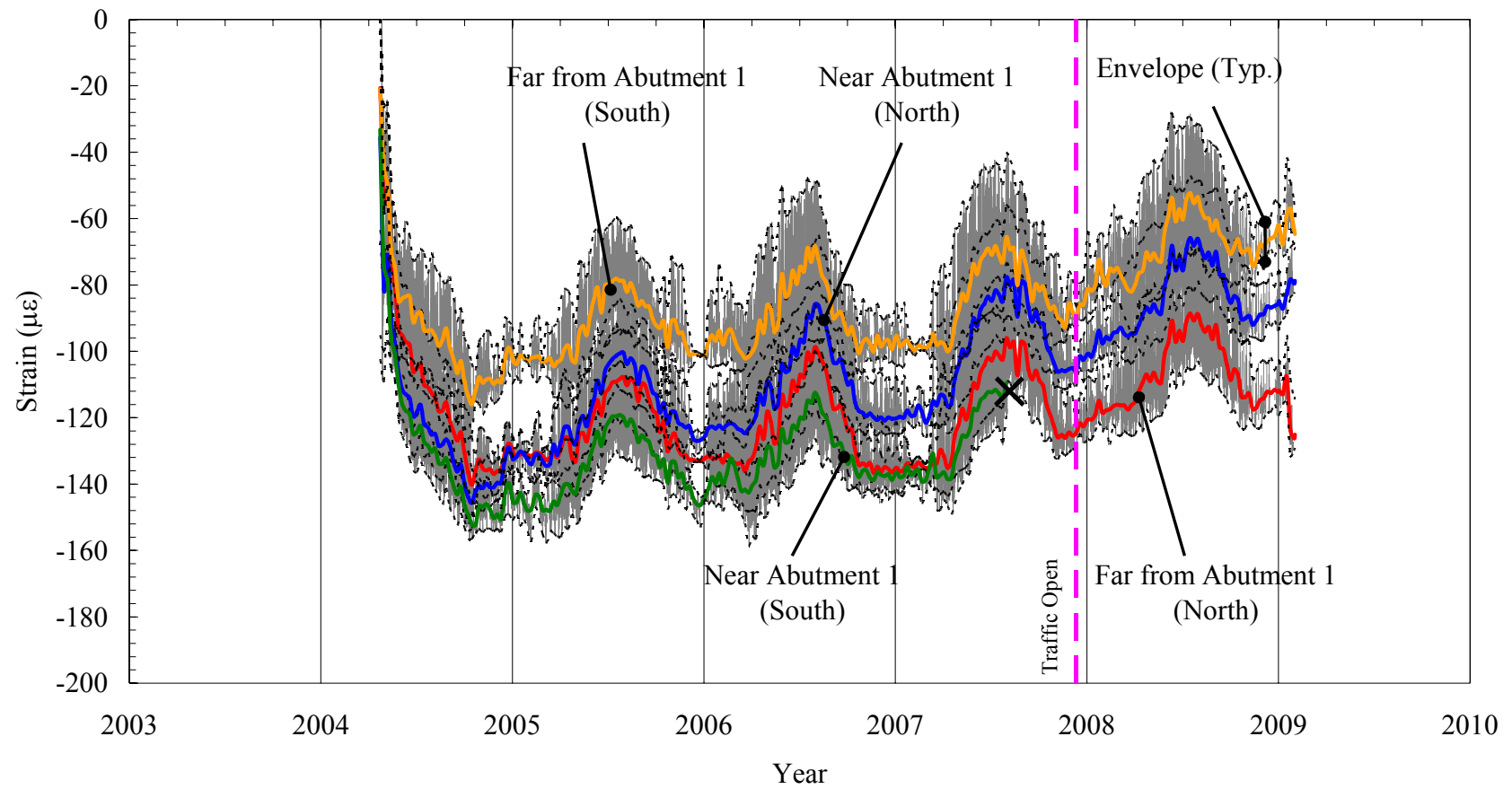


Figure 4.86. Bridge 222: Sister-Bar Gages in Approach Slab near Abutment 1.

4.6 Weather Station

Data obtained from the weather station consist of ambient temperature, relative humidity, air pressure, solar radiation, wind speed, wind direction, and rainfall. Presented here are ambient temperature, relative humidity, air pressure, and solar radiation.

Ambient temperature data, 7-day mean temperature, and maximum and minimum envelopes are presented in Figure 4.87. Maximum and minimum temperatures ranged from -7.7°F in January 2005 to 95.1°F in October 2002. During summer, the average, minimum, and maximum temperatures measured approximately 65 , 32 , and 91°F , respectively. During the winter, the average, minimum, and maximum temperatures measured approximately 37 , -4 , and 81°F , respectively. Daily temperature variation ranges approximately from 25°F to 40°F .

Relative humidity data are presented in Figure 4.88. Relative humidity varied over the time period from 10 to 100 percent, with the 7-day average ranging from 45 to 96 percent. An overall average relative humidity over the data collection period is 76 percent, 6 percent greater than the design value of 70 percent specified in AASHTO LRFD (2007) for central Pennsylvania. Average relative humidity was 76 percent during summer and 75 percent during winter.

Barometric pressure data are presented in Figure 4.89. The barometric pressure varied from 27.8 to 29.4 inches Hg (941 to 996 mbar) over the data collection period. The average pressure over the period is 28.5 inches Hg (965 mbar). Daily barometric pressure variation during winter (approximately 1 inHg) was larger than during summer (approximately 0.5 inHg). Barometric pressure serves as an input parameter used in

conjunction with pressure cell data to determine earth pressures behind abutments and backwalls.

Solar radiation data are presented in Figure 4.90. Solar radiation varied from 0 to 1108 watts. During the winter, solar radiation decreases, and during summer, solar radiation increases. Seven-day mean solar radiation varied from 15 watts in January to 265 watts in July. The difference between winter and summer is approximately 190 watts.

Weather Station Processed Response Data Figure List:

Figure 4.87. Ambient Air Temperature.

Figure 4.88. Relative Humidity.

Figure 4.89. Air Pressure.

Figure 4.90. Solar Radiation.

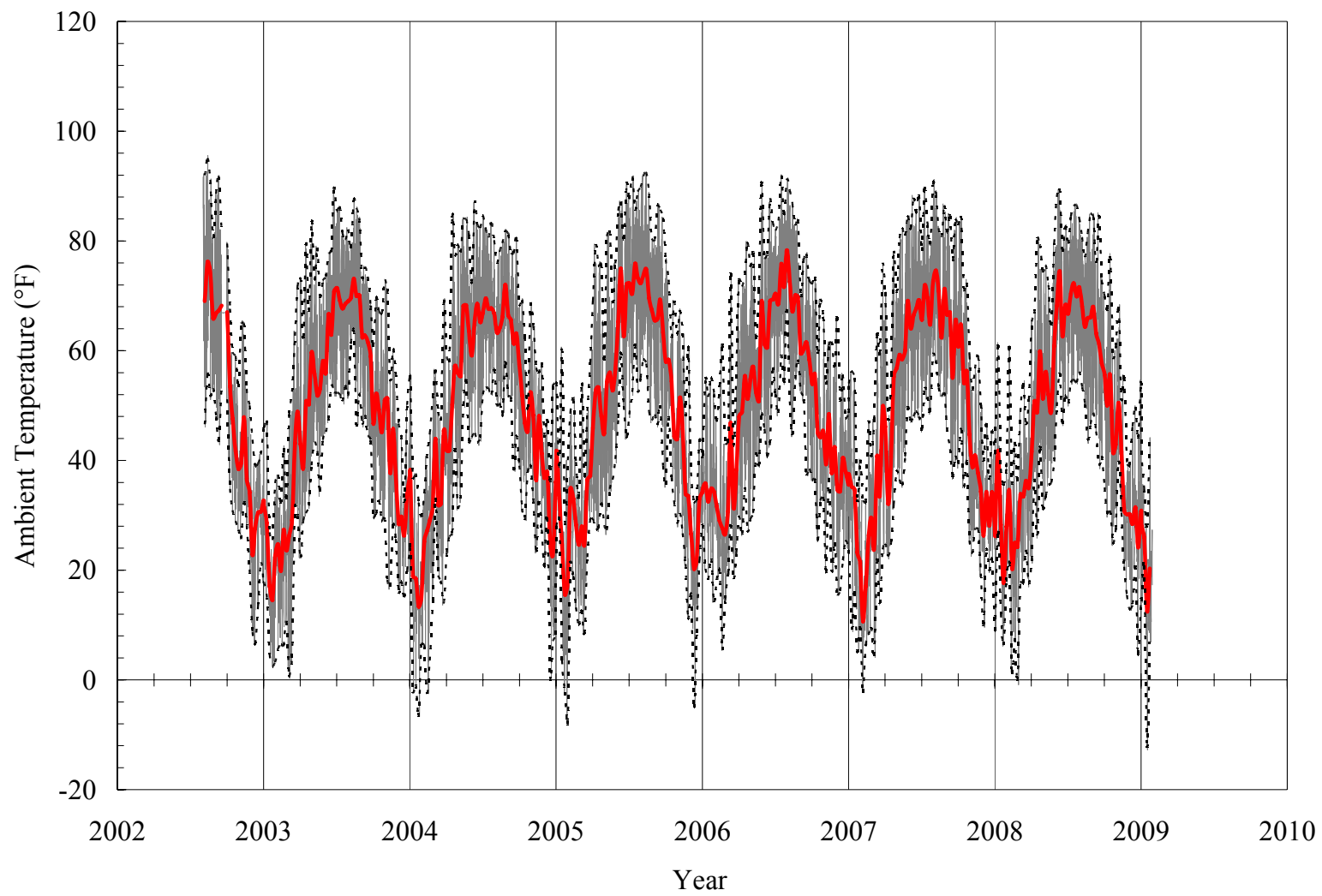


Figure 4.87. Ambient Air Temperature.

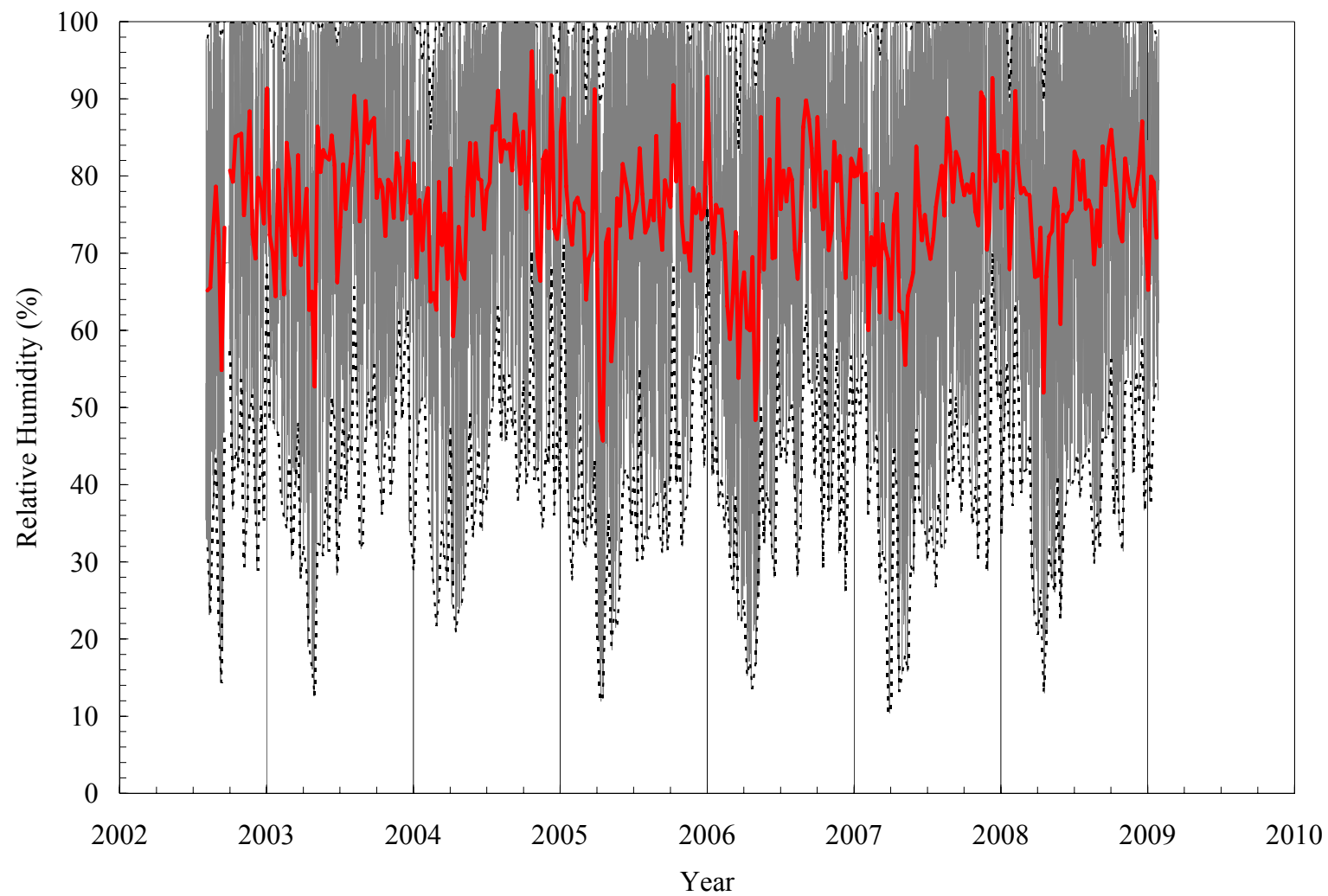


Figure 4.88. Relative Humidity.

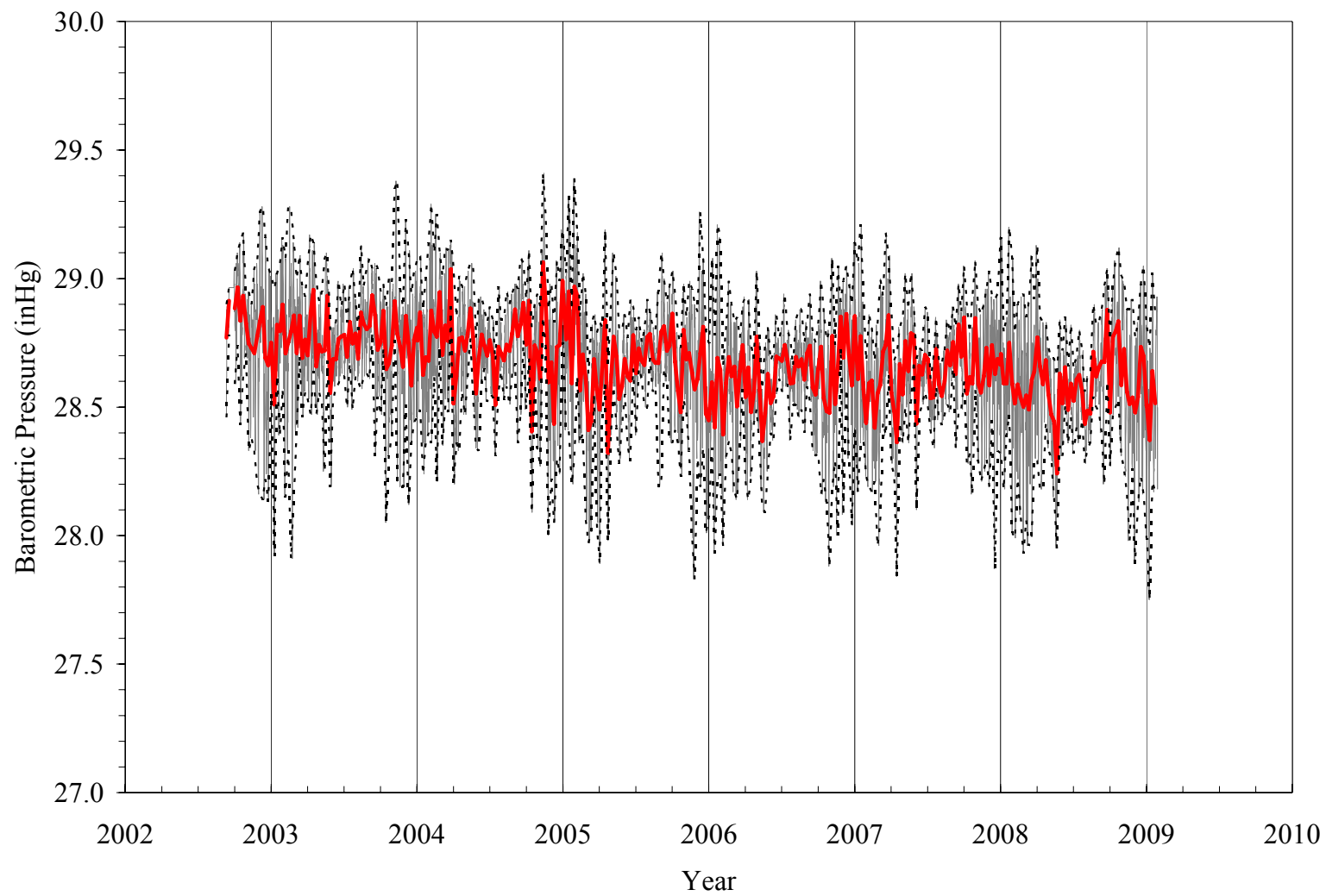


Figure 4.89. Barometric Pressure.

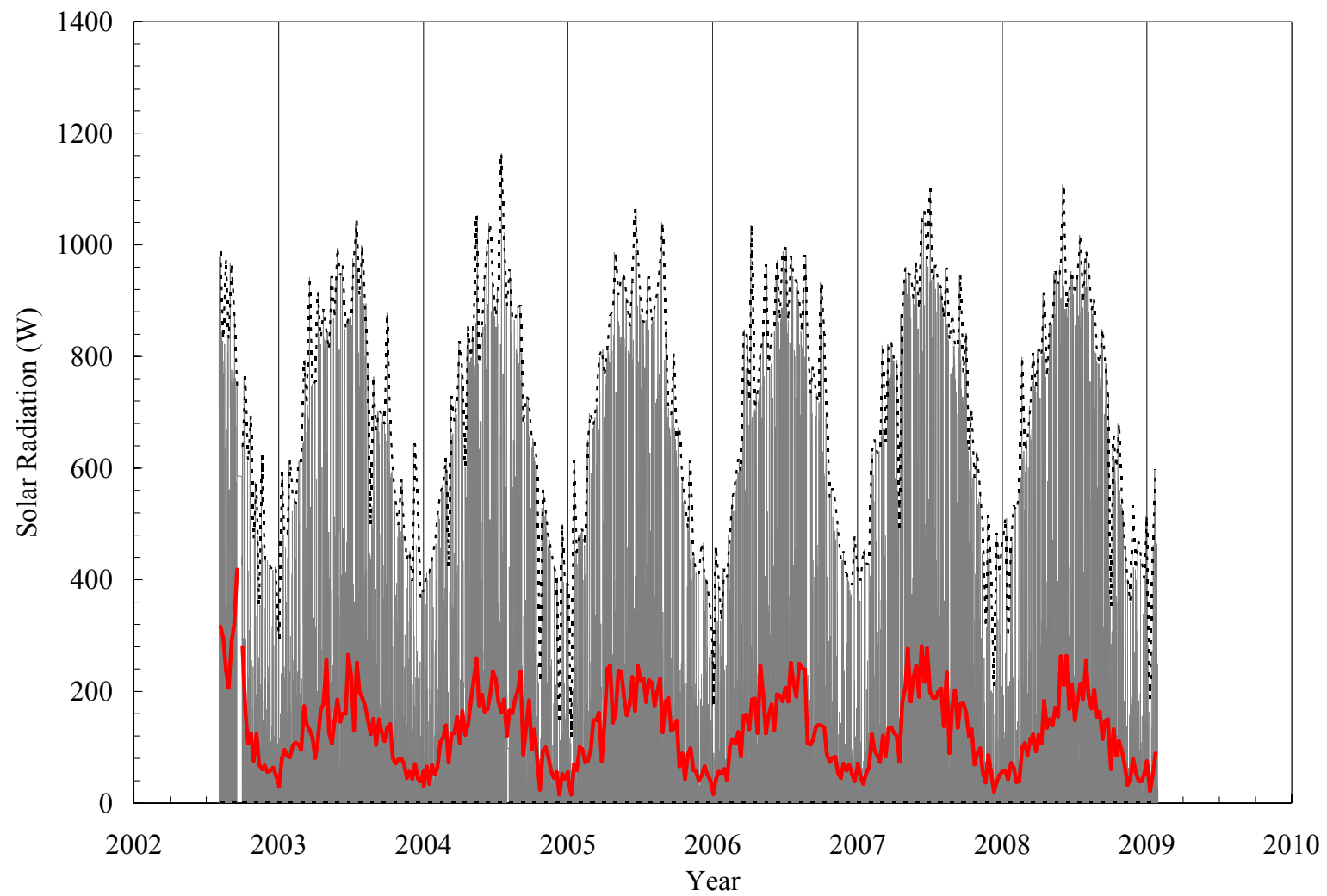


Figure 4.90. Solar Radiation.

4.7 Concluding Remarks

IA bridges 203, 211, 222, and 109 have been instrumented and monitored since November 2002, September 2004, November 2003, and September 2005, respectively. Sixty-four gages each were mounted for bridges 203, 211, and 109, and 48 gages were mounted for bridge 222 to investigate daily and seasonal thermal response of IA bridges.

A general trend of extensometers had a ratcheting effect that explains an unrecoverable displacement. Top extensometers indicated wide fluctuations compared to bottom extensometers. However, the bottom extensometers indicated more significant unrecoverable displacements (see Table 4.10). An obvious trend of backfill pressure was a constant difference between top and bottom pressure cell measurements during the first several years. The constant difference between pressure cells was not as large as the expected, and the difference decreased over the monitored period. A larger daily backfill pressure variation during the summer supports the fact that the upper backfill soil is subjected to higher pressure due to bridge expansion. When a bridge contracts, the lower backfill soil experiences a higher pressure. Thus, displacement amplitudes of top extensometers tend to range widely compared to those of bottom extensometers.

Table 4.10. Summary of Maximum Abutment Displacements and Backfill Pressures.

Response	Gage Location	B109	B203	B211	B222
Abutment Displacement (in)	Top	1.935	0.626	0.239	0.056
	Bottom	2.029	0.299	0.282	0.186
Backfill Pressure (psi)	Top	10.6	16.1	16.6	24.0
	Bottom	37.0	20.3	12.3	16.0

The rotation of tiltmeters on interior girders or abutment produced results in agreement with extensometers (see Table 4.11). However, the rotation of tiltmeters on exterior girder tends to vary within a narrow range. This tiltmeter result was highly dependent on each bridge's dimensions and boundary conditions. Abutment rotations produced different rotations compared to girder rotations because construction joint between backwall and abutment below girder seats was expected to rotate. Generally, abutment rotations were less than girder rotations.

Table 4.11. Summary of Maximum Girder and Abutment Rotations.

Response	Gage Location	B109	B203	B211	B222
Abutment Rotation (degree)	Interior*	0.139	0.322	0.232	0.184
	Exterior*	0.184	0.187	0.162	0.096
Girder Rotation (degree)	Interior**	0.157	0.181	0.225	0.160
	Exterior**	0.152	0.255	0.151	0.135

* abutment rotations were measured under interior and exterior girders

** girder rotations were measured at interior and exterior girders

Pile moments generally ranged within pile section capacity (see Table 4.12). Pile bending moments from strain gage sets at a greater depth are generally smaller due to the location of the gages near the point of fixity. Pile moments at the top locations vary in correspondence to temperature. Pile moments continuously increase with the pile head moving toward the bridge. The first year, abutment displacement of bridge 211 was similar to the third year abutment displacement of bridge 203 although bridge 211 had a single span, 114-ft length, and bridge 203 had a three-span, 172-ft length. Pile axial forces had a similar trend to each other and fluctuated within a small range with respect to superstructure thermal movements.

Table 4.12. Summary of Maximum Pile Moments and Axial Forces.

Response	Gage Location	B109	B203	B211	B222
Moment (ft-kip)	Top	108.3 (35.3)*	80.4 (12.9)*	43.7 (2)*	46.5 (2.3)*
	Bottom	65.0 (42.8)*	-16.2 (-4.9)*	10.9 (-8.8)*	47.4 (9.2)*
Compressive Axial Force (kips)	Top	192.0 (137)*	150 (64)*	123.3 (104)*	77.6 (5)*
	Bottom	416.0 (164)*	91.8 (56)*	120.0 (42)*	123.0 (70)*

* initial readings after pile driving

Girder moments from girder strain produced well-matched results to abutment rotation and girder rotation (see Table 4.13). Generally, girders near abutments had negative moment increasing trends and compressive axial force increasing trends. These trends agree with the contraction abutment displacement and abutment rotation results. Bridges 109 and 211 produced clear trends of girder moments and axial forces. However, for bridges 203 and 222, difficulties in determining general behavior of exterior and interior girders, such as opposite responses to each other with respect to temperature and different amplitudes, were observed. This fact implies that each girder is subjected to different backfill earth pressure or abutment distortion.

Table 4.13. Summary of Maximum Girder Moments and Axial Forces.

Response	Sign	B109	B203	B211	B222
Moment (ft-kip)	Positive	1818	2230	1072	1120
	Negative	-5173	-3160	-6100	-1265
Axial Force (kips)	Tensile	1407	2627	1561	1515
	Compressive	-1559	-1361	-1485	-590

Sister-bar gages in approach slabs initially had significant decreases due to creep and shrinkage (approximately $100 \mu\epsilon$). As observed in extensometers, the decrease of sister-bar gages was not recovered at the original location, but compressive strain decreased over the years. The maximum compressive strains in sister-bar gages are presented in Table 4.14.

Table 4.14. Summary of Maximum Compressive Sister-Bar Strain.

Response	Gage Location	B109	B203	B211	B222
Compressive Strain ($\mu\epsilon$)	near abutment	215	276	141	159
	away from abutment	194	255	101	152

Chapter 5

Numerical Modeling and Response Prediction

5.1 Introduction

Because of the structural continuity inherent to IABs and structure interaction with driven piles and backfill, accurate numerical modeling of IABs is complex. It has been observed that numerical methods commonly employed to predict behavior of conventional bridges is inadequate for IABs, requiring additional incorporated features in the analysis. An accurate IAB modeling process requires the inclusion of material property identification and representation (concrete, steel, soil, elastomeric, foam, etc.), environmental and time-dependent load modeling, and boundary condition modeling of critical bridge components. For the present study, measured material properties and dimensions have been used (Laman *et al.* 2003, 2006) in all analyses presented. Methodologies to incorporate critical structural elements, behaviors, and soil-structure interaction are the primary focus of this chapter. This study focuses on three key bridge response issues: (1) soil-pile interaction, (2) backfill-abutment interaction, and (3) abutment-backwall joint. The Winkler spring model is used to represent abutment-backfill interaction based on classical Rankine active and passive pressure theory. Soil-pile interaction is modeled utilizing nonlinear p - y curves derived on the basis of American Petroleum Institute (API) (1993) recommendations. The abutment-to-backwall joint, depending on construction, may deform significantly into the inelastic region in the case of long bridges; therefore, the joint was modeled based on moment-rotation characteristics of the joints.

Considered loads include backfill pressure, time-dependent effects, temperature load, and temperature gradient load. Backfill pressure applied to abutments is modeled as the traditional, linearly varying distribution with depth. Time-dependent effects consist of concrete creep,

shrinkage, and prestressing steel relaxation that are implemented using an equivalent temperature method and the age-adjusted effective modulus method (AAEM). The temperature gradient of the superstructure is modeled as an equivalent linear variation along the depth because of modeling limitations to represent the complex variation recommended by AASHTO LRFD (2007).

5.2 Model Components

The material used in the numerical modeling was assumed to be homogeneous and isotropic. The predicted response of IABs is largely dependent on the numerical characterization of surrounding soil. To accurately simulate the soil-structure interaction caused by backfill and soils around piles, nonlinear stress-strain curves were adopted for soil models. Soil models that represent nonlinear and path-dependent soil response under cyclic movement are required. In addition, compatibility of soil and structure deformations corresponding to forces (soil-structure interaction) must be maintained in the model at all points in time.

Soil-structure interaction is distinguished by two components: soil-pile interaction and backfill-abutment interaction. A linear Winkler spring, within the range of the upper and lower bound defined by the passive and active failure limit, simulates backfill-abutment interaction. For soil-pile interaction, a family of Winkler springs based on API p - y curves is used.

The typical IAB is constructed with a joint between the backwall and abutment. This construction joint is generally under-reinforced at less than 25 percent of AASHTO LRFD minimum reinforcement; therefore, rotation between superstructure and abutments occurs under expansion and contraction. This study modeled the construction joint as a pre-cracked section

with a rotational stiffness derived from moment-curvature relationships of the reinforcement detail.

5.2.1 Material Properties

This study has taken the material properties for structural members and soils from the concrete mix design, design calculations, and geotechnical reports. All material properties of the four field monitored bridges are presented in Table 5.1. Each bridge structural component is assumed to respond within the linear-elastic range. Soil behavior is modeled based on the measured engineering properties of the backfill and soil strata surrounding H-piles (Figures 5.1 through 5.7). Figures 5.1 and 5.2 illustrate soil strata properties at bridge 109 abutments 1 and 2, and Figure 5.3 describes soil strata properties at abutment 2 of bridge 203. Figures 5.4, 5.5, 5.6, and 5.7 present soil strata properties under each abutment of bridges 211 and 222. The upper 10 ft of soil strata under bridges 203, 211, and 222 abutments, except bridge 222 abutment 2 (4.4 ft only), is stiff clay. Bridge 109 soil strata below each abutment is a sand layer.

Table 5.1. Bridges 109, 203, 211, 222 Material Properties.

Material	Strength (f'_c or F_y) (ksi)	Young's Modulus (ksi)	Poisson's Ratio	Thermal Expansion Coefficient (in/in/°F)
Concrete (Prestressed Girder)	8.0	5154	0.20	5.0 E-6
Concrete AAA (Deck and Backwall)	4.0	3644	0.20	5.0 E-6
Concrete AA (Parapet and Diaphragm)	3.5	3409	0.20	5.0 E-6
Concrete A (Pier and Abutment)	3.0	3156	0.20	5.0 E-6
Steel (H-Piles)	50	29000	0.3	6.5 E-6
Elastomer Rubber	n/a	0.39	0.4985	n/a

	Backfill Overburden (PennDOT OGS) $\gamma = 18.7 \text{ kN/m}^3 \text{ (0.069 pci)}$ $\phi = 34^\circ$		3.4m 135"
	$\gamma = 20.4 \text{ kN/m}^3 \text{ (0.075 pci)}$ $\phi = 28^\circ$	$k_{cyclic} = 15.6 \text{ MN/m}^3 \text{ (57.5 pci)}$	4.6m 180"
	$\gamma = 20.4 \text{ kN/m}^3 \text{ (0.075 pci)}$ $C = 143 \text{ kN/m}^2 \text{ (20.8 psi)}$	$k_{cyclic} = 407.2 \text{ MN/m}^3 \text{ (1500 pci)}$ $\epsilon_{50} = 0.005$	3.5m 138"
	$\gamma = 9.8 \text{ kN/m}^3 \text{ (0.036 pci)}$ $C = 143 \text{ kN/m}^2 \text{ (20.8 psi)}$	$k_{cyclic} = 407.2 \text{ MN/m}^3 \text{ (1500 pci)}$ $\epsilon_{50} = 0.005$	3.0m 120"
	$\gamma = 11.4 \text{ kN/m}^3 \text{ (0.042 pci)}$ $\phi = 34^\circ$	$k_{cyclic} = 15.6 \text{ MN/m}^3 \text{ (57.5 pci)}$	4.6m 180"
	$\gamma = 11.4 \text{ kN/m}^3 \text{ (0.042 pci)}$ $\phi = 34^\circ$	$k_{cyclic} = 24.4 \text{ MN/m}^3 \text{ (90 pci)}$	4.6m 180"
	$\gamma = 20.4 \text{ kN/m}^3 \text{ (0.075 pci)}$ $C = 143 \text{ kN/m}^2 \text{ (20.8 psi)}$ $\gamma = 13 \text{ kN/m}^3 \text{ (0.048 pci)}$ $C = 2896 \text{ kN/m}^2 \text{ (420 psi)}$	$k_{cyclic} = 407.2 \text{ MN/m}^3 \text{ (1500 pci)}$ $\epsilon_{50} = 0.005$ $k_{cyclic} = 1,086.8 \text{ MN/m}^3 \text{ (4,000 pci)}$ $\epsilon_{50} = 0.001$	3.0m 120"
			Bed Rock

Figure 5.1. Bridge 109 Soil Properties under Abutment 1.

	Backfill Overburden (PennDOT OGS) $\gamma = 18.7 \text{ kN/m}^3 \text{ (0.069 pci)}$ $\phi = 34^\circ$		3.5m 138"
	$\gamma = 20.4 \text{ kN/m}^3 \text{ (0.075 pci)}$ $\phi = 28^\circ$	$k_{cyclic} = 15.5 \text{ MN/m}^3 \text{ (57.2 pci)}$	4.6m 180"
	$\gamma = 20.4 \text{ kN/m}^3 \text{ (0.075 pci)}$ $C = 143 \text{ kN/m}^2 \text{ (20.8 psi)}$	$k_{cyclic} = 407.2 \text{ MN/m}^3 \text{ (1500 pci)}$ $\epsilon_{50} = 0.005$	2.5m 98.4"
	$\gamma = 9.8 \text{ kN/m}^3 \text{ (0.036 pci)}$ $C = 143 \text{ kN/m}^2 \text{ (20.8 psi)}$	$k_{cyclic} = 407.2 \text{ MN/m}^3 \text{ (1500 pci)}$ $\epsilon_{50} = 0.005$	3.0m 120"
	$\gamma = 11.4 \text{ kN/m}^3 \text{ (0.042 pci)}$ $C = 143 \text{ kN/m}^2 \text{ (20.8 psi)}$	$k_{cyclic} = 407.2 \text{ MN/m}^3 \text{ (1500 pci)}$ $\epsilon_{50} = 0.005$	3.0m 120"
	$\gamma = 8.1 \text{ kN/m}^3 \text{ (0.030 pci)}$ $\phi = 34^\circ$	$k_{cyclic} = 24.4 \text{ MN/m}^3 \text{ (90 pci)}$	4.2m 168"
	$\gamma = 9.0 \text{ kN/m}^3 \text{ (0.033 pci)}$ $C = 143 \text{ kN/m}^2 \text{ (20.8 psi)}$ $\gamma = 9.0 \text{ kN/m}^3 \text{ (0.033 pci)}$ $\phi = 36^\circ$	$k_{cyclic} = 407.2 \text{ MN/m}^3 \text{ (1500 pci)}$ $\epsilon_{50} = 0.005$ $k_{cyclic} = 33.9 \text{ MN/m}^3 \text{ (125 pci)}$	4.9m 192"
	$\gamma = 13 \text{ kN/m}^3 \text{ (0.048 pci)}$ $C = 2896 \text{ kN/m}^2 \text{ (420 psi)}$	$k_{cyclic} = 1,086.8 \text{ MN/m}^3 \text{ (4,000 pci)}$ $\epsilon_{50} = 0.001$	4.6m 180"
			Bed Rock

Figure 5.2. Bridge 109 Soil Properties under Abutment 2.

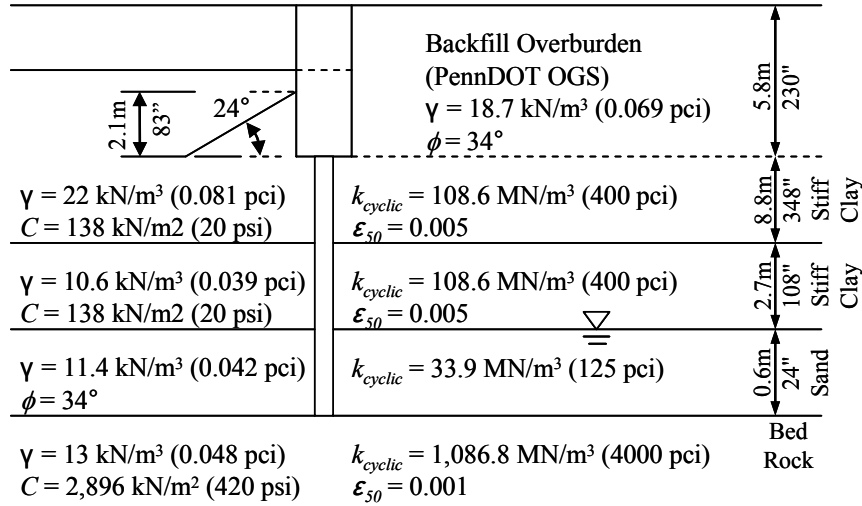


Figure 5.3. Bridge 203 Soil Properties under Abutment 2.
(Note: Abutment 1 has a spread footing on bedrock)

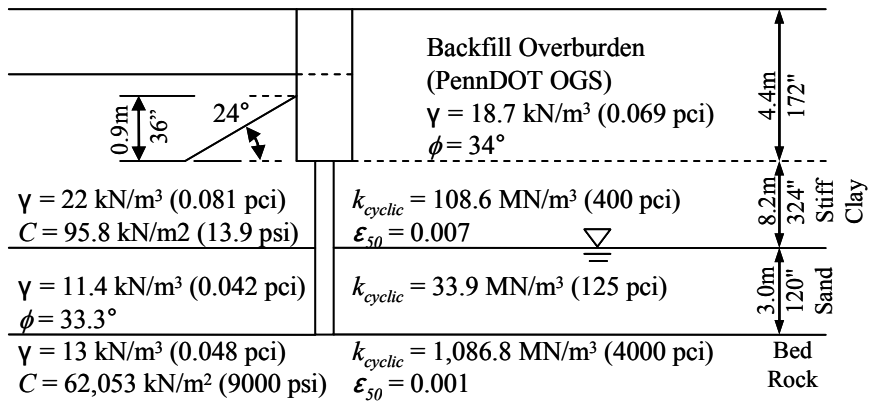


Figure 5.4: Bridge 211 Soil Properties under Abutment 1

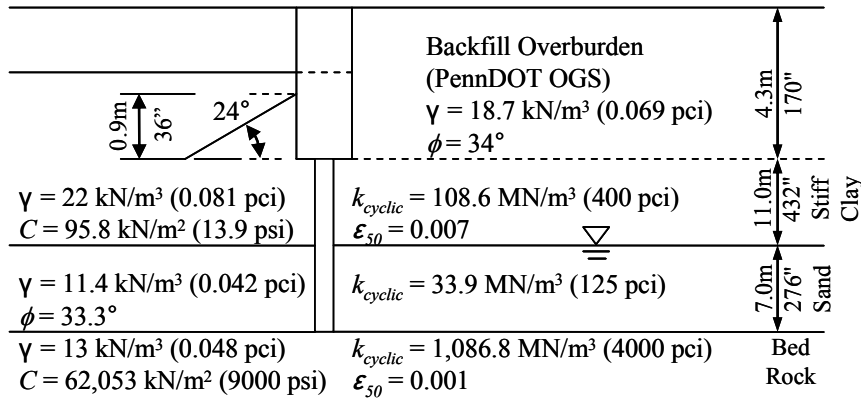


Figure 5.5: Bridge 211 Soil Properties under Abutment 2

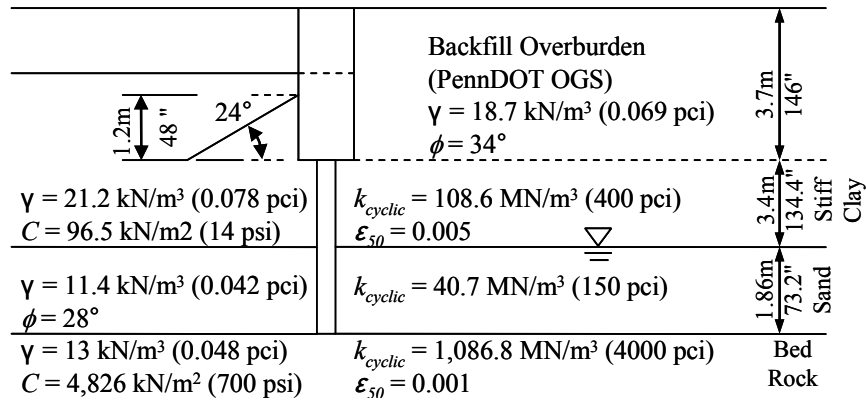


Figure 5.6: Bridge 222 Soil Properties under Abutment 1

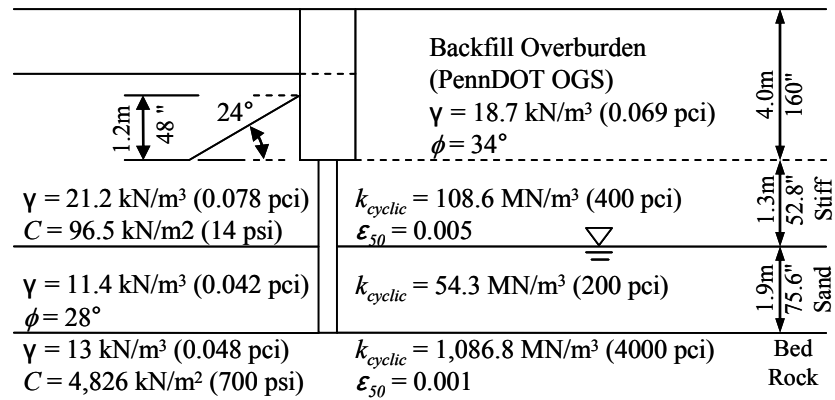


Figure 5.7. Bridge 222 Soil Properties under Abutment 2.

5.2.2 Abutment-backfill Interaction

The abutment backfill interacts with the abutment and backwall. As the abutment and backwall move away from the backfill (bridge contraction), active earth pressure develops. When the abutment and backwall move toward the backfill (bridge expansion), soil resistance gradually increases up to the passive earth pressure limit after large displacements. Figure 5.8 presents a typical earth pressure versus displacement relationship with respect to abutment and backwall.

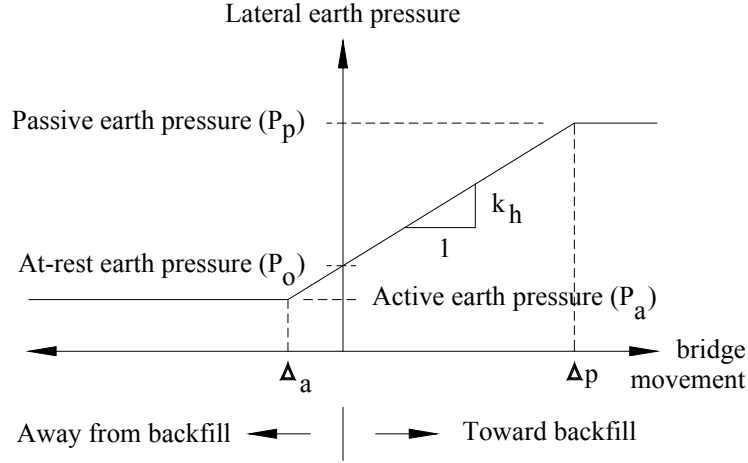


Figure 5.8. Qualitative Lateral Earth Pressure at the Abutment and Backwall.

The prediction accuracy of abutment backfill pressure relies primarily on the determination of the coefficient of the lateral subgrade reaction, k_h . In the present study, k_h is determined from the slope of lateral displacements versus pressures obtained from extensometer and pressure cell data. According to Boulanger *et al.* (1999), stiffness of granular soil, typically used as backfill, is generally proportional to the square root of confinement. Thus, the equation of k_h at any depth z is expressed as:

$$k_h(z) = k_{ref} \left(\frac{z}{h_{ref}} \right)^{0.5} \quad (5.1)$$

where:

h_{ref} = a reference depth measured from soil surface to the pressure cell elevation,

z = a depth of the interested elevation.

Figure 5.8 is used to define the Winkler spring model as required by the ANSYS COMBIN39 element. In addition, the backfill exhibits a hysteretic response as defined by the force-displacement of cyclic loading and unloading. To incorporate this hysteretic behavior in

the abutment backfill, classical plasticity theory is adopted with an assumption that the unloading branch slope is parallel to the initial loading slope. Therefore, the numerical model represents the unrecoverable backfill behavior observed in the monitoring program.

5.2.3 Soil-pile Interaction

Soil-pile interaction modeling requires an accurate depiction of the piles and the surrounding soil. In the case of an IAB, soil resistance developed under bridge expansion is not the same as that of bridge contraction due to the unsymmetrical soil geometry surrounding the abutment. Soil response developed under bridge contraction is the result of a small soil overburden and downhill slope on the bridge side of the abutment. Soil response developed under bridge expansion is the result of a high soil overburden on the approach side of the abutment. These unequal soil resistances are one of the fundamental sources of unequal structural response between bridge expansion and contraction.

A method based on p - y curves (Reese, 1984) is used for the soil-pile interaction modeling. This method was originally developed using finite difference techniques to solve an approximate solution of the 4th order governing equation (see Figure 5.9) based on the modulus of the subgrade reaction approach.

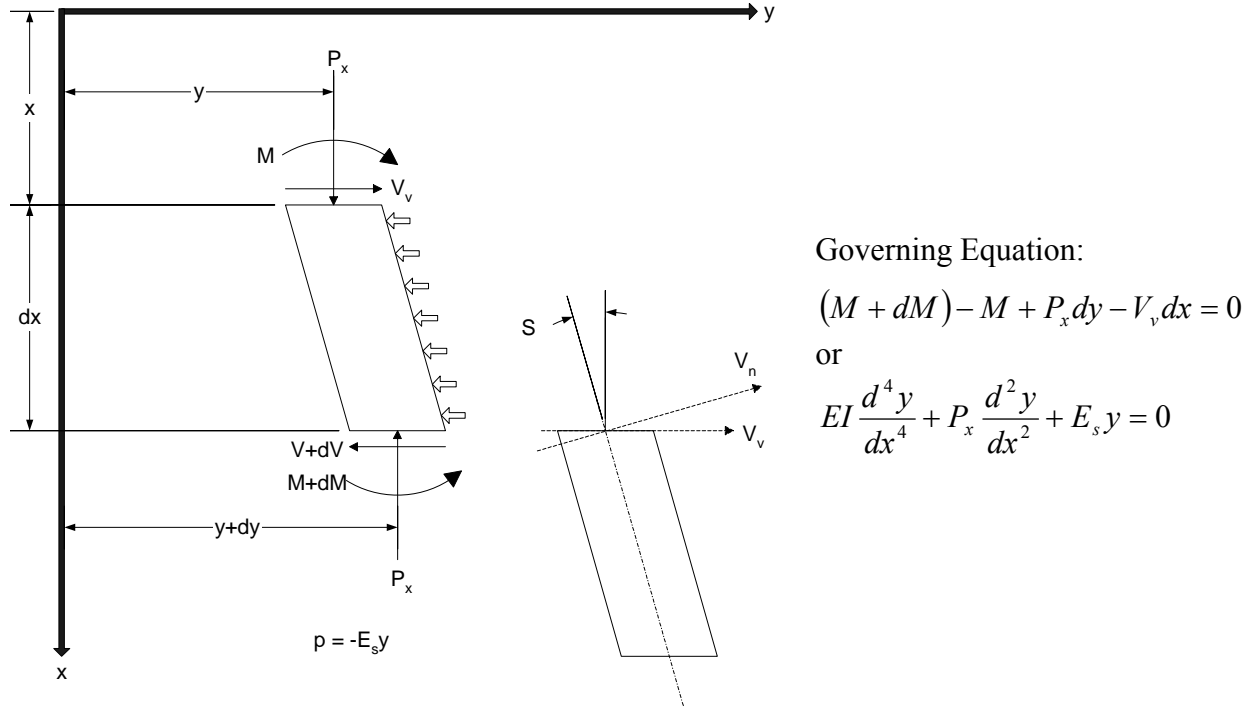


Figure 5.9. Straight Bar Under Axial and Transverse Loading.

The substitution of nonlinear p - y curve springs for the governing equation is performed herein rather than incorporating a traditional linear Winkler spring. The American Petroleum Institute (API) provides equations for p - y curves:

For granular soil:

$$p = Ap_u \tanh \left[\frac{k_i X}{Ap_u} y \right] \quad (5.2)$$

For clayey soil:

$$p = 0.5 p_u \left(\frac{y}{y_{50}} \right)^{1/4} \quad (5.3)$$

$$p_u = \min \left\{ p_{uf} = 9cD, \quad p_{uw} = \left(3 + \frac{\gamma'}{c} X + \frac{J}{D} X \right) cD \right\} \quad (5.4)$$

where:

p = lateral force (kip/in),

A = empirical factor accounting for static or cyclic loading,

X = a specific depth,

p_u = ultimate bearing capacity (kip/in), taken as the lesser of p_{uf} (flow around failure) and p_{uw} (wedge type failure),

k_i = initial modulus of subgrade reaction (kip/in³),

y = lateral deflection (in), y_{50} = deflection when $p = 0.5p_u$,

ϕ_f = internal friction angle,

γ' = effective soil weight,

c = unconfined cohesion at depth X ,

J = empirical parameter (0.5 for soft clay, and 0.25 for medium clay) and

D = effective pile diameter.

Using the equations 5.2, 5.3 and 5.4, p - y curve at each depth can be manually computed. In the present study, p - y curves are implemented with element COMBIN39. Validation of this approach was completed by comparison against the widely accepted COM624P to confirm its accuracy. Figures 5.10 and 5.11 present a sample of p - y curves (in dashed lines) generated from COM624P. Soil parameters are taken from the bridge 222 soil profile for clay above the water table and sand, respectively (see Figure 5.6). The multi-linear curves (in solid lines) represent a nonlinear soil spring in ANSYS.

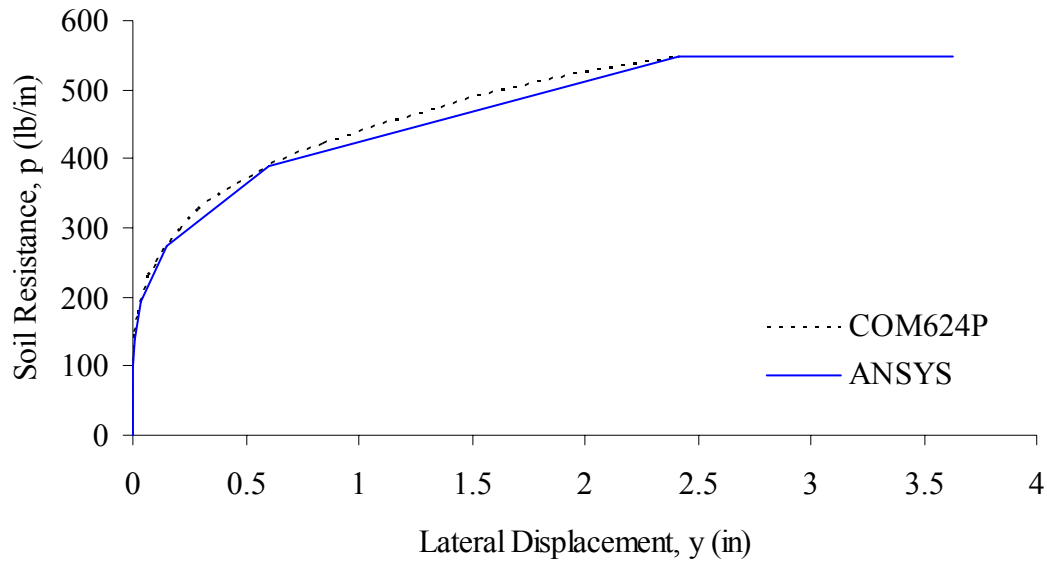


Figure 5.10. p - y Curve at Pile Head - Clay above Water Table.

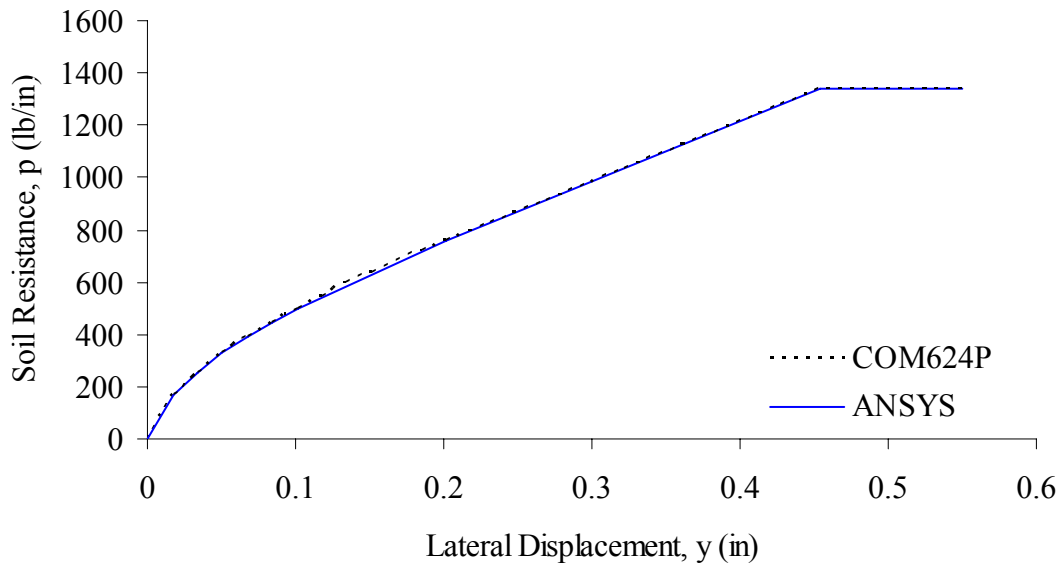


Figure 5.11. p - y Curve at 11.5 Ft below Pile Head – Sand.

An analysis test case was evaluated using the pile geometry and soil profile of bridge 222. A lateral force of 5 kips that produces a working displacement range of the actual structure and a free end boundary condition were applied at the pile head. COM624P and ANSYS comparisons of lateral displacements versus depth, bending moments versus depth, and shear forces versus depth are presented in Figures 5.12 through 5.14.

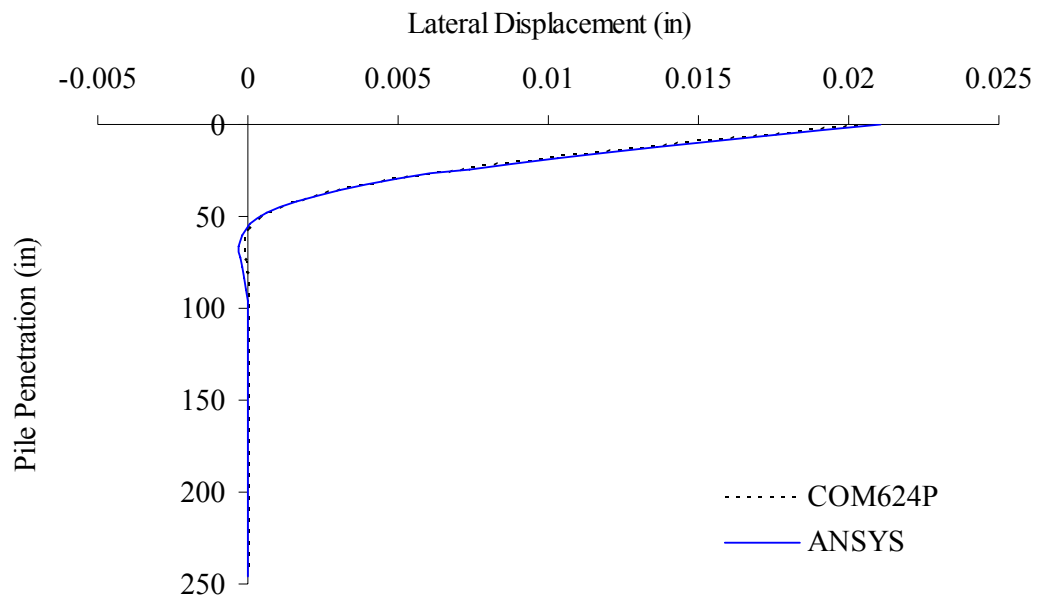


Figure 5.12. Lateral Displacement Due to 5-kip Load at Pile Head.

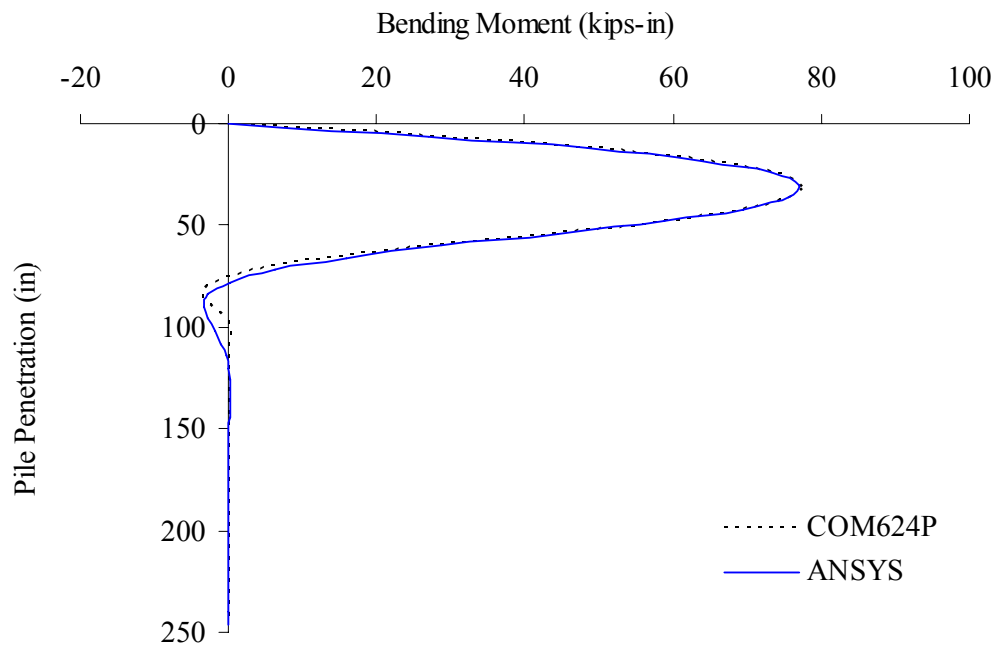


Figure 5.13. Pile Bending Moment Due to 5 kip Load at Pile Head.

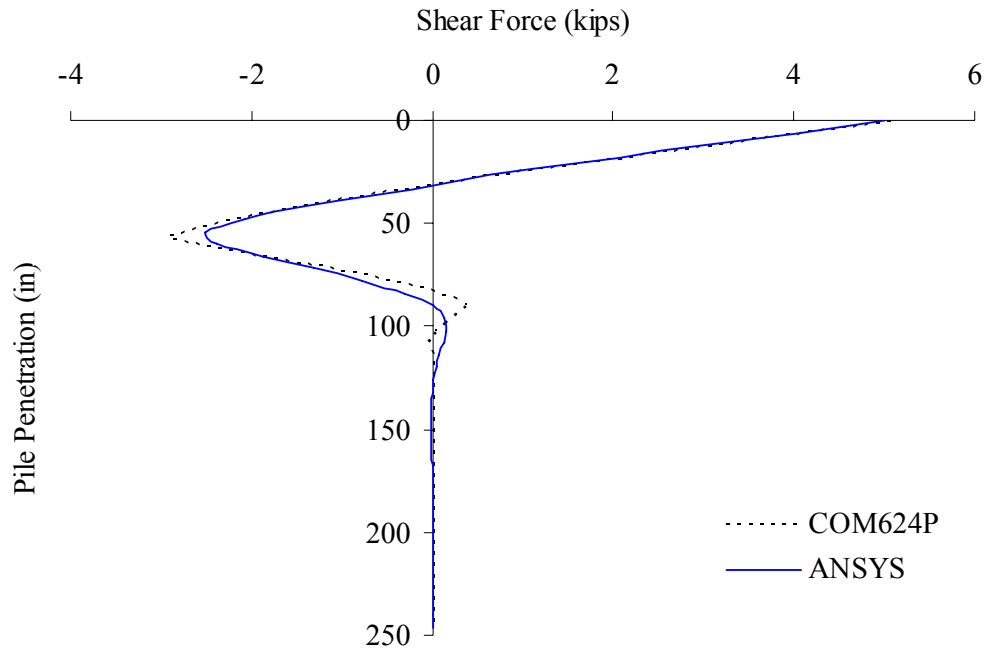


Figure 5.14. Pile Shear Force Due to 5 kip Load at Pile Head.

The maximum difference between ANSYS and COM624P predictions is 3.9 percent for maximum lateral displacement at the pile head, 0.1 percent for maximum bending moment at approximately 4 ft below the pile head, and 1.5 percent for maximum shear (at the pile head). Element length in the ANSYS model is relatively coarse (12-inch grid) compared to the length used in COM624P (1.2 inches). Therefore, differences in moments and shears at a depth of approximately 10 ft are expected to appear where a short distance of two adjacent inflection points occurs.

The unrecoverable characteristics of soil must also be considered when soil is subjected to cyclic loading. Modifications to the original p - y curves (Reese, 1984; and Wang and Reese, 1993) were proposed by several researchers (e.g., Boulanger, 1999; Lin. and Liao, 1999; and Taciroglu *et al.*, 2003). Among the proposed models, an elasto-plastic p - y curve proposed by Taciroglu *et al.* (2003) has proven to be numerically robust and is adopted herein. ANSYS COMBIN39 is capable of incorporating the elasto-plastic behavior by generating an unloading

branch using classical plasticity theory as implemented in the abutment-backfill interaction model. A qualitative diagram of the elasto-plastic p - y curve is presented in Figure 5.15.

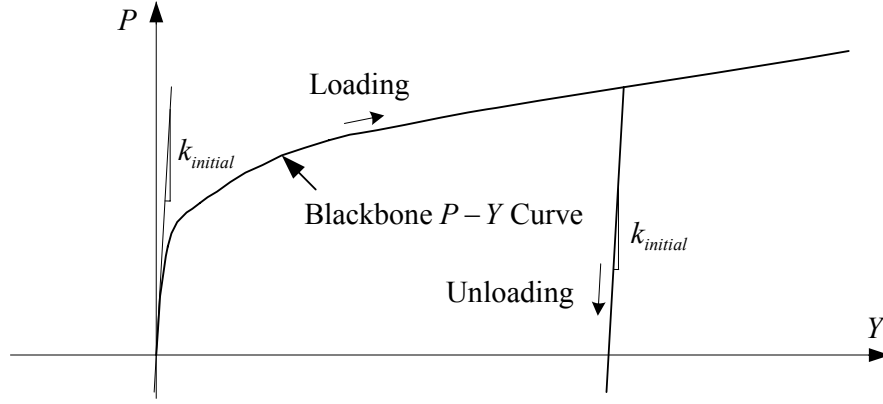


Figure 5.15. Qualitative Diagram of Elasto-Plastic p - y Curve.

For a group of piles in a 2D analysis, an efficiency factor, η may be considered:

$$P_{Group} = \eta n_p p = \left[1 - \frac{\alpha}{90^\circ} \left(\frac{(n-1)m + (m-1)n}{mn} \right) \right] n_p p \quad (5.5)$$

where:

P_{Group} = group pile lateral force,

n_p = number of piles, $\alpha = \tan^{-1}(D/S)$,

D = effective pile diameter,

S = pile spacing,

m = number of pile rows (generally, $m = 1$), and

n = number of pile columns.

However, field data comparison revealed that a $\eta = 1.0$ is valid for 2D analysis of integral abutment bridges.

5.2.4 Abutment-Backwall Construction Joint

The construction joint at the abutment and backwall is a common detail found in IAB construction. Steel reinforcement bar details of this joint vary from state to state (see Table 5.2).

Table 5.2. Construction Joint Reinforcing Details.

State Agency	U-shape Rebar (Concrete Girder)	Anchor Rod (Steel Girder)	Remarks
IL	(#5 at 12")	N/A	
PA	(#5 at 9")	(#5 at 9")	use the same rebar details for concrete and steel girder
MA	(#5 at 6")	($\phi 1\frac{1}{2}$ ")	up to 100' span, otherwise design
NJ	(#5 at 12")	use but not specified	
NY	(#5 at 12")	use but not specified	
VA	N/A	($\phi \frac{7}{8}$ " at 12")	Sometimes shear key is used

The PennDOT standard IA joint detail specifies a U-shape #5 bar at 9 inches (PennDOT Standard BD-667). This joint reinforcement is much less than the reinforcement provided in the abutment and permits significant rotation between the superstructure and abutment. Although many previously completed studies assume that the abutment-backwall joint behaves rigidly, the cold joint condition and low reinforcing results in differential rotation as observed in field monitoring (Laman *et al.* 2003, 2006). Investigating the PennDOT standard abutment-to-backwall joint detail, Paul *et al.* (2005) demonstrated that strength and joint stiffness determined from moment-curvature relationships is much lower than those calculated for abutments. Paul also proposed an elasto-plastic model for this abutment-to-backwall joint.

In order to evaluate abutment-backwall construction joint and abutment stiffness, moment curvature relationships for four monitored bridges were developed as presented in Figure 5.16. Strain compatibility and Whitney's equivalent stress block are used to compute all ultimate moment capacities. Because of restraint by girders, the reinforced area at the construction joint is different between near the face toward the bridge (the front face) and near the face toward backfill (the rear face). Figure 5.17 illustrates construction joint behavior with respect to superstructure expansion and contraction.

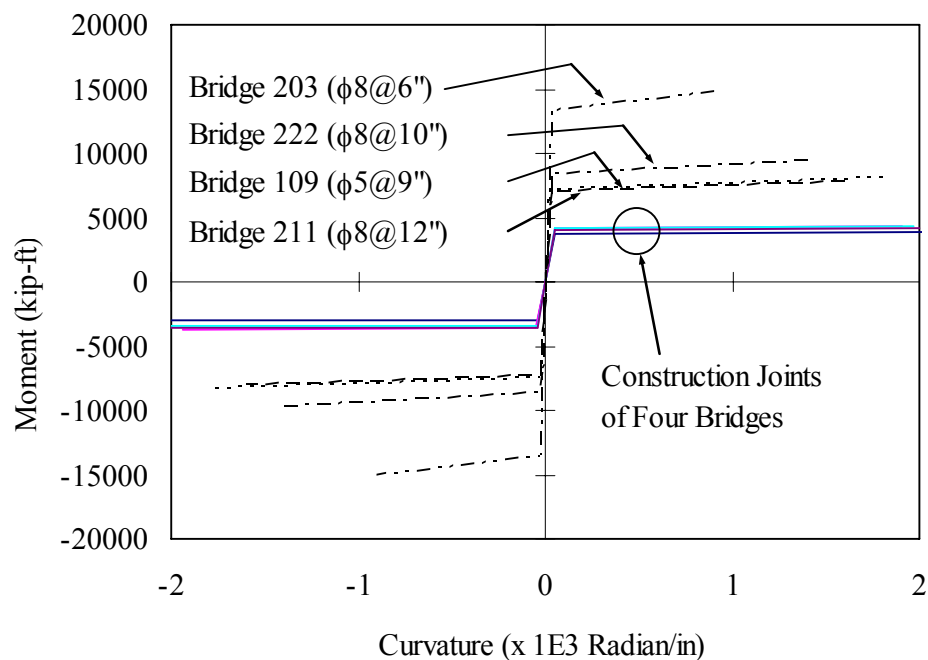


Figure 5.17. Moment-Curvatures of Construction Joints and Abutment Members.

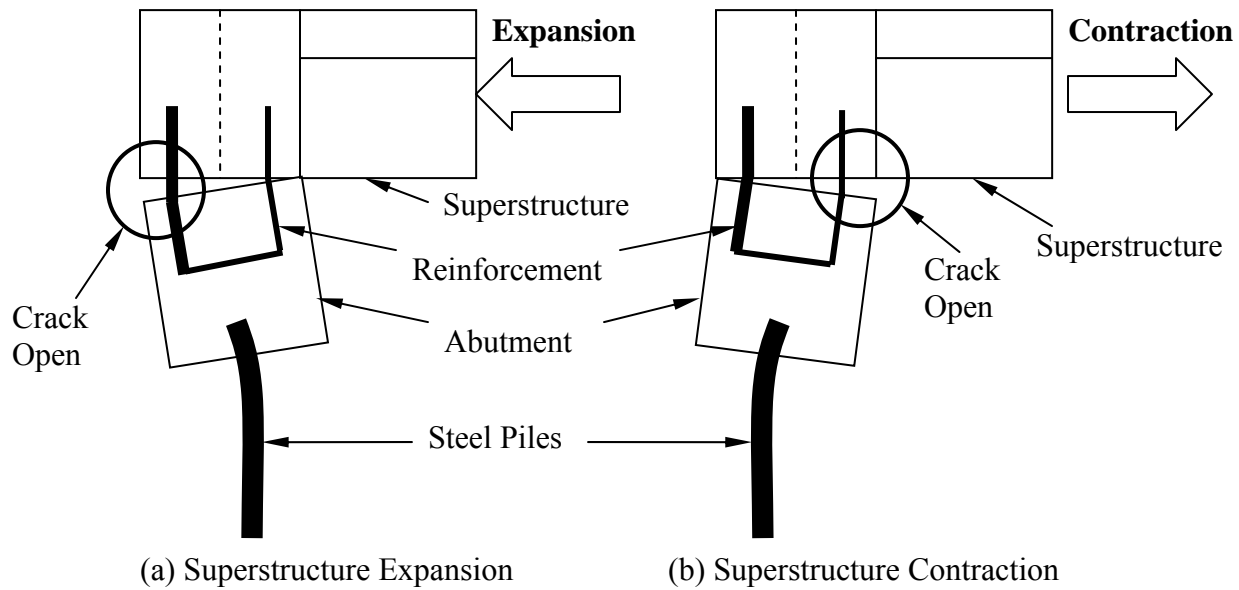


Figure 5.16. Construction Joint Reinforcement and Behavior.

The rotational strength and stiffness (by means of initial slopes) of the expansion case are greater than the contraction by about 20 percent. Additionally, abutment rotational stiffness is 16 to 20 times that of the joint.

To convert joint moment-curvature to moment-rotation for element stiffness properties in the numerical model, Equation 4.7, based small deformation and constant moment over a joint length L , will be used (NCHRP Recommended Provisions, 2000; and Paul, 2003):

$$\theta = \int_0^L \frac{M}{EI} dx = \frac{M}{EI} L = \phi L \quad (5.6)$$

According to Paul (2003), a joint length L is associated with a development length of an epoxy-coated reinforcement, which is equal to 16 inches based on AASHTO LRFD (2007). By assuming a linear variation over the development length and fully mobilized tension on reinforcement at one end and zero at the other end, half of this length, i.e., $L = 8$ inches, has been assumed in the present study.

5.3 Loading

This study considered four loads on IABs: (1) backfill pressure, (2) time-dependent effect, (3) superstructure temperature change, and (4) temperature gradient in superstructure. Dead loads are not considered in the numerical model because the analysis starts after the abutment/backwall connection has cured. In addition, the stress due to the secondary load effect of dead load is negligible compared to the bridge member capacity. The abutment displacement is very small, so the secondary load effect is insignificant compared to the pile moment capacity. Therefore, backfill pressure on abutment and backwall, time-dependent effects, temperature change, and temperature gradient loads in the superstructure have been considered in the numerical model.

5.3.1 Backfill Pressure

Pressure behind the abutment was considered in the numerical model as a triangular distribution along the abutment depth with a unit weight of 18.7 kN/m^3 (119 pcf). Backfilling generally begins after curing of the abutment and backwall so that the superstructure, backwall, and abutment behave integrally. Initially applied backfill pressure is based on at-rest lateral earth pressure coefficient of $K_o = 1.0$, assumed compacted condition by Barker *et al.* (1991). During the simulation, the lateral earth pressure varies between active and passive pressure as presented in Figure 5.8. The backfill pressure was simultaneously applied to the bridge with time-dependent loads and temperature loads. Each backfill pressure in at-rest, active and passive state are computed as:

$$P_o = K_o \gamma' z w = (1) \gamma' z w \quad (5.7)$$

$$P_a = K_a \gamma' z w = \frac{1 - \sin \phi_f}{1 + \sin \phi_f} \gamma' z w$$

$$P_p = K_p \gamma' z w = \frac{1 + \sin \phi_f}{1 - \sin \phi_f} \gamma' z w$$

where:

K_o is the lateral earth pressure coefficient for at-rest,

K_a is the lateral earth pressure coefficient for active,

K_p is the lateral earth pressure coefficient for passive,

γ' is the effective soil weight,

ϕ_f is the internal friction angle,

z is the depth of soil, and

w is the effective backfill width.

5.3.2 Time-dependent Effects

Time-dependent effects in IAB analysis are the result of a combination of creep, shrinkage, and steel relaxation found in all prestressed concrete structures. These effects cause short- and long-term length instability of a superstructure component, producing secondary effects and displacements at the abutments and piles. Therefore, time-dependent effects must be included in numerical models for accurate movement predictions.

ACI 209 (2004) recommendations were used to predict creep and shrinkage of prestressed elements. In order to incorporate time-dependent effects into numerical models, age-adjusted elastic modulus (AAEM), based on a time-varying concrete modulus, was used because it is capable of solving all common time-dependent effect problems (Neville *et al.*, 1983; Jirásek and Bažant, 2001). Creep and aging coefficients taken from ACI 209 (2004) are used as a key

parameter to obtain such time-varying concrete modulus. In addition, time-dependent strains can be determined using the AAEM method and are consequently imposed on the superstructure component by means of an equivalent temperature loading. An equation of intrinsic relaxation in prestressing steel recommended by AASHTO LRFD (2007) has also been incorporated into the numerical models.

5.3.2.1 Concrete Creep

Creep is a well-known phenomenon in concrete members, normally separated into two components: basic creep and drying creep. Basic creep occurs in a condition where moisture is constantly controlled. An uncontrolled condition leads to a drying creep that allows moisture in concrete to diffuse to the environment.

Most specifications, including ACI 209, use a dimensionless term referred to as the creep coefficient, $\varphi(t, t_o)$, to characterize creep (basic and drying creeps). The creep coefficient is defined as the ratio of load duration, $t - t_o$, to the initial elastic strain at time t_o . Therefore, the total strain can be expressed as (Jirásek and Bažant, 2001):

$$\varepsilon(t) = \frac{\sigma(t_o)}{E(t_o)} [1 + \varphi(t, t_o)] \quad (5.8)$$

where:

$\varepsilon(t)$ = a total strain at time t

$\sigma(t_o)$ = an initial stress at time t_o

$E(t_o)$ = a concrete modulus of elasticity at time t_o

$\varphi(t, t_o)$ = a creep coefficient at time t corresponding to the age at loading t_o

Figure 5.18 presents a sample creep coefficient curve based on bridge 222 girder properties.

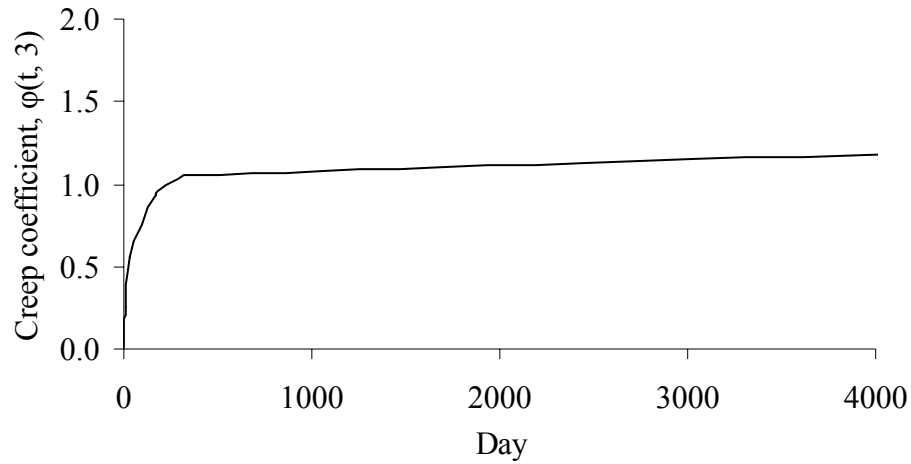


Figure 5.18. Creep Coefficient.

Another important issue related to creep is the effect of varying stress on creep behavior. AAEM incorporates this effect by using a simplified aging coefficient, $\chi(t, t_o)$. ACI 209 (2004) includes a provision for computing this coefficient in a table format. Figure 5.19 presents a sample of the aging coefficient based on bridge 222 girder properties. The procedure used to incorporate creep and aging coefficients into numerical models are discussed later in this chapter.

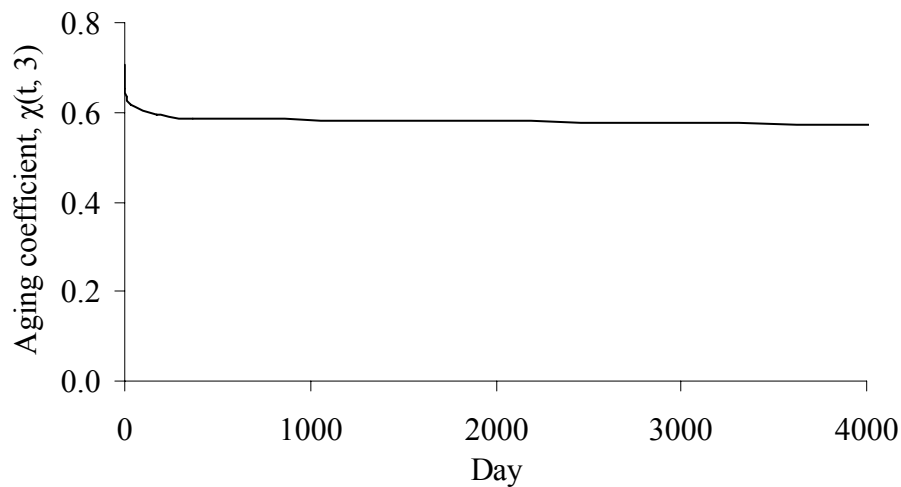


Figure 5.19. ACI 209 Aging Coefficient for Bridge 222.

5.3.2.2 Concrete Shrinkage

Total shrinkage in concrete members is composed of four types: carbonation shrinkage, plastic shrinkage, autogenous shrinkage, and drying shrinkage. A detailed discussion of each shrinkage type is presented in Jirásek and Bažant (2001). Figure 5.20 presents shrinkage strain based on ACI 209 (2004) and bridge 222 girder properties.

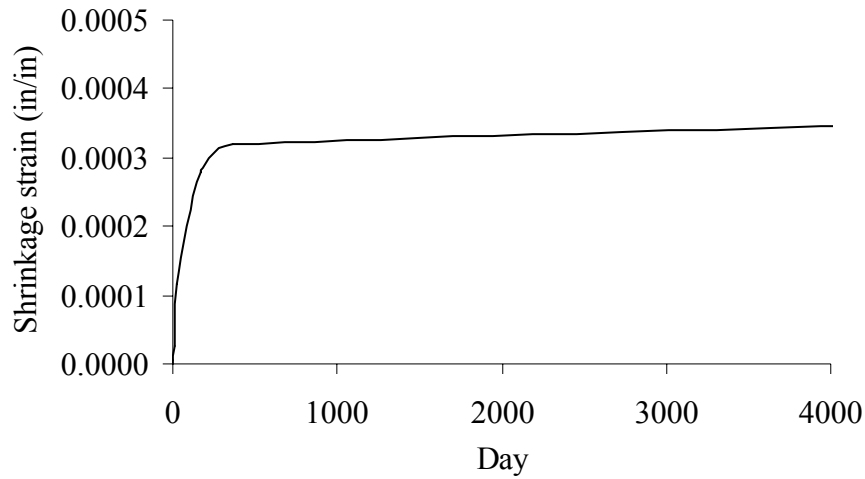


Figure 5.20. ACI 209 Shrinkage Strains for Bridge 222.

5.3.2.3 Relaxation of Prestressing Steel

Compared to creep and shrinkage, relaxation of prestressing steel is more readily predicted with accuracy. An equation of intrinsic relaxation in AASHTO LRFD (2007) for low-relaxation strand is expressed as:

$$\Delta f_{RE} = \frac{[\log(24t) - \log(24t_o)]}{40} \left[\frac{f_{pj}}{f_{py}} - 0.55 \right] f_{pj} \quad (5.9)$$

where:

t = time at the end of the time interval in days,

t_o = time at the beginning of the time interval in days,

f_{pj} = stress in the prestressing steel at jacking in ksi,

f_{py} = a specified yield strength of prestressing steel in ksi.

Intrinsic relaxation occurs under a condition where constant strain is imposed to the strand. For a prestressed concrete member immediately after transfer, the condition of constant strain no longer holds due to the effects of elastic shortening, creep, and shrinkage. As a result, a reduction of the intrinsic relaxation must be made and can be simplified by applying a dimensionless coefficient of reduced relaxation, χ_r . The reduced relaxation Δf_R is given as:

$$\Delta f_R = \chi_r \Delta f_{RE} \quad (5.10)$$

An equation approximating χ_r , taken from Ghali et al (2002), is expressed as:

$$\chi_r = \exp[(-6.7 + 5.3\lambda)\Omega] \quad (5.11)$$

where:

$$\lambda = \frac{\text{steel stress immediately after transfer}}{\text{characteristic tensile stress}},$$
$$\Omega = \frac{\text{total prestress change - intrinsic relaxation}}{\text{steel stress immediately after transfer}}.$$

It can be observed that the total prestress change is required for the calculation of χ_r ; however, this is not normally known in advance. Thus, it is imperative that an iterative procedure be employed in determining the coefficient of reduced relaxation.

5.3.2.4 Age-Adjusted Effective Modulus (AAEM) Method

There are several analysis methods for time-dependent effects, including effective modulus method, rate of creep method, rate of flow method, improved Dischinger method, and AAEM

method (Neville *et al.*, 1983). Among these methods, the AAEM method is the most widely accepted because it is capable of solving all common time-dependent problems with excellent agreement with more sophisticated step-by-step solutions (Neville *et al.*, 1983; Jirásek and Bažant, 2001).

The derivative of aging coefficient, χ , and the basic equation of AAEM is taken from Jirásek and Bažant (2001). The basic AAEM equation is:

$$\varepsilon(t) = \frac{\sigma(t_o)}{E(t_o)} [1 + \varphi(t, t_o)] + \frac{(\sigma(t) - \sigma(t_o))}{\bar{E}(t, t_o)} + \varepsilon_{sh}(t, t_{sh,o}) \quad (5.12)$$

with notation consistent with Equation 1.1:

$\bar{E}(t, t_o)$ is the age-adjusted effective modulus of concrete,

$\sigma(t)$ is total applied stress at time t ,

χ is an aging coefficient at time t corresponding to the age at loading t_o , and

$\varepsilon_{sh}(t, t_{sh,o})$ is a total shrinkage strain at time t .

A more detailed discussion of the AAEM method is available in Ghali et al (2002).

The time-dependent strains at the top and bottom girder fibers for bridge 222 are presented in Figures 5.21 and 5.22, respectively. Three graphs corresponding to 174 (6 months), 365 (1 year), and 36,500 (100 years) days after the concrete deck was poured are presented. For reference, the concrete bridge deck was placed at the 171st day.

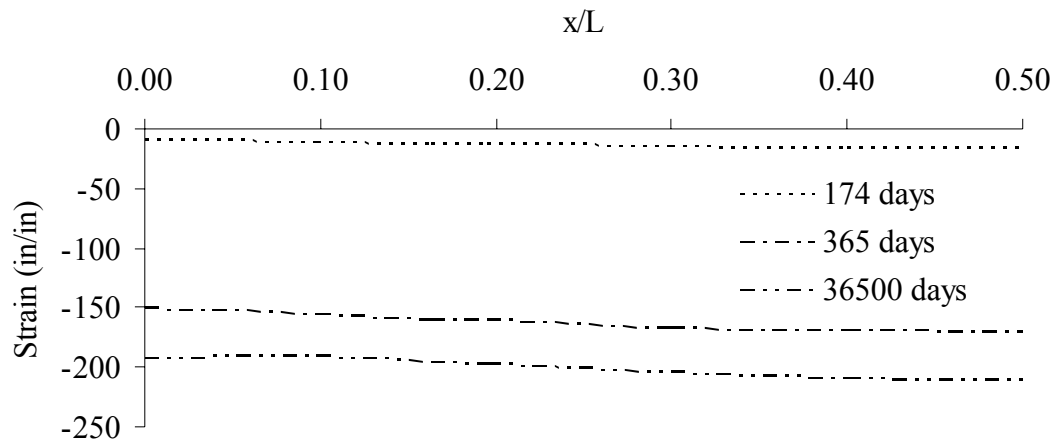


Figure 5.21. Strain at Top Fiber of Bridge 222 Girder.

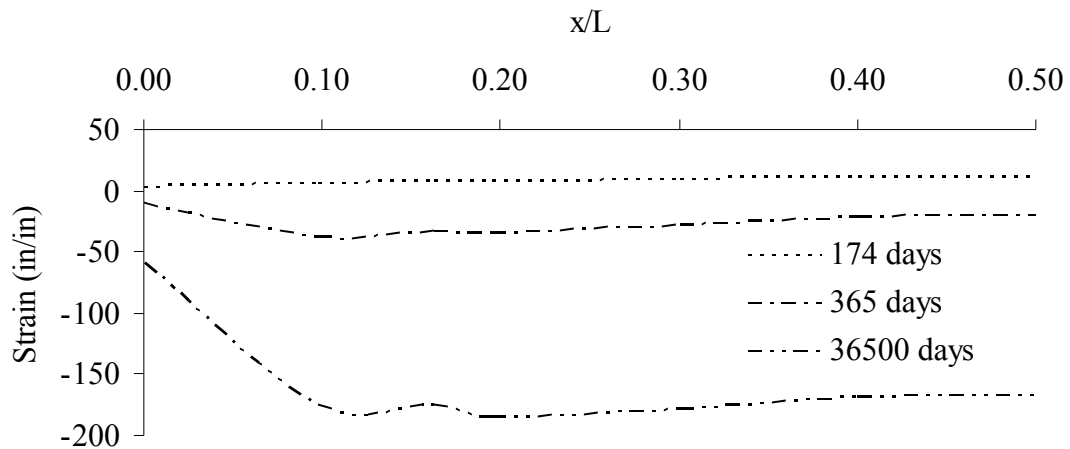


Figure 5.22. Strain at Bottom Fiber of Bridge 222 Girder.

An unrestrained longitudinal boundary condition was assumed in analyzing the time-dependent strains presented above. In order to account for effects of force redistribution due to structural continuity and support restraint to longitudinal movement, an analysis of time-dependent effect for statically indeterminate structures is investigated.

5.3.2.5 Time-Dependent Effects in Indeterminate Structures

Superstructure end restraint conditions prevent free contraction due to time-dependent effects. Longitudinal restraint causes time-dependent strains to develop in the girders. The force or displacement method is usually employed to solve this type of structural problem and is used here. The AAEM method replaces a typical elastic modulus in the stiffness matrix by a time-dependent age-adjusted effective modulus $\bar{E}(t, t_o)$. In order to determine the force vector, an additional procedure is required. Time-dependent strains are converted to an equivalent temperature loading for constructing the force vector.

5.3.3 Temperature Load

Superstructure thermal loading is one of the most significant influences affecting bridge behavior. The primary component of structure thermal loading in areas with weather such as is experienced in Pennsylvania is ambient air temperature. To demonstrate this effect, ambient temperature is compared to instrument temperatures embedded in the bridge. Girder temperature at eight instrument locations on bridge 222 girders (each channel number refers to Figure 3.14) is presented in Figure 5.23. Bridge 109 deck temperature measured by 13 instruments inside the concrete deck is presented in Figure 5.24. The black, heavy line represents ambient temperature, and all instrument temperatures are represented by light gray lines. It can be observed that all instrument temperatures (or structure temperatures) closely track the ambient temperature.

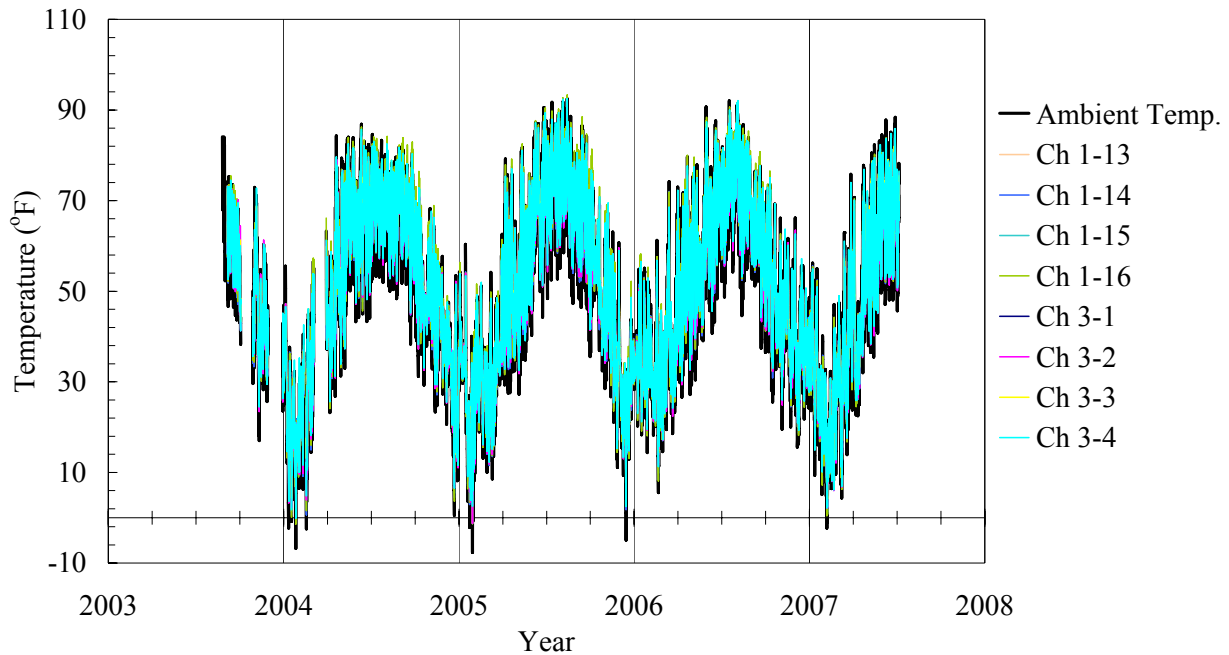


Figure 5.23. Ambient Temperature Versus Girder Temperature (Bridge 222).

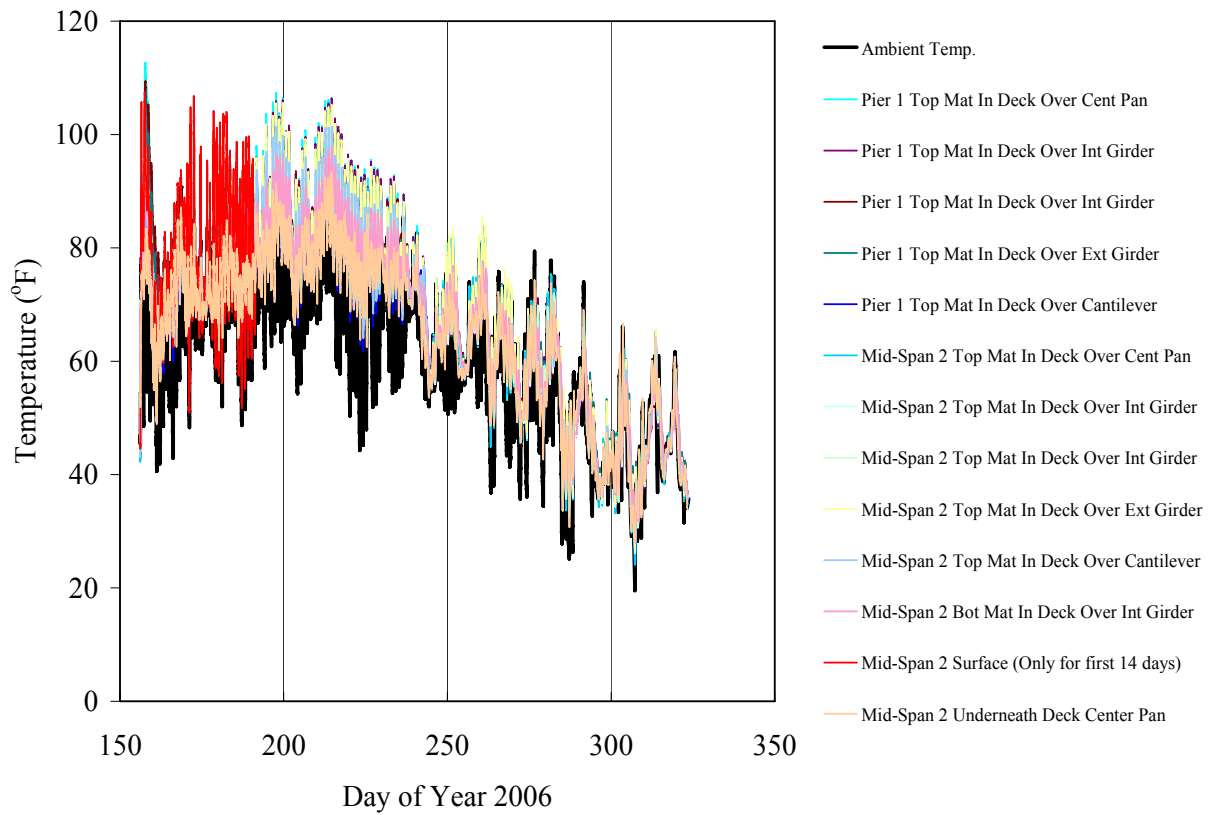


Figure 5.24. Ambient Temperature Versus Deck Slab Concrete Temperature (Bridge 109).

Ambient temperature was collected from a nearby weather station and was applied in the numerical model. Ambient temperature data were collected from September 2002 and are presented in Figure 5.25. The temperature loads specified in AASHTO LRFD are considered conservative for steel and unconservative for concrete members and can be used only for one-way action of expansion or contraction. However, applying actual ambient temperature is not practical because too many loading steps in the analysis (4 temperature loads per day \times 365 days = 1460 loading steps for one year) are required. In addition, structure temperature tends to follow a 7-day running average ambient temperature because of the thermal mass. Hence, the 7-day mean temperature, the thick gray line in Figure 5.25, is used as the basis for the nominal superstructure temperature load model. To represent temperature loading mathematically, temperature loading was assumed as a sinusoidal variation over a year and is represented as:

$$T(t) = T_m + A \sin(\omega t + \phi) \quad (5.12)$$

where:

T_m = mean temperature,

A = amplitude of temperature fluctuation,

ω = frequency,

t = analysis time (year),

ϕ = phase lag (radian).

The mathematical prediction is presented as the thick black line in Figure 5.25, with the numerical temperature model for the four field monitored bridges presented in Table 5.3.

5.3.4 Temperature Gradient

The numerical model included a superstructure temperature gradient that exerts significant stresses. A concrete deck and/or girder has relatively low thermal conductivity; therefore, the

distribution of temperature along the girder depth is nonlinear. Because the AASHTO LRFD (2007) multi-linear temperature gradient cannot be modeled without significant complications, an equivalent temperature gradient was developed based on the axial and bending strains obtained from the AASHTO gradient profile. The thermal stress induced by temperature gradient

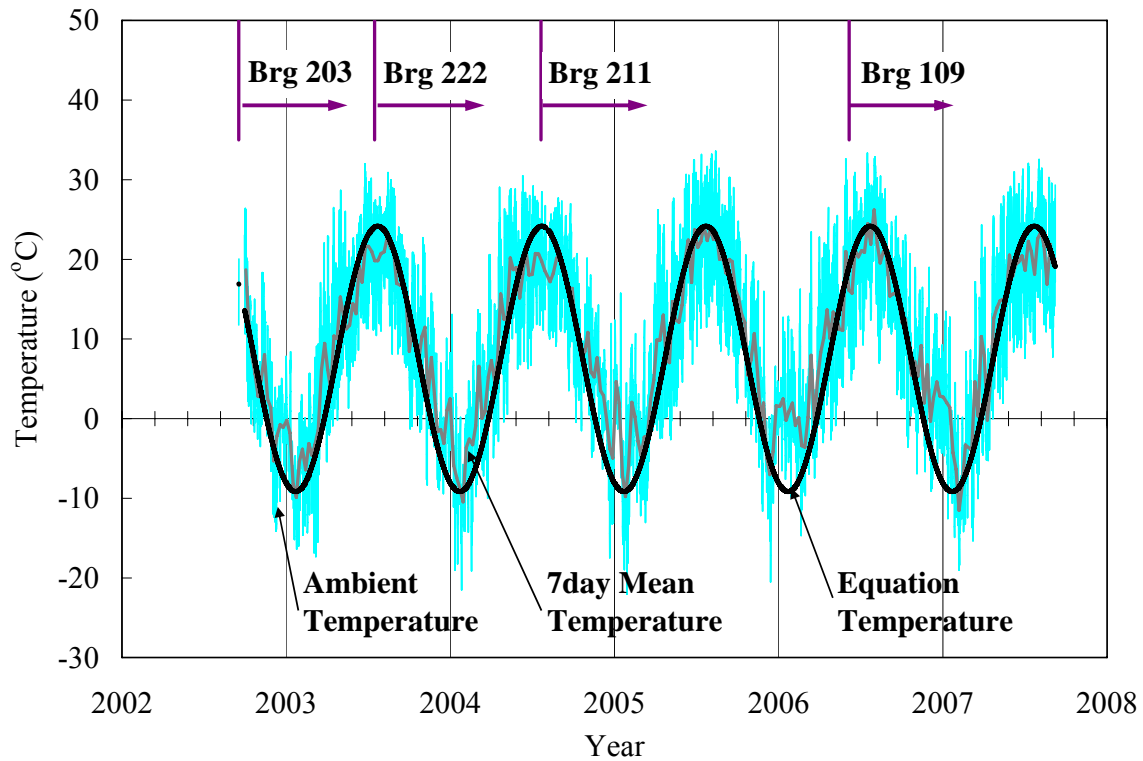


Figure 5.25. Temperature Model Based on 7-Day Average Ambient.

Table 5.3. Coefficients of the Mathematical Temperature Model.

Bridge	Mean Temperature (T_m) °C (F°)	Amplitude (A) °C (F°)	Phase lag (radian) (ϕ)
109	7.5 (45.5)	16.7 (30)	0.751
203	7.5 (45.5)	16.7 (30)	2.54
211	7.5 (45.5)	16.7 (30)	1.53
222	7.5 (45.5)	16.7 (30)	1.45

along depth can be represented as:

$$\sigma_t(y) = E \cdot \alpha \cdot T(y) \quad (5.14)$$

where:

$\sigma_t(y)$ = longitudinal thermal stress at a fiber located a distance y ,

E = elastic modulus,

α = thermal expansion coefficient,

$T(y)$ = temperature at a depth y .

Thus, the axial force (P_t) and moment (M_t) due to thermal stress is respectively:

$$\begin{aligned} P_t &= \int E \alpha T(y) b(y) dY \\ M_t &= \int E \alpha T(y) b(y) Y dY \end{aligned} \quad (5.15)$$

The solid line in Figure 5.26 illustrates the calculated equivalent temperature gradient for bridge 211 that produces the same axial force and bending moment as the AASHTO gradient load. This equivalent temperature gradient is applied throughout the superstructure. In the numerical implementation, Figure 5.27 presents the applied temperature gradient at each top and bottom section during 1 year.

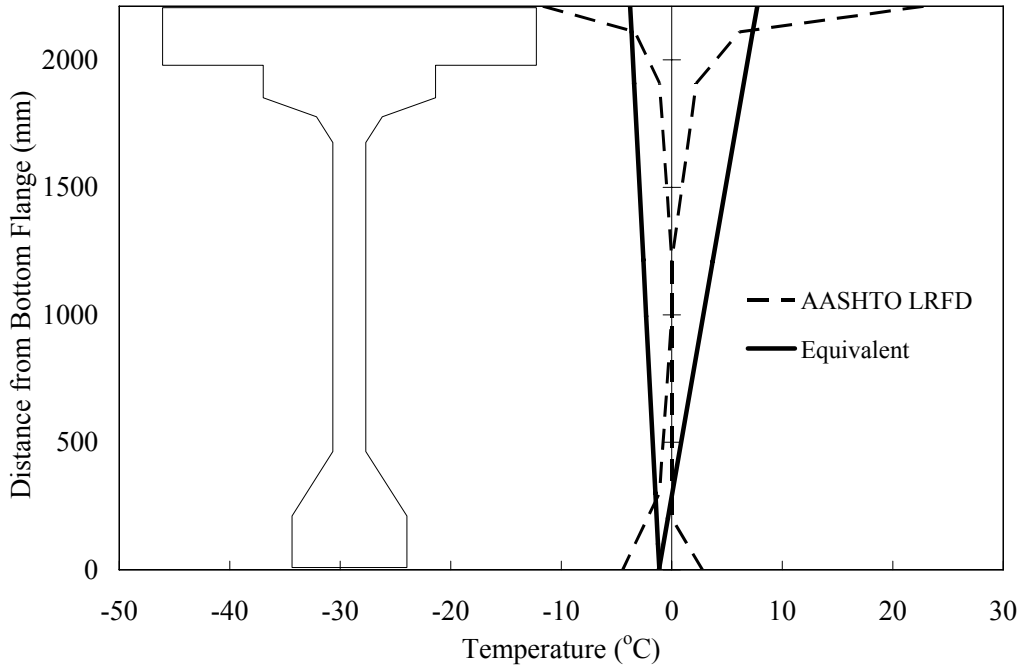


Figure 5.26. Temperature Gradient of Cross-Section.

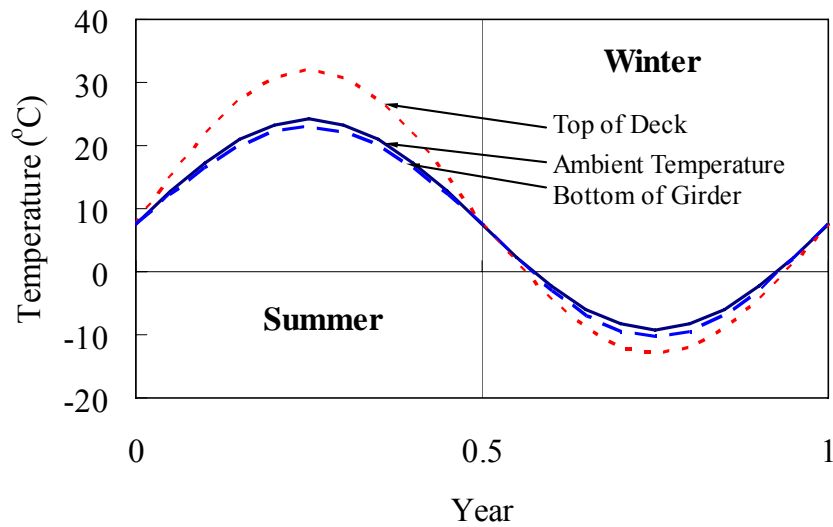


Figure 5.27. Temperature Variation with Temperature Gradient.

5.4 IAB Model Description

5.4.1 Bridge 109 Numerical Model

Numerical models were assembled using the elements described above. Prestressed concrete girders, deck, intermediate diaphragms, backwalls, and abutments were modeled using

SHELL63 elements, and piles were modeled with BEAM4 elements. Each Winkler spring representing soil at the abutment and pile utilized COMBIN39 elements. The horizontal construction joint between the backwall and the abutment was included in the model using COMBIN39. A view of the completed bridge 109 numerical model is presented in Figure 5.28.

To limit the numerical model size for bridge 109, the middle two spans employed a larger element aspect ratio. Spans 2 and 3 element aspect ratios are approximately 13:1 for deck and girder elements. A larger aspect ratio may affect analysis results; however, the aspect ratio used did not produce significant differences in results when compared to more densely meshed models for the same bridge.

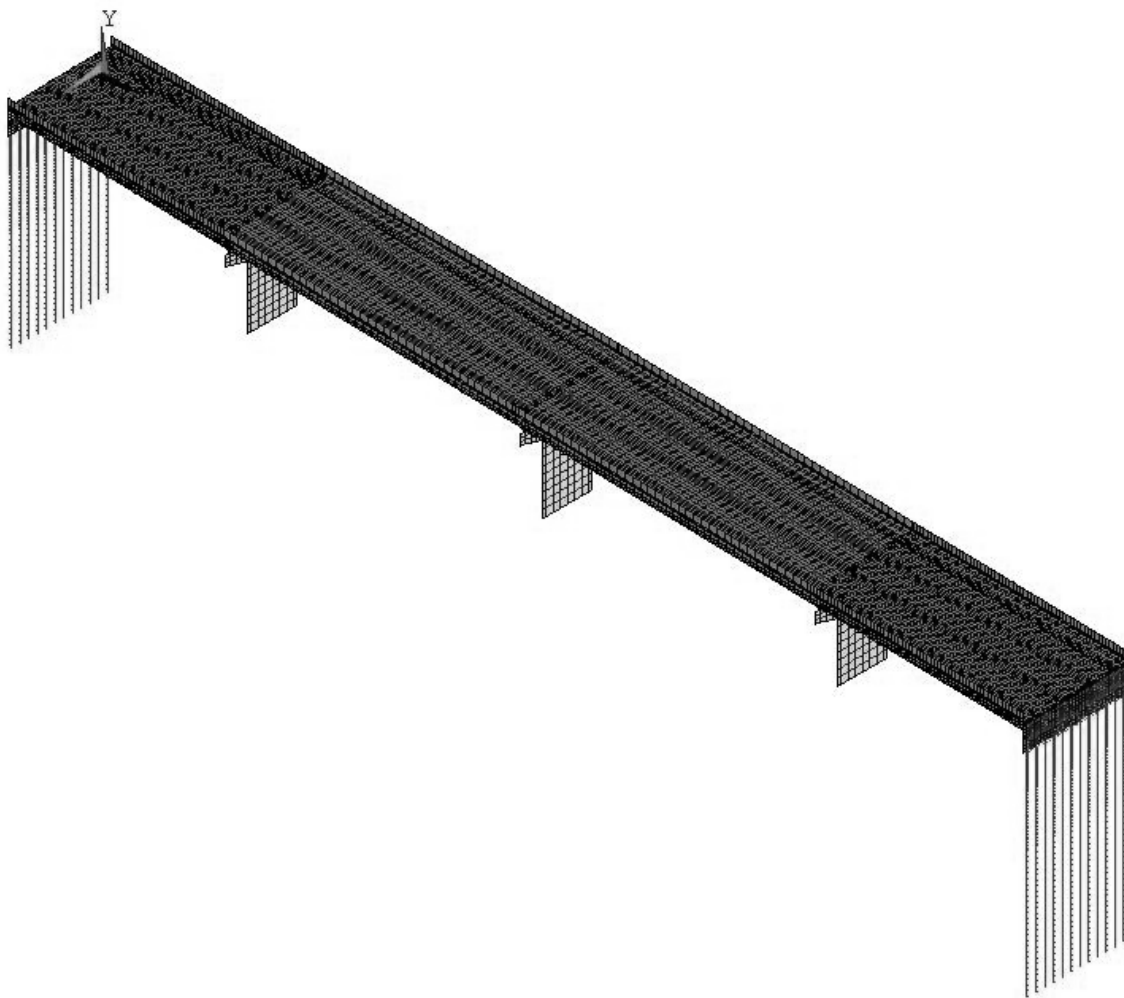


Figure 5.28. Completed Structure 109 Numerical Model.

The numerical modeling of piles closely matches actual constructed conditions. Piles are rigidly attached to the abutment with a pin restraint at the pile tip. Soil-pile interaction is modeled using COMBIN39 based on active and passive soil pressure theory and traditional p-y relationships. The pile mesh for beam elements is 6 inches at the top soil layer and 12 inches below to the tip.

Piers are modeled with SHELL63 elements with rotation and translation fixed at the base as shown in Figure 5.29. Elastomeric pier bearings are modeled as 3-inch beam elements assigned a shear modulus of elasticity consistent with the low-bearing shear stiffness. The axial modulus was increased to an effective compressive modulus of elasticity (E_c) to include the effect of embedded steel shims, computed using Equation 5.2 (AASHTO):

$$E_c = 6GS^2 \quad (5.16)$$

A modification for converting bearing area and stiffness to a function of E_c in the numerical analysis was included:

$$A_e = A_{bearing} \frac{E_c}{E} \quad (5.17)$$

$$I_e = \frac{GA_{bearing}H^2}{12E} \quad (5.18)$$

where:

A_e = equivalent area,

$A_{bearing}$ = actual area of bearing pad,

E = elastic modulus of bearing pad,

G = shear modulus of bearing pad,

H = thickness of bearing pad.

Elastomeric bearing pad properties for Structure 109, including equivalent area and elastic modulus, are presented in Table 5.4.

Table 5.4. Bridge 109 Elastomeric Bearing Properties.

Component	Elastic Modulus (ksi)	Poisson's Ratio	Area (in ²)	Inertia (in ⁴)
Bearing at abutment 1 and 2 (Typ.)	0.39	0.4985	28,046	57.1
Bearing at piers (Typ.)	0.39	0.4985	42,108	70.4

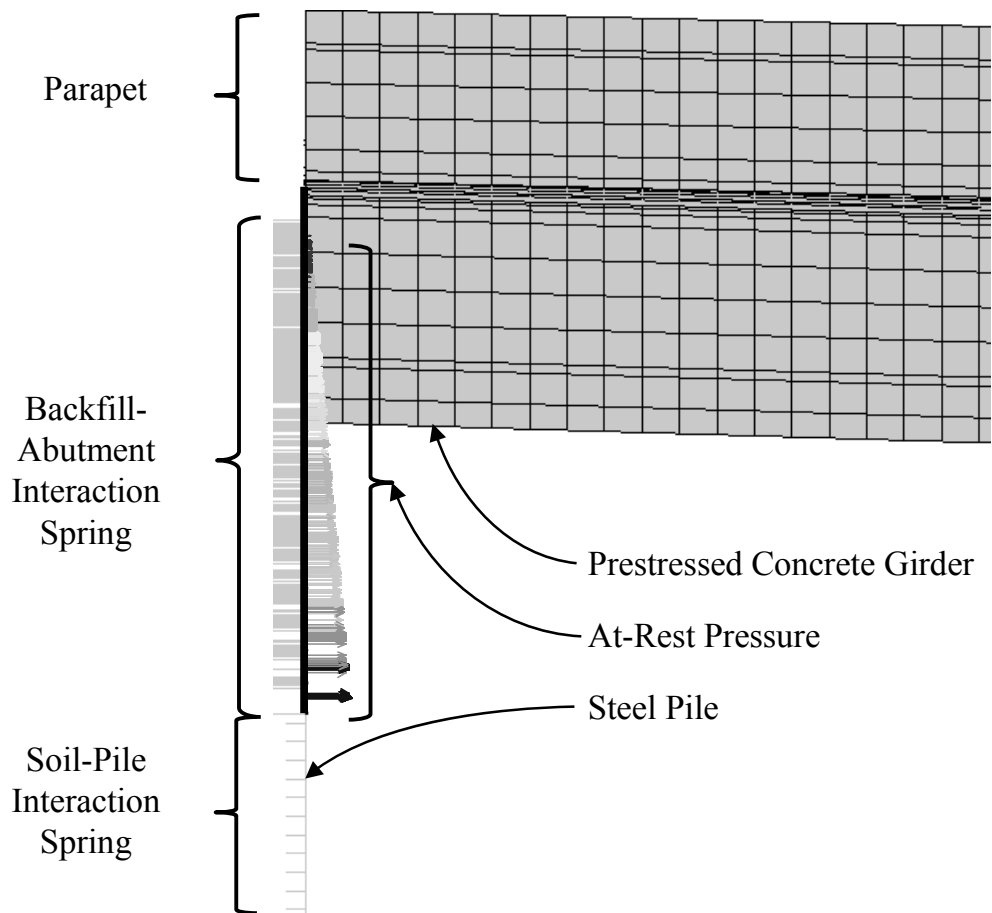


Figure 5.29. At-Rest Pressure Application.

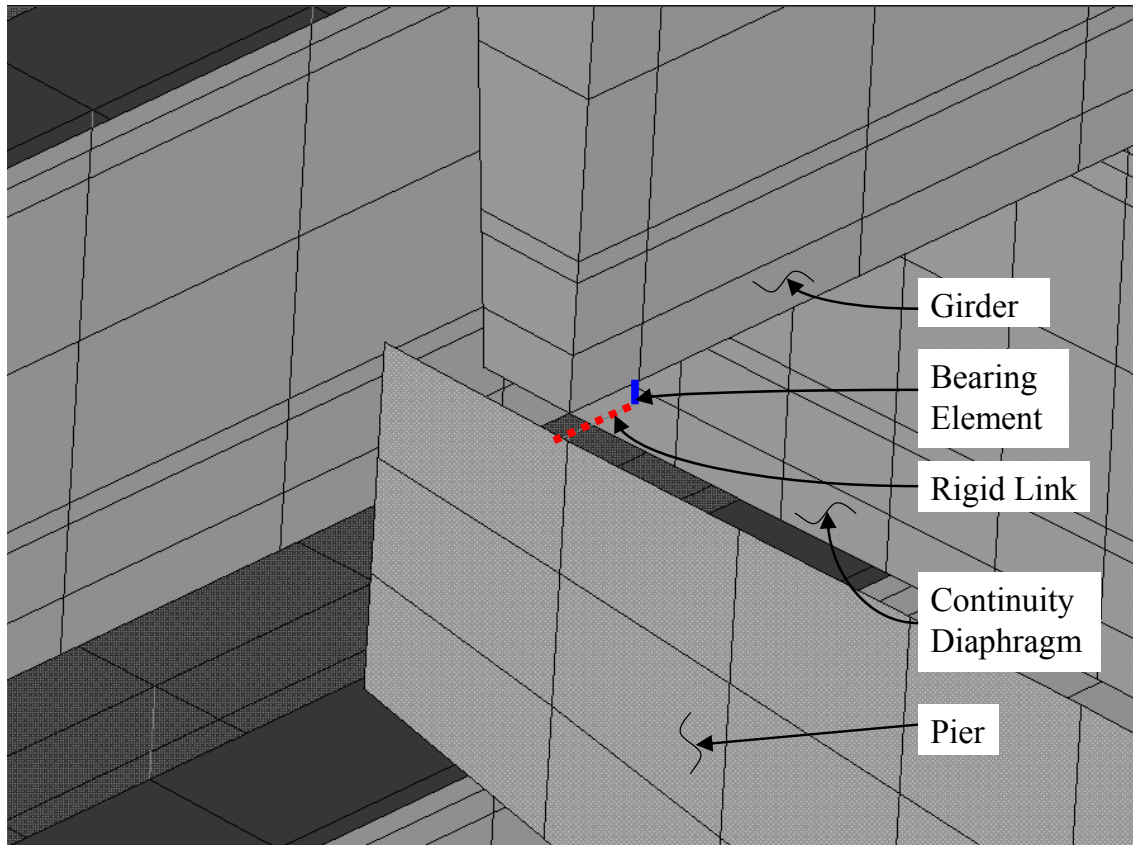


Figure 5.30. Bridge 109 Pier Exploded View.

5.4.2 Bridge 203 Numerical Model

The numerical model developed for bridge 203 (see Figure 5.31) consists of three spans and follows the same element modeling scheme as bridge 109. Details of the numerical modeling can be found in Laman *et al.* (2003). Properties of SHELL63 elements used for piers, abutments, and deck are presented in Table 5.1. Element material properties are as presented in Table 5.1.

Bridge 203 is unique among the four instrumented bridges in that abutment 1 is supported on rock and abutment 2 is supported on piles and is constructed as a standard PennDOT integral abutment. Reflecting the actual construction, abutment 1 foundation element boundary conditions consist of restrained translation, effectively fixing the abutment against all rotations and translations. Abutment 2 is modeled in the same manner as the abutments for bridge 109.

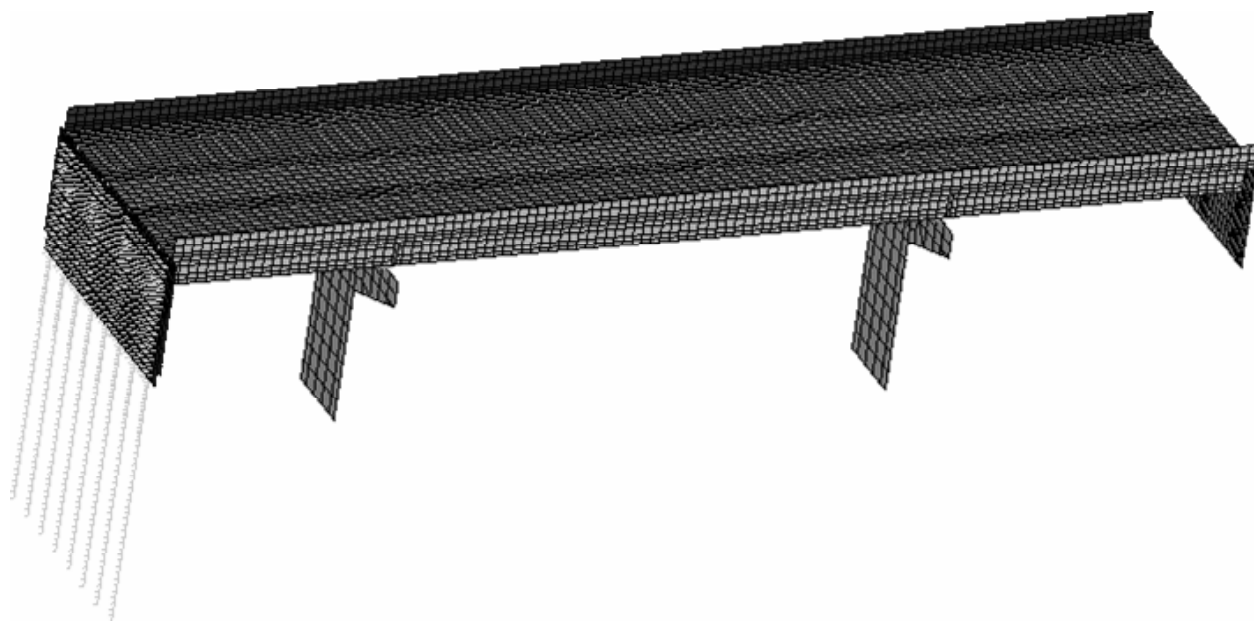


Figure 5.31. Complete Bridge 203 Numerical Model.

5.4.3 Bridge 211 Numerical Model

The numerical model developed for bridge 211 (see Figure 5.32) consists of one span and follows the same element modeling scheme as bridge 109. Details of the numerical modeling can be found in Laman et al. (2003). Element material properties are as presented in Table 5.1.

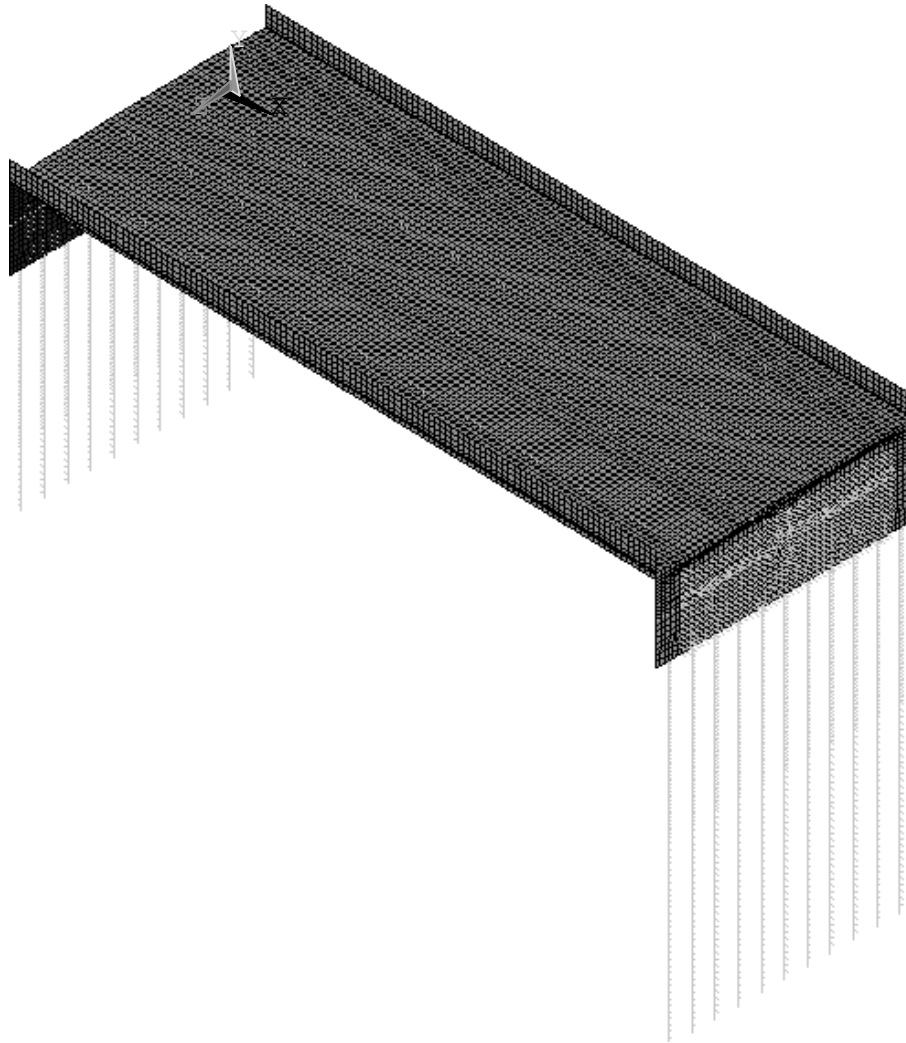


Figure 5.32. Complete Bridge 211 Numerical Model.

5.4.4 Bridge 222 Numerical Model

The numerical model developed for bridge 222 (see Figure 5.33) consists of one span and also follows the same element modeling scheme as bridge 109. Details of the numerical modeling can be found in Laman et al. (2003). Element material properties are as presented in Table 5.1.

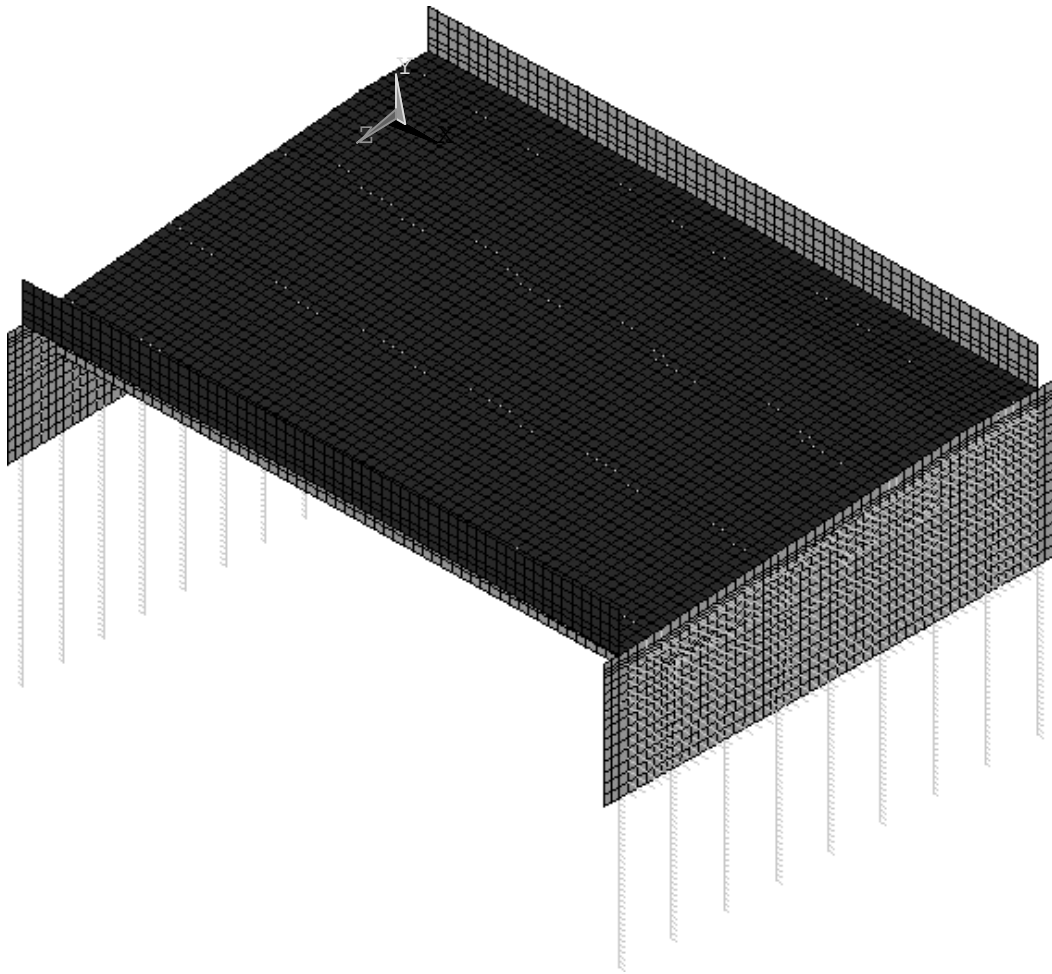


Figure 5.33. Bridge 222 Numerical Model.

Four prestressed concrete girders were modeled with SHELL63 elements and rigidly connected to abutment backwalls. Deck and parapets were also modeled with SHELL63. Deck

slabs were attached to girders using rigid link (BEAM4) and located at the mid-thickness of the deck slab. Parapets were rigidly connected to the deck, and each parapet segment was connected to the adjacent parapet with the restraint of all translation. Both abutments were composed of SHELL63 and located at the mid-thickness of the abutments. Both abutments were rigidly connected and rested on nine steel HP piles. The back face of both abutments was laterally supported by soil-abutment interaction spring. Steel HP12×74 piles were continuously modeled with a 6-inch length for the top soil layer and a 12-inch length for the rest of the soil layer using BEAM4 elements. Nonlinear soil-pile springs attached to the piles laterally supported the HP piles, and boundary conditions of vertical restrained translation were applied to supporting piles.

5.5 Comparison of Predicted to Measured Response

5.5.1 Bridge 109

Predicted and measured abutment displacements and backfill pressures are compared and discussed. For the purposes of accurate comparison, the values of measured and predicted data were initialized with identical starting point established. This adjustment was required due to constraints on field instrumentation imposed by construction sequences and schedules, which cannot be explicitly modeled and do not allow the measured data to have the same zero starting point with the numerical models.

Predicted and measured longitudinal abutment displacements of bridge 109 at the top and bottom locations are presented in Figures 5.34 through 5.37. The top extensometer at abutment 1 measured no contraction displacement during the first year but measured a 0.22 inches lower bound increase during the following year, while the top extensometer at abutment 2 measured 0.41 and 0.51 inches contraction displacement increase over 2 years. The numerical model

predicts that abutment 1 displacements increase 0.50 and 0.21 inches contraction and abutment 2 displacements increase 0.46 and 0.20 inches over 2 years. As shown in Figure 5.35, the extensometer at the bottom location of abutment 1 measured a significant contraction displacement, increasing, compared to the preceding year, 0.56 and 0.20 inches. The numerical model predicts the abutment 1 displacement as 0.62 and 0.19 inches increase compared to the preceding year. The extensometer at the bottom location of abutment 2 measured 0.57 and 0.34 inches as presented in Figure 5.37. The numerical model predicts similar displacements of 0.57 and 0.21 inches, but displacement prediction does not increase as rapidly as the extensometer measurements from the second year.

Predicted earth pressures from the numerical model versus observed earth pressures from both top and bottom pressure cells at both abutment 1 and 2 are presented in Figures 5.38 through 5.41. All predicted pressures showed a similar trend as the measured pressures. Both top pressure cells from both abutment 1 and 2 measured approximately 5 to 10 psi smaller backfill pressures due to the approximately 8 ft 1 inch and 7 ft 10 inches shallower placement, respectively. During summer seasons, both bottom pressure cells measured significant daily variation backfill pressures. However, the numerical model predicts that backfill pressures reach the passive pressure. As shown in Figures 5.38 and 5.40, both pressure cells at the top location from both abutments measured approximately 6.9 and 10.4 psi of maximum backfill pressure during bridge expansion while the numerical model represents approximately 6.8 to 7.4 psi of passive backfill pressure.

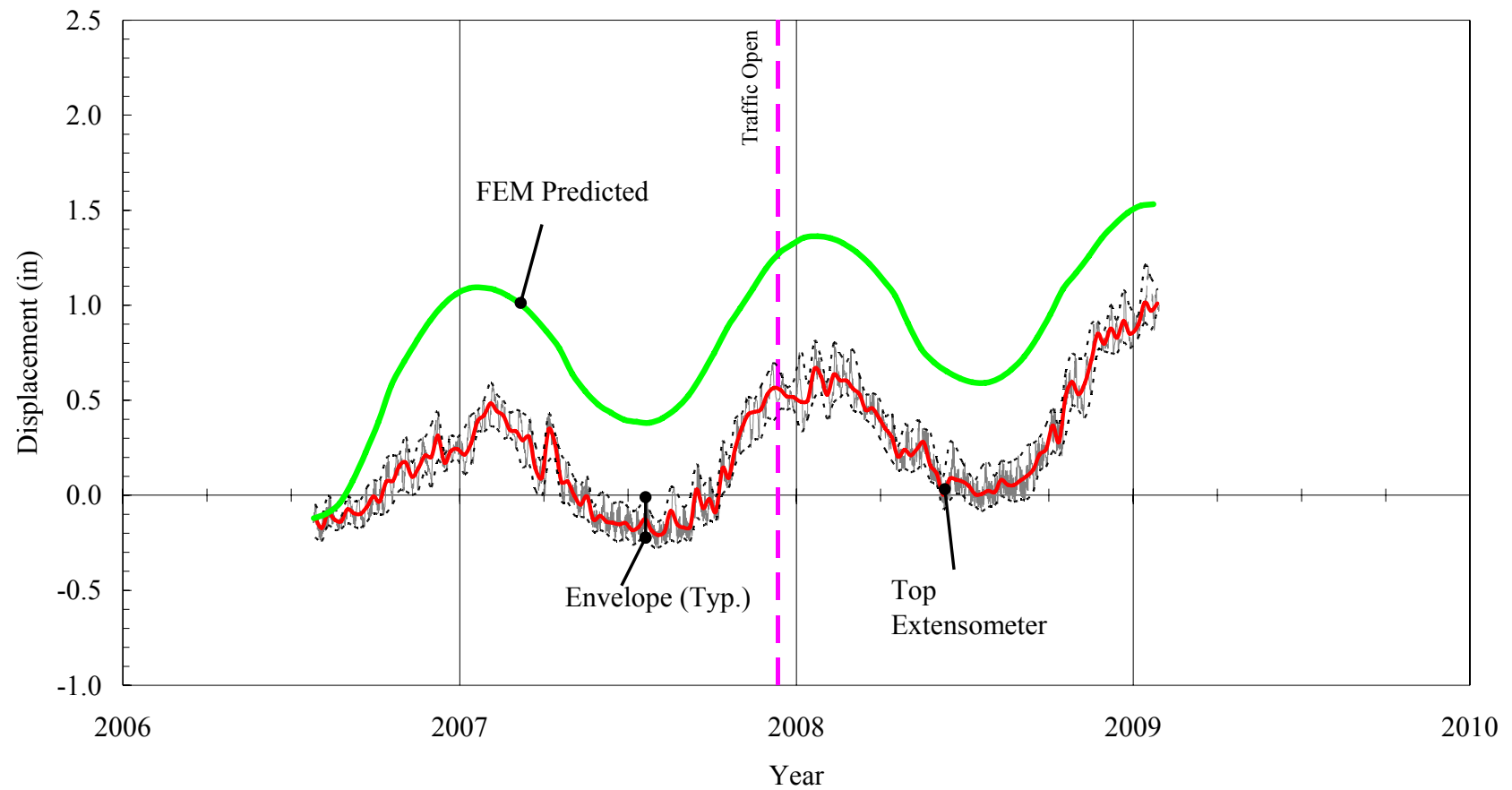


Figure 5.34: Measured and Predicted Bridge 109 Top Extensometer at Abutment 1

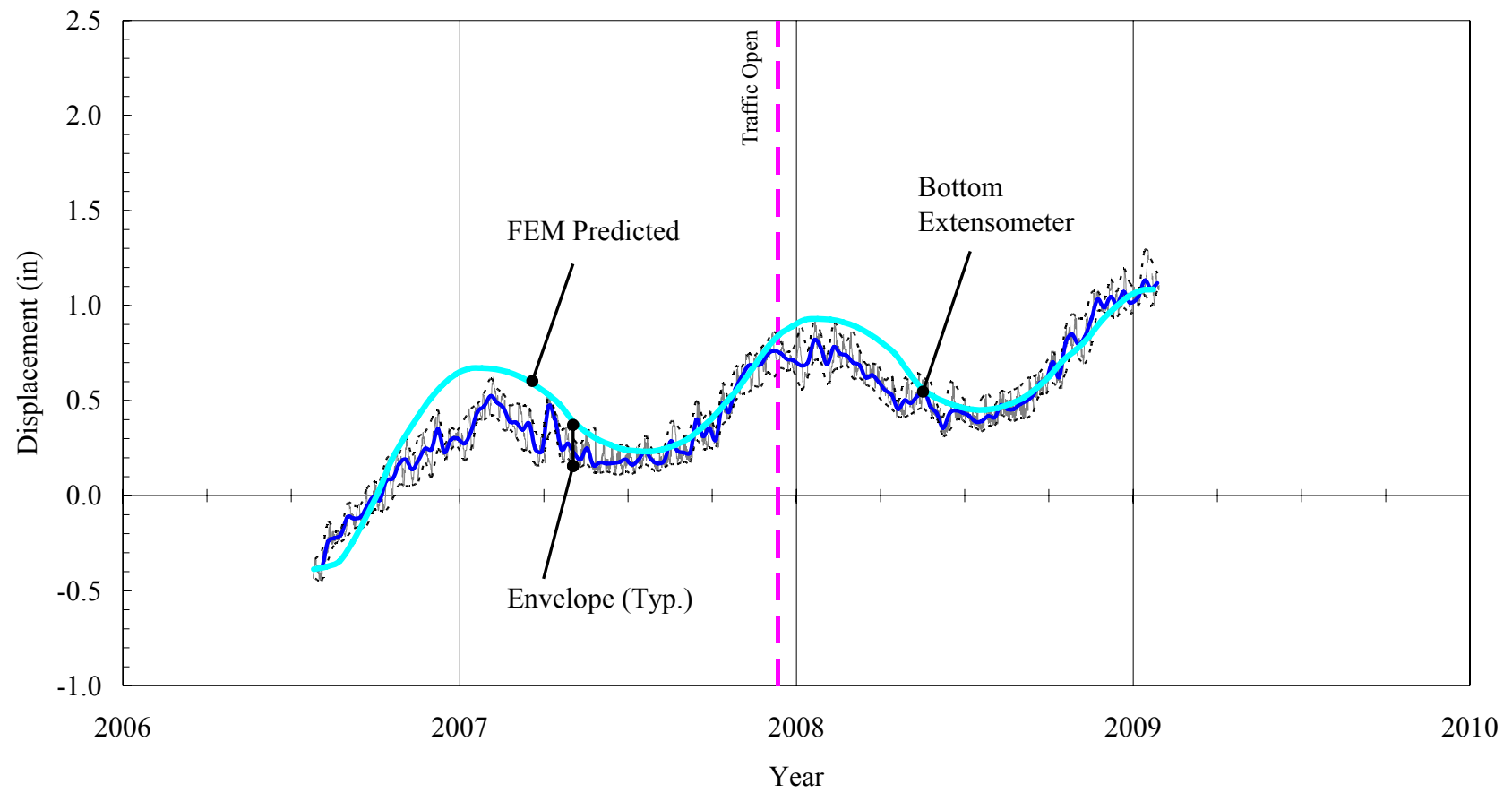


Figure 5.35: Measured and Predicted Bridge 109 Bottom Extensometer at Abutment 1

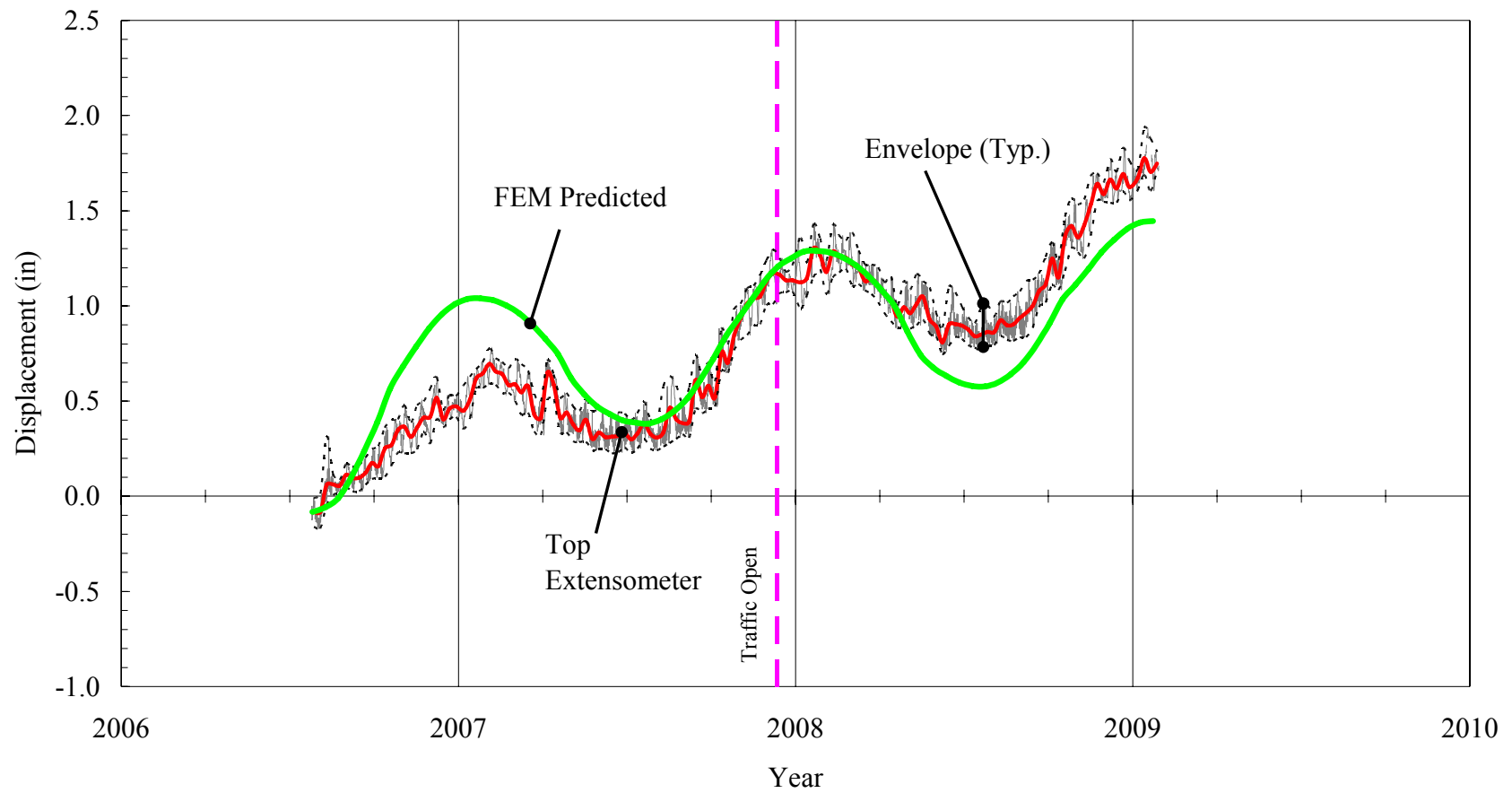


Figure 5.36: Measured and Predicted Bridge 109 Top Extensometer at Abutment 2

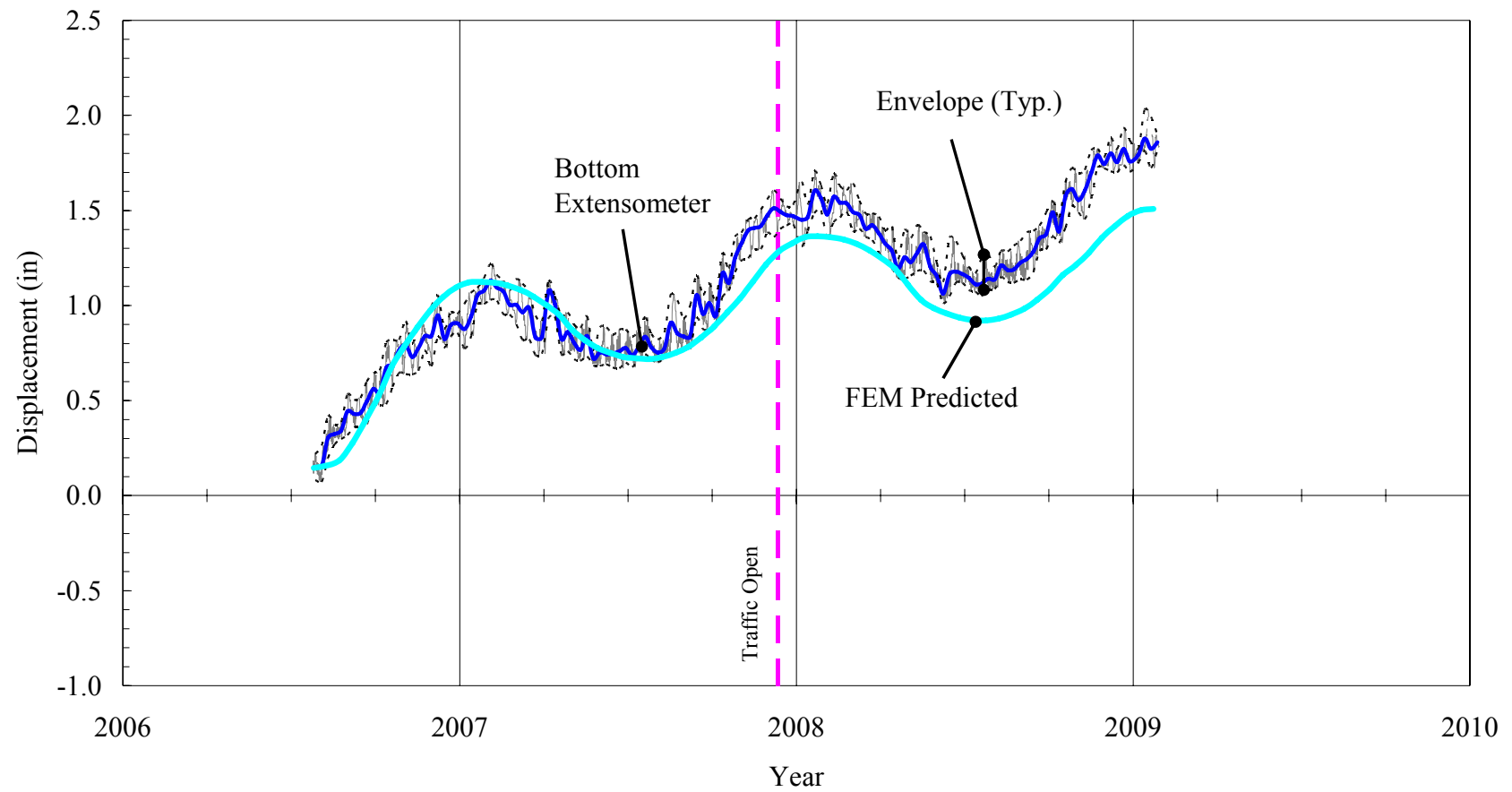


Figure 5.37: Measured and Predicted Bridge 109 Bottom Extensometer at Abutment 2

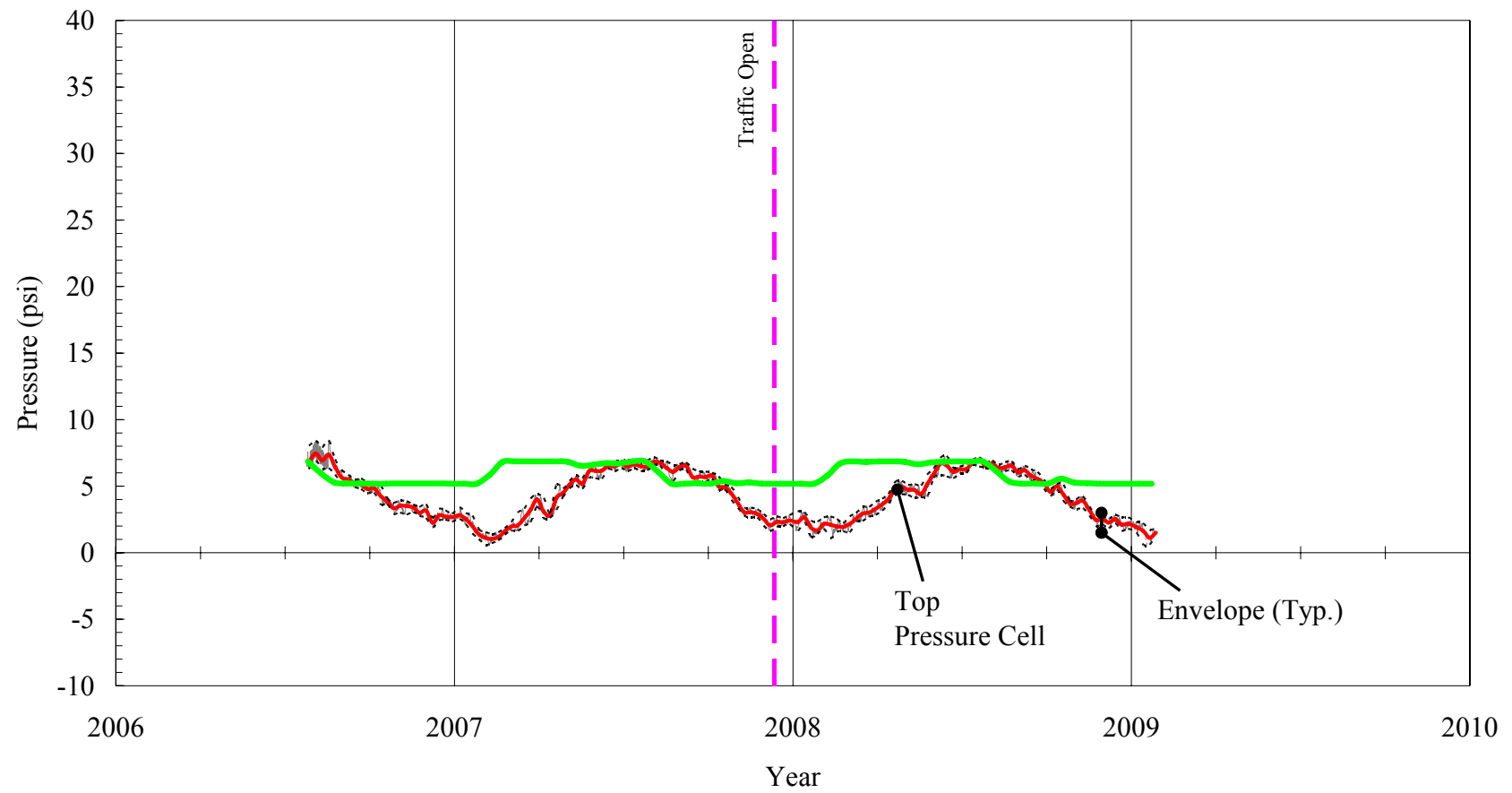


Figure 5.38: Measured and Predicted Bridge 109 Top Pressure Cell at Abutment 1

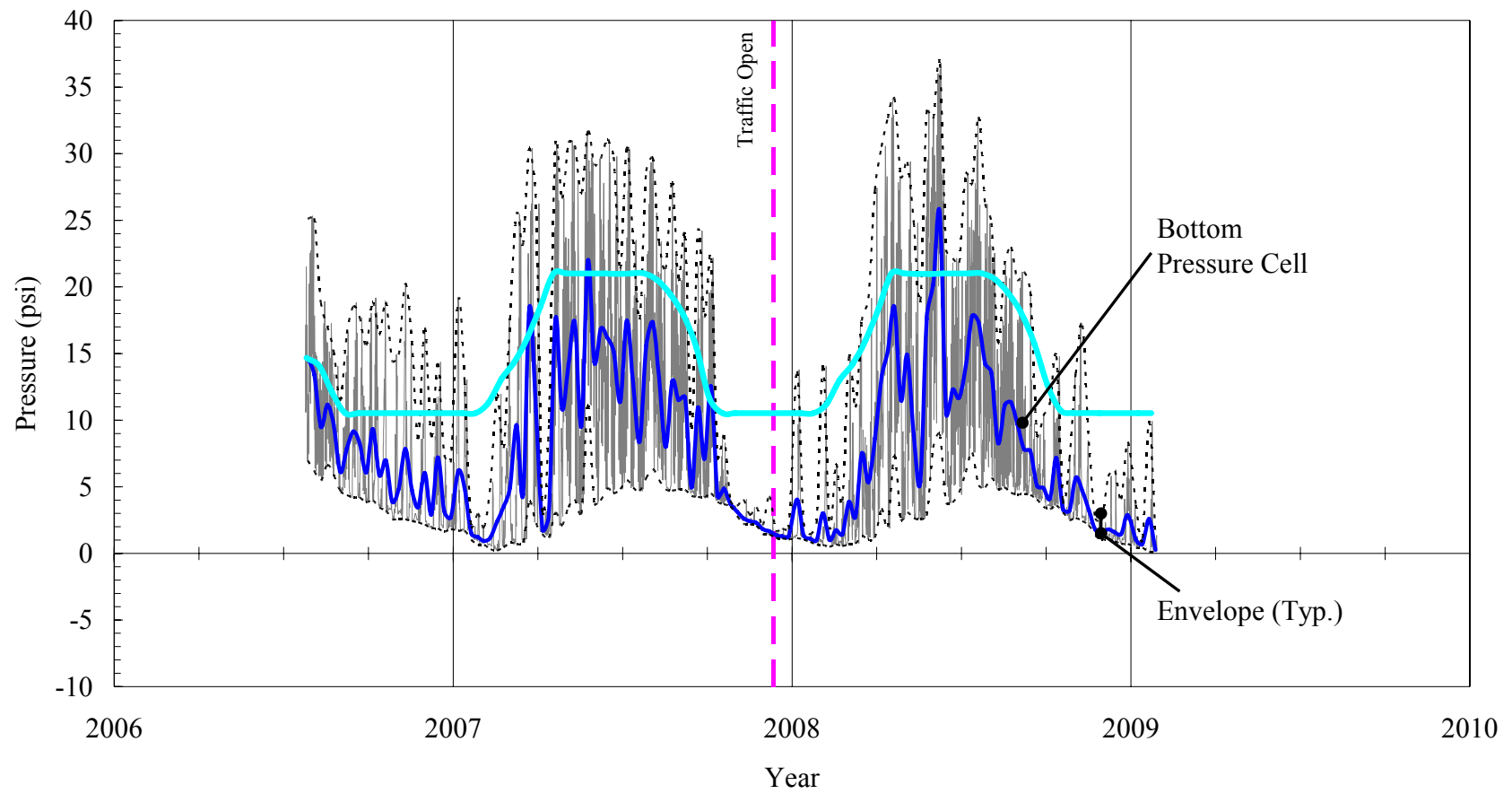


Figure 5.39: Measured and Predicted Bridge 109 Bottom Pressure Cell at Abutment 1

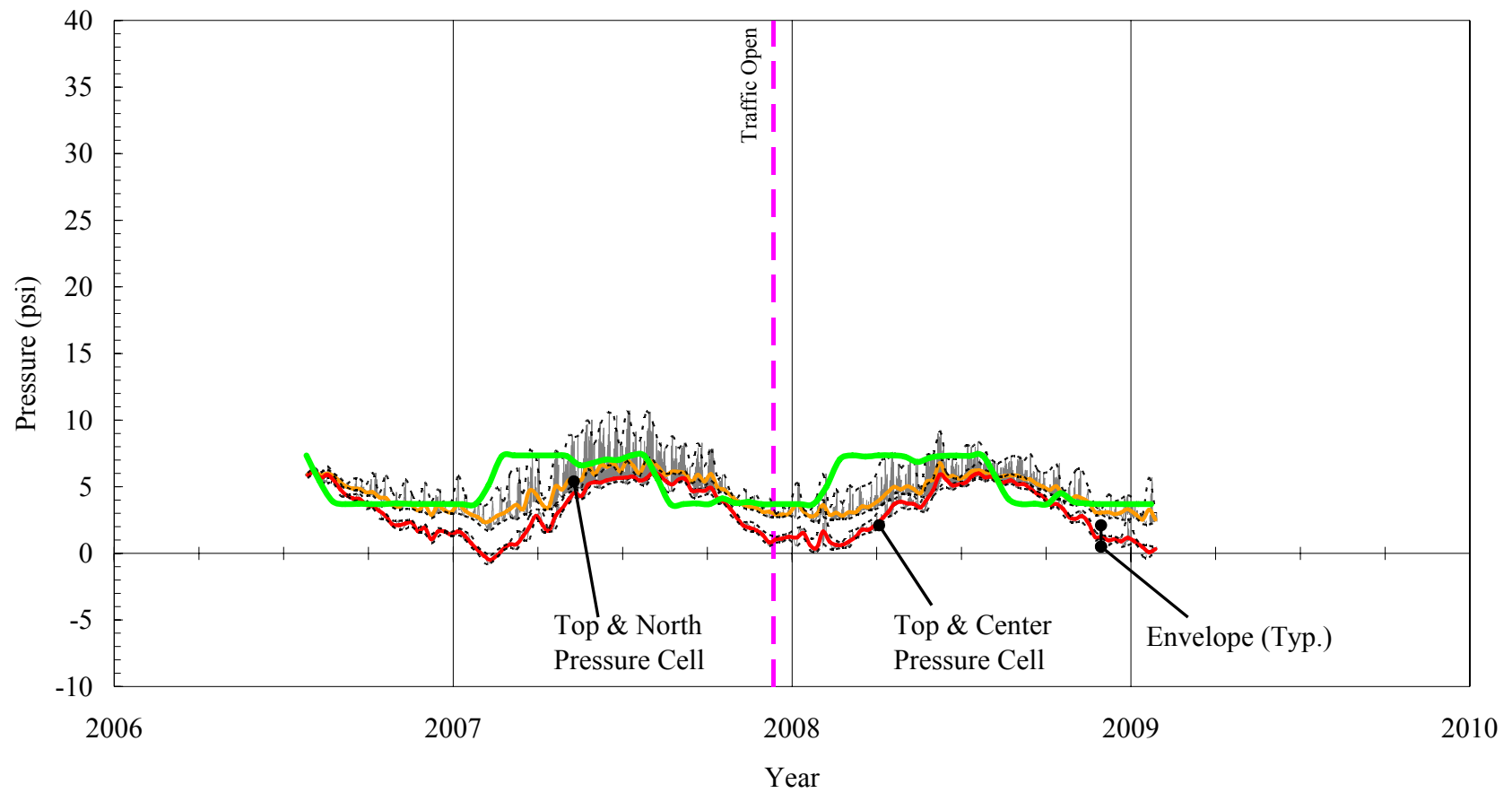


Figure 5.40: Measured and Predicted Bridge 109 Top Pressure Cell at Abutment 2

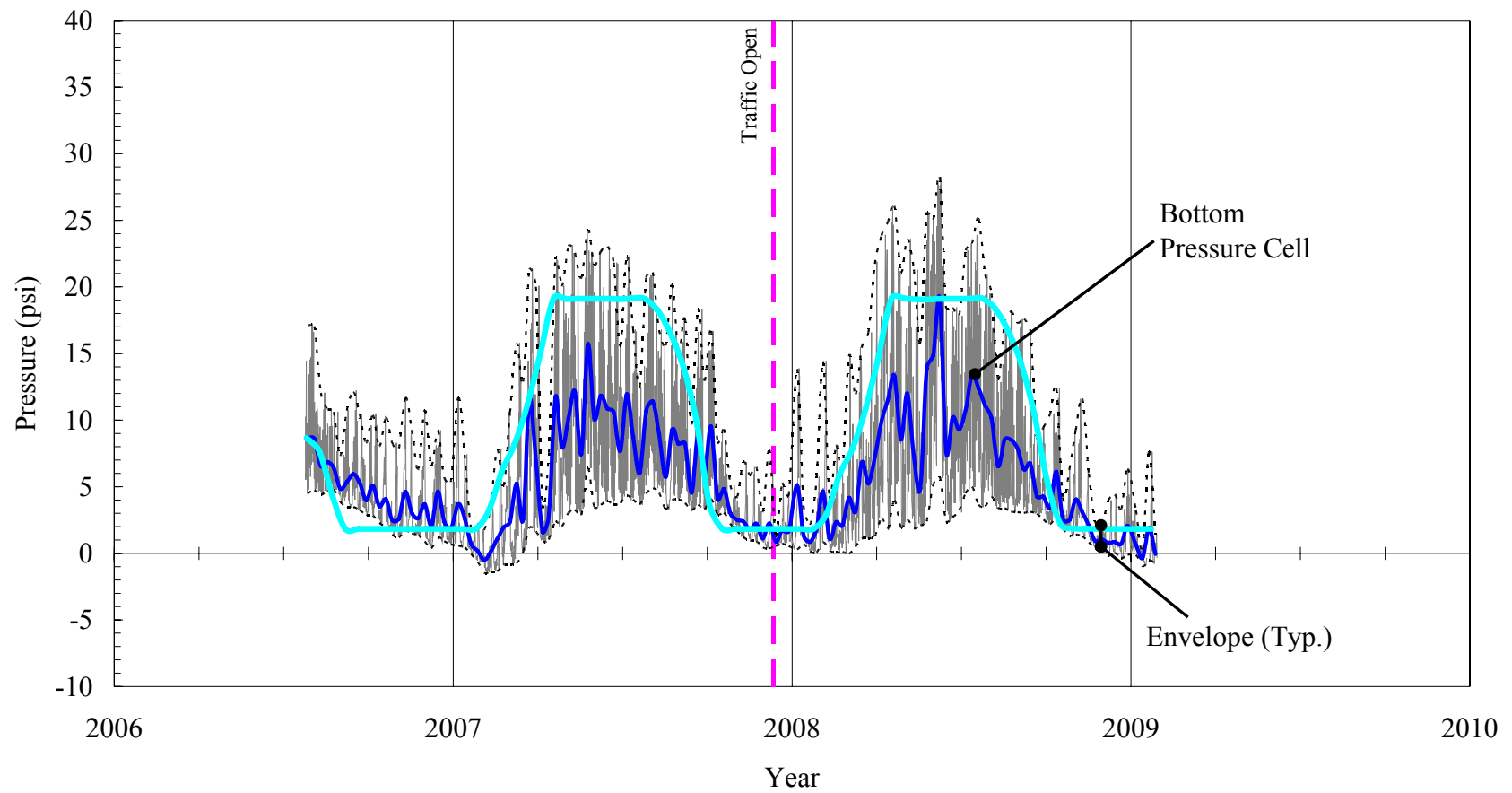


Figure 5.41: Measured and Predicted Bridge 109 Bottom Pressure Cell at Abutment 2

5.5.2 Bridge 203

Predicted and measured abutment displacements and backfill pressures are compared and discussed. For the purposes of accurate comparison, the values of measured and predicted data were initialized with identical starting point established. This adjustment was required due to constraints on field instrumentation imposed by construction sequences and schedules, which cannot be explicitly modeled and do not allow the measured data to have the same zero starting point with the numerical models.

Predicted and measured longitudinal abutment displacements of bridge 203 at the top and bottom locations are presented in Figures 5.42 and 5.43. It can be observed from Figure 5.42 that the numerical model predicts well the displacements at the Mid and West location during the first 4 years. The extensometer at the Mid and Center location measured an expansion trend. However, the extensometer measured a significant abutment displacement (approximately 0.130 inch increase compared to the preceding year's contraction), approximately 0.207 inches larger than the numerical model prediction, occurred during winter 2006/2007.

The Mid and Center extensometer measured a different trend of abutment displacements from the numerical prediction and the Mid and West extensometer. Contrary to the Mid and West and Bottom and Center extensometers, the Mid and Center extensometer exhibits an expansion trend during the first 2 years, and thereafter, neither an expansion nor a contraction trend is observed. Also, the Mid and Center extensometer has approximately 0.20 inches of seasonal amplitude while the Mid and West and Bottom and Center extensometers have approximately 0.32 and 0.11 inches, respectively.

The Bottom and Center extensometer measured approximately 0.03 inches contraction every year while the numerical model predicts 0.15 inches contraction during the first 2 years and 0.02 inches thereafter.

Predicted earth pressures from the numerical model versus observed earth pressures from the three pressure cells are presented in Figures 5.44 and 5.45. All predicted pressures showed the same trend as the observed pressures. During the first 3 years, the Top and West pressure cell measured lower pressures compared to the Top and Center pressure cell. Thereafter both pressure measurements become similar to each other. The predicted pressures for both top pressure cells exhibit a good match with the measured pressures. Both predicted top pressures represent the backfill pressure reaches the active and passive pressures. However, the predicted bottom pressure reaches neither of the active and passive pressures.

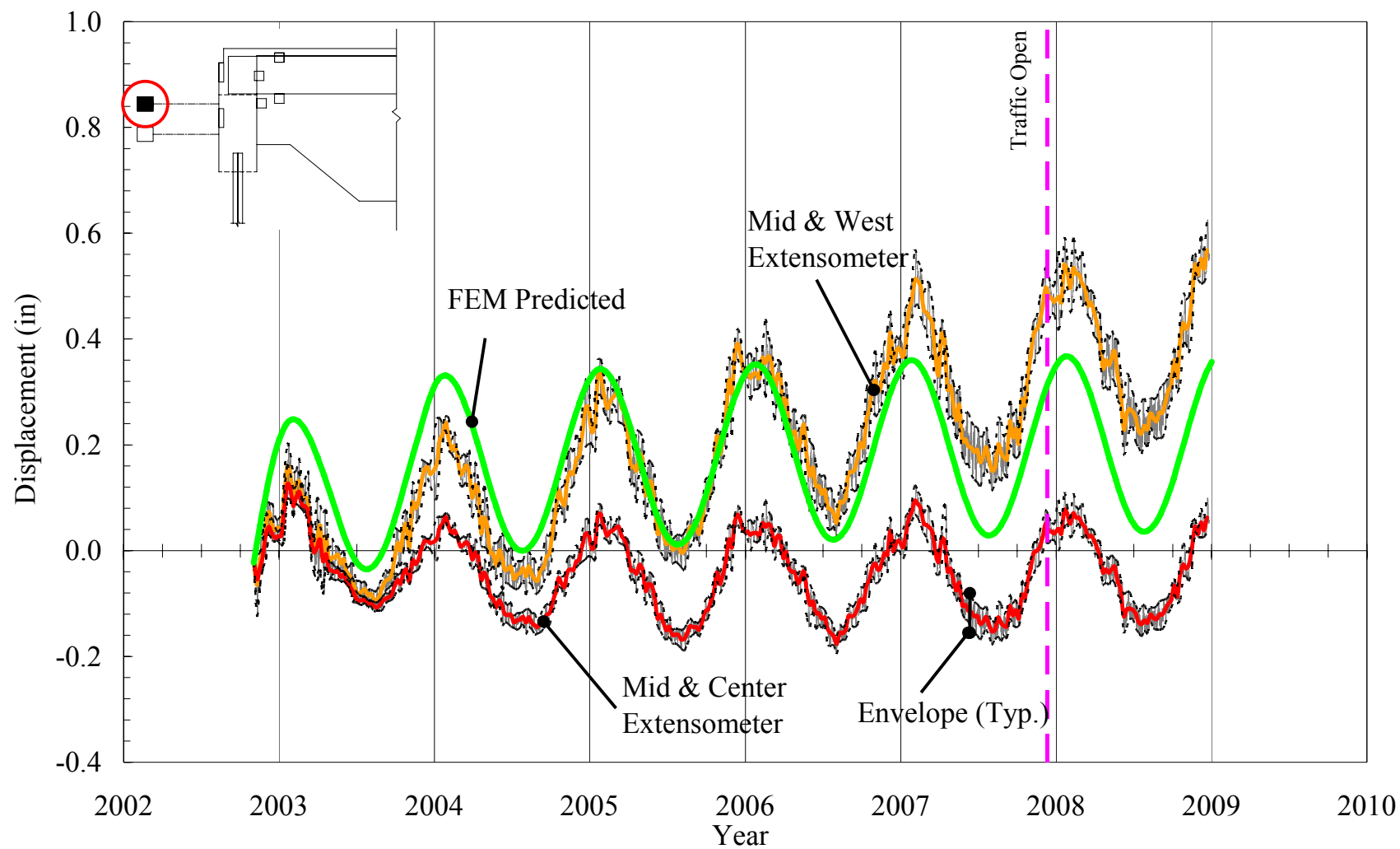


Figure 5.42: Bridge 203 Top Extensometer Comparison

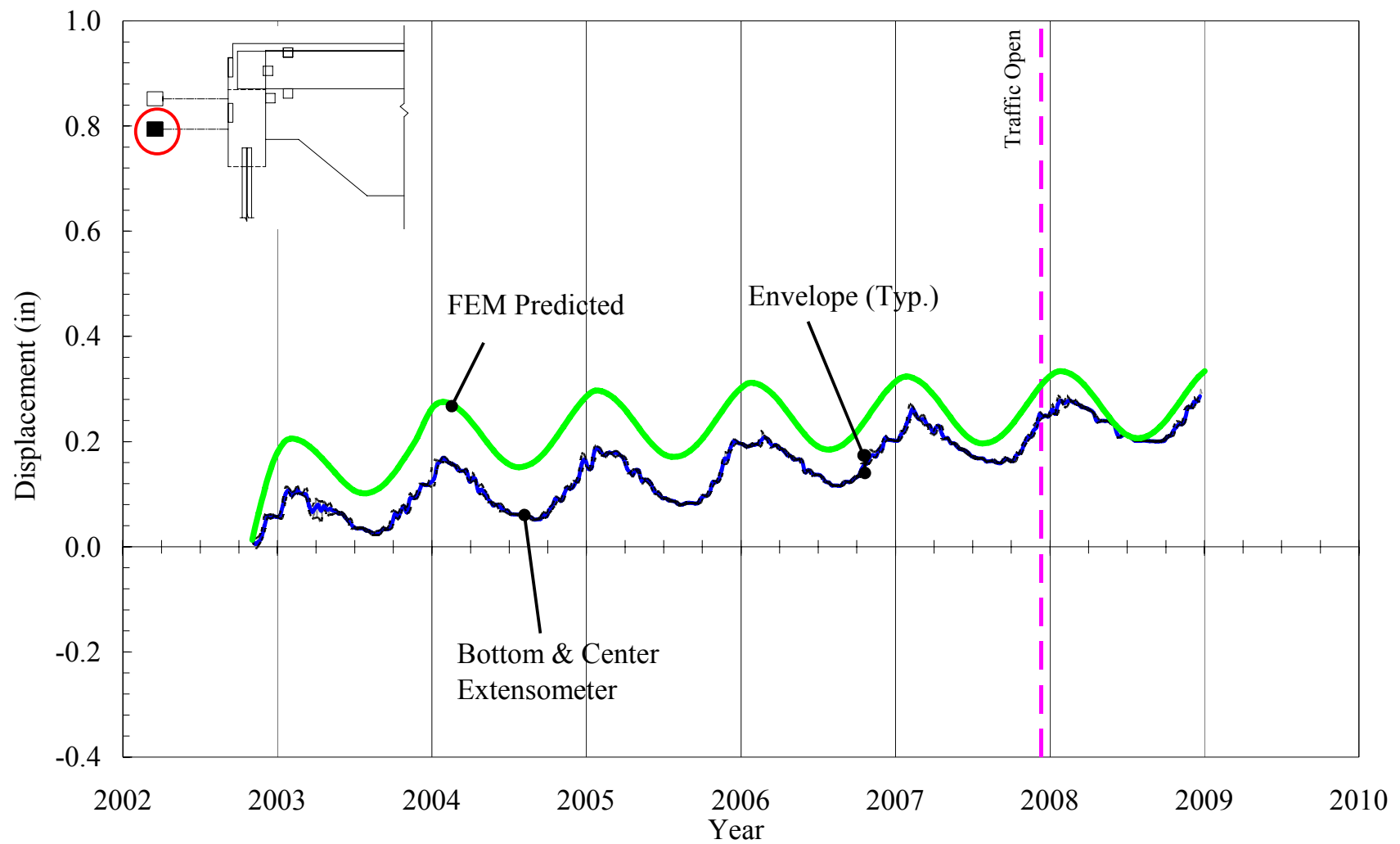


Figure 5.43: Bridge 203 Bottom Extensometer Comparison

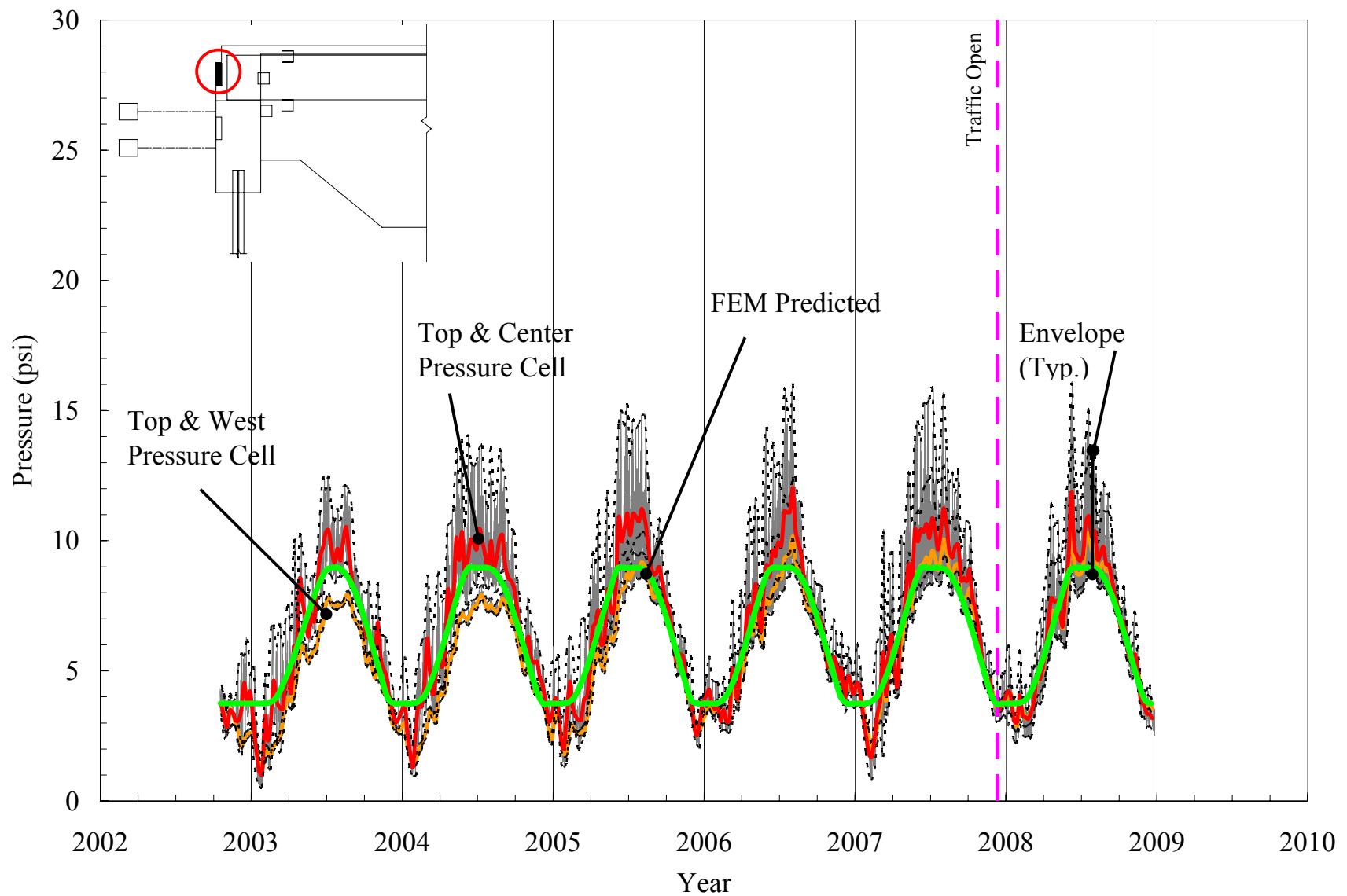


Figure 5.44: Bridge 203 Top Pressure Cell Comparison

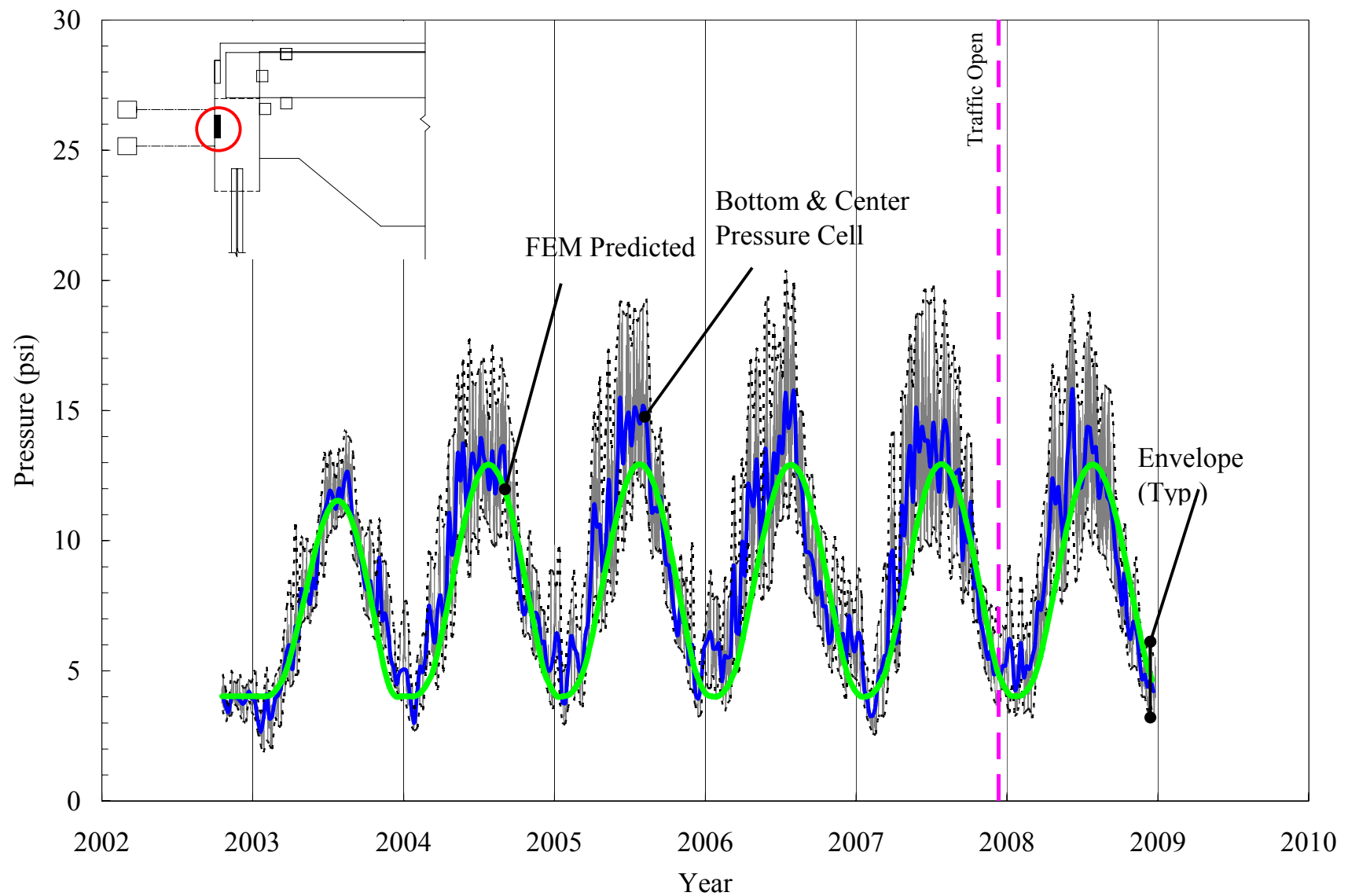


Figure 5.45: Bridge 203 Bottom Pressure Cell Comparison

5.5.3 Bridge 211

Predicted and measured abutment displacements and backfill pressures are compared and discussed. For the purposes of accurate comparison, the values of measured and predicted data were initialized with identical starting point established. This adjustment was required due to constraints on field instrumentation imposed by construction sequences and schedules, which cannot be explicitly modeled and do not allow the measured data to have the same zero starting point with the numerical models.

Predicted and measured longitudinal abutment displacements of bridge 211 at the top and bottom locations are presented in Figures 5.46 through 5.49. It can be observed from Figures 5.46 and 5.48 that the numerical model predicts well the displacements at both abutments top locations over 4 years of monitoring. As shown in Figure 5.47, the extensometer at the bottom location of abutment 1 measured a significant contraction displacement, increasing, compared to the preceding year, 0.09, 0.04, 0.04, and 0.02 inches. However, the numerical model predicts the abutment 1 displacement as 0.08, 0.01, 0.005, and 0.005 increase compared to the preceding year. Contrary to the abutment 1 displacement, the extensometer at the bottom location of abutment 2 measured seasonal fluctuation without a residual displacement, as presented in Figure 5.49. The numerical model predicts similar displacements, but a 0.06-inch residual displacement is observed during the first winter 2004/2005.

Predicted earth pressures from the numerical model versus observed earth pressures from both top and bottom pressure cells at both abutment 1 and 2 are presented in Figures 5.50 through 5.53. All predicted pressures showed a similar trend as the observed pressures while pressure cells at abutment 1 measured a large daily fluctuation during summers. As shown in Figures 5.50 and 5.52, both pressure cells at the top location from both abutments measured

approximately 8.5 psi during bridge expansion while the numerical model represents 4.2 psi of passive backfill pressure. Both bottom pressure cell measurements from both abutments agree better with the numerical model prediction than the top pressure cells. As shown in Figure 5.51, the bottom pressure cells measured peak mean backfill pressures during summers as 7.9, 8.5, 7.3, and 6.1 psi while the numerical model predicts 9.2, 9.1, 9.1, and 9.1 psi. As shown in Figure 5.53, the bottom pressure cells measured peak mean backfill pressures during summers as 10.1, 11.0, 9.7, and 9.1 psi while the numerical model predicts 10.2, 10.5, 10.5, and 10.5. Overall trend predictions by the numerical model are better for the bottom backfill pressures.

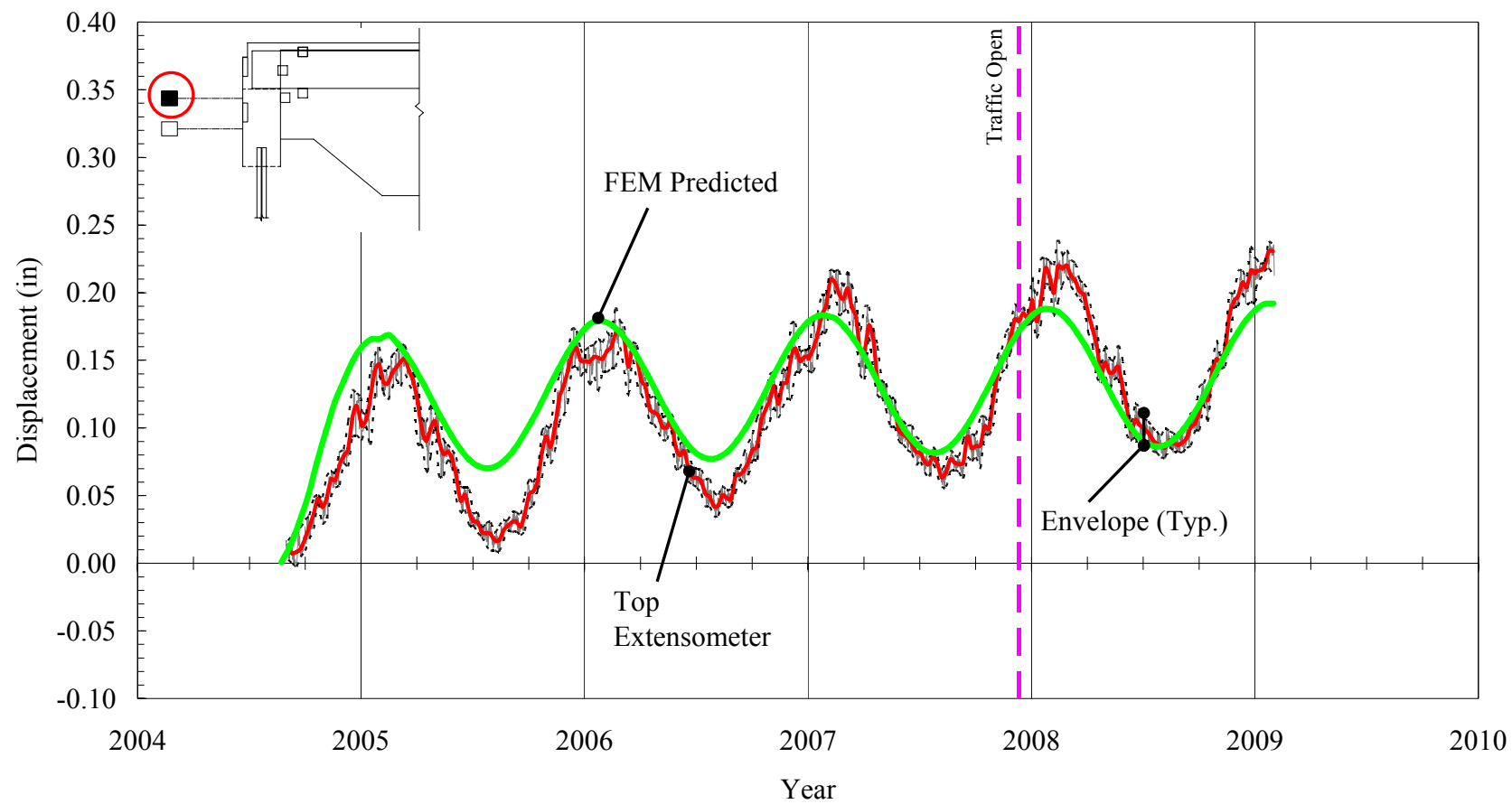


Figure 5.46: Measured and Predicted Bridge 211 Top Extensometer at Abutment 1

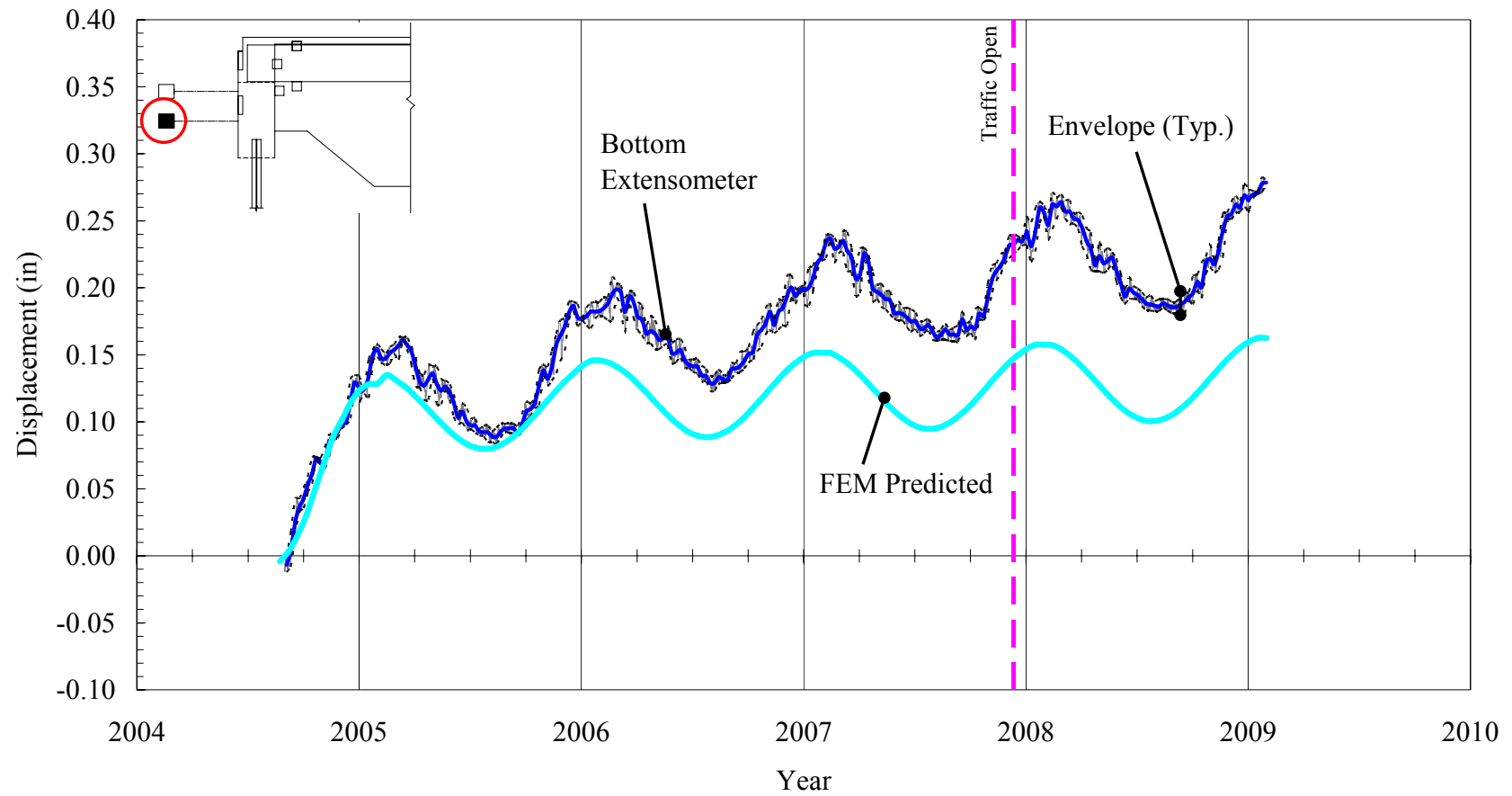


Figure 5.47: Measured and Predicted Bridge 211 Bottom Extensometer at Abutment 1

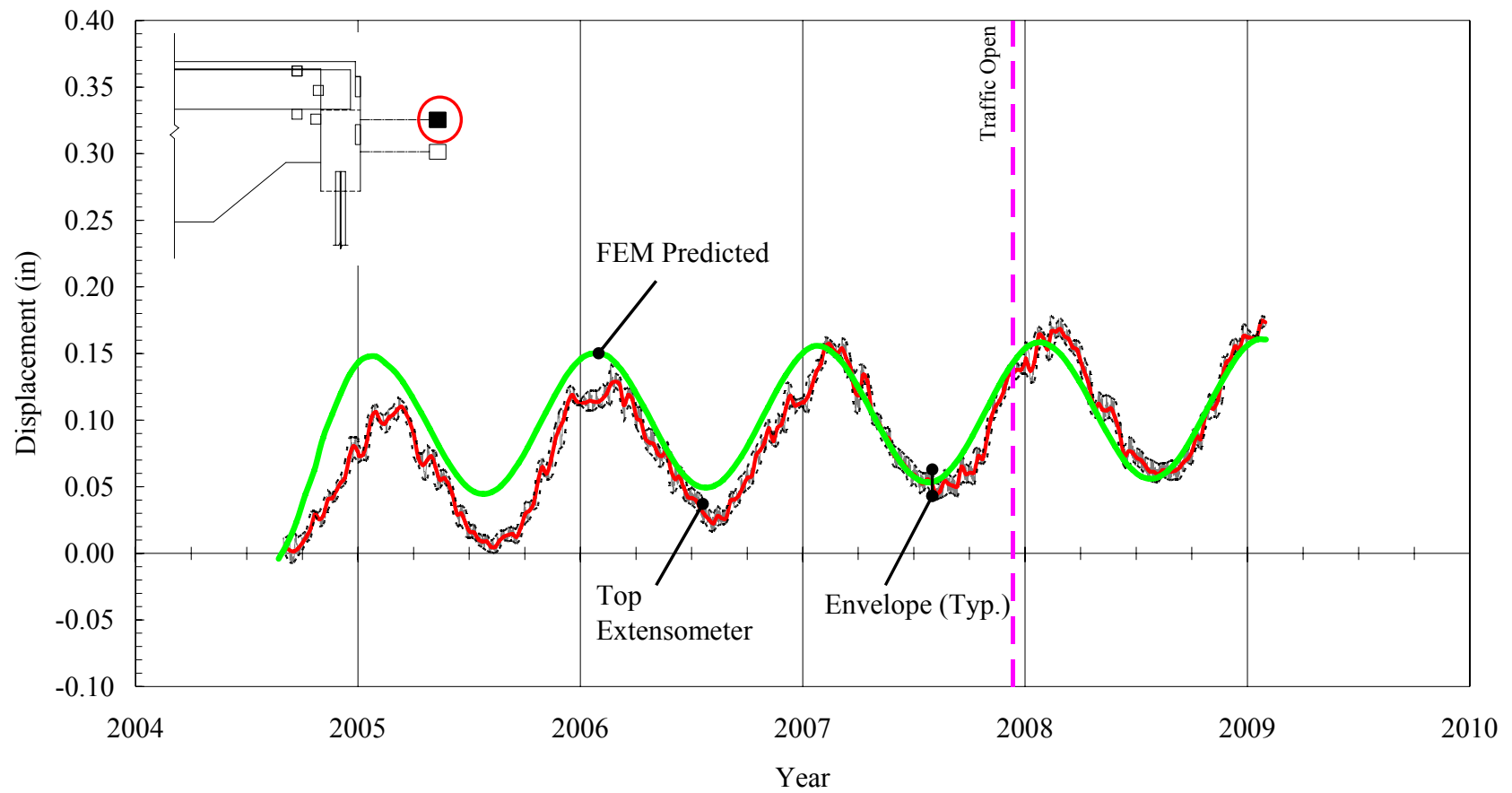


Figure 5.48: Measured and Predicted Bridge 211 Top Extensometer at Abutment 2

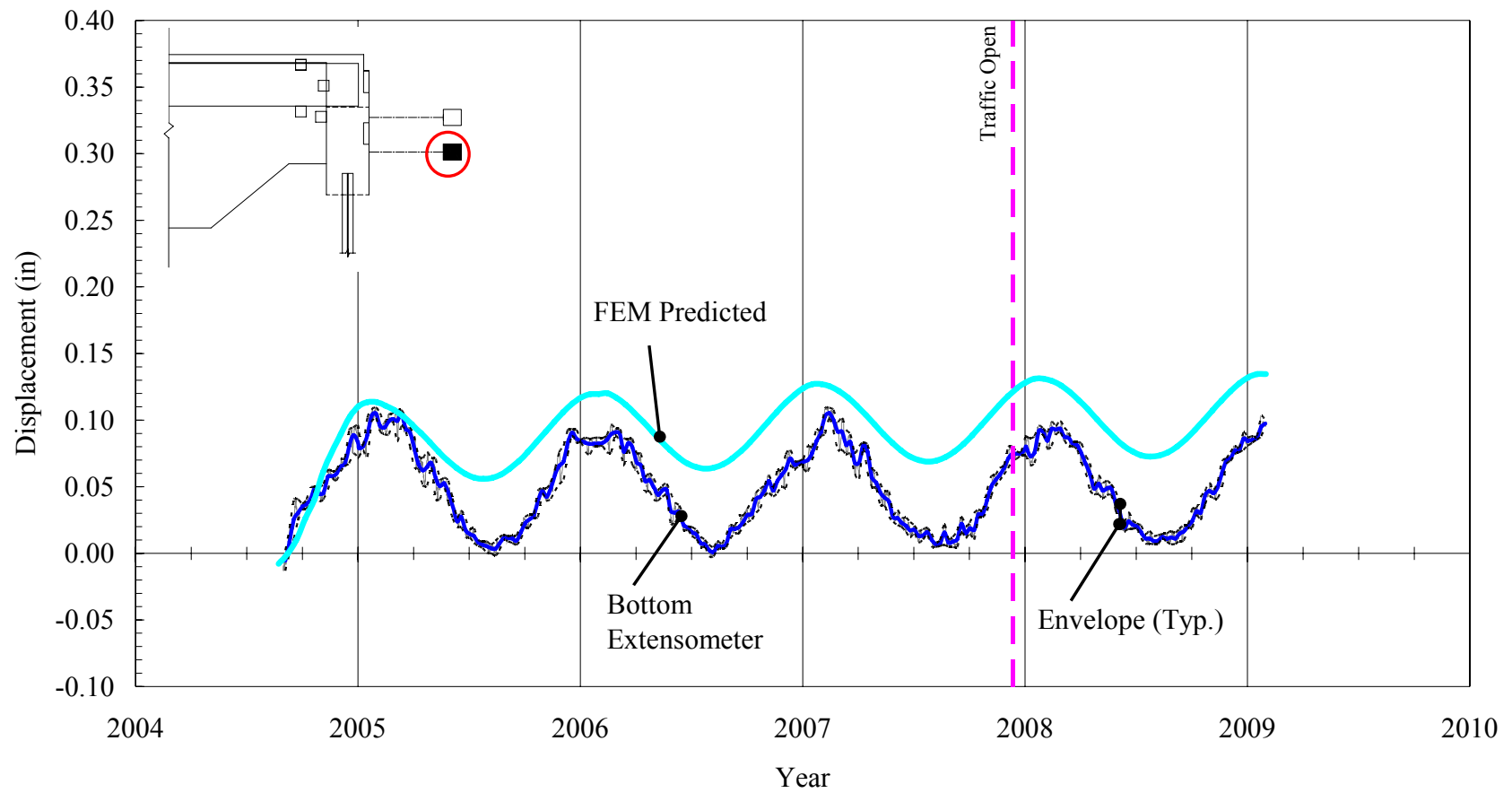


Figure 5.49: Measured and Predicted Bridge 211 Bottom Extensometer at Abutment 2

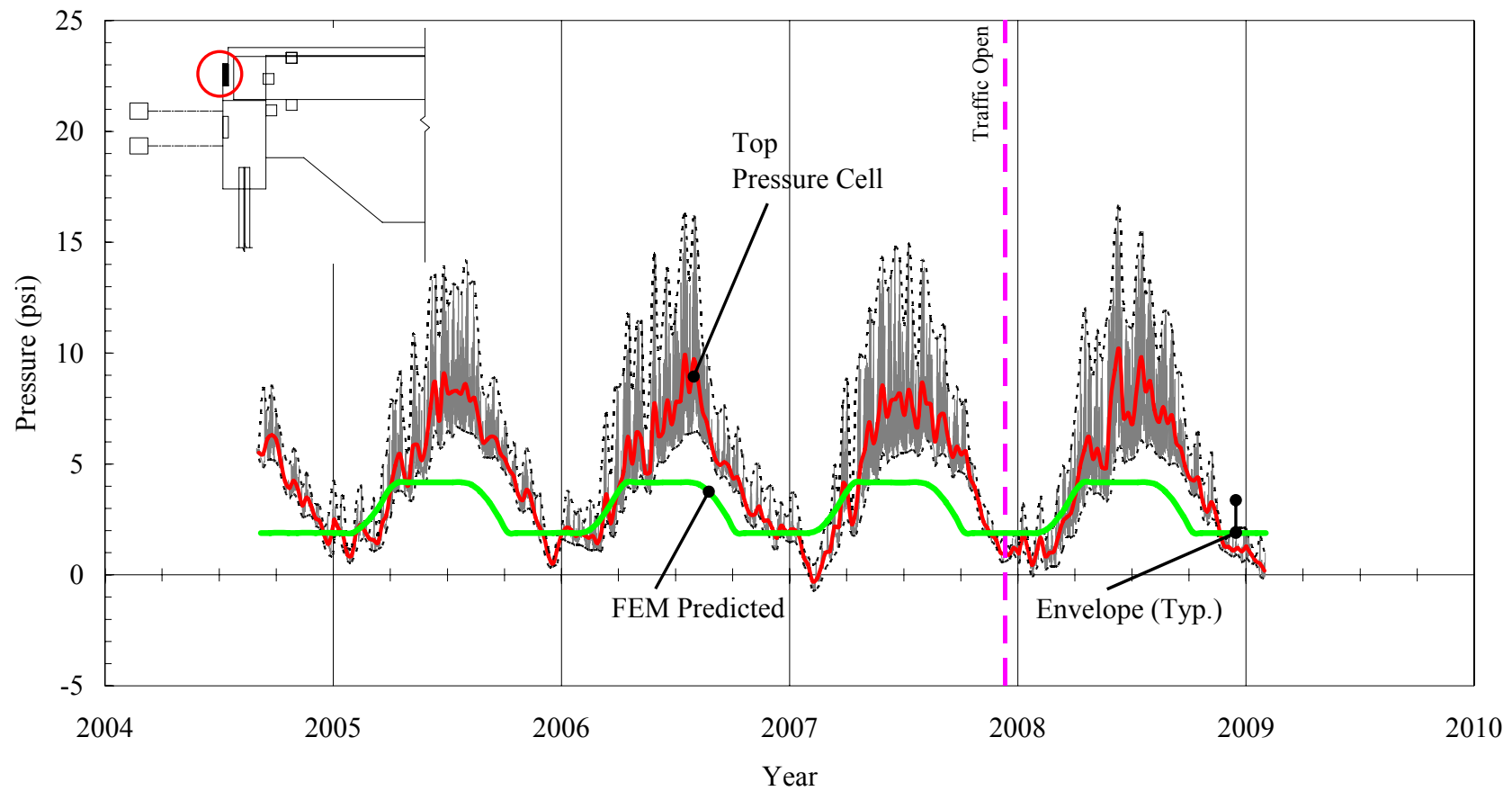


Figure 5.50: Measured and Predicted Bridge 211 Top Pressure Cell at Abutment 1

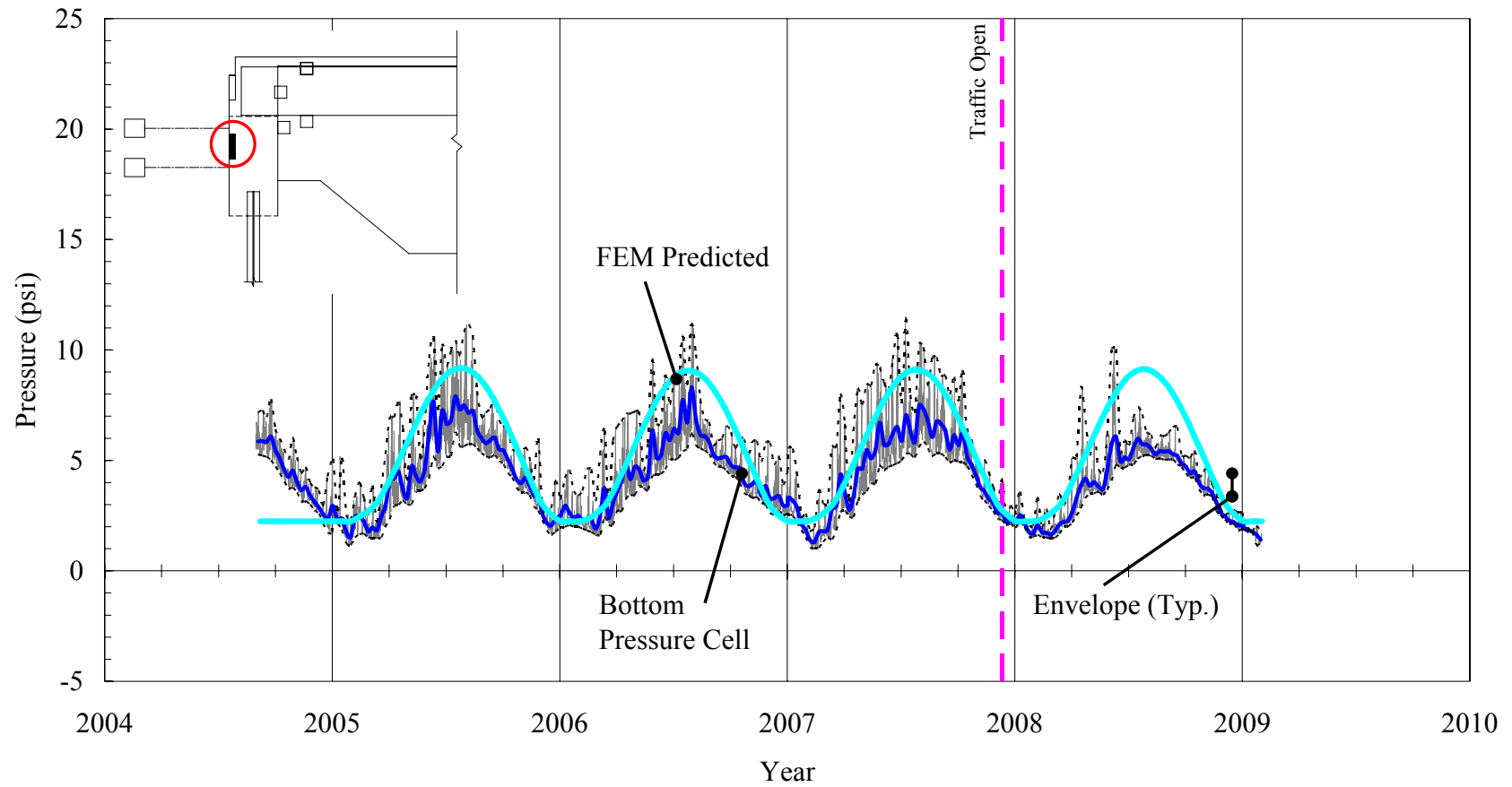


Figure 5.51: Measured and Predicted Bridge 211 Bottom Pressure Cell at Abutment 1

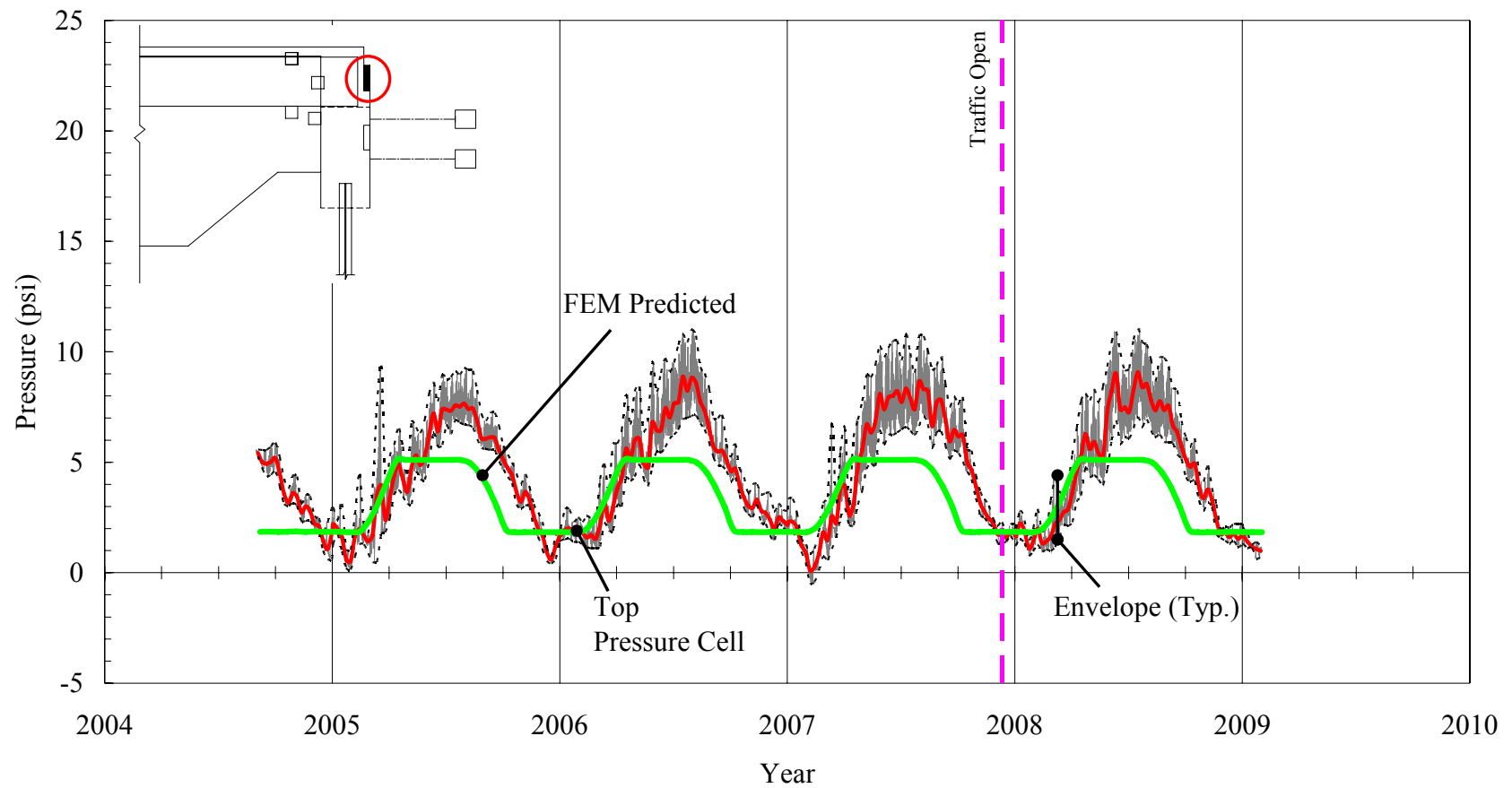


Figure 5.52: Measured and Predicted Bridge 211 Top Pressure Cell at Abutment 2

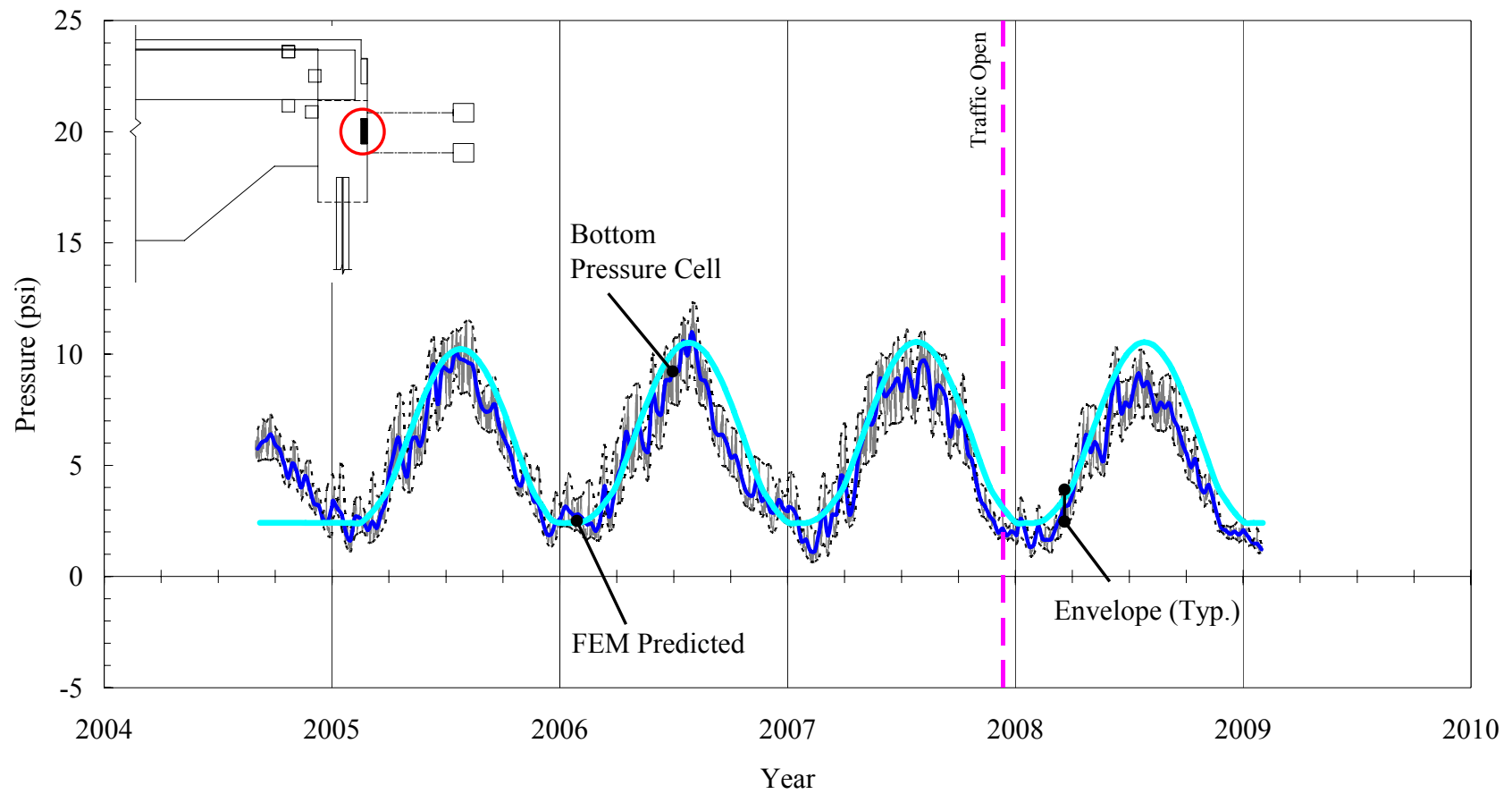


Figure 5.53: Measured and Predicted Bridge 211 Bottom Pressure Cell at Abutment 2

5.5.4 Bridge 222

Predicted and measured abutment displacements and backfill pressures are compared and discussed. For the purposes of accurate comparison, the values of measured and predicted data were initialized with identical starting point established. This adjustment was required due to constraints on field instrumentation imposed by construction sequences and schedules, which cannot be explicitly modeled and do not allow the measured data to have the same zero starting point with the numerical models.

Predicted and measured longitudinal abutment displacements of bridge 222 at the top and bottom locations are presented in Figures 5.54 through 5.57. The top extensometer at abutment 1 measured a contraction displacement increase trend over more than 5 years of monitoring while the top extensometer at abutment 2 measured an expansion displacement increase trend. However, the numerical model predicts that abutment 1 displacements are stable and no residual displacement and abutment 2 displacements increase in approximately 0.005 inches every year. As shown in Figure 5.55, the extensometer at the bottom location of abutment 1 measured a significant contraction displacement, increasing, compared to the preceding year, 0.06, 0.02, 0.03, 0.02, and 0.02 inches. However, the numerical model predicts the abutment 1 displacement as -0.006, 0.003, 0.002, 0.001, and 0.001 increase compared to the preceding year. The extensometer at the bottom location of abutment 2 measured seasonal fluctuation with a zero increase during the first 3 years and a residual displacement of 0.01 inches thereafter as presented in Figure 5.57. The numerical model predicts similar displacements, but a 0.006-inch residual displacement is observed over the simulation period. Both abutment bottom extensometers commonly reported that peak displacements during winter seasons are approximately between late March and early

April, while measured the lowest peak ambient temperature is between late January and late February.

Predicted earth pressures from the numerical model versus observed earth pressures from both top and bottom pressure cells at both abutments 1 and 2 are presented in Figures 5.58 through 5.61. All predicted pressures showed a similar trend as the observed pressures while the top pressure cells at abutment 2 measured a large daily fluctuation (approximately 10 psi) during summers. During winter seasons, both top pressure cells from both abutments 1 and 2 measured approximately 2.5 psi larger backfill pressures despite the approximately 4 ft 7 inches and 5 ft 10 inches shallower placement, respectively. During summers seasons, both top and bottom pressure cells measured similar backfill pressures. However, the numerical model predicts 0.5 and 2.5 psi larger backfill pressure at the top and bottom locations. As shown in Figures 5.58 and 5.60, both pressure cells at the top location from both abutments measured approximately 12.5 psi during bridge expansion while the numerical model represents approximately 10.7 and 12.0 psi of passive backfill pressure. Both bottom pressure cell measurements from both abutments match better with the numerical model prediction during bridge expansion. As shown in Figure 5.59, the bottom pressure cells measured peak mean backfill pressures during summers as 11.0, 12.7, 14.3, 13.9, and 13.9 psi while the numerical model predicts 13.4, 13.6, 13.6, 13.6, and 13.7 psi. As shown in Figure 5.61, the bottom pressure cells measured peak mean backfill pressures during summers as psi while the numerical model predicts 13.2, 13.5, 13.5, 13.6, and 13.7 psi. Overall trend predictions by the numerical model are better for the bottom backfill pressures.

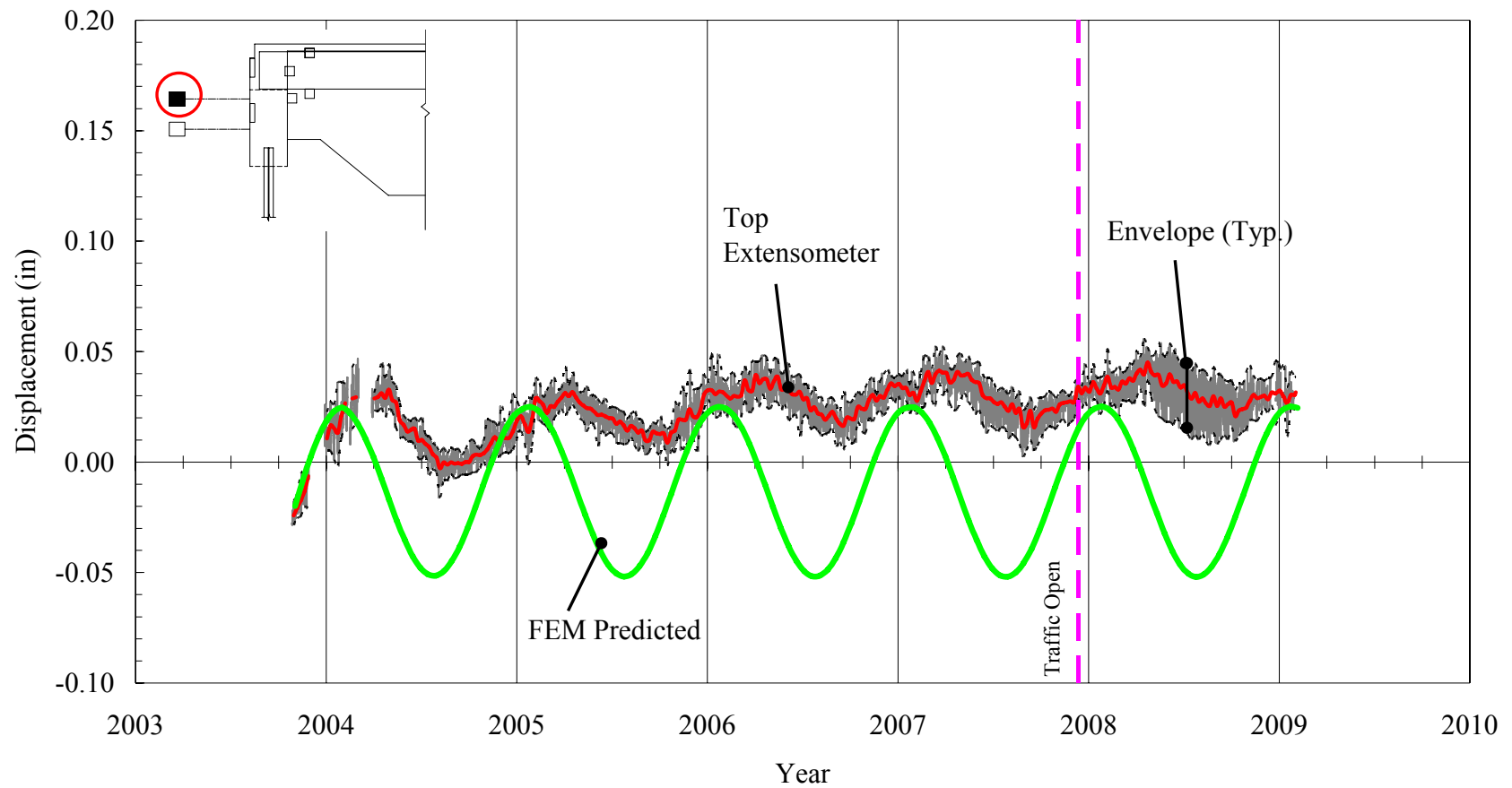


Figure 5.54: Measured and Predicted Bridge 222 Top Extensometer at Abutment 1

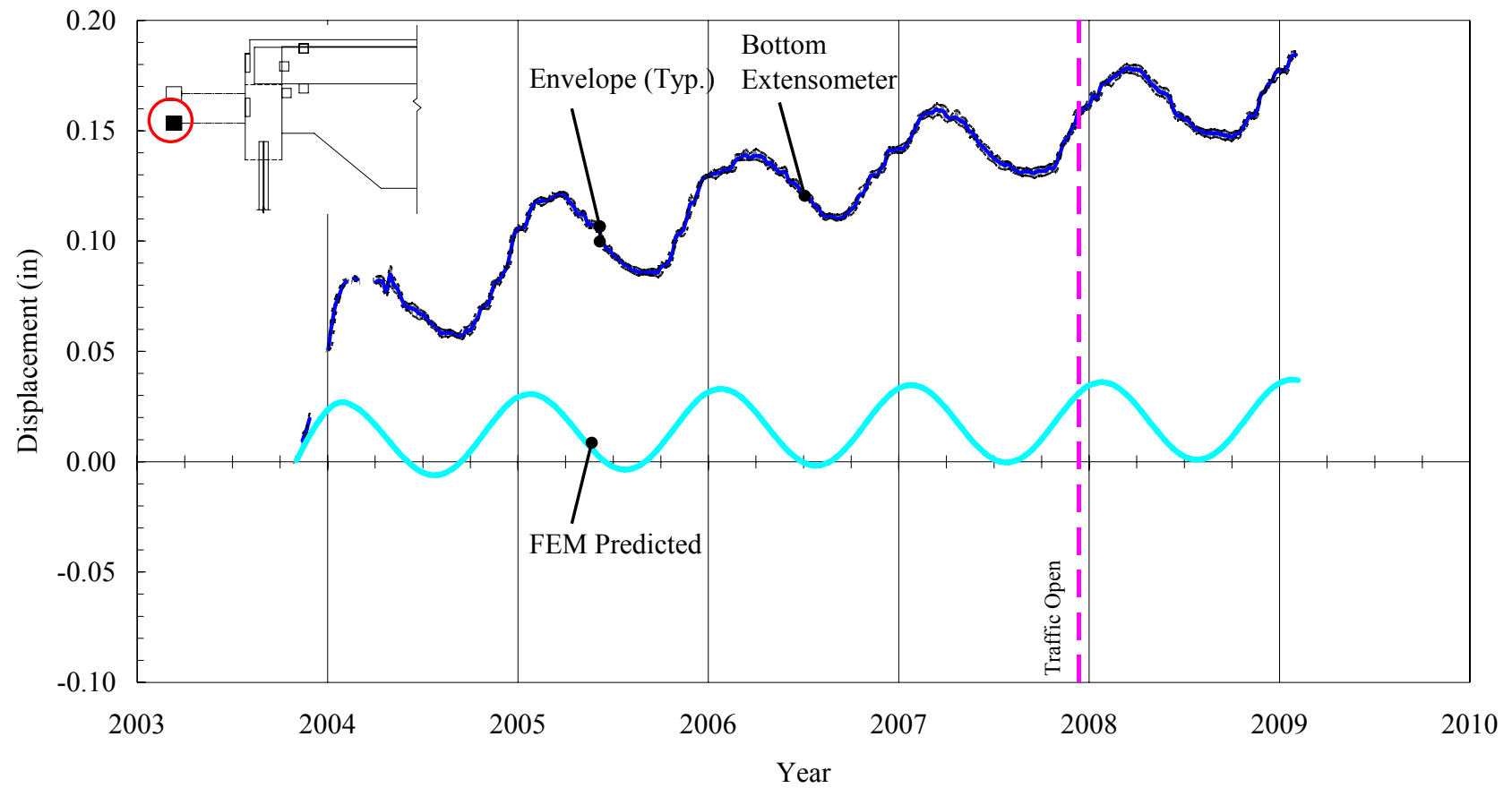


Figure 5.55: Measured and Predicted Bridge 222 Bottom Extensometer at Abutment 1

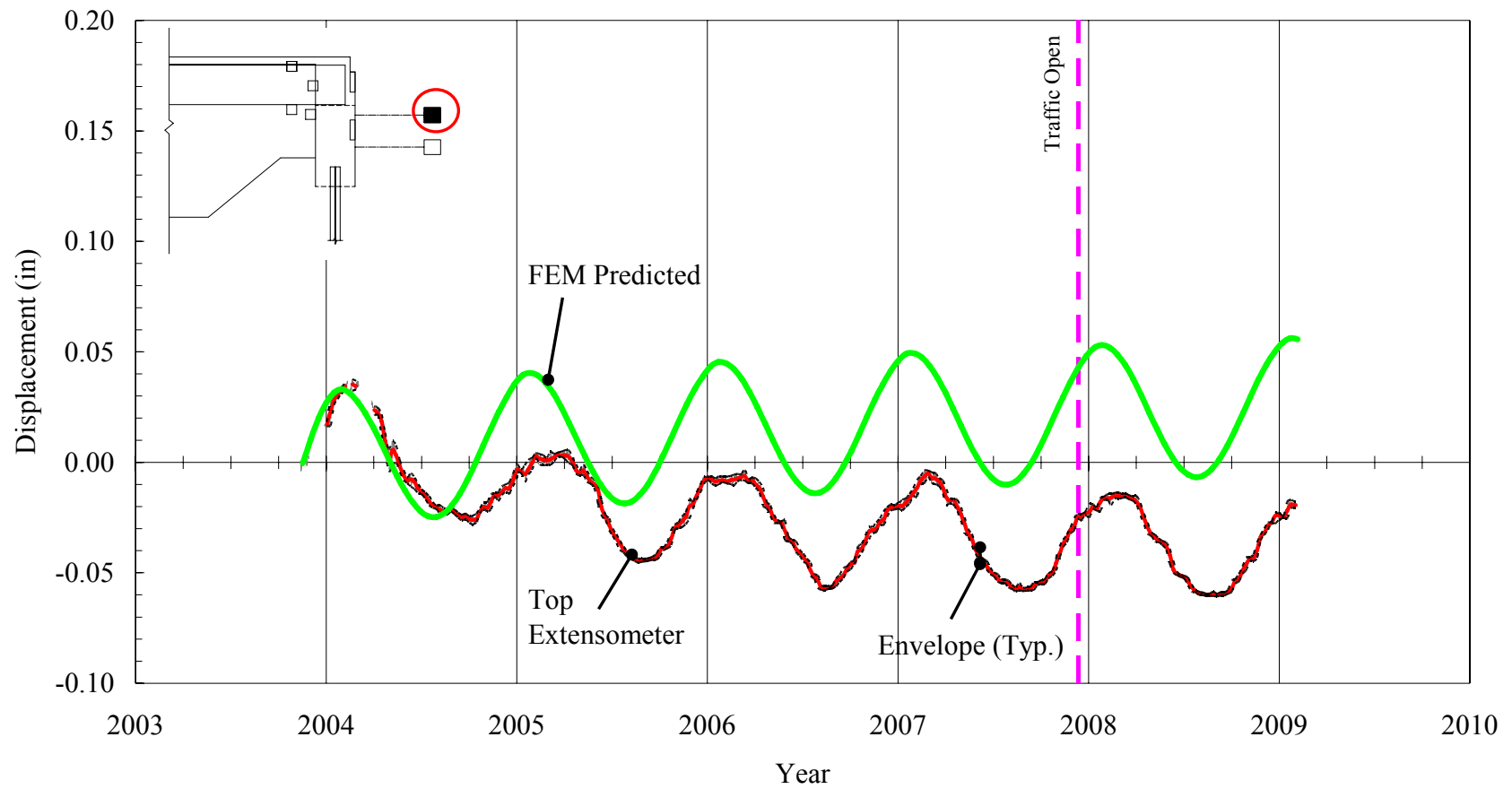


Figure 5.56: Measured and Predicted Bridge 222 Top Extensometer at Abutment 2

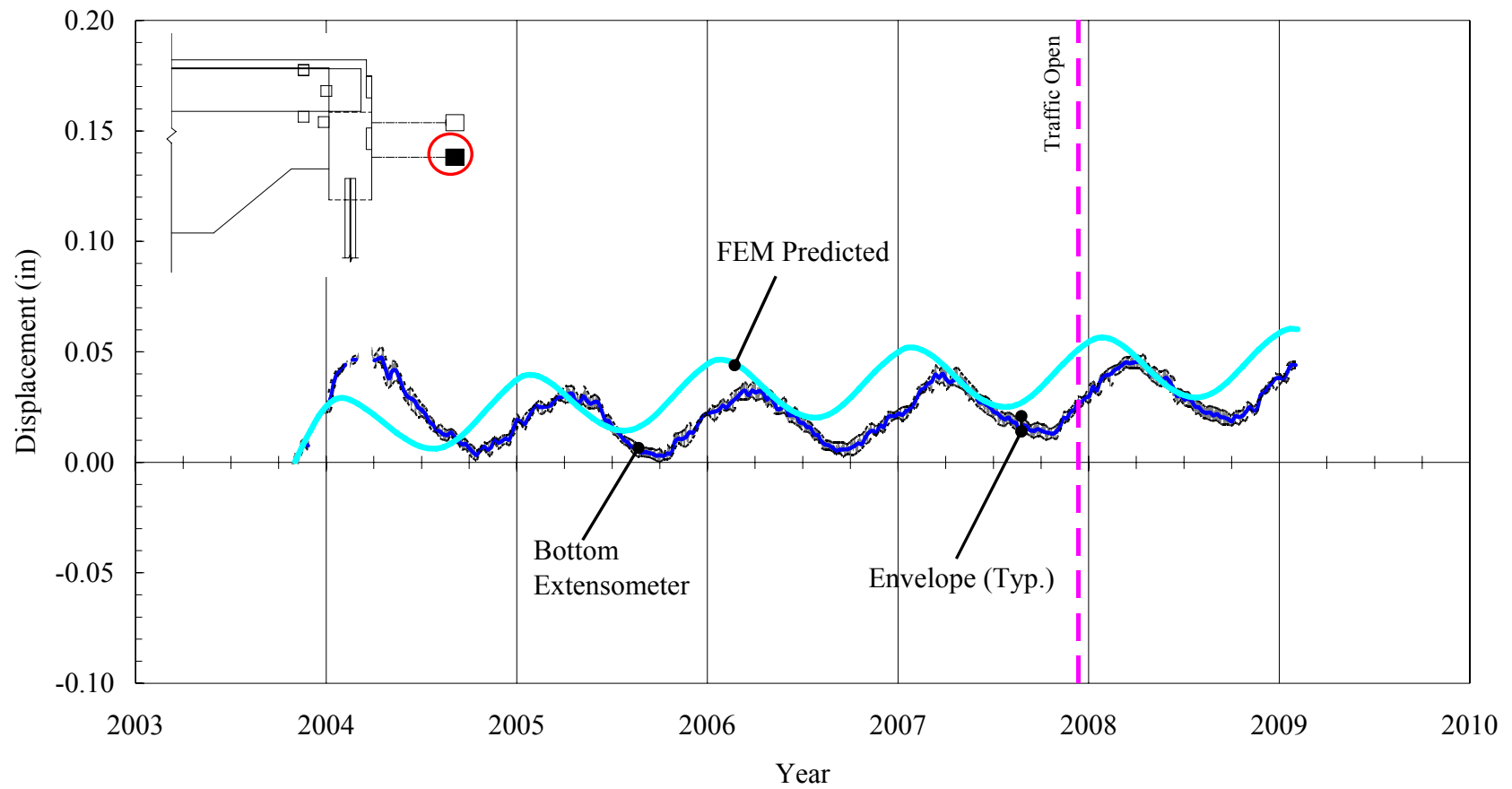


Figure 5.57: Measured and Predicted Bridge 222 Bottom Extensometer at Abutment 2

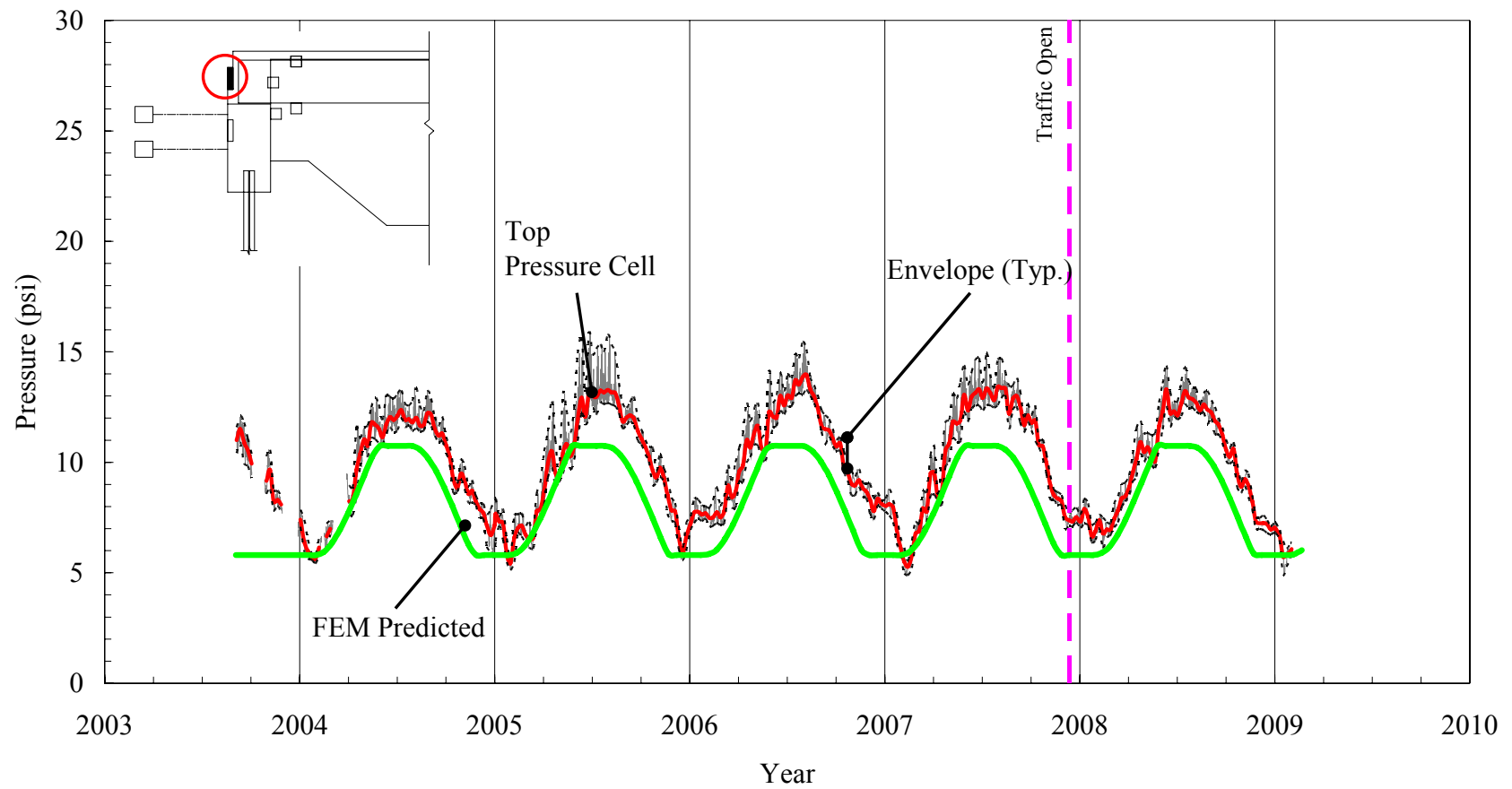


Figure 5.58: Measured and Predicted Bridge 222 Top Pressure Cell at Abutment 1

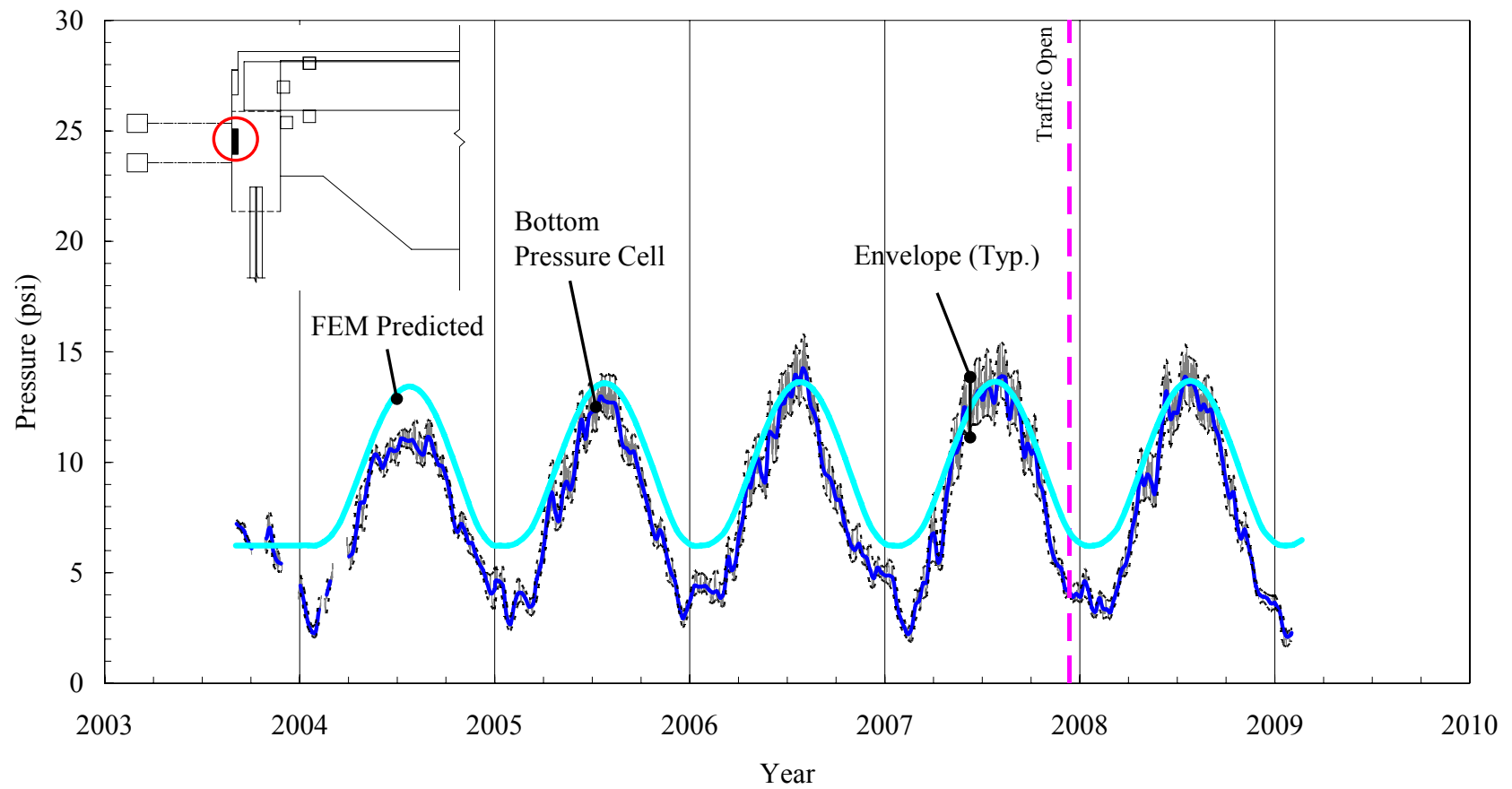


Figure 5.59: Measured and Predicted Bridge 222 Bottom Pressure Cell at Abutment 1

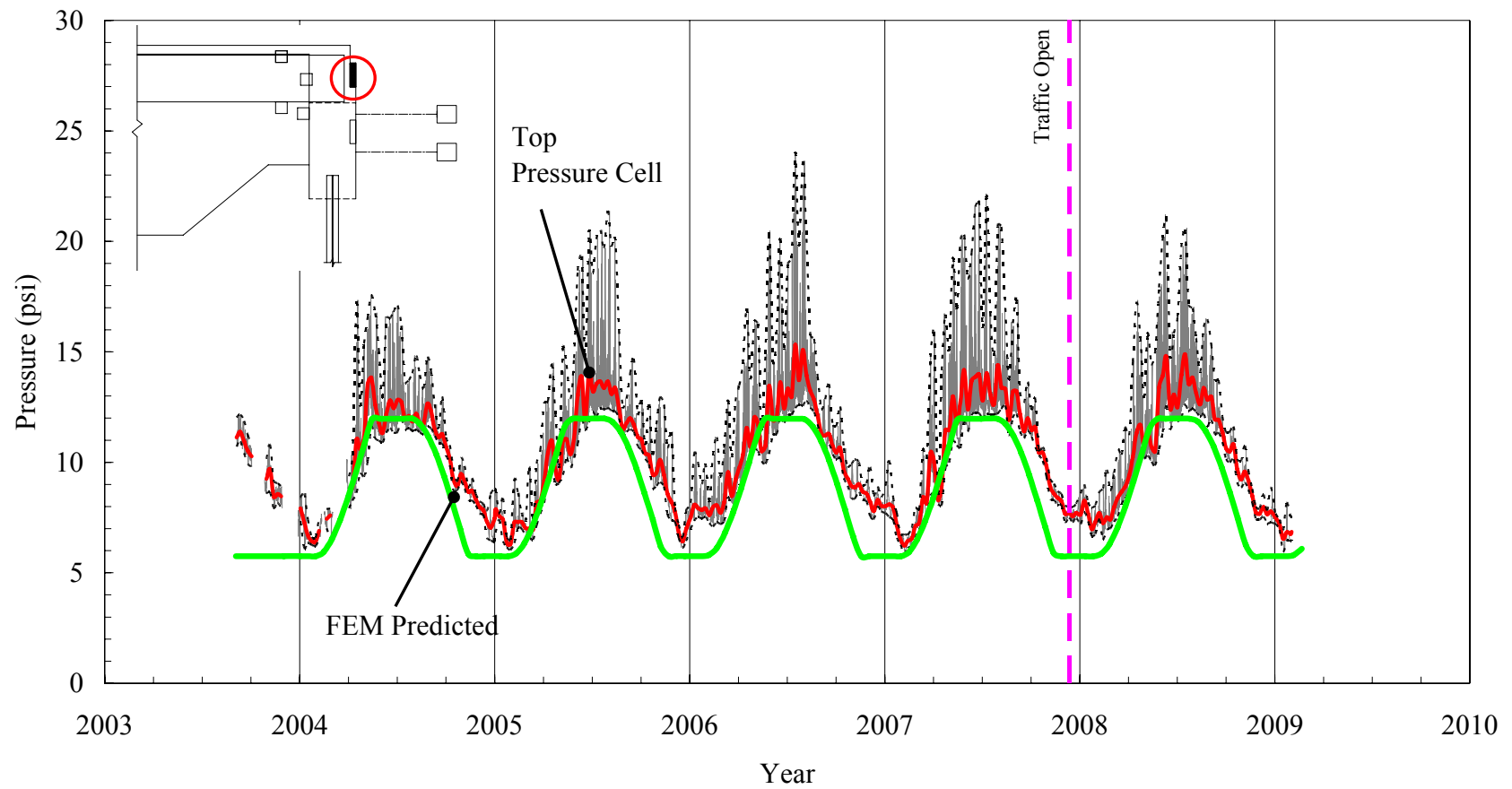


Figure 5.60: Measured and Predicted Bridge 222 Top Pressure Cell at Abutment 2

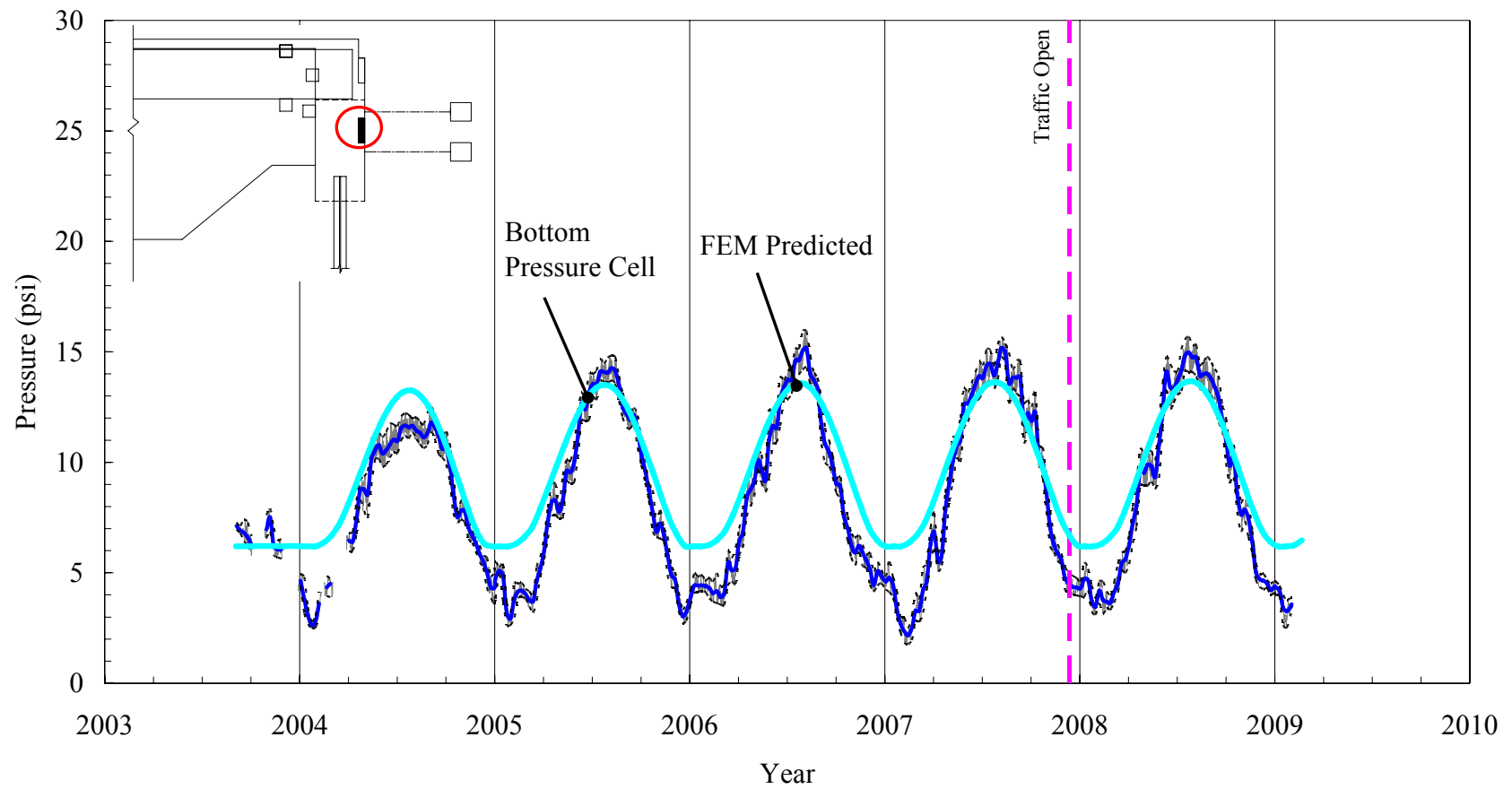


Figure 5.61: Measured and Predicted Bridge 222 Bottom Pressure Cell at Abutment 2

5.6 Concluding Remarks

An accurate numerical modeling methodology was established and numerical models for four instrumented and monitored IABs were constructed. The employed numerical model includes material properties and nonlinear characteristics, temperature load and time-dependent load modeling, and boundary condition modeling of critical bridge components. This study focuses on three key bridge response issues: (1) soil-pile interaction, (2) backfill-abutment interaction, and (3) abutment-backwall joint. The Winkler spring model is used to represent abutment-backfill interaction based on classical Rankine active and passive pressure theory. Soil-pile interaction is modeled utilizing nonlinear p - y curves derived on the basis of American Petroleum Institute (API) (1993) recommendations. The abutment-to-backwall joint, depending on construction, may deform significantly into the inelastic region in the case of long bridges; therefore, the joint was modeled based on moment-rotation characteristics of the joints.

Based on the established numerical modeling methodology, four monitored IABs were modeled and the numerical model response predictions were compared to the measured responses. The established numerical models predicted well the measured responses and were capable of accurately predicting overall IAB behavior and responses over a long-term period.

Chapter 6

Integral Abutment Bridge Parametric Study

6.1 Introduction

Approximate analysis models are a desirable tool for complex design problems where preliminary results are needed to proceed with a more sophisticated analysis. The results of this parametric study formed the basis of an approximate analysis prediction model for IABs. The parametric study is based on the previously presented calibrated numerical models. Base-line numerical models were calibrated against field data in Chapter 5 and previously developed 3D finite element models to increase the accuracy of results.

The parametric study evaluated the effect of four primary parameters based on preliminary analysis: (1) girder material, (2) bridge length, (3) backfill height, and (4) construction joint stiffness between backwall and abutment below girder seats. General parameters that cannot be entirely controlled by bridge designers include: (1) bridge construction timeline, (2) concrete thermal expansion coefficient, (3) backfill stiffness, and (4) pile soil stiffness. Therefore, a parametric study with four parameters results in 72 parametric study cases, and each study case is investigated for both AASHTO extreme bridge expansion and contraction static analyses. Representative values for each of the four parameters were selected and are presented in Table 6.1. The analyses investigated five critical responses: (1) girder axial force, (2) girder bending moment, (3) pile moment, (4) pile lateral force, and (5) pile head displacement.

6.2 Primary Parameters

The four parameters listed in Table 6.1 have been selected based on previous research, IAB monitoring results (Laman *et al.* 2003, 2006), and transportation agency input. The prestressed concrete girder bridge superstructure cross-section selected consists of four or five girders with $f'_c = 8$ ksi and a cast-in-place concrete deck with $f'_c = 4$ ksi (see Figure 6.1). The steel girder bridges have four or five steel plate girders with $F_y = 50$ ksi.

Table 6.1. Primary Parameters and Ranges.

Parameter	Variable
Girder Material	Prestressed Concrete, Steel
Bridge Length (ft)	100, 200, 400, 600
Backfill Height (ft)	10, 15, 20
Construction Joint Stiffness	Min: Hinge; Mean: PennDOT standard (#5@9"); Max: Rigid

Note: total number of parametric study = $2 \times 4 \times 3 \times 3 = 72$ cases

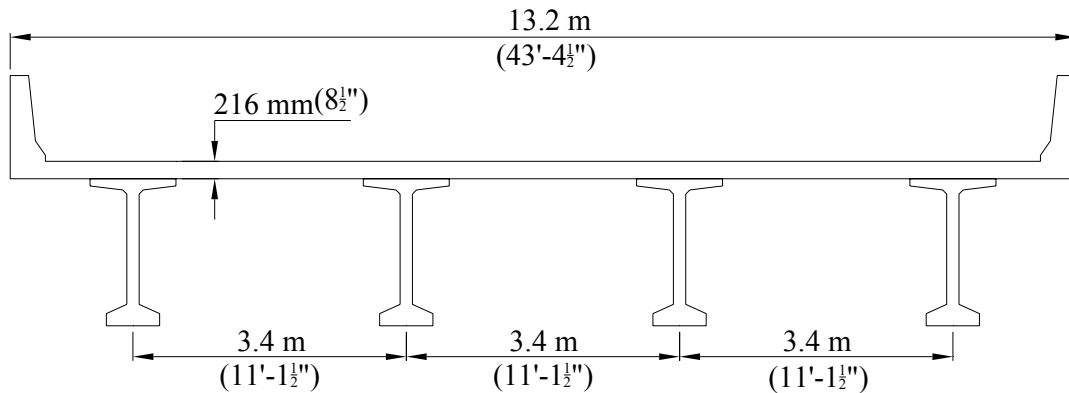


Figure 6.1. Typical Cross-Section for Parametric Study.

6.2.1 Girder Material

Both prestressed concrete and steel plate girders superstructures IAB are commonly constructed. Therefore, the study includes both girder materials to investigate the

influence of girder material on response. Each girder section was designed with respect to the unique bridge dimensions for each parametric case study.

6.2.2 Bridge Length

The two bridge dimensional parameters evaluated in the study are bridge length (L) and abutment backfill height (H). Bridge lengths were selected to represent short to medium length bridges. Based on the selected cross-section, four bridge lengths were considered for both concrete and steel girder bridges in the parametric study. The number of spans depended on bridge length: a single span for a 100-ft bridge, two spans for a 200-ft bridge, three spans for a 400-ft bridge, and four spans for a 600-ft bridge. Table 6.2 presents each bridge girder section dimensions. Each girder section was designed in accordance with *AASHTO LRFD* (2007) and *PCI Bridge Design Manual* (2005).

Table 6.2. Girder Sections and Dimensions for Parametric Study.

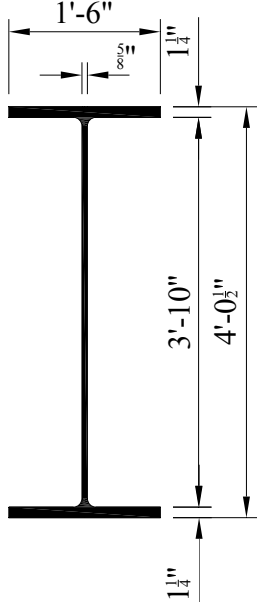
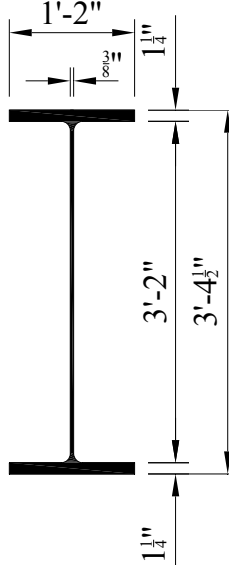
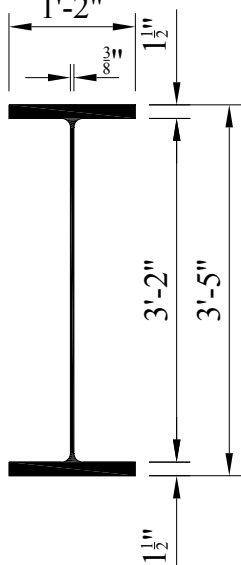
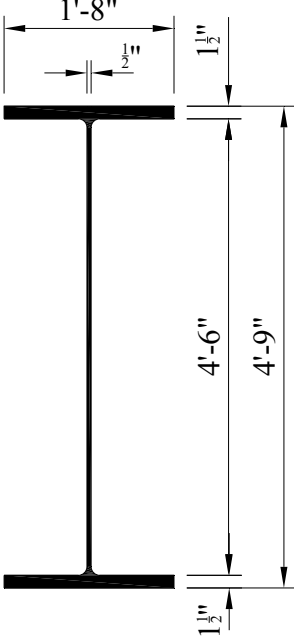
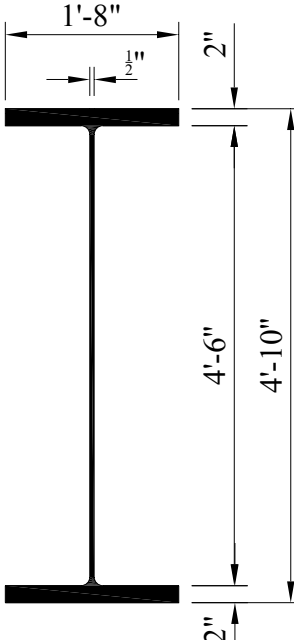
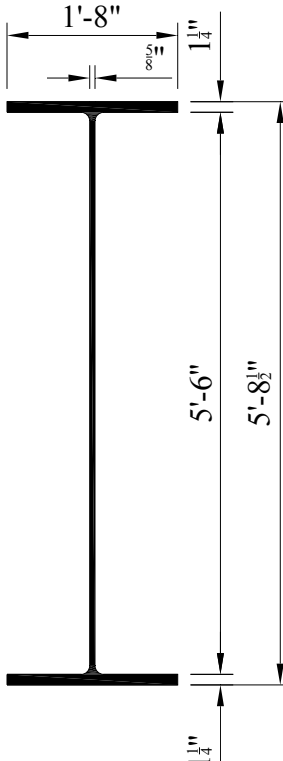
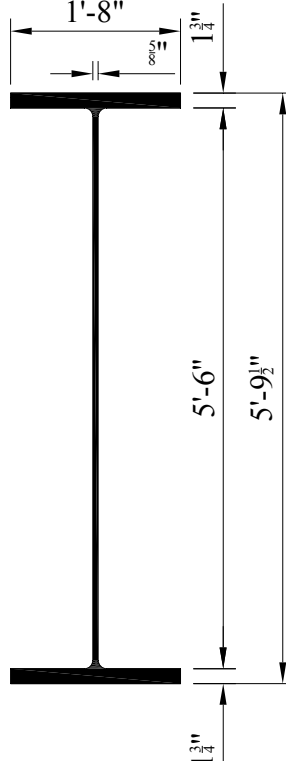
Bridge Type	PS Concrete Girder	Steel Plate Girder	
		Positive Flexure	Negative Flexure
<p>Bridge Length = 100' (Single) Number of Girder = 4 Girder Spacing = 11'-1½"</p>	AASHTO PCI BT72		Not Available
<p>Bridge Length = 200' (100'+100') Number of Girder = 4 Girder Spacing = 11'-1½"</p>	AASHTO PCI BT72		

Table 6.2. Girder Sections and Dimensions for Parametric Study (Cont.).

Bridge Type	PS Concrete Girder	Steel Plate Girder	
		Positive Flexure	Negative Flexure
<p>Bridge Length = 400' (133'+134'+133') Number of Girder = 5 Girder Spacing = 8'-6"</p>	AASHTO PCI BT81		
<p>Bridge Length = 600' (150'+150'+150'+150') Number of Girder = 5 Girder Spacing = 8'-6"</p>	AASHTO PCI BT90		

6.2.3 Backfill Height

A common IAB abutment configuration was adopted consisting of a single row of 13 steel H-piles supporting a cast-in-place wall abutment with $f'_c = 3$ ksi supporting girders and a backwall with $f'_c = 3.5$ ksi. Backfill heights range from short- to medium-high abutments. As presented in Figure 6.2, H represents the total backfill height from the bottom of the abutment/pile cap to the bottom of the approach slab. The roadway elevation was maintained for each IAB, while the abutment below the girder seat height (h_2 in Figure 6.2) varies because of different girder heights (h_1 in Figure 6.2) for different bridge lengths. As a result, the construction joint between backwall and abutment is located at different elevations.

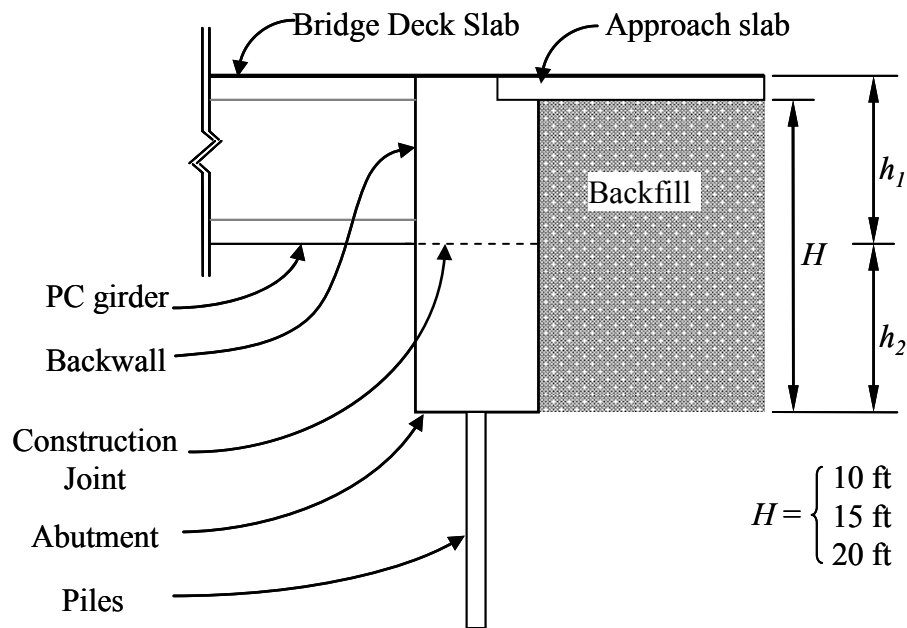


Figure 6.2. Backfill Height Parameter.

6.2.4 Construction Joint Stiffness

The construction joint between abutment and backwall has a significant influence on abutment response and, therefore, has been considered in the study as an important parameter. The specified reinforcement ratio of bars crossing the joint is often very low. PennDOT DM4 uses #5 at 9-inch U-shaped reinforcing bars, resulting in joint reinforcement ratios for the field-tested bridges generally less than 25 percent of the recommended AASHTO minimum reinforcement ratio. A joint with this low reinforcing ratio will permit significant rotation in response to superstructure expansion and contraction. However, the joint is often not modeled in the analysis with the abutment-backwall considered to be a single, rigid element. Field monitoring (Laman *et al.*, 2006) observed differential rotations of the backwall and abutment because of the lack of rotational stiffness in the construction joint. Because of the significance of the construction joint in its influence on IAB behavior, three levels of joints are considered: (1) hinge (free rotation); (2) PA Standard (#5 at 9 inch U-shaped reinforcing bars); and (3) rigid (all translations are restraint).

Construction joint reinforcement details vary from state to state. Most states, however, specify U-shaped steel reinforcing bars as presented in Table 6.3. Table 6.3 presents a survey summary of construction joint reinforcing details from state agencies. Based on the survey results, the U-shape rebar with #5 at 9 inches is a representative construction joint reinforcement.

Table 6.3. Construction Joint Reinforcing Details.

State Agency	U-shape Rebar (Concrete Girder)	Anchor Rod (Steel Girder)	Remarks
IL	(#5 at 12")	N/A	
PA	(#5 at 9")	(#5 at 9")	same rebar details for concrete and steel girder
MA	(#5 at 6")	($\phi 1\frac{1}{2}$ ")	up to 100' span, otherwise design
NJ	(#5 at 12")	use but not specified	
NY	(#5 at 12")	use but not specified	
VA	N/A	($\phi \frac{7}{8}$ " at 12")	Sometimes shear key is used

Rotational moment-curvature relationships for each of the four field-tested bridges were developed as presented in Figure 6.3. The reinforcement detail of all bridges adopted #5 at 9 inches, U-shaped rebar. From the joint and abutment stiffnesses presented in Figure 6.3, it can be observed that the abutment stiffness is approximately two to four times greater than joint strength.

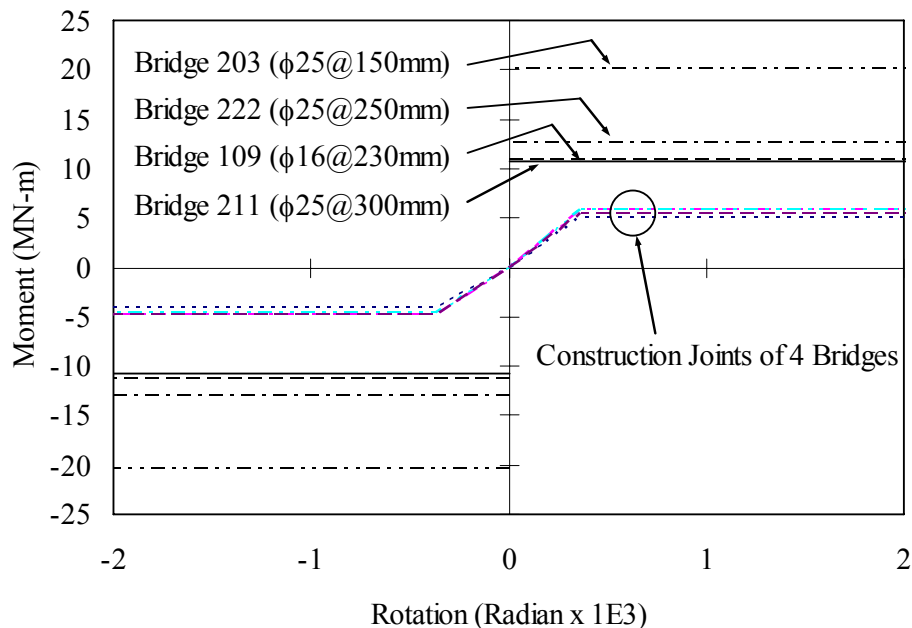


Figure 6.3. Rotational Stiffness of Construction Joints.

6.3 General Parameters

Construction and environmental conditions, which cannot be easily controlled, significantly influence the IAB response. In order to proceed with an IAB analysis over time, an initial time must be established. Environmental loads, soil stiffness, and time-dependent concrete effects must also be evaluated to determine representative magnitudes.

6.3.1 Bridge Construction Timeline

The bridge construction timeline influences IAB behavior due to time-dependent effects inherent in the concrete deck, backwall, and superstructure. Prior to completion of construction, all structural elements are substantially free to undergo creep and shrinkage with no significant effect on the substructure. After the concrete backwall, girders and deck become structurally integrated, the bridge superstructure and substructure become a unit, developing complex frame action resisting vertical loads (dead loads and live loads), as well as horizontal loads (thermal loads, time-dependent effects, and temperature gradients).

The actual construction sequence and concrete cast dates of the four monitored IABs are presented in Table 6.4 and Table 6.5. Cast-in-place concrete deck slabs and backwalls were completed 253 days and 273 days after girder manufacture, respectively. It should be noted that the construction of the monitored bridges was delayed because of unusual construction site problems. However, backwall concrete was consistently placed 20 days after deck slab concrete.

Table 6.4. Deck Placement Date of Field Tested IABs.

Bridge No.	Deck Placement Date	Starting Date (Date of Girder Manufacture)
109	Span 1: 6/6/2006 (487 days) Span 2: 6/6/2006 (238 days) Span 3: 6/20/2006 (252 days) Span 4: 6/20/2006 (501 days)	Span 1&4: approx. 02/05/2005 Span 2&3: approx. 10/12/2005
203	Span 1, 2, 3: 9/17/02 (121 days)	5/20/2002
211	7/20/04 (266 days)	10/29/2003
222	7/16/03 (169 days)	1/29/2003

*Average deck placement: 253 days from girder manufacture date

Table 6.5. Integral Backwall Placement Date of Field Tested IABs.

Bridge	Abutment 1	Abutment 2	Starting Date (from Girder Manufacture)
109	6/29/2006 (510 days)	6/29/2006 (510 days)	Span 1&4: approx. 02/05/2005
203	—	9/19/2002 (123 days)	5/20/2002
211	7/23/2004 (269 days)	8/9/2004 (286 days)	10/29/2003
222	7/24/2003 (177 days)	7/28/2003 (181 days)	1/29/2003

*Average backwall placement: 273 days

*Average gap between abutment 1 and 2: 5 days

The bridge construction timeline adopted for this study is presented in Figure 6.4.

Deck concrete placement lags girder manufacture by 60 to as much as 180 days.

Backwall placement lags deck placement by 10 to as much as 100 days. Deck and

backwall placement are generally the last components completed; therefore, it is assumed that deck concrete is placed 100 days after girder manufacture and the backwall is placed 20 days after the deck placement.

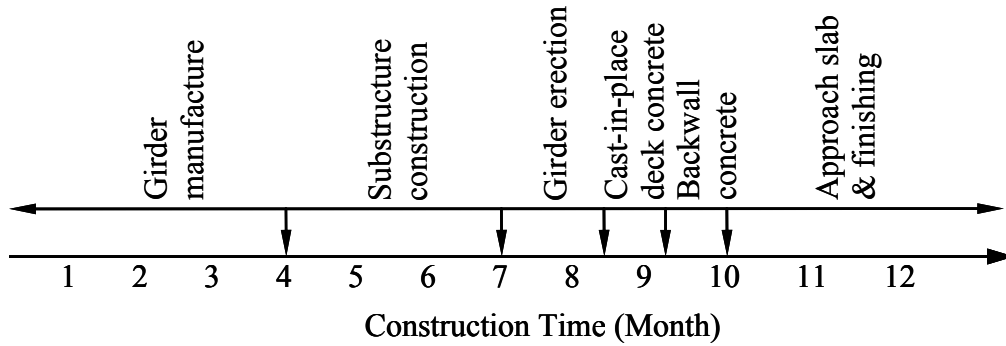


Figure 6.4. Typical Bridge Construction Timeline.

6.3.2 Thermal Expansion Coefficient

The thermal expansion coefficient, α , directly influences superstructure strain in response to concrete temperature changes. Estimates of α vary significantly because of variations in concrete mix properties, aggregate properties and proportions, water-to-cement ratio, relative humidity, age of concrete, and other factors. Table 6.6 presents six sources for the determination of α . When test data are not available, AASHTO LRFD (2007) recommends $6.0 \times 10^{-6}/^{\circ}\text{F}$ with a range of 3 to $8 \times 10^{-6}/^{\circ}\text{F}$. However, the AASHTO recommendation is conservative compared to other research findings. Nilson (1991) reported that α generally varies from 4 to $7 \times 10^{-6}/^{\circ}\text{F}$. Based on over 200 sources, Oesterle *et al.* (1998) reported a mean of $4.87 \times 10^{-6}/^{\circ}\text{F}$ and a range of 2.3 to $8.1 \times 10^{-6}/^{\circ}\text{F}$. Tanesi *et al.* (2007) reported a mean thermal expansion coefficient of $5.54 \times 10^{-6}/^{\circ}\text{F}$. Therefore, the present study has selected α as $5.5 \times 10^{-6}/^{\circ}\text{F}$ for concrete and $6.5 \times 10^{-6}/^{\circ}\text{F}$ for steel.

Table 6.6. Variation of Concrete Thermal Expansion Coefficient.

Source	Thermal Expansion Coefficient, $\times 10^{-6}/^{\circ}\text{F}$		
	Lower Bound	Mean	Upper Bound
AASHTO LRFD	3.0	6.0	8.0
Kada <i>et al.</i> (2002)	3.6	-	4.2
Oesterle <i>et al.</i> (1998)	2.26	4.87	7.49
Nison (1991)	4.0	-	7.0
Russell <i>et al.</i> (2006)	4.52	6.32	8.76
Tanesi <i>et al.</i> (2007)	4.71	5.54	6.50

6.3.3 Backfill Stiffness

Backfill materials and associated stiffness are also evaluated in the parametric study. Typical backfill soil properties were investigated and are presented in Table 6.7. Density and friction angle of backfill soils of the four monitored bridges are all the same compacted PennDOT No. OGS aggregates.

Table 6.7. Backfill Properties

Property	PennDOT No. OGS Backfill
Density (ρ), pcf	119
Angle of friction (ϕ_f), degree	34
Subgrade Modulus (K_h), pci	43.8

Backfill pressure and abutment displacement measurements taken from the four monitored bridges were analyzed to determine the subgrade modulus. Based on the extensive data available from each bridge for each year of monitoring, a line was fitted as shown in Figure 6.5. The slopes of the fitted lines (subgrade modulus) of each bridge,

then, were averaged to obtain a representative subgrade modulus. The results are presented in Figure 6.6.

The bridge 222 subgrade modulus is significantly larger than the other three bridges despite identical backfill material specifications. This abnormality may be attributed to the short bridge 222 length, very small abutment displacement, and high water table susceptible to freeze-thaw. Therefore, the subgrade modulus of bridge 222 was excluded from the calculation of the representative subgrade modulus.

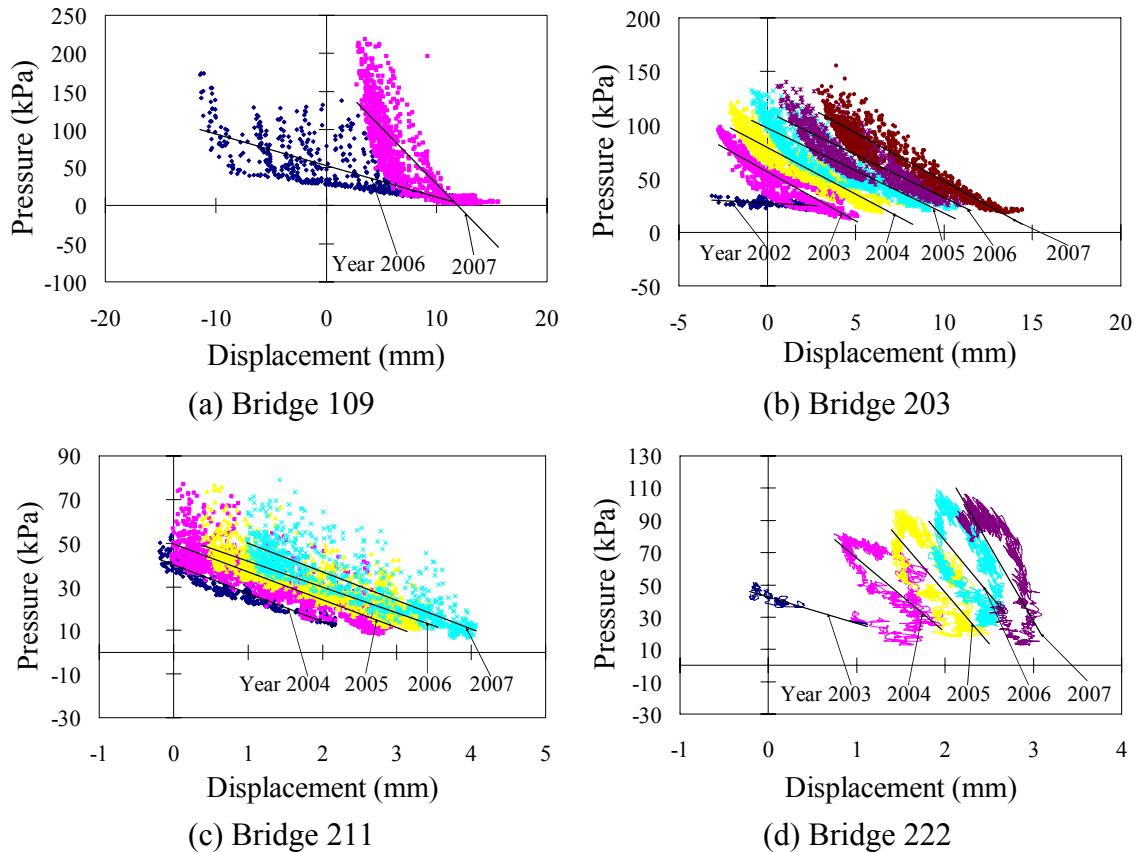


Figure 6.5. Backfill Pressure Versus Abutment Displacement.

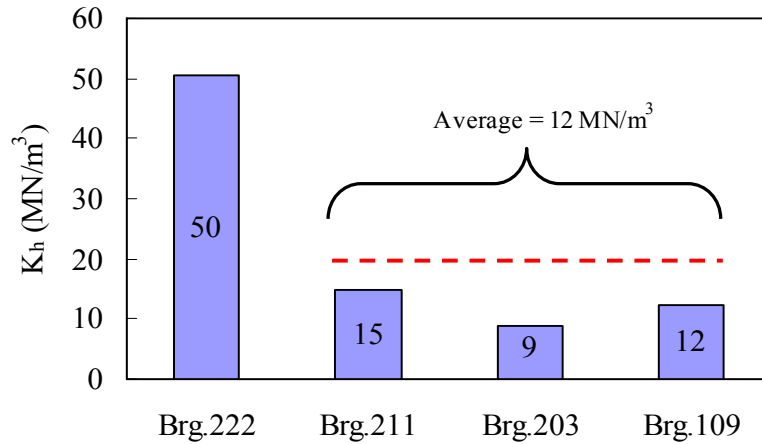


Figure 6.6. Subgrade Modulus of Monitored Bridges.

6.3.4 Pile Soil Stiffness

The present study considered soil properties for soil-pile interaction characteristics. A total of 13 HP12×74, $F_y = 50$ ksi piles were used for the parametric study. Soil strata properties under abutment 2 of bridge 211 was selected as representative (see Figure 6.7).

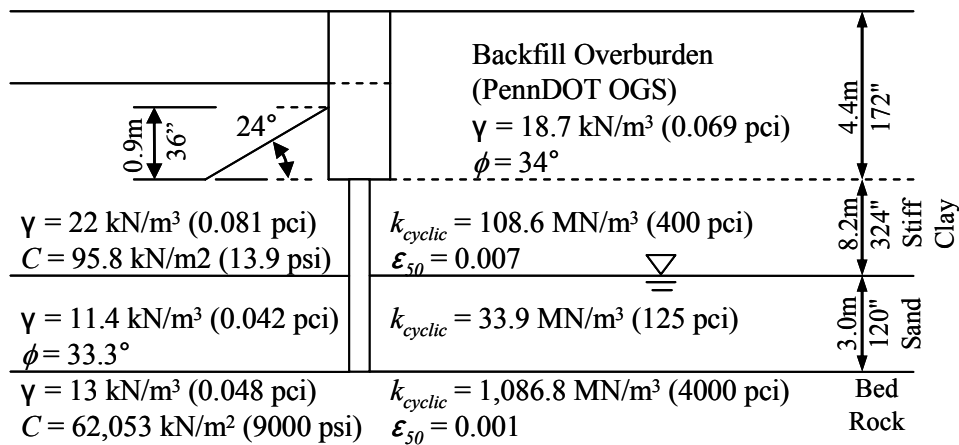


Figure 6.7. Soil Properties under Bridge 211 Abutment 1.

6.4 Description of Numerical Models

The 3D numerical modeling methodology employed in Chapter 5 to predict behavior and response of instrumented IABs is also utilized in a parametric study. The models include the critical aspects of behavior including soil-structure interaction and abutment-backwall joint behavior. Soil-structure interaction is distinguished by two components: soil-pile interaction and backfill-abutment interaction. A linear Winkler spring, within the range of the upper and lower bound defined by the passive and active failure limit, simulates backfill-abutment interaction. For soil-pile interaction, a family of Winkler springs based on American Petroleum Institute (API) (1993) p - y curves is used. The abutment-to-backwall joint, depending on construction, may deform significantly into the inelastic region in the case of long bridges; therefore, the joint was modeled based on #5 bars at 9-inch details and moment-rotation characteristics of the joints.

Bridge loads include backfill pressure, time-dependent effects, temperature load, and temperature gradient load. Backfill pressure applied to abutments is the traditional, linearly varying distribution with depth. Time-dependent effects consist of concrete creep, shrinkage, and prestressing steel relaxation that are implemented using an equivalent temperature method and the age-adjusted effective modulus method (AAEM). The temperature gradient of the superstructure is modeled as an equivalent linear variation along the depth because of modeling limitations to represent the complex variation recommended by AASHTO LRFD (2007).

6.5 Parametric Study Results

The parametric study encompasses practical ranges of key parameters with results presented in this section. Bridge response of girder axial force, girder bending moment, pile moment, pile lateral force and pile head displacement is discussed with respect to four parameters: (1) girder material, (2) construction joint stiffness, (3) backfill height (H), and (4) bridge length (L).

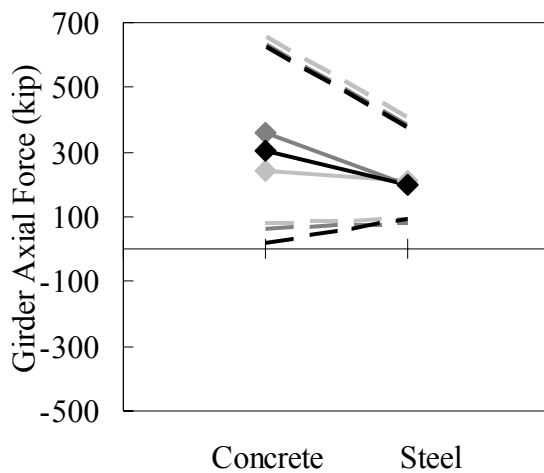
6.5.1 Girder Axial Force

Girder axial force with respect to girder material, construction joint stiffness, backfill height, and bridge length is presented for both bridge expansion and contraction in Figures 6.8 through 6.15. Due to time-dependent effects, prestressed concrete girder IABs experience larger girder tensile axial forces during bridge contraction (see Figures 6.8 and 6.9). Overall, the influence of a flexible construction joint on girder tensile and compressive axial force does not follow a distinct trend. As the construction joint becomes stiffer, both girder tensile force during bridge contraction and compressive axial force during bridge expansion increase (see Figures 6.10 and 6.11).

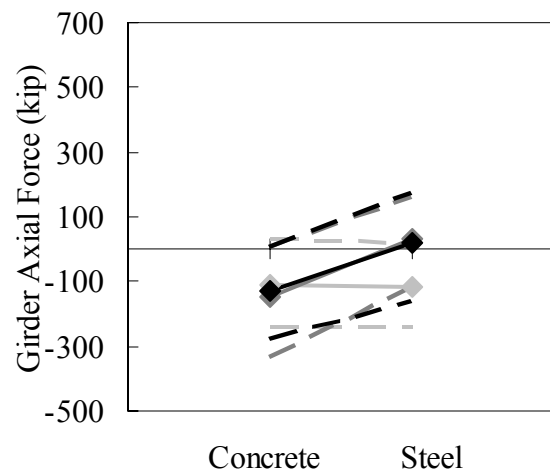
As backfill height increases, girder tensile axial force decreases during contraction (see Figures 6.12 and 6.13). Girder tensile axial force during bridge expansion and girder compressive axial force during bridge contraction are not significantly influenced by backfill height. However, as backfill height increases, girder compressive axial force increases under a given expansion.

Both girder tensile and compressive axial forces change as bridge length increases (see Figures 6.14 and 6.15). However, a clear trend cannot be observed. For prestressed

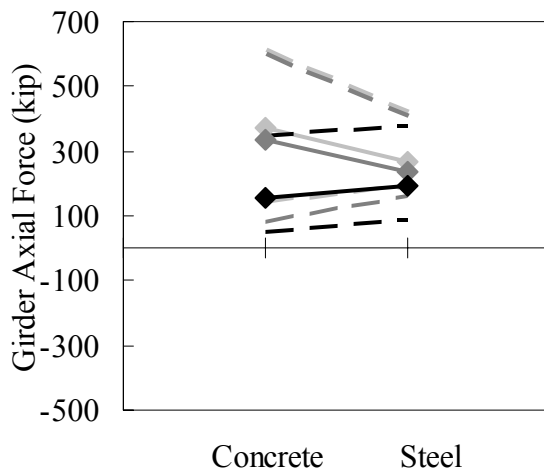
concrete, a 200-ft-long bridge experiences the largest tensile axial force and a 400-ft-long bridge experiences the largest compressive axial force. For steel girder bridges, a 400-ft-long bridge experiences the largest tensile and compressive axial forces. Overall, girder axial force tends to increase for lengths up to 400-ft, but a 600-ft bridge will experience a smaller girder axial force than 400-ft bridges. Girder axial force is most strongly related to bridge length, and the responses within the parametric study exhibit the least variability.



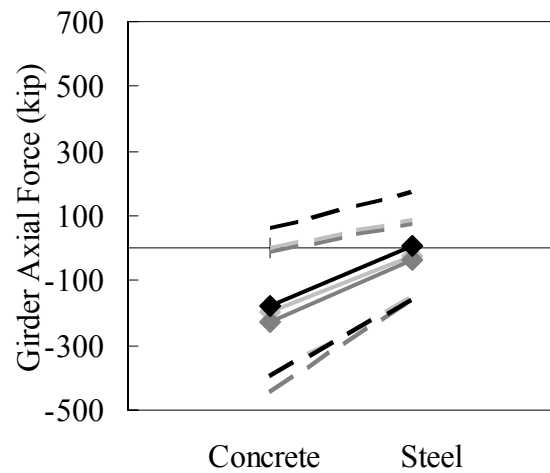
(a) Hinge and Bridge Contraction



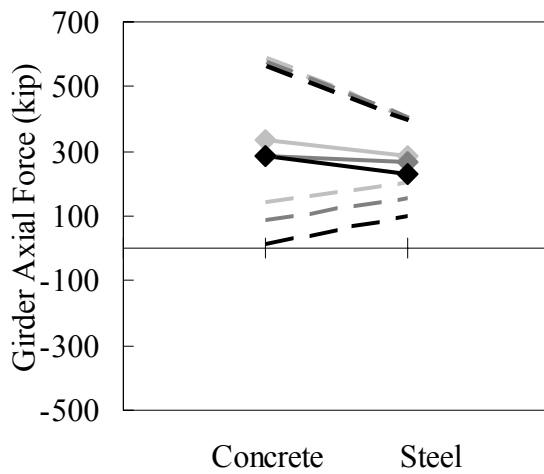
(b) Hinge and Bridge Expansion



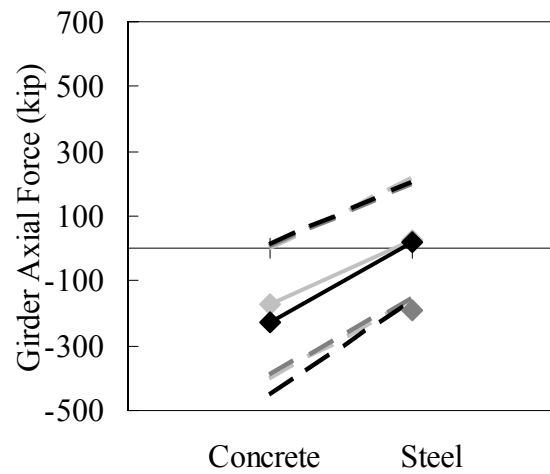
(c) PA Standard and Bridge Contraction



(d) PA Standard and Bridge Expansion

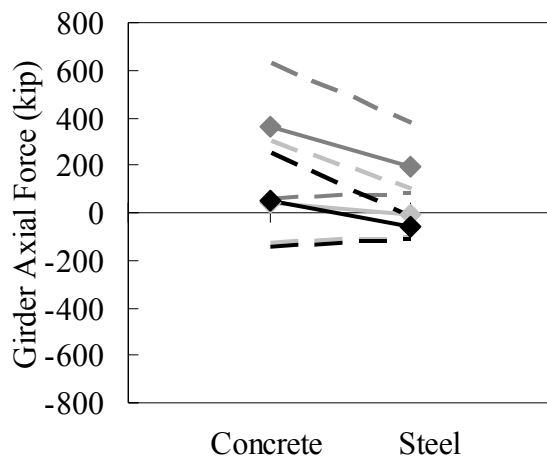


(e) Rigid and Bridge Contraction

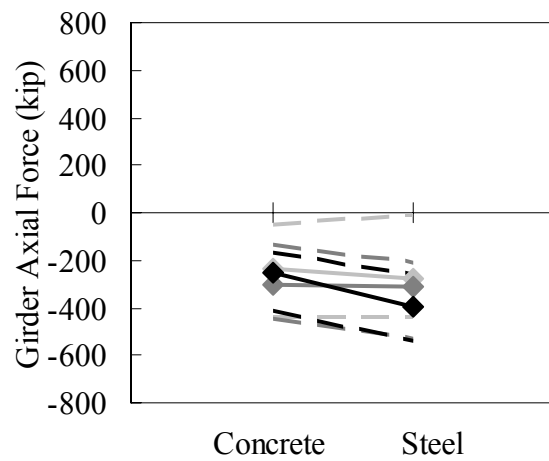


(f) Rigid and Bridge Expansion

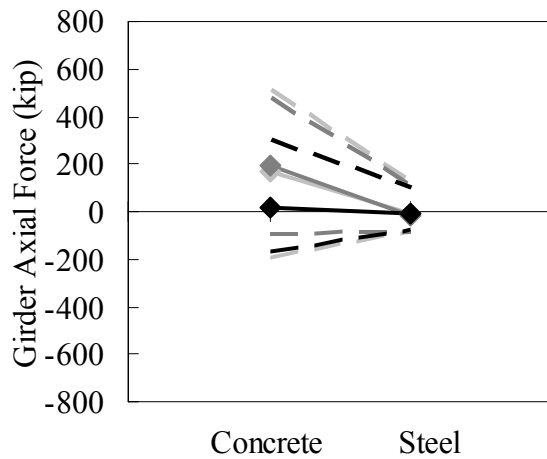
Figure 6.8: Girder Material Influence on Girder Tensile Axial Force
(\diamond : H = 10 ft; \blacklozenge : H = 15 ft; \blacklozenge : H = 20 ft; - - : Envelopes)



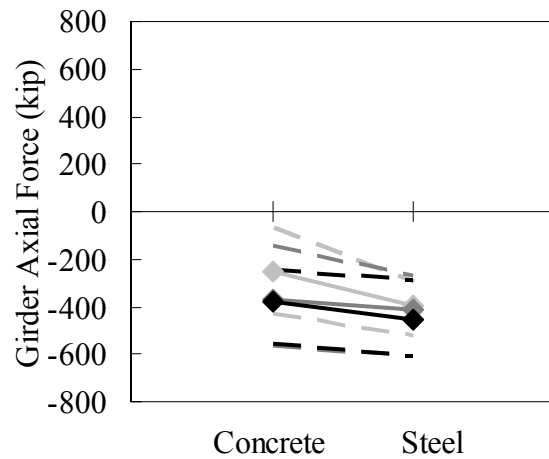
(a) Hinge and Bridge Contraction



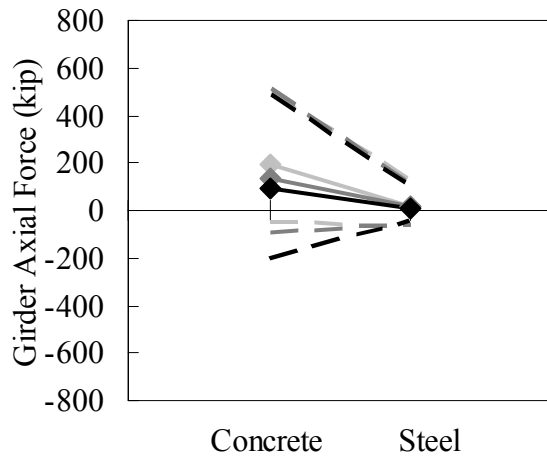
(b) Hinge and Bridge Expansion



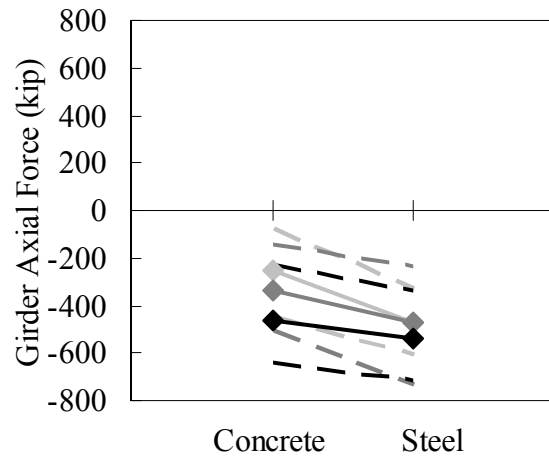
(c) PA Standard and Bridge Contraction



(d) PA Standard and Bridge Expansion

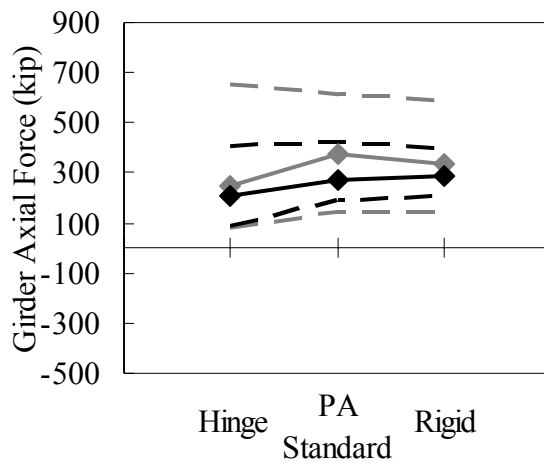


(e) Rigid and Bridge Contraction

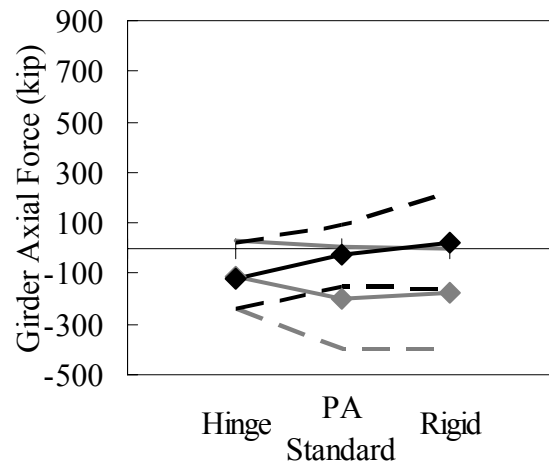


(f) Rigid and Bridge Expansion

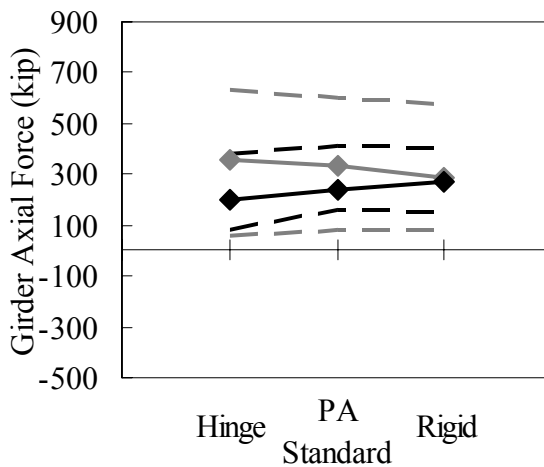
Figure 6.9: Girder Material Influence on Girder Compressive Axial Force
(—◆— : H = 10 ft; —◆— : H = 15 ft; —◆— : H = 20 ft; - - : Envelopes)



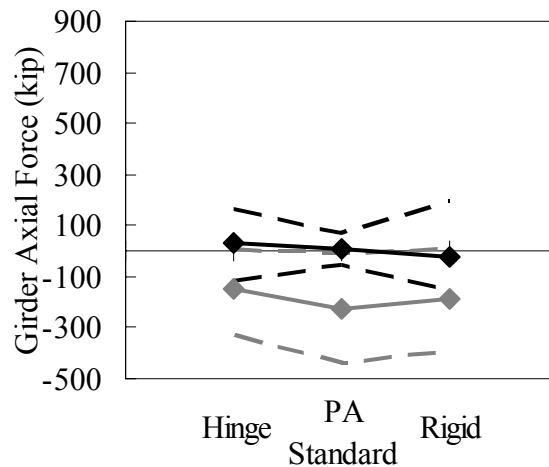
(a) $H = 10$ ft and Bridge Contraction



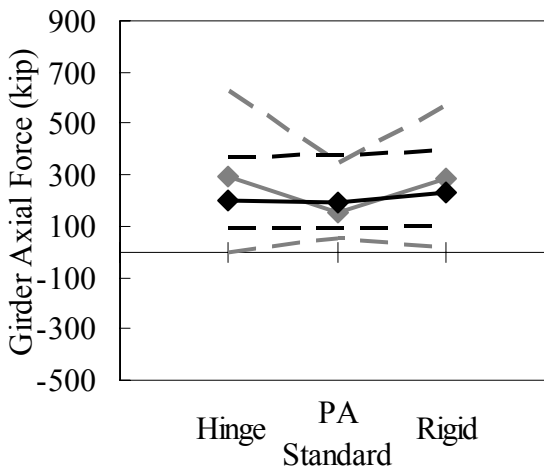
(b) $H = 10$ ft and Bridge Expansion



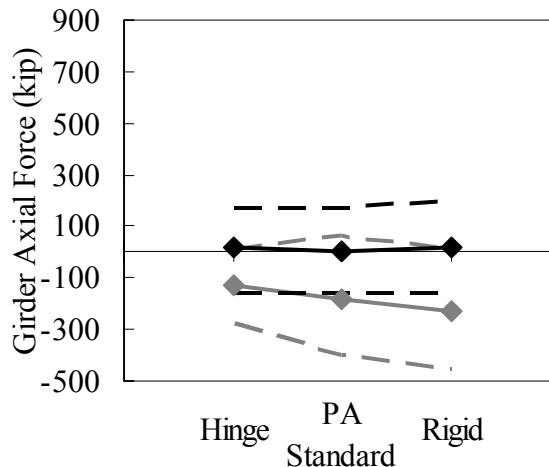
(c) $H = 15$ ft and Bridge Contraction



(d) $H = 15$ ft and Bridge Expansion

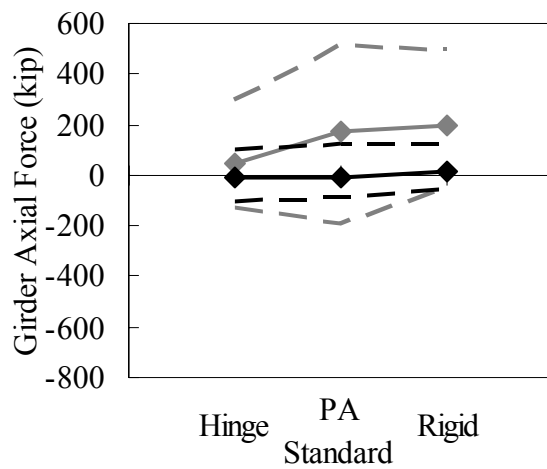


(e) $H = 20$ ft and Bridge Contraction

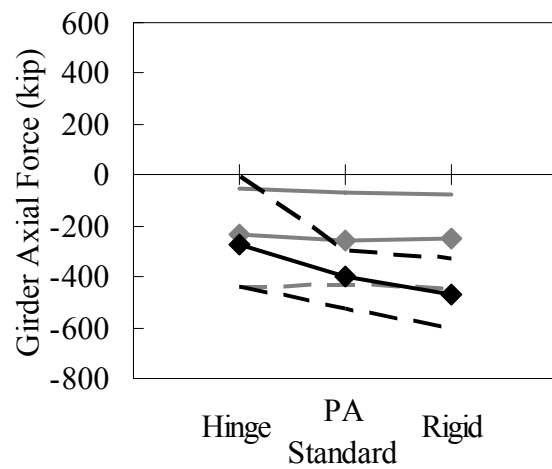


(f) $H = 20$ ft and Bridge Expansion

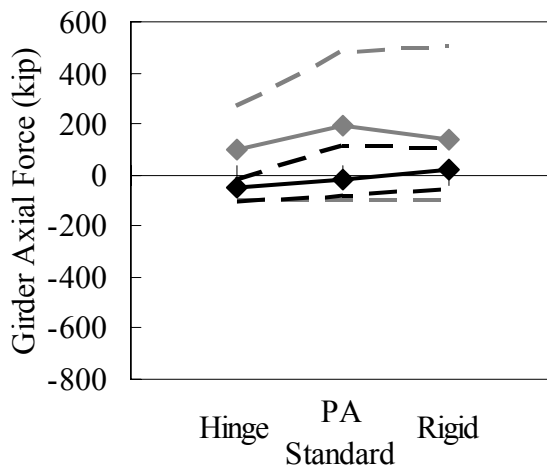
Figure 6.10: Construction Joint Stiffness Influence on Girder Tensile Axial Force
(—◆— : Steel Girder; —◆— : Concrete Girder; - - : Envelopes)



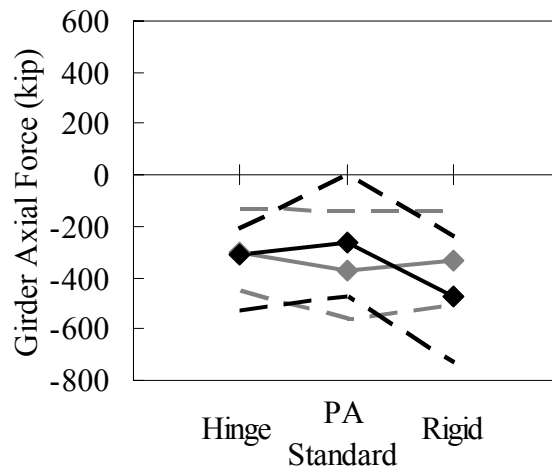
(a) $H = 10$ ft and Bridge Contraction



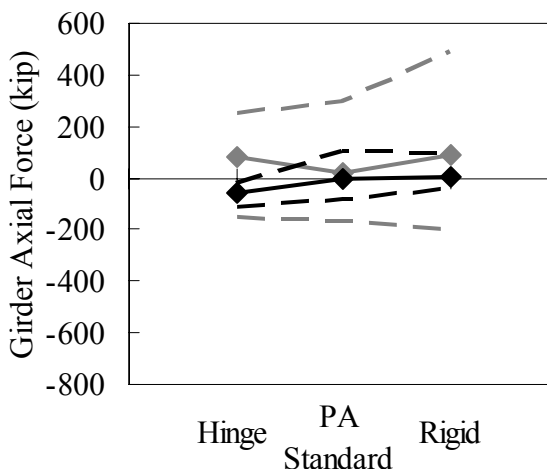
(b) $H = 10$ ft and Bridge Expansion



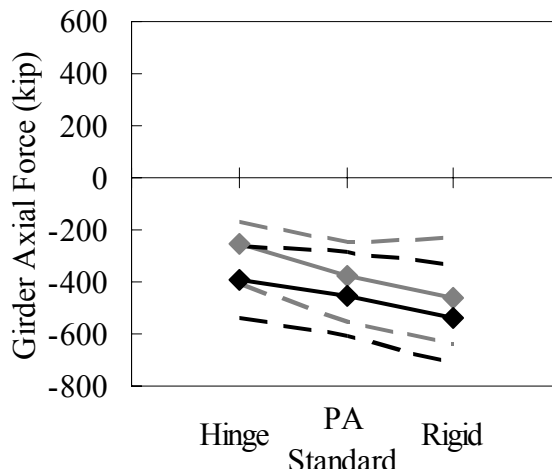
(c) $H = 15$ ft and Bridge Contraction



(d) $H = 15$ ft and Bridge Expansion

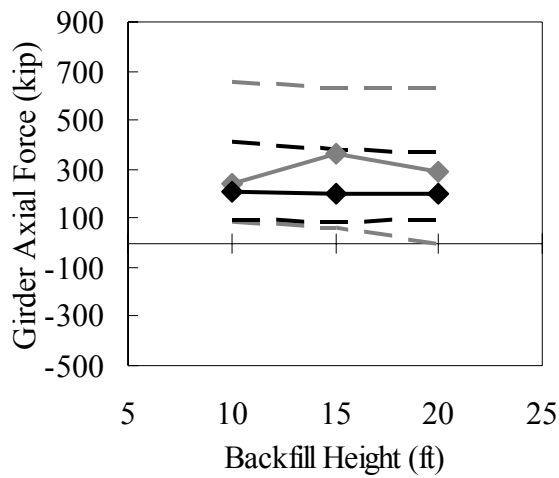


(e) $H = 20$ ft and Bridge Contraction

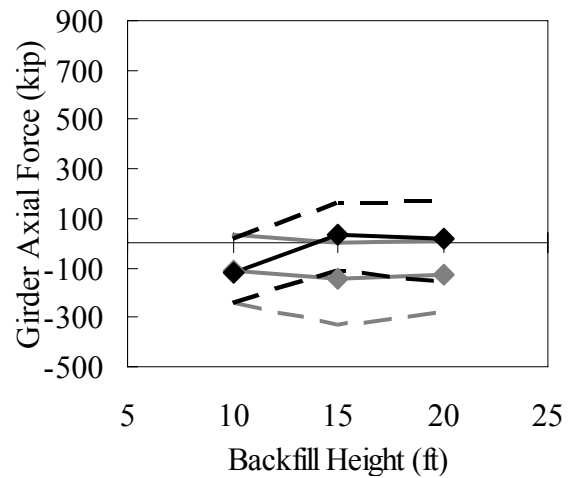


(f) $H = 20$ ft and Bridge Expansion

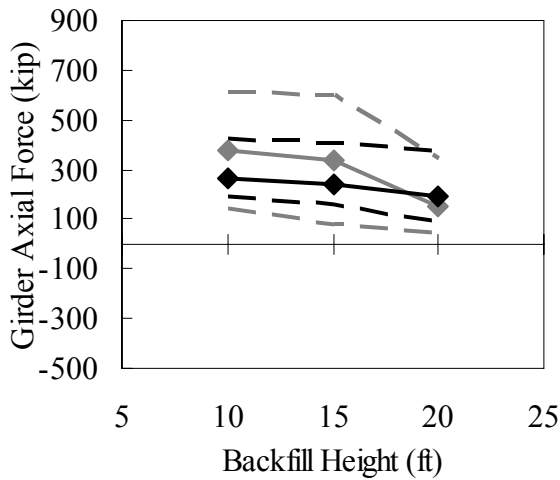
Figure 6.11: Construction Joint Stiffness Influence on Girder Compressive Axial Force
(—◆— : Steel Girder; —◆— : Concrete Girder; - - : Envelopes)



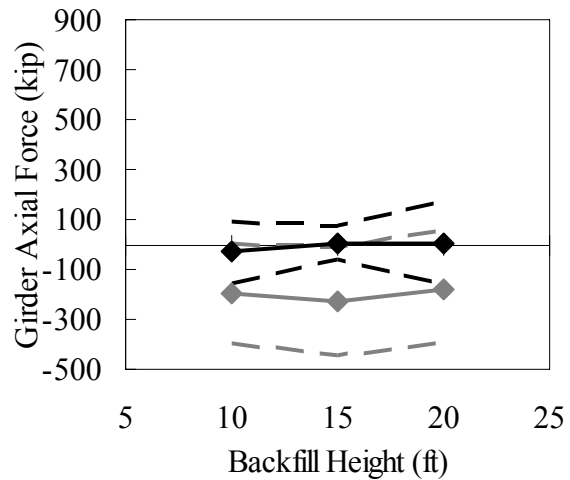
(a) Hinge and Bridge Contraction



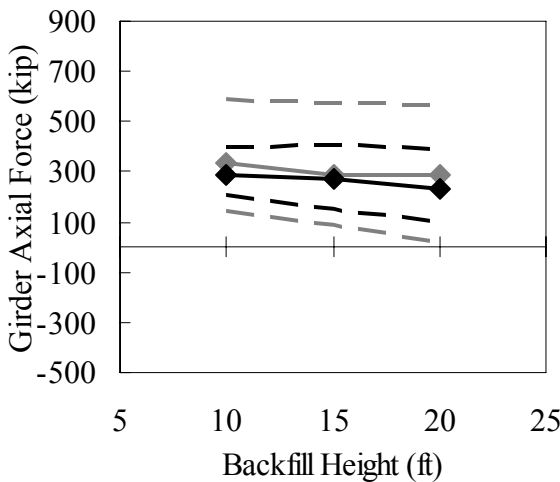
(b) Hinge and Bridge Expansion



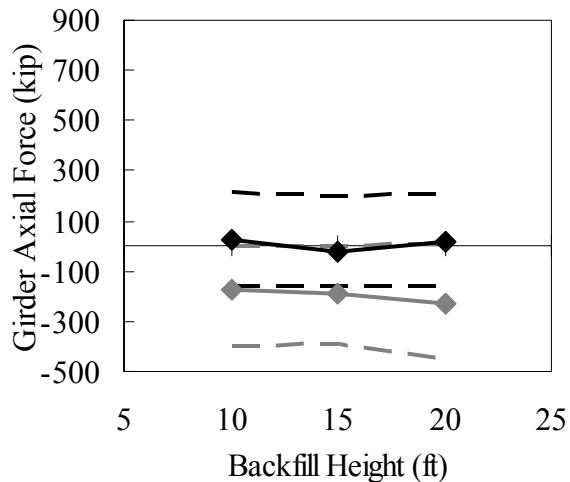
(c) PA Standard and Bridge Contraction



(d) PA Standard and Bridge Expansion

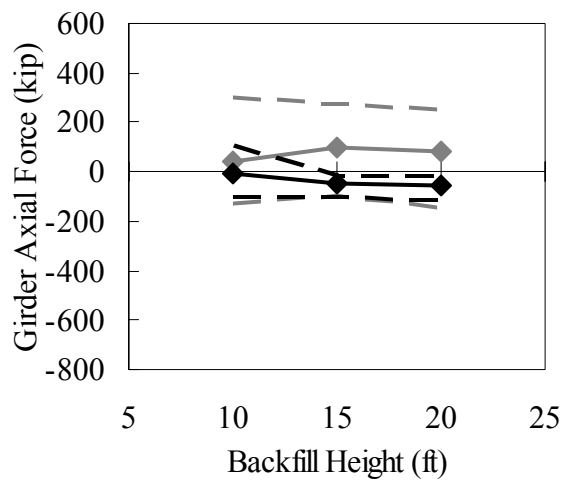


(e) Rigid and Bridge Contraction

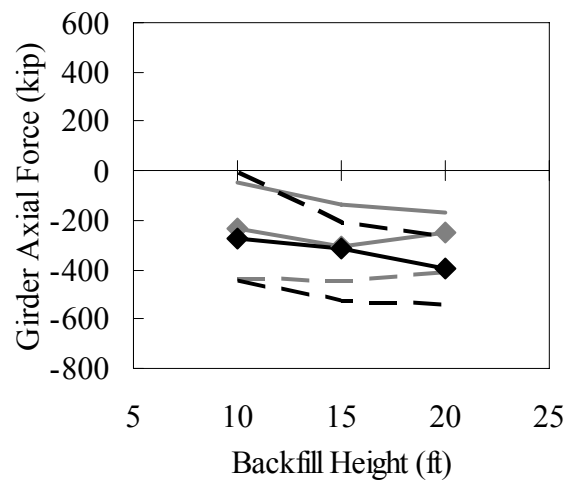


(f) Rigid and Bridge Expansion

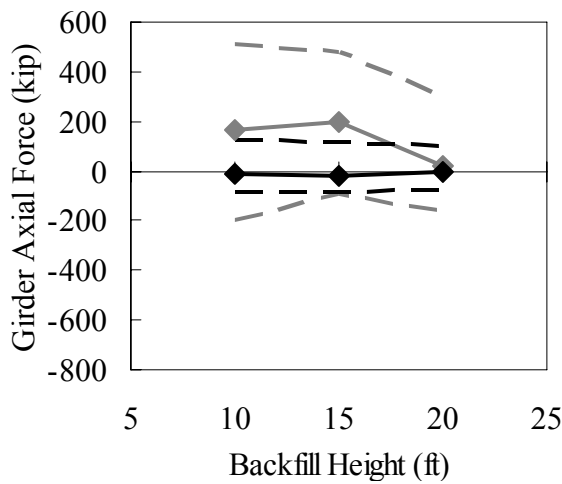
Figure 6.12: Backfill Height Influence on Girder Tensile Axial Force
(—◆— : Steel Girder; —◆— : Concrete Girder; - - : Envelopes)



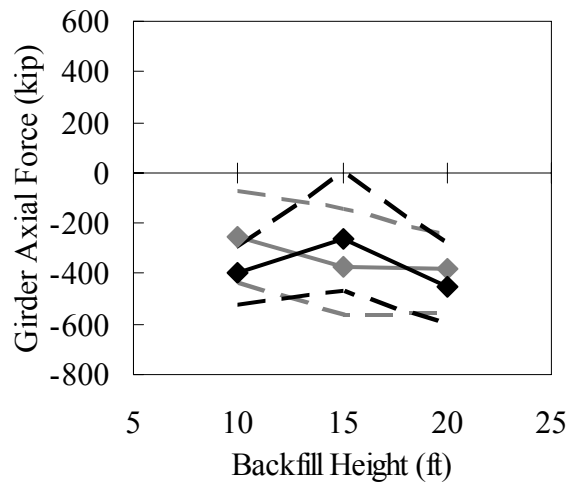
(a) Hinge and Bridge Contraction



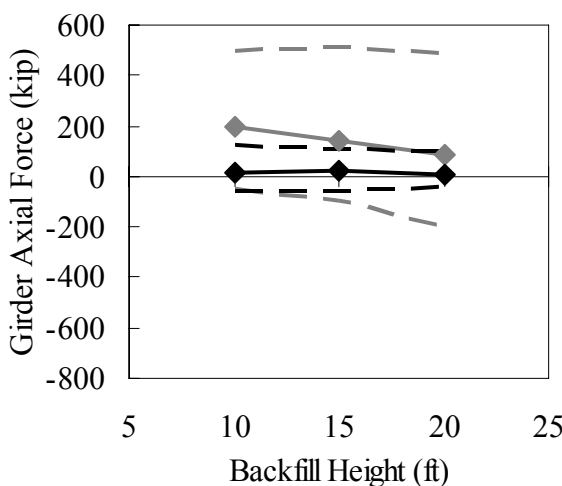
(b) Hinge and Bridge Expansion



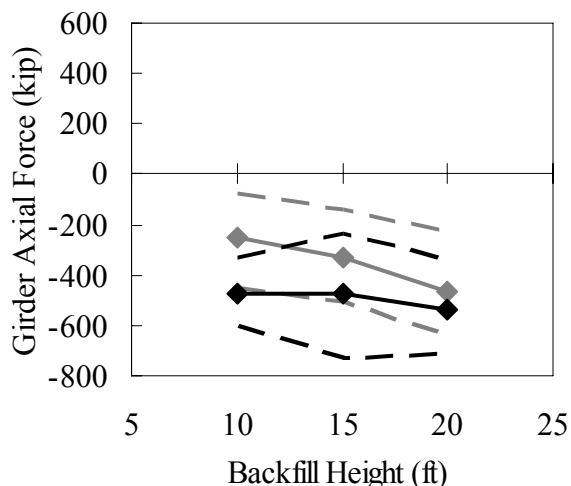
(c) PA Standard and Bridge Contraction



(d) PA Standard and Bridge Expansion

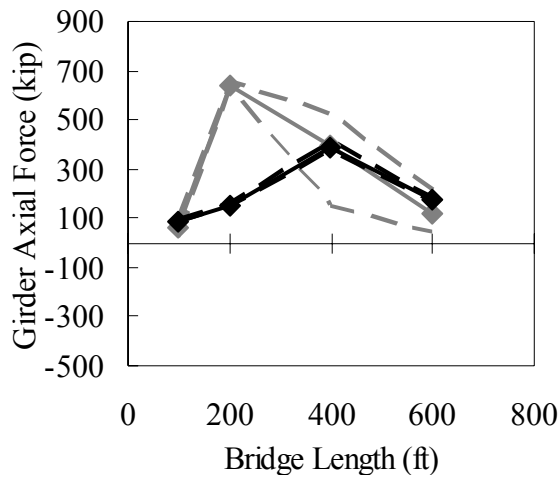


(e) Rigid and Bridge Contraction

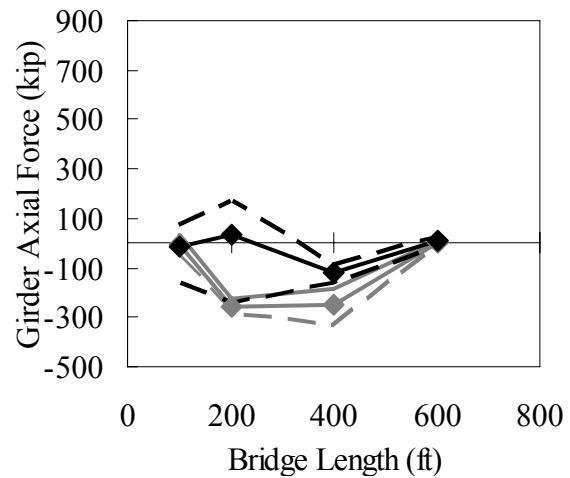


(f) Rigid and Bridge Expansion

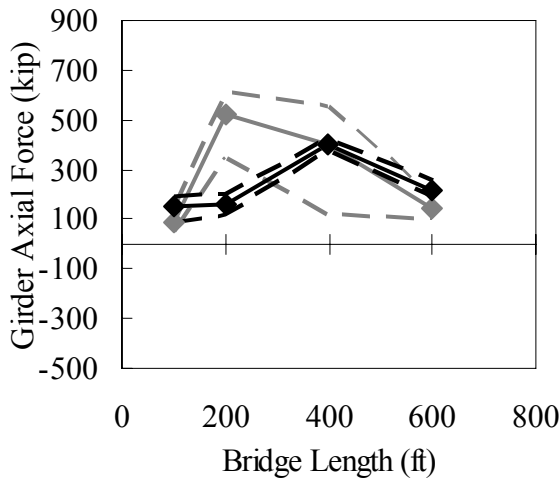
Figure 6.13: Backfill Height Influence on Girder Compressive Axial Force
(—◆— : Steel Girder; —◆— : Concrete Girder; - - : Envelopes)



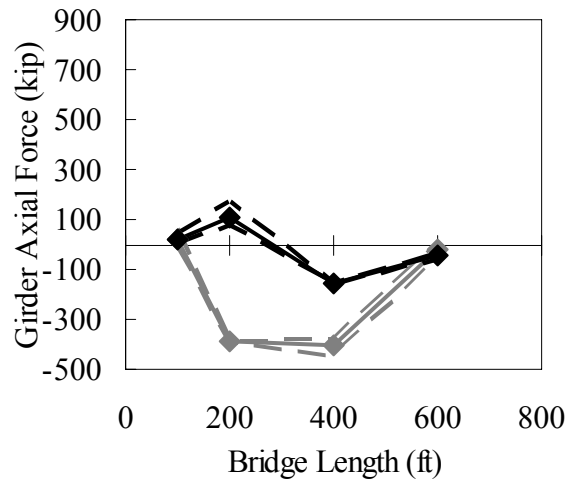
(a) Hinge and Bridge Contraction



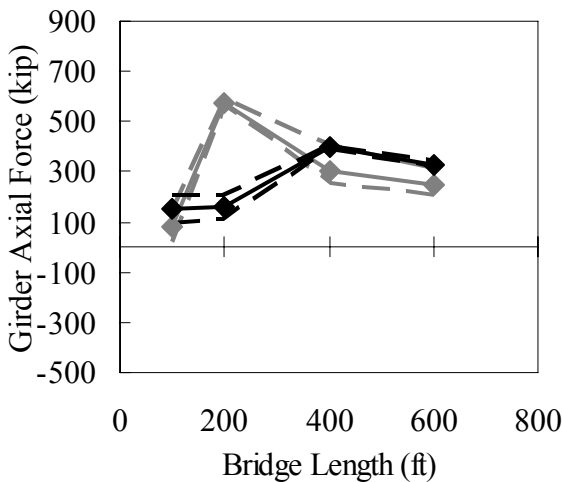
(b) Hinge and Bridge Expansion



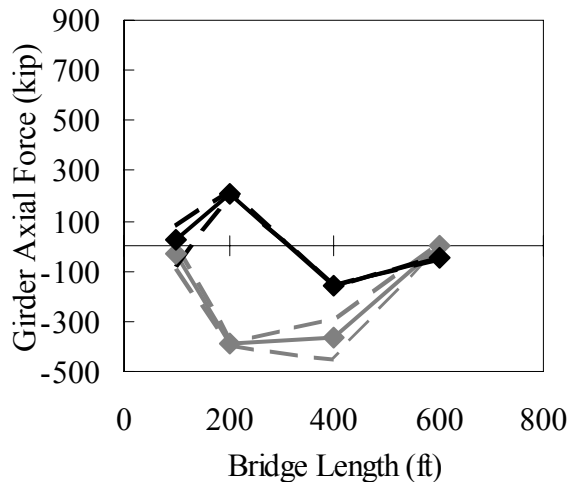
(c) PA Standard and Bridge Contraction



(d) PA Standard and Bridge Expansion

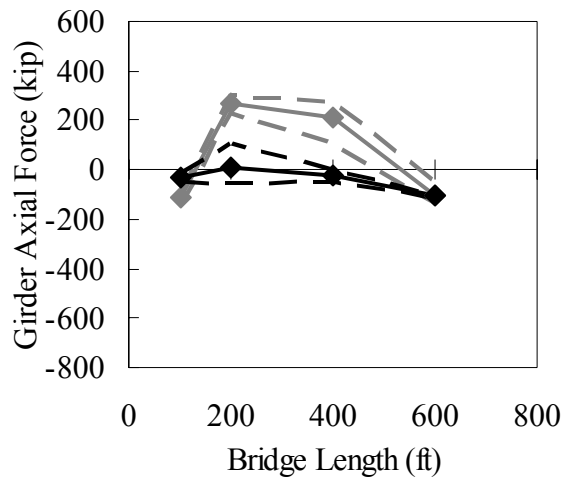


(e) Rigid and Bridge Contraction

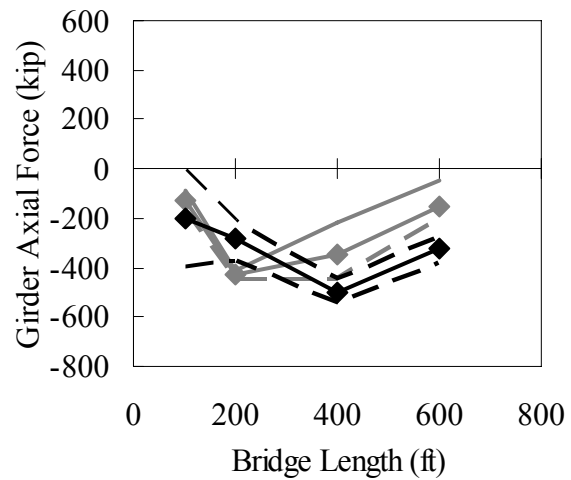


(f) Rigid and Bridge Expansion

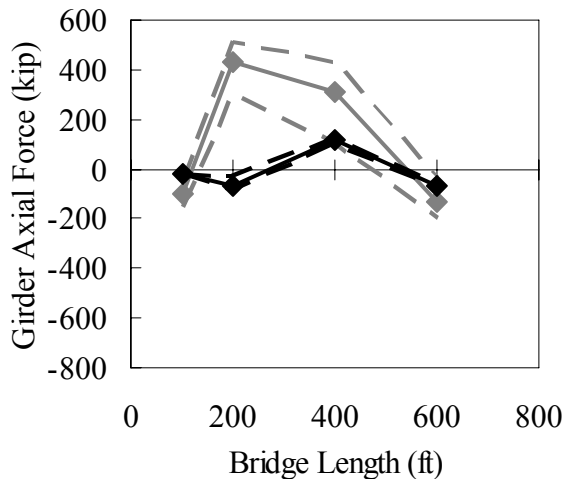
Figure 6.14: Bridge Length Influence on Girder Tensile Axial Force
(—◆— : Steel Girder; - -◆- : Concrete Girder; - - : Envelopes)



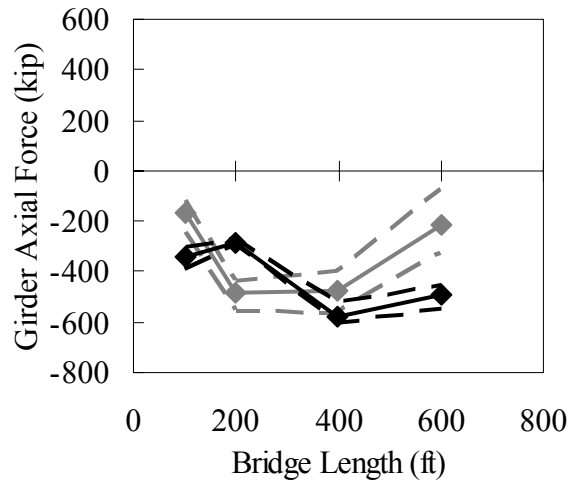
(a) Hinge and Bridge Contraction



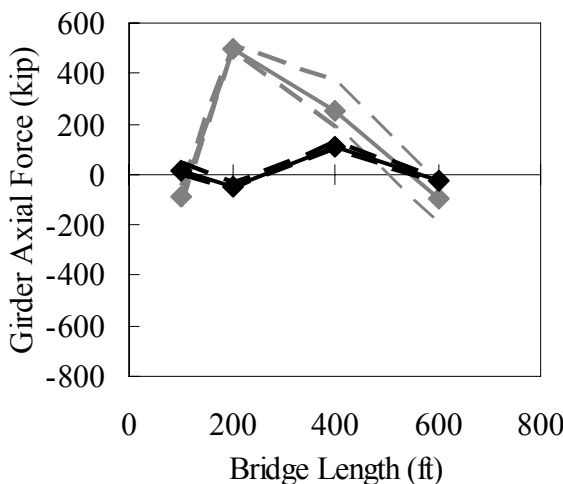
(b) Hinge and Bridge Expansion



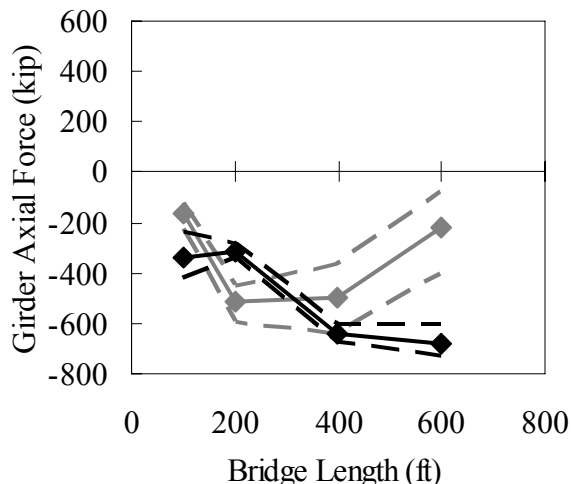
(c) PA Standard and Bridge Contraction



(d) PA Standard and Bridge Expansion



(e) Rigid and Bridge Contraction



(f) Rigid and Bridge Expansion

Figure 6.15: Bridge Length Influence on Girder Compressive Axial Force
(—◆— : Steel Girder; - -◆- - : Concrete Girder; - - : Envelopes)

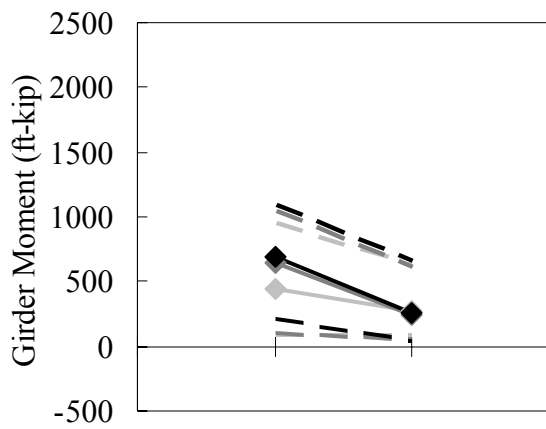
6.5.2 Girder Moment

Girder moment with respect to girder material, construction joint stiffness, backfill height, and bridge length is presented for both bridge expansion and contraction in Figures 6.16 through 6.23. Due to time-dependent effects, prestressed concrete girder IABs experience larger positive girder moments and smaller negative girder moments during bridge contraction and expansion, respectively (see Figures 6.16 and 6.17). During bridge expansion, both positive and negative moments of steel girder IABs are significantly larger than prestressed concrete girder IABs.

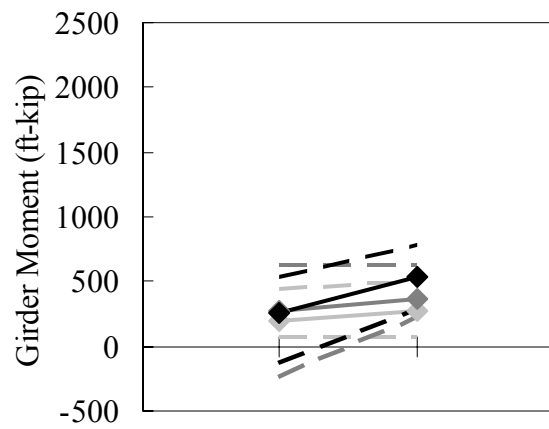
A flexible construction joint also influences girder moments (see Figures 6.18 and 6.19). During bridge expansion, positive moment significantly increases as the construction joint becomes stiffer. Also, negative moments of both prestressed concrete girder bridges and steel girder bridges increase as the construction joint becomes stiffer.

The influence of backfill height does not follow a distinct trend. However, as backfill height increases, positive girder moment increases slightly during bridge expansion (see Figures 6.20 and 6.21).

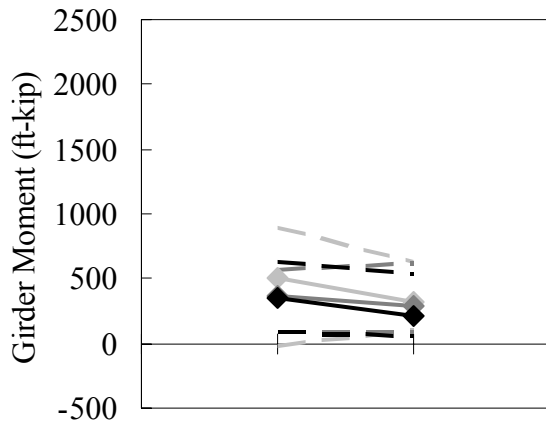
Both girder positive and negative moments are significantly influenced by bridge length increases (see Figures 6.22 and 6.23). During bridge expansion, both positive and negative moments of steel girder bridges change more significantly than in prestressed concrete girder bridges. Positive moments during bridge expansion rapidly increase with respect to bridge length increase, while negative moments during bridge expansion become stable.



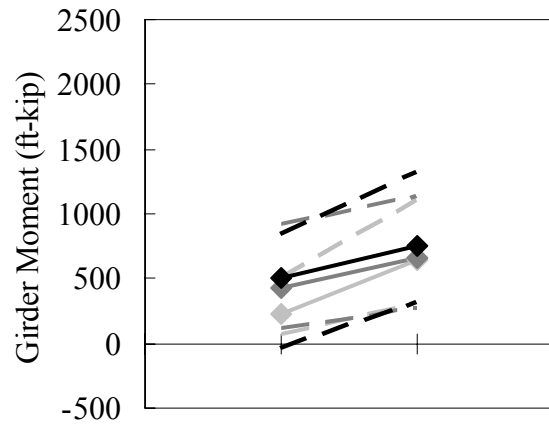
(a) Hinge and Bridge Contraction



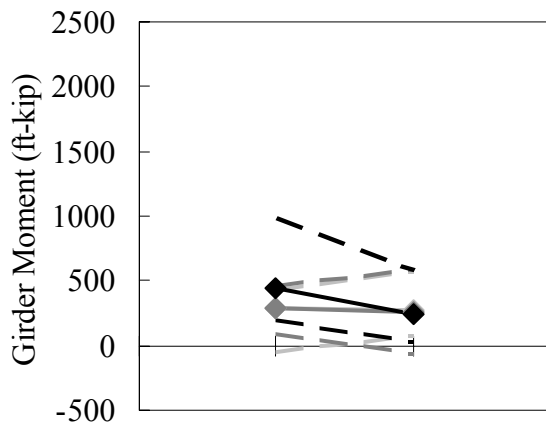
(b) Hinge and Bridge Expansion



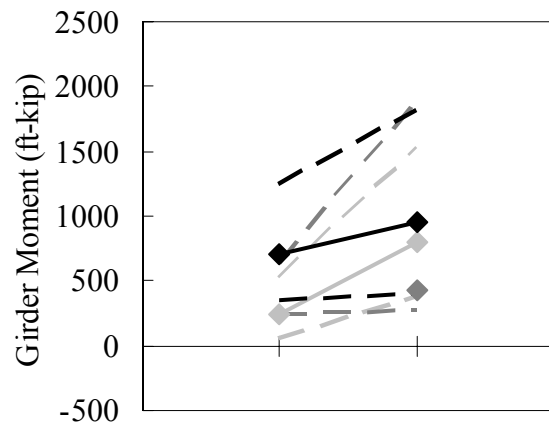
(c) PA Standard and Bridge Contraction



(d) PA Standard and Bridge Expansion

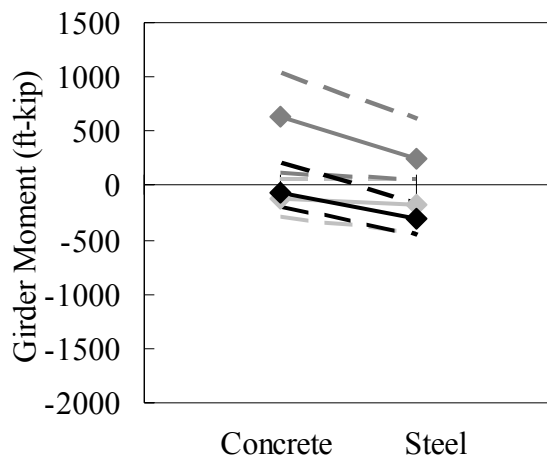


(e) Rigid and Bridge Contraction

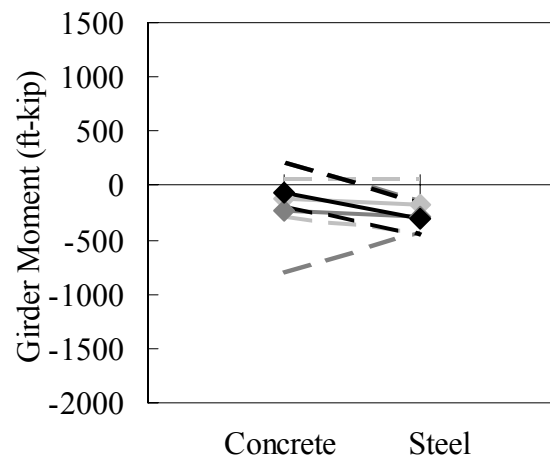


(f) Rigid and Bridge Expansion

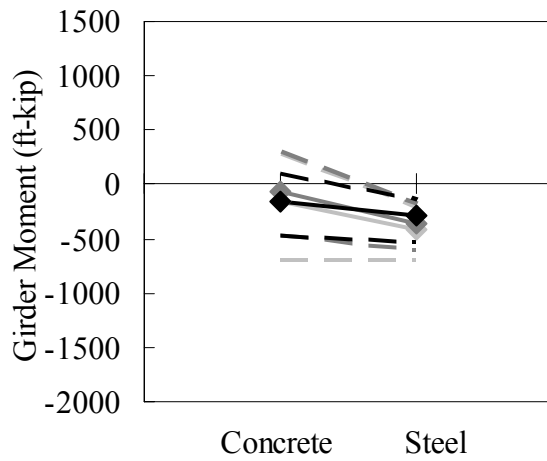
Figure 6.16: Girder Material Influence on Positive Girder Moment
(\blacklozenge : H = 10 ft; \blacklozenge : H = 15 ft; \blacklozenge : H = 20 ft; - - : Envelopes)



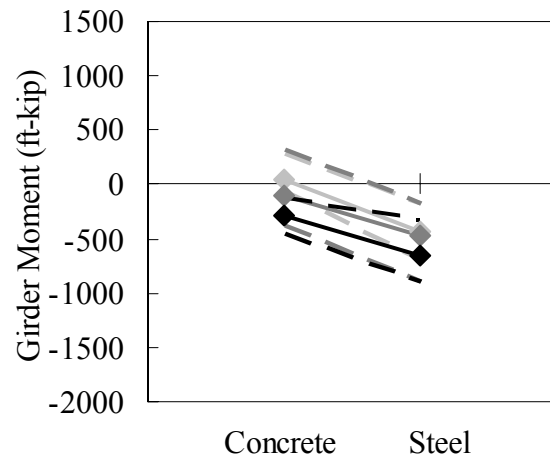
(a) Hinge and Bridge Contraction



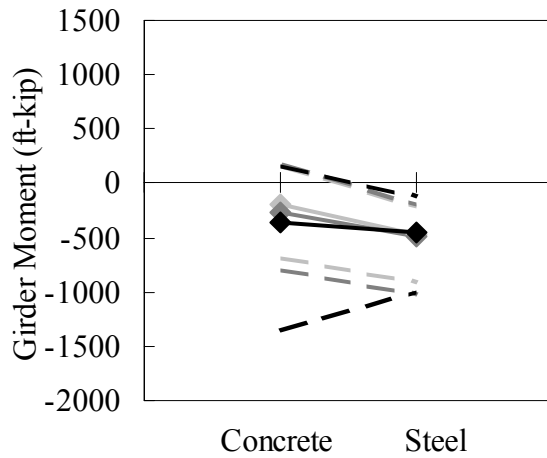
(b) Hinge and Bridge Expansion



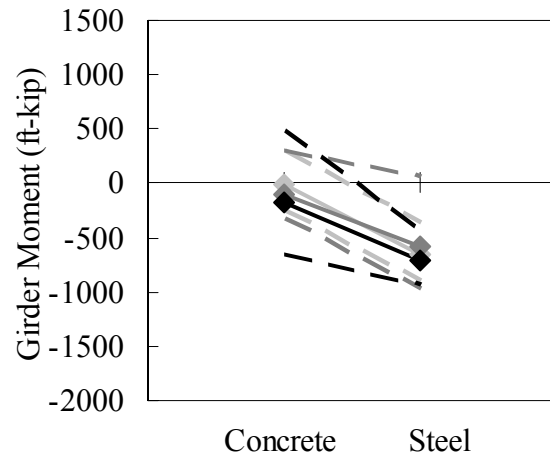
(c) PA Standard and Bridge Contraction



(d) PA Standard and Bridge Expansion

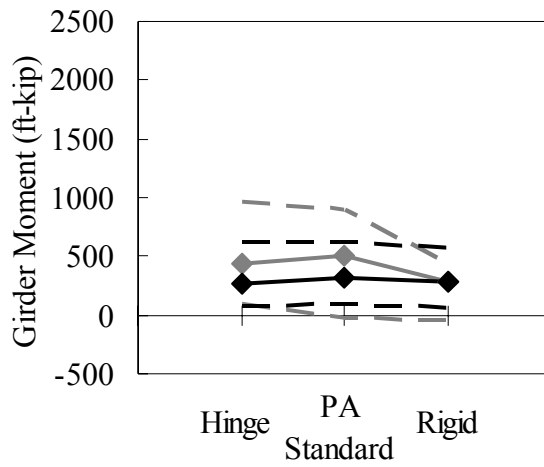


(e) Rigid and Bridge Contraction

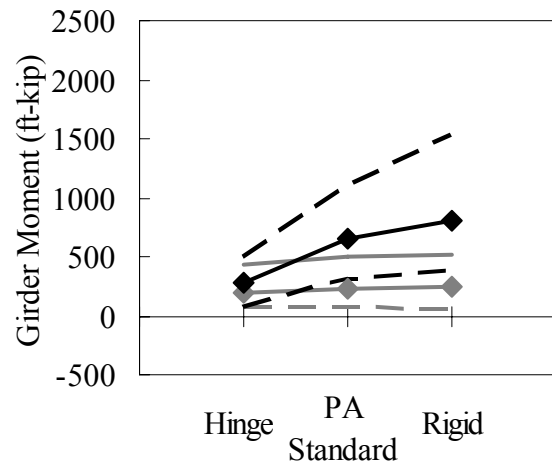


(f) Rigid and Bridge Expansion

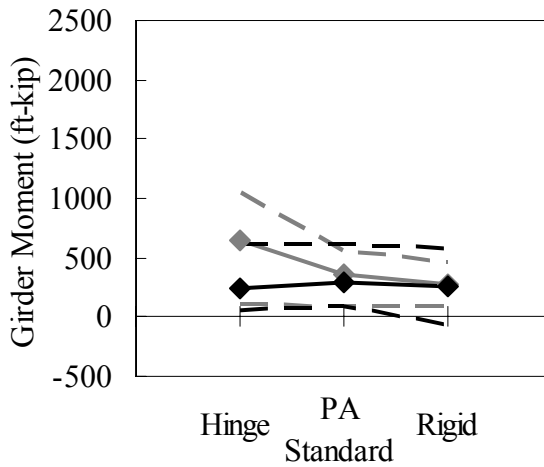
Figure 6.17: Girder Material Influence on Negative Girder Moment
(—◆— : H = 10 ft; —◆— : H = 15 ft; —◆— : H = 20 ft; - - : Envelopes)



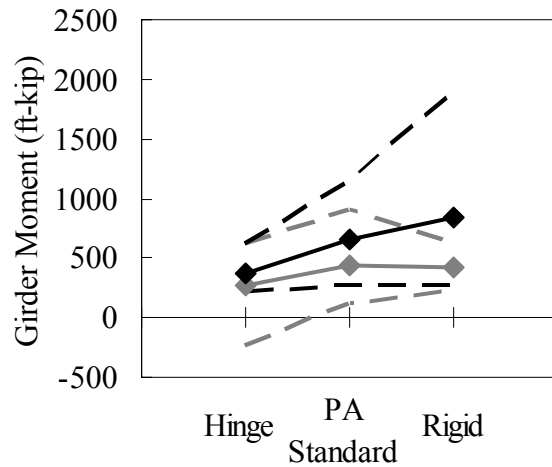
(a) $H = 10$ ft and Bridge Contraction



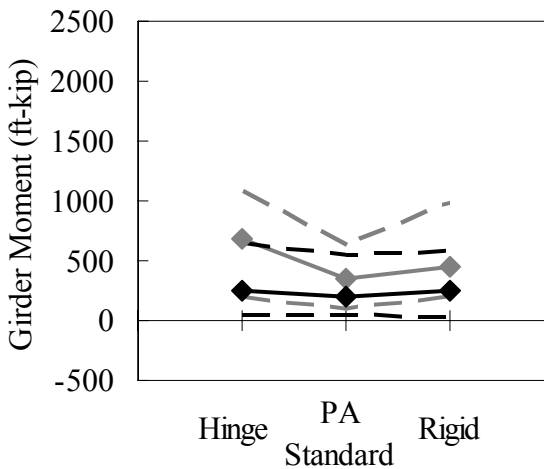
(b) $H = 10$ ft and Bridge Expansion



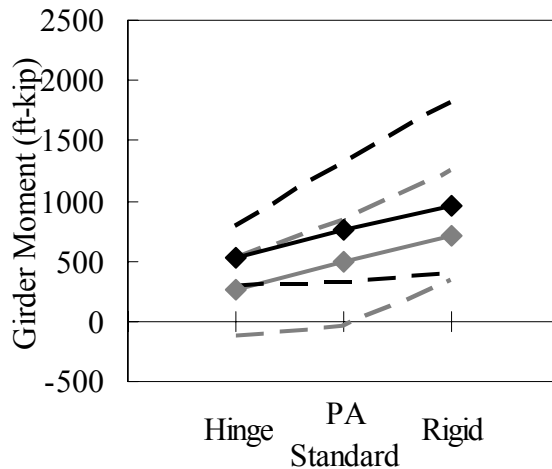
(c) $H = 15$ ft and Bridge Contraction



(d) $H = 15$ ft and Bridge Expansion

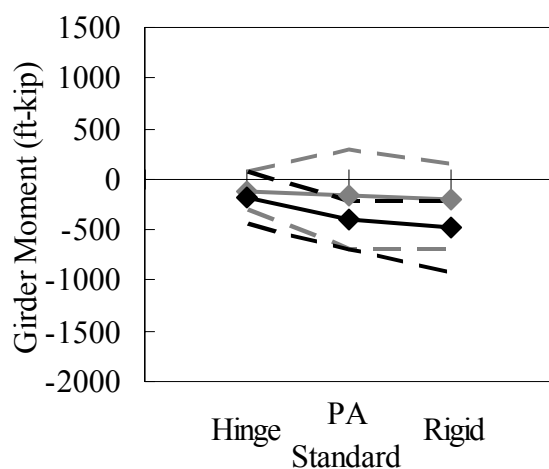


(e) $H = 20$ ft and Bridge Contraction

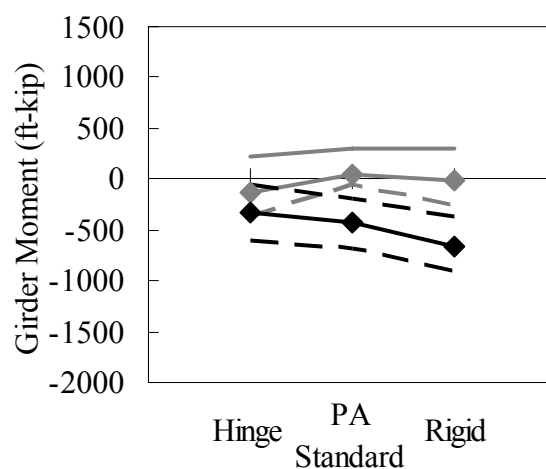


(f) $H = 20$ ft and Bridge Expansion

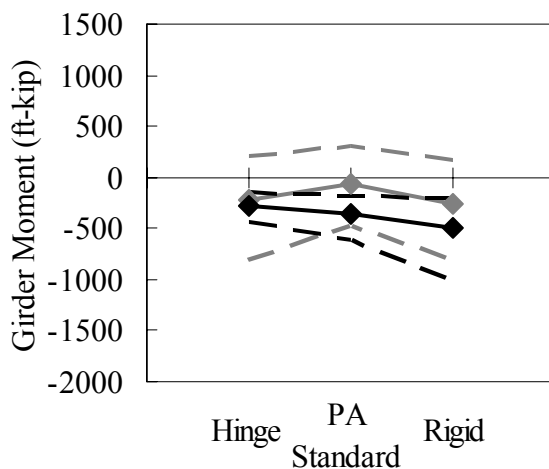
Figure 6.18: Construction Joint Stiffness Influence on Positive Girder Moment
(—◆— : Steel Girder; —◆— : Concrete Girder; - - : Envelopes)



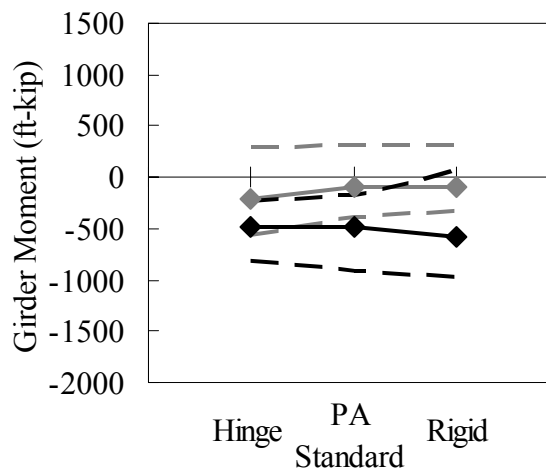
(a) $H = 10$ ft and Bridge Contraction



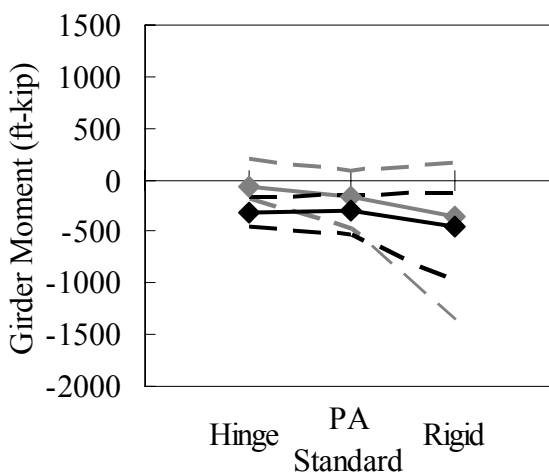
(b) $H = 10$ ft and Bridge Expansion



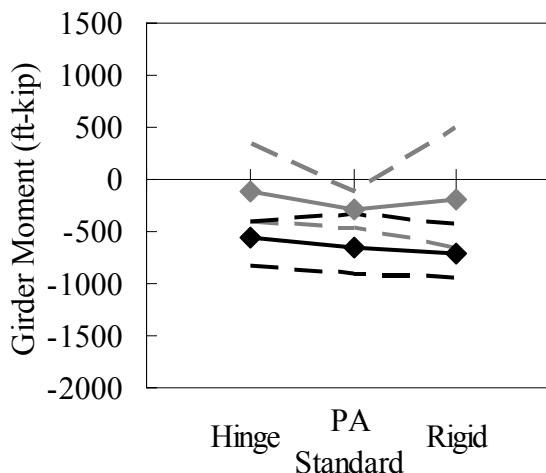
(c) $H = 15$ ft and Bridge Contraction



(d) $H = 15$ ft and Bridge Expansion

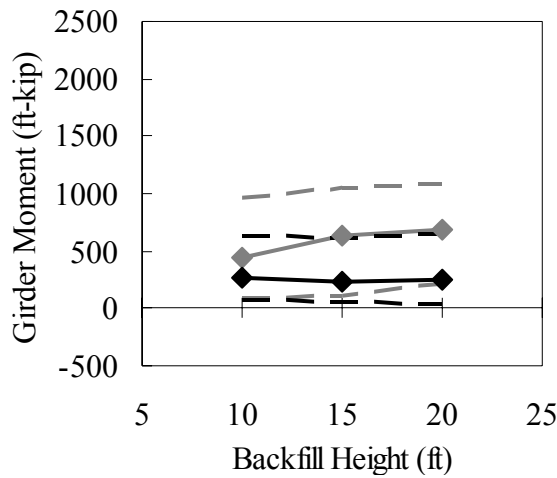


(e) $H = 20$ ft and Bridge Contraction

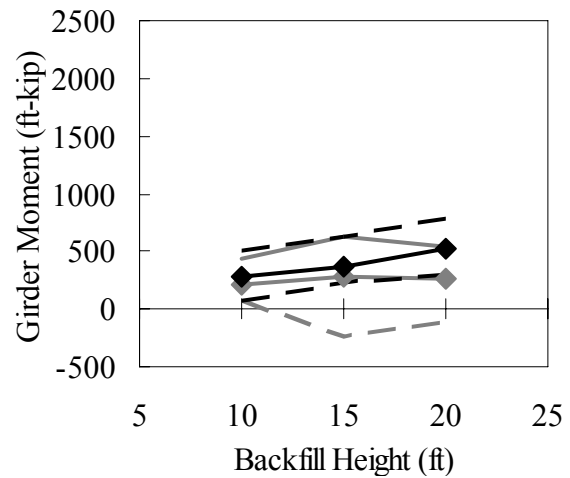


(f) $H = 20$ ft and Bridge Expansion

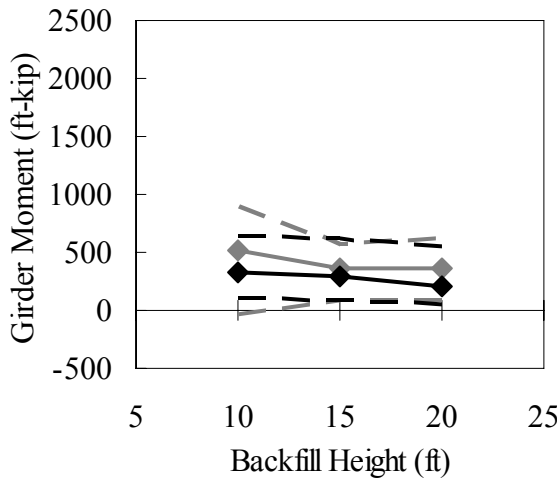
Figure 6.19: Construction Joint Stiffness Influence on Negative Girder Moment
(—◆— : Steel Girder; - -◆- - : Concrete Girder; - - : Envelopes)



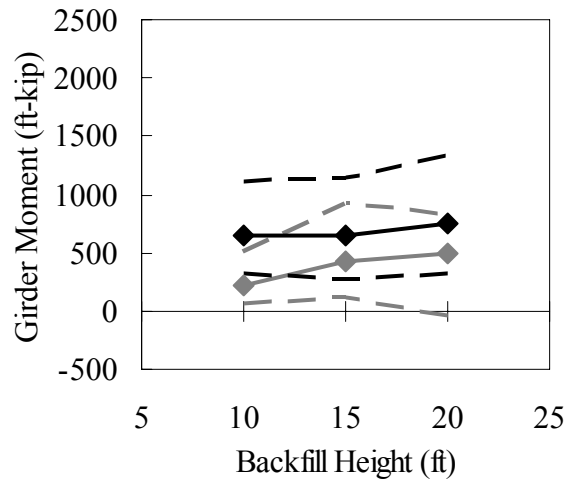
(a) Hinge and Bridge Contraction



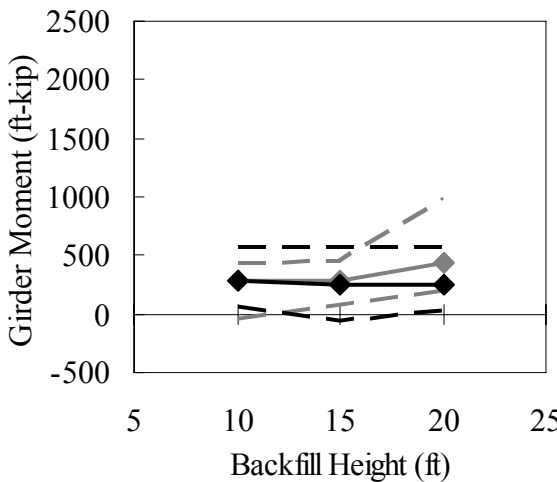
(b) Hinge and Bridge Expansion



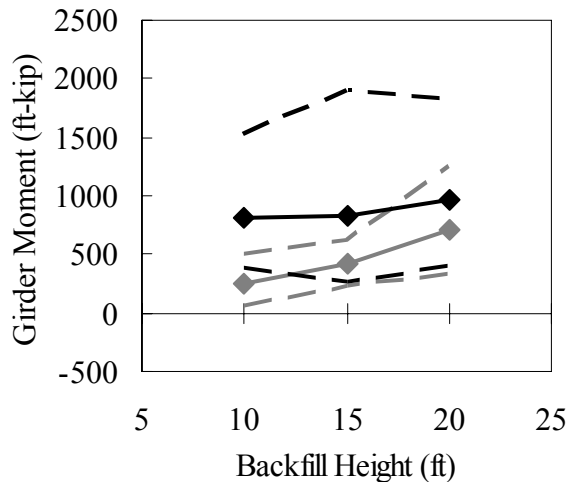
(c) PA Standard and Bridge Contraction



(d) PA Standard and Bridge Expansion

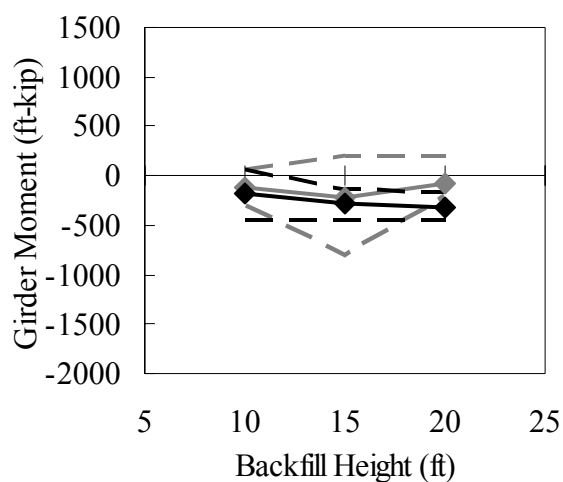


(e) Rigid and Bridge Contraction

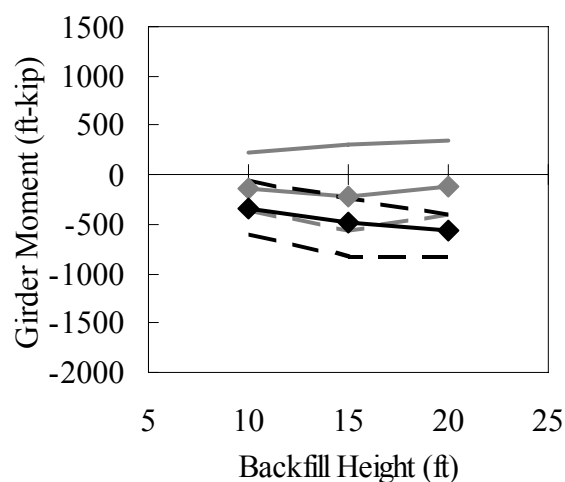


(f) Rigid and Bridge Expansion

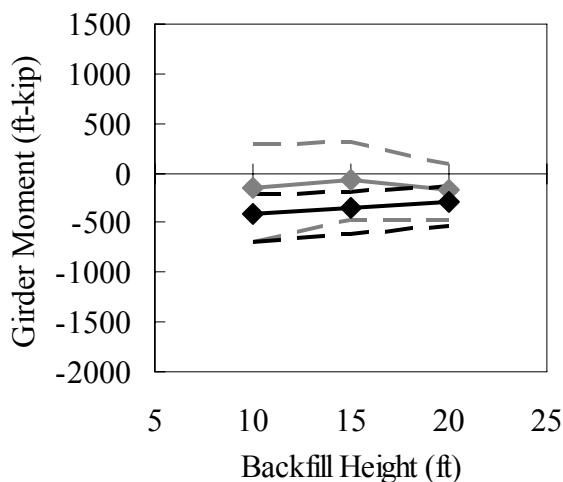
Figure 6.20: Backfill Height Influence on Positive Girder Moment
(—◆— : Steel Girder; —◆— : Concrete Girder; - - : Envelopes)



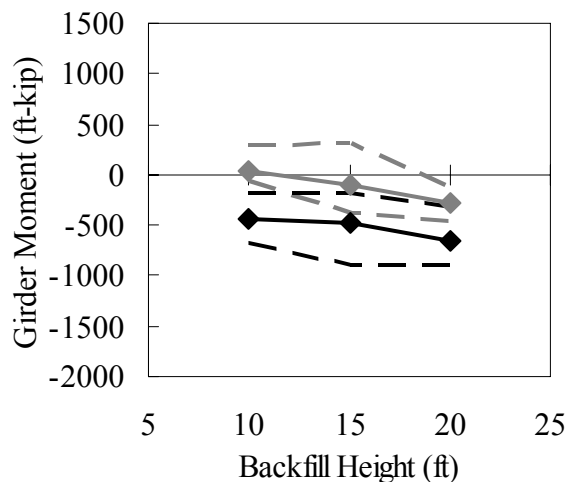
(a) Hinge and Bridge Contraction



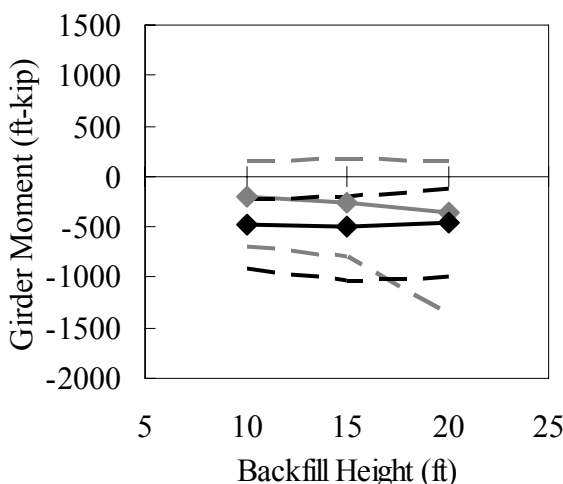
(b) Hinge and Bridge Expansion



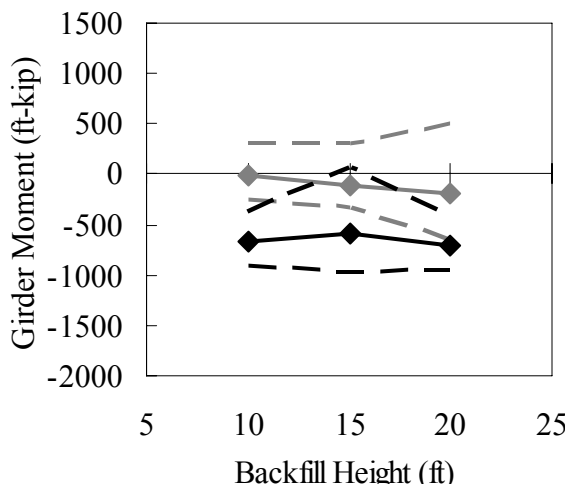
(c) PA Standard and Bridge Contraction



(d) PA Standard and Bridge Expansion

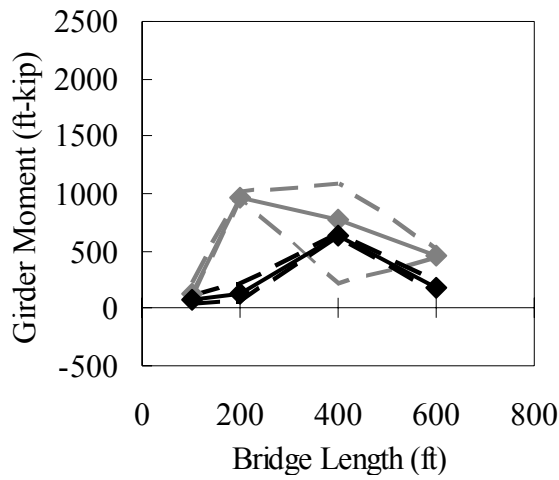


(e) Rigid and Bridge Contraction

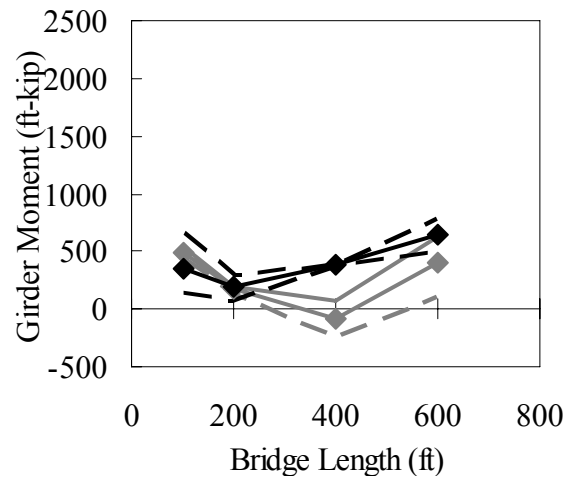


(f) Rigid and Bridge Expansion

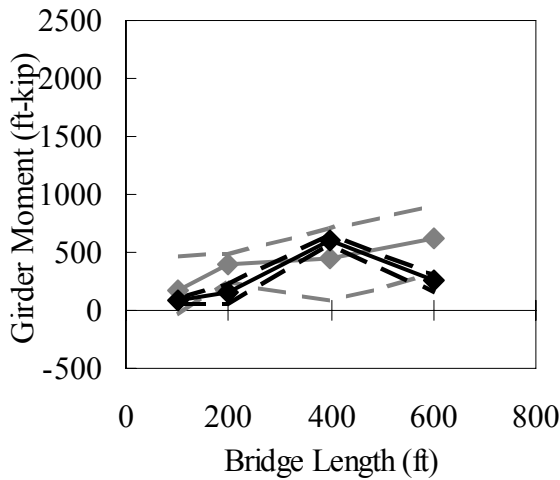
Figure 6.21: Backfill Height Influence on Negative Girder Moment
(—◆— : Steel Girder; —◆— : Concrete Girder; - - : Envelopes)



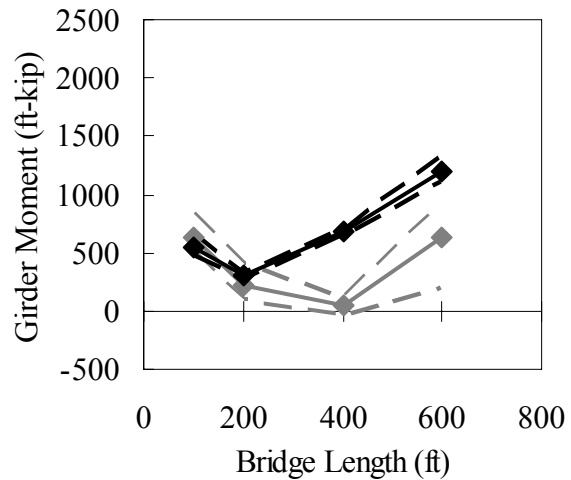
(a) Hinge and Bridge Contraction



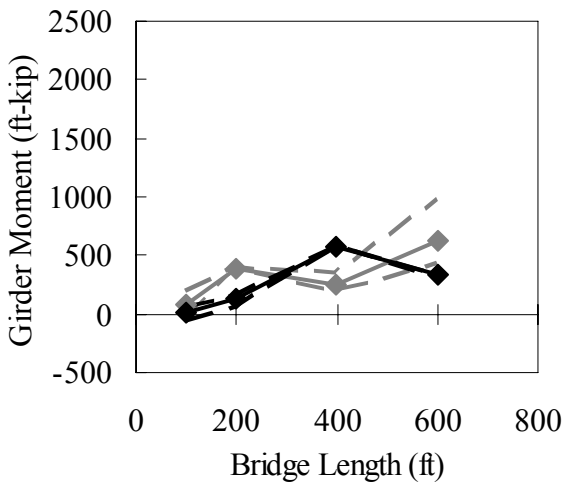
(b) Hinge and Bridge Expansion



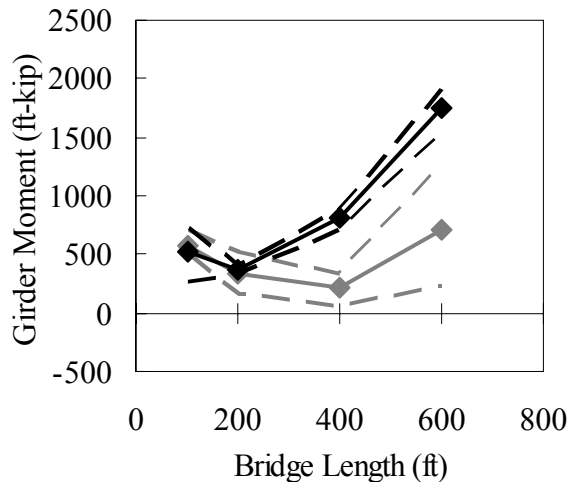
(c) PA Standard and Bridge Contraction



(d) PA Standard and Bridge Expansion

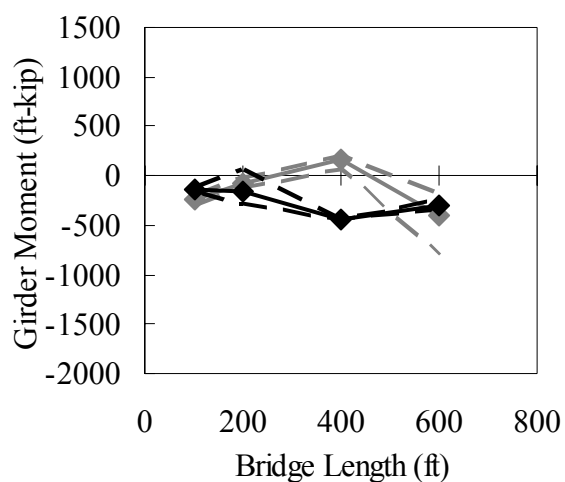


(e) Rigid and Bridge Contraction

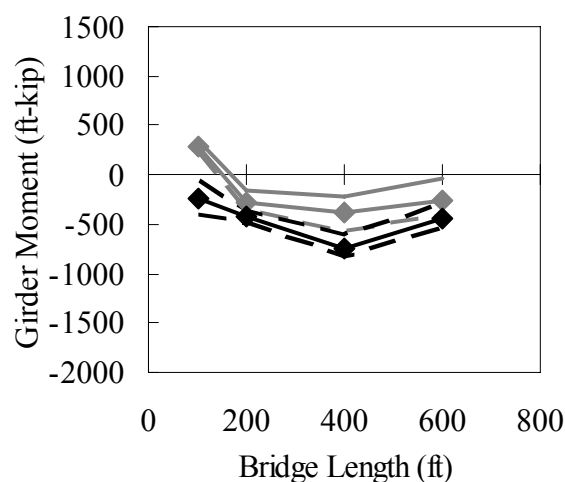


(f) Rigid and Bridge Expansion

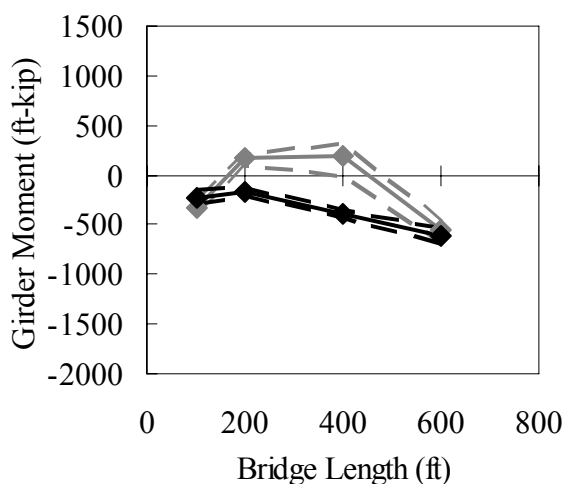
Figure 6.22: Bridge Length Influence on Positive Girder Moment
(—◆— : Steel Girder; - -◆- - : Concrete Girder; - - : Envelopes)



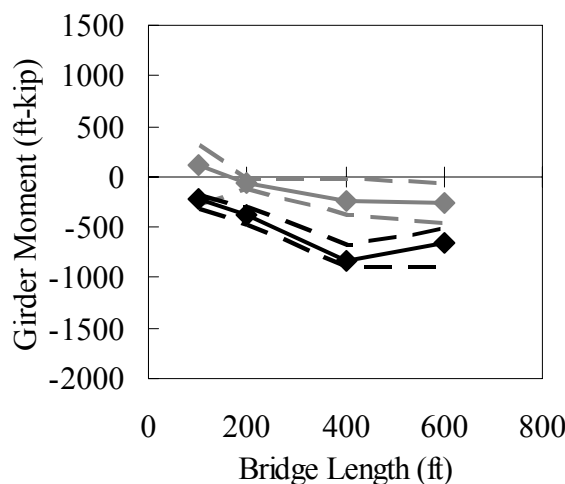
(a) Hinge and Bridge Contraction



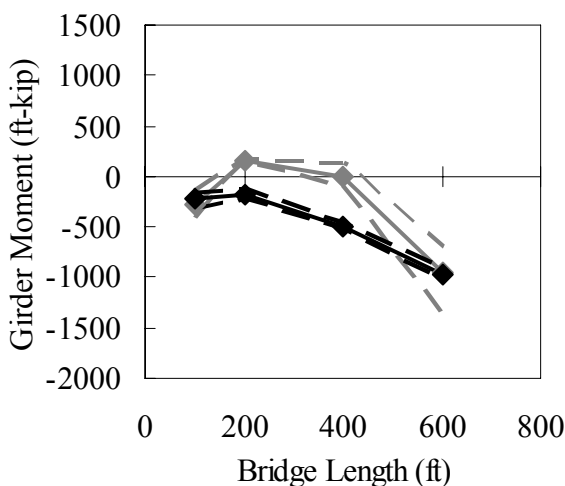
(b) Hinge and Bridge Expansion



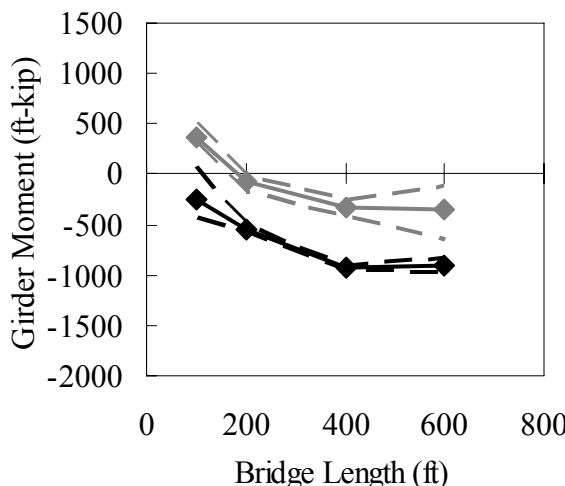
(c) PA Standard and Bridge Contraction



(d) PA Standard and Bridge Expansion



(e) Rigid and Bridge Contraction



(f) Rigid and Bridge Expansion

Figure 6.23: Bridge Length Influence on Negative Girder Moment
(—◆— : Steel Girder; —◆— : Concrete Girder; - - : Envelopes)

6.5.3 Pile Moment

Pile moment with respect to girder material, construction joint stiffness, backfill height, and bridge length is presented for both bridge expansion and contraction in Figures 6.24 through 6.27. The bending capacity of the HP12×74 pile is $\phi M_{yielding} = 127$ ft-kip and $\phi M_{plastic} = 194$ ft-kip based on $F_y = 50$ ksi.

Girder materials influence pile moments (see Figure 6.24). Pile moments in steel girder bridges are significantly larger than in prestressed concrete girder bridges during bridge expansion. However, pile moments in steel girder bridges during bridge contraction do not follow a distinct trend.

A flexible construction joint significantly influences pile moments (see Figure 6.25). During bridge contraction, pile moments rapidly increase as the construction joint becomes stiffer. During bridge expansion, pile moments rapidly decrease as the construction joint becomes stiffer. Pile moment decrease during bridge expansion becomes more significant as backfill height increases.

As backfill height increases, pile moment increases during bridge expansion (see Figure 6.26). Pile moment during bridge contraction does not exhibit a distinct trend with respect to backfill height. Backfill height influences on pile moments become more significant as the construction joint becomes more flexible.

Bridge length significantly influences pile moment (see Figure 6.27). During both bridge contraction and expansion, pile moments of both prestressed concrete and steel girder bridges significantly increase as bridge length increases. This bridge length influence becomes less significant in bridge contraction and more significant in bridge expansion as the construction joint becomes stiffer.

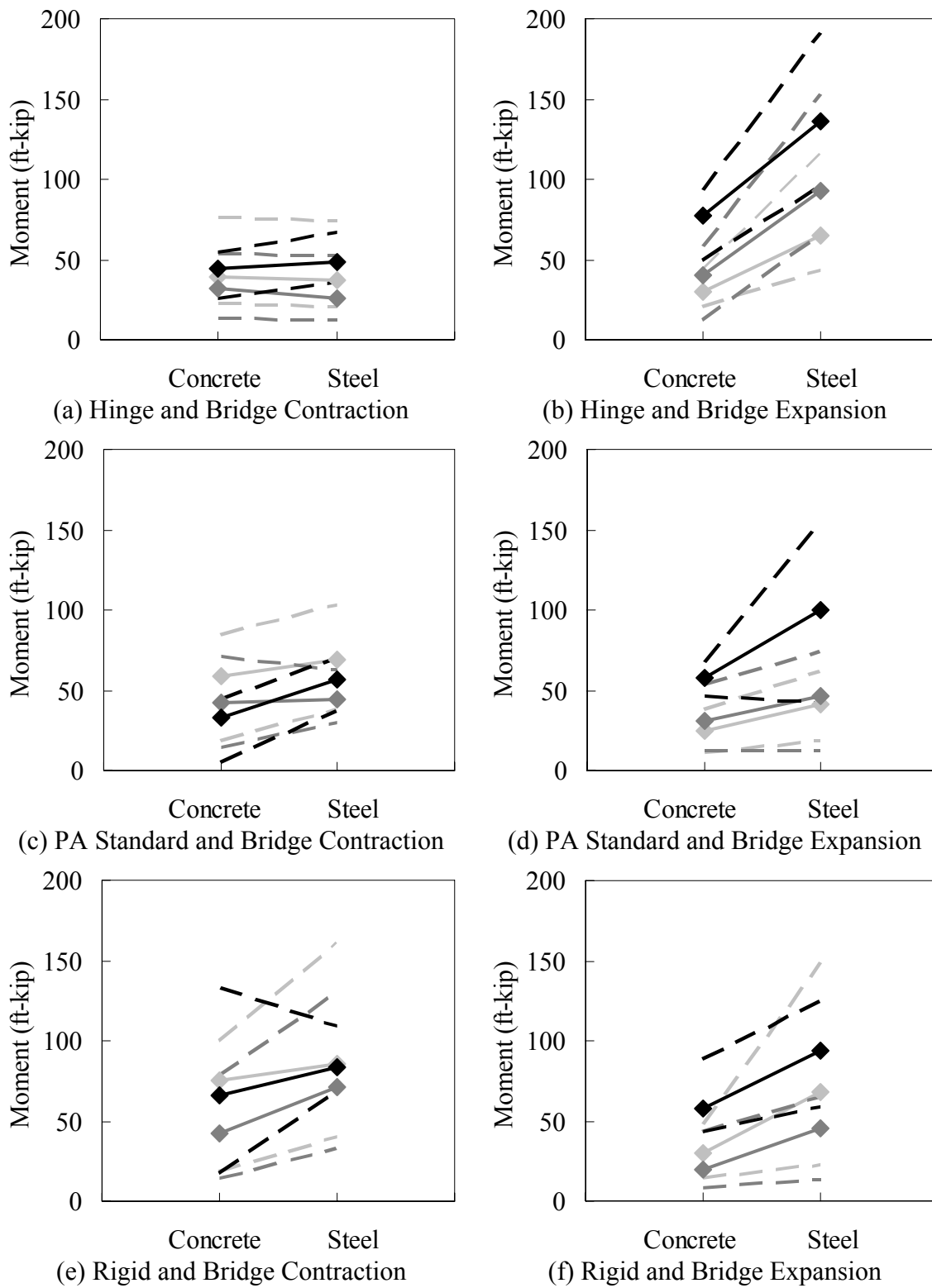
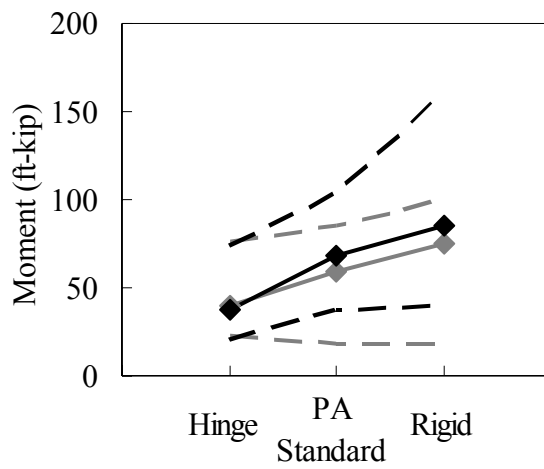
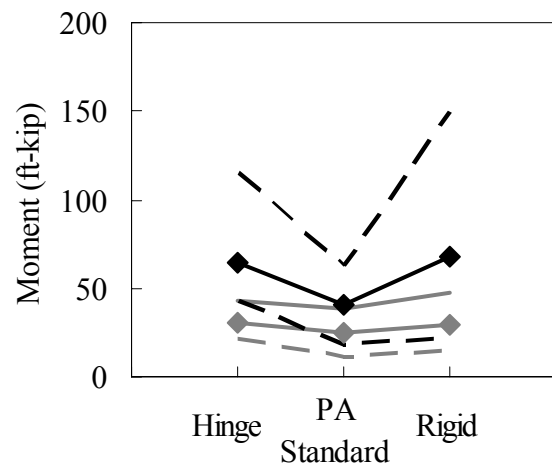


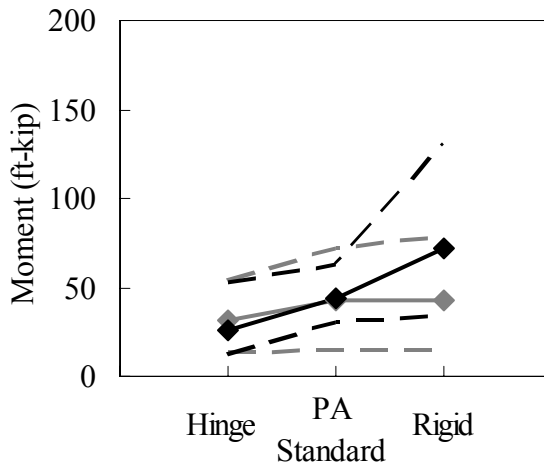
Figure 6.24: Girder Material Influence on Pile Moment
 (—◆— : H = 10 ft; —◆— : H = 15 ft; —◆— : H = 20 ft; - - : Envelopes)



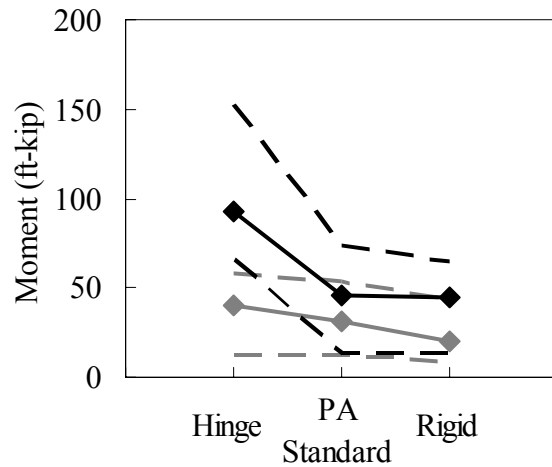
(a) $H = 10$ ft and Bridge Contraction



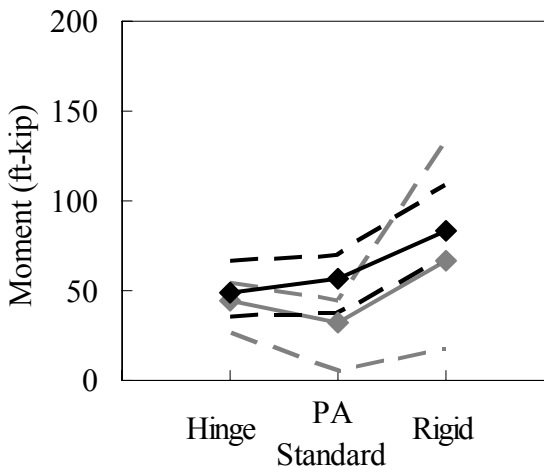
(b) $H = 10$ ft and Bridge Expansion



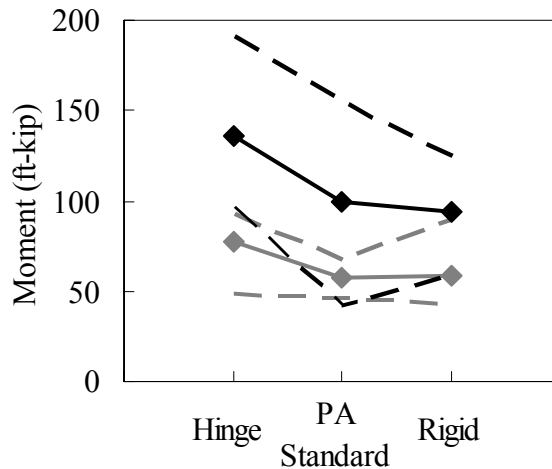
(c) $H = 15$ ft and Bridge Contraction



(d) $H = 15$ ft and Bridge Expansion

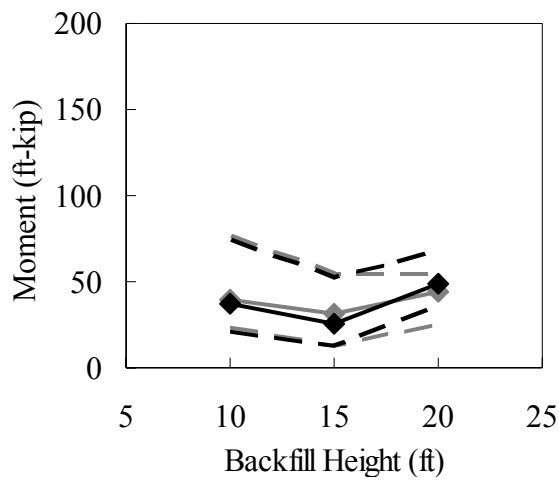


(e) $H = 20$ ft and Bridge Contraction

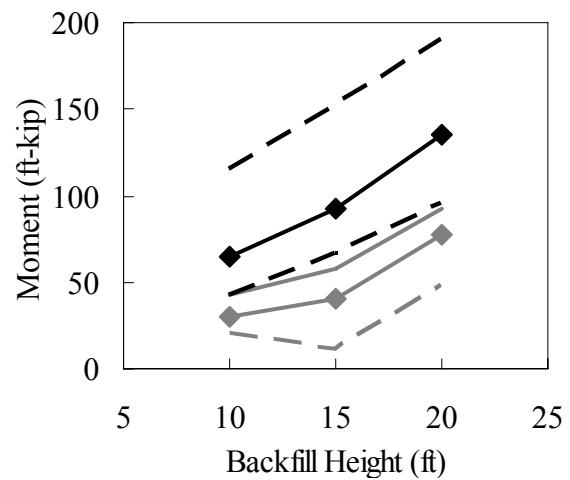


(f) $H = 20$ ft and Bridge Expansion

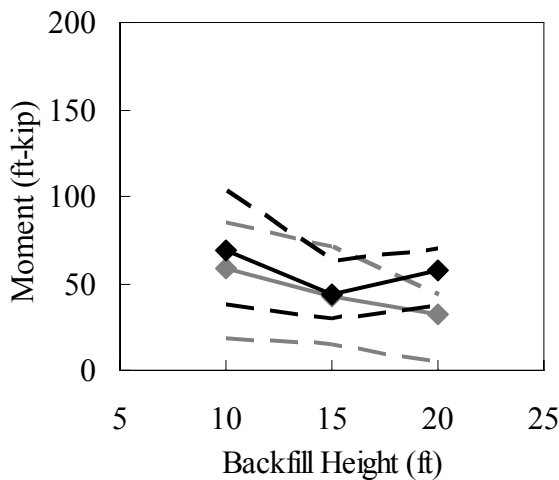
Figure 6.25: Construction Joint Stiffness Influence on Pile Moment
(—◆— : Steel Girder; —■— : Concrete Girder; - - : Envelopes)



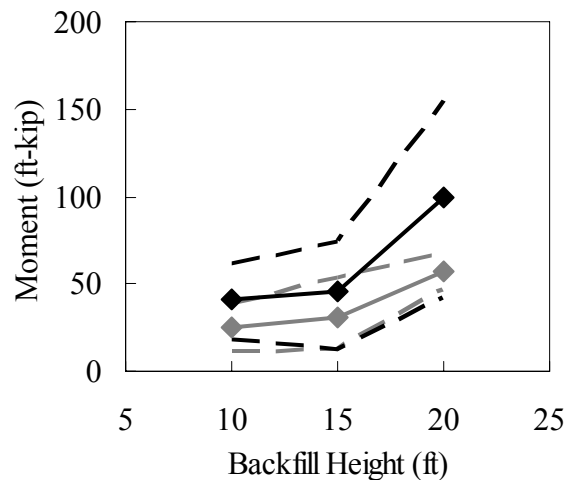
(a) Hinge and Bridge Contraction



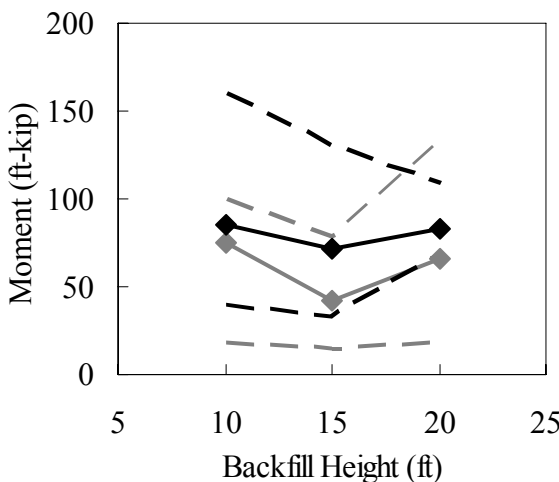
(b) Hinge and Bridge Expansion



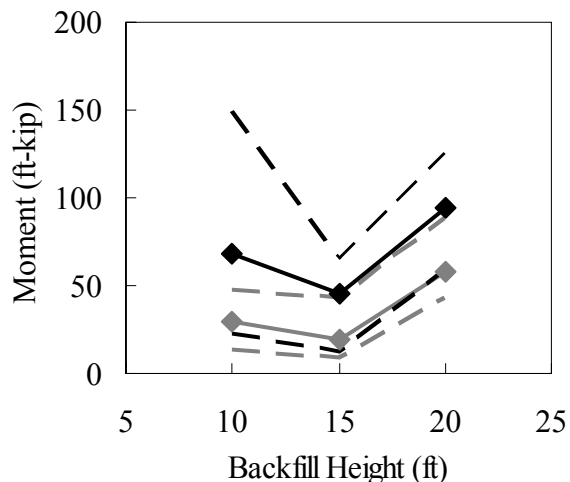
(c) PA Standard and Bridge Contraction



(d) PA Standard and Bridge Expansion

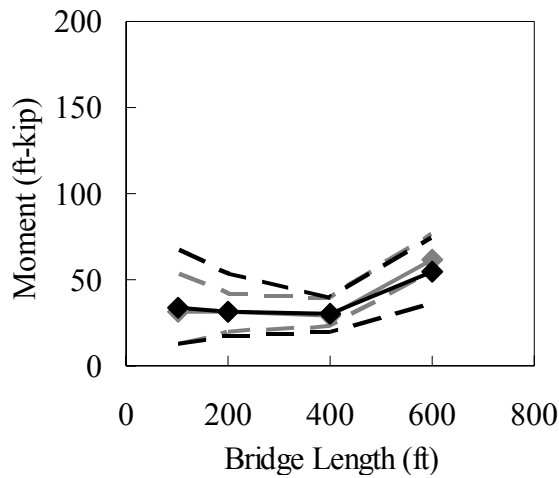


(e) Rigid and Bridge Contraction

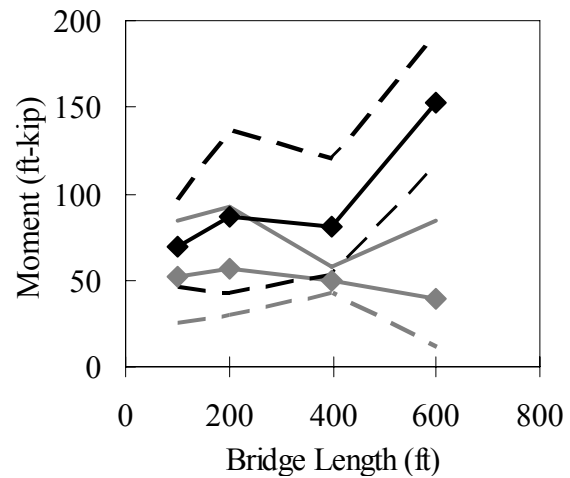


(f) Rigid and Bridge Expansion

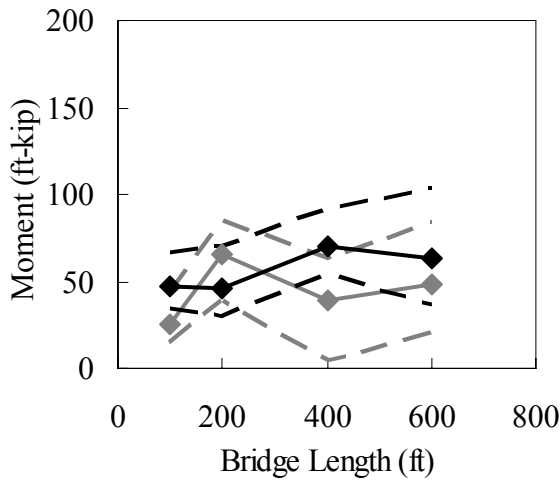
Figure 6.26: Backfill Height Influence on Pile Moment
(—◆— : Steel Girder; —◆— : Concrete Girder; - - : Envelopes)



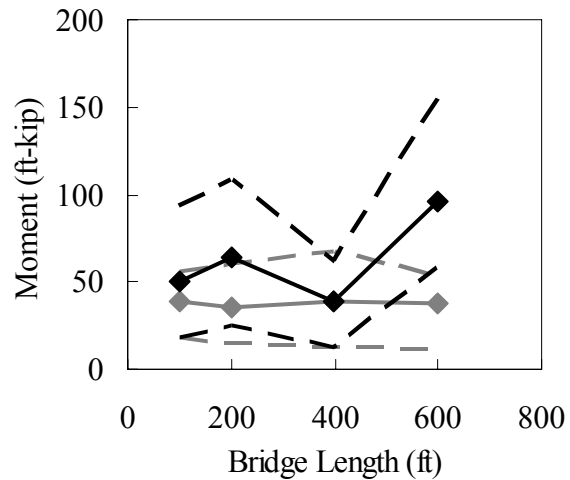
(a) Hinge and Bridge Contraction



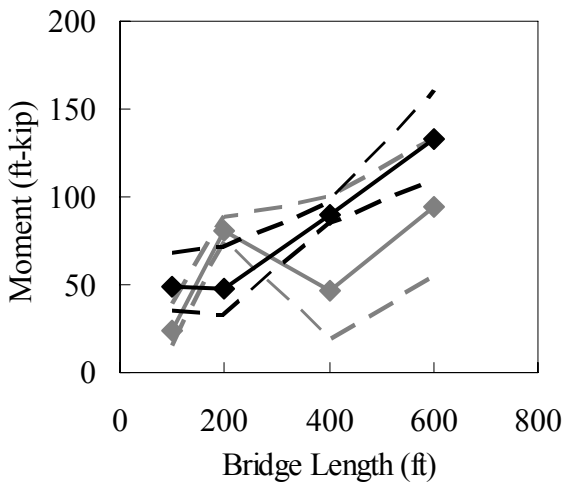
(b) Hinge and Bridge Expansion



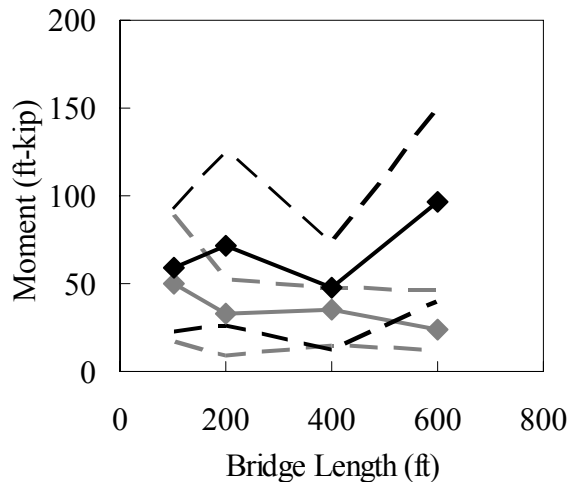
(c) PA Standard and Bridge Contraction



(d) PA Standard and Bridge Expansion



(e) Rigid and Bridge Contraction



(f) Rigid and Bridge Expansion

Figure 6.27: Bridge Length Influence on Pile Moment
(—◆— : Steel Girder; —■— : Concrete Girder; - - : Envelopes)

6.5.4 Pile Lateral Force

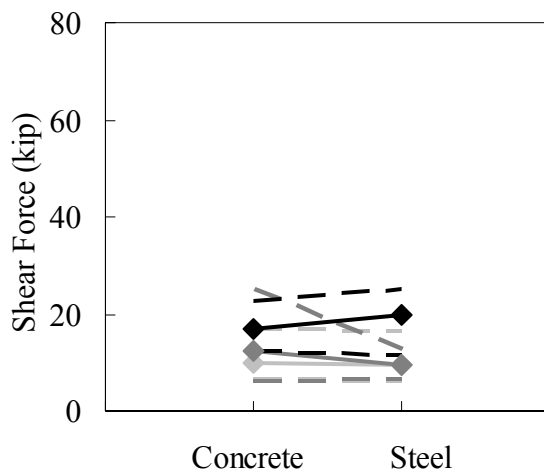
Pile lateral force with respect to girder material, construction joint stiffness, backfill height, and bridge length is presented for both bridge expansion and contraction in Figures 6.28 through 6.31. The shear capacity of the HP12×74 pile is $\phi V_n = 583$ kips based on $F_y = 50$ ksi.

Girder materials influence pile lateral forces (see Figure 6.28). Pile lateral forces in steel girder bridges are significantly larger than prestressed concrete girder bridges during bridge expansion. However, pile moment during bridge contraction does not follow a distinct trend.

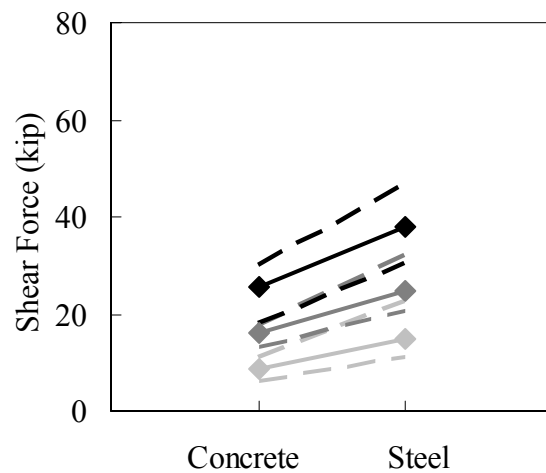
A flexible construction joint significantly influences pile lateral force (see Figure 6.29). During bridge contraction, pile lateral forces of both prestressed concrete and steel girder bridges rapidly increase as the construction joint becomes stiffer. During bridge expansion, pile lateral forces increase for $H = 10$ ft and decrease for $H = 15$ and 20 ft as the construction joint becomes stiffer.

Pile lateral force does not follow a distinct trend with respect to backfill height changes (see Figure 6.30). Only pile lateral forces with hinge construction joint and bridge expansion clearly increase as backfill height increases.

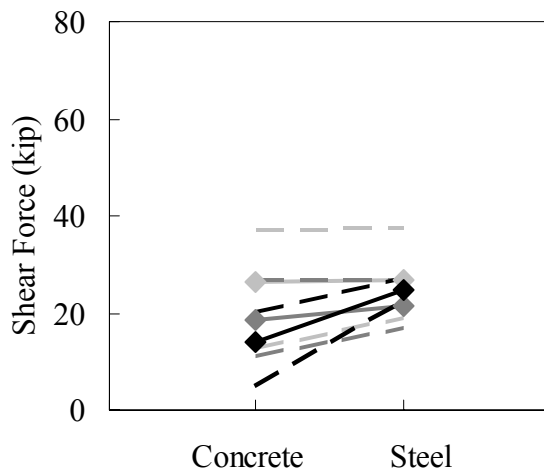
Pile lateral forces increase as bridge length increases (see Figure 6.31). During bridge contraction, pile lateral forces in both prestressed concrete and steel girder bridges increase in proportion to bridge lengths. During bridge expansion, pile lateral forces in steel girder bridges increase with respect to bridge length, while pile lateral forces in prestressed concrete girder bridges are not distinctly influenced. Bridge length influence becomes more significant as the construction joint becomes stiffer.



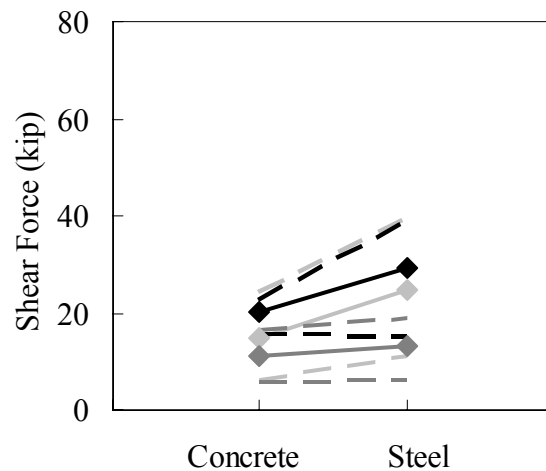
(a) Hinge and Bridge Contraction



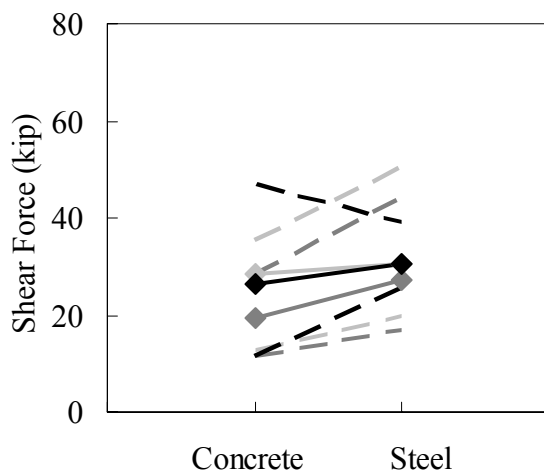
(b) Hinge and Bridge Expansion



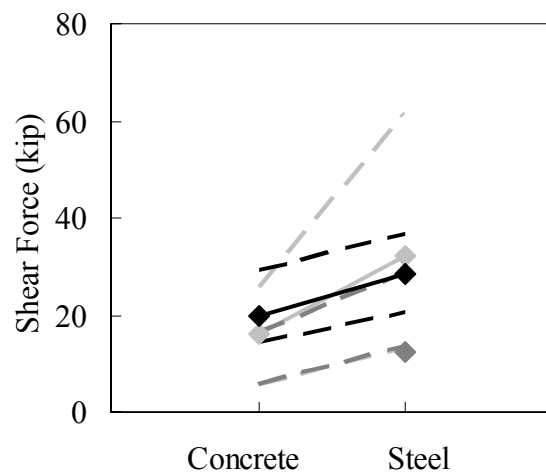
(c) PA Standard and Bridge Contraction



(d) PA Standard and Bridge Expansion

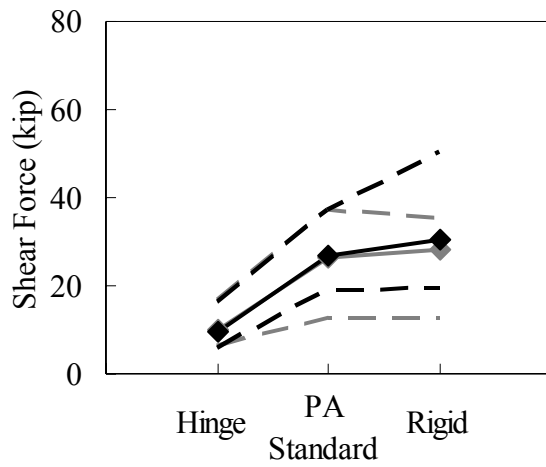


(e) Rigid and Bridge Contraction

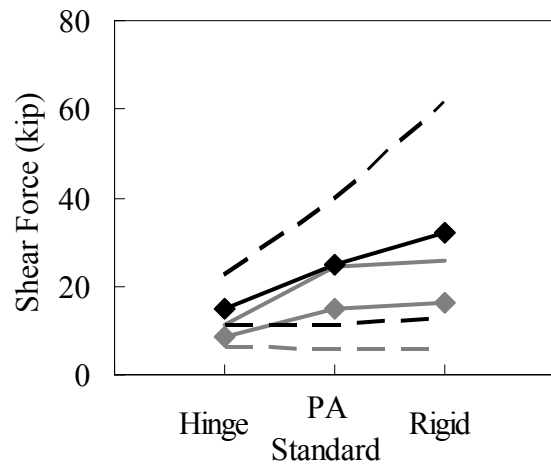


(f) Rigid and Bridge Expansion

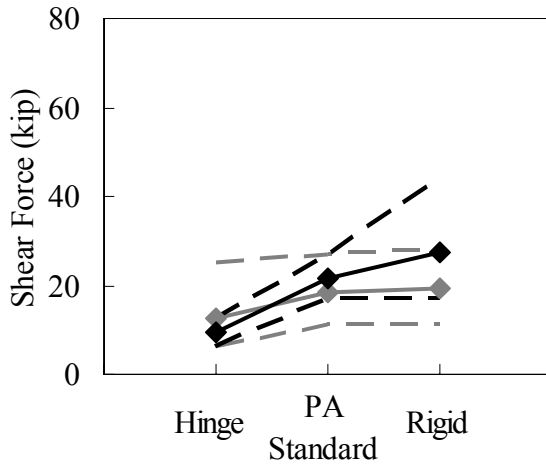
Figure 6.28: Girder Material Influence on Pile Lateral Force
(\diamond : H = 10 ft; \blacklozenge : H = 15 ft; \blacklozenge : H = 20 ft; - - : Envelopes)



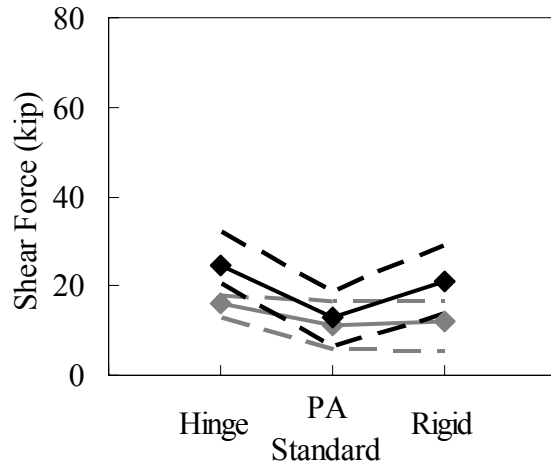
(a) $H = 10$ ft and Bridge Contraction



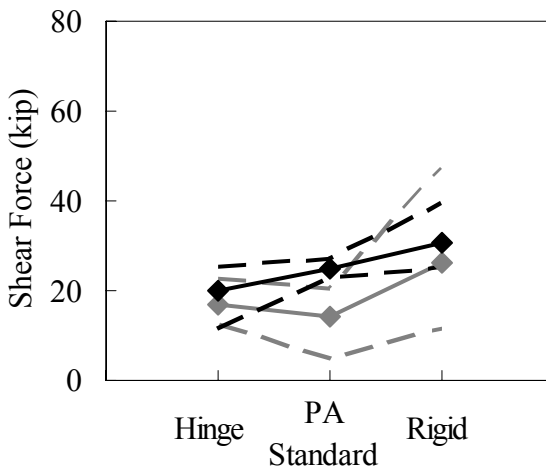
(b) $H = 10$ ft and Bridge Expansion



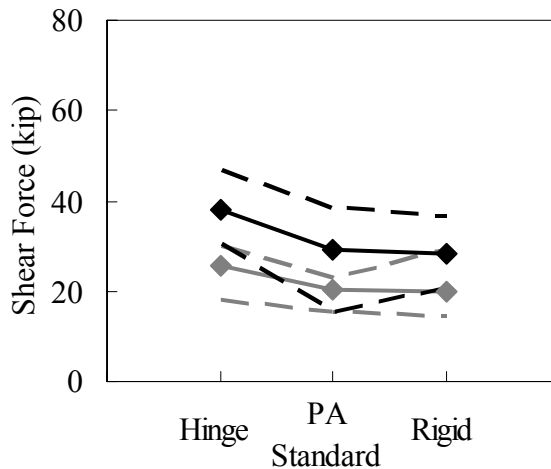
(c) $H = 15$ ft and Bridge Contraction



(d) $H = 15$ ft and Bridge Expansion

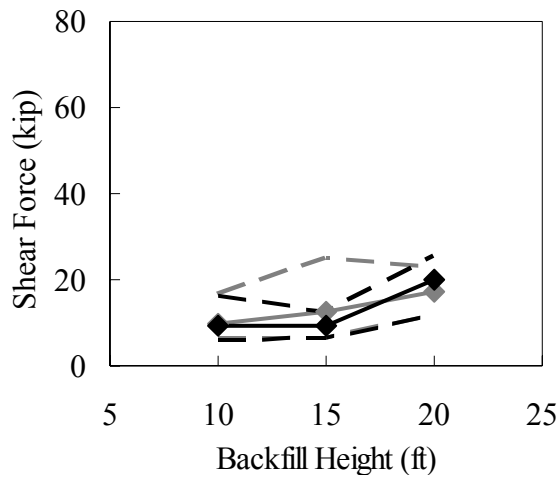


(e) $H = 20$ ft and Bridge Contraction

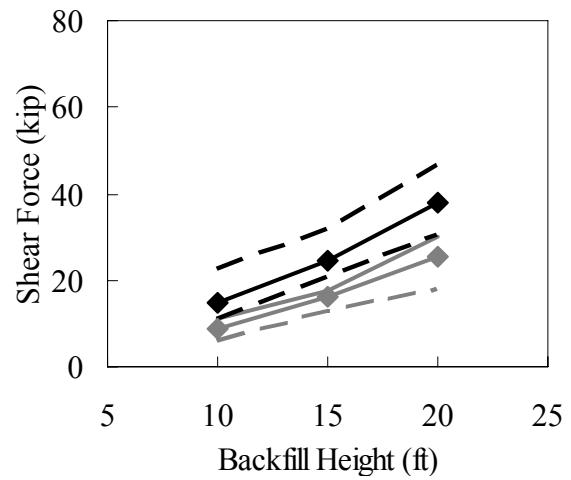


(f) $H = 20$ ft and Bridge Expansion

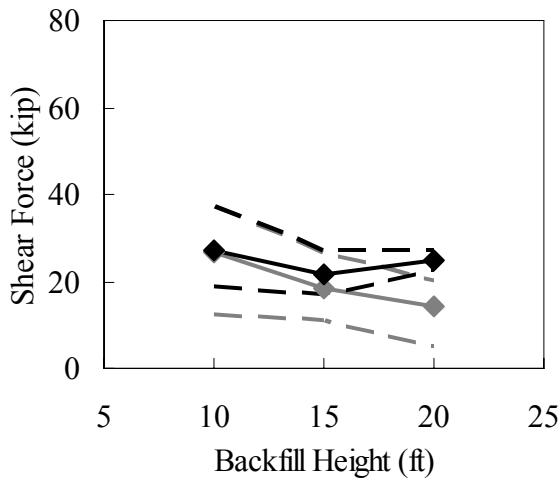
Figure 6.29: Construction Joint Stiffness Influence on Pile Lateral Force
(—◆— : Steel Girder; —◆— : Concrete Girder; - - : Envelopes)



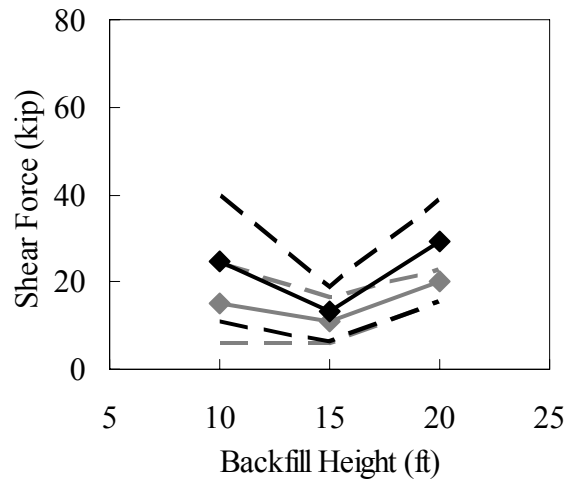
(a) Hinge and Bridge Contraction



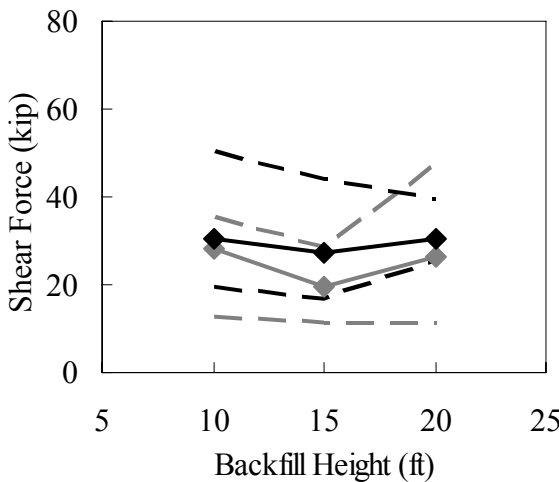
(b) Hinge and Bridge Expansion



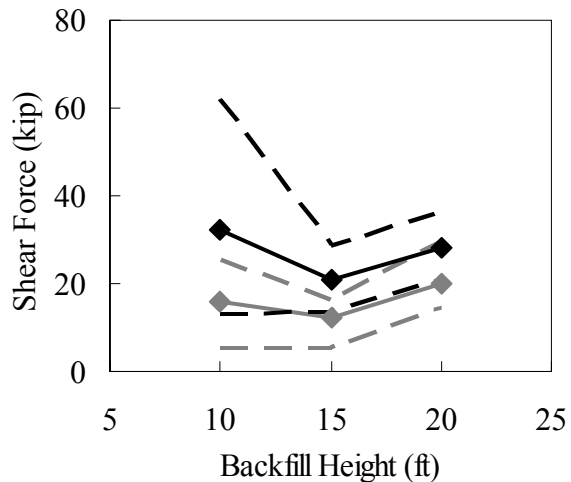
(c) PA Standard and Bridge Contraction



(d) PA Standard and Bridge Expansion

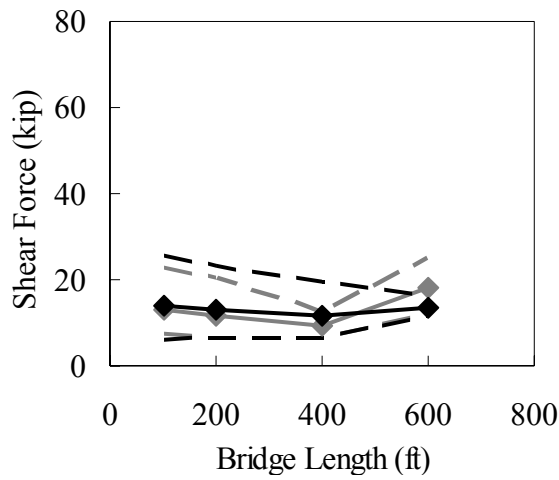


(e) Rigid and Bridge Contraction

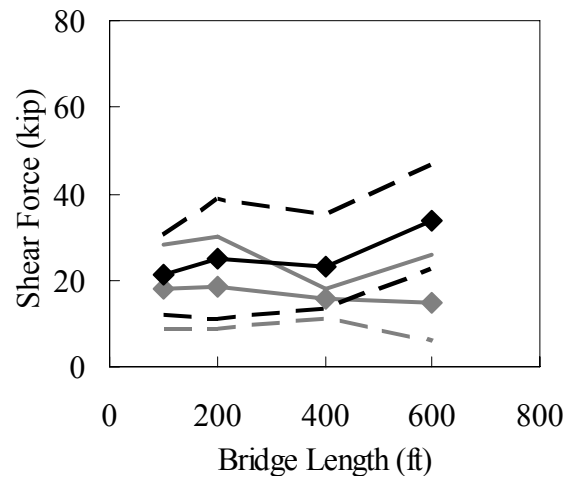


(f) Rigid and Bridge Expansion

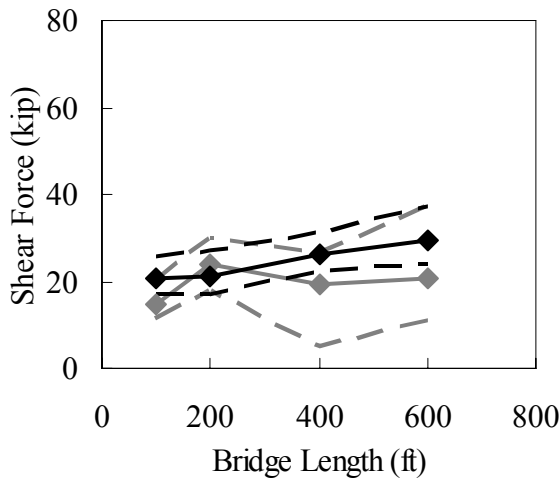
Figure 6.30: Backfill Height Influence on Pile Lateral Force
(—◆— : Steel Girder; —◆— : Concrete Girder; - - : Envelopes)



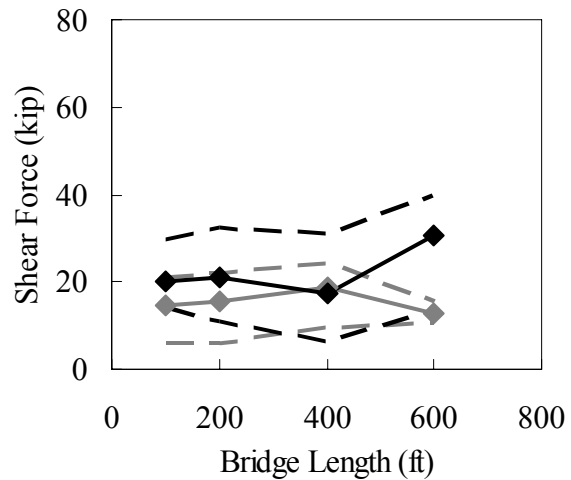
(a) Hinge and Bridge Contraction



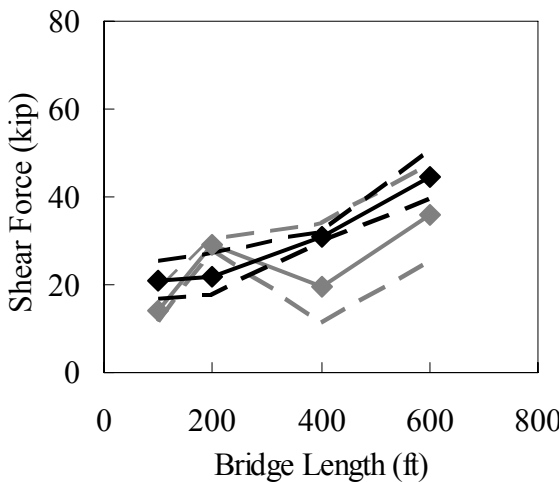
(b) Hinge and Bridge Expansion



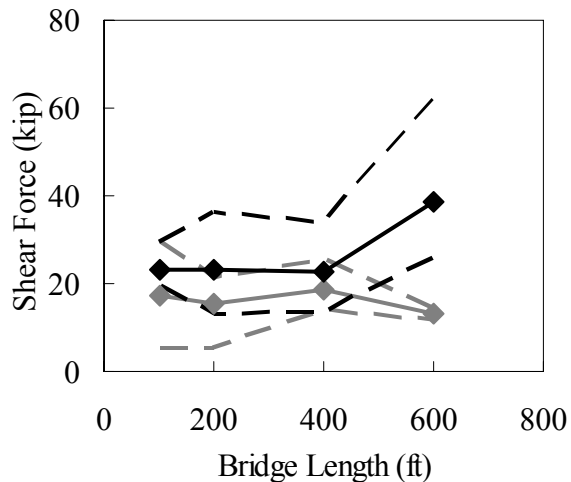
(c) PA Standard and Bridge Contraction



(d) PA Standard and Bridge Expansion



(e) Rigid and Bridge Contraction



(f) Rigid and Bridge Expansion

Figure 6.31: Bridge Length Influence on Pile Lateral Force
(—◆— : Steel Girder; —■— : Concrete Girder; - - : Envelopes)

6.5.5 Pile Head Displacement

Pile head displacement with respect to girder material, construction joint stiffness, backfill height and bridge length are presented for both bridge expansion and contraction in Figures 6.32 through 6.35. Bridge contraction displacement toward the bridge is positive.

The influence of girder materials on pile displacement does not exhibit a distinct trend (see Figure 6.32) for both bridge expansion and contraction.

Pile displacement increases as the construction joint becomes stiffer during bridge contraction (see Figure 6.33). During bridge expansion, pile displacements decrease (piles move toward backfill) as construction joint becomes stiffer.

Backfill height influences pile displacement (see Figure 6.34). During bridge contraction, pile displacement decreases as backfill height increases. When a bridge with a low backfill height expands, the pile moves toward the backfill due to the relatively small backfill pressure.

Pile displacement increases as bridge length increases (see Figure 6.35). During bridge contraction, pile displacement increases as bridge length increases. During bridge expansion, pile displacement decreases as bridge length increases. Due to time-dependent effects, contraction displacements in prestressed concrete girder bridges are similar to steel girder bridges despite the thermal expansion coefficient difference. However, pile displacements in steel girder bridges are larger than during bridge expansion.

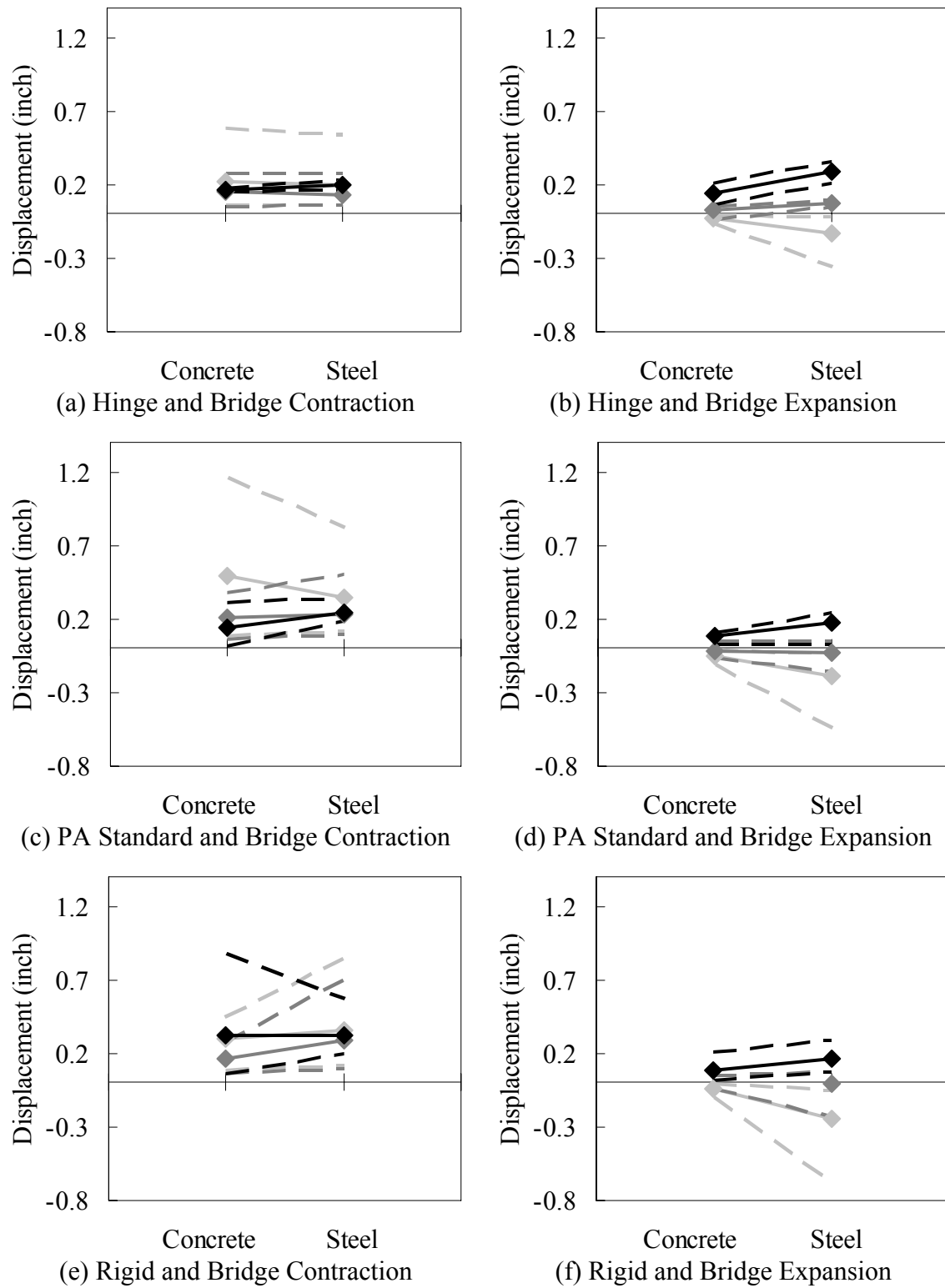
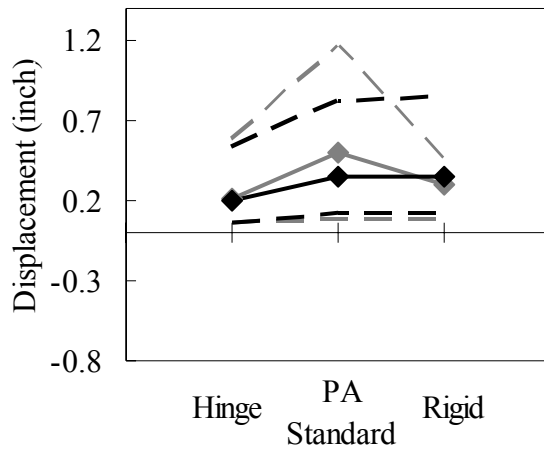
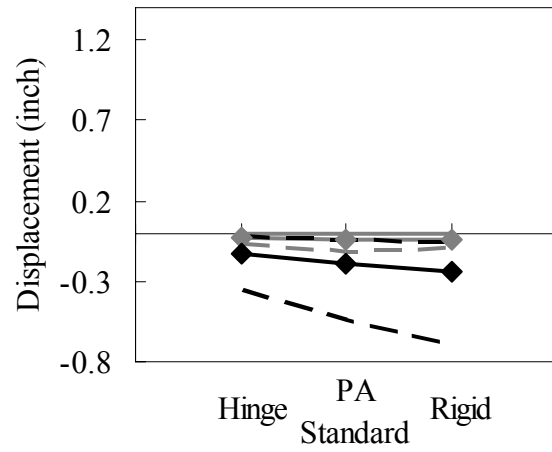


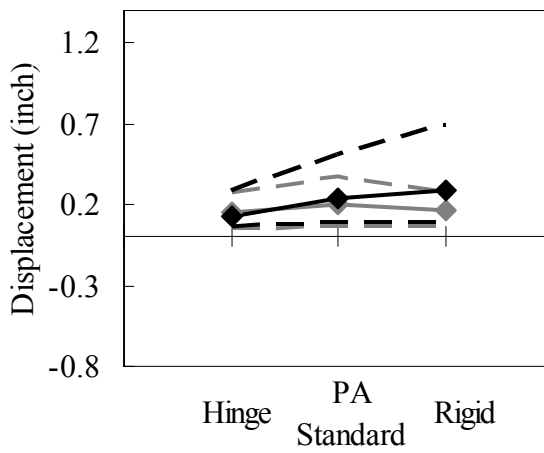
Figure 6.32: Girder Material Influence on Pile Displacement
 (—◆— : H = 10 ft; —◆— : H = 15 ft; —◆— : H = 20 ft; --- : Envelopes)



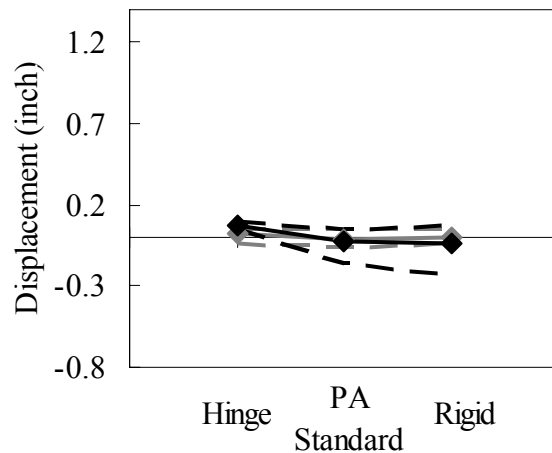
(a) $H = 10$ ft and Bridge Contraction



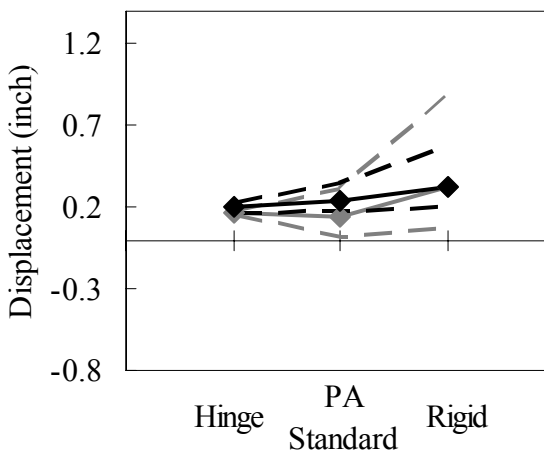
(b) $H = 10$ ft and Bridge Expansion



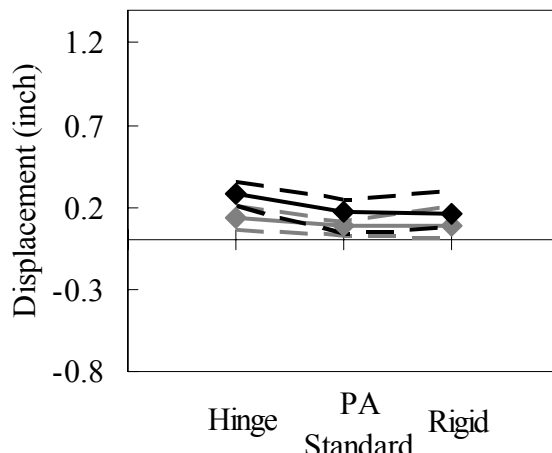
(c) $H = 15$ ft and Bridge Contraction



(d) $H = 15$ ft and Bridge Expansion

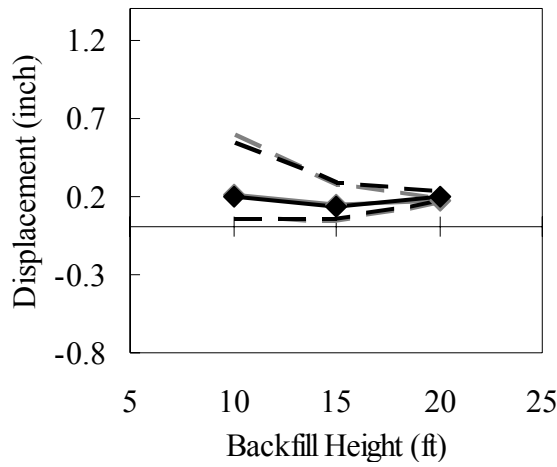


(e) $H = 20$ ft and Bridge Contraction

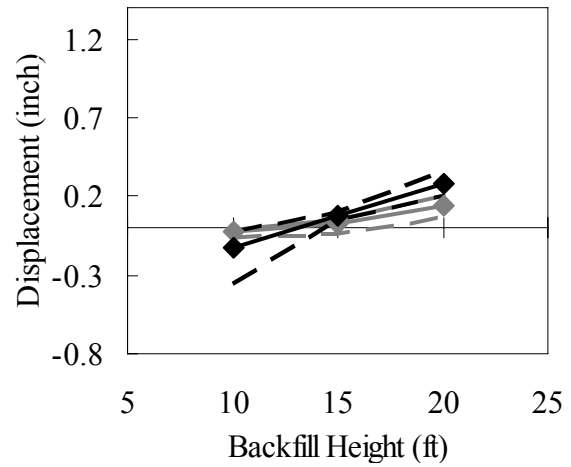


(f) $H = 20$ ft and Bridge Expansion

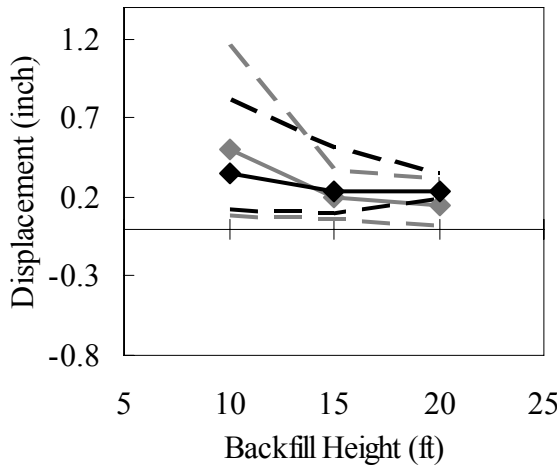
Figure 6.33: Construction Joint Stiffness Influence on Pile Displacement
(—◆— : Steel Girder; —■— : Concrete Girder; - - : Envelopes)



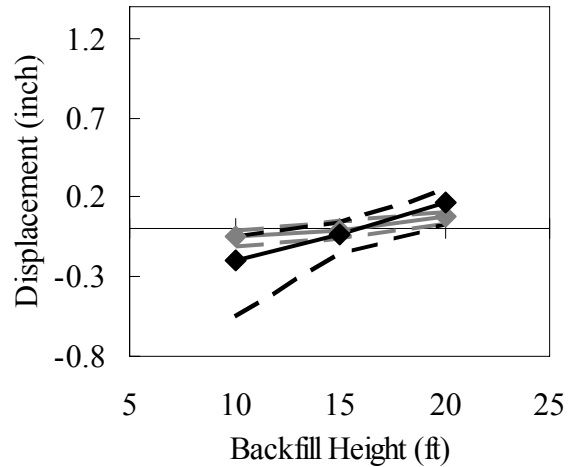
(a) Hinge and Bridge Contraction



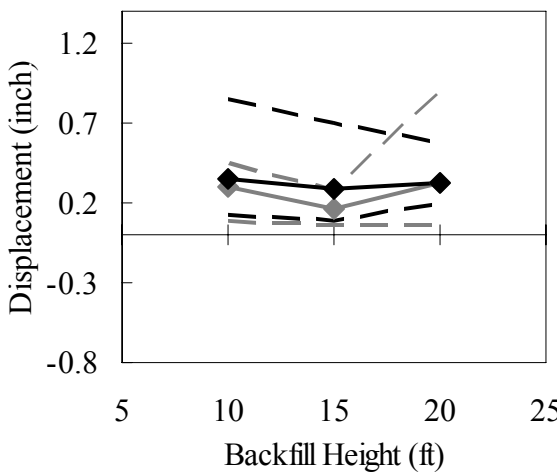
(b) Hinge and Bridge Expansion



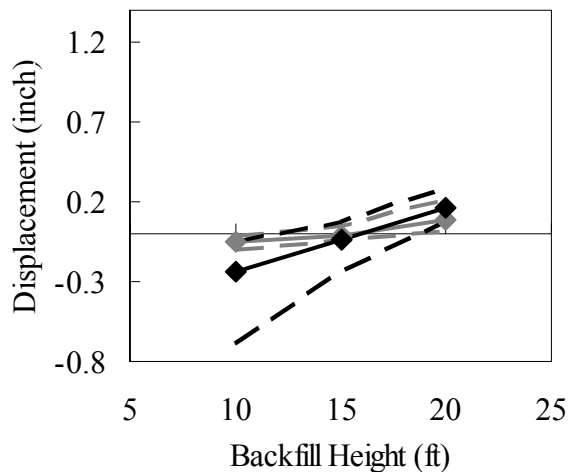
(c) PA Standard and Bridge Contraction



(d) PA Standard and Bridge Expansion

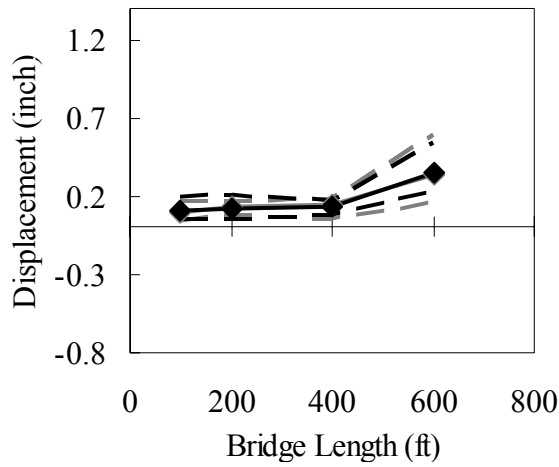


(e) Rigid and Bridge Contraction

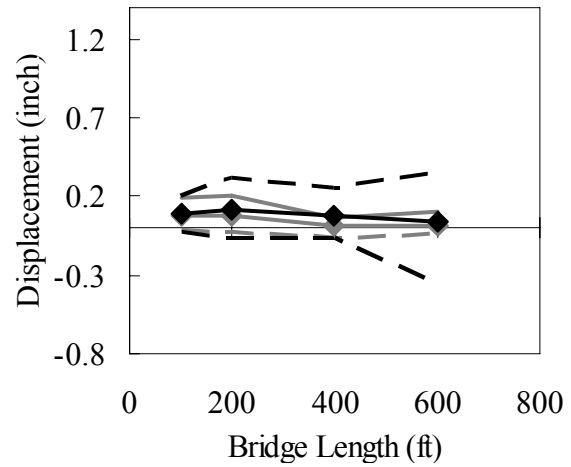


(f) Rigid and Bridge Expansion

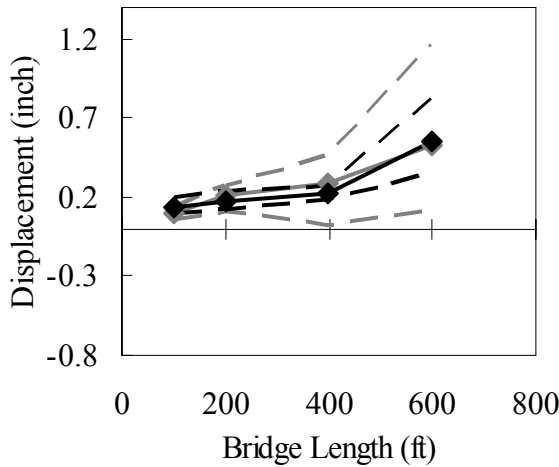
Figure 6.34: Backfill Height Influence on Pile Displacement
(—◆— : Steel Girder; —■— : Concrete Girder; - - : Envelopes)



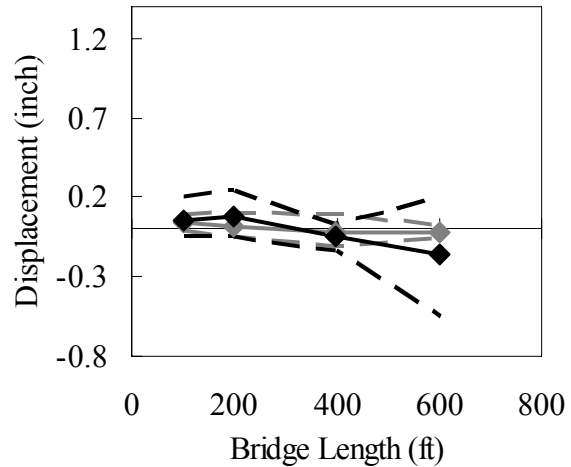
(a) Hinge and Bridge Contraction



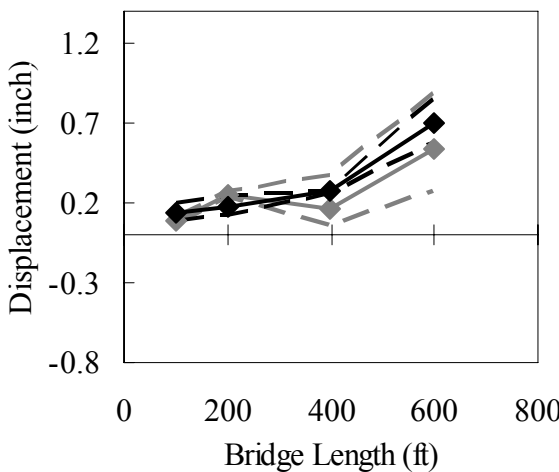
(b) Hinge and Bridge Expansion



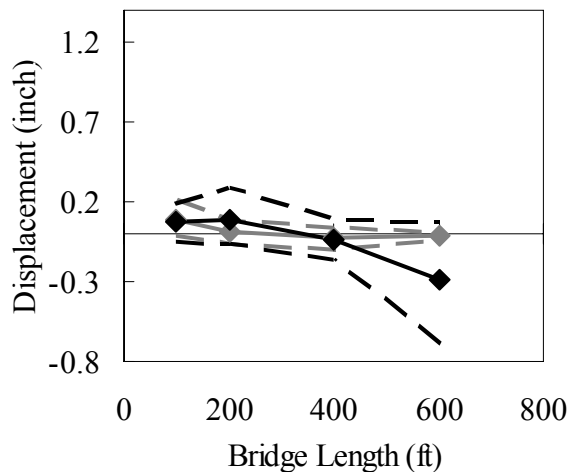
(c) PA Standard and Bridge Contraction



(d) PA Standard and Bridge Expansion



(e) Rigid and Bridge Contraction



(f) Rigid and Bridge Expansion

Figure 6.35: Bridge Length Influence on Pile Displacement
(—◆— : Steel Girder; - -◆- - : Concrete Girder; - - : Envelopes)

6.6 Concluding Remarks

The parametric study is based on the analysis methodology of Chapter 5 that was developed through the study of monitored bridge results and the process of developing calibrated numerical models. The parametric study was performed to construct IAB response trends over limited but practical ranges. The parametric study evaluated the effect of four parameters: (1) girder material, (2) construction joint stiffness, (3) backfill height, and (4) bridge length. Prestressed concrete girder bridges and steel plate girder bridges were evaluated to include girder material in the study. To investigate the influence of the backwall-to-abutment construction joint on IAB behavior, three joint conditions were considered: (1) hinge, (2) PA Standard (#5 rebars at 9 inches), and (3) rigid (no joint). Three magnitudes of backfill height were included in the study: 10, 15, and 20 ft. Bridge lengths evaluated were 100, 200, 400, and 600 ft. Thus, the parametric study evaluated four parameters resulting in a total of 72 separate study cases. Numerical models for each study case were developed and investigated for both AASHTO extreme bridge expansion and contraction static analyses. The analyses results were evaluated for five critical responses: (1) girder axial force, (2) girder bending moment, (3) pile moment, (4) pile lateral force, and (5) pile head displacement.

Based on the parametric study, the following observations are summarized:

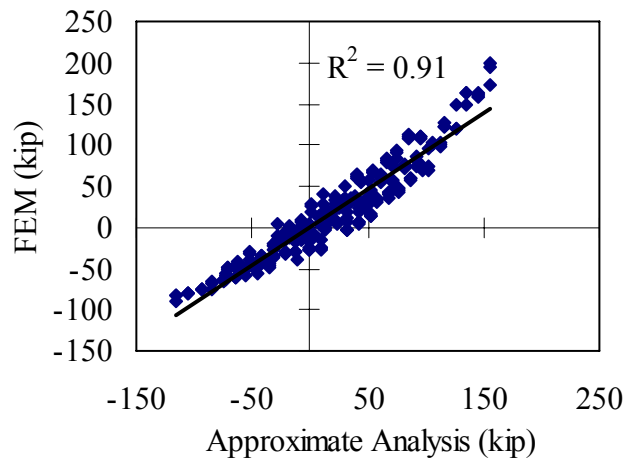
1. Steel girders and a large abutment height reduce girder tensile axial force.

Prestressed concrete girders, hinged construction joints, and low backfill height are appropriate to reduce girder compressive axial force. Priority for design will necessarily be given to the tensile axial force in a prestressed concrete girder, which is generally more critical than the compressive axial force.

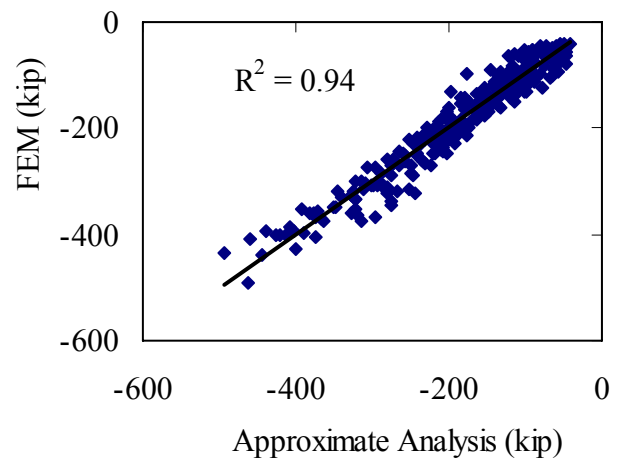
2. A hinged construction joint, low abutment height and short bridge length reduce the girder positive moment. A negative girder moment counteracts gravity loads, and therefore is not an issue. A rigid construction joint and high abutment height increase the negative girder moment.
3. A prestressed concrete girder, PA standard construction joint, and low abutment height are effective in reducing pile moments. A hinged construction joint connection reduces pile moment for bridge contraction, and a rigid connection tends to reduce pile moments under bridge expansion. The construction joint rebar detail of the current PA standard (#5 bars at 9 inches) is between a hinged and rigid joint; therefore, adding more rebars at the front face of the abutment and/or reducing rebars at the rear face of the abutment may reduce pile moment compared to the current PA standard.
4. A prestressed concrete girder, PA standard construction joint and short bridge length reduce the pile lateral force. A hinged construction joint connection tends to reduce the pile lateral force under bridge contraction. Under bridge expansion, the pile lateral force increases for a hinged construction joint and decreases for a rigid construction joint.
5. A hinged construction joint and high abutment height tends to reduce pile head displacement in IABs.

An approximate analysis method has been developed that is based on results and numerical modeling methodology of the above-discussed parametric study. The approximate analysis method allows the generalization of predicted integral abutment

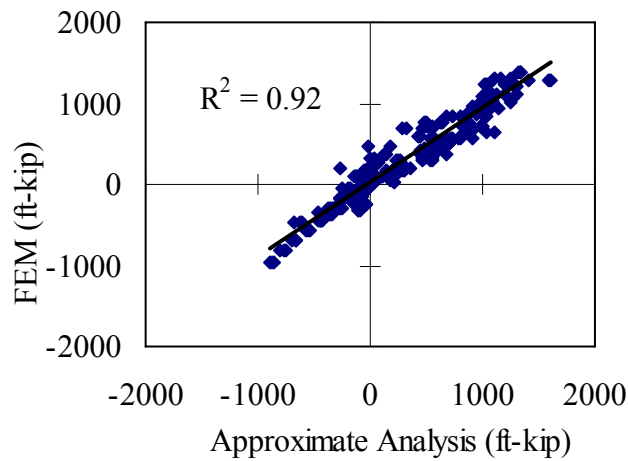
bridge behavior within certain limitations. The studied parameters considered in the parametric study--thermal expansion coefficient, bridge length, backfill height, backfill stiffness, and pile soil stiffness--are inputs to the approximate analysis that predicts key responses through the use of best-fit curves. Extensive numerical simulations resulted in a large dataset for analysis and curve fitting: three variables of each parameter resulted in 243 parametric study cases for both prestressed concrete girder bridges and steel girder bridges. A total of 486 separate study cases were analyzed for a 75-year time-history analysis to account for long-term effects. 3D models discussed in this chapter do not permit such an extensive study, demanding unmanageable storage and computing time; therefore, 2D numerical models were utilized. The established approximate analysis methods include: (1) maximum (tensile) girder axial force; (2) minimum (compressive) girder axial force; (3) maximum (positive) girder moment at the girder end adjacent to the abutment; (4) minimum (negative) girder moment at the girder end adjacent to the abutment; (5) maximum girder moment at the girder mid-span in the end span; (6) minimum girder moment at the girder mid-span in the end span; (7) pile lateral force; (8) pile moment; and (9) pile head displacement. Each approximate analysis prediction was compared to the results of 2D numerical models and presented in Figure 6.36. Each approximate analysis prediction is strongly correlated to a numerical analysis result, exhibiting approximately more than 80% correlations. The approximate analysis method and resulting simplified equations are presented in Chapter 7.



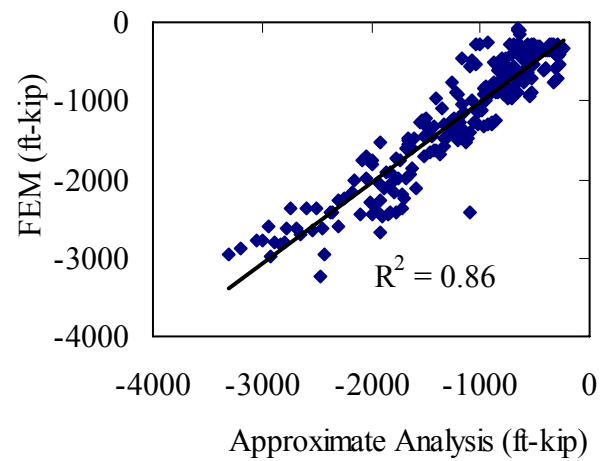
(a) Maximum Girder Axial Force



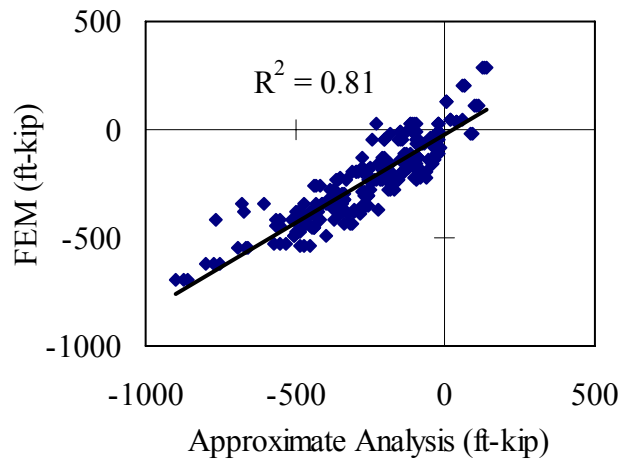
(b) Minimum Girder Axial Force



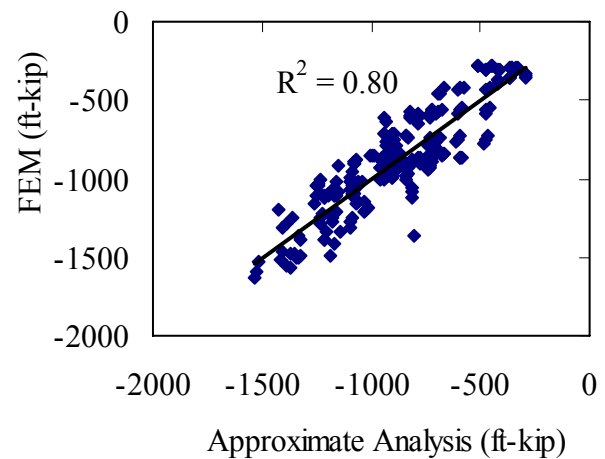
(c) Maximum Girder Moment at the Girder End adjacent to the Abutment



(d) Minimum Girder Moment at the Girder End adjacent to the Abutment

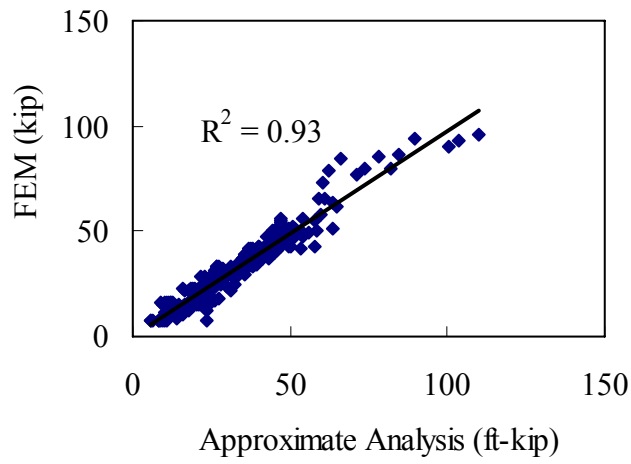


(e) Maximum Girder Moment at the Girder Mid-span in the End Span

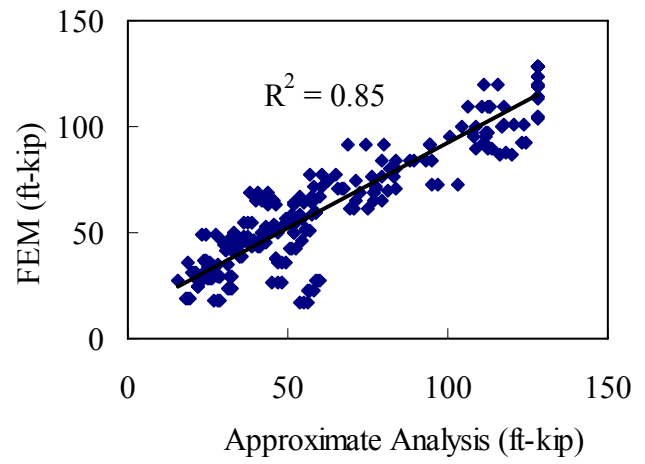


(f) Minimum Girder Moment at the Girder Mid-span in the End Span

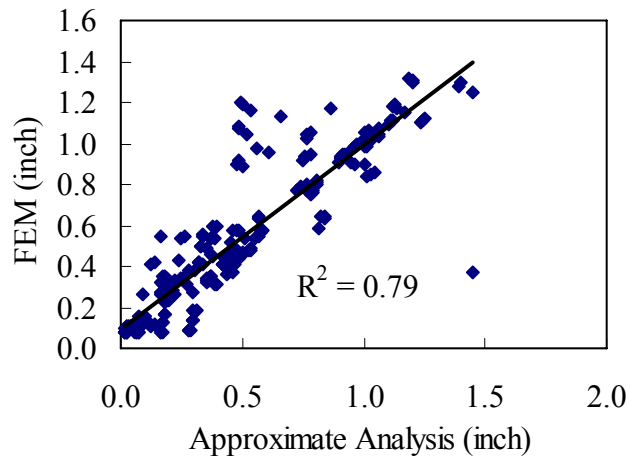
Figure 6.36: Correlation between Approximate Analysis and 2D Model Prediction



(g) Pile Lateral Force



(h) Pile Moment



(i) Pile Head Displacement

Figure 6.36: Correlation between Approximate Analysis and 2D Model Prediction (Cont.)

Chapter 7

Integral Abutment Bridge Thermal Loading Analysis

IAB analysis and design comprises a complex process due to the highly nonlinear behavior of the system. The combined effects of pile-soil interaction, abutment-soil interaction, backwall-soil interaction, and nonlinear joint behavior under thermal loading require a carefully conceived and executed analysis. Stresses that develop under thermal loading conditions must be accurately determined and combined with other load effects using applicable AASHTO load combinations. The purpose of this chapter is to present the state-of-the-art for integral abutment analysis under thermal loading and the subsequent determination of resulting thermal stresses. The presented methodologies represent the outcomes of approximately 6 years of monitoring four IABs and executing hundreds of numerical models devised to evaluate and calibrate an accurate approach.

Integral abutment bridge analysis procedures presented here are separated into a three-level approach: 1) approximate method of analysis, 2) simplified 2D method of analysis, and 3) refined 3D method of analysis. The approximate method of analysis is based on results of an extensive parametric study that allowed the generalization of predicted integral abutment bridge behavior within certain limitations. The simplified 2D analysis method is based on extensive development and calibration of condensed bridge models considering both the observed field behavior and refined 3D finite element modeling. Refined 3D finite element modeling procedures are based on extensive calibration of detailed models with observed behavior at actual bridge sites. Also presented in this chapter are guidelines for material property selection,

specifications for modeling, and requirements for the loading environment with respect to thermal and earth pressures.

7.1. Scope

This chapter presents methodologies for analyzing IABs under thermal loading. In order for the scope of this document and the applicability of the methods to be clearly understood by the user, the following should be considered:

- The abutments are integral to the superstructure with standard PennDOT-type of construction details.
- Abutments are supported on a single row of steel HP section piles oriented to bend about the weak axis.
- Steel HP piles are sufficiently embedded into the concrete abutment in order to create a complete and rigid connection, transferring all translation and rotation between the two elements.
- Steel HP piles are driven in either pre-drilled holes, pre-compacted fill, or native soils.
- Steel HP piles must be long piles:

$$L \geq l_c = \sqrt[4]{\frac{4E_p I_p}{K}} \quad (7.1)$$

where:

L = pile length,

l_c = characteristic length,

E_p = elastic modulus of pile,

I_p = moment of inertia of pile cross-section,

K = soil spring constant ($= kD$),

k = modulus of sub-grade reaction,

D = pile diameter.

- A free-draining, compacted, engineered backfill is placed both behind and in front of the abutments.
- Bridge structural elements are expected to behave within the linear-elastic range, except for supporting steel piles.
- Steel piles behave elasto-plastic.
- Soil boundaries, including backfill and soil surrounding piles, are anticipated to behave inelastically.
- Vertical displacement in supporting piles is negligible.
- Soil layers surrounding piles are continuously and horizontally stratified.
- Bridge length is less than 600 ft.
- The bridge is a right bridge, the abutment having no significant skew with respect to the roadway axis.
- IAB construction is standard concrete slab on steel or concrete girders.
- The loading considered herein includes temperature with applicable thermal gradient, backfill pressure, and time-dependent effects.
- Bridge construction is completed during the spring, summer, or fall season.

It is anticipated that the above scope will encompass the vast majority of IAB structures considered for construction within the Commonwealth of Pennsylvania.

7.2. Approximate Method of Analysis

7.2.1 Introduction

For an approximate analysis, verification of another analysis, or preliminary design and analysis, the approximate analysis method presented herein is very useful. This approximate analysis method is based on results of an extensive 2D numerical analysis parametric study in which results were generalized within short to medium-length bridges (100 ft to 400 ft). The approximate analysis determines five key responses: (1) superstructure bending moment, (2) superstructure axial force, (3) pile moment, (4) pile lateral force, and (5) abutment/pile-head displacement. The approximate method was developed using regression analyses based on an extensive numerical parametric study with numerical simulations run over an expected bridge life of 75 years.

The approximate analysis method requires five input parameters: (1) a concrete thermal expansion coefficient, (2) bridge length, (3) backfill height, (4) backfill stiffness, and (5) pile soil stiffness. The definition and determination of backfill height is illustrated in Figure 7.1. Backfill soil properties and soil layers around piles are classified into three levels and presented in Tables 7.1 and 7.2. Soil stiffness properties in terms of soil stiffness have been classified as low, intermediate, and high stiffness.

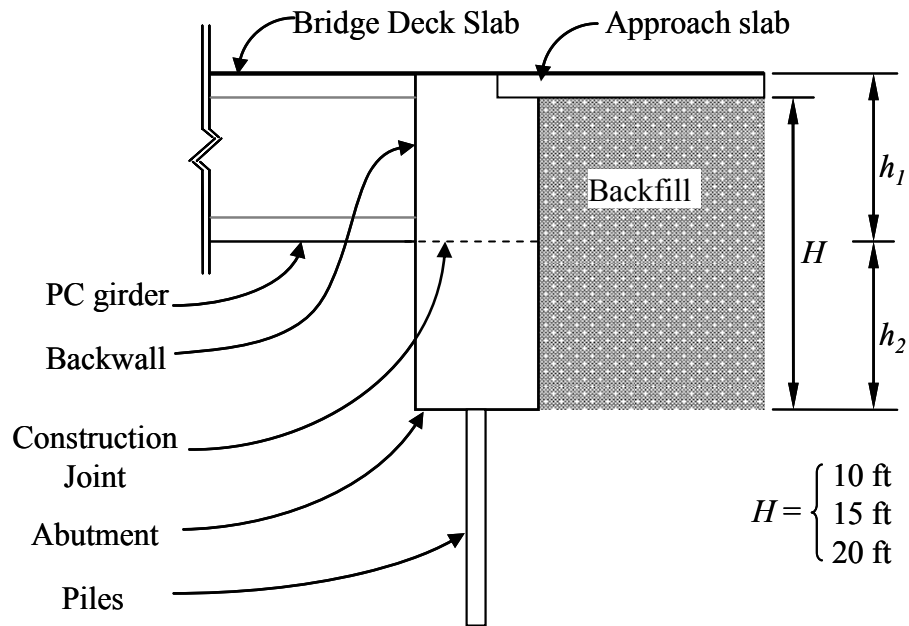


Figure 7.1. Backfill Height Parameter.

Table 7.1. Backfill Properties and Range Determination.

Property	<i>Low</i>	<i>Intermediate</i>	<i>High</i>
Density (γ) (pcf)	116	119	123
Angle of friction (ϕ_f) (Degree)	30.6	34	37.4
Subgrade Modulus (K_h) (pci)	22.5	43.8	65

Note: *Low* = 1, *Intermediate* = 2, *High* = 3 in the approximate method.

Table 7.2. Soil Layer Properties and Range Determination.

Property	<i>Low</i>	<i>Intermediate</i>	<i>High</i>
Sand Density (pcf)	100	121	142
Clay Density (pcf)	100	121	142
Angle of Friction (Sand) (Degree)	28	35	42
Undrained Shear Strength (clay) (psi)	7	17.5	28
Elastic Modulus (K) (pci)	700	1000	1,300
ε_{50} , (in)	0.01	0.008	0.005

Note: *Low* = 1, *Intermediate* = 2, *High* = 3 in the approximate method.

7.2.2 Superstructure Moments

Positive and negative moments due to thermal loading and time-dependent effects occur throughout the superstructure. During bridge contraction, maximum positive moment occurs at mid-span in the end span, and the maximum negative moment occurs adjacent to the abutment. During bridge expansion, a negative moment occurs at mid-span in the end span, and a positive moment occurs adjacent to the abutment. Positive and negative girder moments at the abutment are always larger at mid-span. The maximum bridge total positive and negative moments are estimated at the girder end adjacent to the abutment as:

For prestressed concrete girder IABs:

$$\begin{aligned} M_{pos} = & 120\alpha - 190H + 690P - 14 \geq 0 & \text{for } L \leq 130\text{ft} \\ & 210\alpha + 53H + 170P - 3400 \geq 0 & \text{for } 130 \leq L \leq 300\text{ft} \\ & 59\alpha + 740P - 2600 \geq 0 & \text{for } L \geq 300\text{ft} \end{aligned} \quad (7.2)$$

$$\begin{aligned} M_{neg} = & -74\alpha^{0.35}L^{0.6}P^{0.2} & \text{for } H \leq 13\text{ft} \\ & -280\alpha^{0.4}L^{0.35} & \text{for } 13 \leq H \leq 18\text{ft} \\ & -4000\alpha^{0.1}P^{0.4} & \text{for } H \geq 18\text{ft} \end{aligned} \quad (7.3)$$

For steel girder IABs:

$$M_{pos} = -12\alpha + 3L - 208H - 10B + 863P + 1570 \geq 0 \quad (7.4)$$

$$M_{neg} = -158\alpha^{0.2}L^{0.7}H^{0.3}B^{0.1}P^{0.2} - 1990 \quad (7.5)$$

and at the girder mid-span in the end span (in a multi-span IAB) as:

For prestressed concrete girder IABs,

$$\begin{aligned} M_{pos} = & 134\alpha + 11L + 1040P - 3300 \geq 0 & \text{for } H \leq 13\text{ft} \\ & 118\alpha + 13L + 1100P - 4000 \geq 0 & \text{for } 13 \leq H \leq 18\text{ft} \\ & 213\alpha + 14L + 1500P - 6700 \geq 0 & \text{for } H \geq 18\text{ft} \end{aligned} \quad (7.6)$$

$$\begin{aligned} M_{neg} = & -17\alpha^{0.7}L^{0.80}B^{0.1}P^{0.3} & \text{for } H \leq 13\text{ft} \\ & -26\alpha^{1.0}L^{0.65}B^{0.1}P^{0.08} & \text{for } 13 \leq H \leq 18\text{ft} \\ & -700\alpha^{0.55}L^{0.25}B^{0.04}P^{0.7} & \text{for } H \geq 18\text{ft} \end{aligned} \quad (7.7)$$

For steel girder IABs,

$$M_{pos} = -166\alpha + 0.5L - 5.9H - 5.6B + 269P + 1803 \quad (7.8)$$

$$M_{neg} = 179\alpha - 4.5L + 17.5H - 40.9B + 156P - 2480 \quad (7.9)$$

$$M_g = \frac{M_{pos} \text{ or } M_{neg}}{N_g} \quad (7.10)$$

where:

M_{pos} = bridge total positive moment (kip-ft),

M_{neg} = bridge total negative moment (kip-ft),

M_g = girder moment (kip-ft),

N_g = number of girders,

α = thermal expansion coefficient (in/in/°F) $\times 1\text{E}+6$,

L = total bridge length (ft),

H = backfill height (ft) in Figure 7.1,

B = backfill stiffness in Table 7.1 (*Low* = 1, *Intermediate* = 2, *High* = 3),

P = soil pile stiffness in Table 7.2 (*Low* = 1, *Intermediate* = 2, *High* = 3).

As shown in Equation 7.10, the moment per girder is determined by dividing the bridge moment by the number of girders. Some bridges do not always experience positive moments, and therefore, approximated positive moments may be zero.

7.2.3 Superstructure Axial Forces

Both tension and compression superstructure axial forces develop because of thermal loading and must be considered in the design. The bridge axial force due to temperature load is considered to be constant along the bridge length. The maximum bridge tension and compression axial forces can be approximated using equations as:

For prestressed concrete girder IABs,

$$F_t = 16.6\alpha + 1.2L - 34.9H + 118.8P - 2.1 \geq 0 \quad (7.11)$$

$$F_c = \begin{cases} -2.9\alpha^{0.7}L^{0.8}B^{0.2}P^{0.3} & \text{for } H \leq 13\text{ft} \\ -5.4\alpha^{0.8}L^{0.6}B^{0.2}P^{0.02} & \text{for } 13 \leq H \leq 18\text{ft} \\ -28.6\alpha^{0.6}L^{0.4}B^{0.4}P^{0.2} & \text{for } H \geq 18\text{ft} \end{cases} \quad (7.12)$$

For steel girder IABs,

$$F_t = 4.4\alpha + 0.5L - 30H + 14B + 62P + 127 \geq 0 \quad (7.13)$$

$$F_c = -32\alpha - 2L - 18H - 101B + 16P + 374 \quad (7.14)$$

$$F_g = \frac{F_t \text{ or } F_c}{N_g} \quad (7.15)$$

where:

F_t = bridge tension force (kip),

F_c = bridge compression force (kip),

F_g = girder axial force (kip),

N_g = number of girders,

α = thermal expansion coefficient (in/in/°F) $\times 1\text{E}+6$,

L = total bridge length (ft),

H = backfill height (ft) in Figure 7.1,

B = backfill stiffness in Table 7.1 (*Low* = 1, *Intermediate* = 2, *High* = 3),

P = soil pile stiffness in Table 7.2 (*Low* = 1, *Intermediate* = 2, *High* = 3).

As shown in Equation 7.15, the force per girder is determined by dividing the bridge axial force by the number of girders.

7.2.4 Pile Head Moments

H-pile head moments (at the bottom of the abutment) are critical in determining the required pile strength. Figure 7.2 illustrates calculated pile head responses with respect to the lateral loading. The maximum pile displacement, moment, and shear force occur at the pile head. The maximum pile head moments resisted by the piles are estimated as follows.

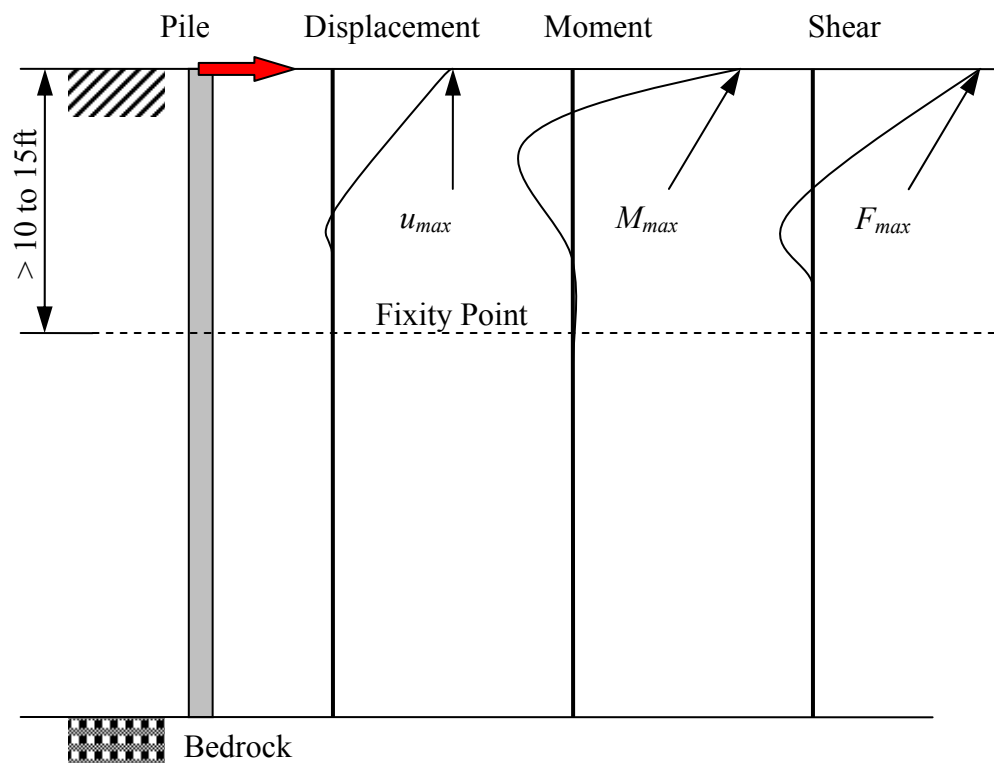


Figure 7.2. Pile Response Displacement, Moment, and Shear Profile

For prestressed concrete girder IABs,

$$\Sigma M_{piles} = 21\alpha^{0.5}L^{0.5}H^{0.1}P^{0.6} \leq M_{y\,pile} N_p \quad (7.16)$$

For steel girder IABs,

$$\begin{aligned} \Sigma M_{piles} &= 12\alpha^{0.4}L^{0.6}P^{0.5} + 203 && \text{for } H \leq 13\text{ft} \\ &= 30\alpha^{0.4}L^{0.4}P^{0.5} + 287 && \text{for } 13 \leq H \leq 18\text{ft} \\ &= 223\alpha^{0.3}L^{0.2}P^{0.2} + 324 && \text{for } H \geq 18\text{ft} \end{aligned} \quad (7.17)$$

$$M_{pile} = \frac{\Sigma M_{piles}}{N_p} \quad (7.18)$$

where:

ΣM_{piles} = total moment resisted by the piles (kip-ft),

$M_{y\,pile}$ = single pile yielding moment (kip-ft),

N_p = number of piles,

M_{pile} = maximum single pile moment (kip-ft),

α = thermal expansion coefficient (in/in/°F) $\times 1\text{E}+6$,

L = total bridge length (ft),

H = backfill height (ft) in Figure 7.1,

B = backfill stiffness in Table 7.1 (*Low* = 1, *Intermediate* = 2, *High* = 3),

P = soil pile stiffness in Table 7.2 (*Low* = 1, *Intermediate* = 2, *High* = 3).

As shown in Equation 7.18, the moment per pile is determined by dividing the total moment by the number of piles.

7.2.5 Pile Axial Forces

Based on measurements and analyses, gravity loads do not significantly influence forces determined as a result of thermal loading. The pile lateral displacement is not sufficient to produce a significant $P-\Delta$ effect. All bridges studied exhibited lateral displacements within an acceptable AASHTO LRFD horizontal displacement limit of 1.5 inches. Therefore, a usual gravity load evaluation is sufficient.

7.2.6 Pile Lateral Forces

Pile lateral shear forces are another aspect of critical factors in designing supporting piles. The maximum lateral shear forces occur at the pile head, which can be determined using the approximate analysis method. The total lateral pile shear force is computed as:

For prestressed concrete girder IABs,

$$\begin{aligned} \Sigma F_{piles} &= 2\alpha^{0.5} L^{0.7} B^{-0.1} P^{0.9} \leq F_{y_pile} N_p & \text{for } H \leq 13\text{ft} \\ &19\alpha^{0.2} L^{0.4} B^{-0.1} P^{0.8} \leq F_{y_pile} N_p & \text{for } 13 \leq H \leq 18\text{ft} \\ &418\alpha^{-0.01} L^{-0.07} B^{-0.05} P^{0.6} \leq F_{y_pile} N_p & \text{for } H \geq 18\text{ft} \end{aligned} \quad (7.19)$$

For steel girder IABs,

$$\begin{aligned} \Sigma F_{piles} &= 4.8\alpha^{0.35} L^{0.6} B^{-0.2} P^{0.7} + 52 \leq F_{y_pile} N_p & \text{for } H \leq 13\text{ft} \\ &241P^{0.45} + 42 \leq F_{y_pile} N_p & \text{for } 13 \leq H \leq 18\text{ft} \\ &555P^{0.27} + 45 \leq F_{y_pile} N_p & \text{for } H \geq 18\text{ft} \end{aligned} \quad (7.20)$$

$$F_{pile} = \frac{\Sigma F_{piles}}{N_p} \quad (7.21)$$

where:

ΣF_{piles} = maximum total lateral shear force (kips),

F_{y_pile} = single pile shear capacity (kips),

N_p = number of piles,

F_{pile} = maximum lateral shear force per pile (kips),

α = thermal expansion coefficient (in/in/°F) $\times 1E+6$,

L = total bridge length (ft),

H = backfill height (ft) in Figure 7.1,

B = backfill stiffness in Table 7.1 (*Low* = 1, *Intermediate* = 2, *High* = 3),

P = soil pile stiffness in Table 7.2 (*Low* = 1, *Intermediate* = 2, *High* = 3).

7.2.7 Abutment/Pile-head Displacements

Due to bridge superstructure contraction and expansion, the pile head experiences lateral displacement, with the maximum displacement occurring at the pile head as presented in Figure

7.2. The maximum pile-head displacement can be estimated as:

For prestressed concrete girder IABs,

$$u_{max} = \begin{cases} 0.0004\alpha^{0.3}L^{1.2}B^{0.02}P^{-0.06} & \text{for } H \leq 13\text{ft} \\ 0.0006\alpha^{0.7}L^{1.0}B^{-0.02}P^{-0.1} & \text{for } 13 \leq H \leq 18\text{ft} \\ 0.2\alpha^{0.3}L^{0.1}B^{-0.02}P^{-1.0} & \text{for } H \geq 18\text{ft} \end{cases} \quad (7.22)$$

For steel girder IABs,

$$u_{max} = \begin{cases} 0.011\alpha^{0.4}L^{0.9}B^{0.1}P^{-0.1} + 0.08 & \text{for } H \leq 13\text{ft} \\ 0.022\alpha + 0.001L - 0.011B - 0.163P + 0.68 & \text{for } 13 \leq H \leq 18\text{ft} \\ 1.5\alpha^{0.02}L^{-0.1}B^{0.1}P^{-0.1} + 0.096 & \text{for } H \geq 18\text{ft} \end{cases} \quad (7.23)$$

where:

u_{max} = maximum pile-head displacement (in),

α = thermal expansion coefficient (in/in/°F) $\times 1E+6$,

L = total bridge length (ft),

H = backfill height (ft) in Figure 7.1,

B = backfill stiffness in Table 7.1 (*Low* = 1, *Intermediate* = 2, *High* = 3),

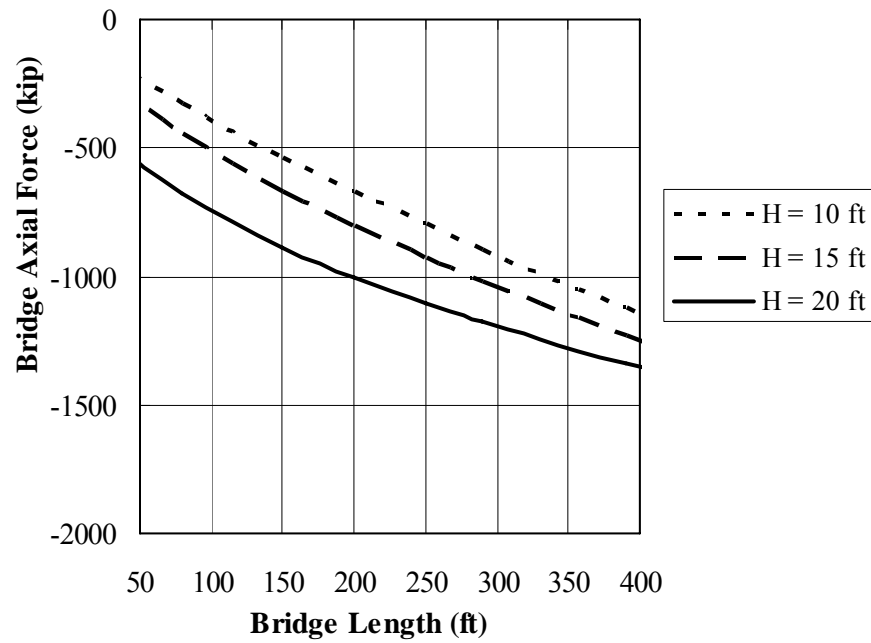
P = soil pile stiffness in Table 7.2 (*Low* = 1, *Intermediate* = 2, *High* = 3).

7.3.8 Graphs for Approximate Analysis

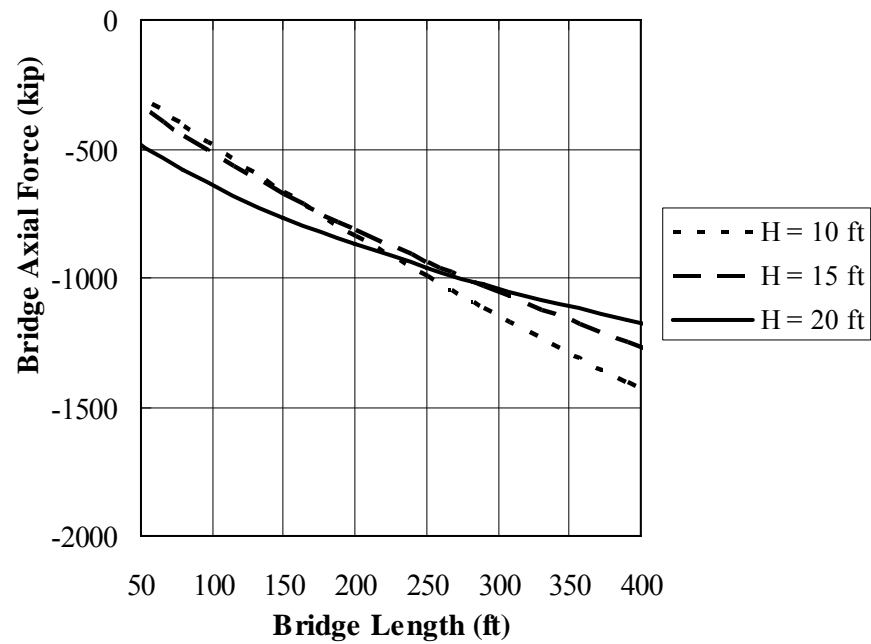
Included here are graphs developed on the basis of the above approximate IAB analysis equations. These graphs provide a convenient means of conducting a preliminary and rapid bridge superstructure and substructure analysis. The graphs were developed based on backfill soil classifications defined in Table 7.1 with PennDOT standard backfill and soil stiffness around piles defined in Table 7.2. The approximate analysis graphs provide IAB thermal bridge axial forces, bridge bending moments, the minimum number supporting piles, and pile head/abutment displacement on the substructure.

7.3.8.1 Bridge Axial Force

From Figures 7.3 and 7.4, the compressive and tensile bridge axial forces are determined based on bridge length (L) and backfill height (H). If the soil layer immediately below the abutment is very stiff, then Figures 7.3(c) and 7.4(c) are used. For soil conditions of low or intermediate stiffness, Figures 7.3(a), 7.3(b), 7.4(a) and 7.4(b) are used. Compressive bridge axial force is closely related to backfill height and pile soil stiffness. When soil pile stiffness is low, a lower backfill height reduces the compressive force. However, when pile soil stiffness is high, a higher backfill reduces the compressive bridge axial force. Bridge axial tensile force increases as backfill height decreases and/or pile soil stiffness increases.

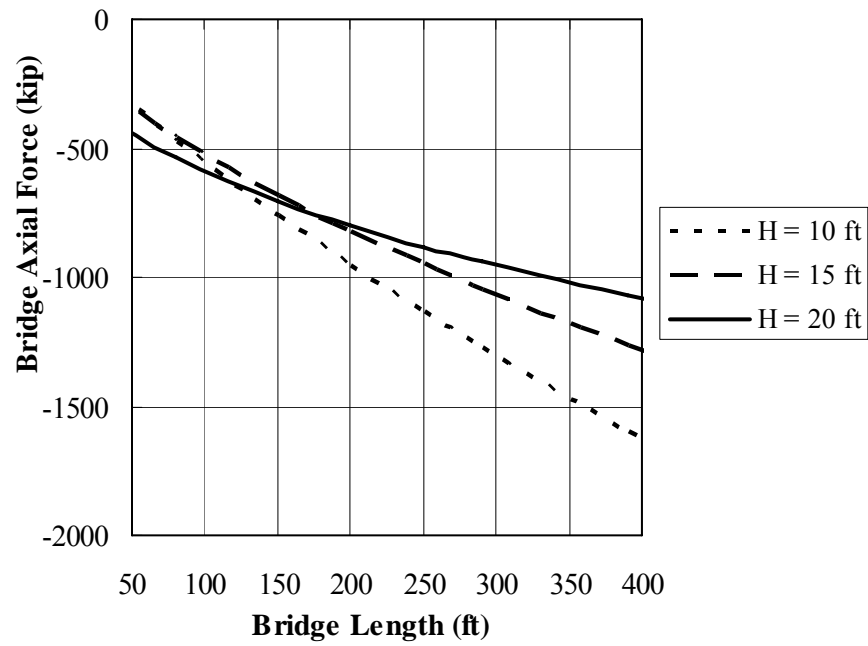


(a) Prestressed Concrete Girder IAB: Soil Pile Stiffness (P) = *Low*

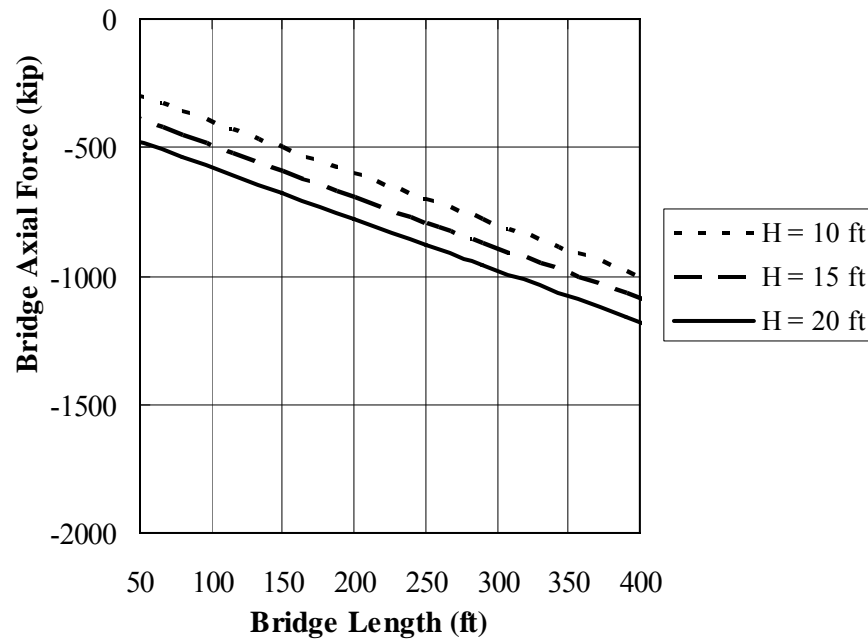


(b) Prestressed Concrete Girder IAB: Soil Pile Stiffness (P) = *Intermediate*

Figure 7.3. Bridge Total Compressive Axial Force.

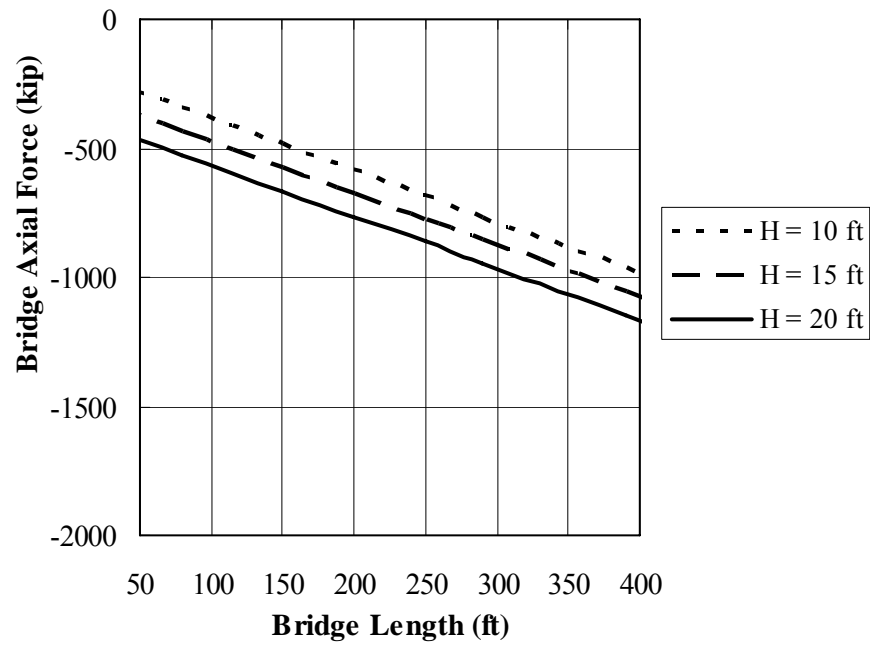


(c) Prestressed Concrete Girder IAB: Soil Pile Stiffness (P) = *High*

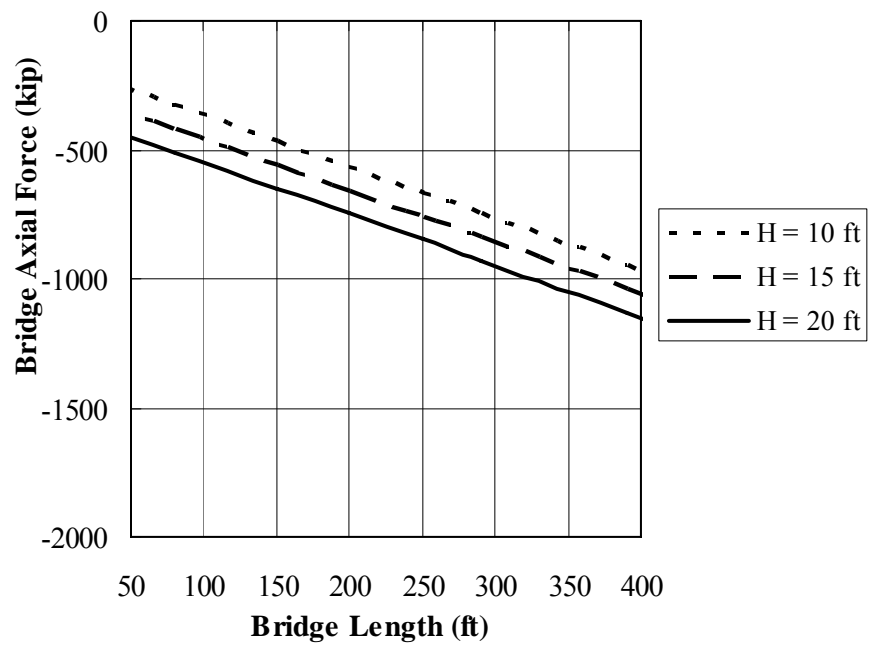


(d) Steel Girder IAB: Soil Pile Stiffness (P) = *Low*

Figure 7.3. Bridge Total Compressive Axial Force (Cont.).

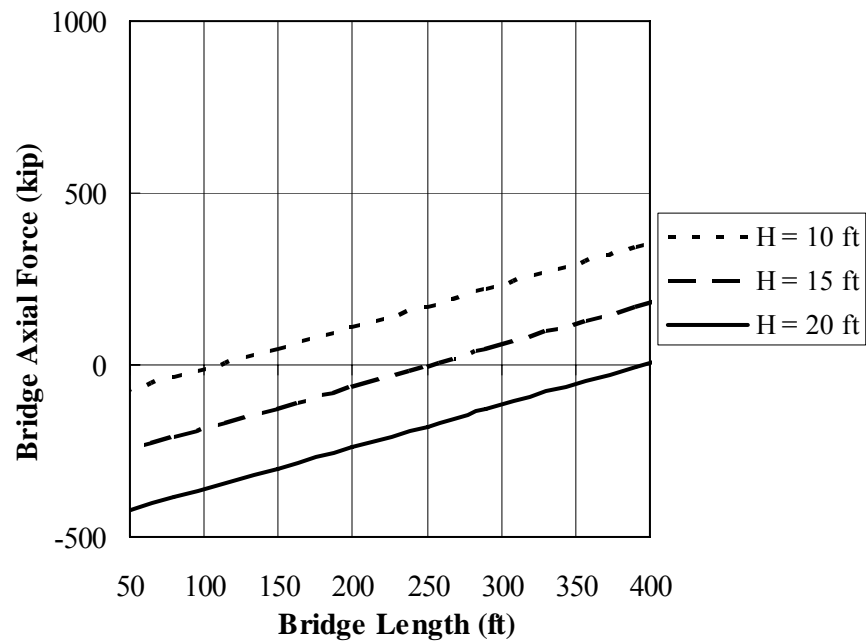


(e) Steel Girder IAB: Soil Pile Stiffness (P) = *Intermediate*

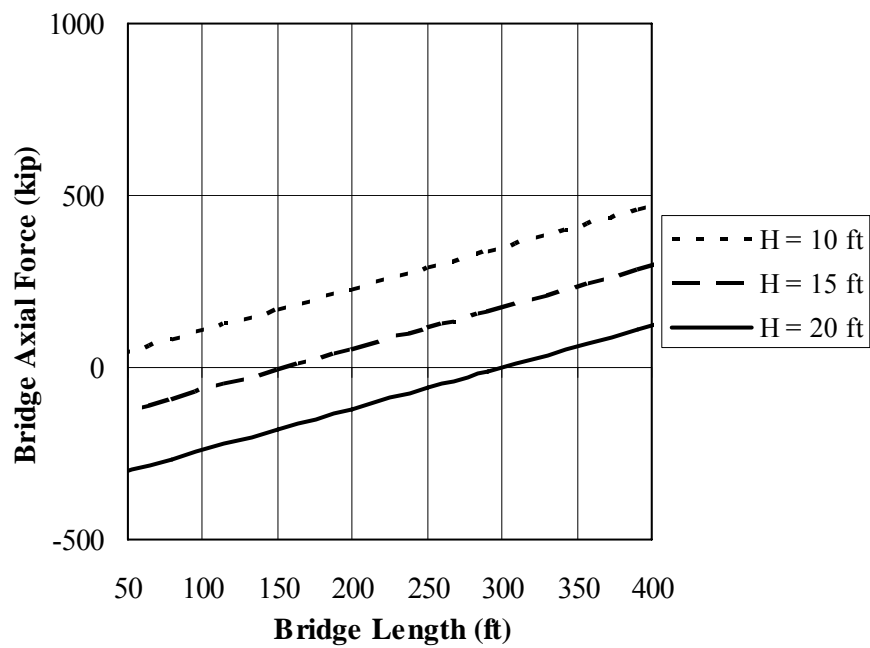


(f) Steel Girder IAB: Soil Pile Stiffness (P) = *High*

Figure 7.3. Bridge Total Compressive Axial Force (Cont.).

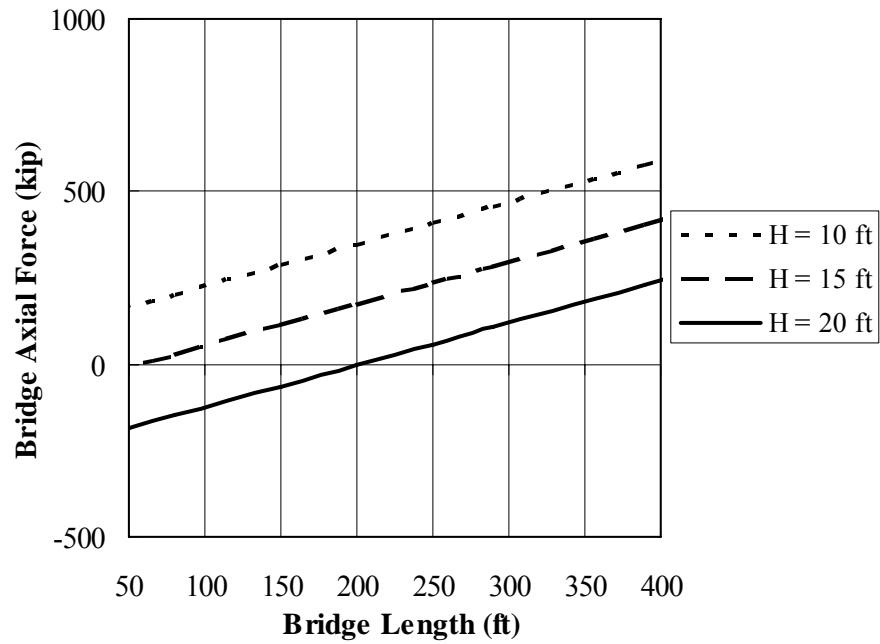


(a) Prestressed Concrete Girder IAB: Soil Pile Stiffness (P) = *Low*

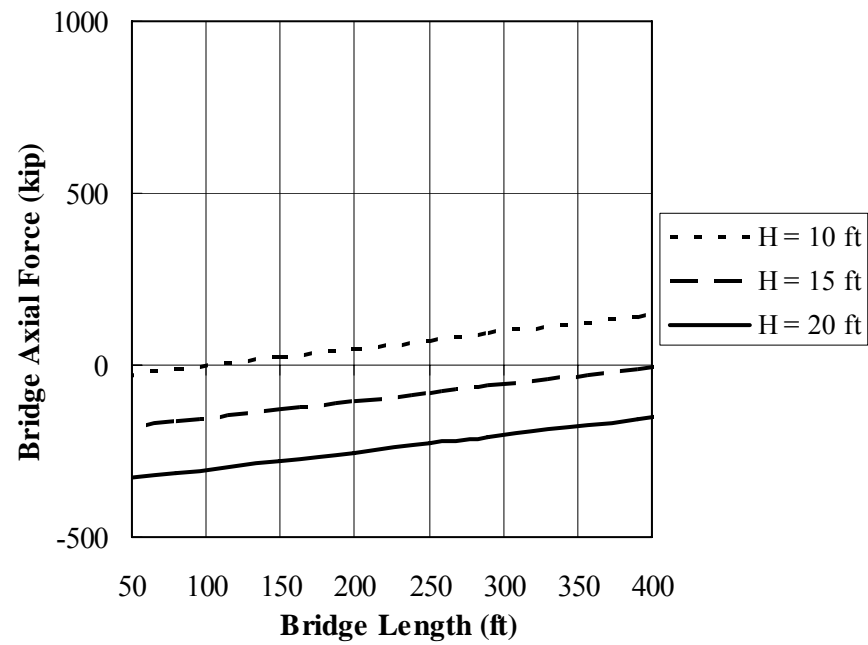


(b) Prestressed Concrete Girder IAB: Soil Pile Stiffness (P) = *Intermediate*

Figure 7.4. Bridge Total Tensile Axial Force.

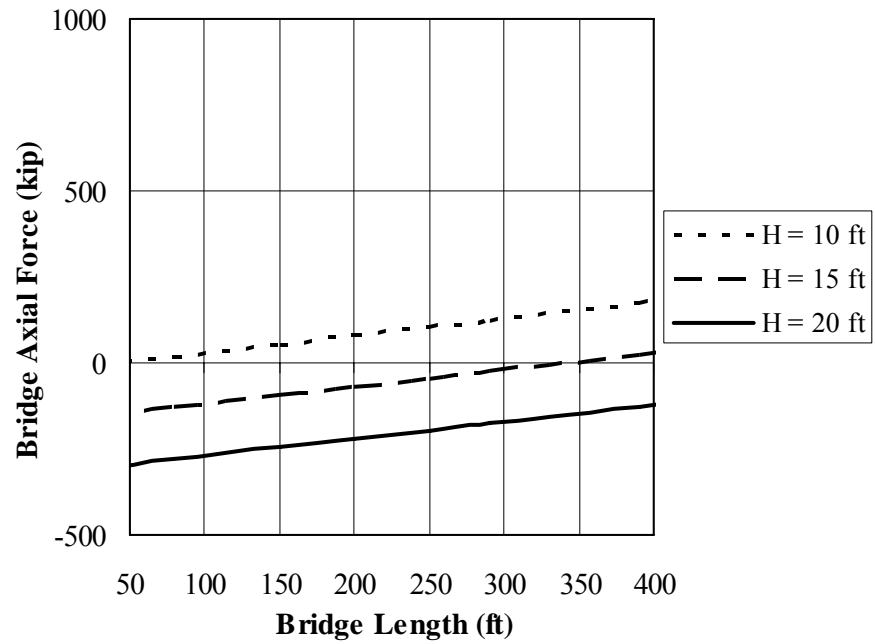


(c) Prestressed Concrete Girder IAB: Soil Pile Stiffness (P) = *High*

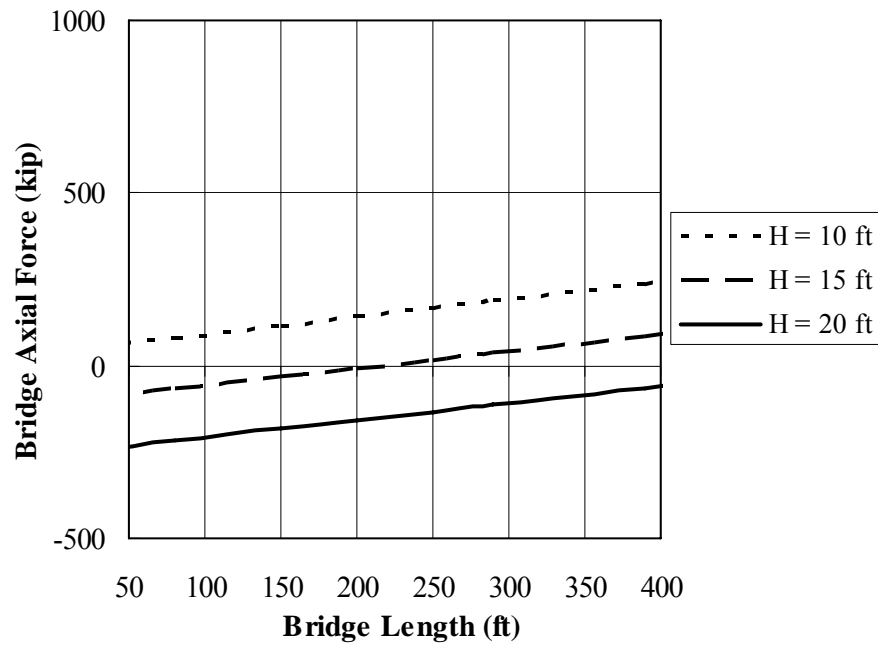


(d) Steel Girder IAB: Soil Pile Stiffness (P) = *Low*

Figure 7.4. Bridge Total Tensile Axial Force (Cont.).



(e) Steel Girder IAB: Soil Pile Stiffness (P) = *Intermediate*

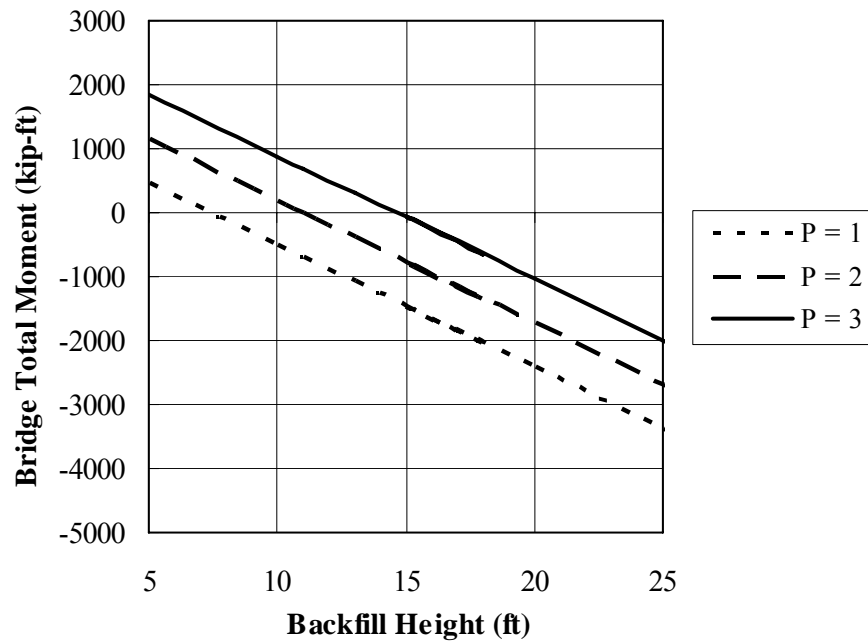


(f) Steel Girder IAB: Soil Pile Stiffness (P) = *High*

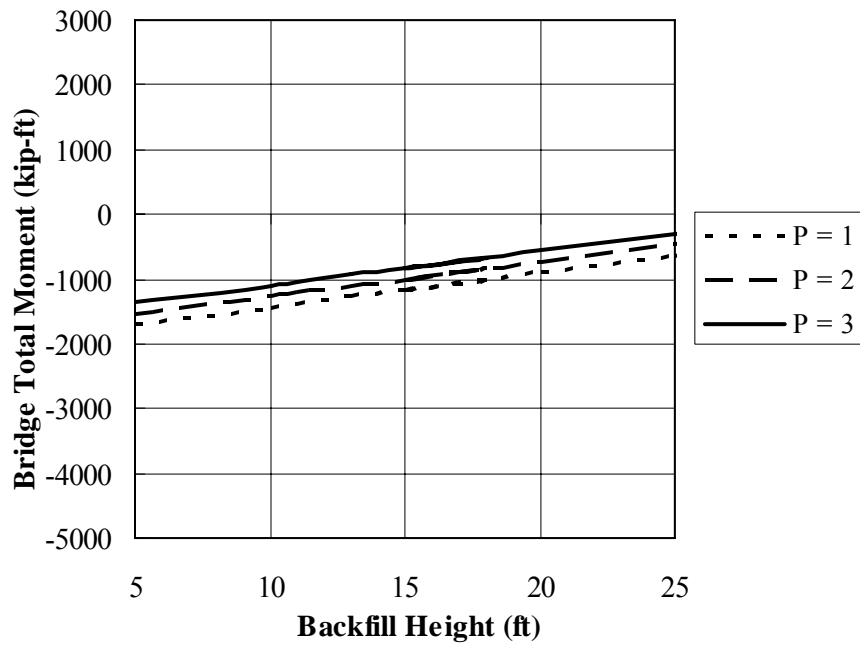
Figure 7.4. Bridge Total Tensile Axial Force (Cont.).

7.3.8.2 Bridge Total Bending Moment

Figures 7.5 and 7.6 present bridge total positive and negative bending moments at mid-span of the exterior span. Figures 7.7 and 7.8 present bridge total positive and negative bending moments at the abutment. Bridge total bending moments are determined based on bridge length (L) and backfill height (H). Bridge total positive bending moments at mid-span are a function of three bridge lengths: 60 ft, 200 ft, and 400 ft. Bridge total negative bending moments at girder mid-span are a function of three backfill heights: 10 ft, 15 ft, and 20 ft. Bridge total positive and negative bending moments at the abutment are also a function of backfill height.

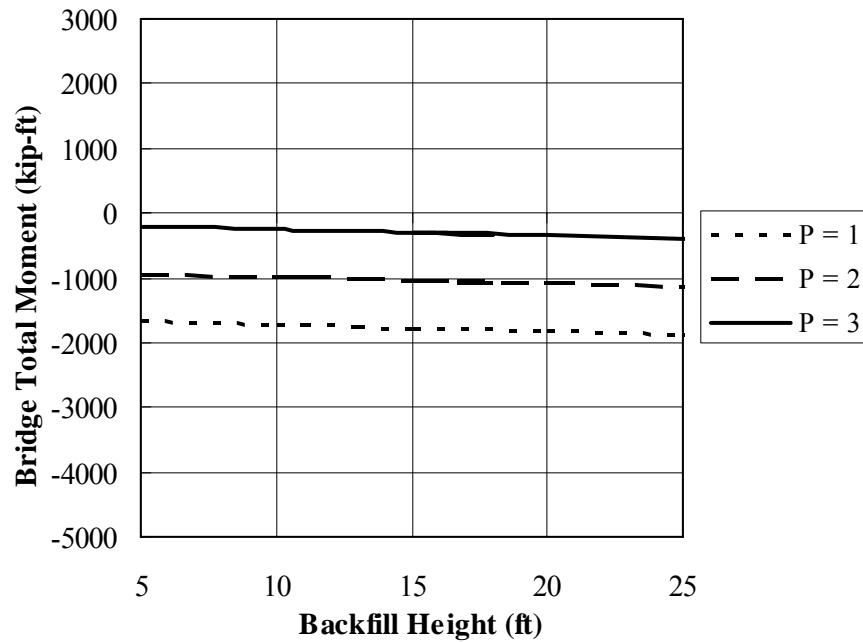


(a) Prestressed Concrete Girder IAB: Bridge Length (L) = 60ft

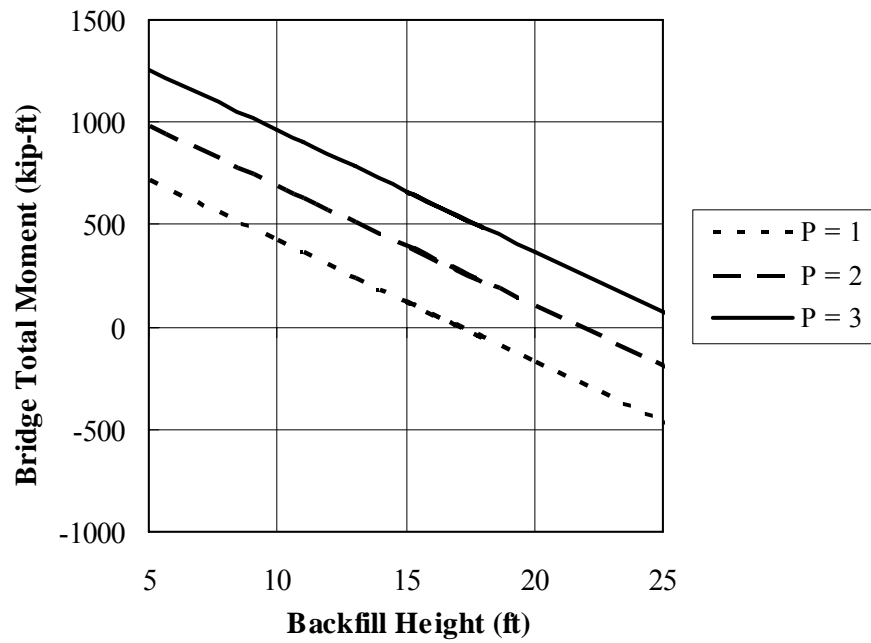


(b) Prestressed Concrete Girder IAB: Bridge Length (L) = 200ft

Figure 7.5. Bridge Total Positive Bending Moment at mid-span of the exterior span.

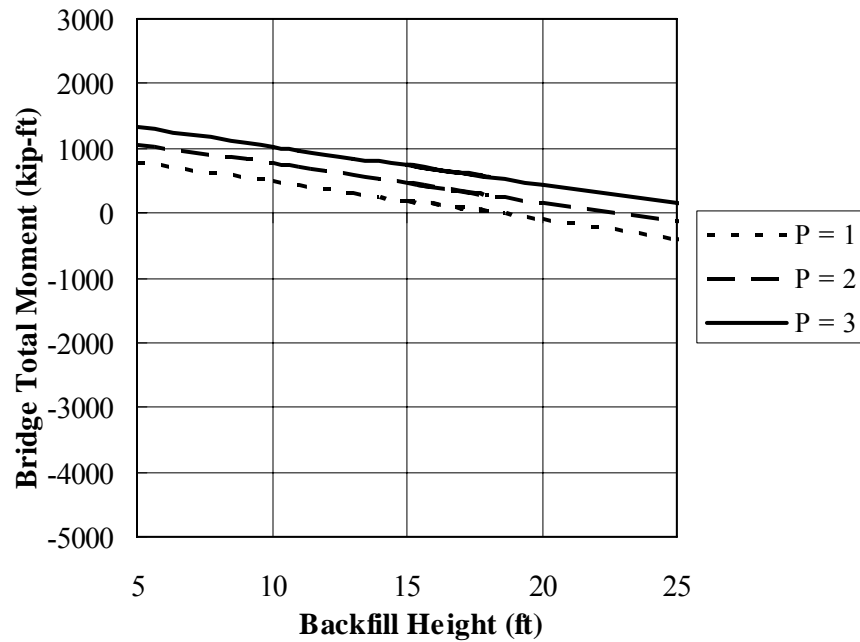


(c) Prestressed Concrete Girder IAB: Bridge Length (L) = 400ft

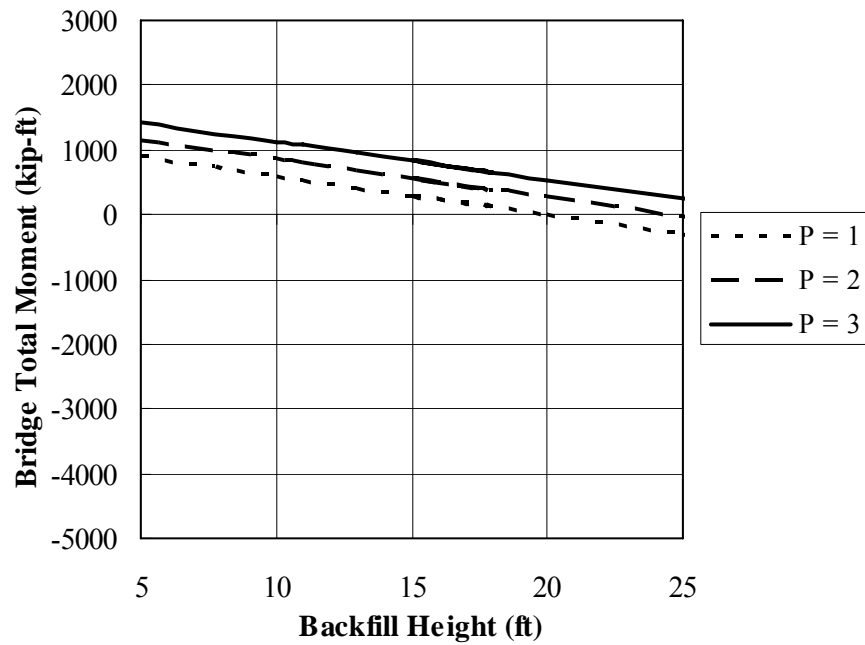


(d) Steel Girder IAB: Bridge Length (L) = 60ft

Figure 7.5. Bridge Total Positive Bending Moment at Mid-Span of the Exterior Span (Cont.).

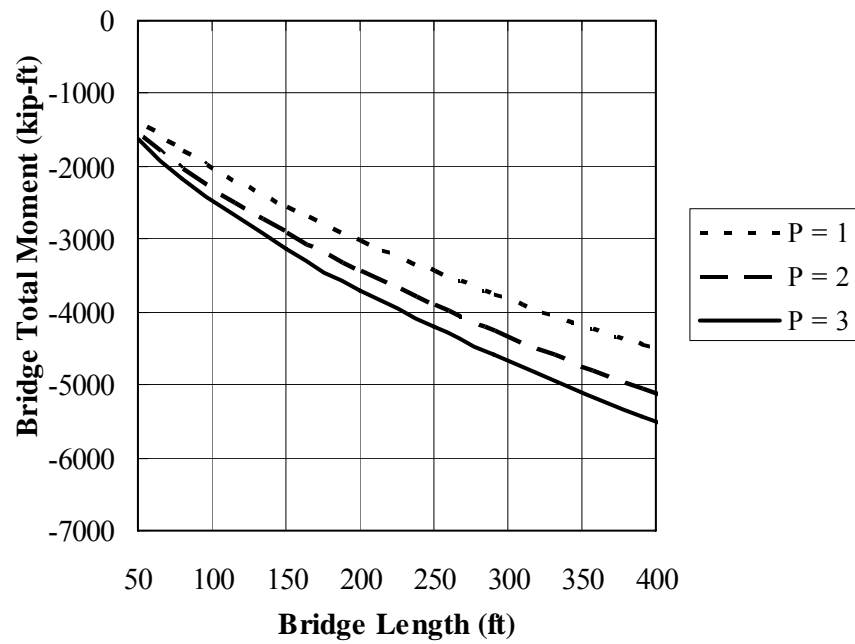


(e) Steel Girder IAB: Bridge Length (L) = 200ft

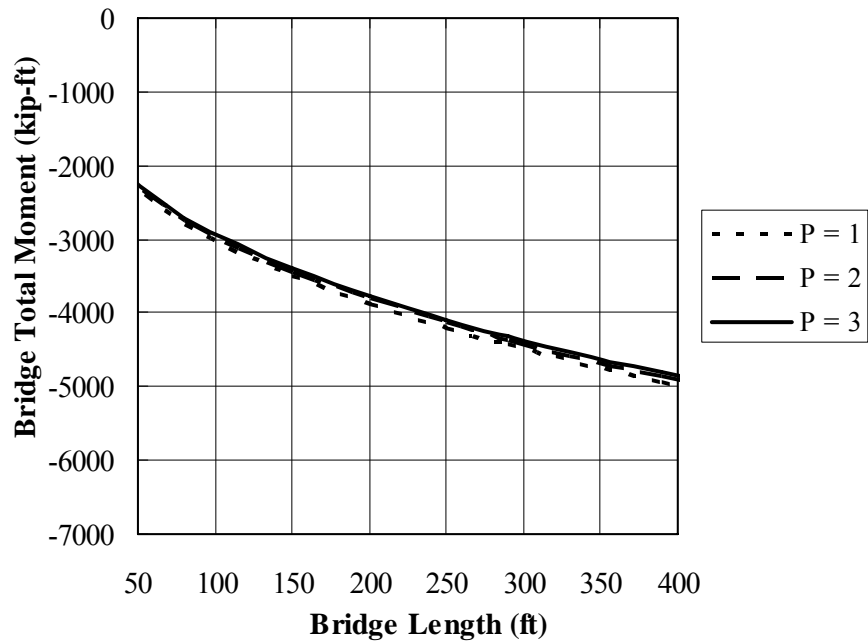


(f) Steel Girder IAB: Bridge Length (L) = 400ft

Figure 7.5. Bridge Total Positive Bending Moment at Mid-Span of the Exterior Span (Cont.).

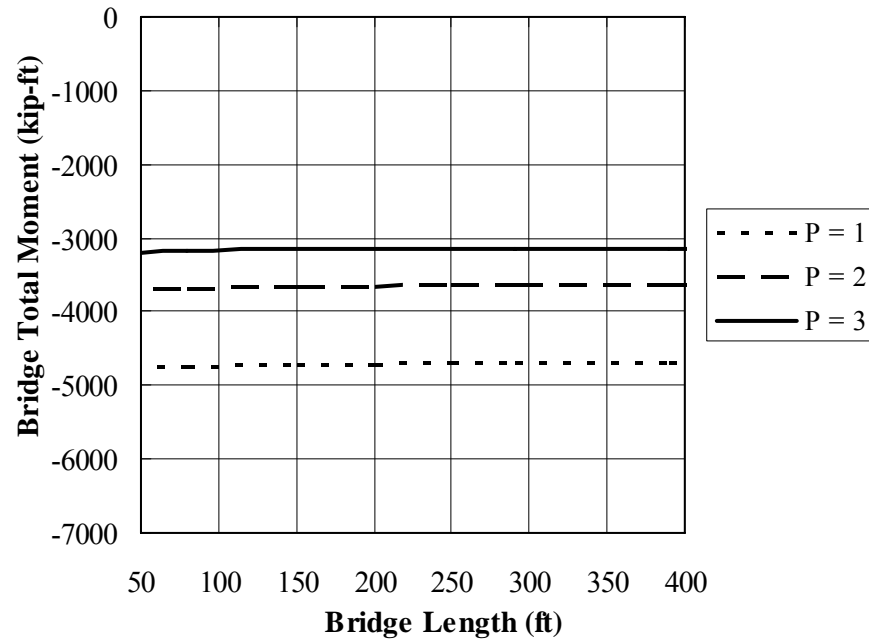


(a) Prestressed Concrete Girder IAB: Backfill Height (H) = 10 ft

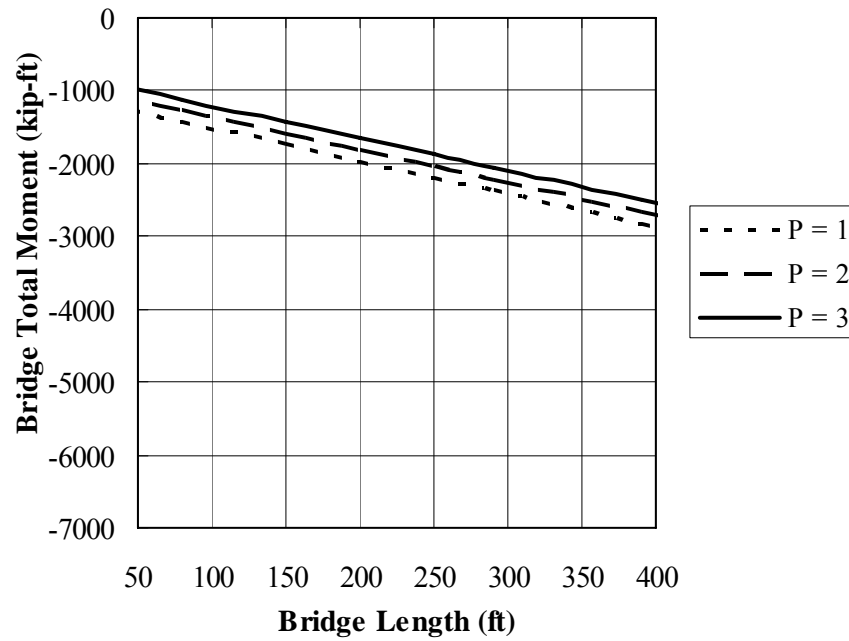


(b) Prestressed Concrete Girder IAB: Backfill Height (H) = 15 ft

Figure 7.6. Bridge Total Negative Bending Moment at Mid-Span of the Exterior Span.

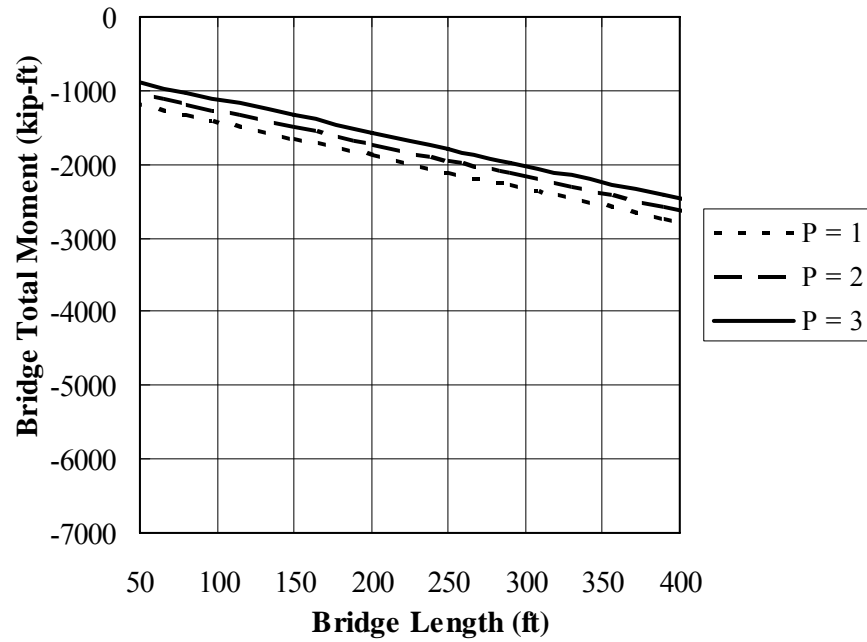


(c) Prestressed Concrete Girder IAB: Backfill Height (H) = 20 ft

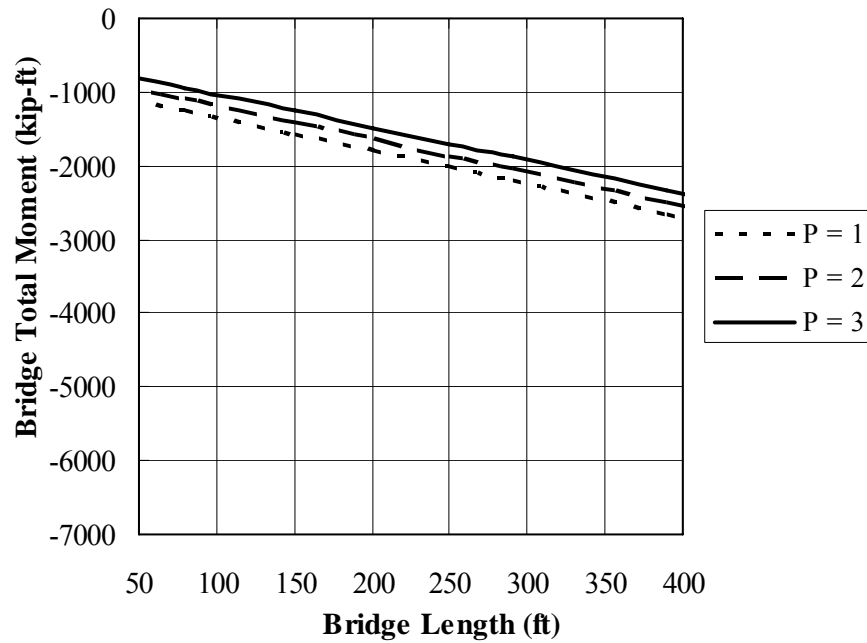


(d) Steel Girder IAB: Backfill Height (H) = 10 ft

Figure 7.6. Bridge Total Negative Bending Moment at Mid-Span of the Exterior Span (Cont.).

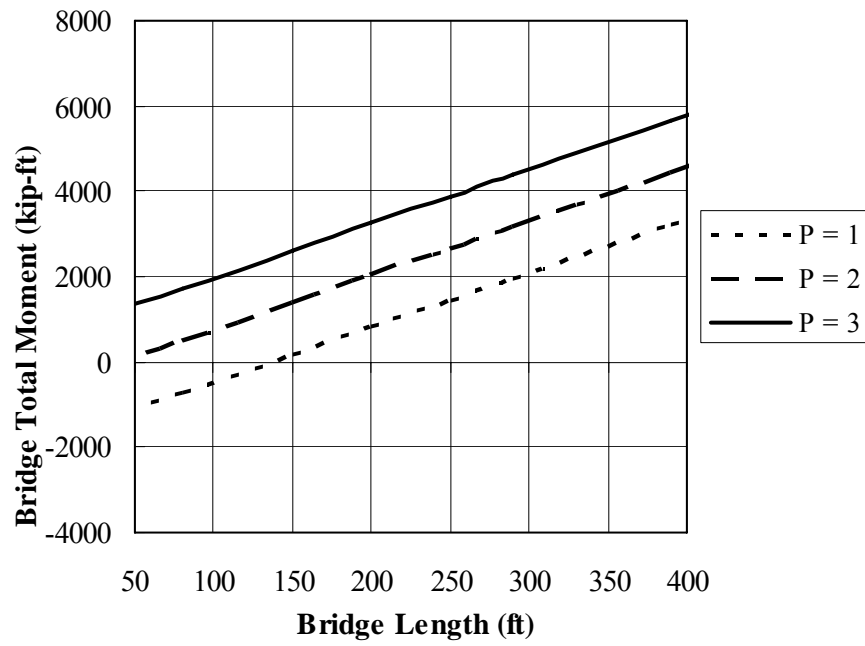


(e) Steel Girder IAB: Backfill Height (H) = 15 ft

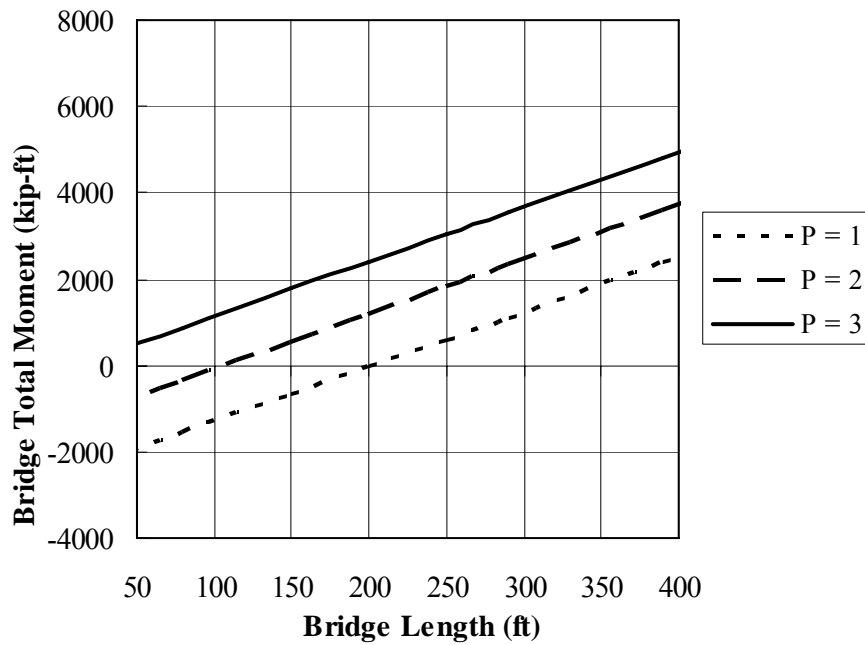


(f) Steel Girder IAB: Backfill Height (H) = 20 ft

Figure 7.6. Bridge Total Negative Bending Moment at Mid-Span of the Exterior Span (Cont.).

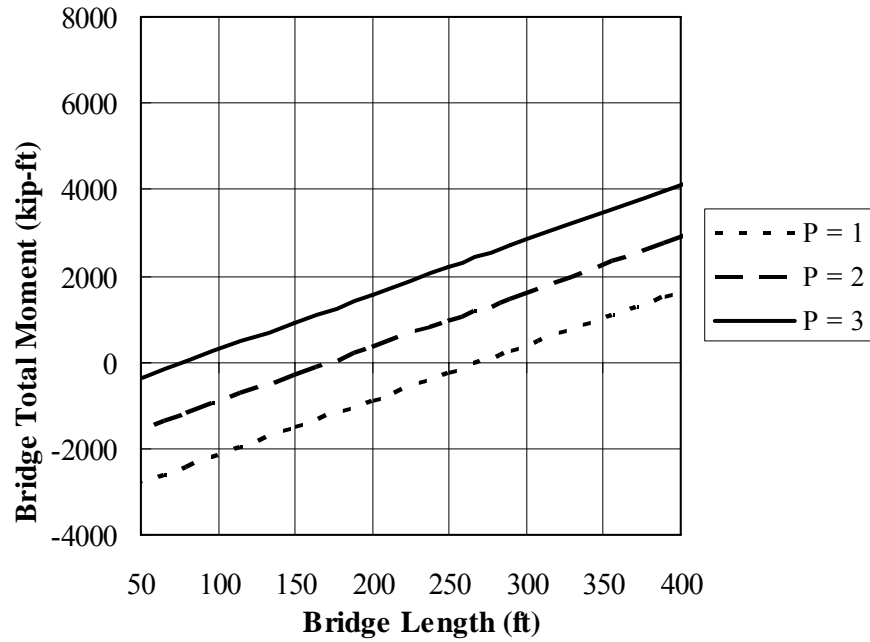


(a) Prestressed Concrete Girder IAB: Backfill Height (H) = 10 ft

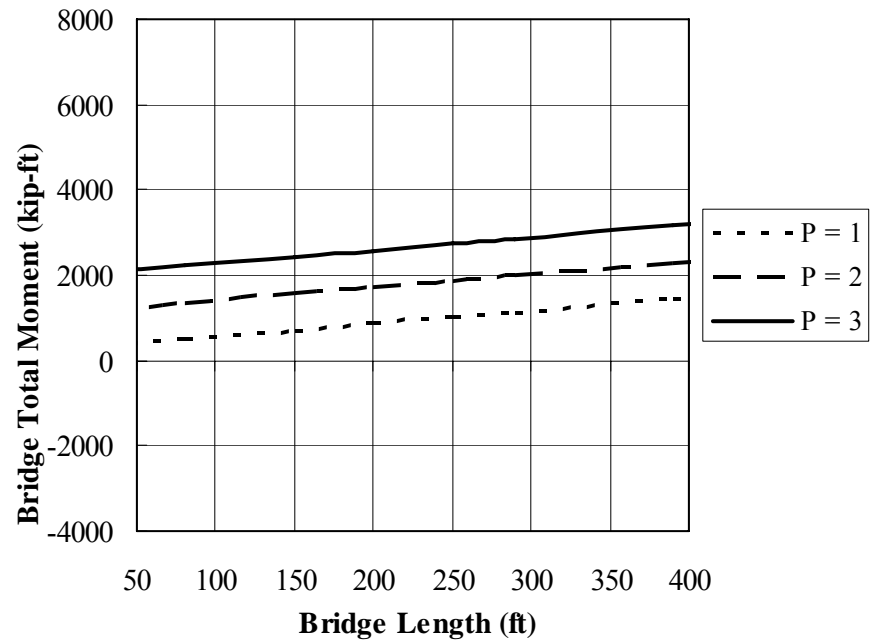


(b) Prestressed Concrete Girder IAB: Backfill Height (H) = 15 ft

Figure 7.7. Bridge Total Positive Bending Moment at Abutment.

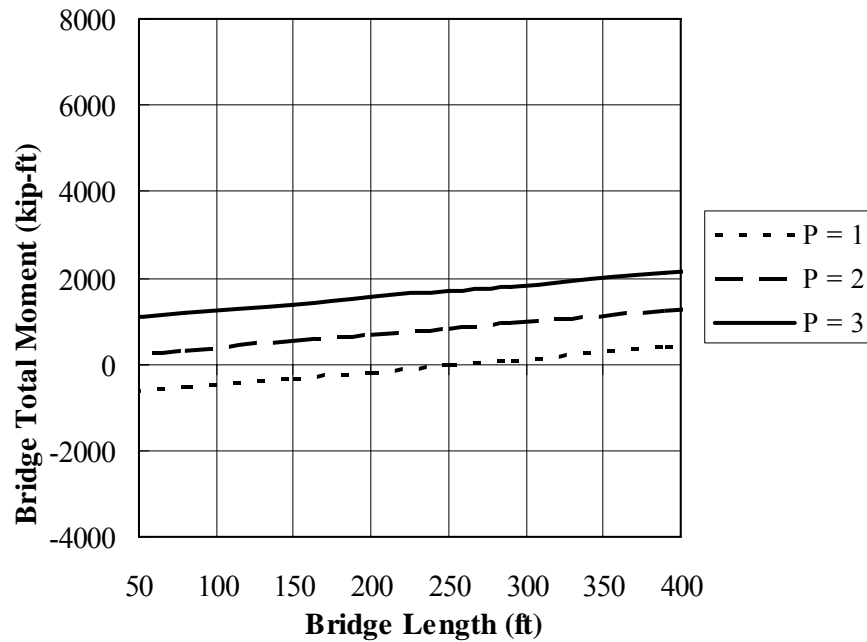


(c) Prestressed Concrete Girder IAB: Backfill Height (H) = 20 ft

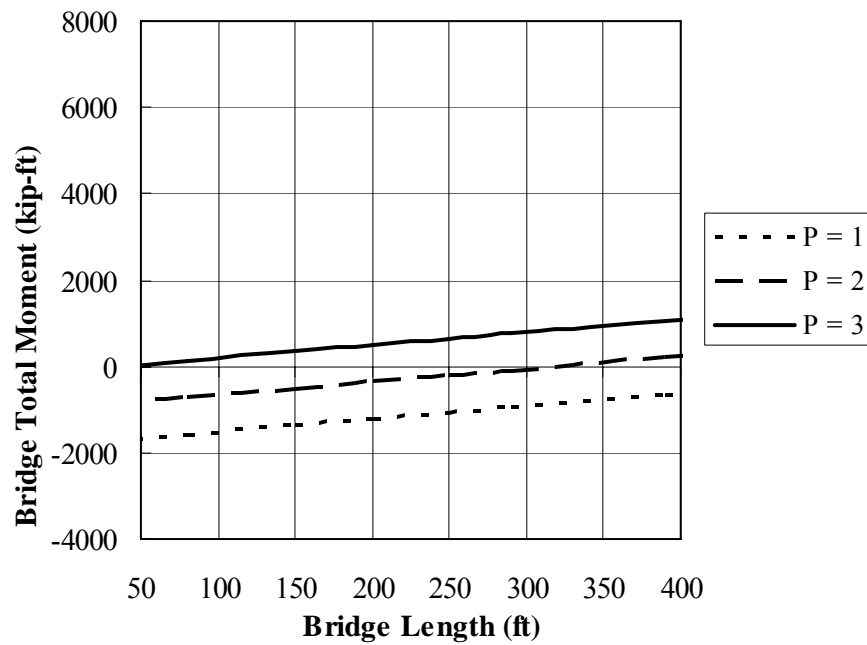


(d) Steel Girder IAB: Backfill Height (H) = 10 ft

Figure 7.7. Bridge Total Positive Bending Moment at Abutment (Cont.).

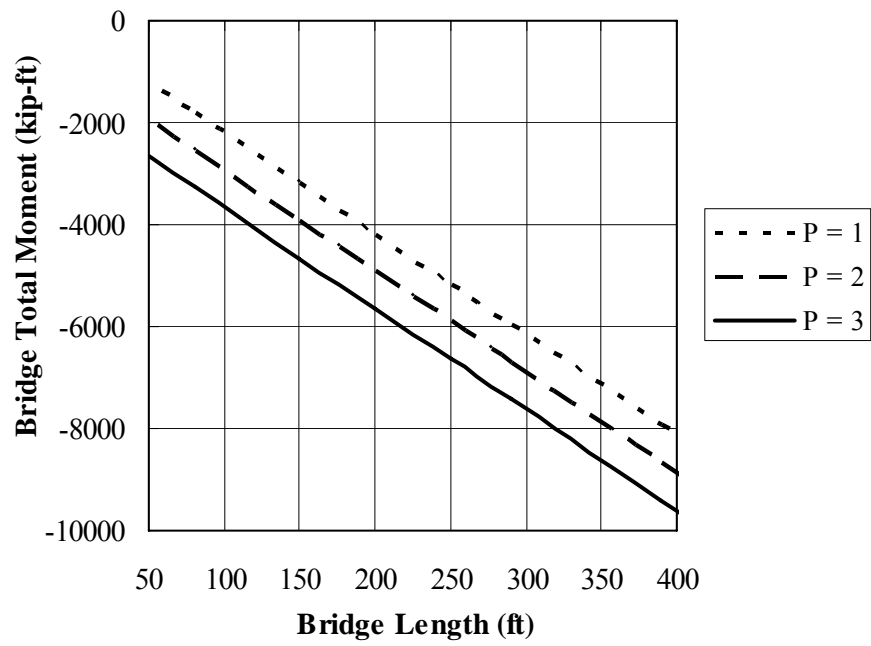


(e) Steel Girder IAB: Backfill Height (H) = 15 ft

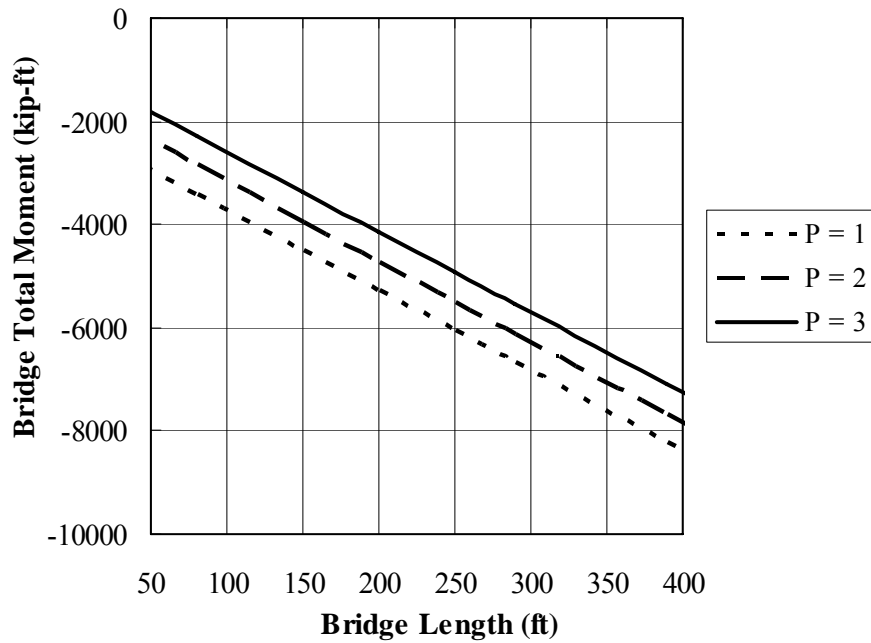


(f) Steel Girder IAB: Backfill Height (H) = 20 ft

Figure 7.7. Bridge Total Positive Bending Moment at Abutment (Cont.).

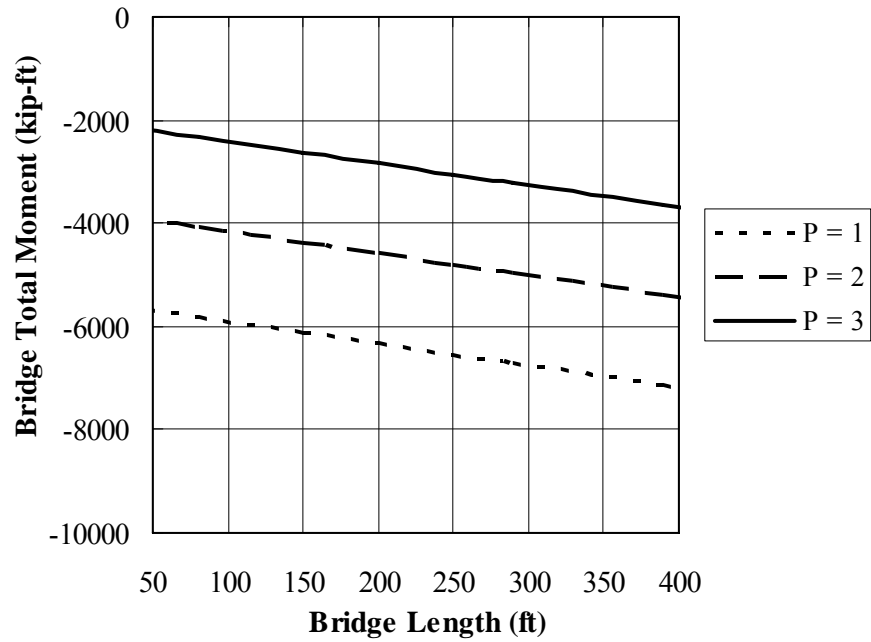


(a) Prestressed Concrete Girder IAB: Backfill Height (H) = 10ft

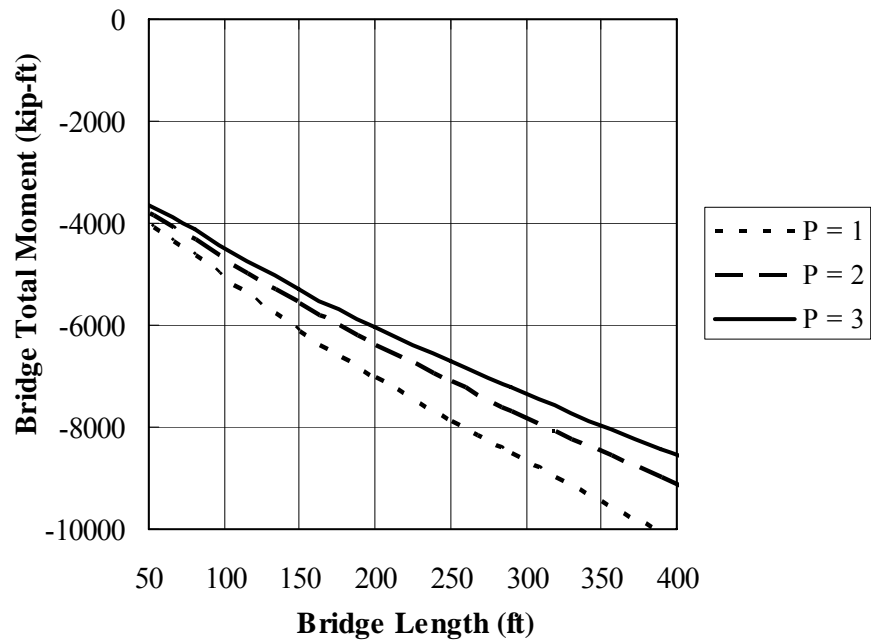


(b) Prestressed Concrete Girder IAB: Backfill Height (H) = 15ft

Figure 7.8. Bridge Total Negative Bending Moment at Abutment.

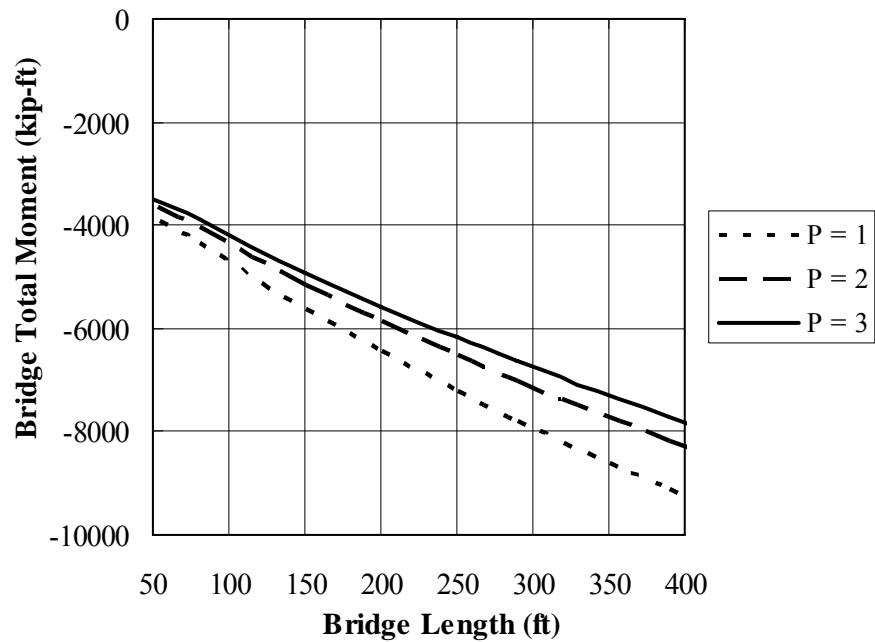


(c) Prestressed Concrete Girder IAB: Backfill Height (H) = 20ft

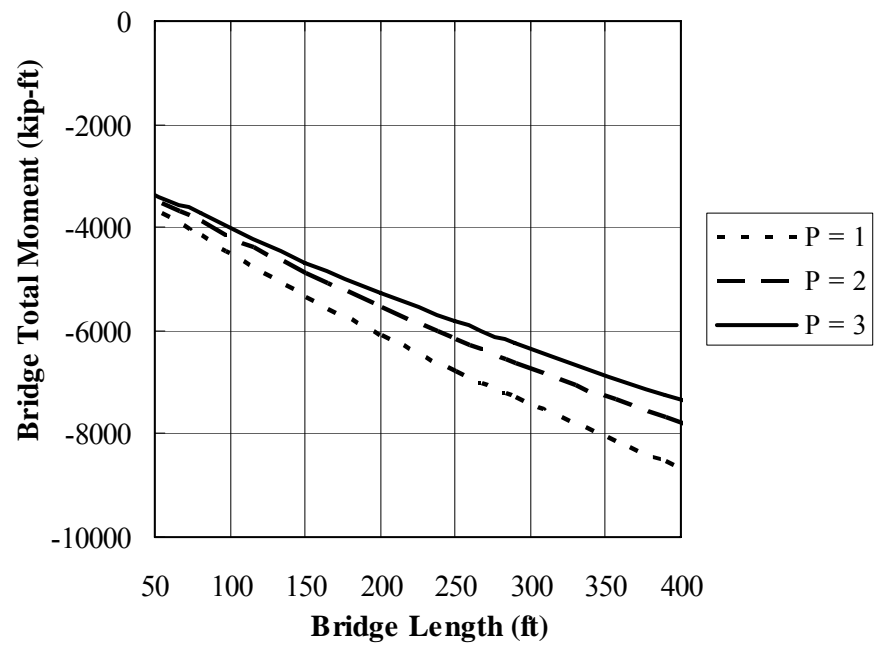


(d) Steel Girder IAB: Backfill Height (H) = 10 ft

Figure 7.8. Bridge Total Negative Bending Moment at Abutment (Cont.).



(e) Steel Girder IAB: Backfill Height (H) = 15 ft

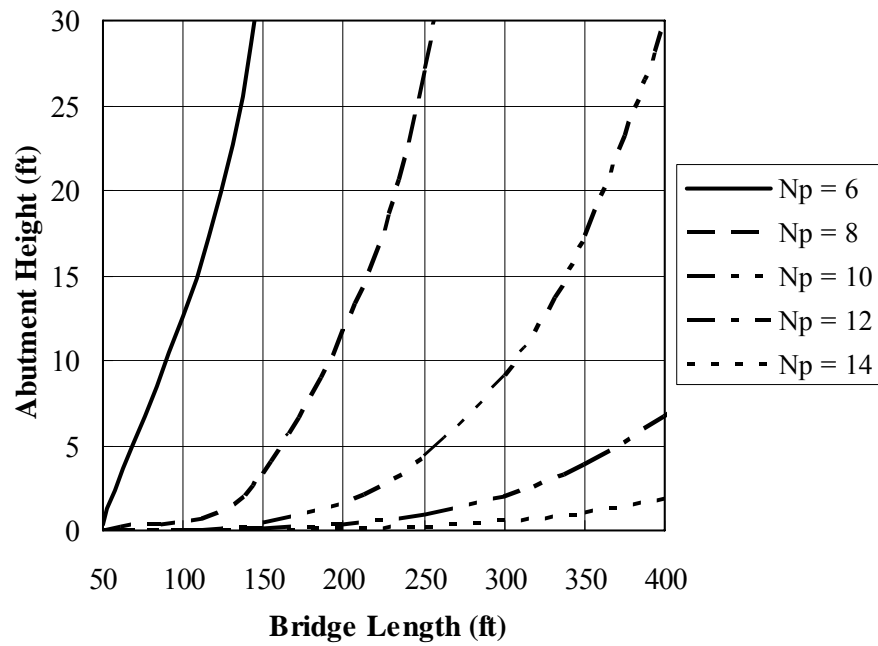


(f) Steel Girder IAB: Backfill Height (H) = 20 ft

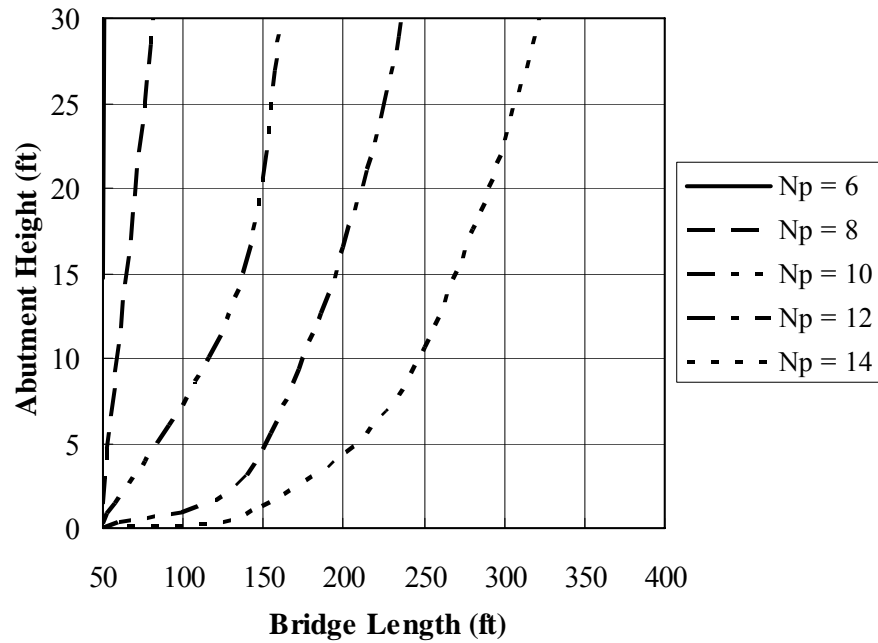
Figure 7.8. Bridge Total Negative Bending Moment at Abutment (Cont.).

7.3.8.3 Minimum Number of Laterally Supporting Piles

Figure 7.9 demonstrates the effect of the number of piles, N_p , and is used to determine the minimum number supporting piles. IAB abutment height versus bridge length is plotted on the graph. All IABs plotted on this graph must be below and to the right of each curve to prevent pile yielding due to thermal loading. The developed plots are based on the assumption that 50 percent of pile section yielding capacity ($F_y = 50$ ksi) is consumed by thermal loading and $\alpha = 6.0$ in/in/°F. When backfill height is high and soil pile stiffness is low, the pile bending moment decreases. However, as soil pile stiffness increases, the pile bending moment rapidly increases.

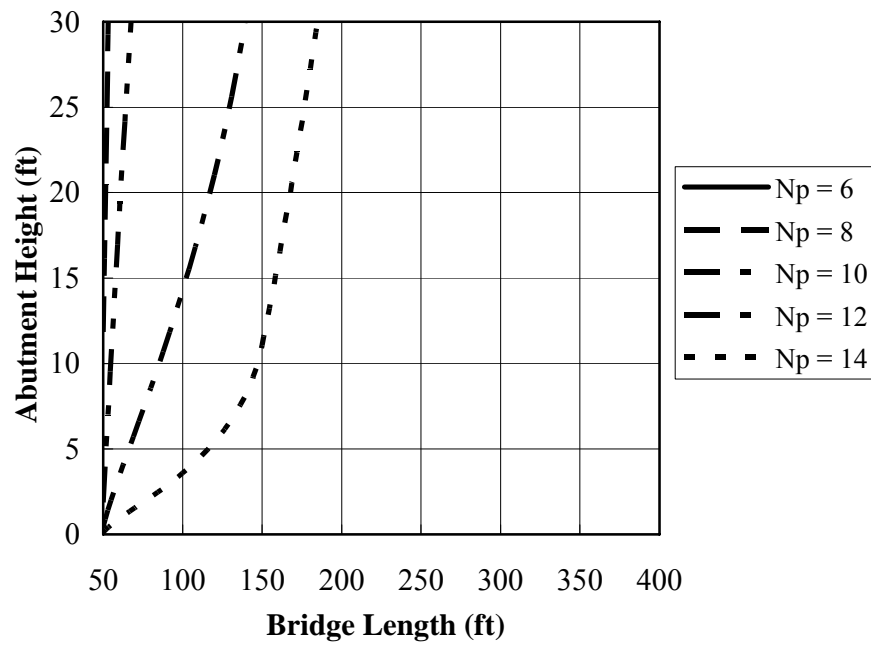


(a) Prestressed Concrete Girder IAB: Soil Pile Stiffness (P) = *Low*

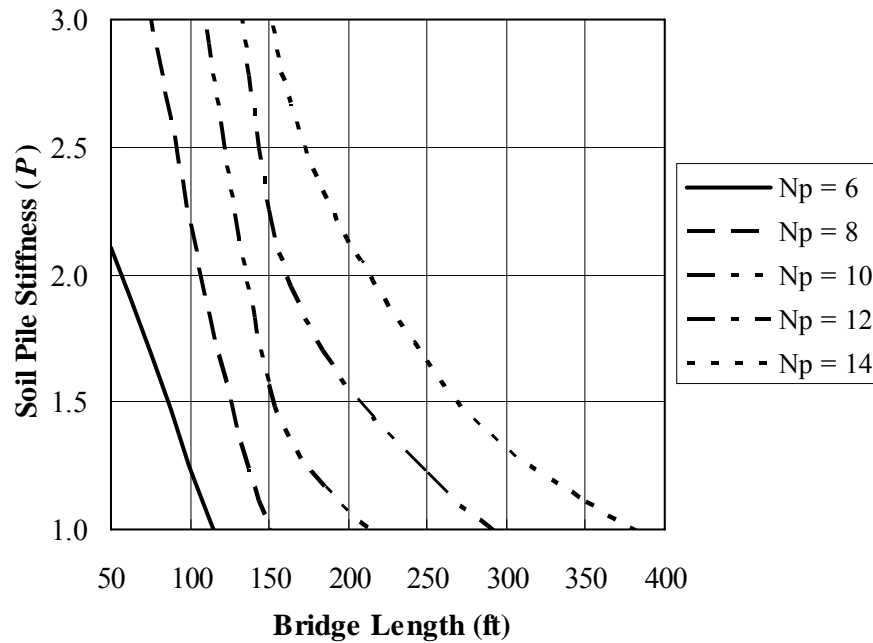


(b) Prestressed Concrete Girder IAB: Soil Pile Stiffness (P) = *Intermediate*

Figure 7.9. Minimum Number of Laterally Supporting Piles.



(c) Prestressed Concrete Girder IAB: Soil Pile Stiffness (P) = *High*

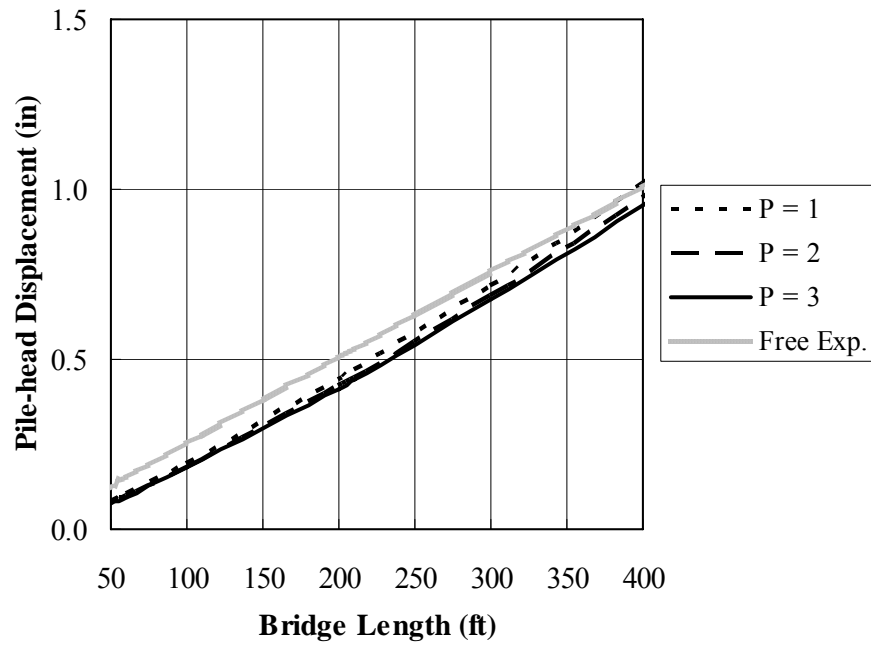


(d) Steel Girder IAB

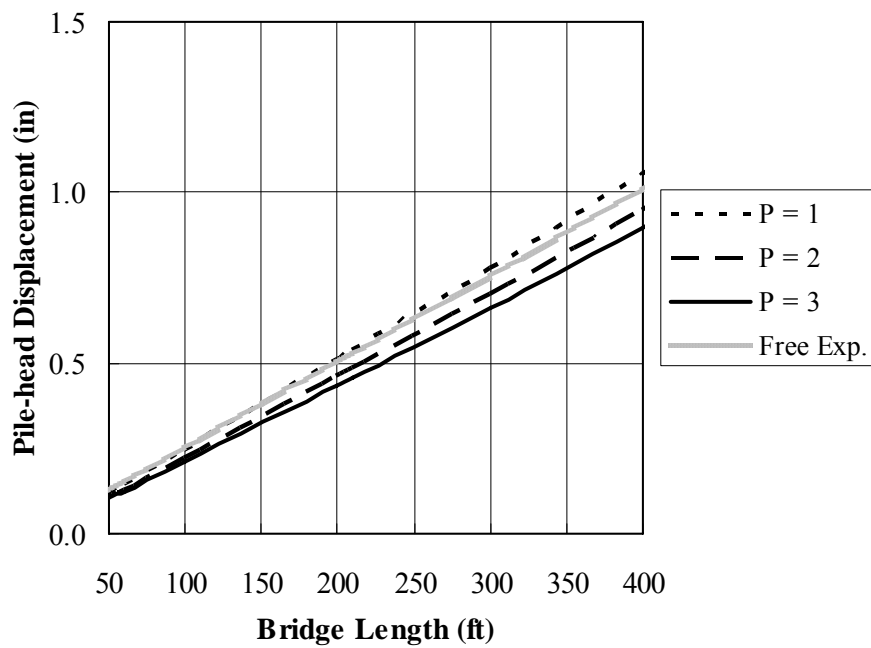
Figure 7.9. Minimum Number of Laterally Supporting Piles (Cont.).

7.3.8.4 Pile Head/Abutment Displacement

Figure 7.10 presents pile head displacement for different backfill heights based on bridge length. The graph is based on $\alpha = 6.0$ in/in/°F for concrete girder and $\alpha = 6.5$ in/in/°F for steel girder and backfill stiffness = *intermediate*. For comparison purposes, free expansion is also plotted based on $\alpha = 6.0$ in/in/°F and a 70°F temperature change for concrete girder bridges and 120°F temperature change for steel girder bridges (AASHTO LRFD, 2008).

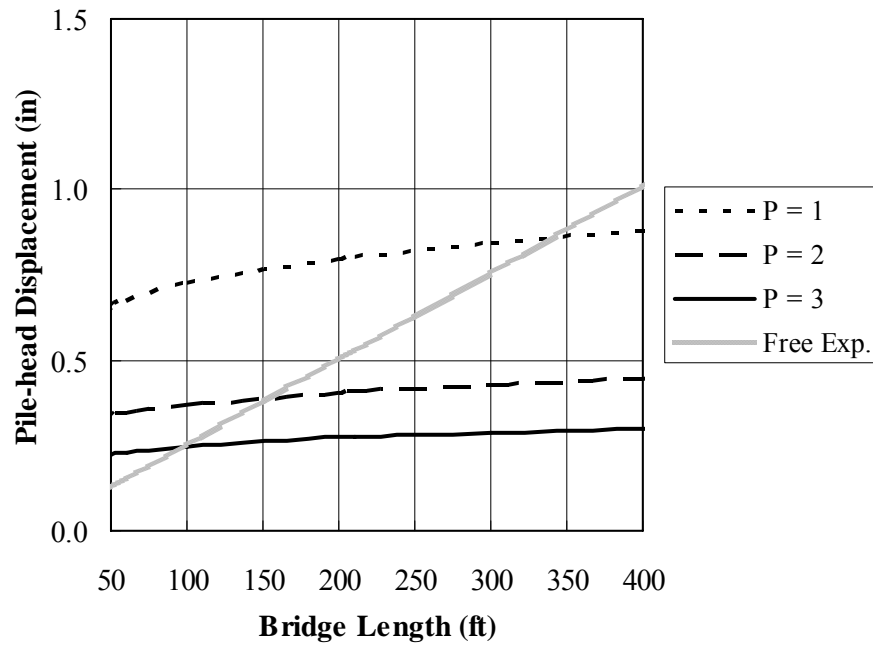


(a) Prestressed Concrete Girder IAB: Backfill Height (H) = 10 ft

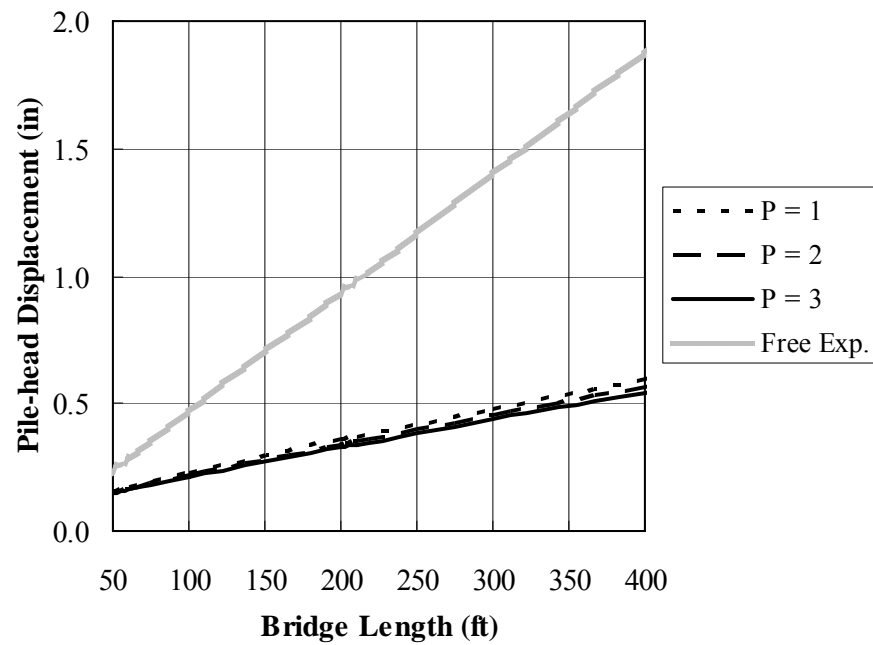


(b) Prestressed Concrete Girder IAB: Backfill Height (H) = 15 ft

Figure 7.10. Maximum Pile Head Displacement.

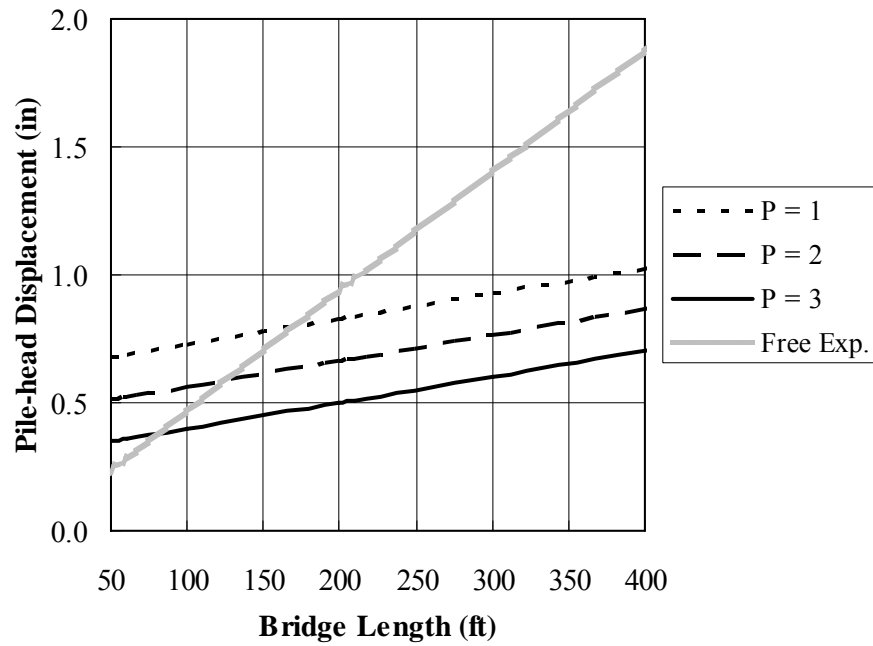


(c) Prestressed Concrete Girder IAB: Backfill Height (H) = 20 ft

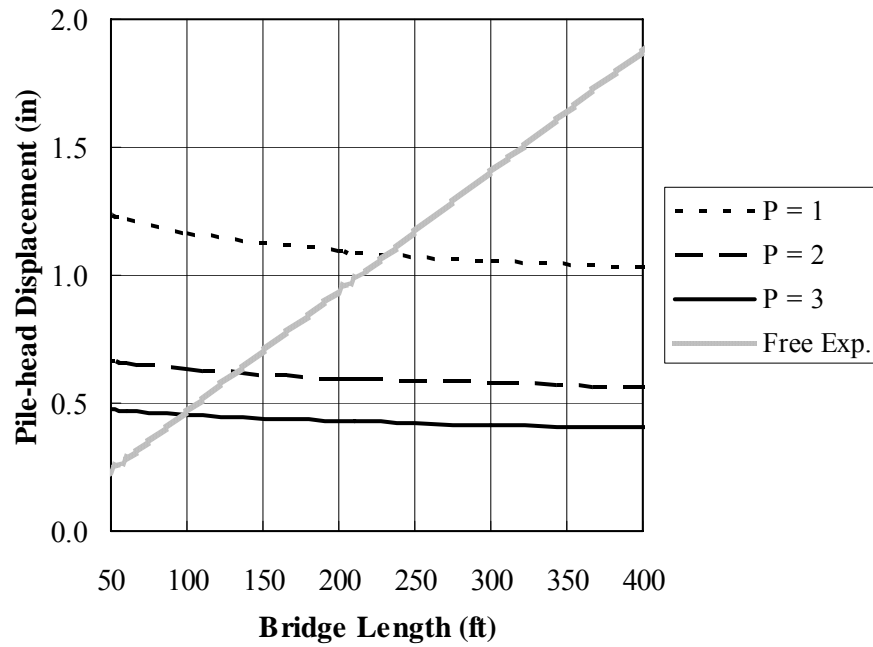


(d) Steel Girder IAB: Backfill Height (H) = 10 ft

Figure 7.10. Maximum Pile Head Displacement (Cont.).



(e) Steel Girder IAB: Backfill Height (H) = 15 ft



(f) Steel Girder IAB: Backfill Height (H) = 20 ft

Figure 7.10. Maximum Pile Head Displacement (Cont.).

7.3. Structure Numerical Modeling

7.3.1 Introduction

The numerical methods developed in this study provide accurate IAB analysis for a complete range of geometries. In this section, detailed explanations of the 2D and 3D numerical modeling methodologies are presented. The modeling process begins with boundary condition modeling, structural element modeling, material property characterization, and load modeling. The analysis details are based on AASHTO LRFD (2007), ACI 209 (2004), and PCI (2005).

Three numerical models are available for the structural element modeling: (1) simplified 2D numerical models with condensed piles, (2) 2D numerical models with full piles, and (3) refined 3D numerical models. A simplified 2D numerical model is used primarily for an analysis that requires extremely high computing time efficiency, such as a 75-year simulation. If the bridge is transversely and longitudinally symmetrical, and the assumption is that all girders and piles are the same, the simplified 2D model is capable of predicting bridge axial force and moment, abutment displacement, and pile lateral force and moment. The 2D numerical model with full piles also determines pile response along the pile depth. The refined 3D numerical analysis is used to investigate specific member responses or to evaluate bridges lacking transverse symmetry. The refined 3D model is most useful for evaluating unidirectional temperature load and/or a single temperature cycle (1-year) analysis.

IAB boundary conditions and the proper modeling are the primary differences from conventional jointed bridges. Because of the lack of an expansion joint system, the superstructure is rigidly connected to the substructure that is supported by flexible steel piles and compacted backfills. In addition, the added complication of boundaries at piles and backfill behaving nonlinearly must be considered.

IAB structural components are modeled as linear-elastic in each of the three modeling methods. Two key behaviors of IABs include (1) soil-structure interaction and (2) nonlinear behavior of construction joint between abutments and backwalls. Soil-structure interaction is categorized into two parts: (1) abutment-backfill interaction and (2) soil-pile interaction.

IAB loads include (1) backfill pressure on abutments, (2) time-dependent effects of the concrete superstructure, (3) superstructure temperature change, and (4) temperature gradient along the superstructure depth. Other loads, such as dead load and vehicle load, are well documented elsewhere and should be included in the analysis.

7.3.2 Simplified 2D Analysis

The simplified 2D models are extremely versatile, rapidly constructed, and can be used in many different situations. The simplified 2D model assumes that the bridge is transversely symmetrical, having a uniform deck slab thickness and evenly spaced identical girders and supporting piles. Intermediate continuity diaphragms cannot be considered in a 2D analysis because this element exists in a plane that is not included in the model.

7.3.2.1 Symmetry Considerations

Consideration of symmetry in the development of the model normally significantly reduces the complexity. If the bridge is not symmetric, then the analysis must consider the entire structure, as in the case of significant super-elevation, non-symmetric girder placement, non-symmetric substructure geometry, significantly dissimilar span lengths, or when both abutments are not expected to be constructed similarly, particularly with respect to pile placement and length. In Figure 7.1, the mid-span at the bridge superstructure centerline is restrained in x-axis translation

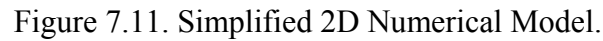
and z-axis rotation. The single row of weak axis-oriented steel HP-piles is assumed. When the bridge is modeled as a symmetric structure, the mid-span at the bridge superstructure centerline is restrained in x-axis translation and z-axis rotation.

7.3.2.2 Boundary Conditions

The determination of representative boundary conditions is critical to the accuracy of the numerical analysis and must represent the conditions of the intended bridge design. The following recommendations for symmetry and pile element modeling are provided to allow the analysis to best predict IAB behavior. An example 2D numerical IAB model is presented in Figure 7.11 for the purposes of illustrating the methodologies.

H-piles are embedded in, and rigidly connected to, the abutment at the top and typically driven to bedrock at the bottom. This end condition prevents significant abutment settlement from developing over time. Therefore, H-pile elements and their associated boundary definitions do not attempt to accommodate the potential for pile settlement or negative friction. The pile vertical (y-axis) displacement degree of freedom is, therefore, justifiably restrained.

Vertical pile elements are replaced at the abutment connection with an equivalent longitudinal (x-axis) nonlinear spring, a rotational (z-axis) nonlinear spring, and a vertical (y-axis) rigid support. The longitudinal, x-axis nonlinear spring definition is equivalent to the characteristics of abutment-backfill interaction elements and soil-pile interaction elements. The additional restraint provided by the approach slab is not included in the longitudinal, nonlinear spring because the contribution to total restraint is relatively small, an observation based on bridge monitoring and numerical analysis.



The simplified 2D numerical model incorporates a condensed soil-pile interaction approach as shown in Figure 7.12. In a more refined numerical model, a nonlinear load (p)-displacement (y) curve is developed to characterize the soil-pile interaction relationship and implemented through the use of multiple Winkler springs along the pile depth. In the simplified 2D model, soil-pile interaction is condensed into a single, equivalent element, or spring, from the full pile model. Figure 7.12 illustrates both the full pile 2D model and the condensed, simplified 2D numerical model.

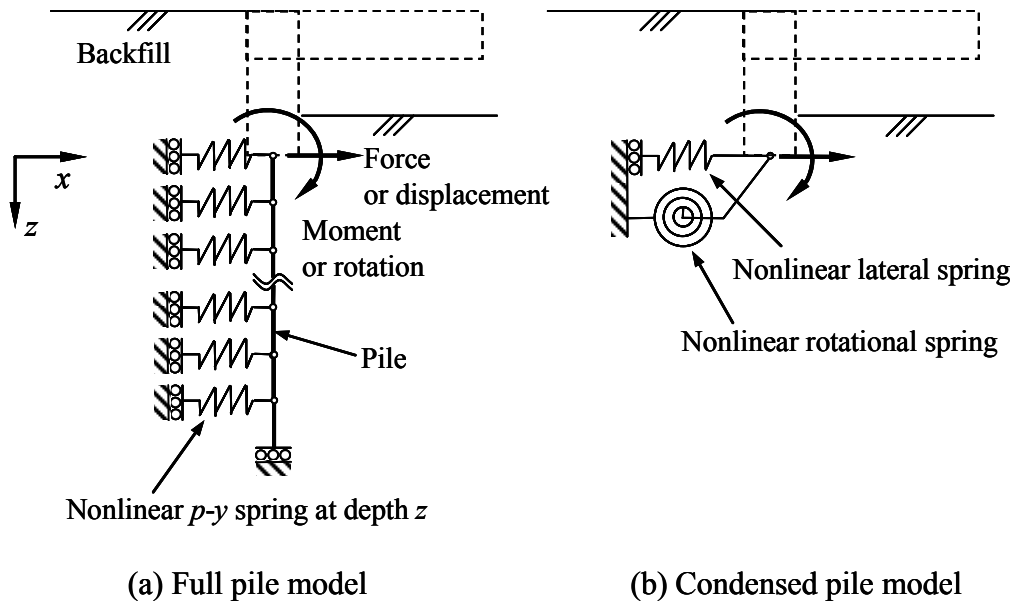


Figure 7.12. Full and Condensed Soil-Pile Interaction Model.

Considering the full pile model, two different p - y curves, one each for expansion and contraction, are required to represent pile-soil interaction. The soil resistance developed under bridge expansion must include the backfill overburden pressure where bridge contraction requires the development of the down-slope soil passive resistance. The widely accepted p - y curves developed by the API (1993) are recommended as a means to establish p - y curves at each depth for specific soil layers around piles. The nonlinear p - y spring near the pile head should be spaced at less than 1 ft because the fixity point generally occurs within the upper 15 ft. To generate a p - y curve at each depth, API simple equations are used:

For granular soil:

$$p = Ap_u \tanh \left[\frac{k_i X}{Ap_u} y \right] \quad (5.2)$$

For clayey soil:

$$p = 0.5 p_u \left(\frac{y}{y_{50}} \right)^{1/4} \quad (5.3)$$

$$p_u = \min \left\{ p_{uf} = 9cD, \quad p_{uw} = \left(3 + \frac{\gamma'}{c} X + \frac{J}{D} X \right) cD \right\} \quad (5.4)$$

where,

p = lateral force (kip/in),

A = empirical factor accounting for static or cyclic loading,

X = a specific depth,

p_u = ultimate bearing capacity (kip/in), taken as the lesser of p_{uf} (flow around failure) and

p_{uw} (wedge type failure),

k_i = initial modulus of subgrade reaction (kip/in³),

y = lateral deflection (in),

y_{50} = deflection when $p = 0.5p_u$,

ϕ_f = internal friction angle,

γ' = effective soil weight,

c = unconfined cohesion at depth X ,

J = empirical parameter (0.5 for soft clay, and 0.25 for medium clay) and

D = effective pile diameter.

For various displacement (y) values, load (p) can be computed to obtain a smooth curve, but usually the upper bound for y is equal to $16y_{50}$ where a p - y curve converges its maximum and becomes stable.

The condensed pile model is derived from the full pile model. The nonlinear lateral spring is derived from the gradually increased lateral force at the pile head with the fixed pile head

rotation. The nonlinear rotation spring is derived from the gradually increased moment at the pile head with fixed lateral displacement. As another approach, nonlinear spring properties of lateral translation and rotation can be obtained from commercial soil-pile interaction programs, such as COM624P (1993) and Lpile (2002).

7.3.2.3 Backwall- and Abutment-Soil Interface

The interaction between abutment displacement and backfill pressure can be implemented using the backfill pressure (P)-displacement (Δ) curve in the numerical model. The relationship between backfill pressure and abutment displacement is assumed as a linear variation between active (P_a) and passive pressure (P_p) as presented in Figure 7.13. For numerical implementation, a modified earth pressure model, shown in Figure 7.13(b), is used to represent active and passive pressure with an external earth pressure of at-rest pressure (P_o). When active or passive pressure is reached, the model behaves perfectly plastic with an unloading branch defined as a slope parallel to the initial slope. Rankine's lateral earth pressure theory is used to obtain active and passive coefficients (K_a and K_p) with backfills initially compacted to at-rest conditions ($K_o = 1.0$). The initial slope of the curve (k_h) in Figure 7.13 is determined from field testing or local geotechnical information. When in-situ soil information is not available, 43.8pci (12MN/m³) can be used for PennDOT OGS backfills.

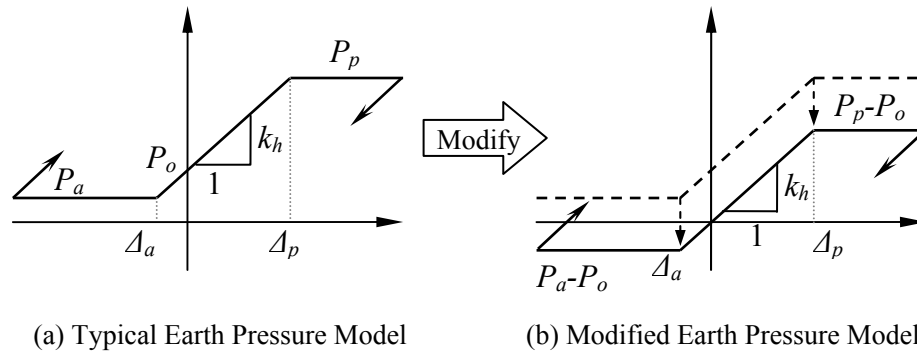


Figure 7.13. Abutment-Backfill Numerical Implementation Modification.

7.3.2.4 Abutment and Backwall Elements

As presented in Figure 7.1, the abutment is modeled as a beam element discrete from the backwall (or end diaphragm). The abutment height is taken from the superstructure bearing down to the supporting pile elements, and the backwall is taken from the top of the abutment to the composite superstructure centroid. The construction joint between the abutment and backwall elements is discussed in more detail in section 7.3.2.8.

7.3.2.5 Pier Elements

Piers and pier bearings in the simplified 2D numerical model are represented as either pinned or roller supports, depending on the intended final design configuration. Pier stems and supporting piles are not considered in the simplified 2D model because the effect on abutments is not significant.

7.3.2.6 Superstructure Elements

All girders and the entire deck are modeled as a single beam element located at the centroid of the composite section with composite beam section properties. All materials are modeled as responding in the liner-elastic range for the thermal loading analysis. The superstructure is divided into beam elements incorporating equivalent gradient temperature loads, time-dependent

loads, and prestress losses. In the case of steel girders with a concrete deck, the composite superstructure is constructed of materials with a dissimilar thermal expansion coefficient; therefore, the following equivalent thermal expansion coefficient, α_{eq} , is determined:

$$\alpha_{eq} = \frac{\alpha_g E_g A_g + \alpha_d E_d A_d}{E_g A_g + E_d A_d} \quad (7.24)$$

where:

α_g = girder material thermal expansion coefficient,

E_g = girder elastic modulus,

A_g = sum of girder sectional area,

α_d = deck material thermal expansion coefficient,

E_d = deck elastic modulus,

A_d = sum of deck sectional area.

7.3.2.7 Elastomeric Bearing Element

Elastomeric bearings at abutments and piers do not significantly influence the behavior and predicted response; therefore, they are neglected in the simplified 2D model in order to limit complexity.

7.3.2.8 Backwall-to-Abutment Construction Joint

The construction joint between abutment and backwall must be considered in the numerical model because the effect of the joint is significant. The joint allows rotation between the backwall and abutment because the reinforcement crossing the joint in the standard detail adopted by several states is very low. The Pennsylvania Department of Transportation (PennDOT) uses #5 at 10-inch U-shaped reinforcing bars, resulting in low reinforcement ratios of the monitored bridges (less than 25 percent of AASHTO minimum reinforcement ratio). In

addition, the cold joint results in a pre-cracked condition and loss of uncracked section stiffness.

The elasto-plastic joint properties can be derived from a moment versus curvature relationship of the construction joint based on the joint reinforcement ratio. Joint degrees of freedom are deleted for all translations and rotations except z-axis rotation. The moment-curvature relationship is converted into a moment-rotation relationship based on small deformations. Paul (2005) recommends a constant stress over a joint length as:

$$\theta = \int_0^L \frac{M}{EI} dx = \frac{M}{EI} L = \phi L \quad (5.6)$$

For the joint length (L), half of AASHTO LRFD (2007) minimum development length of 8 inches is adopted. For the unloading path of the rotational stiffness, a conservative approach that follows the same path of loading without residual rotation is recommended.

7.3.3 Refined 3D Analysis

A more refined 3D IAB analysis requires significant effort and expertise to develop; however, the results are much more extensive and generally more accurate. In addition, transverse direction bridge behaviors and deck and girder stresses can be obtained directly. This section discusses in detail the features of a refined 3D analysis including boundary conditions, soil-pile, soil-abutment, joint, pier, and superstructure elements.

7.3.3.1 Boundary Conditions

Boundary conditions at the piers and abutments must be modeled as closely as possible to the intended bridge design, taking into account directional restraints and stiffness, as well as overall influence on the thermal response. Where symmetry is used, the conditions at the axis of symmetry must be carefully modeled with respect to rotation and displacement restraint. The single row of weak axis-oriented H-piles is assumed to be rigidly restrained in the y-axis

direction at the pile tip. Boundaries at the abutments and backwalls are subjected to longitudinal active and passive backfill pressure, which are modeled with the same fundamental principles as in the 2D model and is discussed in 7.3.3.2. Where an isolated wing-wall is intended in the design, no interaction is required. Pier foundations are supported with rigid restraints because the rotation and displacement of the foundation is small and has little effect on the thermal response in the superstructure longitudinal and transverse directions.

7.3.3.2 Pile-Soil Interface

Piles and soil layers around piles are modeled using beam elements and nonlinear spring elements. Each pile is the same as the full pile model in Figure 7.12(a). Two different p - y relationships, one for expansion and one for contraction, are required to develop the pile-soil interactions. The soil resistance for bridge expansion must include backfill overburden pressure in the determination of the spring constants. The following equations by API (1993) are used to calculate p - y curves at a depth for specific soil layers around piles:

For granular soil:

$$p = Ap_u \tanh \left[\frac{k_i X}{Ap_u} y \right] \quad (5.2)$$

For clayey soil:

$$p = 0.5 p_u \left(\frac{y}{y_{50}} \right)^{1/4} \quad (5.3)$$

$$p_u = \min \left\{ p_{uf} = 9cD, \quad p_{uw} = \left(3 + \frac{\gamma'}{c} X + \frac{J}{D} X \right) cD \right\} \quad (5.4)$$

where,

p = lateral force (kip/in),

A = empirical factor accounting for static or cyclic loading,

X = a specific depth,

p_u = ultimate bearing capacity (kip/in), taken as the lesser of p_{uf} (flow around failure) and

p_{uw} (wedge type failure),

k_i = initial modulus of subgrade reaction (kip/in³),

y = lateral deflection (in),

y_{50} = deflection when $p = 0.5p_u$,

ϕ_f = internal friction angle,

γ' = effective soil weight,

c = unconfined cohesion at depth X ,

J = empirical parameter (0.5 for soft clay, and 0.25 for medium clay) and

D = effective pile diameter.

For various displacement (y) values, load (p) can be computed to obtain a smooth curve, but usually the upper bound for y is equal to $16y_{50}$ where a p - y curve converges its maximum and becomes stable. The nonlinear p - y spring near the pile head should be spaced at less than 1 ft because the lateral and rotational pile displacements generally occur within top 15 ft of piles.

7.3.3.3 Backwall- and Abutment-Soil Interface

The principals of soil-structure interaction incorporated into the 2D numerical model are also incorporated into the refined 3D analysis. Interaction between backfill pressure and abutment displacement is captured through the backfill pressure versus displacement (P - Δ) relationship defined in the 3D numerical model. The relationship between backfill pressure and abutment displacement is assumed to be a linear variation between active (P_a) and passive pressure (P_p) as presented Figure 7.13. To define the behavior numerically, a modified earth pressure model in

Figure 7.13(b) is used to represent active and passive response with an external earth pressure of at-rest pressure (P_o). When active or passive pressure is reached, the model behaves perfectly plastic. The unloading branch is defined along a slope parallel to the initial slope descending from the point of load reversal. Rankine's lateral earth pressure is applied to obtain active and passive coefficients (K_a and K_p). The initial slope, k_h , is taken as 43.8pci (12MN/m³) for PennDOT OGS backfills. Therefore, the effective interaction force between backwall- and abutment-soil interface is:

$$F = K\sigma'_v A_{tributary} \quad (7.25)$$

where:

F = effective interaction force,

K = ratio of horizontal to vertical effective stress,

σ'_v = vertical effective normal stress at depth z (= soil density x depth),

$A_{tributary}$ = spring tributary area as defined by model design and mesh.

7.3.3.4 Abutment and Backwall Elements

Linear-elastic shell elements represent the backwall and abutment in the 3D model. The abutment and backwall are normally both dissimilar concrete mix designs and separated by the previously discussed cold joint; therefore, these two elements are modeled distinctly. Abutment and backwall shell elements are positioned at the center of the thickness and aligned with supporting piles. The abutment and backwall elements at the construction joint interface are meshed to match nodes from abutment and backwall with an equal spacing.

7.3.3.5 Pier Elements

Pier heads and stems are modeled with beam or shell elements, depending on pier shape and dimensions. Pier stems are modeled with fixed rotation and translation at the base (see boundary

conditions). Pedestals on piers are modeled with beam elements with a shape and size corresponding to the intended design. Bearing pads on piers are discussed in section 7.3.3.7 and are modeled accordingly.

7.3.3.6 Superstructure Elements

Superstructure elements include girders, deck slab, and diaphragms. All superstructure elements are assumed to be linear-elastic. The inclusion of parapets or crash barriers in the superstructure can be considered; however, contributions of this element to thermal load response are normally minimal due to both construction joints and expansion joints.

Girders are modeled with linear-elastic beam line elements. The beam element longitudinal axis is positioned along the center of gravity of the gross concrete girder cross-section. In lieu of a line beam element, a more refined 3D modeling of the girder cross-section can be incorporated, depicting the cross-section with shell elements. The refinement of shell elements permits the analysis to determine stresses at each strategically placed node on the girder cross-section, which eliminates the need for further evaluation of analysis results to determine stress. The inclusion of prestressing strands is not necessary due to the relatively low thermal stress and strain levels induced and to limit model complexity to a reasonable level. Prestress forces directly influence longitudinal creep and shrinkage, however, and are included in the 3D numerical model through a force method discussed in section 7.4.

Concrete deck slabs are modeled with linear-elastic shell elements. Shell element nodes are placed at the deck slab mid-thickness with element thickness defined with the shell. Where full composite action between girder and deck is anticipated, the deck shell elements are connected to girder beam elements using rigid connection elements that transfer all displacements as illustrated in Figure 7.14.

IAB deck transverse and longitudinal elevation changes may affect the bridge response and should be included in the numerical 3D model. The transverse deck elevation determines the transverse top of the abutment elevation. Longitudinal elevation changes between abutments also affect bridge response because of an imposed horizontal gravity force component.

The inclusion of parapets is a refinement that can be included in the 3D numerical analysis where a higher degree of accuracy is sought. Parapets are modeled using shell elements with careful evaluation of connections between parapets, deck, and separate sections of the parapet, itself. It has been reported that parapets with a rigid or stiff connection to the deck provide longitudinal stiffness against superstructure flexure, as well as axial displacement.

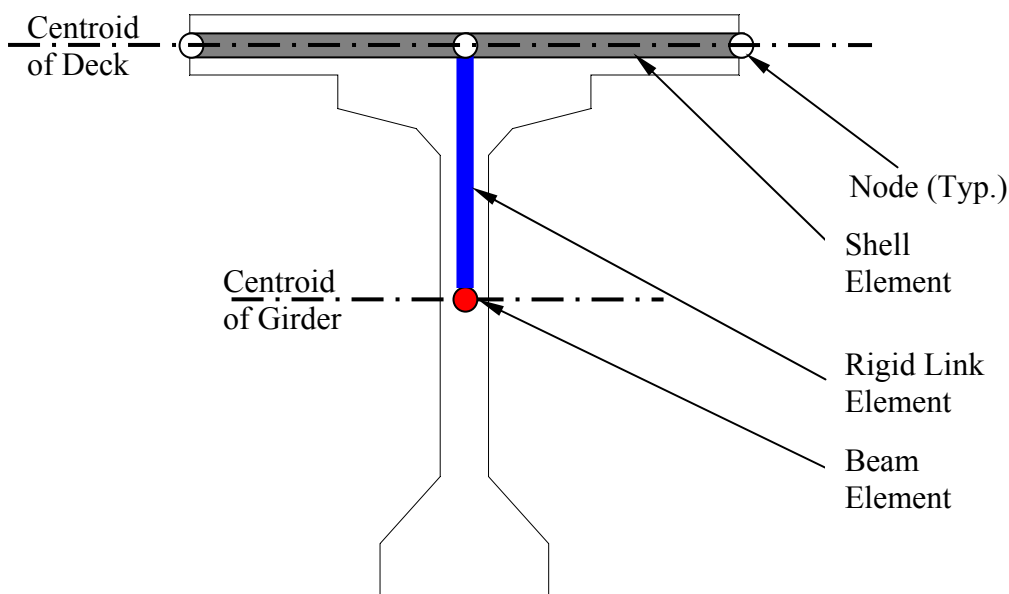


Figure 7.14. Cross-Section of 3D Model Superstructure.

7.3.3.7 Elastomeric Bearing Element

Elastomeric bearings on piers are modeled as beam line elements with assigned shear modulus of elasticity representing the low shear stiffness of the elastomeric material. The axial

modulus of the bearing element is adjusted to reflect an effective compressive modulus of elasticity (E_c) to include the effect of embedded steel shims by using the following (AASHTO LRFD):

$$E_c = 6GS^2 \quad (5.16)$$

To include E_c in a numerical analysis, a modification method using equivalent area and moment of inertia is:

$$A_e = A_{bearing} \frac{E_c}{E} \quad (5.17)$$

$$I_e = \frac{GA_{bearing}H^2}{12E} \quad (5.18)$$

where:

A_e = equivalent area,

$A_{bearing}$ = actual area of bearing pad,

E = the elastic modulus of bearing pad,

G = shear modulus of bearing pad,

H = thickness of bearing pad.

7.3.3.8 Backwall-Abutment Joint

The construction joint between the abutment and backwall is modeled substantially following section 7.3.2.8 as presented for the simplified 2D numerical model. The moment versus rotation properties are derived through the same procedure described in the simplified 2D numerical analysis. For the refined 3D analysis, construction joints are represented by rotational nonlinear spring elements. As presented in Figure 7.15, equally spaced nodes at the construction joint are

coupled for x, y, and z translations and x and y rotations. Z-axis rotation is dependent on rotational property of the construction joint.

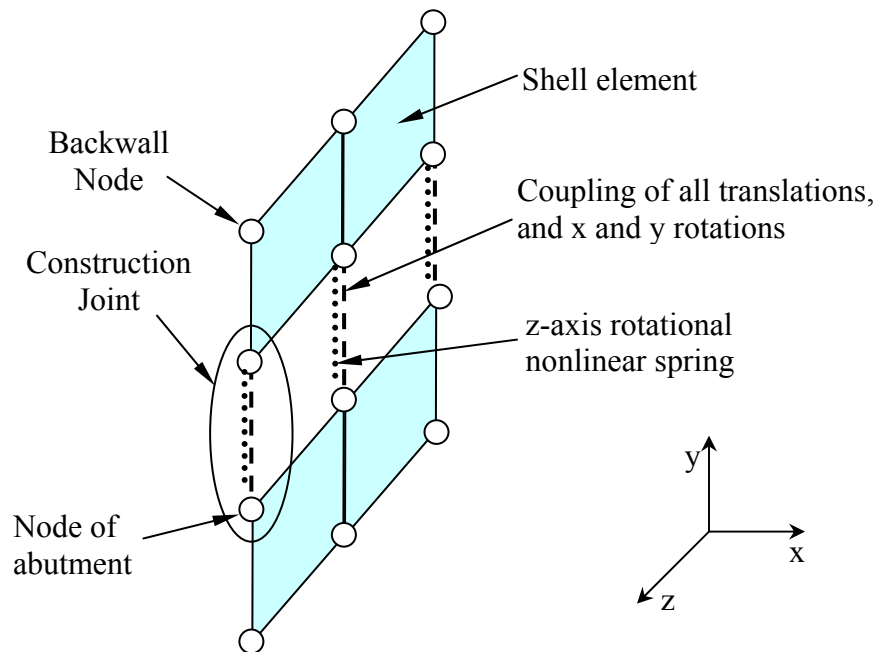


Figure 7.15. Abutment to Backwall Construction Joint.

7.4. Bridge Structure Material Properties

7.4.1 Introduction

Important material properties include elastic modulus, thermal expansion coefficient, and creep and shrinkage of concrete girders. Bridge structure materials are assumed linear-elastic, homogeneous, and isotropic. Where material properties are not available from tests, AASHTO LRFD (2007) and/or ACI209 (2004) procedures can be used to determine the expected values.

7.4.2 Concrete Elastic Modulus

The concrete elastic modulus, E_c , may be determined from tests conducted on previous projects following the same concrete mix design. When tests of a similar concrete mix design are not available, the elastic modulus of concrete will not be available for the analysis; however, E_c can be predicted with reasonable accuracy by the equation proposed by NCHRP 18-07:

$$E_c = 33,000 K_1 K_2 \left(0.140 + \frac{f'_c}{1000} \right)^{1.5} \sqrt{f'_c} \quad (7.26)$$

where:

K_1 = difference of mix unit weight between national average and local average,

K_2 = upper bound or lower-bound value.

If a standard unit weight concrete mix is specified, Equation 7.17 results in the well-known AASHTO LRFD equation as:

$$E_c = 33,000 w_c^{1.5} \sqrt{f'_c} \quad (7.27)$$

where w_c = unit weight of concrete (ksf).

7.4.3 Thermal Expansion Coefficient

The thermal expansion coefficient of a superstructure is a critical parameter in determining thermal movements of IABs. Laboratory tests of concrete mix designs should be conducted where possible for accurate determination. When test results are not available, a thermal expansion coefficient of $6.0\text{E-}6$ in/in/ $^{\circ}\text{F}$ can be conservatively used for concrete bridges in accordance with AASHTO LRFD. When specific concrete mix test data are available, an empirical equation (Emanuel and Hulsey 1997) may be used.

$$\alpha = f_T (f_M f_A \beta_P \alpha_S + \beta_{FA} \alpha_{FA} + \beta_{CA} \alpha_{CA}) \quad (7.28)$$

where:

α = thermal expansion coefficient,

f_T = temperature condition correction factor (1.0 = controlled condition, 0.86 = outside exposure condition).

f_M = concrete moisture content correction factor,

f_A = concrete age correction factor,

β_P = cement paste concrete mix volume proportion,

β_{FA} = fine aggregate concrete mix volume proportion,

β_{CA} = coarse aggregate concrete mix volume proportion,

α_S = saturated, hardened, neat cement paste thermal expansion coefficient,

α_{FA} = fine aggregate thermal expansion coefficient,

α_{CA} = coarse aggregate thermal expansion coefficient.

The thermal expansion coefficients based on the aggregate type are tabulated in Table 7.4.

Table 7.4. Thermal Expansion Coefficient by Aggregate Type.

Aggregate Type	AASHTO Guide (1989)	ACI209 (2004) & PCI (2005)
Basalt	5.0	3.6
Chert	.	6.6
Dolerite	5.3	3.8
Granite	5.3	3.8
Gravel	6.9	.
Limestone	4.0	3.1
Marble	2.4 — 4.1	4.6
Quartz	6.4	6.2
Quartzite	7.1	5.7
Sandstone	6.5	5.2
Siliceous Limestone	.	4.6

For the majority of bridge construction, the girder mix design is substantially different from the deck slab mix design. Based on the axial strength, an equivalent thermal expansion coefficient, α_{eq} can be derived and presented as (Oesterle, et al. 1999):

$$\alpha_{eq} = \frac{\alpha_g E_g A_g + \alpha_d E_d A_d}{E_g A_g + E_d A_d} \quad (7.24)$$

where:

α_g = girder material thermal expansion coefficient,

E_g = girder elastic modulus,

A_g = sum of girder sectional area,

α_d = deck material thermal expansion coefficient,

E_d = deck elastic modulus,

A_d = sum of deck sectional area.

7.4.4 Time-dependent effects

Time-dependent effects of creep, shrinkage, and prestressing steel relaxation have a significant influence on IAB long-term behavior. The procedure described and summarized herein is based on AASHTO LRFD (2007) by CEB-FIP (1990) and ACI209 (2004).

Total strain in a concrete member can be expressed as:

$$\varepsilon(t) = \varepsilon_{\sigma} + \varepsilon_{cr} + \varepsilon_{sh} = \frac{\sigma(t_o)}{E(t_o)} [1 + \varphi(t, t_o)] + \varepsilon_{sh} \quad (7.25)$$

where:

$\varepsilon(t)$ = total concrete strain at analysis time t due to constant stress at analysis time t due to constant stress,

ε_{σ} = the immediate strain due to applied stress, σ ,

ε_{cr} = the time-dependent creep strain,

ε_{sh} = free shrinkage strain,

$\sigma(t_o)$ = the initial stress at the initial loading time t_o ,

$E(t_o)$ = modulus of elasticity at t_o ,

$\varphi(t, t_o)$ = creep coefficient at time t corresponding to the age at loading t_o .

However, Equation 7.21 cannot be used directly because the applied stress, σ , is dependent on time. Figure 7.16 illustrates the strain variation under variable stress. To consider the strain variation, the effects of a series of applied stress are determined individually, and then, all strains are combined based on the principle of superposition. For stress variation, Jirásek and Bažant used the aging coefficient, χ , to adjust the creep coefficient. PCI bridge manual (2004) summarizes that the concept of χ accounts for:

- The concrete member experiences the maximum force only at the end of the time interval (t_o, t) .

- The modulus is increasing with time because the concrete is gaining strength.
- The total creep is larger for a given environment when the concrete is young.

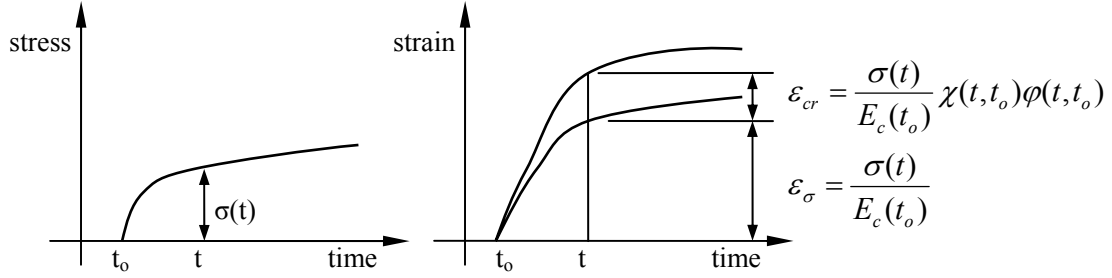


Figure 7.16. Concrete Strain under Variable Stress.

Equation 7.22 is used when the applied stress is variable:

$$\varepsilon = \frac{\sigma(t)}{E_c(t_o)} [1 + \chi(t, t_o)\phi(t, t_o)] + \varepsilon_{sh} \quad (7.26)$$

For time-dependent elastic modulus variation, the effective modulus (E_c^*) method simplifies creep analysis because the method allows a pseudo-elastic analysis within a given time interval.

E_c^* relates the immediate strain and time-dependant strain and is defined as:

$$E_c^*(t, t_o) = \frac{E_c(t_o)}{1 + \chi(t, t_o)\phi(t, t_o)} \quad (7.27)$$

The aging coefficient can be precisely computed and tabulated in ACI Committee 209, but $\chi = 0.7$ for a relatively young concrete age and $\chi = 0.8$ for all other uncertainties generally produces sufficiently accurate results.

ACI 209 shrinkage prediction equation is:

$$\varepsilon_{sh}(t) = \frac{t - t_o}{55 + (t - t_o)} \alpha \gamma_{sh} \quad (7.28)$$

where:

α = a constant equal to 0.00078,

γ_{sh} = a value determined by ambient relative humidity and size, shape effect, concrete slump test, fine aggregate percentage, and air content in concrete.

Most prestressing strand steel materials exhibit relaxation that is similar to creep in that relaxation and creep both result in a loss of prestressing and concrete compressive stress. AASHTO LRFD (2007) specifies determination of intrinsic relaxation of prestressing steel for low-relaxation strand as:

$$\Delta f_{RE} = \frac{[\log(24t) - \log(24t_o)]}{40} \left[\frac{f_{pj}}{f_{py}} - 0.55 \right] f_{pj} \quad (7.29)$$

where

f_{pj} = prestressing jacking stress (ksi),

f_{py} = yield strength of prestressing steel (ksi).

However, Equation 7.28 describes the intrinsic relaxation, while the relaxation of prestressing steel is relieved due to the effects of elastic shortening, creep, and shrinkage. An approximate reduced relaxation coefficient χ_r was derived by Ghali (2002). The reduced relaxation, Δf_R , is expressed as:

$$\Delta f_R = \chi_r \Delta f_{RE}$$

$$\chi_r = \exp[(-6.7 + 5.3\lambda)\Omega]$$

$$\lambda = \frac{\text{steel stress immediately after transfer}}{\text{characteristic tensile stress}} \quad (7.30)$$

$$\Omega = \frac{\text{total prestress change - intrinsic relaxation}}{\text{steel stress immediately after transfer}}$$

However, for low-relaxation prestressing steel, the relaxation effects are very small compared to creep and shrinkage. Thus, in most practical situations, a factor of 0.8 may be applied to the relaxation portion for reducing strain. Therefore, the total strain due to time-dependent effects is expressed as:

$$\varepsilon(t) = \frac{\sigma(t_o)}{E_c(t_o)} [1 + \phi(t, t_o)] + \frac{(\sigma(t) - \sigma(t_o))}{E_c^*(t, t_o)} + \varepsilon_{sh}(t, t_{sh,o}) \quad (7.31)$$

7.5. Loading Environment

7.5.1 Introduction

This section introduces general types of loads that are applied to account for the effects of temperature changes. Loads in the context of this discussion will refer to all types of loads due to removing expansion joints from a bridge, which includes thermal load and associated gradient and backfill pressure. Other load analyses and estimations such as dead loads and live loads are well documented elsewhere and are not discussed here. IAB loads considered may be incorporated in accordance with appropriate load combinations in Table 3.4.1-1 and 2 of AASHTO LRFD (2007).

7.5.2 Thermal Gradient

Where a vertical superstructure temperature gradient exists, a significant strain differential develops. Because the concrete deck and concrete and/or steel girders has a relatively low thermal conductivity, the distribution of temperature along the superstructure depth is nonlinear. AASHTO LRFD (2007) specifies a multi-linear thermal gradient profile for concrete girders and steel girders as presented in Figure 7.17. A negative thermal gradient is determined by

multiplying the positive temperature values by -0.30 for plain concrete decks and -0.20 for decks with an asphalt overlay.

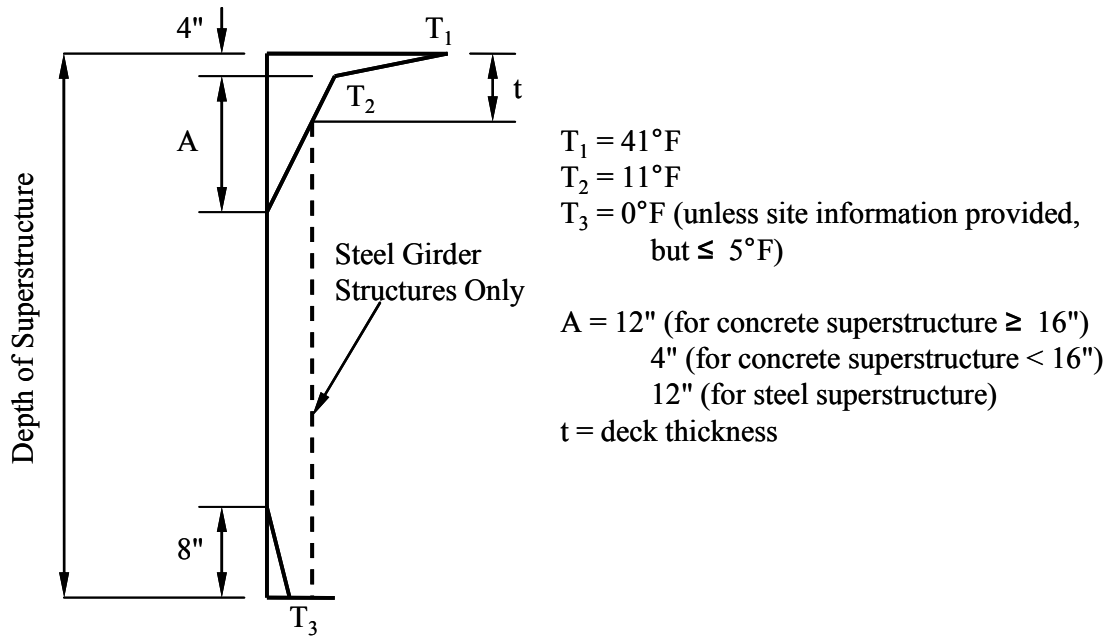


Figure 7.17. Temperature Gradient for Transformed Section.

To facilitate a numerical characterization of the thermal gradient effect, an equivalent, simplified temperature profile has been determined that results in an equal axial force and bending moment. The axial force and bending moment due to thermal stress are represented as:

$$\begin{aligned}
 P_t &= \int E \alpha T(y) b(y) dY \\
 M_t &= \int E \alpha T(y) b(y) Y dY
 \end{aligned}
 \tag{5.15}$$

where:

P_t = axial force,

M_t = bending moment,

E = elastic modulus,

α = thermal expansion coefficient,

$T(Y)$ = temperature at depth Y ,

$b(Y)$ = cross-section width at depth Y .

7.5.3 Temperature Load

Superstructure thermal loading is affected by many factors, the most significant of which for bridges in Pennsylvania is the ambient air temperature. Actual bridge temperature is dependent on the additional factors of solar radiation, wind speed, precipitation, and heat conductivity of bridge components. Because of the high thermal mass of bridge superstructures and the environmental conditions prevalent in Pennsylvania, the average ambient temperature corresponds well with bridge superstructure temperature.

Actual ambient temperature data were collected from September 2002 to September 2007 in the area adjacent to the four monitored bridges. To represent temperature loading mathematically, a full sinusoidal variation is assumed over 12 months:

$$T = A \cdot \sin[2\pi \cdot t - \phi] + T_{mean} \quad (7.32)$$

where:

T_{mean} = mean temperature,

A = amplitude of temperature fluctuation,

t = analysis time (year),

ϕ = phase lag (radian).

Based on the collected temperature data, $T_{mean} = 45.5^\circ\text{F}$ and $A = 30^\circ\text{F}$ are recommended for central Pennsylvania. For a specific area, actual data analysis and weather records may be required.

When a time-history analysis as described above is not feasible, static design extreme temperature load can be used instead of Equation 7.32. PennDOT DM-4 (2007) App. G 1.2.7.4

provided that design temperature for thermal loading in IABs is ± 100 °F for steel and ± 80 °F for concrete bridges. Design temperature by AASHTO LRFD (2007) ranges from 0 °F to 120 °F for steel and from 10 °F to 80 °F for concrete. Maximum and minimum ambient temperatures at the weather station at Port Matilda, including data from the Pennsylvania State Climatologist (PSC) and the National Climate Data Center (NCDC), have been collected and presented in Table 7.5. PSC has collected weather information since 1888 and NCDC since 1971. As can be seen, design extreme temperature by PennDOT DM-4 is conservative and AASHTO temperature is closer to measurements and collected data.

Table 7.5. Maximum and Minimum Temperature Data

	Weather Station at Port Matilda, PA (°F)	PA by PSC (°F)	Mid-Atlantic by NCDC (°F)
Maximum (T_{max})	95.1	102	107
Minimum (T_{min})	-12.9	-18	-47
Annual Mean (T_{mean})	45.5	49.5	50.0
Temperature Rise Temperature Fall	$T_{max} - T_{mean} = 49.6$ °F $T_{min} - T_{mean} = -58.4$ °F	$T_{max} - T_{mean} = 52.5$ °F $T_{min} - T_{mean} = -67.5$ °F	$T_{max} - T_{mean} = 57$ °F $T_{min} - T_{mean} = -97$ °F

7.5.4 Backfill Pressure

Backfill pressure is represented as a triangular distribution along abutment depth based on a unit weight of porous granular backfill equal to 119 pcF (PennDOT OGS). Initially applied backfill pressure is based on the at-rest lateral earth pressure coefficient of $K_o = 1.0$ (compacted condition). The lateral earth pressure coefficients are varied between passive and active pressure. An equivalent hydrostatic pressure corresponding to the backfill depth is applied to the backwall and abutment to represent at-rest soil backfill pressure. Execution of the numerical analysis is

completed in two analysis stages: (1) an initial analysis to compute the displacements at each abutment-backfill interaction springs due to the at-rest pressure and (2) the previously computed at-rest displacements are applied as initial displacements at the other end of the interaction elements, and then at-rest soil pressure is externally applied. This procedure results in the abutment-backfill interaction spring to be in the zero-force state, but the abutment is subjected to the at-rest pressure. The abutment-backfill interaction spring must be modified as presented in Figure 7.13. At-rest pressure is applied to the structure as an external pressure.

Chapter 8

Integral Abutment Analysis Examples

Presented here are three detailed integral abutment analysis examples illustrating the three analysis methods developed in the present study: (1) a 100'- 0" prestressed girder bridge, (2) a 200' - 0" steel girder bridge, and (3) a 400'- 0" prestressed girder bridge. Details of the three bridge structures are summarized in Table 8.1 and bridge elevations are presented in Figures 8.1 and 8.2. Each of the three example analysis bridges has the same superstructure cross-section other than girder size for span. The abutment configuration is also the same for each example analysis bridge with identical pile size, spacing and number. The example bridge abutment backfill height is 15'-0", measured from the bottom of the abutment to the bottom of the approach slab, and is consistent with the PennDOT-monitored bridges. This 15'-0" backfill height results in an abutment height equal to 9'-9" to 8'-3", which exceeds PennDOT standard BD-667M (4'-6" maximum abutment height) but does not alter the analysis procedure presented here in any way.

Each of the example analyses focuses on aspects unique to integral abutment bridge behavior and response to thermal loading effects. Analysis of bridge structures under dead load, vehicle load, wind, ice, collision, and other AASHTO-specified loading is well documented elsewhere and therefore is not included here. The analysis examples focus on the three methods developed during the course of the present study: (1) approximate, (2) 2D numerical model, and (3) 3D numerical model. Each of the analysis results provides thermally induced stresses developed in several bridge components to be combined with other stresses in the AASHTO-specified load

combinations: (1) girder axial force, (2) girder bending moment, (3) pile lateral force, (4) pile moment, and (5) pile head displacement.

Table 8.1. Example Bridges

Bridge	Girder Material	Bridge Length, L (ft)	Backfill Height, H (ft)
Bridge 1	Prestressed Concrete	100 (Single)	15
Bridge 2	Steel	200 (100'-100')	15
Bridge 3	Prestressed Concrete	400 (133'-134'-133')	15

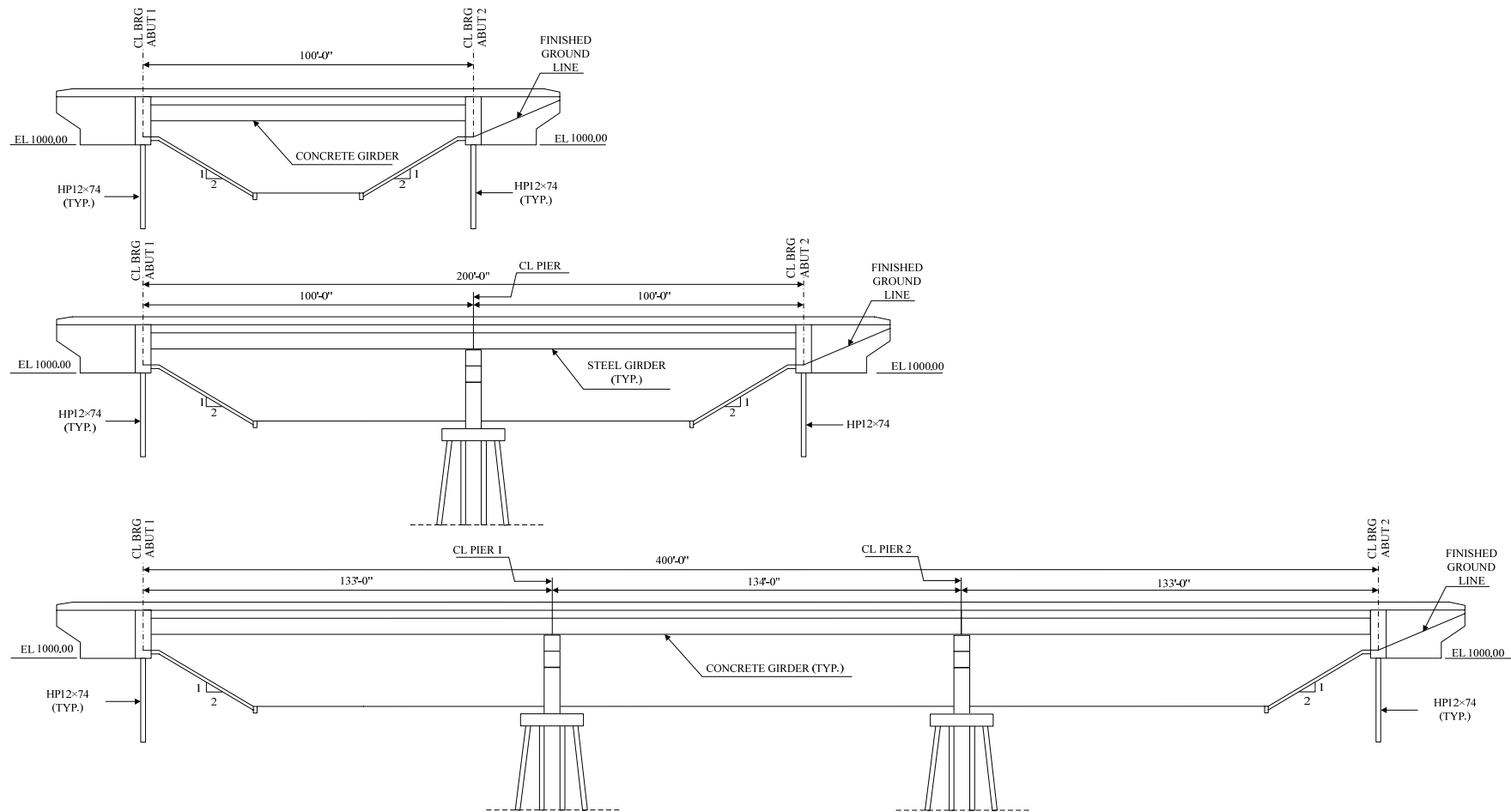


Figure 8.1: Bridge Elevation, Top – Example 1, Middle – Example 2, Bottom – Example 3.

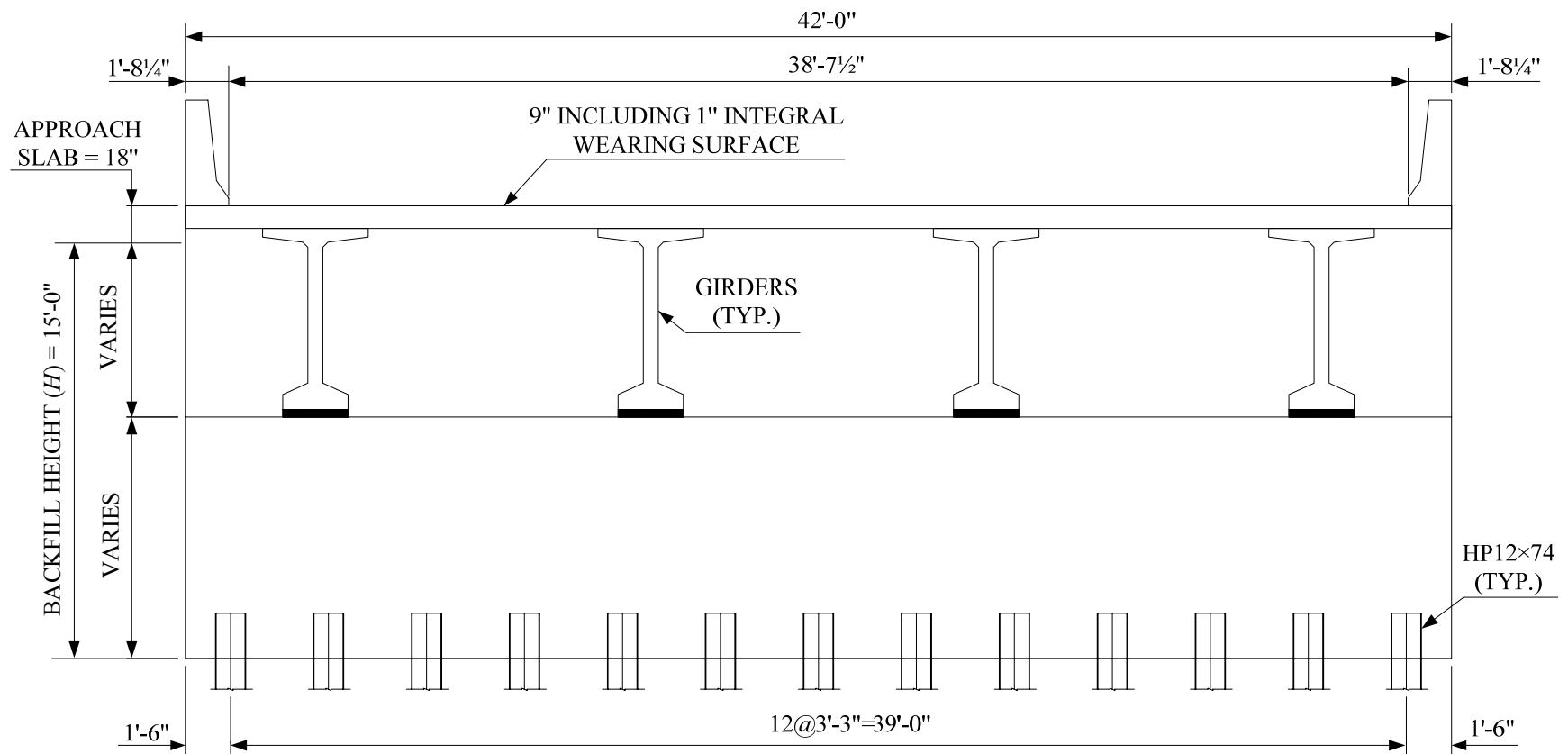


Figure 8.2. Typical Example Bridge Cross-Section and Abutment Dimensions.

8.1 Example 1: Single-span Concrete Girder Bridge

The integral abutment bridge configuration for Example 1 is a single-span, precast, prestressed concrete girder bridge supporting a 9-inch, normally reinforced cast-in-place concrete deck and PennDOT standard barriers. The girder design has been based on widely accepted AASHTO girder bridge practices for gravity load, with the controlling load combination of Service III with HL-93 live load (HS20 basis). The initial analysis under gravity load follows the AASHTO LRFD approximate load distribution method for a multi-lane bridge. Four AASHTO PCI BT72 girders and detailed cross-section dimensions are presented in Figures 8.3 and 8.4. Reinforcement details and construction joint, Section A-A in Figure 8.4, appear in Figure 8.5.

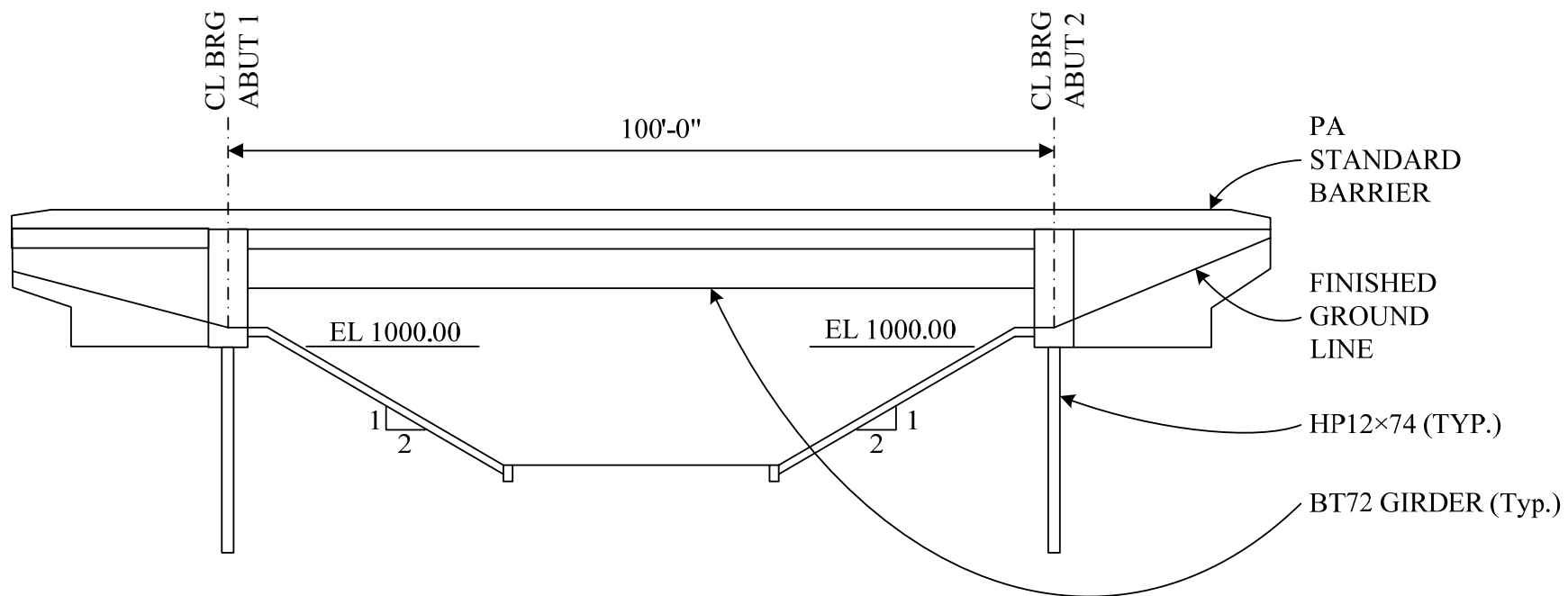


Figure 8.3: Example 1 Bridge Elevation

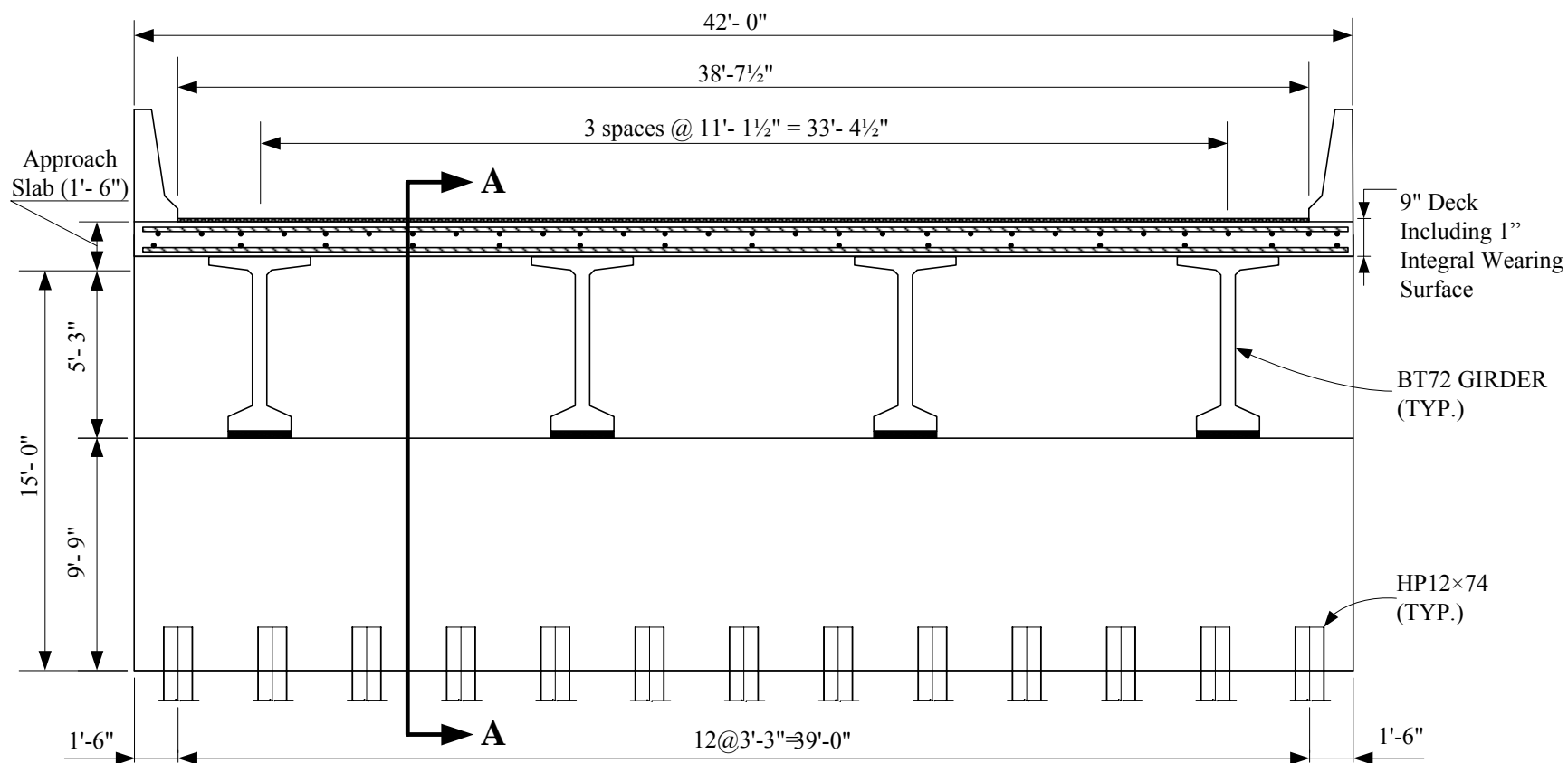


Figure 8.4: Example 1 Bridge Dimensions

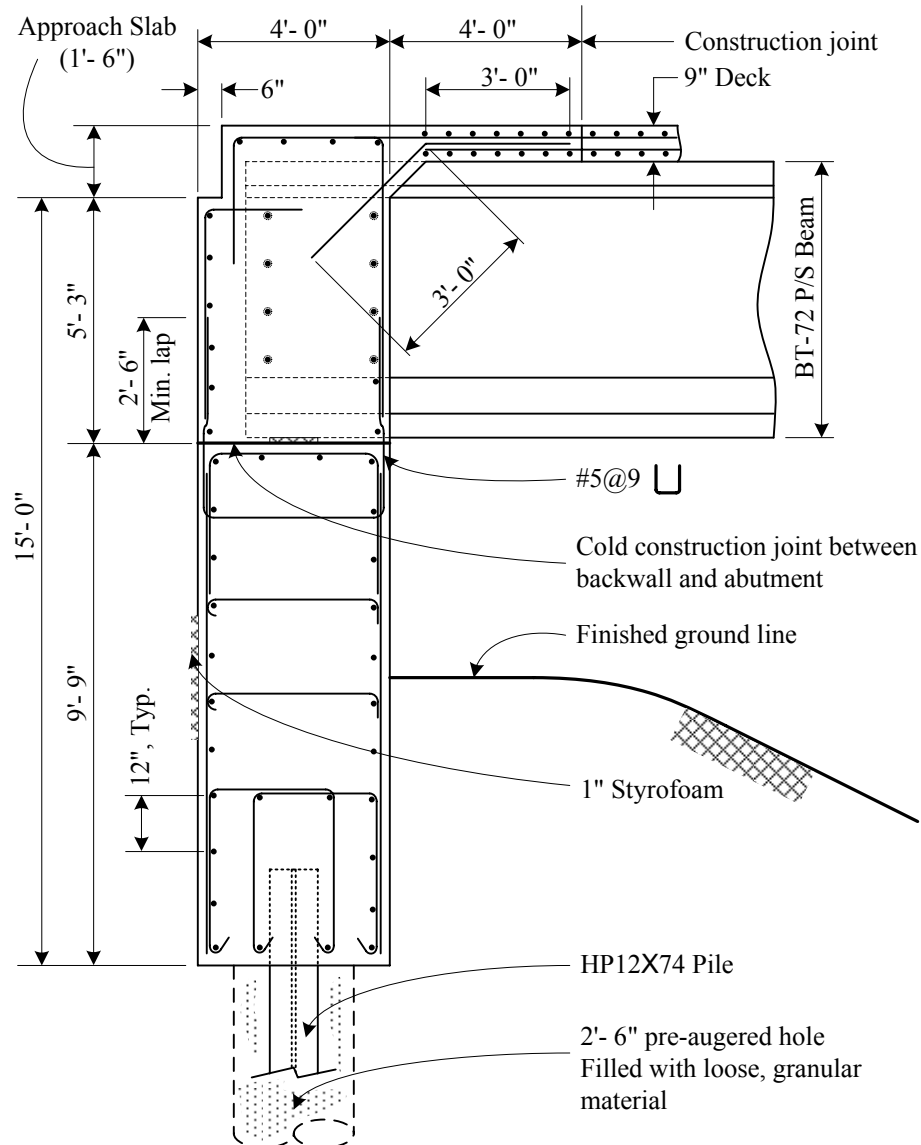


Figure 8.5: Example 1 Bridge Section A-A

Normal weight concrete compressive strengths of bridge components are presented in Table 8.2. A single row of 13, weak-axis oriented, end-bearing, HP12×74 piles are driven to refusal into soil type described in Table 8.3. The soil type for example 1 is taken as *intermediate*. This soil classification is as discussed in Chapter 7, which is also PennDOT No. OGS backfill as described in Table 8.4. The normally reinforced concrete

deck is placed 100 days after the girder manufacture date, which influences how time-dependent effects are computed.

Table 8.2. Example 1 Component Concrete and Steel Strength

Strength (psi)	Bridge Component
High Performance Concrete (8000 psi)	Prestressed Concrete Girders
PennDOT Class AAA (4000 psi)	Deck, Back-wall
PennDOT Class AA (3500 psi)	Parapets, Diaphragms and Cheek Walls
PennDOT Class A (3000 psi)	Abutment below Girder Seats, and Pedestals
$F_y = 50$ ksi	Steel Pile (HP12×74)
$f_y = 60$ ksi	Steel Rebars

Table 8.3. Soil Layer Properties for Soil Pile Stiffness (P)

Property	<i>Intermediate*</i>
Density (pcf)	121
Undrained Shear Strength (psi)	17.5
Soil Modulus (K) (pci)	1000
ε_{50} (in)	0.008

**Intermediate* refers to Table 7.2.

Note: soil pile stiffness (P) is represented as *Low* = 1, *Intermediate* = 2, *High* = 3 in the approximate method.

Table 8.4. Backfill Properties for Backfill Stiffness (B)

Property	<i>Intermediate*</i>
Density (γ) (pcf)	119
Angle of friction (ϕ_f) (Degree)	34
Subgrade Modulus (K_h) (pci)	43.8

**Intermediate* refers to Table 7.1.

Note: backfill stiffness (B) is represented as *Low* = 1, *Intermediate* = 2, *High* = 3 in the approximate method.

8.1.1 Example 1: Approximate Analysis Method

The approximate integral abutment analysis method utilizes equations 7.2 through 7.14, developed and presented in Chapter 7. The approximate method presented herein considers only temperature load, temperature gradient, backfill pressure, and time-dependent loads for a 75-year bridge life. In addition, backfill-abutment interaction, soil-pile interaction, and the nonlinear behavior of the back-wall to abutment construction joint are accounted for in the approximate analysis method, returning maximum, 75-year bridge responses.

AASHTO LRFD (5.4.2.2) recommends a concrete thermal expansion coefficient of $6\text{E-}6/^{\circ}\text{F}$ for normal-weight concrete and $5\text{E-}6/^{\circ}\text{F}$ for light-weight concrete in the absence of measurement data. The AASHTO-recommended thermal expansion coefficient for normal-weight concrete is adopted in the approximate analysis method presented here.

8.1.1.1 Girder Axial Force

Based on the given bridge dimensions and soil property classification, girder axial force is computed from the bridge axial force based on the assumption that all axial forces are evenly distributed to individual girders. Calculated positive and negative girder axial forces represent maximum tensile and compressive axial force over a 75-year bridge life.

Bridge tension force is computed as:

$$F_t = 16.6\alpha + 1.2L - 34.9H + 118.8P - 2.1 \geq 0 \quad (7.7)$$

$$\alpha = 6.0/^{\circ}\text{F} \text{ (AASHTO concrete thermal expansion} \times 1\text{E+6)}$$

$$L = 100 \text{ ft (bridge overall length)}$$

$H = 15$ ft (abutment height)

$P = 2$ (soil pile stiffness based on Table 8.3)

$$F_t = 16.6(6.0 / ^\circ\text{F}) + 1.2(100 \text{ ft}) - 34.9(15 \text{ ft}) + 118.8(2) - 2.1 \geq 0$$

$= -68$ kips per bridge < 0 ; therefore, no superstructure tension is predicted.

A single-span bridge does not experience significant thermal expansion and contraction displacements or time-dependent effects due to the relatively short total bridge length.

The example bridge considered herein has a large backfill pressure effect relative to the thermal expansion and contraction effects. Therefore, this example bridge case does not experience any superstructure tensile forces and no tensile axial force needs to be considered.

Bridge longitudinal compression force, F_c , is computed as:

$$F_c = -5.4\alpha^{0.8}L^{0.6}B^{0.2}P^{0.02} \quad \text{for } 13 \leq H \leq 18\text{ft} \quad (7.8)$$

$\alpha = 6.0 / ^\circ\text{F}$ (AASHTO concrete thermal expansion $\times 1\text{E}+6$)

$L = 100$ ft (bridge overall length)

$B = 2$ (backfill pile stiffness coefficient based on Table 8.4)

$P = 2$ (soil pile stiffness based on Table 8.3)

$$F_c = -5.4(6.0 / ^\circ\text{F})^{0.8}(100 \text{ ft})^{0.6}(2)^{0.2}(2)^{0.02} = -470 \text{ kips per bridge}$$

Compression Force per Girder $= -470 \text{ kips} / (4 \text{ girders}) = -120 \text{ kips per girder}$

8.1.1.2 Girder Bending Moment

The girder bending moment is computed from bridge bending moment, calculated from the approximate analysis equations 7.2 through 7.6 in Chapter 7 of this report. In a single-span bridge, the superstructure moment due to thermal loading is constant throughout the span. An illustration of bending moment under bridge expansion and contraction is presented in Figure 8.6. Bending moments at the mid-span and at the abutment are the same in a single span bridge.

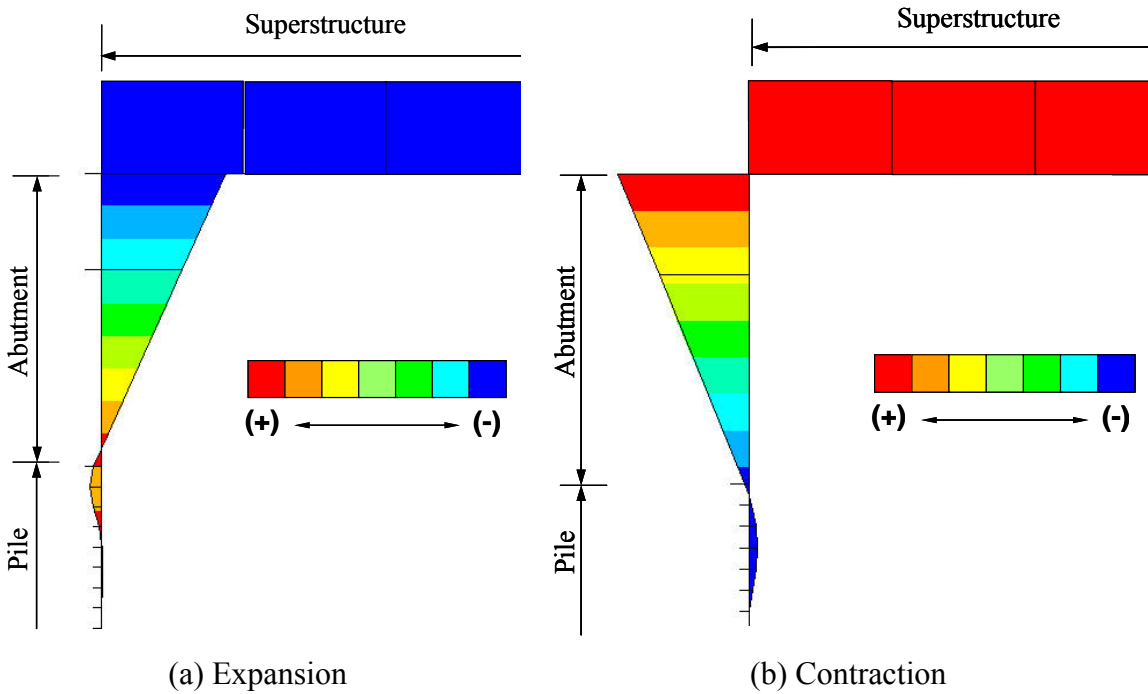


Figure 8.6: Moment Diagram of 2D Model

Bridge positive moment, M_{pos} , at the abutment is computed as:

$$M_{pos} = 120\alpha - 190H + 690P - 14 \geq 0 \quad \text{for } L \leq 130\text{ft} \quad (7.2)$$

$$\alpha = 6.0 \text{ } ^\circ\text{F} \text{ (AASHTO concrete thermal expansion } \times 1\text{E}+6)$$

$$H = 15 \text{ ft (abutment height)}$$

$$P = 2 \text{ (soil pile stiffness based on Table 8.3)}$$

$$M_{pos} = 120(6.0 \text{ } ^\circ\text{F}) - 190(15 \text{ ft}) + 690(2) - 14 = -760 \text{ ft-kips per bridge}$$

M_{pos} at the mid-span per girder = -760 ft-kip / (4 girders) = -190 ft-kips per girder < 0.

The computed bridge moment at the abutment is less than zero; therefore, positive moment at the abutment does not occur under thermal load. Due to the example single-span and a relatively short bridge total length, thermal contraction and expansion and time-dependent effects do not overcome the initial abutment displacement caused by at-rest backfill pressure. Bridge superstructure thermal behavior corresponding to the (a) initial (at-rest), (b) bridge expansion, and (c) contraction are illustrated in Figure 8.7.

Initial abutment displacement due to backfill pressure is sufficiently large, and the superstructure curvature is always convex, to cause the superstructure moment to always be negative.

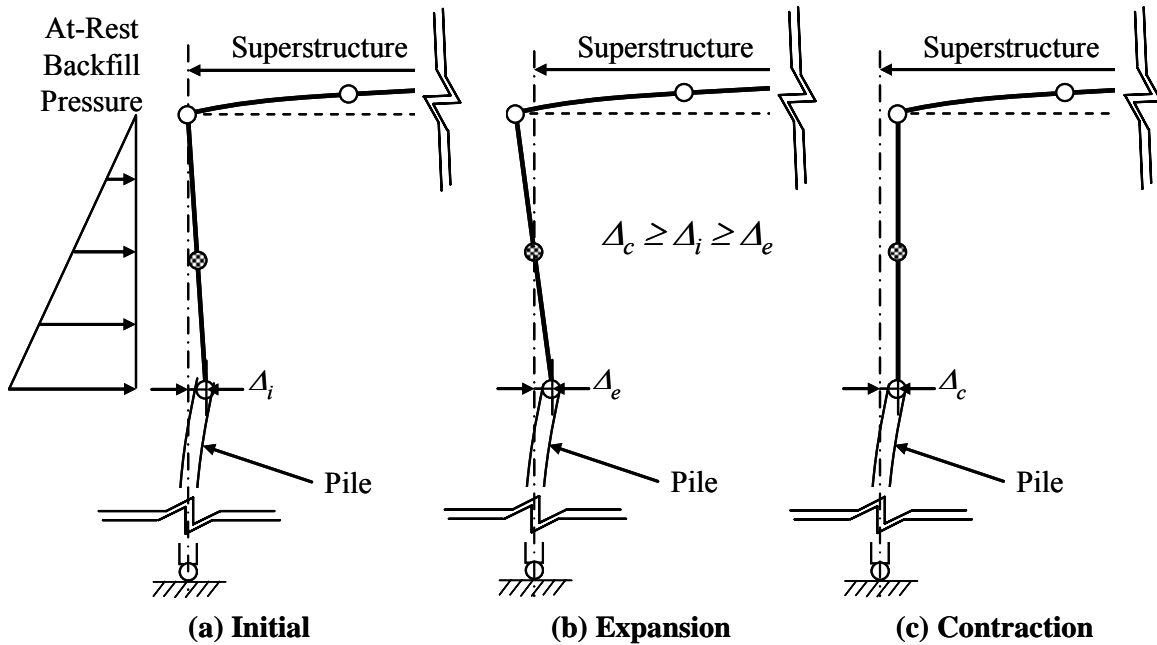


Figure 8.7: Single Span Bridge Thermal Behavior

Bridge negative moment, M_{neg} , at the abutment is computed as:

$$M_{neg} = -280\alpha^{0.4}L^{0.35} \quad \text{for } 13 \leq H \leq 18\text{ft} \quad (7.3)$$

$$\alpha = 6.0 / ^\circ\text{F} \text{ (AASHTO concrete thermal expansion } \times 1\text{E}+6)$$

$$L = 100 \text{ ft (bridge overall length)}$$

$$M_{neg} = -280(6.0 / ^\circ\text{F})^{0.4}(100\text{ft})^{0.35} = -2,900 \text{ ft-kips per bridge}$$

$$M_{neg} \text{ at the abutment per girder} = -2,900 \text{ ft-kip} / (4 \text{ girders}) = -730 \text{ ft-kips per girder.}$$

Bridge positive moment, M_{pos} , at the mid-span is computed as:

$$M_{pos} = 118\alpha + 13L + 1100P - 4000 \geq 0 \quad \text{for } 13 \leq H \leq 18\text{ft} \quad (7.4)$$

$$\alpha = 6.0 / ^\circ\text{F} \text{ (AASHTO concrete thermal expansion } \times 1\text{E}+6)$$

$$L = 100 \text{ ft (bridge overall length)}$$

$$P = 2 \text{ (soil pile stiffness based on Table 8.3)}$$

$$M_{pos} = 118(6.0 / ^\circ\text{F}) + 13(100\text{ft}) + 1100(2) - 4000 = +210 \text{ ft-kips per bridge}$$

$$M_{pos} \text{ at the mid-span per girder} = 210 \text{ ft-kip} / (4 \text{ girders}) = +53 \text{ ft-kips per girder.}$$

Bridge negative moment, M_{neg} , at the mid-span is computed as:

$$M_{neg} = -26\alpha^{1.0}L^{0.65}B^{0.1}P^{-0.08} \quad \text{for } 13 \leq H \leq 18\text{ft} \quad (7.5)$$

$$\alpha = 6.0 / ^\circ\text{F} \text{ (AASHTO concrete thermal expansion } \times 1\text{E}+6)$$

$$L = 100 \text{ ft (bridge overall length)}$$

$$B = 2 \text{ (backfill pile stiffness coefficient based on Table 8.4)}$$

$$P = 2 \text{ (soil pile stiffness based on Table 8.3)}$$

$$M_{neg} = -26(6.0 / ^\circ\text{F})^{1.00}(100 \text{ ft})^{0.65}(2)^{0.10}(2)^{-0.08} = -4,950 \text{ ft-kips per bridge}$$

$$M_{neg} \text{ at the abutment per girder} = -4,950 \text{ ft-kip} / (4 \text{ girders}) = -1,240 \text{ ft-kips per girder}$$

While a single-span IAB experiences a constant bending moment over the span, the approximate analysis method is able to determine girder bending moment for both mid-span and abutment locations. However, as presented in Figure 8.6, the superstructure moment is constant along the entire length. For this example approximate analysis, the larger of the moments is accepted to ensure a conservative result. Therefore, +53 ft-kips, which is a larger positive moment than -190 ft-kips, is selected as the positive girder bending moment and -1,240 ft-kips, which is a larger negative moment than -730 ft-kips, is selected as a negative girder bending moment.

8.1.1.3 Pile Head Moment

Pile head moments are computed using the approximate analysis equations 7.10 through 7.11 from Chapter 7 of this report. Typical IAB abutment pile displacement, moment, and shear are presented in Figure 8.8. While pile response depends significantly on bridge length and time-dependent effects, pile points of fixity are normally established above a 15-ft depth. Maximum supporting pile displacement, moment, and shear in occur at the pile head; therefore, these values are used for pile design.

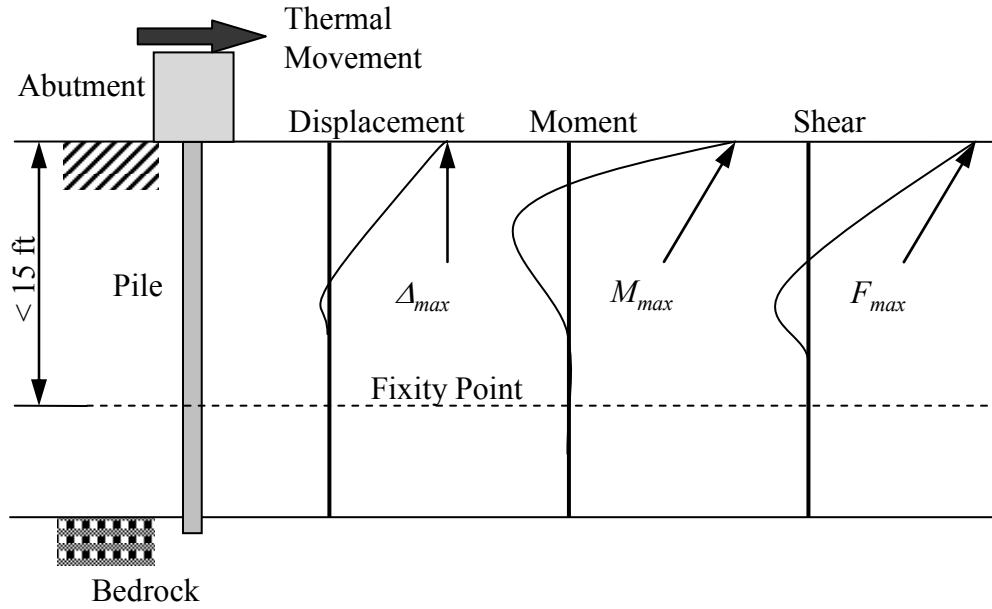


Figure 8.8: Typical IAB Pile Displacement, Moment, and Shear Response.

Total pile head moment is computed as:

$$M_{piles} = 21\alpha^{0.5}L^{0.5}H^{-0.1}P^{0.6} \leq M_{ypile} N_p \quad (7.10)$$

$$\alpha = 6.0 \text{ } ^\circ\text{F} \text{ (AASHTO concrete thermal expansion } \times 1\text{E}+6)$$

$$L = 100 \text{ ft (bridge overall length)}$$

$$H = 15 \text{ ft (abutment height)}$$

$$P = 2 \text{ (soil pile stiffness based on Table 8.3)}$$

$$M_{piles} = 21(6.0 \text{ } ^\circ\text{F})^{0.5}(100 \text{ ft})^{0.5}(15 \text{ ft})^{-0.1}(2)^{0.6} = 595 \text{ ft-kips per bridge}$$

$$\text{Pile head moment per pile: } M_{pile} = 595 \text{ ft-kips} / (13 \text{ piles}) = 46 \text{ ft-kips per pile}$$

A single pile is expected to experience a maximum of 46 ft-kip weak axis bending moment at the pile head over the 75-year bridge life.

8.1.1.4 Pile Lateral Force

Total pile lateral shear force is computed as:

$$F_{piles} = 19\alpha^{0.2}L^{0.4}B^{-0.1}P^{0.8} \leq F_{y_pile} N_p \quad \text{for } 13 \leq H \leq 18\text{ft} \quad (7.12)$$

The total pile lateral force is limited to single pile shear capacity (F_{y_pile}) times the number of piles (N_p). The minimum number of piles can be determined based on this limitation so that $F_{piles} \leq F_{y_pile} N_p$. For Example 1, the total pile lateral force is:

$$F_{piles} = 19\alpha^{0.2}L^{0.4}B^{-0.1}P^{0.8}$$

$$\alpha = 6.0 / ^\circ\text{F} \text{ (AASHTO concrete thermal expansion } \times 1\text{E}+6)$$

$$L = 100 \text{ ft (bridge overall length)}$$

$$B = 2 \text{ (backfill pile stiffness coefficient based on Table 8.4)}$$

$$P = 2 \text{ (soil pile stiffness based on Table 8.3)}$$

$$F_{piles} = 19(6.0 / ^\circ\text{F})^{0.2}(100 \text{ ft})^{0.3}(2)^{-0.1}(2)^{0.7} = 164 \text{ kips per bridge}$$

Pile lateral force, $F_{pile} = 164 \text{ kips} / (13 \text{ piles}) = 13 \text{ kips per pile}$

8.1.1.5 Pile Head/abutment Displacement

As presented in Figure 8.8, pile head/abutment displacement reaches its maximum at the pile head. This pile head/abutment displacement may also be used to determine the number of piles or other bridge dimensions because AASHTO LRFD (2007) limits the abutment displacement to $\leq 1\frac{1}{2}$ inches. For the current bridge example, maximum displacement is computed as:

$$u_{max} = 0.0006\alpha^{0.7}L^{1.0}B^{-0.02}P^{-0.1} \quad 13 \leq H \leq 18\text{ft} \quad (7.14)$$

$$\alpha = 6.0 / ^\circ\text{F} \text{ (AASHTO concrete thermal expansion } \times 1\text{E}+6)$$

$$L = 100 \text{ ft (bridge overall length)}$$

$$B = 2 \text{ (backfill pile stiffness coefficient based on Table 8.4)}$$

$$u_{max} = 0.0006(6.0 / ^\circ\text{F})^{0.7}(100 \text{ ft})^{1.0}(2)^{-0.15} = 0.19 \text{ inch}$$

8.1.2 Example 1: Two-Dimensional Model Analysis

A more refined and potentially more accurate relative to the IAB approximate analysis method is an analysis method that utilizes a two-dimensional, numerical, finite-element model. The methodology presented here permits the incorporation of individual bridge elements and the respective material and geometric properties through a demonstrated effective 2D model approach.

To construct a 2D model of the three-dimensional structure, the four girders and composite concrete deck are represented as a single beam element using ANSYS BEAM189 elements. Supporting piles are represented as two-dimensional beam elements, also using BEAM189 elements with soil-pile interaction springs (COMBIN39) spaced vertically at 1'-0" representing the soil. Similarly, abutment to backfill interaction is represented using nonlinear interaction springs. The development of material and geometric properties for each element is discussed in detail below. A schematic of the 2D bridge model developed for example 1 is presented in Figure 8.9.

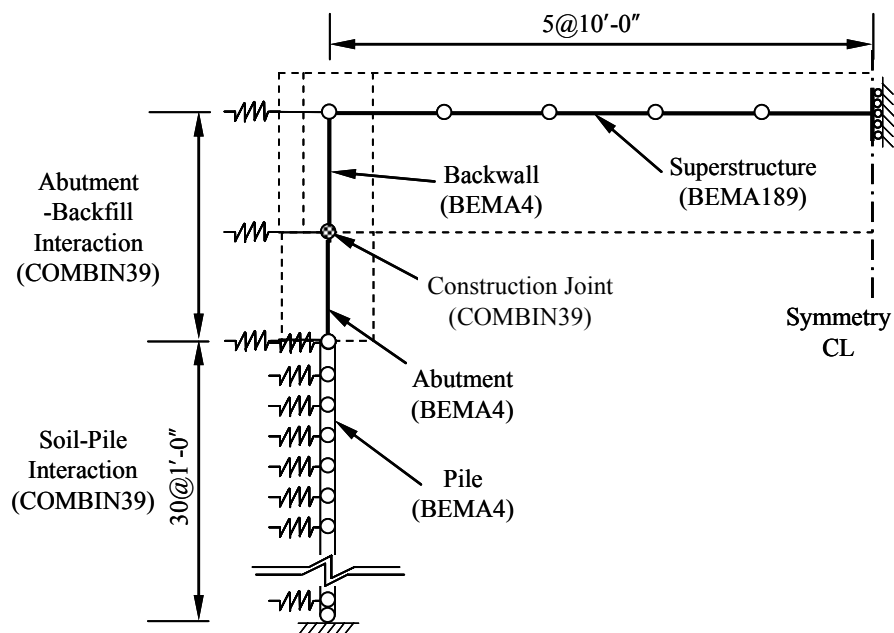


Figure 8.9: 2D Example 1 ANSYS Bridge Model.

The incorporation of transverse bridge components, such as diaphragms, in a two-dimensional model is not possible; however, the effects of the transverse elements on the longitudinal response to temperature loading are not significant. Key bridge components include girders, deck, abutment/backwall, construction joint and piles. Loading includes superstructure temperature variation, temperature gradient, and backfill pressure. A completed 2D numerical model with actual cross section of each member of the bridge is presented in Figure 8.10.

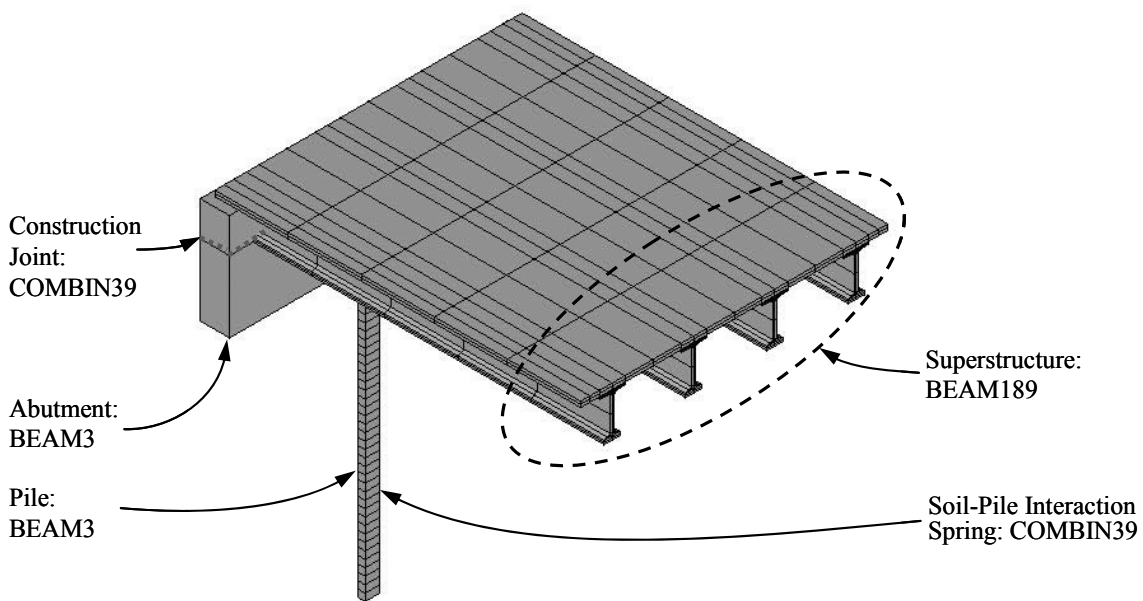


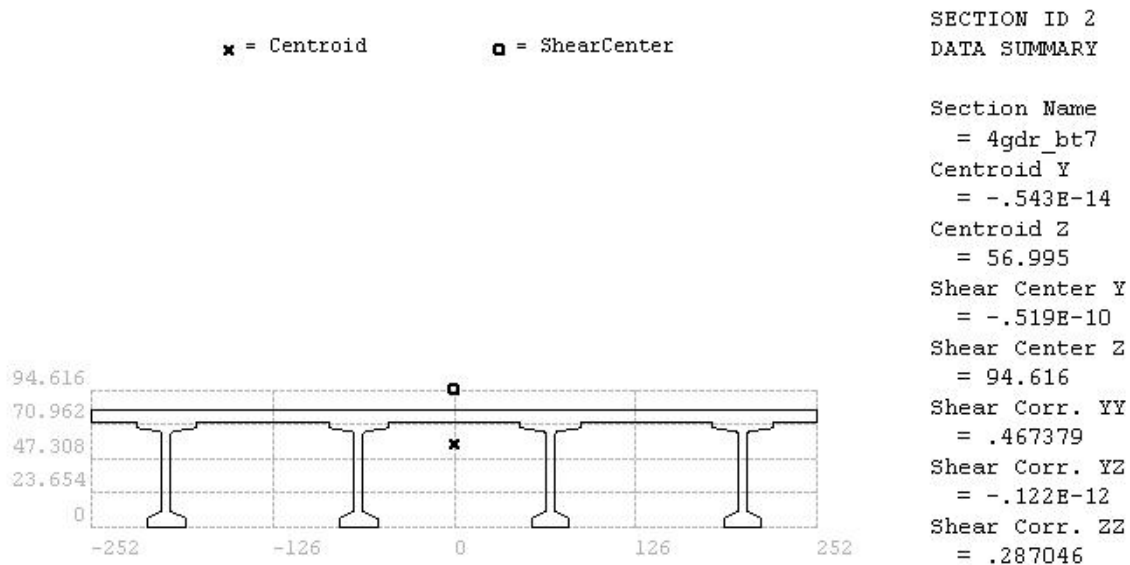
Figure 8.10: 2D Example 1 ANSYS Model Perspective View

8.1.2.1 Bridge Components

Each bridge component and its definition are described in detail in the following sections to allow the reader to develop future models for other IABs. The discussion includes girder and deck, abutment/backwall, construction joint, piles, and soil springs.

8.1.2.1.1 Girder and Deck

The bridge superstructure is modeled using a beam element based on the entire superstructure cross section properties, as shown in Figure 8.11. Computed superstructure section properties are presented in Table 8.5. Due to the 28-day strength difference between deck concrete (4,000 psi) and girder concrete (8,000 psi), a transformed deck concrete area is used in the calculation of area and moment of inertia. Based on AASHTO recommendations, the concrete thermal expansion coefficient for deck concrete and girder concrete is taken as $6.0\text{E-}6 \text{ in/in/}^{\circ}\text{F}$.



Note: All dimensions in inches.

Figure 8.11: Beam Element (BEAM189) Cross Section for Superstructure

Table 8.5: Superstructure Composite Section Property of Single Span Prestressed Girder IAB

Section Property	Centroid (in)	Area (in ²)	Moment of Inertia (in ⁴)	Elastic Modulus (ksi)	Thermal Expansion Coefficient (in/in/ [°] F)
Beam Element	56.995	7,604	6,648,258.33	5154	$6.0\text{E-}6$

8.1.2.1.2 Abutment/Back-wall

For a 2D model, the abutment (or pile cap) and back-wall (or end diaphragm) are modeled using beam elements. The full height of the abutment (base to beam seats) determines the length of the abutment beam element; however, the back-wall is modeled from the beam seat to the superstructure centroid. The superstructure is represented as a beam line element; therefore, the portion of the back-wall above the superstructure centroid is extraneous and eliminated.

Generally, higher-strength concrete is used in the back-wall as compared to the abutment concrete because the back-wall is placed monolithically with the deck. The example 1 bridge specifies 4,000 psi and 3,000 psi 28-day compressive strength concrete for the back-wall and abutment, respectively, resulting in the elastic modulus for the back-wall as 3,640 ksi and the elastic modulus for abutment as 3,160 ksi.

8.1.2.1.3 Construction Joints

The construction joint between the back-wall and abutment is modeled using a joint element with defined rotational stiffness, but all translations are directly compatible with adjacent elements. The computed rotational stiffness of the construction joint is presented in Figure 8.12.

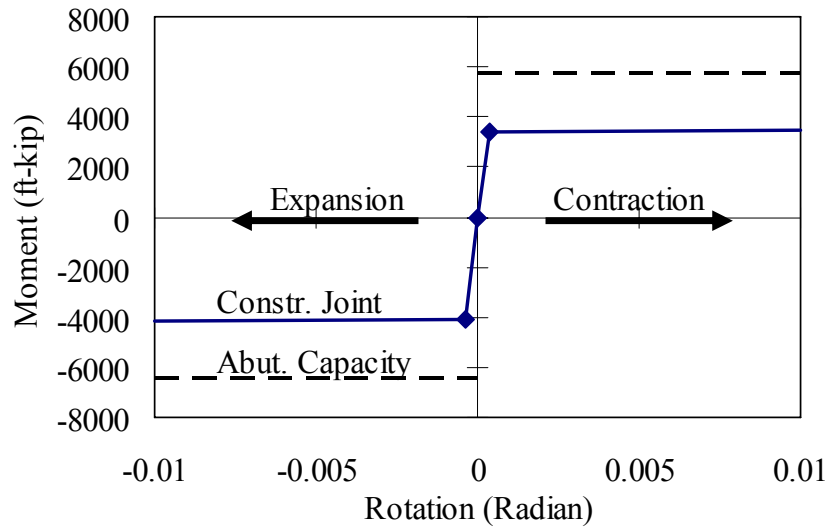


Figure 8.12: Construction Joint Rotational Stiffness

Rotational stiffness is determined based on reinforcing bars crossing the joint. A reinforcement detail consisting of #5 bars at 9" center-to-center is a typical PennDOT specification and is therefore adopted here. In addition, the reinforcement adjacent to the backfill side of the joint is different from the reinforcement adjacent to the abutment front face because girders interfere with the reinforcement placement (see Figure 8.5). This causes the rotational stiffness for superstructure expansion to be different from the rotational stiffness for superstructure contraction.

The construction joint is a cold joint; therefore, concrete tension is not considered in the development of moment-curvature definition. To convert curvature into rotation, half of the AASHTO LRFD embedment length is utilized to compute the displacement, crack opening between the abutment and the back-wall during superstructure expansion and contraction, due to strain in the reinforcement.

8.1.2.1.4 Steel H-Piles

Weak axis oriented steel H-piles are modeled using beam elements and soil-structure interaction is modeled using nonlinear spring elements. Beam element steel H-pile properties of area and moment of inertia are assigned directly. The pile length must be at least 20 ft because the pile fixity point (zero rotation and zero displacement) occurs between 10 and 15 ft. However, longer bridges develop a deeper fixity point, and therefore piles should be modeled to the full expected driven depth. The pile fixity point of the numerical model must be evaluated to determine whether the pile has been properly modeled. For the given example bridge, a 30-ft pile length has been modeled.

8.1.2.1.5 Soil Springs

Soil non-linear stiffness definition at each depth is represented using equivalent Winkler spring elements based on p - y curves spaced at 1-ft vertical intervals. Alternatively, commercial programs such as COM624P and Lpile can directly generate p - y curves at various soil conditions and depths (refer to section 5.2.3 of this report). In the 2D ANSYS bridge model, COMBIN39 nonlinear spring elements are used to represent the hysteretic behavior of soil-pile interaction. Each p - y spring is spaced at 1'-0" intervals from the pile head to the pile bearing tip. Spring element properties defined by lateral force vs. lateral displacement (p - y) at a given depth consider the total number of abutment piles and the tributary area along the pile. For illustration, under the bridge contraction case, a p - y curve at the 10'-0" depth of the given soil strata is computed as:

$$p_u = \min \left\{ p_{uf} = 9cD, \quad p_{uw} = \left(3 + \frac{\gamma'}{c} X + \frac{J}{D} X \right) cD \right\} \quad (5.4)$$

$$p_{uf} = 9cD = 9(13.9 \text{ psi})(12.1 \text{ inches}) = 1510 \text{ lbs/inch}$$

$$p_{uw} = \left(3 + \frac{140 \text{ pcf}}{2000 \text{ psf}} (120 \text{ inches}) + \frac{0.5}{12.1 \text{ inches}} (120 \text{ inches}) \right) (2000 \text{ psf}) (12.1 \text{ inches})$$

$$= 1460 \text{ lb/inch} \rightarrow \text{governs}$$

For the tributary length of 1'-0", $p_u = (1460 \text{ lbs/inch})(12 \text{ inches}) = 17.5 \text{ kips}$

$$p = 0.5 p_u \left(\frac{y}{y_{50}} \right)^{1/4} \text{ and if } y = 0.1 \text{ inches,}$$

$$p = 0.5 (17.5 \text{ kips}) \left(\frac{0.1 \text{ inches}}{0.212 \text{ inches}} \right)^{1/4} = \underline{7.24 \text{ kips}}$$

Similarly, for expansion, $X = 120 \text{ inches} + 180 \text{ inches (backfill height)} = 300 \text{ inches}$:

$$p_{uf} = 9cD = 9(13.9 \text{ psi})(12.1 \text{ inches}) = 1510 \text{ lbs/inch}$$

$$p_{uw} = \left(3 + \frac{140 \text{ pcf}}{2000 \text{ psf}} (300 \text{ inches}) + \frac{0.5}{12.1 \text{ inches}} (300 \text{ inches}) \right) (2000 \text{ psf}) (12.1 \text{ inches})$$

$$= 2880 \text{ lb/inch}$$

For the tributary length of 1'-0", $p_u = (1510 \text{ lbs/inch})(12 \text{ inches}) = 18.2 \text{ kips}$

$$p = 0.5 p_u \left(\frac{y}{y_{50}} \right)^{1/4} \text{ and if } y = 0.1 \text{ inches,}$$

$$p = 0.5 (18.2 \text{ kips}) \left(\frac{0.1 \text{ inches}}{0.212 \text{ inches}} \right)^{1/4} = \underline{7.53 \text{ kips}}$$

This procedure is repeated for several y values to form a smooth p - y curve, computed up to $16y_{50} = 16(2.5D\varepsilon_{50}) = 16(2.5)(12.1 \text{ inches})(0.007 \text{ inches}) = 3.39 \text{ inches}$ because p - y curves in clay soils start to become constant after $16y_{50}$. For the given case, example computations for a soil-pile interaction spring at a depth of 10'-0" are tabulated as:

Table 8.6: p - y curve ordinates for a depth of 10'-0"

	P_u (kip)	y (inches)								
		9.8E-5	7.8E-4	0.025	0.1	0.42	0.85	1.69	3.39	4.5
Cont.	17.5	1.28	2.15	5.12	7.24	10.4	12.4	14.7	17.5	17.5
Exp.	18.2	1.33	2.24	5.32	7.53	10.8	12.8	15.3	18.2	18.2

Based on the sign convention that bridge expansion induces negative displacement and force, the data of Table 8.6 is plotted in Figure 8.13 and compared to results generated by the Lpile program. The API equations in Table 8.6 and the Lpile program produce identical results. Soil springs at each depth require this procedure to generate a p - y curve.

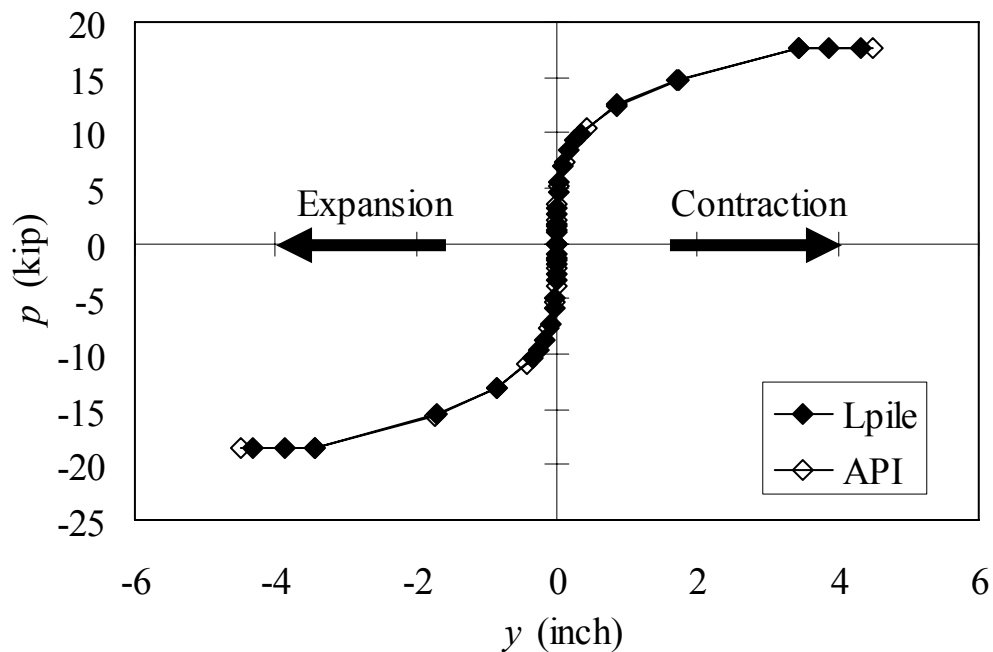


Figure 8.13: Comparison of p - y Curve by the API Equation and Lpile.

8.1.2.1.6 Miscellaneous Components (diaphragms, interior supports, bearings)

Girder bearings (normally elastomeric) at both abutments are embedded in the back-wall concrete and are not modeled explicitly. The superstructure is rigidly connected to the back-wall and is modeled as such. Interior supports (piers) are modeled as roller restraints. Because both ends of an IAB superstructure are restrained at the abutments, interior supports are not designed to provide longitudinal restraint. In addition, because elastomeric bearings allow longitudinal displacement with very low resistance during bridge contraction and expansion, a roller support condition is appropriate for interior supports. Diaphragms at the mid-span or pier supports are not considered due to modeling restrictions.

8.1.2.2 Loads

Loads considered in the 2D model include the overall superstructure temperature fluctuation, temperature gradient through the superstructure depth, and backfill pressure. Each load component is described in the sections below. Two approaches are presented for the 2D analysis example: (1) a 2D time-history analysis, and (2) an extreme design static 2D analysis. The 2D time-history analysis evaluates a 75-year bridge life as a result of a sinusoidal temperature fluctuation. This simulation considers a sinusoidal temperature change, time-dependent effects and cyclic soil-structure interaction over time, and is close to actual conditions. However, the 2D design analysis is a static analysis based on AASHTO specified an extreme temperature rise (+30°F) and fall (-40°F) for concrete bridges. This analysis approach is typically used for DOT design, is easy to implement and the required computing resources are low. Time-dependent effects are not

included for the design temperature rise analysis in order to obtain the maximum bridge expansion response. This approach recognizes that initial bridge expansion will likely occur before significant, counteracting time-dependent effects occur. Time-dependent effects are combined with design temperature fall to obtain the maximum bridge contraction response.

8.1.2.2.1 Sinusoidal Temperature Fluctuation Simulation

Superstructure temperature fluctuation over time is simulated with a sinusoidal curve that is based on field-collected data at monitored bridges and a weather station. The 2D model is configured to simulate a 75-year bridge life; therefore, the sinusoidal temperature simulation must represent a nominal temperature fluctuation over the expected bridge life. Although bridge structures possess relatively low thermal conductivity and high thermal inertia, the average superstructure temperature is reasonably assumed to be equal to ambient temperature. The temperature fluctuation is plotted in Figure 8.14. Depending on the availability of local meteorological data, annual mean temperature, annual temperature amplitude, frequency ($2\pi t$) and phase lag (ϕ) can be determined. Based on the present study monitoring results and information obtained from the National Climate Data Center, central Pennsylvania annual mean = 49 °F and the annual temperature amplitude = 30 °F. A phase lag = π is adopted when the bridge backwall concrete is placed during fall season around annual mean temperature.

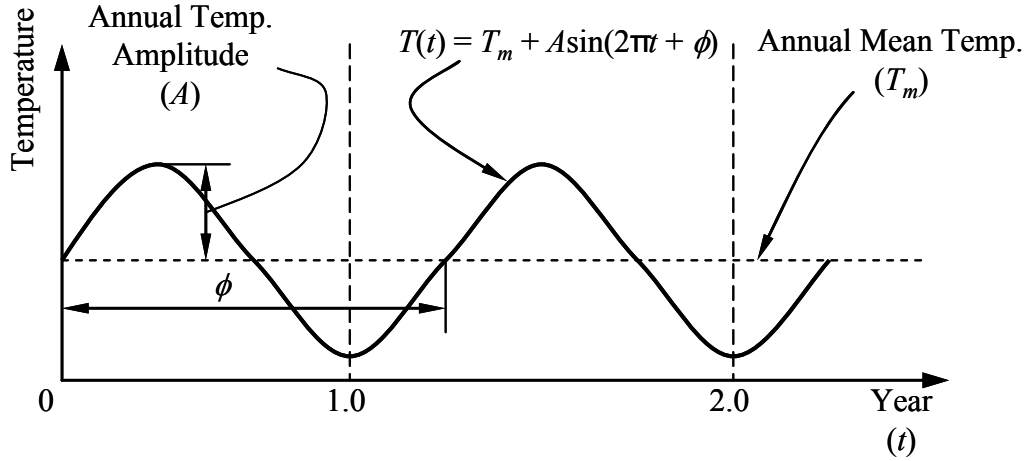


Figure 8.14: Temperature Model

8.1.2.2.2 Temperature Gradient

Based on AASHTO multi-linear temperature gradient requirements, an equivalent temperature gradient is computed. Thermal stress (σ_t) induced by the temperature gradient along the superstructure depth is represented as:

$$\sigma_t(y) = E \cdot \alpha \cdot T(y) \quad (5.14)$$

where y = distance from the extreme bottom fiber, $\sigma_t(y)$ = longitudinal thermal stress at a fiber located at y ; E = elastic modulus; α = thermal expansion coefficient, and $T(y)$ = temperature at y . Thus, the axial force, P_t , and moment, M_t , due to thermal stresses are:

$$P_t = \int E \alpha T(y) b(y) dY, \text{ and} \quad (5.15)$$

$$M_t = \int E \alpha T(y) b(y) Y dY$$

For an AASHTO-PCI BT72 girder, the equivalent temperature at the top fiber is 14.9 °F and the equivalent temperature at the bottom fiber is -1.9 °F. A similar computation for the negative temperature gradient results in -7.3 °F and -2.0 °F at the top and bottom fiber, respectively.

The temperature gradient application in a 2D numerical analysis is presented in Figure 8.15. The AASHTO gradient represents maximum and minimum temperature gradient across the superstructure. During warm months of summer, the maximum temperature gradient is reached. During the cold months of winter, the minimum temperature gradient is reached. During the transitional months from spring to summer to fall, the temperature gradient is applied using a sinusoidal fluctuation with the amplitude of positive temperature gradient. Thus, the sinusoidal temperature gradient is superimposed on the thermal fluctuation. During the transitional months from fall to winter to spring, the temperature gradient is also applied using a sinusoidal fluctuation; however, the sinusoidal amplitude of the negative temperature gradient is used. The sinusoidal temperature gradient, as appropriate for the season, is effectively superimposed on the thermal fluctuation.

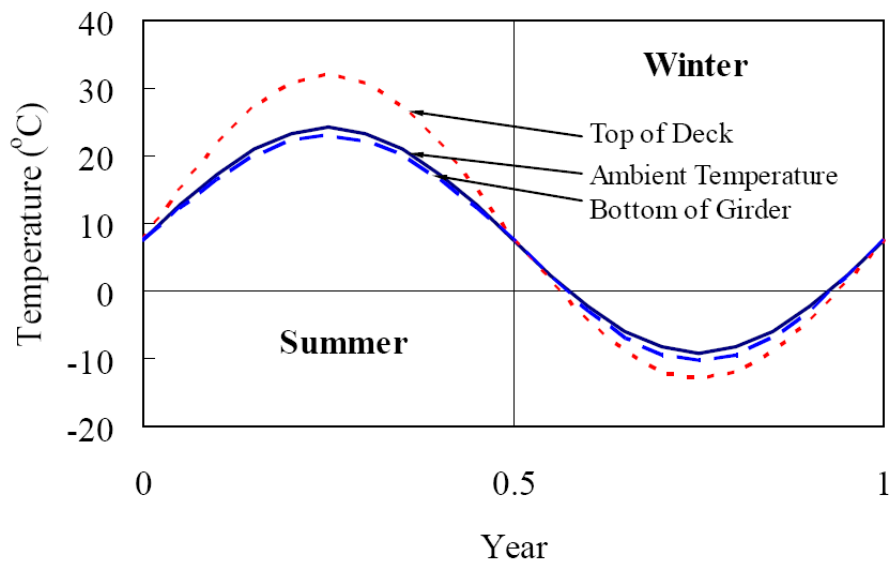


Figure 8.15: Temperature Variation with Temperature Gradient

8.1.2.2.3 Backfill Pressure

Earth pressure behind the abutments and back-walls is assumed as a hydrostatic pressure distribution, increasing with depth resulting in a triangular pressure distribution. As presented in Figure 8.16, backfill pressure varies according to a pressure-displacement relationship. The initial earth pressure is taken as the familiar at-rest pressure, but the pressure ranges between active (P_a) and passive pressure (P_p) depending on abutment displacement. In the numerical simulation, a typical abutment-to-backfill interaction relationship is presented in Figure 8.16, where active and passive backfill pressure limit is determined based on equation 5.7:

$$\begin{aligned}
 P_o &= K_o \gamma' z w = (1) \gamma' z w \\
 P_a &= K_a \gamma' z w = \frac{1 - \sin \phi_f}{1 + \sin \phi_f} \gamma' z w \\
 P_p &= K_p \gamma' z w = \frac{1 + \sin \phi_f}{1 - \sin \phi_f} \gamma' z w
 \end{aligned} \tag{5.7}$$

where K_o , K_a and K_p are the lateral earth pressure coefficients for at-rest, active and passive condition, respectively, γ' is the effective soil weight, ϕ_f is the internal friction angle, z is the depth of soil, and w is the effective backfill width. For example 1, K_o , K_a and $K_p = 1.0$, 0.283 and 3.537 , respectively, and $\gamma' = 119$ pcf, $\phi_f = 34^\circ$, and $w = 36'-10''$.

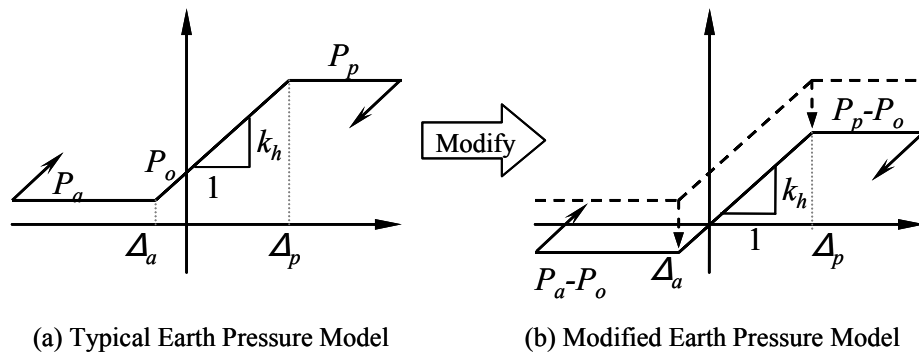


Figure 8.16: Backfill Pressure

The slope (k_h) in Figure 8.16 between active and passive pressure is computed by Boulanger et al. (1999):

$$k_h(z) = k_{ref} \left(\frac{z}{h_{ref}} \right)^{0.5} \quad (5.1)$$

where h_{ref} is the reference depth measured from the soil surface to the pressure cell elevation and z is the depth. Based on monitoring results, $k_{ref} = 0.044$ kci at 4 ft from the bottom of the abutment may be used for backfill height ranging from 10 to 20 ft.

To modify the backfill-abutment interaction as presented in Figure 8.16(b), at-rest backfill pressure (P_o) is applied externally and presented in Figure 8.17.

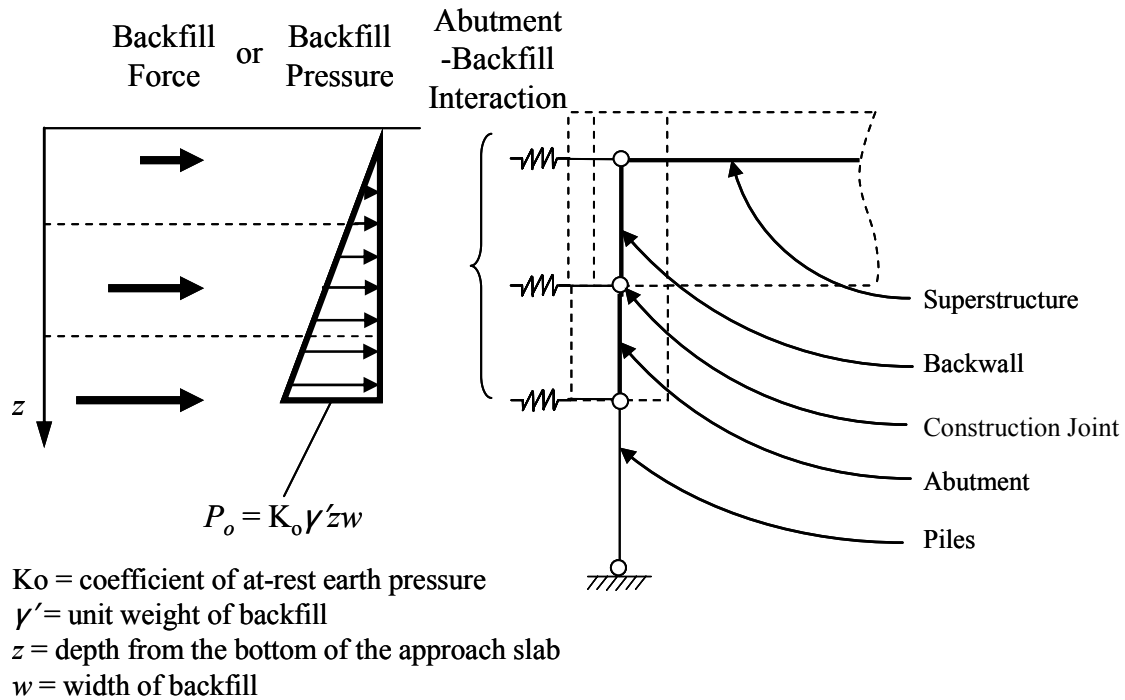


Figure 8.17: Backfill Pressure

In the 2D numerical model, the backfill pressure is applied either by (1) line loads on abutment and backwall elements or (2) forces on nodes based on tributary area divided by

the dotted lines in backfill pressure diagram in Figure 8.17. Both produce the same results.

Backfill pressure applied to 2D numerical model is represented as a triangular-shaped line load and is presented in Figure 8.18.

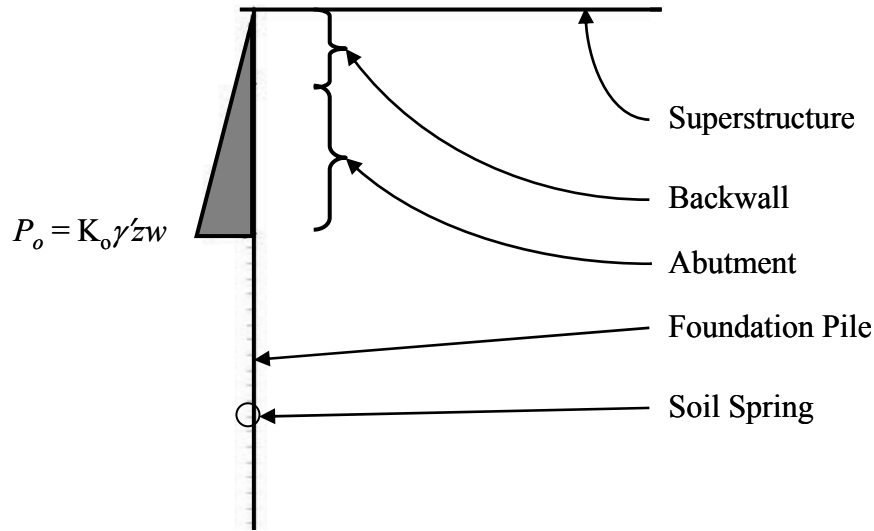


Figure 8.18: Backfill Pressure in 2D Numerical Model

8.1.2.2.4 Time-dependent Loads

To accurately simulate time-dependent effects (creep and shrinkage), the superstructure is divided into five segments and each element is subjected to an applied computed equivalent temperature load based on Section 5.3.2 of this report, ACI 209 creep and shrinkage strain and AASHTO LRFD prestressing steel relaxation. Figure 8.19 presents the temperature load and time-dependent load application. Each time-dependent effect at time t is computed at each location (both end of elements) and computed strain is transformed into temperature based on thermal expansion coefficient. Computed time-dependent temperature is added to temperature load and temperature gradient load, and applied at each top and bottom location of elements.

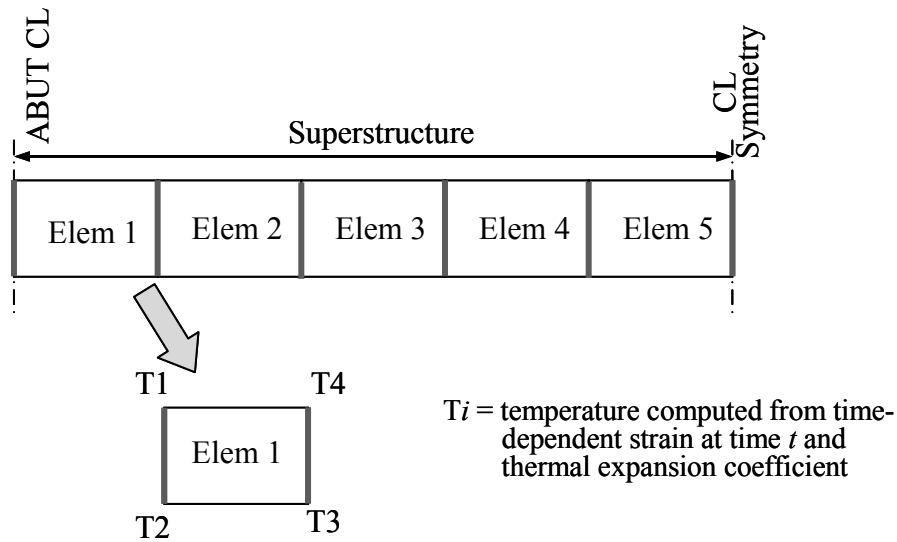


Figure 8.19: Time-dependent Load Application

When an equivalent rectangular cross section is used for the superstructure I-girder, the time-dependent load for the superstructure section is required to be offset. Because the composite section elastic neutral axis (ENA) (Figure 8.20(a)) is not coincident with the equivalent rectangular section ENA (Figure 8.20(c)), the equivalent rectangular section is aligned and located at its ENA; that is, the distance from ENA to the extreme top fiber is the same as to the distance from ENA to the extreme bottom fiber. However, computed time-dependent effects are based on the actual section (Figure 8.20(a)) whose distance from ENA to the extreme top fiber is different from the distance from ENA to the extreme bottom fiber. The computed strains (Figure 8.20(b)) due to time-dependent effects plus temperature loads (T'_i in Figure 8.20) must be corrected as an offset temperature load (T_i in Figure 8.20) to induce the same moment and axial force as presented in Figure 8.20(d). If computed strains are applied to the rectangular section without an offset, a different rotation of ϕ is subjected to the section, as appears in Figure 8.20(e).

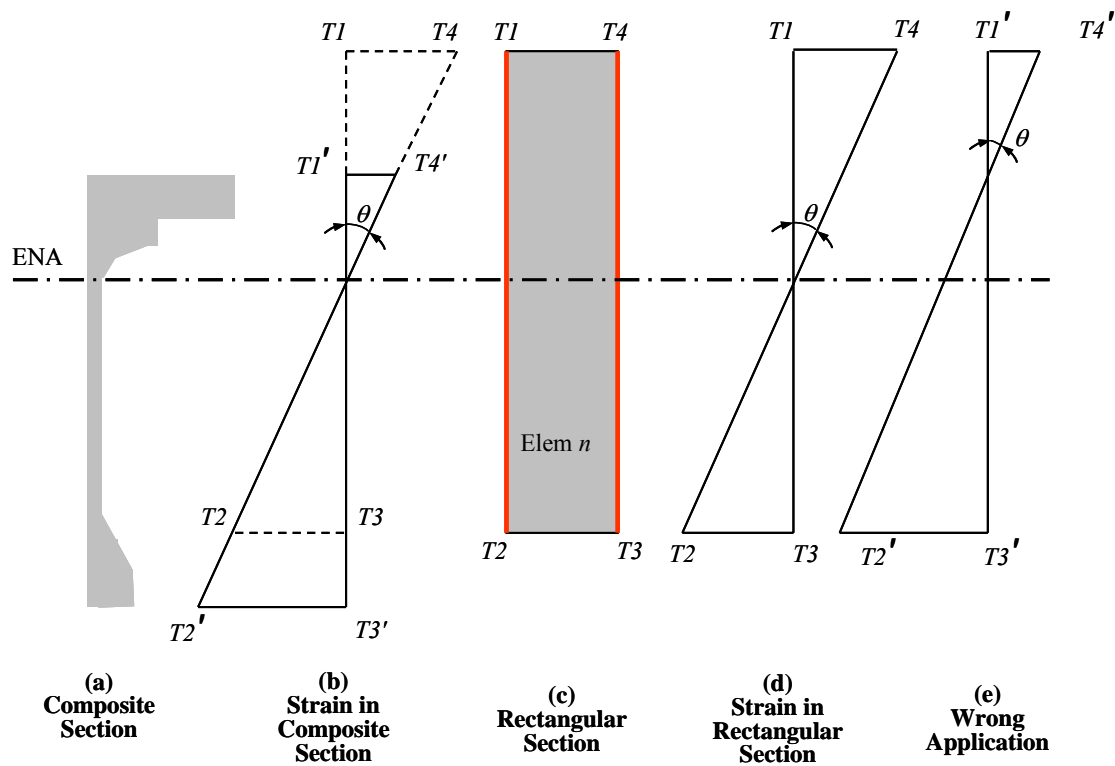


Figure 8.20: Temperature Load Application in Offset Element Section

8.1.2.3 Example 1: 2D Analysis Results

Two analysis approaches are demonstrated in this example: (1) 2D extreme design temperature static analysis and (2) 2D time-history analysis. The 2D extreme design temperature range static analysis runs for both AASHTO extreme temperature rise (+30°F) and fall (-40°F). To obtain the maximum response, time-dependent effects are considered only for the bridge contraction case. For the bridge expansion case, only thermal load is considered because the initial bridge expansion will occur before significant time-dependent effects have occurred. If time-dependent loads are desired, 2D models are capable of considering time-dependent loads. The time-history analysis, considering time-dependent effects, runs for a 75-year bridge life with a sinusoidal temperature load. Superimposed results of both approaches are presented on the same

graph for girder axial force, girder bending moment, pile lateral force, pile moment, and pile head displacement.

8.1.2.3.1 Girder Axial Force

Girder axial forces by both extreme design temperature range static analysis (dashed lines) and time-history analysis (solid line) are presented in Figure 8.21. While the temperature range in the extreme temperature static analysis is larger than the time-history analysis, the time-history analysis results in a larger compressive girder axial force.

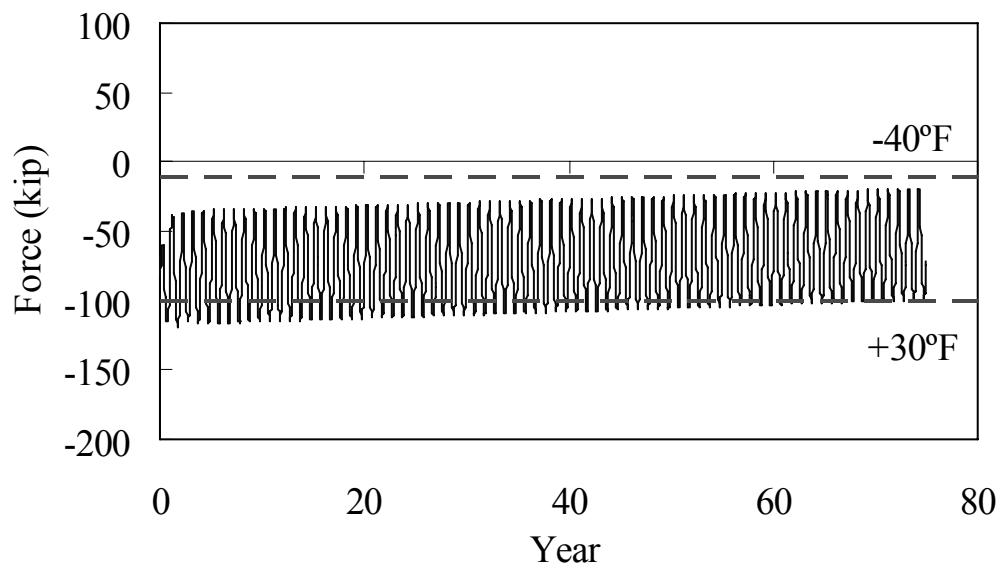


Figure 8.21: Example 1: 2D Analysis—Girder Axial Force (Static and Time-History)

8.1.2.3.2 Girder Bending Moment

Girder bending moments by both extreme design temperature static analysis (dashed lines) and time-history analysis (solid line) are presented in Figure 8.22. Although the

temperature range for the extreme design temperature static analysis is larger than time-history analysis, the time-history analysis results in a larger negative girder moment.

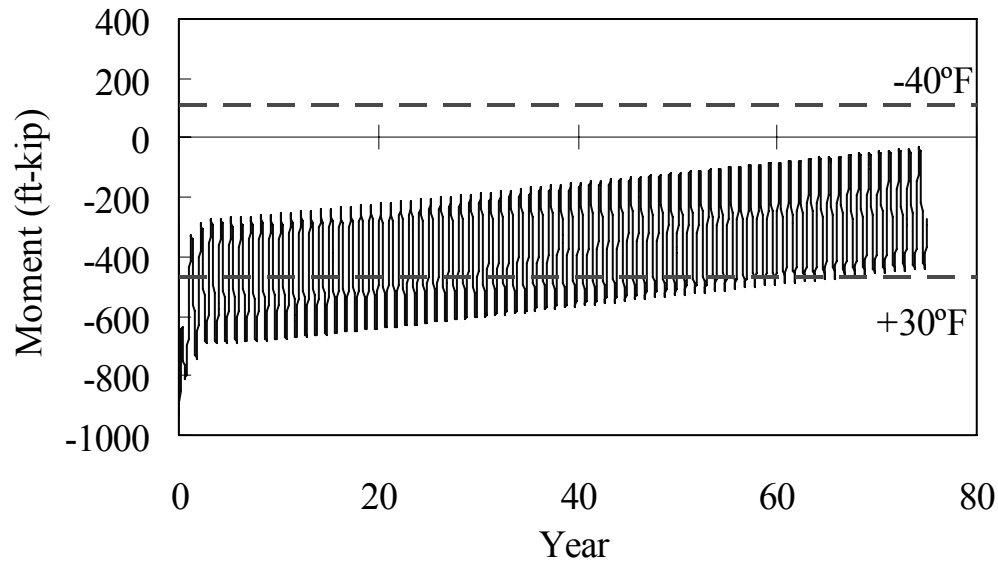


Figure 8.22: Example 1: 2D Analysis—Girder Bending Moment (Static and Time-history)

8.1.2.3.3 Pile Lateral Force

Pile lateral force by both the extreme design temperature static analysis (dashed lines) and the time-history analysis (solid line) are presented in Figure 8.23. Again, even though the extreme design temperature range is larger than the time-history analysis, the time-history analysis predicts a larger girder axial force.

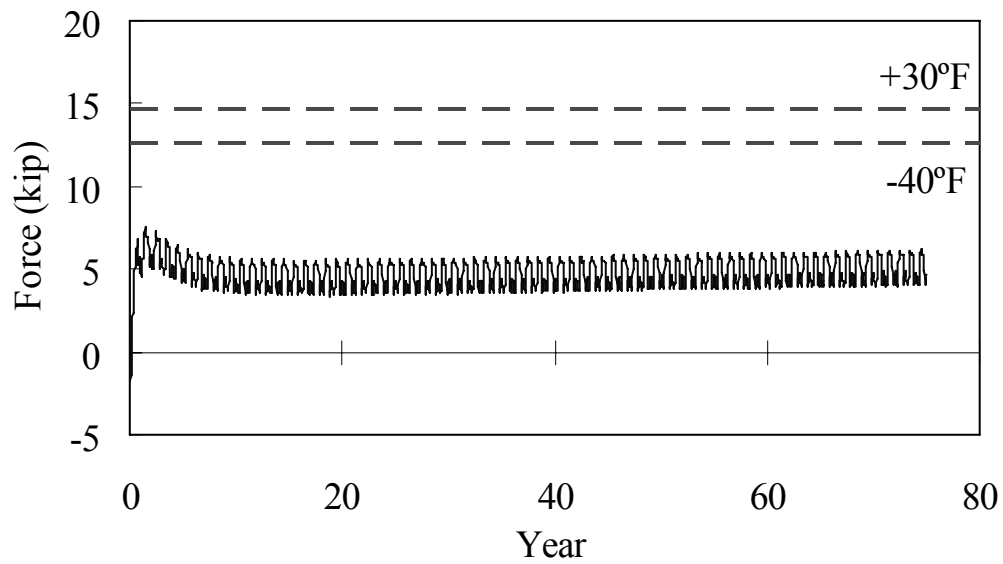


Figure 8.23: Example 1: 2D Analysis - Pile Lateral Force (Static and Time-history)

8.1.2.3.4 Pile Moment

Pile moment by both extreme design temperature static analysis (dashed lines) and time-history analysis (solid line) are presented in Figure 8.24. While the temperature range of the extreme design temperature analysis is larger than the time-history analysis, the time-history analysis predicts a larger pile moment.

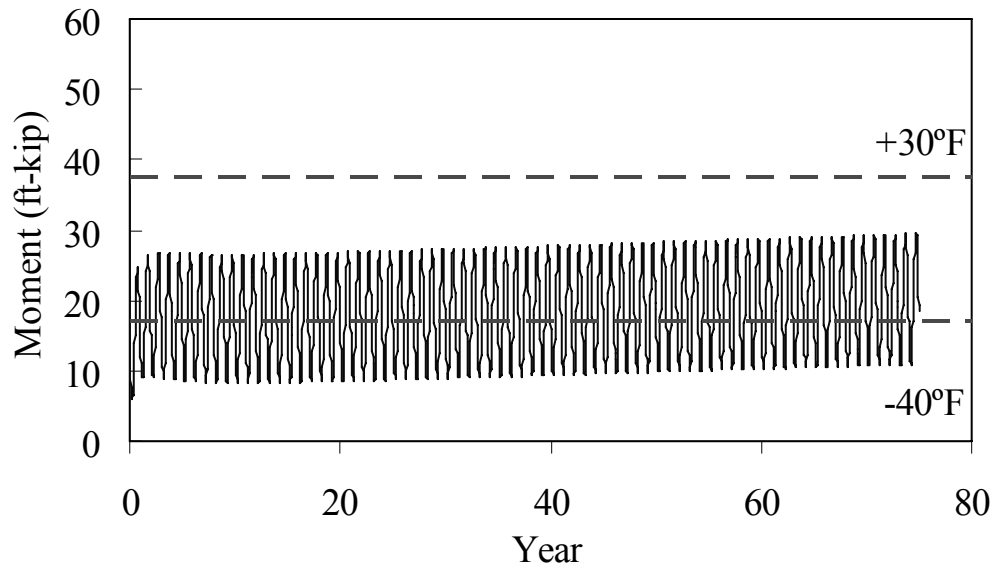


Figure 8.24: Example 1: 2D Analysis - Pile Moment (Static and Time-history)

8.1.2.3.5 Pile Head Displacement

Pile head displacement by both extreme design temperature static analysis (dashed lines) and time-history analysis (solid line) are presented in Figure 8.25. Although the extreme design temperature range is larger than time-history analysis, the time-history analysis results in a larger pile head displacement.

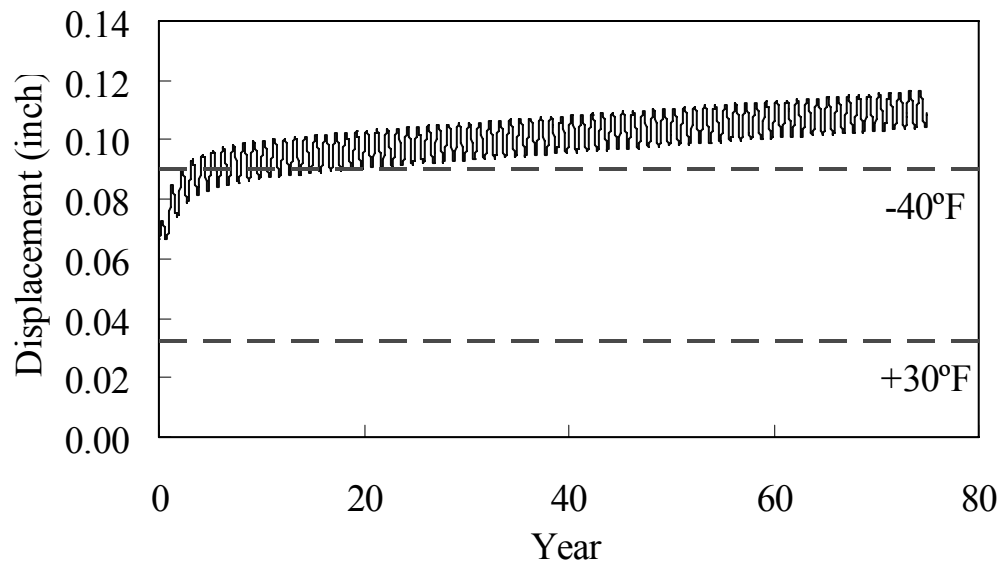


Figure 8.25: Example 1: 2D Analysis - Pile Head Displacement (Static and Time-History)

8.1.3 Example 1: Three-dimensional Analysis Model

Three-dimensional numerical simulations offer increased predictive accuracy over two-dimensional simulations. In addition, individual element response to load is available from the 3D analysis rather than grouped response as in a 2D analysis. Transverse effects are also determined with a 3D simulation due to the added third, transverse dimension to the model. The methodology presented here permits the incorporation of individual bridge elements and the respective material and geometric properties through a demonstrated effective 3D model approach using the commercially available, general analysis program ANSYS. The example 1, 3D analysis evaluates two separate loading cases that consist of the AASHTO extreme temperature rise (+30°F) and extreme temperature fall (-40°F). Any other thermal loading may be applied to the 3D, however.

The example 1, 3D ANSYS schematic model in isometric view is presented in Figure 8.26. Each of the four prestressed concrete girders is represented using ANSYS BEAM189 elements that have a BT72 cross section. At the mid-point of the 9-inch bridge deck thickness are ANSYS SHELL63 elements, which have 6 degrees of freedom at each of four corner nodes. To connect the deck to the four girders, ANSYS rigid link MPC184 elements are included at a longitudinal spacing equal to 2 ft. The connection of girders and deck accomplishes the effects of a composite section as is intended in the original design. Abutment piles are included in the 3D model with ANSYS BEAM189 elements defined with the pile HP12×74 cross section. Soil-pile interaction springs modeled using ANSYS COMBIN39 elements spaced at the maximum of 1 ft are included along the full height of each pile. The abutment and back-wall elements are modeled using ANSYS SHELL63 with a maximum of 1 ft side dimension. Abutment to

backfill interaction is represented with ANSYS COMBIN39 elements nonlinear springs.

Bridge diaphragms are included in the 3D model using BEAM189 elements. An isometric view of the completed solid ANSYS 3D numerical model with actual cross sections of each member of the bridge is presented in Figure 8.27.

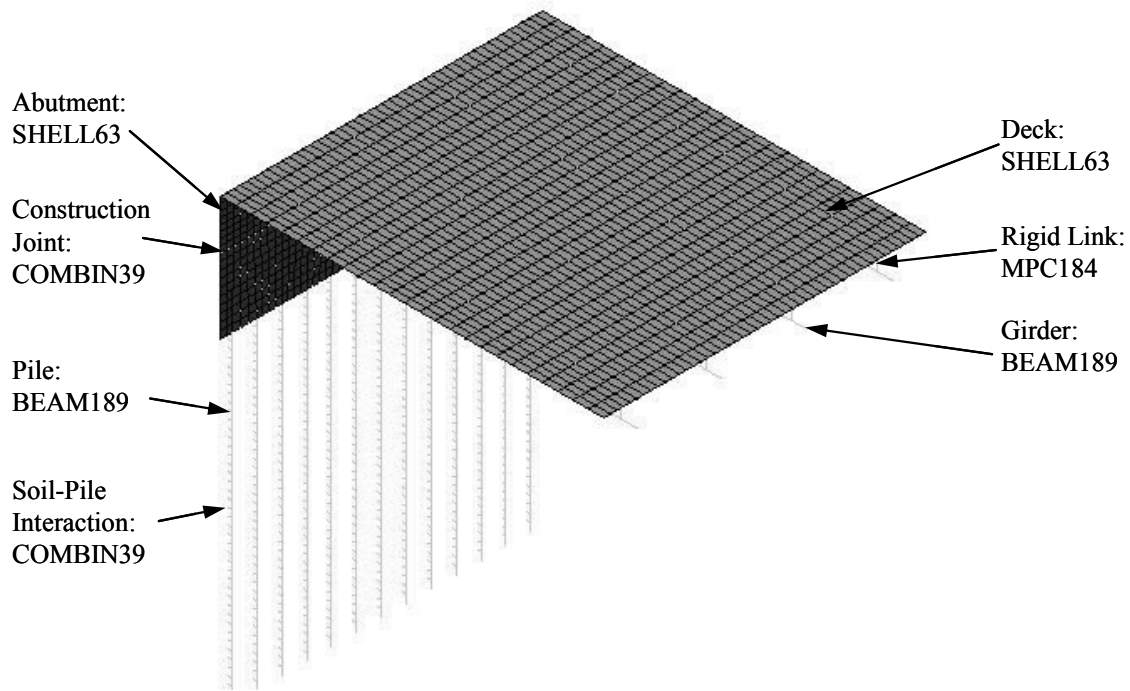


Figure 8.26: Example 1, 3D Schematic ANSYS Bridge Model – Isometric View.

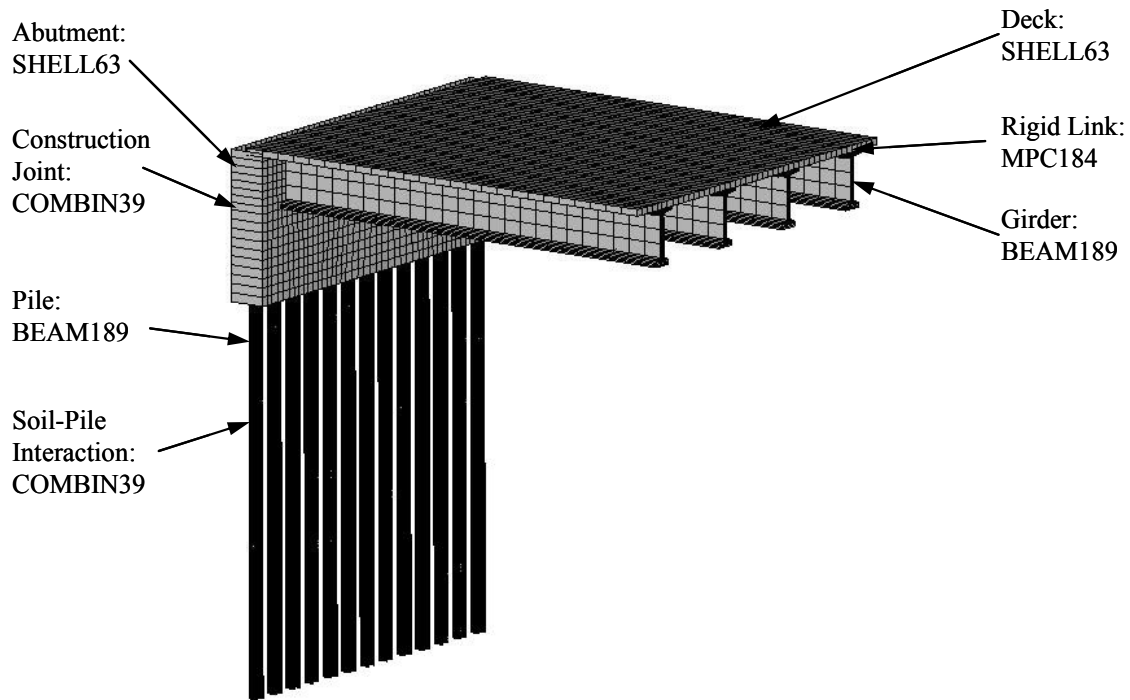


Figure 8.27: Example 1, Solid 3D Bridge Model – Isometric View

Bridge load includes the superstructure temperature fluctuation, temperature gradient, and backfill pressure. As with the 2D simulation, the thermal loading model developed on the basis of actual measurements is utilized for the 3D model. However, a time-history analysis with the 3D numerical model is not practical due to unmanageable computing time and memory demand; therefore, a static analysis under design level thermal loads is performed.

8.1.3.1 Bridge Components

Each bridge component and its material and geometric definition are described in detail in the following sections to permit development of future models for other IABs. The discussion includes girder and deck, abutment/backwall, construction joint, piles, and soil springs and analysis results.

8.1.3.1.1 Girder and Deck

The bridge girders are modeled using the ANSYS 3D beam element BEAM189 based on the BT72 girder cross section in Figure 8.28. ANSYS computes all geometric properties of the cross-section as shown in the figure. The 9-inch concrete deck is modeled using the solid element SHELL63 that has both bending and membrane capabilities. Girder and deck 28-day concrete strengths are specified as 8,000 psi and 4,000 psi, respectively. The elastic modulus of concrete is computed using the widely accepted AASHTO and ACI formula:

$$E_c = 33000w_c^{1.5}\sqrt{f'_c} \quad (8.1)$$

resulting in E_c for girders and deck equal to 5,150 ksi and 3,640 ksi.

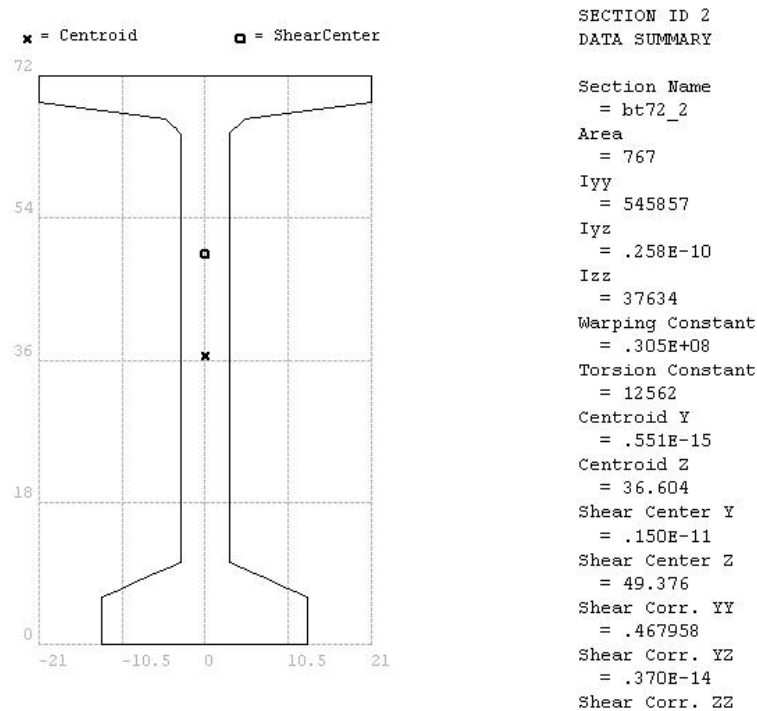


Figure 8.28: Cross Section of BT72 Girder (units are inches).

Based on AASHTO LRFD recommendations, the thermal expansion coefficient for deck concrete and girder concrete is assigned a value of 6.0E-6 in/in/°F.

To model the bridge girder and deck composite section, ANSYS rigid link MPC184 elements are included to connect the girder and deck. This is necessary because the geometric center of the slab and the girder are offset in the model, requiring a connection that enforces compatible displacements, three translational and three rotational. Details of the rigid link connection are presented in Figure 8.29. Each girder element and deck element is located at its respective geometric center, as shown in the figure. The rigid link, which is a multi-point constraint element, connects the girder and deck at 2-ft intervals, forcing displacement compatibility and, therefore, composite behavior.

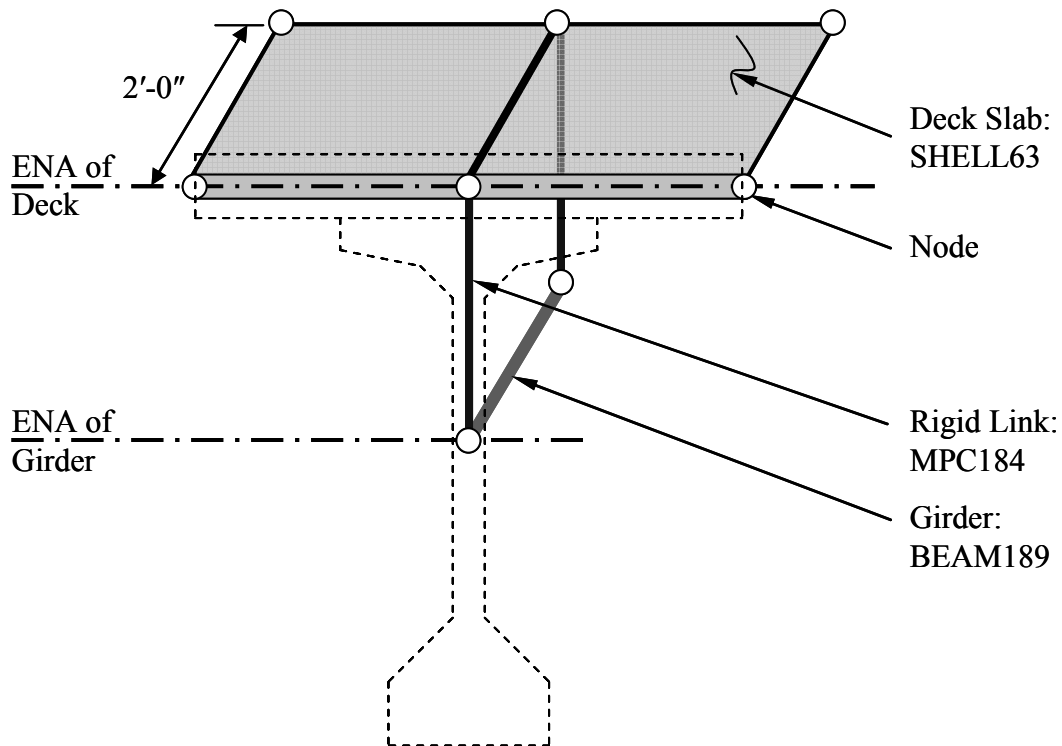


Figure 8.29: Girder and Deck Slab Connection

8.1.3.1.2 Abutment/Backwall

Both the abutment (or pile cap) and back-wall (or end diaphragm) are modeled using ANSYS solid element SHELL63. The full height of the abutment and back-wall are

modeled with the SHELL63 element located at the abutment centerline. Each SHELL 63 element is meshed at 1 ft in both directions to increase accuracy and to facilitate connections of abutment elements to back-wall, girder, and deck elements. The model element assembly of the abutment and back-wall is shown in Figure 8.30, viewed from the backfill side.

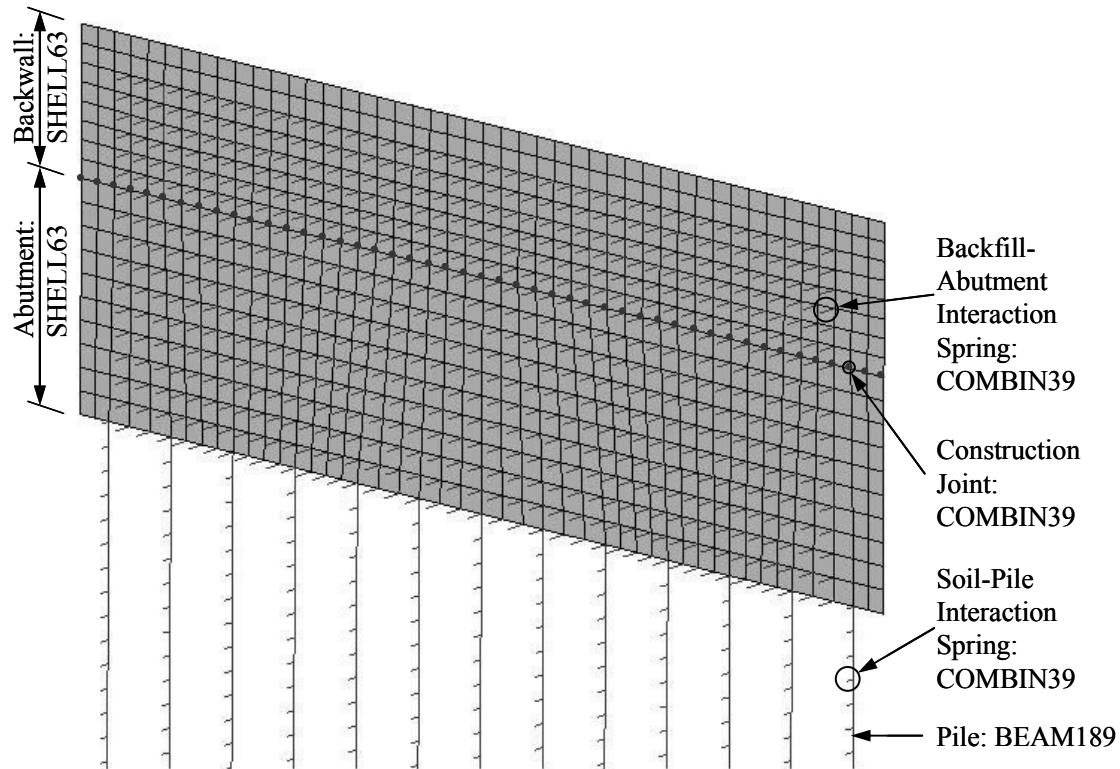


Figure 8.30: Example 1 3D Abutment and Back-wall – Viewed from Backfill

Normally higher-strength concrete is used for the back-wall concrete as compared to abutment concrete because the back-wall is placed with the deck. Example 1 bridge specifications are for 28-day compressive strength concrete equal to 4,000 psi and 3,000 psi at the back-wall and abutment, respectively, resulting in computed elastic moduli for the back-wall equal to 3,640 ksi and for abutment equal to 3,160 ksi.

Two nodes (separate but coincident) are placed at the construction joint between the back-wall and the abutment and are connected by the ANSYS joint element COMBIN39. The properties of this joint element are discussed in the following section.

8.1.3.1.3 Construction Joints

Rotational stiffness of the back-wall to abutment joint is modeled using the ANSYS COMBIN39 element, as presented in Section 5.2.4 of this report. All translations and rotations except z-axis rotation are coupled where rotation is defined by COMBIN39. A graphical illustration of the construction joint modeling, showing all nodes and elements, is presented in Figure 8.31. The computed construction joint rotational stiffness is based on the PennDOT standard detail BD-667 that specifies #5 “U” reinforcing bars at 9 inches. The imbalance of reinforcement between the backfill face and the front face is also considered in the definition of the joint element. For the expansion case, moment-rotation properties are computed:

For backfill side, rebar area is:

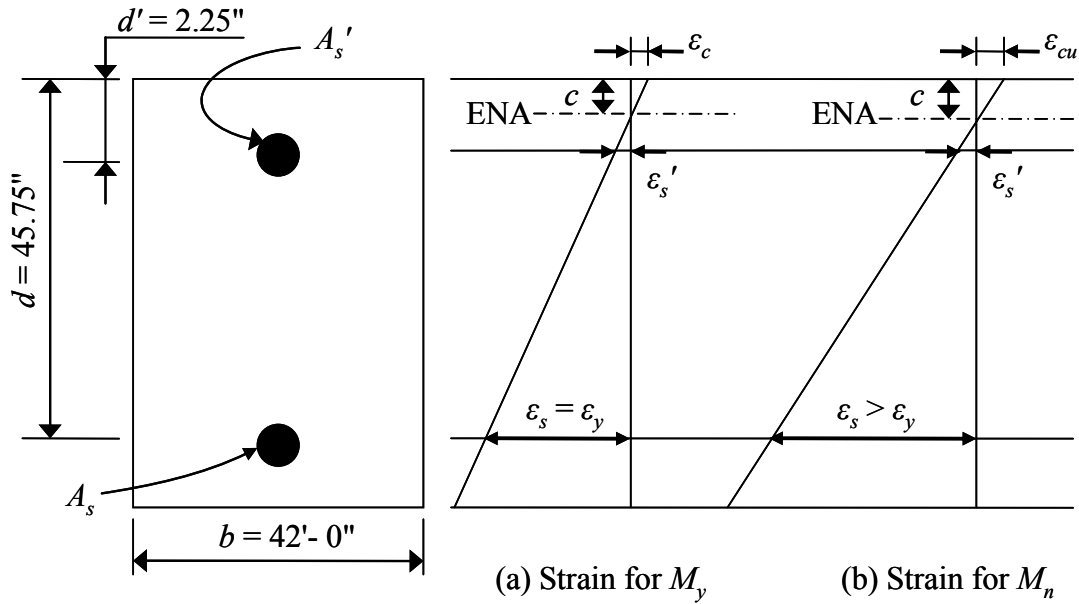
$$\begin{aligned}
 A_s &= (\text{\#5 rebar area}) \times (\text{number of rebars}) \\
 &= (\text{\#5 rebar area}) \frac{(\text{abutment width})}{(\text{rebar spacing})} = (0.31 \text{ in}^2) \frac{42'}{9''} \\
 &= (0.31 \text{ in}^2) \times (56 \text{ rebars}) \\
 &= 17.36 \text{ in}^2
 \end{aligned}$$

For front face side, rebar area is:

$$A_s' = (\text{\#5 rebar area})(\text{number of rebars})$$

$$\begin{aligned}
&= (\#5 \text{ rebar area}) \frac{(\text{abutment width}) - (\text{number of girders})(\text{girder width})}{(\text{rebar spacing})} \\
&= (0.31 \text{ in}^2) \frac{(42') - (4)(26'')}{9''} \\
&= (0.31 \text{ in}^2)(45 \text{ rebars}) \\
&= 13.95 \text{ in}^2
\end{aligned}$$

Based on the specified abutment reinforcing, two bending capacities of (1) yielding moment (M_y) and (2) ultimate moment (M_n) are evaluated and strain compatibility is presented in Figure 8.31.



d = distance from the extreme fiber to the centroid of tension reinforcement
 d' = distance from the extreme fiber to the centroid of compression reinforcement
 A_s = tension reinforcement area
 A_s' = compression reinforcement area
 b = beam width
 ϵ_c = strain in concrete at the extreme compressive fiber corresponding stress f_c
 ϵ_{cu} = ultimate concrete compression strain (= 0.003) corresponding stress f_c'
 ϵ_s = strain in tension reinforcement corresponding stress f_s
 ϵ_s' = strain in compression reinforcement corresponding stress f_s'
 ϵ_y = yielding strain of steel rebars (= 0.00207)

Figure 8.31: Strains in Doubly Reinforced Beam

The distance between the ENA and the extreme compressive fiber, c , for yielding capacity M_y is computed as follows:

From strain compatibility in Figure 8.31, tensile forces, T , are:

$$T = A_s f_y + A_s' f_s' = A_s f_y + A_s' E_s \varepsilon_s' = A_s f_y + A_s' E_s \left(\frac{\varepsilon_y (d' - c)}{(d - c)} \right)$$

$$= (17.36 \text{ in}^2)(60 \text{ ksi}) + (13.95 \text{ in}^2)(29000 \text{ ksi}) \left(\frac{0.00207(2.25 \text{ in} - c)}{45.75 \text{ in} - c} \right)$$

Similarly, compressive force, C , is:

$$C = \frac{1}{2} f_c c b = \frac{1}{2} \left(\frac{c}{d - c} f_y \right) b = \frac{1}{2} \left(\frac{c}{45.75 \text{ in} - c} (60 \text{ ksi}) \right) (42 \text{ ft})$$

From $C = T$,

$$c = 1.75 \text{ inches and } \varepsilon_c = c \frac{\varepsilon_y}{d - c} = 0.000082 < \varepsilon_{cu} = 0.003.$$

Thus, $M_y = A_s f_y (d - c) + A_s' f_s' (d' - c) = \underline{550,000 \text{ ft-kips}}$

Curvature (ϕ) is computed as:

$$\phi = \frac{\varepsilon_c}{c} = 0.000047$$

Based on half the minimum development length, l_d , rotation (θ) is computed as:

$$\theta = \phi \cdot l_d = (0.000047)(8 \text{ inches}) = \underline{0.00038 \text{ radians}}$$

For the nominal moment capacity, M_n , ultimate concrete strain (ε_{cu}) is used in the calculation:

$$T = A_s f_y + A_s' f_s' = A_s f_y + A_s' E_s \varepsilon_s' = A_s f_y + A_s' E_s \left(\frac{\varepsilon_{cu} (d' - c)}{c} \right)$$

$$= (17.36 \text{ in}^2)(60 \text{ ksi}) + (13.95 \text{ in}^2)(29000 \text{ ksi}) \left(\frac{0.003(2.25 \text{ in} - c)}{c} \right)$$

Similarly, the compressive force, C , is:

$$C = 0.85 f'_c b (\beta_1 c) = 0.85(3 \text{ ksi})(42 \text{ ft})(0.85 \times c)$$

From $C = T$,

$$c = 1.50 \text{ inches and } \varepsilon_c = \varepsilon_{cu} = 0.003.$$

$$\text{Thus, } M_n = A_s f_y (d - c) + A'_s f'_s (d' - c) = \underline{558,000 \text{ ft-kips}}$$

Curvature (ϕ) is computed as:

$$\phi = \frac{\varepsilon_c}{c} = 0.00199$$

Based on half the minimum development length, l_d , rotation (θ) is computed as:

$$\theta = \phi \cdot l_d = (0.00199)(8 \text{ inches}) = \underline{0.0159 \text{ radian}}$$

For the bridge contraction case, a similar computation can be performed exchanging A_s and A'_s . The moment-rotation curve in Figure 8.32 is obtained.

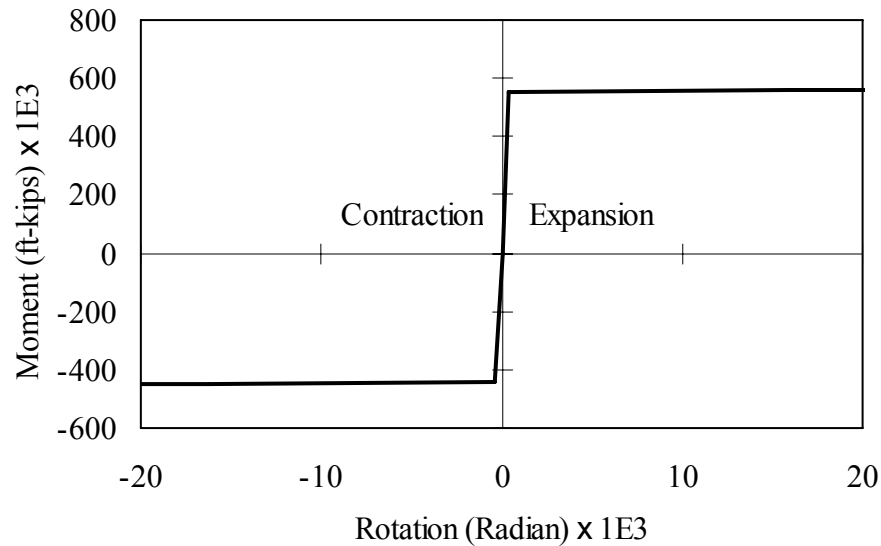


Figure 8.32: Moment-Rotation Curve

An average transverse distance (z-axis direction in Figure 8.33) between two adjacent nodes along the construction joint is computed. The foregoing total doubly-reinforced moment-to-rotation property of the construction joint is evenly distributed at each node pair based on the computed average distance.

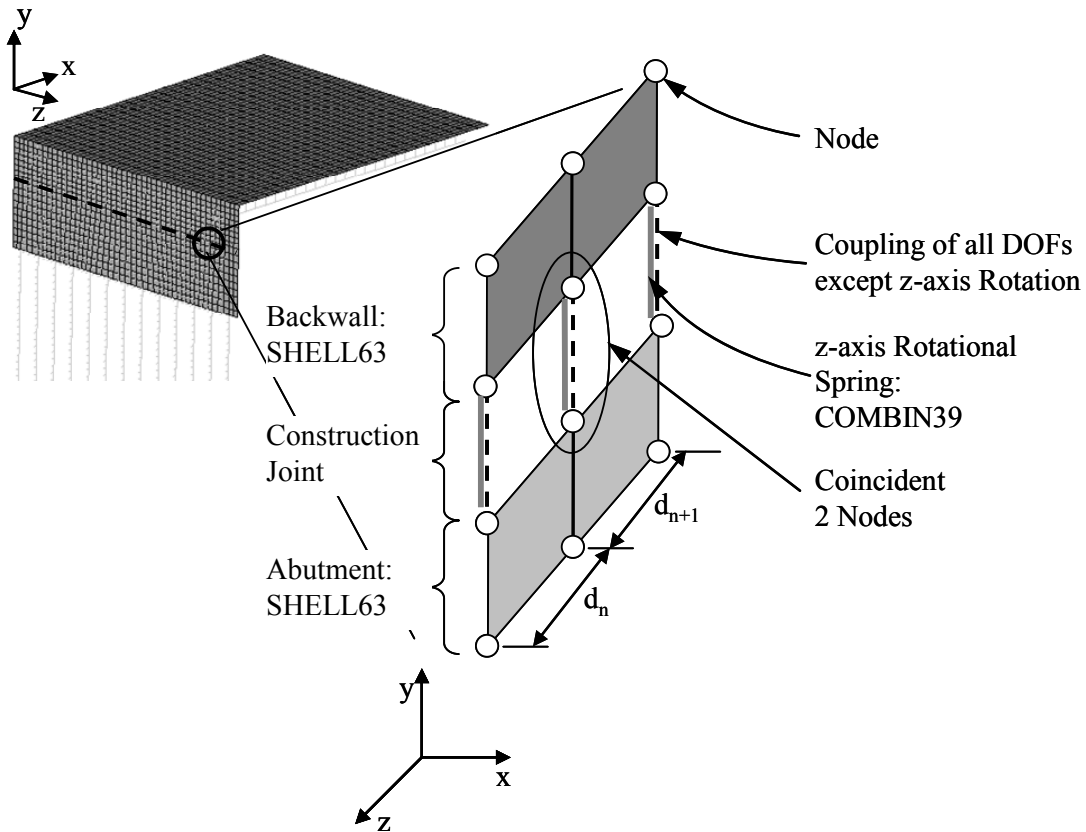


Figure 8.33: Example 1 Abutment to Back-wall Construction Joint Modeling
(Note: All nodes are coincident at construction joints)

8.1.3.1.4 Pile Foundations

Weak axis oriented steel HP12×74 piles are modeled using ANSYS beam elements BEAM189 and soil-pile interaction is modeled using nonlinear spring elements COMBIN39. For beam elements, the pile section and computed properties provided in Figure 8.34 are used in the example 1, 3D model.

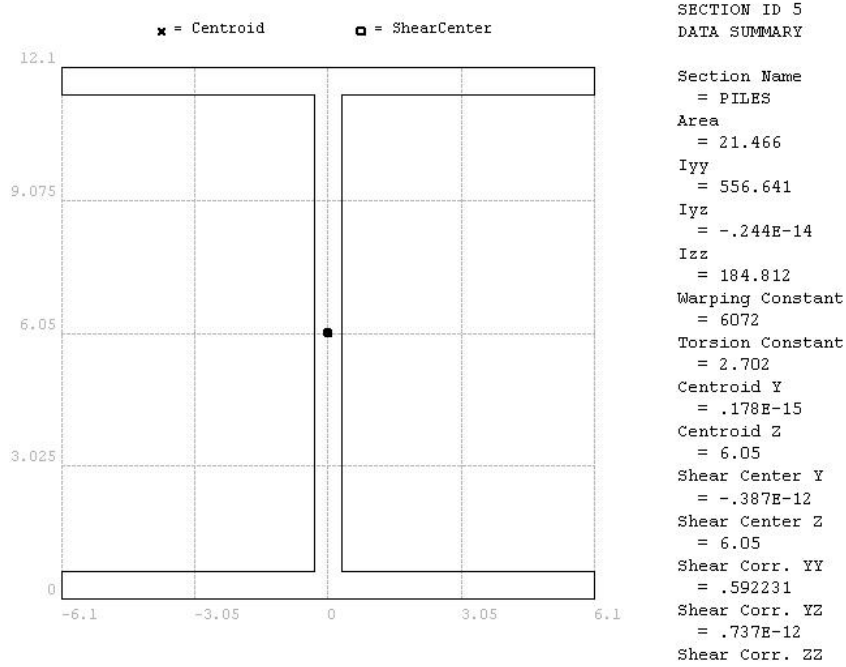


Figure 8.34: HP12×74 Foundation Pile Section

A total of thirteen HP12×74 piles by 30 ft long are used in this example 1, 3D model, as presented in Figure 8.34. The specified soil unit weight, $\gamma = 121$ pcf, undrained shear strength (c) = 17.5 psi, and $\epsilon_{50} = 0.008$. The soil-pile interaction is represented by a Winkler spring using ANSYS COMBIN39 elements developed on the basis of p - y curves. The same p - y curve equations in Equations 5.3 and 5.4 are used to generate force-displacement properties at each depth, as shown in Figure 8.35:

$$p = 0.5 p_u \left(\frac{y}{y_{50}} \right)^{1/4} \quad (5.3)$$

$$p_u = \min \left\{ p_{uf} = 9cD, \quad p_{uw} = \left(3 + \frac{\gamma'}{c} X + \frac{J}{D} X \right) cD \right\} \quad (5.4)$$

For this 3D example, a p - y curve at each depth at a 1-ft increment is computed.

Alternatively, commercial programs such as COM624P and Lpile can directly generate p -

y curves at a wide range of soil conditions and depths. The COMBIN39 springs are distributed along the full depth of the pile, spaced at 1'-0". The spring element lateral force versus lateral displacement properties at a given depth include the tributary area (1'-0" tributary depth \times pile effective diameter $b_f = 12.1"$) (see Figure 8.35) of the spring at each location.

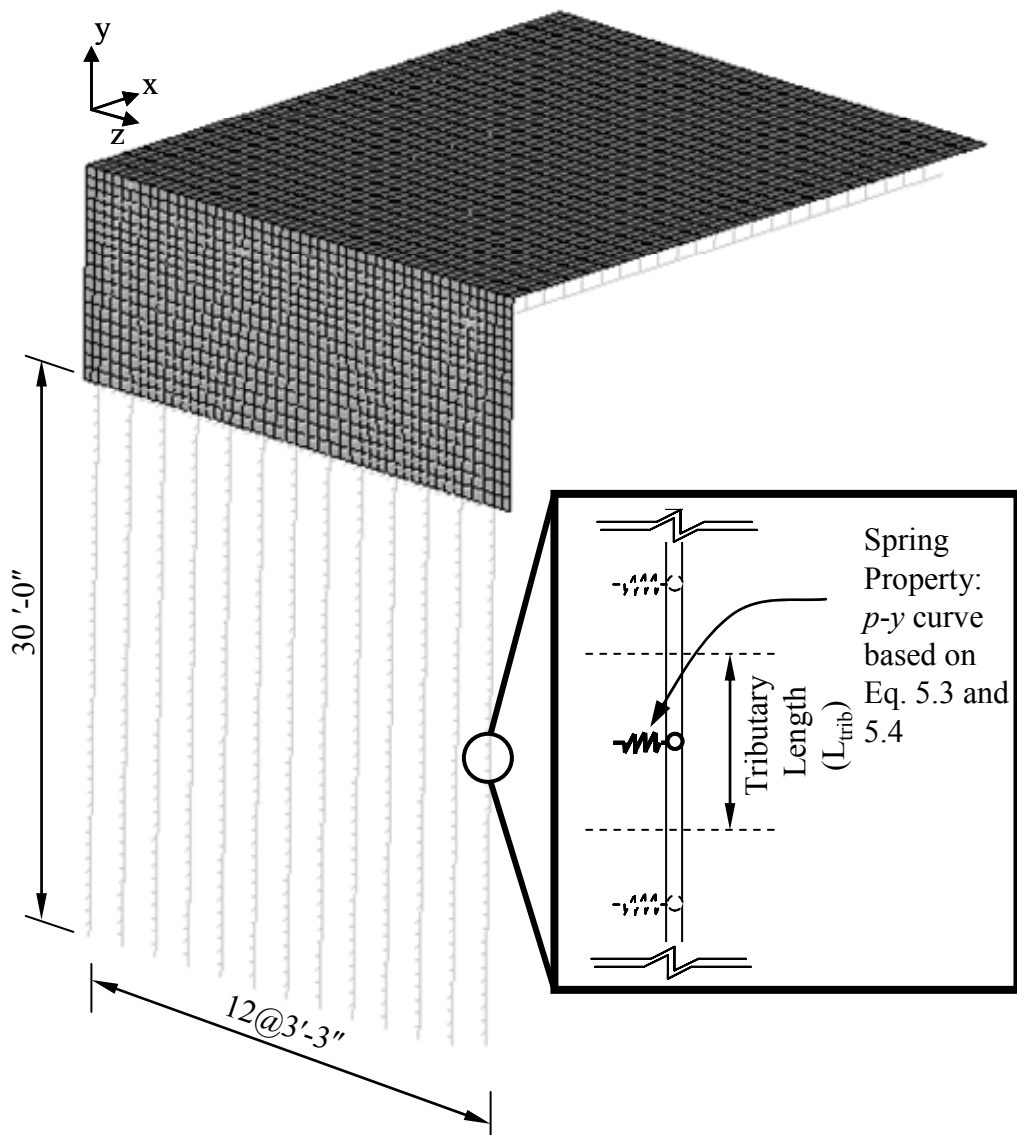


Figure 8.35: Foundation Pile Section Soil Spring Definition.

8.1.3.1.5 Miscellaneous Components

The mid-span bridge diaphragm is coincident with the bridge transverse axis of symmetry and is not explicitly modeled. A boundary condition in a single span bridge is applied at the bridge symmetry centerline. At the transverse axis of symmetry the x (longitudinal) and z (transverse) translations and y (in deck plane twisting) and z (girder strong axis bending) rotations are restrained. Piles are driven into bedrock and vertical translation is restraint at the pile tips. To expedite numerical computation convergence, z-axis translation is provided from pile tip to the characteristic length, l_c .

$$l_c = \sqrt[4]{\frac{4E_p I_p}{K}} \quad (7.1)$$

$$l_c = \sqrt[4]{\frac{4(29000 \text{ ksi})(186 \text{ in}^4)}{1000 \text{ psi}}} = 68 \text{ inches} \approx 6 \text{ ft}$$

If pile head displacements in the z direction are expected, the same p - y curve description in Section 8.1.3.1.4 of this report should be employed.

8.1.3.2 Loads

The loads applied in the example 1, 3D model include superstructure temperature load, temperature gradient, backfill pressure and time-dependent loads. Each load case is described in the subsequent sections.

8.1.3.2.1 Temperature Load

The superstructure thermal load definition for this example is taken from AASHTO LRFD (2007): 0°F to 120°F for steel and 10°F to 80°F for concrete. PennDOT DM-4 Appendix 1.2.7.4 (2007) describes extreme temperature loads for concrete bridges as an

80°F temperature rise or fall ranging 160°F. Monitoring conducted under the present study revealed a temperature rise or fall equal to 80°F is very conservative. Based on the example procedure described in *AASHTO Guide Specifications: Thermal Effects in Concrete Bridge Superstructures* (1989), the extreme temperature for bridge expansion and contraction is 30°F increase and 40°F decrease for the current example bridge. Therefore, a uniform temperature load equal to a 30°F increase and 40°F decrease is applied to the bridge girders and deck.

8.1.3.2.2 Temperature Gradient

Based on AASHTO multi-linear temperature gradient, an equivalent temperature gradient is computed. Equivalent temperature loads by Equation 5.14 and 5.15 are computed. AASHTO LRFD 3.12.3 provide temperature gradient model for Pennsylvania area as presented in Figure 8.36.

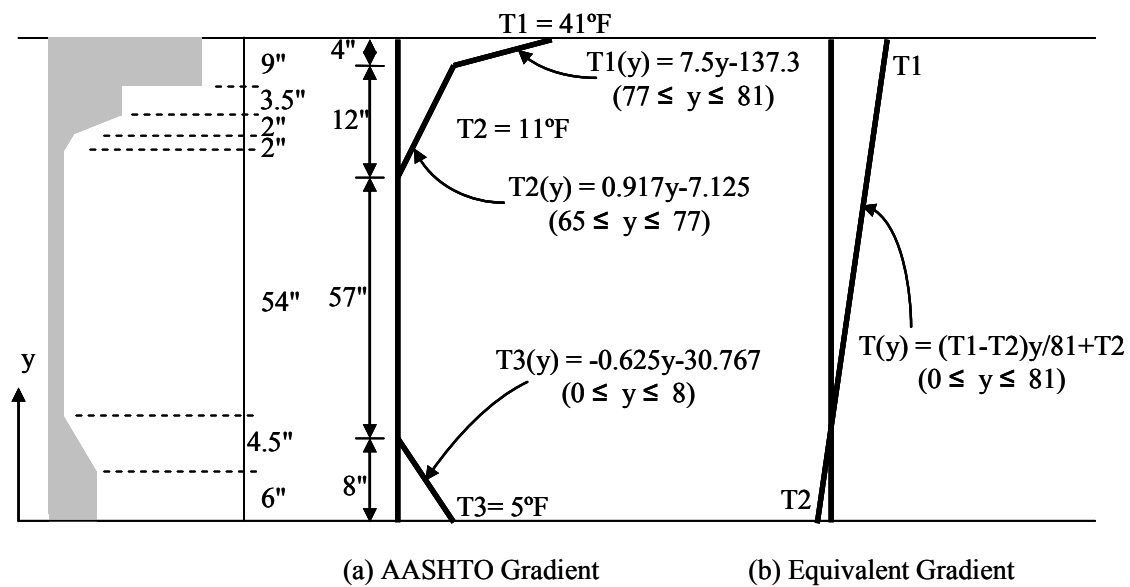


Figure 8.36: Temperature Gradient for BT72 Girder in Pennsylvania

Axial force can be obtained as:

$$\begin{aligned}
 P &= \int \sigma_t(y) b(y) dy = \int E \alpha T(y) b(y) dy \\
 &= \int_0^6 (5154 \text{ ksi}) (6.0 \times 10^{-6} / ^\circ \text{ F}) [-0.625y - 30.767] (26") dy \\
 &+ \int_6^8 (5154 \text{ ksi}) (6.0 \times 10^{-6} / ^\circ \text{ F}) [-0.625y - 30.767] (21.56") dy \\
 &+ \int_{65}^{66.5} (5154 \text{ ksi}) (6.0 \times 10^{-6} / ^\circ \text{ F}) [0.917y - 7.125] (13") dy \\
 &+ \int_{66.5}^{68.5} (5154 \text{ ksi}) (6.0 \times 10^{-6} / ^\circ \text{ F}) [0.917y - 7.125] (29") dy \\
 &+ \int_{68.5}^{72} (5154 \text{ ksi}) (6.0 \times 10^{-6} / ^\circ \text{ F}) [0.917y - 7.125] (42") dy \\
 &+ \int_{72}^{77} (5154 \text{ ksi}) (6.0 \times 10^{-6} / ^\circ \text{ F}) [0.917y - 7.125] (91.22") dy \\
 &+ \int_{77}^{81} (5154 \text{ ksi}) (6.0 \times 10^{-6} / ^\circ \text{ F}) [7.5y - 137.291] (91.22") dy \\
 &= 415.7 \text{ kips}
 \end{aligned}$$

Similarly, moment can be obtained as:

$$\begin{aligned}
 M &= \int \sigma_t(y) b(y) y dy = \int E \alpha T(y) b(y) y dy \\
 &= \int_0^6 (5154 \text{ ksi}) (6.0 \times 10^{-6} / ^\circ \text{ F}) [-0.625y - 30.767] (26") y dy \\
 &+ \int_6^8 (5154 \text{ ksi}) (6.0 \times 10^{-6} / ^\circ \text{ F}) [-0.625y - 30.767] (21.56") y dy \\
 &+ \int_{65}^{66.5} (5154 \text{ ksi}) (6.0 \times 10^{-6} / ^\circ \text{ F}) [0.917y - 7.125] (13") y dy \\
 &+ \int_{66.5}^{68.5} (5154 \text{ ksi}) (6.0 \times 10^{-6} / ^\circ \text{ F}) [0.917y - 7.125] (29") y dy \\
 &+ \int_{68.5}^{72} (5154 \text{ ksi}) (6.0 \times 10^{-6} / ^\circ \text{ F}) [0.917y - 7.125] (42") y dy
 \end{aligned}$$

$$\begin{aligned}
& + \int_{72}^{77} (5154 \text{ ksi}) (6.0 \times 10^{-6} / ^\circ \text{ F}) [0.917y - 7.125] (91.22'') y dy \\
& + \int_{77}^{81} (5154 \text{ ksi}) (6.0 \times 10^{-6} / ^\circ \text{ F}) [7.5y - 137.291] (91.22'') y dy \\
& = 612.4 \text{ ft-kips}
\end{aligned}$$

Based on the obtained axial force and moment, an equation is built:

$$\begin{aligned}
P_{eq} &= \int \sigma_t(y) b(y) dy = \int E \alpha T(y) b(y) dy \\
&= \int_0^6 (5154 \text{ ksi}) (6.0 \times 10^{-6} / ^\circ \text{ F}) \left[\frac{T1 - T2}{81} y + T2 \right] (26'') dy \\
&+ \int_6^{10.5} (5154 \text{ ksi}) (6.0 \times 10^{-6} / ^\circ \text{ F}) \left[\frac{T1 - T2}{81} y + T2 \right] (16'') dy \\
&+ \int_{10.5}^{64.5} (5154 \text{ ksi}) (6.0 \times 10^{-6} / ^\circ \text{ F}) \left[\frac{T1 - T2}{81} y + T2 \right] (6'') dy \\
&+ \int_{64.5}^{66.5} (5154 \text{ ksi}) (6.0 \times 10^{-6} / ^\circ \text{ F}) \left[\frac{T1 - T2}{81} y + T2 \right] (8'') dy \\
&+ \int_{66.5}^{68.5} (5154 \text{ ksi}) (6.0 \times 10^{-6} / ^\circ \text{ F}) \left[\frac{T1 - T2}{81} y + T2 \right] (26'') dy \\
&+ \int_{68.5}^{72} (5154 \text{ ksi}) (6.0 \times 10^{-6} / ^\circ \text{ F}) \left[\frac{T1 - T2}{81} y + T2 \right] (42'') dy \\
&+ \int_{72}^{81} (5154 \text{ ksi}) (6.0 \times 10^{-6} / ^\circ \text{ F}) \left[\frac{T1 - T2}{81} y + T2 \right] (91.22'') dy \\
M_{eq} &= \int \sigma_t(y) b(y) y dy = \int E \alpha T(y) b(y) y dy \\
&= \int_0^6 (5154 \text{ ksi}) (6.0 \times 10^{-6} / ^\circ \text{ F}) \left[\frac{T1 - T2}{81} y + T2 \right] (26'') y dy \\
&+ \int_6^{10.5} (5154 \text{ ksi}) (6.0 \times 10^{-6} / ^\circ \text{ F}) \left[\frac{T1 - T2}{81} y + T2 \right] (16'') y dy
\end{aligned}$$

$$\begin{aligned}
& + \int_{10.5}^{64.5} (5154 \text{ ksi}) (6.0 \times 10^{-6} / ^\circ \text{F}) \left[\frac{T1 - T2}{81} y + T2 \right] (6'') y dy \\
& + \int_{64.5}^{66.5} (5154 \text{ ksi}) (6.0 \times 10^{-6} / ^\circ \text{F}) \left[\frac{T1 - T2}{81} y + T2 \right] (8'') y dy \\
& + \int_{66.5}^{68.5} (5154 \text{ ksi}) (6.0 \times 10^{-6} / ^\circ \text{F}) \left[\frac{T1 - T2}{81} y + T2 \right] (26'') y dy \\
& + \int_{68.5}^{72} (5154 \text{ ksi}) (6.0 \times 10^{-6} / ^\circ \text{F}) \left[\frac{T1 - T2}{81} y + T2 \right] (42'') y dy \\
& + \int_{72}^{81} (5154 \text{ ksi}) (6.0 \times 10^{-6} / ^\circ \text{F}) \left[\frac{T1 - T2}{81} y + T2 \right] (91.22'') y dy
\end{aligned}$$

Now, let $P = P_{eq}$ and $M = M_{eq}$, and a trial and error procedure yields $T1 = 15.45^\circ\text{F}$ and $T2 = -0.45^\circ\text{F}$. Negative gradient is obtained by multiplying -0.3 for the positive temperature gradient in Figure 8.36.

For the AASHTO-PCI BT72 girder, the equivalent temperature at the top fiber of deck slab is 15.5°F , the temperature at the top fiber of girder is 13.7°F , and the temperature at the bottom fiber is -0.45°F . For negative temperature gradient, -4.6°F , -4.1°F and 0.13°F at the top fiber of deck slab, the top fiber of girder and bottom fiber of girder. The final positive and negative temperature gradient is presented in Figure 8.37. These temperature gradients are added to the previously discussed uniform temperature increase and decrease.

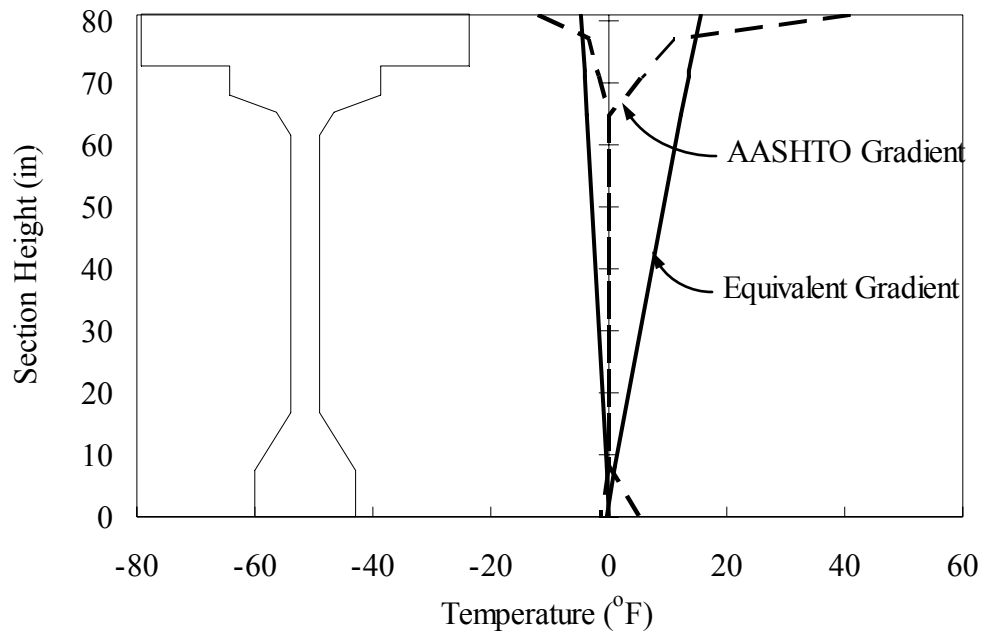


Figure 8.37: Temperature Gradient for BT72 Girder and Deck Slab

8.1.3.2.3 Backfill Pressure

Hydrostatic pressure behind the back-wall and abutment must be determined, accounting for the 1'-6" approach slab and 2'-7" wing-walls at both sides, as presented in Figure 8.38.

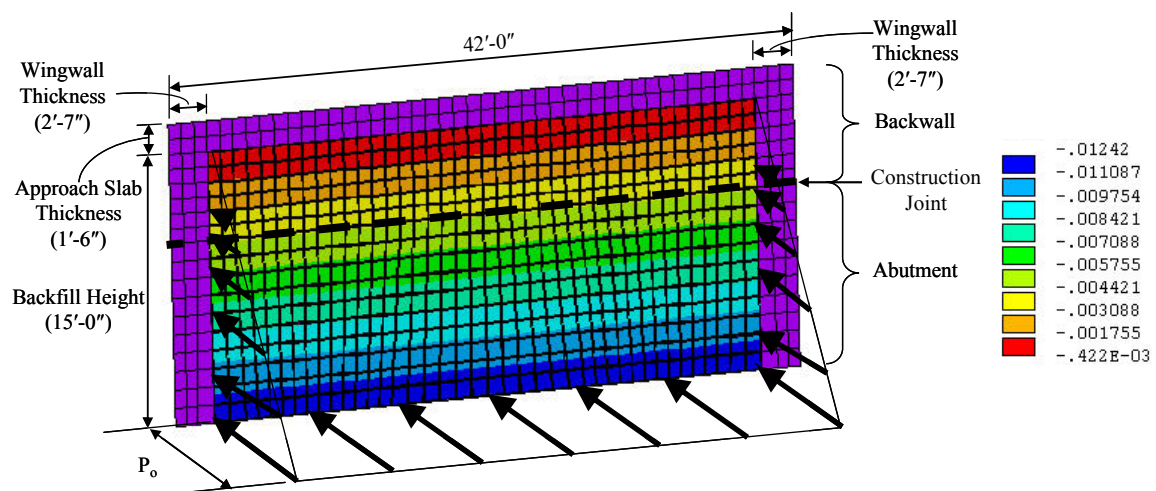


Figure 8.38: Backfill Pressure Contour in Example 1 3D Model

A triangular hydrostatic pressure and abutment-to-backfill interaction springs are clearly identified in Figures 8.39 and 8.40.

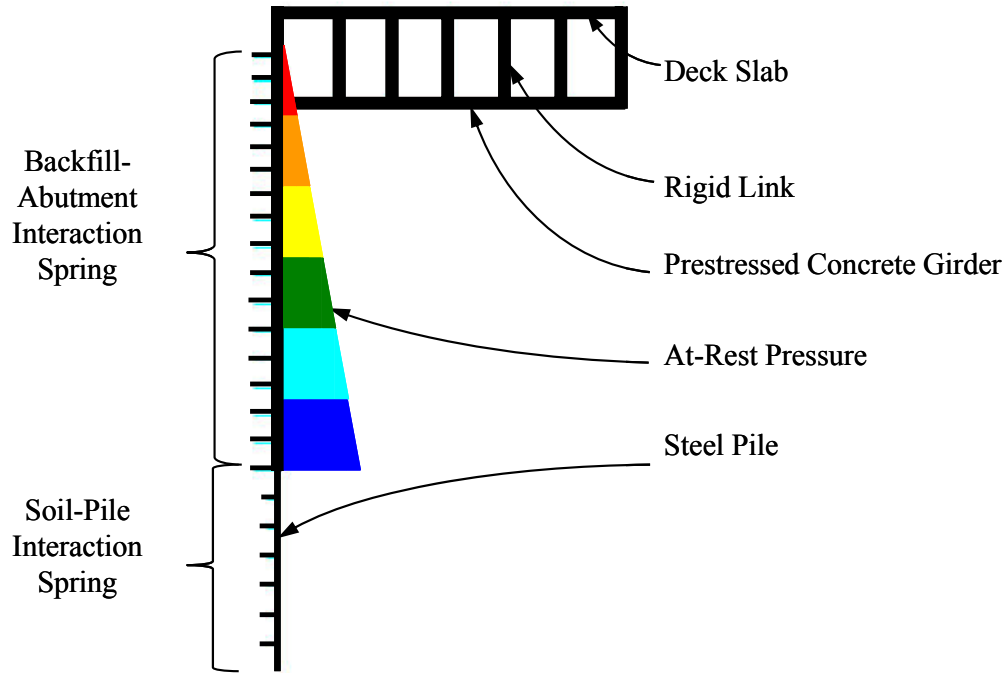


Figure 8.39: Example 1 3D Analysis Abutment Backfill Pressure

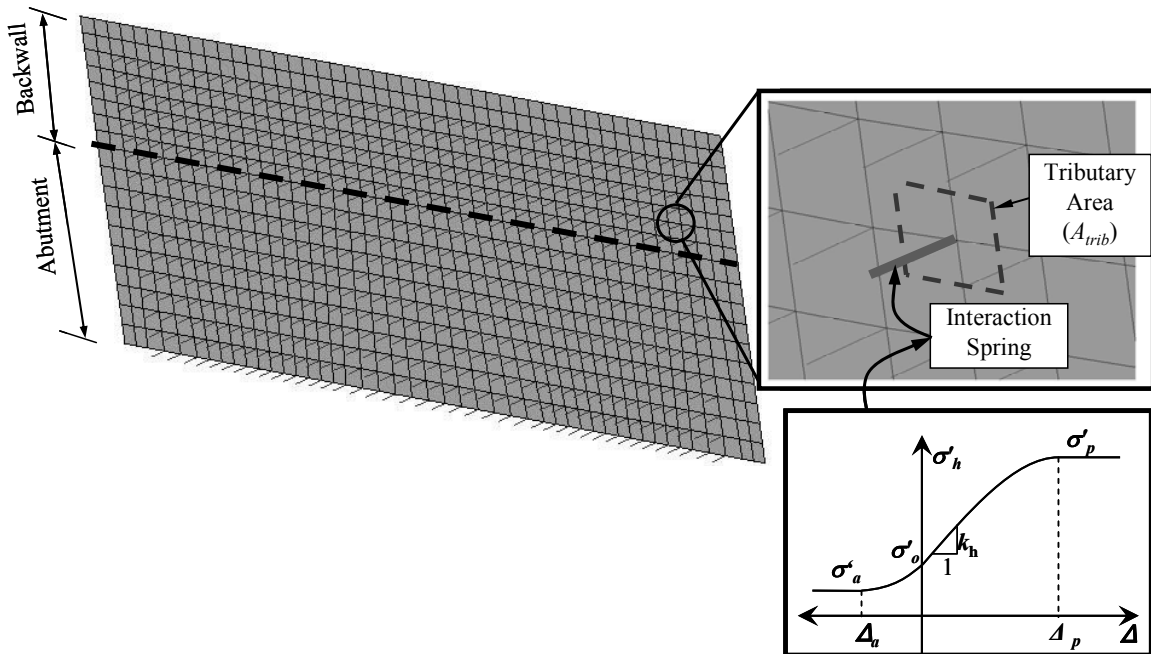


Figure 8.40: Example 1 3D Analysis Backfill Pressure Tributary Area for Spring

To determine the backfill pressure, each soil spring tributary area is computed as presented in Figure 8.40. At-rest pressure, active pressure, and passive pressure at each spring element location are computed as:

$$\begin{aligned}
 P_o &= K_o \gamma' z A_{trib} = \gamma' z A_{trib} \\
 P_a &= K_a \gamma' z A_{trib} = \frac{1 - \sin \phi_f}{1 + \sin \phi_f} \gamma' z A_{trib} \\
 P_p &= K_p \gamma' z A_{trib} = \frac{1 + \sin \phi_f}{1 - \sin \phi_f} \gamma' z A_{trib}
 \end{aligned} \tag{5.7}$$

where K_o , K_a and K_p are at-rest, active and passive coefficients, $\gamma' = 119$ pcf, A_{trib} = tributary area and $\phi_f = 34^\circ$. For each node location on the back-wall and abutment a different z and A_{trib} is computed. For example, at $z = 3$ ft and $A_{trib} = 1.0$ ft²:

$$\begin{aligned}
 P_o &= (119 \text{ pcf})(3 \text{ ft})(1 \text{ ft}^2) = 357 \text{ lbs} \\
 P_a &= K_a \gamma' z A_{trib} = \frac{1 - \sin \phi_f}{1 + \sin \phi_f} \gamma' z A_{trib} = \frac{1 - \sin 34^\circ}{1 + \sin 34^\circ} (119 \text{ pcf})(3 \text{ ft})(1.0 \text{ ft}^2) = 101 \text{ lbs} \\
 P_p &= K_p \gamma' z A_{trib} = \frac{1 + \sin \phi_f}{1 - \sin \phi_f} \gamma' z A_{trib} = \frac{1 + \sin 34^\circ}{1 - \sin 34^\circ} (119 \text{ pcf})(3 \text{ ft})(1.0 \text{ ft}^2) = 1260 \text{ lbs}
 \end{aligned}$$

The slope of the spring element response between P_a and P_p is computed from equation 5.1, discussed in Chapter 5 of this report:

$$k_h(z) = k_{ref} \left(\frac{z}{h_{ref}} \right)^{0.5} A_{trib} \tag{5.1}$$

where h_{ref} = reference depth and z = backfill depth. As discussed in Section 5.2.2, $k_{ref} = 0.044$ kci at 4 ft from the bottom of the abutment and is used for this example:

$$k_h(3 \text{ ft}) = (0.044 \text{ kci}) \left(\frac{3 \text{ ft}}{15 \text{ ft} - 4 \text{ ft}} \right)^{0.5} (144 \text{ inches}) = 3.31 \text{ kips/inch}$$

Displacements u_a and u_p corresponding to P_a and P_p are computed as:

$$u_a = \frac{101 \text{ lbs}}{3310 \text{ lbs/inch}} = 0.0305 \text{ inches}$$

$$u_p = \frac{1260 \text{ lbs}}{3310 \text{ lbs/inch}} = 0.381 \text{ inches}$$

Therefore, the example backfill-abutment interaction spring, defined generally in Figure 8.40, is presented in Figure 8.41.

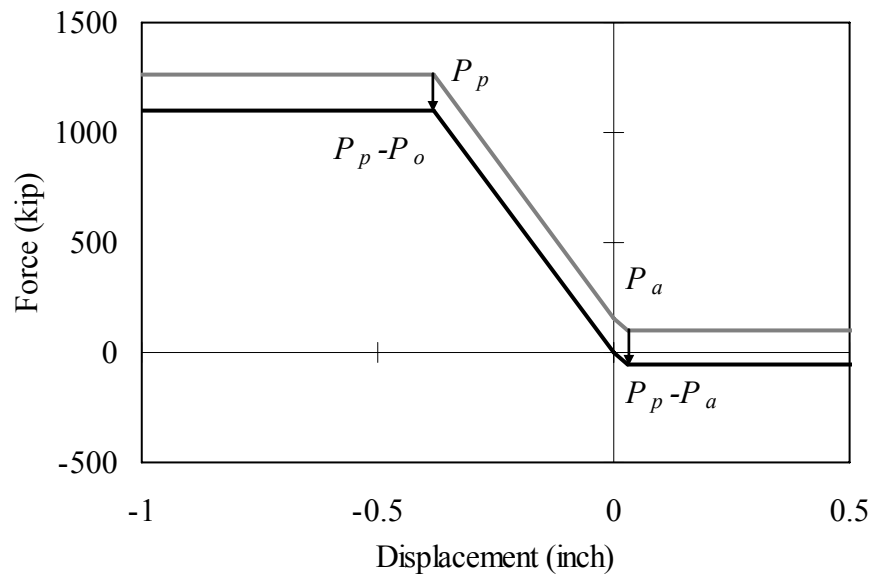


Figure 8.41: Backfill-Abutment Interaction Spring Property

8.1.3.2.4 Time-dependent Loads

The time-dependent effects of concrete creep and shrinkage result in bridge shortening; however, this effect is not included with thermal expansion. To determine the maximum bridge contraction and corresponding response, time-dependent effects are combined with thermal contraction, temperature gradient, and backfill pressure. For maximum expansion response, it is anticipated that the initial bridge expansion will occur prior to when significant creep and shrinkage have occurred. Time-dependent strains over

75 years are computed for the top fiber of the deck, top fiber of the girder and bottom fiber of the girder and applied for the maximum contraction response. The strains at each location are converted to temperature loads based on the thermal expansion coefficient. Uniform temperature load, temperature gradient, and time-dependent effects are then summed and applied to the girders and deck.

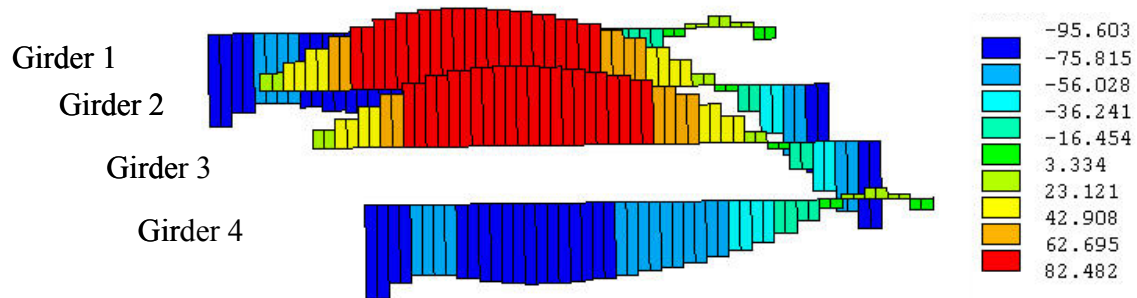
To accurately account for thermal loads and time-dependent effects, the girder and deck elements are meshed at 2 ft and time-dependent effects are computed at every node. Each element is assigned thermal loads from time-dependent strains.

8.1.3.3 Example 1: 3D Analysis Results

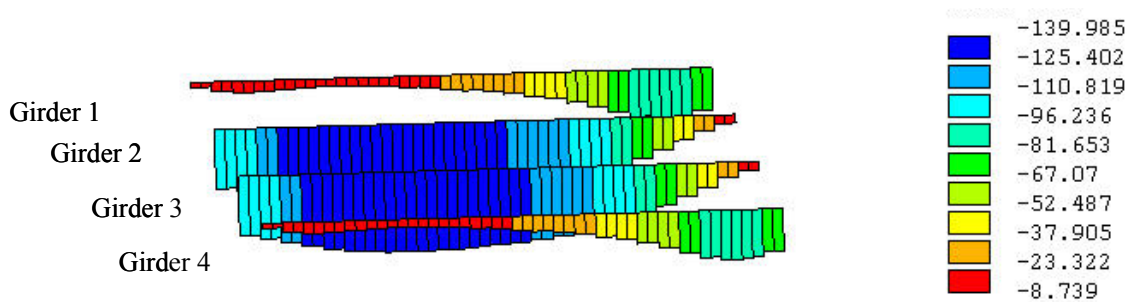
An extreme design static 3D analysis is demonstrated for the example 1 bridge. Although a time-history analysis is not performed in this example, 3D models are capable of performing a time-history analysis with a sinusoidal temperature fluctuation load. However, a 3D time-history analysis would require extensive and unmanageable computing time and storage; therefore, this analysis is not demonstrated here. The two loading cases of extreme design temperature are demonstrated based on AASHTO extreme temperature rise (+30°F) and fall (-40°F). To obtain the maximum contraction response, time-dependent effects are included with the thermal effects. For the expansion case, only thermal effects are considered. Example 1 girder axial force, girder bending moment, pile lateral force, pile moment, and pile head displacement are presented, using the analysis methods described in the body of this report.

8.1.3.3.1 Girder Axial Force

Girder axial forces predicted by a 3D extreme design temperature static analysis are presented in Figure 8.42 for both (a) bridge contraction; and (b) bridge expansion. Axial forces in each girder differ due to the larger interior girder abutment and deck tributary area and the retaining backfill force differences between interior girders and exterior girders. When the bridge contracts, tensile axial forces occur in the interior girders due to significant time-dependent effects. When the bridge expands, significant compressive axial forces develop in the interior girders due to the larger abutment and back-fill tributary area as compared to the exterior girders.



(a) Bridge Contraction (All units in kips)



(b) Bridge Expansion (All units in kips)

Figure 8.42: Example Bridge 1 3D Analysis Girder Axial Force Comparison

8.1.3.3.2 Girder Bending Moment

Girder bending moments predicted by a 3D extreme design temperature static analysis are presented in Figure 8.43 for both (a) bridge contraction and (b) bridge expansion. Girder moments differ between interior and exterior girders, again due to time-dependent effects and the difference in abutment and corresponding backfill forces. When the bridge contracts, significant positive and negative moments occur in the interior girders due to significant time-dependent effects and differences in tributary backfill forces. When the bridge expands, all four girders are subjected to similar bending moments; however, interior girders are subjected to higher moments due to the larger backfill forces.

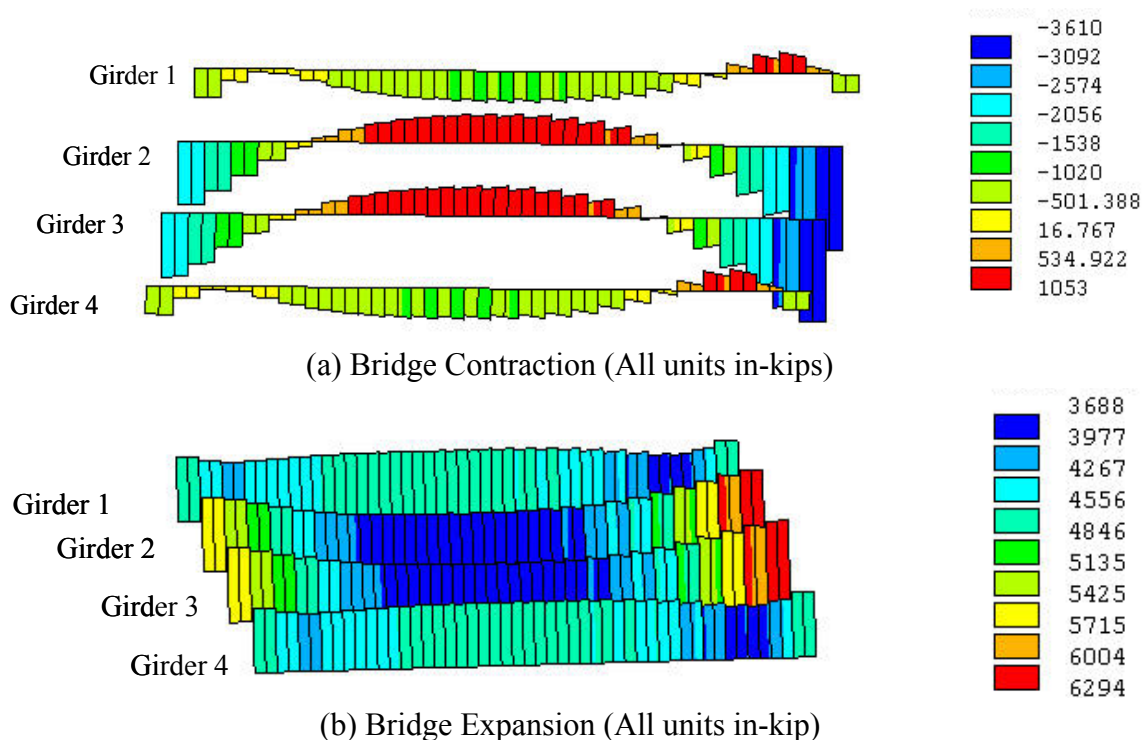
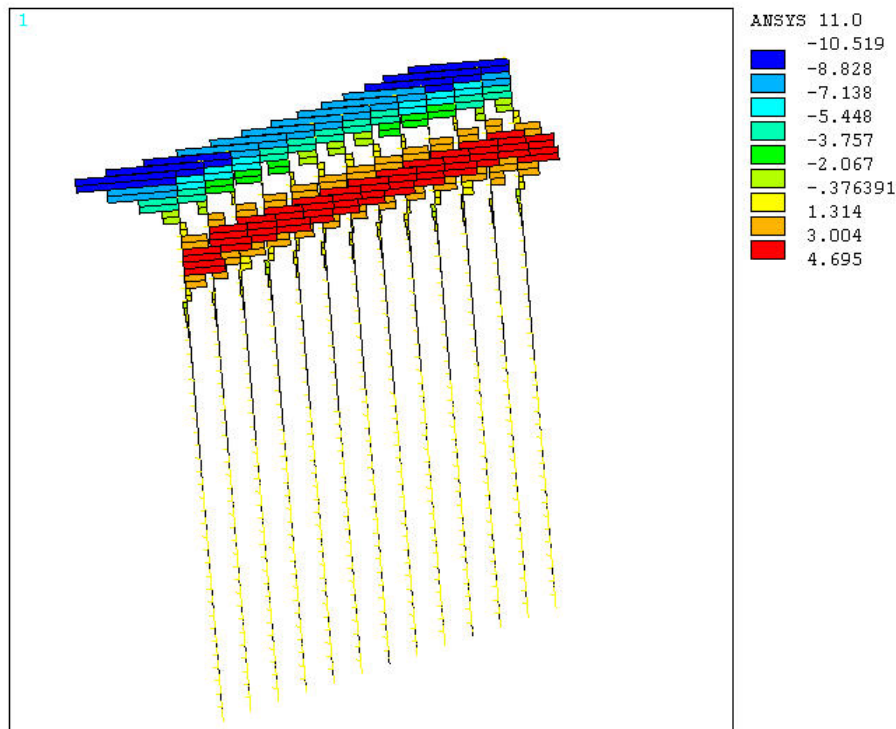


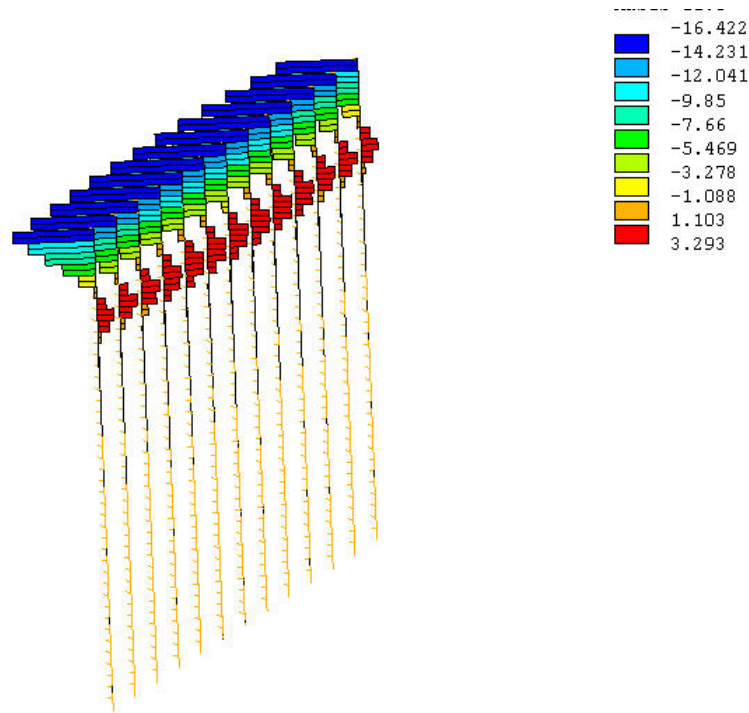
Figure 8.43: Example Bridge 1 3D Analysis Girder Bending Moment

8.1.3.3.3 Pile Lateral Force

The lateral forces on piles predicted by the 3D extreme design temperature static analysis are presented in Figure 8.44 for both (a) bridge contraction and (b) bridge expansion. Pile lateral forces vary with respect to pile depth; when the bridge contracts, exterior piles are subjected to larger lateral force compared to interior piles. This is a direct result of the smaller abutment and backfill tributary forces restraining the superstructure movement, resulting in larger forces at this location. Relative displacement and rotation in the exterior piles due to bridge contraction are larger than those of interior piles. All piles are predicted to experience larger lateral forces under expansion as compared to contraction.



(a) Bridge Contraction (All units in kip)

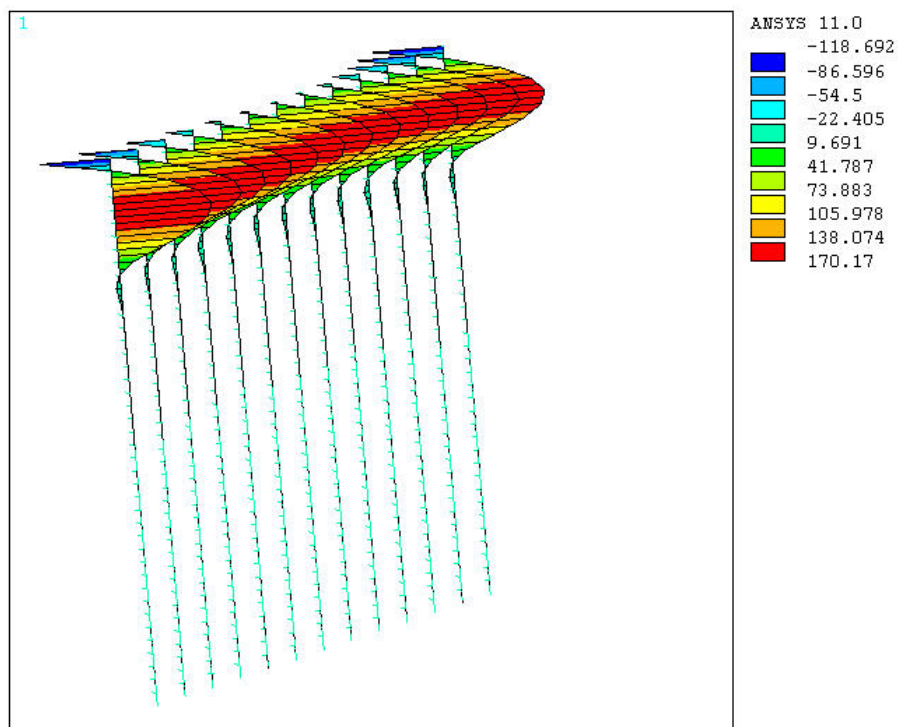


(b) Bridge Expansion (All units in kip)

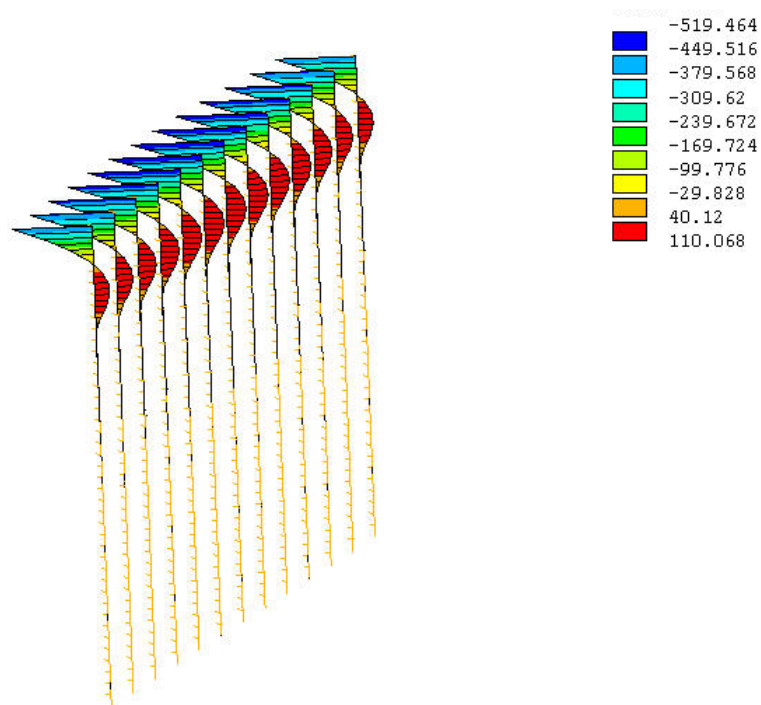
Figure 8.44: Example 1 3D Analysis Model Pile Lateral Force.

8.1.3.3.4 Pile Moment

The pile moments based on the 3D extreme design temperature static analysis are presented in Figure 8.45 for both (a) bridge contraction and (b) bridge expansion. Weak axis bending moments across all piles are very similar and vary with respect to vertical depth. Under superstructure contraction, exterior piles experience larger moments as compared to interior piles, again due to the larger restraint offered by the backfill at this location. Under superstructure expansion, significantly larger pile moments are predicted as compared to the contraction case.



(a) Bridge Contraction (All units in-kips)



(b) Bridge Expansion (All units in in-kip)

Figure 8.45: Example Bridge 1 Pile Moment by 3D Analysis

8.1.3.3.5 Pile Head Displacement

Pile head displacement predicted by the 3D extreme design temperature static analysis is presented in Figure 8.46 for superstructure contraction. Pile head displacements in all piles are very similar for this case. As expected, interior piles experience slightly larger displacements as compared to exterior piles.

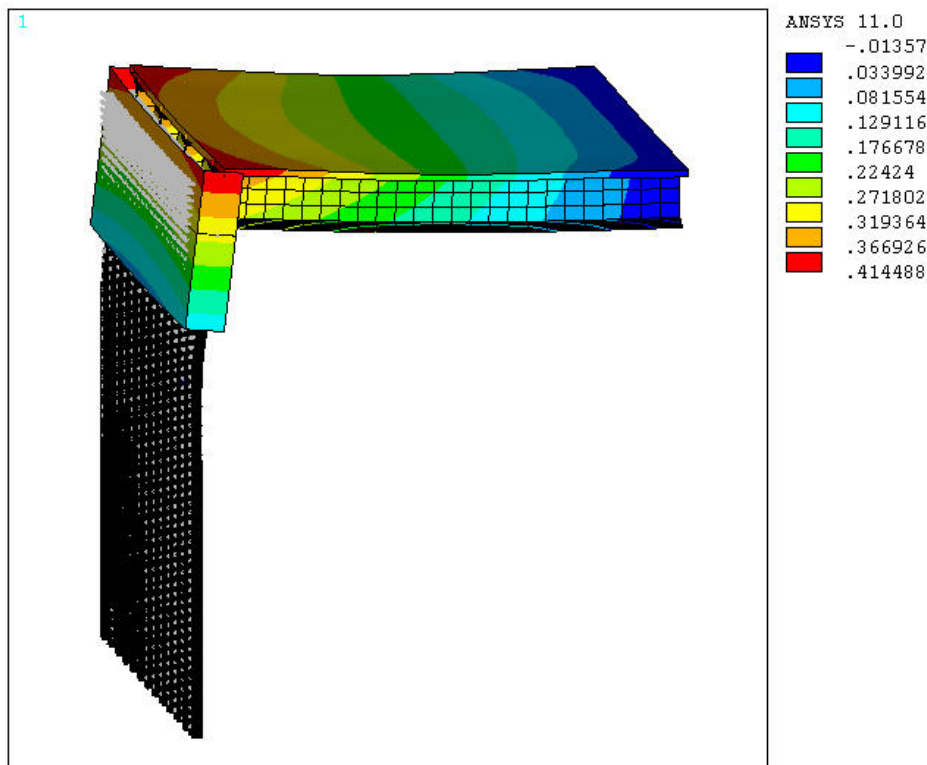


Figure 8.46: Example Bridge 1 Pile Head Displacement by 3D Analysis
(All units in inches)

8.1.4 Example 1 Analysis Results

The Example 1 bridge has been analyzed by the approximate method, the 2D extreme design temperature static analysis method, the 2D time-history analysis method, and the 3D extreme design temperature static analysis method. Results of these four analyses are compared in this section. The extracted results include: (1) girder axial force,

(2) girder bending moment, (3) pile lateral force, (4) pile moment, and (5) pile head displacement.

8.1.4.1 Girder Axial Force

Girder axial force results by approximate method (Approx.), 2D time-history analysis (2D-TH), 2D design analysis (2D-DA), and 3D design analysis (3D-DA) are presented in Figure 8.47. Girder compressive axial force predictions range from 15% to 28% lower as compared to the 3D-DA analysis results. The approximate method and both 2D analyses results report girder average axial force while the maximum compressive axial force from 3D-DA reports a single girder maximum value. When 3D-DA girder axial forces are averaged (see Figure 8.42), the predicted girder axial force is nearly identical to the other analysis results. Similarly, the girder tensile axial force from 3D-DA reports a positive axial force while the approximate method and both 2D analyses do not, due to the averaging effect of a 2D analysis.

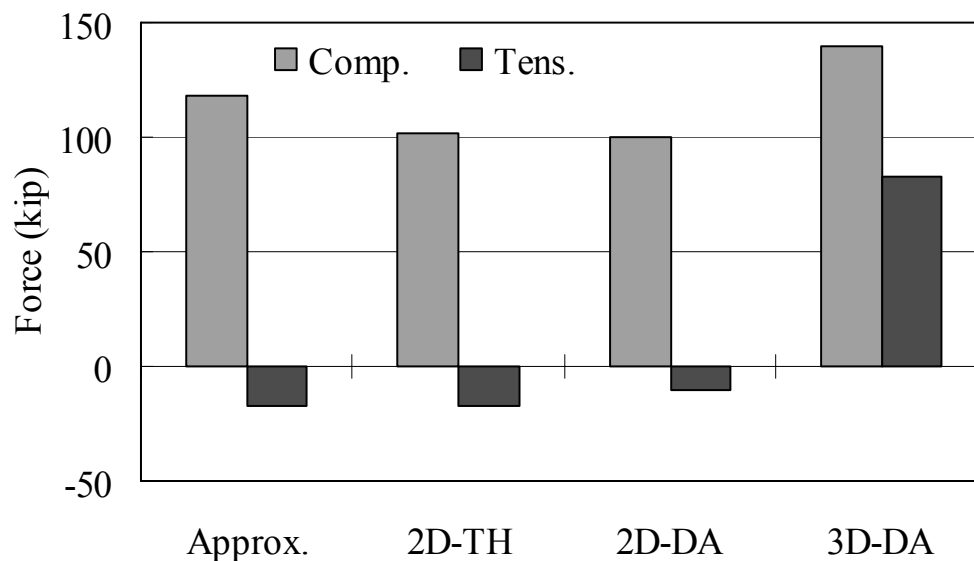


Figure 8.47: Example Bridge 1 Girder Axial Force Comparison

8.1.4.2 Girder Bending Moment

Girder bending moment results by Approx., 2D-TH, 2D-DA and 3D-DA are presented in Figure 8.48. Similar to the girder axial force results, 3D-DA reports larger positive and negative girder bending moments. The 3D-DA reports positive girder moments that are larger than the approximate analysis method and both 2D analyses by 83%, 77% and 63%, and 41%, 19% and 11% smaller negative moments. Again, this is due to the fact that the approximate analysis and the 2D analysis necessarily report average moments whereas the 3D reports the maximum moments in any of the four girders.

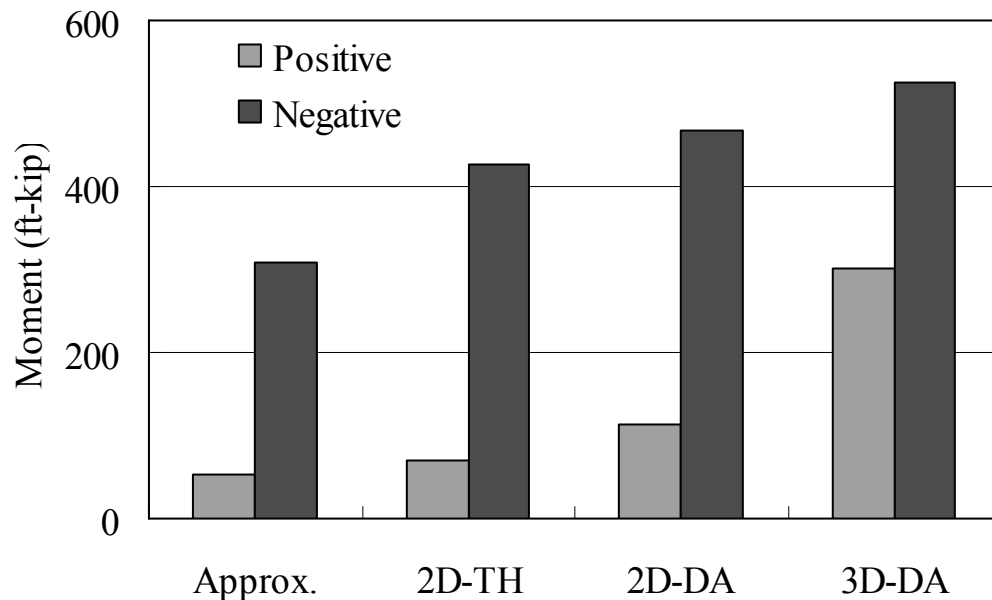


Figure 8.48: Example Bridge 1 Girder Bending Moment Comparison

8.1.4.3 Pile Lateral Force

Pile lateral force results obtained by the Approx., 2D-TH, 2D-DA and 3D-DA are presented in Figure 8.49. Compared to 3D-DA, the Approx., 2D-TH and 2D-DA report smaller lateral pile forces by 23%, 1.5% and 10%. For comparison purposes, the single pile lateral force, F_{pile} , due to a superstructure-free expansion, is computed as:

$$F_{pile} = \frac{12EI\Delta}{L_{pile}^3} = \frac{12EI}{L_{pile}^3}(\alpha \cdot \Delta T \cdot L)$$

$$= \frac{6(29000 \text{ ksi})(186 \text{ in}^4)}{(30 \text{ ft})^3} (6 \times 10^{-6} / ^\circ \text{F})(70 ^\circ \text{F}) \left(\frac{100 \text{ ft}}{2} \right) = 0.35 \text{ kips}$$
(8.2)

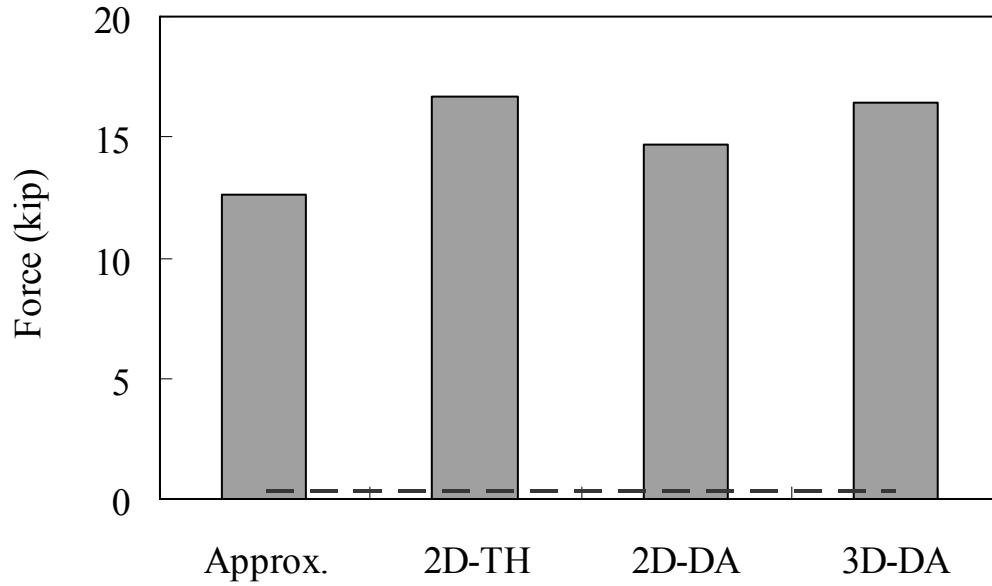


Figure 8.49: Example Bridge 1 Pile Lateral Force Comparison

8.1.4.4 Pile Moment

Pile head moment results obtained by the Approx., 2D-TH, 2D-DA, and 3D-DA are presented in Figure 8.50. All analyses report similar pile head moments. Compared to 3D-DA, the Approx., 2D-TH and 2D-DA report moments that are 5.6% larger, 12% larger, and 13% smaller. For comparison purposes, the single pile moment, M_{pile} , due to a superstructure-free expansion, is computed as:

$$M_{pile} = \frac{6EI\Delta}{L_{pile}^2} = \frac{6EI}{L_{pile}^2}(\alpha \cdot \Delta T \cdot L)$$
(8.3)

$$= \frac{6(29000 \text{ ksi})(186 \text{ in}^4)}{(30 \text{ ft})^2} (6 \times 10^{-6} / ^\circ \text{F})(70 ^\circ \text{F}) \left(\frac{50 \text{ ft}}{2} \right) = 5.2 \text{ ft-kip}$$

All analysis predictions are smaller than the moment by free expansion.

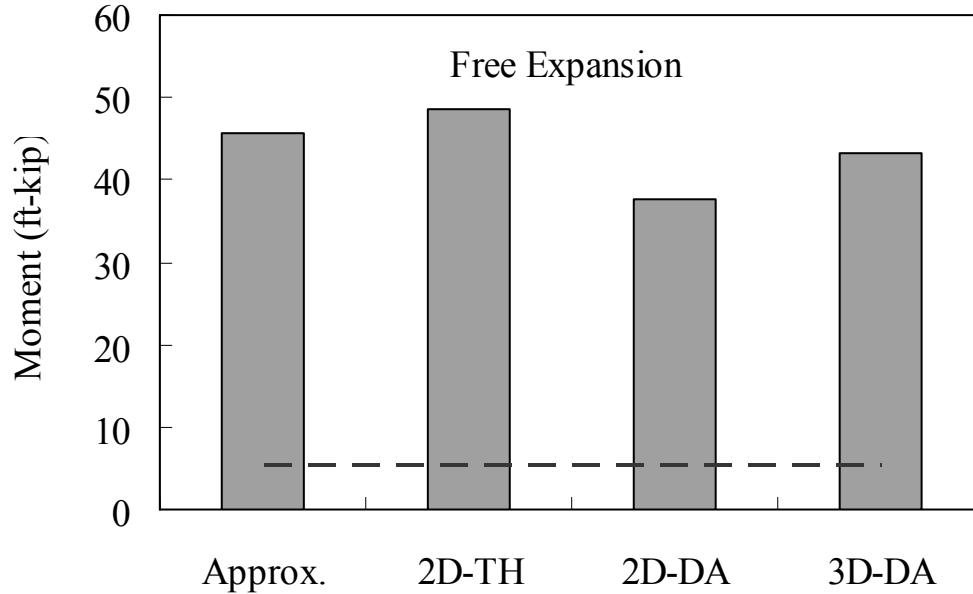


Figure 8.50: Example Bridge 1 Pile Moment Comparison

8.1.4.5 Pile Head Displacement

Pile head displacement results obtained by the Approx., 2D-TH, 2D-DA, 3D-DA are presented in Figure 8.51. Except for the approximate method, all analyses report similar pile head displacements. Compared to the 3D-DA, the approximate method, 2D-TH, and 2D-DA report pile head displacements 10% larger, 14% larger, and 3% smaller. For comparison purposes, the pile head displacement due to superstructure-free expansion is computed as:

$$\delta_{pile} = \alpha \cdot \Delta T \cdot L = (6 \times 10^{-6}) (70 ^\circ \text{F}) \left(\frac{100 \text{ ft}}{2} \right) = 0.25 \text{ inches} \quad (8.4)$$

All analysis predictions are smaller than the displacement by free expansion.

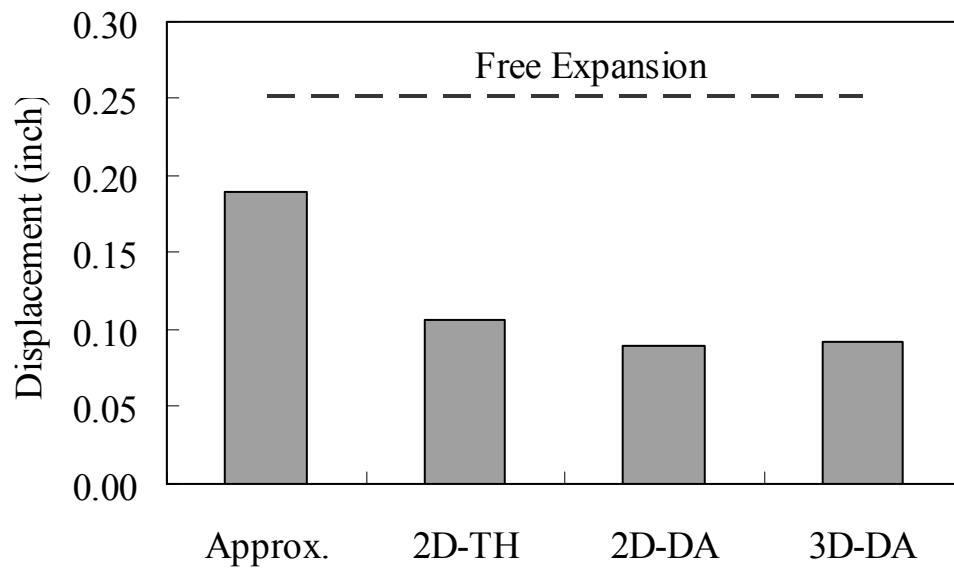


Figure 8.51: Example Bridge 1 Pile Head Displacement Comparison

8.2 Example 2: 2-span Steel Girder Bridge

The integral abutment bridge configuration for Example 2 is a 2-span, 200' (100'-100'), steel plate girder bridge supporting a 9", normally reinforced cast-in-place concrete deck and PennDOT standard barriers. The girder design has been based on widely accepted AASHTO girder bridge practices for gravity load, with the controlling load combination of Strength I with HL-93 live load (HS20 basis). The initial analysis under gravity load follows the AASHTO LRFD approximate load distribution method for a multi-lane bridge. Four steel girders and detailed cross section dimensions are presented in Figures 8.52 through 8.54. Reinforcement details and construction joint, Section A-A in Figure 8.54, appears in Figure 8.55.

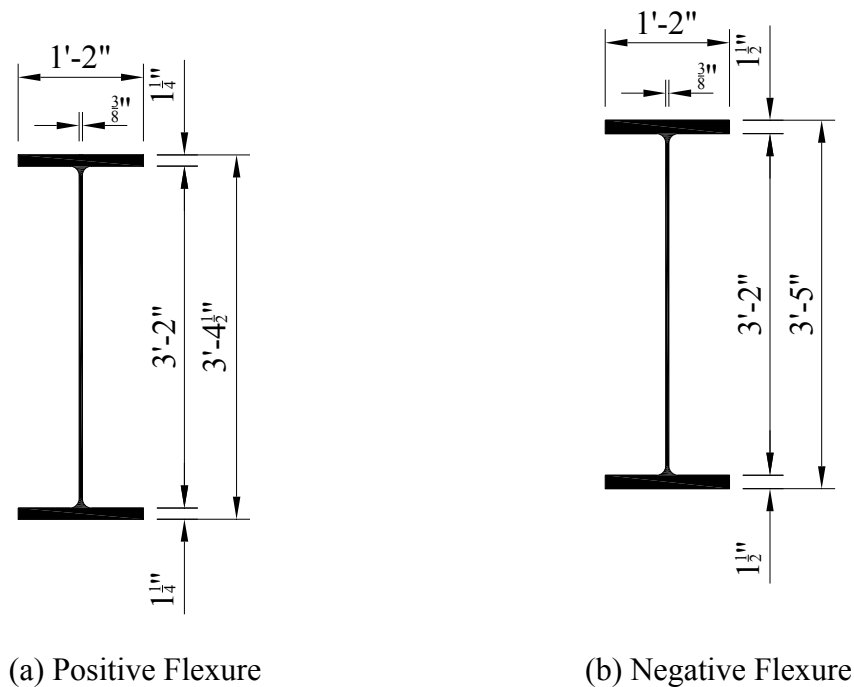


Figure 8.52: Example Bridge 2 Girder Section

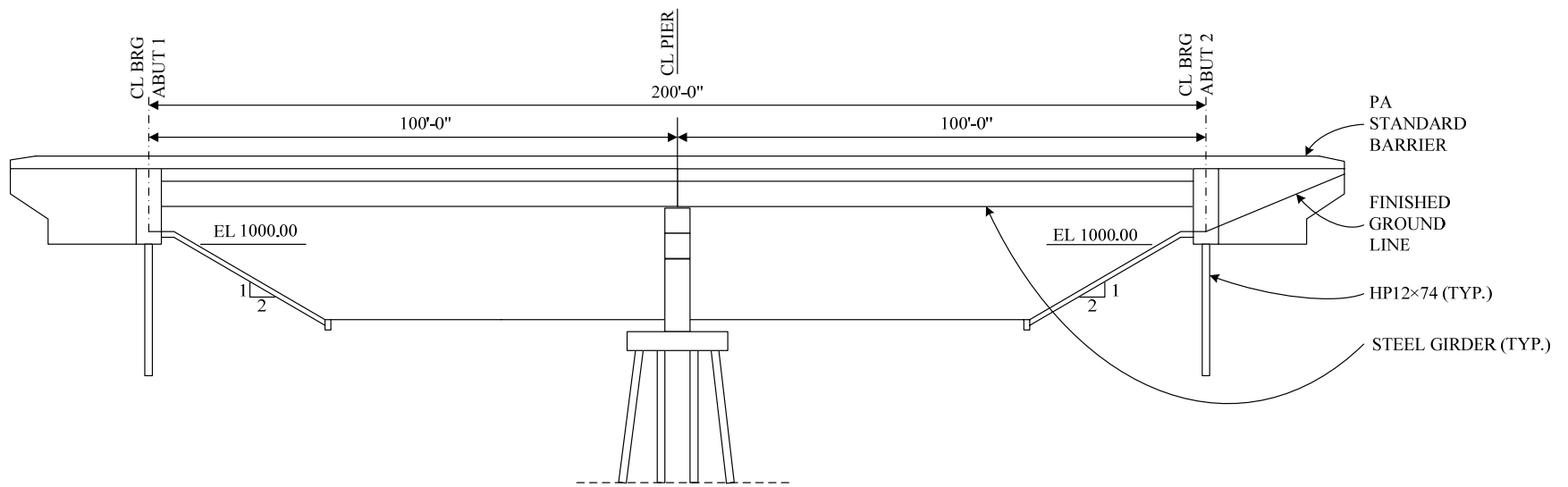


Figure 8.53: Example Bridge 2 Elevation

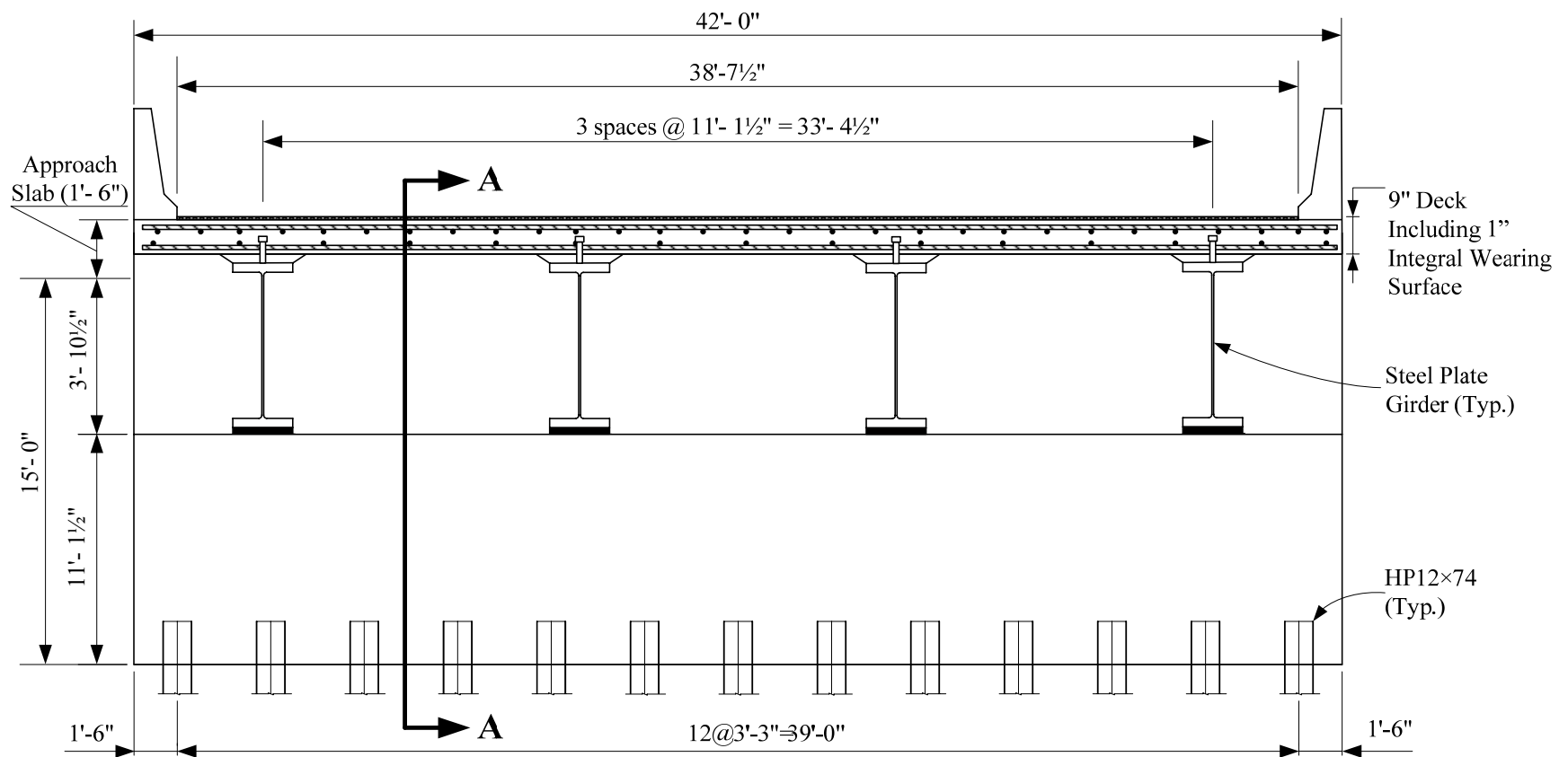


Figure 8.54: Example Bridge 2 Dimensions

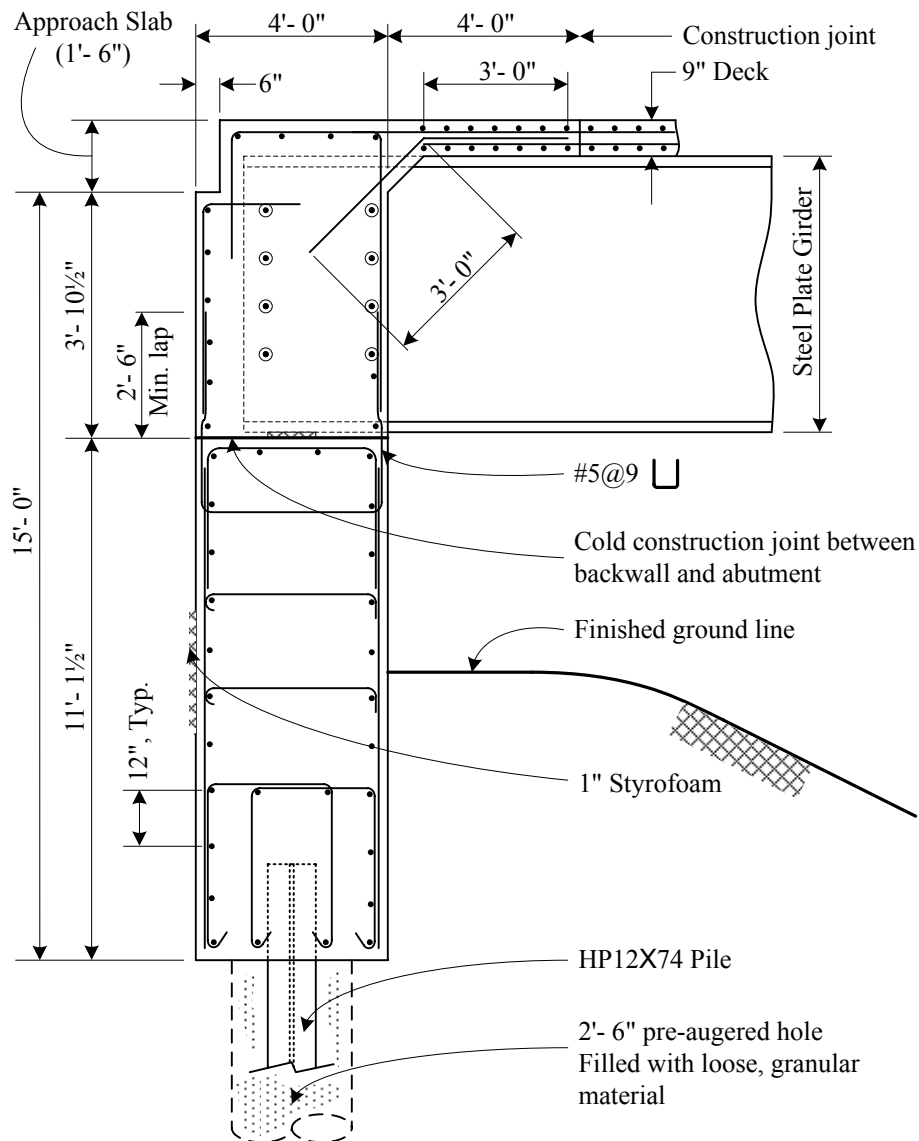


Figure 8.55: Example Bridge 2 Section A-A

Normal weight concrete compressive strengths of bridge components are presented in Table 8.7. A single row of 13, weak-axis oriented, end-bearing, HP12×74 piles are driven to refusal into soil type described in Table 8.8. The soil type for example 2 is taken as *intermediate*. This soil classification is as discussed in Chapter 7, which is also PennDOT No. OGS backfill as described in Table 8.9. The normally reinforced concrete

deck is placed 100 days after the girder manufacture date, which influences how time-dependent effects are computed.

Table 8.7. Example 2 Component Concrete and Steel Strength

Strength (psi)	Bridge Component
PennDOT Class AAA (4000 psi)	Deck, Back-wall
PennDOT Class AA (3500 psi)	Parapets, Diaphragms and Cheek Walls
PennDOT Class A (3000 psi)	Abutment below Girder Seats, and Pedestals
$F_y = 50$ ksi	Steel Plate Girder, Steel Pile (HP12X74)
$f_y = 60$ ksi	Steel Rebars

Table 8.8. Soil Layer Properties for Soil Pile Stiffness (P)

Property	<i>Intermediate*</i>
Density (pcf)	121
Undrained Shear Strength (psi)	17.5
Soil Modulus (K) (pci)	1000
ε_{50} (in)	0.008

**Intermediate* refers to Table 7.2.

Note: soil pile stiffness (P) is represented as *Low* = 1, *Intermediate* = 2, *High* = 3 in the approximate method.

Table 8.9. Backfill Properties for Backfill Stiffness (B)

Property	<i>Intermediate*</i>
Density (γ) (pcf)	119
Angle of friction (ϕ_f) (Degree)	34
Subgrade Modulus (K_h) (pci)	43.8

**Intermediate* refers to Table 7.1.

Note: backfill stiffness (B) is represented as *Low* = 1, *Intermediate* = 2, *High* = 3 in the approximate method.

8.2.1 Example 2: Approximate Analysis Method

The approximate integral abutment analysis method utilizes equations 7.2 through 7.14 developed and presented in Chapter 7. The approximate method presented herein considers only temperature load, temperature gradient and backfill pressure for a 75-year bridge life. In addition, backfill-abutment interaction, soil-pile interaction, and the nonlinear behavior of the back-wall to abutment construction joint are accounted for in the approximate analysis method, returning maximum, 75-year bridge responses.

AASHTO LRFD (5.4.2.2) recommends a thermal expansion coefficient of $6.5\text{E-}6/^{\circ}\text{F}$ for structural steel and $6\text{E-}6/^{\circ}\text{F}$ for normal-weight concrete in the absence of measurement data. The AASHTO-recommended thermal expansion coefficient for normal-weight concrete is adopted in the approximate analysis method presented here.

8.2.1.1 Girder Axial Force

Based on the given bridge dimensions and soil property classification, girder axial force is computed from the bridge axial force based on the assumption that all axial forces are evenly distributed to individual girders. Calculated positive and negative girder axial forces represent maximum tensile and compressive axial force over a 75-year bridge life.

Bridge tension force is computed as:

$$F_t = 4.4\alpha + 0.5L - 30H + 14B + 62P + 168 \geq 0 \quad (7.7)$$

$$\alpha = 6.0 /^{\circ}\text{F} \text{ (concrete deck slab thermal expansion} \times 1\text{E+6)}$$

$$L = 200 \text{ ft (bridge overall length)}$$

$$H = 15 \text{ ft (abutment height)}$$

$$P = 2 \text{ (soil pile stiffness based on Table 8.3)}$$

$$F_t = 4.4(6.0 \text{ } ^\circ\text{F}) + 0.5(200 \text{ ft}) - 30(15 \text{ ft}) + 14(2) + 62(2) + 168 \geq 0$$

$$= -3.6 \text{ kips per bridge} < 0, \text{ therefore, no superstructure tension is predicted.}$$

The example bridge considered herein has a large backfill pressure effect relative to the thermal expansion and contraction effects. Therefore, this example bridge case does not experience any superstructure tensile forces and no tensile axial force needs to be considered.

Bridge longitudinal compression force, F_c , is computed as:

$$F_c = -32\alpha - 2L - 18H - 101B + 16P + 169 \quad (7.8)$$

$$\alpha = 6.0 \text{ } ^\circ\text{F (concrete deck slab thermal expansion} \times 1\text{E}+6)$$

$$L = 200 \text{ ft (bridge overall length)}$$

$$H = 15 \text{ ft (abutment height)}$$

$$B = 2 \text{ (backfill pile stiffness coefficient based on Table 8.4)}$$

$$P = 2 \text{ (soil pile stiffness based on Table 8.3)}$$

$$F_c = -32(6.0 \text{ } ^\circ\text{F}) - 2(200 \text{ ft}) - 18(15) - 101(2) + 16(2) + 374 = -863 \text{ kips per bridge}$$

$$\text{Compression Force per Girder} = -863 \text{ kips} / (4 \text{ girders}) = -216 \text{ kips per girder}$$

8.2.1.2 Girder Bending Moment

The girder bending moment is computed from bridge bending moment, calculated from the approximate analysis equations 7.2 through 7.6 in Chapter 7 of this report.

Bridge positive moment, M_{pos} , at the abutment is computed as:

$$M_{pos} = -12\alpha + 3L - 208H - 10B + 863P + 1570 \geq 0 \quad (7.2)$$

$$\alpha = 6.0 / ^\circ\text{F} \text{ (concrete deck slab thermal expansion } \times 1\text{E}+6)$$

$$L = 200 \text{ ft (bridge overall length)}$$

$$H = 15 \text{ ft (abutment height)}$$

$$B = 2 \text{ (backfill pile stiffness coefficient based on Table 8.4)}$$

$$P = 2 \text{ (soil pile stiffness based on Table 8.3)}$$

$$M_{pos} = -12(6.0 / ^\circ\text{F}) + 3(200 \text{ ft}) - 208(15 \text{ ft}) - 10(2) + 863(2) + 1570 = 684 \text{ ft-kips per bridge}$$

$$M_{pos} \text{ at the abutment per girder} = 684 \text{ ft-kip} / (4 \text{ girders}) = 171 \text{ ft-kips per girder.}$$

Bridge negative moment, M_{neg} , at the abutment is computed as:

$$M_{neg} = -158\alpha^{0.2}L^{0.7}H^{0.3}B^{0.1}P^{0.2} - 1990 \quad (7.3)$$

$$\alpha = 6.0 / ^\circ\text{F} \text{ (concrete deck slab thermal expansion } \times 1\text{E}+6)$$

$$L = 200 \text{ ft (bridge overall length)}$$

$$H = 15 \text{ ft (abutment height)}$$

$$B = 2 \text{ (backfill pile stiffness coefficient based on Table 8.4)}$$

$$P = 2 \text{ (soil pile stiffness based on Table 8.3)}$$

$$M_{neg} = -158(6.0 / ^\circ\text{F})^{0.2}(200\text{ft})^{0.7}(15 \text{ ft})^{0.3}(2)^{0.1}(2)^{0.2} - 1990 = -5,810 \text{ ft-kips per bridge}$$

$$M_{neg} \text{ at the abutment per girder} = -5,810 \text{ ft-kip} / (4 \text{ girders}) = -1,450 \text{ ft-kips per girder.}$$

8.2.1.3 Pile Head Moment

Pile head moments are computed using the approximate analysis equations 7.10 through 7.11 from Chapter 7 of this report. Typical IAB abutment pile displacement, moment, and shear are presented in Figure 8.56. While pile response depends significantly on

bridge length, pile points of fixity are normally established above a 15-ft depth.

Maximum supporting pile displacement, moment and shear in occur at the pile head;

therefore, these values are used for pile design.

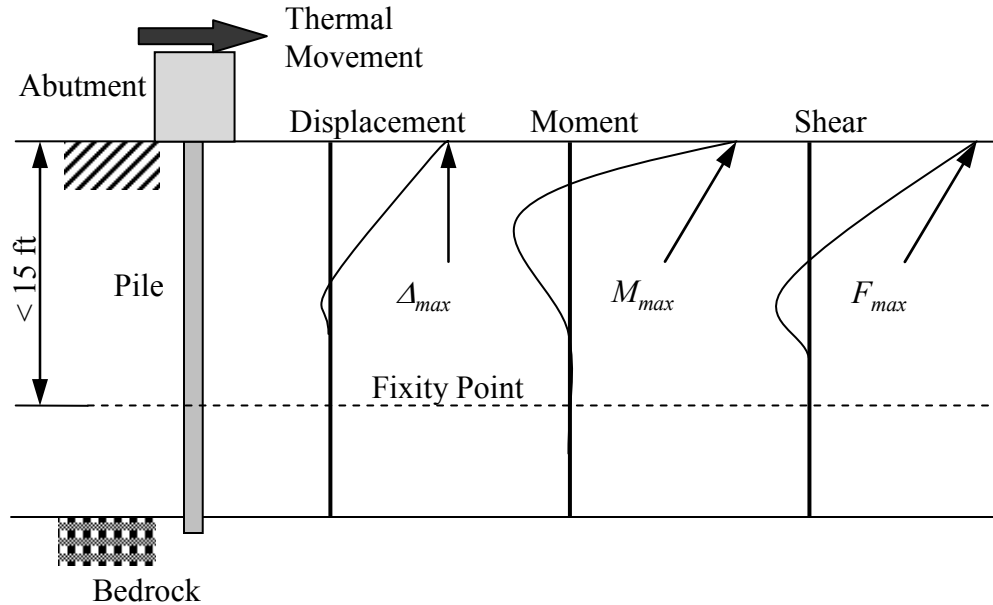


Figure 8.56: Typical IAB Pile Displacement, Moment, and Shear Response.

Total pile head moment is computed as:

$$M_{piles} = 30\alpha^{0.4}L^{0.4}P^{0.5} + 287 \leq M_{ypile} N_p \quad \text{for } 13 \leq H \leq 18\text{ft} \quad (7.10)$$

$$\alpha = 6.0 \text{ } ^\circ\text{F} \text{ (concrete deck slab thermal expansion } \times 1\text{E}+6)$$

$$L = 200 \text{ ft (bridge overall length)}$$

$$P = 2 \text{ (soil pile stiffness based on Table 8.3)}$$

$$M_{piles} = 30(6.0 \text{ } ^\circ\text{F})^{0.4}(200 \text{ ft})^{0.4}(2)^{0.5} + 287 = 1010 \text{ ft-kips per bridge}$$

$$\text{Pile head moment per pile: } M_{pile} = 1010 \text{ ft-kips} / (13 \text{ piles}) = 78 \text{ ft-kips per pile}$$

A single pile is expected to experience a maximum of 55.6 ft-kip weak axis bending moment at the pile head over the 75-year bridge life.

8.2.1.4 Pile Lateral Force

Total pile lateral shear force is computed as:

$$F_{piles} = 241L^{-0.01}B^{-0.04}P^{0.45} + 42 \leq F_{y_pile} N_p \quad (7.12)$$

The total pile lateral force is limited to single pile shear capacity (F_{y_pile}) times the number of piles (N_p). The minimum number of piles can be determined based on this limitation so that $F_{piles} \leq F_{y_pile} N_p$. For Example 2, the total pile lateral force is:

$$F_{piles} = 241L^{-0.01}B^{-0.04}P^{0.45} + 42$$

$$L = 200 \text{ ft (bridge overall length)}$$

$$B = 2 \text{ (backfill pile stiffness coefficient based on Table 8.4)}$$

$$P = 2 \text{ (soil pile stiffness based on Table 8.3)}$$

$$F_{piles} = 241(200 \text{ ft})^{-0.01}(2)^{-0.04}(2)^{0.45} + 42 = 346 \text{ kips per bridge}$$

Pile lateral force, $F_{pile} = 346 \text{ kips} / (13 \text{ piles}) = 26.6 \text{ kips per pile}$

8.2.1.5 Pile Head/Abutment Displacement

As presented in Figure 8.56, pile head/abutment displacement reaches its maximum at the pile head. This pile head/abutment displacement may also be used to determine the number of piles or other bridge dimensions because AASHTO LRFD (2007) limits the abutment displacement to $\leq 1\frac{1}{2}$ inches. For the current bridge example, maximum displacement is computed as:

$$u_{max} = 0.022\alpha + 0.001L - 0.011B - 0.163P + 0.68 \quad \text{for } 13 \leq H \leq 18\text{ft} \quad (7.14)$$

$$\alpha = 6.0 / ^\circ\text{F (concrete deck slab thermal expansion} \times 1\text{E}+6)$$

$$L = 200 \text{ ft (bridge overall length)}$$

$B = 2$ (backfill pile stiffness coefficient based on Table 8.4)

$P = 2$ (soil pile stiffness based on Table 8.3)

$$u_{max} = 0.022(6.0 / ^\circ\text{F}) + 0.001(200 \text{ ft}) - 0.01(2) - 0.16(2) + 0.68 = 0.67 \text{ inches}$$

8.2.2 Example 2: Two-Dimensional Model Analysis

A more refined, and potentially more accurate relative to the IAB approximate analysis method, is an analysis method that utilizes a two-dimensional, numerical, finite-element model. The methodology presented here permits the incorporation of individual bridge elements and the respective material and geometric properties through a demonstrated effective 2D model approach.

To construct a 2D model of the three-dimensional structure, the four girders and composite concrete deck are represented as a single beam element using ANSYS BEAM189 elements. Supporting piles are represented as two-dimensional beam elements, also using BEAM189 elements with soil-pile interaction springs (COMBIN39) spaced vertically at 1'- 0" representing the soil. Similarly, abutment-to-backfill interaction is represented using nonlinear interaction springs. The development of material and geometric properties for each element is discussed in detail below. A schematic of the 2D bridge model developed for example 2 is presented in Figure 8.57.

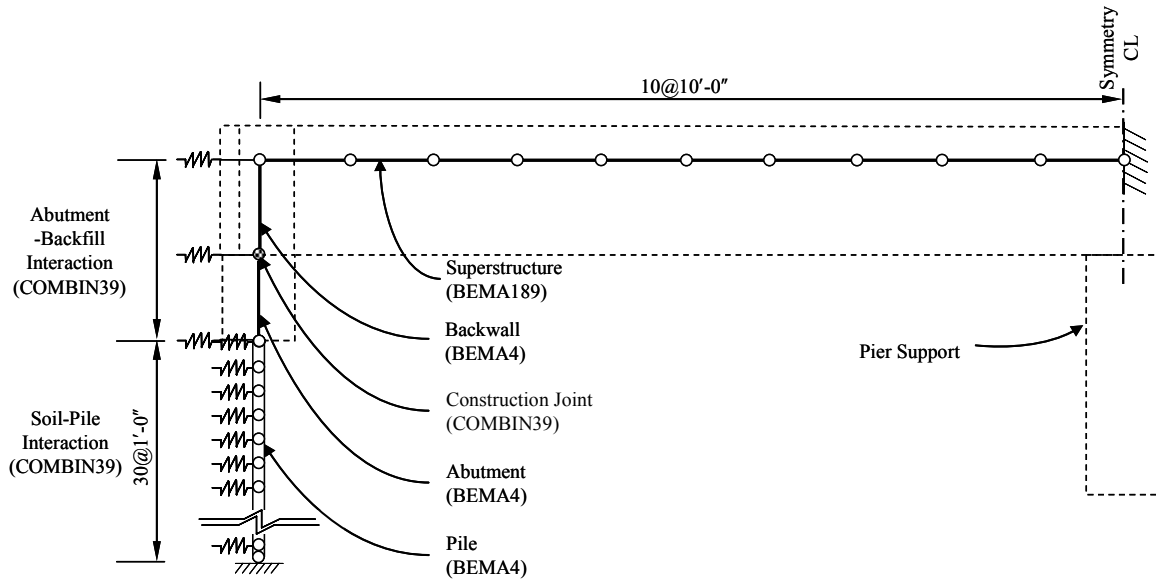


Figure 8.57: 2D Example 2 ANSYS Bridge Model.

The incorporation of transverse bridge components, such as diaphragms, in a two-dimensional model is not possible; however, the effects of the transverse elements on the longitudinal response to temperature loading is not significant. Key bridge components include girders, deck, abutment/backwall, construction joint, and piles. Loading includes superstructure temperature variation, temperature gradient, and backfill pressure. A completed 2D numerical model with actual cross section of each member of the bridge is presented in Figure 8.58.

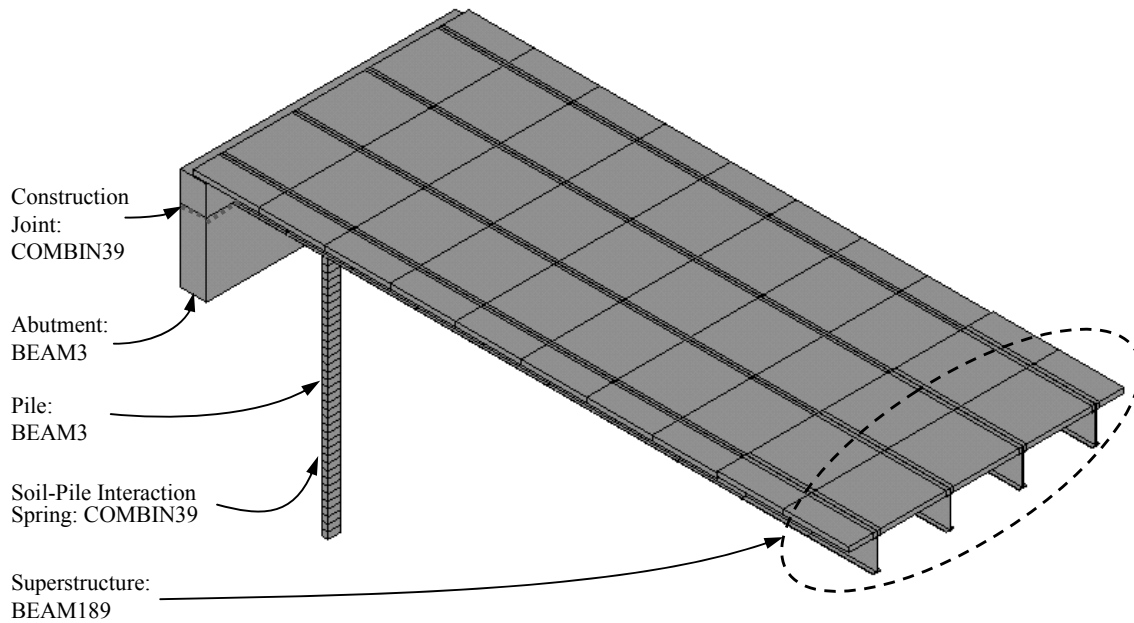


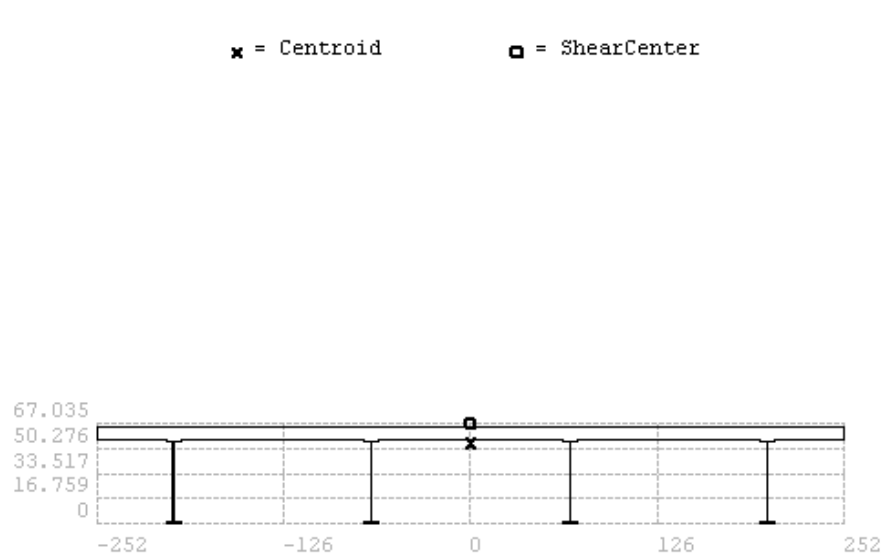
Figure 8.58: 2D Example 2 ANSYS Model Perspective View

8.2.2.1 Bridge Components

Each bridge component and its definition are described in detail in the following sections to allow the reader to develop future models for other IABs. The discussion includes girder and deck, abutment/backwall, construction joint, piles, and soil springs.

8.2.2.1.1 Girder and Deck

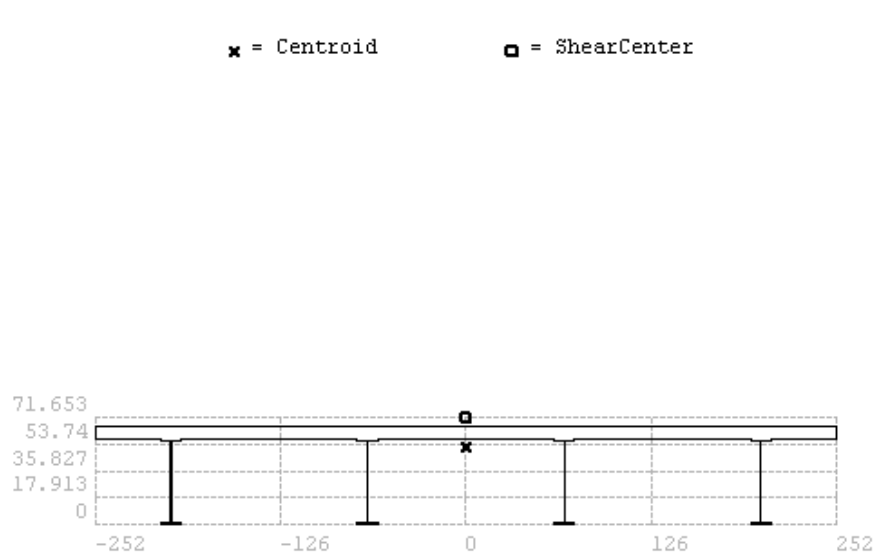
The bridge superstructure is modeled using a beam element based on the entire superstructure cross section properties as shown in Figure 8.59. Computed superstructure section properties are presented in Table 8.10. Due to the 28-day strength difference between deck concrete (4,000 psi) and girder concrete (8,000 psi), a transformed deck concrete area is used in the calculation of area and moment of inertia. Based on AASHTO recommendations, the concrete thermal expansion coefficient for deck concrete and girder concrete is taken as $6.0\text{E-}6 \text{ in/in/}^{\circ}\text{F}$.



SECTION ID 2
DATA SUMMARY

Section Name
= 4stl200p
Centroid Y
= $-.189\text{E-}12$
Centroid Z
= 53.797
Shear Center Y
= $.154\text{E-}08$
Shear Center Z
= 67.035
Shear Corr. YY
= .728373
Shear Corr. YZ
= $-.074365$
Shear Corr. ZZ
= .172819

(a) Positive Flexure



SECTION ID 3
DATA SUMMARY

Section Name
= 4stl200n
Centroid Y
= $-.233\text{E-}12$
Centroid Z
= 51.955
Shear Center Y
= $.319\text{E-}09$
Shear Center Z
= 71.653
Shear Corr. YY
= .656696
Shear Corr. YZ
= $-.060172$
Shear Corr. ZZ
= .167398

(b) Negative Flexure

Figure 8.59: Beam Element (BEAM189) Cross Section for Superstructure
(Note: All dimensions in inches)

Table 8.10: Superstructure Composite Section Property of Steel Girder IAB

Section Property	Centroid (in)	Area (in ²)	Moment of Inertia (in ⁴)	Elastic Modulus (ksi)	Thermal Expansion Coefficient (in/in/°F)
Positive	53.8	4,680	1,433,200	29,000	6.5E-6
Negative	52.0	4,780	2,580,000	29,000	6.5E-6

8.2.2.1.2 Abutment/Back-wall

For a 2D model, the abutment (or pile cap) and back-wall (or end diaphragm) are modeled using beam elements. The full height of the abutment (base to beam seats) determines the length of the abutment beam element; however, the back-wall is modeled from the beam seat to the superstructure centroid. The superstructure is represented as a beam line element; therefore, the portion of the back-wall above the superstructure centroid is extraneous and eliminated.

Generally, higher-strength concrete is used in the back-wall as compared to the abutment concrete because the back-wall is placed monolithically with the deck. The example 2 bridge specifies 4,000 psi and 3,000 psi 28-day compressive strength concrete for the back-wall and abutment, respectively, resulting in the elastic modulus for the back-wall as 3,640 ksi and the elastic modulus for abutment as 3,160 ksi.

8.2.2.1.3 Construction Joints

The construction joint between the back-wall and abutment is modeled using a joint element with defined rotational stiffness, but all translations are directly compatible with

adjacent elements. The computed rotational stiffness of the construction joint is presented in Figure 8.60.

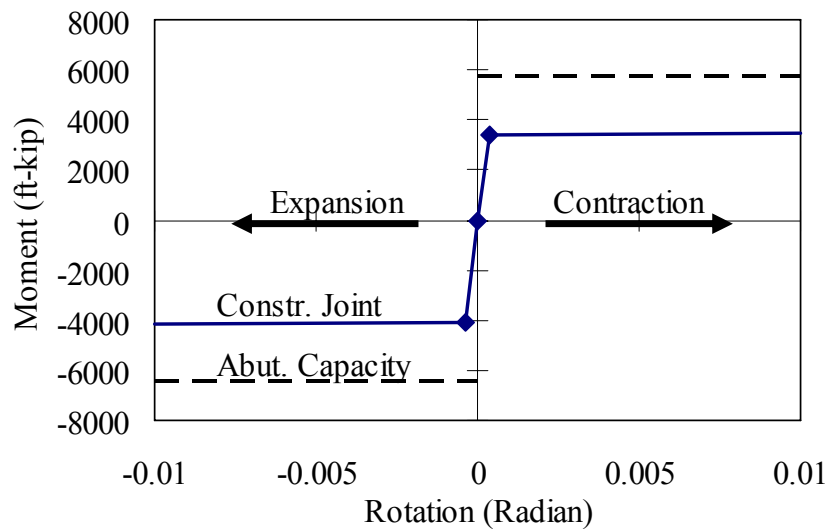


Figure 8.60: Construction Joint Rotational Stiffness

Rotational stiffness is determined based on reinforcing bars crossing the joint. A reinforcement detail consisting of #5 bars at 9 inches center-to-center is a typical PennDOT specification and is therefore adopted here. In addition, the reinforcement adjacent to the backfill side of the joint is different from the reinforcement adjacent to the abutment front face because girders interfere with the reinforcement placement (see Figure 8.55). This causes the rotational stiffness for superstructure expansion to be different from the rotational stiffness for superstructure contraction.

The construction joint is a cold joint; therefore, concrete tension is not considered in the development of moment-curvature definition. To convert curvature into rotation, half of the AASHTO LRFD embedment length is utilized to compute the displacement, crack opening between the abutment and the back-wall during superstructure expansion and contraction, due to strain in the reinforcement.

8.2.2.1.4 Steel H-Piles

Weak axis oriented steel H-piles are modeled using beam elements and soil-structure interaction is modeled using nonlinear spring elements. Beam element steel H-pile properties of area and moment of inertia are assigned directly. The pile length must be at least 20 ft because the pile fixity point (zero rotation and zero displacement) occurs between 10 and 15 ft. However, longer bridges will develop a deeper fixity point; therefore, piles should be modeled to the full expected driven depth. The pile fixity point of the numerical model must be evaluated to determine whether the pile has been properly modeled. For the given example bridge, a 30-ft pile length has been modeled.

8.2.2.1.5 Soil Springs

Soil non-linear stiffness definition at each depth is represented using equivalent Winkler spring elements based on p - y curves that are spaced at 1-ft vertical intervals. Alternatively, commercial programs such as COM624P and Lpile can directly generate p - y curves at various soil conditions and depths (refer to section 5.2.3 of this report). In the 2D ANSYS bridge model, COMBIN39 nonlinear spring elements are used to represent the hysteretic behavior of soil-pile interaction. Each p - y spring is spaced at 1'-0" intervals from the pile head to pile bearing tip. Spring element properties defined by lateral force vs. lateral displacement (p - y) at a given depth consider the total number of abutment piles and the tributary area along the pile. For illustration, under the bridge contraction case, a p - y curve at the 10'-0" depth of the given soil strata is computed as:

$$p_u = \min \left\{ p_{uf} = 9cD, \quad p_{uw} = \left(3 + \frac{\gamma'}{c} X + \frac{J}{D} X \right) cD \right\} \quad (5.4)$$

$$p_{uf} = 9cD = 9(13.9 \text{ psi})(12.1 \text{ inches}) = 1510 \text{ lbs/inch}$$

$$p_{uw} = \left(3 + \frac{140 \text{ pcf}}{2000 \text{ psf}} (120 \text{ inches}) + \frac{0.5}{12.1 \text{ inches}} (120 \text{ inches}) \right) (2000 \text{ psf}) (12.1 \text{ inches})$$

= 1460 lb/inch → governs

For the tributary length of 1'-0", $p_u = (1460 \text{ lbs/inch})(12 \text{ inches}) = 17.5 \text{ kips}$

$$p = 0.5 p_u \left(\frac{y}{y_{50}} \right)^{1/4} \text{ and if } y = 0.1 \text{ inches,}$$

$$p = 0.5(17.5 \text{ kips}) \left(\frac{0.1 \text{ inches}}{0.212 \text{ inches}} \right)^{1/4} = \underline{7.24 \text{ kips}}$$

Similarly, for expansion, $X = 120 \text{ inches} + 180 \text{ inches (backfill height)} = 300 \text{ inches}$:

$$p_{uf} = 9cD = 9(13.9 \text{ psi})(12.1 \text{ inches}) = 1510 \text{ lbs/inch} \rightarrow \text{governs}$$

$$p_{uw} = \left(3 + \frac{140 \text{ pcf}}{2000 \text{ psf}} (300 \text{ inches}) + \frac{0.5}{12.1 \text{ inches}} (300 \text{ inches}) \right) (2000 \text{ psf}) (12.1 \text{ inches}) =$$

2880 lbs/inch

For the tributary length of 1'-0", $p_u = (1510 \text{ lbs/inch})(12 \text{ inches}) = 18.2 \text{ kips}$

$$p = 0.5 p_u \left(\frac{y}{y_{50}} \right)^{1/4} \text{ and if } y = 0.1 \text{ inches,}$$

$$p = 0.5(18.2 \text{ kips}) \left(\frac{0.1 \text{ inches}}{0.212 \text{ inches}} \right)^{1/4} = \underline{7.53 \text{ kips}}$$

This procedure is repeated for several y values to form a smooth p - y curve, computed up to $16y_{50} = 16(2.5D\epsilon_{50}) = 16(2.5)(12.1 \text{ inches})(0.007 \text{ inches}) = 3.39 \text{ inches}$ because p - y curves in clay soils start to become constant after $16y_{50}$. For the given case, example computations for a soil-pile interaction spring at a depth of 10'-0" are tabulated as:

Table 8.11: p - y curve ordinates for a depth of 10'-0"

	P_u (kip)	y (inches)								
		9.8E-5	7.8E-4	0.025	0.1	0.42	0.85	1.69	3.39	4.5
Cont.	17.5	1.28	2.15	5.12	7.24	10.4	12.4	14.7	17.5	17.5
Exp.	18.2	1.33	2.24	5.32	7.53	10.8	12.8	15.3	18.2	18.2

Based on the sign convention that bridge expansion induces negative displacement and force, the data of Table 8.11 are plotted in Figure 8.61 and compared to results generated by the Lpile program. The API equations in Table 8.11 and the Lpile program produce identical results. Soil springs at each depth require this procedure to generate a p - y curve.

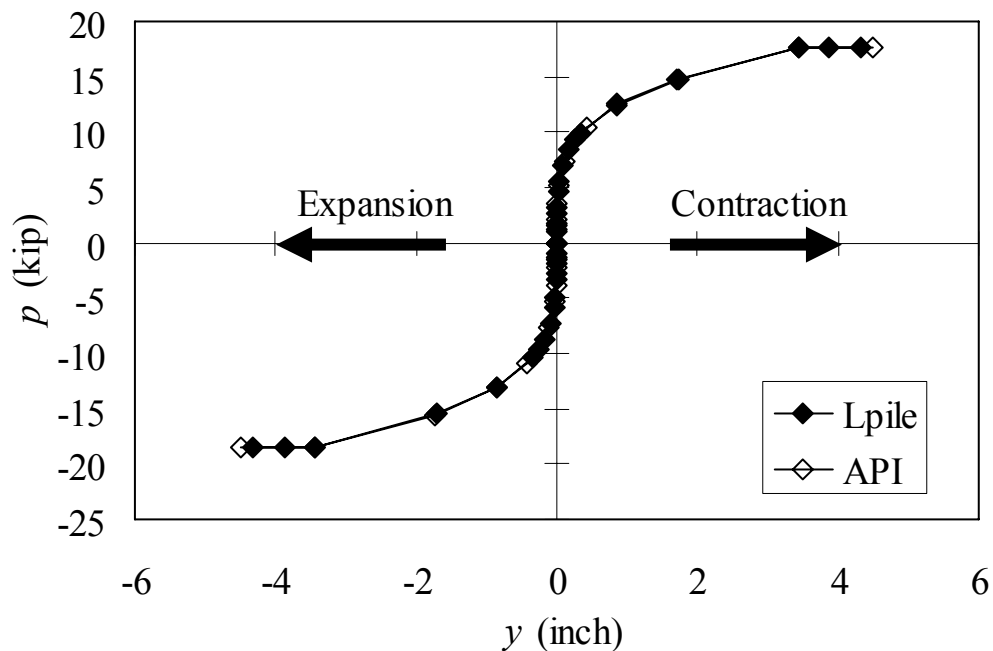


Figure 8.61: Comparison of p - y Curve by the API Equation and Lpile.

8.2.2.1.6 Miscellaneous Components (diaphragms, interior supports, bearings)

Girder bearings (normally elastomeric) at both abutments are embedded in the back-wall concrete and are not modeled explicitly. The superstructure is rigidly connected to the back-wall and is modeled as such. Because both ends of an IAB superstructure are restrained at the abutments, interior supports are not designed to provide longitudinal restraint. In addition, because elastomeric bearings allow longitudinal displacement with very low resistance during bridge contraction and expansion, a roller support condition is appropriate for interior supports. However, the interior support (pier) in this example is coincident with the bridge axis of symmetry; therefore, vertical translation, longitudinal translation, and z-axis rotation (see Figure 8.57) are restrained. Diaphragms at the mid-span or pier supports are not considered due to modeling restrictions.

8.2.2.2 Loads

Loads considered in the 2D model include the overall superstructure temperature fluctuation, temperature gradient through the superstructure depth, and backfill pressure. Each load component is described in the sections below. Two approaches are presented for the 2D analysis example: (1) a 2D time-history analysis and (2) an extreme design static 2D analysis. The 2D time-history analysis evaluates a 75-year bridge life as a result of a sinusoidal temperature fluctuation. This simulation considers a sinusoidal temperature change, time-dependent effects and cyclic soil-structure interaction over time, and is close to actual conditions. However, the 2D design analysis is a static analysis based on an AASHTO-specified extreme temperature rise (+30°F) and fall (-40°F) for concrete bridges. This analysis approach is typically used for DOT design and is easy to

implement, and the required computing resources are low. Time-dependent effects are not included for the design temperature rise analysis in order to obtain the maximum bridge expansion response. This approach recognizes that initial bridge expansion will likely occur before significant, counteracting time-dependent effects occur. Time-dependent effects are combined with design temperature fall to obtain the maximum bridge contraction response.

8.2.2.2.1 Sinusoidal Temperature Fluctuation Simulation

Superstructure temperature fluctuation over time is simulated with a sinusoidal curve that is based on field collected data at monitored bridges and a weather station. The 2D model is configured to simulate a 75-year bridge life; therefore, the sinusoidal temperature simulation must represent a nominal temperature fluctuation over the expected bridge life. Although bridge structures possess relatively low thermal conductivity and high thermal inertia, the average superstructure temperature is reasonably assumed to be equal to ambient temperature. The temperature fluctuation is plotted in Figure 8.62. Depending on the availability of local meteorological data, annual mean temperature, annual temperature amplitude, frequency ($2\pi t$) and phase lag (ϕ) can be determined. Based on the present study monitoring results and information obtained from the National Climate Data Center, central Pennsylvania annual mean = 49 °F and the annual temperature amplitude = 30 °F. A phase lag = π is adopted when the bridge backwall concrete is placed during fall season around annual mean temperature.

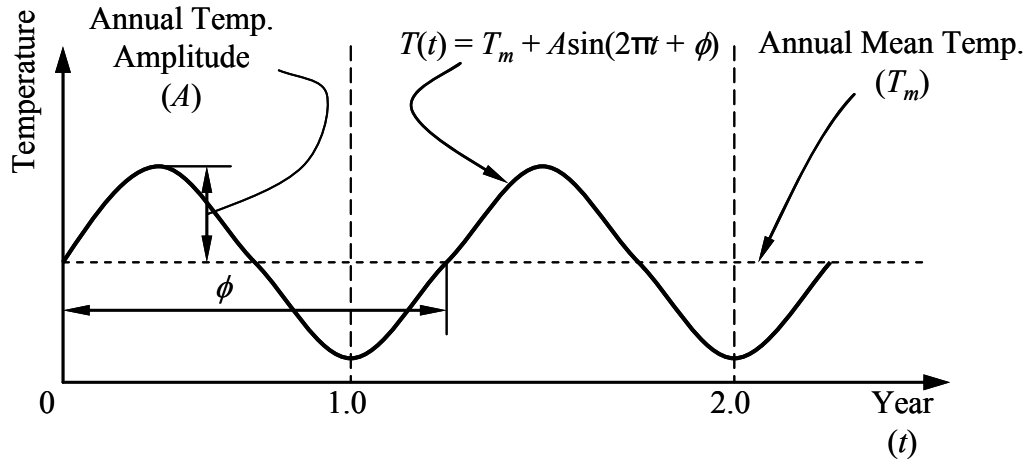


Figure 8.62: Temperature Model

When an equivalent rectangular cross section is used for the superstructure I-girder, the time-dependent load for the superstructure section is required to be offset. Because the composite section elastic neutral axis (ENA) (Figure 8.63(a)) is not coincident with the equivalent rectangular section ENA (Figure 8.63(c)), the equivalent rectangular section is aligned and located at its ENA, i.e. the distance from ENA to the extreme top fiber is the same as to the distance from ENA to the extreme bottom fiber. However, computed time-dependent effects are based on the actual section (Figure 8.63(a)) whose distance from ENA to the extreme top fiber is different from the distance from ENA to the extreme bottom fiber. The computed strains (Figure 8.63(b)) due to time-dependent effects plus temperature loads (T'_i in Figure 8.63) must be corrected as an offset temperature load (T_i in Figure 8.63) to induce the same moment and axial force as presented in Figure 8.63(d). If computed strains are applied to the rectangular section without an offset, a different rotation of ϕ is subjected to the section as appears in Figure 8.63(e).

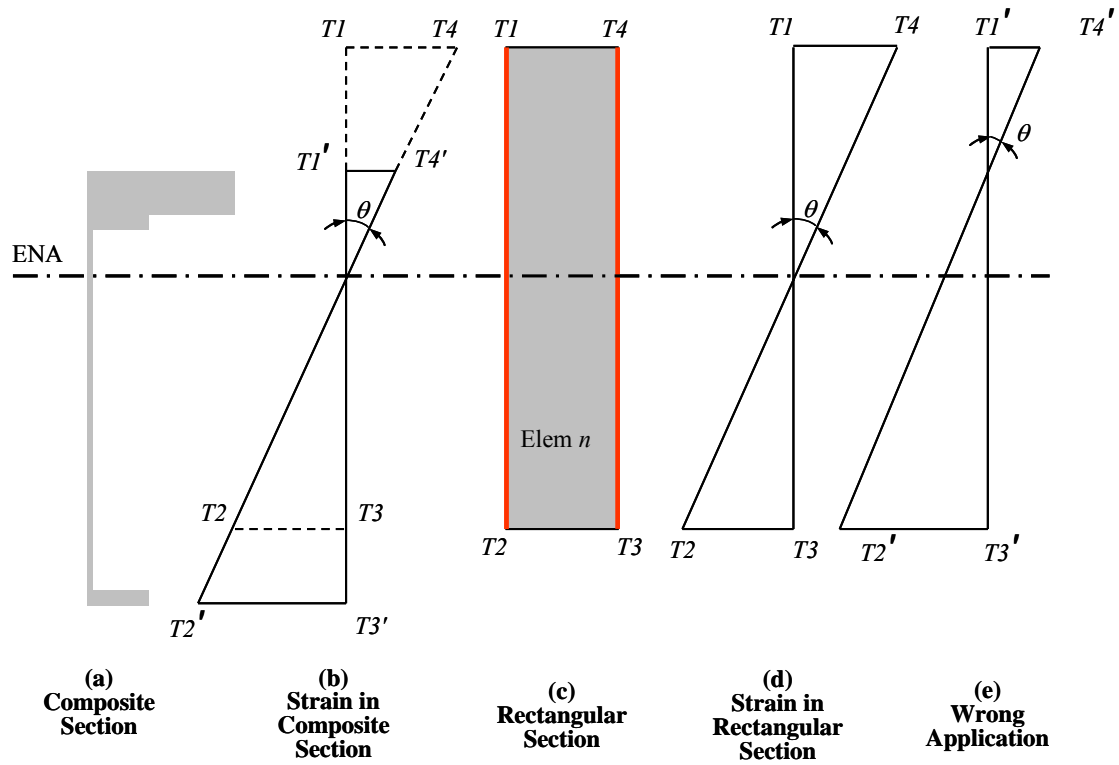


Figure 8.63: Temperature Load Application in Offset Element Section

8.2.2.2.2 Temperature Gradient

Based on AASHTO multi-linear temperature gradient requirements, an equivalent temperature gradient is computed. Thermal stress (σ_t) induced by the temperature gradient along the superstructure depth is represented as:

$$\sigma_t(y) = E \cdot \alpha \cdot T(y) \quad (5.14)$$

where y = distance from the extreme bottom fiber, $\sigma_t(y)$ = longitudinal thermal stress at a fiber located at y , E = elastic modulus, α = thermal expansion coefficient, and $T(y)$ = temperature at y . Thus, the axial force (P_t) and moment (M_t) due to thermal stresses are respectively:

$$\begin{aligned} P_t &= \int E \alpha T(y) b(y) dY, \text{ and} \\ M_t &= \int E \alpha T(y) b(y) Y dY \end{aligned} \quad (5.15)$$

For steel plate girders in Figure 8.52, the equivalent temperature at the top fiber is 17.42 °F and the equivalent temperature at the bottom fiber is -0.57 °F. A similar computation for the negative temperature gradient results in -5.23 °F and 0.17 °F at the top and bottom fiber, respectively.

The temperature gradient application in a 2D numerical analysis is presented in Figure 8.64. The AASHTO gradient represents maximum and minimum temperature gradient across the superstructure. During the warm months of summer, the maximum temperature gradient is reached. During the cold months of winter, the minimum temperature gradient is reached. During the transitional months from spring to summer to fall, the temperature gradient is applied using a sinusoidal fluctuation with the amplitude of positive temperature gradient. Thus, the sinusoidal temperature gradient is superimposed on the thermal fluctuation. During the transitional months from fall to

winter to spring, the temperature gradient is also applied using a sinusoidal fluctuation; however, the sinusoidal amplitude of the negative temperature gradient is used. The sinusoidal temperature gradient, as appropriate for the season, is effectively superimposed on the thermal fluctuation.

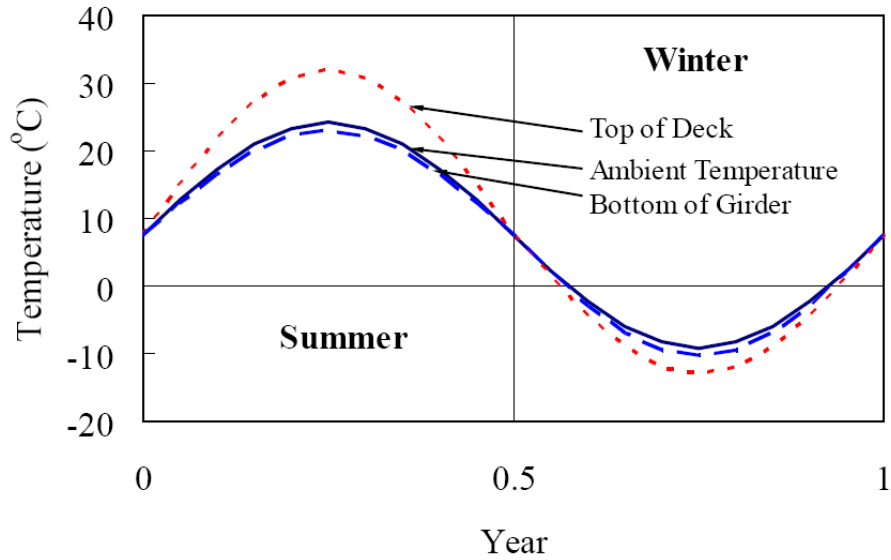


Figure 8.64: Temperature Variation with Temperature Gradient

8.2.2.2.3 Backfill Pressure

Earth pressure behind the abutments and back-walls is assumed as a hydrostatic pressure distribution, increasing with depth resulting in a triangular pressure distribution. As presented in Figure 8.65, backfill pressure varies according to a pressure-displacement relationship. The initial earth pressure is taken as the familiar at-rest pressure, but the pressure ranges between active (P_a) and passive pressure (P_p) depending on abutment displacement. In the numerical simulation, a typical abutment-to-backfill interaction relationship is presented in Figure 8.65, where the active and passive backfill pressure limit is determined based on equations 5.7:

$$P_o = K_o \gamma' z w = (1) \gamma' z w$$

$$P_a = K_a \gamma' z w = \frac{1 - \sin \phi_f}{1 + \sin \phi_f} \gamma' z w \quad (5.7)$$

$$P_p = K_p \gamma' z w = \frac{1 + \sin \phi_f}{1 - \sin \phi_f} \gamma' z w$$

where K_o , K_a and K_p are the lateral earth pressure coefficients for at-rest, active and passive condition, respectively, γ' is the effective soil weight, ϕ_f is the internal friction angle, z is the depth of soil, and w is the effective backfill width. For example 2, K_o , K_a and $K_p = 1.0$, 0.283 and 3.537 , respectively, and $\gamma' = 119$ pcf, $\phi_f = 34^\circ$, and $w = 36'-10''$.

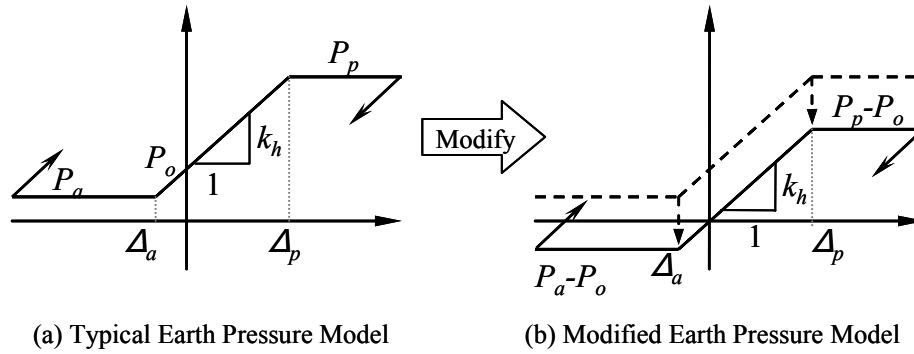


Figure 8.65: Backfill Pressure

The slope (k_h) in Figure 8.65 between active and passive pressure is computed by Boulanger et al. (1999):

$$k_h(z) = k_{ref} \left(\frac{z}{h_{ref}} \right)^{0.5} \quad (5.1)$$

where h_{ref} is the reference depth measured from the soil surface to the pressure cell elevation and z is the depth. Based on monitoring results, $k_{ref} = 0.044$ kci at 4 ft from the bottom of the abutment may be used for backfill height ranging from 10 to 20 ft.

To modify the backfill-abutment interaction as presented in Figure 8.65(b), at-rest backfill pressure (P_o) is applied externally and presented in Figure 8.66.

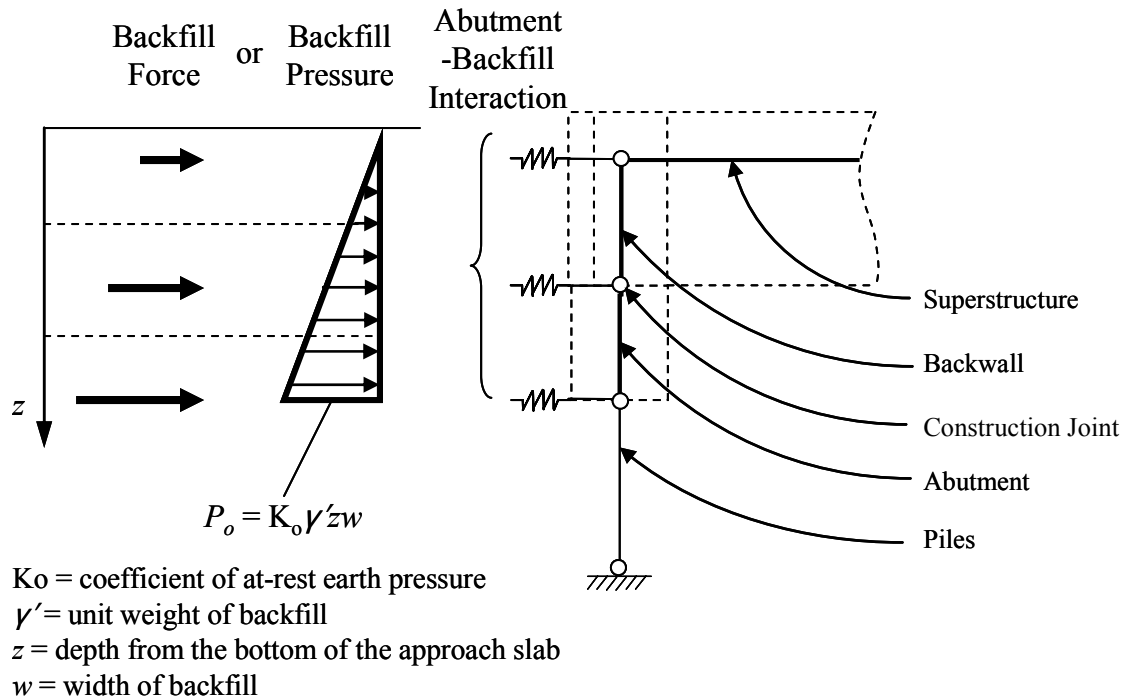


Figure 8.66: Backfill Pressure

In the 2D numerical model, the backfill pressure is applied either by (1) line loads on abutment and backwall elements or (2) forces on nodes based on tributary area divided by the dotted lines in the backfill pressure diagram in Figure 8.66. Both produce the same results. Backfill pressure applied to 2D numerical model is represented as a triangular-shaped line load and is presented in Figure 8.67.

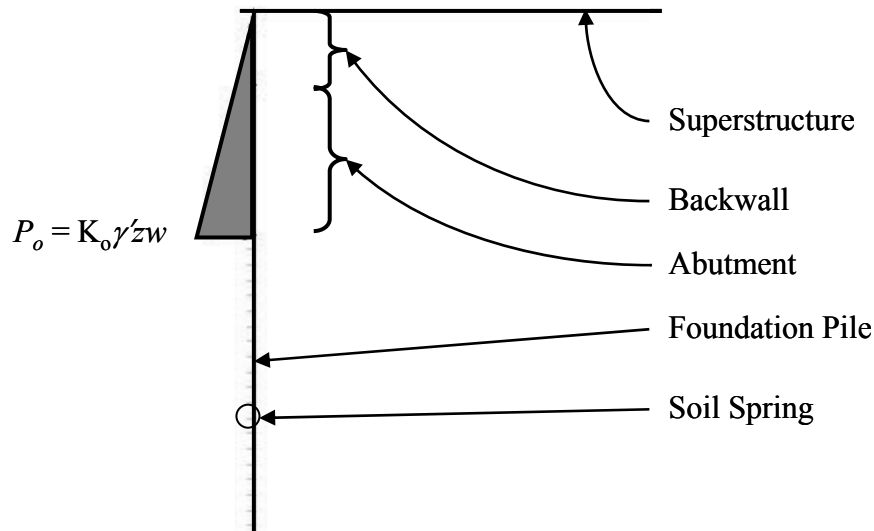


Figure 8.67: Backfill Pressure in 2D Numerical Model

8.2.2.2.4 Time-dependent Loads

For a steel girder bridge, time-dependent effects of concrete creep and shrinkage are not considered.

8.2.2.3 Example 2: 2D Analysis Results

Two analysis approaches are demonstrated in this example: (1) 2D extreme design temperature static analysis and (2) 2D time-history analysis. 2D extreme design temperature range static analysis runs for both AASHTO extreme temperature rise (+60°F) and fall (-60°F). For both the bridge expansion and the contraction case, only thermal load is considered. The time-history analysis, considering hysteretic behavior of soil-structure interaction, runs for a 75-year bridge life with a sinusoidal temperature load. Superimposed results of both approaches are presented on the same graph for girder axial force, girder bending moment, pile lateral force, pile moment, and pile head displacement.

8.2.2.3.1 Girder Axial Force

Girder axial forces by both extreme design temperature range static analysis (dashed lines) and time-history analysis (solid line) are presented in Figure 8.68. The temperature range in the extreme temperature static analysis is larger than the time-history analysis, and therefore, the time-history analysis results in a 21% smaller compressive girder axial force during bridge expansion. The time-history analysis has no tensile axial force during bridge contraction while the extreme design temperature static analysis predicts 16 kips of tensile girder axial force.

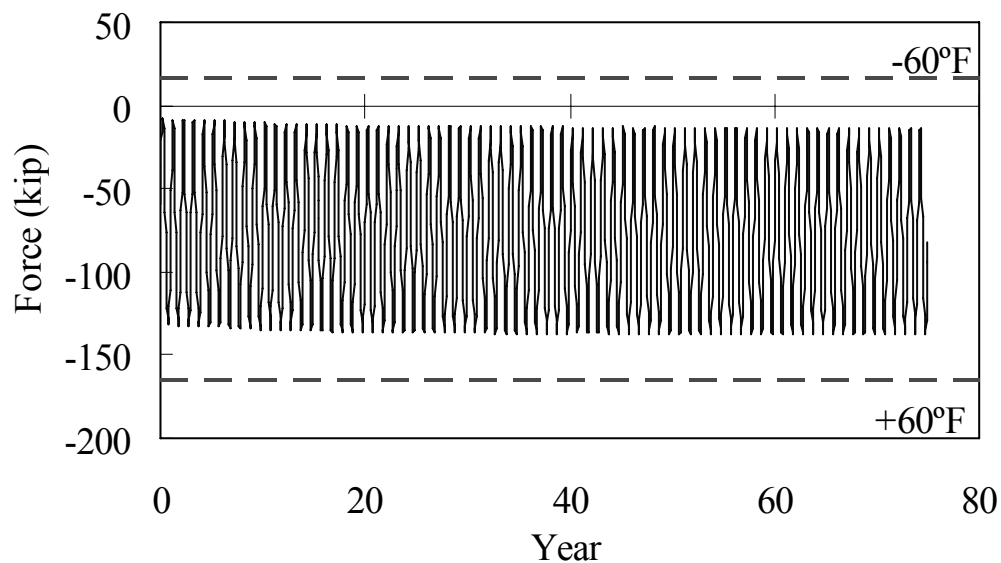


Figure 8.68: Example 2: 2D Analysis—Girder Axial Force (Static and Time-History)

8.2.2.3.2 Girder Bending Moment

Girder bending moments by both extreme design temperature static analysis (dashed lines) and time-history analysis (solid line) are presented in Figure 8.69. The extreme design temperature static analysis predicts a 178% larger positive girder bending moment

and 27% larger negative girder bending moment, compared to the time-history analysis predictions.

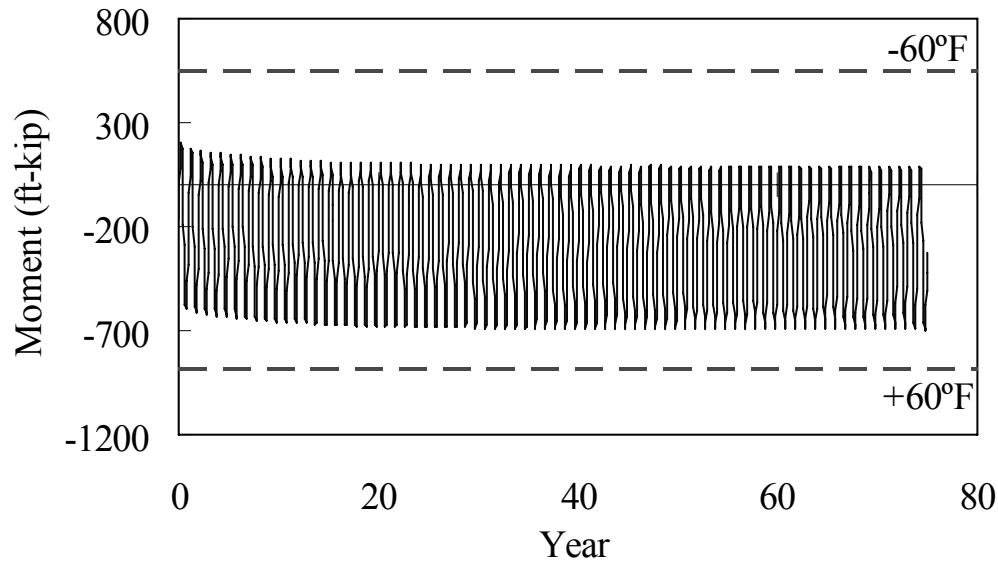


Figure 8.69: Example 2: 2D Analysis—Girder Bending Moment (Static and Time-history)

8.2.2.3.3 Pile Lateral Force

Pile lateral force by both the extreme design temperature static analysis (dashed lines) and the time-history analysis (solid line) is presented in Figure 8.70. Initially, the time-history analysis prediction of pile lateral force is approximately 18 kips. However, after 7 years, the pile lateral force decreases to 7.5 kips and is almost constant. The extreme design temperature static analysis predicts 2.4% smaller pile lateral forces during bridge expansion and 188% larger pile lateral force during bridge contraction. The initial pile lateral force in the time-history analysis predicts a similar pile lateral force (only 2.4% different), but cyclic soil-pile interaction and backfill-abutment interaction over time decrease the pile lateral force.

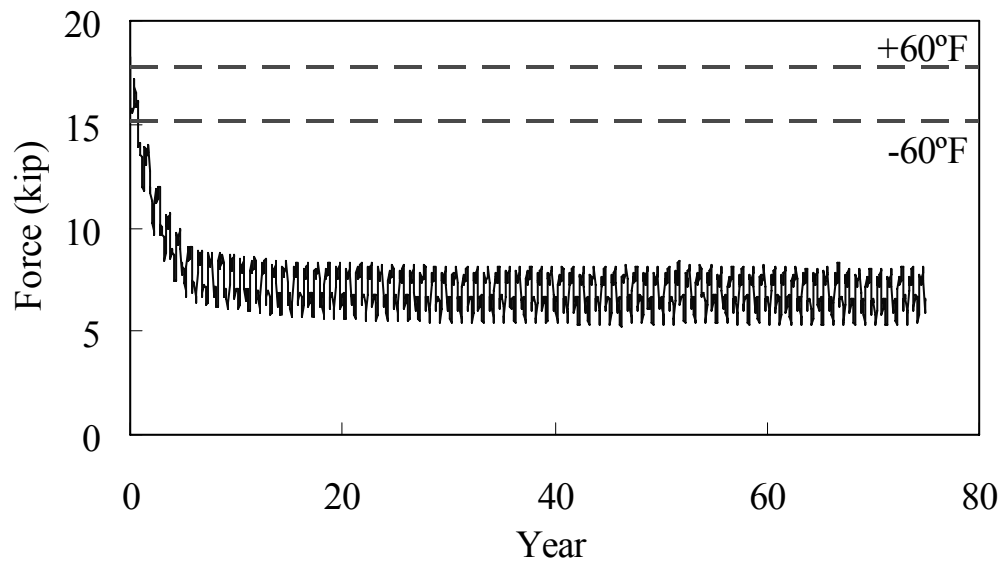


Figure 8.70: Example 2: 2D Analysis - Pile Lateral Force (Static and Time-history)

8.2.2.3.4 Pile Moment

Pile moment by both extreme design temperature static analysis (dashed lines) and time-history analysis (solid line) is presented in Figure 8.71. While the temperature range of the extreme design temperature analysis is larger than the time-history analysis, the design static analysis predicts a 4.5% larger pile moment during bridge expansion and a 14.5% larger pile moment during bridge contraction. The time history analysis pile moment fluctuates within the pile moment bounds established by the extreme design temperature static analysis.

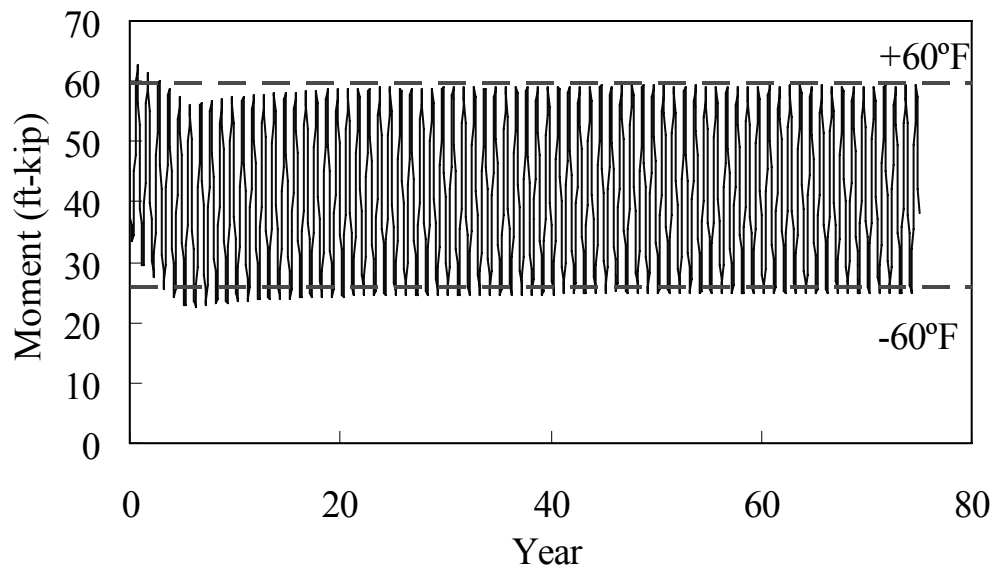


Figure 8.71: Example 2: 2D Analysis - Pile Moment (Static and Time-history)

8.2.2.3.5 Pile Head Displacement

Pile head displacement by both extreme design temperature static analysis (dashed lines) and time-history analysis (solid line) are presented in Figure 8.72. Although the extreme design temperature range is larger than time-history analysis, the time-history analysis results in a larger pile head displacement.

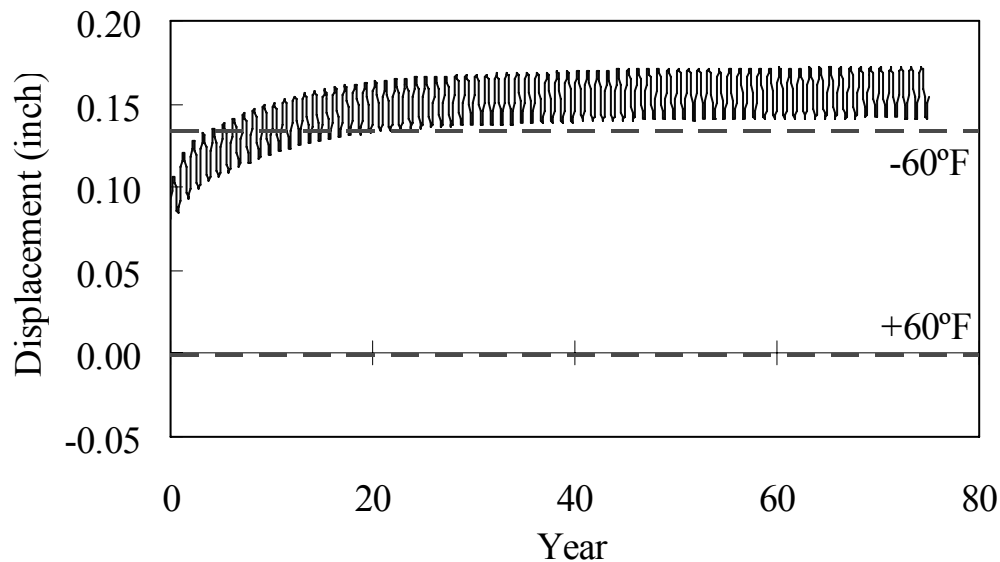


Figure 8.72: Example 2: 2D Analysis— Pile Head Displacement (Static and Time-history)

8.2.3 Example 2: Three-dimensional Analysis Model

Three dimensional numerical simulations offer increased predictive accuracy over two-dimensional simulations. In addition, individual element response to load is available from the 3D analysis rather than grouped response, as in a 2D analysis. Transverse effects are also determined with a 3D simulation due to the added third, transverse dimension to the model. The methodology presented here permits the incorporation of individual bridge elements and the respective material and geometric properties through a demonstrated effective 3D model approach using the commercially available, general analysis program ANSYS. The example 2, 3D analysis evaluates two separate loading cases that consist of the AASHTO extreme temperature rise (+60°F) and extreme temperature fall (-60°F). Any other thermal loading may be applied to the 3D, however.

The example 2, 3D ANSYS schematic model in isometric view is presented in Figure 8.73. Each of the four steel plate girders is represented using ANSYS BEAM189

elements. At the mid-point of the 9-inch bridge deck thickness are ANSYS SHELL63 elements, which have 6 degrees of freedom at each of four corner nodes. To connect the deck to the four girders, ANSYS rigid link MPC184 elements are included at a longitudinal spacing equal to 2 ft. The connection of girders and deck accomplishes the effects of a composite section as is intended in the original design. Abutment piles are included in the 3D model with ANSYS BEAM189 elements defined with the pile HP12×74 cross section. Soil-pile interaction springs modeled using ANSYS COMBIN39 elements spaced at the maximum of 1 ft are included along the full height of each pile. The abutment and back-wall elements are modeled using ANSYS SHELL63 with a maximum of 1 ft side dimension. Abutment-to-backfill interaction is represented with ANSYS COMBIN39 elements nonlinear springs. Bridge diaphragms are included in the 3D model using BEAM189 elements. An isometric view of the completed solid ANSYS 3D numerical model with actual cross sections of each member of the bridge is presented in Figure 8.74.

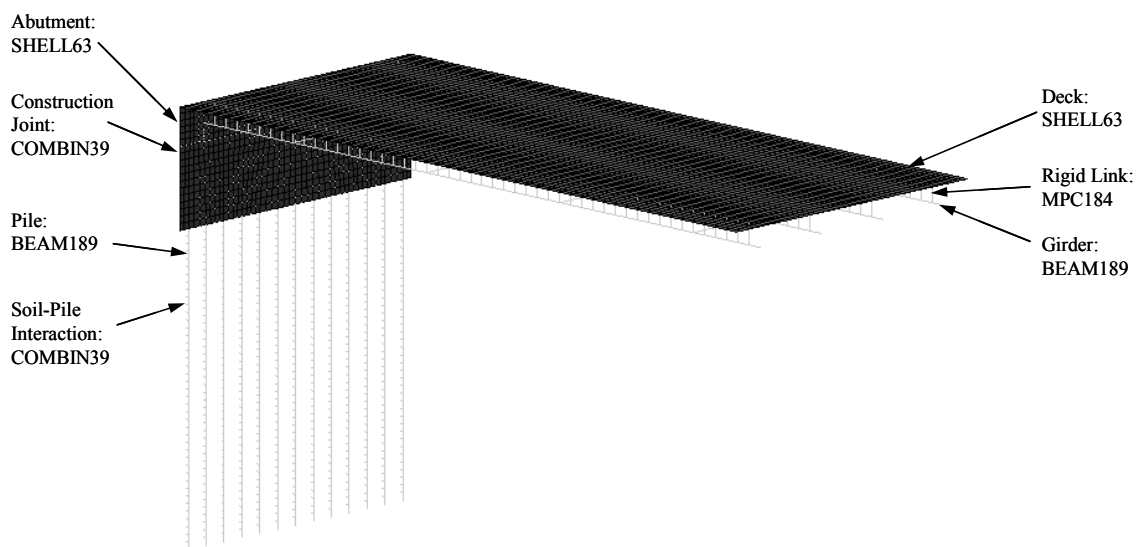


Figure 8.73: Example 2 3D Schematic ANSYS Bridge Model – Isometric View.

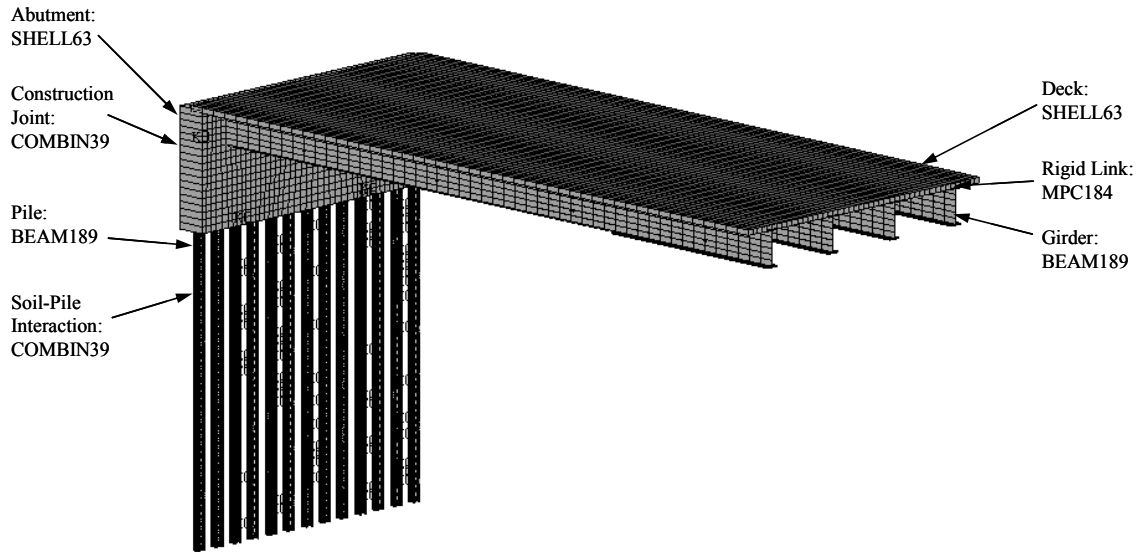


Figure 8.74: Example 2 Solid 3D Bridge Model – Isometric View

Bridge load includes the superstructure temperature fluctuation, temperature gradient, and backfill pressure. As with the 2D simulation, the thermal loading model developed on the basis of actual measurements is utilized for the 3D model. However, a time-history analysis with the 3D numerical model is not practical due to unmanageable computing time and memory demand; therefore, a static analysis under design level thermal loads is performed.

8.2.3.1 Bridge Components

Each bridge component and its material and geometric definition are described in detail in the following sections to permit development of future models for other IABs. The discussion includes girder and deck, abutment/backwall, construction joint, piles, and soil springs and analysis results.

8.2.3.1.1 Girder and Deck

The bridge girders are modeled using the ANSYS 3D beam element BEAM189 based on the steel plate girder cross section in Figure 8.52. Both positive flexure and negative flexure section geometry and properties are presented in Figure 8.75 as computed by ANSYS. The 9-inch concrete deck is modeled using the solid element SHELL63 that has both bending and membrane capabilities. Girder yield strength is specified as $F_y = 50$ ksi and concrete deck 28-day concrete strength is specified as $f'_c = 4,000$ psi. The elastic modulus of steel is specified as 29,000 ksi and the elastic modulus of concrete deck is computed using the widely accepted AASHTO and ACI formula:

$$E_c = 33000w_c^{1.5}\sqrt{f'_c} \quad (8.1)$$

resulting in E_c for deck equal to 3,640 ksi.

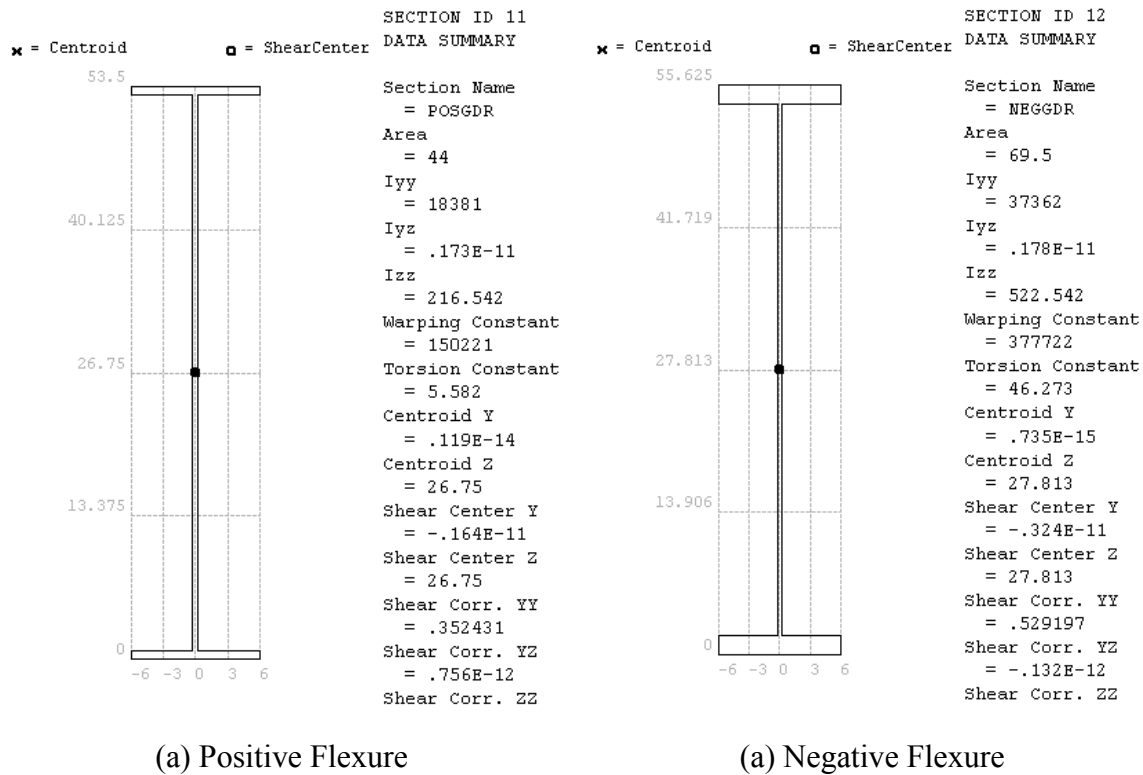


Figure 8.75: Cross Section of Steel Plate Girder (units are inches).

Based on AASHTO LRFD recommendations, the thermal expansion coefficient for structural steel is $6.5\text{E-}6$ and deck concrete is $6.0\text{E-}6$ in/in/ $^{\circ}\text{F}$.

To model the bridge girder and deck composite section, ANSYS rigid link MPC184 elements are included to connect the girder and deck. This is necessary because the geometric center of the slab and the girder are offset in the model, requiring a connection that enforces compatible displacements, three translational and three rotational. Details of the rigid link connection are presented in Figure 8.76. Each girder element and deck element is located at its respective geometric center, as shown in the figure. The rigid link, which is a multi-point constraint element, connects the girder and deck at 2-ft intervals, forcing displacement compatibility and, therefore, composite behavior.

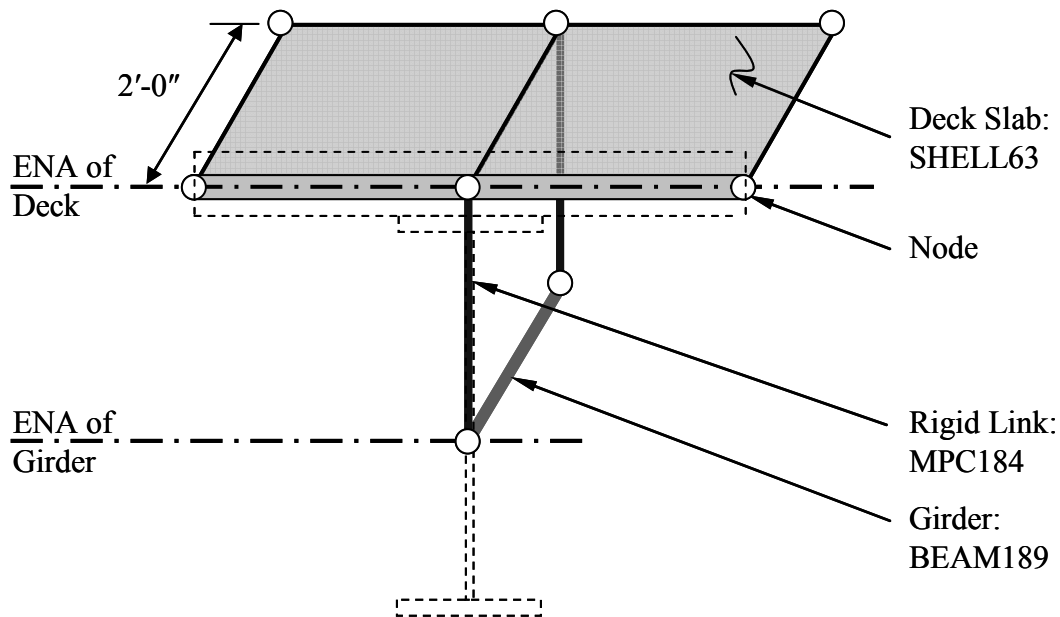


Figure 8.76: Girder and Deck Slab Connection

8.2.3.1.2 Abutment/Backwall

Both the abutment (or pile cap) and back-wall (or end diaphragm) are modeled using ANSYS solid element SHELL63. The full height of the abutment and back-wall are

modeled with the SHELL63 element located at the abutment centerline. Each SHELL 63 element is meshed at 1 ft in both directions to increase accuracy and to facilitate connections of abutment elements to back-wall, girder, and deck elements. The model element assembly of the abutment and back-wall is shown in Figure 8.77, viewed from the backfill side.

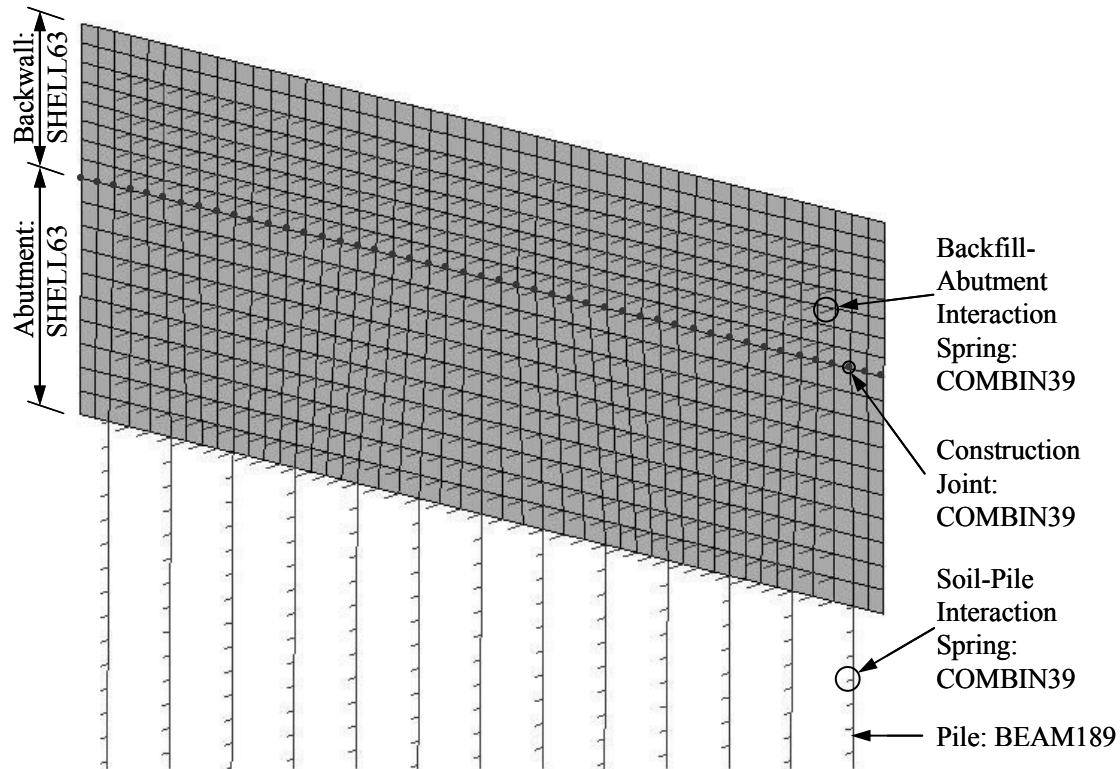


Figure 8.77: Example 2 3D Abutment and Back-wall – Viewed from Backfill

Normally higher-strength concrete is used for the back-wall concrete as compared to abutment concrete because the back-wall is placed with the deck. Example 2 bridge specifications are for 28-day compressive strength concrete equal to 4,000 psi and 3,000 psi at the back-wall and abutment, respectively, resulting in computed elastic moduli for the back-wall equal to 3,640 ksi and for abutment equal to 3,160 ksi.

Two nodes (separate but coincident) are placed at the construction joint between the back-wall and the abutment and are connected by the ANSYS joint element COMBIN39. The properties of this joint element are discussed in the following section.

8.2.3.1.3 Construction Joints

Rotational stiffness of the back-wall to abutment joint is modeled using the ANSYS COMBIN39 element, as presented in Section 5.2.4 of this report. All translations and rotations except z-axis rotation are coupled where rotation is defined by COMBIN39. A graphical illustration of the construction joint modeling, showing all nodes and elements, is presented in Figure 8.78. The computed construction joint rotational stiffness is based on the PennDOT standard detail BD-667 that specifies #5 “U” reinforcing bars at 9 inches. The imbalance of reinforcement between the backfill face and the front face is also considered in the definition of the joint element. For the expansion case, moment-rotation properties are computed:

For backfill side, rebar area is:

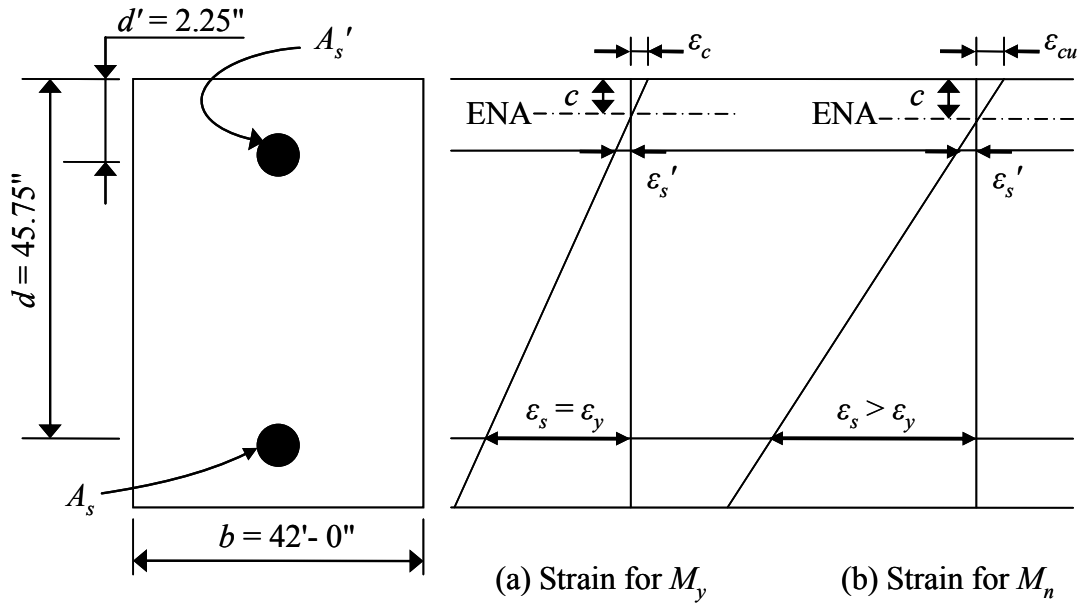
$$\begin{aligned}
 A_s &= (\text{\#5 rebar area}) \times (\text{number of rebars}) \\
 &= (\text{\#5 rebar area}) \frac{(\text{abutment width})}{(\text{rebar spacing})} = (0.31 \text{ in}^2) \frac{42'}{9''} \\
 &= (0.31 \text{ in}^2) \times (56 \text{ rebars}) \\
 &= 17.36 \text{ in}^2
 \end{aligned}$$

For front face side, rebar area is:

$$A_s' = (\text{\#5 rebar area})(\text{number of rebars})$$

$$\begin{aligned}
&= (\#5 \text{ rebar area}) \frac{(\text{abutment width}) - (\text{number of girders})(\text{girder width})}{(\text{rebar spacing})} \\
&= (0.31 \text{ in}^2) \frac{(42') - (4)(26'')}{9''} \\
&= (0.31 \text{ in}^2)(45 \text{ rebars}) \\
&= 13.95 \text{ in}^2
\end{aligned}$$

Based on the specified abutment reinforcing, two bending capacities of (1) yielding moment (M_y) and (2) ultimate moment (M_n) are evaluated and strain compatibility is presented in Figure 8.78.



d = distance from the extreme fiber to the centroid of tension reinforcement
 d' = distance from the extreme fiber to the centroid of compression reinforcement
 A_s = tension reinforcement area
 A_s' = compression reinforcement area
 b = beam width
 ϵ_c = strain in concrete at the extreme compressive fiber corresponding stress f_c
 ϵ_{cu} = ultimate concrete compression strain (= 0.003) corresponding stress f_c'
 ϵ_s = strain in tension reinforcement corresponding stress f_s
 ϵ_s' = strain in compression reinforcement corresponding stress f_s'
 ϵ_y = yielding strain of steel rebars (= 0.00207)

Figure 8.78: Strains in Doubly Reinforced Beam

The distance between the ENA and the extreme compressive fiber, c , for yielding capacity M_y is computed as follows:

From strain compatibility in Figure 8.78, tensile forces, T , are:

$$\begin{aligned} T &= A_s f_y + A_s' f_s' = A_s f_y + A_s' E_s \varepsilon_s' = A_s f_y + A_s' E_s \left(\frac{\varepsilon_y (d' - c)}{(d - c)} \right) \\ &= (17.36 \text{ in}^2)(60 \text{ ksi}) + (13.95 \text{ in}^2)(29000 \text{ ksi}) \left(\frac{0.00207(2.25 \text{ in} - c)}{45.75 \text{ in} - c} \right) \end{aligned}$$

Similarly, compressive force, C , is:

$$C = \frac{1}{2} f_c c b = \frac{1}{2} \left(\frac{c}{d - c} f_y \right) b = \frac{1}{2} \left(\frac{c}{45.75 \text{ in} - c} (60 \text{ ksi}) \right) (42 \text{ ft})$$

From $C = T$,

$$c = 1.75 \text{ inches and } \varepsilon_c = c \frac{\varepsilon_y}{d - c} = 0.000082 < \varepsilon_{cu} = 0.003.$$

Thus, $M_y = A_s f_y (d - c) + A_s' f_s' (d' - c) = \underline{550,000 \text{ ft-kips}}$

Curvature (ϕ) is computed as:

$$\phi = \frac{\varepsilon_c}{c} = 0.000047$$

Based on half the minimum development length, l_d , rotation (θ) is computed as:

$$\theta = \phi \cdot l_d = (0.000047)(8 \text{ inches}) = \underline{0.00038 \text{ radians}}$$

For the nominal moment capacity, M_n , ultimate concrete strain (ε_{cu}) is used in the calculation:

$$T = A_s f_y + A_s' f_s' = A_s f_y + A_s' E_s \varepsilon_s' = A_s f_y + A_s' E_s \left(\frac{\varepsilon_{cu} (d' - c)}{c} \right)$$

$$= (17.36 \text{ in}^2)(60 \text{ ksi}) + (13.95 \text{ in}^2)(29000 \text{ ksi}) \left(\frac{0.003(2.25 \text{ in} - c)}{c} \right)$$

Similarly, the compressive force, C , is:

$$C = 0.85 f'_c b (\beta_1 c) = 0.85 (3 \text{ ksi}) (42 \text{ ft}) (0.85 \times c)$$

From $C = T$,

$$c = 1.50 \text{ inches and } \varepsilon_c = \varepsilon_{cu} = 0.003.$$

$$\text{Thus, } M_n = A_s f_y (d - c) + A'_s f'_s (d' - c) = \underline{558,000 \text{ ft-kips}}$$

Curvature (ϕ) is computed as:

$$\phi = \frac{\varepsilon_c}{c} = 0.00199$$

Based on half the minimum development length, l_d , rotation (θ) is computed as:

$$\theta = \phi \cdot l_d = (0.00199)(8 \text{ inches}) = \underline{0.0159 \text{ radian}}$$

For the bridge contraction case, a similar computation can be performed exchanging A_s and A'_s . The moment-rotation curve in Figure 8.79 is obtained.

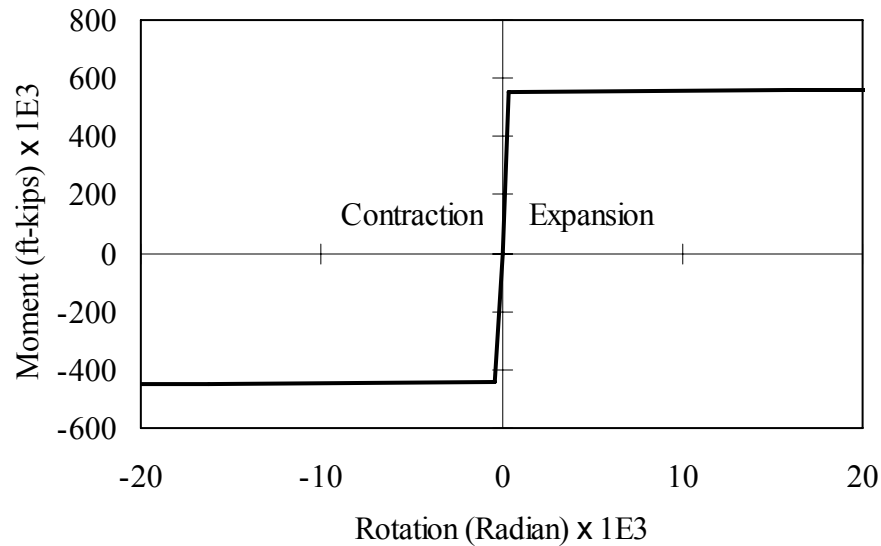


Figure 8.79: Moment-Rotation Curve

An average transverse distance (z-axis direction in Figure 8.80) between two adjacent nodes along the construction joint is computed. The foregoing total doubly-reinforced moment-to-rotation property of the construction joint is evenly distributed at each node pair based on the computed average distance.

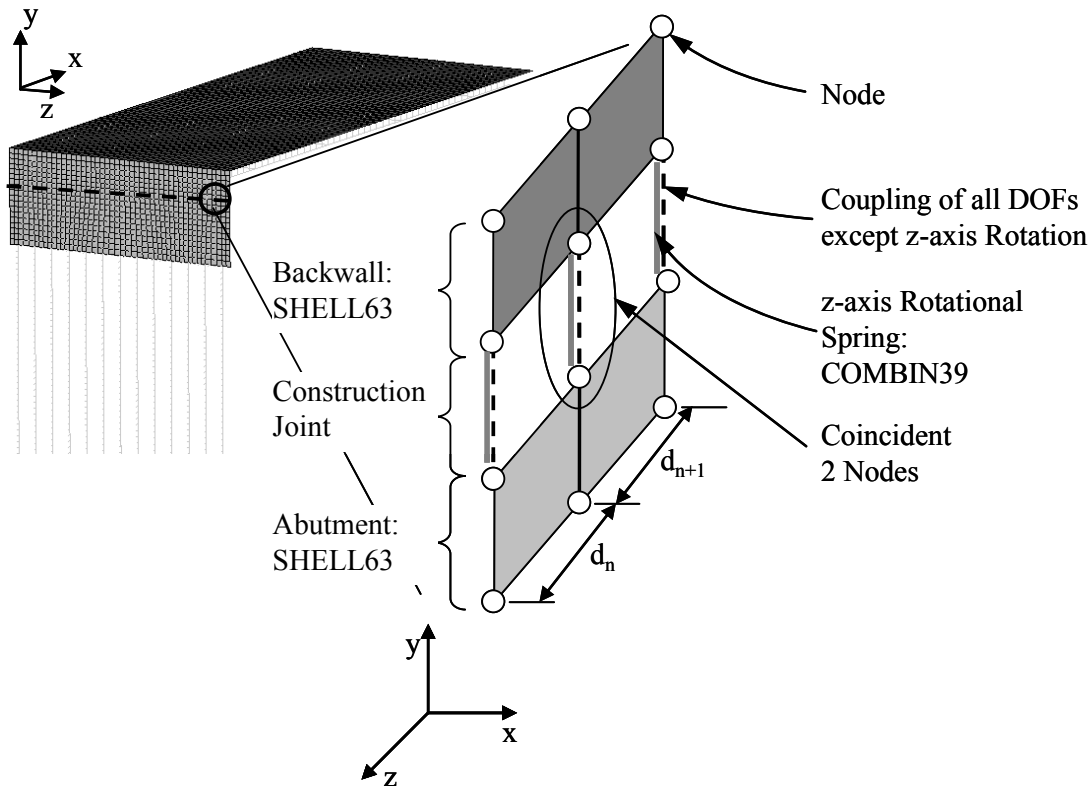


Figure 8.80: Example 2 Abutment to Back-wall Construction Joint Modeling
(Note: All nodes are coincident at construction joints)

8.2.3.1.4 Pile Foundations

Weak axis oriented steel HP12×74 piles are modeled using ANSYS beam elements BEAM189 and soil-pile interaction is modeled using nonlinear spring elements COMBIN39. For beam elements, the pile section and computed properties provided in Figure 8.81 are used in the example 2, 3D model.

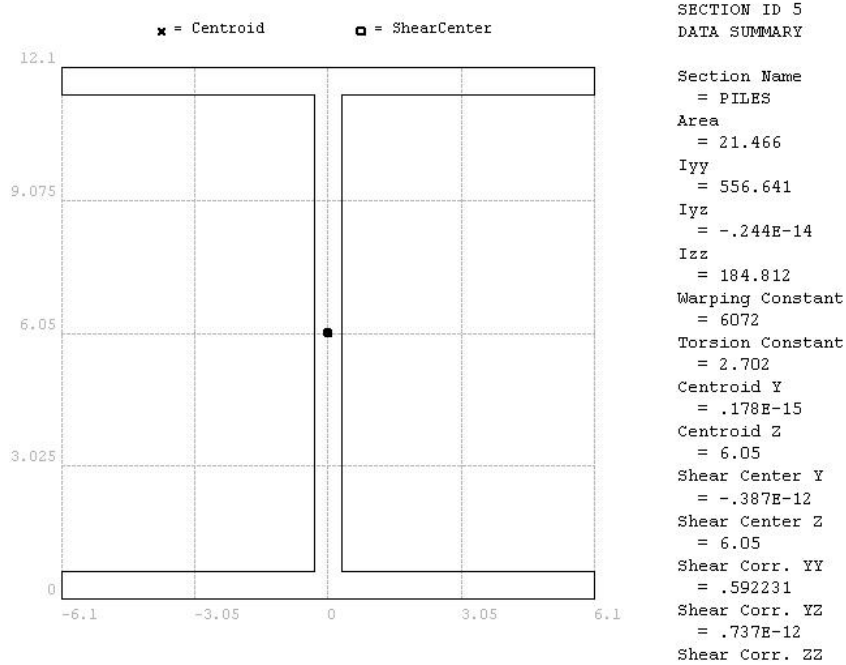


Figure 8.81: HP12×74 Foundation Pile Section

A total of thirteen HP12×74 piles by 30 ft long are used in this example 2, 3D model as presented in Figure 8.81. The specified soil unit weight, $\gamma = 121$ pcf, undrained shear strength (c) = 17.5 psi, and $\varepsilon_{50} = 0.008$. The soil-pile interaction is represented by a Winkler spring using ANSYS COMBIN39 elements developed on the basis of p - y curves. The same p - y curve equations in Equations 5.3 and 5.4 are used to generate force-displacement properties at each depth as shown in Figure 8.82:

$$p = 0.5 p_u \left(\frac{y}{y_{50}} \right)^{1/4} \quad (5.3)$$

$$p_u = \min \left\{ p_{uf} = 9cD, \quad p_{uw} = \left(3 + \frac{\gamma'}{c} X + \frac{J}{D} X \right) cD \right\} \quad (5.4)$$

For this 3D example, a p - y curve at each depth at a 1-ft increment is computed.

Alternatively, commercial programs such as COM624P and Lpile can directly generate p -

p -y curves at a wide range of soil conditions and depths. The COMBIN39 springs are distributed along the full depth of the pile, spaced at 1'-0". The spring element lateral force versus lateral displacement properties at a given depth include the tributary area (1'-0" tributary depth \times pile effective diameter $b_f = 12.1$ ") (see Figure 8.82) of the spring at each location.

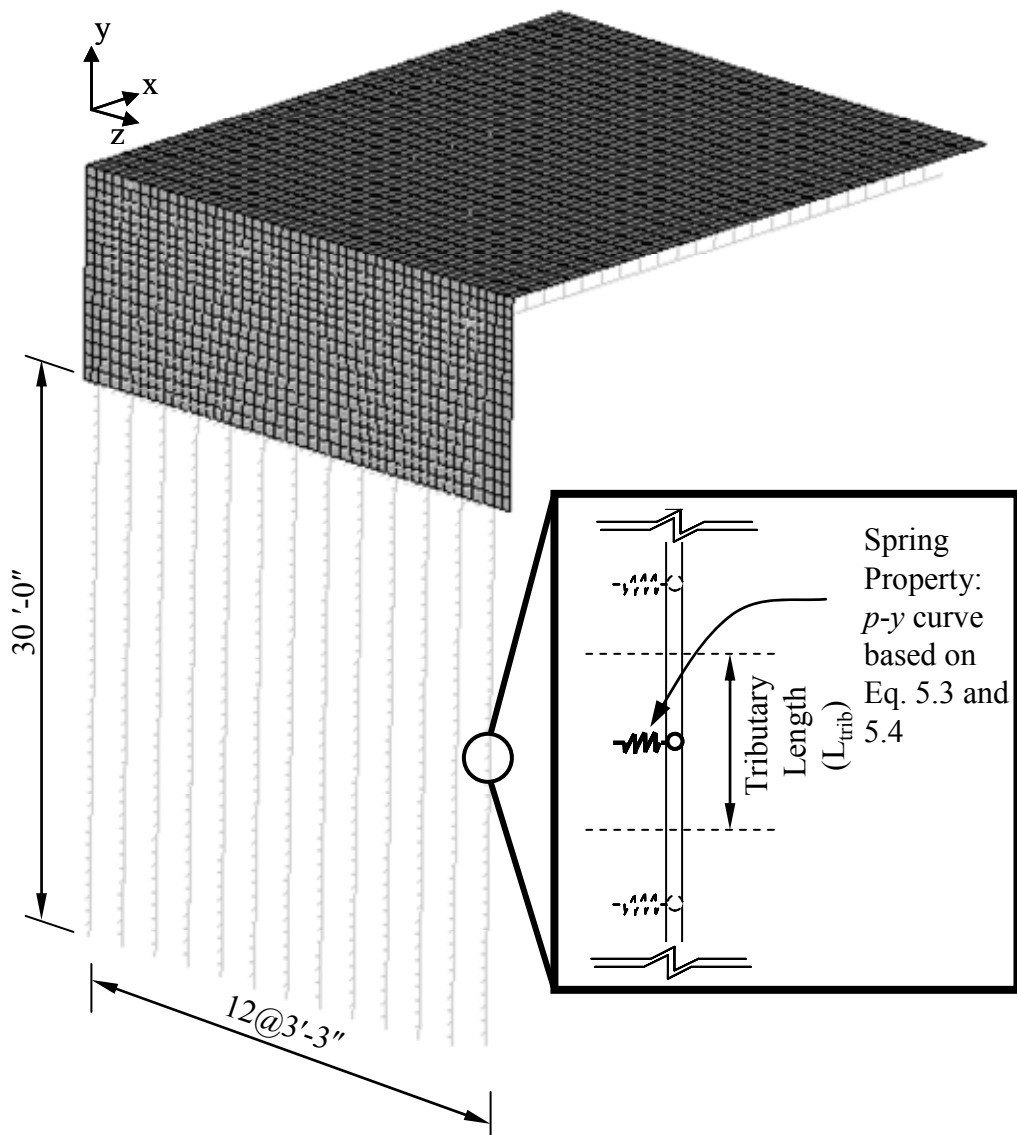


Figure 8.82: Foundation Pile Section Soil Spring Definition.

8.2.3.1.5 Miscellaneous Components

The mid-span bridge diaphragm is coincident with the bridge transverse axis of symmetry and is not explicitly modeled. A boundary condition in a single-span bridge is applied at the bridge symmetry centerline. At the transverse axis of symmetry the x (longitudinal) and z (transverse) translations and y (in deck plane twisting) and z (girder strong axis bending) rotations are restrained. Piles are driven into bedrock and vertical translation is restrained at the pile tips. To expedite numerical computation convergence, z-axis translation is provided from pile tip to the characteristic length, l_c .

$$l_c = \sqrt[4]{\frac{4E_p I_p}{K}} \quad (7.1)$$

$$l_c = \sqrt[4]{\frac{4(29000 \text{ ksi})(186 \text{ in}^4)}{1000 \text{ psi}}} = 68 \text{ inches} \approx 6 \text{ ft}$$

If pile head displacements in the z direction are expected, the same p - y curve description in Section 8.2.3.1.4 of this report should be employed.

8.2.3.2 Loads

The loads applied in the example 2, 3D model include superstructure temperature load, temperature gradient, and backfill pressure. Time-dependent loads are not considered due to the steel girder material. Each load case is described in the subsequent sections.

8.2.3.2.1 Temperature Load

The superstructure thermal load definition for this example is taken from AASHTO LRFD (2007): 0°F to 120°F for steel and 10°F to 80°F for concrete. PennDOT DM-4

Appendix 1.2.7.4 (2007) describes extreme temperature loads for steel bridges as a 100°F temperature rise or fall, resulting in a range equal to 200°F. Monitoring conducted under the present study revealed that an ambient temperature rise or fall equal to 100°F is very conservative. Thus, a temperature rise and fall of 100°F is extremely conservative. Based on the example procedure described in *AASHTO Guide Specifications: Thermal Effects in Concrete Bridge Superstructures* (1989), the extreme temperature for bridge expansion and contraction is 60°F increase and 60°F decrease for the current example bridge. Therefore, a uniform temperature load equal to a 60°F increase and 60°F decrease is applied to the bridge girders and deck.

8.2.3.2.2 Temperature Gradient

Based on AASHTO multi-linear temperature gradient, an equivalent temperature gradient is computed. Equivalent temperature loads by Equation 5.14 and 5.15 are computed. AASHTO LRFD 3.12.3 provides a temperature gradient model for Pennsylvania as presented in Figure 8.83.

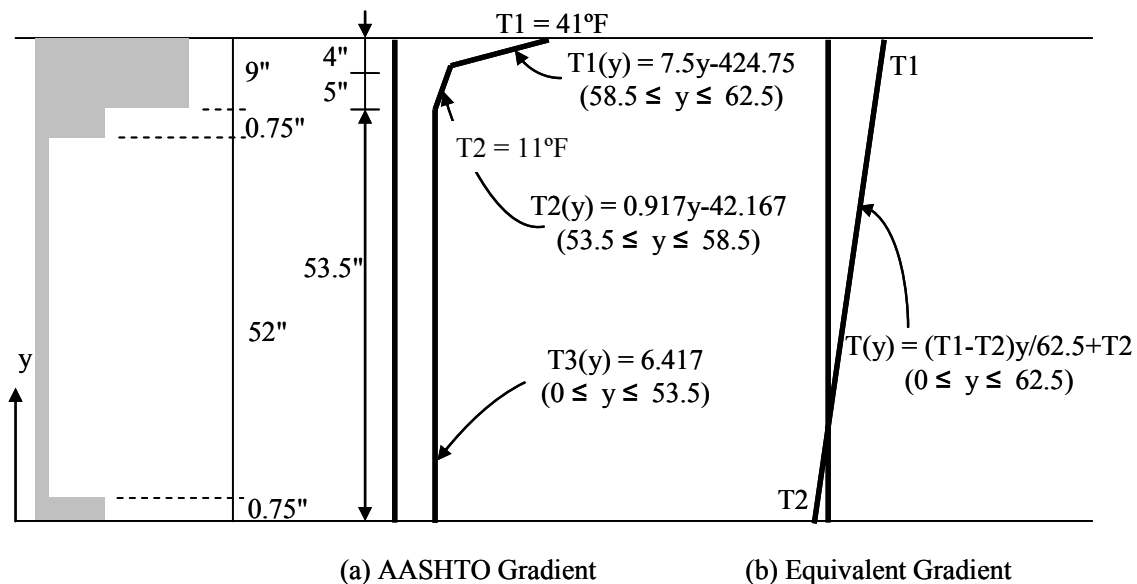


Figure 8.83: Temperature Gradient for BT72 Girder in Pennsylvania

Axial force can be obtained as:

$$\begin{aligned}
 P &= \int \sigma_t(y)b(y)dy = \int E\alpha T(y)b(y)dy \\
 &= \int_0^{0.75} (29000 \text{ ksi}) (6.5 \times 10^{-6} / ^\circ \text{ F}) [0.6417^\circ \text{ F}] (12'') dy \\
 &\quad + \int_{0.75}^{52.75} (29000 \text{ ksi}) (6.5 \times 10^{-6} / ^\circ \text{ F}) [0.6417^\circ \text{ F}] (0.5'') dy \\
 &\quad + \int_{52.75}^{53.5} (29000 \text{ ksi}) (6.5 \times 10^{-6} / ^\circ \text{ F}) [0.6417^\circ \text{ F}] (12'') dy \\
 &\quad + \int_{53.5}^{58.5} (29000 \text{ ksi}) (6.5 \times 10^{-6} / ^\circ \text{ F}) [0.917y - 42.167] (^\circ \text{ F}) (14.17'') dy \\
 &\quad + \int_{58.5}^{62.5} (29000 \text{ ksi}) (6.5 \times 10^{-6} / ^\circ \text{ F}) [7.5y - 427.75] (^\circ \text{ F}) (14.17'') dy = 447 \text{ kips}
 \end{aligned}$$

Similarly, moment can be obtained as:

$$\begin{aligned}
 M &= \int \sigma_t(y)b(y)ydy = \int E\alpha T(y)b(y)ydy \\
 &= \int_0^{0.75} (29000 \text{ ksi}) (6.5 \times 10^{-6} / ^\circ \text{ F}) [0.6417^\circ \text{ F}] (12'') ydy \\
 &\quad + \int_{0.75}^{52.75} (29000 \text{ ksi}) (6.5 \times 10^{-6} / ^\circ \text{ F}) [0.6417^\circ \text{ F}] (0.5'') ydy \\
 &\quad + \int_{52.75}^{53.5} (29000 \text{ ksi}) (6.5 \times 10^{-6} / ^\circ \text{ F}) [0.6417^\circ \text{ F}] (12'') ydy \\
 &\quad + \int_{53.5}^{58.5} (29000 \text{ ksi}) (6.5 \times 10^{-6} / ^\circ \text{ F}) [0.917y - 42.167] (^\circ \text{ F}) (14.17'') ydy \\
 &\quad + \int_{58.5}^{62.5} (29000 \text{ ksi}) (6.5 \times 10^{-6} / ^\circ \text{ F}) [7.5y - 427.75] (^\circ \text{ F}) (14.17'') ydy = 2,073 \text{ ft-kips}
 \end{aligned}$$

Based on the obtained axial force and moment, an equation for P_{eq} is constructed:

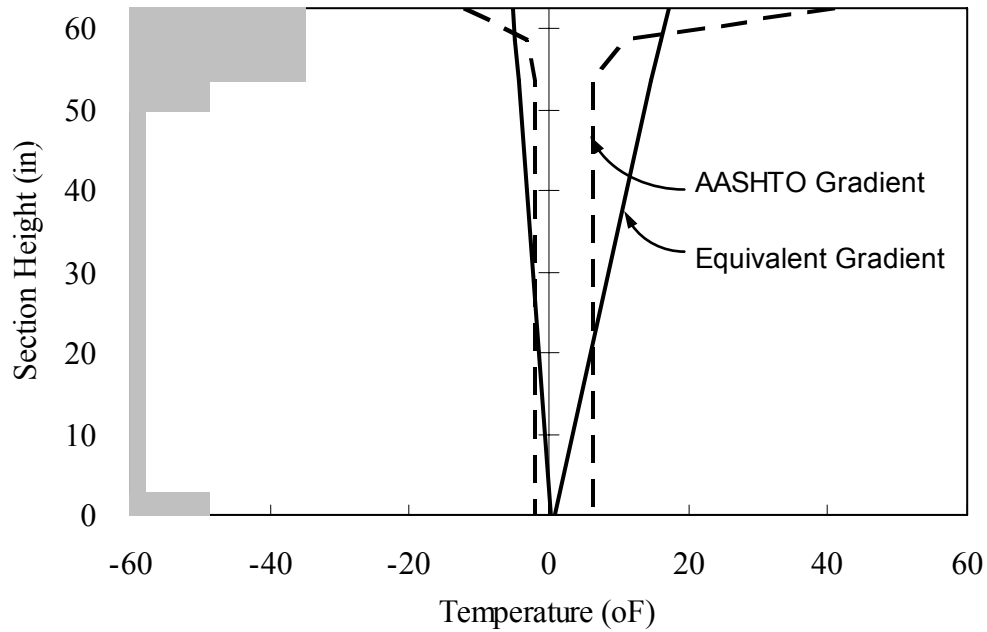
$$\begin{aligned}
 P_{eq} &= \int \sigma_t(y)b(y)dy = \int E\alpha T(y)b(y)dy \\
 &= \int_0^{0.75} (29000 \text{ ksi}) (6.5 \times 10^{-6} / ^\circ \text{ F}) \left[\frac{T1 - T2}{62.5} y + T2 \right] (12'') dy
 \end{aligned}$$

$$\begin{aligned}
& + \int_{0.75}^{52.75} (29000 \text{ ksi}) (6.5 \times 10^{-6} / ^\circ \text{F}) \left[\frac{T1 - T2}{62.5} y + T2 \right] (0.5'') dy \\
& + \int_{52.75}^{53.5} (29000 \text{ ksi}) (6.5 \times 10^{-6} / ^\circ \text{F}) \left[\frac{T1 - T2}{62.5} y + T2 \right] (12'') dy \\
& + \int_{53.5}^{62.5} (29000 \text{ ksi}) (6.5 \times 10^{-6} / ^\circ \text{F}) \left[\frac{T1 - T2}{62.5} y + T2 \right] (14.17'') dy \\
M_{eq} & = \int \sigma_t(y) b(y) y dy = \int E \alpha T(y) b(y) y dy \\
& = \int_0^{0.75} (29000 \text{ ksi}) (6.5 \times 10^{-6} / ^\circ \text{F}) \left[\frac{T1 - T2}{62.5} y + T2 \right] (12'') y dy \\
& + \int_{0.75}^{52.75} (29000 \text{ ksi}) (6.5 \times 10^{-6} / ^\circ \text{F}) \left[\frac{T1 - T2}{62.5} y + T2 \right] (0.5'') y dy \\
& + \int_{52.75}^{53.5} (29000 \text{ ksi}) (6.5 \times 10^{-6} / ^\circ \text{F}) \left[\frac{T1 - T2}{62.5} y + T2 \right] (12'') y dy \\
& + \int_{53.5}^{62.5} (29000 \text{ ksi}) (6.5 \times 10^{-6} / ^\circ \text{F}) \left[\frac{T1 - T2}{62.5} y + T2 \right] (14.17'') y dy
\end{aligned}$$

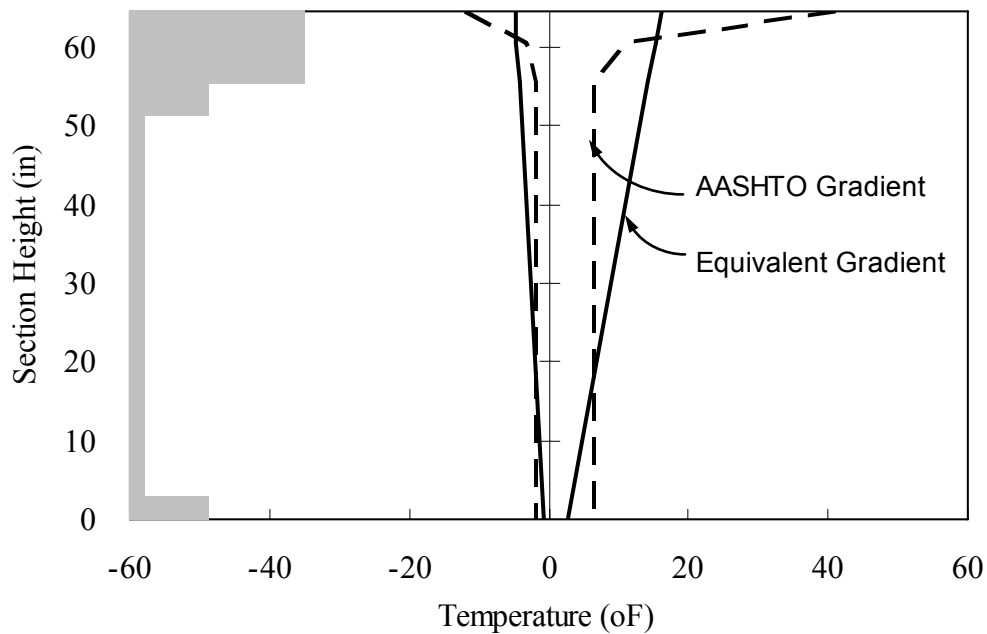
Now, let $P = P_{eq}$ and $M = M_{eq}$, and a trial-and-error procedure yields $T1 = 17.1^\circ\text{F}$ and $T2 = 0.8^\circ\text{F}$. For the negative flexure section, $T1 = 16.4^\circ\text{F}$ and $T2 = 2.3^\circ\text{F}$. Negative gradient is obtained by multiplying the positive gradient by -0.3 to obtain the positive temperature gradient presented in Figure 8.83.

For a steel girder, the equivalent temperature at the top fiber of deck slab is 17.2°F , the temperature at the top fiber of girder is 14.4°F and the temperature at the bottom fiber is 1.57°F . For negative temperature gradient, -5.3°F , -4.4°F and -0.4°F at the top fiber of deck, the top fiber of girder and bottom fiber of girder are applied for the equivalent temperature gradient. The final positive and negative temperature gradients are presented

in Figure 8.84(a) and (b). These temperature gradients are added to the previously discussed uniform temperature increase and decrease.



(a) Positive Flexure Section



(b) Negative Flexure Section

Figure 8.84: Temperature Gradient for Steel Girder and Deck Slab

8.2.3.2.3 Backfill Pressure

Hydrostatic pressure behind the back-wall and abutment must be determined, accounting for the 1'-6" approach slab and 2'-7" wing-walls at both sides as presented in Figure 8.85.

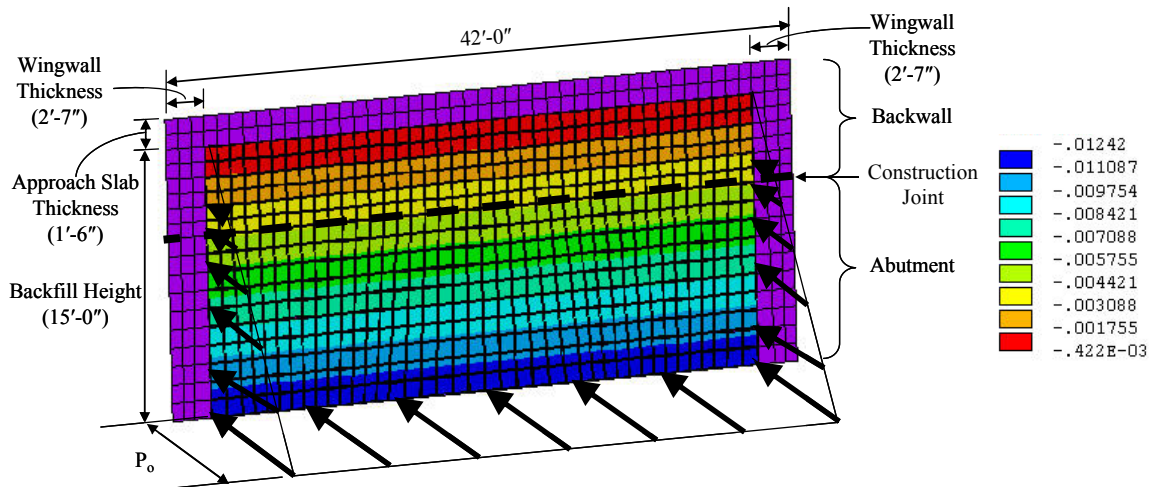


Figure 8.85: Backfill Pressure Contour in Example 2 3D Model

A triangular hydrostatic pressure and abutment-to-backfill interaction springs are clearly identified in Figures 8.86 and 8.87.

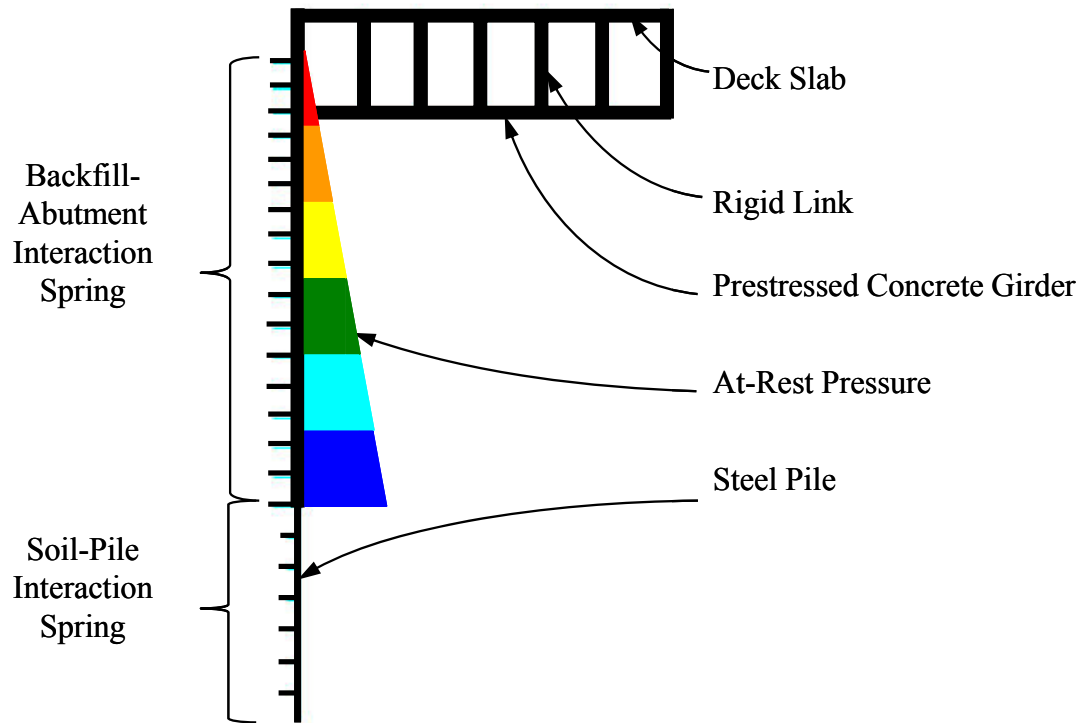


Figure 8.86: Example 2 3D Analysis Abutment Backfill Pressure

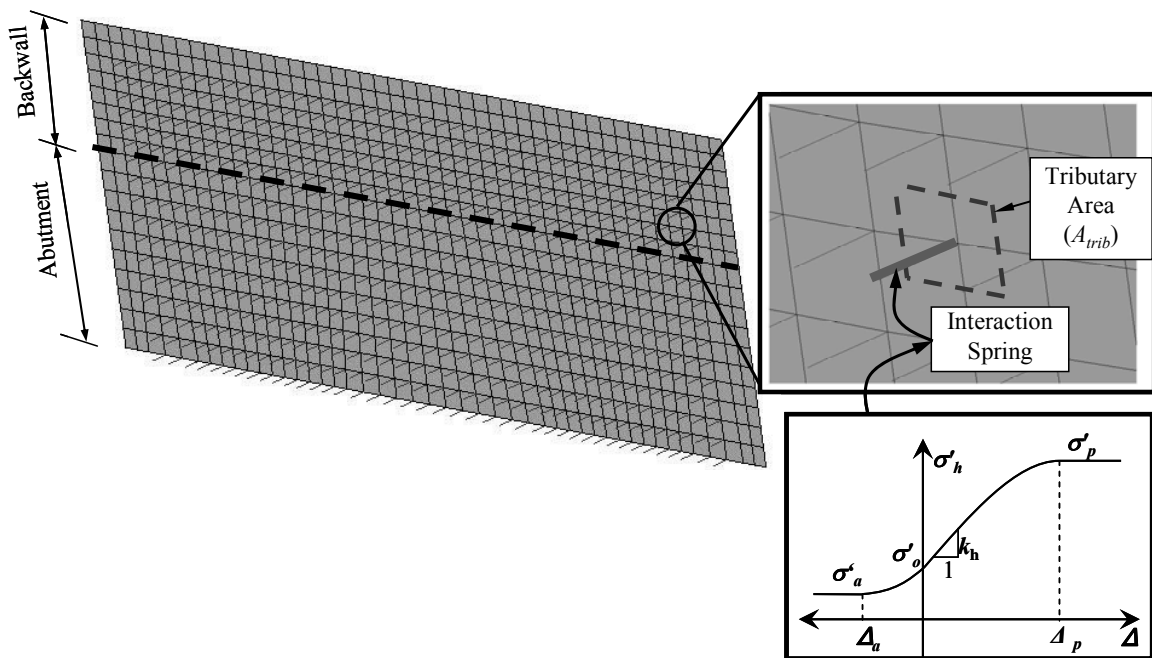


Figure 8.87: Example 2 3D Analysis Backfill Pressure Tributary Area for Spring

To determine the backfill pressure, each soil spring tributary area is computed as presented in Figure 8.87. At-rest pressure, active pressure, and passive pressure at each spring element location are computed as:

$$\begin{aligned}
 P_o &= K_o \gamma' z A_{trib} = \gamma' z A_{trib} \\
 P_a &= K_a \gamma' z A_{trib} = \frac{1 - \sin \phi_f}{1 + \sin \phi_f} \gamma' z A_{trib} \\
 P_p &= K_p \gamma' z A_{trib} = \frac{1 + \sin \phi_f}{1 - \sin \phi_f} \gamma' z A_{trib}
 \end{aligned} \tag{5.7}$$

where K_o , K_a and K_p are at-rest, active and passive coefficients, $\gamma' = 119$ pcf, A_{trib} = tributary area and $\phi_f = 34^\circ$. For each node location on the back-wall and abutment a different z and A_{trib} are computed. For example, at $z = 3$ ft and $A_{trib} = 1.0$ ft²:

$$\begin{aligned}
 P_o &= (119 \text{ pcf})(3 \text{ ft})(1 \text{ ft}^2) = 357 \text{ lb} \\
 P_a &= K_a \gamma' z A_{trib} = \frac{1 - \sin \phi_f}{1 + \sin \phi_f} \gamma' z A_{trib} = \frac{1 - \sin 34^\circ}{1 + \sin 34^\circ} (119 \text{ pcf})(3 \text{ ft})(1.0 \text{ ft}^2) = 101 \text{ lbs} \\
 P_p &= K_p \gamma' z A_{trib} = \frac{1 + \sin \phi_f}{1 - \sin \phi_f} \gamma' z A_{trib} = \frac{1 + \sin 34^\circ}{1 - \sin 34^\circ} (119 \text{ pcf})(3 \text{ ft})(1.0 \text{ ft}^2) = 1260 \text{ lbs}
 \end{aligned}$$

The slope of the spring element response between P_a and P_p is computed from equation 5.1, discussed in Chapter 5 of this report:

$$k_h(z) = k_{ref} \left(\frac{z}{h_{ref}} \right)^{0.5} A_{trib} \tag{5.1}$$

where h_{ref} = reference depth and z = backfill depth. As discussed in Section 5.2.2, $k_{ref} = 0.044$ kci at 4 ft from the bottom of the abutment and is used for this example:

$$k_h(3 \text{ ft}) = (0.044 \text{ kci}) \left(\frac{3 \text{ ft}}{15 \text{ ft} - 4 \text{ ft}} \right)^{0.5} (144 \text{ inches}) = 3.31 \text{ kips/inch}$$

Displacements u_a and u_p corresponding to P_a and P_p are computed as:

$$u_a = \frac{101 \text{ lbs}}{3310 \text{ lbs/inch}} = 0.0305 \text{ inches}$$

$$u_p = \frac{1260 \text{ lbs}}{3310 \text{ lbs/inch}} = 0.381 \text{ inches}$$

Therefore, the example backfill-abutment interaction spring, defined generally in Figure 8.87, is presented in Figure 8.88.

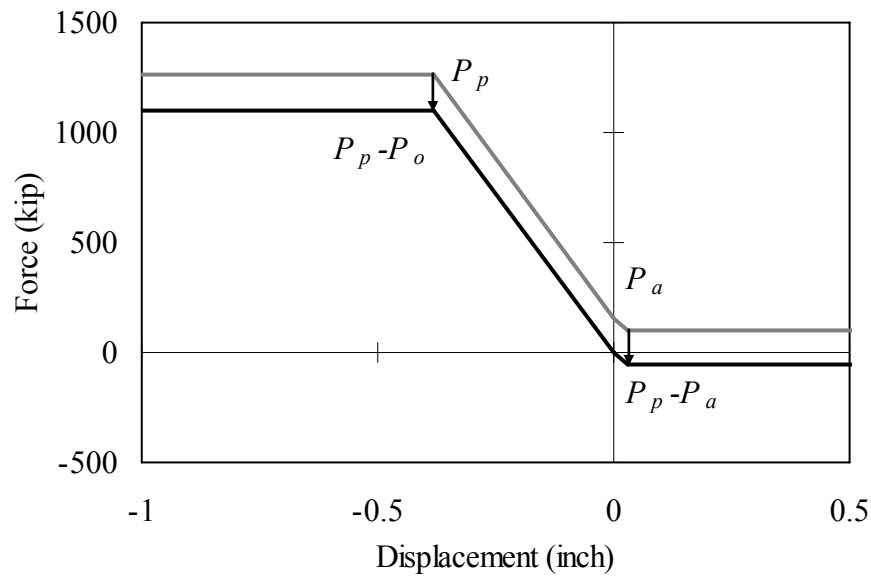


Figure 8.88: Backfill-Abutment Interaction Spring Property

8.2.3.2.4 Time-dependent Loads

The time-dependent effects of concrete creep and shrinkage are not considered in this example because the bridge girder material is structural steel.

8.2.3.3 Example 2: 3D Analysis Results

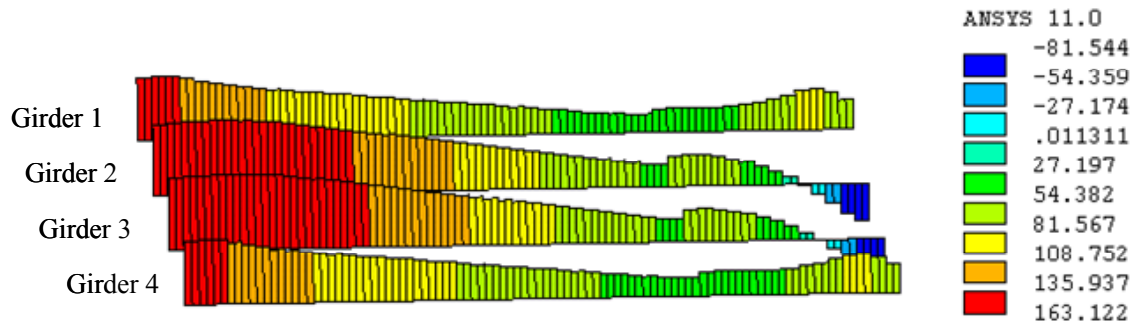
An extreme design static 3D analysis is demonstrated for the example 2 bridge.

Although a time-history analysis is not performed in this example, 3D models are capable

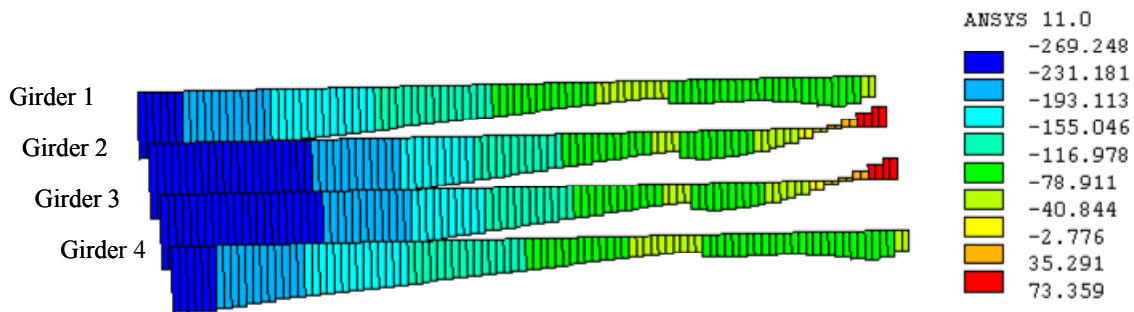
of performing a time-history analysis with a sinusoidal temperature fluctuation load. However, a 3D time-history analysis would require extensive and unmanageable computing time and storage; therefore, this analysis is not demonstrated here. The two loading cases of extreme design temperature are demonstrated based on AASHTO extreme temperature rise (+60°F) and fall (-60°F). For example 2, steel girder time-dependent effects do not exist; therefore, only temperature loading, temperature gradient and backfill pressure are incorporated in the analysis. Girder axial force, girder bending moment, pile lateral force, pile moment, and pile head displacement are presented, using the analysis methods described in the body of this report.

8.2.3.3.1 Girder Axial Force

Girder axial forces predicted by a 3D extreme design temperature static analysis are presented in Figure 8.89 for both (a) bridge contraction and (b) bridge expansion. Axial forces in each girder differ due to the larger interior girder abutment and deck tributary area and the retaining backfill force differences between interior girders and exterior girders. When the bridge contracts, tensile axial forces occur in all girders due to the large thermal coefficient of structural steel. When the bridge expands, significant compressive axial forces develop in the interior girders due to the larger abutment and backfill tributary area as compared to the exterior girders.



(a) Bridge Contraction (All units in kips)

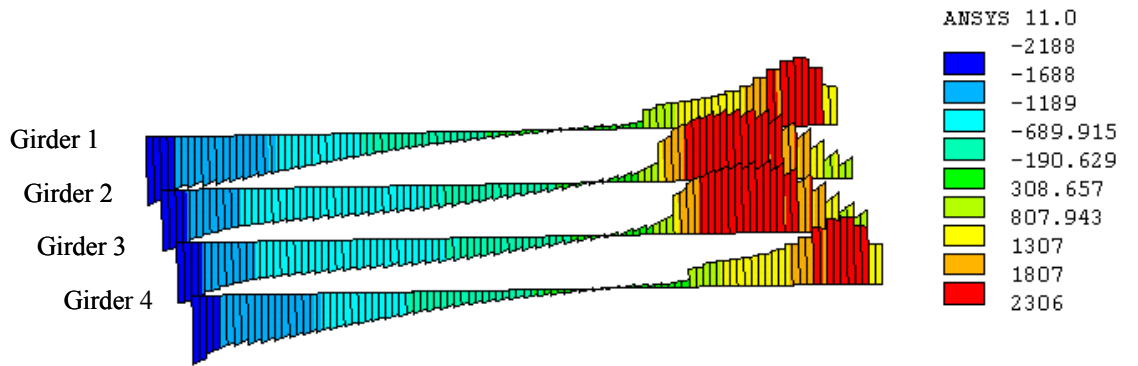


(b) Bridge Expansion (All units in kips)

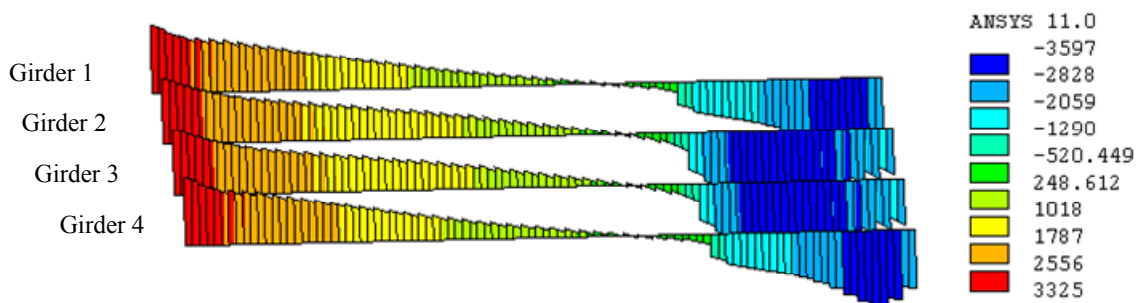
Figure 8.89: Example Bridge 2 3D Analysis Girder Axial Force Comparison

8.2.3.3.2 Girder Bending Moment

Girder bending moments predicted by a 3D extreme design temperature static analysis are presented in Figure 8.90 for both (a) bridge contraction and (b) bridge expansion. Girder moments differ between interior and exterior girders, again due to the difference in abutment and corresponding backfill forces. When the bridge contracts, significant positive and negative moments occur in the interior girders near the interior pier support due to significant differences in tributary backfill forces. When the bridge expands, all four girders are subjected to similar bending moments; however, interior girders are subjected to higher moments due to the larger backfill forces.



(a) Bridge Contraction (All units in-kips)

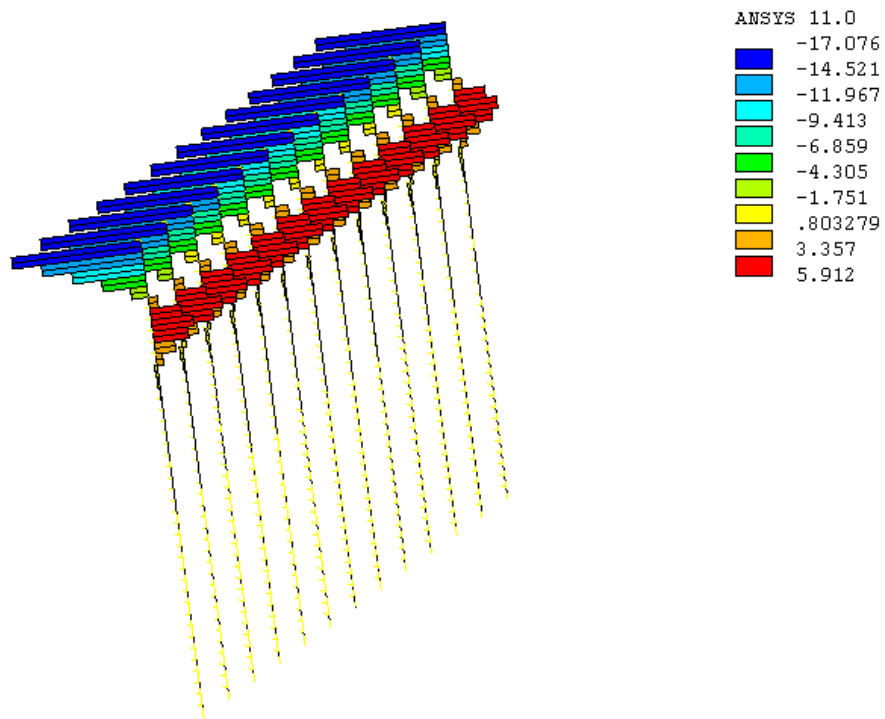


(b) Bridge Expansion (All units in-kip)

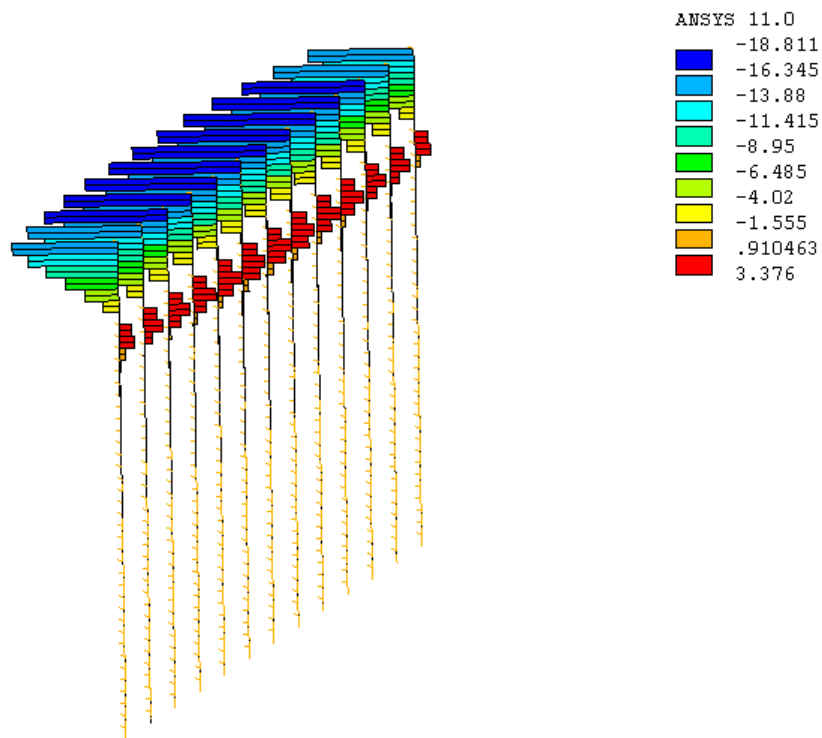
Figure 8.90: Example Bridge 2 3D Analysis Girder Bending Moment

8.2.3.3.3 Pile Lateral Force

The lateral forces on piles predicted by the 3D extreme design temperature static analysis are presented in Figure 8.91 for both (a) bridge contraction and (b) bridge expansion. Pile lateral forces vary with respect to pile depth; when the bridge expands, exterior piles are subjected to larger lateral force compared to interior piles. This is a direct result of the smaller abutment and backfill tributary forces restraining the superstructure movement, resulting in larger forces at this location. Relative displacement and rotation in the exterior piles due to bridge expansion are larger than those of interior piles. All piles are predicted to experience larger lateral forces under expansion as compared to contraction.



(a) Bridge Contraction (All units in kip)

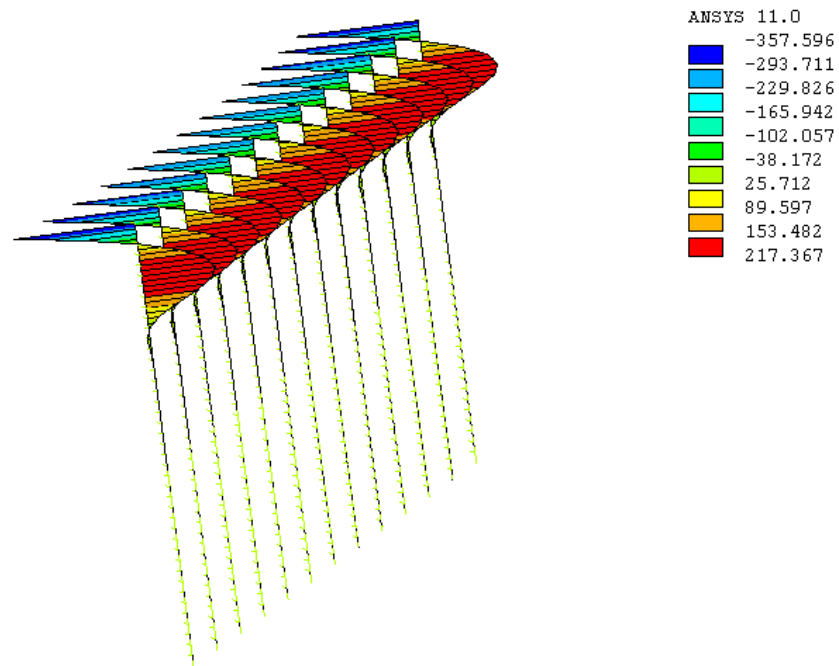


(b) Bridge Expansion (All units in kip)

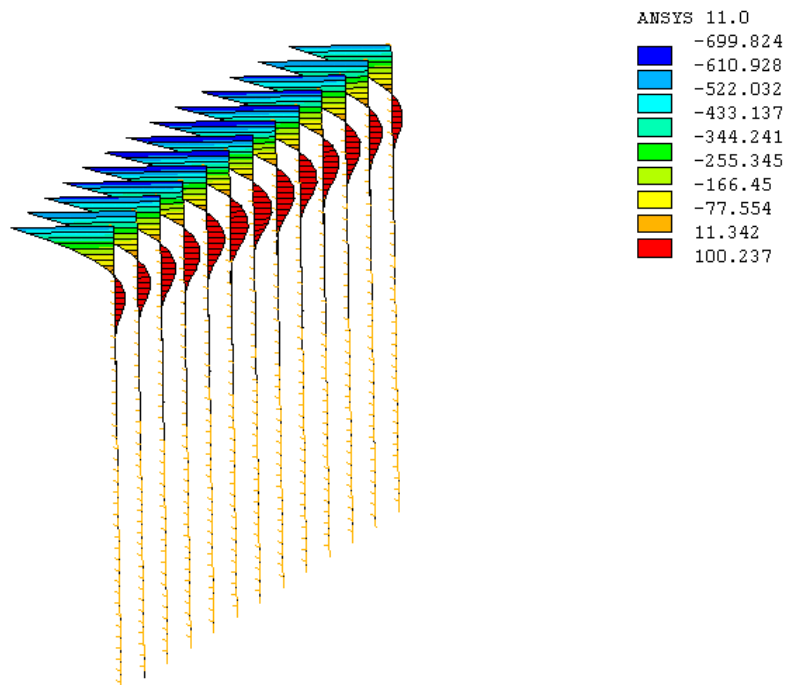
Figure 8.91: Example 2 3D Analysis Model Pile Lateral Force.

8.2.3.3.4 Pile Moment

Pile moments based on the 3D extreme design temperature static analysis are presented in Figure 8.92 for both (a) bridge contraction and (b) bridge expansion. Weak axis bending moments across all piles are very similar and vary with respect to vertical depth. Under superstructure contraction, exterior piles experience larger moments as compared to interior piles, again due to the larger restraint offered by the backfill at this location. Under superstructure expansion, significantly larger pile moments are predicted as compared to the contraction case.



(a) Bridge Contraction (All units in-kips)



(b) Bridge Expansion (All units in in-kip)

Figure 8.92: Example Bridge 2 Pile Moment by 3D Analysis

8.2.3.3.5 Pile Head Displacement

Pile head displacement predicted by the 3D extreme design temperature static analysis is presented in Figure 8.93 for superstructure contraction. Pile head displacements in all piles are very similar for this case. As expected, interior piles experience slightly larger displacements as compared to exterior piles.

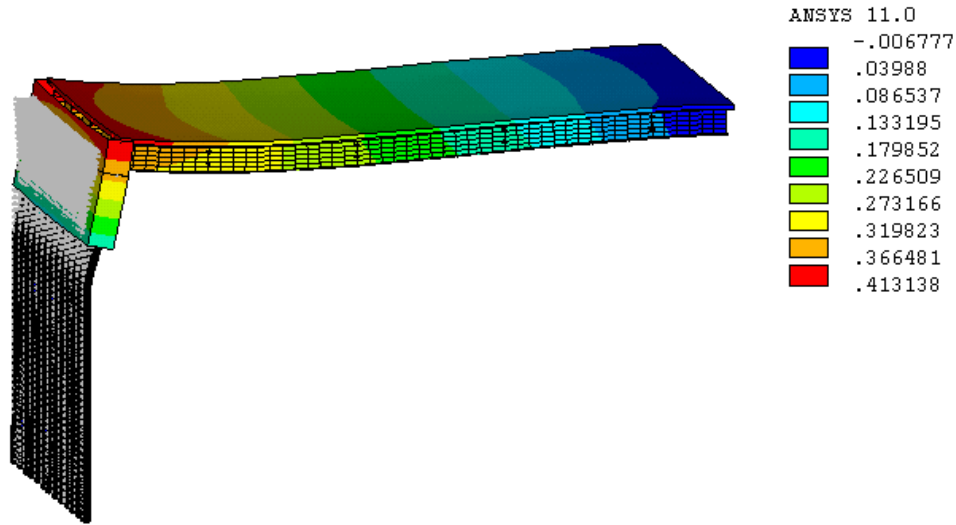


Figure 8.93: Example Bridge 2 Pile Head Displacement by 3D Analysis
(All units in inches)

8.2.4 Example 2 Analysis Results

The Example 2 bridge has been analyzed by the approximate method, the 2D extreme design temperature static analysis method, the 2D time-history analysis method, and the 3D extreme design temperature static analysis method. Results of these four analyses are compared in this section. The extracted results include: (1) girder axial force, (2) girder bending moment, (3) pile lateral force, (4) pile moment, and (5) pile head displacement.

8.2.4.1 Girder Axial Force

Girder axial force results by approximate method (Approx.), 2D time-history analysis (2D-TH), 2D design analysis (2D-DA), and 3D design analysis (3D-DA) are presented in Figure 8.94. Girder compressive axial force predictions range from 20% to 50% lower as compared to the 3D-DA analysis results. The approximate method and both 2D analyses results predict girder average axial force while the maximum compressive axial force from 3D-DA reports a single girder maximum value. When 3D-DA girder axial forces are averaged (see Figure 8.89), the predicted girder axial force is similar to the other analysis results. Similarly, the girder tensile axial force from 3D-DA reports a positive axial force while the approximate method and both 2D analyses do not, due to the averaging effect of a 2D analysis.

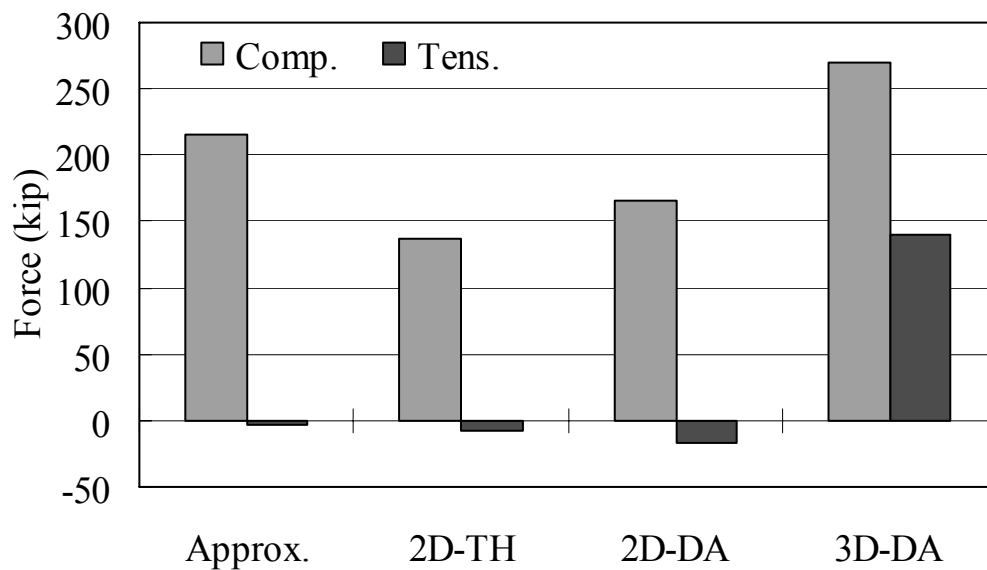


Figure 8.94: Example Bridge 2 Girder Axial Force Comparison

8.2.4.2 Girder Bending Moment

Girder bending moment results predicted by Approx., 2D-TH, 2D-DA and 3D-DA are presented in Figure 8.95. The approximate analysis method, 2D-TH and 2D-DA analyses predicts moments 38% smaller, 28% smaller and 99% larger, as compared to 3D-DA. For negative moment, 3D-DA predicts 384%, 132% and 194% smaller moments. Again, this is due to the fact that the approximate analysis and the 2D analysis necessarily report average moments whereas the 3D reports the maximum moments in any of the four girders.

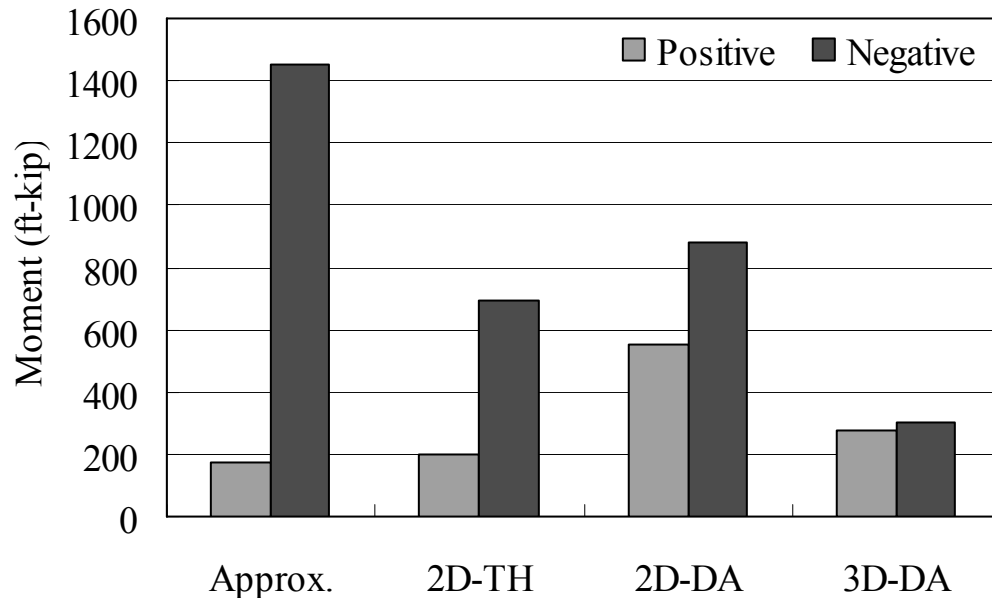


Figure 8.95: Example Bridge 2 Girder Bending Moment Comparison

8.2.4.3 Pile Lateral Force

Pile lateral force results obtained by the Approx., 2D-TH, 2D-DA and 3D-DA are presented in Figure 8.96. Compared to 3D-DA, the Approx. predicts a larger lateral pile force by 41% while 2D-TH and 2D-DA predict smaller lateral pile forces by 3% and 5%.

For comparison purposes, the single pile lateral force, F_{pile} , due to a superstructure-free expansion is computed as:

$$F_{pile} = \frac{12EI\Delta}{L_{pile}^3} = \frac{12EI}{L_{pile}^3}(\alpha \cdot \Delta T \cdot L) \quad (8.2)$$

$$= \frac{12(29000 \text{ ksi})(186 \text{ in}^4)}{(30 \text{ ft})^3} (6 \times 10^{-6} / ^\circ \text{F})(70 ^\circ \text{F}) \left(\frac{200 \text{ ft}}{2} \right) = 0.70 \text{ kips}$$

Therefore, pile lateral forces are mainly dependent on backfill pressure because pile lateral force by bridge movement is significantly smaller as compared to the results in Figure 8.96.

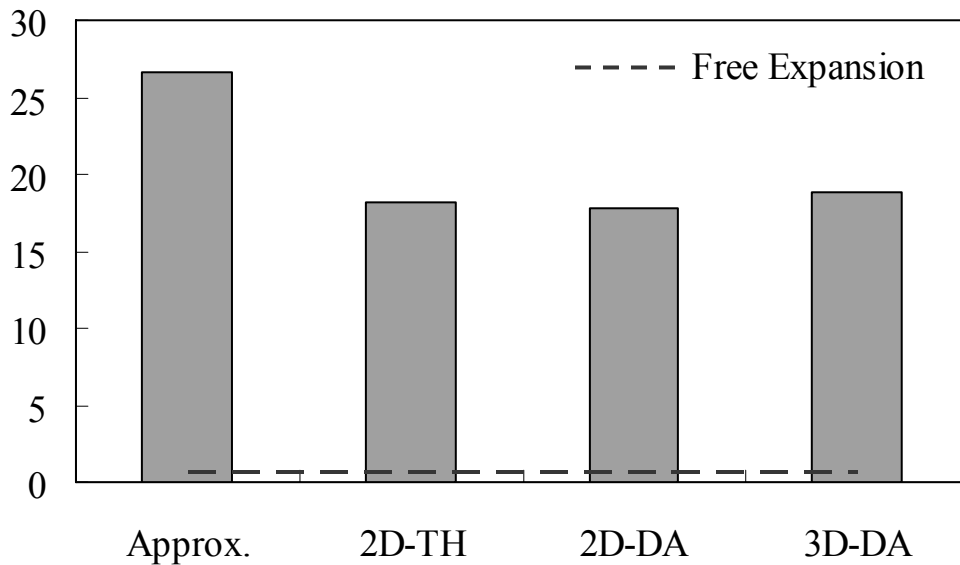


Figure 8.96: Example Bridge 2 Pile Lateral Force Comparison

8.2.4.4 Pile Moment

Pile head moment results obtained by the Approx., 2D-TH, 2D-DA, and 3D-DA are presented in Figure 8.97. All analyses report similar pile head moments. Compared to 3D-DA, the Approx., 2D-TH and 2D-DA report moments that are 34%, 8%, and 3%

larger. For comparison purposes, the single pile moment, M_{pile} , due to a superstructure-free expansion is computed as:

$$M_{pile} = \frac{6EI\Delta}{L_{pile}^2} = \frac{6EI}{L_{pile}^2}(\alpha \cdot \Delta T \cdot L)$$

$$= \frac{6(29000 \text{ ksi})(186 \text{ in}^4)}{(30 \text{ ft})^2} (6 \times 10^{-6} / ^\circ \text{F})(70 ^\circ \text{F}) \left(\frac{100 \text{ ft}}{2} \right) = 10.5 \text{ ft-kip} \quad (8.3)$$

All analyses predictions are larger than the moment by free expansion. Therefore, pile moments due to thermal loading are not significant and backfill pressure and abutment rotation may have significant influences.

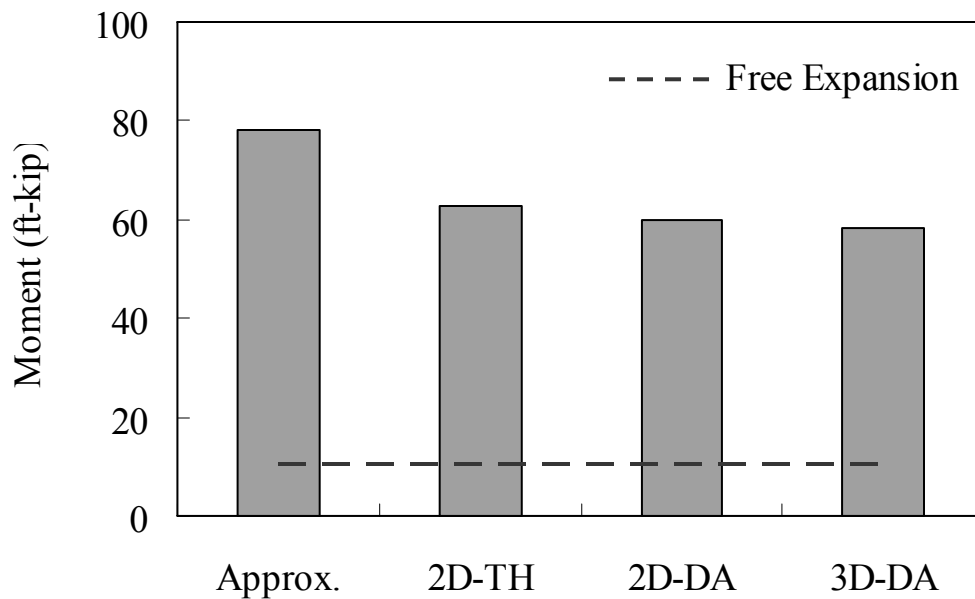


Figure 8.97: Example Bridge 2 Pile Moment Comparison

8.2.4.5 Pile Head Displacement

Pile head displacement results obtained by the Approx., 2D-TH, 2D-DA, 3D-DA are presented in Figure 8.98. Except for the approximate method, all analyses report similar pile head displacements. Compared to the 3D-DA, the approximate method, 2D-TH and

2D-DA report pile head displacements are 370% larger, 14% larger, and 3% smaller. For comparison purposes, the pile head displacement due to superstructure-free expansion is computed as:

$$\delta_{pile} = \alpha \cdot \Delta T \cdot L = (6 \times 10^{-6}) (70^\circ \text{F}) \left(\frac{200 \text{ ft}}{2} \right) = 0.50 \text{ inches} \quad (8.4)$$

All analyses predictions except the Approx. analysis are smaller than the displacement by free expansion.

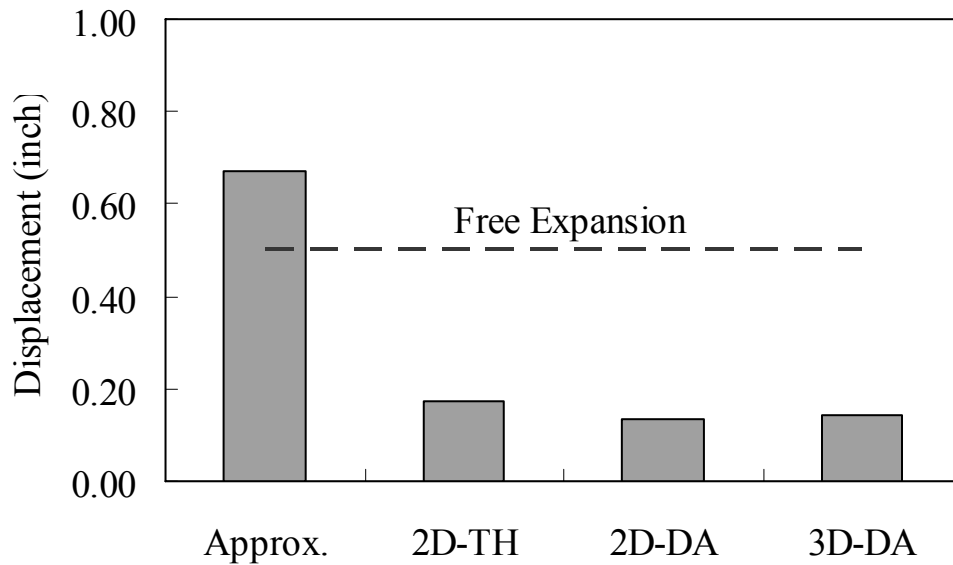


Figure 8.98: Example Bridge 2 Pile Head Displacement Comparison

8.3 Example 3: 3-span Concrete Girder Bridge

The integral abutment bridge configuration for Example 3 is a 3-span, precast, prestressed concrete girder bridge supporting a 9-inch, normally reinforced cast-in-place concrete deck and PennDOT standard barriers. The girder design has been based on widely accepted AASHTO girder bridge practices for gravity load, with the controlling load combination of Service III with HL-93 live load (HS20 basis). The initial analysis under gravity load follows the AASHTO LRFD approximate load distribution method for a multi-lane bridge. Five AASHTO PCI BT81 girders and detailed cross section dimensions are presented in Figures 8.99 and 8.100. Reinforcement details and construction joint, Section A-A in Figure 8.100, appear in Figure 8.101.

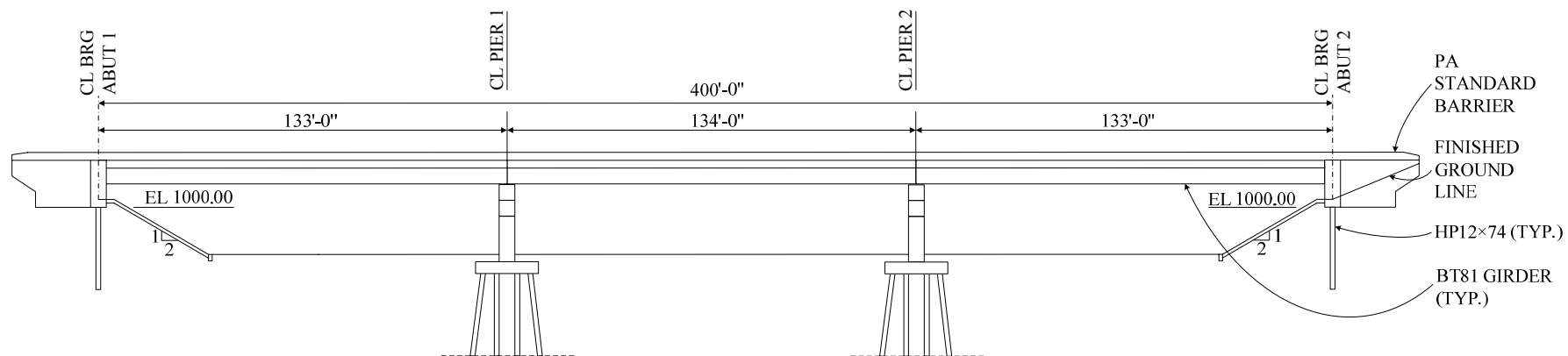


Figure 8.99: Example 3 Bridge Elevation

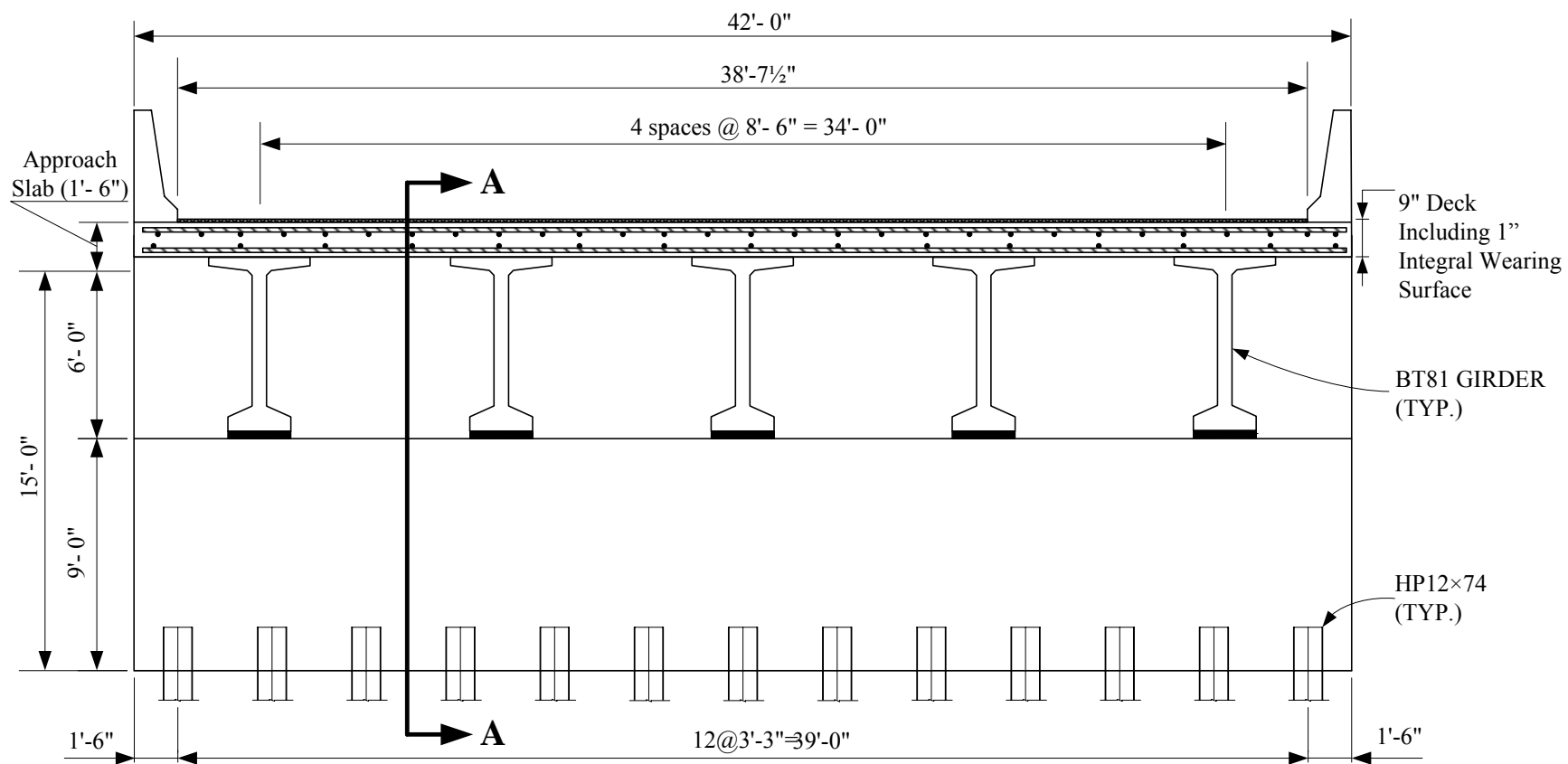


Figure 8.100: Example 3 Bridge Cross-Section and Abutment Elevation

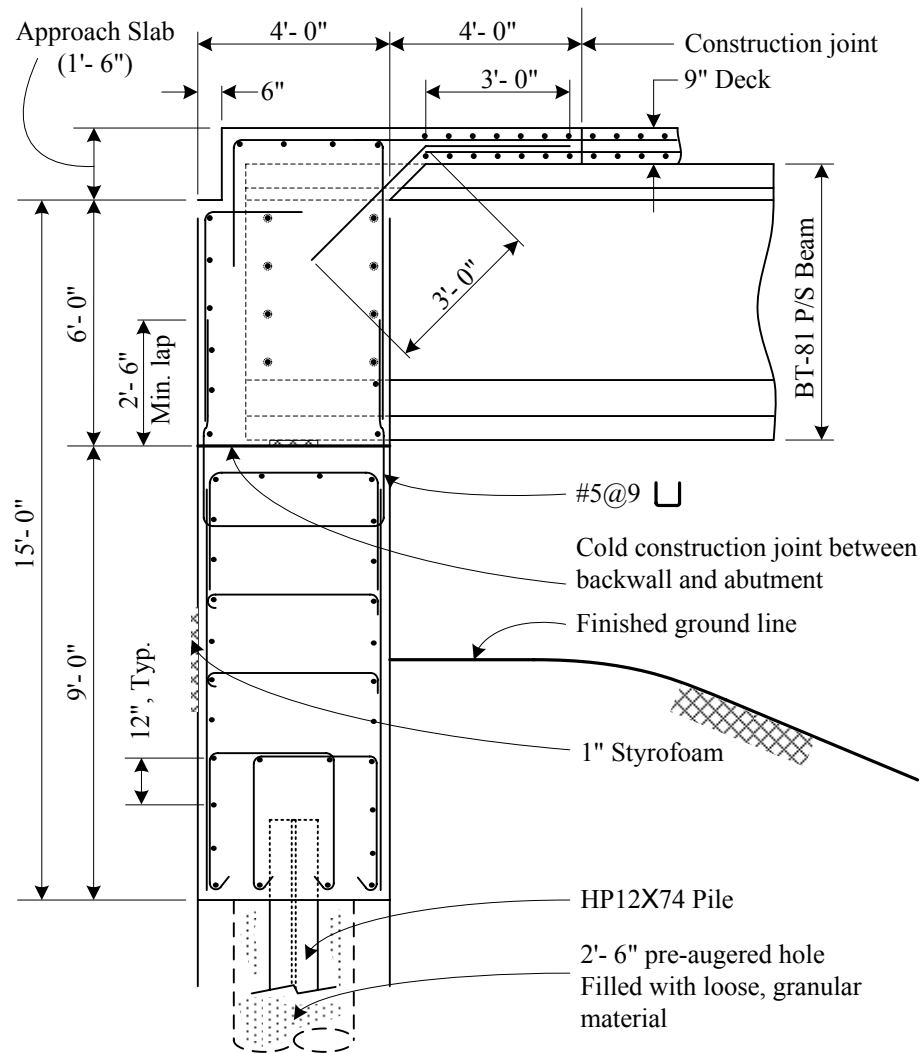


Figure 8.101: Example 3 Bridge Section A-A

Normal weight concrete compressive strengths of bridge components are presented in Table 8.12. A single row of 13, weak-axis oriented, end-bearing, HP12×74 piles are driven to refusal into the soil type described in Table 8.13. The soil type for Example 3 is taken as *intermediate*. This soil classification is as discussed in Chapter 7, which is also PennDOT No. OGS backfill as described in Table 8.14. The normally reinforced concrete deck is placed 100 days after the girder manufacture date, which influences how time-dependent effects are computed.

Table 8.12. Example 3 Component Concrete and Steel Strength

Strength (psi)	Bridge Component
High Performance Concrete (8000 psi)	Prestressed Concrete Girders
PennDOT Class AAA (4000 psi)	Deck, Back-wall
PennDOT Class AA (3500 psi)	Parapets, Diaphragms and Cheek Walls
PennDOT Class A (3000 psi)	Abutment below Girder Seats, and Pedestals
$F_y = 50$ ksi	Steel Pile (HP12×74)
$f_y = 60$ ksi	Steel Rebars

Table 8.13. Soil Layer Properties for Soil Pile Stiffness (P)

Property	<i>Intermediate*</i>
Density (pcf)	121
Undrained Shear Strength (psi)	17.5
Soil Modulus (K) (pci)	1000
ε_{50} (in)	0.008

**Intermediate* refers to Table 7.2.

Note: soil pile stiffness (P) is represented as *Low* = 1, *Intermediate* = 2, *High* = 3 in the approximate method.

Table 8.14. Backfill Properties for Backfill Stiffness (B)

Property	<i>Intermediate*</i>
Density (γ) (pcf)	119
Angle of friction (ϕ_f) (Degree)	34
Subgrade Modulus (K_h) (pci)	43.8

**Intermediate* refers to Table 7.1.

Note: backfill stiffness (B) is represented as *Low* = 1, *Intermediate* = 2, *High* = 3 in the approximate method.

8.3.1 Example 3: Approximate Analysis Method

The approximate integral abutment analysis method utilizes equations 7.2 through 7.14 developed and presented in Chapter 7. The approximate method presented herein considers only temperature load, temperature gradient, backfill pressure and time-dependent loads for a 75-year bridge life. In addition, backfill-abutment interaction, soil-pile interaction, and the nonlinear behavior of the back-wall to abutment construction joint are accounted for in the approximate analysis method, returning maximum, 75-year bridge responses.

AASHTO LRFD (5.4.2.2) recommends a concrete thermal expansion coefficient of $6\text{E-}6/^{\circ}\text{F}$ for normal-weight concrete and $5\text{E-}6/^{\circ}\text{F}$ for light-weight concrete in the absence of measurement data. The AASHTO-recommended thermal expansion coefficient for normal-weight concrete is adopted in the approximate analysis method presented here.

8.3.1.1 Girder Axial Force

Based on the given bridge dimensions and soil property classification, girder axial force is computed from the bridge axial force based on the assumption that all axial forces are evenly distributed to individual girders. Calculated positive and negative girder axial forces represent maximum tensile and compressive axial force over a 75-year bridge life.

Bridge tension force is computed as:

$$F_t = 16.6\alpha + 1.2L - 34.9H + 118.8P - 2.1 \geq 0 \quad (7.7)$$

$$\alpha = 6.0 \text{ }/^{\circ}\text{F} \text{ (AASHTO concrete thermal expansion} \times 1\text{E+6)}$$

$$L = 400 \text{ ft (bridge overall length)}$$

$$H = 15 \text{ ft (abutment height)}$$

$$P = 2 \text{ (soil pile stiffness based on Table 8.13)}$$

$$\begin{aligned} F_t &= 16.6(6.0 \text{ } ^\circ\text{F}) + 1.2(400 \text{ ft}) - 34.9(15 \text{ ft}) + 118.8(2) - 2.1 \\ &= 292 \text{ kips per bridge} \end{aligned}$$

$$\text{Tensile Force per Girder} = 292 \text{ kips} / (5 \text{ girders}) = 58 \text{ kips}$$

Bridge longitudinal compression force, F_c , is computed as:

$$F_c = -5.4\alpha^{0.8}L^{0.6}B^{0.2}P^{0.02} \quad \text{for } 13 \leq H \leq 18\text{ft} \quad (7.8)$$

$$\alpha = 6.0 \text{ } ^\circ\text{F (AASHTO concrete thermal expansion} \times 1\text{E}+6)$$

$$L = 400 \text{ ft (bridge overall length)}$$

$$B = 2 \text{ (backfill pile stiffness coefficient based on Table 8.14)}$$

$$P = 2 \text{ (soil pile stiffness based on Table 8.13)}$$

$$F_c = -5.4(6.0 \text{ } ^\circ\text{F})^{0.8}(400 \text{ ft})^{0.6}(2)^{0.2}(2)^{0.02} = -960 \text{ kips per bridge}$$

$$\text{Compression Force per Girder} = -960 \text{ kips} / (5 \text{ girders}) = -192 \text{ kips per girder}$$

The Example 3 bridge experiences both tensile and compressive axial forces in the girders. When temperature falls, significant thermal contraction and time-dependent effects are predicted due to the relatively long bridge length, resulting in a significant girder axial tensile force. When temperature rises, significant thermal expansion due to the long length and large passive backfill pressure results in a significant compressive axial force in the girders.

8.3.1.2 Girder Bending Moment

The girder bending moment is computed from the bridge bending moment, calculated from the approximate analysis equations 7.2 through 7.6 in Chapter 7 of this report. The superstructure moment due to thermal loading is not constant throughout the span. Therefore, moments at the abutment and moments at the girder midspan in the end span are different.

Bridge positive moment, M_{pos} , at the abutment is computed as:

$$M_{pos} = 59\alpha + 740P - 2,600 \geq 0 \quad \text{for } L \geq 300\text{ft} \quad (7.2)$$

$$\alpha = 6.0 \text{ } ^\circ\text{F (AASHTO concrete thermal expansion} \times 1\text{E}+6)$$

$$P = 2 \text{ (soil pile stiffness based on Table 8.13)}$$

$$M_{pos} = 59(6.0 \text{ } ^\circ\text{F}) + 740(2) - 2,600 = -766 \text{ ft-kips per bridge}$$

$$M_{pos} \text{ at the mid-span per girder} = -766 \text{ ft-kip} / (5 \text{ girders}) = -153 \text{ ft-kips per girder} < 0.$$

The computed bridge moment at the abutment is less than zero; therefore, positive moment at the abutment does not occur under thermal load.

Bridge negative moment, M_{neg} , at the abutment is computed as:

$$M_{neg} = -280\alpha^{0.4}L^{0.35} \quad \text{for } 13 \leq H \leq 18\text{ft} \quad (7.3)$$

$$\alpha = 6.0 \text{ } ^\circ\text{F (AASHTO concrete thermal expansion} \times 1\text{E}+6)$$

$$L = 400 \text{ ft (bridge overall length)}$$

$$M_{neg} = -280(6.0 \text{ } ^\circ\text{F})^{0.4}(400 \text{ ft})^{0.35} = -4,670 \text{ ft-kips per bridge}$$

$$M_{neg} \text{ at the abutment per girder} = -4,670 \text{ ft-kip} / (5 \text{ girders}) = -934 \text{ ft-kips per girder.}$$

Bridge positive moment, M_{pos} , at the mid-span is computed as:

$$M_{pos} = 118\alpha + 13L + 1100P - 4000 \geq 0 \quad \text{for } 13 \leq H \leq 18\text{ft} \quad (7.4)$$

$$\alpha = 6.0 \text{ } ^\circ\text{F (AASHTO concrete thermal expansion} \times 1\text{E}+6)$$

$$L = 400 \text{ ft (bridge overall length)}$$

$$P = 2 \text{ (soil pile stiffness based on Table 8.13)}$$

$$M_{pos} = 118(6.0 \text{ } ^\circ\text{F}) + 13(400 \text{ ft}) + 1100(2) - 4000 = +4,110 \text{ ft-kips per bridge}$$

$$M_{pos} \text{ at the mid-span per girder} = 4,110 \text{ ft-kip} / (5 \text{ girders}) = +822 \text{ ft-kips per girder.}$$

Bridge negative moment, M_{neg} , at the mid-span is computed as:

$$M_{neg} = -26\alpha^{1.0}L^{0.65}B^{0.1}P^{-0.08} \quad \text{for } 13 \leq H \leq 18\text{ft} \quad (7.5)$$

$$\alpha = 6.0 \text{ } ^\circ\text{F (AASHTO concrete thermal expansion} \times 1\text{E}+6)$$

$$L = 400 \text{ ft (bridge overall length)}$$

$$B = 2 \text{ (backfill pile stiffness coefficient based on Table 8.14)}$$

$$P = 2 \text{ (soil pile stiffness based on Table 8.13)}$$

$$M_{neg} = -26(6.0 \text{ } ^\circ\text{F})^{1.00}(400 \text{ ft})^{0.65}(2)^{0.10}(2)^{-0.08} = -7,770 \text{ ft-kips per bridge}$$

$$M_{neg} \text{ at the abutment per girder} = -7,770 \text{ ft-kip} / (5 \text{ girders}) = -1,550 \text{ ft-kips per girder}$$

8.3.1.3 Pile Head Moment

Pile head moments are computed using the approximate analysis equations 7.10 through 7.11 from Chapter 7 of this report. Typical IAB abutment pile displacement, moment, and shear are presented in Figure 8.102. While pile response depends significantly on bridge length and time-dependent effects, pile points of fixity are normally established above a 15-ft depth. Maximum supporting pile displacement, moment, and shear in occur at the pile head; therefore, these values are used for pile design.

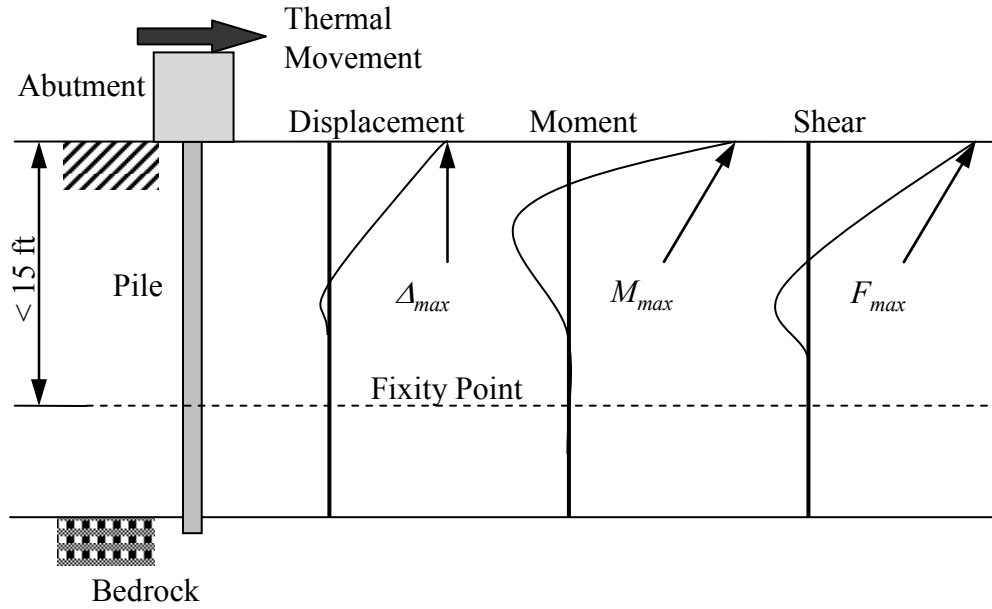


Figure 8.102: Typical IAB Pile Displacement, Moment, and Shear Response.

Total pile head moment is computed as:

$$M_{piles} = 21\alpha^{0.5}L^{0.5}H^{0.1}P^{0.6} \leq M_{y\ pile} N_p \quad (7.10)$$

$$\alpha = 6.0 \text{ /}^\circ\text{F (AASHTO concrete thermal expansion} \times 1\text{E+6)}$$

$$L = 400 \text{ ft (bridge overall length)}$$

$$H = 15 \text{ ft (abutment height)}$$

$$P = 2 \text{ (soil pile stiffness based on Table 8.13)}$$

$$M_{piles} = 21(6.0 \text{ /}^\circ\text{F})^{0.5}(400 \text{ ft})^{0.5}(15 \text{ ft})^{-0.1}(2)^{0.6} = 1,190 \text{ ft-kips per bridge}$$

Pile head moment per pile: $M_{pile} = 1,190 \text{ ft-kips} / (13 \text{ piles}) = 91 \text{ ft-kips per pile}$

A single pile is expected to experience a maximum of 91 ft-kip weak axis bending moment at the pile head over the 75-year bridge life.

8.3.1.4 Pile Lateral Force

Total pile lateral shear force is computed as:

$$F_{piles} = 19\alpha^{0.2}L^{0.4}B^{-0.1}P^{0.8} \leq F_{y_pile} N_p \quad \text{for } 13 \leq H \leq 18\text{ft} \quad (7.12)$$

The total pile lateral force is limited to single-pile shear capacity (F_{y_pile}) times the number of piles (N_p). The minimum number of piles can be determined based on this limitation so that $F_{piles} \leq F_{y_pile} N_p$. For Example 3, the total pile lateral force is:

$$F_{piles} = 19\alpha^{0.2}L^{0.4}B^{-0.1}P^{0.8}$$

$$\alpha = 6.0 \text{ /}^\circ\text{F (AASHTO concrete thermal expansion} \times 1\text{E}+6)$$

$$L = 400 \text{ ft (bridge overall length)}$$

$$B = 2 \text{ (backfill pile stiffness coefficient based on Table 8.14)}$$

$$P = 2 \text{ (soil pile stiffness based on Table 8.13)}$$

$$F_{piles} = 19(6.0 \text{ /}^\circ\text{F})^{0.2}(400 \text{ ft})^{0.3}(2)^{-0.1}(2)^{0.7} = 250 \text{ kips per bridge}$$

Pile lateral force, $F_{pile} = 250 \text{ kips} / (13 \text{ piles}) = 19 \text{ kips per pile}$

8.3.1.5 Pile Head/abutment Displacement

As presented in Figure 8.102, pile head/abutment displacement reaches its maximum at the pile head. This pile head/abutment displacement may also be used to determine the number of piles or other bridge dimensions because AASHTO LRFD (2007) limits the abutment displacement to $\leq 1\frac{1}{2}$ inches. For the current bridge example, maximum displacement is computed as:

$$u_{max} = 0.0006\alpha^{0.7}L^{1.0}B^{-0.02}P^{-0.1} \quad \text{for } 13 \leq H \leq 18\text{ft} \quad (7.14)$$

$$\alpha = 6.0 \text{ /}^\circ\text{F (AASHTO concrete thermal expansion} \times 1\text{E}+6)$$

$$L = 400 \text{ ft (bridge overall length)}$$

$$B = 2 \text{ (backfill pile stiffness coefficient based on Table 8.14)}$$

$$u_{max} = 0.0006(6.0 \text{ } ^\circ\text{F})^{0.7}(400 \text{ ft})^{1.0}(2)^{-0.15} = 0.76 \text{ inch}$$

8.3.2 Example 3: Two-Dimensional Model Analysis

A more refined, and potentially more accurate relative to the IAB approximate analysis method, is an analysis method that utilizes a two-dimensional, numerical, finite element model. The methodology presented here permits the incorporation of individual bridge elements and the respective material and geometric properties through a demonstrated effective 2D model approach.

To construct a 2D model of the three-dimensional structure, the five girders and composite concrete deck are represented as a single beam element using ANSYS BEAM189 elements. Supporting piles are represented as two-dimensional beam elements, also using BEAM189 elements with soil-pile interaction springs (COMBIN39) spaced vertically at 1'- 0" representing the soil. Similarly, abutment-to-backfill interaction is represented using nonlinear interaction springs. The development of material and geometric properties for each element is discussed in detail below. A schematic of the 2D bridge model developed for Example 3 is presented in Figure 8.103.

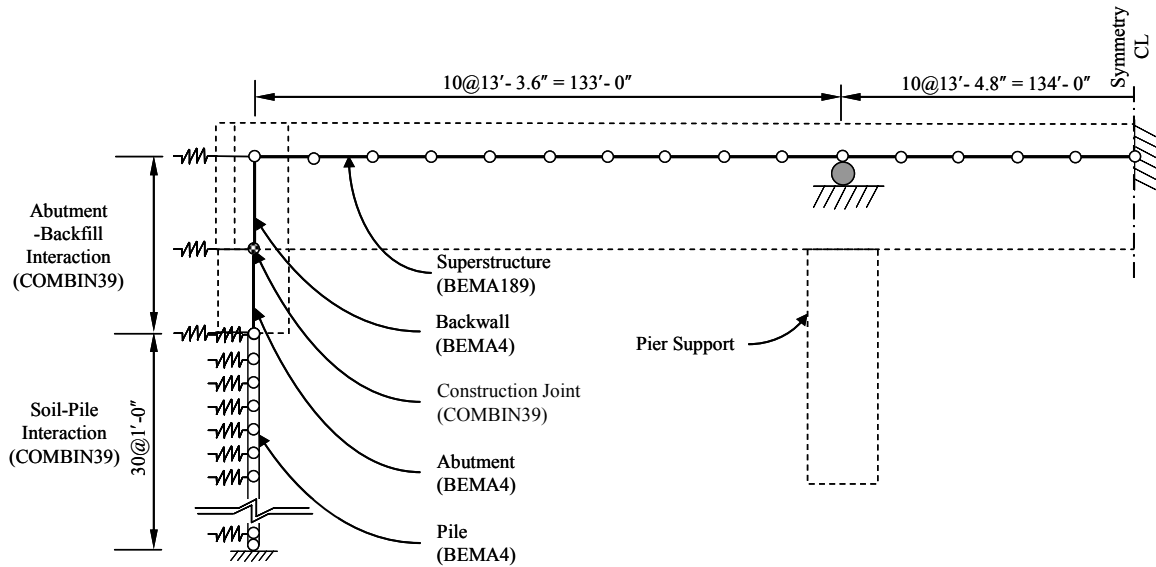


Figure 8.103: 2D Example 3 ANSYS Bridge Model.

The incorporation of transverse bridge components, such as diaphragms, in a two-dimensional model is not possible; however, the effects of the transverse elements on the longitudinal response to temperature loading is not significant. Key bridge components include girders, deck, abutment/backwall, construction joint and piles. Loading includes superstructure temperature variation, temperature gradient, and backfill pressure. A completed 2D numerical model with actual cross section of each member of the bridge is presented in Figure 8.104.

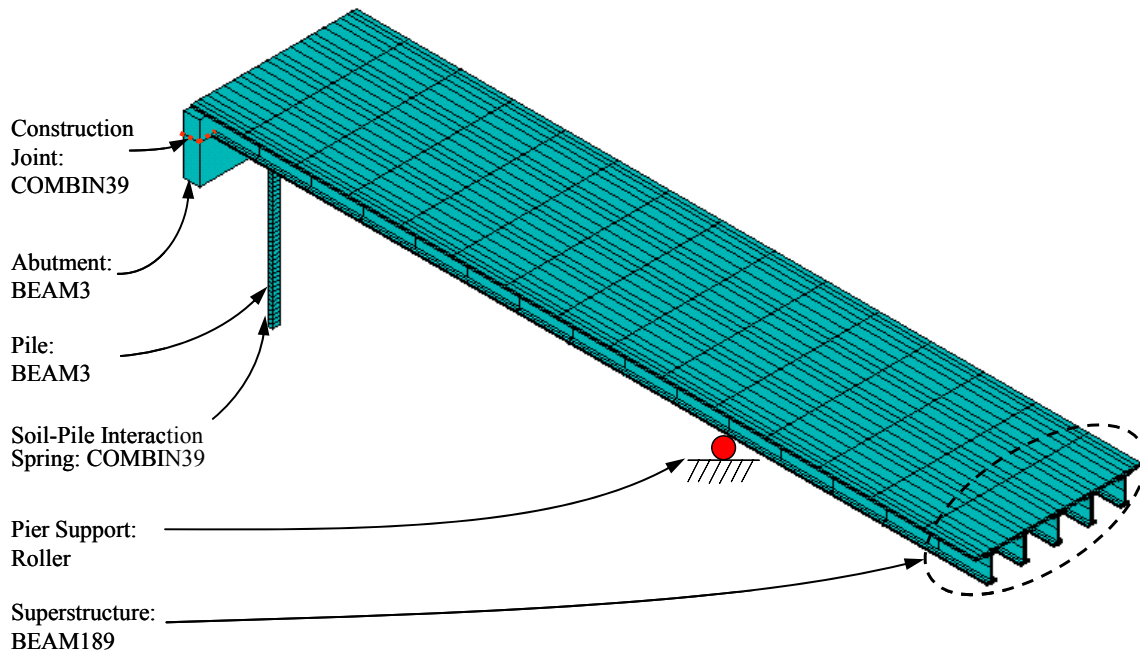


Figure 8.104: 2D Example 3 ANSYS Model Perspective View

8.3.2.1 Bridge Components

Each bridge component and its definition are described in detail in the following sections to allow the reader to develop future models for other IABs. The discussion includes girder and deck, abutment/backwall, construction joint, piles, and soil springs.

8.3.2.1.1 Girder and Deck

The bridge superstructure is modeled using a beam element based on the entire superstructure cross section properties as shown in Figure 8.105. Computed superstructure section properties are presented in Table 8.15. Due to the 28-day strength difference between deck concrete (4,000 psi) and girder concrete (8,000 psi), a transformed deck concrete area is used in the calculation of area and moment of inertia. Based on AASHTO recommendations, the concrete thermal expansion coefficient for deck concrete and girder concrete is taken as $6.0\text{E-}6 \text{ in/in/}^{\circ}\text{F}$.

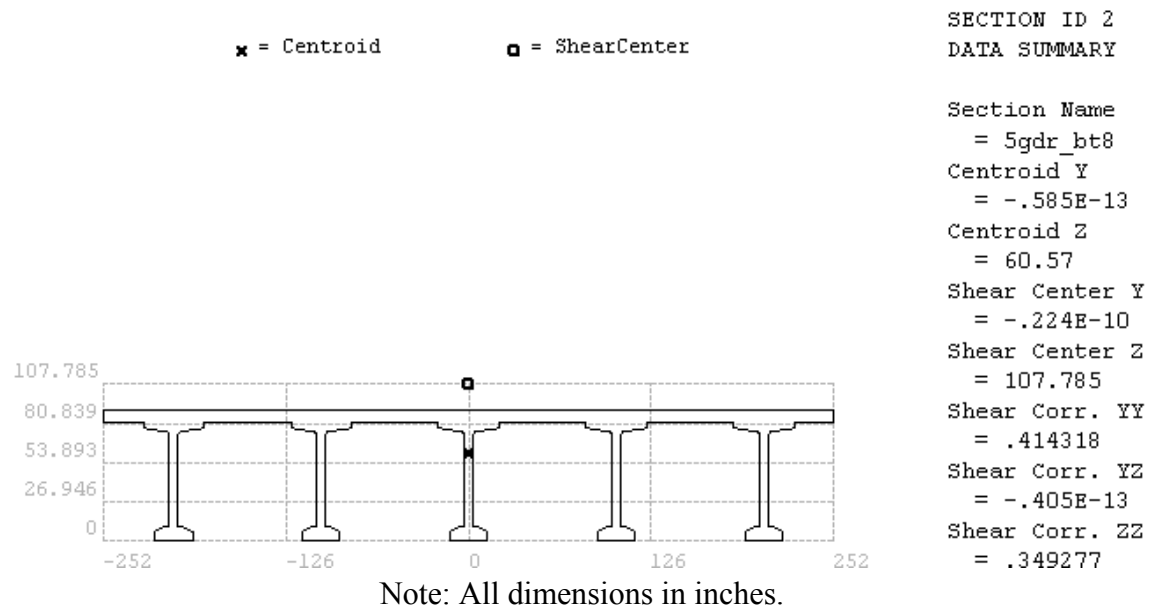


Figure 8.105: Beam Element (BEAM189) Cross Section for Superstructure

Table 8.15: Superstructure Composite Section Property of 3-Span Prestressed Girder IAB

Section Property	Centroid (in)	Area (in ²)	Moment of Inertia (in ⁴)	Elastic Modulus (ksi)	Thermal Expansion Coefficient (in/in/°F)
Beam Element	61.570	8,641	10,216,146.8	5,154	6.0E-6

8.3.2.1.2 Abutment/Back-wall

For a 2D model, the abutment (or pile cap) and back-wall (or end diaphragm) are modeled using beam elements. The full height of the abutment (base to beam seats) determines the length of the abutment beam element; however, the back-wall is modeled from the beam seat to the superstructure centroid. The superstructure is represented as a beam line element; therefore, the portion of the back-wall above the superstructure centroid is extraneous and eliminated.

Generally, higher strength concrete is used in the back-wall as compared to the abutment concrete because the back-wall is placed monolithically with the deck. The Example 3 bridge specifies 4,000 psi and 3,000 psi 28-day compressive strength concrete for the back-wall and abutment, respectively, resulting in the elastic modulus for the back-wall as 3,640 ksi and the elastic modulus for the abutment as 3,160 ksi.

8.3.2.1.3 Construction Joints

The construction joint between the back-wall and abutment is modeled using a joint element with defined rotational stiffness, but all translations are directly compatible with adjacent elements. The computed rotational stiffness of the construction joint is presented in Figure 8.106.

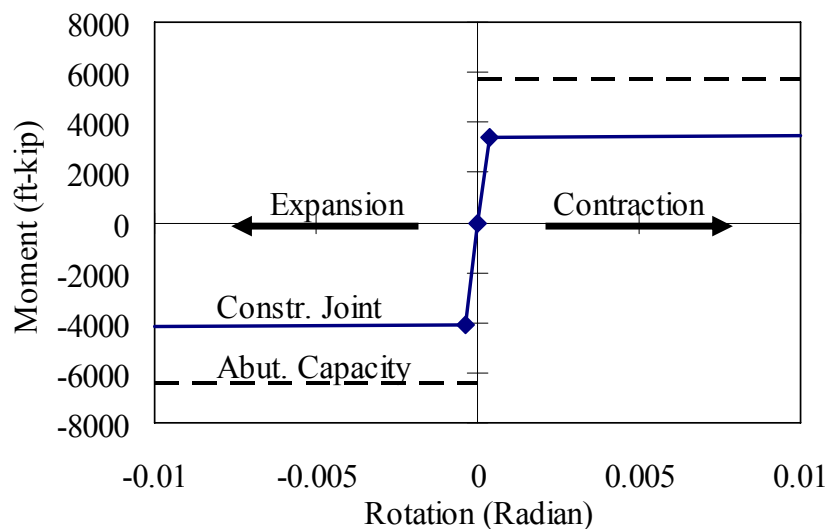


Figure 8.106: Construction Joint Rotational Stiffness

Rotational stiffness is determined based on reinforcing bars crossing the joint. A reinforcement detail consisting of #5 bars at 9 inches center-to-center is a typical PennDOT specification and is therefore adopted here. In addition, the reinforcement adjacent to the backfill side of the joint is different from the reinforcement adjacent to

the abutment front face because girders interfere with the reinforcement placement (see Figure 8.101). This causes the rotational stiffness for superstructure expansion to be different from the rotational stiffness for superstructure contraction.

The construction joint is a cold joint; therefore, concrete tension is not considered in the development of moment-curvature definition. To convert curvature into rotation, half of the AASHTO LRFD embedment length is utilized to compute the displacement, crack opening between the abutment and the back-wall during superstructure expansion and contraction due to strain in the reinforcement.

8.3.2.1.4 Steel H-Piles

Weak axis oriented steel H-piles are modeled using beam elements and soil-structure interaction is modeled using nonlinear spring elements. Beam element steel H-pile properties of area and moment of inertia are assigned directly. The pile length must be at least 20 ft because the pile fixity point (zero rotation and zero displacement) occurs between 10 and 15 ft. However, longer bridges will develop a deeper fixity point; therefore, piles should be modeled to the full expected driven depth. The pile fixity point of the numerical model must be evaluated to determine whether the pile has been properly modeled. For the given example bridge, a 30-ft pile length has been modeled.

8.3.2.1.5 Soil Springs

Soil non-linear stiffness definition at each depth is represented using equivalent Winkler spring elements based on p - y curves that are spaced at 1-ft vertical intervals.

Alternatively, commercial programs such as COM624P and Lpile can directly generate p -

y curves at various soil conditions and depths (refer to section 5.2.3 of this report). In the 2D ANSYS bridge model, COMBIN39 nonlinear spring elements are used to represent the hysteretic behavior of soil-pile interaction. Each p - y spring is spaced at 1'-0" intervals from the pile head to the pile bearing tip. Spring element properties defined by lateral force versus lateral displacement (p - y) at a given depth consider the total number of abutment piles and the tributary area along the pile. For illustration, under the bridge contraction case, a p - y curve at the 10'-0" depth of the given soil strata is computed as:

$$p_u = \min \left\{ p_{uf} = 9cD, \quad p_{uw} = \left(3 + \frac{\gamma'}{c} X + \frac{J}{D} X \right) cD \right\} \quad (5.4)$$

$$p_{uf} = 9cD = 9(13.9 \text{ psi})(12.1 \text{ inches}) = 1510 \text{ lbs/inch}$$

$$p_{uw} = \left(3 + \frac{140 \text{ pcf}}{2000 \text{ psf}} (120 \text{ inches}) + \frac{0.5}{12.1 \text{ inches}} (120 \text{ inches}) \right) (2000 \text{ psf})(12.1 \text{ inches})$$

$$= 1460 \text{ lb/inch} \rightarrow \text{governs}$$

For the tributary length of 1'-0", $p_u = (1460 \text{ lbs/inch})(12 \text{ inches}) = 17.5 \text{ kips}$

$$p = 0.5 p_u \left(\frac{y}{y_{50}} \right)^{1/4} \quad \text{and if } y = 0.1 \text{ inches,}$$

$$p = 0.5(17.5 \text{ kips}) \left(\frac{0.1 \text{ inches}}{0.212 \text{ inches}} \right)^{1/4} = \underline{7.24 \text{ kips}}$$

Similarly, for expansion, $X = 120 \text{ inches} + 180 \text{ inches (backfill height)} = 300 \text{ inches}$:

$$p_{uf} = 9cD = 9(13.9 \text{ psi})(12.1 \text{ inches}) = 1510 \text{ lbs/inch}$$

$$p_{uw} = \left(3 + \frac{140 \text{ pcf}}{2000 \text{ psf}} (300 \text{ inches}) + \frac{0.5}{12.1 \text{ inches}} (300 \text{ inches}) \right) (2000 \text{ psf})(12.1 \text{ inches})$$

$$= 2880 \text{ lb/inch}$$

For the tributary length of 1'-0", $p_u = (1510 \text{ lbs/inch})(12 \text{ inches}) = 18.2 \text{ kips}$

$$p = 0.5 p_u \left(\frac{y}{y_{50}} \right)^{1/4} \text{ and if } y = 0.1 \text{ inches,}$$

$$p = 0.5(18.2 \text{ kips}) \left(\frac{0.1 \text{ inches}}{0.212 \text{ inches}} \right)^{1/4} = \underline{7.53 \text{ kips}}$$

This procedure is repeated for several y values to form a smooth p - y curve, computed up to $16y_{50} = 16(2.5D\epsilon_{50}) = 16(2.5)(12.1 \text{ inches})(0.007 \text{ inches}) = 3.39 \text{ inches}$ because p - y curves in clay soils start to become constant after $16y_{50}$. For the given case, example computations for a soil-pile interaction spring at a depth of 10'-0" are tabulated as:

Table 8.16: p - y curve ordinates for a depth of 10'-0"

	P_u (kip)	y (inches)								
		9.8E-5	7.8E-4	0.025	0.1	0.42	0.85	1.69	3.39	4.5
Cont.	17.5	1.28	2.15	5.12	7.24	10.4	12.4	14.7	17.5	17.5
Exp.	18.2	1.33	2.24	5.32	7.53	10.8	12.8	15.3	18.2	18.2

Based on the sign convention that bridge expansion induces negative displacement and force, the data of Table 8.16 are plotted in Figure 8.107 and compared to results generated by the Lpile program. The API equations in Table 8.16 and the Lpile program produce identical results. Soil springs at each depth require this procedure to generate a p - y curve.

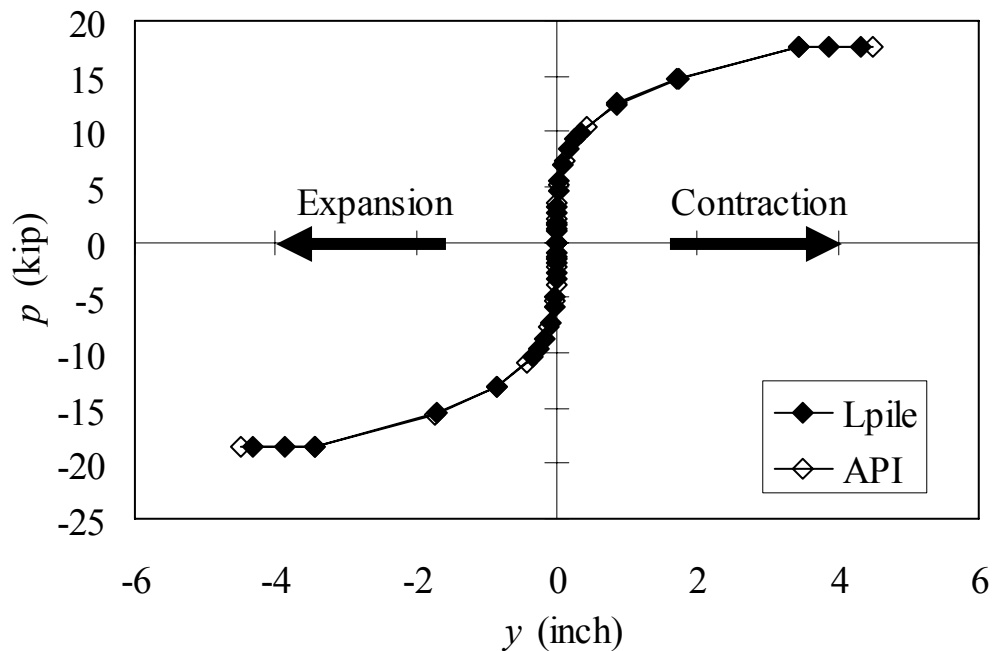


Figure 8.107: Comparison of p - y Curve by the API Equation and Lpile.

8.3.2.1.6 Miscellaneous Components (diaphragms, interior supports, bearings)

Girder bearings (normally elastomeric) at both abutments are embedded in the back-wall concrete and are not modeled explicitly. The superstructure is rigidly connected to the back-wall and is modeled as such. Interior supports (piers) are modeled as roller restraints. Because both ends of an IAB superstructure are restrained at the abutments, interior supports are not designed to provide longitudinal restraint. In addition, because elastomeric bearings allow longitudinal displacement with very low resistance during bridge contraction and expansion, a roller support condition is appropriate for interior supports. Diaphragms at the mid-span or pier supports are not considered due to modeling restrictions.

8.3.2.2 Loads

Loads considered in the 2D model include the overall superstructure temperature fluctuation, temperature gradient through the superstructure depth, and backfill pressure. Each load component is described in the sections below. Two approaches are presented for the 2D analysis example: (1) a 2D time-history analysis and (2) an extreme design static 2D analysis. The 2D time-history analysis evaluates a 75-year bridge life as a result of a sinusoidal temperature fluctuation. This simulation considers a sinusoidal temperature change, time-dependent effects, and cyclic soil-structure interaction over time, and is close to actual conditions. However, the 2D design analysis is a static analysis based on an AASHTO-specified extreme temperature rise (+30°F) and fall (-40°F) for concrete bridges. This analysis approach is typically used for DOT design and is easy to implement, and the required computing resources are low. Time-dependent effects are not included for the design temperature rise analysis in order to obtain the maximum bridge expansion response. This approach recognizes that initial bridge expansion will likely occur before significant, counteracting time-dependent effects occur. Time-dependent effects are combined with design temperature fall to obtain the maximum bridge contraction response.

8.3.2.2.1 Sinusoidal Temperature Fluctuation Simulation

Superstructure temperature fluctuation over time is simulated with a sinusoidal curve that is based on field-collected data at monitored bridges and a weather station. The 2D model is configured to simulate a 75-year bridge life; therefore, the sinusoidal temperature simulation must represent a nominal temperature fluctuation over the

expected bridge life. Although bridge structures possess relatively low thermal conductivity and high thermal inertia, the average superstructure temperature is reasonably assumed to be equal to ambient temperature. The temperature fluctuation is plotted in Figure 8.108. Depending on the availability of local meteorological data, annual mean temperature, annual temperature amplitude, frequency ($2\pi t$), and phase lag (ϕ) can be determined. Based on the present study monitoring results and information obtained from the National Climate Data Center, central Pennsylvania annual mean = 49 °F and the annual temperature amplitude = 30 °F. A phase lag = π is adopted when the bridge backwall concrete is placed during fall season around annual mean temperature.

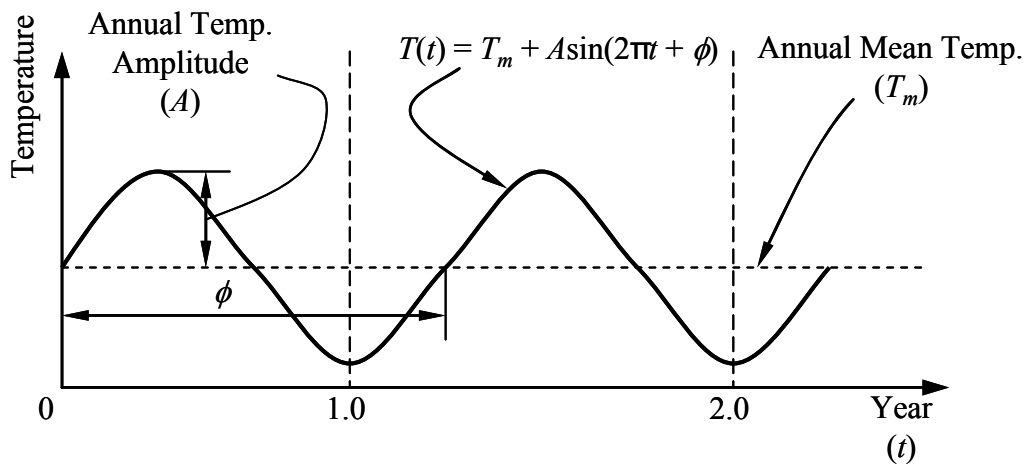


Figure 8.108: Temperature Model

8.3.2.2.2 Temperature Gradient

Based on AASHTO multi-linear temperature gradient requirements, an equivalent temperature gradient is computed. Thermal stress (σ_t) induced by the temperature gradient along the superstructure depth is represented as:

$$\sigma_t(y) = E \cdot \alpha \cdot T(y) \quad (5.14)$$

where y = distance from the extreme bottom fiber, $\sigma_t(y)$ = longitudinal thermal stress at a fiber located at y , E = elastic modulus, α = thermal expansion coefficient, and $T(y)$ = temperature at y . Thus, the axial force (P_t) and moment (M_t) due to thermal stresses are respectively:

$$P_t = \int E\alpha T(y)b(y)dY, \text{ and} \quad (5.15)$$

$$M_t = \int E\alpha T(y)b(y)YdY$$

For an AASHTO-PCI BT81 girder, the equivalent temperature at the top fiber is 14.8 °F and the equivalent temperature at the bottom fiber is 0.2 °F. A similar computation for the negative temperature gradient results in -4.4 °F and -0.1 °F at the top and bottom fiber, respectively.

The temperature gradient application in a 2D numerical analysis is presented in Figure 8.109. The AASHTO gradient represents maximum and minimum temperature gradient across the superstructure. During warm months of summer, the maximum temperature gradient is reached. During the cold months of winter, the minimum temperature gradient is reached. During the transitional months from spring to summer to fall, the temperature gradient is applied using a sinusoidal fluctuation with the amplitude of positive temperature gradient. Thus, the sinusoidal temperature gradient is superimposed on the thermal fluctuation. During the transitional months from fall to winter to spring, the temperature gradient is also applied using a sinusoidal fluctuation; however, the sinusoidal amplitude of the negative temperature gradient is used. The sinusoidal temperature gradient, as appropriate for the season, is effectively superimposed on the thermal fluctuation.

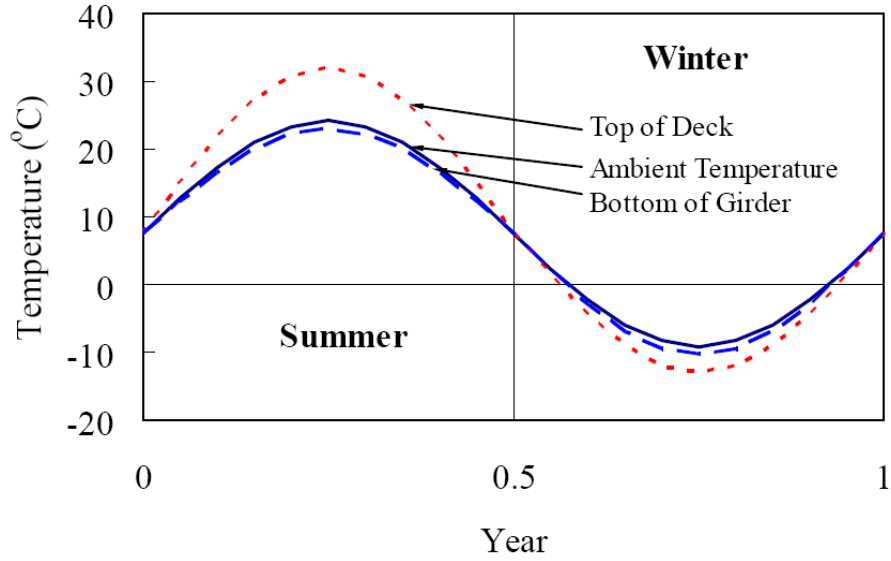


Figure 8.109: Temperature Variation with Temperature Gradient

8.3.2.2.3 Backfill Pressure

Earth pressure behind the abutments and back-walls is assumed as a hydrostatic pressure distribution, increasing with depth resulting in a triangular pressure distribution. As presented in Figure 8.110, backfill pressure varies according to a pressure-displacement relationship. The initial earth pressure is taken as the familiar at-rest pressure, but the pressure ranges between active (P_a) and passive pressure (P_p) depending on abutment displacement. In the numerical simulation, a typical abutment-to-backfill interaction relationship is presented in Figure 8.110, where active and passive backfill pressure limit is determined based on equations 5.7:

$$P_o = K_o \gamma' z w = (1) \gamma' z w$$

$$P_a = K_a \gamma' z w = \frac{1 - \sin \phi_f}{1 + \sin \phi_f} \gamma' z w \quad (5.7)$$

$$P_p = K_p \gamma' z w = \frac{1 + \sin \phi_f}{1 - \sin \phi_f} \gamma' z w$$

where K_o , K_a and K_p are the lateral earth pressure coefficients for at-rest, active and passive condition, respectively, γ' is the effective soil weight, ϕ_f is the internal friction angle, z is the depth of soil, and w is the effective backfill width. For Example 3, K_o , K_a and $K_p = 1.0$, 0.283 , and 3.537 , respectively, and $\gamma' = 119$ pcf, $\phi_f = 34^\circ$, and $w = 36'$ - $10''$.

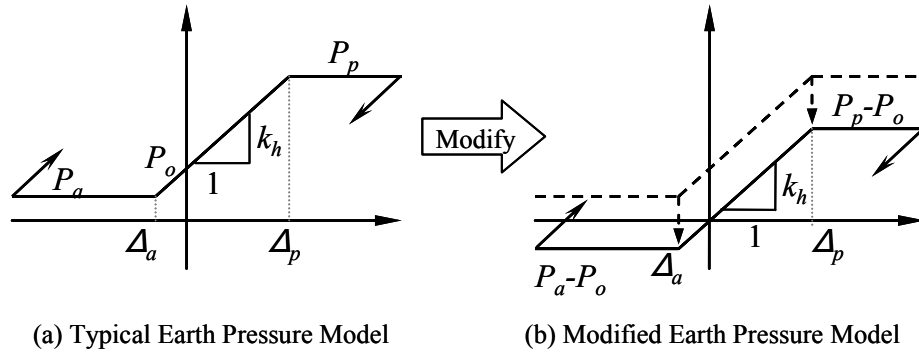


Figure 8.110: Backfill Pressure

The slope (k_h) in Figure 8.110 between active and passive pressure is computed by Boulanger et al. (1999):

$$k_h(z) = k_{ref} \left(\frac{z}{h_{ref}} \right)^{0.5} \quad (5.1)$$

where h_{ref} is the reference depth measured from the soil surface to the pressure cell elevation and z is the depth. Based on monitoring results, $k_{ref} = 0.044$ kci at 4 ft from the bottom of the abutment may be used for backfill height ranging from 10 to 20 ft.

To modify the backfill-abutment interaction as presented in Figure 8.110(b), at-rest backfill pressure (P_o) is applied externally and presented in Figure 8.111.

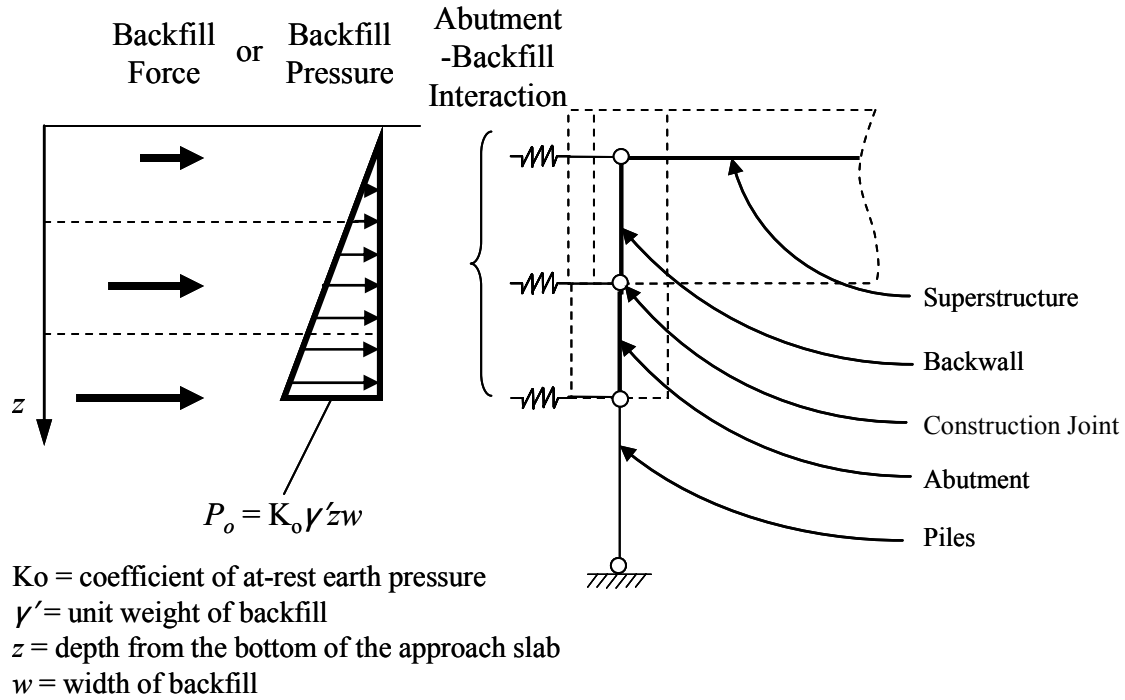


Figure 8.111: Backfill Pressure

In the 2D numerical model, the backfill pressure is applied either by (1) line loads on abutment and backwall elements or (2) forces on nodes based on tributary area divided by the dotted lines in backfill pressure diagram in Figure 8.111. Both produce the same results. Backfill pressure applied to 2D numerical model is represented as a triangular-shaped line load and is presented in Figure 8.112.

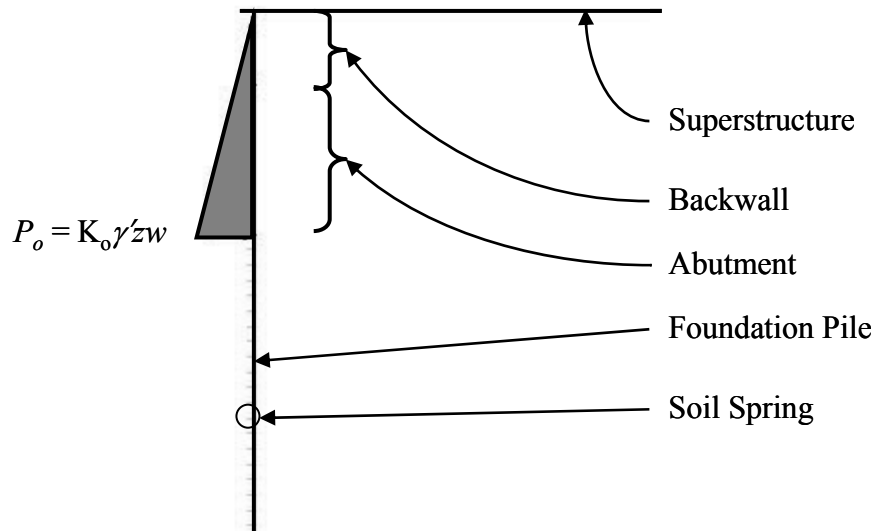


Figure 8.112: Backfill Pressure in 2D Numerical Model

8.3.2.2.4 Time-dependent Loads

To accurately simulate time-dependent effects (creep and shrinkage), the superstructure is divided into 5 segments and each element is subjected to an applied computed equivalent temperature load based on Section 5.3.2 of this report, ACI 209 creep and shrinkage strain and AASHTO LRFD prestressing steel relaxation. Figure 8.113 presents the temperature load and time-dependent load application. Each time-dependent effect at time t is computed at each location (both ends of elements) and computed strain is transformed into temperature based on thermal expansion coefficient. Computed time-dependent temperature is added to temperature load and temperature gradient load, and applied at each top and bottom location of elements.

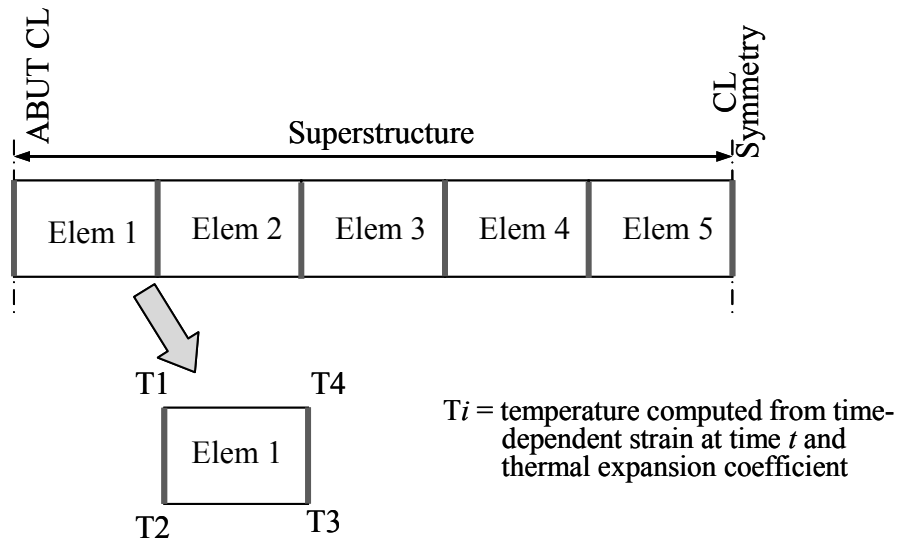


Figure 8.113: Time-dependent Load Application

When an equivalent rectangular cross section is used for the superstructure I-girder, the time-dependent load for the superstructure section is required to be offset. Because the composite section elastic neutral axis (ENA) (Figure 8.114(a)) is not coincident with the equivalent rectangular section ENA (Figure 8.114(c)), the equivalent rectangular section is aligned and located at its ENA; that is, the distance from ENA to the extreme top fiber is the same as to the distance from ENA to the extreme bottom fiber. However, computed time-dependent effects are based on the actual section (Figure 8.114(a)), whose distance from ENA to the extreme top fiber is different from the distance from ENA to the extreme bottom fiber. The computed strains (Figure 8.114(b)) due to time-dependent effects plus temperature loads (T'_i in Figure 8.114) must be corrected as an offset temperature load (T_i in Figure 8.114) to induce the same moment and axial force as presented in Figure 8.114(d). If computed strains are applied to the rectangular section without an offset, a different ENA is subjected to the section as appears in Figure 8.114(e).

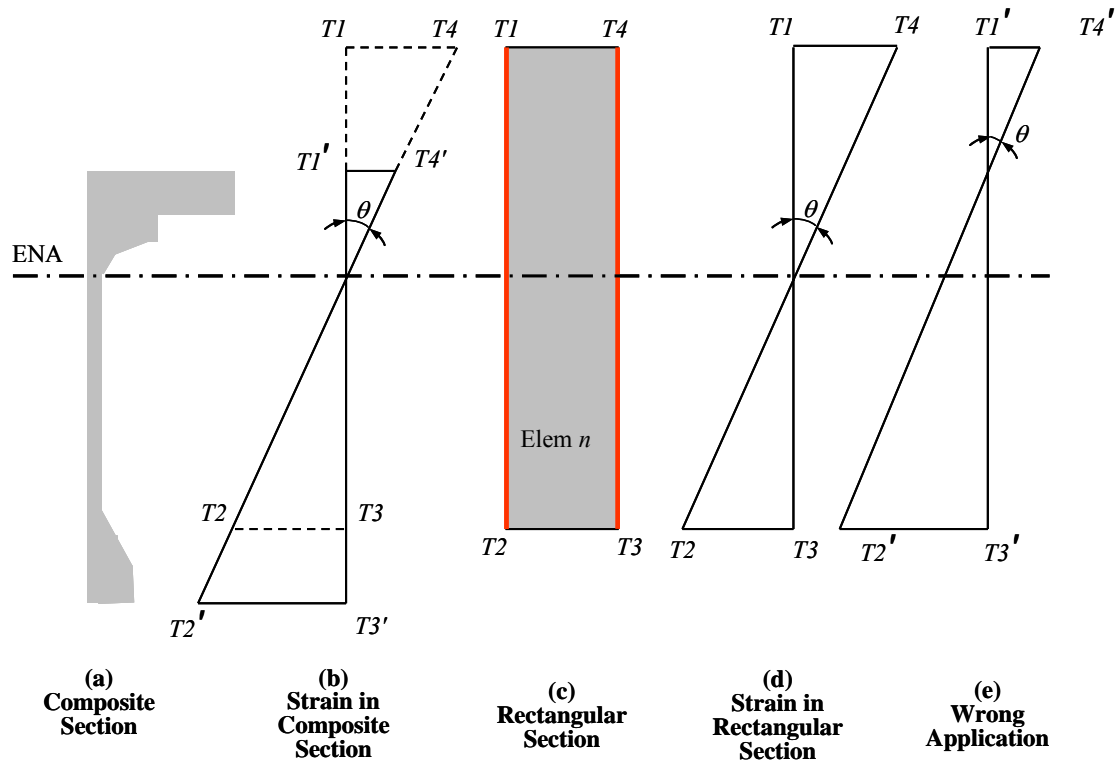


Figure 8.114: Temperature Load Application in Offset Element Section

8.3.2.3 Example 3: 2D Analysis Results

Two analysis approaches are demonstrated in this example: (1) 2D extreme design temperature static analysis and (2) 2D time-history analysis. 2D extreme design temperature range static analysis runs for both AASHTO extreme temperature rise (+30°F) and fall (-40°F). To obtain the maximum response, time-dependent effects are considered only for the bridge contraction case. For the bridge expansion case, only thermal load is considered because the initial bridge expansion will occur before significant time-dependent effects have occurred. If time-dependent loads are desired, 2D models are capable of considering time-dependent loads. The time-history analysis, considering time-dependent effects, runs for a 75-year bridge life with a sinusoidal temperature load. Superimposed results of both approaches are presented on the same

graph for girder axial force, girder bending moment, pile lateral force, pile moment, and pile head displacement.

8.3.2.3.1 Girder Axial Force

Girder axial forces by both extreme design temperature range static analysis (dashed lines) and time-history analysis (solid line) are presented in Figure 8.115. While the temperature range in the extreme temperature static analysis is larger than the time-history analysis temperature range, both analyses predict similar tensile and compressive axial forces. Compared to the time-history analysis, the design analysis predicts 58% larger tensile force and 5% smaller compressive axial force.

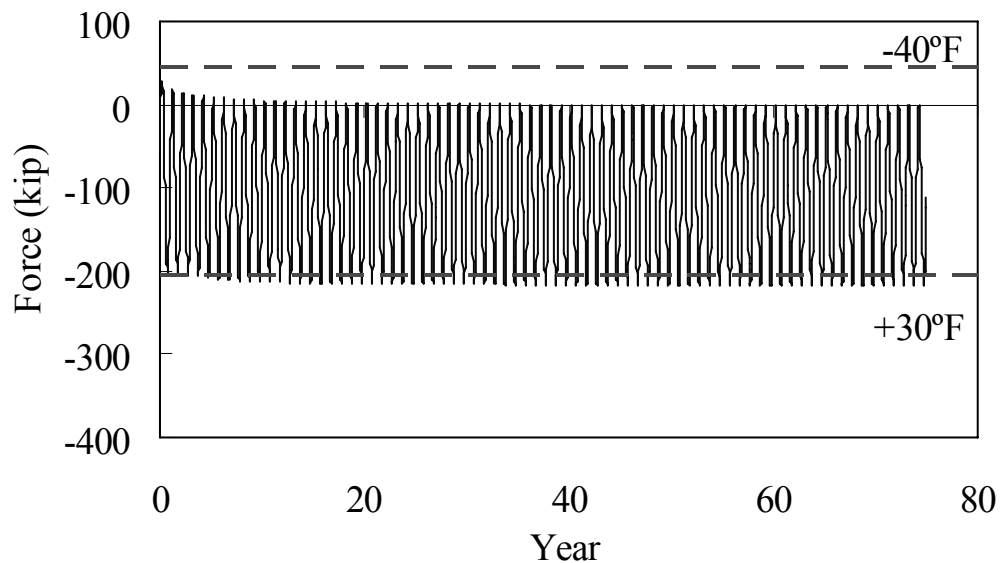


Figure 8.115: Example 3: 2D Analysis—Girder Axial Force (Static and Time-History)

8.3.2.3.2 Girder Bending Moment

Girder bending moments by both extreme design temperature static analysis (dashed lines) and time-history analysis (solid line) are presented in Figure 8.116. The design

analysis predicts a 33% larger positive moment and a 5% larger negative moment compared to the time-history analysis. The time-history analysis prediction fluctuates within the extreme design static analysis predictions.

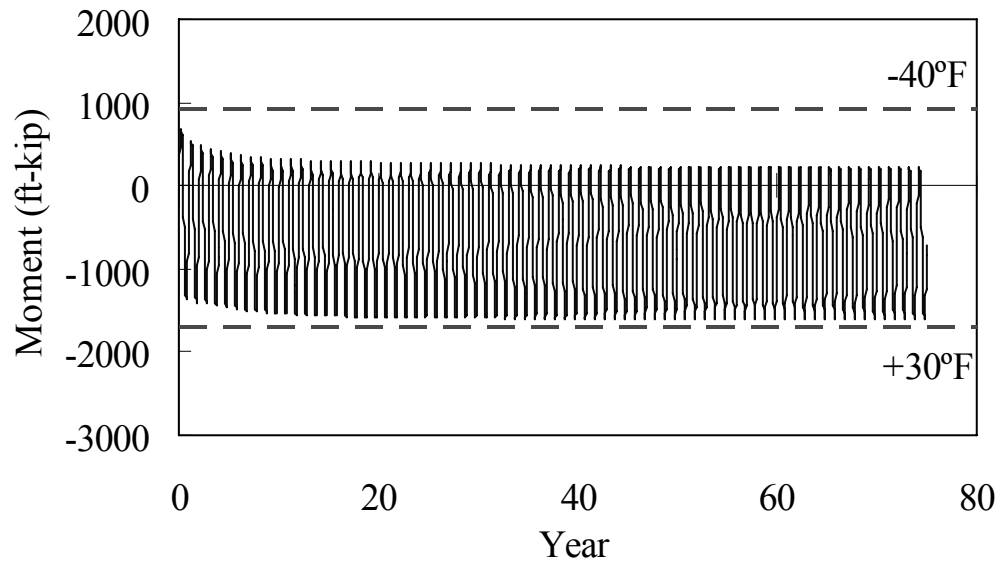


Figure 8.116: Example 3: 2D Analysis—Girder Bending Moment (Static and Time-history)

8.3.2.3.3 Pile Lateral Force

Pile lateral force by both the extreme design temperature static analysis (dashed lines) and the time-history analysis (solid line) is presented in Figure 8.117. The design analysis predicts 25% larger positive pile lateral force and 68% smaller negative pile lateral force compared to the time-history analysis. Initially, the time-history analysis results are bounded by the design analysis results, but the negative pile lateral force increases during the first 10 years.

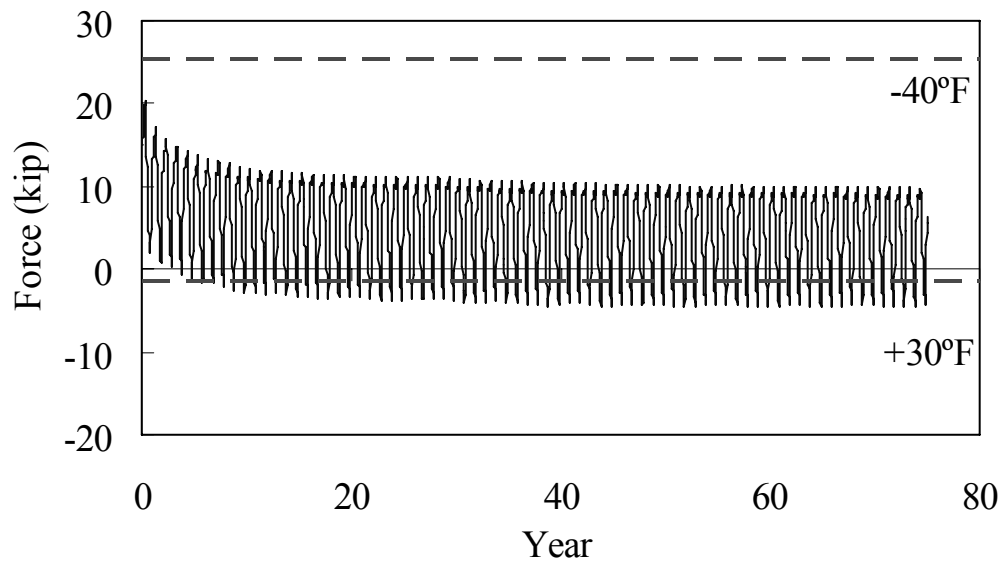


Figure 8.117: Example 3: 2D Analysis - Pile Lateral Force (Static and Time-history)

8.3.2.3.4 Pile Moment

Pile moment by both extreme design temperature static analysis (dashed lines) and time-history analysis (solid line) is presented in Figure 8.118. The design analysis predicts 39% smaller positive moment and 5% larger negative moment compared to the time-history analysis. Initially the time-history analysis prediction starts between the design analysis upper and lower boundary, but pile moments increase during the first 5 years. Thereafter, pile moments start to decrease over 40 years.

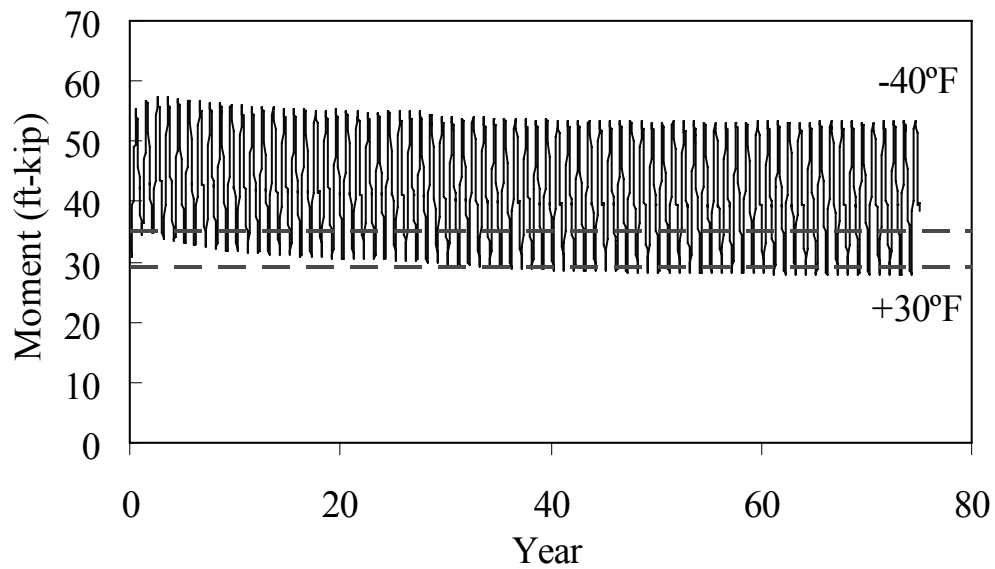


Figure 8.118: Example 3: 2D Analysis - Pile Moment (Static and Time-History)

8.3.2.3.5 Pile Head Displacement

Pile head displacement by both extreme design temperature static analysis (dashed lines) and time-history analysis (solid line) is presented in Figure 8.119. The design analysis predicts 50% larger maximum pile head displacement compared to the time-history analysis.

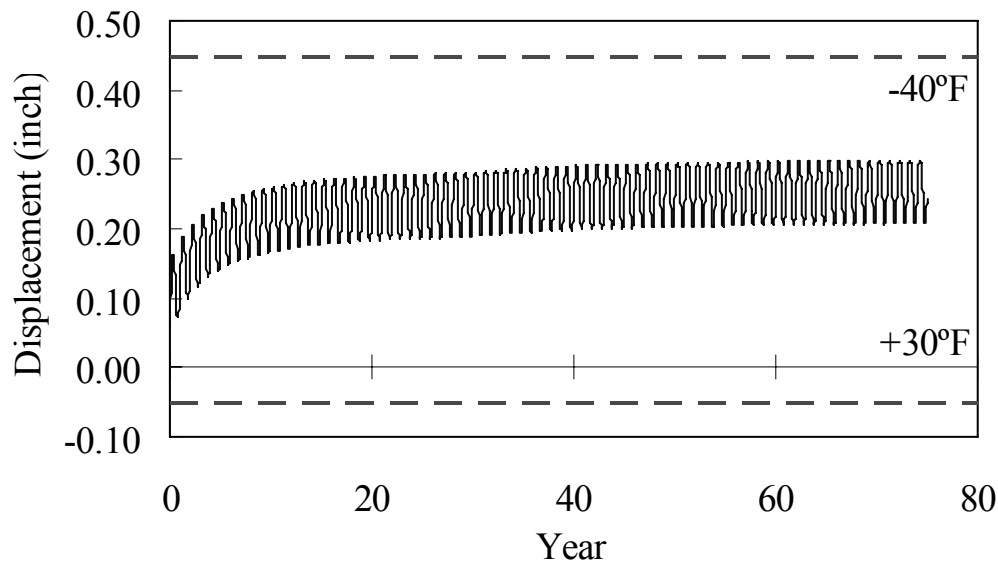


Figure 8.119: Example 3: 2D Analysis—Pile Head Displacement (Static and Time-History)

8.3.3 Example 3: Three-dimensional Analysis Model

Three-dimensional numerical simulations offer increased predictive accuracy over two-dimensional simulations. In addition, individual element response to load is available from the 3D analysis rather than grouped response as in a 2D analysis. Transverse effects are also determined with a 3D simulation due to the added third, transverse dimension to the model. The methodology presented here permits the incorporation of individual bridge elements and the respective material and geometric properties through a demonstrated effective 3D model approach using the commercially available, general analysis program ANSYS. The Example 3, 3D analysis evaluates two separate loading cases that consist of the AASHTO extreme temperature rise (+30°F) and extreme temperature fall (-40°F). Any other thermal loading may be applied to the 3D, however.

The Example 3, 3D ANSYS schematic model in isometric view is presented in Figure 8.120. Each of the five prestressed concrete girders is represented using ANSYS BEAM189 elements that have a AASHTO PCI BT81 cross section. At the mid-point of the 9-inch bridge deck thickness are ANSYS SHELL63 elements, which have 6 degrees of freedom at each of four corner nodes. To connect the deck to the five girders, ANSYS rigid link MPC184 elements are included at a longitudinal spacing equal to 2 ft. The connection of girders and deck accomplishes the effects of a composite section as is intended in the original design. Abutment piles are included in the 3D model with ANSYS BEAM189 elements defined with the pile HP12×74 cross section. Soil-pile interaction springs modeled using ANSYS COMBIN39 elements spaced at the maximum of 1 ft are included along the full height of each pile. The abutment and back-wall elements are modeled using ANSYS SHELL63 with a maximum of 1 ft side dimension. Abutment-to-backfill interaction is represented with ANSYS COMBIN39 elements nonlinear springs. Bridge diaphragms are included in the 3D model using BEAM189 elements. An isometric view of the completed solid ANSYS 3D numerical model with actual cross sections of each member of the bridge is presented in Figure 8.121.

Bridge load includes the superstructure temperature fluctuation, temperature gradient, and backfill pressure. As with the 2D simulation, the thermal loading model developed on the basis of actual measurements is utilized for the 3D model. However, a time-history analysis with the 3D numerical model is not practical due to unmanageable computing time and memory demand; therefore, a static analysis under design level thermal loads is performed.

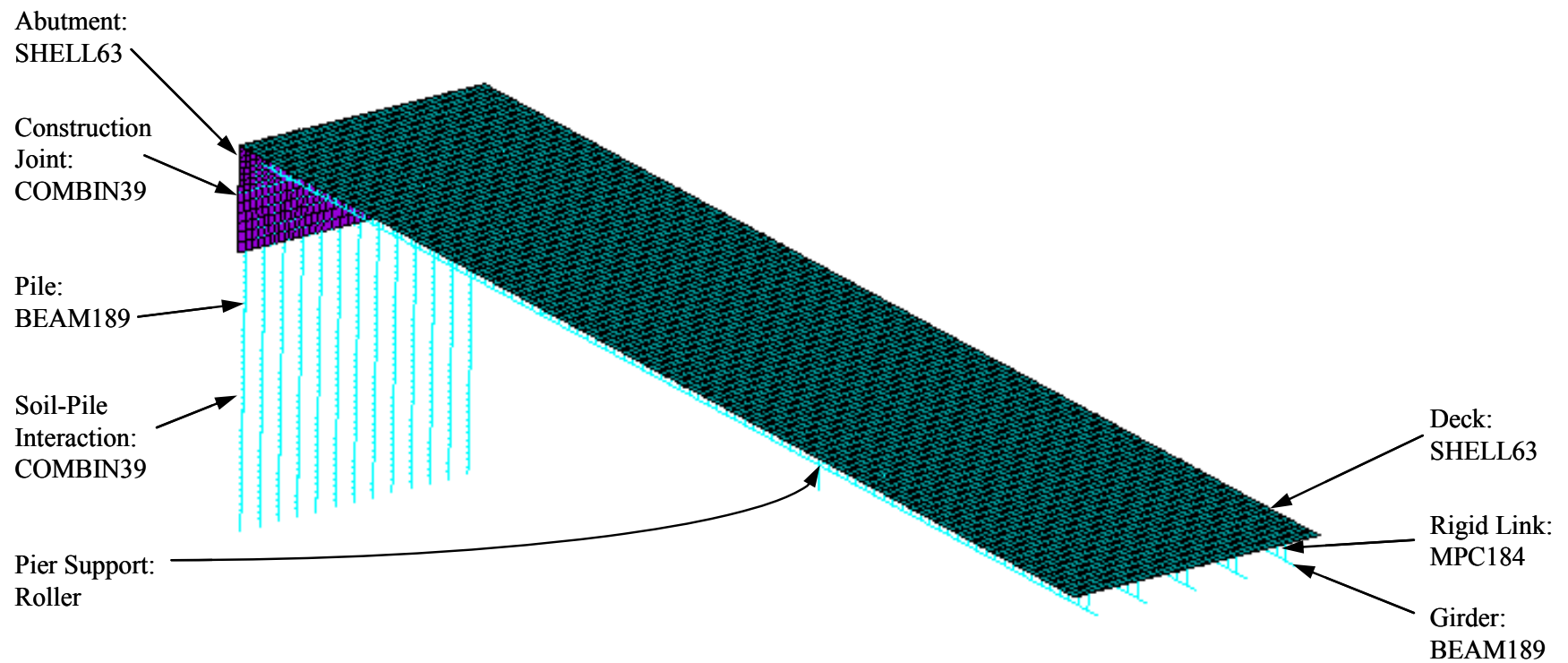


Figure 8.120: Example 3 3D Schematic ANSYS Bridge Model – Isometric View.

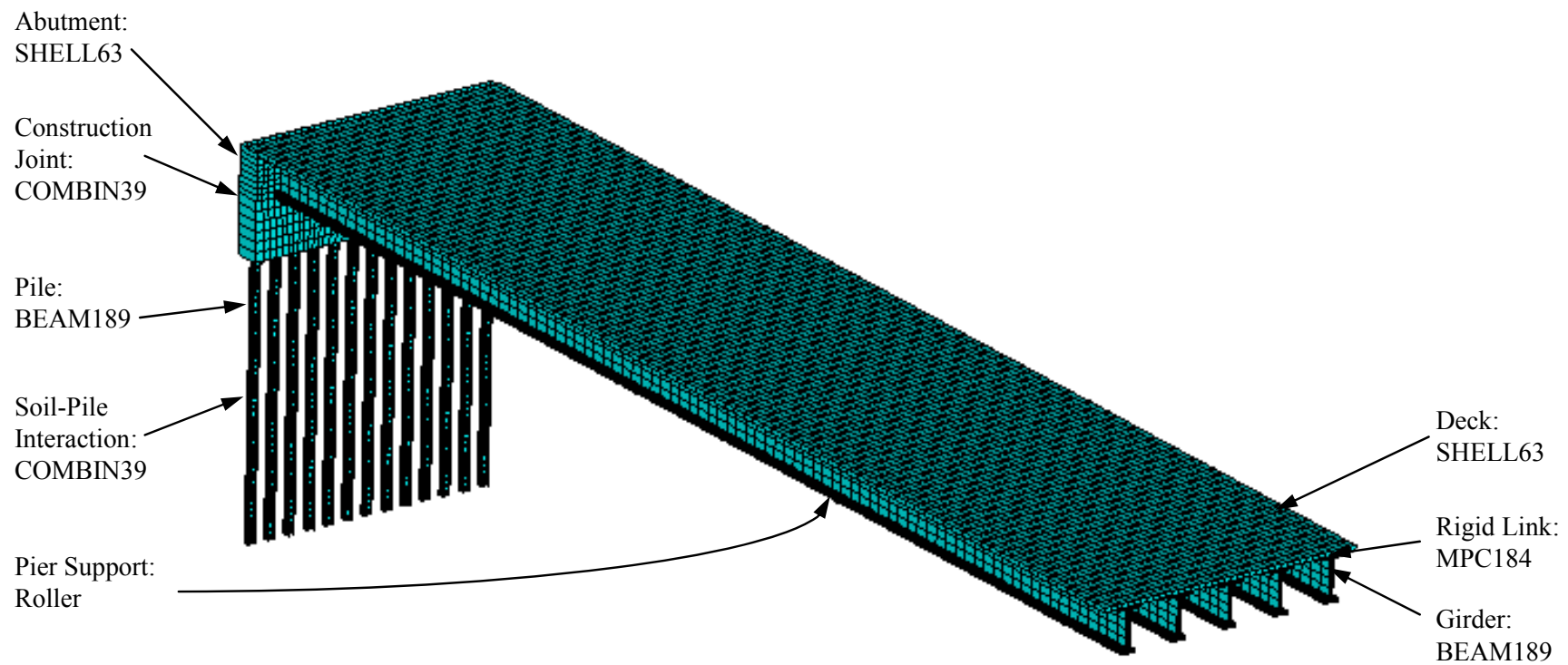


Figure 8.121: Example 3 Solid 3D Bridge Model – Isometric View

8.3.3.1 Bridge Components

Each bridge component and its material and geometric definition is described in detail in the following sections to permit development of future models for other IABs. The discussion includes girder and deck, abutment/backwall, construction joint, piles, and soil springs and analysis results.

8.3.3.1.1 Girder and Deck

The bridge girders are modeled using the ANSYS 3D beam element BEAM189 based on the BT81 girder cross section in Figure 8.122. ANSYS computes all geometric properties of the cross-section, as shown in the figure. The 9-inch concrete deck is modeled using the solid element SHELL63 that has both bending and membrane capabilities. Girder and deck 28-day concrete strengths are specified as 8,000 psi and 4,000 psi, respectively. The elastic modulus of concrete is computed using the widely accepted AASHTO and ACI formula:

$$E_c = 33000w_c^{1.5}\sqrt{f'_c} \quad (8.1)$$

resulting in E_c for girders and deck equal to 5,150 ksi and 3,640 ksi.

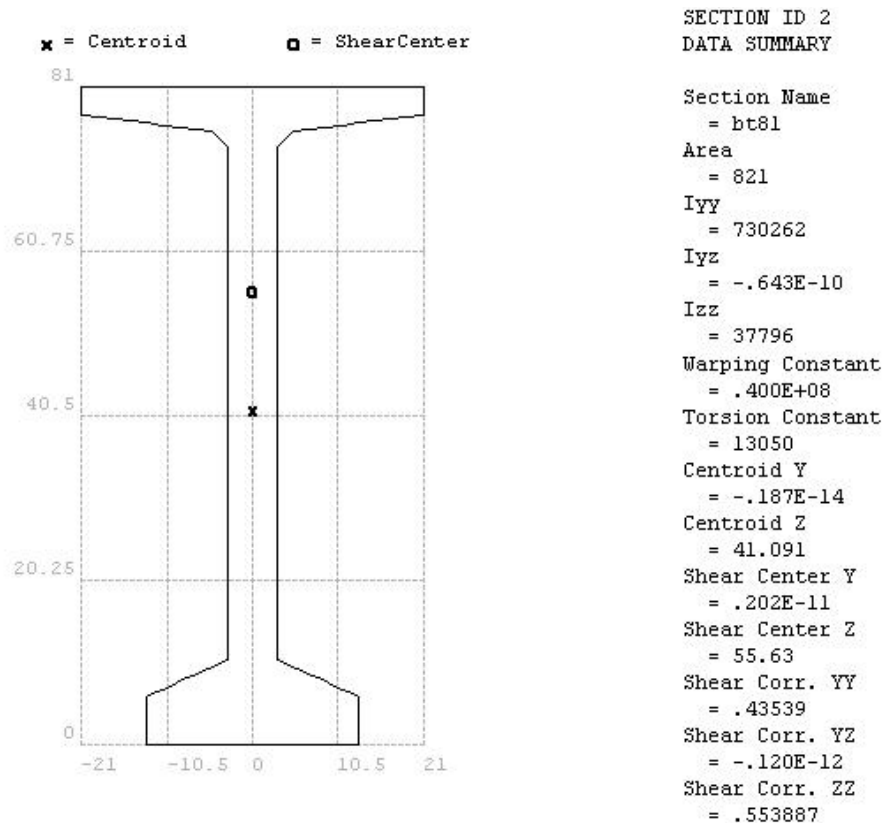


Figure 8.122: Cross Section of BT81 Girder (units are inches).

Based on AASHTO LRFD recommendations, the thermal expansion coefficient for deck concrete and girder concrete is assigned a value of $6.0\text{E-}6$ in/in/°F.

To model the bridge girder and deck composite section, ANSYS rigid link MPC184 elements are included to connect the girder and deck. This is necessary because the geometric center of the slab and the girder are offset in the model, requiring a connection that enforces compatible displacements, three translational and three rotational. Details of the rigid link connection are presented in Figure 8.123. Each girder element and deck element is located at its respective geometric center, as shown in the figure. The rigid link, which is a multi-point constraint element, connects the girder and deck at 2-ft intervals, forcing displacement compatibility and, therefore, composite behavior.

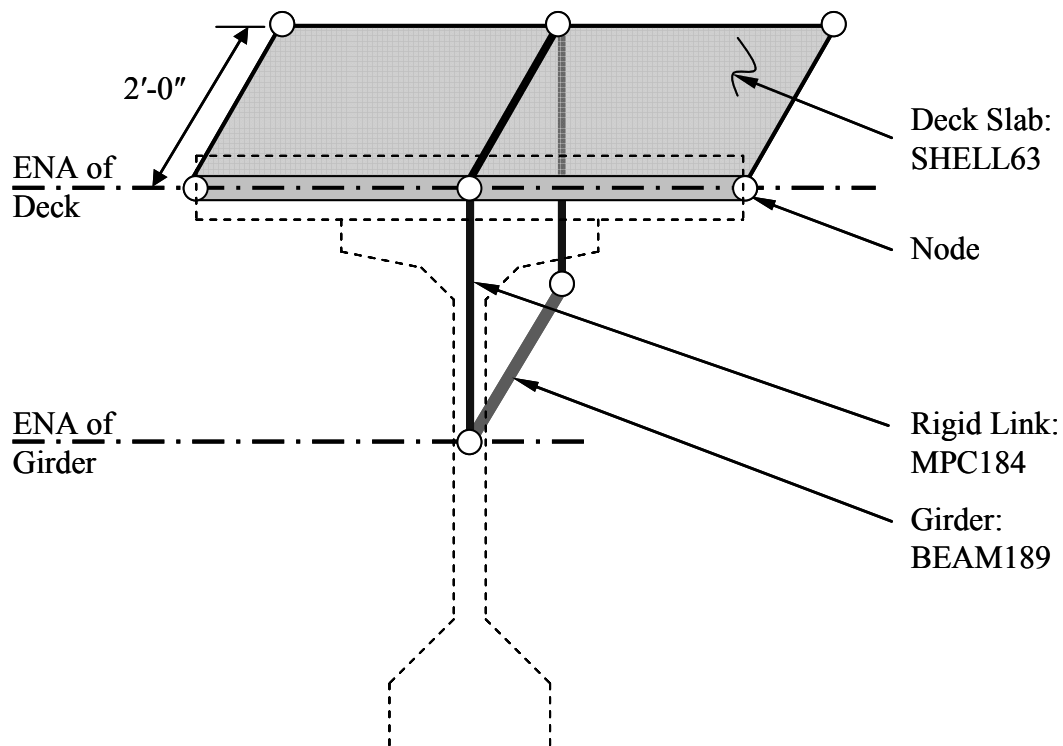


Figure 8.123: Girder and Deck Slab Connection

8.3.3.1.2 Abutment/Backwall

Both the abutment (or pile cap) and back-wall (or end diaphragm) are modeled using ANSYS solid element SHELL63. The full height of the abutment and back-wall are modeled with the SHELL63 element located at the abutment centerline. Each SHELL 63 element is meshed at 1 ft in both directions to increase accuracy and to facilitate connections of abutment elements to back-wall, girder, and deck elements. The model element assembly of the abutment and back-wall is shown in Figure 8.124, viewed from the backfill side.

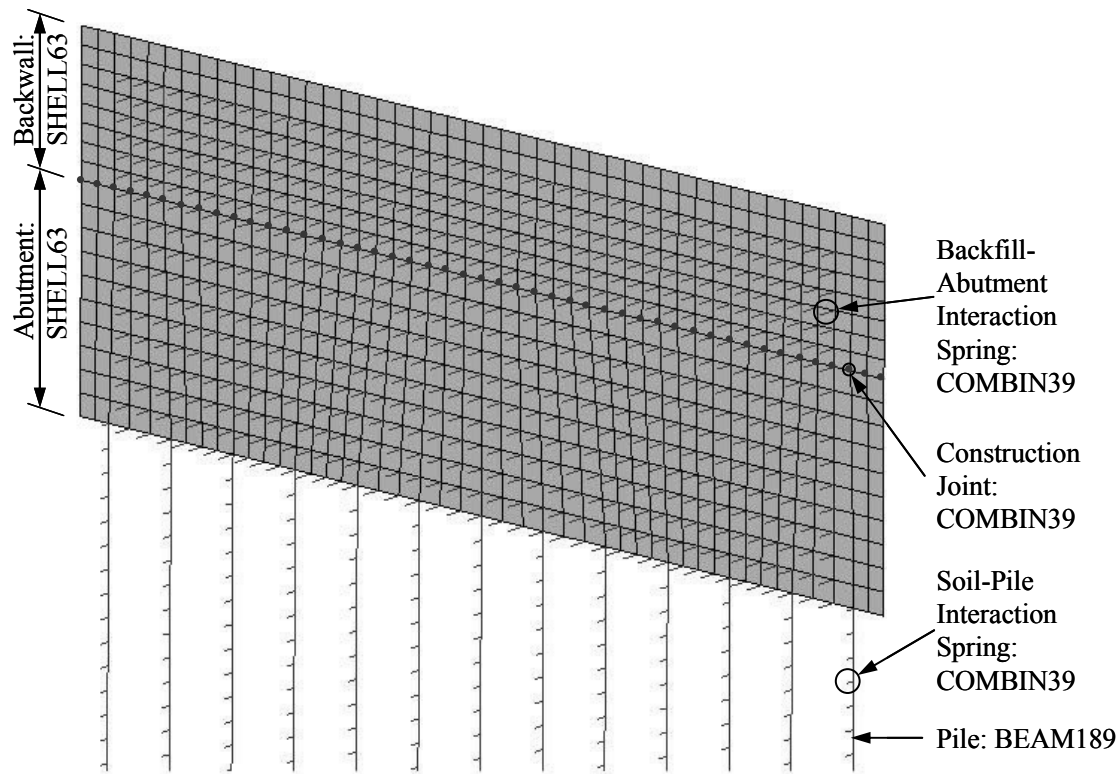


Figure 8.124: Example 3 3D Abutment and Back-wall – Viewed from Backfill

Normally, higher-strength concrete is used for the back-wall concrete as compared to abutment concrete because the back-wall is placed with the deck. Example 3 bridge specifications are for 28-day compressive strength concrete equal to 4,000 psi and 3,000 psi at the back-wall and abutment, respectively, resulting in computed elastic moduli for the back-wall equal to 3,640 ksi and for the abutment equal to 3,160 ksi.

Two nodes (separate but coincident) are placed at the construction joint between the back-wall and the abutment and are connected by the ANSYS joint element COMBIN39. The properties of this joint element are discussed in the following section.

8.3.3.1.3 Construction Joints

Rotational stiffness of the back-wall to abutment joint is modeled using the ANSYS COMBIN39 element as presented in Section 5.2.4 of this report. All translations and rotations except z-axis rotation are coupled where rotation is defined by COMBIN39. A graphical illustration of the construction joint modeling, showing all nodes and elements, is presented in Figure 8.125. The computed construction joint rotational stiffness is based on the PennDOT standard detail BD-667 that specifies #5 “U” reinforcing bars at 9 inches. The imbalance of reinforcement between the backfill face and the front face is also considered in the definition of the joint element. For the expansion case, moment-rotation properties are computed:

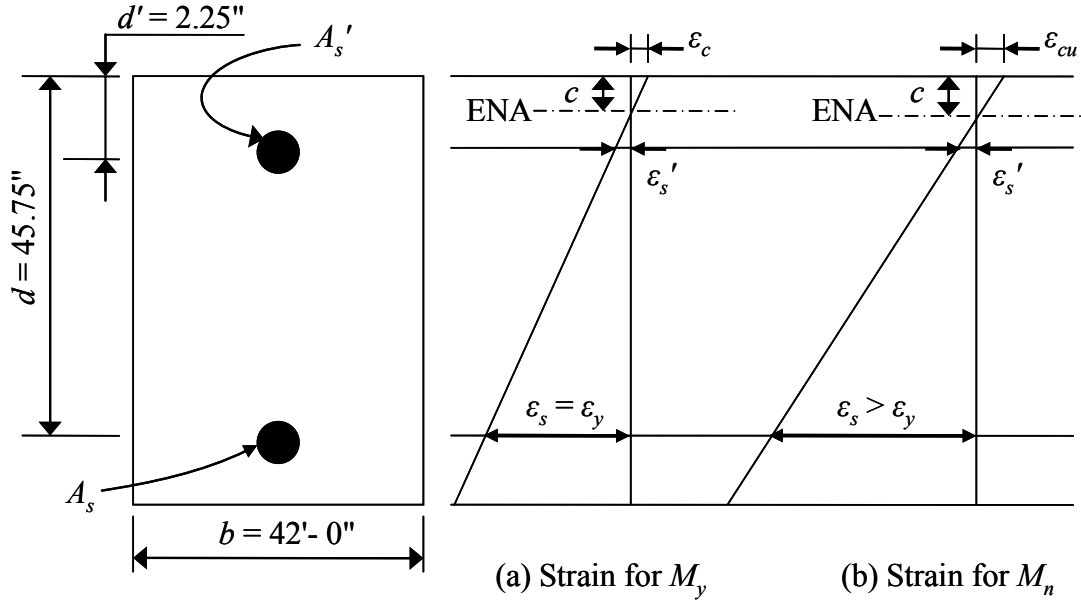
For backfill side, rebar area is:

$$\begin{aligned} A_s &= (\text{\#5 rebar area}) \times (\text{number of rebars}) \\ &= (\text{\#5 rebar area}) \frac{(\text{abutment width})}{(\text{rebar spacing})} = (0.31 \text{ in}^2) \frac{42'}{9''} \\ &= (0.31 \text{ in}^2) \times (56 \text{ rebars}) \\ &= 17.36 \text{ in}^2 \end{aligned}$$

For front face side, rebar area is:

$$\begin{aligned} A_s' &= (\text{\#5 rebar area})(\text{number of rebars}) \\ &= (\text{\#5 rebar area}) \frac{(\text{abutment width}) - (\text{number of girders})(\text{girder width})}{(\text{rebar spacing})} \\ &= (0.31 \text{ in}^2) \frac{(42') - (4)(26'')}{9''} \\ &= (0.31 \text{ in}^2)(45 \text{ rebars}) \\ &= 13.95 \text{ in}^2 \end{aligned}$$

Based on the specified abutment reinforcing, two bending capacities of (1) yielding moment (M_y) and (2) ultimate moment (M_n) are evaluated and strain compatibility is presented in Figure 8.125.



d = distance from the extreme fiber to the centroid of tension reinforcement
 d' = distance from the extreme fiber to the centroid of compression reinforcement
 A_s = tension reinforcement area
 A_s' = compression reinforcement area
 b = beam width
 ϵ_c = strain in concrete at the extreme compressive fiber corresponding stress f_c
 ϵ_{cu} = ultimate concrete compression strain (= 0.003) corresponding stress f_c'
 ϵ_s = strain in tension reinforcement corresponding stress f_s
 ϵ_s' = strain in compression reinforcement corresponding stress f_s'
 ϵ_y = yielding strain of steel rebars (= 0.00207)

Figure 8.125: Strains in Doubly Reinforced Beam

The distance between the ENA and the extreme compressive fiber, c , for yielding capacity M_y is computed as follows:

From strain compatibility in Figure 8.125, tensile forces, T , are:

$$T = A_s f_y + A_s' f_s' = A_s f_y + A_s' E_s \epsilon_s' = A_s f_y + A_s' E_s \left(\frac{\epsilon_y (d' - c)}{(d - c)} \right)$$

$$= (17.36 \text{ in}^2)(60 \text{ ksi}) + (13.95 \text{ in}^2)(29000 \text{ ksi}) \left(\frac{0.00207(2.25 \text{ in} - c)}{45.75 \text{ in} - c} \right)$$

Similarly, compressive force, C , is:

$$C = \frac{1}{2} f_c c b = \frac{1}{2} \left(\frac{c}{d - c} f_y \right) b = \frac{1}{2} \left(\frac{c}{45.75 \text{ in} - c} (60 \text{ ksi}) \right) (42 \text{ ft})$$

From $C = T$,

$$c = 1.75 \text{ inches and } \varepsilon_c = c \frac{\varepsilon_y}{d - c} = 0.000082 < \varepsilon_{cu} = 0.003.$$

Thus, $M_y = A_s f_y (d - c) + A_s' f_s' (d' - c) = \underline{550,000 \text{ ft-kips}}$

Curvature (ϕ) is computed as:

$$\phi = \frac{\varepsilon_c}{c} = 0.000047$$

Based on half the minimum development length, l_d , rotation (θ) is computed as:

$$\theta = \phi \cdot l_d = (0.000047)(8 \text{ inches}) = \underline{0.00038 \text{ radians}}$$

For the nominal moment capacity, M_n , ultimate concrete strain (ε_{cu}) is used in the calculation:

$$\begin{aligned} T &= A_s f_y + A_s' f_s' = A_s f_y + A_s' E_s \varepsilon_s' = A_s f_y + A_s' E_s \left(\frac{\varepsilon_{cu}(d' - c)}{c} \right) \\ &= (17.36 \text{ in}^2)(60 \text{ ksi}) + (13.95 \text{ in}^2)(29000 \text{ ksi}) \left(\frac{0.003(2.25 \text{ in} - c)}{c} \right) \end{aligned}$$

Similarly, the compressive force, C , is:

$$C = 0.85 f_c' b (\beta_1 c) = 0.85 (3 \text{ ksi}) (42 \text{ ft}) (0.85 \times c)$$

From $C = T$,

$$c = 1.50 \text{ inches and } \varepsilon_c = \varepsilon_{cu} = 0.003.$$

Thus, $M_n = A_s f_y (d - c) + A_s' f_s' (d' - c) = \underline{558,000 \text{ ft-kips}}$

Curvature (ϕ) is computed as:

$$\phi = \frac{\varepsilon_c}{c} = 0.00199$$

Based on half the minimum development length, l_d , rotation (θ) is computed as:

$$\theta = \phi \cdot l_d = (0.00199)(8 \text{ inches}) = \underline{0.0159 \text{ radian}}$$

For the bridge contraction case, a similar computation can be performed exchanging A_s and A_s' . The moment-rotation curve in Figure 8.126 is obtained.

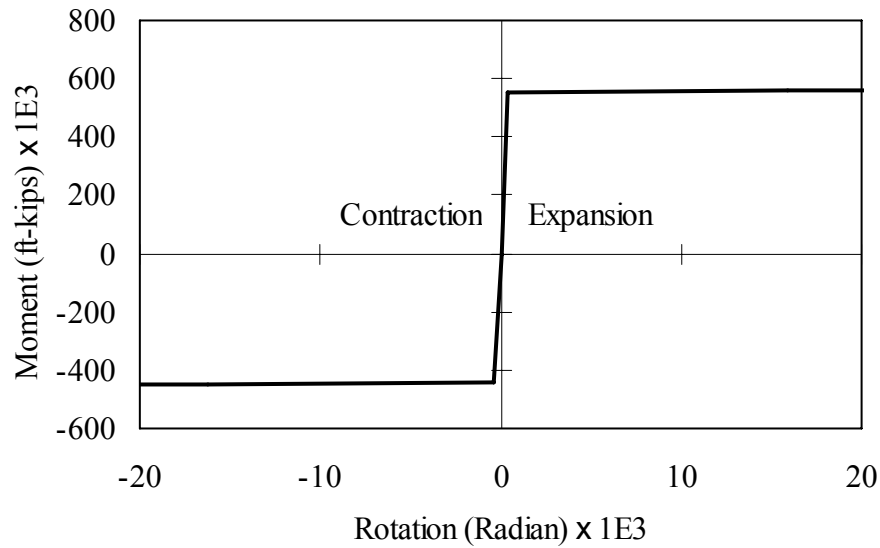


Figure 8.126: Moment-Rotation Curve

An average transverse distance (z-axis direction in Figure 8.127) between two adjacent nodes along the construction joint is computed. The foregoing total, doubly reinforced moment-to-rotation property of the construction joint is evenly distributed at each node pair based on the computed average distance.

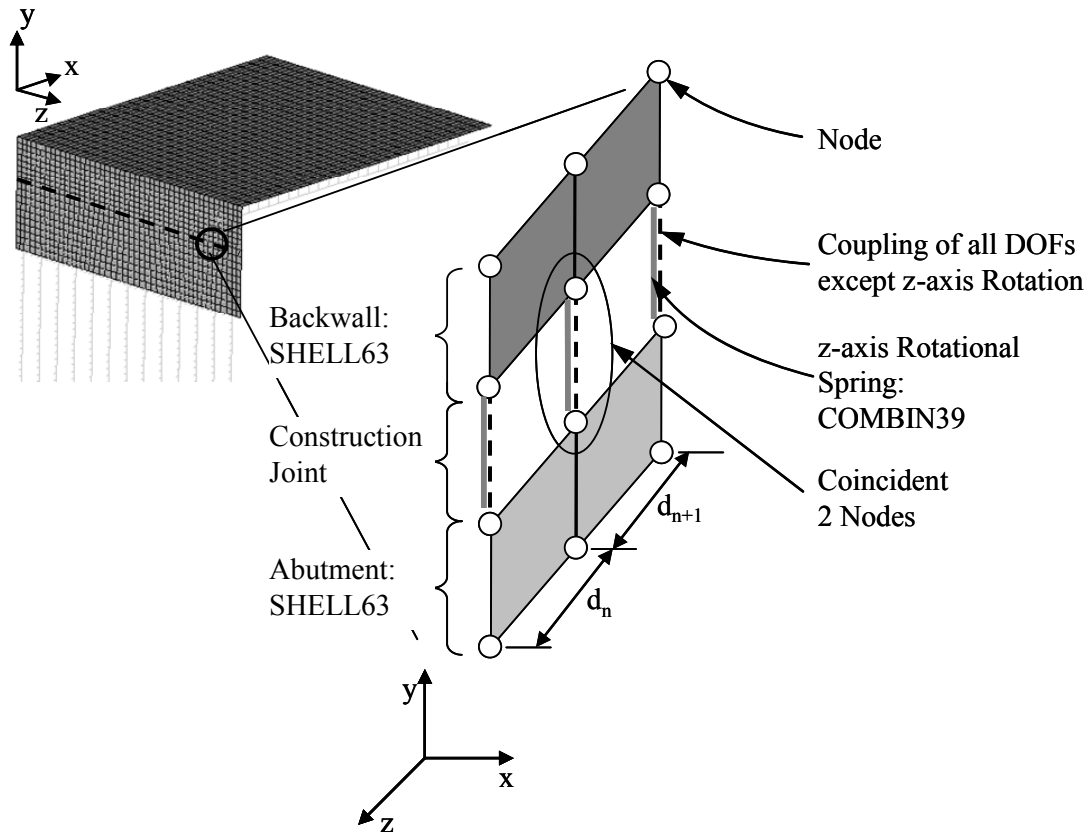


Figure 8.127: Example 3 Abutment to Back-wall Construction Joint Modeling
(Note: All nodes are coincident at construction joints)

8.3.3.1.4 Pile Foundations

Weak axis oriented steel HP12×74 piles are modeled using ANSYS beam elements BEAM189 and soil-pile interaction is modeled using nonlinear spring elements COMBIN39. For beam elements, the pile section and computed properties provided in Figure 8.128 are used in the Example 3, 3D model.

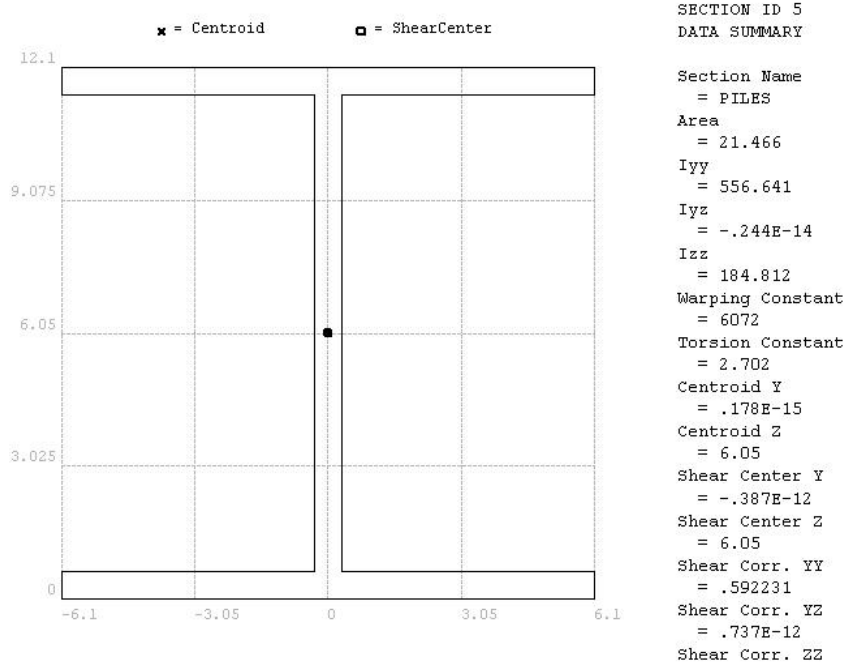


Figure 8.128: HP12×74 Foundation Pile Section

A total of thirteen HP12×74 piles by 30 ft long are used in this Example 3 3D model as presented in Figure 8.128. The specified soil unit weight, $\gamma = 121$ pcf, undrained shear strength (c) = 17.5 psi, and $\varepsilon_{50} = 0.008$. The soil-pile interaction is represented by a Winkler spring using ANSYS COMBIN39 elements developed on the basis of p - y curves. The same p - y curve equations in Equations 5.3 and 5.4 are used to generate force-displacement properties at each depth as shown in Figure 8.129:

$$p = 0.5 p_u \left(\frac{y}{y_{50}} \right)^{1/4} \quad (5.3)$$

$$p_u = \min \left\{ p_{uf} = 9cD, \quad p_{uw} = \left(3 + \frac{\gamma'}{c} X + \frac{J}{D} X \right) cD \right\} \quad (5.4)$$

For this 3D example, a p - y curve at each depth at a 1-ft increment is computed.

Alternatively, commercial programs such as COM624P and Lpile can directly generate p -

p -y curves at a wide range of soil conditions and depths. The COMBIN39 springs are distributed along the full depth of the pile, spaced at 1'-0". The spring element lateral force versus lateral displacement properties at a given depth include the tributary area (1'-0" tributary depth \times pile effective diameter $b_f = 12.1$ ") (see Figure 8.129) of the spring at each location.

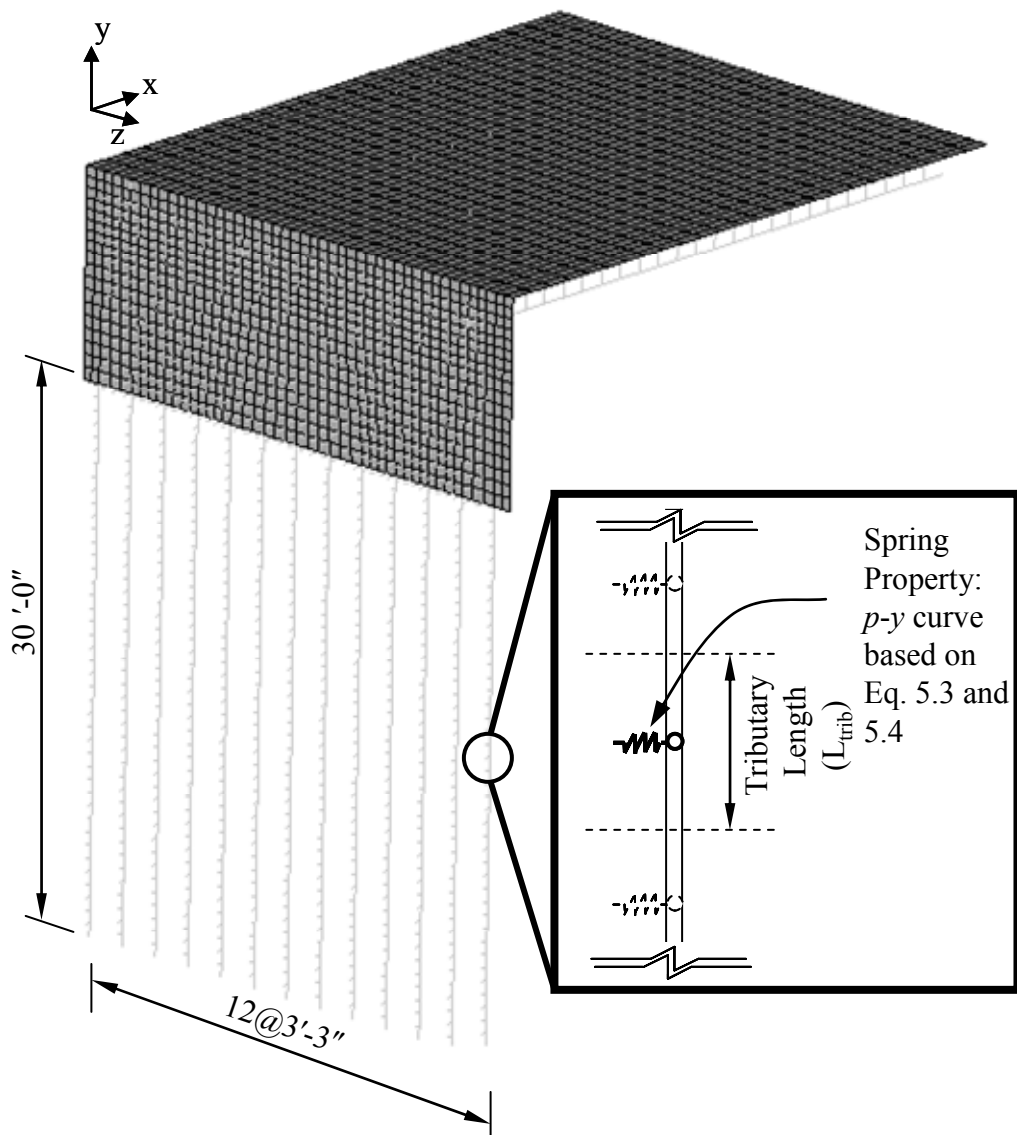


Figure 8.129: Foundation Pile Section Soil Spring Definition.

8.3.3.1.5 Miscellaneous Components

The mid-span bridge diaphragm is coincident with the bridge transverse axis of symmetry and is not explicitly modeled. A boundary condition in a 3-span bridge is applied at the bridge symmetry centerline. At the transverse axis of symmetry the x (longitudinal) and z (transverse) translations and y (in deck plane twisting) and z (girder strong axis bending) rotations are restrained. Piles are driven into bedrock and vertical translation is restrained at the pile tips. To expedite numerical computation convergence, z-axis translation is provided from pile tip to the characteristic length, l_c .

$$l_c = \sqrt[4]{\frac{4E_p I_p}{K}} \quad (7.1)$$

$$l_c = \sqrt[4]{\frac{4(29000 \text{ ksi})(186 \text{ in}^4)}{1000 \text{ psi}}} = 68 \text{ inches} \approx 6 \text{ ft}$$

If pile head displacements in the z direction are expected, the same p - y curve description in Section 8.3.3.1.4 of this report should be employed.

8.3.3.2 Loads

The loads applied in the Example 3, 3D model include superstructure temperature load, temperature gradient, backfill pressure, and time-dependent loads. Each load case is described in the subsequent sections.

8.3.3.2.1 Temperature Load

The superstructure thermal load definition for this example is taken from AASHTO LRFD (2007): 0°F to 120°F for steel and 10°F to 80°F for concrete. PennDOT DM-4 Appendix 1.2.7.4 (2007) describes extreme temperature loads for concrete bridges as an

80°F temperature rise or fall, equivalent to a 160°F range. Monitoring conducted under the present study revealed that a temperature rise or fall equal to 80°F is extremely conservative. Based on the example procedure described in *AASHTO Guide Specifications: Thermal Effects in Concrete Bridge Superstructures* (1989), the extreme temperature for bridge expansion and contraction is 30°F increase and 40°F decrease for the current example bridge. Therefore, a uniform temperature load equal to a 30°F increase and 40°F decrease is applied to the bridge girders and deck for the purposes of this example.

8.3.3.2.2 Temperature Gradient

Based on AASHTO multi-linear temperature gradient, an equivalent temperature gradient is computed. Equivalent temperature loads by Equation 5.14 and 5.15 are computed. AASHTO LRFD 3.12.3 provide temperature gradient model for Pennsylvania area as presented in Figure 8.130.

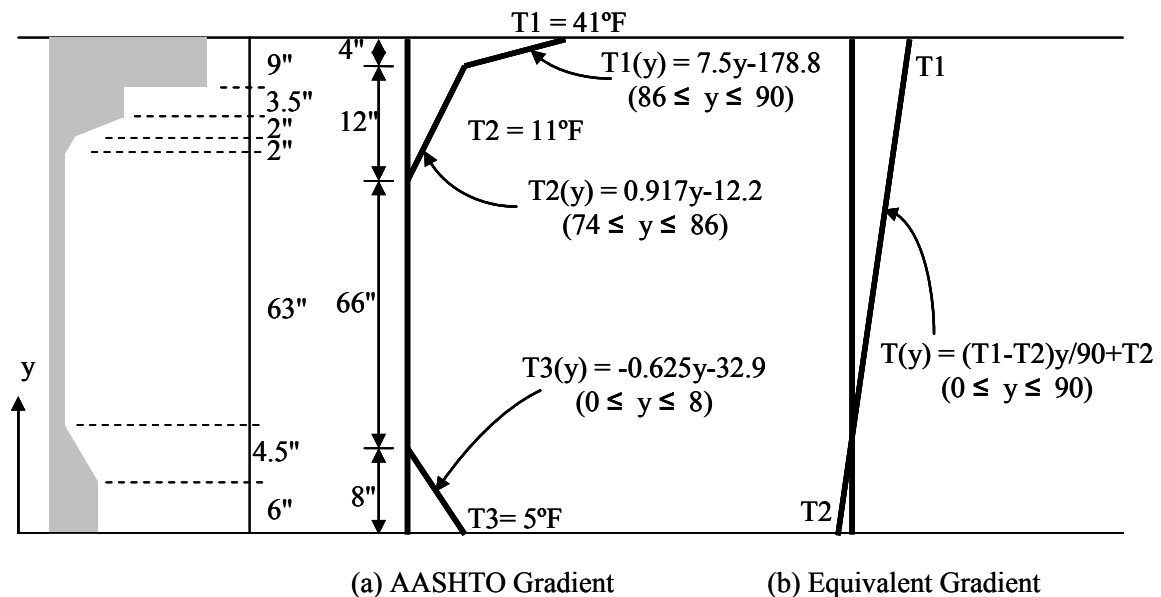


Figure 8.130: Temperature Gradient for BT81 Girder in Pennsylvania

Axial force can be obtained as:

$$\begin{aligned}
 P &= \int \sigma_t(y)b(y)dy = \int E\alpha T(y)b(y)dy \\
 &= \int_0^6 (5154 \text{ ksi})(6.0 \times 10^{-6} / ^\circ \text{ F})[-0.625y - 32.9](26'')dy \\
 &\quad + \int_6^8 (5154 \text{ ksi})(6.0 \times 10^{-6} / ^\circ \text{ F})[-0.625y - 32.9](21.56'')dy \\
 &\quad + \int_{76}^{77.5} (5154 \text{ ksi})(6.0 \times 10^{-6} / ^\circ \text{ F})[0.917y - 12.2](30'')dy \\
 &\quad + \int_{77.5}^{81} (5154 \text{ ksi})(6.0 \times 10^{-6} / ^\circ \text{ F})[0.917y - 12.2](42'')dy \\
 &\quad + \int_{81}^{86} (5154 \text{ ksi})(6.0 \times 10^{-6} / ^\circ \text{ F})[0.917y - 12.2](72.12'')dy \\
 &\quad + \int_{86}^{90} (5154 \text{ ksi})(6.0 \times 10^{-6} / ^\circ \text{ F})[7.5y - 137.291](72.12'')dy \\
 &= 336.7 \text{ kips}
 \end{aligned}$$

Similarly, moment can be obtained as:

$$\begin{aligned}
 M &= \int \sigma_t(y)b(y)ydy = \int E\alpha T(y)b(y)ydy \\
 &= \int_0^6 (5154 \text{ ksi})(6.0 \times 10^{-6} / ^\circ \text{ F})[-0.625y - 32.9](26'')ydy \\
 &\quad + \int_6^8 (5154 \text{ ksi})(6.0 \times 10^{-6} / ^\circ \text{ F})[-0.625y - 32.9](21.56'')ydy \\
 &\quad + \int_{76}^{77.5} (5154 \text{ ksi})(6.0 \times 10^{-6} / ^\circ \text{ F})[0.917y - 12.2](30'')ydy \\
 &\quad + \int_{77.5}^{81} (5154 \text{ ksi})(6.0 \times 10^{-6} / ^\circ \text{ F})[0.917y - 12.2](42'')ydy \\
 &\quad + \int_{81}^{86} (5154 \text{ ksi})(6.0 \times 10^{-6} / ^\circ \text{ F})[0.917y - 12.2](72.12'')ydy \\
 &\quad + \int_{86}^{90} (5154 \text{ ksi})(6.0 \times 10^{-6} / ^\circ \text{ F})[7.5y - 137.291](72.12'')ydy \\
 &= 619.8 \text{ ft-kips}
 \end{aligned}$$

Based on the obtained axial force and moment, an equation is built:

$$\begin{aligned}
 P_{eq} &= \int \sigma_t(y) b(y) dy = \int E \alpha T(y) b(y) dy \\
 &= \int_0^6 (5154 \text{ ksi}) (6.0 \times 10^{-6} / ^\circ \text{F}) \left[\frac{T1 - T2}{90} y + T2 \right] (26") dy \\
 &+ \int_6^{10.5} (5154 \text{ ksi}) (6.0 \times 10^{-6} / ^\circ \text{F}) \left[\frac{T1 - T2}{90} y + T2 \right] (16") dy \\
 &+ \int_{10.5}^{72.5} (5154 \text{ ksi}) (6.0 \times 10^{-6} / ^\circ \text{F}) \left[\frac{T1 - T2}{90} y + T2 \right] (6") dy \\
 &+ \int_{72.5}^{74.5} (5154 \text{ ksi}) (6.0 \times 10^{-6} / ^\circ \text{F}) \left[\frac{T1 - T2}{90} y + T2 \right] (8") dy \\
 &+ \int_{74.5}^{76.5} (5154 \text{ ksi}) (6.0 \times 10^{-6} / ^\circ \text{F}) \left[\frac{T1 - T2}{90} y + T2 \right] (26") dy \\
 &+ \int_{76.5}^{81} (5154 \text{ ksi}) (6.0 \times 10^{-6} / ^\circ \text{F}) \left[\frac{T1 - T2}{90} y + T2 \right] (42") dy \\
 &+ \int_{81}^{90} (5154 \text{ ksi}) (6.0 \times 10^{-6} / ^\circ \text{F}) \left[\frac{T1 - T2}{90} y + T2 \right] (72.12") dy
 \end{aligned}$$

$$\begin{aligned}
 M_{eq} &= \int \sigma_t(y) b(y) y dy = \int E \alpha T(y) b(y) y dy \\
 &= \int_0^6 (5154 \text{ ksi}) (6.0 \times 10^{-6} / ^\circ \text{F}) \left[\frac{T1 - T2}{90} y + T2 \right] (26") y dy \\
 &+ \int_6^{10.5} (5154 \text{ ksi}) (6.0 \times 10^{-6} / ^\circ \text{F}) \left[\frac{T1 - T2}{90} y + T2 \right] (16") y dy \\
 &+ \int_{10.5}^{72.5} (5154 \text{ ksi}) (6.0 \times 10^{-6} / ^\circ \text{F}) \left[\frac{T1 - T2}{90} y + T2 \right] (6") y dy \\
 &+ \int_{72.5}^{74.5} (5154 \text{ ksi}) (6.0 \times 10^{-6} / ^\circ \text{F}) \left[\frac{T1 - T2}{90} y + T2 \right] (8") y dy
 \end{aligned}$$

$$\begin{aligned}
& + \int_{74.5}^{76.5} (5154 \text{ ksi}) (6.0 \times 10^{-6} / ^\circ \text{F}) \left[\frac{T1 - T2}{90} y + T2 \right] (26'') y dy \\
& + \int_{76.5}^{81} (5154 \text{ ksi}) (6.0 \times 10^{-6} / ^\circ \text{F}) \left[\frac{T1 - T2}{90} y + T2 \right] (42'') y dy \\
& + \int_{81}^{90} (5154 \text{ ksi}) (6.0 \times 10^{-6} / ^\circ \text{F}) \left[\frac{T1 - T2}{90} y + T2 \right] (72.12'') y dy
\end{aligned}$$

Now let $P = P_{eq}$ and $M = M_{eq}$, and a trial-and-error procedure yields $T1 = 14.8^\circ\text{F}$ and $T2 = 0.2^\circ\text{F}$. A negative gradient is obtained by multiplying the positive gradient by -0.3 to obtain the positive temperature gradient presented in Figure 8.130.

For an AASHTO-PCI BT81 girder, the equivalent temperature at the deck top fiber is 14.8°F , the temperature at the girder top fiber is 7.8°F , and the temperature at the bottom fiber is 0.18°F . For the negative temperature gradient, -4.4°F , -2.3°F and -0.1°F at the deck top fiber, the girder top fiber, and girder bottom fiber are applied for the equivalent temperature gradient. The final positive and negative temperature gradient is presented in Figure 8.131. These temperature gradients are added to the previously discussed uniform temperature increase and decrease.

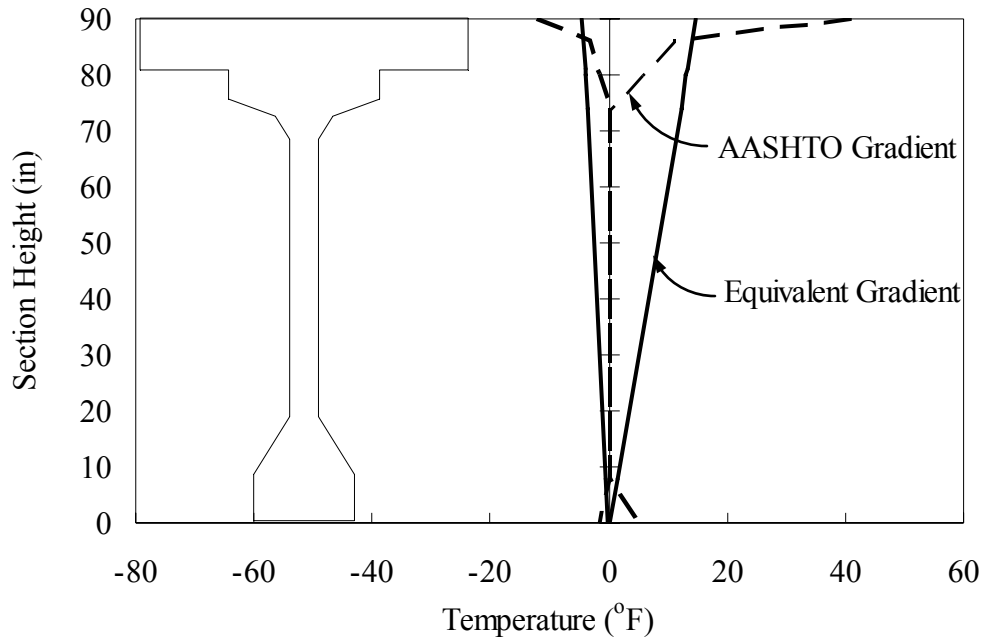


Figure 8.131: Temperature Gradient for BT81 Girder and Deck Slab

8.3.3.2.3 Backfill Pressure

Hydrostatic pressure behind the back-wall and abutment must be determined, accounting for the 1'-6" approach slab and 2'-7" wing-walls at both sides as presented in Figure 8.132. A triangular hydrostatic pressure and abutment-to-backfill interaction springs are identified in Figures 8.133 and 8.134.

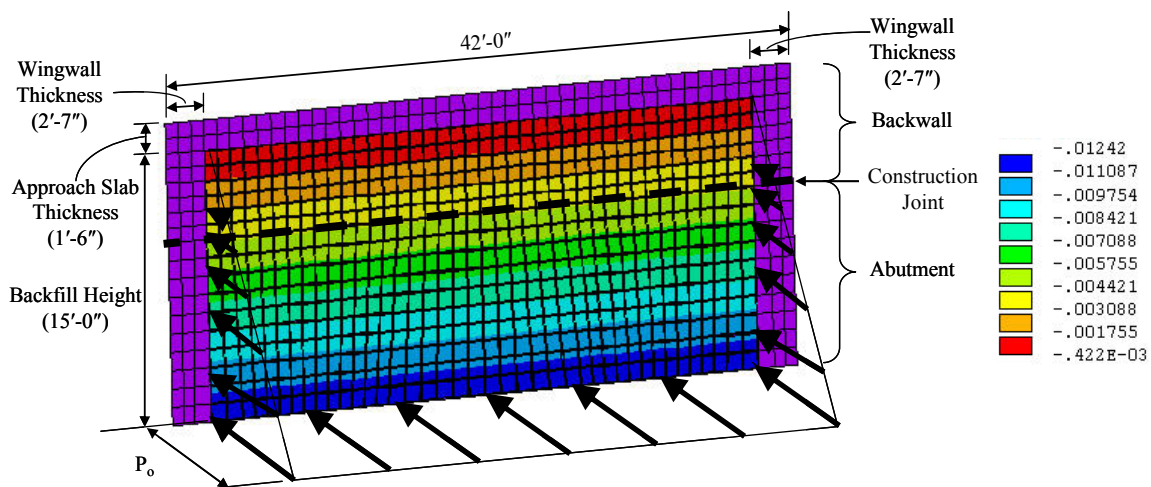


Figure 8.132: Backfill Pressure Contour in Example 3 3D Model

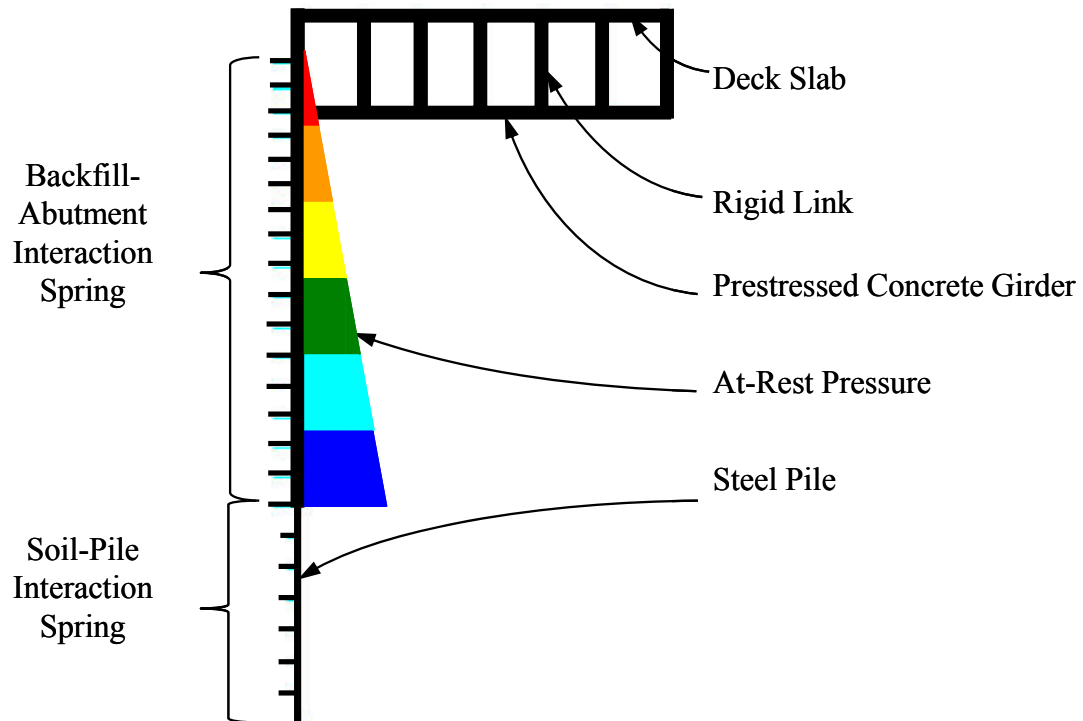


Figure 8.133: Example 3 3D Analysis Abutment Backfill Pressure

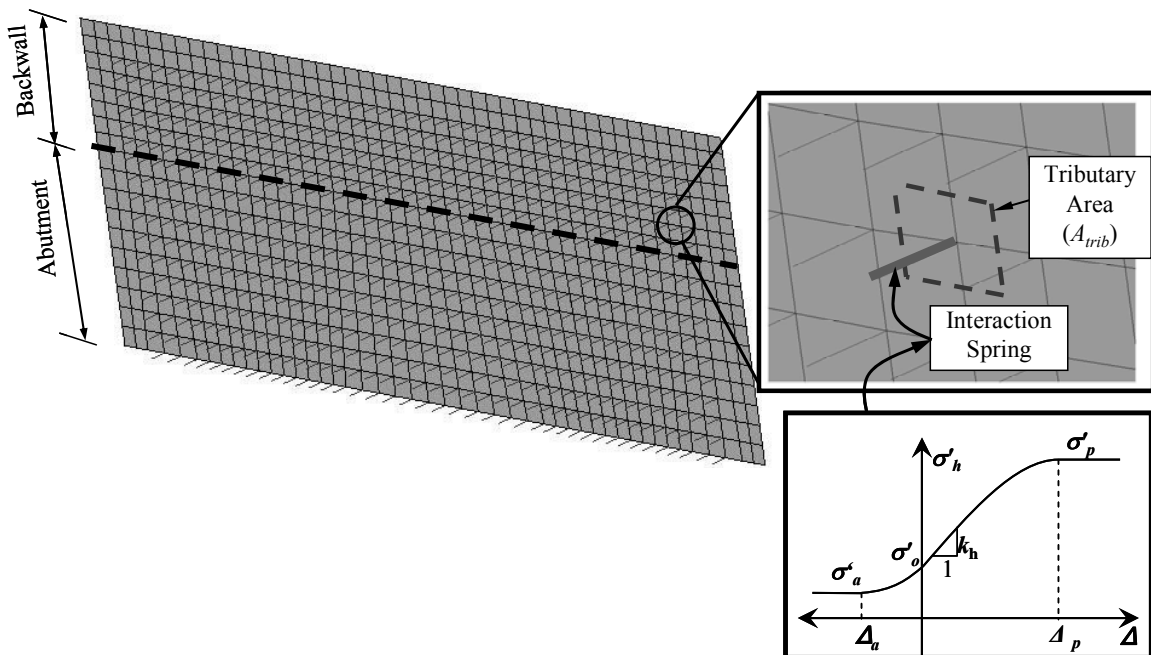


Figure 8.134: Example 3 3D Analysis Backfill Pressure Tributary Area for Spring

To determine the backfill pressure, each soil spring tributary area is computed as presented in Figure 8.134. At-rest pressure, active pressure, and passive pressure at each spring element location are computed as:

$$\begin{aligned}
 P_o &= K_o \gamma' z A_{trib} = \gamma' z A_{trib} \\
 P_a &= K_a \gamma' z A_{trib} = \frac{1 - \sin \phi_f}{1 + \sin \phi_f} \gamma' z A_{trib} \\
 P_p &= K_p \gamma' z A_{trib} = \frac{1 + \sin \phi_f}{1 - \sin \phi_f} \gamma' z A_{trib}
 \end{aligned} \tag{5.7}$$

where K_o , K_a and K_p are at-rest, active and passive coefficients, $\gamma' = 119$ pcf, A_{trib} = tributary area and $\phi_f = 34^\circ$. For each node location on the back-wall and abutment a different z and A_{trib} is computed. For example, at $z = 3$ ft and $A_{trib} = 1.0$ ft²:

$$\begin{aligned}
 P_o &= (119 \text{ pcf})(3 \text{ ft})(1 \text{ ft}^2) = 357 \text{ lbs} \\
 P_a &= K_a \gamma' z A_{trib} = \frac{1 - \sin \phi_f}{1 + \sin \phi_f} \gamma' z A_{trib} = \frac{1 - \sin 34^\circ}{1 + \sin 34^\circ} (119 \text{ pcf})(3 \text{ ft})(1.0 \text{ ft}^2) = 101 \text{ lbs} \\
 P_p &= K_p \gamma' z A_{trib} = \frac{1 + \sin \phi_f}{1 - \sin \phi_f} \gamma' z A_{trib} = \frac{1 + \sin 34^\circ}{1 - \sin 34^\circ} (119 \text{ pcf})(3 \text{ ft})(1.0 \text{ ft}^2) = 1260 \text{ lbs}
 \end{aligned}$$

The slope of the spring element response between P_a and P_p is computed from equation 5.1, discussed in Chapter 5 of this report:

$$k_h(z) = k_{ref} \left(\frac{z}{h_{ref}} \right)^{0.5} A_{trib} \tag{5.1}$$

where h_{ref} = reference depth and z = backfill depth. As discussed in Section 5.2.2, $k_{ref} = 0.044$ kci at 4 ft from the bottom of the abutment and is used for this example:

$$k_h(3 \text{ ft}) = (0.044 \text{ kci}) \left(\frac{3 \text{ ft}}{15 \text{ ft} - 4 \text{ ft}} \right)^{0.5} (144 \text{ inches}) = 3.31 \text{ kips/inch}$$

Displacements u_a and u_p corresponding to P_a and P_p are computed as:

$$u_a = \frac{101 \text{ lbs}}{3310 \text{ lbs/inch}} = 0.0305 \text{ inches}$$

$$u_p = \frac{1260 \text{ lbs}}{3310 \text{ lbs/inch}} = 0.381 \text{ inches}$$

Therefore, the example backfill-abutment interaction spring, defined generally in Figure 8.135, is presented in Figure 8.41.

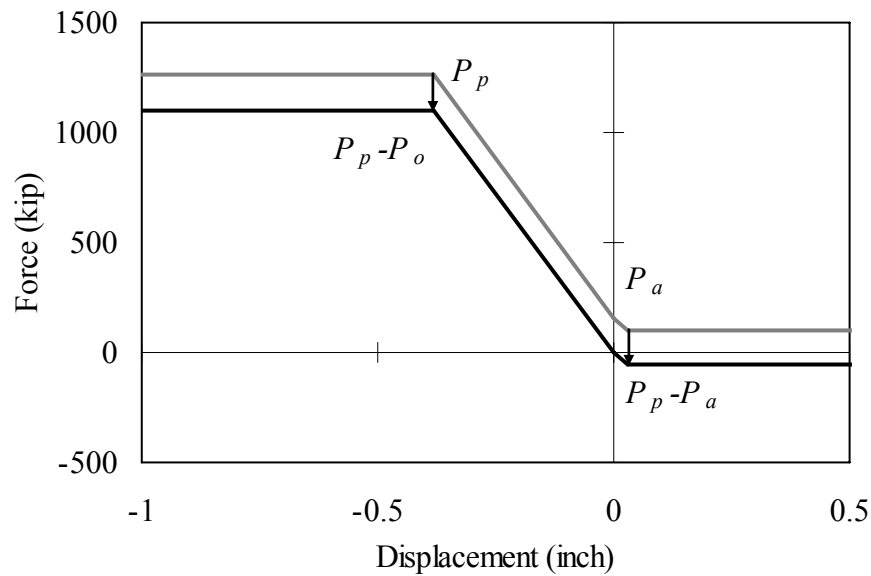


Figure 8.135: Backfill-Abutment Interaction Spring Property

8.3.3.2.4 Time-dependent Loads

The time-dependent effects of concrete creep and shrinkage result in bridge shortening; however, this effect is not included with thermal expansion. To determine the maximum bridge contraction and corresponding response, time-dependent effects are combined with thermal contraction, temperature gradient, and backfill pressure. For maximum expansion response, it is anticipated that the initial bridge expansion will occur prior to when significant creep and shrinkage have occurred. Time-dependent strains over

75 years are computed for the top fiber of the deck, top fiber of the girder, and bottom fiber of the girder and applied for the maximum contraction response. The strains at each location are converted to temperature loads based on the thermal expansion coefficient. Uniform temperature load, temperature gradient, and time-dependent effects are then summed and applied to the girders and deck.

To accurately account for thermal loads and time-dependent effects, the girder and deck elements are meshed at 2 ft and time-dependent effects are computed at every node. Each element is assigned thermal loads from time-dependent strains.

8.3.3.3 Example 3: 3D Analysis Results

An extreme design static 3D analysis is demonstrated for the Example 3 bridge. Although a time-history analysis is not performed in this example, 3D models are capable of performing a time-history analysis with a sinusoidal temperature fluctuation load. However, a 3D time-history analysis would require extensive and unmanageable computing time and storage; therefore, this analysis is not demonstrated here. The two loading cases of extreme design temperature are demonstrated based on AASHTO extreme temperature rise (+30°F) and fall (-40°F). To obtain the maximum contraction response, time-dependent effects are included with the thermal effects. For the expansion case, only thermal effects are considered. Example 3 girder axial force, girder bending moment, pile lateral force, pile moment, and pile head displacement are presented, using the analysis methods described in the body of this report.

8.3.3.3.1 Girder Axial Force

Girder axial forces predicted by a 3D extreme design temperature static analysis are presented in Figure 8.136 for both (a) bridge contraction and (b) bridge expansion. Axial forces in each girder differ due to the larger interior girder abutment and deck tributary area and the retaining backfill force differences between interior girders and exterior girders. When the temperature falls, tensile axial forces develop in all five girders due to significant thermal loads and time-dependent effects. When the temperature rises, significant compressive axial forces develop in all five girders. Due to the larger abutment and back-fill tributary area, interior girders develop larger tensile and compressive axial forces compared to exterior girders.

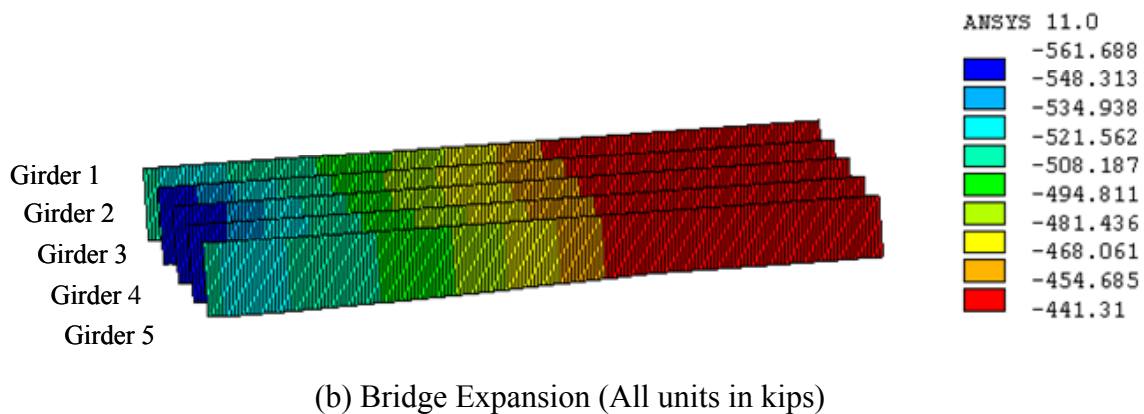
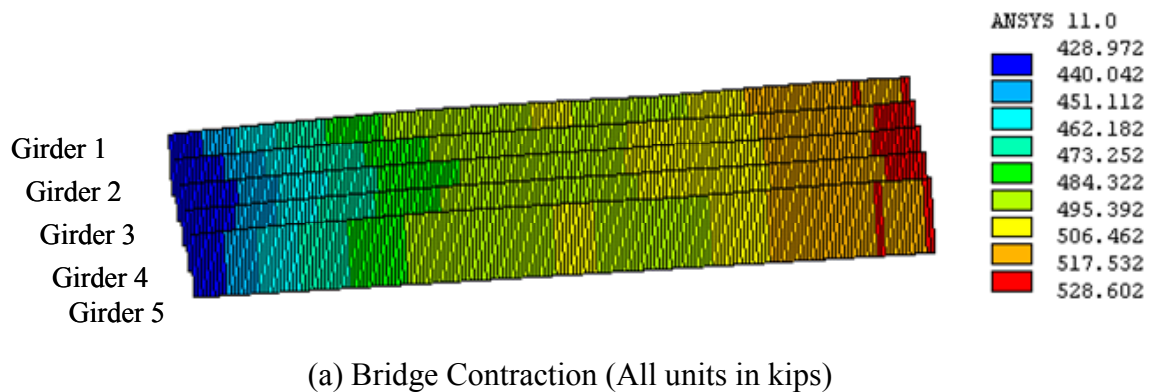
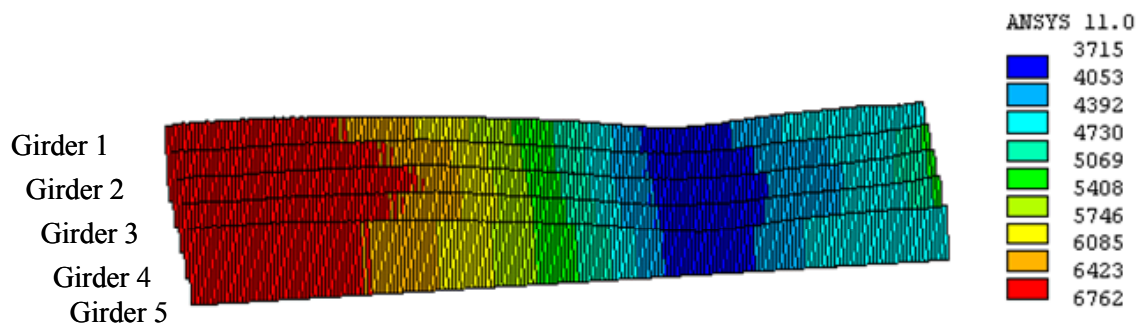


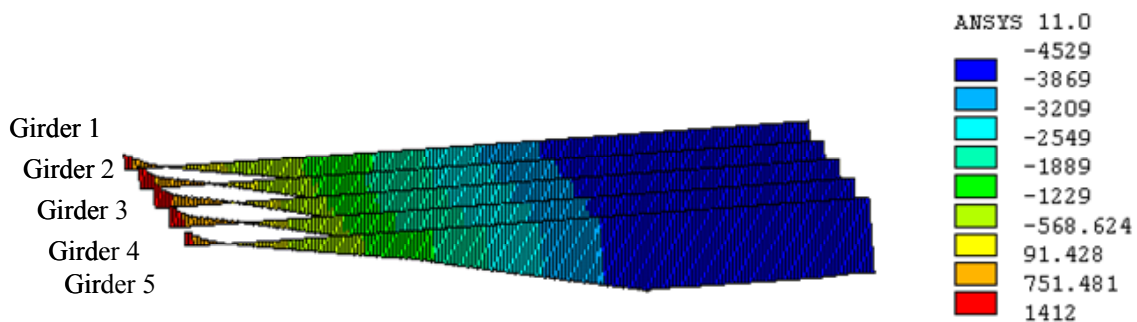
Figure 8.136: Example 3 Bridge 3D Analysis Girder Axial Force Comparison

8.3.3.3.2 Girder Bending Moment

Girder bending moments predicted by a 3D extreme design temperature static analysis are presented in Figure 8.137 for both (a) bridge contraction and (b) bridge expansion. When the temperature falls, significant positive moments develop in all five girders due to significant thermal loads and time-dependent effects. The interior girders develop larger higher moments than the exterior due to larger tributary back-wall area and consequently larger backfill forces. When the bridge expands, all five girders are subjected to similar bending moments; however, interior girders are subjected to somewhat higher moments, again due to the larger backfill forces.



(a) Bridge Contraction (All units in-kips)

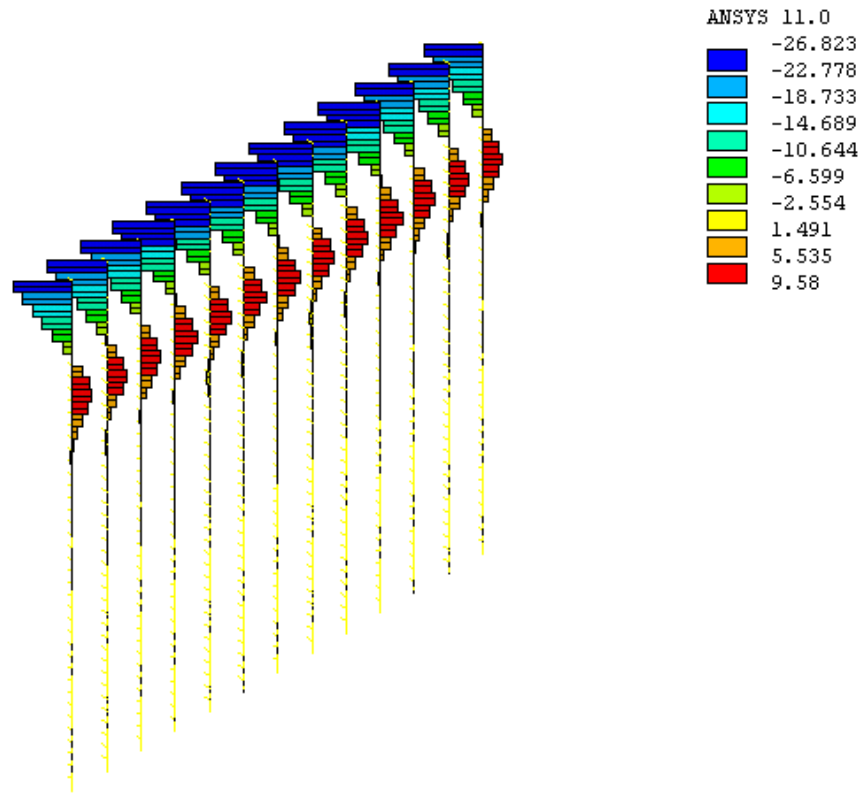


(b) Bridge Expansion (All units in-kip)

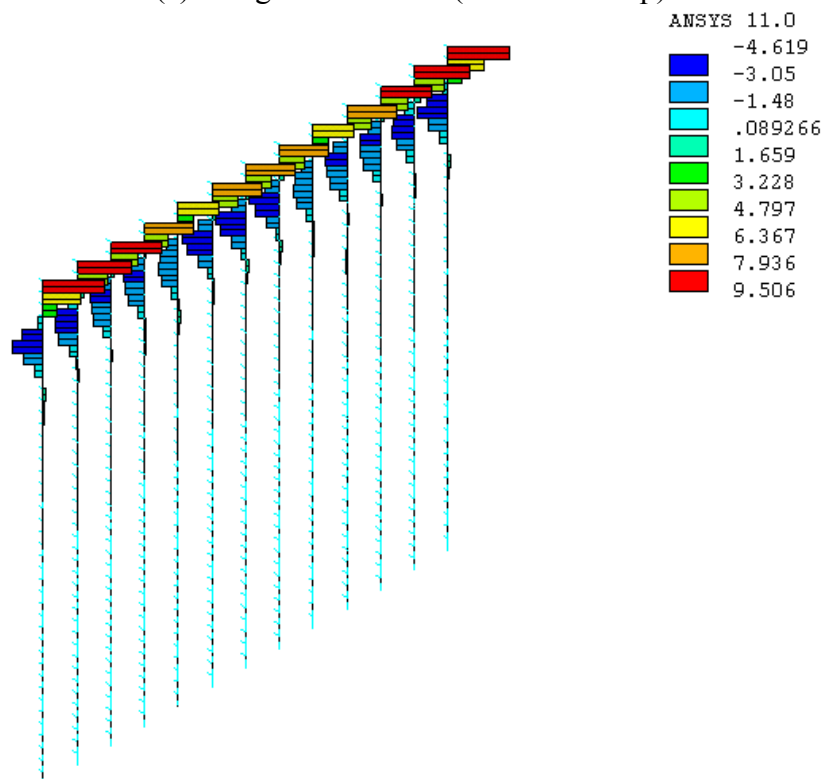
Figure 8.137: Example 3 Bridge 3D Analysis Girder Bending Moment

8.3.3.3.3 Pile Lateral Force

The lateral forces on piles predicted by the 3D extreme design temperature static analysis are presented in Figure 8.138 for both (a) bridge contraction and (b) bridge expansion. Relative displacement and rotation in the exterior piles due to bridge contraction are larger than those of interior piles. All piles are predicted to experience larger lateral forces under expansion as compared to contraction.



(a) Bridge Contraction (All units in kip)

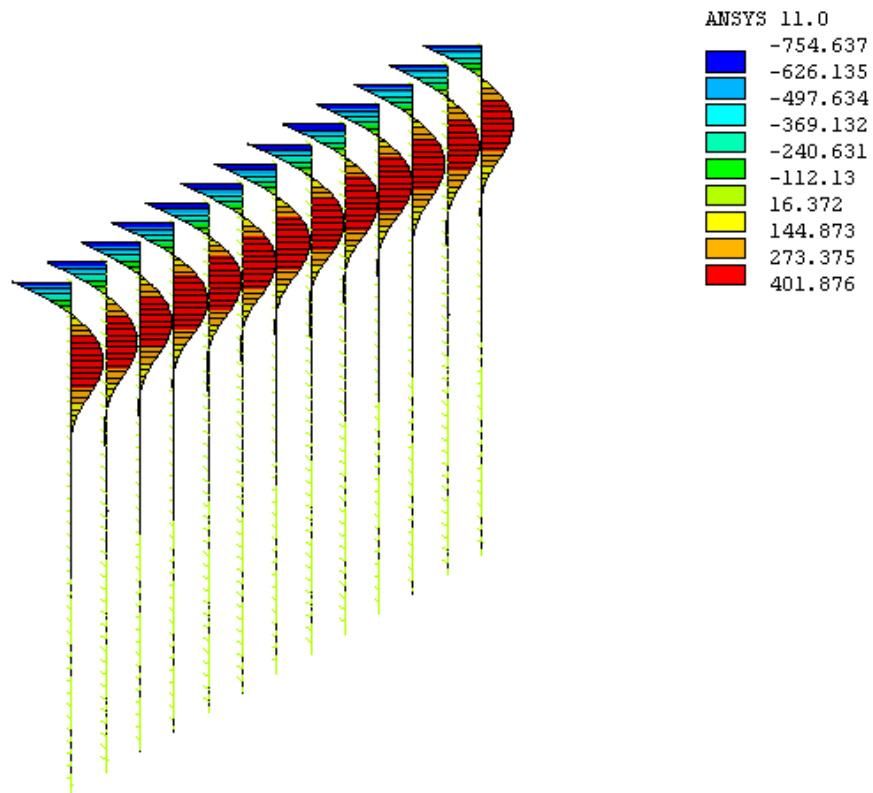


(b) Bridge Expansion (All units in kip)

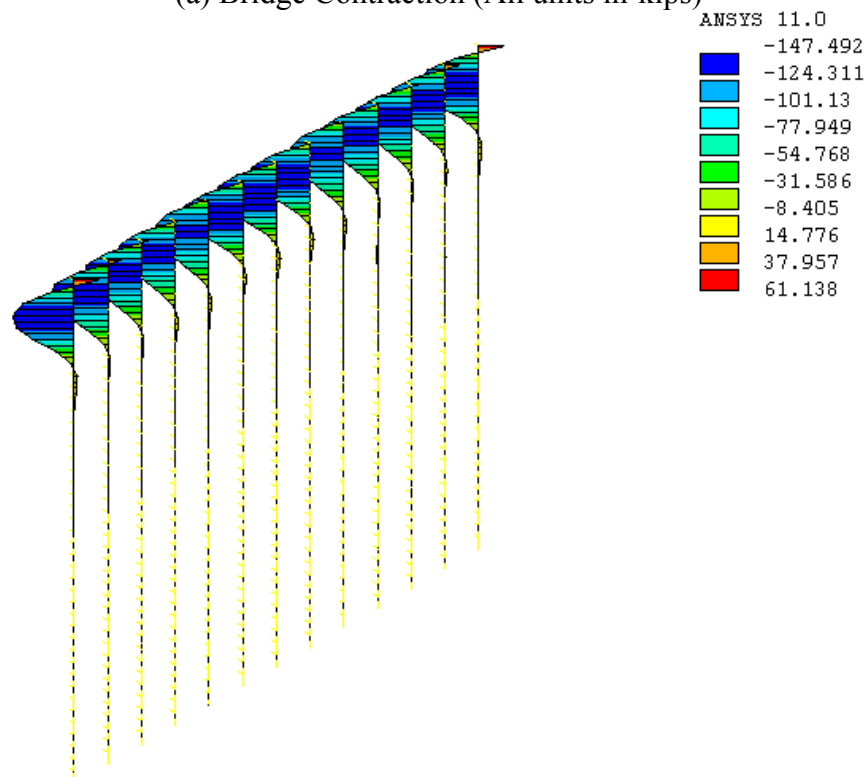
Figure 8.138: Example 3 3D Analysis Model Pile Lateral Force.

8.3.3.3.4 Pile Moment

The pile moments based on the 3D extreme design temperature static analysis are presented in Figure 8.139 for both (a) bridge contraction and (b) bridge expansion. Weak axis bending moments across all piles are very similar and vary with respect to vertical depth. Under superstructure expansion, significantly larger pile moments are predicted as compared to the contraction case, and exterior piles experience larger pile moments compared to interior piles due to the smaller restraining backfill pressure. In addition, pile maximum moments are located approximately 3 ft below the pile head, although typically it is thought that the maximum moment occurs at the pile head. The piles are subjected to lateral displacement and rotation simultaneously; therefore, the maximum moment occurs away from the pile head.



(a) Bridge Contraction (All units in-kips)



(b) Bridge Expansion (All units in in-kip)

Figure 8.139: Example 3 Bridge Pile Moment by 3D Analysis

8.3.3.3.5 Pile Head Displacement

Pile head displacement predicted by the 3D extreme design temperature static analysis is presented in Figure 8.140 for superstructure contraction. Pile head displacements in all piles are very similar for this case. As expected, interior piles experience slightly larger displacements as compared to exterior piles.

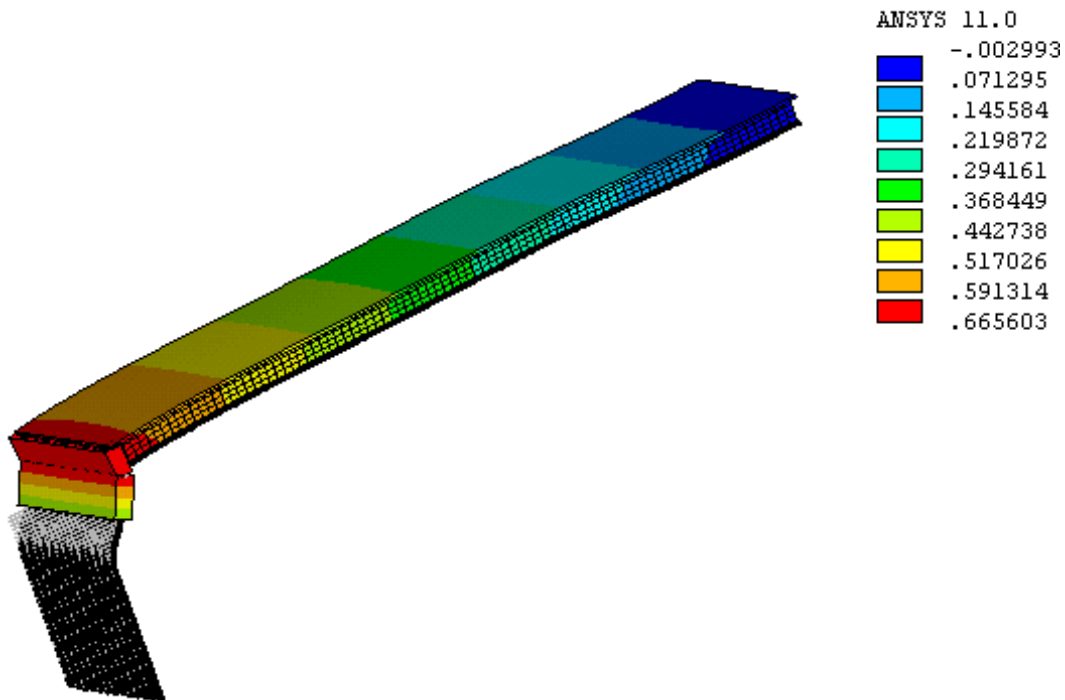


Figure 8.140: Example 3 Bridge Pile Head Displacement by 3D Analysis
(All units in inches)

8.3.4 Example 3 Analysis Results

The Example 3 bridge has been analyzed by the approximate method, the 2D extreme design temperature static analysis method, the 2D time-history analysis method, and the 3D extreme design temperature static analysis method. Results of these four analyses are compared in this section. The extracted results include: (1) girder axial force,

(2) girder bending moment, (3) pile lateral force, (4) pile moment, and (5) pile head displacement.

8.3.4.1 Girder Axial Force

Girder axial force results by approximate method (Approx.), 2D time-history analysis (2D-TH), 2D design analysis (2D-DA), and 3D design analysis (3D-DA) are presented in Figure 8.141. The Approx., 2D-TH and 2D-DA predict similar girder axial forces. Girder compressive axial force predictions range from 61% to 95% lower as compared to the 3D-DA analysis results.

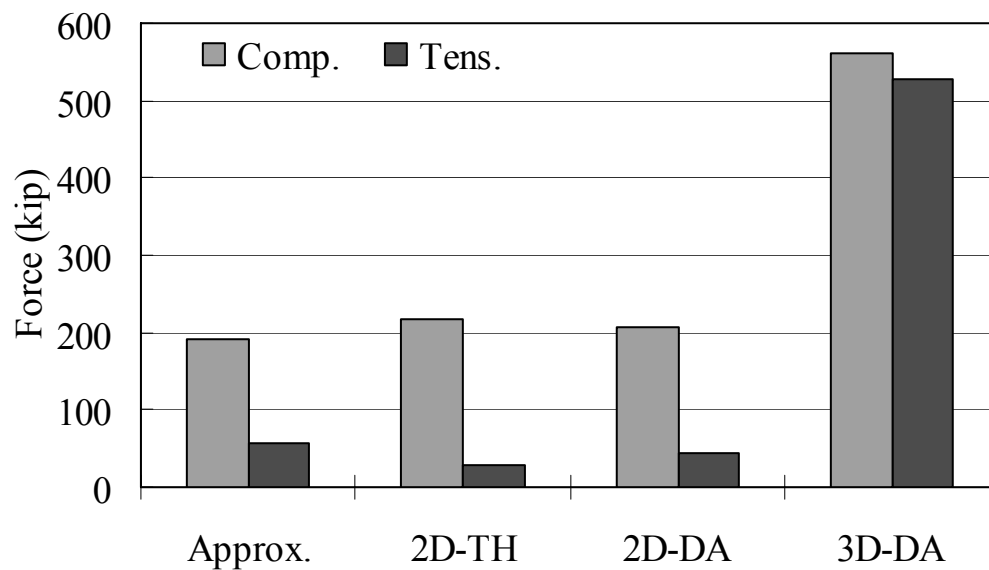


Figure 8.141: Example 3 Bridge Girder Axial Force Comparison

8.3.4.2 Girder Bending Moment

Girder bending moment results by Approx., 2D-TH, 2D-DA, and 3D-DA are presented in Figure 8.142. The 3D-DA reports smaller moments compared to the other

methods. Approx., 2D-TH, and 2D-DA predict 46%, 21%, and 62% larger positive moments and 311%, 327%, and 350% larger negative moments.

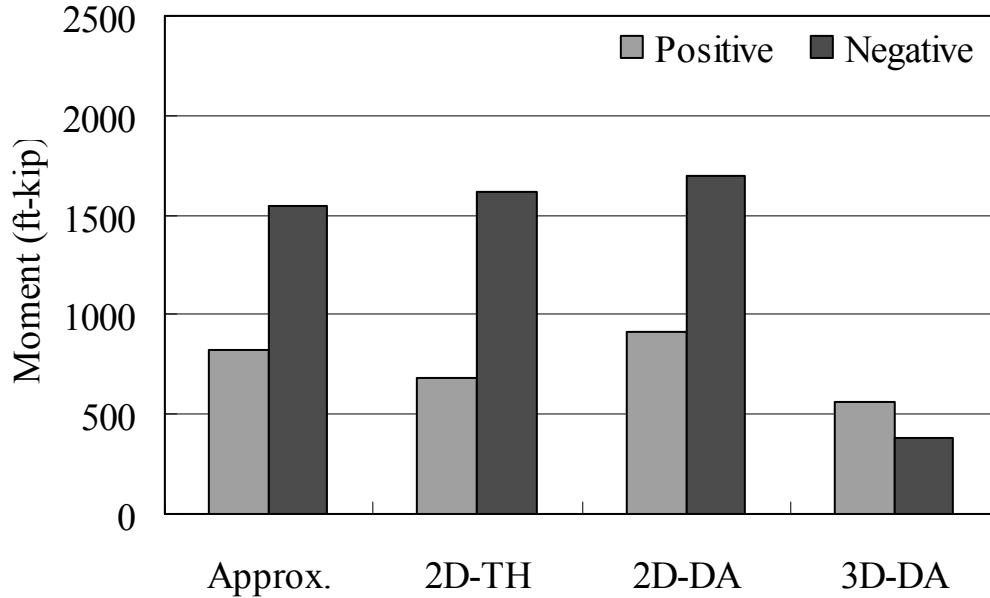


Figure 8.142: Example 3 Bridge Girder Bending Moment Comparison

8.3.4.3 Pile Lateral Force

Pile lateral force results obtained by the Approx., 2D-TH, 2D-DA, and 3D-DA are presented in Figure 8.143. Compared to 3D-DA, the Approx., 2D-TH, and 2D-DA report smaller lateral pile forces by 29%, 24%, and 6%. For comparison purposes, the single-pile lateral force, F_{pile} , due to a superstructure-free expansion is computed as:

$$\begin{aligned}
 F_{pile} &= \frac{12EI\Delta}{L_{pile}^3} = \frac{12EI}{L_{pile}^3}(\alpha \cdot \Delta T \cdot L) \\
 &= \frac{6(29000 \text{ ksi})(186 \text{ in}^4)}{(30 \text{ ft})^3}(6 \times 10^{-6} / ^\circ \text{F})(70 ^\circ \text{F})\left(\frac{400 \text{ ft}}{2}\right) = 1.4 \text{ kips}
 \end{aligned}
 \tag{8.2}$$

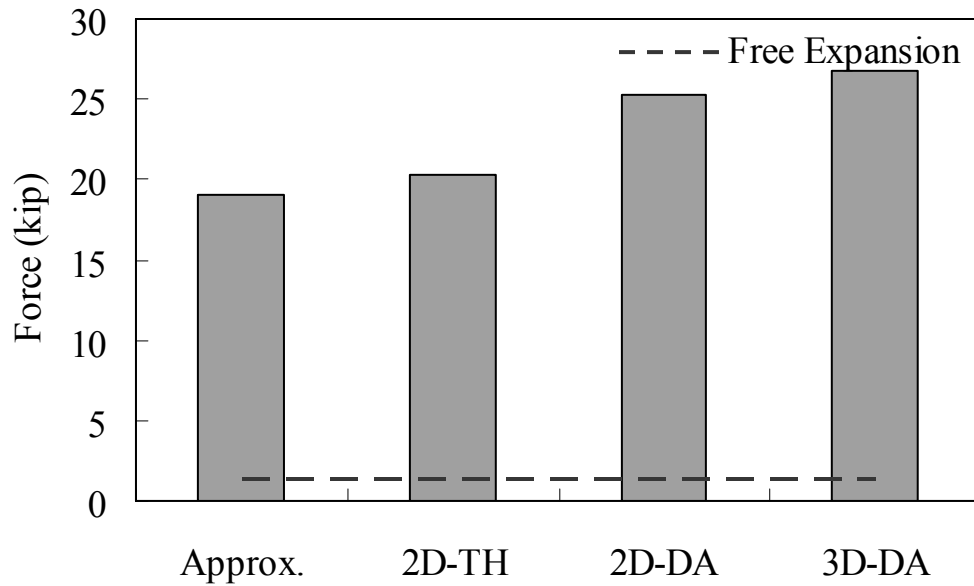


Figure 8.143: Example 3 Bridge Pile Lateral Force Comparison

8.3.4.4 Pile Moment

Pile head moment results obtained by the Approx., 2D-TH, 2D-DA, and 3D-DA are presented in Figure 8.144. All analyses report similar pile head moments. Compared to 3D-DA, the Approx., 2D-TH, and 2D-DA report moments are 45% larger, 9% smaller, and 44% smaller. For comparison purposes, the single pile moment, M_{pile} , due to a superstructure-free expansion is computed as:

$$M_{pile} = \frac{6EI\Delta}{L_{pile}^2} = \frac{6EI}{L_{pile}^2}(\alpha \cdot \Delta T \cdot L) \quad (8.3)$$

$$\frac{6(29000 \text{ ksi})(186 \text{ in}^4)}{(30 \text{ ft})^2} (6 \times 10^{-6} / ^\circ \text{F})(70 ^\circ \text{F}) \left(\frac{400 \text{ ft}}{2} \right) = 21 \text{ ft-kip}$$

All analyses predictions are smaller than the moment by free expansion.

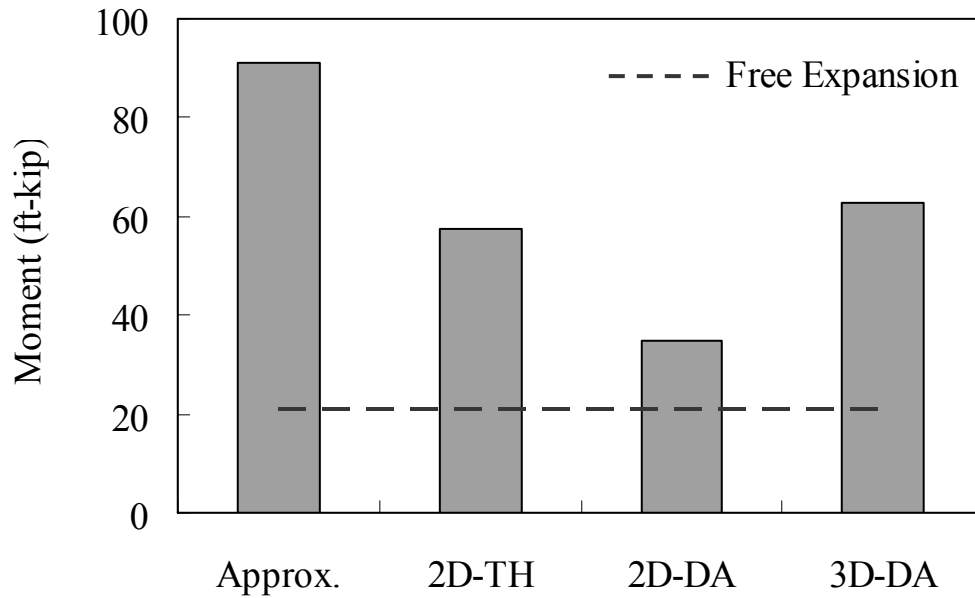


Figure 8.144: Example 3 Bridge Pile Moment Comparison

8.3.4.5 Pile Head Displacement

Pile head displacement results obtained by the Approx., 2D-TH, 2D-DA, and 3D-DA are presented in Figure 8.145. Except for the approximate method, all analyses report similar pile head displacements. Compared to the 3D-DA, the approximate method, 2D-TH, and 2D-DA report pile head displacements 103% larger, 20% smaller, and 20% larger. For comparison purposes, the pile head displacement due to superstructure-free expansion is computed as:

$$\delta_{pile} = \alpha \cdot \Delta T \cdot L = (6 \times 10^{-6}) (70^\circ \text{F}) \left(\frac{400 \text{ ft}}{2} \right) = 1.01 \text{ inches} \quad (8.4)$$

All analyses predictions are smaller than the displacement by free expansion.

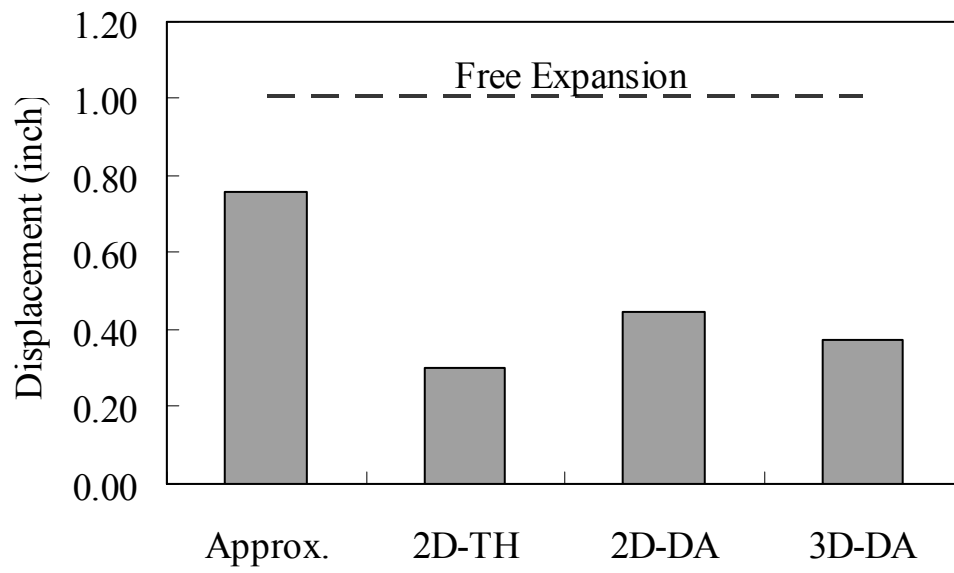


Figure 8.145: Example 3 Bridge Pile Head Displacement Comparison

Chapter 9

Discussion of PennDOT IAB Analysis and Design Provisions

Predicted behavior of the four instrumented bridges using the PennDOT IAB design program was evaluated by comparison to the measured behavior obtained from the bridge monitoring program. Bridge parameters taken from design drawings, design calculations, and geotechnical reports provided by the engineer of record are used as input to the PennDOT program. A summary of the PennDOT spreadsheet program is described and considered on a design subsection basis. Comparisons are discussed and suggested program improvements are provided, where appropriate.

In addition, on the basis of the analysis development undertaken in this study, a discussion of PennDOT DM4 provisions is provided. Because the four instrumented bridges in this study represent a somewhat limited range of IAB bridge conditions, the parametric study has allowed a more complete consideration of the range of configurations and construction situations.

9.1 PennDOT IAB Design Procedure

The PennDOT IAB design program was developed to aid analysis and design of IAB piles. AASHTO LRFD Bridge Design Specification (1994) and PennDOT Design Manual Part 4, DM-4 Appendix G (2000) were used for this design program development. There are two additional features incorporated into the PennDOT IAB program: (1) design of abutment/pile cap reinforcement; and (2) pile design under scour

conditions. Pile design for scour is not discussed or evaluated herein as it is beyond the scope of the study.

The PennDOT IAB program consists of five main sections: (1) bridge data; (2) integral abutment data; (3) load data; (4) pile data; and (5) analysis summary. The following descriptions of these five sections are limited to the design of abutment/pile cap reinforcement and piles under normal conditions.

The bridge data section allows users to specify girder material, type of girders, and bridge superstructure geometric data. Material options are steel and concrete. Where concrete is specified, an I-girder or spread box girder is listed. All descriptive geometric dimensions are required, including total bridge length, length of integral span, skew angle, bridge width, number of girders, girder spacing, girder depth, bearing pad thickness, deck and haunch thickness, and parapet height.

The integral abutment data section requires input of abutment height and wingwall length. Abutment length and width are automatically generated by the program based on the PennDOT Standard Drawing (BD-667M) and PennDOT Design Manual (DM-4) recommendations. Data input and generated information in this section are primarily used to determine abutment and wingwall dead loads.

The load data section requires the AASHTO LRFD load modifier, η_i , girder reactions due to dead loads and live loads, girder end rotations due to composite dead loads and live loads, wind pressure, and centrifugal force. Unfactored dead and live load girder reactions and rotations can be obtained from the PennDOT prestressed concrete girder design program, PSLRFD, for input to the program. Wind pressure and centrifugal force are also determined using AASHTO LRFD. Maximum and minimum factored

dead load and live load girder reactions are calculated by the program using AASHTO LRFD load combinations. Maximum and minimum unfactored girder reactions due to effects of wind and centrifugal force are also computed.

The pile data section requires pile properties, number of piles per abutment, pile spacing, pile length, soil resistance factors, pile resistance factors, and unit soil resistance. Soil and pile resistance factors are obtained from DM-4 while unit soil resistances must be obtained from geotechnical reports. In addition, a separate, iterative procedure to estimate depth to pile fixity must be performed to determine the moment arm and resulting axial pile force due to overturning moments of wind force on structure, wind force on live load, and centrifugal force. Normally, COM624P is utilized to determine these pile moments. The final design is performed by checking both geotechnical and structural pile axial force limits, axial-moment interaction, ductility, and abutment/pile cap reinforcements.

The analysis summary section repeats all input and reports warnings and errors to be addressed, if any. Critical design results including factored axial force versus axial capacities (both structural and geotechnical), and magnitude of axial-moment interaction evaluation are also provided.

9.2 PennDOT IAB Design Spreadsheet Discussion

The PennDOT IAB analysis and design program was compared with measured results from the present study and the original design for each of the four bridges. The five program design sections were addressed individually and are summarized in Table 9.1. Page numbers presented in the first column correspond to the program page numbers.

Table 9.1: PennDOT IAB Design Spreadsheet Evaluation

Design Section	Discussion	Recommendation
1) Bridge Data (pp. 1-3)	Input data sequence and explanations are clearly presented. Minor warning is reported concerning girder depth greater than the specified value by DM-4.	-
2) Integral Abutment Data (pp. 3-4)	Input data sequence and explanations are clearly presented.	-
3) Load Data (pp. 5-8) <ul style="list-style-type: none"> Dead and live load girder reactions (p. 6) Girder end rotation due to composite dead and live loads (pp. 6-7) 	<p>Calculation in the program strictly follows DM-4 App. G 1.2.7.2, which is based on the assumptions of equally distributed loads to all piles and removal of the multiple presence provision.</p> <p>Considers effects of girder-end rotations on the pile head rotations. Discussion of this issue is continued in section 4 of this Table 9.1.</p>	<p>More study may be required to ensure that this assumption does not over- or under-estimate pile loads for narrow and wide bridges.</p> <p>See design section 4 of this Table 9.1 under <i>iterative procedure interacting with COM624P</i>.</p>

<p>4) Pile Data (pp. 9-18)</p> <ul style="list-style-type: none"> • Pile properties (p. 9) • Temperature range (p. 11) • Maximum abutment movement (p. 12) 	<p>Typically, $\frac{1}{16}$ inch pile thickness loss (all around) due to corrosion is recommended. The pile properties used in the PennDOT IAB program do not consider this.</p> <p>DM-4 design temperature, App.G 1.2.7.4, is ± 100 °F for steel and ± 80 °F for concrete bridges. Maximum and minimum ambient temperature during this project's seven-year monitoring period ranged from -12.9 °F to 95.1 °F. Based on an average bridge construction temperature of 68 °F, temperature rise and fall is approximately 30 °F rise and 80 °F fall. These temperatures are site specific and may not be representative of all regions of Pennsylvania.</p> <p>Maximum measured abutment thermal displacements are approximately 50% of the PennDOT IAB program prediction.</p>	<p>Input of the anticipated pile thickness loss as well as an option to automatically compute deteriorated pile properties are suggested. This follows normal geotechnical consultant recommendations also stipulated in the geotechnical report for the study bridges.</p> <p>It appears that the DM-4 specified design temperature range as in App.G 1.2.7.4 is overly large. AASHTO temperature ranges of 0 °F to 120 °F for steel and 10 °F to 80 °F for concrete should be considered. As presented in Section 7.5.3, this study collected data from Pennsylvania State Climatology (PSC) (since 1888), and the National Climate Data Center (NCDC) (since 1971). These data support AASHTO temperature ranges. The proposed time-history analysis method presented in Chapter 7.5.3 utilized an annual average temperature of 45.5 °F with a temperature fluctuation equal to 30 °F.</p> <p>The PennDOT IAB program overestimates the abutment displacement, largely due to the current DM-4 large design temperature range. A modification of the temperature range will result in a more realistic displacement prediction. In</p>
---	--	--

<ul style="list-style-type: none"> • Coefficient of passive earth pressure (p. 12) • Iterative procedure interacting with COM624P (p. 14) • Axial load-moment interaction (p. 16) • Abutment/pile cap reinforcement (p. 18) 	<p>The maximum measured earth pressure was very close ($\pm 1\%$) to the design passive earth pressure.</p> <p>Measured girder and abutment rotations, pile strains, and abutment displacements all indicate that the abutment-to-backwall connection is not rigid and the abutment rotates away from the backfill. The PennDOT IAB program assumption of a rigid connection contributes to a conservative prediction of pile response. Measured pile moments were approximately 25% of the predicted pile moments.</p> <p>The PennDOT IAB program does not account for x-axis pile bending under wind loads and thermally induced abutment movements in the transverse direction.</p> <p>The PennDOT IA program is limited to the design of abutment/pile cap longitudinal reinforcement.</p>	<p>addition, the proposed 2D and 3D analysis methods significantly improve displacement prediction.</p> <p>It appears that the passive earth pressure assumption for IAB design is appropriate.</p> <p>The analysis methods proposed in this study incorporate rotational flexibility of the construction joint, superstructure and substructure partial continuity, superstructure time-dependent effects, abutment height and backfill pressure, and cyclic thermal loading. Incorporating the actual bridge component interactions results in a much more accurate prediction of pile response.</p> <p>Corrections of structure flexibility as described above and the inclusion of wind and transverse thermal behavior are needed to more accurately predict behavior. Wind loading and corresponding response is beyond the scope of this study.</p> <p>The design of vertical reinforcement for the abutment/pile cap should be considered.</p>
5) Analysis Summary (pp. 19-20)	Analysis summary is concisely and clearly presented.	-

Further detailed review of PennDOT DM-4 integral abutment provisions as compared to both the measured bridge responses of the four study structures and the subsequent numerical modeling studies performed are discussed below. The issues are addressed in approximate organization of PennDOT DM-4 as they relate to the present study.

Table 9.2: PennDOT DM-4 IAB Design Discussion

Design Section	Design Issue	Discussion/Suggested Improvements
Design Procedure	PennDOT analysis procedure	The proposed three IAB analysis methods of Chapter 7 can be used to improve the current PennDOT analysis procedure accuracy. The proposed procedure includes load effects that are not considered in the current DM-4 such as time-dependent effects, cyclic soil-structure interaction, construction joint influence, axial force and moment in girders due to thermal loading, and pile displacement, shear, and moment due to thermal loading. In addition, all of these load effects are from a single analysis, while the current procedure requires separate analysis and computations. This procedure does not consider continuity and component interactions of the structure.
Superstructure	Creep and shrinkage	Concrete creep and shrinkage in Section 7.4.4 is a major driving force, inducing significant, irreversible abutment displacement over time. Therefore, creep and shrinkage should be considered in the IAB analysis due to the longitudinal restraint.
	Thermal effects on girder	As presented in the parametric study of this report in Chapter 6 and monitoring results in Chapter 4, significant girder axial force and moment is observed due to thermal loading. Abutment restraint induces this girder response and corresponding stresses. Abutment rotation also interacts with the girders to influence this response. Therefore, both abutment displacement and rotation must be considered in beam design, as demonstrated by the proposed 2D and 3D analysis methods.

Integral Abutment	Construction joint detail: #5 @ 9 inches	The construction joint detail between the abutment and back-wall significantly influences IAB behavior over time. Current PennDOT IAB analysis assumes the construction joint to be rigid; however, IAB monitoring results demonstrate that differential rotations between back-wall and abutment routinely occur. The current #5 @ 9" construction joint rebar detail is between perfectly hinged and rigid as discussed in Section 6.2.4. Chapter 6 parametric study results demonstrate that a rigid joint may perform better – all bridge responses due to thermal loading decrease during bridge contraction.
	Pile cap depth specified in PennDOT BD-667: maximum depth of 4'-3" for skews < 80°, and maximum depth of 4'-6" for skews ≥ 80°	The four monitored IABs are all constructed with abutment heights > 4'-6". Each was observed to be performing well during the monitoring period. An abutment height increase influences bridge responses both positively and negatively. The present study results in Chapter 6 revealed that bridges with a backfill height of 10 and 15 ft (from the bottom of the abutment to the bottom of the approach slab) perform well and do not cause pile yielding or other problems evaluated within the scope of this study.
	Earth pressure distribution	The current linear earth pressure distribution provides satisfactory analysis model results compared to the measured earth pressure. However, backfill earth pressure approaches a uniform distribution over time as presented in field monitoring results in Chapter 4. The top of abutment location likely becomes compacted due to daily and annual superstructure thermal movement compared to the bottom that has more restraint. More measurements of earth pressure are required to support this hypothesis.

Foundation Pile	Pile deflection	Current DM-4 does not specify a pile head deflection limit; however, the AASHTO limit is 1.5 inches. The present study demonstrates that IABs less than 600 ft long experience pile head deflections less than 1 inch, as can be observed in Section 6.5.5. The AASHTO provision should be followed; however, it should be understood that pile head deflection limitations are indirect limitations for other issues such as pile moment, approach slab performance and others. Where all bridge component design and performance issues are properly accounted for, the pile head deflection is not relevant.
	Interior vs. exterior piles	The maximum response difference between interior and exterior piles is not significant. The example bridges of Chapter 8 of this report illustrate an approximately 4 kips shear and 5 ft-kip moment difference between piles. If average pile response is considered, this difference is reduced further.
	Pile forces due to thermal expansion and thermal contraction	As presented in Chapter 8, maximum pile responses are obtained through two different analysis procedures: maximum contraction effects are the result of thermal load, thermal gradient, and time-dependent loads (considering long-term to maximum time-dependent loads); maximum expansion effects are the result of thermal load and temperature gradient only (considers initial conditions to minimize time-dependent loads).
	Short-length bridges	Short-length bridges experience a small thermal loading effect and time-dependent effects. Thus, pre-augered holes for foundation piles are not necessary below a bridge length of approximately 100 ft under normal conditions. Observed construction practice indicates that the pre-augering and sand fill does accomplish the original intent as the pile driving significantly compacts the sand fill, likely to a density in excess of the surrounding material.

	Backfill placement requirements and details	DM-4 App.1.2.9 specifies O.G.S. backfill material compacted in 4-inch lifts. A 1 inch sheet of foam board is also used to reduce passive pressure. However, the passive pressure reduction achieved by including the foam board is doubtful because the board compresses and loses its elasticity due to daily and annual abutment movements.
	Minimum acceptable pile length of 15 ft in PennDOT DM-4 App.G 1.4.2.1	<p>Minimum pile length must be determined in conjunction with pile head displacement, which is strongly related to pile size and type, bridge length, abutment height, and pile soil stiffness. The bridges in this study were observed to have a fixity point less than 10 ft below the bottom of abutment as in Chapter 8. The proposed 2D and 3D analysis methods can be used to predict the pile head displacement and a fixity point. For preliminary pile length selection as in Section 7.1, the following equation can be used to be sure that the pile behaves as a long pile:</p> $L \geq l_c = \sqrt[4]{\frac{4E_p I_p}{K}}$ <p>where: L = pile length, l_c = characteristic length, E_p = elastic modulus of pile, I_p = moment of inertia of pile cross-section, K = soil spring constant ($= kD$), k = modulus of sub-grade reaction, and D = pile diameter.</p>
	Pre-augering requirement in DM-4 App.G 1.4.2.1	Pile fixity points of bridges less than 600 ft are formed above 10 to 15 ft below the bottom of the abutment; therefore, minimum pre-augering requirements of 10 ft may be applicable to the bridges of interest. However, as mentioned above, in order for the pre-augering and sand placement to be effective, the placement of sand should take place after pile driving.
	Soil-structure interaction	For soil-pile interaction, p - y curves based on API equations are used, which is the identical basis for COM624P and Lpile (Section 5.2.3).

Miscellaneous	Wing-wall	DM-4 App.G 1.4.4 allows only “U” wing-walls with three configurations. All three types of wing-walls can be regarded as minimally influencing IAB responses. In addition, IAB analysis models may omit wing-walls to determine bridge responses.
	Approach slab	The evaluation of approach slab effects in this study is not conclusive, as instrumentation was very limited. However, based on the success of 2D and 3D models that do not include the approach slab in matching the measured responses, it can be concluded that approach slabs minimally influence responses.
	Vertical thermal loading	High-rise piers (> 30 ft) may produce vertical displacements (> 0.1 inch) at the piers, and additional moments in the superstructure occur. The proposed numerical methods can account for the vertical displacement influence in IAB behavior and response.

9.3 Implementation Plan

An implementation plan that provides detail on the broader use of the results of this project is provided below. Primarily, PennDOT relies on the PennDOT Integral Abutment Spread Sheet configured in EXCEL, as discussed above. The spread sheet was developed to aid analysis and design and to ensure consistency, and is based on AASHTO LRFD Bridge Design Specification (1994) and PennDOT Design Manual Part 4, DM-4 Appendix G (2000).

The current spread sheet analysis is a two-step procedure that requires iteration with other software, containing limitations and requiring the user to exit the spreadsheet. Certain proposed Chapter 7 analysis methods can be incorporated into the current PennDOT spread sheet analysis procedure. The proposed methods provide three levels of analysis: (1) approximate; (2) 2D numerical analysis; and (3) 3D numerical analysis. The approximate analysis equations developed in the present study can readily be included in an EXCEL spreadsheet, however, a 2D analysis may require further investigation of EXCEL macro capabilities. Time-dependent effects, cyclic soil-structure interaction, construction joint flexibility, girder axial force and moment due to thermal loading, and pile displacement, shear, and moment due to thermal loading are included in the approximate analysis equations; all are important aspects of the predicted bridge behavior. The approximate analysis method estimates critical thermal load effects during a 75-year bridge life: (1) girder bending moment; (2) girder axial force; (3) pile moment; (4) pile lateral force; and (5) pile head displacement. However, the approximate method is limited within a scope discussed in Chapter 7.

The 2D analysis method, while more accurate from a perspective of compatible distortions, is not able to include time-dependent effects explicitly. However, this can be remedied by the inclusion of a compensation factor or more directly, the provisions of ACI 209. The 2D analysis method is capable of, with better accuracy, performing both a time-history analysis and an extreme design temperature analysis. Time-history is able to simulate IAB behavior over a 75-year bridge life and provides response fluctuations over time. Extreme design temperature analysis is based on AASHTO design temperature for bridge expansion and contraction. As mentioned, the actual implementation details of including an explicit and limited scope 2D finite element analysis into an EXCEL spread sheet would need to be further evaluated; however, the benefits of a 2D analysis may be viewed as significant relative to the cost of implementation.

A 3D bridge analysis procedure is beyond the capability of an EXCEL spread sheet, but most accurately predicts bridge behavior in the longitudinal and transverse directions. 3D analysis provides each member shear and moment response for bridge expansion and contraction for both interior and exterior girders. Also, ACI 209 time-dependent effects can be incorporated into a 3D analysis. It is suggested that a 3D analysis be included as an optional prediction tool in the case of more complex structures with either long length or unusual geometry such as skew or dissimilar abutments. Consideration should be given to the development of a user interface or other tool that guides the 3D model development in a manner consistent with the findings of the present study.

9.4 Concluding Remarks

PennDOT IAB design procedures and other design issues have been discussed in this chapter. The PennDOT design spread sheet was developed to aid analysis and design of IABs; however, the IAB program does not realistically represent actual IAB behavior. Based on the long-term IAB monitoring program and extensive numerical studies, suggestions have been presented and discussed to improve current PennDOT IAB design protocols.

Chapter 10

Summary and Conclusions

10.1 Summary

The primary objectives of this research project included: (1) connection of wireless data transfer at the four previously instrumented IABs and weather station; (2) continuous monitoring and collection of engineering bridge response data; (3) conduct of a parametric study to determine IAB behavior trends relative to several variables over practical ranges; (4) development of a preliminary, approximate analysis procedure to be used for initial design; (5) develop accurate 2D and 3D analysis methodologies calibrated to measured response; and (6) presentation of three IAB analysis examples that include steel and concrete superstructures of three different lengths and illustrate the approximate, 2D, and 3D analysis methodologies.

To effectively present bridge field monitoring results and details of the numerical studies of this research project, this report consists of nine chapters: Chapter 1 presents project objectives and tasks; Chapter 2 presents detailed dimensions and locations of the four instrumented IABs and weather station; Chapter 3 summarizes the previous PennDOT/PSU research projects conducted on the four IABs; Chapter 4 presents processed data and measurements from all instruments installed at each of the four IABs and the weather station; Chapter 5 presents the developed IAB numerical modeling methodologies; Chapter 6 presents the parametric study conducted in order to observe overall trends for several key variables including results; Chapter 7 discusses the three

IAB analyses methods; Chapter 8 presents the three detailed IAB analyses examples; and Chapter 9 presents an overall Summary and Conclusions.

The present study utilized a wireless connection between the base computer and bridge monitoring sites to download data approximately once per month. The data loggers and instrumentation were installed under two previous research contracts (Laman et al. 2003, 2006): research conducted from October 2000 to March 2003 installed instruments on bridges 203, 211, and 222, and research conducted from June 2005 to July 2006 installed instruments on bridge 109. The four instrumented IABs and weather station are located on the I-99 extension near Port Matilda in central Pennsylvania and, therefore, all thermal loading data are based on data collected there. Data loggers installed at bridges 203, 222, 211, and 109 were activated in November 2002, November 2003, September 2004, and July 2006, respectively. Measured bridge response data at each site are composed of longitudinal abutment displacements, abutment earth pressures, abutment and girder rotations, H-pile bending moments about the weak axis and axial forces, girder axial forces and moments, and approach slab strains.

Four 3D numerical models were developed and calibrated to predict IAB responses for bridges 109, 203, 211, and 222. Key features of the models include soil-pile interaction, backfill-abutment interaction, construction joint behavior, seasonal temperature fluctuation, superstructure temperature gradient, time-dependent effects and backfill pressure. Comparisons between measured bridge responses and predicted bridge responses are presented and discussed. Based on the numerical modeling methodologies developed in this study, an extensive parametric study utilizing these 3D numerical modeling methodologies was performed to determine trends of IAB responses. The

parameters considered include girder material, bridge length, backfill height, and construction joint stiffness. Girder materials considered are prestressed concrete girders and steel plate girders with cast-in-place deck slab concrete. The four bridge lengths of the study are single-span 100 ft, two-span 200 ft, three-span 400 ft, and four-span 600 ft. Based on the monitored bridge dimensions, backfill heights range from 10 to 20 ft. The construction joint between the backwall and abutment was included in three levels: (1) a hinged joint, (2) the PennDOT standard reinforcement detail (#5 rebars at 9 inches), and (3) a rigid joint. Thus, the 3D parametric study results in 72 study cases. Each was analyzed based on an AASHTO extreme temperature static analysis for both temperature rise and fall. Variations of girder axial force, girder moment, pile lateral force, pile moment, and pile head displacement with respect to the four parameters were investigated and discussed. In addition, a parametric study utilizing 486 2D numerical models was performed considering six parameters: (1) girder material, (2) thermal expansion coefficient, (3) bridge length, (4) backfill height, (5) backfill stiffness, and (6) pile soil stiffness. The parametric study results provided a basis to establish goodness-of-fit curves for the approximate analysis. Response equations for maximum and minimum girder axial force, maximum and minimum girder moment at the girder end adjacent to the abutments, maximum and minimum girder moment at the girder mid-span in the end span, maximum pile lateral force, maximum pile moment, and maximum pile head displacement have been developed.

The three bridge analysis methods developed as part of this study, (1) approximate analysis method, (2) 2D analysis methodology, and (3) 3D analysis methodology, are described in detail and each of the analysis methods was demonstrated with three integral

abutment bridge examples. The bridge analysis example are: (1) single-span 100-ft prestressed concrete girder bridge; (2) two-span steel plate girder bridge; and (3) three-span 400-ft prestressed concrete girder bridge.

10.2 Conclusions

The following conclusions are derived from this research:

- (1) The wireless connection to the data loggers provides real-time bridge monitoring of remote or inaccessible bridges. Bridge and weather station data can be retrieved from any site located in the United States.
- (2) Measured bridge responses fluctuated with respect to daily and seasonal temperature variation. All measurements of abutment displacements, backfill pressures, abutment and girder tiltmeters, pile moments and axial forces, girder moments and axial forces, and approach slab strains are significantly influenced by thermal loadings.
- (3) Measured bridge responses are significantly influenced by time-dependent effects and long-term behavior. Bridge responses to thermal load must be considered in the IAB design and analysis process.
- (4) Comparisons between measured ambient and bridge temperatures revealed that an average daily ambient temperature can reasonably be used to represent bridge temperature. Despite massive concrete area and low thermal conductivity, temperatures of prestressed concrete girders and deck slabs are very similar to the measured average daily ambient temperatures.

- (5) Measured abutment displacements and rotations exhibited unrecoverable residual movements over the monitoring period. The rate of increase in residual displacement and rotation tends to decrease over time and is expected to stabilize to zero. However, the movements continued to increase over the 7-year monitoring period.
- (6) Despite backfill height differences, top and bottom pressure cells measured similar backfill pressures and this trend became clearer over time. When a tall abutment is subjected to forces as a result of superstructure thermal loading, abutment rotation rather than abutment displacement occurs. This rotation may cause larger soil pressure cell measurements at the top as monitored. For a short abutment, superstructure thermal loading induces abutment displacement that results in larger bottom pressure cell measurements.
- (7) Tiltmeters measured abutment and girder rotations due to superstructure thermal loading. Differential rotations between abutments and girders were also observed, which implies a potential crack opening or rebar yielding at the construction joints between abutments and backwalls.
- (8) Due to the larger thermal movement experienced by longer bridges, construction joint rotations were clearly observed. This construction joint behavior under cyclic loading requires more study for better understanding.
- (9) Pile moments near the abutment base fluctuate significantly with respect to daily and seasonal superstructure temperature variations, while pile moments at deeper locations do not fluctuate significantly. In addition, pile axial forces do not fluctuate significantly.

- (10) The numerical modeling methods developed as a result of this study, considering soil-pile interaction, backfill-abutment interaction, and construction joint behavior under thermal loading, temperature gradient, time-dependent effects, and backfill pressure, accurately predict measured IAB responses.
- (11) Time-dependent effects significantly influence both short-term and long-term IAB behavior and responses.
- (12) Soil-pile interaction and backfill-abutment interaction influence only short-term (less than 10 years) behavior and responses.
- (13) The triangular-shaped passive lateral earth pressure distribution theory is not always appropriate to model backfill pressure in IABs. Pressure cells at bridges 211 and 222 measured similar backfill pressures at the top and bottom locations despite a more than 7-ft height difference. Also, pressure cell measurements indicate that backfill may be compacted and become stiffer over time as a result of the cyclic superstructure thermal loading.
- (14) Girder material and bridge length significantly influence IAB behavior. Steel girder bridge integral abutments experience significant forces as a result of the superstructure thermal expansion. The resulting steel girder compressive axial force as compared to concrete girder bridges is larger.
- (15) Long concrete girder bridges experience significant bridge contraction due to the time-dependent effects of creep and shrinkage.
- (16) Increasing bridge length increases girder axial force, girder moment, pile lateral force, pile moment, and abutment displacement.

- (17) The 400-ft and 600-ft prestressed concrete girder bridges in the parametric study experienced significant time-dependent effects so that their contraction displacements are similar to steel girder bridges of the same length. However, expansion displacements of steel girder bridges are larger than for prestressed concrete girder bridges.
- (18) Steel girders and a large abutment height result in a reduced girder tensile axial force. Prestressed concrete girders, a hinged construction joint, and a low backfill height tend to result in a reduced girder compressive axial force. Priority for design will necessarily be given to the tensile axial force in a prestressed concrete girder, which is generally more critical than the compressive axial force.
- (19) A hinged construction joint, low abutment height, and short bridge length tend to result in a reduced girder positive moment. A negative girder moment counteracts gravity loads, and therefore is generally not an issue. A rigid construction joint and high abutment height tends to result in an increased negative girder moment.
- (20) A prestressed concrete girder, PA standard construction joint, and low abutment height result in lower pile moments. A hinged construction joint tends to reduce pile moments for bridge contraction and a rigid connection tends to reduce pile moments under bridge expansion.
- (21) The construction joint rebar detail of the current PA standard (#5 bars at 9 inches) is between a hinged and rigid joint; therefore, adding more rebars at the

front face of the abutment and/or reducing rebars at the rear face of the abutment may reduce pile moments as compared to the current PA standard.

- (22) A prestressed concrete girder, PA standard construction joint, and short bridge length result in a reduced pile lateral force. A hinged construction joint connection tends to reduce the pile lateral force under bridge contraction. Under bridge expansion, the pile lateral force increases for a hinged construction joint and decreases for a rigid construction joint.
- (23) A hinged construction joint and high abutment height tend to reduce pile head displacement.
- (24) Pile fixity points are formed at approximately 10 to 15 ft below the surface.
- (25) This research considered only long piles for flexibility, but IABs with short piles may experience pile tip lateral translations due to superstructure thermal loads. IABs with short piles (less than 20 ft) require more study.
- (26) As the abutment height decreases, girder compressive axial forces, pile moments and pile lateral forces decrease, but pile displacements increase.
- (27) The developed approximate analysis methods for both prestressed concrete girder IABs and steel girder IABs are very useful to estimate and predict bridge responses for preliminary analyses and/or designs.
- (28) 2D analysis is necessary for a time-history analysis and long-term response prediction, while 3D analysis can be chosen for a detailed individual member analysis under static loading definitions.
- (29) A time-history analysis with the 3D numerical model is not practical due to unmanageable computing time and memory demand.

- (30) An extreme design temperature static analysis by AASHTO LRFD temperature ranges (70°F range for concrete and 120°F range for steel) predicts similar results to a time-history analysis based on averaged measured temperature fluctuations.
- (31) A 2D extreme temperature static analysis tends to predict larger responses than 2D time-history analysis, but covers the upper and lower bounds of a 2D time-history analysis.
- (32) Interior girders and piles are subjected to larger backfill restraints than exterior girders and piles. Therefore, interior girders experience larger compressive axial force and moments and interior piles experience smaller pile moments during thermal expansion.
- (33) Due to 3D effects, 3D analysis predicts significantly higher individual element responses while 2D analysis predicts average responses.

Bibliography

Abendroth, R. E. and Greimann, L. F. (2005). Field Testing of Integral Abutments. Final Report No. HR-399. Iowa Department of Transportation, Ames, IA.

Alaska Department of Transportation and Public Facilities (AKDOT). (2004). Standard Specifications for Highway Construction, Alaska Department of Transportation and Public Facilities, Juneau, Alaska.

American Association of State Highway and Transportation Officials (AASHTO). (2002). AASHTO Standard Specifications, 17th Ed., Washington, D.C.

American Association of State Highway and Transportation Officials (AASHTO LRFD). (2007). AASHTO LRFD Bridge Design Specifications, Washington, D.C.

American Association of State Highway and Transportation Officials (AASHTO Guide). AASHTO Guide Specifications Thermal Effects in Concrete Bridge Superstructures. (1989). Washington, D.C.

American Concrete Institute Committee 209 (ACI 209). (2004). "Prediction of Creep, Shrinkage, and Temperature Effects in Concrete Structures," ACI Manual of Concrete Practice Part I, American Concrete Institute, Farmington Hills, MI.

American Concrete Institute Committee 363 (ACI 363). (1998). Guide to Quality Control and Testing of High-Strength Concrete, American Concrete Institute, Farmington Hills, MI.

ANSYS Release 11.0, ANSYS University Advanced, ANSYS Inc.

American Petroleum Institute (API) (1993). Recommended Practice for Planning, Designing, and Constructing Fixed Offshore Platforms—Working Stress Design. 20th Ed., API RP2A-WSD, Washington, D.C.

Arockiasamy, M., Butrieng, N. and Sivakumar, M. (2004). "State-of-the-Art of Integral Abutment Bridges: Design and Practice," Journal of Bridge Engineering, ASCE, Vol. 9, No. 5.

Arockiasamy, M. and Sivakumar, M. (2005). "Time-Dependent Behavior of Continuous Composite Integral Abutment Bridges," Practice Periodical on Structural Design and Construction, ASCE, Vol. 10, No. 3.

Arsoy, S., and R. M. Barker, and J. M. Duncan, and C. E. Via (1999). "Behavior of Integral Abutment Bridges," Final Report FHWA/VTRC-00/CR3, Virginia Transportation Research Council, Charlottesville.

Ashour, M. and Norris, G. (2000). "Modeling Lateral Soil-Pile Response Based on Soil-Pile Interaction," *Journal of Geotechnical and Geoenvironmental Engineering*, ASCE, Vol. 126, No. 5.

Barker, R. M., Duncan, J. M., Rojiani, K. B., Ooi, P. S. K., Tan, C. K., and Kim., S. G. (1991). "Manuals for the Design of Bridge Foundations," NHCRP Report 343, Transportation Research Board.

Baker, R. M., Mattei, N. J., Almalik, B. K., Carr, S. P., and Homes, D. (2005). "Evaluation of DOTD Semi-Integral Bridge and Abutment System," Report No. FHWA/LA.05/397, Louisiana Transportation Research Center, Baton Rouge, LA.

Barr, P. J., Stanton, J. F. and Eberhard, M. O. (2005). "Effects of Temperature Variation on Precast, Prestressed Concrete Bridge Girders," *Journal of Bridge Engineering*, ASCE, Vol. 10, No. 2.

Bazănt, Z. P., and Baweja, S. (1995). "Justification and Refinement of Model B3 for concrete creep and shrinkage models—I. Statistics and sensitivity," *Materials and Structures*, Vol. 28, No. 181, pp. 415-430.

Bazănt, Z. P., and Baweja, S. (2000). "Creep and Shrinkage Prediction Model for Analysis and Design of Concrete Structures: Model B3—Short Form," *Adam Neville Symposium: Creep and Shrinkage: Structural Design Effects*, American Concrete Institute, pp. 85-100.

BD-667M (2005), "Standard Integral Abutment Drawings," Bureau of Design, Commonwealth of Pennsylvania, Department of Transportation.

Boulanger, R. W., Curras, C. J., Kutter, B. L., Wilson, D. W., and Abghari, A. (1999). "Seismic Soil-Pile-Structure Interaction Experiments and Analysis," *Journal of Geotechnical and Geoenvironmental Engineering*, ASCE, V.125, No.9, pp750-759.

Breña, S. F., Bonczar, C. H., Civjan, S. A., DeJong, J. T., and Crovo, D. S. (2007). "Evaluation of Seasonal and Yearly Behavior of an Integral Abutment Bridge," *Journal of Bridge Engineering*, ASCE, Vol. 12, No. 3, pp. 296-305.

Burke Jr., M. P. (1990). "Integral bridge design is on the rise," *Modern Steel Construction*, 30(4), 9-11.

California Department of Transportation (CALTRAN). (2006). *Bridge Design Specifications*, California Department of Transportation, Sacramento, CA.

Civjan, S. A., Bonczar, C., Breña, S. F., DeJong, J., and Crovo, D. (2007). "Integral Abutment Bridge Behavior: Parametric Analysis of Massachusetts Bridge," *Journal of Bridge Engineering*, ASCE, Vol.12, No.1, pp.64-71.

Clough, G. W., and Duncan, J. M. (1991). *Foundation Engineering Manual*, 2nd Ed., H. Y. Fang, ed., Van Nostrand Reinhold, New York.

Colorado Department of Transportation (CODOT). (2002). *Bridge Design Manual*, Colorado Department of Transportation, Denver.

Comite Euro-Internationale du Beton (CEB) (1990). *CEB-FIP Model Code for Concrete Structures*, Buletin D'Information No. 213/214, Lausanne, Switzerland.

Darley, P., Carder, D. R. and Alderman, G. H. (1996). "Seasonal Thermal Effects on the Shallow Abutment of an Integral Bridge in Glasgow," TRL Report 178, E465A/BG, Transport Research Laboratory, ISSN 0968-4107.

Das, B. M. (1999). *Principles of Foundation Engineering*, Brooks/Cole Publishing Company, 4th Ed. ISBN: 0-534-95403-0

Das, B. M. (2002). *Soil Mechanics Laboratory Manual*, 6th Ed., Oxford University Press.

DeJong, J. T., Howey, D. S., Civjan, S. A., Brena, S. F., Butler, D. S., Crovo, D. S., Hourani, N. and Connors, P. (2004). "Influence of Daily and Annual Thermal Variations on Integral Abutment Bridge Performance," *Proceedings of Geotechnical Engineering for Transportation Projects, GeoTrans 2004*, ASCE, pp.496-505.

Dicleli, M. (2000). "Simplified Model for Computer-Aided Analysis of Integral Bridges," *Journal of Bridge Engineering*, Vol. 5, No. 3, pp. 240-248.

Dicleli, M and Albhaisi, S. M. (2003). "Estimation of Length Limits for Integral Bridges Built on Clay," *Journal of Bridge Engineering*, ASCE, Vol. 9, No. 6.

Dicleli, M and Albhaisi, S. M. (2004). "Effect of Cyclic Thermal Loading on the Performance of Steel H-Piles in Integral Bridges with Stub-Abutments," *Journal of Construction Steel Research*, 60, pp. 161-182.

Dicleli, M. and Albhaisi, S. M. (2004). "Performance of abutment-backfill system under thermal variations in integral bridges built on clay," *Engineering Structures*, Elsevier, No. 26, pp. 949-962.

Dicleli, M. (2005). "Integral Abutment-Backfill Behavior on Sand Soil—Pushover Analysis Approach," *Journal of Bridge Engineering*, ASCE, Vol. 10, No. 3.

Delattre, L. (2001). "A Century of Design Methods for Retaining Walls – The French Point of View: I. Calculation – Based Approaches – Conventional and Subgrade Reaction Methods," BLPC-2001/234, Laboratoire Central des Ponts et Chaussées.

Duncan, J. M. and Mokwa, R. L. (2001). "Passive Earth Pressure: Theories and Tests", *Journal of Geotechnical and Geoenvironmental Engineering*, ASCE, Vol. 127, No. 3.

Dunker, K. F., and Liu, D. (2007). "Foundations for Integral Abutments," *Practical Periodical on Structural Design and Construction*, ASCE, Vol. 12, No.1, pp. 22-30.

Elbadry, M. M. and Ghali, A. (2001). "Analysis of Time-Dependent Effects in Concrete Structures Using Conventional Linear Computer Programs," *Canadian Journal of Civil Engineering*, CNRC Canada, Vol. 28, pp.190-200.

Emanuel, J. H. and Hulsey, J. L. (1977). Prediction of the Thermal Coefficient of Expansion of Concrete. *Journal of American Concrete Institute*, Vol. 74, No. 4, pp, 149-155, April.

Faraji, S., Ting, J. M., Crovo, D. S. and Ernst, H. (2001). "Nonlinear Analysis of Integral Bridges: Finite-Element Model", *Journal of Geotechnical and Geoenvironmental Engineering*, ASCE, Vol. 127, No. 5.

Fennema, J. L., Laman, J. A., and Linzell, D. G. (2005). "Predicted and Measured Response of an Integral Abutment Bridge," *Journal of Bridge Engineering*, ASCE, Vol. 10, No. 6, pp. 666-677.

Florida Department of Transportation (FDOT) (2007). *Structures Design Guidelines*, Florida Department of Transportation, Tallahassee, FL.

Fu, K. and Lu, F. (2003). "Nonlinear Finite-Element Analysis for Highway Bridge Superstructures," *Journal of Bridge Engineering*, ASCE, Vol. 8, No. 3.

Galambos, T. V., Ellingwood, B., MacGreger, J. G., and Cornell, C. A. (1982). "Probability Based Load Criteria: Assessment of Current Design Practice," *Journal of Structural Engineering*, ASCE, Vol. 108, No. ST5, pp.959-977.

Ghali, A., Favre, R., and Elbadry, M. (2002). *Concrete Structures: Stresses and Deformation*, 3th Ed., Spon Press, London.

Girton, D. D., and T. R. Hawkinson, and L. F. Greimann (1991). "Validation of Design Recommendations for Integral-Abutment Piles," *Journal of Structural Engineering*, ASCE, Vol. 117, No. 7, pp. 2117-2134.

Greimann, L. F., Yang, P., and Wolde-Tinsae, A. M. (1986). "Nonlinear Analysis of Integral Abutment Bridges," *Journal of Structural Engineering*, ASCE, Vol. 112, No. 10, pp.2263-2280.

Horvath, J. S. (2004). "Integral-Abutment Bridges: A Complex Soil-Structure Interaction Challenge," *Proceedings Geotechnical Engineering for Transportation Projects, GeoTrans 2004*, ASCE.

Huang, J., Shield, C. K., and French, C. (2005). "Time-dependent Behavior of a Concrete Integral Abutment Bridges," *Transportation Research Record: Journal of the*

Transportation Research Board, CD 11-S, Transportation Research Board of the National Academies, Washington D.C., pp 299-309.

Hwang, E-S., and Nowak, A. S. (1991). "Simulation of dynamic load for bridges." *Journal of Structural Engineering*, ASCE, 117(5), 1413-1434.

Illinois Department of Transportation (ILDOT). (2003). *Bridge Manual*, Illinois Department of Transportation, Springfield, Illinois.

Iowa Department of Transportation (IADOT). (2006). *Bridge Design Manual*, Iowa Department of Transportation, Ames, Iowa.

Imbsen, R. A., Vandershaf, D. E., Shamber, R. A., and Nutt, R. V. (1985). *Thermal Effects in Concrete Superstructures*. NCHRP Report No. 276, Transportation Research Board, Washington, D.C.

Ingram, E. E., Burdette, E. G., Goodpasture, D. W., Deatherage, J.H., and Bennett, R. M. (2004). "Behavior of Steel H-piles Supporting Integral Abutments," *Proceedings Structure 2004*, ASCE, pp. 1-7.

Jaky, J. (1944). "The Coefficient of Earth Pressure at Rest," *J. Soc. Hung. Eng. Arch.*, 355-358.

Jirásek, M. and Bažant, Z. P. (2002). *"Inelastic Analysis of Structures,"* John Wiley & Sons, New York.

Julian, O. G. (1966). "Discussion of strength variations in ready-mixed concrete by A. E. Cummings." *ACI Journal*, 51(9), 772-2-772-8.

Kada, H., Lachemi, M., Petrov, N., Bonneau, O., and Aïtcin, P.-C. (2002). "Determination of the coefficient of thermal expansion of high performance concrete from initial setting," *Materials and Structures*, Vol. 35, pp. 35-41.

Kim, W. (2008). "Simplified Nonlinear Numerical Analysis Method for Integral Abutment Bridges," *Proceedings of the 2008 International Bridge Conference*, Pittsburgh, PA, IBC-08-43, June 2-4.

Kim, W. (2008). "Load and Resistance Factor Design for Integral Abutment Bridges," Ph.D. Dissertation, The Pennsylvania State University, University Park, PA.

Knickerbocker, D., and Basu, P. K. (2004). "Analysis of Prestressed Concrete Jointless Bridges with Integral Abutments," *Proceedings: Structure 2004*, ASCE, pp. 1-10.

Koskinen, M. *Soil-Structure-Interaction of Jointless Bridges on Piles*. Geotechnical Laboratory, Tampere University of Technology, Finland, pp. 1091-1096.

Kulhawy, F. H. (1992). "On the evaluation of soil properties," ASCE Geotech. Special Publication, No. 31, pp.95–115.

Kunin, J., and S. Alampalli (2000). "Integral Abutment Bridges: Current Practice in United States and Canada," Journal of Performance of Constructed Facilities, ASCE, Vol. 14, No. 3, pp. 104-111.

Laman, J. A., Linzell, D. G., Leighty, C. A., and Fennema, J. L. (2003). "Methodology to Predict Movement and Stresses in Integral Abutment Bridges," Report No. FHWA-PA-2002-039-97-04(80), Pennsylvania Transportation Research Council.

Laman, J. A., Pugasp, K., and Kim, W. (2006). "Field Monitoring of Integral Abutment Bridges," Report No. FHWA-PA-2006-006-510401-01, Pennsylvania Transportation Research Council.

Lpile Plus Version 4.0, ENSOFT Inc.

Ministry of Transportation. (1991). Ontario highway bridge design code, 3rd Ed., Quality and Standards Division, Downsview, Ont. Canada.

Maine Department of Transportation. (2003). Maine DOT Bridge Design Guide, Maine Department of Transportation, Augusta, Maine.

Massachusetts Highway Department. (2005). Bridge Manual. Commonwealth of Massachusetts, Massachusetts Highway Department, Boston, MA.

Moorty, S., and Roeder, C. W. (1992). "Temperature Dependent Bridge Movements," Journal of Structural Engineering, ASCE, Vol. 118, No. 4, pp. 1090-1105.

Moulton, L. K., GangaRao, H. V. S., and Halverson, G. T. (1985) Tolerable Movement Criteria for Highway Bridges, FHWA/RD-85/107, FHWA, U.S. Department of Transportation, Washington, D.C., 118 pp.

Mourad, S., and S. W. Tabsh (1999). "Deck Slab Stresses in Integral Abutment Bridges," Journal of Bridge Engineering, ASCE, Vol. 4, No. 2, pp. 125-130.

National Climate Data Center (NCDC). (2006). Comparative Climate Data for the United States through 2006. National Oceanic and Atmospheric Administration. (<http://www.noaa.gov/>).

National Cooperative Highway Research Program (NCHRP). (1991). Manuals for the Design of Bridge Foundations, R. M. Baker, J. M. Duncan, K. B. Rojiani, P. S. D. Ooi, C. K. Tan, and S. G. Kim, eds. Rep 343, Transportation Research Board, Washington, D. C.

National Cooperative Highway Research Program (NCHRP 18-07). (1999). Prestress Losses in Pretensioned High-Strength Concrete Bridge Girders, M. K. Tadros, N. Al-

- Omaishi, S. J. Seguirant, J. G. Gallt. Rep 496, Transportation Research Board, Washington, D. C.
- New Jersey Department of Transportation. (2004). Bridges and Structures Design Manual, New Jersey Department of Transportation, Trenton, N.J.
- Nilson, A.H. (1991). Design of Concrete Structures, Eleventh Edition, McGraw-Hill Inc., New York.
- North Dakota Department of Transportation. (2002). Standard Specifications for Road and Bridge Construction, North Dakota Department of Transportation, Bismarck, ND.
- Ndon, U. J., and K. L. Bergeson (1995). "Thermal Expansion of Concretes: Case Study in Iowa. Journal of Materials in Civil Engineering, ASCE, Vol. 7, No. 4, 246-251.
- New York Department of Transportation. (2006). Bridge Manual, New York Department of Transportation, Albany, N.Y.
- Noorzaei, J., Viladkar, M. N. and Godbole, P. N. (1995). "Elasto-Plastic Analysis for Soil-Structure Interaction in Framed Structures", Computers & Structures, Vol. 55, No. 5, 797-807.
- Oesterle, R. G, Refai, T. M., Volz, J. S., Scanlon, A., and Weiss, W. J. (1998). "Jointless and Integral Abutment Bridges Analytical Research and Proposed Design Procedures", Construction Technology Laboratories, Inc., Draft Final Report to Federal Highway Administration, Washington, D.C.
- Paul, M. D. (2003). "Thermally Induced Superstructure Stress in Prestressed Girder Integral Abutment Bridges," M.S. Thesis, The Pennsylvania State University.
- Paul, M. D., Laman, J. A., and Linzell, D. G. (2005). "Thermally Induced Superstructure Stresses in Prestressed Girder Integral Abutment Bridges," Transportation Research Record: Journal of the Transportation Research Board, Transportation Research Board of the National Academies, Washington D.C., 287-297.
- PCI (2001). "The State of the Art of Precast/Prestressed Integral Bridges," ISBN 0-937040-66-5, Precast/Prestressed Concrete Institute, Chicago, IL.
- PCI (2005). PCI Bridge Manual, Precast/Prestressed Concrete Institute, Chicago, IL.
- Pennsylvania Department of Transportation (PennDOT). (2007). Design Manual Part 4, "Structures: Procedures-Design-Plans Presentation," PennDOT Design Manual Part 4, Commonwealth of Pennsylvania, Department of Transportation, Harrisburg, PA.
- The Pennsylvania State Climatologist (PSC), http://pasc.met.psu.edu/PA_Climatologist.

Pugasap, K. (2006). "Hysteresis Model Based Prediction of Integral Abutment Bridge Behavior," Ph.D. Dissertation, The Pennsylvania State University, University Park, PA.

Pugasap, K., Kim, W., and Laman, J. A. (2009). "Long-term Response Prediction of Integral Abutment Bridges," *Journal of Bridge Engineering*, ASCE, Vol. 14, No. 2, March/April, pp. 129-139.

Pugasap, K., and Laman, J. A. (2009). "Integral Abutment Bridge Hysteresis Model for Long Prediction," *Proceedings of the Institute of Civil Engineers, Bridge Engineering*, March, Issue BE1, pp. 37-49.

Shoukry, S. N., William, G. W., and Riad, M. Y. (2006). "Structural Behaviour of an Integral Abutment Bridge under Environmental Conditions," *Proceedings of Structures 2006*, ASCE.

South Dakota Department of Transportation (SDDOT). *Structures Construction Manual*, South Dakota Department of Transportation, Pierre, SD.

Tanesi, J., Kutay, M. E., Abbas, A., and Meininger, R. (2007). "Effect of CTE Variability on Concrete Pavement Performance as Predicted Using the Mechanistic-Empirical Pavement Design Guide," *Proceedings: TRB 86th Annual Meeting*, Jan.25-27, 2007. Transportation Research Board, Washington D.C.

Terzaghi, K. E., and Peck, R. B. (1948). *Soil Mechanics in Engineering Practice*, John Wiley and Sons, Inc.

Theodoer A. Thomson, Jr. and Lutenecker, A. J. (1998). "Passive Earth Pressure Tests On An Integral Bridge Abutment", *Proceedings: Fourth International Conference on Case Histories in Geotechnical Engineering*, St. Louis, Missouri.

Thippeswamy, H. K., GangaRao, H. V. S. and Franco, J. M. (2002). "Performance Evaluation of Jointless Bridges," *Journal of Bridge Engineering*, ASCE, Vol. 7, No. 5.

Thomas, M. E. (1999). "Field Study of Integral Abutment Bridges," M.S. Thesis, Iowa State University, Ames, Iowa.

Turkstra, C. J. (1970). "Theory of Structural Design Decisions," *Solid Mechanics Study No.2*, University of Waterloo, Waterloo, Canada.

Vintzēleou, E. N., and Tassios, T. P. (1987). "Behavior of Dowels under Cyclic Deformations," *ACI Structural Journal*, ACI, pp. 18-30.

Virginia Department of Transportation (2007). *Design Aids and Typical Details, Volume V, Part 2*. Commonwealth of Virginia, Department of Transportation, Richmond, VA.

Wang, S. and Reese, L. C. (1993). "COM624P—Laterally Loaded Pile Analysis Program for the Microcomputer," Report No. FHWA-SA-91-048, U.S. Department of Transportation.

West Virginia Department of Transportation. (2004). Bridge Design Manual, West Virginia Department of Transportation, Charleston, W.Va.

Yazdani, N., Eddy, S. and Cai, C. S. (2000). "Effect of Bearing Pads on Precast Prestressed Concrete Bridges", Journal of Bridge Engineering, ASCE, Vol. 5, No. 3, pp. 224-231.